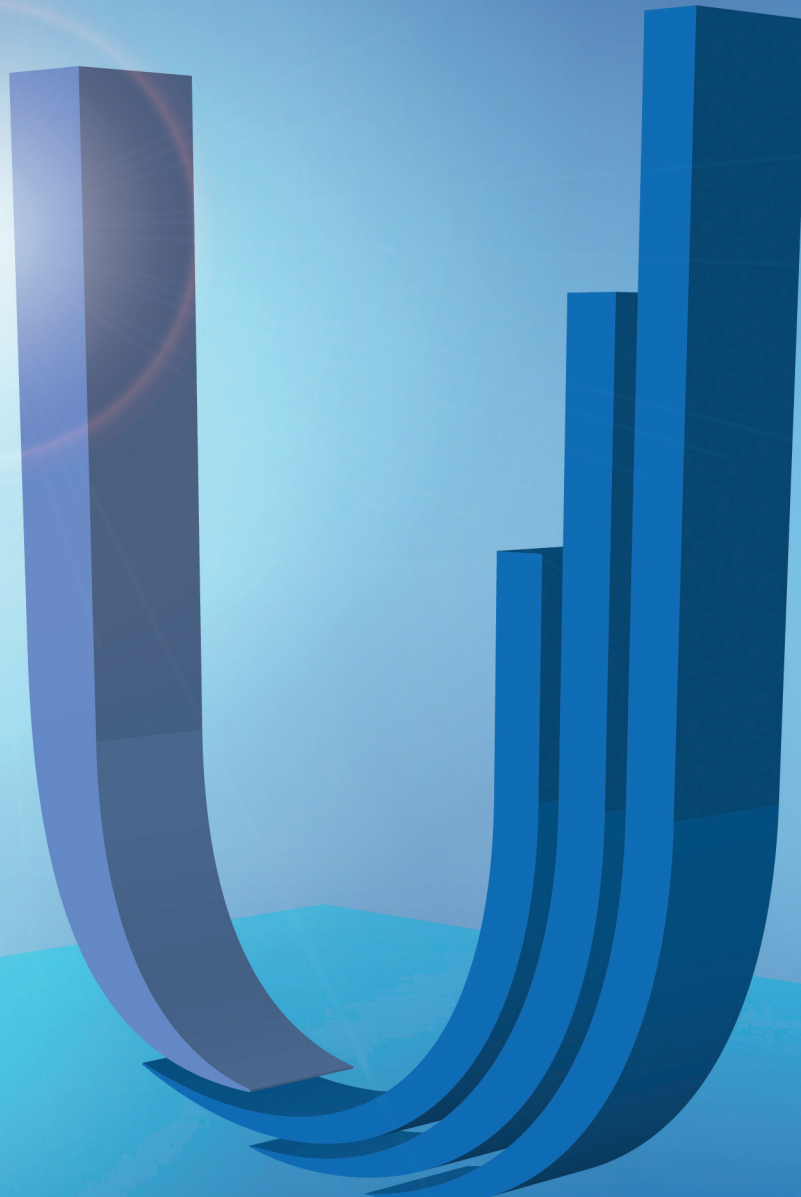


LHC INJECTORS UPGRADE

Technical Design Report - Volume I: Protons

CERN-ACC-2014-0337 - 15 December 2014



Edited by J. Coupard, H. Damerau, A. Funken, R. Garoby, S. Gilardoni, B. Goddard, K. Hanke,
A. Lombardi, D. Manglunki, M. Meddahi, B. Mikulec, G. Rumolo, E. Shaposhnikova, M. Vretenar



Copyright © CERN, 2014

The colour version of this report is available online at <https://cds.cern.ch/>

 Creative Commons Attribution 4.0

Knowledge transfer is an integral part of CERN's mission.

CERN publishes this report Open Access under the Creative Commons Attribution 4.0 license (<http://creativecommons.org/licenses/by/4.0/>) in order to permit its wide dissemination and use.

This monograph should be cited as:

LHC Injectors Upgrade, Technical Design Report, Vol. I: Protons,
edited by J. Coupard, H. Damerau, A. Funken, R. Garoby, S. Gilardoni, B. Goddard, K. Hanke,
A. Lombardi, D. Manglunki, M. Meddahi, B. Mikulec, G. Rumolo, E. Shaposhnikova, M. Vretenar
CERN-ACC-2014-0337 (CERN, Geneva, 2014)



LHC Injectors Upgrade

Technical Design Report Vol. I: Protons

Editors

J. Coupard, H. Damerau, A. Funken, R. Garoby, S. Gilardoni,
B. Goddard, K. Hanke, A. Lombardi, D. Manglunki, M. Meddahi,
B. Mikulec, G. Rumolo, E. Shaposhnikova, M. Vretenar

Copyright © CERN, 2014

The colour version of this report is available online at <https://cds.cern.ch/>

 Creative Commons Attribution 4.0

Knowledge transfer is an integral part of CERN's mission.

CERN publishes this report Open Access under the Creative Commons Attribution 4.0 license (<http://creativecommons.org/licenses/by/4.0/>) in order to permit its wide dissemination and use.

This monograph should be cited as:

LHC Injectors Upgrade, Technical Design Report, Vol. I: Protons, edited by J. Coupard, H. Damerau, A. Funken, R. Garoby, S. Gilardoni, B. Goddard, K. Hanke, A. Lombardi, D. Manglunki, M. Meddahi, B. Mikulec, G. Rumolo, E. Shaposhnikova, M. Vretenar, CERN-ACC-2014-0337 (CERN, Geneva, 2014).



LHC Injectors Upgrade

Technical Design Report

J. Abelleira, O. Aberle, D. Aguglia, M. Aiba, A. Akroh, A. Aloev, M. E. Angoletta, G. Arduini,
T. Argyropoulos, L. Arnaudon, M. Arruat, M. G. Atanasov, S. Aumon (GSI), J. Axensalva,
B. Balhan, R. A. Barlow, M. Barnes, W. Bartmann, S. Bartolome Jimenez, H. Bartosik, J. Bauche,
C. Baud, P. Baudrenghien, C. Bedel, J. Belleman, G. Bellodi, D. Belohrad, E. Benedetto, O. E. Berrig,
S. Bertolasi, C. Bertone, J. Betz, C. Bhat, N. Biancacci, T. W. Birtwistle, A. Blas, F. Boattini,
D. Bodart, T. Bohl, J. Borburgh, C. Bracco, E. Bravin, M. Brugger, S. Burger, A. Burns,
A. Butterworth, M. Buzio, S. Calatroni, C. Carli, E. Carlier, F. Caspers, M. Cerqueira-Bastos,
F. Cerutti, P. Chiggiato, E. C. Coeffic, J. Cole, K. Cornelis, J.-P. Corso, P. Costa Pinto, J. Coupard,
J.-M. Cravero, P. Dahlen, A. Dalloccchio, H. Damerau, S. Damjanovic, H. Day, B. Dehning, A. Deleu,
S. Deleval, M. Delonca, J. D. Devine, T. Dobers, J. Double, L. Drosdal, L. Ducimetiere, G. Dumont,
J. Emery, G. Favia, S. Federmann, L. M. C. Feliciano, J. A. Ferreira Somoza, A. J. Findlay,
G. J. Focker, R. Folch, V. Forte, J. D. Fox (SLAC), R. Froeschl, J.-F. Fuchs, A. Funken, S. Gabourin,
M. Garlasche, R. Garoby, M. Gasior, D. Gerard, E. Gianfelice-Wendt (Fermi National Accelerator
Laboratory, Batavia IL, USA), S. Gibson, S. Gilardoni, M. Giovannozzi, B. Goddard, J. L. Gonzalez,
D. Gonzalez Outeda, M. Gourber-Pace, J.-J. Gras, S. Grau, G. Graver, J.-L. Grenard, G. Hagmann,
S. Hancock, K. Hanke, J. Hansen, M. Haase, D. Hay, A. J. Henriques, T. Hermanns, W. Hofle,
E. B. Holzer, M. Hourican, A. Huschauer, G. Iadarola, M. Jaussi, L. Jensen, S. Jensen, J. M. Jimenez,
A. J. Jones, R. Jones, M. Juchno, V. Kain, A. Kosmicki, M. A. Kowalska, W. S. Kozlowska,
I. Kozsar, T. Kramer, D. Kuchler, J.-M. Lacroix, A. Lasheen, P. Le Roux, T. Lefevre, P. M. Leinonen,
J. Lettry, T. Levens, A. Lombardi, L. A. Lopez-Hernandez, R. Losito, R. Louwerse, F. L. Maciariello,
C. Maglioni, E. Mahner, L. Mainoli, D. Manglunki, C. Martin, M. Martini, A. Masi, S. Mataguez,
S. Mathot, H. Maury Cuna, M. J. Mcateer, D. Mcfarlane, M. Meddahi, A. Mereghetti, O. Mete
(University of Manchester, UK), E. Metral, G. Metral, M. Migliorati, B. Mikulec, G. Minchev
Georgiev, D. Missiaen, S. Moccia, J. Molendijk, R. Mompo, E. Montesinos, M. M. Morgenstern,
M. Morville, J. E. Muller, Y. Muttoni, A. Newborough, D. Nisbet, C. Noels, M. Nonis, R. Noulibus,
R. Nunes, M. R. Obrecht, P. Odier, T. Otto, M. Paoluzzi, Y. Papaphilippou, F. Pasdeloup,
C. Pasquino, S. B. Pedersen, A. Perillo Marcone, D. Perrelet, S. Persichelli, J. Pierlot, G. Piero Di
Giovanni, X. Piroux, S. Pittet, E. J. Prebys, A. Prost, B. Puccio, D. Quatraro, U. Raich, V. Raginel,
B. Riffaud, S. Rioja Fuentelsaz (Universidad de Zaragoza, Spain), S. Roesler, A. Romano,
F. Roncarolo, R. Rosol, C. Rossi, I. Ruehl, G. Rumolo, B. Salvant, J.-L. Sanchez Alvarez, J. Sanchez
Quesada, A. Sanz Ull, M. Sapinski, A. Sarrio Martinez, D. Schoerling, M. Scholz, R. Scrivens,
V. Senaj, L. Sermeus, E. Shaposhnikova, K. Shing Bruce Li, J. Simonin, L. Soby, G. Steele,
R. Steerenberg, G. Sterbini, Z. Szoke, M. Taborelli, J. Tan, M. Tavlet, H. Timko, B. Todd,
G. Tranquille, J. Uythoven, L. Vanherpe, P. Van Trappen, J. E. Varela Campelo, F. M. Velotti,
R. Veness, L. Ventura, V. Venturi, H. Vincke, J. Vollaire, M. Vretenar, R. Wasef, S. Weisz,
J. Wenninger, W. Weterings, M. Widorski, E. Wildner, C. Yin Vallgren, C. Yu, Z. Zaharieva,
C. Zamantzas, C. Zannini, M. Zerlauth, F. Zocca, S. Zorzetti, L. Zuccalli

Contents

1	Executive Summary.....	9
1.1	Introduction.....	9
1.1.1	Motivation and mandate.....	9
1.1.2	Project organization	9
1.1.3	Beam parameters through the injector chain.....	10
1.2	LIU-PSB	11
1.2.1	Scope of the LIU-PSB upgrade	11
1.2.2	Outlook/concluding remarks for the LIU-PSB	11
1.3	LIU-PS	13
1.3.1	Scope of the LIU-PS upgrade	13
1.3.2	Outlook/concluding remarks for the LIU-PS	14
1.4	LIU-SPS	14
1.4.1	Scope of the LIU-SPS upgrade	14
1.4.2	Outlook/concluding remarks for the LIU-SPS.....	15
1.5	LIU-IONS	16
1.5.1	Scope of the LIU-IONS upgrade	16
1.5.2	Outlook/concluding remarks for LIU-IONS	16
1.6	LIU project cost and schedule.....	16
1.6.1	LIU project cost.....	16
1.6.2	Schedule	17
1.7	Safety	18
1.7.1	Safety organisation	18
1.7.2	Safety objectives for LIU	19
2	Introduction and Overview.....	21
2.1	Introduction.....	21
2.2	Current LHC proton injectors	22
2.2.1	Mode of operation.....	22
2.2.2	Present performance and future needs.....	23
2.3	Upgrade plan of the LHC proton injectors.....	26
2.3.1	Transverse phase plane.....	26
2.3.2	Longitudinal phase plan	27
2.3.3	Electron clouds	28
2.3.4	Other upgrades.....	28
2.3.5	Beam characteristics after the upgrades	28
3	Proton Synchrotron Booster	33
3.1	Upgrade path.....	33
3.1.1	Scope of the LIU-PSB project	33
3.1.2	Energy upgrade of the PSB to 2 GeV.....	34
3.2	Beam dynamics and collective effects	34
3.2.1	Introduction	34
3.2.2	Optics model.....	35
3.2.3	Performance with space charge (emittance and losses).....	36
3.2.4	Beam coupling impedance	40
3.2.5	Beam stability	46
3.3	Injection line and PSB injection systems	50
3.3.1	Injection beam dynamics	50
3.3.2	Injection systems	54
3.4	Magnets.....	73
3.4.1	PS Booster injection magnets	74
3.4.2	PS Booster ring magnets	80
3.4.3	PS Booster transfer line magnets (BT, BTP, BTY and BTM)	86

TABLE OF CONTENTS

3.4.4	Magnetic measurements and B-train	101
3.5	RF systems	109
3.5.1	Introduction	109
3.5.2	Wideband RF system	111
3.5.3	Accelerating current and beam loading	116
3.5.4	Amplifier response	119
3.5.5	Low-level RF upgrade	122
3.5.6	Support for Finemet research and development after LS1	127
3.5.7	Future upgrades	127
3.5.8	Summary of DLLRF features	128
3.5.9	Transverse feedback	131
3.6	Power systems	139
3.6.1	Injection power supplies	139
3.6.2	Main power supply	151
3.7	Beam instrumentation	177
3.7.1	Screen monitors	177
3.7.2	Beam observation system (BTV) for the PSB H ⁻ injection region	179
3.7.3	H ⁰ /H ⁻ intensity measurement at the injection dump	182
3.7.4	Injection matching monitor	183
3.7.5	Intensity watchdog	184
3.7.6	PSB orbit and trajectory system	185
3.8	Beam intercepting devices	187
3.8.1	PS Booster main dump	187
3.8.2	Injection dumps	196
3.9	Vacuum systems	207
3.9.1	Vacuum	207
3.9.2	Vacuum layout	208
3.9.3	Vacuum equipment	208
3.10	PSB extraction systems and PSB-PS transfer line	209
3.10.1	Extraction and transfer line beam dynamics	209
3.10.2	Extraction and transfer line systems	210
3.11	Controls	215
3.11.1	Upgrade of hardware platform for front-end computers	215
3.11.2	Timing network	215
3.11.3	Drivers	216
3.11.4	Control software framework	216
3.11.5	Controls configuration database (CCDB)	217
3.11.6	CMW, work on the middle tier	217
3.11.7	InCA/LSA	218
3.12	PSB upgrade electrical infrastructure	218
3.12.1	Introduction	218
3.12.2	Power requirements	219
3.12.3	PSB complex: HV electrical network	219
3.12.4	Technical description of the LV infrastructure	223
3.13	Cooling and ventilation	227
3.13.1	Introduction	227
3.13.2	New PSB-MPS building 245: water-cooling requirements	228
3.13.3	New PSB-MPS building 245: ventilation requirements	231
3.14	Installation, transport and handling	237
3.14.1	Transport and handling equipment	237
3.14.2	Transport and handling services	238
3.15	Civil engineering	238
3.15.1	Introduction	238
3.15.2	Proposed location	238
3.15.3	Proposed layout	239

3.15.4	Civil engineering works	241
3.16	Radiological protection.....	242
3.16.1	Injection dumps	242
3.16.2	Main dump	243
3.16.3	Consolidation of water-cooling infrastructure.....	244
3.16.4	Collimation system.....	244
3.17	Machine interlocks.....	244
3.17.1	Beam interlock system	244
3.17.2	Magnet interlock system.....	250
3.17.3	The layout.....	252
3.17.4	Supervision	253
3.18	Survey	254
3.A	Appendix.....	254
3.A.1	MPC dimensioning results.....	254
3.A.1.1	Booster 2GeV MPC: electrical design	255
3.A.1.2	Booster 2GeV MPC: thermal design.....	256
3.A.1.3	Booster 2GeV MPC: output filter design	261
3.A.1.4	Booster 2GeV MPS: mechanical design and integration in building 245	262
3.A.2	Power supplies for extraction and transfer.....	264
3.A.2.1	RMS current reduction	264
3.A.2.2	Converter upgrade	265
4	Proton Synchrotron	285
4.1	Introduction.....	285
4.1.1	Schemes for 25 ns beam production.....	285
4.1.2	Challenges of traditional schemes and proposed solutions	285
4.1.3	Summary of upgrade interventions	286
4.2	Beam dynamics.....	287
4.2.1	Space-charge and resonance compensation.....	287
4.2.2	Control of the working point	293
4.2.3	The PS 2 GeV injection	296
4.2.4	The HT instability for the LIU-PS beams	301
4.2.5	Transition energy crossing for PS upgrade	311
4.2.6	EC studies in the CERN PS	316
4.2.7	Longitudinal instabilities and transient beam loading.....	324
4.3	Injection and operation at 2 GeV	331
4.3.1	Magnetic injection devices	331
4.3.2	Injection kickers	333
4.3.3	Magnets	336
4.3.4	Power converters	337
4.3.5	Low-energy power converters	340
4.4	The PS Transverse Damper	341
4.4.1	Description of the present system.....	342
4.4.2	The power amplifiers.....	345
4.4.3	The damper kicker	346
4.4.4	Upgrade of the PS damper	346
4.5	RF.....	349
4.5.1	The longitudinal damper.....	349
4.5.2	RF-HL	360
4.5.3	RF-low-level feedbacks and beam control	365
4.6	EC studies in the PS	374
4.6.1	Introduction	374
4.6.2	The existing EC set-up in the PS	374
4.6.3	New proposals for EC studies in the PS magnet	374
4.6.4	Implementation in the PS	378

TABLE OF CONTENTS

4.7	Impedance models	380
4.7.1	Longitudinal impedance	380
4.7.2	PS transverse impedances: current and future.....	385
4.8	Radioprotection and civil engineering	395
4.8.1	Radiation protection requirements for the shielding improvements above the injection and extraction areas of the PS.....	395
4.8.2	Civil engineering: Route Goward	398
4.8.3	Civil engineering: Septum 16	401
4.9	Beam instrumentation	406
4.9.1	Additional wideband PUs in the BTP line and PS ring.....	406
4.9.2	Modifications of the beam diagnostics around the PS injection septum	407
4.9.3	Ghost and satellite detection.....	408
4.9.4	IPM.....	408
4.9.5	Matching monitor	412
4.10	PS internal dump in the FLUKA Monte Carlo simulation	412
4.10.1	Introduction and motivation	412
4.10.2	Internal dump current state.....	413
4.10.3	Upgraded beam parameters	418
5	Super Proton Synchrotron	435
5.1	Overview.....	435
5.1.1	Summary of performance requirements and limitations for SPS	435
5.1.2	SPS upgrade baseline	435
5.2	Longitudinal beam dynamics	436
5.2.1	Introduction	436
5.3	Transverse beam dynamics	442
5.3.1	Low gamma transition optics	442
5.3.2	Transverse mode coupling instability at injection	443
5.3.3	Simulation study of the electron cloud-driven single bunch instability	446
5.3.4	Space charge.....	447
5.4	RF power systems (200, 800 MHz)	449
5.4.1	200 MHz RF system.....	449
5.4.2	800 MHz RF system.....	451
5.5	LLRF upgrade and control.....	474
5.5.1	The 800 MHz system	474
5.5.2	The 200 MHz system.....	476
5.5.3	Beam control	478
5.6	Transverse feedback systems	478
5.6.1	Upgrade of bunch-by-bunch SPS transverse feedback.....	478
5.6.2	New high-bandwidth transverse feedback system.....	486
5.7	Electron cloud	490
5.7.1	Observed and simulated performance, limitations	490
5.7.2	Mitigation by scrubbing	494
5.7.3	Mitigation by amorphous carbon coating.....	498
5.7.4	Planning.....	499
5.8	Beam scraping	500
5.8.1	Introduction	500
5.8.2	Beam scraping on a fixed mask	500
5.8.3	Feasibility studies	501
5.8.4	Operational flexibility and limitations.....	502
5.8.5	Material studies	503
5.8.6	Radiation protection considerations	503
5.8.7	Endurance test of the present scraper blades	504
5.8.8	Summary	506
5.9	Dump system	506

5.9.1	Limitations and proposed upgrades of the present system	508
5.9.2	External dump design	511
5.9.3	Conclusions	514
5.10	SPS to LHC transfer line collimators	515
5.10.1	Motivation	515
5.10.2	Requirements	515
5.10.3	LIU TCDIs for TI 2 and TI 8—possible layout	517
5.10.4	Summary and outlook	519
5.11	Beam Instrumentation	520
5.11.1	Orbit and trajectory monitoring system upgrade	520
5.11.2	Fast beam current transformer system upgrade	523
5.11.3	Head–tail monitor system upgrade	526
5.11.4	Upgrade of the SPS synchrotron light monitor	526
5.11.5	Spectral components of the source	527
5.11.6	Source size	527
5.11.7	Plans and schedule	528
5.11.8	Upgrade of the SPS ionization profile monitor	528
5.12	Vacuum system	529
5.12.1	Halving the length of long vacuum sectors	529
5.12.2	x10 vacuum sectors	532
5.12.3	x60 vacuum sectors	533
5.12.4	Improving protection for kicker MKDH 11757	534
5.12.5	Protection of TIDVG dump	535
5.12.6	Re-sectorization of RF cavities	537
5.12.7	Fast valves	537
5.12.8	Costs	538
5.12.9	Conclusions	539
5.13	Impedance budget	539
5.13.1	Transverse impedance model	539
5.13.2	SPS longitudinal impedance model	542
5.13.3	Kicker impedance heating and mitigation	549
5.13.4	Beam measurements	552
5.14	Electrostatic septa	556
5.14.1	Vacuum improvements	556
5.14.2	Impedance reduction	557
5.15	Extraction protection elements upgrade	560
5.15.1	Purpose	560
5.15.2	Validation of existing design and failure assumptions	563
5.15.3	Upgrade	563
5.16	Orbit stability and correction	564
5.16.1	Orbit at extraction through BPM fit	564
5.16.2	Source investigations	566
5.16.3	Orbit correction strategies	570
6	Common Beam Instrumentation	593
6.1	Beam loss measurement	593
6.1.1	Acquisition electronics	594
6.1.2	Processing electronics	595
6.1.3	Installation and planning	595
6.2	Beam loss observation system	595
6.3	New wire scanner system	596
6.3.1	System design	596
6.3.2	Incremental optical angular sensor	596
6.3.3	Control and acquisition electronics	597
6.3.4	Planning	599

TABLE OF CONTENTS

6.4	DC beam current transformers.....	599
7	Commissioning and Optimization	601
7.1	General considerations.....	601
7.1.1	Training	601
7.1.2	Hardware commissioning.....	602
7.1.3	Dry runs	602
7.1.4	Commissioning with beam.....	602
7.1.5	Validation	603
7.1.6	Optimization	603
7.2	PSB	603
7.2.1	Scope	603
7.2.2	Preparation phase before LS2.....	603
7.2.3	Hardware commissioning and dry runs following LS2.....	604
7.2.4	Beam commissioning up to validation	604
7.2.5	Summary of beam commissioning planning	605
7.2.6	Optimization	606
7.3	PS	606
7.3.1	Scope	606
7.3.2	Preparation before LS2.....	607
7.3.3	Hardware commissioning and dry runs following LS2.....	607
7.3.4	Beam commissioning up to validation	607
7.3.5	Optimization	608
7.4	SPS.....	608
7.4.1	Scope	609
7.4.2	Preparation before LS2.....	610
7.4.3	Hardware commissioning and dry runs following LS2.....	610
7.4.4	Beam commissioning up to validation	610
7.4.5	Optimization	611
7.5	Integrated planning	612

TABLE OF CONTENTS

Chapter 1

Executive Summary

1.1 Introduction

1.1.1 Motivation and mandate

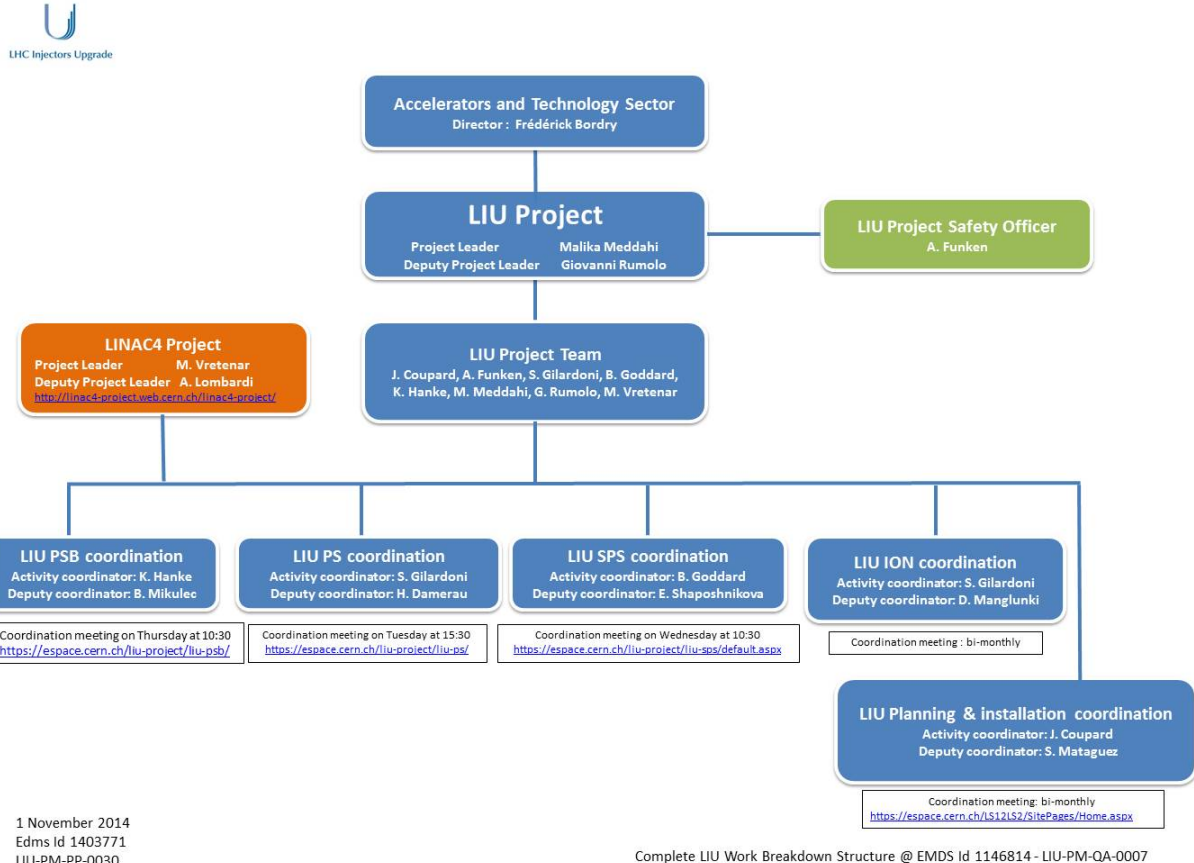
The accelerators of the injector complex gave a decisive contribution to the excellent performance of the Large Hadron Collider (LHC) during its first run, which finished in February 2013, and was crowned with the discovery of the Higgs boson. The injectors demonstrated a remarkable flexibility, providing many different types of beams over a wide range of intensities, emittances and distances between bunches, which were crucial for safely commissioning and efficiently setting-up the collider. The brightness of the beam injected into the LHC comfortably exceeded the nominal requirements from the LHC design report (e.g. 1.2×10^{11} protons/bunch (p/b) with 25 ns bunch spacing within emittances of 2.6 μm at ejection from the Super Proton Synchrotron (SPS)).

The performance achieved during Run 1 is, however, not sufficient to meet the requirements of the High Luminosity LHC (HL-LHC) Project [1], which aims at a levelled luminosity of $5 \times 10^{34} \text{ cm}^{-2} \text{ s}^{-1}$ with protons during Run 4 beyond 2024. To achieve this target, the intensity of the injected beam has to be doubled, and its brightness multiplied by 2.5 (2.3×10^{11} p/b with 25 ns bunch spacing within emittances of 2.1 μm). A similar challenge is set for lead (Pb) ions. Solutions must therefore be found and implemented in all the accelerators that comprise the LHC injector complex to overcome present limitations and reliably reach this new level of performance in day-by-day operation.

The LHC Injectors Upgrade (LIU) project has the ultimate goal of making the injectors capable of delivering reliably the beams required by the HL-LHC. The project covers Linac4 and the upgrades of the PS-Booster (PSB), the Proton Synchrotron (PS) and the SPS. The injectors specific to the heavy ion chain, i.e. Linac3 and the Low Energy Ion Ring (LEIR), are also included in LIU. All upgrades must be implemented by the end of the second Long Shutdown (LS2) to be in position to attain the specified beam characteristics by the end of Run 3.

1.1.2 Project organization

LIU is a CERN-wide project reporting to the Director of the Accelerators and Technology Sector. Led by the project leader and a deputy, the project team is composed of one coordinator per proton injector synchrotron (PSB, PS, SPS) plus one coordinator for the ions throughout the whole injection chain (Linac3, LEIR, PS, SPS), the leader of the Linac4 project, the technical coordinator for planning and installation, and the project safety officer (Fig. 1.1).

**Fig. 1.1:** LIU project organization

1.1.3 Beam parameters through the injector chain

The proton beam characteristics that are estimated as reliably achievable after the completion of the LIU project are shown in Table 1.1 [2]. The beam characteristics for Pb ions are given in Table 1.2 [3]. Multiple injections are used in the PS, SPS and LHC for protons, and in LEIR, SPS and LHC for Pb ions. RF beam gymnastics are applied in the PS and SPS to reach the distance between bunches required by the LHC.

Table 1.1: Achievable proton beam characteristics at injection for the different accelerators after LIU

Kinetic energy (GeV)	Number of bunches	Distance between bunches (ns)	Bunch intensity (10^{11} p/b)	Transverse emittance (m)	Longitudinal emittance (eVs)	Bunch length (ns)
PSB	0.160	1/ring		29.6	1.5	1.4
PS	2	2 + 4	284	28.1	1.6	3
SPS	25 ^a	4 × 72	25	2.2	1.7	0.35
LHC	449 ^a	~10 × 288	25	2	1.9	0.6

^aThese values correspond to momenta of 26 GeV/c and 450 GeV/c.

It must be noted that, projecting from present knowledge, the bunch intensity achievable at LHC injection after the full injector upgrade will still be about 15% below the HL-LHC specification (Table 1.3). Nevertheless, the present performance estimates (Table 1.1) will have to be regularly revised over the full duration of the LIU programme. As past experience with the CERN accelerators has shown, it is reasonable to anticipate that, as a result of the intense effort invested in both modelling and beam experiments, the beam characteristics will eventually go beyond the current estimates and

may eventually match the HL-LHC requirements. Tuning the successive accelerators to get the full benefit of the upgrades will require a large amount of machine development and dedicated commissioning time spread between the end of LS2 and the start of LS3.

Table 1.2: Optimum lead ion beam characteristics at injection of the different synchrotrons after LIU

	Energy (GeV/u)	Charge state	Number of bunches	Distance between bunches (ns)	Bunch intensity (10^8 ions/bunch)	Transverse emittance (m)	Longitudinal emittance (eVs/u)	Bunch length (ns)
LEIR	0.0042	54+	Coasting		10^a	0.5	0.02	
PS	0.072	54+	2	350	8	0.7	0.025	200
SPS	5.9	82+	12×4	100	1.8	1.0	0.045	3.9
LHC	176.4	82+	26×48	50	1.2	1.2	0.24	1.8

^aTotal beam intensity

Table 1.3: HL-LHC requested proton beam characteristics at injection

	Energy (GeV)	Number of bunches	Distance between bunches (ns)	Bunch intensity (10^{11} p/b)	Transverse emittance (m)	Longitudinal emittance (eVs)	Bunch length (ns)
LHC	450	$\sim 10 \times 288$	25	2.32	2.08	0.65	1.65

1.2 LIU-PSB

1.2.1 Scope of the LIU-PSB upgrade

The LIU-PSB project consists of two major upgrade programmes: the upgrade of the injection line and injection period to accommodate the injection of 160 MeV H⁻ ions from Linac4, and the upgrade of the PSB rings, extraction and recombination transfer lines to permit acceleration and extraction at 2 GeV.

The main PSB upgrade items necessary to deliver the specified LHC beam parameters are listed in Table 1.4, and they are accompanied by a brief description. In addition, the foreseen duration (in months), the start time, the consequences if not done, and the current status are indicated for each activity.

1.2.2 Outlook/concluding remarks for the LIU-PSB

The two main parts of the PSB upgrade, i.e. the modification of the injection and the energy upgrade, are scheduled to be implemented simultaneously during LS2, while it should be noted that it is planned that all equipment required for Linac4 connection will be available in 2016. All design choices have been made, with only the final decision on the High Level (HL) Radio Frequency (RF) still pending. Preparation, design and procurement are in progress in essentially all areas. Many items are partially consolidation items, i.e. some work on the equipment would need to be done independently of the injection and energy upgrade. This has been detailed in Ref. [4].

Table 1.4: Scope of the LIU-PSB upgrade

Activity	Baseline or option	Description	Risk if not done	Time (months)	Can start	Work status
Magnets	Baseline	Modification/replacement of magnets for 160 MeV injection and 2 GeV operation	Some magnets are currently urgent consolidation items; no Linac4 connection; no 2 GeV upgrade	4 to 5	Extended end of the year technical stop (EYTS)	Design and procurement in progress
Low Level (LL) RF	Baseline	Full renovation of the LL RF	Old system obsolete and inappropriate for Linac4 and new HL RF	For new HL RF: 7 For Linac4: 1.5	Extended EYTS; Transverse Feedback modifications planned by the end of 2014	Partly completed
HL RF	Baseline	Replacement of the C02 and C04 RF cavity system by new wideband cavities and renovation of the C16 RF cavity system	Old system obsolete and will not work with Linac4 intensities and 2 GeV; baseline is new RF system	10.5	LS2	Prototype installation being tested
Power converters L4 injection	Baseline	New power converters for 160 MeV H ⁻ injection	No Linac4 connection		Extended EYTS	Design and procurement in progress
Power converters ring, extraction and transverse lines	Baseline	Modification/replacement of power converters for 2 GeV operation	No 2 GeV; some items were also consolidation items (reliability issue); the present Main Power Supply (MPS) system would need consolidation		LS2	Design and procurement in progress
Beam instrumentation	Baseline	Improved instrumentation for measurement of high brightness beams and for 160 MeV H ⁻ injection	Commissioning with Linac4 impossible; quality of emittance diagnostics insufficient	9	Extended EYTS	Design phase
Beam intercepting devices	Baseline	New main dump and new injection dumps for H ⁻ injection	No Linac4 connection		Extended EYTS	Main dump completed, injection dumps design phase
Linac4 injection	Baseline	Rebuild injection line and injection period for H ⁻ injection	No Linac4 connection	9 + 1.5 cool down	Extended EYTS	Integration phase
2 GeV extraction and transfer	Baseline	Upgrade extraction and transfer hardware from 1.4 GeV to 2.0 GeV operation	No 2 GeV upgrade	7	LS2 (to be checked if some equipment could be installed before in an EYTS...)	Design phase
Vacuum	Baseline	Vacuum system for the new injection period, other vacuum work as imposed by the hardware upgrade	No Linac4 connection		Extended EYTS	
Electrical systems	Baseline	Upgrade of the electrical distribution for increased power need (2 GeV operation and increased cooling needs)	Inappropriate for increased power needs		In parallel with MPS building construction; can some items from the renovation be done during an EYTS?	
Cooling and ventilation	Baseline	Full refurbishment of the PSB cooling plant in order to satisfy the needs of 2 GeV operation	Obsolete system and inappropriate for new needs		In parallel with MPS building construction; otherwise LS2	
Installation, transport and handling	Baseline	Consolidation of handling equipment and adaptation of equipment for installation in the frame of the energy upgrade	Equipment not ready, delays		LS1	Partially completed
Civil engineering	Baseline	New building for the new MPS, various work in the PSB ring to create space for cables	No 2 GeV upgrade	Not shutdown-dependent		New building design in progress
Interlock systems	Baseline	New interlocks for operation with Linac4	No Linac4 connection	Extended EYTS		
Control	Baseline	Controls needs driven by the other activities	New equipment cannot be controlled	Extended EYTS		

1.3 LIU-PS

1.3.1 Scope of the LIU-PS upgrade

The LIU-PS project consists of two major upgrade programmes: the upgrade of the injection energy at 2 GeV, with the necessary interventions in the injection area, and the upgrade of the RF systems.

The main PS upgrade items (baseline and optional) necessary to deliver the specified LHC beam parameters are listed in Table 1.5, and they are accompanied by a brief description. In addition, the foreseen duration (in months), the start time, the consequences if not done, and the current status are indicated for each activity.

Table 1.5: Scope of the LIU-PS upgrade

Activity	Baseline or option	Description	Risk if not done	Time (months)	Can start	Work status
Beam instrumentation	Baseline	Renovation of Beam Wire Scanner (BWS) (including turn-by-turn measurements). Ring SEMGRID turn-by-turn acquisition. New: fast Beam Loss Monitor (BLM), injection SEMGRID, Ionisation Profile Monitors (IPM), longitudinal profile monitor	Quality of emittance diagnostics insufficient. Injected beam profiles not measurable, new injection setup very difficult	1.5	EYTS/ Extended EYTS	In design and procurement phases. Longitudinal profile monitor ready for installation
Corrector magnets	Baseline	New vertical correctors and new skew quadrupoles	Not compatible for 2 GeV operation	4	Extended EYTS	Design phase
Resonance compensation magnet	Option	New or renovated skew sextupoles and/or octupoles to compensate resonances	Eventually reduced margin on maximum acceptable direct space-charge tune shift at injection	0.5	n/a	Beam dynamics study phase. Magnets existing
Transverse damper	Baseline	New power amplifiers	Not compatible with 2 GeV operation. Limited DC power and bandwidth	Not shutdown dependent	LS1	Partially completed
Longitudinal damper	Baseline	Finemet cavity to damp longitudinal coupled bunch instabilities	Limited intensity/bunch that can be accelerated not compatible with HL-LHC beam parameters	Not shutdown dependent	LS1	Partially completed
Radiation shielding	Baseline	Increase of radiation shielding on top of extraction septum and route Goward	RP related issues	Not shutdown dependent	LS1	Finished
Correctors power converters	Baseline	Low energy quadrupoles, orbit correctors, skew quadrupoles/sextupoles	Increased number of failures due to large RMS current and old thermal protections for magnet power converters. Not compatible with 2 GeV operation	Not shutdown dependent	Extended EYTS	Procurement
Beam dumps	Baseline	New beam dumps (also replace ‘ralentisseur’ for first turn dump)	Existing dumps not compliant with future beam parameters (mechanical and operational risks). Present mechanics prone to vacuum leaks	1	LS2	Conceptual design study
General 2 GeV injection devices	Baseline	New injection septum. New injection extra kicker. New injection magnet bumpers. Low beta insertion elements. Appropriate new power converters and new instrumentation	2 GeV injection not possible with existing hardware	4	LS2	Design phase
10 MHz High Power (HP) RF	Baseline	10 MHz system renovation baseline, upgrade of feedback amplifiers	Reduced longitudinal beam stability, degradation of beam quality	11 ^a	LS2	Study phase
40–80 MHz HP RF	Option	Add a new 40 MHz or 80 MHz cavity	Increased losses at SPS capture	1	LS2	Review progressing. New power converter being built

Activity	Baseline or option	Description	Risk if not done	Time (months)	Can start	Work status
80 MHz fast tuners and new feedback amplifiers 40 MHz and 80 MHz	Baseline	New fast tuner against beam loading and for fast change to operation with ions	Reduced longitudinal beam quality at extraction. Not possible to use all available 80 MHz cavities simultaneously if ions and protons in parallel operation	0.5	LS2	Test phase
LL RF	Baseline	New 1-turn delay feedbacks, 10 MHz and 20 MHz/40 MHz/80 MHz cavities. Coupled-bunch feedback and beam loading compensation for Finemet cavity	Transient beam loading issues at high intensity, degraded beam quality and bunch-to-bunch spread. Degraded beam stability. Existing system on 10 MHz cavities not operationally usable for LHC-type beams	Not shutdown dependent	EYTS	System for 10 MHz finished during LS1
LL RF	Baseline	Replace existing beam control by fully digital beam control	Degradation of beam quality due to drifts, risk of frequent breakdown, insufficient spare old hardware	n/a	LS2	Options being investigated
Vacuum	Baseline	New vacuum chambers. New electron cloud monitors. Activities for other groups	Needed for 2 GeV injection	n/a	LS2	E-cloud monitor installed

^aUpgrade activities and normal maintenance included.

1.3.2 Outlook/concluding remarks for the LIU-PS

The timelines, whenever the information was not available because the new devices are not yet in an advanced enough design stage, are either planned or deduced from similar interventions made in the recent past. Whenever possible, the activities will be advanced with respect to LS2.

1.4 LIU-SPS

1.4.1 Scope of the LIU-SPS upgrade

The SPS upgrade items (baseline and optional), necessary to deliver the specified LHC beam parameters are listed in Table 1.6, and they are accompanied by a brief description. In addition, the foreseen duration (in months), the start time, the consequences if not done, and the current status are indicated for each activity.

Table 1.6: Scope of the LIU-SPS upgrade

Activity	Baseline or option	Description	Risk if not done	Time (months)	Can start	Work status
Machine interlocks	Baseline	Replace relays with standard safety PLC-based solution	Poor reliability; maintenance costs; need to maintain obsolete LL system	6	LS1	Finished
800 MHz upgrade	Baseline	Install digital control and new 1-turn low-level feedback and feed-forward for amplitude and phase stability. Consolidation of power system. Doubling of available power to match 200 MHz upgrade	Instabilities, impedance, and poor beam quality; difficult controlled emittance blow-up; longer LHC filling time; resources and reliability risk with obsolete low-level system	12	LS1	Finished
Long Straight Section (LSS) 1 vacuum sectorization	Baseline	Add sector valves around internal dump (TIDVG) and injection/dump kickers (MKP/D) to reduce dose, protect equipment and reduce pump times	Risk of venting and damage to sensitive/very radioactive equipment. Increased radiation dose to personnel	6	LS1	Finished
Scraper improvement	Baseline	Construction of additional spares and local shielding improvement	Reduced LHC performance, with losses from beam tails	0	n/a	Active: assembly

EXECUTIVE SUMMARY

Activity	Baseline or option	Description	Risk if not done	Time (months)	Can start	Work status
Beam instrumentation	Baseline	Upgrade Multi Orbit Position System (MOPOS) electronics; new wire scanners; upgrade Beam Gas Ionisation (BGI), Beam Synchrotron Radiation Telescope (BSRT), IPM and head-tail monitors	Poor beam size measurement; insufficient resolution, no bunch-by-bunch; extra cost, resources and reliability risk with obsolete systems	24 ^a	LS1	Active: cabling, design, prototypes
Transverse damper upgrade	Baseline	Dedicated pickups; digital low-level control; 200 MHz local oscillator; cable consolidation	Larger emittances; extra cost; resources and reliability risk with obsolete system, no damping for ions	9	LS1	Finished
Arc vacuum sectorization	Baseline	Reduce length of arc sectors by factor of 2; reduce pumping times; preserve better e-cloud scrubbing	Longer scrubbing times for e-cloud; longer recovery from vacuum interventions	6	LS2	Active: cabling
Upgrade TIDVG	Baseline	Upgrade TIDVG core to accept future LHC beams	TIDVG damage for intense LHC beams; long (months) recovery time	3	LS2	Active: design
Reduce kicker impedance	Baseline	Addition of transition pieces in MKD; serigraphy of tune kickers (MKQ)	Intensity limitation with high-duty cycle beams (scrubbing)	3	2015/2016	Active: MKD
Electrostatic Extraction septa (ZS) improvements	Baseline	More pumping; reduce impedance; improve ion traps and anode circuit	Sparking; limit Fixed Target beams; longer switch to LHC cycle	3	2015/2016	Active: design
200 MHz low level upgrade	Baseline	Upgrade drivers, cavity controllers, High Voltage (HV) power supplies, cooling and ventilation and power couplers; digital LL control	Poor beam control; instability; poor LHC performance; extra cost, resources and reliability risk with obsolete system	6	2016/2017	Active: design
Extraction septum protection (TPSG) upgrade	Baseline	Replacement of TSPG4/6 by upgraded versions with better robustness and protection of extraction septum MSE	Damage of TPSG or MSE in the event of a mis-steered beam at extraction	3	LS2	To start
200 MHz power upgrade	Baseline	Rearrange to six RF cavities with two additional 1.4 MW power plants. Reduce impedance by 15%, double RF voltage to increase RF current	25 ns bunch intensity limited at about 1.3e11 p+; longer bunches to LHC; beam losses in SPS and LHC	12	LS2	Active: building, tendering, design
Transfer lines (TL) protection devices	Baseline	Upgrade TL collimators (TCDI) for robustness and protection; new locations in TI2/TI8 TLs	Damage to TCDI or TI2/8 magnets in case of steering error; higher LHC injection losses	3	LS2	Active: design
New wide band feedback system	Option	Intra-bunch damping system to damp instabilities from Transverse Mode Coupling Instabilities (TMCI) or Electron Cloud Instabilities (ECI)	Longer scrubbing times for ecloud; increased need for amorphous Carbon (aC) coating; lower instability thresholds	3	LS2	Active: prototype
New external high energy beam dump	Baseline	New dump system outside SPS ring, using existing fast extraction, and new switching series of magnets	Increased TIDVG activation; TIDVG damage; longer setting up times; reduced LHC availability	6–18	LS2	Active: design
Upgrade MSE septa converters aC coating of vacuum chambers	Option	Replace MSE/T converters with high stability versions	Longer LHC setting up time for injection; LHC injection loss	6	LS2	Active: study
	Baseline	Coat all SPS main magnets and chambers to suppress electron cloud. Coat chamber inside magnet in building BHAS	25 ns intensity limitation; poor beam quality; long conditioning times; higher beam losses; larger emittance	18	LS2	Active: prototype
100 ns rise time kickers for ions	Baseline	Upgrade Injection kickers (MKP) Pulse Forming Lines (PFL), new in-vacuum septum, dump and instrumentation	Lower luminosity in LHC for Pb ions	6	LS2	Active: design

^aTotal.

1.4.2 Outlook/concluding remarks for the LIU-SPS

The SPS upgrade is well under way, with some activities already complete and most of the other activities well into the design or construction phase. Major works are planned for LS2, which will require careful preparation and coordination, and the decision on whether the complete machine needs aC coating to suppress the electron cloud needs to be taken in 2015, to allow proper preparation of the shutdown and overall logistics. Most other technical decisions have been taken.

1.5 LIU-IONS

1.5.1 Scope of the LIU-IONS upgrade

The upgrade items for all accelerators in the heavy ion injection chain (baseline and optional), necessary to deliver the specified LHC beam parameters are listed in Table 1.7, and they are accompanied by a brief description. In addition, the foreseen duration (in months), the start time, the consequences if not done, and the current status are indicated for each activity.

Table 1.7: Scope of the LIU-IONS upgrade

Activity	Baseline or option	Description	Risk if not done	Time (months)	Can start	Work status
10 Hz	Baseline	Allow injection into LEIR every 100 ms	Too low intensity in LEIR	18	2016	Study started
Spectrometer measurement line (LBS)	Baseline	New spectrometer line after connection of Linac4 to PSB	No energy measurement of Linac3 beam	18	LS2	Study started
Low Energy Beam Transport (LEBT)	Baseline	Rematched optics in LEBT, between source and Radio Frequency Quadrupole (RFQ)	Lower intensity in Linac3/LEIR	18	2017	Study started
Oven test stand	Baseline	Additional lead oven to study the dynamics of the existing one	Insufficient knowledge of oven behaviour	6	2015	Active: design
Source test stand	Option	Alternate source for machine experiments, independent of operational one; can be used as a spare in the case of an emergency	No spare source, no training of supervisors			Not started
LEIR dump	Baseline	Allowing to safely and cleanly dump the ion beam when not desired by PS or LHC	Vacuum degradation in LEIR and PS	18	LS2	Study started
100 ns rise time kickers (see SPS)	Baseline	Upgrade MKP PFLs, new in-vacuum septum, dump and instrumentation	~23% less peak luminosity in LHC for Pb ions	6	LS2	Active: design
SPS momentum slip stacking	Baseline	RF gymnastics to merge PS trains in the SPS, effectively decreasing the bunch spacing from 100 ns to 50 ns	~43% less peak luminosity in LHC for Pb ions	6	LS2	Active: design
SPS damper	Baseline	Upgrade transverse damper for ion injection in SPS	Too large ion emittances		2015	Active: prototype

1.5.2 Outlook/concluding remarks for LIU-IONS

In order to reach the required performance level—seven times the design peak luminosity for Pb–Pb collisions—the intensity limitation bottleneck currently experienced in LEIR has to be overcome. This can only be achieved with an extensive study programme, including more advanced modelling and simulations as well as more time and resources for machine development activities with the beam.

1.6 LIU project cost and schedule

1.6.1 LIU project cost

The project costs to completion are summarized in Table 1.8.

EXECUTIVE SUMMARY

Table 1.8: Cost to completion (all numbers in kCHF)

	2008	2009	2010	2011	2012	2013	2014	2015	2016	2017	2018	2019	2020	Grand total
LIU-MNG						55	764	1 668	2 000	2 000	2 000	2 000	1 000	11 487
LIU-PSB	138	313	340	955	1 711	4 195	6 351	13 827	21 694	11 863	4 165	396	0	65 948
LIU-PS				245	461	3 429	3 246	4 814	4 936	3 297	1 795	240	75	22 538
LIU-SPS				504	2 126	3 450	5 856	8 712	13 583	18 308	15 085	9 168	1 075	77 867
LIU-ION						50	400	500	2 100	2 300	2 000	0		7 350
LIU project grand total	138	313	340	1 704	4 298	11 129	16 267	29 421	42 713	37 568	25 345	13 804	2 150	185 190

1.6.2 Schedule

The estimated time required for recovering pre-LS2 performance from the injector complex accelerators is summarized in Table 1.9. The main conclusion is that, to fit within the allocated slot of 18 months of beam stop in the LHC, beam commissioning in the PSB, PS and SPS has to begin after no more than 13.5, 15 and 16.5 months, respectively. A first estimate prepared for the Review of LHC and Injectors Upgrade Plans [5] in October 2013 showed that this will be challenging, especially in the PSB, where the extensive amount of cabling work is on the critical path. A detailed schedule remains to be prepared, making the optimum use of the access time during the machine stops before LS2 and taking properly into account all of the activities.

The commissioning of the final HL-LHC beams with double the brightness is expected to take around two years of parallel machine development and dedicated tests. Many new systems and functionalities must be commissioned across the complex, including a completely new type of injection in the PSB (160 MeV H⁻) with brand new hardware, and it is expected that much of Run 3 will be needed to learn how to operate and optimize the adjustment of the newly installed equipment and to routinely produce the new beams. This implies that LIU has to be completed ~one LS before the HL-LHC upgrades are implemented in the collider (LIU completed during LS2 if HL-LHC is completed during LS3).

Table 1.9: Preliminary estimates of shutdown time required for the LHC injectors during LS2

	Month																			
	1			//	13		14		15		16		17		18		19		20	
	1	2	//		1	2	1	2	1	2	1	2	1	2	1	2	1	2	1	2
	LS2 start	End of beams in LHC			Start of Beam commissioning in injectors											Start of Beam commissioning in LHC				
PSB	PSB LS2 works (Linac4 connection + 2 GeV upgrade)			Beam commissioning LHCprobe					LHCprod											
PS	PS LS2 works (2 GeV injection + RF upgrades etc.)							Beam commissioning LHCprobe			LHCprod									

SPS	SPS LS2 works (200 MHz high-power RF upgrade + aC coating + external beam dump + 100 ns rise-time injection kickers for ions)	Beam commissioning LHCProbe	LHCProd (with scrubbing)	
LHC	LHC LS2 works		Beam commissioning	

1.7 Safety

1.7.1 Safety organisation

In accordance with the Safety Regulation [SR-SO](#) ‘Responsibilities and organisational structure in matters of Safety at CERN’, the safety structure within the project is described in (Fig. 1.2).

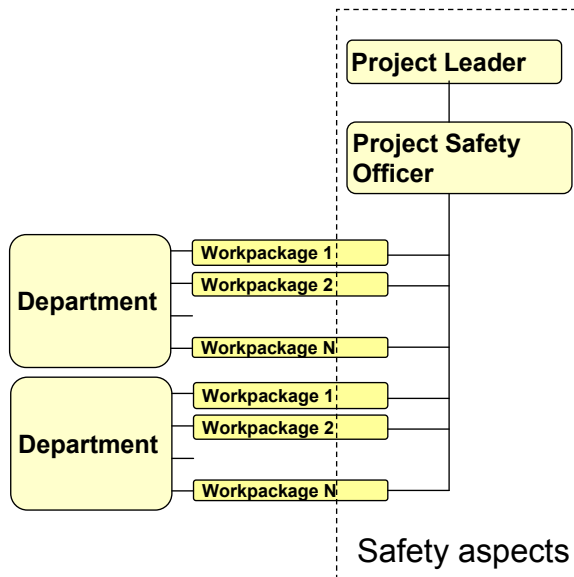


Fig. 1.2: LIU project safety structure

The project leader is responsible for safety in the project.

As defined in the General Safety Instruction [GSI-SO-7](#), the project safety officer (PSO) is appointed by the project leader to oversee and coordinate Safety aspects of the project. The mandate is twofold:

- the PSO verifies that safety aspects have been correctly considered within the different work packages, that the solutions proposed are consistent with the general safety policy of the project and that the safety measures are correctly applied by the different work packages;
- the PSO verifies that there are no safety issues arising at the interface between work packages. If this happens, he/she asks the relevant work packages to apply the appropriate measures.

The work package holders are responsible for proposing and applying the correct safety measures for the work and equipment included in their work package. Because all work packages are contained within one department, the department of the work package is finally responsible for the safety conditions of the work attributed to it by the project.

EXECUTIVE SUMMARY

Territorial safety is the responsibility of the department where the work is done. The department nominates territorial safety officers (TSO).

The Radiation Protection group takes responsibility for all radiation protection aspects during the design, commissioning, operation and dismantling of the facility. In particular, the Radiation Protection group takes responsibility for the results of all radiation protection studies (e.g. stray radiation, material activation, and air and water activation) and the derived radiation protection requirements for the facility.

1.7.2 Safety objectives for LIU

The program of upgrade of the injectors will ensure that the present level of safety for the people and the environment is maintained during all project phases (simulations, design, prototyping, installation, commissioning, operation and dismantling) and whenever possible or required, it will be improved. This will be demonstrated in the LIU Safety File, which will be published in a separate document.

In particular, the aim is to optimize the beam losses, to favour technical solutions which minimise the dose rates according to the ALARA principle (keep doses to persons as low as reasonably achievable) and minimize radioactive waste.

Some examples which illustrate that safety is integrated in the LIU project are the following:

- new beam dumps for LEIR, PSB, PS, and SPS;
- design of a dedicated cavern for hosting the SPS beam dump;
- overall design of protection elements (transfer line collimators, beam dumps...);
- remote handling of radioactive equipment foreseen from the design phase;
- upgrades of the cooling stations at SPS point 3 minimizing the impact on the environment.

Besides these technical measures, organisational measures are also in place (non-exhaustive list):

- work and dose planning (DIMR) aiming at optimization of the job to reduce the individual and collective doses;
- use of TREC tool installed in the buffer zones to trace potentially radioactive equipment;
- correct management of the planning through the organisation of regular meetings (“LIU installation and planning meetings”);
- safety visits before the start of the works (VIC in French for “Visite d’Inspection Commune”);
- management of the interventions inside the accelerators using IMPACT. This web-based tool is used for inputting work declarations, planning, scheduling, preparing and coordinating all activities. The system also provides an approval process including radiation protection;
- any modification to the project baseline, including safety, is subject to an Engineering Change Request (ECR) process with an appropriate approval procedure. The impact of the modification on safety is also assessed.

Tables

1.1. Achievable proton beam characteristics at injection of the different accelerators after LIU	10
--	----

1.2.	Optimum lead ion beam characteristics at injection of the different synchrotrons after LIU	11
1.3.	HL-LHC requested proton beam characteristics at injection.....	11
1.4.	Scope of the LIU-PSB upgrade	12
1.5.	Scope of the LIU-PS upgrade.....	13
1.6.	Scope of the LIU-SPS upgrade.....	14
1.7.	Scope of the LIU-IONS upgrade.....	16
1.8.	Cost to completion.....	17
1.9.	Preliminary estimates of shutdown time required for the LHC injectors during LS2.....	17

Figures

1.1.	LIU project organization	10
1.2.	LIU project safety structure	18

References

- [1] S. Myers, Projects Structure in the Accelerators and Technology Sector, DG-DAT-2010-005, 2010.
- [2] G. Rumolo *et al.*, LIU Beam Parameters, EDMS Id. 1296306v.1, 2014.
- [3] D. Manglunki *et al.*, Provisional List of Parameters for Ions in HL-LHC, EDMS Id. 1311644, 2014.
- [4] K. Hanke *et al.*, PS Booster Energy Upgrade Feasibility Study – First Report, <https://edms.cern.ch/document/1082646/3>, 2010.
- [5] B. Mikulec,*et al.*, Work Effort in the LHC Injector Complex for the Upgrade Scenarios, in Proceedings of RLIUP: Review of LHC and Injector Upgrade Plans, Centre de Convention, Archamps, France, 29–31 October 2013, edited by B. Goddard and F. Zimmermann, CERN-2014-006 (CERN, Geneva, 2014), pp. 75 – 79.

Chapter 2

Introduction and Overview

2.1 Introduction

Built many years ago (in 1959 for the Proton Synchrotron (PS)), the accelerators of the injector complex were extensively consolidated and upgraded during the past decade in preparation for their role in the Large Hadron Collider (LHC) [1, 2]. They are shown in Fig. 2.1: Linac2 (50 MeV), the Proton Synchrotron Booster (PSB) (1.4 GeV), PS (25 GeV), and the Super Proton Synchrotron (SPS) (449 GeV) for protons –kinetic energy quoted-, plus Linac3 and the Low Energy Ion Ring (LEIR) for other ions. After optimization and extensive beam scrubbing, they were able to provide a beam with characteristics exceeding the nominal LHC requirements (Table 2.1) and decisively contributed to the excellent performance of the LHC during its first run until February 2013, which was crowned with the discovery of the Higgs boson.

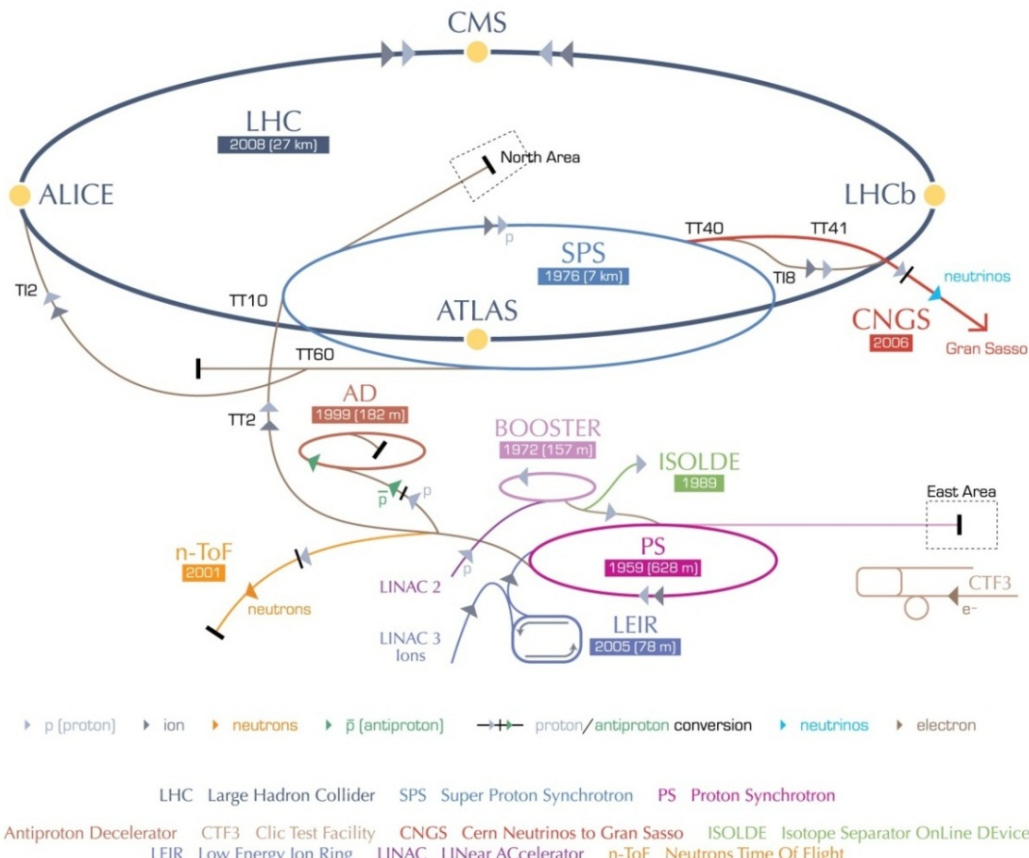


Fig. 2.1: CERN accelerator complex in 2012

Their flexibility was also crucial to the LHC's success. It is typically illustrated by the comparison between the proton beam effectively used for physics (1.65×10^{11} p/b with 50 ns bunch spacing within emittances of $1.6 \mu\text{m}$ at ejection from the SPS) and the nominal beam described in the LHC Design Report (1.15×10^{11} p/b with 25 ns bunch spacing within emittances of $3.5 \mu\text{m}$ at ejection from the SPS) [1]. During the LHC's second run, from 2015 until mid-2018, a beam with 25 ns bunch spacing will be used for physics (1.2×10^{11} p/b with 25 ns bunch spacing within emittances of $2.6 \mu\text{m}$

at ejection from the SPS). This is expected to contribute to exceeding the nominal peak luminosity of $10^{34} \text{ cm}^{-2}\text{s}^{-1}$ in LHC before its second Long Shutdown (LS2).

This is, however, not enough for the High Luminosity LHC (HL-LHC) project, which aims at a levelled luminosity of $5 \times 10^{34} \text{ cm}^{-2} \text{ s}^{-1}$ with protons during run 4, after ~ 2022 [3]. For that purpose, the injected beam has to be approximately 2 times more intense and 2.5 times brighter ($2.3 \times 10^{11} \text{ p/b}$ with 25 ns bunch spacing within emittances of $2.1 \mu\text{m}$). Solutions must therefore be found and implemented in all of the LHC injector complex accelerators to reach and reliably operate at this new level of performance. The necessary work, which is the core of the LHC Injectors Upgrade (LIU) project, is the subject of this report.

Table 2.1: Proton beam characteristics in 2012

	50 ns bunch trains at LHC injection	50 ns bunch trains at start of collisions	25 ns bunch trains at LHC injection^a
Number of bunches (n_b)	1374	1374	2748
Protons/bunch (N_b)	1.65×10^{11}	1.6×10^{11}	1.1×10^{11}
Normalised transverse emittance (ε_n) (μm)	1.6	2.4	2.8

^a The number of 25 ns-spaced bunches that the LHC could effectively accelerate was limited to 804 because of electron cloud effects [4].

Integrated luminosity with heavy ions in the LHC is also expected to progress during the High Luminosity era by approximately an order of magnitude. The required upgrades in the injectors are managed by the LIU project and the tentative ions beam parameters are summarised in [5]. A dedicated LIU-IONS TDR will be written in 2015.

2.2 Current LHC proton injectors

2.2.1 Mode of operation

In the PSB and PS, the main concern is the induced tune spread resulting from the high beam brightness. It is brought to an acceptable level in the PSB by dividing the intensity per pulse by a factor of 2, filling the PS with two batches instead of a single one. This was made possible by operating the PSB on harmonic 1, hence with a single bunch per ring. In the PS, where the first batch of bunches stays at injection energy for 1.2 s, the space charge-induced tune spread has been reduced by a factor of 1.5 by increasing the transfer energy from the PSB from 1 GeV to 1.4 GeV (a ratio of $\beta\gamma^2$).

The long and intense bunches delivered by the PSB are transformed within the PS into trains of bunches spaced by 25 ns (or 50 ns) before ejection, as shown in Fig. 2.2 (Refs. [1, pp. 5–8, 45–52] and [6]). This is obtained with quasi-adiabatic bunch-splitting gymnastics that keep the beam bunched and under RF control. As a result, the gap without beam corresponding to the empty bucket at injection (six PSB bunches being sent to the PS on $h = 7$) is preserved and used for the rise time of the ejection kicker, avoiding beam loss at ejection. Moreover, shorter bunch trains can be obtained simply, with fewer bunches from the PSB.

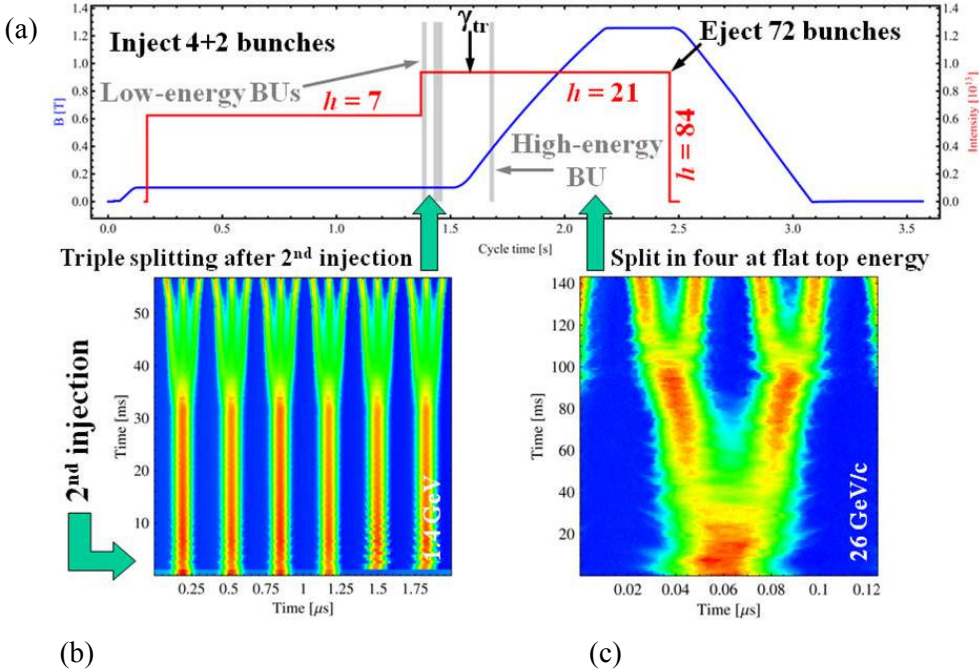


Fig. 2.2: Longitudinal bunch-splitting to generate a 25 ns bunch train in the PS. (a) B field (blue) and beam current (red) during a PS cycle. Longitudinal controlled blow-ups (BU) are used for optimizing the gymnastics and avoiding longitudinal beam instabilities. 2D displays of longitudinal density at (b) 1.4 GeV) and (c) 25 GeV. Time during the process is along the vertical axis. Longitudinal density is colour-coded from blue (no beam) to red (maximum).

Bunch splitting is done in multiple steps.

- Splitting into three takes place at injection energy (1.4 GeV) combining the simultaneous use of three RF systems on harmonics 7, 14 and 21. At the end of the process the beam is held on $h = 21$, on which it is accelerated up to top energy.
- Splitting into four takes place at 25 GeV, in two successive steps, using RF systems on $h = 21$ and $h = 42$ for the first step, and on $h = 42$ and $h = 84$ for the second step. Without this last step, bunch spacing is 50 ns.

In addition, the longitudinal emittance is submitted to controlled blow-ups to improve longitudinal stability, pulsing the 200 MHz cavities a few times during the cycle. Finally, a non-adiabatic bunch length reduction process is used before ejection to the SPS for reducing bunch length to ~ 4 ns, which can be captured in a 200 MHz SPS bucket. In total, five families of RF systems are necessary in the PS (3–10 MHz, 20 MHz, 40 MHz, 80 MHz and 200 MHz) to generate the proton beams for the LHC.

In the SPS the injected bunches are captured with the main RF system operating at 200 MHz. Up to four batches of 25 ns (or 50 ns) bunch trains from the PS are accumulated on a 10.8 s-long flat bottom (at injection energy). Longitudinal stability is obtained adding the fourth harmonic RF (800 MHz) in bunch shortening mode (increasing Landau damping) and applying a longitudinal controlled blow-up during acceleration. In the transverse phase plane the electron clouds that were limiting performance by provoking vertical instability are significantly reduced at present intensities thanks to the scrubbing of the surface of the vacuum chamber.

2.2.2 Present performance and future needs

The beam characteristics that were available at injection in the LHC before its first long shutdown in 2013 are summarized in Table 2.1. The corresponding brightness at injection in the LHC is 20%

higher than the ‘nominal’ value considered in the LHC design report [1] for a bunch spacing of 25 ns. During the first run of the LHC, 50 ns spacing has been preferred, benefiting from bunches of the ultimate intensity ($\sim 1.7 \times 10^{11}$ p/b) within half the emittance (twice the nominal brightness) at 450 GeV. In spite of transverse blow-up in the LHC (centre column in Table 2.1), it consistently allowed the attainment of 75% of the nominal peak luminosity ($7.5 \times 10^{33} \text{ cm}^{-2} \text{ s}^{-1}$ instead of $10^{34} \text{ cm}^{-2} \text{ s}^{-1}$), mostly compensating for the effect of the larger geometric emittance due to the reduced beam collision energy (4 TeV instead of 7 TeV).

With these beam characteristics, the injector complex is performing as foreseen but without any margin. For the High Luminosity LHC (HL-LHC) project, which aims at accumulating $\sim 250 \text{ fb}^{-1}/\text{year}$, beam characteristics in collision have to progress to the level described in Table 2.2. Assuming 20% emittance blow-up and 5% beam loss between injection and collision in the LHC [3], the beam intensity required from the injectors has to double in the baseline case (25 ns) and the brightness has to become nearly threefold.

Table 2.2: Beam characteristics for the High Luminosity LHC project

	25 ns bunch trains at start of collisions	25 ns bunch trains at injection (estimate)	50 ns ^a bunch trains at start of collisions	50 ns ^a bunch trains at injection (estimate)
Number of bunches (n_b)	2748 ^b	2748	1374 ^b	1374
Prottons/bunch (N_b)	2.2×10^{11}	2.3×10^{11}	3.5×10^{11}	3.7×10^{11}
Normalised transverse emittance (ε_n) (μm)	2.5	2.1	3	2.5

^aThe 50 ns scenario is a back-up, in case fundamental limitations of the LHC (e.g. due to electron clouds or total intensity) are encountered with the 25 ns baseline parameters.

^bThe filling schemes in the accelerator chain, the maximization of colliding bunches in the four experiments, and the need for non-colliding bunches will slightly reduce the number of colliding bunches in the high luminosity interaction points.

The currently identified limitations of the injectors are illustrated in Fig. 2.3, together with the achieved and expected beam performances. In the coordinate system emittance versus intensity, a constant space charge-induced tune spread is represented by a straight line passing through the origin. Below that line, the space charge effect is excessive (the curve for the PS is not a straight line because it takes into account the energy spread assuming a constant longitudinal emittance). The other limitations restrict the maximum intensity per bunch, which corresponds to a vertical line parallel to the Y axis. For 25 ns bunch spacing, 1.2×10^{11} p/b is the maximum intensity in the SPS because of the available RF power and because of longitudinal coupled bunch instabilities. The limit due to electron clouds is currently beyond this intensity. For 50 ns, the main limitations result from heat dissipated in the equipment because of the beam image current and from longitudinal instabilities ($N_b < 1.7 \times 10^{11}$ p/b).

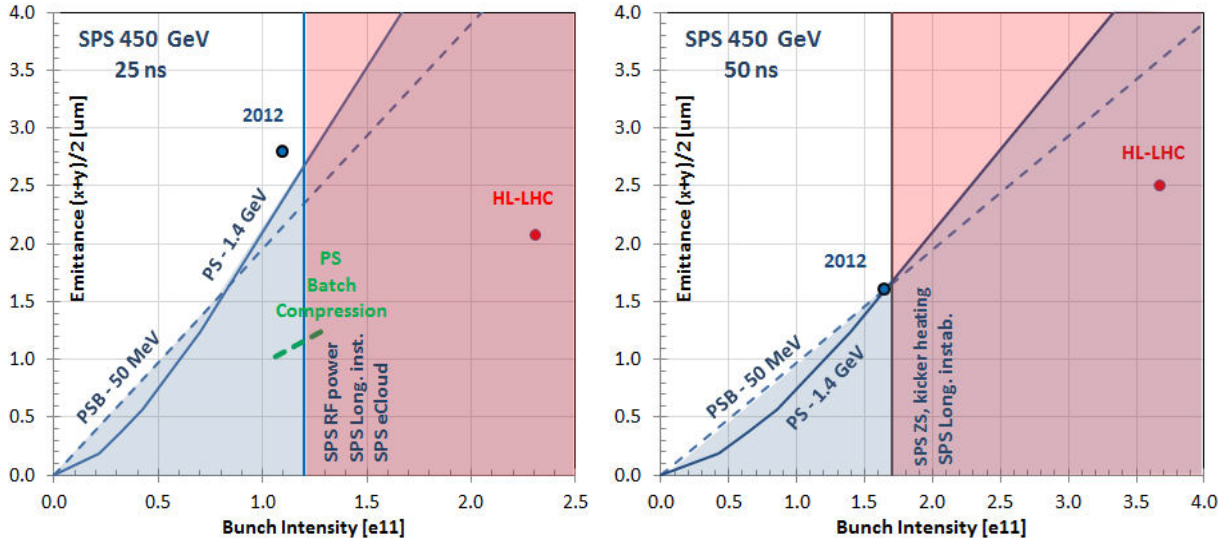


Fig. 2.3: Status and limitations of the beam characteristics of the LHC proton injector complex at SPS ejection, in 2012. (a) 25 ns bunch spacing; (b) 50 ns bunch spacing.

Before the implementation of the upgrades described below, new sophisticated beam gymnastics have been proposed for the PS for generating 25 ns batches with a brightness similar to 50 ns [7]. The principle is to split the PSB beam into fewer bunches while keeping spacing at 25 ns. For that purpose, the batch of PSB bunches that fills most of the PS circumference at injection is compressed into a smaller fraction of the circumference. A typical scenario is illustrated in Fig. 2.4:

- i) two consecutive batches of four bunches from the PSB are injected in eight PS buckets on $h = 9$;
- ii) after acceleration up to an intermediate energy of 2.5 GeV where space charge is smaller and longitudinal acceptance larger, the beam is compressed into 57% of the circumference by adiabatically increasing the harmonic number from $h = 9$ to $h = 14$;
- iii) bunches are merged two by two (the reverse of the process of splitting in two), which results in four bunches on $h = 7$;
- iv) triple splitting is finally applied, generating 12 bunches on $h = 21$.

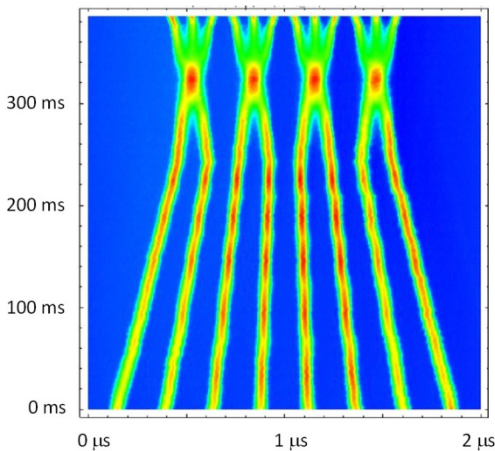


Fig. 2.4: 2D display (simulated) of longitudinal density in the PS during batch compression merging and splitting (BCMS) at 2.5 GeV. Time follows the vertical axis. Longitudinal density is colour-coded from blue (no beam) to red (maximum).

These 12 bunches are then accelerated to high energy and split into four, using the current method (Fig. 2.2(c)). Compared to the present process, batch compression merging and splitting (BCMS) provides only 48 bunches with 25 ns spacing, instead of 72, increasing the filling time of the LHC and decreasing by approximately 10% the maximum number of bunches in the collider because of the gaps required for the rise time of the kickers in the SPS and LHC.

The corresponding beam characteristics at LHC injection, shown as a dashed green line in Fig. 2.3(a), can potentially increase luminosity with respect to the 50 ns scheme while reducing the number of events per crossing and hence easing operation of the detectors in the experiments. The interest of the scheme will, however, depend upon the LHC's capability to preserve small emittances at the maximum circulating current acceptable (nominally ~ 0.58 A).

This scheme has already been successfully tested in the injectors at the end of 2012. A much higher brightness than with the nominal scheme has been obtained, with bunches of 1.15×10^{11} p/b within emittances of $1.4 \mu\text{m}$ reproducibly injected in the LHC.

2.3 Upgrade plan for the LHC proton injectors

This section is only a brief summary. Details for the PSB, PS and SPS are given in this report in Chapters 3, 4 and 5, respectively.

2.3.1 Transverse phase plane

The primary limitation due to the space charge-induced tune spread in the PSB and in the PS will again be addressed by increasing the injection energy.

In the case of the PSB, this will be obtained with a new linear accelerator (Linac4 [8]), which will provide a beam at a kinetic energy of 160 MeV, doubling $\beta\gamma^2$ with respect to the present 50 MeV Linac2. The main parameters of Linac4 are summarized in Table 2.3. Charge exchange injection in the PSB will replace multi-turn betatron stacking, increasing the efficiency up to $\sim 98\%$ and providing the means to tailor the transverse distribution of protons. Painting is also foreseen in the longitudinal phase plane, to maximize capture efficiency and to optimize the longitudinal particle distribution. Operating with the same space charge tune spread $|\Delta Q_y|$, as has been achieved with the current configuration with Linac2 (0.44), the higher injection energy is expected to allow for a brightness of 1.8×10^{12} p/ μm , twice the present level. With the nominal beam gymnastics and some margin for emittance blow-up, this corresponds to a brightness of 10^{11} p/ μm for 25 ns bunch spacing at ejection from the SPS (and with 2×10^{11} p/ μm for 50 ns).

Table 2.3: Linac4 beam parameters

Parameter	Value
Ion species	H^-
Output energy	160 MeV
Bunch frequency	352.2 MHz
Maximum repetition rate	2 Hz
Beam pulse length	400 μs
Mean pulse current	40 mA
Maximum number of particles per pulse	1.0×10^{14}
Number of particles per bunch	1.14×10^9
Transverse emittance	$0.4 \pi \mu\text{m}$ (rms)

In the case of the PS, the beam injection energy will be increased from 1.4 GeV to 2 GeV kinetic, increasing $\beta\gamma^2$ and decreasing the space charge tune spread by a factor of ~ 1.6 . This energy is attainable in the PSB [9], provided that some equipment, such as the power supply for the main dipoles, is upgraded or redesigned. Likewise, in the PS, important modifications and new equipment must be added for beam injection at 2 GeV [10]; and the existing transverse damper will be renovated to avoid transverse instabilities, providing more flexibility in the choice of tunes at low energy and, hopefully, stabilizing the beam on the high energy flat top.

Beyond these major changes, an extensive campaign is in progress to optimize the transverse tunes and improve the compensation of resonances [11]. As a result, operation with vertical tune spreads greater than those currently obtained is foreseen to be manageable in all synchrotrons, and especially in the PS.

In the SPS, the integer part of the tunes have recently been changed from 26 ('Q26') to 20 ('Q20'), reducing the transition energy and enhancing the slip factor $|\eta| = |1/\gamma_t^2 - 1/\gamma^2|$ to increase the thresholds of longitudinal and transverse mode coupling instabilities [12, 13]. With these optics, operation with a space charge tune shift in excess of 0.15 is expected to be manageable, corresponding to a brightness of $\sim 10^{11}$ p/ μ m at SPS ejection, matched to the capability of the upgraded PSB for 25 ns bunch spacing.

2.3.2 Longitudinal phase plane

The PSB is not expected to suffer from limitations in the longitudinal phase plane when providing the high brightness beams for the LHC. A major renovation of the main RF systems is, however, required to guarantee reliable operation during the lifetime of the LHC and to let other users (e.g. Isotope Separator On Line Device (ISOLDE) benefit from the higher intensity beams allowed with Linac4.

In the PS, the measures presently used to stabilize the beam in the longitudinal phase plane (controlled longitudinal blow-up and coupled bunch instability damper) cannot handle a bunch intensity larger than $\sim 1.7 \times 10^{11}$ p/b, both for 25 and 50 ns bunch spacing. This limitation will be addressed by a new longitudinal damper using a dedicated 'broad band' cavity, aimed at bringing the instability threshold beyond 3×10^{11} p/b. Moreover, transient beam loading in the five families of RF systems will increase with beam intensity, degrading the quality of the multiple beam gymnastics. Fast RF feedback on all high-power RF systems will therefore be upgraded and one-turn delay feedbacks will be renovated on the 3–10 MHz ferrite cavities and implemented on the other cavities. More RF voltage at 40 MHz will be installed to improve longitudinal capture efficiency in the SPS [14]. The combined effect of all these actions is expected to allow for an operational availability of 3×10^{11} p/b at PS ejection.

In the SPS, two new 1.6 MW RF power plants will be installed, doubling the available power at 200 MHz, and the cavities will be reorganized into six assemblies (currently four), reducing the beam impedance. This will allow the acceleration of a beam current of up to 3 A, and 10 MV will be available on the high energy flat top, before ejection. Up to 2×10^{11} p/b with 25 ns bunch spacing could then be transferred to the LHC. Longitudinal stability of the beam in the SPS is presently obtained through the combined effects of controlled longitudinal blow-up up to 0.6 eVs and 800 MHz RF voltage used in bunch shortening mode. The instability threshold will increase with the new Q20 optics thanks to the increased slip factor $|\eta|$, although this will be balanced by the smaller longitudinal emittance imposed by the reduced acceptance of the buckets. The lower impedance of the reorganized 200 MHz RF system will also be beneficial, as well as the planned renovation of the low- and high-power equipment of the 800 MHz system. The present estimate is that 2.3×10^{11} p/b with 25 ns bunch spacing and 3.5×10^{11} p/b with 50 ns bunch spacing should be attainable. Such intensities might require transferring longer bunches (1.6–1.8 ns) to the LHC, where mitigation measures have to be studied [15].

2.3.3 Electron clouds

Electron cloud formation is observed in the PS on the 25 ns beam a few milliseconds before ejection, and at the same time a transverse instability has repeatedly been diagnosed. Although not presently affecting performance, it is a subject of theoretical and experimental investigation to determine the risk with the future beam characteristics and to prepare cures or mitigation measures.

In the SPS, electron clouds have been a major concern as soon as an LHC-like beam has been injected [16]. They trigger vacuum pressure rises, instabilities, beam losses and transverse emittance blow-up. Cures and mitigation measures have been developed through modelling/simulation and experimental tests. Beam scrubbing is showing an interesting potential, as demonstrated by the continuous improvement of the SPS since the beginning of LHC operation. It suffers, however, from degradation whenever the vacuum chambers are exposed to atmosphere and the minimum obtainable secondary electron yield (SEY) is limited, depending upon the nature and cleanliness of the vacuum chamber. Coating of the vacuum chamber with a low SEY material would be a perfect cure, completely avoiding the appearance of electron clouds. Amorphous carbon is especially efficient in that respect, and adequate coating processes for the SPS vacuum chambers have been developed and experimentally demonstrated. The use of clearing electrodes has also been considered, but no satisfying engineering solution has been found that would not reduce the available aperture. In any case, getting rid of the electron cloud limitations in the SPS is considered as feasible, either with scrubbing or with amorphous carbon coating [17]. As a mitigation measure, a wideband (GHz bandwidth) transverse damper is also envisaged as a possible means of counteracting electron cloud-triggered instabilities [18].

2.3.4 Other upgrades

The equipment in all accelerators must match the increased level of performance and be capable of operating reliably:

- new beam instrumentation has to be developed for measuring with adequate accuracy beams of reduced size and high brightness and intensity. The capability to detect and quantify the intensity in ‘spurious’ bunches in the PS and in the SPS is an important and challenging need;
- new beam interception and protection devices have to be built that will withstand impacts from the higher brightness/higher intensity beam. That concerns beam dumps in all machines, as well as the SPS scraper system for halo shaping and the devices in the SPS-to-LHC transfer lines protecting the LHC;
- a number of power supplies need to be replaced because of aging and/or because of more demanding specifications;
- civil engineering and building construction are also necessary for radiation shielding (PS injection and ejection sectors) and to host new, large equipment (new PSB main power supply and new SPS high-power RF amplifiers).

It is not planned that very expensive items like the main dipoles will be changed, but their ageing will be carefully monitored and spares have to be available.

2.3.5 Beam characteristics after the upgrades

The performance reach of the LHC proton injector complex after the improvements described in the previous section are graphically represented in Fig. 2.5 for 25 ns bunch spacing, which is the baseline option preferred by the LHC experiments. Compared to the present situation (Fig. 2.3), the intensity per bunch is 70% higher and brightness is more than doubled. The beam characteristics expected by the HL-LHC project (yellow dot) are approximately compatible with all identified limitations, except with the SPS one at 2×10^{11} p/b due to beam loading and longitudinal instabilities.

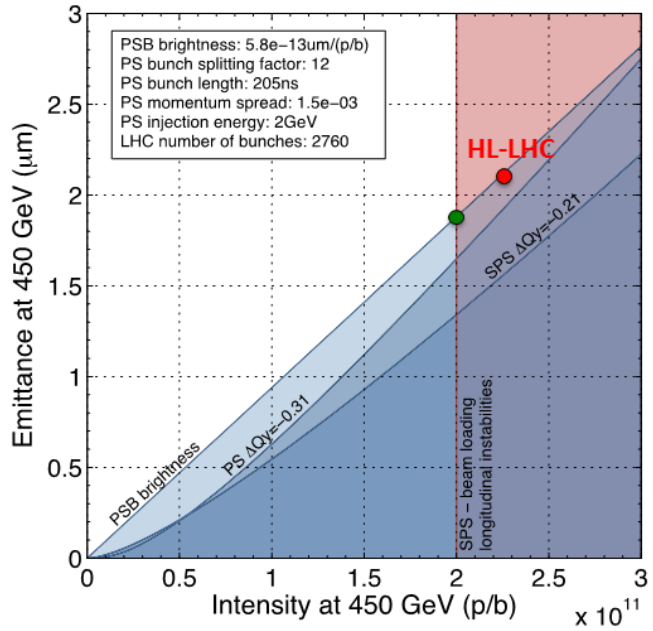


Fig. 2.5: Performance at SPS ejection of the upgraded LHC proton injector complex for 25 ns bunch spacing

The beam characteristics at injection in the successive accelerators [19] are summarized in Table 2.4 and compared to the achieved performance and to the ultimate goal of HL-LHC.

As a spare solution, in case the 25 ns beam cannot be used in the LHC (e.g. because of electron clouds or total beam intensity), 50 ns bunch spacing could be considered. More limitations would then have to be faced in the injectors:

- in the PS, mainly because of longitudinal instability, with an estimated limit is 2.7×10^{11} p/b, while the HL-LHC specification is at 3.5×10^{11} p/b;
- in the SPS, because of longitudinal instability and because of space-charge (the tune spread will reach 0.22 on the injection flat porch).

The performances shown in Fig. 2.5 and Table 2.4 are however only estimates which will have to be regularly revised during the ~10 years duration of the injectors' upgrade programme. As past experience with the CERN accelerators has shown, it is not unreasonable to hope that, as a result of the intense effort invested both in theory and in beam experiments [20], beam characteristics will finally exceed the present expectation and meet the present HL-LHC requirements. Similarly, the possibility cannot be discarded that the HL-LHC beam specifications will evolve as experience with the collider progresses.

Table 2.4: Beam characteristics at injection in the injection complex accelerators (cases in red are presently estimated to be beyond feasibility).

		PSB (1 b after capture, c=285 ms)						
		$N (10^{11} \text{ p})$	$\epsilon_{x,y} (\mu\text{m})$	$E (\text{GeV})$	$\epsilon_z (\text{eVs})$	$B_t (\text{ns})$	$\delta p/p_0$	$\Delta Q_{x,y}$
Achieved	50 ns	12.56	1.41	0.05	1.0	1100	$2.4 \cdot 10^{-3}$	(0.51, 0.61)
	25 ns	17.73	2.14	0.05	1.0	1100	$2.4 \cdot 10^{-3}$	(0.51, 0.59)
After LIU	50 ns	19.94	1.61	0.16	1.4	650	$1.8 \cdot 10^{-3}$	(0.36, 0.43)
	25 ns	29.55	1.55	0.16	1.4	650	$1.8 \cdot 10^{-3}$	(0.55, 0.66)
HL-LHC	50 ns	27.21	2.06	0.16	1.4	650	$1.8 \cdot 10^{-3}$	(0.40, 0.47)
	25 ns	34.21	1.72	0.16	1.4	650	$1.8 \cdot 10^{-3}$	(0.58, 0.69)

		PS (4+2 b/inj)						
		$N (10^{11} \text{ p/b})$	$\epsilon_{x,y} (\mu\text{m})$	$E (\text{GeV})$	$\epsilon_z (\text{eVs/b})$	$B_t (\text{ns})$	$\delta p/p_0$	$\Delta Q_{x,y}$
Achieved	50 ns	11.93	1.48	1.4	1.2	180	$0.9 \cdot 10^{-3}$	(0.24, 0.31)
	25 ns	16.84	2.25	1.4	1.2	180	$0.9 \cdot 10^{-3}$	(0.25, 0.30)
After LIU	50 ns	18.95	1.69	2.0	1.91	205	$1.0 \cdot 10^{-3}$	(0.15, 0.21)
	25 ns	28.07	1.63	2.0	3.00	205	$1.5 \cdot 10^{-3}$	(0.16, 0.28)
HL-LHC	50 ns	25.85	2.16	2.0	1.91	205	$1.0 \cdot 10^{-3}$	(0.18, 0.23)
	25 ns	32.50	1.80	2.0	3.00	205	$1.5 \cdot 10^{-3}$	(0.18, 0.30)

		SPS (4 × 36-72 b/inj)						
		after filamentation ($\epsilon_z = 0.35 \text{ eVs}$, $B_t = 4 \text{ ns}$ @inj)						
		$N (10^{11} \text{ p/b})$	$\epsilon_{x,y} (\mu\text{m})$	$p (\text{GeV/c})$	$\epsilon_z (\text{eVs/b})$	$B_t (\text{ns})$	$\delta p/p_0$	$\Delta Q_{x,y}$
Achieved	50 ns	1.89	1.55	26	0.42	3.0	$1.5 \cdot 10^{-3}$	(0.09, 0.15)
	25 ns	1.33	2.36	26	0.42	3.0	$1.5 \cdot 10^{-3}$	(0.05, 0.07)
After LIU	50 ns	3.00	1.77	26	0.42	3.0	$1.5 \cdot 10^{-3}$	(0.13, 0.21)
	25 ns	2.22	1.71	26	0.42	3.0	$1.5 \cdot 10^{-3}$	(0.09, 0.16)
HL-LHC	50 ns	4.09	2.27	26	0.42	3.0	$1.5 \cdot 10^{-3}$	(0.14, 0.24)
	25 ns	2.57	1.89	26	0.42	3.0	$1.5 \cdot 10^{-3}$	(0.10, 0.17)

		LHC ($n \times 144\text{-}288 \text{ b/inj}$)				
		$N (10^{11} \text{ p/b})$	$\epsilon_{x,y} (\mu\text{m})$	$p (\text{GeV/c})$	$\epsilon_z (\text{eVs/b})$	$B_t (\text{ns})$
Achieved	50 ns	1.70	1.71	450	0.46	1.60
	25 ns	1.20	2.60	450	0.39	1.47
After LIU	50 ns	2.70	1.95	450	0.60	1.65
	25 ns	2.00	1.88	450	0.60	1.65
HL-LHC	50 ns	3.68	2.50	450	0.67	1.70
	25 ns	2.32	2.08	450	0.65	1.65

Tables

2.1. Proton beam characteristics in 2012	22
2.2. Beam characteristics for the High Luminosity LHC project	24
2.3. Linac4 beam parameters	26
2.4. Beam characteristics at injection in the injection complex accelerators (cases in red are presently estimated to be beyond feasibility).	30

Figures

2.1. CERN accelerator complex in 2012	21
---	----

2.2. Longitudinal bunch-splitting to generate a 25 ns bunch train in the PS. (a) B field (blue) and beam current (red) during a PS cycle. Longitudinal controlled blow-ups (BU) are used for optimizing the gymnastics and avoiding longitudinal beam instabilities. 2D displays of longitudinal density at (b) 1.4 GeV and (c) 25 GeV. Time during the process is along the vertical axis. Longitudinal density is colour-coded from blue (no beam) to red (maximum)	23
2.3. Status and limitations of the beam characteristics of the LHC proton injector complex at SPS ejection, in 2012, (a) 25 ns bunch spacing; (b) 50 ns bunch spacing.....	25
2.4. 2D display (simulated) of longitudinal density in the PS during BCMS at 2.5 GeV. Time follows the vertical axis. Longitudinal density is colour-coded from blue (no beam) to red (maximum).	25
2.5. Performance at SPS ejection of the upgraded LHC proton injector complex for 25 ns bunch spacing.....	29

References

- [1] M. Benedikt, P. Collier, V. Mertens, J. Poole and K. Schindl (ed.), LHC Design Report Vol. III: the LHC injector chain, CERN–2004–003 (2004).
- [2] A. Blas *et al.*, Conversion of the PS complex as LHC proton pre-injector, CERN–PS–DI–97–048–DI, <http://cdsweb.cern.ch/record/328735/files/ps-97-048.pdf>, 1997.
- [3] O.S. Bruning, HL-LHC parameter space and scenarios, Proc. Chamonix Workshop on LHC Performance, Chamonix, 2012, CERN–2012–006, p. 315.
- [4] G. Iadarola *et al.*, Electron cloud and scrubbing studies for the LHC, IPAC2013, Shanghai, China, 2013, TUPFI002, p. 1331.
- [5] D. Manglunki *et al.*, Provisional List of Parameters for Ions in HL-LHC, EDMS Id. 1311644, 2014
- [6] R. Garoby, Status of the nominal proton beam for LHC in the PS, CERN–PS–99–013–RF (1999) <http://cdsweb.cern.ch/record/382971/files/ps-99-013.pdf>.
- [7] H. Damerau, Performance potential of the injectors after LS1, Proc. LHC Performance Workshop, Chamonix, 2012, p. 268.
- [8] M. Vretenar *et al.*, The Linac4 project at CERN, IPAC2011, San Sebastian, 2011, TUOAA03, p. 900.
- [9] K. Hanke *et al.*, PS Booster energy upgrade feasibility study (2010) <https://edms.cern.ch/document/1082646/3>.
- [10] S. Gilardoni *et al.*, PS potential performance with a higher injection energy, Proc. LHC Performance Workshop, Chamonix, 2011, p. 349.
- [11] S. Gilardoni *et al.*, Tune and space charge studies for high brightness and high intensity at CERN PS, IPAC2011, San Sebastian, Spain, 2011, MOPS014, p. 625.
- [12] E. Shaposhnikova, Lessons from SPS studies in 2010, Proc. LHC Performance Workshop, Chamonix, 2011, p. 359.
- [13] H. Bartosik *et al.*, Low gamma transition optics for the SPS: simulation and experimental results for high brightness beams, Proc. HB2012 Workshop, Beijing, China, 2012, WEO1B01.

- [14] H. Timko *et al.*, Longitudinal beam loss studies of the CERN PS to SPS transfer, Proc. HB2012 Workshop, Beijing, China, 2012, WEO1C03.
- [15] L. Drosdal *et al.*, MD on Injection Quality: Longitudinal and Transverse Parameters, CERN–ATS–Note–2011–063 MD, 2011.
- [16] G. Rumolo *et al.*, Proc. CARE-HH-APD Beam'07 Workshop (CERN, Geneva, 2007).
- [17] J.M. Jimenez, SPS: scrubbing or coating? Proc. LHC Performance Workshop, Chamonix, 2012, p. 339.
- [18] K.S.B. Li *et al.*, Modelling and studies for a wideband feedback system for mitigation of transverse single bunch instabilities, IPAC2013, Shanghai, China, 2013, WEPME042, p. 3019.]
- [19] G. Rumolo *et al.*, LIU Beam Parameters, EDMS Id. 1296306v.1, 2014.
- [20] G. Rumolo *et al.*, Summary of the LIU beam studies review, CERN–ATS–Note–2012–083 PERF (2012).

Chapter 3

Proton Synchrotron Booster

3.1 Upgrade path

3.1.1 Scope of the LIU-PSB project

The LIU-PSB project can be divided in two upgrade projects, which could either be implemented simultaneously or in two phases: the modification of the Booster injection (BI) line and injection region for 160 MeV H⁻ injection, and the energy upgrade of the Booster rings and extraction, including the transfer line to the PS, to 2 GeV.

The modifications of the injection region cover the section of the Linac4–PSB transfer line downstream of the concrete wall that separates the Linac and PSB access zones (downstream of BI.QNO20). The section of the transfer line upstream of this wall falls into the Linac4 project. The LIU-PSB project therefore comprises the modifications of most of the BI line as well as the modifications in the injection period of the PSB (periods 1/16). This includes the beam separation scheme (distributor and vertical septum), as well as the stripping foil and painting hardware and other associated modifications.

3.1.1.1 Upgrade of the PSB injection for 160 MeV H⁻

The change from Linac2 (50 MeV protons) to Linac4 (160 MeV H⁻) requires significant modifications to the injection line and injection period. The present beam separation scheme (distributor and vertical septum) cannot operate at the increased beam energy and needs to be replaced. This essentially implies re-building most of the BI line. More importantly, the charge-exchange injection scheme is fundamentally different from the present multi-turn injection scheme using a horizontal injection septum. The horizontal septum will be replaced by a stripper foil mechanism. In addition, new hardware is needed for the injection and painting bumps, diagnostics, etc. The details of the modifications and the new injection scheme will be described below.

3.1.1.2 Expected gain

The incoherent space charge tune shift at Booster injection can be expressed as

$$\Delta Q_x = \frac{R_p N_b}{2\pi^{3/2} \gamma^3 \beta^2 \sigma_z} \oint \frac{\beta_x(s) ds}{\sigma_x(s)[\sigma_x(s) + \sigma_y(s)]} \quad (3.1a)$$

and

$$\Delta Q_y = \frac{R_p N_b}{2\pi^{3/2} \gamma^3 \beta^2 \sigma_z \sqrt{\epsilon_y}} \oint \frac{\sqrt{\beta_y(s)} ds}{\sigma_x(s) + \sigma_y(s)} \quad (3.1b)$$

where R_p is the classical proton radius and N_b is the number of protons per bunch.

With the increase of beam energy from 50 MeV to 160 MeV the relativistic $\beta\gamma^2$ factor increases by a factor of 2, thus doubling the intensity that can be accumulated within a given emittance. This

would result in a factor of 2 increase in brilliance for the PSB. The main benefit would be for the ISOLDE type beams, where the intensity is expected to roughly double. The LHC will ultimately take advantage of the increased beam brilliance once the 2 GeV upgrade is in place.

A real gain is expected by changing the injection scheme to charge-exchange injection. While the present multi-turn injection is associated with a beam loss of about 50% of the intensity delivered by Linac2, the new scheme will be essentially loss-free (apart from a few percent lost due to stripping efficiency). Longitudinal capture losses are expected to be comparable with today's situation. Moreover, the new injection scheme will make it possible to tailor emittances by means of phase space painting according to the needs of individual users.

3.1.2 Energy upgrade of the PSB to 2 GeV

Following the Chamonix 2010 workshop [1] a study was performed to confirm the feasibility of an energy upgrade of the PS Booster to 2 GeV [2]. The underlying idea is to reduce space charge effects at injection into the PS, thus removing this bottleneck. This would increase beam brilliance through the LHC injector chain and eventually enable the injectors to deliver LHC-type beams to the highest specifications. The upgrade of the PSB to 2 GeV is presently planned for LS2.

3.1.2.1 Expected gain

The expected gain can be deduced from the ratio of the $\beta\gamma^2$ factor at 1.4 GeV and 2.0 GeV, which is 1.63 and that corresponds to an intensity increase of 60% within given emittance values.

3.2 Beam dynamics and collective effects

3.2.1 Introduction

Beam dynamics studies need to ensure the production and the optimization of the required high-brilliance and high-intensity beams, taking into account the upgrade modifications (Section 3.1), in particular the higher injection and extraction energies, the implementation of the H⁻ injection from Linac4, and the installation of new hardware.

On the one hand, studies are going on in parallel with the equipment specifications, to verify the impact of new hardware on the performance of the machine, and if necessary to find mitigation measures. On the other hand, a large effort is ongoing to improve our comprehension of the PS Booster and build optics and impedance models, refine our simulation tools and increase our confidence in their predictive power. This effort includes the validation of the code for the non-ultrarelativistic case and the benchmark for measurements of space charge dominated beams.

The beam dynamics issues during the fall of the H⁻ injection chicane bump are detailed in Section 3.3.1. The extra focusing induced by the edge effect of the rectangular chicane magnets induce beta beating. Moreover, multipolar components are also present due to eddy currents in the Inconel vacuum chamber during ramp-down. A correction scheme is discussed and beam simulations including space charge are shown, to validate it.

Section 3.2.2 describes the studies to build up the linear and non-linear optics models of the PS Booster. The final goal is to implement, in a deterministic way, a resonance compensation scheme to accommodate a large space charge tune spread. The outcome of the optics studies is used in the space charge simulations, described in Section 3.2.3, which require the best possible knowledge of the optics model to have good predictive power.

Space charge studies, the topic of Section 3.2.3, are used to evaluate the performance of the machine at low energy, in terms of emittances and losses, and will eventually help in optimizing the

working point, including chromaticity. The goal of these studies is to validate the effectiveness of the resonance compensation scheme for the production of high brightness beams and to minimize losses at low energy. Preliminary considerations for loss management are also presented in this section.

Section 3.2.4 describes the ongoing effort to build an impedance model for the PS Booster, including present and future hardware, in order to assess the stability limits in the machine, which is the topic of Section 3.2.5. A major complication in these studies is that the electromagnetic codes are not yet fully validated for the non-ultrarelativistic case. Studies are ongoing in this field.

Finally, Section 3.2.5 describes the instability studies in the PSB, which are useful to validate and improve the impedance model and that will eventually predict the stability limits, assess the impact of the new hardware and quantify the upgrade requirements for gain and bandwidth of the feedback system, which the PSB relies upon in operation.

3.2.2 Optics model

We are conducting optics studies in the PSB using two approaches: orbit response matrix measurements for linear optics and turn-by-turn studies for nonlinear optics. Orbit response analysis will allow for the measurement and correction of beta and dispersion beating and of linear coupling. It can also be useful for determining the distribution of errors in the machine, making the lattice model and therefore simulation results more accurate. The nonlinear optics analysis from turn-by-turn measurements will allow for characterization and correction of higher-order resonances. This resonance compensation will be necessary when beam intensity is increased and the tune footprint is larger, as it will no longer be possible to avoid all potentially dangerous resonance lines that could cause emittance growth and beam loss.

Turn-by-turn measurements can be used to determine linear optics as well as nonlinear optics, but we decided to make orbit response measurements as well, because orbit response should give more precise information about linear optics for the PSB. The current working point of the machine is not ideal for optics measurements using either of these methods; the phase advance between BPMs is close to 90° , and sampling a sinusoidal signal like betatron oscillations or closed orbit distortions at 90° intervals increases the uncertainty in determining amplitude and phase. However, the orbit response measurements contain information about the optics at the location of the dipoles in addition to information about the optics at the location of the BPMs, which should help to mitigate this problem. The precision of measurements via both techniques could likely be improved by changing the tune by $+0.5$ or -1.0 , thereby moving the phase advance per turn away from 90° .

3.2.2.1 Linear optics from closed orbits

The linear optics from closed orbits (LOCO) method involves measuring the linear response of the closed orbit to each orbit corrector dipole, at each beam position monitor. This matrix of (i BPMs \times j correctors) measured orbit responses is then compared to the model predictions, and one can solve for the set of variable model parameter values that minimizes the difference between measurements and model:

$$f = \sum_{i,j} \frac{1}{\sigma_{ij}^2} \left(\left(\frac{\partial x_i}{\partial \theta_j} \right)_{\text{model}} - \left(\frac{\partial x_i}{\partial \theta_j} \right)_{\text{meas}} \right)^2 \quad (3.2)$$

where $\partial x_i / \partial \theta_j$ is the measured or model orbit response at the i th BPM to the j th corrector, and σ_{ij}^2 is the uncertainty of the measurement. These variable model parameters typically include dipole and corrector gains and tilts, and normal and skew quadrupole errors. If the goal is to correct optics distortions, the variable quadrupole parameters should be placed at the location of normal and skew quadrupole corrector elements in the machine. Then, if there are enough correctors available, one can correct beta beating and transverse linear coupling by setting the normal and skew quads according to

the results of the LOCO fitting. If the quad correctors are not adequate to fully correct the observed distortions, one can still use LOCO to calibrate the model so that errors are properly described. In this case it may be more useful to place the variable quad parameters at the location of the focusing triplet quads.

We measured the response of all 13 available orbit corrector dipoles per plane, in each of the four rings. We also measured the dispersion in each ring and included those measurements as a column in the orbit response matrix for the analysis, which reduces the ambiguity between dipole strength errors and BPM gain errors found from LOCO fitting. The orbit was measured with three settings for each dipole (negative, zero and positive current), and was measured five times at each setting to reduce the uncertainty from pulse-to-pulse orbit variation. Linear fits were done of the measured orbit position at each BPM vs. each dipole kick, and the slope and the standard error of the slope were used as the measured orbit response and the uncertainty of the measurement. The MADX model used for the analysis included alignment data for bending magnets, triplet quads and BPM/multipole stacks from the most recent survey.

The orbit response measurements are consistent with very small quadrupole errors and beta beating of only a few percent, but the uncertainty on the calculated quadrupole errors is very large. This analysis can be improved by repeating the measurements at different working points. Also, some of the measurements had relatively large uncertainty due to pulse-to-pulse variation in closed orbit, which increased the uncertainty of the calculated parameter errors. This effect can be mitigated by automating the measurement process, allowing for more precise measurements with larger statistical samples to be made quickly.

These measurements show that there is significant transverse coupling, but it is consistent with MADX predictions when surveyed magnet tilts and offsets are included in the model. The realignment campaign during Long Shutdown 1 (LS1) should reduce transverse coupling, but any remaining coupling could be corrected with the skew quad correctors based on LOCO results.

In addition, the polarities of all BPMs and orbit correctors in all rings have been determined through these measurements.

3.2.2 Turn-by-turn nonlinear optics measurements

Nonlinear resonances will be characterized by analysis of turn-by-turn trajectory measurements. This method involves creating coherent betatron oscillations in the beam and measuring the trajectory at all BPMs around the ring, and then analysing the amplitude and phase of higher-order frequencies in the spectra of the trajectories at each BPM. These resonances will then be compensated using multipole correctors, which will reduce beam losses and emittance growth in the case that the tune footprint crosses these resonance lines.

All BPMs in the rings are being upgraded during LS1 to make them capable of acquiring turn-by-turn position data. A few BPMs were available for trajectory measurements before LS1, and trial measurements were made with these BPMs using a variety of methods for exciting coherent transverse oscillations. The issues and challenges discovered from these trial measurements are being resolved, and we expect to be ready to proceed quickly with the full measurements after LS1.

3.2.3 Performance with space charge (emittance and losses)

The PSB beam dynamics at low energy is dominated by space charge effects. The new charge-exchange injection at 160 MeV will yield higher brightness beams compared to the conventional 50 MeV multi-turn injection from Linac2. Since the space charge tune spread scales with $1/(\beta\gamma^2)$, the increase of the injection energy from 50 MeV to 160 MeV leads to potentially a factor 2 brightness increase for the same ΔQ . Moreover, thanks to the H⁻ charge exchange injection, it will be possible to paint in the transverse phase space and produce tailored emittances.

Studies aim to understand the maximum space charge tune spread acceptable at injection and, more precisely, to predict the curve emittance vs. intensity with Linac4, after optimization of the longitudinal distribution and of the working point (including chromaticity) and possibly by compensating for harmful resonances.

3.2.3.1 Measurements of maximum tune spread for injection from Linac2

In 2012 measurements were performed to identify the maximum achievable tune spread in the present configuration [3]. Figure 3.1 shows the curve emittance vs. beam intensity for a longitudinal distribution corresponding to cavities $h = 1$ and $h = 2$ in anti-phase and at maximum voltage ($V = 8$ kV), in order to maximise the acceptance and the bunching factor. This results in a vertical space charge tune spread $\Delta Q_y = 0.77$ at 60 MeV for the highest possible intensity of $\sim 1000 \times 10^{10}$ and with relative losses of maximum 14%. One can notice that for intensities smaller than 500×10^{10} , i.e. for vertical tune spreads smaller than 0.5, there is no emittance blow-up along the ramp and the losses are below 5%. Moreover, the measured points lay on a straight line, the slope of which is actually a function of the longitudinal emittance.

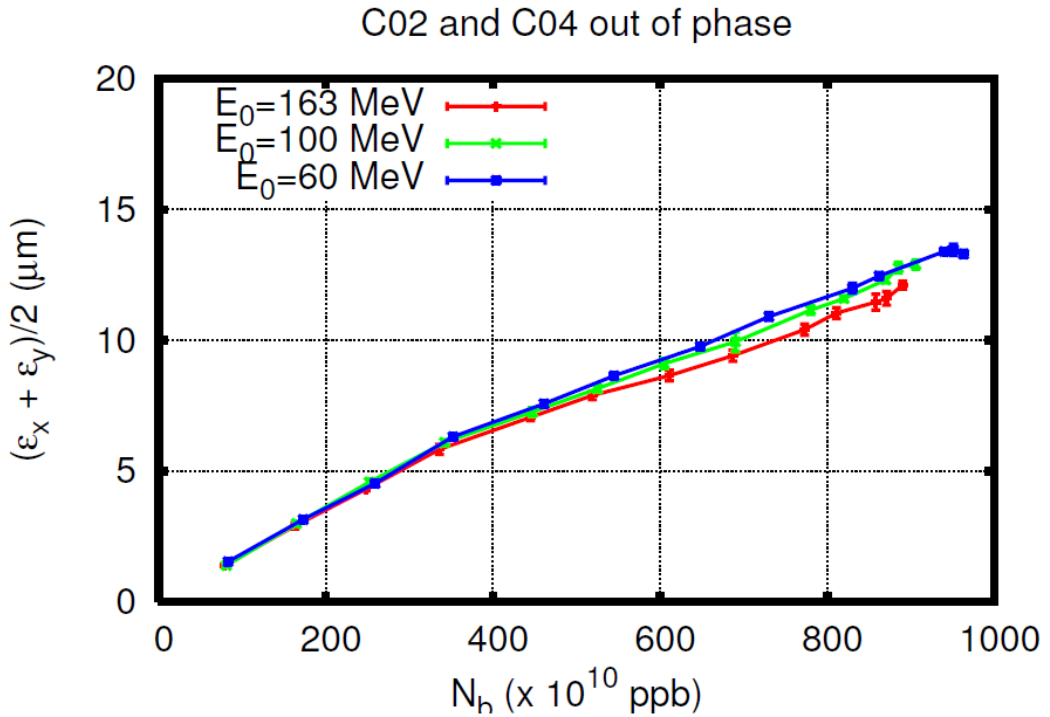


Fig. 3.1: Measured rms normalized average transverse emittance as a function of bunch intensity for 60 MeV, 100 MeV and 163 MeV [3].

The conclusion of this work is that the PSB is able to successfully accelerate beams with a tune spread much larger than 0.5, with limited losses. These studies were done without optimizing the working point and without resonance compensation, and give us reasonable confidence that the production of beams for the LHC Injector Upgrade and the HL-LHC, with a maximum tune spread close to 0.5, is within reach.

One question that still remains to be addressed is whether the conservation of transverse emittance still holds when a tune spread of 0.5 is obtained with lower intensities and much lower transverse emittances (i.e. 350×10^{10} ppb within 2 μm instead of 500×10^{10} ppb within 8 μm rms averaged emittance). To answer this question, simulations of the full H⁻ injection process based on a consistent and fully benchmarked optics model are required.

3.2.3.2 Code benchmark with measurements

A large set of measurements were made in 2012–2013 to benchmark our simulation tools [4].

PTC-Orbit [5], the code chosen for the studies, is made out of a combination of PTC libraries, for accurate single-particle tracking, with Orbit for the collective effects calculations. The PSB ring is divided into 200 nodes in which the space charge is computed in a self-consistent way using 2.5 D particle-in-cell methods, while the tracking in between the nodes, through the accelerator elements, is done in a symplectic way with PTC.

Code benchmarking with the measurements gives very good results [6] when the optics errors, derived from the analysis described in Section 3.2.2, are included in the model. In particular there is a very good quantitative agreement in terms of beam losses, longitudinal profiles and transverse emittance evolution between the simulations and the measurements close to the half-integer.

Figure 3.2 shows the evolution of the beam intensity and the comparison between the measurements and the simulations including or not including field and alignment errors, for a programmed tune of $Q_x = 4.28$, $Q_y = 4.53$. Simulations for the ideal machine (matched to a $Q_y = 4.517$, which is closer to the measured tune) show no losses as expected while, if all the errors are properly included, there is a very good agreement in term of loss evolution. The simulations also manage to well reproduce the change of slope at around 570 ms. Figure 3.3 presents the measured and simulated longitudinal phase space tomogram at the beginning and at the end of the measurement window, which shows how the simulations are correctly reproducing the physics behind the losses: particles with large synchrotron amplitudes, which are sitting exactly on the half-integer resonance line, are lost. As the intensity decreases, the space charge tune spread is also reduced and new particles are brought onto this line and lost again [7]. One should note here how the code’s predictive power relies on the machine optics model.

Measurements close to the integer [6] are more difficult to reproduce in a quantitative way, since knowledge of both linear and non-linear models is required. Simulations close to the $Q_v = 4.0$ line, however, are evidence for the strong contribution of the chromaticity and of the closed orbit distortion in the dynamics of the losses. Further simulations and measurements are planned to better study the effect of chromaticity and how it entangles with space charge effects, e.g. one of the measurements planned for the 2014 run foresees a corrected vertical chromaticity.

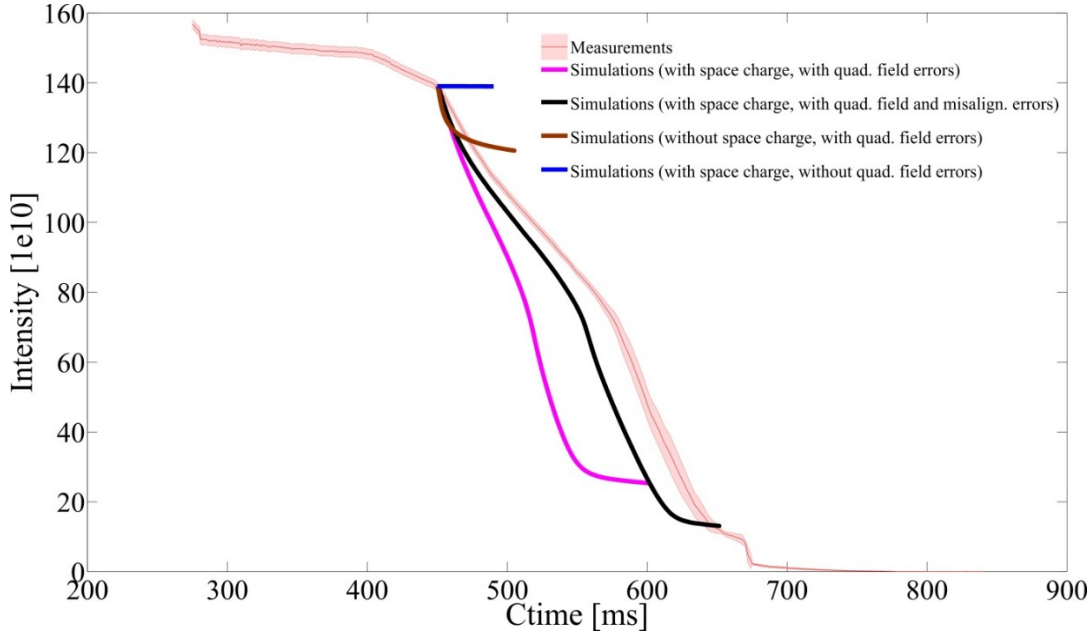


Fig. 3.2: Intensity evolution for $Q_x = 4.28$, $Q_y = 4.53$ (programmed). In red, the measurement results with the error bar; in blue the simulations for an ideal lattice (no errors); in magenta the simulations with only field errors (Section 3.2.2); in black with the full set of field and alignment errors. For comparison, in brown, simulations with errors but no space charge [6].

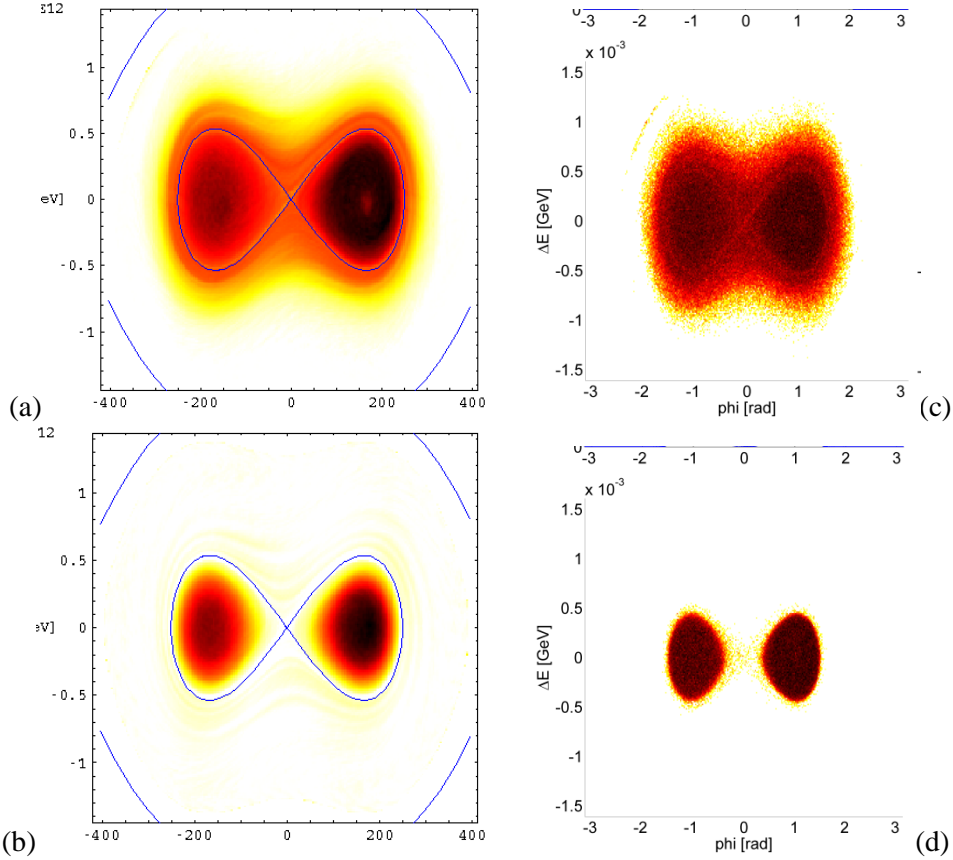


Fig. 3.3: Tomoscope profiles at (a) C450 and (b) C600 compared with simulated beam profiles (c) C450 and (d) C600 [6].

3.2.3.3 Space charge studies for losses

The increase of beam intensity and energy will lead to potentially more harmful losses and a strategy to mitigate them and/or to control their location needs to be envisaged.

Studies are ongoing to understand the present PS Booster beam loss pattern and activation mechanisms via machine development studies with high-intensity, large emittance beams. PTC-Orbit simulations are being set up to reproduce the measurements of intensity evolution and beam profiles at low energy, where space charge plays a major role in the creation of halo and beam losses. This will allow gauging the computational tools against experimental data and using them reliably to predict losses in future scenarios with higher injection energy and H⁻ injection.

In parallel, the feasibility and effectiveness of a collimation system in the machine is being investigated, to remove the halo and thereby control the location of the beam losses. Since a multi-stage collimation system such as in the LHC is not suited at 160 MeV [8], the studies are now focusing on a one-stage collimator, which makes use of a scraper (or absorber).

Currently in the machine there is a well-localized aperture restriction, the so-called beam scope window (BSW), which was used in the past for destructive profile measurements and currently for ‘shaving’ operational beams to a controlled and reproducible intensity value. The goal is to identify from beam physics considerations the appropriate aperture, thickness and material for a new absorber to replace the BSW, taking into account the existing PSB space constraints. Simulations will be the tool to validate and eventually optimize the choices.

3.2.4 Beam coupling impedance

An accurate impedance model is needed in order to determine the effect on beam stability and assess the impact of the new devices to be installed in the machine, with both the present and future beam parameters [9, 10].

3.2.4.1 PSB impedance model

A first attempt to build the PSB impedance model was made in the PhD thesis of D. Quatraro [11]. In particular, attention is focused on the model of the wall impedance, which includes a resistive wall and indirect space charge. Moreover, based on tune shift measurements and the wall impedance model, a so-called ‘broadband impedance’ was also estimated (i.e. measured impedance after subtracting the wall impedance) at different energies. These studies led to the conclusion that at injection about 50% of the measured tune shift can be attributed to indirect space charge and that the broadband impedance decreases with the relativistic beta.

A more detailed impedance model of the PSB could help explain the behaviour of the measured tune shift at different energies. Presently, there is an ongoing effort to build an impedance model and continuously refine it according to the modifications in the machine or new understandings. The first version of the impedance model, which we present here, includes the extraction kicker with cables, a detailed model of the resistive wall, the transitions between different vacuum chambers and the indirect space charge.

Indirect space charge impedance

Up to now the indirect space charge impedance was estimated assuming the PSB to have an elliptic beam pipe (half-height $h = 32$ mm and half-width $w = 80$ mm) for one-third of the circumference and a circular one for the remaining two-thirds (radius $r = 80$ mm) [11].

However, since indirect space charge impedance is expected to play a major role, a more accurate calculation based on the PSB aperture model [12] has been performed. For a circular chamber

the indirect space charge impedance has been analytically calculated. Using the appropriate form factors [13], the calculation has been extended to rectangular or elliptic geometries.

Resistive wall impedance

As for the indirect space charge in Ref. [11] the resistive wall impedance was estimated assuming the PSB to have an elliptic beam pipe (stainless steel half-height $h = 32$ mm and half-width $w = 80$ mm), and a circular one for the remaining two-thirds (stainless steel radius $r = 80$ mm). The elliptical pipe was approximated to a circular pipe with radius $r = h$. Stainless steel was used with an electrical conductivity $\sigma_{\text{el}} = 10^6$ S/m and a relative permeability $\mu_r = 8$.

Here we present a more accurate calculation based on the aperture model that accounts for the different PSB vacuum chambers. The calculation has been performed with the new TL wall code, based on a transmission line model [14]. In Table 3.1 the main parameters used for the calculation are summarized. As an example, Fig. 3.4 shows the generalized horizontal and vertical resistive wall impedance of the PSB at $E_{\text{kin}} = 160$ MeV. The largest contribution to the resistive wall impedance is given by the bending magnets due to the very thin wall (0.4 mm). Due to the very thin layer, assuming an electrical conductivity of 7.7×10^5 S/m, the skin depth becomes larger than the wall thickness for frequencies below 2 MHz. Therefore, below this frequency the impedance becomes strongly dependent on the background material. Figure 3.5 shows a comparison of the resistive wall impedance with vacuum and iron backgrounds. The iron has been modelled as a silicon-steel similar to that of the SPS [14]. The dispersion model for the permeability μ has been obtained as

$$\mu = \mu_0 \mu_r(B) = \mu_0 \left(1 + \frac{\mu_i(B)}{1 + j f / f_{\text{rel}}} \right) \quad (3.3)$$

where $f_{\text{rel}} = 10$ kHz [15]. The relative permeability μ_r is a function of the magnetic field B and thus of the particle momentum. The behaviour of μ_i as a function of B can be found in Ref. [16]. The variation of the resistive wall impedance due to the variation of μ_r during the PSB cycle has been estimated to be lower than 5%.

Table 3.1: Main parameters of the resistive wall calculation for the different vacuum chambers: thickness of the wall, electrical conductivity of the wall and background material.

	Wall thickness	Wall (σ_{el})	Background material
Dipoles	0.4 mm	7.7×10^5 S/m	Iron (silicon steel)
Quadrupoles	1.5 mm	1.3×10^6 S/m	Iron (silicon steel)
Straight sections	1 mm	1.3×10^6 S/m	Vacuum

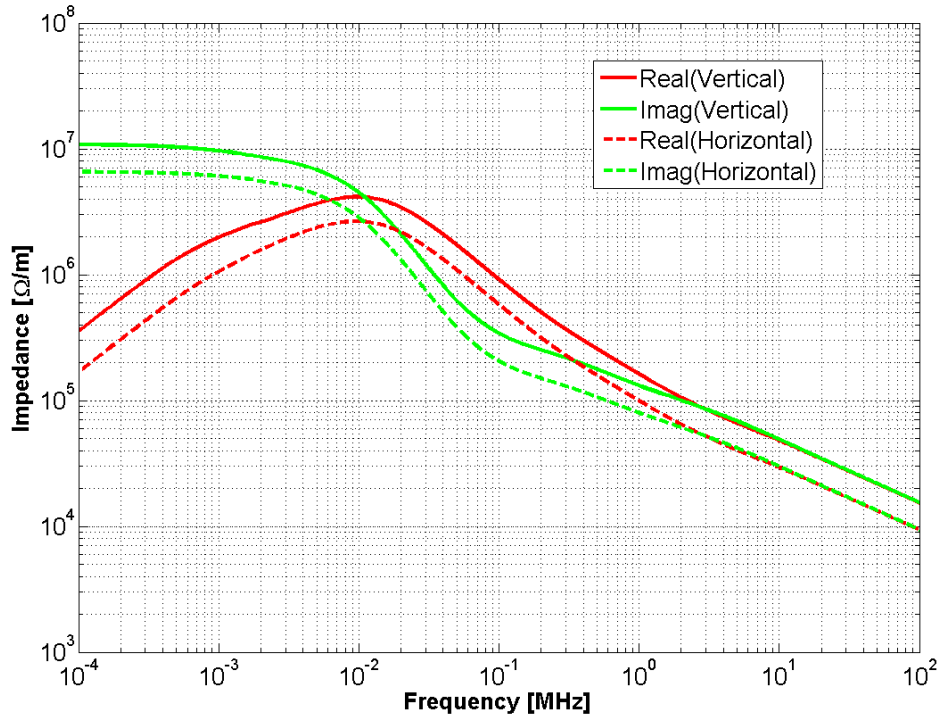


Fig. 3.4: Vertical (full lines) and horizontal (dashed lines) generalized (driving + detuning) resistive wall impedance of the PSB at 160 MeV kinetic energy.

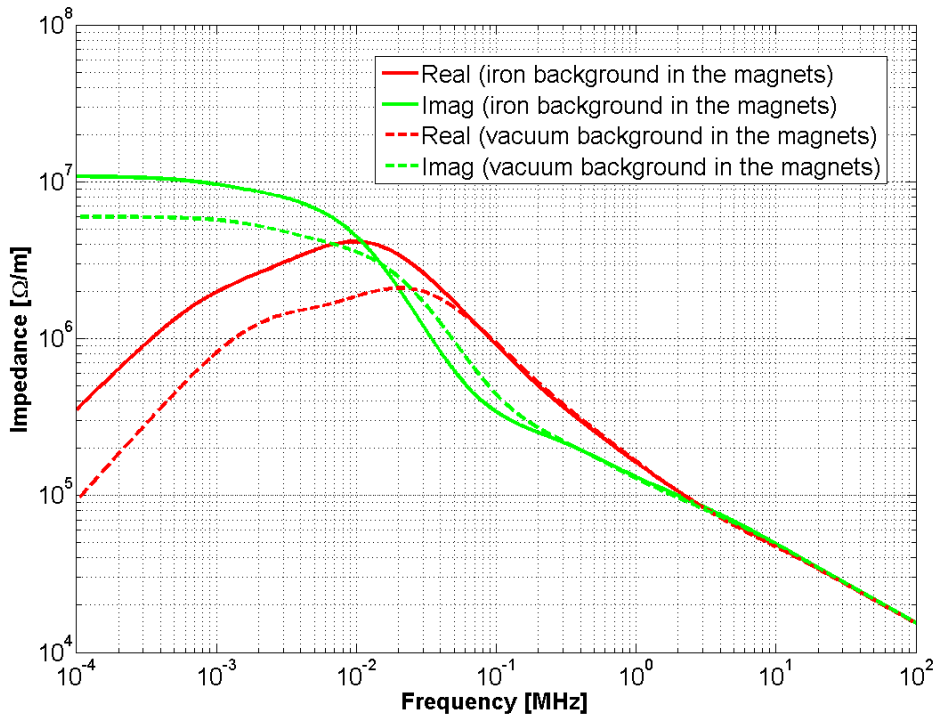


Fig. 3.5: Vertical generalized impedance of the PSB at 160 MeV kinetic energy: comparison between the calculations assuming iron background in the magnets (full lines) and those assuming vacuum background (dashed lines).

PSB extraction kicker

The contribution of the PSB extraction kicker has been estimated, resorting to the theoretical model described in Refs. [14, 17]. The broadband impedance of the ferrite-loaded structure is separated from the impedance due to the coupling to the external circuits. Due to the geometry of the kicker, the ferrite mainly determines the vertical impedance, while the external cable connections have an important impact on the horizontal impedance. The contribution due to the ferrite-loaded structure is calculated by means of the Tsutsui model extended to the nonrelativistic case [18, 19]. The impedance due to the coupling to the external circuits has been obtained approximating the kicker as an ideal transformer [14, 17] placed in a transmission line with different terminations of the cables on either side (short-short, open-open, open-matched and open-short). As an example, Fig. 3.6 shows the contribution due to the ferrite-loaded structure of the kicker for the vertical impedance and Fig. 3.7 shows the contribution due to the coupling to the external circuits for the horizontal impedance in the open-short configuration, which is the closest to reality [20].

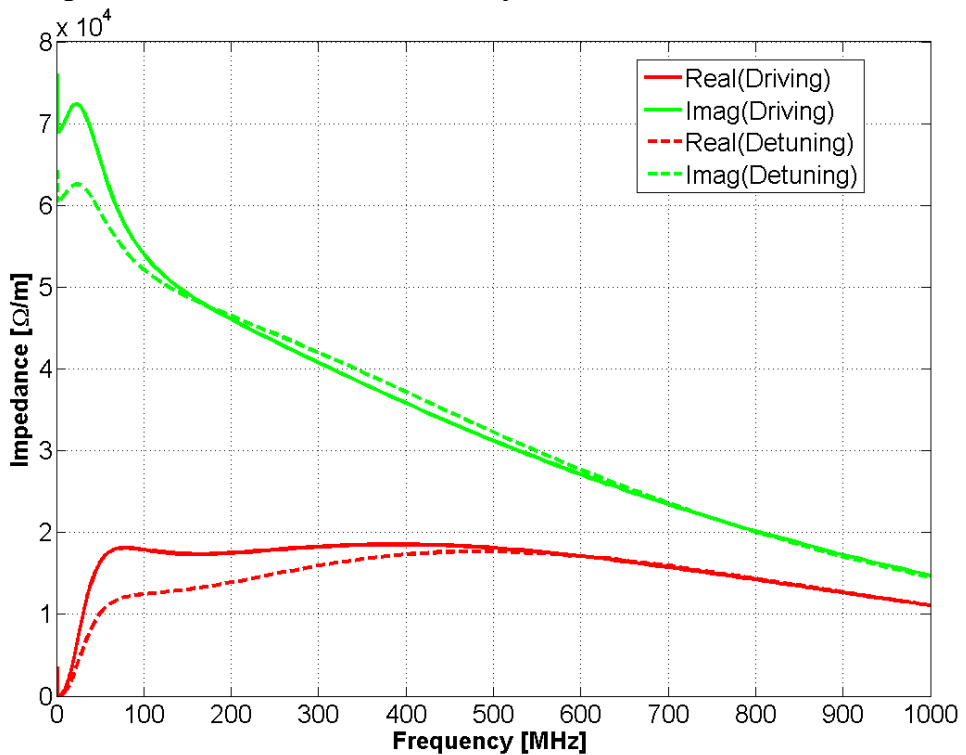


Fig. 3.6: Vertical driving (full lines) and detuning (dashed lines) impedance of the ferrite-loaded structure of the PSB extraction kicker at 160 MeV kinetic energy.

Transitions

Based on the results of 3D EM simulations, the broadband impedance contribution due to an abrupt transition is independent of the relativistic beta. Therefore, based on the aperture model, the generalized broadband impedance of the PSB transitions has been calculated as:

$$Z_{\text{transitions}} = \sum_{i=1}^N Z_i n_i \quad (3.4)$$

where N is the number of different transitions, Z_i is the broadband impedance of the transition i and n_i is the number of occurrence of the transition i .

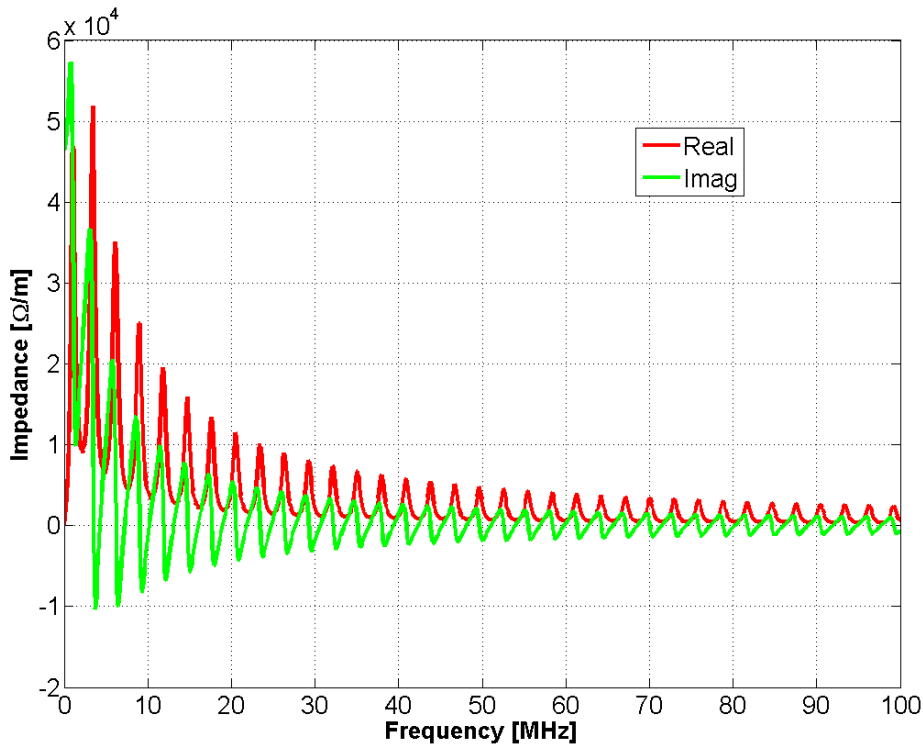


Fig. 3.7: Horizontal driving impedance due to the coupling to the external circuits of the PSB extraction kicker at 160 MeV kinetic energy.

New devices to be installed: Finemet cavities and vacuum chamber of the new H^- region

CST EM studio [21] simulations based on the 3D model described in Ref. [22] indicate that the beam coupling impedance of the Finemet cavities is weakly dependent on the relativistic beta. So, the study that was done for the PS [19] should also be representative for the PSB.

Concerning the vacuum chamber for the H^- injection region, two different solutions have been studied: a corrugated Inconel chamber and a titanium coated ceramic chamber. The studies led to the conclusion that the corrugated chamber and ceramic chamber are equivalent from the impedance point of view [23].

3.2.4.2 Summary

Figure 3.8 shows the full PSB impedance model including all the impedance sources analysed, weighted by the respective length and beta functions (resistive wall, indirect space charge and kicker with cables and steps) for the horizontal and vertical driving impedances. Table 3.2 summarizes the contribution to the coherent tune shift of the different elements in terms of effective impedance at 160 MeV, 1 GeV and 1.4 GeV. The last row also displays the measured tune shifts [11]. From the comparison between the expected and measured values, it is clear that, while both measurements at 1 GeV and 1.4 GeV are consistent with a missing $\sim 2 \text{ M}\Omega/\text{m}$, the measurement at 160 MeV seems to suggest a discrepancy of $\sim 4 \text{ M}\Omega/\text{m}$.

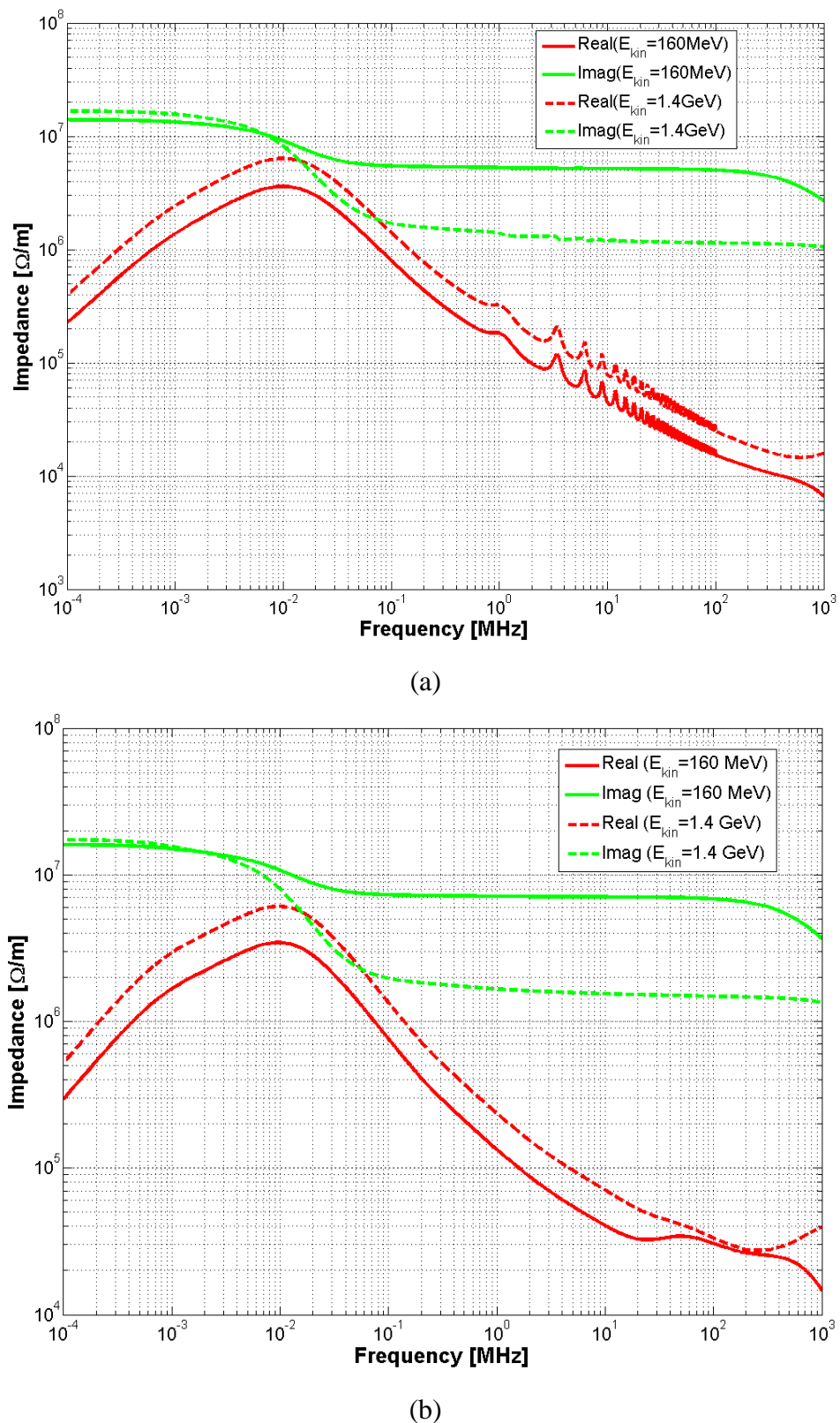


Fig. 3.8: Total (a) horizontal and (b) vertical driving impedance of the PSB at 160 MeV and 1.4 GeV kinetic energy.

3.2.4.3 Conclusions

The present PSB impedance model compared to the measured coherent tune shift underestimates the vertical impedance by a factor of between 1.4 and 2 depending on the particle momentum. Concerning the horizontal impedance, only a few data measurements were available, and measurements should probably be repeated with corrected chromaticity. The small slope of the horizontal tune with intensity can be explained by a combination of the lower impedance effect (see Table 3.2) and the presence of machine elements with negative generalized impedance in the horizontal plane (e.g. kickers [14]).

3.2.4.4 Future plans

CST 3-D EM simulations are widely used to estimate the impedance contribution of the different devices along the CERN accelerator complex.

Unlike the highly relativistic case, in which the reliability of the EM solver has been proved in many specific cases by comparing simulations with analytical results or bench measurements, the nonrelativistic case has not yet been fully validated. In order to use CST 3-D EM simulations systematically for the PS Booster a validation campaign is in progress. The main complication to singling out the beam coupling impedance, as resulting from the interaction of the beam with the surroundings, consists of defining a reliable procedure for removing the strong contribution of the direct space charge of the source bunch, which is included in the EM calculation.

CST 3D EM simulations will be used to continue characterizing the PSB devices in terms of impedance.

Table 3.2: Vertical effective impedance of the elements included in the PSB impedance model for the mode $l = 0$. The last row shows the vertical effective impedance extrapolated from the measured coherent tune shift in Ref. [11]. In the horizontal plane the measured tune shift was almost negligible.

	$E_{\text{kin}} = 160 \text{ MeV}$ ($\text{M}\Omega/\text{m}$) (x/y)	$E_{\text{kin}} = 1.0 \text{ GeV}$ ($\text{M}\Omega/\text{m}$) (x/y)	$E_{\text{kin}} = 1.4 \text{ GeV}$ ($\text{M}\Omega/\text{m}$) (x/y)
Indirect space charge	1.50/8.80	0.29/1.68	0.19/1.10
Kicker cables	0.0084/0	0.012/0	0.0105/0
Kicker ferrite	-0.044/0.13	-0.04/0.11	-0.04/0.11
Steps	0.53/0.63	0.53/0.63	0.53/0.63
Resistive wall	0.03/0.05	0.04/0.07	0.04/0.07
Total (expected)	2.03/9.62	0.83/2.49	0.73/1.91
Total (measured)	?/13.4	?/4.6	?/3.8

3.2.5 Beam stability

Transverse instabilities in the CERN PS Booster have been observed since the beginning of its operation in the early 1970s [24] and were among the first experimental observations of head-tail modes in bunches. In the following years, the problems of transverse beam instability in the PS Booster were successfully addressed and cured by the installation of a transverse feedback system [25]. Currently, no operational beam going through the PS Booster suffers from transverse instabilities, and intensities up to 10^{13} protons per ring can be accelerated and extracted in routine operation. High-intensity beams (i.e. with intensities in the range 5×10^{12} – 10^{13} protons per ring) are presently used for ISOLDE experiments or for fixed target physics in the downstream machines (PS and SPS). The LHC beams can be ranked as low intensity for the PS Booster in their current parameter range as well as for the beam parameter space targeted within the LIU and HL-LHC project [9].

However, it is well known that, especially when accelerating high intensity beams, beam stability in the PSB is strongly dependent on the correct operation of the horizontal feedback system. At some specific timings of the PSB magnetic cycle, coherent oscillations in the horizontal plane

appear in the absence (or failure) of the damper, leading to unstable centroid motion and losses. These coherent instabilities are observed to occur at reproducible cycle timings, as indicated by the blue lines in Fig. 3.9. Since these losses are intensity-dependent, they usually can be observed at later cycle timings than the one at which the first instability sets in, though only if the feedback switch-off time is set to permit the beam to go through the first instability without losses. While not posing any operational limitation for the PSB, these instabilities have been an object of study during several machine development sessions over the years. The reason is that a detailed analysis of their features could potentially lead to the identification of the responsible impedance sources in the PSB. This would be an important result, in terms both of extrapolating the stability of the PSB operation with future (possibly higher) intensity beams and opening the possibility of implementing impedance reduction measures to remove the cause of the instability.

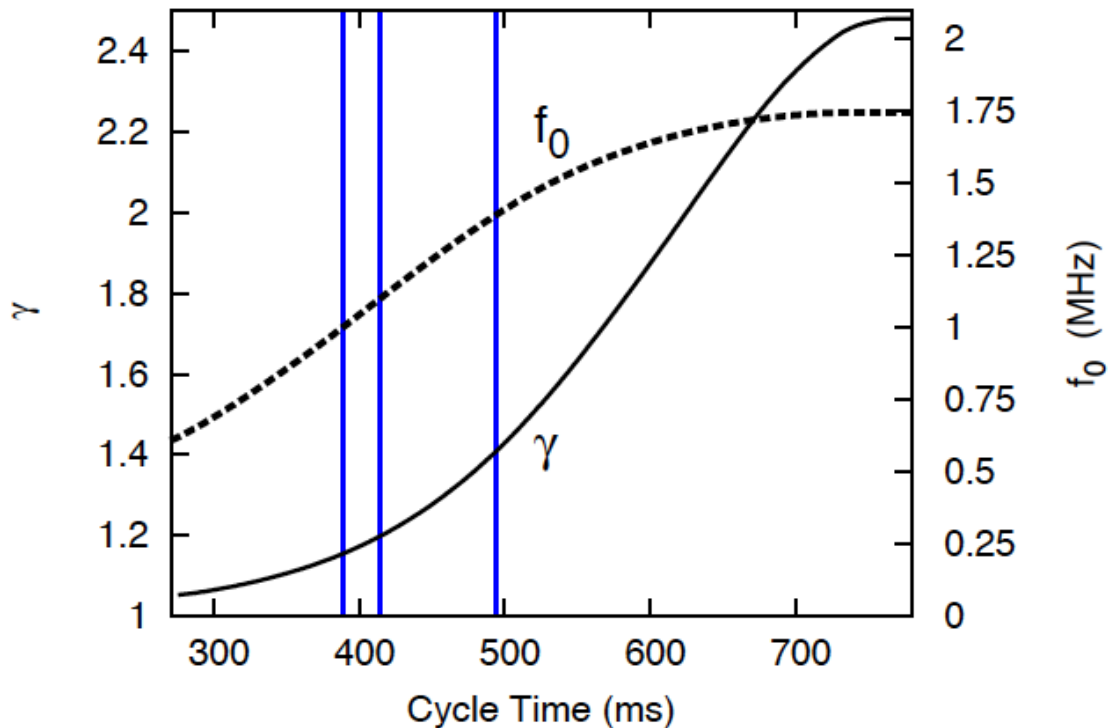


Fig. 3.9: The PS Booster cycle: the full line shows the relativistic Lorentz factor (left vertical axis), the dashed line corresponds to the revolution frequency (right vertical axis). The blue lines indicate the cycle times at which unstable transverse oscillations and the related losses are observed.

3.2.5.1 Some experimental observations

Several machine development sessions were devoted during the 2012–2013 run to better characterize the PSB instabilities, in an attempt to gain a deeper insight into the impedance that triggers them. The main observation in all cases is a strong oscillation in the horizontal plane (the oscillation in the vertical plane appears later and is driven by x - y coupling), for which the delta pick-up signal shows a clear exponential growth accompanied by a coherent intra-bunch motion. The first unstable motion, which is also the most widely studied, occurs at a cycle time of about 380 ms and manifests itself only above a certain intensity threshold (depending on machine settings, i.e. bunch shape and working point). The possible conditions that have been explored over the different MD sessions are: different working points, different RF settings (allowing for single RF, double RF in bunch lengthening and shortening modes), horizontal damper gain and chromaticity. We will describe some of the main findings from these MD sessions below.

Scan of the working point

A systematic shift of the instability occurrence time has been observed in a series of measurements while varying the horizontal tune around the time of the instability. Table 3.3 shows the horizontal tune in PSB (around cycle time 380 ms) and the corresponding instability occurrence time.

Table 3.3: Horizontal tune and instability occurrence time

Tune	Instability cycle time (ms)
4.19	384
4.20	386
4.23	389
4.25	392

RF settings

Measurements of instabilities were taken with different settings of the two main RF systems (C02 and C04) in order to tailor differently the longitudinal bunch shape. In particular, the instability (threshold and rise times) was studied for different configurations over several different MD sessions. During a first study, measurements were conducted with single RF (C02, i.e. $h = 1$, with $V_1 = 8$ kV) and then with double RF ($h = 1 + 2$) with two different voltage values on the C04 RF system ($V_2 = 4$ kV and $V_2 = 8$ kV). The first $h = 1 + 2$ configuration produced a bunch with flattened longitudinal profile, while the second configuration corresponds to the PSB operational standard setting in the first part of the magnetic cycle. The typical bunch profiles for the two cases with double harmonic as well as the relative horizontal delta signals, which show the instability form, are displayed in Fig. 3.10.

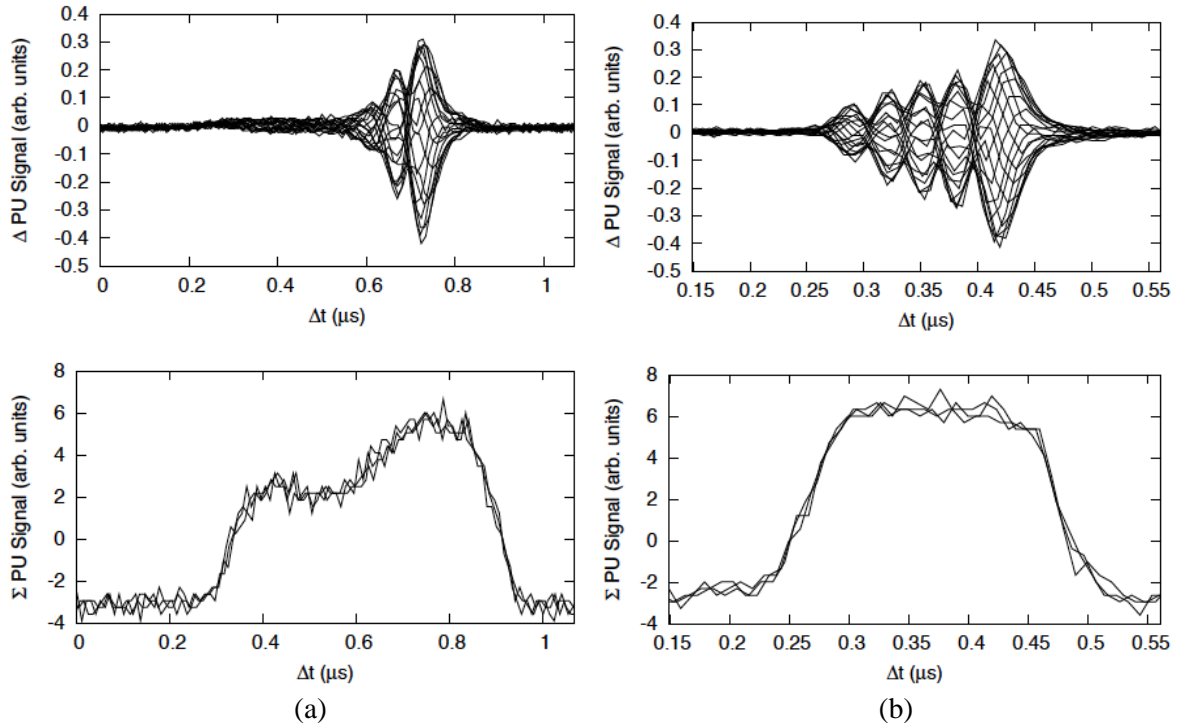


Fig. 3.10: The pick-up signals of the instability observed in the PSB with double-RF operation. (a) Standard operation, (b) flattened bunch profile, at the cycle time 493 ms, with $N_p = 500 \times 10^{10}$ ppb and a measured growth rate of 0.08×10^{-3} .

The instability growth rates (as the inverse of thousands of turns) as a function of intensity for the different voltage settings are plotted in Fig. 3.11 [26]. The intensity thresholds, above which the

instability appears, are also highlighted. The figure shows that the most unstable case is the flattened bunch longitudinal profile, while the most stable one is the PSB standard double harmonic bunch. This reveals that the magnitude and spread of the synchrotron tunes play a role in the instability mechanism.

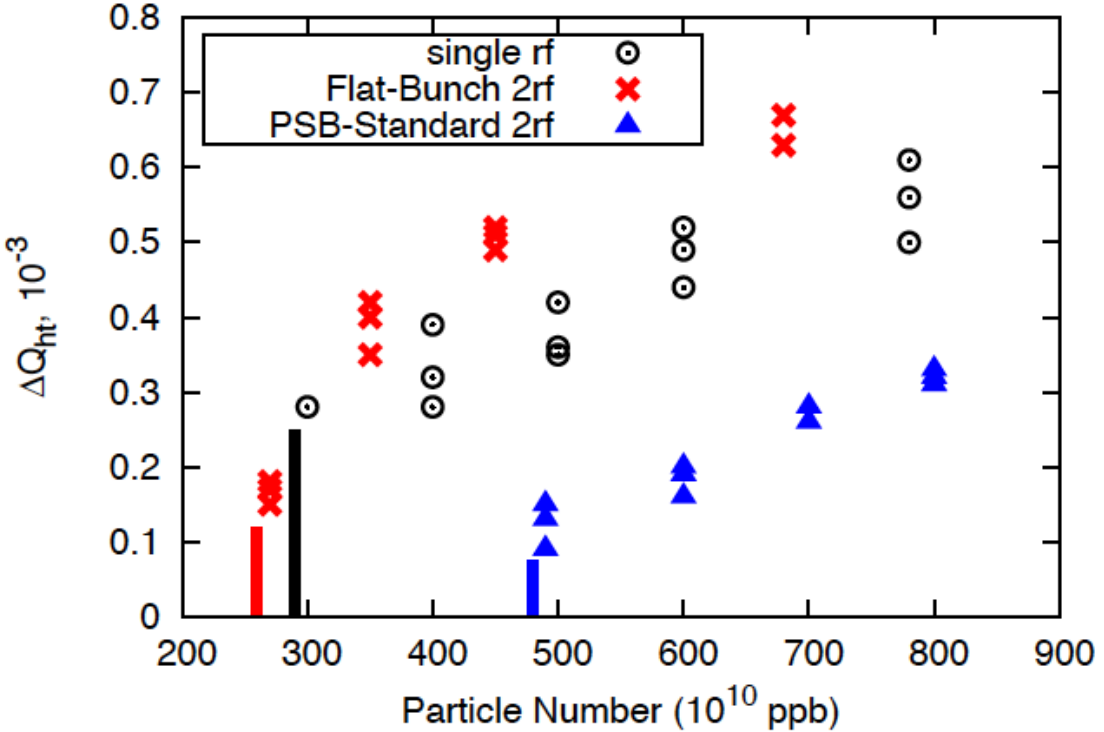


Fig. 3.11: Summary for the growth rates of the horizontal instability in the PSB observed around the cycle time 386 ms. The vertical bars indicate the intensity thresholds of instability for RF operation with the corresponding colour.

At the beginning of 2013, additional measurements have been taken with single RF and double RF in bunch lengthening and shortening mode (i.e. with $V_2 = 4$ kV and then C04 in opposition of phase or in phase with C02, respectively). The results of these MD sessions are still being analysed.

Chromaticity and damper gain

Although the results of these measurements can be still considered very preliminary, it is worth mentioning that a few MD sessions in 2013 were also devoted to studying the dependence of the occurrence of instability on the chromaticity and damper gain settings. In particular, the horizontal chromaticity was trimmed between -8 and $+8$ (Q' units) with respect to the operational value of around -4 . We should emphasize at this point that, since the PSB only has one family of sextupoles for chromaticity trims, the change of the horizontal chromaticity also resulted in an opposite change of the vertical chromaticity. During this exercise, it was observed that the chromaticity setting had a clear impact on both the instability threshold and the measured intra-bunch pattern. In particular, the bunch was found to be much more stable with chromaticity around -8 , while the instability also still appeared with positive chromaticity values. Concerning the influence of the damper gain, a scan of the values was made in PSB operational conditions. In general, it was found that even the lowest gain was enough to suppress the instability up to very large intensity values. A more detailed analysis of these MD data will be conducted in the near future to be able to quantify the needed feedback system gain to ensure stability of all the PSB operational beams.

3.3 Injection line and PSB injection systems

3.3.1 Injection beam dynamics

3.3.1.1 Introduction

The substitution of Linac2 with Linac4, in CERN’s injector chain, will allow an increase of the injection energy into the PSB from 50 MeV to 160 MeV. This will mitigate the direct space charge detuning and permit to increase the beam intensity at the Booster. A new multi-turn H⁻ charge-exchange injection system, consisting of a horizontal chicane (BSW) and a thin carbon stripping foil will be put in place. A controlled distribution of the injected particles will provide further space charge attenuation. Energy modulation of the Linac4 beam will be used to attempt equalizing the beam density within the PSB RF bucket. Transverse painting will be performed in the horizontal plane, by means of four existing PSB kicker magnets (KSW), to uniformly fill the horizontal phase space area. The vertical emittance can be adjusted by setting a few millimetres of vertical offset for the injected beam.

The PSB has to provide beams with different emittance and intensity (see Table 3.4). Tracking simulations are performed with the code objective ring beam injection and tracking (ORBIT) to define the optimum KSW decay modulation for all the PSB users, according to their specific requirements and, in general, for injection studies. The number of turns needed to fill the PSB (taking into account a PSB revolution time of 1 μ s) depends both on the target intensity and Linac4 performance. In case of nominal operation, the Linac4 source will produce pulses of 1×10^{14} protons, corresponding to an average 40 mA beam current after chopping. A minimum number of 40 turns has to be taken into account to complete the longitudinal painting in the bucket. H⁻ charge exchange, foil scattering, space charge, acceleration and apertures are included in the simulations.

3.3.1.2 Transverse painting in the horizontal plane

The chicane bump stays constant at 46 mm during injection and then decays to zero in 5 ms. The painting bump is at full amplitude (35 mm) at the start-up of the painting process and then decays in a controlled way, until injection is accomplished.

A high flexibility in the KSW current decay is needed to fulfil the requirements of all the different users. A multiple-linear waveform is chosen for the KSW generators as schematically shown in Fig. 3.12. Ideally, an initial fast decay, over few turns (until t_1), has to be followed by an almost constant slope until the end of injection (t_2). This allows the filling first of the centre and then the outer area of the transverse phase space, reducing the charge density in the core of the bunch and thus the space charge effects. On the other hand, the flat part of the waveform implies that the circulating beam crosses the stripping foil over several turns. This can induce emittance blow-up, losses in the injection region and foil heating. Dedicated studies have to be performed to find a trade-off between particle distribution uniformity and minimization of drawback effects related to foil crossing. Once injection is finished, the circulating beam is moved away from the foil, as fast as possible, until a negative bump of -9.2 mm (one-fifth of the BSW bump) to avoid any further interaction with the foil. Also at this point, the chicane starts decaying and the KSW bump goes to zero in 1 ms (one-fifth of the BSW decay time). Preliminary simulations were performed to define envelope conditions, required precision and needed flexibility for the design and construction of the KSW generators (see the section entitled KSW pulse generator below). Additional studies take into account different optics (matched or zero horizontal dispersion, beta functions at the injection point, offsets, etc.), beam conditions (Linac4 delivered current, emittance, energy spread and/or longitudinal painting) and machine imperfections. The final specifications for the KSW waveforms and the optimum optics for the different users will result from these studies.

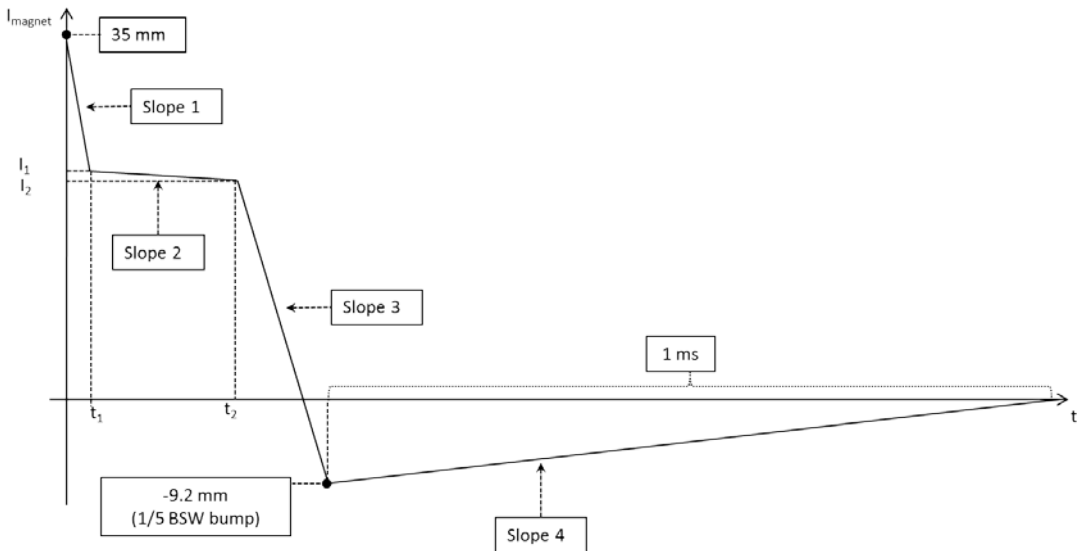


Fig. 3.12: Decay of KSW current as a function of time

3.3.1.3 Possible sources of emittance blow-up for the LHC beams during the injection process

Special attention is dedicated to defining and quantifying possible sources of emittance blow-up for the high-brightness LHC beams. A target intensity (per PSB ring) of 1.65×10^{12} protons in a transverse emittance of $\leq 2 \text{ mm mrad}$ has to be accumulated for the 25 ns beam and of 1.5×10^{12} in 1 mm mrad has to be accumulated for the BCMS beam. No longitudinal painting is used to minimize the number of injection turns and thus the emittance blow-up induced by stripping foil crossing. Also, no transverse painting is applied: the KSW bump stays constant at 35 mm until the end of the injection process and is then switched off as quickly as allowed by the hardware. In ideal conditions, the transfer line optics is matched to the PSB optics at injection (beta functions and dispersion) and no offset is applied between the injected and the circulating beam. A nominal normalized transverse emittance of 0.4 mm mrad is assumed for the beam from Linac4. A uniform distribution in phase ($\pm 1.9 \text{ mrad}$, corresponding to 616 ns bunch length) and parabolic in $\Delta p/p$ ($\pm 1.1 \times 10^{-3}$, corresponding to an energy offset of $\pm 0.336 \text{ MeV}$) is considered for these studies.

Calculations of emittance blow-up are done including space charge effects (for a final intensity of 1.65×10^{12} protons per ring) and assuming:

- ideal optics and nominal Linac4 current;
- 25% mismatch of the optics parameters (beta functions and dispersion);
- mismatch as in (b) plus a constant offset of 2 mm between injected and circulating beam (steering and/or orbit errors);
- mismatch and offset as in (b) and (c) plus Linac4 current limited to 50% of its nominal value. This requires doubling the number of injection turns and, as a consequence, stripping foil crossings.

The result of the simulations, for the different mentioned scenarios, shows a final transverse emittance of $\sim 0.9 \text{ mm mrad}$ (see Fig. 3.13), still in agreement with the specifications. Possible solutions to mitigate the emittance blow-up for the high-brightness beams could be an improved choice of the PSB working point ($Q_V = 4.55$ and $Q_H = 4.28$ is used in these simulations) and of the longitudinal distribution of the particles from Linac4; dedicated studies are being performed for this purpose.

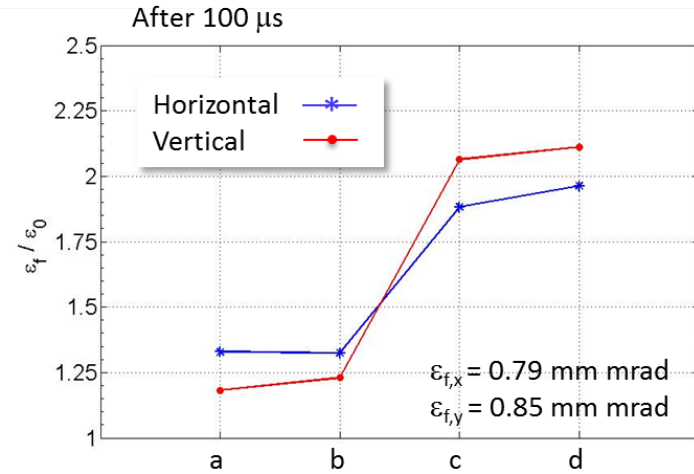


Fig. 3.13: Ratio between final ε_f (after 100 μs) and initial ε_i emittance for different non-ideal scenarios: (a) mismatched optics, (b) orbit offset, (c) reduced Linac4 current. A factor of two emittance blow-up is observed for the most conservative case (d).

3.3.1.4 Perturbations induced by the chicane magnets

The bump created by the BSW chicane magnets located in the injection straight section, described in the section entitled KSW pulse generator below, induces optics perturbations in the lattice by two mechanisms.

First of all, in order to satisfy the stringent geometry constrain, short rectangular magnets with a maximum deflection of 66 mrad are required and introduce focusing errors in the vertical plane [27]. Since the machine vertical tune is close to the half integer resonance, this induces strong beta-beating in the vertical plane. This effect goes to zero as the chicane bump collapses.

The second effect, but of a comparable size, is that the ramp-down of the magnets within 5 ms induces eddy currents in the Inconel vacuum chamber and generates multipolar components varying with time [28]. This translates again into vertical beta-beating due to the large horizontal orbit excursions inside the BSW magnets (see Fig. 3.21 below), which cause quadrupolar feed-down effects. Multipolar components due to eddy currents depend linearly on the ramp rate, and the effects on the beam are proportional to the offset from the magnet's centre.

Detailed magnetic simulations have been performed assuming a linear ramp-down (see the section entitled KSW pulse generator below) and are used as input for the beam dynamics studies. Figure 3.14(a) shows the functions of the dipolar and sextupolar component at one magnet (the other three are similar). We considered an almost linear ramp-down of the power supplies, with roundings at the beginning and at the end to avoid transients (see Section 3.6). The sextupolar component was extracted by scaling the values from Opera simulations by the new values of the derivative of the power supplies function, after cross-checking that it is indeed strictly proportional.

To compensate for the beta-beating caused by the rectangular magnets' edge effects, additional trims on the two defocusing lattice quadrupoles QDE3 and QDE14 are envisaged [29]. These trims are also at the same time found to be effective at correcting the perturbation induced by eddy currents [30]. Figure 3.14 (b) shows the normalized strength required in the lattice quadrupoles, both in the standard quadrupoles and in the two with extra trims for compensation, in the case where the decay of the chicane has the shape discussed above. The vertical beta-beating due to the perturbation and the resulting value after correction is plotted in Fig. 3.15 at 1 ms after injection, when the edge effects are still important and the sextupolar component has reached its maximum.

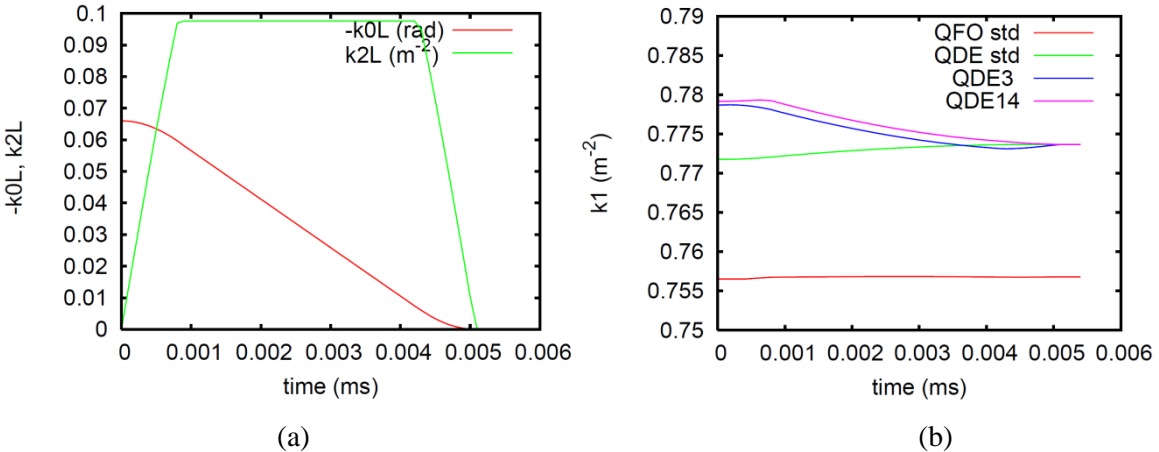


Fig. 3.14: (a) Dipole and sextupolar component at BSW2. (b) Normalized strength required in the lattice quadrupoles, in absolute value, and in the special QDE3 and QDE14 equipped with trims for beta-beating compensation. The working point is $Q_x = 4.28$, $Q_y = 4.55$.

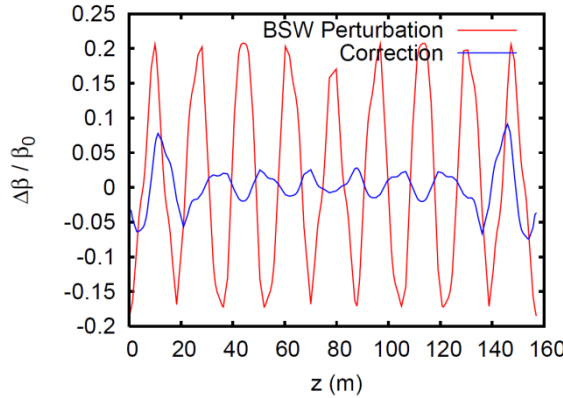


Fig. 3.15: Vertical beta-beating at 1 ms after injection, before and after the correction with the trims on QDE3 and QDE14.

Simulations including space charge effects and the realistic chicane decay shape [28] have been done for two extreme beams whose parameters are summarized in Table 3.4. The aim was to compare the case where only the rectangular dipole edge effects are considered (corresponding to the situation of a ceramic beam pipe) and the effect of the eddy current-induced multipoles (i.e. with an Inconel vacuum chamber).

Table 3.4: Parameters for the two types of simulated beams

	High brightness beam	High intensity/high emittance beam
Intensity	320×10^{10}	1000×10^{10}
Rms normalized emittance	$1.2 \mu\text{m}/1.2 \mu\text{m}$	$8.8 \mu\text{m}/5.7 \mu\text{m}$
Bunching factor	0.60	0.60
Programmed working point	(4.28, 4.55)	(4.28, 4.55)

The PSB model is ‘ideal’: it does not include any non-linearities, errors, misalignments, or other perturbations than those induced by the BSW; therefore the results are valid only as a relative comparison, to determine whether the metallic chamber was not generating any showstoppers. Figure 3.16(a) shows the evolution of the rms vertical normalized emittance for the HB beam, whose parameters are similar to the one required by the High Luminosity LHC, for which emittance control is important. In Fig. 3.16(b) the beam intensity evolution is shown for the HI beam, similar to the one

provided to the ISOLDE nuclear experiments, for which the blow-up translates directly into losses. The efficiency of the correction is here evident and the conclusion is that the inconel eddy-current perturbation has a substantial effect and needs proper compensation, but it does not constitute a showstopper.

Studies to evaluate the tolerance of the compensation settings and on the precision for the control of the chicane magnet power supply are ongoing.

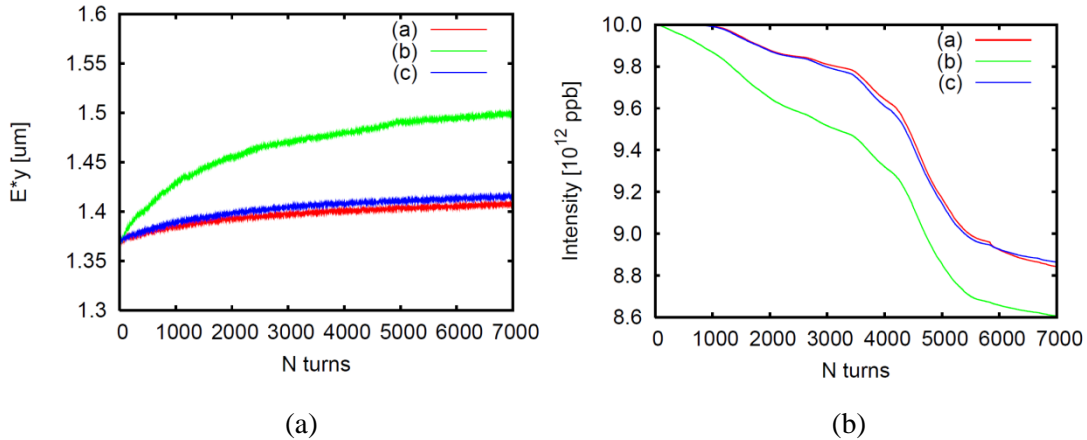


Fig. 3.16: Evolution during the fall of the chicane bump (~5000 turns) of (a) the HB beam rms normalized vertical emittance and (b) the HI beam intensity, for the case of (a) ceramic: only edge effects are taken into account and corrected; (b) inconel: edge and multipole effects, only edge effects corrected; (c) inconel: edge and multipole effects, all corrected.

3.3.2 Injection systems

3.3.2.1 Introduction

The 160 MeV beam from the Linac4 transfer line will be distributed to the four levels of the PSB by a sequence of a vertical bending magnet (BI.DVT30), a system of five pulsed kicker magnets, the so-called proton distributor (BI.DIS), a vertical bending magnet (BI.DVT40), three septum magnets (BI.SMV) and another three vertical bending magnets (BI.BVT). The beam will be subsequently injected horizontally into the PSB by means of a H^- charge exchange injection system, one for each ring, through a graphite foil converting ~98% of the beam to protons. Partially stripped H^0 and ~1% H^- missing the foil will be directed to an internal H^0/H^- dump, as described in Section 3.8.2. The local orbit of the PSB beam is displaced, using two independent closed orbit bump systems, by ~81 mm, to meet the incoming beam. The first, called the injection bump, comprises a set of four pulsed dipole magnets (BSW) located in the injection straight section, and displaces the beam by a constant 46 mm during the injection process. A series of four horizontal kickers (KSW), outside the injection region, will produce a 35 mm closed orbit bump, with falling amplitude during injection, to accomplish transverse phase space painting to the required emittance. The energy of the injected beam can be varied to fill the bucket with an equal density distribution to achieve longitudinal painting [31].

The Linac4 beam injection line will be built keeping the present layout and positions [32] as shown in Fig. 3.17, by modifying the existing equipment or building new equipment with higher performance. In order to make this possible, the required pulse structure from Linac4 will consist of four individual pulses typically 25–100 μ s long, depending on the required number of injected turns per ring, spaced by a 1 μ s gap allowing for the BI.DIS rise-time. The BI.DIS timing will be linked to the Linac4 pulse structure, see Fig. 3.18 [33].

It will be noted that, in case of a lower than expected Linac4 source current, the PSB injection hardware (BI.DIS, BI.BSW, etc.) would be compatible with individual pulses of up to 150 μ s long.

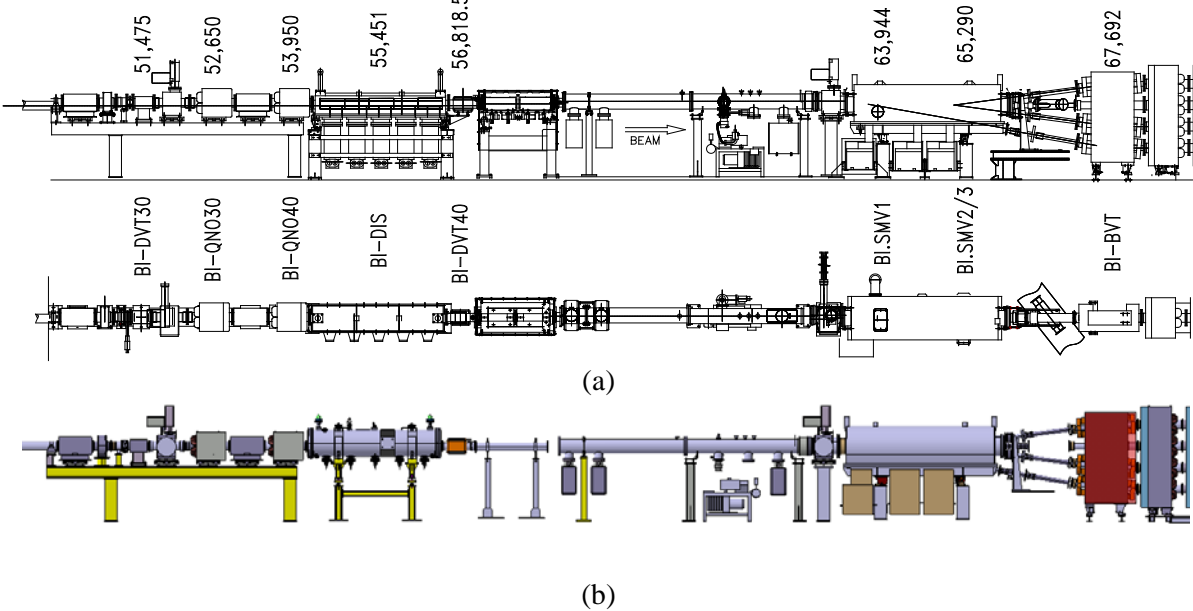


Fig. 3.17: (a) Current layout and (b) future layout study in CATIA (ST0428283) of the PSB BI injection line, giving main components and longitudinal positions (m).

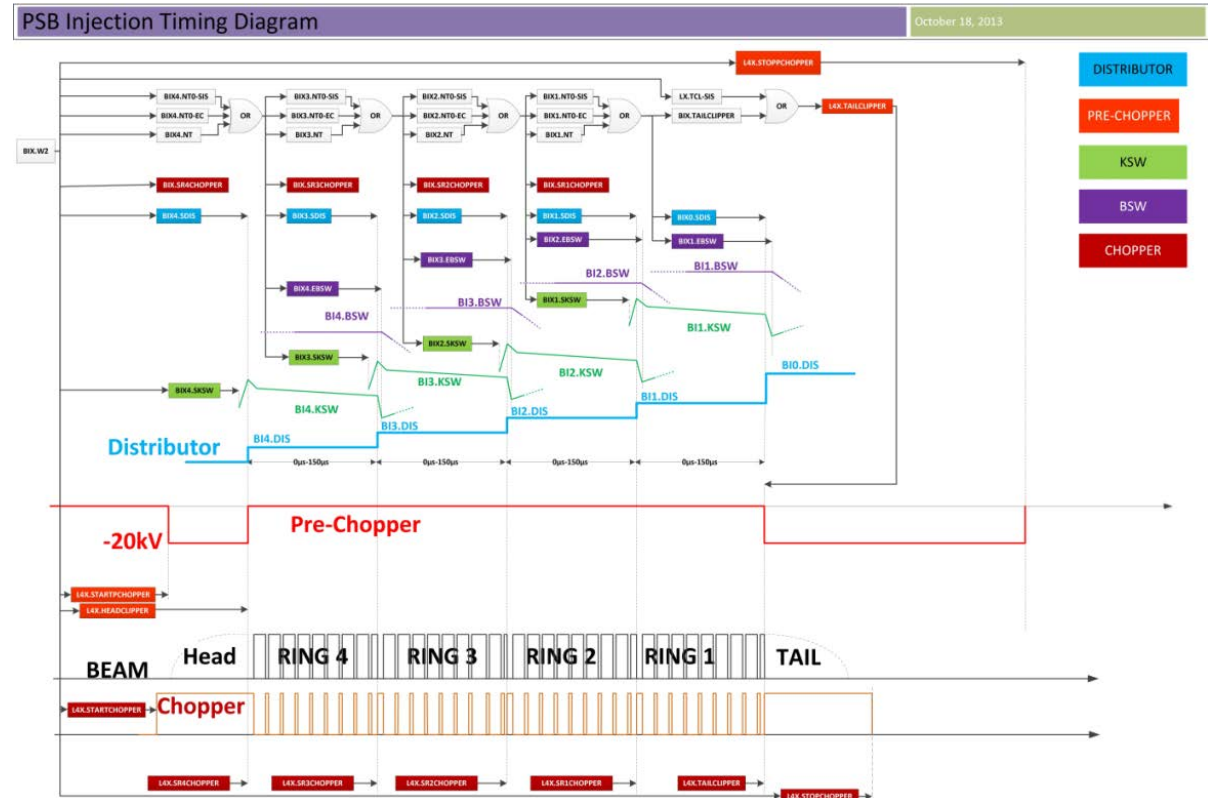


Fig. 3.18: Timing diagram of the PSB injection region for H⁻ injection [33]

3.3.2.2 Beam distribution

The vertical distribution system [34] in the injection line is schematically represented in Fig. 3.19 and consists of the proton distributor BI.DIS, a system of five pulsed ferrite core magnets, which kicks

time-resolved slices of the beam to different vertical positions at the vertical septum BI.SMV. The PSB beam levels are designated counting from the bottom, with ring 3 at the PS beam level. The Linac4 beam enters the BI.DIS with a ~5.7 mm [35] vertical offset and is deflected by a fixed field iron magnet (BI.DVT40) into an absorber block, the so-called head dump, at level 5. Once the rise time of the Linac4 pulse is over, the BI.DIS system, in combination with the BI.DVT40, deflects the beam sequentially into the different apertures of the BI.SMV, which will further deflect the beam vertically into the four separate BI.BVT magnets to achieve the required PSB beam level separation of 360 mm between each ring.

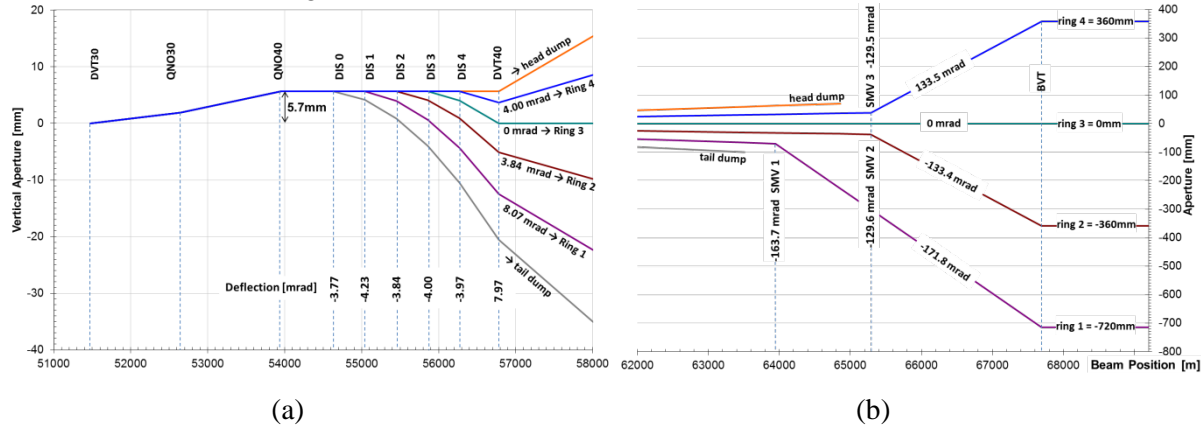


Fig. 3.19: Schematic of the PSB injection line with (a) the BI.DIS and (b) BI.SMV vertical separation schemes [35].

The beam in the fall-time of the Linac4 pulse is deflected to a second absorber block, the so-called tail dump, at level 0. In the case of a complete BI.DIS failure or missing trigger, the full Linac4 pulse will be directed to the head dump, which will be robust enough to withstand a full beam impact at 160 MeV. In the case of individual BI.DIS magnet failures, pulses will be directed to other rings depending on which magnets fails. The head and tail dumps [36, 37], which are described in Section 3.8.2, will be positioned just upstream of the SMV yokes, allowing for maximum beam separation and optimum protection of the septa.

Linac4 pulse structure

The chopper and pre-chopper are be designed [38, 39] such that beam during the rise- and fall-time of the Linac4 pulse will be removed. For this reason no beam should be seen on the tail dumps except in the case of equipment failure, and only some beam escaping the chopper during the LEBT space charge build-up could hit the head dump.

The Linac4 pulse structure will consist of four individual pulses, typically 25–100 μ s long (depending on the required number of injected turns per ring) and separated by a $\geq 1 \mu$ s particle-free gap allowing for the BI.DIS rise time. In order to keep flexibility, the Linac4 pulses and BI.DIS timing can be adjusted, as shown in Fig. 3.20, to fit the required number of injection turns from pulse to pulse, or to not fill a ring if required. Therefore the BI.DIS timing must be linked to the Linac4 chopper, which builds the Linac4 pulse structure, as schematically shown in Fig. 3.18 [33]. The BI.DIS pulse lengths will be fixed, but different for each magnet.

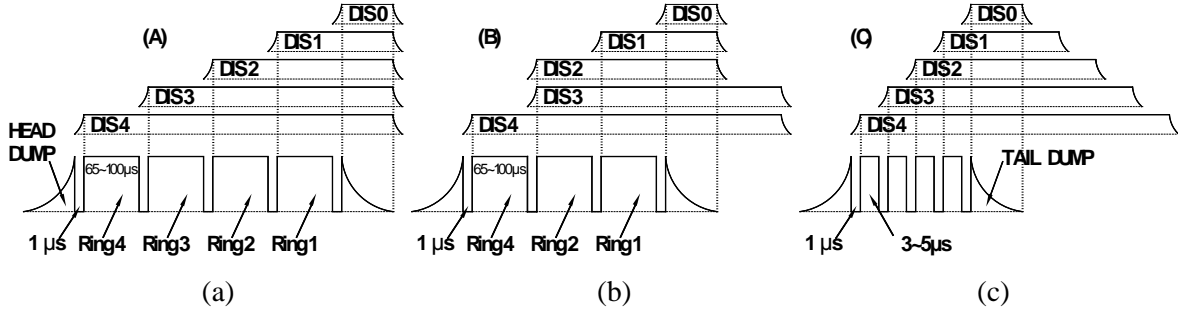


Fig. 3.20: Possible Linac4 pulse structures and BI.DIS timing showing: (a) standard operation with 65–100 injected turns per ring, (b) operation with 0 injected turns for ring 3 and (c) pilot beam with 3–5 injected turns per ring.

3.3.2.3 Distributor BI.DIS

The BI.DIS system, in combination with the BI.DVT30 and BI.DVT40, is designed such that a ~3.5 mrad deflection produces a vertical beam separation of 35 mm at the entrance to the BI.SMV septa. In order to achieve these deflection angles at 160 MeV a new distributor system will be built since an increase by a factor of ~1.9 in the integrated field $\int B \, dl$ is required. This will be possible by modifying the system to provide up to 950 A to the magnet, at a 4.3 mrad design value, compared to 500 A for the current 50 MeV beam distributor system. To attain this, the rise- and fall-times will be increased from 100 ns to less than 1 μs and the BI.DIS pulse lengths will be fixed, but different for each magnet.

BI.DIS magnet

The distributor will consist of five consecutive magnets, which will be powered individually [40]. The main parameters of the BI.DIS magnets are described in Table 3.5. The new BI.DIS magnets are based on the actual design. To improve its voltage hold-off capability and to improve the field homogeneity in the gap a new conductor design is used. The new coil geometry was validated using Vector Fields' Tosca software (Cobham plc, Wimborne, UK). In Fig. 3.21 the finite-element model with the coil is shown. The calculations show that the required integral field will be reached at 1094 A.

Table 3.5: Main BI.DIS magnet parameters

	Unit	DIS
Deflection angle (max)	mrad	5
Integrated field	mTm	9.5
Gap field	mT	27
Gap height	mm	98
Gap width	mm	50
Magnetic length	mm	350
Peak current	kA	1.1
Peak voltage	kV	27
Magnet inductance	μH	1.1
Magnet resistance	mΩ	15
Number of turns		1
Repetition rate	Hz	1.1
Rise time (1–99%)	μs	1
Flat top duration	μs	620

The BI.DIS magnets are installed in a UHV circular tank equipped with end covers at each end, see Figs. 3.22 and 3.23. The five-magnet stack can be inserted into the vessel using a temporary demountable rail guide system that is removed prior to closing the tank. Before insertion into the

vacuum tank the magnets are pre-aligned on a rigid support plate and the complete assembly is then transferred to the rail guide system and rolled into the tank. Subsequently, the assembly is transferred to a tank-mounted lifting system that positions and lowers the magnet stack onto the high voltage (HV) feedthroughs with the aid of precision location shafts. The vacuum tank is equipped with ion pumps and independent vacuum gauges. The system can be baked if necessary but is not equipped with an under-vacuum bake out system. All joints are of the OFE UHV type and the tank is fitted with UHV flanges that allow the magnet system to achieve a pressure in the region of 10^{-9} mbar under storage.

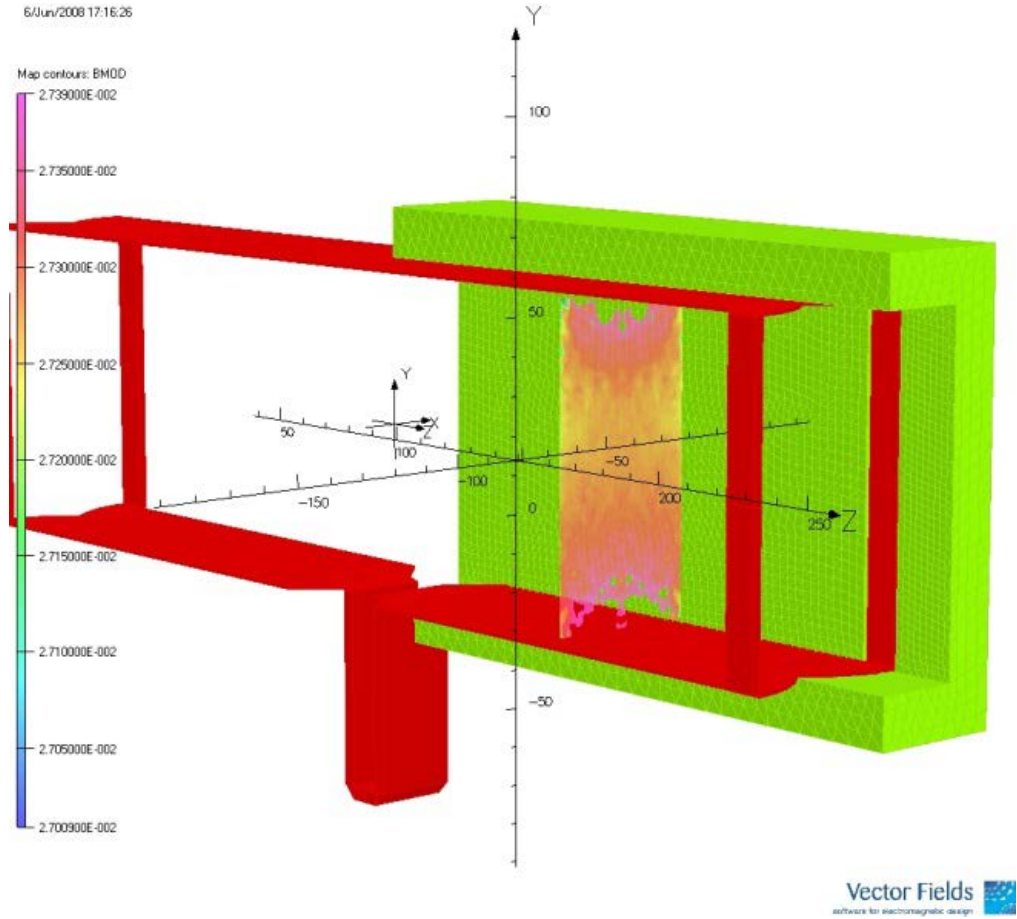


Fig. 3.21: Finite-element model of BI.DIS with the 1% field region plotted

The magnet is short-circuited inside the vacuum vessel. The magnet yoke has reused the existing design and is made using CMD 5005 ferrites (National Magnetics Group, Bethlehem, Pennsylvania, USA). The coils were manufactured from stainless steel and are assembled using a laser welding technique to minimize as much as possible the distortion during localized heating. A precision assembly tool has been designed that will allow precise alignment of all components of the coil prior to welding. In this way the strict geometric tolerances can be respected during welding operations.

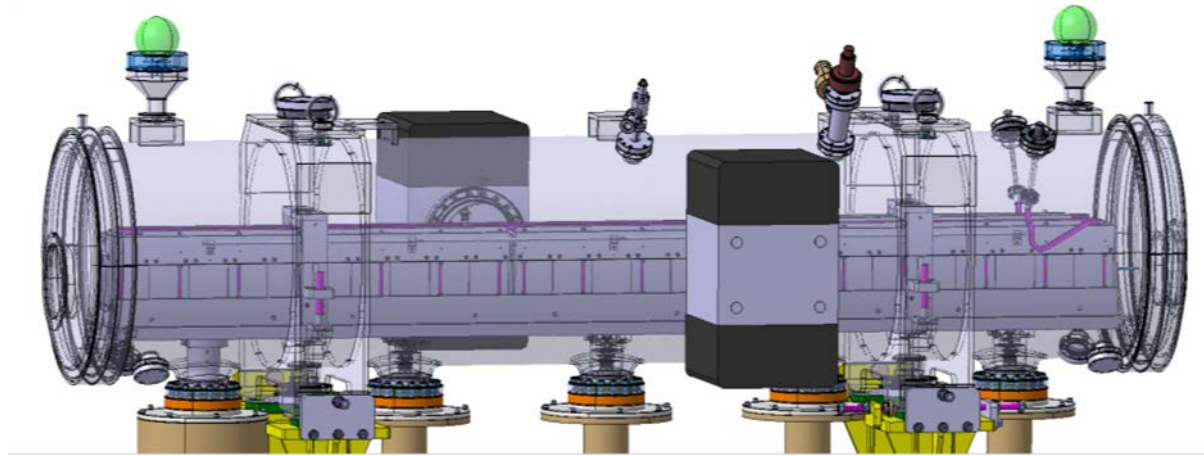


Fig. 3.22: Assembly model of BI.DIS (CATIA ST0221219)



Fig. 3.23: The BIDIS magnets being inserted into their vacuum vessel. In the background the spare vacuum vessel is waiting to be fitted out.

Unlike the previous BI.DIS system, no scrapers are fitted to the upstream end of the magnet stack to protect the ferrites from stray particles in the beam halo. Due to the increase in beam energy, with relation to the present system, the new absorbers would become significantly bigger and the required longitudinal space is not available.

The system has been designed to facilitate ease of exchange in the event of a magnet or HV failure. The complete tank, including the magnet stack, can be removed from the injection line and

replaced by its spare assembly in a relatively short period of time. This will significantly reduce the downtime and also the radiation dose taken by equipment specialists during such an intervention. Although heating effects are considered to be minimal, a cooling system was installed on top of the magnet support to stabilize the temperature of the distributor.

If the need arises to deflect protons instead of H^- ions, the polarity of the magnets can be changed by changing the orientation of the magnets inside the vacuum vessel. Therefore the stack of magnets needs to be removed from the vacuum vessel and the individual magnets can be turned by 180° around the vertical axis. Subsequently the stack is reinstalled in the vacuum vessel. This operation could be performed on a spare magnet. A total of two full BI.DIS magnet assemblies have been built; one will be installed and one is an operational spare.

BI.DIS pulse generator

The present BI.DIS system built in the 1970s could not be upgraded to cope with the Linac4 beam requirements. So, a new design has been developed. This design is still based on fast-switched pulse forming network (PFN) technology but extends the limits of devices built up to the present at CERN. A major constraint for the new design is the use of the same space as the current one (located in the Booster control and electronics room (BCER)) while multiplying the maximum pulse length by a factor of five and current by a factor of two. Fortunately the relaxation of the pulse rise time results in decreasing the PFN impedance and the operating voltage. This allows the use of IGBT semi-conductor devices to replace thyratrons.

The system layout is shown in Fig. 3.24. It features (for the longest) a 60-cell PFN whose characteristic impedance is $6.25\ \Omega$. The PFN is charged at 6.25 kV by a DC power supply and discharged at one end by two IGBT modules connected in series. The resulting current excites the lumped inductance magnet described above via eight parallel connected transmission cables. A fast high-voltage diode is connected at the other PFN end to avoid voltage reversal and to recover about 50% of the 1.2 kJ PFN stored energy. A freewheel high-voltage diode is connected at the switch output to limit high-voltage spikes induced by undesired IGBT switch-off at full current. In normal operation, the PFN is fully discharged before the IGBT is switched off.

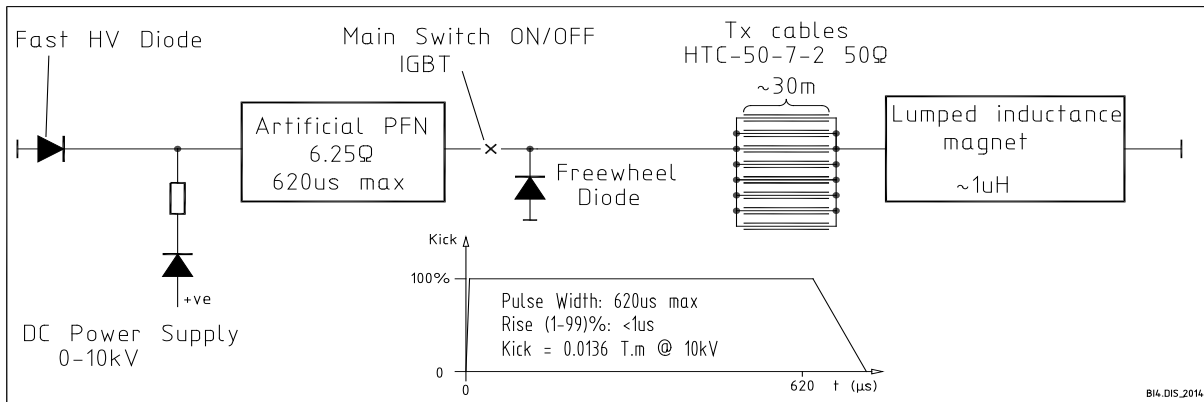


Fig. 3.24: New BI.DIS system layout

Five PFNs plus one spare will be built. The fourth one (DIS4) and the spare will be designed to kick the full foreseen beam length of $620\ \mu s$. The number of cells of the others will be reduced by multiples of $150\ \mu s$ accordingly. Pairs of PFNs will share common racks split horizontally in two separate halves for safety reasons. An automatic CO₂ fire extinguisher system will be installed in each PFN for fire prevention.

BI.DIS controls

The BI.DIS controls [41] will be located into the BCER in building 361. The entire system, as schematically shown in Fig. 3.25, will be housed in nine racks, which comprise a power distribution unit for all five generators and a spare unit. A second rack will be dedicated for user interface (SCADA), central processing unit (CPU) for slow control management and finite state machine. The third rack will contain the BI.DIS signal acquisition and signal logging and a timing distribution system. The remainder of the racks consists of ‘modules’, hence ‘five of’ generator controls plus one spare. Each generator control mainly comprises a fully dedicated fast control interface for managing the ‘fast’ system interlocks but also to manage the fine trigger control on the series IGBTs. This is the IGBT ‘turn off’ system with drift stabilization that will enable fully controlled and smooth running of the series IGBT’s operation. Distributed I/Os will help manage the power supply controls and general-purpose controls such as actuators, temperature readings and micro switches. Housed inside the generator system will be the upstream triggering system for the IGBT’s and the PFN’s electrical and manual earth switch system.

The system architecture is distributed over two main buses, an Ethernet ‘backbone’ and an industrial bus. The Ethernet is for many of the remote control features that are implemented for the control room and experts but it also supports the fast acquisition system and interlocking systems. The industrial bus manages all of the PLC controllers and slow controls.

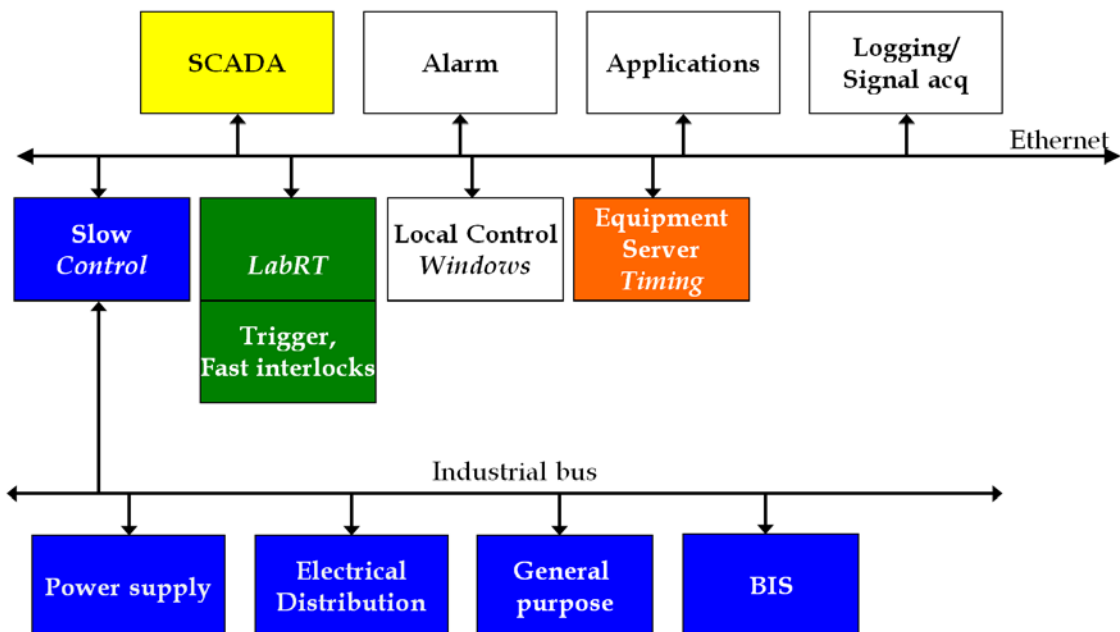


Fig. 3.25: New BI.DIS control architecture

3.3.2.4 Magnetic septa BI.SMV

The three vertical deflection septa [42] will be installed in one vacuum tank, which will provide the space for the head and tail dumps (see Section 3.8.2). All magnets (see Table 3.6 for the main parameters) are identical, but are mounted differently to allow the beams to be deflected to the different PSB rings, which are not at the same height as the LINAC4. SMV1 will deflect the beam towards PSB ring 1, and SMV2 and SMV4 deflect the beams towards rings 2 and 4, respectively. The beam for ring 3 passes straight between SMV2 and SMV4, unaffected by their magnetic fields except for the leak fields.

Table 3.6: Main BISMV (full) magnet parameters

	Unit	SMV1	SMV2
		SMV4	
Deflection angle	mrad	164	130
Integrated field	mTm	312	248
Gap field	mT	325	258
Magnet gap height	mm	64	
Gap width	mm	70	
Vertical beam acceptance	mm	35	
Magnetic length	mm	960	
Septum thickness	mm	4	
Half magnet angle	mrad	129	104
Half magnet offset	mm	4.6	0
Peak current	kA	18.1	14.4
Magnet inductance	μH	1.2	
Magnet resistance	$\text{m}\Omega$	0.2	
Number of turns		1	
Repetition rate	Hz	1.1	
Rise/fall time	ms	1	
Flat top duration	ms	1	

The cross-section through the magnets was optimized using Flux2D finite-element software (CEDRAT S.A., Meylan, France). Each magnet consists of two half magnets powered electrically and hydraulically in series. The septum conductor is 5 mm thick, but at the beam entrance and exit this thickness is reduced to 4 mm over 160 mm in length. Each magnet will consist of two separate magnet blocks, to maximize the magnetic length for the given space available, while keeping the leakage field as low as possible. The magnets have been modelled using Opera 3D software (Cobham plc, Wimborne, UK). The aim was to develop a magnet concept using two identical magnets in order to limit development and manufacturing costs. Subsequently the angle and the offset between the half magnets were optimized (see Fig. 3.26).

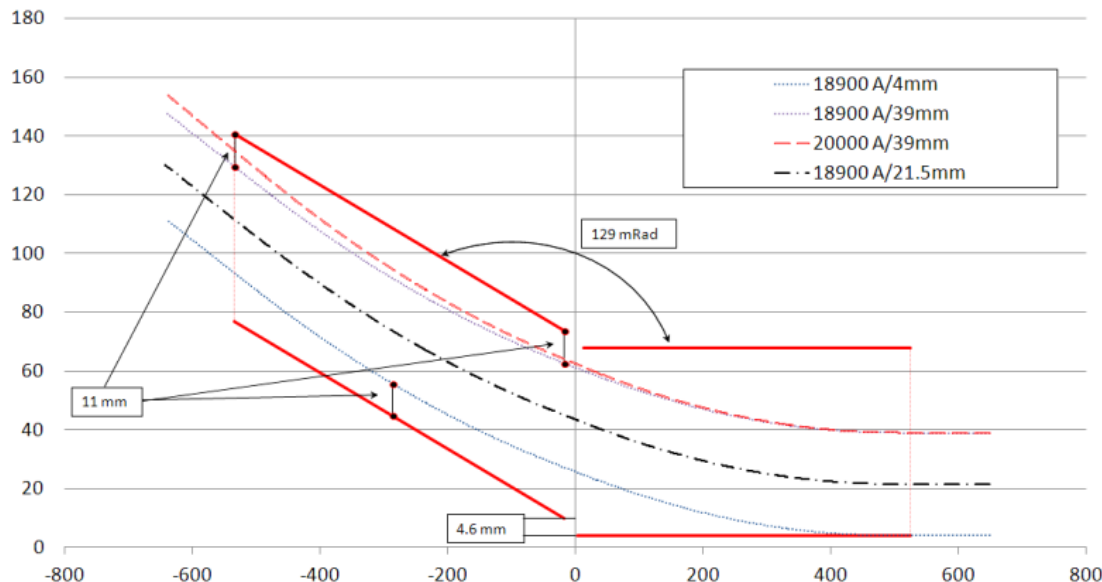


Fig. 3.26: Optimized angle and offset shown for the half magnets of SMV1 resulting from the simulations of the beam trajectory.

The magnetic yoke is made of laminated silicon steel, and its cross-section is designed to minimize the yoke cross-section (reducing outgassing rates due to a lower surface exposed to vacuum) and reduce the stray field. In principle the stable field flat top length needs to be 100 μs , but the actual current flat top is chosen to be longer to limit the effect of eddy currents induced in the yoke and to stabilize the current from the power converter before the passage of the beam through the magnet.

The two half magnets dissipate approximately 50 W, so water cooling is required. The resulting coil, made of OFE copper, contains embedded stainless steel cooling channels located close to the coil edges. The cooling channels in the return conductor are also positioned close to the edges thus reducing the pressure wave in the cooling circuit due to energy deposited by the secondary particles originating from the head and tail dumps (for SMV3 and SMV1, respectively). The head and tail dumps are described in Section 3.8.2. For this coil geometry the simulations show that the stray field will be below 1% of the main field and its quadrupolar component is predicted to be three times less than that of the gap field [43].

Due to the laminated construction of the magnets, the vacuum load will be significant and a substantial pumping system using ion pumps is integrated into the limited space assembly of the septum tank assembly (see Fig. 3.27), with a total pumping capacity fitted to the BI.SMV of 1800 l s^{-1} .

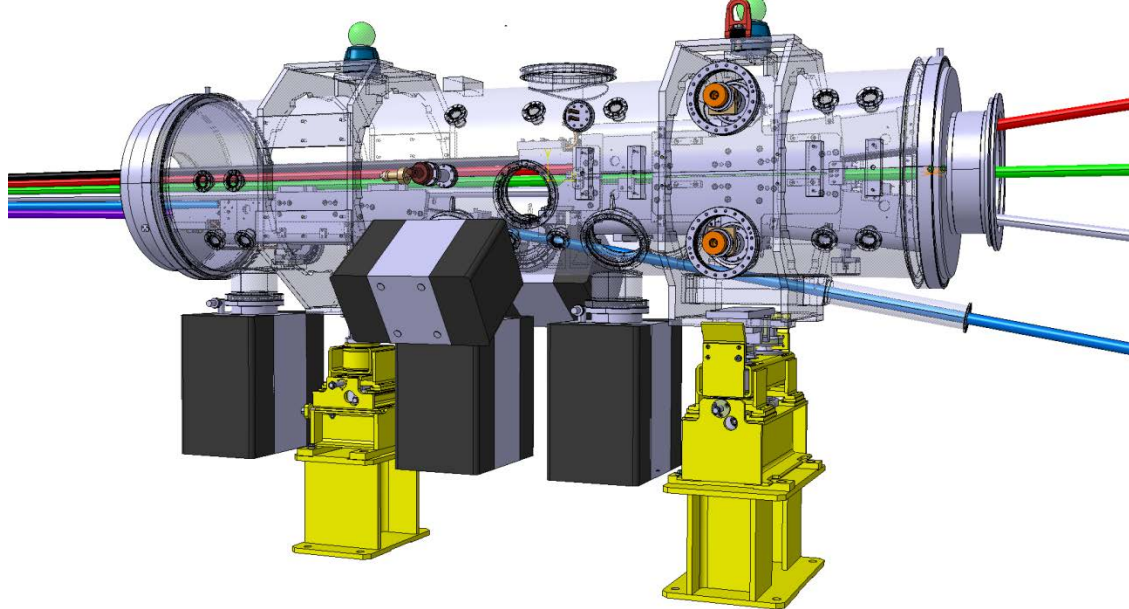


Fig. 3.27: The BI.SMV complete vacuum tank assembly (CATIA ST0318018)

Each magnet has an integrated bake-out resistor, and thermocouples are used to control the magnets' temperature during bake-out. The bake-out resistor consists of a vacuum-compatible heating element fixed to the main magnet support yoke. This element is powered with 220 V and supplies 500 W of heating power. Most of the heating (approximately 85%) is by conduction through the yoke to the magnet laminations, with the remainder by radiation directly to the lower laminations. The system has been designed to allow for the assembly of each magnet pair with their corresponding electrical feedthrough to be performed outside of the vacuum tank. All brazing operations can therefore be completed with easy access, improving reliability. The magnet pairs can then be fixed onto their dedicated supports and precisely aligned before insertion into the vacuum vessel.

Each magnet has a dedicated transformer that will be located as near as possible to the vacuum vessel in order to reduce the inductance of the secondary circuit. The integration of the three transformers adjacent to the vacuum tank will probably require modification to the cooling distribution and perhaps to the cabling of the transfer line. The BI.SMV power convertors are covered in Section

3.6.1. In order to reduce design work the re-use of supports, originally designed for the LHC MKI magnets, has been selected.

3.3.2.5 H^- injection system

For the charge-exchange injection scheme the local orbit of the circulating beam is displaced by up to 81 mm to meet the incoming beam at an angle of 66 mrad. This is done by using two independent closed orbit bump systems. The first bump, called the injection bump, comprises a set of four new pulsed dipole magnets (BSW1–BSW4) located in the injection straight section, and displaces the beam by a constant 46 mm during the injection process. The second bump, called the painting bump, is made using four existing, kicker magnets (KSW1–KSW4) distributed around the ring to produce a closed orbit offset of 35 mm at the injection foil. The amplitude of the painting bump is reduced during injection, to distribute the injected beam over the horizontal PSB aperture. Some of the existing KSW magnets will need to be relocated and re-engineered to achieve this. A schematic view of the PSB injection region configuration is given in Fig. 3.28.

The L1 injection straight section of the PSB is 2.564 m long, as shown in Fig. 3.29, and is redesigned to accommodate the new injection elements. The H^- injection system comprises, in each of the four rings, four new BSW magnets, a foil holder and handling system, and a beam dump for unstripped H^0/H^- , the latter described in Section 3.8.2. Suitable instrumentation for setting up and optimizing the injection process will also be installed, e.g. viewscreens, beam dump current monitors, beam loss monitors, and stripping foil current measurements. Detailed description of the instrumentation can be found in Section 3.7. Furthermore, the H^- injection system will become a dedicated vacuum sector.

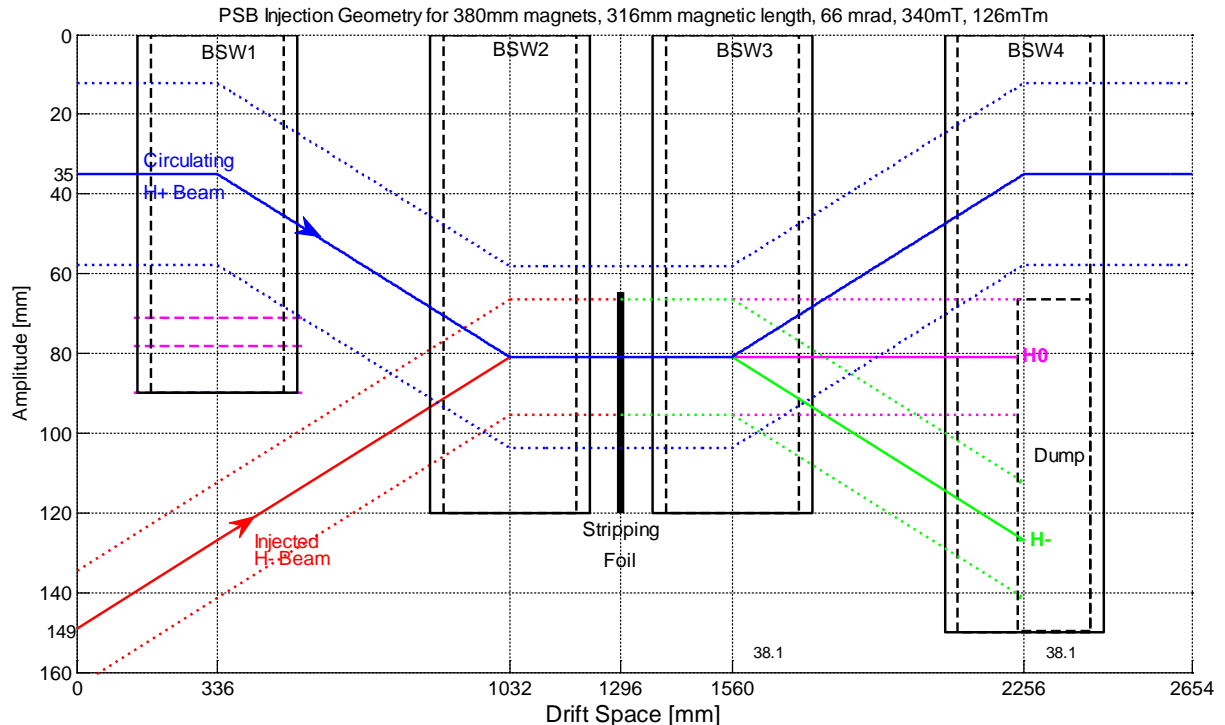


Fig. 3.28: Configuration of the PSB injection region, showing injected and circulating (first turn) beam envelopes of $\pm 4\sigma$ for $\pm 0.4\%$ $\Delta p/p$ variation.

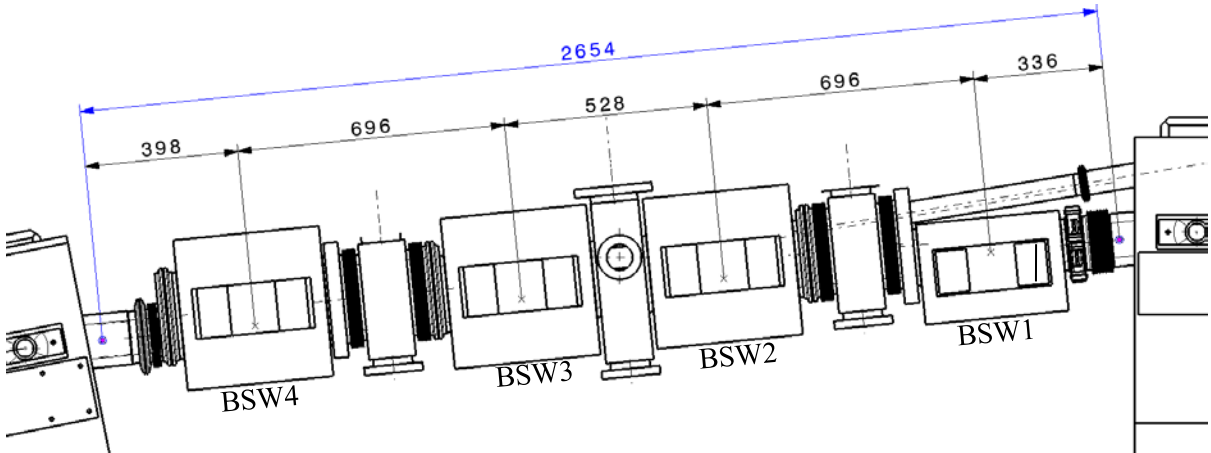


Fig. 3.29: Conceptual layout of the injection straight section, seen from the inside of the ring, showing the available space and position (mm) of the BSW magnets.

KSW painting magnet

The painting bump is made using a series of four horizontal kicker stacks (KSW), outside the injection region to produce a closed orbit offset of 35 mm at the injection foil. The four KSWs will be used to accomplish painting in the horizontal phase space to match the injected beams to the required emittances. Some of the existing KSW magnets will need to be re-engineered and relocated. The present layout configuration and the electrical parameters of the KSW painting magnets will significantly change. The two major modifications are:

- the 1L1 magnet stack will be removed from its present location as shown in Fig. 3.30, for the new injection system;
- a new 16L1 magnet stack will be installed between the bending magnets BHZ152 and BHZ161 as shown in Fig. 3.31.

Other minor changes include the move of the present 16L4 to replace the 2L1, the latter will be reconverted into a spare. In sector 16 a new magnet stack will be installed in 16L4. As a result, the outer magnets 16L1 and 2L1 will be mechanically and electrically identical as the inner ones 16L4 and 1L4.

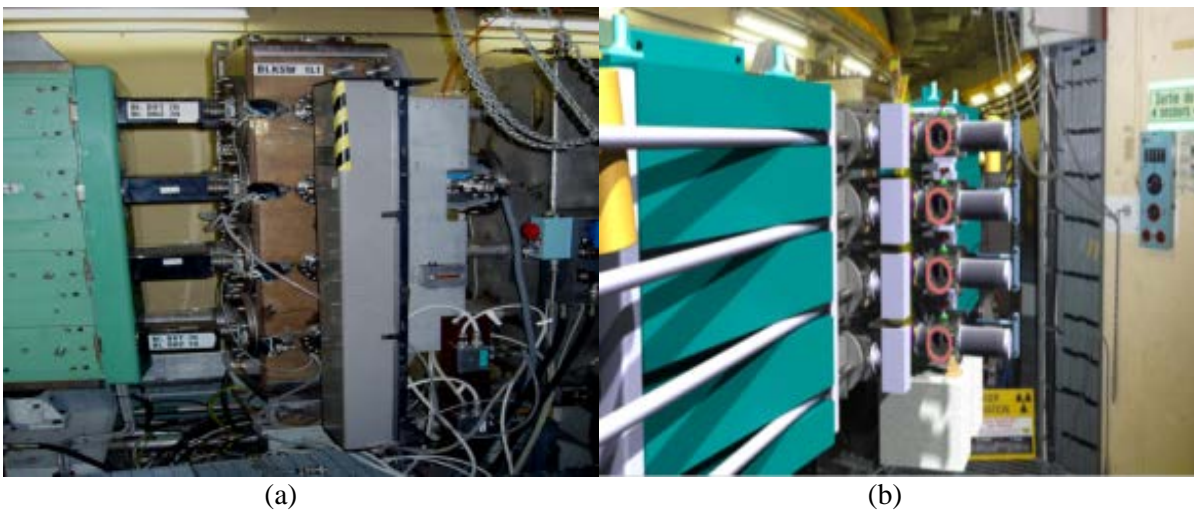


Fig. 3.30: (a) Present and (b) future layout in PS Booster straight section 1

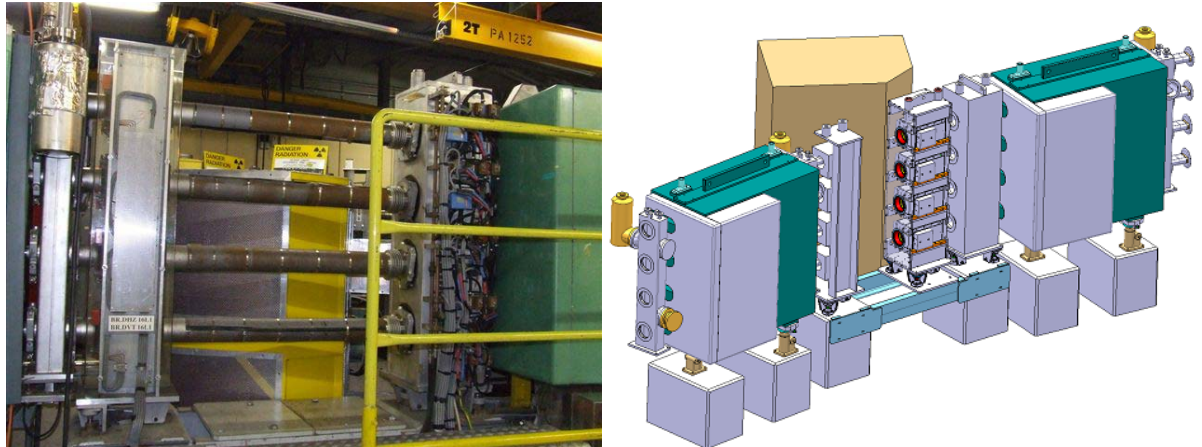


Fig. 3.31: (a) Present and (b) future layout in PS Booster 16L1

All eight new magnets, as well as future spares, will be equipped with new ceramic vacuum chambers, as shown in Fig. 3.32. To reduce the beam coupling impedance, the new ceramic chambers will be coated, on the inner surface of the tube, with a $2\text{ }\mu\text{m}$ titanium layer. The equivalent value of the coating is such that the electrical conductivity from flange to flange is about $0.3\text{ }\Omega$ [44].

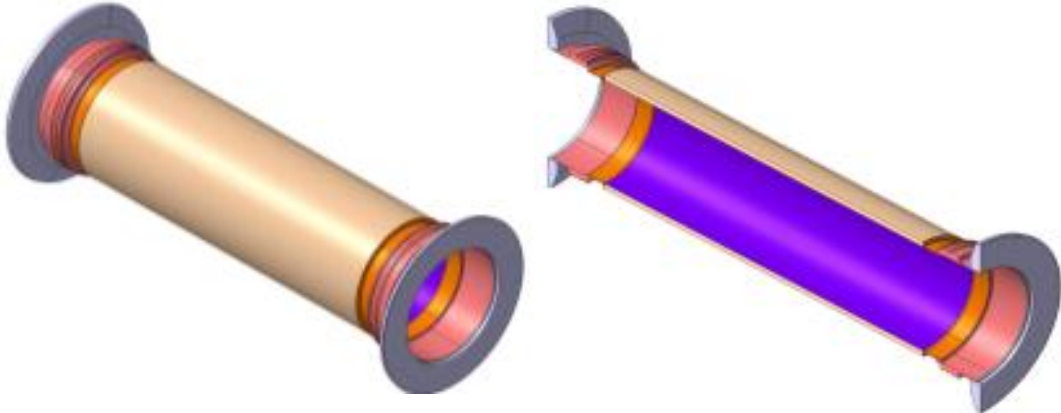


Fig. 3.32: KSW new ceramic chamber 3D and sectional views

Although the new KSW layout only permits two different types of magnets guaranteeing the same kick shape, the kick strength will be slightly different for each magnet, see Table 3.7, and each magnet will be powered individually.

Table 3.7: KSW magnet parameters

	Unit	1L4	2L1	16L1	16L4
Deflection angle (max)	mrad	1.15	5.41	5.85	0.83
Integrated field	T	0.006	0.028	0.030	0.004
Gap height	mm	132	132	132	132
Gap width	mm	132	132	132	132
Magnetic length	mm	370	370	370	370
Magnet inductance	μH	390	39	39	390
Number of turns		48	16	16	48
Repetition rate	Hz	1.1	1.1	1.1	1.1

The energy of the injected beam can be varied to fill the bucket with an equal density distribution to achieve longitudinal painting [31]. The reason for having four different kick values is that the four KSW magnets are not symmetrically distributed in the Booster ring with regards to the

stripping foil. Having unequal kick values will prevent orbit perturbation in the horizontal plane, which would lead to higher beam emittance. The circulating and injected beams are then perfectly matched, and the bump is closed as shown in Fig. 3.33.

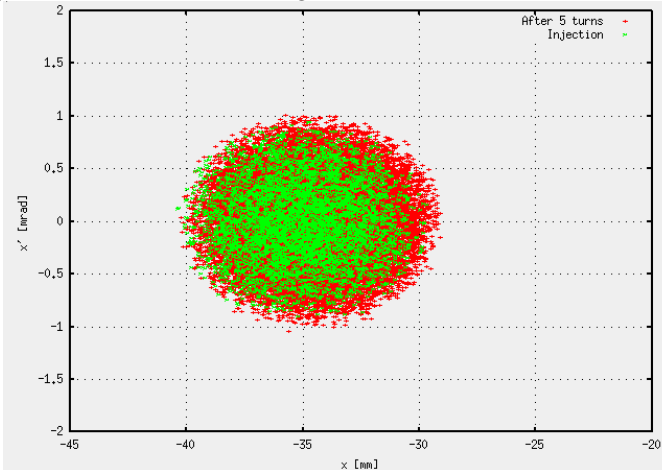


Fig. 3.33: ORBIT simulations of the injected and circulating beams after five turns

The construction of the new KSW magnets is based on current designs, which will be reused. The magnetic circuit is made of Ferroxcube Ni Zn ferrite, grade 8C11 (Ferroxcube Deutschland GMBH, Hamburg, Germany). The ferrite blocks will be excited by a multi-turn winding in which the current will rise from 0 A to 380 A in 48.4 μ s. During the same time, the flux density will vary from 0 T to 0.03 T. The ferrite blocks will be used to homogeneously distribute the flux density inside a ceramic chamber, where the proton beam circulates. A schematic cross-section of the KSW magnet is given in Fig. 3.34 and the main parameters of the KSW circuit are given in Table 3.8.

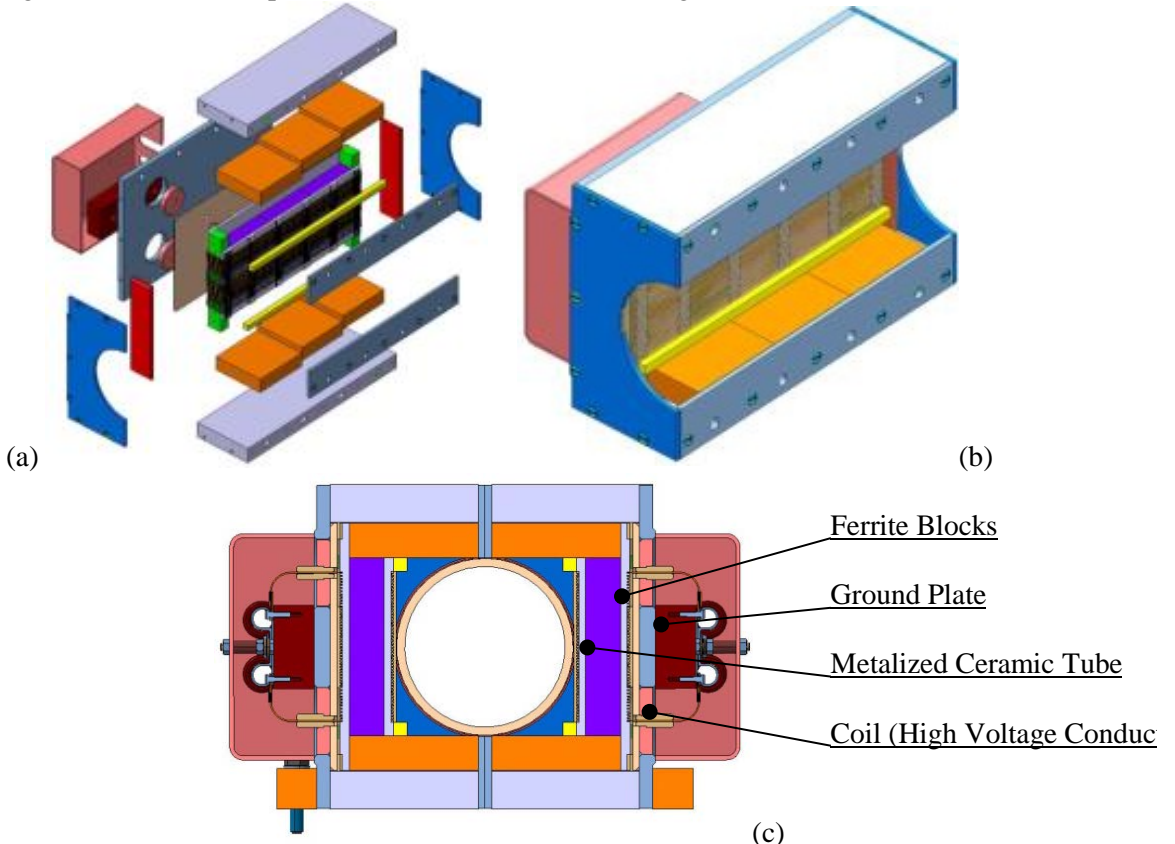


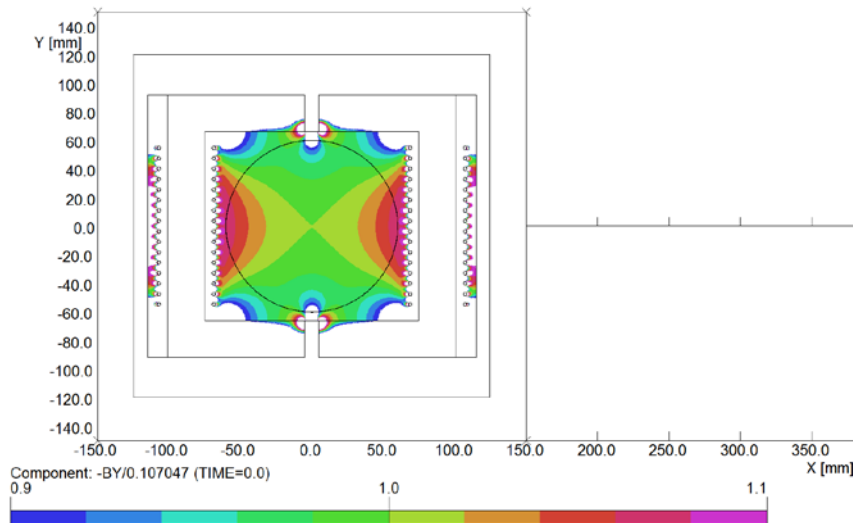
Fig. 3.34: (a, b) CATIA 3D models and (c) schematic cross-section of the KSW magnet

Table 3.8: Parameters of the KSW circuit

	Unit	KSW
Pulse voltage (max)	kV	1
Pulse current	A	380
Rise time (current and field)	μs	48.4
Pulse duration	μs	100
Fall time	μs	10
Repetition period	s	0.9

As shown in Fig. 3.35, the new KSW magnets' field distribution in the gap presents a good homogeneity between 0.9 and 1.1, validated with Vector Fields software (Cobham plc, Wimborne, UK). The current amplitude to reach the required integrated field is 380 A.

There will be only two types of windings, 16 and 48 turns. The winding is impregnated with charged Araldite resin after assembly in the magnet housing and will form half a magnet yoke as shown in Fig. 3.36. When the 2L1 magnet stack is removed from the machine, it will be disassembled. The mechanical parts will be reused and new coils of each type (16- and 48-turn windings) will be built. Two new magnets of each type will be assembled to be used as spares.

**Fig. 3.35:** Finite-element model of the KSW magnet

The present 1L1, which is currently a different design and built under vacuum, will not be reused. In the future, any faulty KSW magnet could be replaced without venting the vacuum sector, which represents an advantage for the duration of the intervention and subsequent collective radiation dose.



Fig. 3.36: KSW magnet (a) before and (b) after impregnation

KSW pulse generator

The KSW painting magnets will operate with many different waveforms depending on the beam user, as shown in Fig. 3.37. Before beam injection, the current rises to I_{MAX} and then starts to fall down to I_{NEG} during the injection with 1, 2 or 3 different linear slopes. The final slope, from I_{NEG} to 0 in 1 ms, is identical for all waveforms. For each PSB ring there are four KSW magnets, the magnets in position 16L1 and 2L1 having an I_{MAX} of 400 A and the magnets in position 16L4 and 1L4 having an I_{MAX} of 40 A. Therefore two generators have to be built; high current and low current versions. The current I_{NEG} is approximately -25% of I_{MAX} . All four generators of one ring must work synchronously and deviation from the reference waveform will be less than 1%. The coordinates of P_1 are variable in time from 5 μ s to 30 μ s as well as in amplitude from 60% to 95% I_{MAX} . However, the maximum $|di/dt|$ from time 0 to P_1 is limited to 10 A/ μ s. P_2 is 30 μ s to 100 μ s after P_1 and 1% lower in amplitude. P_3 is at I_{MAX} and variable in time from 5 μ s to 25 μ s.

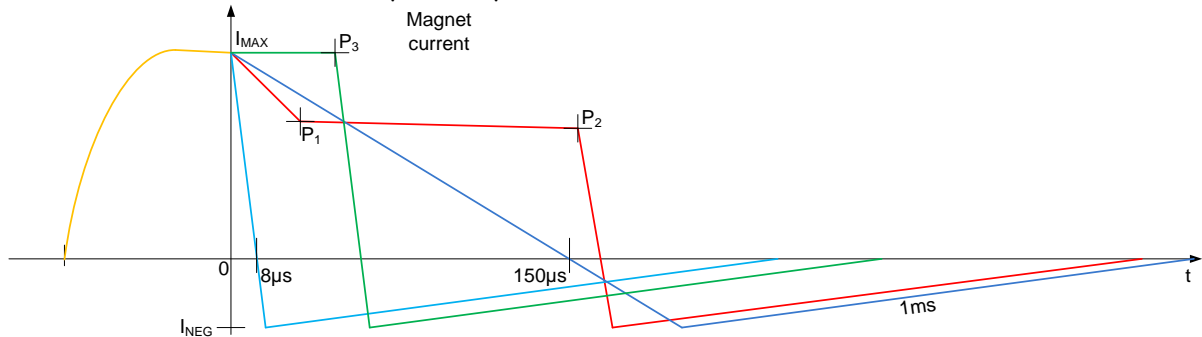
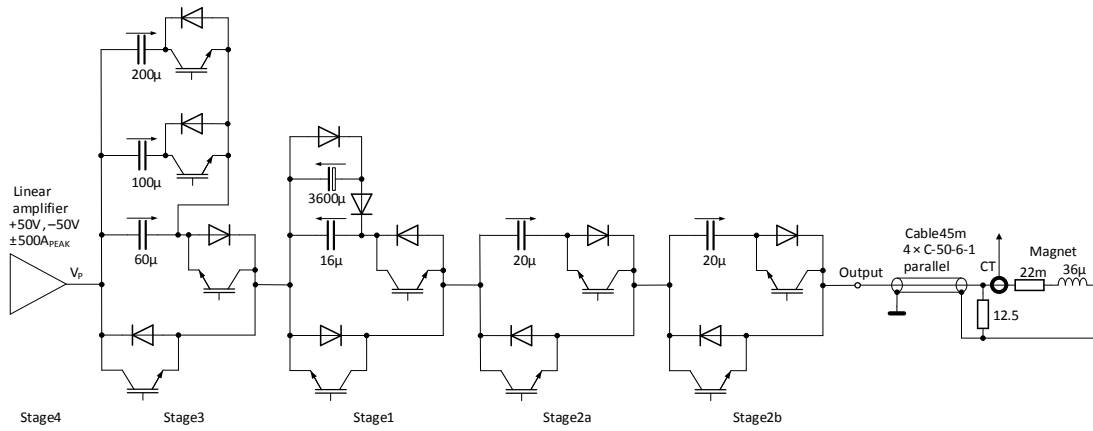


Fig. 3.37: Possible BI.KSW current waveforms (not to scale).

The principle of generator operation is explained schematically in Fig. 3.38. To make the magnet current rise or fall a voltage is applied that is proportional to the required di/dt of the current. The voltage sources are pre-charged capacitors that are switched one after the other to the load (cable, magnet). There are four capacitor switching stages in series that can each supply voltage of one polarity, but the current can flow in both directions. The lower branch of each stage is a bypass switch. When the bypass switch of a stage opens the stage becomes active and the current flows through the upper branch with the capacitor; and the output voltage being the sum of the capacitor voltages of all active stages. The additional circuitry in parallel to the capacitors is used to coarsely linearize the current and its use depends on the waveform. The coarse linearization is already quite good but not sufficient to achieve the required precision. The final linearity correction is done using the linear amplifier in stage 4; only a small voltage is required to bring the linearity error down to zero. In order to reduce the current for the amplifier there is a pulsed current source in parallel supplying a pulse of up to 300 A; the precise waveform of this current source is not important.

**Fig. 3.38:** Conceptual design of the generator, high current version

The magnet current is measured with a current transformer. During operation the measured current is compared with the reference waveform and, in the case of a difference, the capacitor voltages, amplifier voltage and timing are corrected automatically to minimize the error. Continuous automatic correction is necessary since temperature changes and component ageing can cause errors of several percent.

BSW chicane magnets

To fit all elements in the injection straight section, the BSW magnets do not exceed 0.38 m in length, and have a magnetic length of 0.316 m. Because of the symmetric nature of the injection bump, as shown in Fig. 3.28, the deflection angle of the BSW magnets [45] is determined by the 66 mrad injection angle. The main parameters of the BSW magnets are given in Table 3.9. The first magnet (BSW1) is a septum magnet, while the other chicane magnets (BSW2, 3 and 4) are window frame magnets. The BSW2 and BSW3 magnets, installed on each side of the stripping foil, are identical magnets. BSW4 has an enlarged horizontal gap to accommodate the unstripped particle beam as well as the unstripped particle monitor in front of the unstripped particle dump, the latter described in Sections 3.7 and 3.8, respectively. Each magnet is powered individually to allow for maximum flexibility during operation. The BSW power convertors are covered in Section 3.6.1.

Table 3.9: Main BI.BSW magnet parameters

	unit	BSW1	BSW2/3	BSW4
Deflection angle	mrad	66	66	66
Integrated field	mTm	126	126	126
Gap field	mT	399	399	399
Gap height	mm	85	85	85
Gap width	mm	162	218	242
Magnetic length	mm	316	316	316
Septum thickness, including magnetic screen	mm	8	na	na
Peak current	kA	6.7	3.4	3.4
Magnet inductance	μH	13	70	77
Magnet resistance	mΩ	3.5	7	7
Number of turns		4	8	8
Repetition rate	Hz	1.1	1.1	1.1
Rise/fall time	ms	5	5	5
Flat top duration	ms	1	1	1

To assess the impact on the field homogeneity of both the metallic (Inconel) undulated vacuum chambers as well as the unstripped particles dump, dynamic finite-element simulations were performed. The conclusion of these calculations is that the effect of the dump on the magnetic field, located just outside the magnet aperture, is not expected to be significant. The influence of the vacuum chambers was also precisely determined; the field was calculated at top field and several steps during the ramps down. Subsequently for each time step, the field integrals were extracted throughout the gap aperture. The mapped field integrals per time step were then translated in field harmonics and used to analyse the impact on the beam (emittance growth, beta beating etc.), see Section 3.3.1.

Stripping foil and handling system

The material choice and thickness of the foil is driven by the stripping efficiency, beam loss through nuclear scattering, emittance blow-up of the circulating beam and temperature rise of the foil [46]. For thermal stability, high sublimation temperature, radiation resistance and mechanical reasons the stripping foil material will be carbon, either in amorphous or diamond form. The foil thickness is specified by the areal density in $\mu\text{g}/\text{cm}^2$; the equivalent thickness is assumed with a bulk density of $2 \text{ g}/\text{cm}^3$. To ensure a theoretical stripping efficiency $>99\%$ the thickness should be $>150 \mu\text{g}/\text{cm}^2$, but to keep the emittance increase below $0.1 \pi \mu\text{m}$, for the $\varepsilon_x \sim 2 \pi \mu\text{m}$ for the LHC beam at injection, the foil should be $<250 \mu\text{g}/\text{cm}^2$ in thickness. Furthermore, to retain the uncontrolled beam loss below the 10^{-4} level a foil thickness $<200 \mu\text{g}/\text{cm}^2$ is required [47]. Since the benefits of a thicker foil outweigh the disadvantages of extra foil heating, losses and emittance blow-up, a foil thickness of $200 \mu\text{g}/\text{cm}^2$ ($\sim 1 \mu\text{m}$) is specified for PSB H⁻ injection.

Simulations [48] have shown that the highest foil temperatures are obtained for the high-intensity beam, where ε_x around $8 \pi \cdot \mu\text{m}$ and $6 \pi \cdot \mu\text{m}$ are assumed in the horizontal and vertical planes, respectively. The temperature rise for a single injection of $1.3 \times 10^{13} \text{ p}^+$ is about 280 K, as shown in Fig. 3.39. The effect of multiple injections at 1.2 Hz was investigated, assuming only black-body radiation cooling. An equilibrium peak temperature of 650 K is reached after a few cycles. Thermal foil damage is therefore unlikely during the foil's lifetime or a performance issue. The foil lifetime is expected to be dominated by purely mechanical effects or by accidents, such as shocks or being moved into the circulating beam.

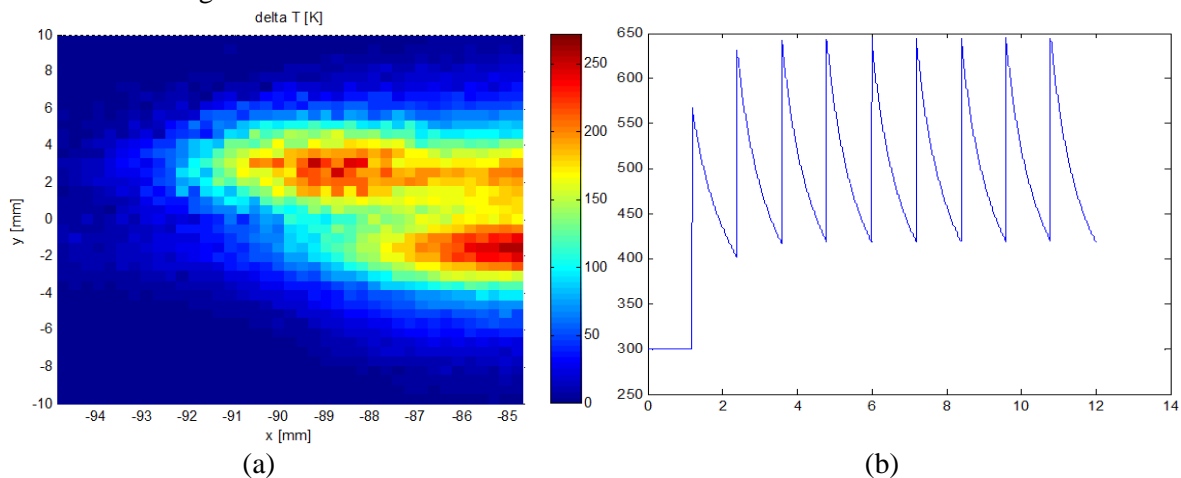


Fig. 3.39: (a) Temperature rise in carbon foil; (b) evolution of maximum temperature for high-intensity $1.3 \times 10^{13} \text{ p}^+$ beam injected at 1.2 s intervals.

The foil changer design is based on a NEC FS6 type foil changer (NEC, Middleton, USA), as shown in Fig. 3.40, and six foils per ring will be available in the exchange unit. Due to the limited space between BSW2 and BSW3 the stripping foil cannot be at the exact theoretical stripping point location, but will be positioned with an offset of ~ 30 mm longitudinal, upstream of the straight section centre. The aim is to have the possibility of moving each foil into the nominal beam position with a

precision of ± 0.1 mm from which a foil movement in the horizontal plane of ± 2 mm is possible in order to adjust the injection and cover the movement for setting up from a retracted position to the nominal position. The foil will cover the total vertical acceptance of the PSB, thus no vertical adjustment is necessary. To minimize the losses occurring from beam missing the foil, the foil size needs to be large enough to fully cover the incoming H^- beam. Nevertheless, a too large foil will result in larger numbers of foil hits per proton during injection, resulting in increases in beam loss, emittance and foil temperature. The width of the foil [47] was found to be 21 mm for injection with zero dispersion at the end of the transfer line and 32 mm for matched dispersion (-1.4 m). The support edges of the foil holder are kept outside the acceptance of the PSB and the lateral edge far enough, in order not to intercept the circulating beam, see Fig. 3.41.

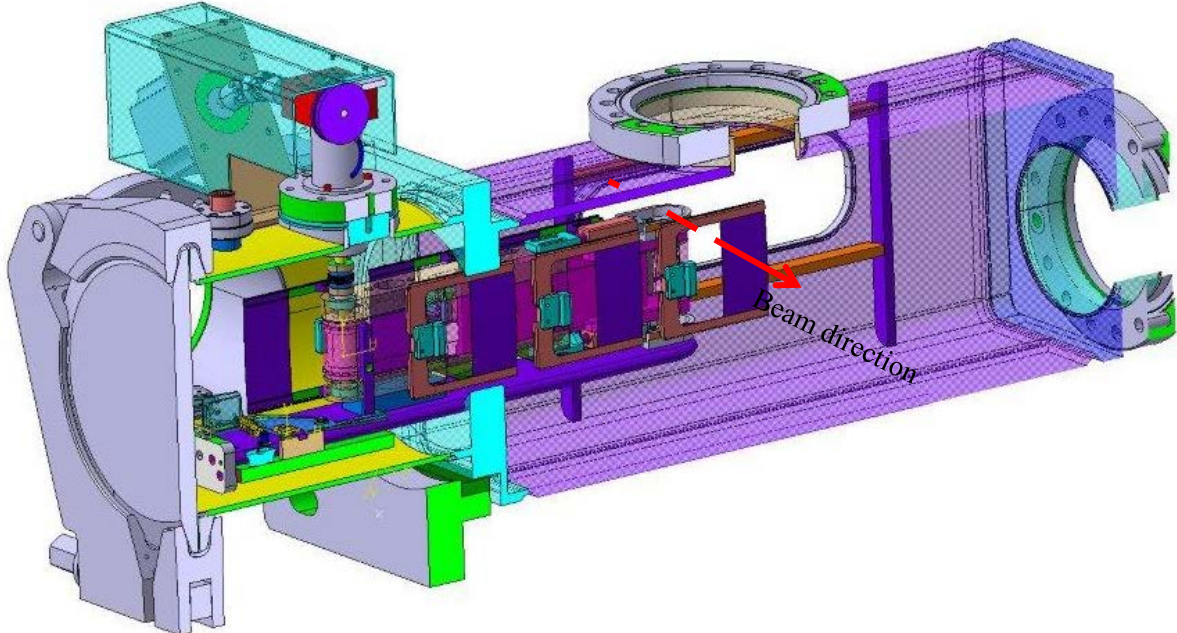


Fig. 3.40: Cross-section of stripping foil charger and handling system (CATIA ST411236)

In order to avoid foil damage due to differential pressure and to optimize intervention times, it will be possible to isolate the foil exchange system from the overall PSB vacuum system. For this reason the H^- injection system will become a dedicated vacuum sector with the sector valves located downstream of the BHZ162 and upstream of the BHZ11 main dipole magnets. An interlock system will be in place to avoid venting of the PSB vacuum system before the H^- injection is isolated.

Taking into account a pulley diameter of 24 mm and a step angle of 1.8° we end up with a step resolution of ≈ 0.38 mm/step. In order to meet the required specification, a gearbox with a 10:1 ratio is used so the final resolution is ≈ 0.038 mm/step when using a full-step drive. The stripping foils are fragile and can easily be damaged by vibration; this requires micro-stepping to smooth foil movement. Nevertheless, microsteps will not be used for positioning; thus the above-mentioned resolution remains. A third-party microstepping driver will be purchased for driving the two-phase stepping motor.

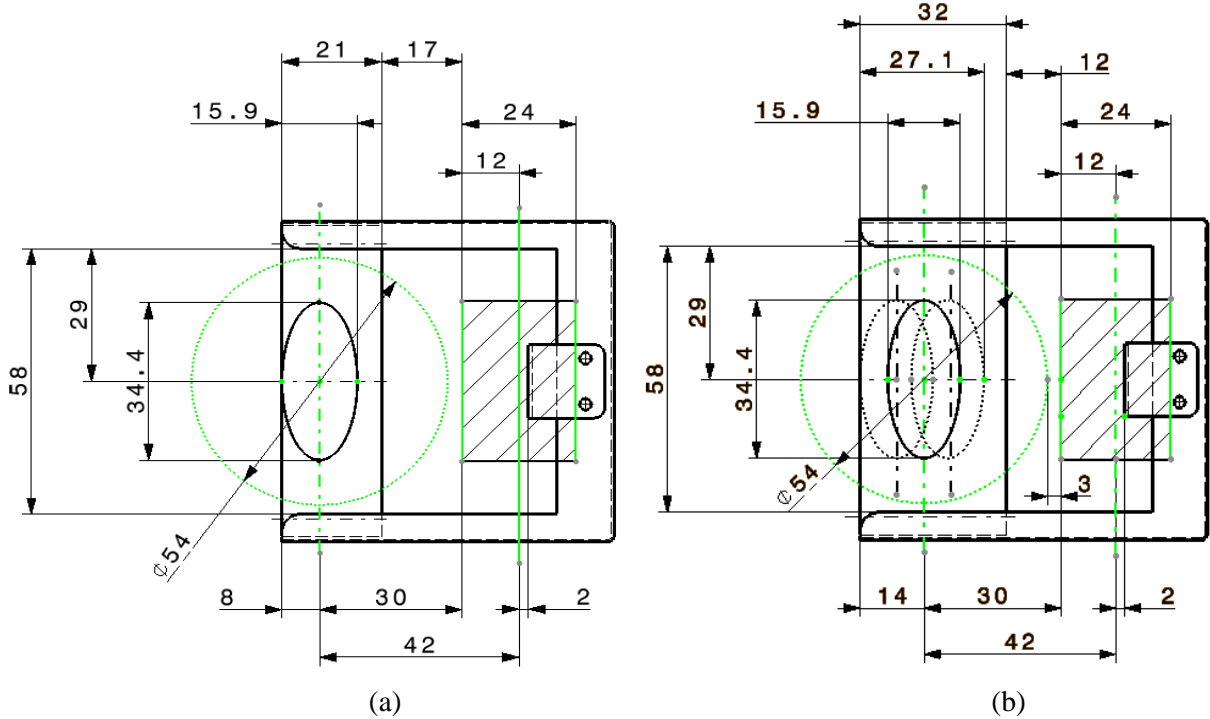


Fig. 3.41: Foil and support size and clearances required (a) for zero dispersion and (b) matched (-1.4 m) dispersion at injection point.

The stepping motor, connected to the gearbox, is connected to the pulley through a magnetic vacuum coupling. This magnetic coupling has a limited holding torque and could slip, meaning that a 180° turn of the pulley could go unnoticed and would result in incorrect position information. For this reason there will be three mechanisms inside the vacuum chamber to inspect and control the foil's frame position:

- a retractable rod/hook to have a zero position for calibration;
 - microswitches that are triggered for a certain range: foil IN or OUT position;
 - a U-shaped potentiometer made of conductive ink on Kapton to deduce a frame's position.

The control system [49] will consist of a relatively small and highly modular PLC [50], an economic solution for the limited computing power needed, and a custom-made electronics card. The PLC will supervise the microswitches, potentiometer and resolver, and control the stepping motor driver. Since the PLC is unable to translate the resolver signals, an electronics card will be made. This card will also control a small stepping motor that controls the retractable rod. Because of the distance between the stripping foil unit and the racks, some signal buffers on the card will also be needed.

3.4 Magnets

This section describes the current and new magnets required for the LIU-PSB project. The section is divided into four sub-sections including the injection line, PS Booster ring, transfer lines magnets from the PS Booster, and finally magnetic measurement requirements.

All of the CERN normal conducting magnets are defined in a database that is accessible when connected to CERN via www.norma.web.cern.ch. Information including characteristics, documentation and drawings can be found. The magnet designs are identified with a unique ten letter identifier; each magnet is then serialized with an additional eight digits as described in [51] and shown

in the example in Fig. 3.42. Throughout this section ‘existing’, ‘new’ and ‘proposed’ magnet designs are referenced using these identifiers.

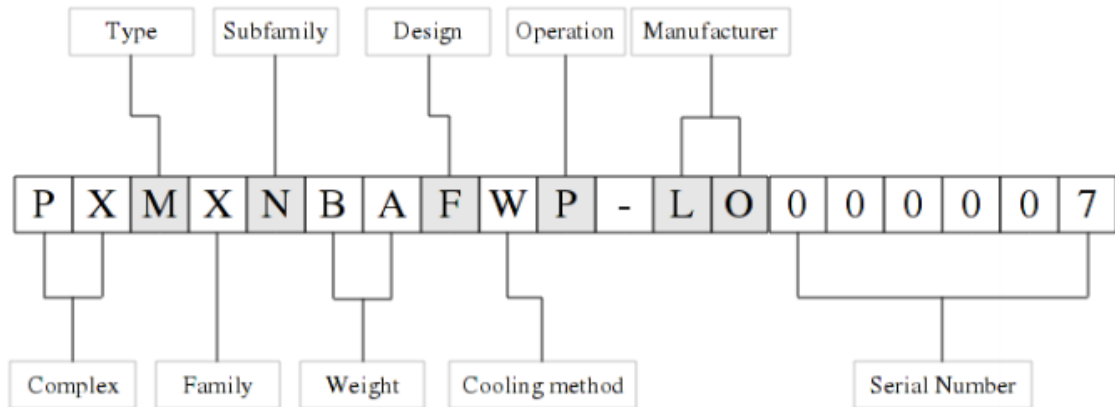


Fig. 3.42: Example of the CERN normal conducting magnet identifier

3.4.1 PS Booster injection magnets

Required modifications in the injection region are dictated by the increase in beam rigidity with the upgrade from Linac2 to Linac4. Additionally we plan to replace other magnets in the frame of a consolidation programme: a summary of the magnets in the injection line and required action is shown in Table 3.10.

Table 3.10: List of Booster injection transfer line magnets

Paragraph	Slot	Magnet type	Magnetic Parameters		Electrical Parameters			ACTION
			Magnetic length (m)	Integrated Field (Tm) / Gradient (T) @ 160 MeV	Ipeak Maximum (@160 MeV) [A]	R (Ohms) per plane	L (mH) per plane	
4.1.1	B1.BVT.R1	PXMBVDB4WC (NEW I-BV)	0.860	0.3320	418.2	0.056	12.2	Replaced LIU
	B1.BVT.R3	PXMCCCLA4WC (type 11)	0.860	0.2560	414.5	0.046	9.5	Replaced LIU
	B1.BVT.R4	PXMCCCLA4WC (type 11)	0.860	0.2560	414.5	0.046	9.5	Replaced LIU
4.1.2	B1.DHZ.DVT10	PXMCCCLA4WP (type 11)	0.388	0.0040	7.9	1.500	42.3	Replaced Consolidation
	B1.DHZ.DVT20	PXMCCCLA4WP (type 11)	0.388	0.0040	7.9	1.500	42.3	Replaced Consolidation
	B1.DHZ.DVT30	PXMCCCLA4WP (type 11)	0.388	0.0040	7.9	1.500	42.3	Replaced Consolidation
4.1.3	B1.DHZ.DVT40	PXMCCCAA4WP (Type 1)	0.440	0.0152	23.0	1.000	75.0	USE AS IS
	B1.QN010	PXMQNBSNAP	0.460	-0.4826	-50.6	0.500	33.0	Replaced Consolidation
	B1.QN020	PXMQNBSNAP	0.460	0.4707	49.3	0.500	33.0	Replaced Consolidation
4.1.4	B1.QN030	PXMQNBSNAP	0.460	-0.4464	-46.8	0.500	33.0	Replaced Consolidation
	B1.QN040	PXMQNBSNAP	0.460	0.4493	47.1	0.500	33.0	Replaced Consolidation
	B1.QN050	PXMQNBSNAP * 4	0.460	-0.8484	-88.9	0.500	33.0	Replaced Consolidation
4.1.2	B1.QN060	PXMQNBSNAP * 4	0.460	-0.9129	-95.7	0.500	33.0	Replaced Consolidation
	B11.DHZ.DVT50	PXMCCCLA4WP (type 11)	0.388	0.0130	25.0	1.500	42.3	Replaced LIU
	B12.DHZ.DVT50	PXMCCCLA4WP (type 11)	0.388	0.0130	25.0	1.500	42.3	Replaced LIU
4.1.2	B13.DHZ.DVT50	PXMCCCLA4WP (type 11)	0.388	0.0130	25.0	1.500	42.3	Replaced LIU
	B14.DHZ.DVT50	PXMCCCLA4WP (type 11)	0.388	0.0130	25.0	1.500	42.3	Replaced LIU
	B11.DHZ.DVT70	PXMCCCLA4WP (type 11)	0.388	0.0160	30.8	1.500	42.3	Replaced LIU
4.1.2	B11.DHZ.DVT70	PXMCCCLA4WP (type 11)	0.388	0.0160	30.8	1.500	42.3	Replaced LIU
	B11.DHZ.DVT70	PXMCCCLA4WP (type 11)	0.388	0.0160	30.8	1.500	42.3	Replaced LIU
	B11.DHZ.DVT70	PXMCCCLA4WP (type 11)	0.388	0.0160	30.8	1.500	42.3	Replaced LIU

3.4.1.1 *Injection bending BI.BVT40 (PXMBVDB4WC—‘new’)*

The vertical injection bending BI.BVT40 is a window-framed DC magnet with four apertures. It is positioned after the PSB injection distributor (BI.DIS) and septum (BI.SMV) to deflect three of the beams (one passes through without deflection) into the path of the four superimposed PSB rings. From bottom to top the required deflection angles are: Level 1: 174.5 mrad, Level 2: 134.5 mrad, Level 3: 0 mrad and Level 4: 134.5 mrad. The configuration of the current magnet uses three pairs of coils all connected in series to one power supply; the differing deflection angles are achieved using different numbers of turns between gap 1 and gaps 2 and 4 (90 and 70, respectively). With the introduction of Linac4 and an increase of beam rigidity a study has shown that the current magnet will not be able to operate due to saturation effects and limitations in the water cooling, and a new magnet has to be used.

A new magnet [52], shown in Fig. 3.43, has been designed to operate in DC, powered by three individual power converters. The iron cross-section has been increased to reduce the saturation at higher field levels and the copper conductor cooling channel cross-section has been increased to allow for an adequate cooling flow with an acceptable pressure drop. The main parameters of the magnet are shown in Table 3.11.

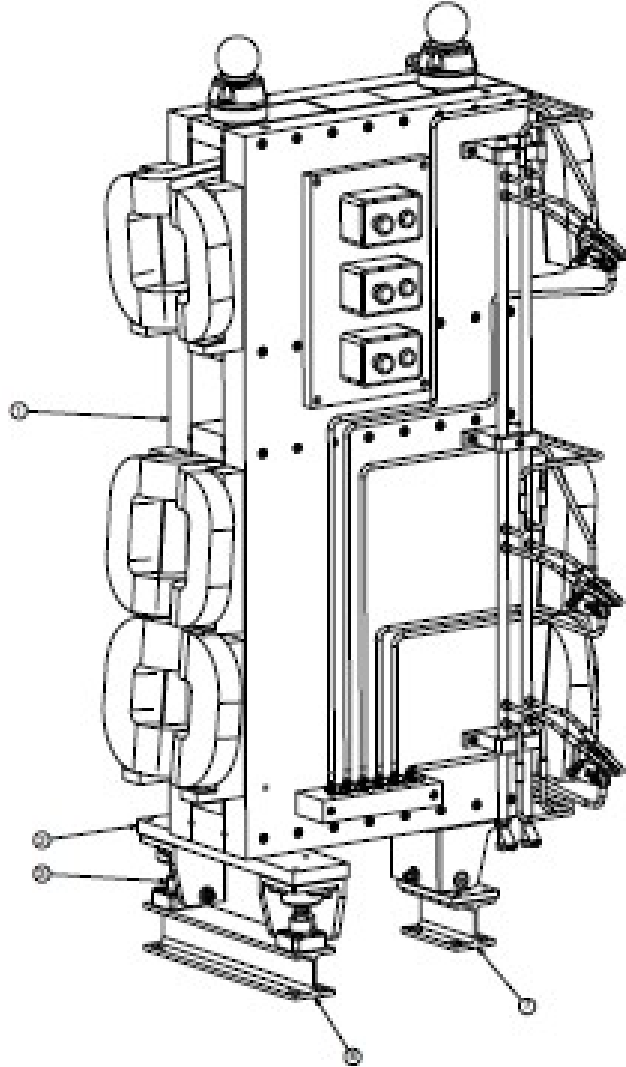


Fig. 3.43: 3D model of the new BI.BVT40 three aperture vertical injection magnet

Table 3.11: Injection bending magnet parameters for 50 MeV and 160 MeV operations

	Unit	50 MeV	160 MeV
Operation		DC	
Cooling		Water	
Deflection angle			
Level 1	mrad	174.5	
Levels 2 and 4	mrad	134.5	
$\int B dl$	T m		
Level 1		0.141	0.332
Levels 2 and 4		0.139	0.256
Effective length	m	0.87	
Gap width (H)	mm	120	
Gap height (V)	mm	124–168	
Operating current	A	220	405
Resistance	$\text{m}\Omega$	44–62	

3.4.1.2 *Injection dipole correctors BI.DHZ.DVT(10,20,30,50,70) (PXMCCLA WAP—‘new’)*

The combined horizontal and vertical dipole corrector magnets BI.DHZ.DVT50 and BI.DHZ.DVT70 are pulsed laminated window-frame magnets after the BI.BVT40 injection dipole used for the final steering of the beam into the PSB. To increase the space available around the injection point of the PSB, the stack of four magnets in slot BI.DHZ.DVT70 must be moved upstream of their current position by approximately 2 m. This movement dictates an increase in integrated field strength by a factor of two for the magnets in slots BI.DHZ.DVT50 and BI.DHZ.DVT70 for the Linac2 beam to arrive at the current same position. When also taking the increase of energy from Linac2 to Linac4 into account, the integrated field strength must be approximately doubled again. In addition, an offset of approximately 10 mm is required at the injection point [53]. To satisfy the most stringent beam dynamic requirements of the two slots a new corrector magnet common design [54] (Fig. 3.44) has been studied to replace both the magnets in slot BI.DHZ.DVT50 and slot BI.DHZ.DVT70. The common design reduces costs and the number of spare magnets required. The new magnet has been designed to be powered with the MidiDiscap power converter [55] and can also be used to replace the other upstream dipole corrector magnets as part of an agreed consolidation plan. The main parameters of the magnets are shown in Table 3.12.

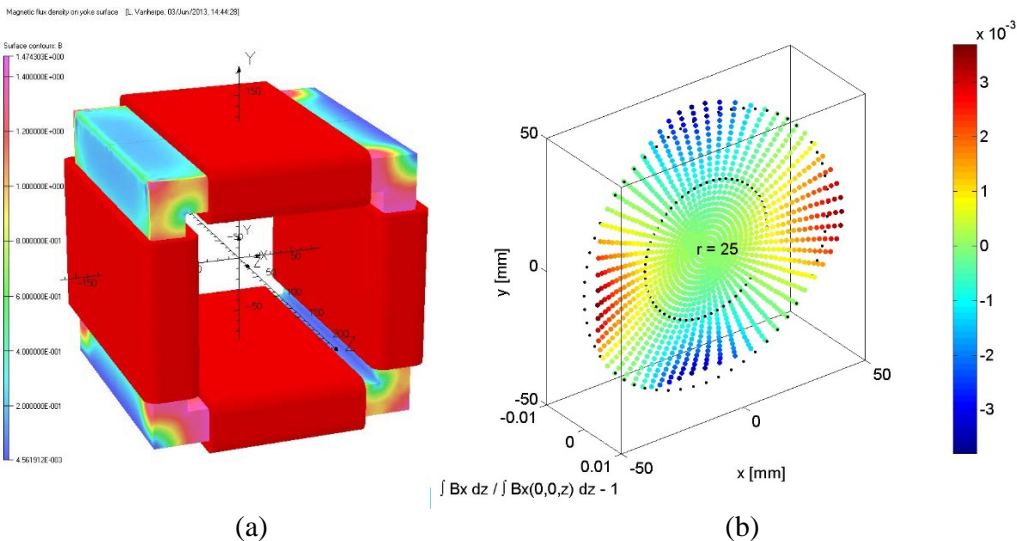


Fig. 3.44: (a) Magnetic design showing Opera 3D model with a map of the magnetic flux density B on the yoke surface: both planes are excited, the value of B does not exceed 1.5 T; (b) field homogeneity of component B_x in good-field region; vertical plane excited.

Table 3.12: Injection dipole corrector magnets parameters for 50 MeV and 160 MeV operations

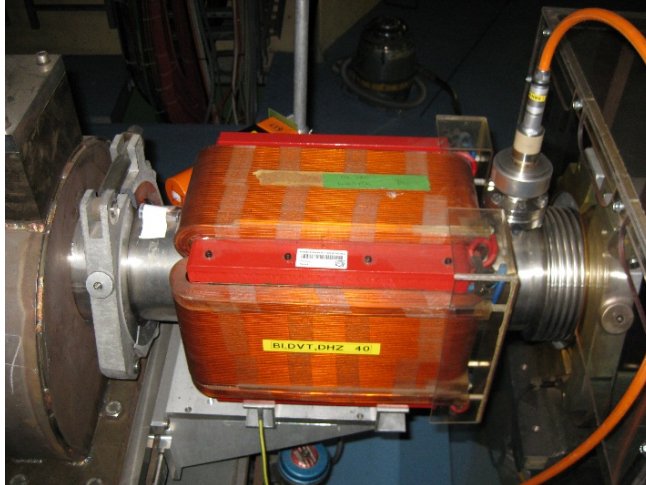
	Unit	50 MeV	160 MeV
Operation		Pulsed.	
Cooling		Air	
$B \cdot dl$	T m	0.08	0.16
Effective length	m		0.387
Gap height (V)	mm		150
Gap width (H)	mm		150
Operating current	A	15.75	31.5
Resistance (per plane)	Ω		1.5
Inductance (per plane)	mH		42.4

3.4.1.3 *Injection dipole corrector magnet BI.DHZ.DVT40 (PXMCCAAWAP—‘existing’)*

The combined horizontal and vertical dipole corrector magnet BI.DHZ.DVT40 (Fig. 3.45) is a pulsed laminated window-frame magnet design common to and used around the PSB ring as an orbit corrector. The BI.DHZ.DVT40 is positioned after the BI.DIS and is used to deflect the beam on the correct path towards the BI.SMV. The increase of beam rigidity from Linac2 to Linac4 dictates an increase of field strength by approximately 2; and in order to achieve sufficient beam separation at the BI.SMV [56] an approximate further 10% increase in the vertical plane is required. The new requirements still fit with the existing magnet design, although as the required current now exceeds the limits of the power supply, replacing the magnet with the design previously described can be considered. The support for the magnet is currently integrated with the BI.DIS; with the new BI.DIS the magnet must be moved to its own support. The main parameters of the magnet are shown in Table 3.13.

Table 3.13: Injection dipole corrector magnet BI.DHZ.DVT40 parameters for 160 MeV operations

	Unit	Value
Operation		Pulsed
Cooling		Air
Deflection angle	mrad	7.97
$B \cdot dl$	T m	0.00825
Effective length	m	0.44
Gap height (V)	mm	145
Gap width (H)	mm	145
Maximum operating current	A	23
Resistance (per plane)	Ω	1.0
Inductance (per plane)	mH	75.0

**Fig. 3.45:** The BI.DVT.DHZ 40 magnet integrated on the support for the existing BI.DIS

3.4.1.4 *Injection quadrupole magnets BI.QNO (10:60) (PXMQNBSNAP—‘new’)*

The current Booster injection quadrupole magnets date from the early 1970s. They are solid DC magnets both air- and water-cooled and, although the optics can be matched to allow the magnets to be used for Linac4 operation, a consolidation programme has been put in place to replace them. A new common air-cooled pulsed magnet design (Fig. 3.46) [57] has been made to operate with the MidiDiscap power converter [55]. The advantages of the new design include lower power consumption and standardization of the magnets and power converters for the injection line. In total there are 12 magnets to be replaced in the BI line: four single units and two stacks of four just before injection to the Booster. The main parameters of the magnets are shown in Table 3.14.

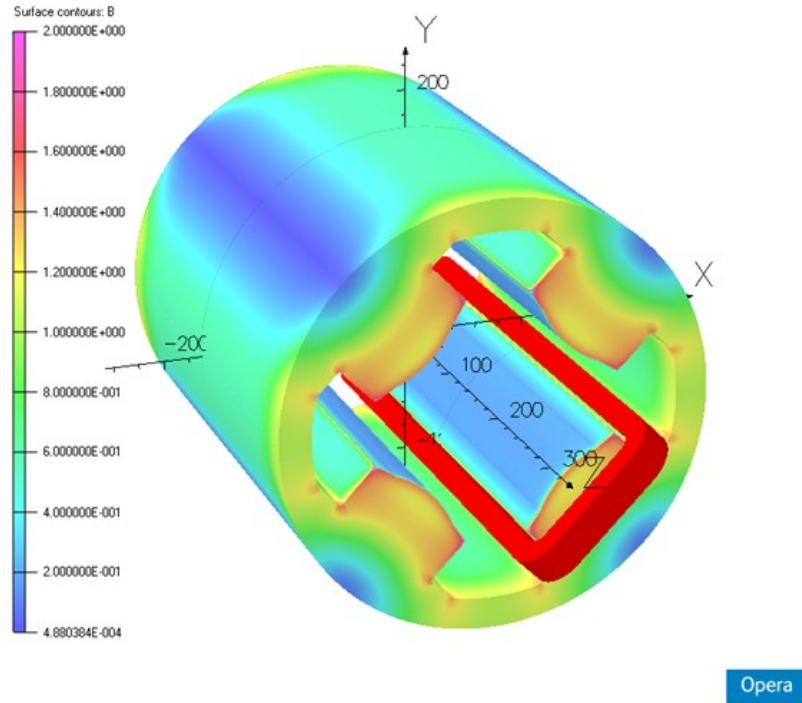


Fig. 3.46: Opera 3D magnetic simulation of the pulsed quadrupole magnet (only one coil is displayed)

Table 3.14: Injection quadrupole magnets BI.QNO (10:60) parameters for 160 MeV operations

	Unit	Value
Operation		Pulsed
Cooling		Air
Maximum $G.d/l$	T	1.04
Effective length	m	0.452
Inscribed radius	mm	75
Maximum operating current	A	95.4
Resistance	Ω	0.5
Inductance	mH	33.0

3.4.2 PS Booster ring magnets

The PS Booster is divided into sixteen periods, each period contains two main horizontal bending magnets, two focusing and one defocusing quadrupole magnet as well as dipole and multipole corrector magnets in the straight sections between the main bending and quadrupole magnets. The dipole and multipole corrector magnets are used at low energy and have already been assessed for operation with the 160 MeV Linac4 beam and confirmed to have adequate margin for operations.

3.4.2.1 Main units

The main bending and quadrupole magnets are connected to the main power supply (MPS) electrically in series with an additional bending magnet situated in the PS Booster power house used as a reference magnet for controlling the RF and power converter. In addition to the MPS, three trim converters on the main circuit are used: one on each of the focusing and defocusing types of quadrupole magnets to add gradient and one on the outer rings (ring 1 + 4) of the bending magnets, which require

approximately 1% increase in current due to saturation effects at 1.4 GeV. Figure 3.47 shows the electrical schematic of the main magnet electrical connections as used at 1.4 GeV operations.

The upgrade to 2.0 GeV operations require a new power converter and powering scheme as detailed in Section 3.6, the principle change for the magnet circuit is that it will be split into two, for which the two new circuits will comprise bending magnet rings 1 + 4 with the focusing quadrupole magnets and bending magnet rings 2 + 3 with the defocusing quadrupole magnets. With this scheme the trim supply on the bending magnet rings 1 + 4 can be suppressed, however modifications, as detailed in the section entitled *Main bending reference magnet (PXMBHGJ4WP—‘existing’)* below, will be required at the reference magnet. Splitting of the circuit into two also reduces the resistive and induced voltage applied to the magnets.

Separate circuits also exist on the main bending and quadrupole magnets, the so-called BDL and Q-Strip. These circuits are additional windings found on each ring for the main bending and focusing/defocusing quadrupole magnets; the windings are connected electrically in series by magnet type and per ring with 12 circuits in total. The 12 circuits are used to adjust each ring in terms of integrated field and gradient strength.

Main bending magnets (PXMBHGC4WP, PXMBHGD4WP, PXMBHGE4WP—‘existing’)

There are 32 main bending magnets in the PS Booster ring, 30 ‘normal’ and two ‘special’ used at the injection and extraction of the ring. The bending magnets (Fig. 3.48) are water-cooled, laminated asymmetric window-frame dipole magnets weighing ~12 tonnes each. The main parameters for the magnets at 1.4 GeV and 2.0 GeV are shown in Table 3.15.

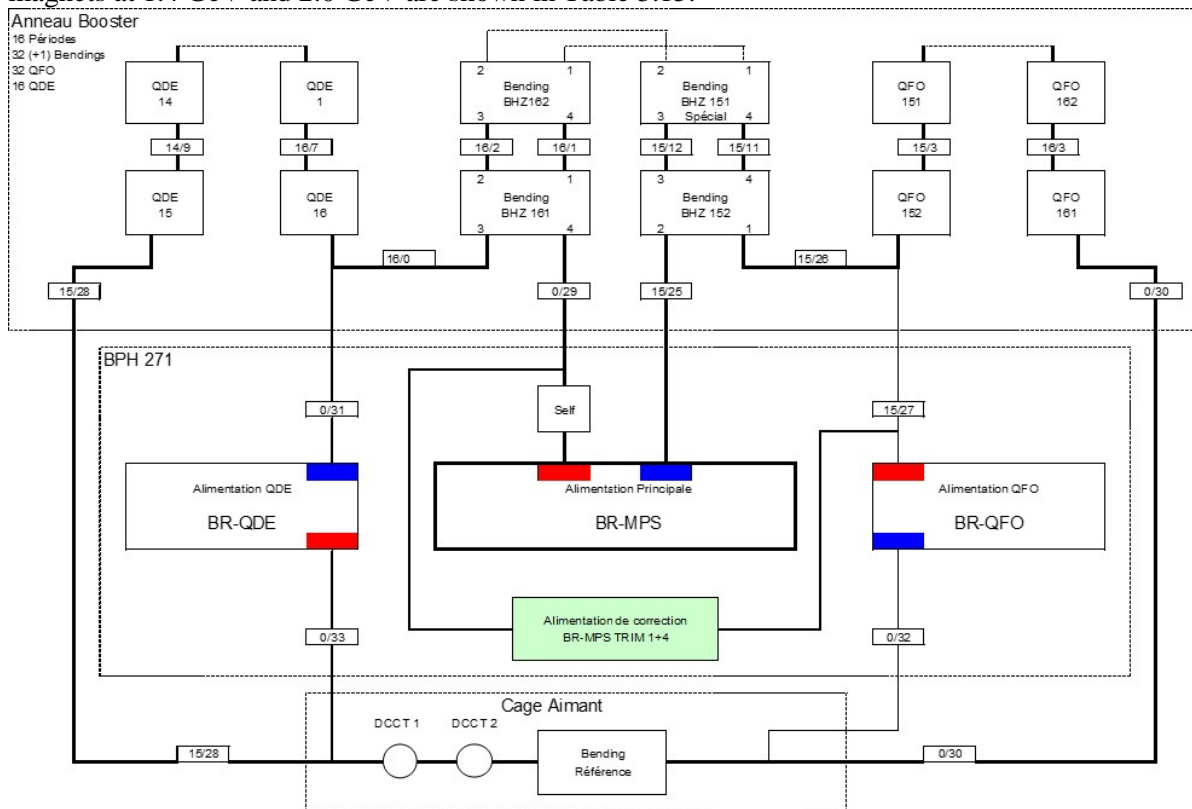


Fig. 3.47: Electrical schematic of the PS Booster main magnets as used at 1.4 GeV operations

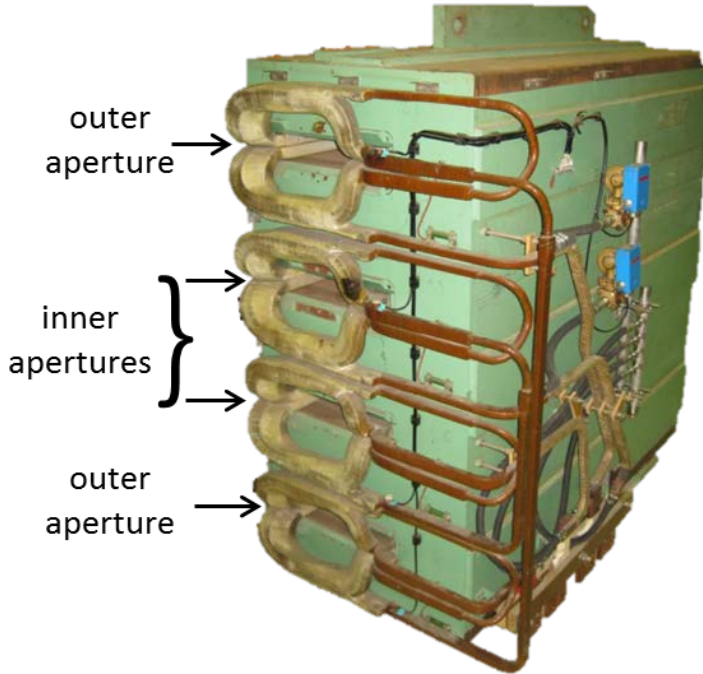


Fig. 3.48: The PSB four aperture main dipole magnet

Table 3.15: Main bending magnet parameters for 1.4 GeV and 2.0 GeV operations

	Unit	1.4 GeV	2.0 GeV
Operation		DC cycled	
Cooling		Water	
$B.dl$	T m	1.376	1.824
Effective length	m		1.63
Gap height (V)	mm		70
Gap width (H)	mm		200
Maximum rms current	A		2495
Nominal peak current	A	4032	5255
Resistance per aperture	$\text{m}\Omega$		2.5
Inductance per aperture	mH		1.5

During the upgrade of the PS Booster to 1.4 GeV in 1999 a study [58] on the bending magnets showed that due to the asymmetric design and saturation effects a difference of approximately 1% could be seen between the inner and outer rings. More recent modelling and measurements of a spare magnet confirm that at 2.0 GeV field levels the difference will increase to approximately 4% due to higher levels of saturation. It has been recently shown [59] that the difference between the inner and outer gaps can be reduced back to below 1% by replacing the solid coil retaining plates with laminated versions as shown in Fig. 3.49 and detailed in Table 3.16. A similar modification will also need to be made to the special injection and extraction bending magnets. These magnets have special coils where the injection and extraction vacuum pipes are allowed to pass through the magnet aperture. The study for these two magnets is ongoing, and at the time of writing a decision to implement this improvement has not been made and will depend on the completion of the relevant magnetic measurements and evaluation of the advantages for doing so.

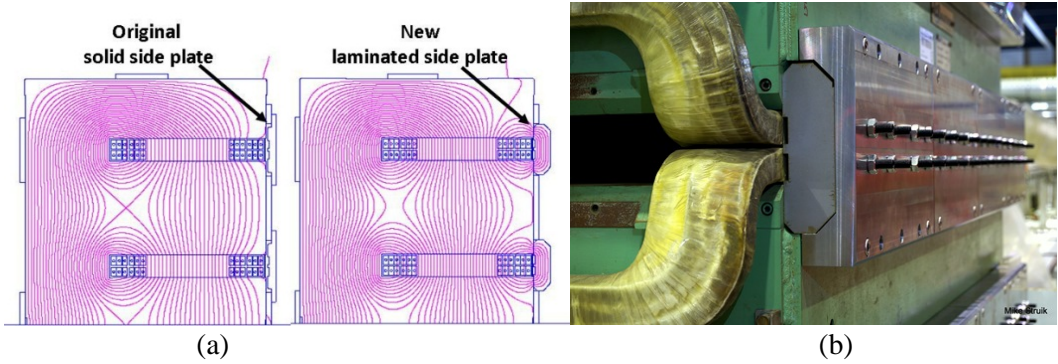


Fig. 3.49: (a) Poisson Superfish 2D simulation showing the effect of introducing the laminated side plate; (b) the prototype installation.

Table 3.16: Measured integrated field strength before and after the introduction of the laminated coil retain plate

	Unit	1.4 GeV	2.0 GeV
Before modification			
Peak current	A	4065	5515
Inner apertures	T m	1.408	1.913
Outer apertures	T m	1.392	1.834
Difference	%	1.10	4.13
After modification			
Peak current	A	4032	5200
Inner apertures	T m	1.397	1.798
Outer apertures	T m	1.394	1.778
Difference	%	0.18	1.10

The mechanical integrity of the bending magnet at 2.0 GeV has been evaluated with particular attention paid to forces acting on the coils and the shimming of these coils in the magnet yoke. The force acting on the coils increases with the square of the field and, compared to 1.4 GeV operations, is to increase by around 70% from 32 kN to 55 kN for 2.0 GeV operations. This increase is considerably more than the PS Booster's first operations at 800 MeV, and an investigation [60] into the method of shimming clearly shows that modifications are required for 2.0 GeV operations. The proposed modifications that can be integrated with or without the laminated side plates aim to improve the method for the application of the shims against the coils and increase the size of the shims, thus reducing localized forces and the risk of mechanical damage.

The cooling performance of the main bending dipole magnets has been assessed during the feasibility study [2]. The relevant findings show that to avoid modifying the magnets where such modifications would dictate removing each one from the machine to perform the modifications, an increase of 10% in rms current can be permitted. To achieve this 10% increase where natural scaling would increase by 30% at 2.0 GeV operations a shorter cycle has been determined [61] increasing both the ramp up and down and minimizing the flat-top. However, even with the increase of 10% it has been required to change the thermal protection switches on the magnet [62]; this work has already been implemented during LS1 of the LHC along with the upgrade to the magnet protection hardware.

Main bending reference magnet (PXMBHGJ4WP—‘existing’)

The main bending reference magnet installed with a real-time magnetic measurement system (‘B-train’) is situated in the PS Booster power house and is used to control the RF and power convertors,

see section 3.4.4. The magnet is similar to the normal bending magnets as described in the previous section, but it was built as the prototype for the Booster and as such the configuration of the coils is not compatible for operation at 2.0 GeV as the four apertures cannot be separated into inner and outer apertures as they can for the ring magnets. For this purpose it is necessary to construct and install four times two pairs of new coils.

Main quadrupole magnets (31 * PXMQNEC4WP, 1 * PXMQNED4WP, 16 * PXMQNFA4WP—‘existing’)

There are 16 defocusing (Fig. 3.50) and 32 focusing quadrupole magnets in the PS Booster of which one of the focusing quadrupole (PXMQNED4WP) has a doubled cooling performance. The magnets are laminated and water-cooled, and weigh between 3.1 and 5.6 tonnes each. Magnetic models show that they operate far from saturation and in terms of magnetic field gradient can operate linearly beyond 2 GeV field levels.

Like the PS Booster main bending magnets, to operate at 2.0 GeV field levels the rms current must be limited to 10% higher than that of 1.4 GeV operations. Again, like the main bending magnets, it has been necessary to replace the thermal protection switches on the magnets that have been completed during LS1.

Another important upgrade that has already been implemented during LS1 is the improvement to the hydraulic circuit integrity [63]. The magnets for the PS Booster were designed to operate with a water pressure drop of around 5 bar, while at 1.4 GeV and 2.0 GeV the operating pressure drop is more than double, at 11 bar. To be able to operate for the next 20-plus years the coil connections have been upgraded with new brazed and crimped connections. The main parameters for the focusing and defocusing magnets at 1.4 GeV and 2.0 GeV are shown in Tables 3.17 and 3.18, respectively.



Fig. 3.50: The four-aperture defocusing main quadrupole magnet

Table 3.17: Focusing quadrupole magnet parameters for 1.4 GeV and 2.0 GeV operations

	Unit	1.4 GeV	2.0 GeV
Operation		DC cycled	
Cooling		Water	
G	T/m	5.61	7.66
Effective length	m	0.503	
Aperture radius	mm	60	
Maximum rms current	A	2495	
Nominal peak current	A	4032	5255
Resistance per magnet	$\text{m}\Omega$	2.4	
Inductance per magnet	mH	0.24	

Table 3.18: Defocusing quadrupole magnet parameters for 1.4 GeV and 2.0 GeV operations

	Unit	1.4 GeV	2.0 GeV
Operation	DC cycled		
Cooling	Water		
G.dl	T	5.61	7.66
Effective length	m		0.881
Aperture radius	mm		60
Maximum rms current	A		2495
Nominal peak current	A	4032	5255
Resistance per magnet	mΩ		3.3
Inductance per magnet	mH		0.42

3.4.3 PS Booster transfer line magnets (BT, BTP, BTY and BTM)

Required modifications in the transfer lines from the Booster are dictated by the increase in beam rigidity from 1.4 GeV to 2.0 GeV operations as well as allowing for pulse-to-pulse modulation (PPM) mode operations. In addition, while some magnets could be used as they are, consideration has been given to the most efficient method to upgrade the complete circuit including the power converter. In many cases the additional voltage required to cycle the magnets would require a new larger and more costly power converter for which more space would be required in the already packed converter rooms. In these scenarios both the magnet and power converter could be changed for a pulsed system that has not only the advantage of requiring less space for the converter but also would considerably lower operation costs in terms of power consumption. A summary of the magnets in the Booster transfer lines BT, BTM and BTP, and required actions is shown in Table 3.19.

3.4.3.1 Recombination bending magnets type: T-BV1, BT1.BVT10 and BT4.BVT10, (PXMBVBCWAP or PXMBVBCWWP—‘proposed’) T-BV2, BT.BVT20, (PXMBVCFWAP or PXMBVCFWWP—‘proposed’)

The T-BV1 bending magnets start the recombination of the four PSB rings by deflecting ring 1 up to ring 2 and 4 down to ring 3, while the T-BV2 magnet further downstream starts the recombination from the two times two combined rings into one by deflecting ring 2 up to ring 3 (Fig. 3.51). The laminated, water-cooled magnets installed in the late 1990s allow operation in PPM between 1.0 GeV and 1.4 GeV field levels; however, due to a limitation in the power converter the field level is only changed when requested and does not drop to zero between cycles. This type of operation between 1.4 and 2.0 GeV will not be possible as the magnets will exceed the maximum allowable rms current when at 2.0 GeV field levels, and therefore must be continuously cycled to a lower current between machine cycles to stay with their cooling limits. Although the magnets are laminated they have not been optimized for this type of cycling as they include magnetic end plates, tie bars and solid magnetic shims. The current and voltage required to cycle the magnets also dictate a new larger and more costly power supply and it is therefore recommended to change the magnet as part of the upgrade. The new magnet type is to be defined but options include a similar ‘slow design’ as currently used, with an improved cooling performance and optimized yoke or an air-cooled ‘fast design’ to be pulsed using a capacitive discharge type power supply. The main parameters for each design option are shown in Tables 3.20 and 3.21.

Table 3.19: List of Booster ejection transfer line magnets

Paragraph	BT line	Slot	Magnet type	Magnetic parameters			Action
				Minimum required integrated field (T m)	Magnetic length (m)	Maximum required integrated field (T m) / gradient (T)	
4.3.1	BT4.BVT 10		T-BV1 (PXMBVBBCWAP or PXMBVBCCWWP ‘proposal’)	0.9059	0.5360	0.6968	New magnet (LIU)
	BT1.BVT 10		T-BV2 (PXMBVCFWAP or PXMBVCFWWWP)	0.9059	0.5380	0.6994	New magnet (LIU)
	BT.BVT 20			0.9260	0.5149	0.6694	New magnet (LIU)
87	BT3.DVT 10		T-DVT (PXMCVABWWP ‘existing’ or PXMCVACWAP ‘proposal’)	0.4037	0.0400	0.0521	Use as is / new magnet (LIU – if pulsed)
	BT2.DVT 10			0.4037	0.0355	0.0461	Use as is / new magnet (LIU – if pulsed)
	BT3.DVT 20			0.4037	0.0743	0.0966	TBD / new magnet (LIU – if pulsed)
	BT2.DVT 20			0.4037	0.0700	0.0910	TBD / new magnet (LIU – if pulsed)
	BT3.DVT 40			0.3333	0.0352	0.0457	Use as is / new magnet (LIU – if pulsed)
	BT4.DHZ 10		8af (PXMCXADWAP ‘existing’)	0.3333	0.0128	0.0166	Use as is
	BT3.DHZ 10			0.3333	0.0089	0.0115	Use as is
4.3.3	BT2.DHZ 10			0.3333	0.0167	0.0218	Use as is
	BT1.DHZ 10			0.3333	0.0069	0.0090	Use as is
	BT.DVT 30			0.3330	0.0167	0.0218	Use as is
	BT2.DVT 40			0.3333	0.0167	0.0218	Use as is
	BT.DVT 50		4af (PXMCXAEWAP ‘existing’)	0.3330	0.0139	0.0181	Use as is
4.3.4	BT.DVT 60			0.3330	0.0176	0.0229	Use as is

Table 3.19: Continued

Magnetic parameters						
Paragraph	Slot	Magnet type	Magnetic length (m)	Minimum required integrated field (T m) / gradient (T)	Maximum required integrated field (T m) / gradient (T)	Action
4.3.7	BT2.QNO 10	Triumf water (PXMQNCRNWP ‘existing’)	0.4660	2.1434	2.8892	Use as is / new magnet (LIU – if pulsed)
	BT3.QNO 10		0.4660	2.1434	2.8892	Use as is / new magnet (LIU – if pulsed)
	BT2.QNO 20		0.4660	0.0820	2.7354	Use as is / new magnet (LIU – if pulsed)
	BT3.QNO 20		0.4660	2.0820	2.7354	Use as is / new magnet (LIU – if pulsed)
	BT.QNO 30		0.4660	0.8710	1.2442	Use as is / new magnet (LIU – if pulsed)
4.3.8	BT.QNO 40	Quadrupole, type BT (PXMQNCRNAP or PXMQNCRUNWP ‘proposal’)	0.6000	3.1500	5.4000	New magnet (LIU)
	BT.QNO 50		0.6000	-2.9100	-4.9900	New magnet (LIU)
	BT.BHZ 10	(PXMMBHGAWWP ‘new’)	2.00	1.14	1.49	New magnet (LIU)
BTM line						
4.3.9	BTM.QNO 05	Q130 (PXMQNCDNWP ‘existing’)	0.5600	2.4461	4.1944	Use as is
	BTM.QNO 10		0.5600	-2.9478	-5.0568	Use as is
	BTM.QNO 20		0.5600	3.4143	5.8520	Use as is
	BTM.BHZ 10	(PXMBBXGECWP ‘new’)	2.4800	2.45	3.19	Replace LIU
4.3.6	BTM.DVT 10	4af (PXMCCXAEWAP ‘existing’)	0.3330	0.0056	0.0072	Use as is
4.3.4	BTM.DHZ 10		0.3330	0.0111	0.0145	Use as is

Table 3.19: Continued

Paragraph	BTP line	Slot	Magnet type	Magnetic parameters			Action
				Minimum required integrated	Maximum required integrated	field (T m) / gradient (T)	
4.3.4	BTP.DHZ 10	4af (new)		0.3330	0.0111	0.0145	TBD/replace LIU – as two combined
	BTP.DVT 10			0.3330	0.0074	0.0096	H/V to allow use in wall
	BTP.DHZ 20	4af (PXM CXAEWAP ‘existing’)		0.3330	0.0046	0.0060	Use as is
	BTP.DVT 20			0.3330	0.0056	0.0072	Use as is
	BTP.DHZ 30			0.3330	0.0046	0.0060	Use as is
	BTP.DVT 30			0.3330	0.0074	0.0096	Use as is
	BTP.DVT 40			0.3330	0.0176	0.0229	Use as is
	BTP.DHZ 40			0.6000	0.0056	0.0072	Use as is
	BTP.DVT 50			0.3330	0.0111	0.0145	Use as is
	BTP.QNO 20	SMIT water (new)		0.6000	2.7049	4.6361	Replace LIU
4.3.8	BTP.QNO 30			0.6000	-3.0206	-5.1801	Replace LIU
	BTP.Q35			0.6000	3.3754	5.7846	Replace LIU
	BTP.QNO 50			0.6000	1.6601	2.8458	Replace LIU
	BTP.Q55			0.6000	-2.0018	-3.4317	Replace LIU
	BTP.QNO 60			0.6000	2.1081	3.6131	Replace LIU

Table 3.20: Recombination bending magnets, T-BV1 (new) parameters for 1.4 GeV and 2.0 GeV operations

	Unit	‘Slow design’ (PXMBVBCWWP)	‘Fast design’ (PXMBVBCWAP)
Operation		Cycled DC	Pulsed
Cooling		Water	Air
Maximum $B.dl$ at 1.4 GeV	T m	0.536	
Maximum $B.dl$ at 2.0 GeV	T m	0.697	
Effective length	m	0.906	
Gap height (V)	mm	124	
Gap width (H)	mm	62	
Maximum current at 1.4 GeV	A	269	1004
Maximum current at 2.0 GeV	A	350	1306
Resistance	Ω	0.236	0.02
Inductance	mH	40	3

Table 3.21: Recombination bending magnet, T-BV2 (new) parameters for 1.4 GeV and 2.0 GeV operations

	Unit	‘Slow design’ (PXMBVCFWWP)	‘Fast design’ (PXMBVCFWAP)
Operation		Cycled DC	Pulsed
Cooling		Water	Air
$B.dl$ at 1.4 GeV	T m	0.515	
$B.dl$ at 2.0 GeV	T m	0.667	
Effective length	m	0.906	
Gap height (V)	mm	124	
Gap width (H)	mm	120	
Maximum current at 1.4 GeV	A	243	972
Maximum current at 2.0 GeV	A	316	1264
Resistance	Ω	0.46	0.03
Inductance	mH	86	5

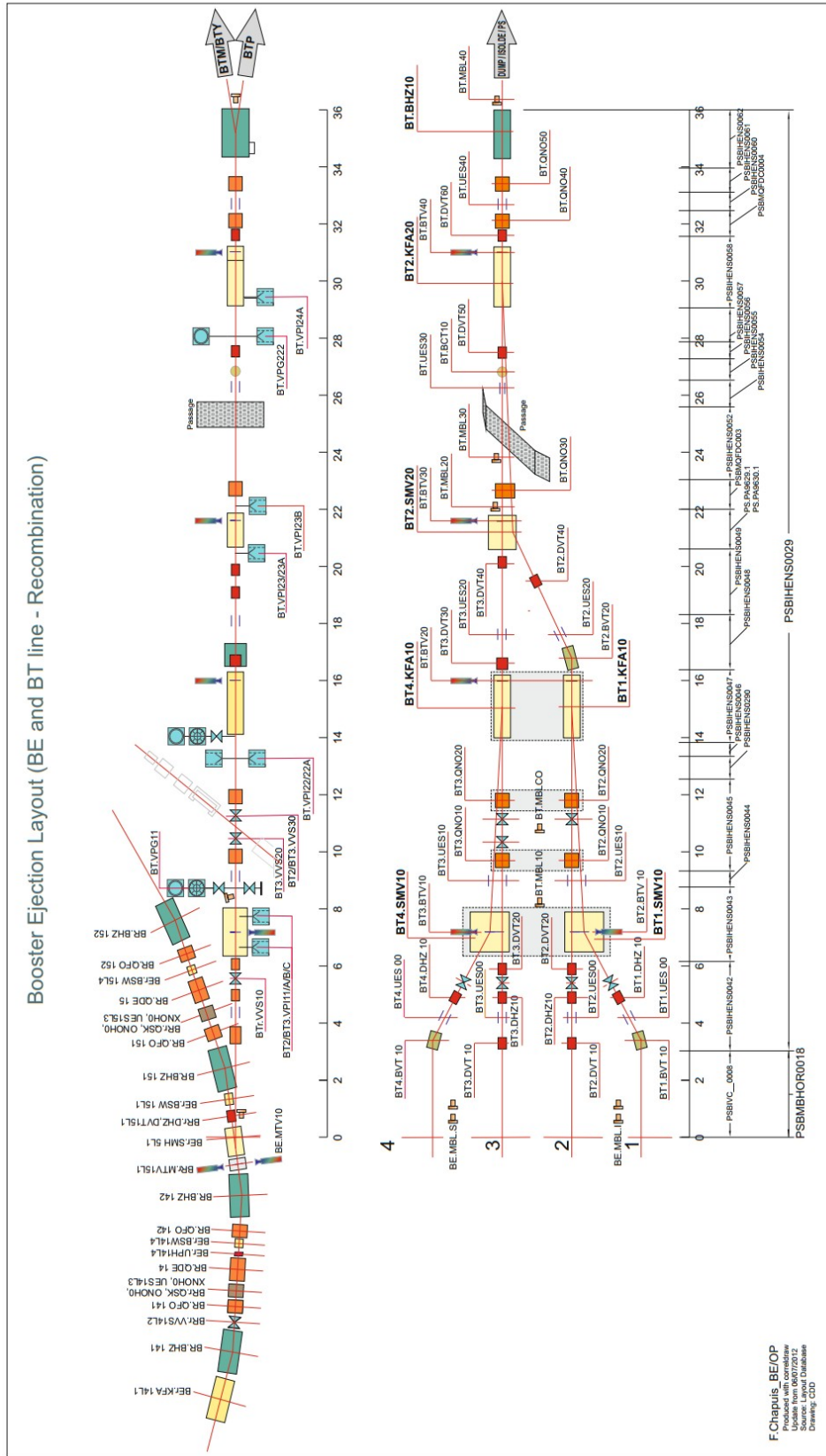


Fig. 3.51: Booster ejection layout (BE and BT line)

3.4.3.2 Recombination dipole corrector magnets type T-DVT (BT2.DVT10, BT3.DVT10, BT2.DVT20, BT3.DVT20 and BT3.DVT40) (PXMCVABWWP—‘existing’ and PXMCVACWAP—‘new’)

The T-DVT corrector magnets form part of the recombination from the four PSB rings to the single transfer line towards the PS, measurement line/dump and ISOLDE facility (Fig. 3.52). The laminated magnets installed in the late 1990s allow operation in PPM between 1.0 GeV and 1.4 GeV field levels; however, due to limitations in the power converter the field levels are only changed when requested and do not drop to zero between cycles. Three out of the five magnets can comfortably be operated in a similar method for 2 GeV operations within the original specification but may require new power supplies. For the remaining two magnets, BT2.DVT20 and BT3.DVT20, this type of operation between 1.4 GeV and 2.0 GeV will not be possible as the magnets will exceed the maximum allowable rms current when at 2.0 GeV field levels, and therefore must be continuously cycled to a lower current between machine cycles to stay with their cooling limits. The required field levels for 2 GeV operations are also beyond the measured magnetic field values available and, as there are currently no spare magnets (only spare coils) in stock, magnetic models are being developed to evaluate field homogeneity at the higher field levels, where the magnets become saturated. The manufacture of new yokes pieces so that spare magnets can be assembled will be considered once the magnetic models have been evaluated and if new magnetic shimming is required. In addition, although the magnets are laminated they have not been optimized for this type of cycling as they include magnetic end plates, tie bars and solid magnetic shims; the required current and voltage will also dictate that new power converters are required and therefore a new air-cooled ‘fast design’ using a capacitive discharge power supply is also being considered. The main parameters of the original ‘slow design’ and new ‘fast design’ magnets are shown in Table 3.22.

Table 3.22: Recombination dipole corrector magnets, T-DVT parameters for 1.4 GeV and 2.0 GeV operations

Unit	‘Slow design’ (PXMCVABWWP)	‘Fast design’ (PXMCVACWAP)
Operation	Cycled DC	Pulsed
Cooling	Water	Air
Maximum $B.dl$ at 1.4 GeV	T m	0.074
Maximum $B.dl$ at 2.0 GeV	T m	0.097
Effective length	m	0.404
Gap height (V)	mm	102
Gap width (H)	mm	104
Maximum current at 1.4 GeV	A	243
Maximum current at 2.0 GeV	A	347
Resistance	Ω	0.082
Inductance	mH	2.7
		26

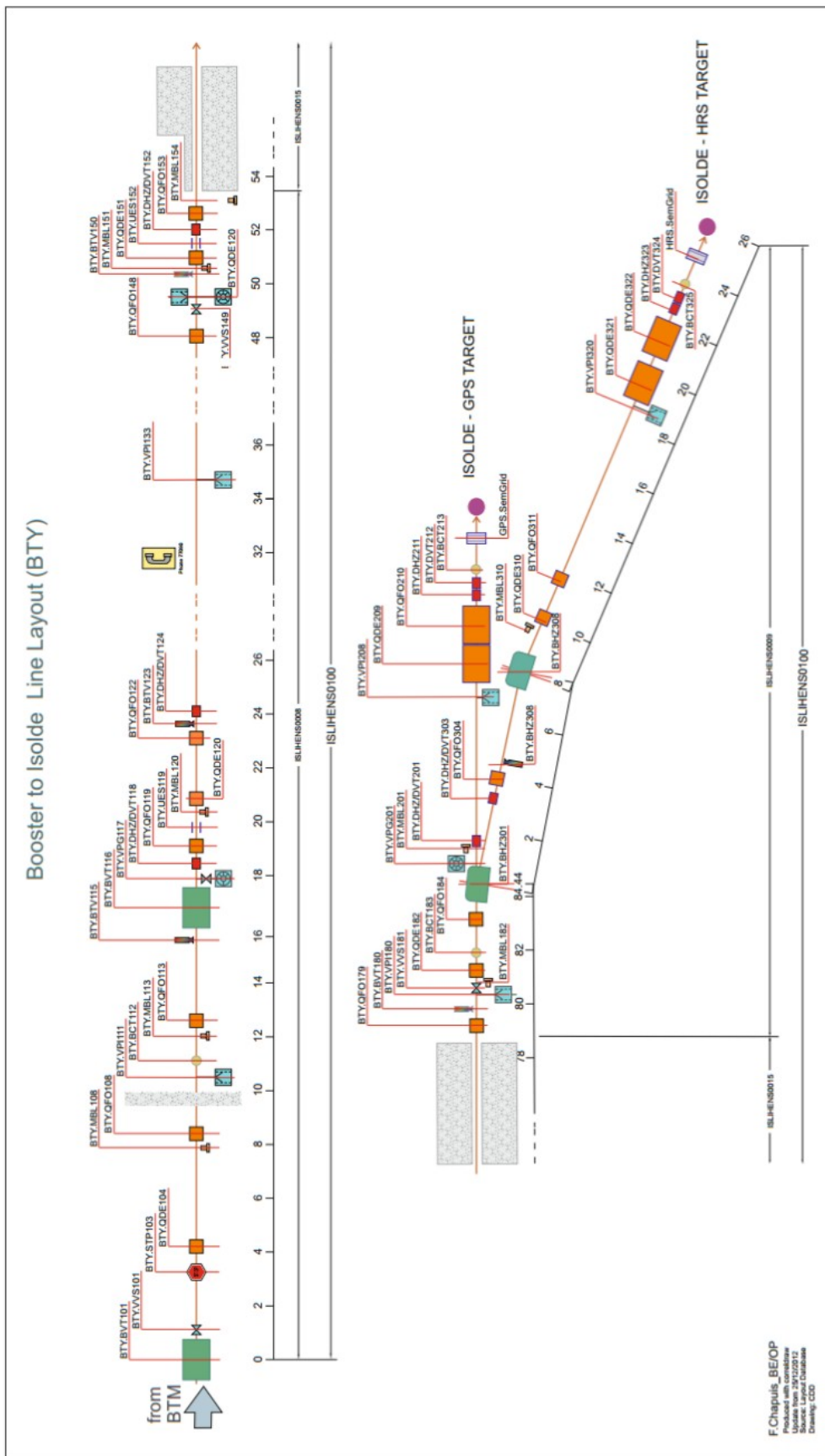


Fig. 3.52: Booster to ISOLDE (BTY)

3.4.3.3 Horizontal or vertical corrector magnets type 8af (BT(1,2,3,4).DHZ10, BT3.DVT30, BT2.DVT40) (PXM CXADWAP—‘existing’)

The six single-plane horizontal or vertical corrector magnets are installed in three positions along the BT transfer line (Fig. 3.51). The first four shown in Fig. 3.53 are stacked one above the other and are used for horizontal correction; the next two, which are used in different longitudinal positions, provide vertical correction. The magnets are air-cooled pulsed magnets powered with the MiniDiscap power system. Scaling from maximum values at 1.4 GeV to 2.0 GeV operations, the field levels go beyond that of the original specifications and measurements. However, simulations show that the magnets are below saturation levels and can be operated in terms of field and electrical performance at 2 GeV beam energy. The scaled current goes beyond that of the connected power supply in half of the cases, and it must be considered if a scaling approach is appropriate in the case of the future required correction in the transfer line. The main parameters of the magnets are shown in Table 3.23.

Table 3.23: Correction dipole magnet parameters for 1.4 GeV and 2.0 GeV operations

	Unit	1.4 GeV	2.0 GeV
Operation		Pulsed	
Cooling		Air	
Maximum $B \cdot dl$	T m	0.0167	0.0218
Effective length	m		0.333
Gap height (V) ^a	mm		105
Gap width (H) ^a	mm		120
Maximum rms current	A		16
Operating current	A	17	21.9
Resistance	Ω		0.65
Inductance	mH		38

^aHorizontal configuration.

3.4.3.4 Horizontal or vertical corrector magnets type 4af (BT.DVT50, BT.DVT60, BTP.DHZ(10...40), BTP.DVT(10...50), BTM.DHZ10, BTM.DVT10) (PXM CXAEWAP—‘existing’)

The eleven single-plane horizontal or vertical corrector magnets are installed along the BT, BTP and BTM transfer lines (Figs. 3.51 and 3.54). The magnets are air-cooled pulsed magnets powered with the MiniDiscap power system with the pair of coils connected in parallel. Scaling from maximum values at 1.4 GeV to 2 GeV operations, the field levels go beyond that of the original specifications and measurements. However, simulations show that the magnets are below saturation levels and can be operated in terms of field and electrical performance at 2 GeV beam energy. The scaled current goes beyond that of the connected power supply in three of the cases and it must be considered if a scaling approach is appropriate in the case of the future required correction in the transfer line.

The first two magnets of this type in the BTP transfer line (BTP.DHZ10 and BTP.DVT10) are positioned in the wall between the PSB and the PS, where repair would be extremely difficult. It can be considered that these two magnets can be replaced by two combined function horizontal and vertical corrector magnets where one is used and the other is considered as a hot spare to allow for operational use. The main parameters of the magnets are shown in Table 3.24.



Fig. 3.53: The BT(1,2,3,4).DHZ10 corrector dipole magnets (PXMCXADWAP)

Table 3.24: Correction dipole magnet parameters for 1.4 GeV and 2.0 GeV operations

	Unit	1.4 GeV	2.0 GeV
Operation		Pulsed	
Cooling		Air	
Maximum $B \cdot dl$	T m	0.0176	0.0230
Effective length	m		0.333
Gap height (V) ^a	mm		150
Gap width (H) ^a	mm		160
Maximum rms current	A		16
Operating current	A	19	24.7
Resistance ^b	Ω		0.83
Inductance ^b	mH		97.8

^a Horizontal configuration; ^b for parallel connection of coils

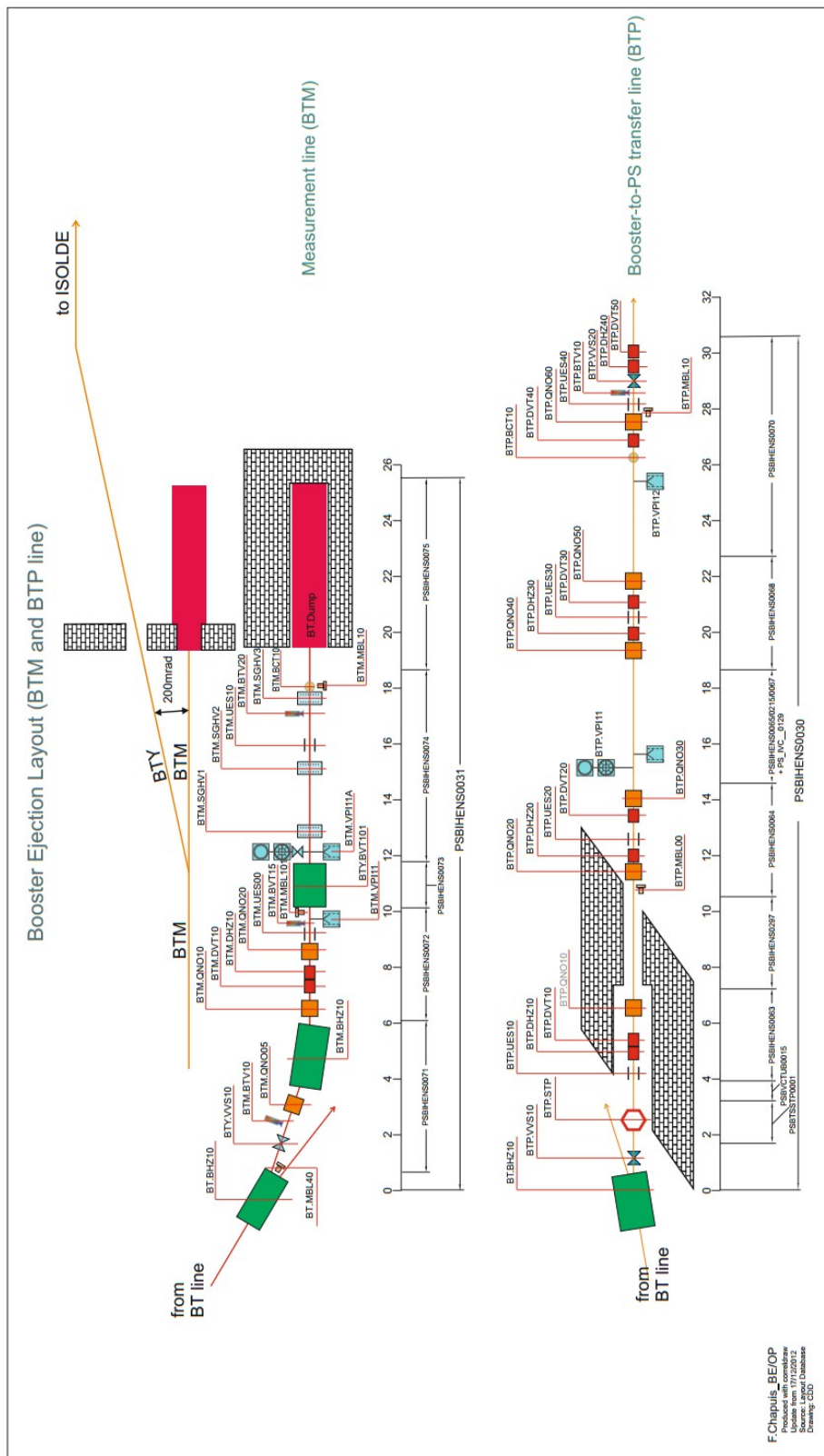


Fig. 3.54: Booster ejection layout (BTM and BTP line)

3.4.3.5 *Horizontal switching magnet, TBH (BT.BHZ10) (PXMBHGAWWP—‘proposed’)*

The horizontal switching magnet is installed at the end of the BT transfer line (Fig. 3.54) where it deflects the beam rightwards into the BTP transfer line towards the PS or leftwards into the BTM transfer line towards the dump and BTY transfer line to ISOLDE. With no field the beam would crash into the y-shaped vacuum chamber. The current magnet weighing 8 tonnes is laminated, water-cooled, and is operated in PPM mode between both polarities. At 2 GeV operations the field levels and cooling performance required both go beyond that of the original specification/measurements and the magnet cannot be considered for operation. As the current magnet is not covered by a spare a study [64] has already been made investigating several scenarios for a replacement that could be installed when ready to operate; firstly at 1.4 GeV and then at 2 GeV. The conclusion of the study was to build a longer magnet, designed to be used with the existing power converter, and then matching the optics to take into account the additional length and change of magnetic centres.

The possibility of pulsing the magnet with a capacitive discharge-type power supply is also being considered. This can be achieved with the same magnet design by configuring the coil connections differently. The design includes two coils: an upper and lower with 95 turns each made up from five layers of 19 turns. For use with the existing power converter, the 190 turns are connected in series requiring 410 A for 2.0 GeV operations with a high resistance and inductance of 257 mΩ and 510 mH, respectively. To be pulsed, the 10 layers can be connected in parallel, in effect reducing the number of turns to 19, requiring a higher current of 4100 A with a lower resistance and inductance of 3 mΩ and 5 mH. The advantage of the pulsed configuration will be a dramatic reduction in the power consumption, where 20-plus years of operation are likely to recuperate the cost of the new power supply several times. As the decision to pulse the magnet may only be arrived at after operations at 2.0 GeV with the existing supply, the yoke will be constructed from a relatively thin lamination, and reduce any dynamic effects such as eddy currents by using exclusively non-magnetic end plates and tie bars. The new magnet design shown in Fig. 3.55 is detailed in Ref. [65], and the main parameters of the magnet configured in the ‘slow configuration’ and ‘fast configuration’ are shown in Table 3.25.

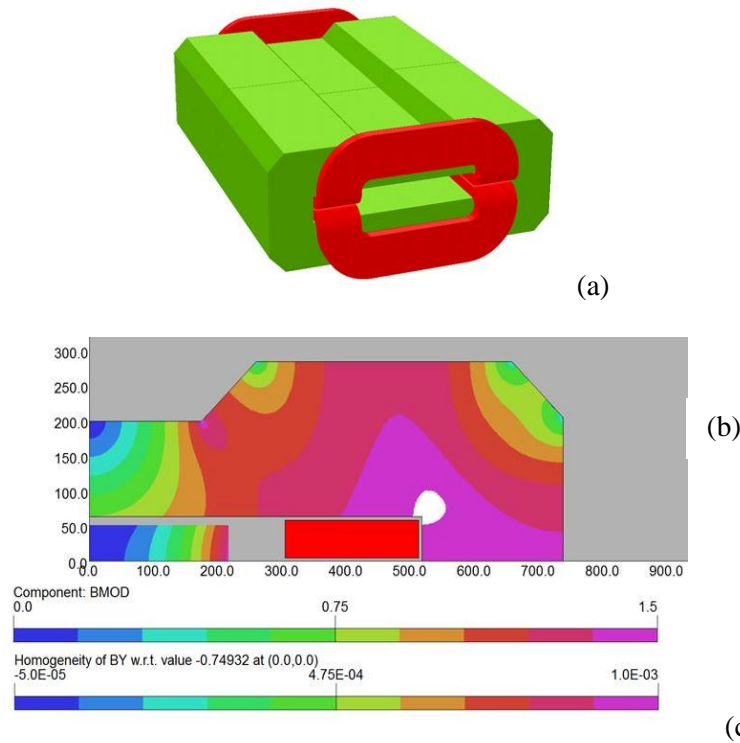


Fig. 3.55: (a) New BT.BHZ10 horizontal switching magnet 3D model; (b) magnetic flux distribution in the yoke; (c) field homogeneity in the GFR less than 10×10^{-3} .

Table 3.25: Horizontal switching magnet PXMBHGAWWP parameters for 1.4 GeV and 2.0 GeV operations

Unit	'Slow configuration'		'Fast configuration'
Operation	Cycled DC		Pulsed
Cooling	Water		Water (reduced consumption)
$B.dl$ at 1.4 GeV	T m	1.143	
$B.dl$ at 2.0 GeV	T m	1.486	
Effective length	m	2.0	
Gap height (V)	mm	128	
Gap width (H)	mm	600	
Current at 1.4 GeV	A	316	3160
Current at 2.0 GeV	A	410	4100
Resistance	Ω	0.25	0.003
Inductance	mH	540	5.4

3.4.3.6 Horizontal bending magnet, VB4 (BTM.BHZ10) (PXMBXGECWP—‘proposed’)

The horizontal bending magnet is an 18 tonne, 2.8 m-long C-shaped magnet originally used in the CERN ISR machine. The magnet completes the bend after BT.BHZ10 towards the PSB dump and BTY transfer line (Fig. 3.54). A preliminary study [66] shows that although the magnet can be operated in terms of cooling performance, at 2 GeV field levels the magnetic circuit becomes heavily saturated, degrading the field quality beyond the point where the magnet can be considered for 2 GeV operations, and therefore a new magnet design is required.

Radiation surveys taken around BTM.BHZ10 over the previous years suggest beam loses due to the vertical aperture of the magnet, and an initial optics study [67] suggested increasing the aperture of the magnet GFR from ~ 100 mm to 124 mm, dictating an increase of mechanical aperture of around

30%. This increase would have resulted in an unrealistic magnet/power converter configuration in terms of power consumption and space requirements; however, the initial optics study was conducted to determine the aperture requirement with the existing optics. Therefore a further optics study [68] was conducted, aimed at reducing the vertical aperture requirements, resulting in a reduction of the GFR to 80 mm and mechanical aperture of 98 mm. For this reduction of ~10% two designs are being considered, a ‘slow design’ based on a longer version of the existing magnet and a ‘fast design’, again with a longer effective length but powered with a capacity discharge power supply allowing for a reduction in power consumption over the next 20-plus years of operations.

One important issue with the new design that needs to be studied is the removal of the existing magnet and the integration of the new heavier (~22 tonnes) and longer magnet into the already crowded beam line and the PSB tunnel itself, where the crane availability is currently limited to 10 tonnes. The main parameters of the preliminary ‘slow design’ and ‘fast design’ magnet are shown in Table 3.26.

Table 3.26: Horizontal bending magnet, BTM.BHZ10 parameters for 1.4 GeV and 2.0 GeV operations

Unit	‘Slow configuration’	‘Fast configuration’
Operation	Cycled DC	Pulsed
Cooling	Water	Water (reduced consumption)
$B.dl$ at 1.4 GeV	T m	2.45
$B.dl$ at 2.0 GeV	T m	3.19
Effective length	m	2.479
Gap height (V)	mm	98
Gap width (H)	mm	420
Current at 1.4 GeV	A	390
Current at 2.0 GeV	A	507
Resistance	Ω	0.161
Inductance	mH	690
		4.8

3.4.3.7 Recombination quadrupoles, Triumf water (BT2.QNO.10, BT3.QNO10, BT2.QNO.20, BT3.QNO20, BT.QNO.30) (PXMQNCRNWP)

The Triumf water quadrupole magnets provide beam focusing at the start of the BT line (Fig. 3.51). The first four magnets shown in Fig. 3.56 are stacked in two pairs on rings 2 and 3 while the fifth magnet is alone on ring 3. The optics in this section of the line has not been changed and the magnetic gradients are scaled with the beam rigidity.



Fig. 3.56: Recombination quadrupole magnets in position BT2.QNO.10, BT3.QNO10

The laminated magnets installed in the 1990s allow operation in PPM between 1.0 GeV and 1.4 GeV field levels, only changing when requested and not dropping to zero between cycles. Operation in this way between 1.4 GeV and 2.0 GeV will also be possible with the required fields still within the original specification. Changing these five magnets may be considered if space permits with those discussed in Section 3.4.3.8 to minimize the number of families used both for magnets and power converters, and if a pulsed design is chosen to reduce power consumption. The main parameters of the quadrupole magnets are shown in Table 3.27.

Table 3.27: Quadrupole magnets, Triumf water parameters for 1.4 GeV and 2.0 GeV operations

	Unit	1.4 GeV	2.0 GeV
Operation		DC cycled	
Cooling		Water	
Maximum $G.dl$	T	2.14	2.89
Effective length	m		0.466
Aperture radius	mm		175
Maximum rms current	A		300
Minimum/maximum operating current	A	72/181	103/244
Resistance	Ω		0.147
Inductance	mH		39.0

3.4.3.8 *BT and BTP quadrupole magnets, BT.QNO.40, 50, BTP.QNO.20, 30, 35, 50, 55, 60 (PXMQNCUNAP or PXMQNCUNWP—‘proposed’)*

The downstream (Figs. 3.51 and 3.54) quadrupole magnets after BT.QNO.30 in the BT and BTP transfer lines consist of three magnet designs: the BT.QNO.40, which is a Triumf water as described in Section 3.4.3.7; the BT.QNO.50, which is a quadrupole magnet originally installed in the CERN ISR that has been modified to have an increased aperture radius of 100 mm; and the BTP quadrupole magnets (Smit water), which are a solid DC magnet design dating from 1970. The 2.0 GeV baseline is to allow PPM operation through to the PS and therefore the existing DC BTP quadrupole magnets cannot be used. In addition the optics studies [67, 68] require higher gradients than can be provided by

the current two BT quadrupole magnets and a longer magnet design must be made. Although between the different slots the maximum integrated gradients vary from 2.85 T to 5.8 T (including a 20% margin for future requirements), a common design is preferred for the eight magnets.

Two designs are currently being considered, a ‘slow design’ similar to the existing Triumf water quadrupole magnet and a ‘fast design’ to be pulsed with a capacitive discharge-type power converter. Assuming a pole-tip field of 0.75 T results in an effective length of 0.6 m when keeping an aperture radius of 75 mm as per the Triumf and Smit designs. The reduction of aperture radius for the BT.QNO50 magnet from 100 mm to 75 mm is acceptable as per the optics studies [67, 68]. Space permitting it could be considered to also change the quadrupole magnets described in Section 3.4.3.7 to the pulsed design when considering the power consumption savings over 20-plus years. The main parameters of the preliminary ‘slow design’ and ‘fast design’ magnet are shown in Table 3.28.

Table 3.28: BT and BTP quadrupole magnet (new) parameters for 1.4 GeV and 2.0 GeV operations

Unit	‘Slow design’ (PXMQNCUNWP)	‘Fast design’ (PXMQNCUNAP)
Operation	Cycled DC	Pulsed
Cooling	Water	Air
Minimum $G.dl$ at 1.4 GeV	T	1.66
Maximum $G.dl$ at 2.0 GeV	T	5.8
Effective length	m	0.6
Aperture radius	mm	75
Minimum current at 1.4 GeV	A	117
Maximum current at 2.0 GeV	A	408
Resistance	Ω	0.234
Inductance	mH	76.8
		23.7

3.4.4 Magnetic measurements and B-train

This section is concerned mainly with the design of the real-time measurement system for the main bending field, also known as the B-train. A campaign of magnetic tests is being conducted on the spare bending and quadrupole magnets in order to characterize their behaviour in terms of saturation, dynamics (eddy currents) and field quality (harmonics) under different working conditions; the results obtained will be the subject of separate reports.

3.4.4.1 Motivation for a B-train upgrade

Six accelerators at CERN, namely the PS Booster (PSB), PS, SPS, LEIR, AD and the upcoming ELENA, require feedback from B-trains to calibrate and/or control RF and, in certain cases, the bending field [69]. This is due to the difficulty of predicting accurately non-linear effects such as eddy currents, saturation and hysteresis, which depend upon the magnetic properties of the iron core, the history of the excitation current, ambient conditions, etc. All of these systems measure the field B of a reference bending magnet according to:

$$B(t) = B_0 + \int_0^t \frac{V_c(\tau)}{A_c} d\tau \quad (3.5)$$

where the rate of change of the field is provided by the voltage V_c developed by a coil (flux loop) of total surface area A_c , while the integration constant B_0 is given by a so-called field marker. In general, emphasis is placed upon the reproducibility of the measured field rather than on its absolute accuracy. Reproducibility is, as a rule, adversely affected by operation at low field (as in ELENA) due to remanent field effects, and by cycling with large pulse-to-pulse modulation (as in PS), which

exacerbates the effects of hysteresis. Conversely, operation at higher fields is beneficial to reset magnetic memory effects in the iron [70].

The PSB is operated since 2000 with a B-train based on the same acquisition electronics used in PS and AD [71]. The PSB B-train uses sensors installed in a reference magnet housed in building 361 and excited in series with the bending magnets in the ring (Fig. 3.57). The main features of the system are:

- a straight coil placed in aperture 2 of a length sufficient to capture the field integral, fringe regions included, to measure the rate of change of the magnetic field;
- the value of the field at the start of the integration is provided by a Metrolab NMR probe, also placed in aperture 2 and operating in marker mode at a fixed frequency of 4.713 MHz [72]. A dedicated electronics card generates a TTL trigger every time that the field reaches the value of 110.7 mT, just before the injection plateau;
- the field measured in aperture 2 is assumed to be the same in all rings. The bending magnets are top-bottom symmetric, and an additional trim circuit compensates the difference between the fields in the inner and outer rings (about 1% due to saturation at 1.4 GeV). The ratio between the currents in the trim and the main excitation circuit is fixed;
- an additional high-field NMR probe was originally installed in the reference magnet to provide a second marker trigger on the flat-top for the purpose of more accurate calibration. This functionality is not implemented in the current B-train.

The current system provides satisfactory performance for operation up to 1.4 GeV in terms of both absolute accuracy (of the order of 1 G) and reliability (no major maintenance interventions on record since 2006, when TE/MSC took charge of the equipment). However, this system is incompatible with the 2 GeV upgrade for two main reasons:

- a) as discussed in Section 3.6, two new power converters will be used to excite independently the bending coils of the inner and outer rings; each converter therefore requires feedback from an independent B-train system. In the present iron yoke configuration, the level of saturation expected at the peak field level (1.2 T), based on calculations and measurements, is about 1% in the inner and 5% in the outer apertures. The resulting 4% difference depends non-linearly upon the excitation current and cannot be compensated with a simple fixed-ratio trim circuit, as in the present system; in this case, a twin B-train is absolutely necessary. Even if the corrective actions discussed in section 3.4.2 (laminated side plates) were taken, we recommend strongly a twin B-train anyway, to ensure precise feedback despite hard-to-predict effects, such as those due to hysteresis and eddy currents, which can imbalance the inner and outer rings;
- b) faster cycles in the upgrade would push the current electronics close to and, in certain cases, above, its limits. The worst case is the acceleration ramp of 900 ms cycles, which is foreseen to have a very steep initial segment lasting about 36 ms, where the current increases by about 830 A and the field by 0.18 T. These conditions define a peak field ramp rate of about 4.8 T/s, which is the highest among all CERN B-trains. At the current resolution of 10 µT (0.1 G), the existing distribution system based on $B_{\text{up}}/B_{\text{down}}$ 24 V pulse channels would have to work at a frequency of about 500 kHz, which recent tests in the PS have shown to be unreachable.

These compelling reasons, together with considerations of long-term maintainability (obsolescence of electronic components, modernization of diagnostic tools), provide the motivation for this upgrade.



Fig. 3.57: The PSB B-train reference magnet in the Power House (building 361)

3.4.4.2 *The CERN-wide B-train renovation project*

The new PSB B-train will be part of a larger upgrade project having the goal of standardizing all CERN systems, improving their performance as required, and ensuring long-term maintainability [73, 74]. This project was motivated initially by the requirements of the PS, where a prototype system is currently being tested. The main design features of the new B-trains are listed below.

- i) Modern electronics for the integrator and the marker trigger generator, based upon off-the-shelf or CERN-supported solutions. These include the standard platform PC Industrial Computers Manufacturers Group CPICMG 1.3 to be used for the front-ends, together with Open Hardware Simple PCI FMC carrier (SPEC) PCI express cards, which provide customized FPGA functionality via the FPGA Mezzanine Card (FMC) architecture [75].
- ii) CERN-supported software compatible with accelerator control systems, i.e. CERN Scientific Linux and FESA (front-end software architecture) C++ classes to exchange low-bandwidth configuration and diagnostic data with the control room.
- iii) Field markers based on commercially available components such as NMR probes for sufficiently uniform dipole fields, or adapted ferrimagnetic resonance (FMR) RF filters for those cases where the field has a significant gradient component.
- iv) Distribution of measurement results in a serial digital format based on the Open Hardware White Rabbit fieldbus [76]. This technology, developed at CERN specifically for the transmission of real-time data in accelerator control systems, is essentially Gbit Ethernet plus built-in nanosecond-accurate timing. The numerical format aims at simplifying data transmission compared to the current cumbersome mechanism, based on sending incremental values, which forces each user to accumulate the field and to reset the counter at every machine cycle. Optical fibre ensures noise immunity and gives the possibility of reaching users kilometres away, which is important, e.g. for remote diagnostics.
- v) New streaming (i.e. continuous) integration and on-the-fly drift/gain correction algorithms, designed to improve the accuracy of the measured field and to make the system more robust by eliminating the need to synchronize with machine timing signals.

The prototype system installed in the PS is shown in Fig. 3.58. The basic functional units are contained in the B-train chassis, which includes the two recently developed SPEC/FMC cards at the heart of the system: a two-channel integrator based on a 2 MHz ADC, and a two-channel marker trigger generator compatible with both FMR and NMR signals (two separate inputs are implemented for a low-field and a high-field marker). The two integration channels operate in parallel and are designed to provide a weighted sum representing the integral of the field over two halves of a magnet.

Upon a suitable calibration, the weights could be modulated as a function of excitation current, measured field, or other variables, in such a way as to model, for example, the change of magnetic length with saturation, or other non-linear effects.

The new system is designed to be modular, compatible with different kinds of physical sensors and adaptable to the different specifications of the synchrotrons at CERN (and elsewhere: for example, the new electronics is being adapted for an ion therapy machine in the framework of the collaboration with MedAustron [77]). The test campaign ongoing in the PS is expected to confirm soon the viability of the concept.

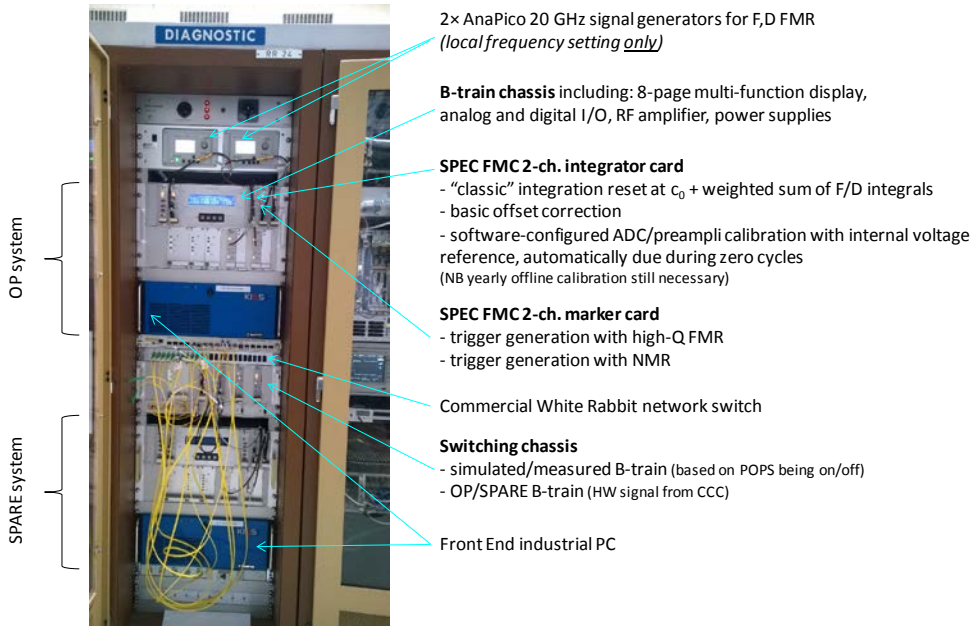


Fig. 3.58: The upgraded PS B-train prototype in the U101 reference magnet room

3.4.4.3 PSB B-train upgrade specifications

The PSB upgrade poses a set of challenges that are unique among all CERN B-train systems. The most critical requirements are given below.

- Two identical B-train systems operating in parallel: each system will send its output to a different set of users, using different cables. This working mode requires that the two magnetic circuits be uncoupled, which is a reasonable first approximation. However, a certain degree of coupling should be expected due to saturation in the common parts of the magnetic circuits; therefore, the dipole field integral, but also the magnetic length and the harmonic errors in one set of rings, will depend upon the current in the other. This implies that a simple one input/one output control strategy might be inadequate. The extent of this dependence will be measured in the spare bending unit.
- High peak field ramp-rate (4.8 T/s): the White Rabbit serial link has a theoretical maximum frame rate of about 2 MHz, where each 64-byte Ethernet frame (the minimum length allowed by the protocol) can hold the current value of the B field, the dB/dt (as required by RF) and higher order multipoles if required. The FPGA integrator, by itself, does not represent a limit since it has been tested to work up to 10 MHz. The major bottlenecks appear to be the latency due to the switch and the interference with the 1 kHz upstream transmission from the main power supply (see Section 3.6). The prototype system has been tested successfully up to 250 kHz, yielding no lost frames and a maximum latency of 5.2 μ s. For the moment, this performance corresponds to

a limit of the measurement resolution about $20 \mu\text{T}$ during the fastest ramp segment. Tests are planned to assess the performance at higher rates.

- High saturation level: the expected (uncorrected) level of saturation of the PSB bending dipoles will be halfway between the worst case among the B-train systems, i.e. 12% in the PS, and more linear machines like the SPS (3%). This is expected to affect strongly the magnetic length as a function of current, and it will have an impact on the calibration of the field markers (these provide actually point-like measurement that must be multiplied by a scaling factor to represent the integral). A coil covering the totality of the field distribution, as in the present system, is mandatory to measure directly the variations of the field integral above the marker level.

We must also mention that the PSB has certain characteristics that mitigate somehow the severity of these constraints:

- the absolute accuracy required is of the order of 0.1 mT (1 G);
- the maximum cycle duration is only 1.2 s , which facilitates the correction of integrator drift.

Based on these considerations, the proposed specifications of the PSB B-train are summarized in Table 3.29.

Table 3.29: PSB B-train specifications

Parameter	Value	Unit
Maximum magnetic field B	1.2	T
Minimum magnetic field B	0.1	T
Maximum field ramp rate $\text{d}B/\text{d}t$	4.8	T/s
Absolute measurement uncertainty	100	μT
Maximum measurement resolution	20	μT
Maximum cycle duration	1.2	s
Field broadcast rate	250	kHz

3.4.4.4 General design of the PSB B-train upgrade

The overall layout of the upgraded system is shown in Fig. 3.59. The system will be installed in the existing reference magnet, taking advantage of the four apertures to fit easily all the required sensors. With respect to the general B-train upgrade described above, the specific requirements of the PSB system are given below.

- Hot spares: according to established practice, both the inner and outer B-trains will have a spare set of identical electronics plus sensors installed in the symmetric aperture. Operational and spare systems will be working continuously in parallel, thus providing a basis for real-time comparisons and diagnostics. Two-bit flags sent by the CCC via FESA allow remote selection of the operational channel, which will be enabled only when the respective power converter is off. An adequate amount of separate spare electronic components is also foreseen (modularity across all CERN systems being beneficial).
- Measurement coils: a new set of four coils is required to equip the whole system. The approximate coil surface area needed to reach a peak 5 V output is 1 m^2 , which as an example translates into a $2000 \text{ mm} \times 10 \text{ mm}$, 50-turn winding. Based on the experience of similar recent projects, the solution proposed consists in the development of a printed circuit board (PCB) fluxmeter, including an array of parallel coils curved to follow the nominal beam path (see Ref.

[78] for an example). The main advantages of this design are higher measurement accuracy, simultaneous measurement of field and commercial availability (with the added bonus of unit cost reducing with volume orders). The PCB solution would allow a number of units to be set aside as spares inexpensively, or as a tool for precise magnetic testing of the spare magnets.

- Field marker: no change is proposed in this respect, since the Metrolab PT2025 teslameter provides good performance in a uniform dipole field. A set of high-field probes, as installed in the original B-train design, could be essential to guarantee the required accuracy in high saturation conditions; a separate study to assess this need will be launched. An adequate number of spare teslameter units are already available at CERN, whereas the (relatively inexpensive) NMR probes are subject to wear and will have to be procured new. In the near future, Metrolab is going to release the new teslameter version PT2026, which will be functionally compatible with the PT2025 and thus able to guarantee maintainability in the long term.

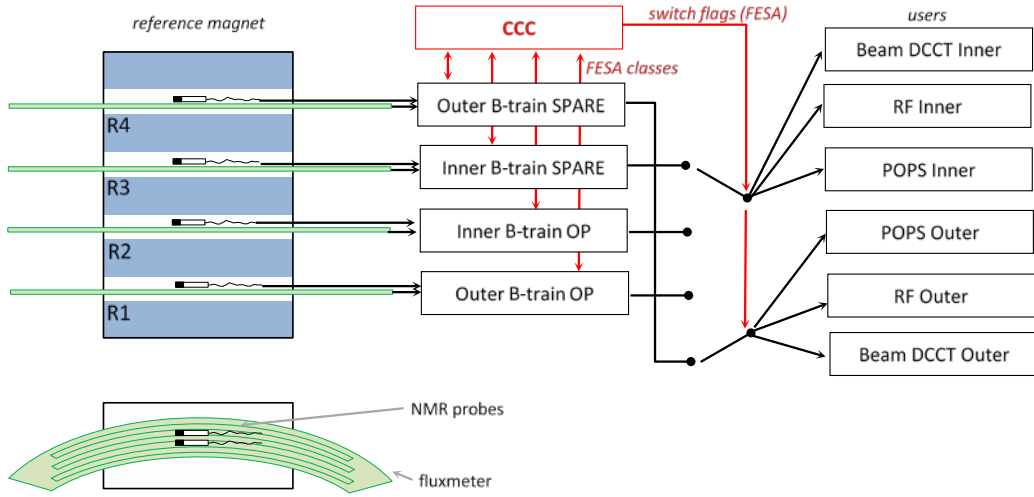


Fig. 3.59: Schematic layout of the 2 GeV PSB B-train

White Rabbit transmission

The proposed format of the data transmitted over the White Rabbit link is given in Fig. 3.60. Each magnetic measurement result is represented by a 32-bit signed integer, and the selected range and resolution are more than adequate to meet all present (and foreseeable) demands at CERN. The main points to remark at this stage are given below.

- Downstream transmission (originating in the B-train) for the PSB includes the B field for the power converters and the dB/dt for the RF. Ample headroom is available to add more measurement results in the future, such as quadrupole or sextupole field harmonics, etc. Should these ever be necessary, PCB fluxmeters provide at little extra cost all the necessary measurement signals; only additional integrator cards would be required.
- An upstream transmission of the excitation current, originating in the power converters where it is measured by the high-precision internal DC current transformers. This transmission, already implemented in POPS and foreseen to be extended to other systems, is required to implement advanced diagnostics and functionality such as timing-independent enabling of marker triggers (useful to prevent noise causing false triggers).
- All transmissions are done in Ethernet broadcast mode. This causes a small penalty at the receiver's end, where sifting for the wanted sender becomes necessary; the main advantage is that the system becomes more flexible, allowing the addition of senders or receivers without needing to pull new cables.

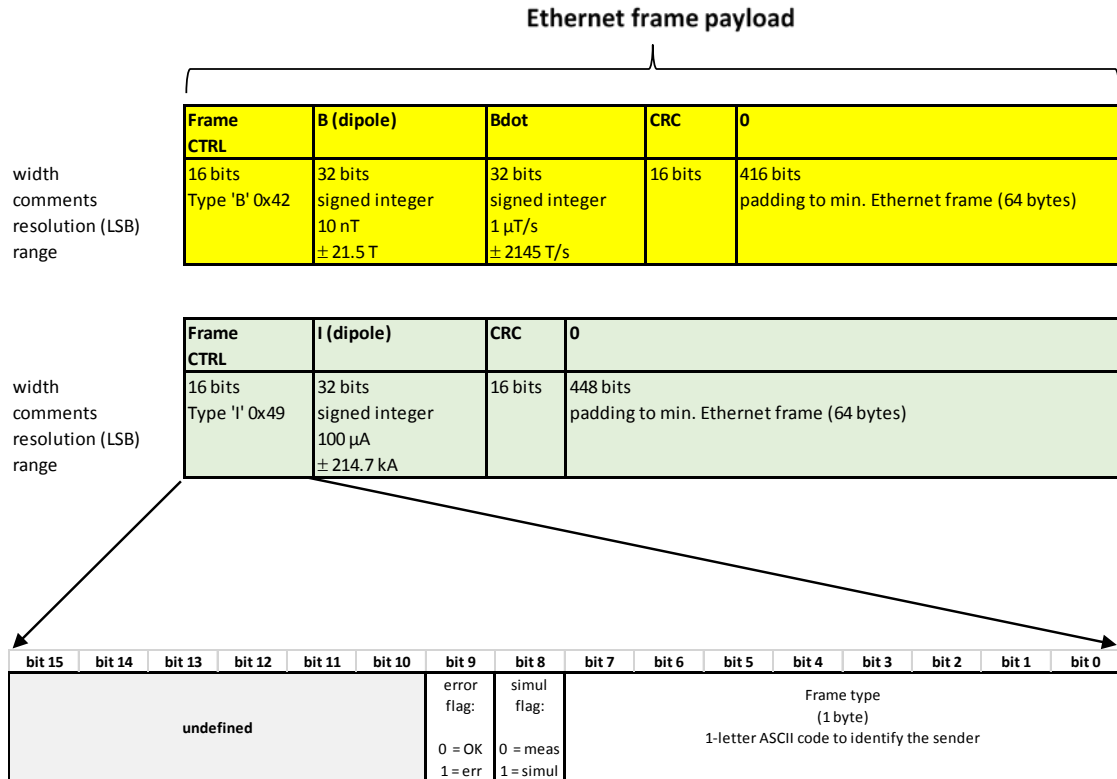


Fig. 3.60: Structure of the White Rabbit Ethernet data packets

3.4.4.5 Interface with other work packages

Floor space requirements

According to the design presented here, the upgraded B-train requires two and a half full-height racks in the Power House, i.e. two acquisition and distribution racks like the one represented in Fig. 3.58, plus another half to house the NMR teslameter units. Considering the analogue nature of the signals transmitted from the reference magnet to the racks, in particular the noise-sensitive coil voltages, their distance should be as small as possible; a cable length of up to about 10 m, as in the current systems, would be acceptable.

During the validation phase in which the new prototype system will be tested against the existing one (Section 3.4.4.6), two B-train chains, i.e. about one full rack, will be needed in addition to the existing electronics, which occupies one and a half racks. In the final operating configuration, the space occupied by the old system will, of course, be recovered.

Input from other WP

The following input is needed to finalize the B-train specifications and design:

- i) from machine operation:
 - absolute accuracy and repeatability of the measured $B(t)$;
 - requirements in terms of diagnostics and signals to be exchanged between the B-train and the machine control system (FESA classes or OASIS/sampler analogue signals);
 - any additional user besides RF, power converters and beam current monitors;
 - level of redundancy required: are the two proposed acquisition chains running in parallel acceptable, as, for example, currently used in the PS (the early system had three). Some space

savings could be made by installing just one hot spare set of electronic components, to be routed to the inner or outer ring sensors as required; this would, however, increase the cost and complexity of the system.

ii) From all users:

- resolution, absolute accuracy, bandwidth, latency and maximum admissible step variation (a possible artefact induced by the on-the-fly error correction) of the measured $B(t)$;
- White Rabbit cabling layout (two standard single-mode optical fibre per user, departing from the B-train rack in a star network configuration).

iii) From RF:

- rate and accuracy of the dB/dt measurement;
- accuracy of the synthetic B-train to be generated during dry runs.

iv) From power converters:

- list and parameters of all foreseen power cycles; in particular, it is very important to assess the impact of overshoots, undershoots and (if applicable) zero cycles, which may affect adversely the reproducibility of the magnetic field by inducing minor hysteresis loops;
- maximum ramp rate;
- constraints on current acceleration/deceleration profiles (necessary to select optimal trigger points NMR markers).

3.4.4.6 Status and outlook

At the time of writing, a prototype of the PS B-train upgrade that will form the basis of the PSB B-train system has just started to undergo field tests. While no problems of principle have been identified so far, a large number of practical details and parameters remain to be fixed; the formal validation of the design will require extensive testing, alongside the existing B-train system, in a variety of beam configurations at the PS.

At the end of this testing phase, when electronics, firmware and software components will have been finalized, it would be advisable to install a partial prototype system in the PSB, taking advantage of the free apertures in the reference magnet to carry out a similar validation campaign. Before getting there, some issues have to be clarified experimentally on the spare magnets:

- impact of higher saturation levels on the field quality (harmonics);
- impact of the planned cycles, in particular concerning the alternation of low- and high-energy cycles, on hysteresis and remanent field;
- evaluation of the coupling between the inner and outer apertures;
- evaluation of the degree of symmetry between the top and bottom rings;
- effectiveness of laminated side plates to equalize inner and outer rings;
- any possible issue associated with the two special insertion units.

We recall that no tests of main quadrupole units have been carried out so far. A dedicated campaign will be scheduled to measure the level of saturation, the time constant of eddy currents at different flat-top levels and the impact of 2 GeV operation on field quality.

Finally, there remain a few technical points to address concerning the sensors and the acquisition system:

- cost/benefit of traditional straight coils vs. PCB fluxmeter;

- possible calibration improvement with high-field NMR;
- improvement of the White Rabbit throughput above 250 kHz.

3.5 RF systems

3.5.1 Introduction

With the coming into operation of Linac4 the PS Booster (PSB) injection energy will be increased to 160 MeV [79]. This will bring the injection beam revolution frequency from ~ 600 kHz to ~ 1 MHz. In parallel, the foreseen PSB energy upgrade programme will raise the extraction energy from 1.4 GeV to 2 GeV with minor influence on the maximum revolution frequency, which rises from 1.75 MHz to 1.81 MHz. A variety of different beams are produced by the PSB machine. For filling the LHC, single bunch intensities at extraction in the order of few 10^{12} protons per bunch (ppb) and bunch length down to 130 ns [9, 80] are foreseen. These intensities are, however, substantially lower than $1.4 \cdot 10^{13}$ protons per ring, with 200 ns bunch length being the intensity goal with Linac4. Moreover, full use of the Linac4 beam implies an absolute maximum of 2.5×10^{13} protons per ring with beam peak current reaching ~ 32 A (half sine approximation) and 13 A, 8.5 A and 7.2 A of fundamental, second harmonic and DC components, respectively. Among other parameters, the ability of the machine to digest the highest intensities depends on the current and power available from the RF systems. Both can be limited, making the accelerating cycle longer, but a major intervention on the RF amplifiers is still required to stay below the main magnet maximum rms current, which will reach ~ 2.5 kA after the upgrades foreseen during LS2.

3.5.1.1 Limits and possible upgrades with existing ferrite-loaded cavities

Three RF systems presently exist in the machine: C02, C04 and C16. The latter is used for controlled blow-up while the first two cover the beam revolution frequency range and its second harmonic. All these systems have a double, ferrite-loaded, $\lambda/4$ line topology with a central gap excited in differential mode. They exhibit reasonably narrow bandwidth (high Q), are driven by vacuum tube-based amplifiers and implement fast RF feedback.

C02 RF system

The C02 amplifiers use a single vacuum tube (RS1084) connected to one side on the cavity gap and coupled to the other side by means of the tuning loops. This configuration is such that the ratio between the gap current I_{Gap} and the tube plate current I_A is

$$I_A/I_{\text{Gap}} = 2 . \quad (3.6)$$

The single tube, working in class B, is conducting for about half an RF cycle and, considering the tube I_A vs. V_G non linearity, an additional factor of ~ 3.5 must be applied so that all together the ratio is

$$I_{A \text{ pk}}/I_{\text{Gap}} = 7 . \quad (3.7)$$

As the RS1084 tetrode can provide up to 40 A plate current and allowing 10% margin for errors, ageing, etc. the maximum peak current available at the gap is:

$$I_{\text{Gap}} = 0.9 \cdot 40/7 \sim 5.1 \text{ A} . \quad (3.8)$$

In ferrite-loaded tuned cavities with reasonably high quality factor, only the beam current harmonic component at the cavity resonance needs to be compensated as the harmonics are shorted by the low cavity impedance. Moreover, the tuning system compensates the reactive part of the beam

current and only the real part that transfers energy for acceleration has to be provided; this is proportional to the sine of the stable phase φ_s . Calculations of the acceleration cycle and parameters show that the maximum intensity that can be handled with the existing equipment is 1.4×10^{13} protons. The goal value of 2.5×10^{13} protons cannot be accelerated without replacing the final amplifier with a push–pull stage. This would double the maximum available RF current and require a completely new design. The results are summarized in Table 3.30 and plotted in Fig. 3.61.

Table 3.30: C02 acceleration cycle relevant parameters

$\varphi_{s\text{ MAX}}$ (°)	f at $\varphi_{s\text{ MAX}}$ (MHz)	R_{Gap} at $\varphi_{s\text{ MAX}}$ (Ω)	\hat{I}_{Gap} (A)	t_{Inj} (ms)	t_{Ext} (ms)	$I_{\text{A pk}}$ (A)	Number of tubes	Notes	$\varphi_{s\text{ Ext}}$ (°)	f_{Ext} (MHz)	R_{Gap} at f_{Ext} (MHz)	\hat{I}_{Gap} (A)
50	1.75	4000	14.1	275	775	98.7	1	Exceeding I_{A} limit (36 A)	31	1.81	4000	14.0
22	1.3	3500	5.1	275	1200	35.7	1	Exceeding $MPS_{\text{Max}} + 10\%$ (2490 A)	10	1.81	4000	5.0
46.9	1.73	4000	10.3	275	785	36	2	OK	34	1.81	4000	8.4
47	1.73	4000	9.6	275	715	67.2	1	Exceeding I_{A} limit (36 A)	15	1.81	4000	5.8
25	1.37	3600	5.1	275	945	35.7	1	Exceeding $MPS_{\text{Max}} + 10\%$ (2490 A)	11	1.81	4000	5.0
31	1.53	3800	5.1	275	755	35.7	1	OK	23	1.81	4000	3.0

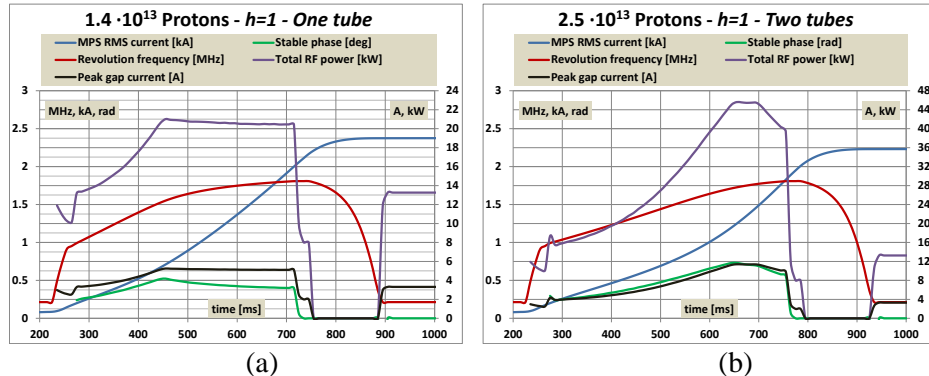


Fig. 3.61: (a) 1.4×10^{13} and (b) 2.5×10^{13} C02 acceleration cycles

From the tuning loop stability point of view there should be no major problems. The cavity current at 8 kV is ~ 2 A, the beam current $I_B = 13$ A and the loop gain $LG = 10$. The ratio is

$$I_B/(I_{\text{Cav}} \cdot LG) = 0.65 \quad (3.9)$$

and, in first approximation, stability requires staying below unity.

C04 RF system

For the C04 system providing the second harmonic, the current constraints are also a limiting factor. The existing system is based on a push–pull amplifier using two RS2012 tetrodes with a maximum current capability of 12 A. Present experience has shown that the existing amplifier is already working at its limit with 1×10^{13} protons accelerated to 1.4 GeV. To achieve 2 GeV extraction energy or

increase the beam intensity the amplifier upgrade towards a system similar to that used in the C02 system is required (single tetrode RS1084). At 3.6 MHz, the fast RF feedback loop provides a loop gain $LG = 13$ (22 dB) and the cavity resistance is $R_{Cav} \sim 12 \text{ k}\Omega$. The maximum second harmonic component of the beam current for tuning stability is then

$$I_B \sim LG \cdot I_{Cav} \sim LG \cdot V_{Gap}/R_{Cav} \quad (3.10)$$

As for the C02 system the tube current will be 3.5 times higher for a two-tube amplifier and 7 times higher for a single tube amplifier. Table 3.31 lists the maximum beam current at the tuning loop stability limit vs. second harmonic gap voltage. It also lists the corresponding number of particles (200 ns bunch length) and the required tube current. It can be seen that, from experience with the present amplifier, 1×10^{13} protons is the practical limit down to 3 kV gap voltages. To go beyond that an upgraded amplifier using the RS1084 tetrode is required. This could digest up to 1.6×10^{13} protons. For the ultimate intensity a push-pull amplifier using the RS 1084 cannot be avoided.

Table 3.31: C04 relevant parameters (single bunch, at extraction)

V_{Gap} (V)	I_B Max (A)	Number of particles	I_A pk ^a (A)	I_A pk ^b (A)
1000	1.1	3.1×10^{12}	3.7	7.5
2000	2.1	6.3×10^{12}	7.5	15.0
3000	3.2	9.4×10^{12}	11.2	22.5
4000	4.3	1.3×10^{13}	15.0	30.0
5000	5.4	1.6×10^{13}	18.7	37.5
6000	6.4	1.9×10^{13}	22.5	45.0
7000	7.5	2.2×10^{13}	26.2	52.5
8000	8.6	2.5×10^{13}	30.0	59.9

^aExisting push-pull amplifier with two RS2012; ^bupgraded single-ended with one RS1084

3.5.2 Wideband RF system

To cope with this new situation, the existing narrowband, tuned RF systems covering the $h = 1$ and $h = 2$ frequency ranges could be replaced by 1.0 MHz to 4 MHz cavities based on the wideband frequency characteristics of Finemet® magnetic alloy (MA) [81]. Full exploitation of the wideband characteristics suggests using a cellular configuration in which an accelerating gap is surrounded by a MA core on each side [82] and produces a fraction of the total accelerating voltage. Each cell can be 130 mm long and 12 cells can be fitted into the space presently used by each C02 and C04 cavity. In this perspective and considering the possible MA core size (dictated by the four superimposed PSB rings' distance), the material's characteristics and the cooling possibilities, each cell can provide ~ 700 V with power levels compatible with what is achievable by solid-state power stages. As 8 kV per cavity can be maintained and three straight sections are presently occupied by the C02 and C04 systems the total maximum voltage can either be kept to 16 kV using just two straight sections or increased to 24 kV. The wideband response will also allow multi-harmonic operation and flexible adjustment of the $h = 1$ and $h = 2$ voltage components ratio that will only be limited by the total maximum voltage. However, installing wideband cavities in the PSB rings introduces longitudinal impedance covering many revolution frequency harmonics, and special care must be taken for compensating the beam loading. A fast RF feedback loop can take partial care of this and additional measures must be implemented in the low-level electronics.

3.5.2.1 Power system description

The wideband RF system design [82] is based on multiple RF cells each providing a fraction of the total RF voltage. Each cell consists of a ceramic gap with a Finemet® FT-3L magnetic alloy core on each side being push-pull driven by solid-state amplifiers (Fig. 3.62). The rings' dimensions are dictated by the vacuum chamber diameter and the distance among the superposed PSB rings (outer diameter 300 mm, inner diameter 200 mm and thickness 25 mm). Longitudinally, the cell is about 130 mm long. Both the amplifiers and MA cores are water-cooled.

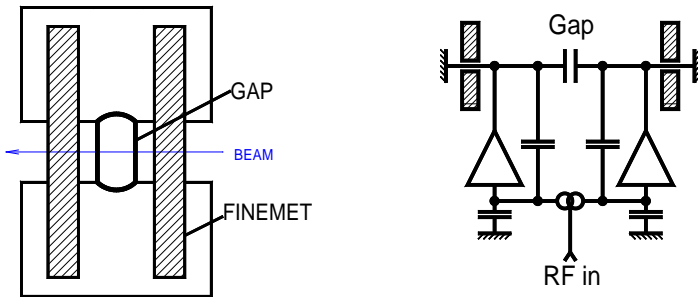


Fig. 3.62: Basic cell configuration. (a) Cell construction; (b) amplifier circuit

3.5.2.2 Thermal considerations

The maximum voltage achievable from one MA core is limited by the ability to remove the energy deposited in it. Among different cooling configurations, indirect cooling has been retained. For this, a water-cooled copper ring is placed on one of the core's sides and isolated from the MA core by a thin kapton foil (Fig. 3.63). Detailed thermal simulations and measurements have been carried out. Figure 3.64 plots the simulation results for 750 W. Extrapolating from this data the maximum temperature in the core is expected to be limited to below 100°C while dissipating 1 kW with an inlet cooling water temperature of 30°C (3 l/min).

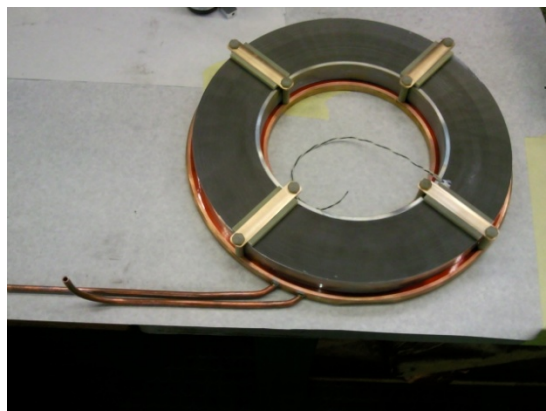


Fig. 3.63: MA core mounted on a copper cooling ring

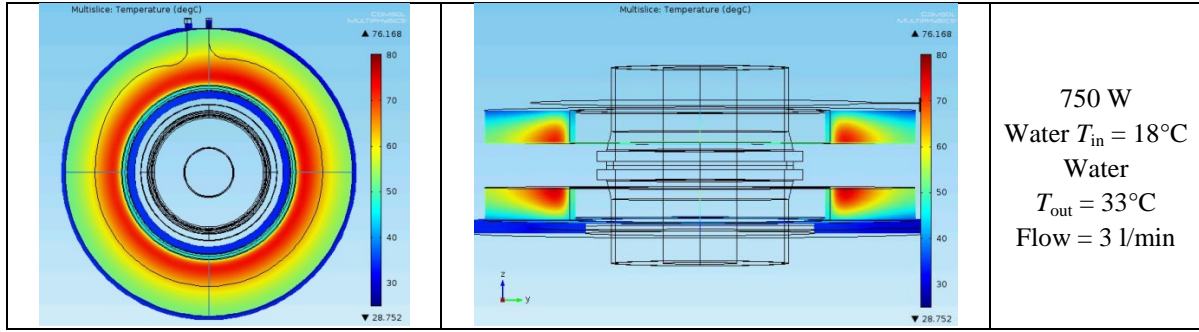


Fig. 3.64: MA core temperature distribution (°C)

3.5.2.3 MA core impedance characterization

At low frequencies the impedance of the cell is mainly dictated by the core characteristics; at high frequencies the system capacitance becomes predominant. Figure 3.65(a) plots the measured impedance on one gap side with a single core inserted into the cell as well as its equivalent parallel R-L-C components. From the parallel resistance the maximum voltage achievable on one core for a given power can be computed. Figure 3.65(b) plots these values for 1 kW.

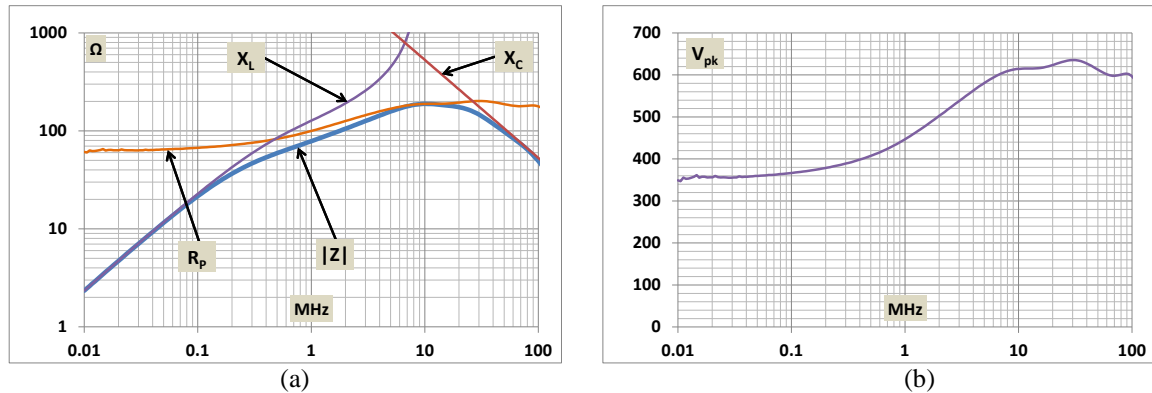


Fig. 3.65: (a) Single core impedance and R-L-C equivalent; (b) maximum voltage for 1 kW dissipation

The impedance behaviour can be reasonably fitted by a ladder R-L network. The system capacitance and the additional capacitance introduced by attaching the core to the cooling ring can complete a model that turns out being very convenient for Spice simulations. The measured and simulated curves as well the equivalent model are plotted on Fig. 3.66.

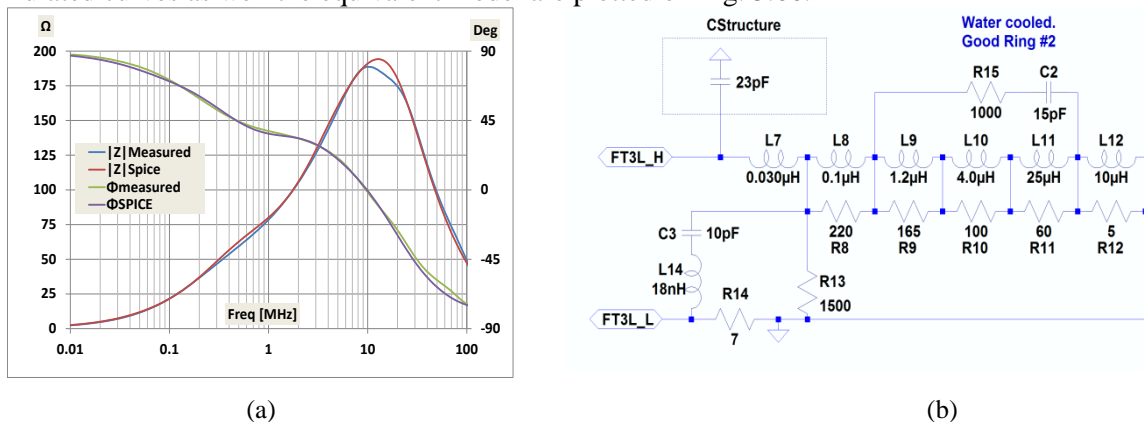


Fig. 3.66: (a) Comparison of measured and simulated impedance; (b) equivalent circuit model

3.5.2.4 Amplifier output circuit configuration

The amplifier has to fulfil strict vertical space limitations as the four superimposed PSB vacuum chambers set the maximum available height. Longitudinally the dimensions are set by the spacing required for the two MA cores, the cooling rings, the ceramic gap and the connection lines. All these limitations result in an available cabinet 295 mm deep, 323 mm high and 125 mm long. Sixteen 200 W amplification modules, the driver, the output combiners and transformers as well as the ancillary circuitry could be housed in this volume. In the first amplifier version (Fig. 3.67) the outputs of eight 200 W modules were combined and a 1:3 RF voltage transformer steps up the impedance to a nominal $50\ \Omega$. The other eight 200 W modules were combined in the same way and driven in anti-phase to obtain a differential output signal on two $50\ \Omega$ ports.

Each 200 W module contains an internal matching transformer with a 1:4 ratio so that the overall voltage increase from the MOSFETs' drain to the push-pull output is 24 times. To improve reliability the maximum DC supply voltage has been reduced from the nominal 50 V to 40 V so that, considering the saturation voltage and other loss phenomena, the maximum gap voltage achievable in this configuration is $\sim 750\text{ V}_{\text{Peak}}$. Using the differential output amplifier version, $8\text{ kV}_{\text{Peak}}$ (with some margin) can be achievable by the 12 cells that can replace a C02 or C04 cavity.

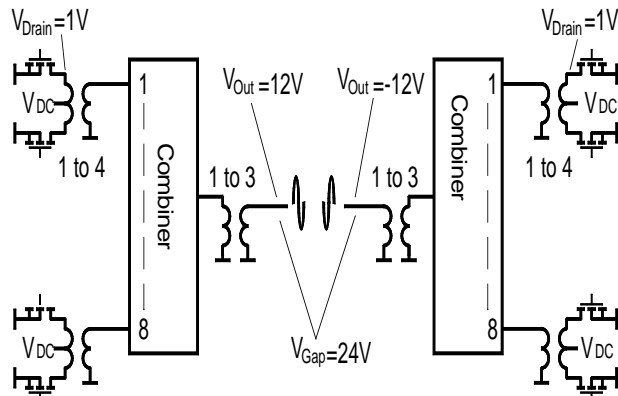


Fig. 3.67: Differential output amplifier: output circuit configuration

To increase the output voltage to $800\text{ V}_{\text{Peak}}$ or above a single-ended version of the amplifier has been designed. It combines the sixteen 200 W modules into a single output, and the output transformer has a 1:4 voltage transformation ratio (Fig. 3.68). Driving each gap side with one amplifier allows increasing the available power per cell to $\sim 5\text{ kW}$ and the voltage to $\sim 1\text{ kV}_{\text{Peak}}$.

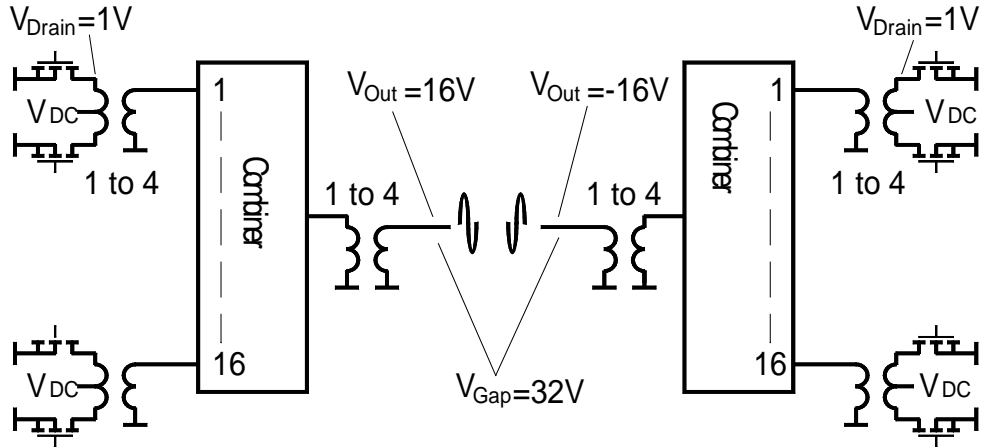


Fig. 3.68: Single-ended output amplifier: output circuit configuration

To evaluate the current available from the amplifier for acceleration and cancellation of wake fields induced by the beam current, it may be noticed that the current at the gap is transformed back to each drain as:

$$I_{\text{Drain}} = I_{\text{Gap}} \times \frac{n}{N} 2 \quad (3.11)$$

where N is the number of combined 200 W modules and n is the voltage transformation ratio from the amplifier output to each MOSFET drain. So, for the two amplifier configurations we have:

Differential output, $N = 8$, $n = 12$

$$\frac{I_{\text{Drain}}}{I_{\text{Gap}}} = 1.5 . \quad (3.12)$$

Single-ended output, $N = 16$, $n = 16$

$$\frac{I_{\text{Drain}}}{I_{\text{Gap}}} = 1 . \quad (3.13)$$

3.5.2.5 MOSFETs' behaviour in radioactive environment

Typically, MOSFETs submitted to radiation exhibit a threshold voltage (V_{TH}) shifting due to charges getting trapped in the gate isolating layer. For N-channel MOSFETs the shift is such that the device goes into conduction with lower V_{TH} values. This effect can be partially recoverable. Different MOSFET types were tested at J-PARC Main Ring (MR) collimator to doses above 10 kGy. MRF151 is a standard device already in use in the PSB and employed in the test system. SD2942 and VRF151 are devices equivalent to MRF151 but the latter has enhanced V_{DS} characteristics. Unlike the previous models with V geometry, the MRFE6VP6300 is a modern L type device with superior performance but lower maximum V_{GS} . Figure 3.69 plots the relative evolution of V_{GS} required for $I_{\text{D}} = 1 \text{ A}$ vs. received dose until device failure. It can be noticed that all devices surviving 2 kGy react in a similar way but the L-MOS type seems less affected and stabilizes at some point.

In the location presently dedicated to the C02 and C04 RF systems the doses measured from April 2012 to March 2013 were:

- C02 in section 7L1: 14 Gy;
- C02 in section 10L1: 30 Gy;

- C04 in section 13L1: 1 Gy;
- C16 in section 5L1: 17 Gy.

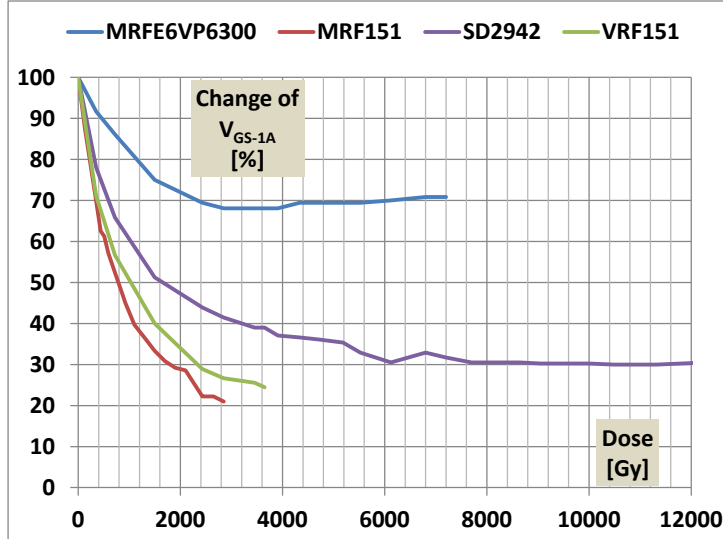


Fig. 3.69: Relative change of V_{GS} vs. received dose

With this level of radiation the effects should become visible in 5–10 years and do not represent a major concern as some kind of compensation/correction measures can be integrated with the amplifier bias circuitry.

3.5.2.6 Amplifier input circuit, bias adjustment and radiation compensation

The amplifier input circuit comprises a driver amplifier acting as a high-impedance push-pull stage that drives all of the 200 W modules' gates in parallel. As the gates' inputs almost behave as ideal capacitors, these resulting ports can be used as summing points for routing back the gap voltage signal through capacitors and implementing a fast RF feedback loop. Due to this kind of coupling, the overall response is that of a low-pass network. An adequate high-pass section can linearize the response at a low level.

To set the MOSFET rest current as required for class AB operation the gate bias is simply fed through $10\text{ k}\Omega$ resistors to the gates. A power MOSFET of the same kind as used in the power stage implements a voltage generator proportional to its threshold voltage. This reference generator is used to modulate the overall bias of the 200 W stages to automatically stabilize the working point vs. any threshold voltage variations. Placing the sensing MOSFET on one of the power devices will provide thermal stabilization but also, as it will have identical exposure to radiation, an automatic radiation compensation effect.

3.5.3 Accelerating current and beam loading

If with the narrowband impedance of ferrite loaded cavities the beam–cavity interaction is mainly limited to the harmonic component at cavity resonance, the wideband response of the Finemet® loaded cells requires acting on more harmonics.

Assuming the gap impedance to be purely resistive (R_{gap}), frequency independent, and driven by the generator and beam currents (Fig. 3.70), to obtain the gap current:

$$I_{\text{Gap}} = V_{\text{Gap}} / R_{\text{gap}} \quad (3.14)$$

the generator must supply:

$$I_{\text{Gen}} = \sqrt{(I_{\text{Beam}}^2 + I_{\text{Gap}}^2 - 2 \cdot I_{\text{Beam}} \cdot I_{\text{Gap}} \cdot \cos(\alpha))} \quad (3.15)$$

This simple relation can be applied to compute the generator current required for acceleration by setting V_{Gap} at the fundamental frequency at the required value. It can also be used for computing what is needed for cancelling the higher harmonic components, zeroing the corresponding V_{Gap} . A linear addition of the different components will then provide the total generator current.

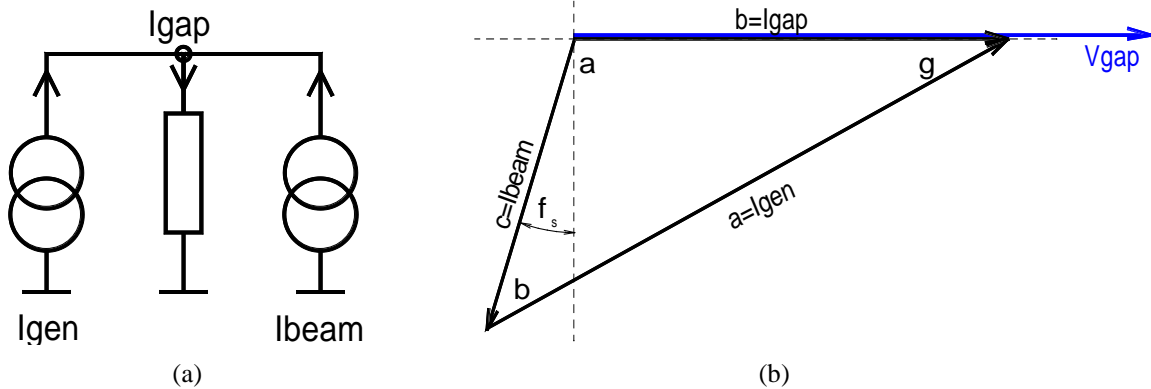


Fig. 3.70: (a) Gap driving currents; (b) vector diagram

To evaluate the RF system requirements, the beam reconstruction is already precise enough using the first four harmonics (Fig. 3.71: half sine distribution, 200 ns bunch length, 1.81 MHz extraction frequency). With the cycles shown in Figs. 3.72 and 3.73 the maximum current is required around 1.74 MHz where the stable phase reaches its maximum (45° and 50° for 1.4×10^{13} and 2.5×10^{13} protons, respectively). The right hand side plots show the computed shapes of the beam and generator currents as well as the gap voltage for one of the 12 accelerating cells. The latter shows perfect compensation of the beam current higher harmonics. From the plots we see that a maximum of 16 A and 26 A, respectively, are required from the generator.

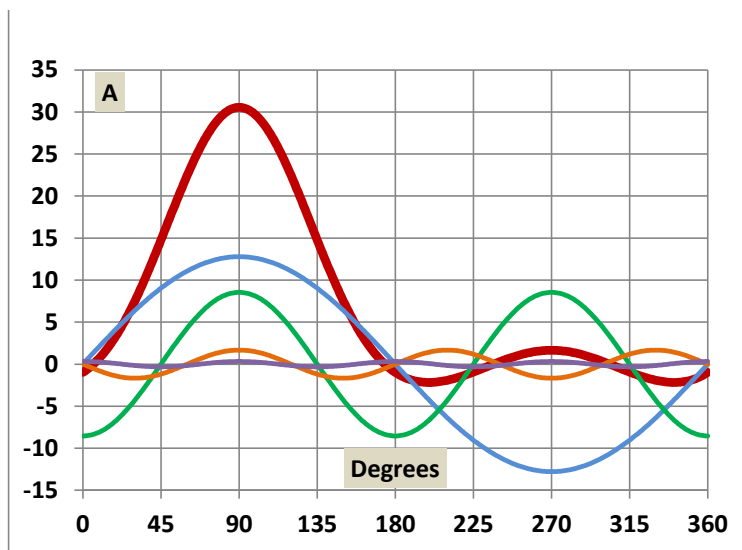


Fig. 3.71: Bunch reconstruction with DC and first four harmonic components (2.5×10^{13} protons, 200 ns, 1.81 MHz).

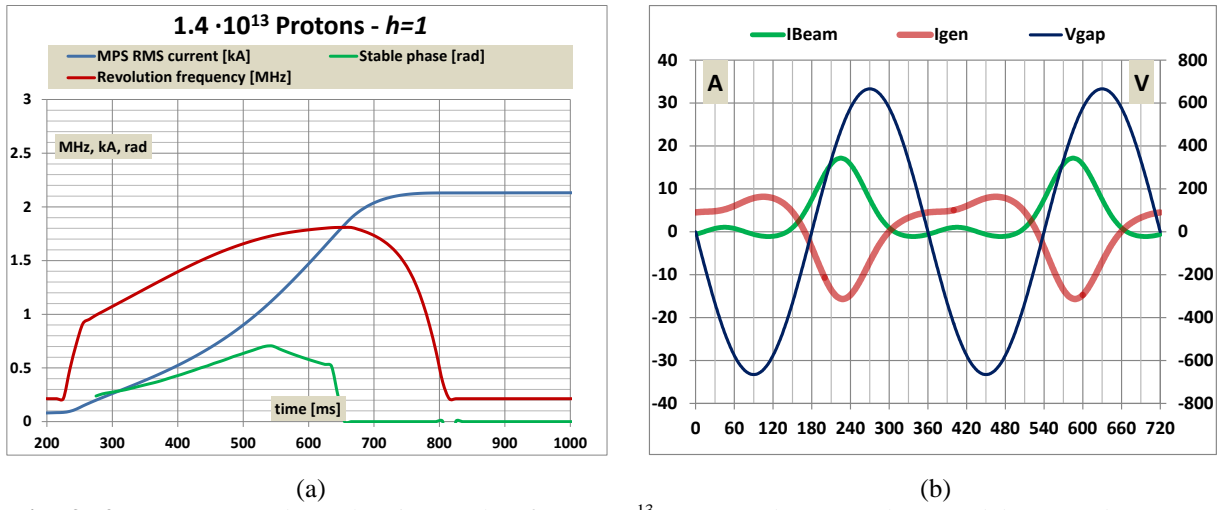


Fig. 3.72: (a) Computed accelerating cycle of 1.4×10^{13} protons; (b) gap voltage and beam and generator currents.

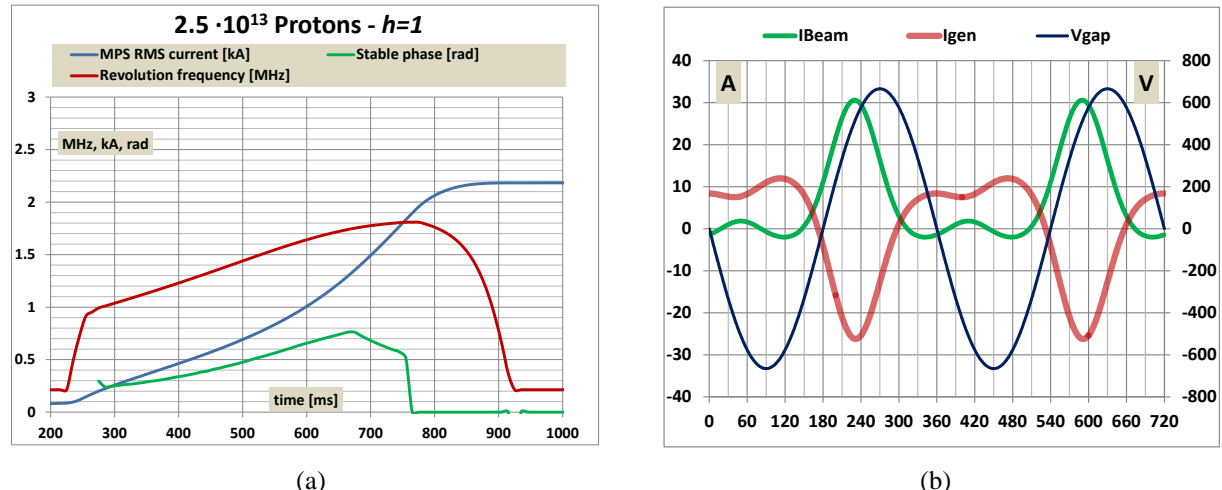


Fig. 3.73: (a) Computed accelerating cycle of 2.5×10^{13} protons; (b) gap voltage and beam and generator currents

As shown in Fig. 3.74, VRF151G, MRF151 and SD2942 drain current saturates at ~ 40 A while the more modern MRFE6VP6300 saturates at ~ 30 A.

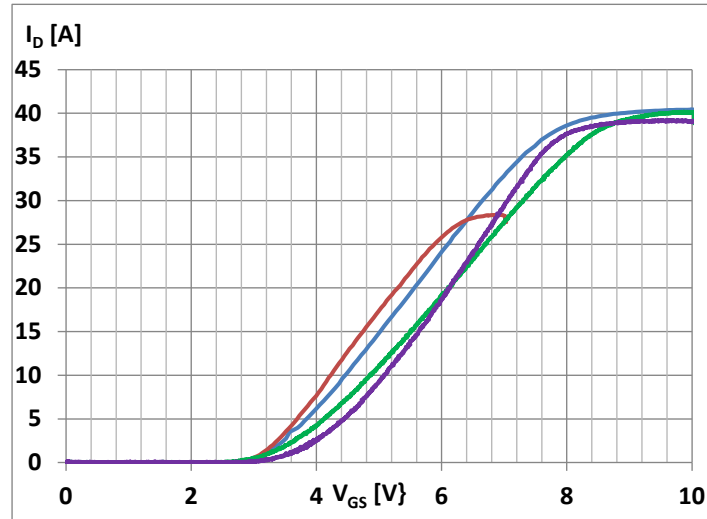


Fig. 3.74: MOSFET saturation currents. Green, VRF151; violet, SD2942; blue, MRF151; red, MRFE6VP6300

The ratio between drain and gap currents is unity for the single-ended amplifier version, so that the maximum required current of 26 A seems within the amplifier's possibilities unless using the MRFE6VP6300 device. The push-pull amplifier configuration has a drain and gap current ratio of 1.5 and therefore can only be used for the intermediate beam intensity requiring 16 A.

3.5.4 Amplifier response

To get a better view of the system possibilities a Spice model of a single-cell system has been simulated. It includes the Finemet® core characteristics derived from measurements and the VRF151 MOSFET model provided by the manufacturer. The amplification system with a push-pull amplifier is shown in Fig. 3.75.

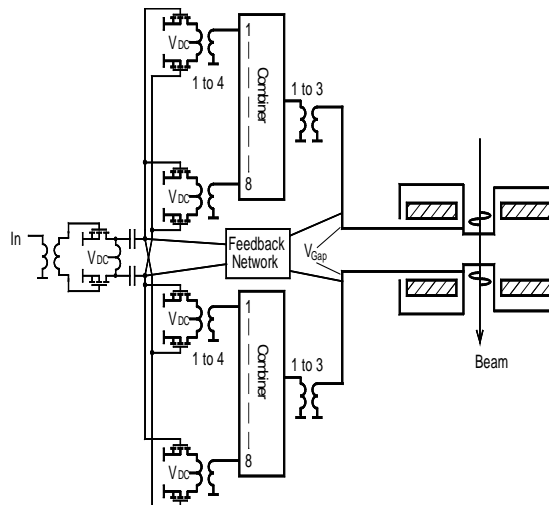


Fig. 3.75: System configuration

It includes some RF feedback to control the gap impedance and partially compensate the beam loading. With a feedback network composed of 150 pF capacitors in series with 100 Ω resistors feeding back each of the gap sides signals to the summing points, the loop gain is ~ 10 dB. A bandwidth limiting circuit composed of a 100 pF capacitor in series with a 10 Ω resistor is also connected from each gap side to ground. Measured and simulated circuit responses are shown in Fig.

3.76 (Add 46 dB for absolute gain). Frequency response linearization is achieved with a series 330 pF capacitor inserted between the driving generator and the amplifier input.

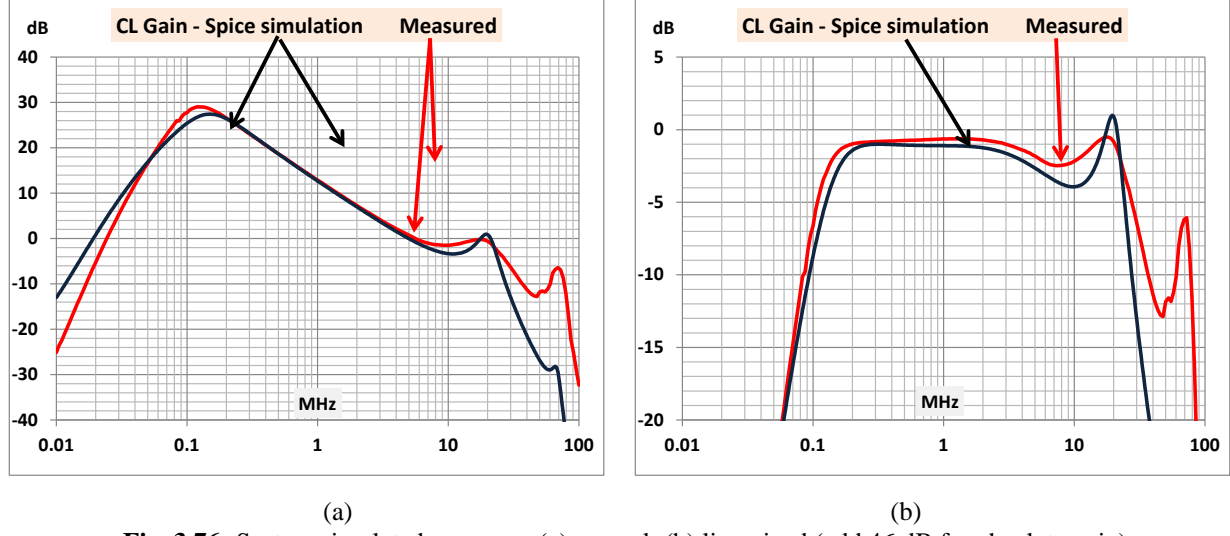


Fig. 3.76: System simulated response: (a) normal; (b) linearized (add 46 dB for absolute gain)

The impedance experienced by the beam going through a gap is defined by the cell impedance, the amplifier output impedance and the connection transmission lines. Figure 3.77 shows the measured and simulated amplifier output impedance.

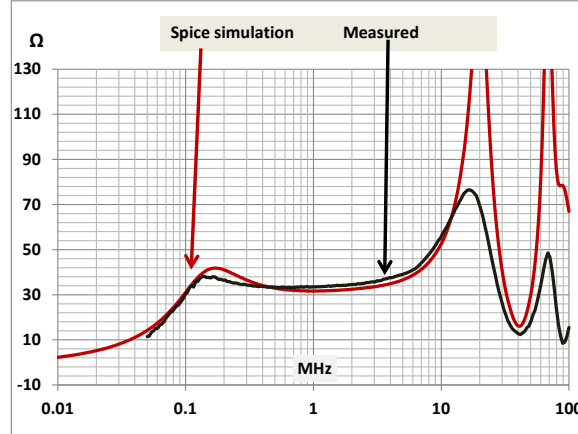


Fig. 3.77: Measured and simulated amplifier output impedance

Time domain simulations of the system providing $V_{\text{Gap}} \sim 670$ V (8 kV/12) with and without beam current allowed checking that the current and power limits of the active devices are not exceeded. The beam current corresponding to 1.4×10^{13} protons circulating at 1.81 MHz revolution frequency (2 GeV, $h = 1$, extraction) has been used for simulations with the push-pull amplifier. As in the previous paragraph the beam has been reconstructed using the first four harmonic components and compensated by a feed forward arrangement coming on top of the fast feedback. The feed forward reduces the equivalent gap resistance to $\sim 4 \Omega$ thus improving the situation by ~ 18 dB. The stable phase has been set around 50° . Figures 3.78 and 3.79 show the gap voltage with and without beam as well as the drain current in one of the 32 active devices comprising the amplifier. As expected the ratio between the drain current and the beam current is approximately 1.5. The power dissipated on each device is about 30 W without beam and it rises to about 75 W with beam. This is well below the 250 W rating for a perfectly cooled device.

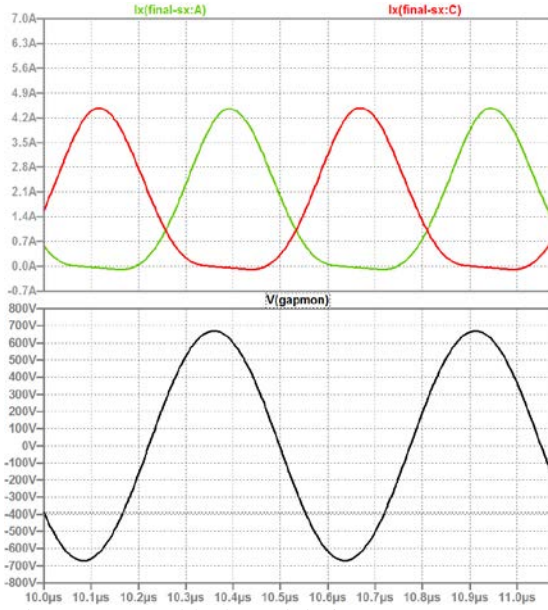


Fig. 3.78: Simulated V_{Gap} (670 V, black) and drain currents (green and red) without beam

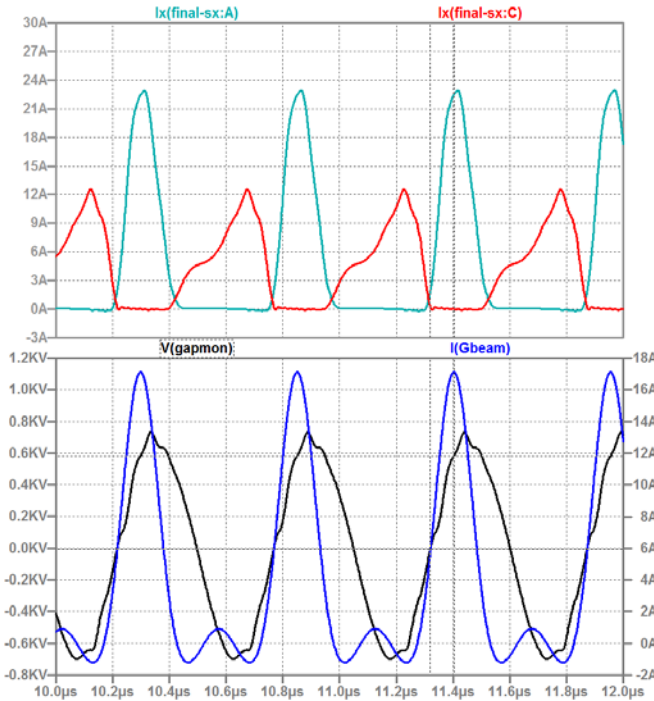


Fig. 3.79: Simulated V_{Gap} (670 V, black), I_{Beam} (1.4×10^{13} protons, stable phase $\sim 50^\circ$, blue) and drain currents (light blue and red).

When manipulating higher intensity beams the response is expected to be similar. For 2.5×10^{13} protons the generator current will rise from 16 A to 26 A thus increasing by a factor smaller than 2. Using two single-ended amplifiers the number of active devices will double and the gap-to-drain current ratio will step down from 1.5 to 1. This means that from a current point of view there will be almost no difference while the situation will be improved as far as the power dissipation is concerned. But increasing the current and power available from the amplifier will not be enough: the equivalent gap impedance must additionally be reduced at least by a factor of ~ 1.6 to replicate the simulated situation.

3.5.5 Low-level RF upgrade

3.5.5.1 *Introduction and reasons for upgrade*

The upgrade of the PSB low-level RF (LLRF) system to a digital LLRF (DLLRF) is part of a global effort carried out by the BE/RF group to replace the existing generation of mixed analogue-digital LLRF systems. The PSB DLLRF system is an evolution of the system that has been successfully operational in LEIR since 2006 [83] and belongs to a new family that will be extensively used for LLRF as well as for diagnostics in many other machines [84–87]. LEIR will also benefit from this development and be upgraded to the new DLLRF.

Advantages of the digital approach [88] include full remote control and archiving capabilities, reproducibility and absence of drift in the electronics. DLLRF allows using built-in diagnostics, essential for system optimization, troubleshooting, low down-time and operations close to the machine's performance limits. Special situations can be handled more precisely and complex algorithms and modern control methods are easier to implement than in analogue. Several operational modes can be implemented by software (FPGA and DSP) in the same hardware and selected in PPM via a software switch.

The new PSB DLLRF will address shortcomings of the current PSB LLRF, such as hardware obsolescence, the absence of full PPM operation and archiving of hardware settings. The full PPM feature will be especially welcome for the PSB where, typically, users in the same supercycle have different characteristics, in terms of RF gymnastics, HLRF combinations and intensities (ranging from 5×10^9 to more than 1×10^{13} protons/ring). Moreover, some users are requiring an intensity that varies from ~10% to 100% of the nominal one, although not in the same supercycle. It is expected that the full PPM operation possible with the DLLRF will provide improved beam performance, since the parameters for each user can be individually tailored, and the setup time required by a significant change in intensity will be minimized.

Last but not least, LLRF standardization across different machines improved general knowledge of the systems for experts, an overall lower maintenance effort and better spares management.

3.5.5.2 *Overview of the PSB LLRF system after LS1*

After LS1 the PSB will restart with the new DLLRF on all four rings as its operational system, although it will still be possible to revert to the previous LLRF if needed.

Hardware and software

The block diagram for one ring is shown in Fig. 3.80. It consists of one VME switched serial (VXS) crate containing three VXS-DSP-FMC-Carrier motherboards, each one equipped with two daughtercards.

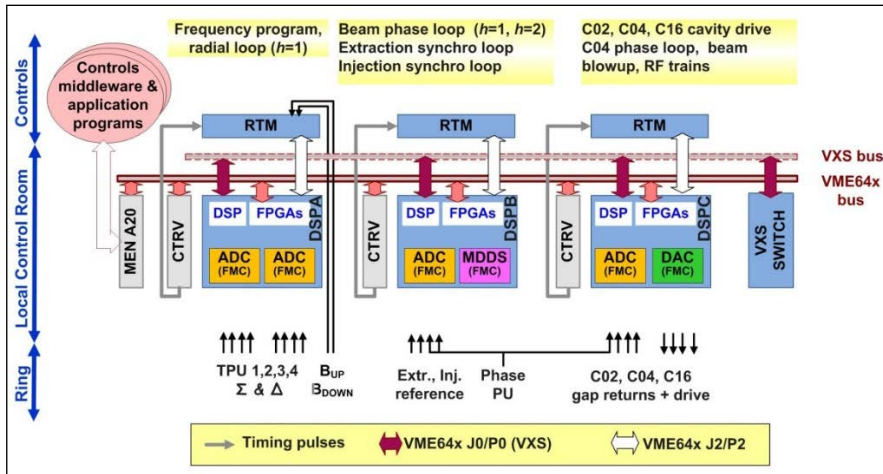


Fig. 3.80: PSB DLLRF block diagram for one ring after LS1. DDS: direct digital synthesiser; AD: analogue-to-digital FMC board; DAC: digital-to-analogue FMC board; DSP A, B, C: VXS-DSP-FMC-Carrier boards; RTM: rear transition module; Phase PU: longitudinal phase pick-up; TPU: transverse pick-up; CTRV: timing receiver module; Men A20: master VME board; BTrain: measured magnetic field.

The VXS standard [89] is an enhancement of the VME64x standard that supports switched serial fabrics over a new, high-speed P0 connector. The VITA57 standard FPGA mezzanine card is used for the daughtercards.

Three kinds of FMC daughtercards have been developed; the direct digital synthesizer (DDS), the analogue-to-digital converter (ADC) and the digital-to-analogue converter (DAC) FMC modules.

The DDS FMC daughtercard is a high-quality, compact clock generator, featuring two independent channels synchronized to the same reference and allowing up to 232 MHz frequency step resolution. It uses the AD9858 IC as the DDS core.

The ADC FMC daughtercard uses an AD9286 ADC and includes four independent digitization channels with up to 125 MSPS of 16 bits resolution. Its analogue front-end provides signal conditioning with DC coupling, low noise, low distortion and a controllable gain switching of 18 dB, corresponding to 3 LSBs. The measured spurious-free dynamic range (SFDR) exceeds 70 dB, the signal-to-noise (SNR) ratio exceeds 74 dB thus allowing 12.5 equivalent number of bits (ENOB).

The DAC FMC daughtercard is based on the AD9747 IC and allows four independent digital-to-analogue conversion channels with 16 bits resolution in the conversion and programmable gain switching of 18 dB. The output is DC coupled, with a 40 MHz analogue bandwidth and a peak output voltage of 2 V peak-to-peak. The sampling rate of the DAC mezzanine can reach up to 250 MSPS and the front-end, like the ADC FMC board, includes low distortion and low-noise electronics.

Both ADC and DAC FMC daughtercards provide features such as voltage/temperature monitoring, precise board identification with a silicon ID chip and EEPROM for storing board specific information such as the FMC family type and version number. Both daughtercard types are also equipped with ADC and DAC ICs for automatic offset compensation.

Two VXS switch boards per crate allow transference of 10b8b-encoded data between VXS-DSP-FMC carrier boards at a raw link rate of 2 Gbit/s. The VXS switch board is also compatible with the future PSB B-train distribution protocol, based upon White Rabbit. Under this scheme, the B-train information is sent to the destination VXS-DSP-FMC carrier board via a spare full-duplex channel.

The VXS-DSP-FMC carrier board, shown in Fig. 3.81, is a 6U unit board carrying a SHARC digital signal processor (DSP) ADSP-21368 and two Xilinx Virtex 5 field programmable gate arrays (FPGAs), referred to as main FPGA (XC5VLX110T) and FMC FPGA (XC5VSX95T). The former is the heart of communications; the latter, optimized for digital signal processing, controls the FMC

hardware and implements the required data treatment. Each carrier board can host up to two FMC daughtercards with a high-pin count format. The carrier board also includes several memory banks for observation purposes. In particular, two $4\text{ M} \times 18$ bit banks are clocked at 100 MHz and two $1\text{ M} \times 4 \times 18$ bit banks are clocked at the RF clock frequency.

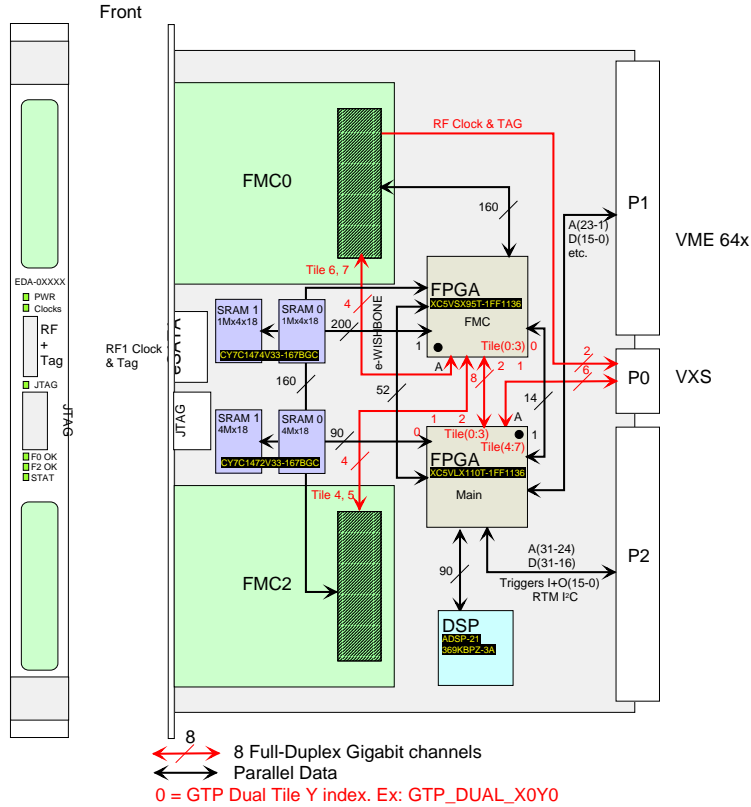
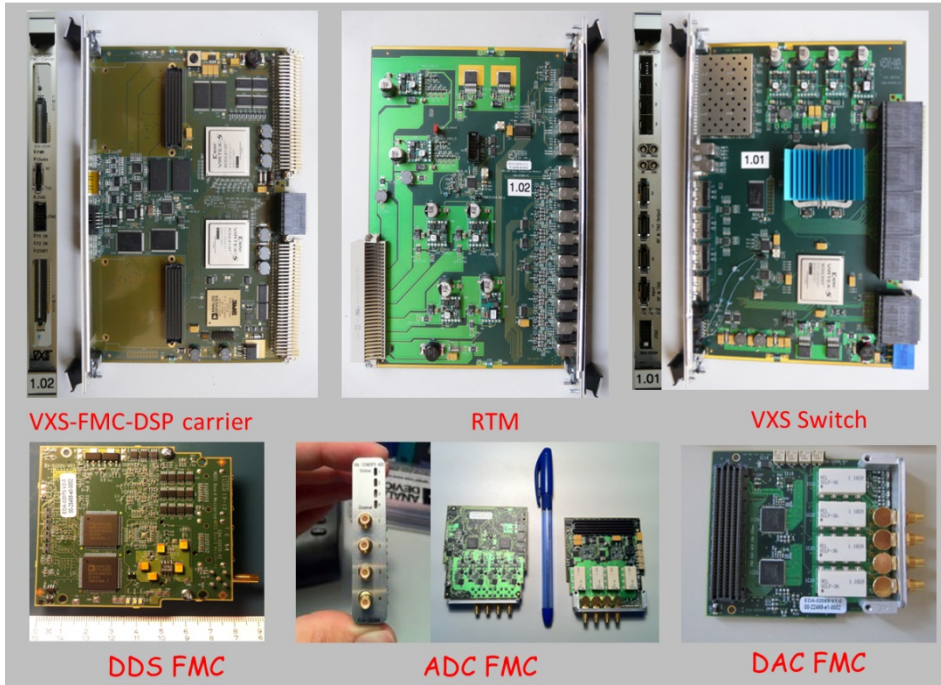
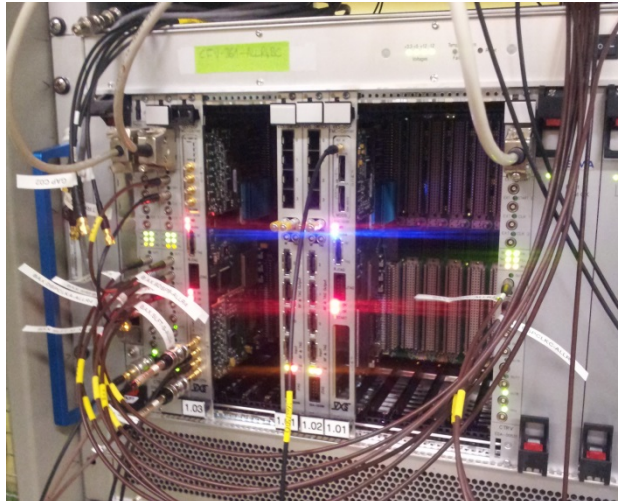


Fig. 3.81: VXS-DSP-FMC carrier board block diagram

Figure 3.82 provides an overview of the main hardware modules comprising the new DLLRF and Fig. 3.83 shows a picture of the prototype system, based upon these new modules, that was installed in the PSB RF cage in early 2013 for test purposes.

**Fig. 3.82:** Picture of the main DLLRF modules**Fig. 3.83:** Test system based upon the new DLLRF modules installed in February 2013 in the PSB RF cage for test purposes.

The firmware running on the main FPGA implements the essential infrastructure for system communication and data exchange. The communication architecture is configured such that no arbitration is required on any of the link or bus interfaces for simplicity and overall system reliability. The same firmware implements other capabilities, such as; i) a dual, 128 channel timing generator, ii) 16 channels, 32 bit \times 1024 vector function generators; iii) 48 channels, 32-bit \times 2048 programmable digital signal observation. The firmware allows remote updating of FPGA and DSP software. Finally, numerous diagnostics functions are available. The firmware will be the same for all boards; the capabilities will be enabled or disabled through controls depending on the desired board function.

The FMC FPGA is optimized for DSP resources and implements the custom FMC hardware control and data treatment via the instantiation of FMC IP cores. Each daughter card is complemented by an FPGA IP core running on the FMC FPGA. The FMC daughter card assembly and corresponding

IP core implements the functionality of a master direct digital synthesizer for the DDS FMC, a digital down converter for the ADC FMC and a slave direct digital synthesizer for the DAC FMC.

The DSP implements the core data treatment functionalities, such as the beam and cavity control loops for the LLRF, thus fully exploiting its floating point processing capabilities. The DSP code will entirely depend on the functionality of the board hosting the DSP itself and will allow full system customization. An advantage of this approach is the short time required to compile the code and download it into the hardware, as opposed to that required by a complex FPGA. This will minimize the downtime due to code modifications during machine studies.

More details about the hardware and software implementation can be found elsewhere [84].

3.5.5.3 *Functionality*

The analogue signal acquisition and generation, and associated processing is clocked by an RF clock, which is a programmable high harmonic of f_{REV} . A revolution ‘tag’ (single or double) marks each turn and guarantees phase synchronism between all boards in the system. The RF clock harmonic is changed within each cycle to maintain its frequency in the 60 MHz to 120 MHz range; the changes are synchronized via a double tag.

The new DLLRF system will implement all beam control capabilities now available with the current LLRF, such as frequency programming and correction, beam phase and radial loops. Several PPM extraction synchronization loop implementations will be available to satisfy the needs of operational as well as of MD beams. The three ferrite high level RF (HLRF) systems will be controlled by the LLRF: in particular, the phase of the C04 HLRF system will be locked to that of the C02 HLRF by feedback, and the C16 HLRF system generating the longitudinal blow-up will be controlled in feedforward. Several RF trains (analogue as well as digital) will be available for distribution to other systems such as tune measurement as well as observation via the OASIS digital oscilloscope.

The sampling period of the loops is expected to be as low as 5 μ s, thus allowing a closed loop bandwidth of several kHz.

Over the past years several successful MD sessions have been carried out using a prototype digital LLRF system installed in PSB ring 4. Features validated included various extraction schemes, such as the single batch transfer, the single batch transfer with re-bucketing, bunch splitting and control of the C04 phase with respect to the C02 and the C16 longitudinal blow-up [90, 91]. These MD sessions have thus allowed validation of implementations and system performance as well as building confidence in the new system deployment.

3.5.5.4 *Installation and layout*

A fifth LLRF system will be installed in addition to the operational DLLRF systems for rings 1 to 4. This will be referred to as ‘ring 0’ and will eventually be connectable to any of the four PSB rings, but will initially be switchable in PPM with the operational LLRF in Ring 4. Ring 0 will allow implementation of dedicated software or hardware configurations for MD sessions in PPM without modifying the operational ring systems. It will also allow testing and validation of new features, prior to their deployment on the operational rings, thus minimizing the risk of malfunction or undesired side-effects.

Figure 3.84 shows the rack layout in the beam observation room (BOR) after LS1. The red-coloured racks are those that house the hardware developed for the PSB LIU upgrade. The current LLRF systems for rings 1 to 4, shown on the left side of the picture, will be left in place for the initial part of the run; they will be removed once the DLLRF is fully commissioned.

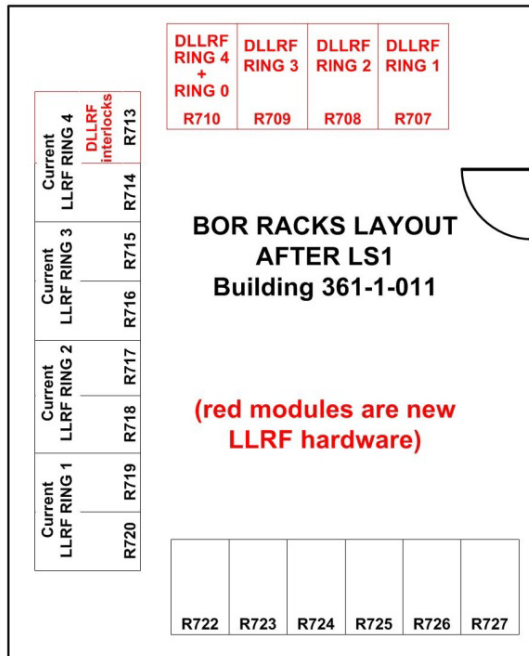


Fig. 3.84: Rack layout in the BOR after LS1

3.5.6 Support for Finemet research and development after LS1

The Ring 0 DLLRF system will support the Finemet research and development effort after LS1, which will lead to a decision on the PSB HLRF consolidation. To this aim, the ring 0 DLLRF will be connected to PSB ring 4 and will control not only the three ferrite HLRF systems but also several harmonics of the Finemet HLRF installed in the same ring.

This activity follows successful MD sessions already carried out in 2012 by using a prototype digital LLRF system installed in PSB ring 4 [92].

3.5.7 Future upgrades

The operation of the DLLRF with the 2 GeV cycle in the PSB should require no major changes, although the systems will have to be commissioned with the new cycle. The DLLRF is also already compatible with the future PSB B-train distribution system based upon White Rabbit.

The HLRF upgrades and operation with Linac4 will require upgrades in the DLLRF systems, both in hardware and software.

3.5.7.1 DLLRF upgrade to follow HLRF upgrades

The DLLRF will be upgraded to satisfy the needs of the HLRF upgrade, which will be decided in 2015. In case the Finemet HLRF solution is retained, the system will be upgraded to the number of feedback and feedforward loops required for operating the wideband cavities with intense beams. In case it is decided to keep the ferrite-based HLRF, the voltage and tuning loops will be integrated in the DLLRF at least for the C02 and the C04 HLRF systems.

The processing power and the modularity of the DLLRF bode well for the feasibility of the required upgrades, although these are as yet unspecified.

3.5.7.2 Operation with Linac4

The future Linac4 beam should be inhibited at low energy in the event of a significant problem being signalled on the RF equipment of any of the four PSB rings, in order to avoid unnecessary beam loss.

A dedicated system called RF interlock interface has been developed to collect the status information from the RF power, RF low-level and Linac4 interlock systems as well as from the machine operating parameters in order to determine which ring(s), if any, should be inhibited. The information is processed in real time and ‘inhibit’ signals are sent to the Chopper and to the LLRF equipment. Figure 3.85 shows a block diagram of the RF interlock interface system and of its connections. The system is well advanced and will be commissioned with the DLLRF by January 2015.

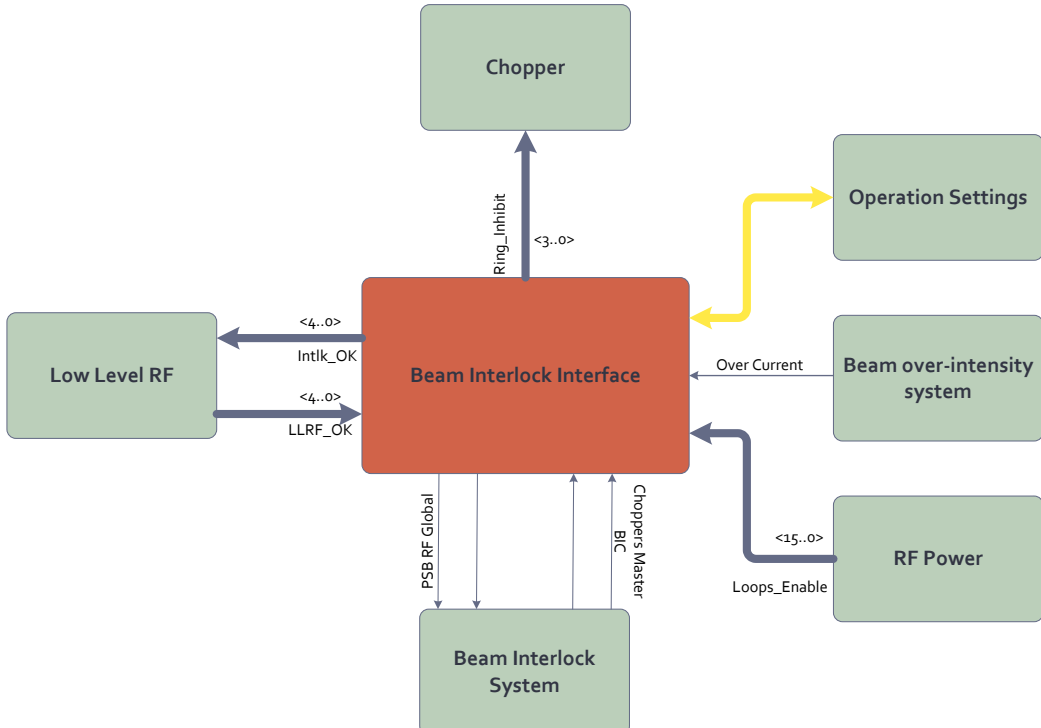


Fig. 3.85: Block diagram of the RF interlock interface and its connections

A second functional upgrade to the DLLRF for operation with Linac4 is the implementation of a synchronization of the four Booster rings prior to injection with respect to a single reference oscillator [93]. This will allow avoidance of a resynchronization of the system generating the required Linac4 beam structure and the fast Booster injection timings at the switching of the injection from one ring to the next. Standard control modules will then be used for the generation of all fast Booster timings. The RF frequency of any of the four rings will start rising with the beginning of the injection, but the transient thus generated is expected to pose no problem.

The DLLRF system deployed in the PSB after LS1 will include the hardware channels as well as the digital signal processing required to carry this out. The software implementation and validation will then be possible well in advance of the Linac4 connection to the PSB.

3.5.8 Summary of DLLRF features

Table 3.32 summarizes the main features of the DLLRF hardware.

Table 3.32: Main features of the DLLRF system

Component	Feature	Description
VXS-FMC-DSP carrier	DSP type	SHARC ADSP-21368 (400 MHz clock)
	FPGAs type	Xilinx XC5VLX110T and XC5VSX95T
	On-board memory	Two banks ($4 \text{ M} \times 18 \text{ bit}$) clocked at 100 MHz Two banks ($1 \text{ M} \times 4 \times 18 \text{ bit}$) clocked at RF clock frequency.
	FMC sites	Two high pin count with independent adjustable power supplies
	VXS data interfaces	Six full duplex serial links each running 2 Gb/s
	Inter FPGA data	Eight full duplex serial links each running 2 Gb/s
	RF clock and tag	Ultra-low jitter differential RF clock and tag distribution with source selectable from front panel eSATA or dedicated VXS-B ports
VXS switch	Crossbar switch	Protocol-agnostic 72×72 crossbar with multicast 4.25 Gb/s Mindspeed M21141
	Control FPGA type	Xilinx XC5VLX50T
	RF clock and tag	Ultra-low jitter differential RF clock and tag distributor via eSATA front panel interface or through VXS
	External data exchange	Quad SFP for full-duplex serial giga-bit fibre optical connections
	VXS compliance	Full support for VXS payload ports 1 up to 12
ADC FMC	Miscellaneous	White Rabbit compliant hardware through a dedicated SFP interface
	Number of channels	Four (fully independent)
	ADC IC	AD9286 (125 MSPS, 16 bits resolution)
	Input impedance	$50 \Omega \pm 5\%$
	Full-scale peak input voltage	1.0 V
	Full-scale input power	+10 dBm
	Bandwidth	40 MHz (300 MHz without input filter)
	Narrowband linearity (spurious content around the carrier, single tone)	Better than 90 dB at $f_s^a = 125 \text{ MHz}$
	Wideband linearity (SFDR)	Better than 70 dB at $f_s = 125 \text{ MHz}$
	Passband ripple	1 dB maximum.
	SNR	70 dB at 125 MSPS (up to Nyquist limit)
	Resolution	16 bit
	ENOB	12.5
	Maximum sample rate	125 MSPS
	Minimum sample rate	20 MSPS (typical)
	Clock random jitter for specified figures	2 ps maximum

Component	Feature	Description
ADC FMC	Front-end variable gain	Two steps: 0 dB, +18 dB (3 bits)
	Gain error	4% (typical)
	Channel isolation	90 dB (typical)
DAC FMC	Input connector	SMC
	Number of channels	Four (fully independent)
	DAC IC	AD9747 (250 MSPS, 16 bits resolution).
	Output impedance	$50 \Omega \pm 5\%$
	Full scale peak output voltage	2.0 V
	Full scale nominal output power	+10 dBm
	Narrowband linearity (spurious content around the carrier, single tone)	Better than 80 dB at $f_s^a = 125$ MHz
	Wideband linearity (SFDR)	Better than 60 dB at $f_s = 125$ MHz
	Maximum sample rate	250 MSPS
DDS FMC	Minimum sample rate	20 MSPS (typical)
	Clock random jitter for specified figures	2 ps maximum
	Front-end variable gain	Two steps: 0 dB, +18 dB (3 bits)
	Gain error	4% (typical)
	Channel isolation	90 dB (typical)
	Input connector	SMC
	Number of channels	2
	DDS IC	AD9858
	Reference input signal	10 MHz, 0 dBm sine wave, or AC coupled square wave
DDS FMC	Minimum amplitude	0 dBm to attain the specified jitter performance
	Maximum amplitude	+10 dBm
	Frequency resolution	32 bits ($\Delta f = 232$ mHz)
	Jitter performance	800 full-scale rms (typical), 2 ps rms (worst case) ^b
	Output dividers	1 to 32
	Signal levels	LVPECL with AC coupling
	Minimum output frequency	20 MHz (typical).
	Maximum output frequency	450 MHz
	Tag generator maximum output frequency	Same as RF_CLK (450 MHz)
	Output connector	Shielded e-SATA

Component	Feature	Description
Loops sampling period		As low as 5 μ s
Expected loops BW		Up to 50 kHz
		Two analogue
Number of independent RF trains		Four digital
		(RF trains at $h = 1$ and $h = 2$ available without limitations)

^a f_s —sampling frequency

^b For certain frequencies, it could peak to bigger values due to the DDS phase truncation. These values are averages along the entire frequency range

3.5.9 Transverse feedback

3.5.9.1 Introduction

In the CERN PS Booster (PSB), the present transverse damper system has been in operation since 1999 and, with the proton beam as supplied by Linac2, this equipment has provided satisfactory operational results.

In the framework of the LHC injector chain upgrade (LIU), this system will nevertheless be modified in 2014 in order to adapt to the expected Linac4 beam and to the demands for new features including transverse blow-up, beam excitation for tune measurement and new remote control and monitoring capabilities. The replacement of the ageing electronic hardware is also advised with regards to maintenance issues. The main changes are as follows.

- i) An increase of kick strength—achieved by an increase in installed RF power—to address the injection errors at a higher kinetic energy with Linac4 (160 MeV instead of 50 MeV) and the doubling of the maximum beam current that translates, due to constraints in the present radial offset suppression unit, to a potential saturation of the amplifier stage. This increased power will also allow for efficient transverse blow-up even at the increased extraction energy of 2 GeV (instead of 1.4 GeV as at present).
- ii) A new water-cooling distribution system for the power amplifier in building 361-1-211 above the PSB ring, with remote control and monitoring, along with automatic shut-down if a leak is detected.
- iii) A new PLC-based remote power control system, as is now the standard for RF power equipment CERN-wide.
- iv) Electronic digital signal processing featuring new functions such as variable betatron phase adjustment along the cycle to track tune changes, a notch filter to remove frequency components related to beam position offsets, the generation of a signal at a chosen harmonic for blow-up purposes and a variable gain.

3.5.9.2 New pick-up head amplifiers

The present amplifiers installed in the ring close to the transverse position pick-ups (PU) need to be redesigned to handle the increased peak voltage caused by the higher intensity beam from the future connection to Linac4. They have also received a radiation dose over the recommended limits for electronic circuits (although they still perform as specified) and sourcing replacement parts is becoming difficult due to outdated components. A prototype of a new circuit underwent some preliminary tests in December 2013 (Fig. 3.86). The effective bandwidth of the amplifier is from 100 Hz to 150 MHz with less than 45° phase error. The bandwidth measurement was made including a

test PU using a so-called ‘wire measurement’ where a conductive wire simulates the beam. This explains the high-pass behaviour at low frequency (Fig. 3.87) while the amplifier stage is DC coupled.

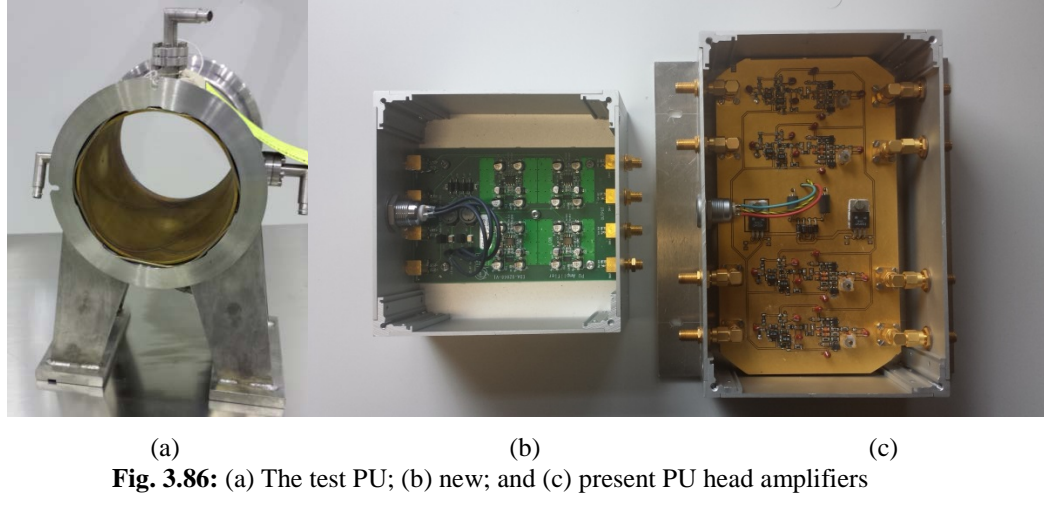


Fig. 3.86: (a) The test PU; (b) new; and (c) present PU head amplifiers

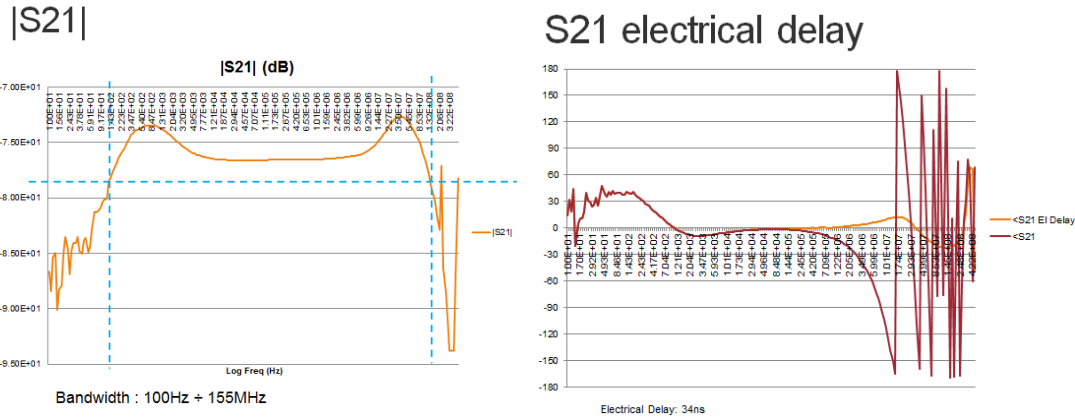


Fig. 3.87: New PU head amplifier frequency response

3.5.9.3 New signal processing board

The digital signal processing board is similar to that used for the PS one turn feedback and for the CPS transverse damper (Fig. 3.88). As used for the transverse dampers, this board has been named the beam synchronous processing unit (BSP), as it is designed to adapt the loop delay to the particles’ varying time of flight. Details concerning the board can be found in Ref. [94].

This board will be clocked at a rate from 60 MHz to 120 MHz with a high harmonic of the beam revolution frequency. The clock will be supplied by the new PSB beam control [91]. The core feature of this board is to shift the analogue signal from the beam pick-ups into the digital domain where it is processed by a powerful Stratix™ II FPGA and then transformed into an analogue corrective signal to be applied to the kickers after amplification [95]. The present ADCs are the elements limiting the sampling rate to a specified value of 100 MS/s, although in practice they have been successfully tested above 125 MHz. A new adaptation board is nevertheless presently being designed to allow for the installation of a faster ADC.



Fig. 3.88: Digital signal processing board or BSP

Figure 3.89 summarizes the details of the signal processing occurring in the BSP. The notch filter removes the revolution frequency bands that convey only the information of the closed orbit, letting through the betatron bands that are to be corrected. The betatron signal is then dephased in order to appear in quadrature phase at the kicker level for optimal damping. At the third stage an automatic delay is applied to ensure the kick is synchronized with the measured beam slice. This automatic delay has a precision of 1 ns, enough to keep the phase error below 7° at 20 MHz (bandwidth of the overall system).

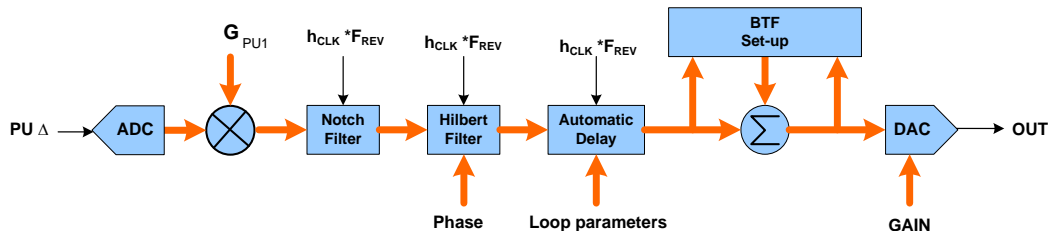


Fig. 3.89: Beam synchronous digital signal processing block diagram

3.5.9.4 New power amplifiers

The new water-cooled power amplifiers will provide 800 W rms on each $50\ \Omega$ kicker strip-line plate instead of the 100 W rms currently in use. The present bandwidth of 100 kHz to 100 MHz will be preserved. These devices are specified to have a 60 dB voltage gain and thermal protection shutting down the power supply when the limit is reached. Their architecture is based on the usage of moderate voltage but high-current transistors driving the low impedance end of a series of impedance to voltage transformers of the transmission line type. Low-voltage MOSFETs have the advantage of allowing for a lower drain-source resistance with an almost unchanged parasitic capacitance, thus allowing for an extended bandwidth. The selected BLF 578 device has a 70 mΩ drain-source resistance. An original feature of this amplifier is that at the transistor output stage it uses a $5.5\ \Omega$ transmission line (flexible ribbon) wound around a high-saturation field ferrite core. The latter assembly has been simulated but not yet tested. Figure 3.90 shows the initially tested version, with a $16.5\ \Omega$ coaxial line impedance, that was found to be prone to instabilities.

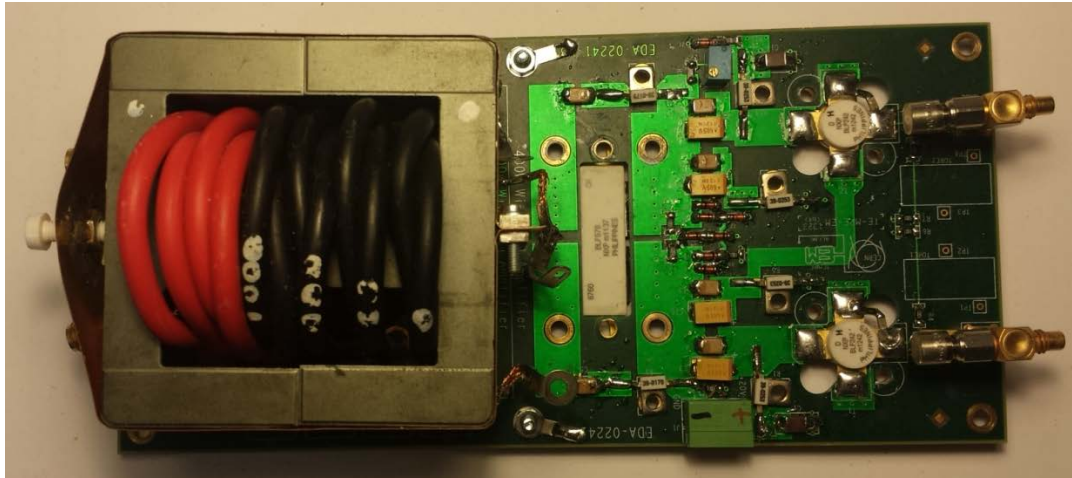


Fig. 3.90: 800 W power stage board

3.5.9.5 New water-cooling system

In the previous amplifier water-cooling system, the two amplifiers of a given plane and one PSB ring were connected in series directly to the main demineralized water circuit, without any protection or monitoring, apart from a flowmeter switch activated below a chosen threshold. The new system is separated into eight channels; one for each plane of the four PSB rings (Fig. 3.91). It has full monitoring of upstream and downstream pressure, temperature and flow, together with control of electric valves; all of this is achieved either locally or via a PLC control system integrated with the global accelerator complex control system (Fig. 3.92).

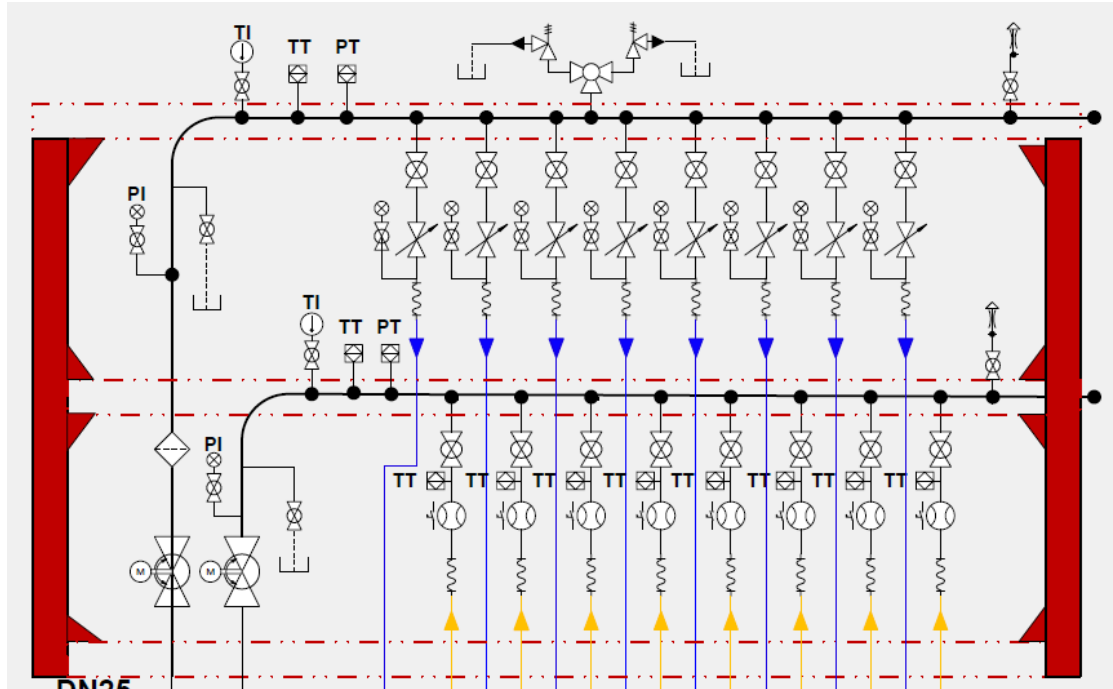


Fig. 3.91: Water-cooling distribution diagram



Fig. 3.92: Water-cooling distribution

3.5.9.6 New PLC control system

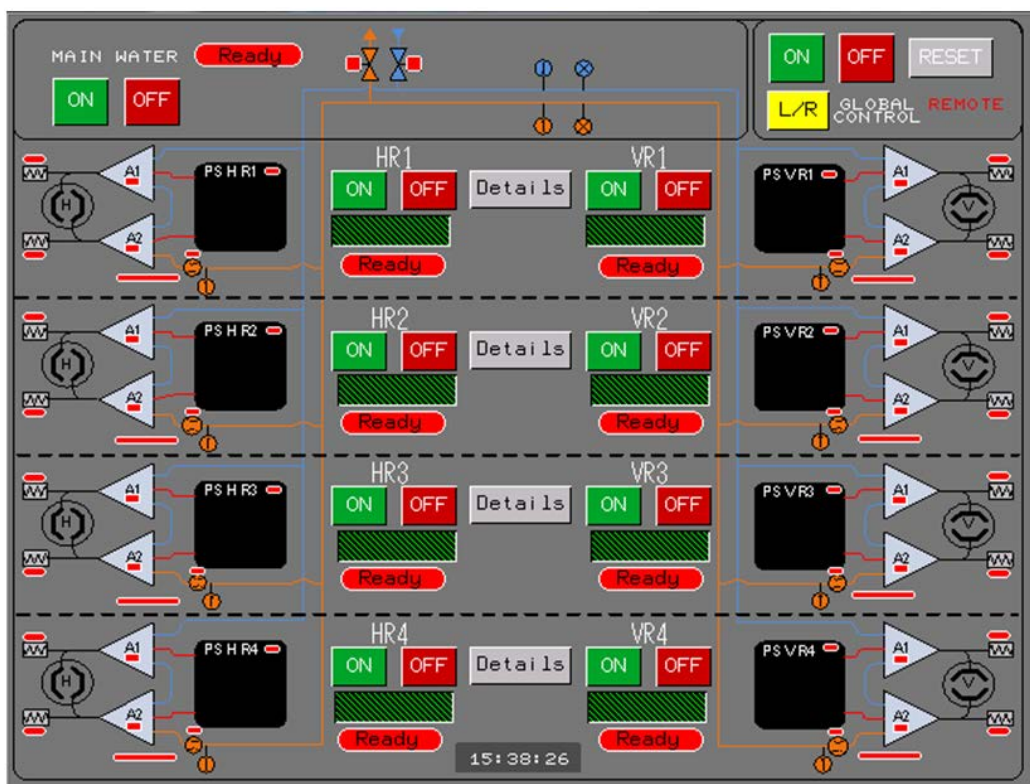
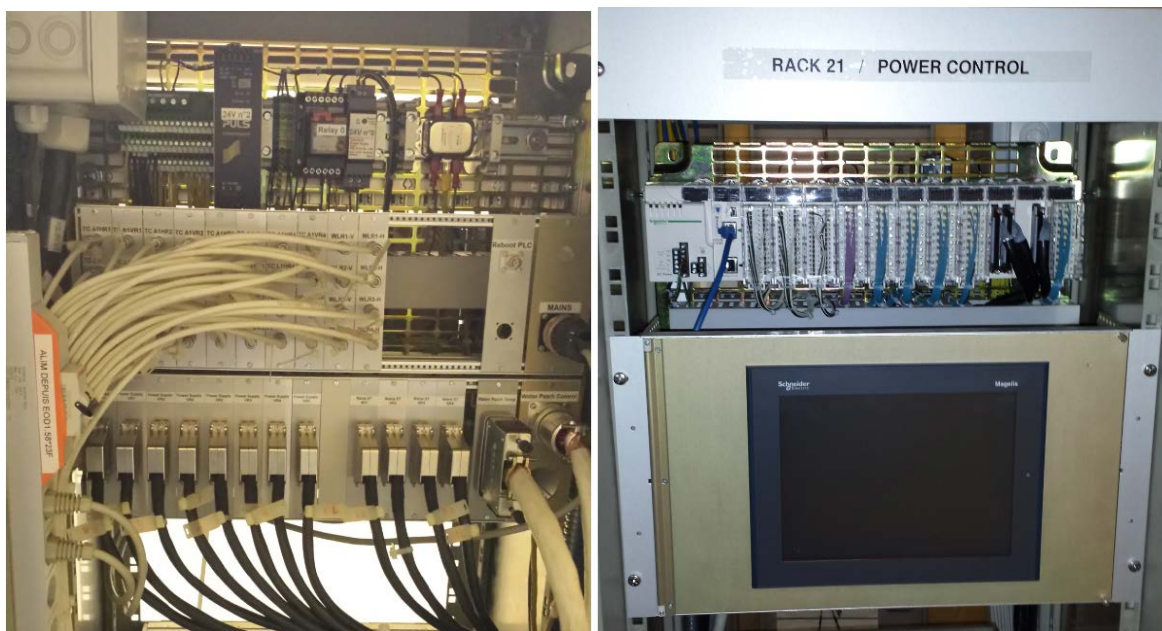
In the previous system, the power equipment was under basic supervision consisting of an exchange of a set of bits with an application in a server for control and monitoring. The features controlled and monitored were: interlock ok/not ok, remote/local, system on/off, loop closed/open, BTF on/off, timing on/off, water flow ok/not ok.

The new PLC system [96] uses an industrial framework designed to offer safer operation. All information is treated by a local processor that continues to deal with the interlocks even when the network is unavailable or disconnected. The range of monitoring points has been extended to include cooling water parameters like pressure, flow and temperature at different locations, together with a water leak detector indication from each set of amplifiers. The monitoring of the voltage and current of the new power-supplies and the over-temperature indication of the final resistive loads has also been added. The status information is available locally on a LCD touch screen as well as remotely (Figs. 3.93 and 3.94). The control of the installation can be set to be local only if required.

3.5.9.7 New OASIS observation system

All crucial signals for the monitoring of the PSB damper system were previously connected to a remote rack hosting VME digitizers multiplexed with other users. Due to the requirement that extra signals be monitored, an independent installation has been included in the racks reserved for the PSB dampers (Fig. 3.95).

In addition to the previous monitored signals, all pick-up plates will be connected to OASIS, along with all kicker plates (compared to the addition of two plates for a given plane, as previously). The amplifier outputs are now also available for monitoring.

**Fig. 3.93:** First page of the PLC control menu**Fig. 3.94:** PLC control hardware

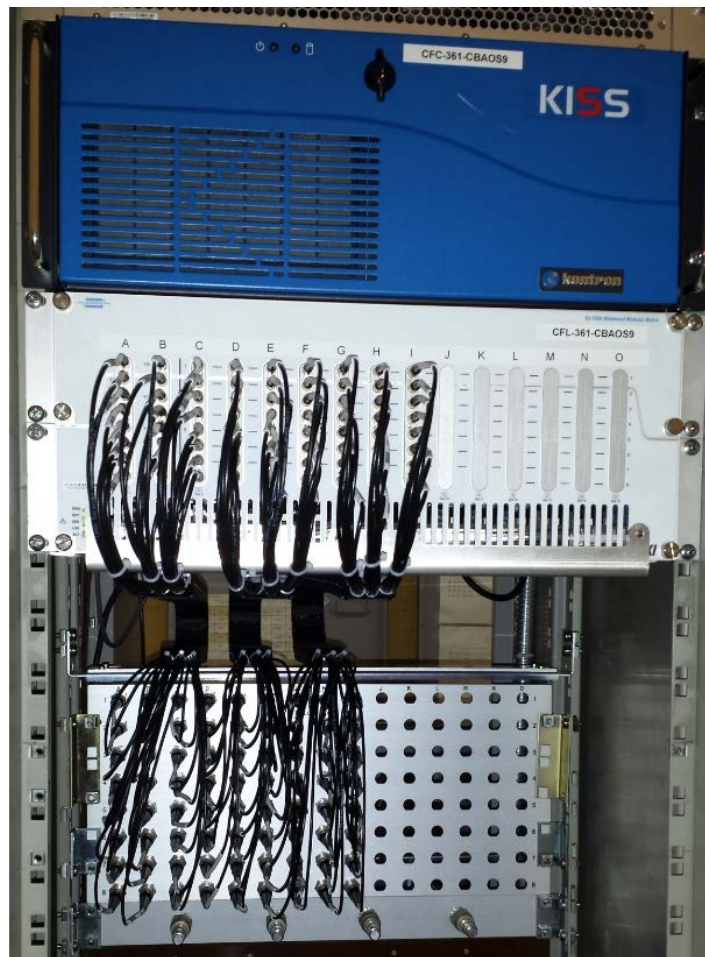


Fig. 3.95: OASIS hardware installation

3.5.9.8 Additional new hardware

The power supplies feeding the power amplifiers have been replaced by a new version (TDK lambda GEN 50 V-85 A) providing the extra power required by the amplifiers' power increase (Fig. 3.96). These devices also offer complete remote control and monitoring capabilities when associated with the new PLC control system.



Fig. 3.96: New power supply for the power amplifiers

The 50Ω loads absorbing the kicker signal are located in the equipment room, but these had to be upgraded to cope with the increased power available (Fig. 3.97). The new units from Diconex have a power specification of 600 W rms that is sufficient to stand the 800 W peak of the installation. They offer an attenuated (-60 dB) image of the input voltage and are protected by a thermal switch connected to the PLC interlock system.



Fig. 3.97: New power attenuators

3.5.9.9 Conclusion

The new PSB transverse damper system is modified to be compatible with the requirements implied by the foreseen increased beam energies at injection with Linac4 and at extraction (2 GeV instead of 1.4 GeV), see Table 3.33.

The PLC control system will allow safer operation of all the equipment remotely, along with reliable monitoring of the system components in parallel with the OASIS observation system.

The enhanced capabilities of the system to adjust the betatron phase and gain along the cycle is expected to improve the loop damping time. An improvement is also expected due to the addition of the notch filter to remove the revolution frequency lines, as these were known to saturate the power amplifiers during the extraction bump, due to the slow response time of the beam offset signal suppressor as previously used.

The new system should allow for transverse blow-up operation and will be available to supply the excitation required for the transverse tune measurement.

Table 3.33: Summary of changes in the PSB transverse feedback system

Equipment	Value	
New power amplifiers	800 W rms for each 50Ω kicker plate	
New digital processing unit	Bandwidth Sampling rate Bandwidth (DC) Automatic delay precision M (1 Hilbert filter phase resolution) Notch filter rejection	100 kHz to 100 MHz 60 MS/s to 125 MS/s 20 MHz 1 ns 1° 72 dB _{FS}
New pick-up head amplifiers	Bandwidth	100 Hz to 150 MHz, pick-up response included
New controls and monitoring		New OASIS monitoring New PLC control New water distribution circuit New three-phase mains distribution

3.6 Power systems

3.6.1 Injection power supplies

3.6.1.1 Introduction

As described elsewhere in the Technical Design Report, the injection region of the PSB will be subject to several modifications to accept H^- particles at an energy of 160 MeV from Linac4, compared with the existing 50 MeV protons from Linac2. Modifications and upgrades to the LT and LTB transfer lines, shared by both the Linac2 and Linac4 accelerators, are briefly described but are under the supervision of the Linac4 project. Modifications and upgrades to the BI lines and the injection region of the PSB are part of the LIU PSB upgrade project and are described below.

For the power converters, the changes can be categorized in three main areas: 1) those required for the 160 MeV injection energy upgrade; 2) those required to implement H^- stripping; 3) associated consolidation activities.

3.6.1.2 160 MeV injection energy upgrade

For the 160 MeV region upgrade, the injection septa (BI.SMV), the vertical bending (BI.BVT) and the correctors BI.DHZ50/70 and BI.DVT50/70 require modifications to the magnet; the power converters will also be replaced.

BI[1, 2, 4].SMV

Compared with the existing BI.SMV, operation with H^- at a higher energy will require a higher pulsed current (20 kA). New power converters were specified for the upgrade. As no suitable system for the required specification is commercially available, a CERN development programme has resulted in a new converter topology, termed the Megadiscap, to meet the requirements, which are summarized in Table 3.34.

Table 3.34: Specification parameters for the vertical septum (BI.SMV) power converters

Parameter	Value
Peak current	21 kA
Operating mode	Pulsed
Flat-top length	1 ms max
Maximum repetition frequency	1.1 Hz
Load inductance	1.22 μ H
Load resistance	0.2 m Ω
Precision (uncertainty)	500 ppm (5×10^{-4}) of nominal
Mechanical dimensions ($h \times w \times d$)	2225 mm \times 1150 mm \times 1000 mm

The Megadiscap operates using a controlled capacitor discharge principle. The converter generates a pulse of up to 2 kA, 3 kV, which must then be transformed to the specified load current through a current transformer. The current is actively controlled during the pulse flat-top using feedback from a high-performance current measurement device that is installed on the secondary side. In the case of the Megadiscap, a transformer with a turns ratio of 1:12 will be used to obtain 20 kA on the secondary.

Measurement of the high pulsed current with sufficient accuracy and bandwidth is a challenge and work is ongoing to find an appropriate solution.

The power electronics topology and waveform are presented below (Figs. 3.98 and 3.99). Further information can be found in the project note *Operational Principle and Tuning of the MegaDiscap Power Converters Control System*, CERN-sLHC-Project-Note-0020.

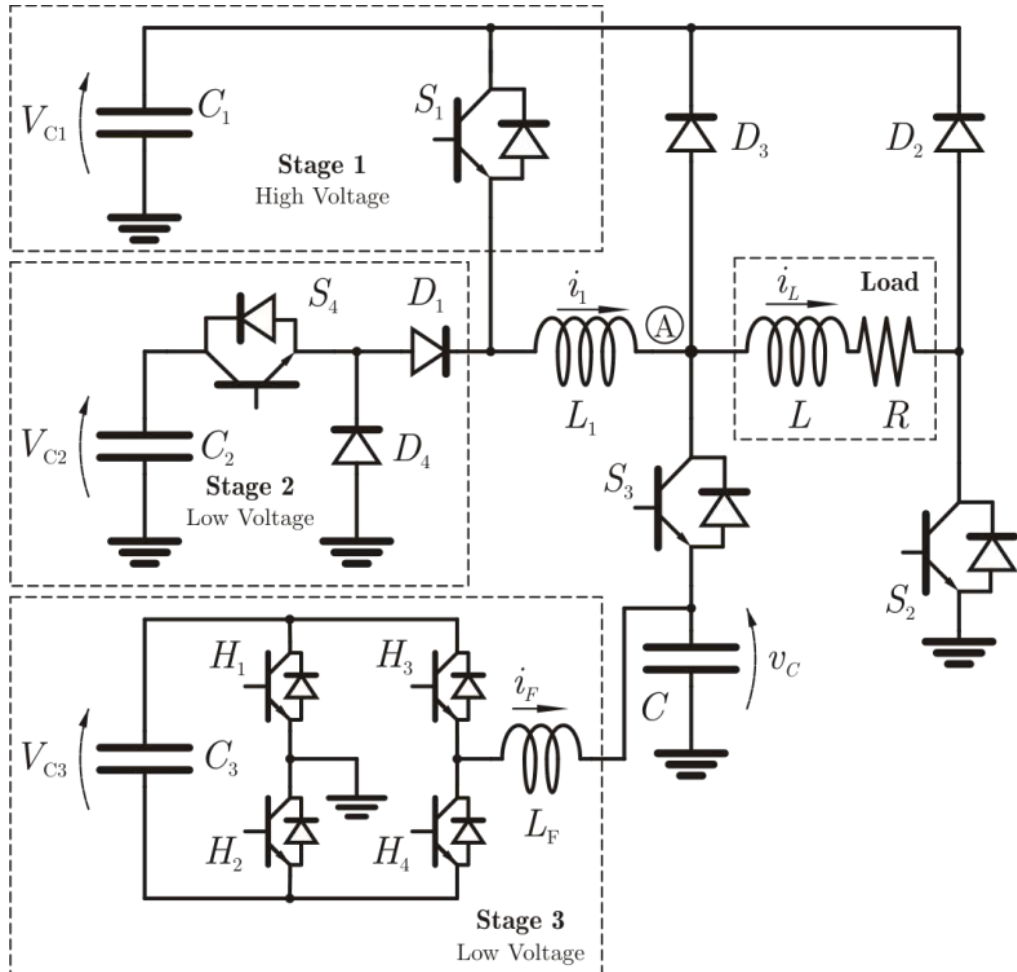


Fig. 3.98: Megadiscap power converter topology

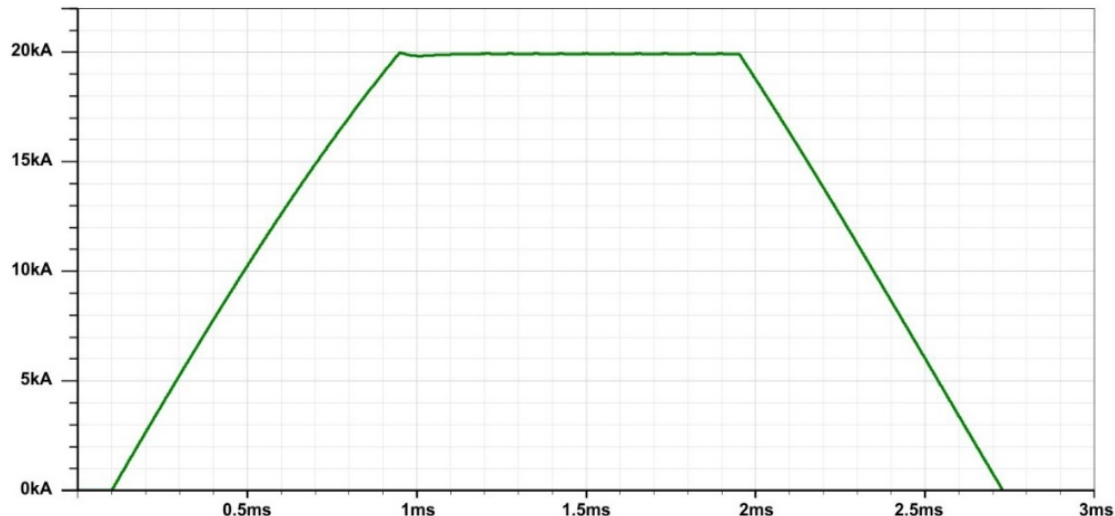


Fig. 3.99: Septum magnet current

Three operational power converters and one spare have been installed in their definitive location during the LS1 shutdown (2014). However the associated new transformers and cables will not be installed until the next long shutdown (LS2) (Fig. 3.100).



Fig. 3.100: Megadiscap power converter

Once the new SMV converters enter into service, the old SMV converters, including a spare system, can be removed. In addition, the BI.SMH converter is no longer required and will also be removed.

BI[1,2,4].BVT

The vertical dipole magnet in the BI line is currently operated in DC with all coils powered in series. The magnet will be upgraded using a similar design but capable of operating for 160 MeV H⁻. Each aperture will however be powered individually. The magnet design report can be found at EDMS 1188530. See Table 3.35.

Table 3.35: Specification parameters for the vertical dipole (BI.BVT) power converters

Parameter	Value
Peak current	450 A
Operating mode	DC
Load inductance	12 mH
Load resistance (without cables)	56 mΩ
Precision (uncertainty)	200 ppm (2×10^{-4}) of nominal
Mechanical dimensions	One rack

Several technical solutions are possible for the powering of these magnets. The preferred solution is to use power converters as designed for the LHC and used principally at LHC points 3 and

7. These converters are capable of delivering [± 600 A, ± 40 V] and require water cooling (Figs. 3.101 and 3.102).

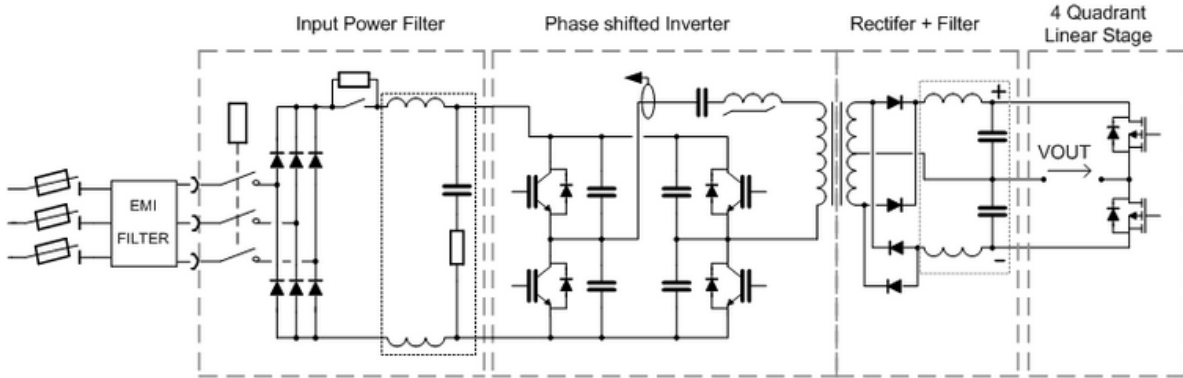


Fig. 3.101: Topology of the [± 600 A, ± 40 V] power converter



Fig. 3.102: [± 600 A, ± 40 V] power converter

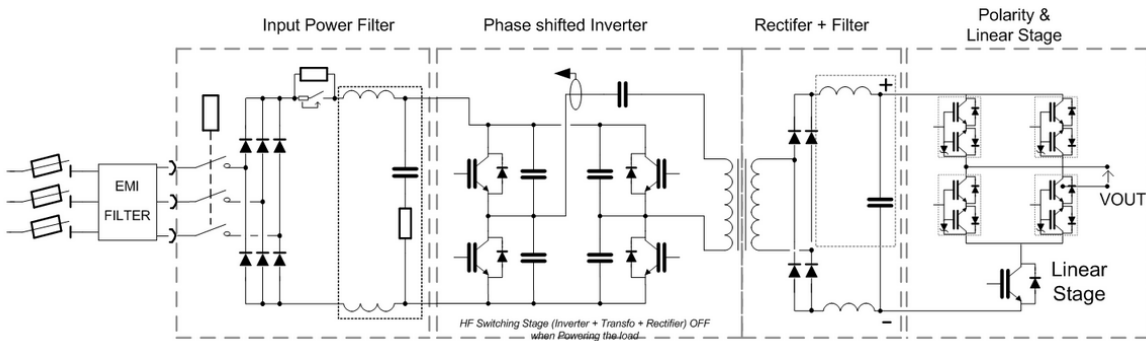
The existing power converter for the BI.BVT will be removed during LS2. For the three power converters and one spare, a total of four racks are required.

BI[1,2,3,4].DHZ[50, 70], BI[1,2,3,4].DVT[50, 70]

The horizontal and vertical corrector magnets for the injection region will require replacement to meet the constraints of the new injection scheme. The new magnets will require a higher operating current that exceeds the maximum current of the installed power converters, and thus new systems must be specified. The new magnet design has been made to ensure compatibility with the Linac4 pulsed corrector power system, where a Mididiscap power converter system is used (Figs. 3.103 and 3.104). The magnet design report can be found in [54]. See Table 3.36.

Table 3.36: Specification parameters for the corrector magnet power converters

Parameter	Value
Peak current	35 A
Operating mode	Pulsed
Flat-top length	2 ms
Maximum repetition frequency	2 Hz
Load inductance	42 mH
Load resistance (without cables)	1.5 Ω
Precision (uncertainty)	1000 ppm (1×10^{-3}) of nominal
Mechanical dimensions	One rack per six converters

**Fig. 3.103:** Topology of the Mididiscap power converter**Fig. 3.104:** Mididiscap power converter

Further details of this power converter can be found at <http://te-epc-lpc.web.cern.ch/te-epc-lpc/converters/mididiscap/general.stm>

The existing power converter for these correctors will be removed during LS2. The new power converters will be installed in the same location. For the 16 power converters and two spares, a total of three racks are required.

3.6.1.3 New requirements for H^- operation

The new H^- injection scheme requires an orbit bump composed of four individually powered pulsed bending magnets, and this for each of the four rings. The perturbations to the optics of the circulating beam due to the collapsing of the bump will require quadrupole correction, and this has been proposed to be implemented using the Qstrips in sectors 3 and 14 of the PSB.

Injection chicane bump

A total of 16 magnets are to be powered individually in a pulsed mode to deviate the H^- beam towards the stripping foil. The H^- beam is injected at the end of the flat-top, following which the circulating beam is present during the ramp down while the bump is collapsed.

As no suitable system for the required specification is commercially available, a CERN development programme has been initiated to meet the requirements, which are summarized in Table 3.37.

Table 3.37: Specification parameters for the injection chicane bump (BSW) power converters

Parameter	Value (BSW1)	Value (BSW2, 3, 4)
Peak current	6.7 kA	3.4 kA
Operating mode	Pulsed	Pulsed
Flat-top length	2 ms max	2 ms max
Controlled ramp down time	5 ms	5 ms
Maximum repetition frequency	1.1 Hz	1.1 Hz
Load inductance	13 μ H	70 μ H (77 μ H for BSW4)
Load resistance (without cables)	3.5 m Ω	7 m Ω
Precision (uncertainty) (flat-top)	100 ppm (1×10^{-4}) of nominal	
Precision (uncertainty) (ramp-down)	1000 ppm (1×10^{-3}) of nominal	
Mechanical dimensions	Three racks per converter	

The reference current waveforms in all BSW magnets are composed of line segments and 125 Hz sinusoidal segments only. As an example, Fig. 3.105 illustrates the reference current for BSW 2, 3, and 4.

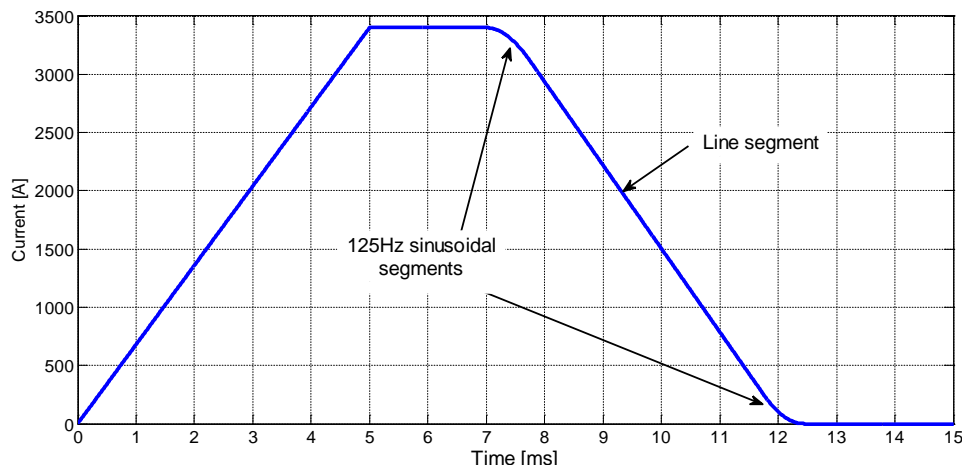


Fig. 3.105: Current ramp for BSW magnets 2, 3 and 4

The actual current will include some higher frequency content. In particular, a 20 kHz–50 kHz harmonic with \sim 50 ppm peak-to-peak amplitude will be present (ripple due to switching-based power converter).

The general simplified integration layout, for one PSB ring alone, is shown in Fig. 3.106. Four pulse transformers will be placed near the BSW1 in the PSB tunnel.

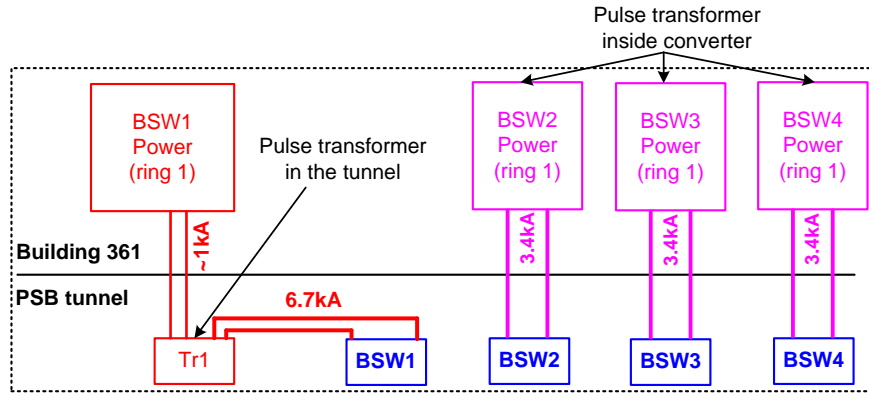


Fig. 3.106: Overview of the BSW power converter system (1 ring)

The utility voltage is rectified and energy is stored in a capacitor bank. Two parallel IGBT-based H-bridges are controlled in current (feedback control) to follow the reference (Fig. 3.107). For every pulse, the energy transferred to the magnet is recovered back to the capacitor bank. The system consumes only the power converter, cable and magnet losses.

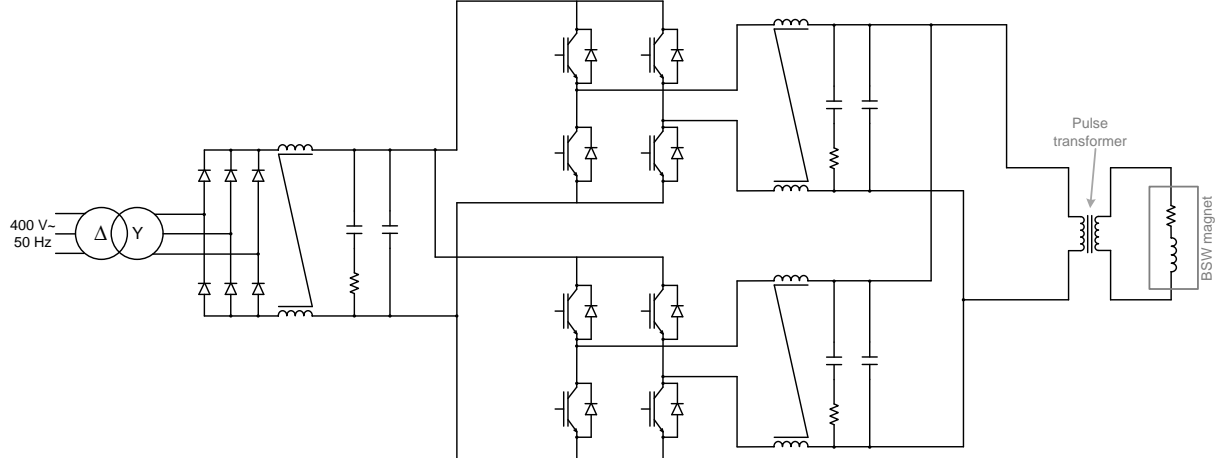


Fig. 3.107: Topology of the BSW power converter using IGBTs

There are several integration issues for these power converters. In total, 54 racks are estimated to be necessary to implement four BSW1 and one spare, and 12 BSW(2, 3, 4) and one spare. The power converters must be implemented as close as is reasonable to the magnet load to limit the maximum voltage and power delivered by the power converter to overcome resistance and cable leakage inductance. It is estimated that should the cables exceed ~ 100 m in length a different power electronics design solution will be required, with an impact on space and cost (note that the maximum cable length is strongly influenced by the final cable characteristics, which are yet to be selected, thus 100 m is provisionally given as a reasonable upper limit).

For the BSW1 magnets, the pulsed current transformers will be installed for each beam-line < 5 m from the magnet for a feasible power converter design. In addition, this will limit the area where bus bars rated for 6.7 kA current are implemented, also limiting excessive losses that must be compensated for by the power converter. Details of the transformer design constraints can be found in the paper *Pulse Transformer Design for Magnet Powering in Particle Accelerators* EDMS 1264513.

The first integration studies are focusing on the use of the Booster building 361/1-017, which is in proximity to the injection area. However, several issues remain such as the routing of cables and adequate air conditioning and/or water cooling. Studies are ongoing, including an evaluation of tunnelling new cable ducts.

Chicane optics correction with Qstrip trims.

During the chicane bump collapse, optical perturbations will be induced on the circulating beam. To compensate for this a trim of the QCD magnets (Qstrip magnets) in sectors 3 and 14 will be implemented.

Two technical solutions can be considered:

- i) A trim of the QCD circuit in sectors 3 and 14;
- ii) Individual powering of the QCD circuit in sectors 3 and 14.

For powering simplicity, a preference is given for the individual powering solution. However, as the current in each QCD magnet should be identical, from the optical design perspective a preference has been expressed for the trim solution.

The trim power converter will be capable of supporting the maximum common mode voltage available from the QCD power system, which is 70 V. The Cancun power converter is capable of delivering the required performance and supporting this common mode voltage (Fig. 3.108). See Table 3.38.



Fig. 3.108: Cancun [$\pm 50 \mu\text{A}$, $\pm 30 \mu\text{V}$] power converter

Table 3.38: Specification parameters for the chicane correction (Qstrip trim) power converters

Parameter	Value
Peak current	30 A
Operating mode	Cycled
Load inductance	62 μH
Load resistance (without cables)	15 m Ω
Precision (uncertainty)	1000 ppm (1×10^{-3}) of nominal
Mechanical dimensions	One rack for six converters

Preliminary examples of the waveform during injection for the QCD circuit and for the QCD trim are given in Fig. 3.109. The form of the trim function is also influenced by the form of the chicane ramp function.

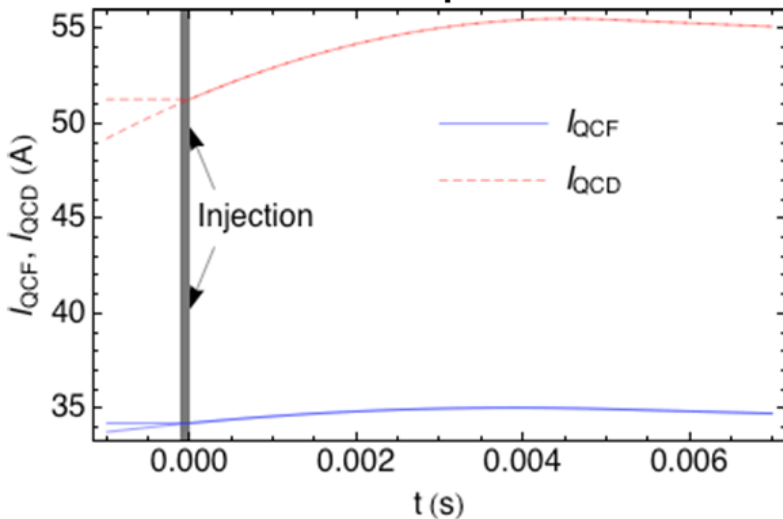


Fig. 3.109: Current waveforms for the QCD circuits during injection

Note that the definitive waveform for the QCD trim circuits in sectors 3 and 14 is not yet known. Thus the function in Fig. 3.110 is the best estimate at the time of submission for the TDR. Figure 3.111 shows the topology of the power converter for the QCD trim.

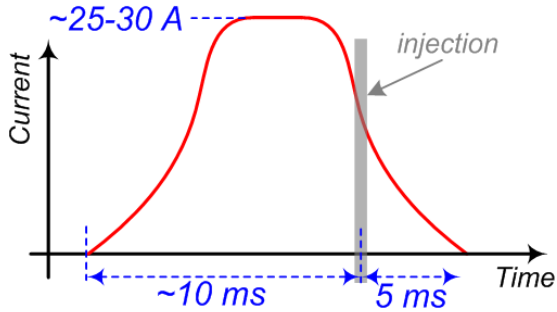


Fig. 3.110: Trim function of the QCD circuit in sectors 3 and 14

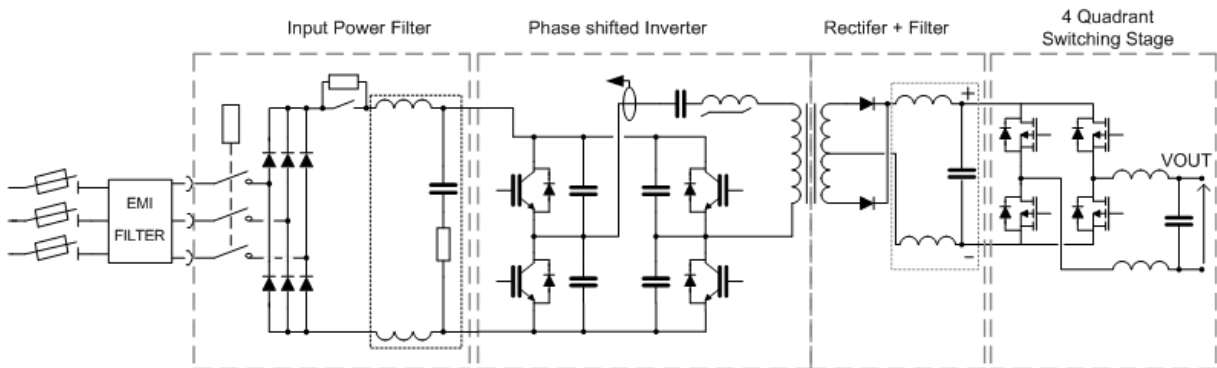


Fig. 3.111: Topology of the power converter for the QCD trim

First integration studies indicate space is available in 361/1-211. The trim solution will require three racks for eight power converters and two spares.

3.6.1.4 Consolidation

Consolidation of the magnet power converters may be initiated either due to the magnet being modified, or the power converter reaching its end-of-life. A further common reason is the update of the controls front-end, without modifying the power converter itself.

In the BI, LT and LTB transfer lines to the PSB, a majority of the existing power converters will be upgraded to the latest generation of power and control electronics. There are, however, several systems that do not require modification for operation with 160 MeV H⁻ particles, but will require to be modified for the reasons mentioned above.

As such, subject to financial and personnel resources, all remaining circuits not required to be modified for 160 MeV H⁻ operation will be consolidated in line with the magnet consolidation programme, and to ensure that all systems from Linac4 to the PSB will use the latest generation of control electronics.

The following sections describe the updates that are under consideration.

BI.QNO[10,20,30,40], BI[1,2,3,4].QNO[50, 60]

The magnets are of a solid yoke construction and therefore cannot be cycled, as such it is proposed to consolidate them with pulsed air-cooled magnets thus reducing power consumption and heat losses. The power converter, which is currently DC, must also be replaced.

In total, 12 power converters will be replaced with Maxidiscap capacitor discharge systems to ensure that all quads in these transfer lines are using the same power and control technology. See Table 3.39.

Table 3.39: Specification parameters for the consolidation of the BI line Quadrupole (QNO [10, 20, 30, 40, 50, 60]) power converters.

Parameter	Value
Peak current	95 A
Operating mode	Pulsed
Flat-top length	2 ms max
Maximum repetition frequency	2 Hz
Load inductance	32 mH
Load resistance (without cables)	0.5 Ω
Precision (uncertainty)	1000 ppm (1×10^{-3}) of nominal
Mechanical dimensions	One rack per three converters

Integration would be in the same rack space as for the existing quadrupole circuits. In principle the same DC cables can be reused, subject to an audit of their condition.

BI.DHZ[10,20,30,40], BI.DVT[10, 20, 30, 40]

To harmonize the power converter and control electronics for the corrector magnets in the BI transfer line, a total of eight corrector power converters will need to be replaced. The Mididiscap capacitor discharge power converter is used for all other steerers in this area and is the most appropriate technical solution. See Table 3.40.

Table 3.40: Specification parameters for the consolidation of the BI line Steerer (DHZ and DVT [10, 20, 30, 40]) power converters.

Parameter	Value
Peak current	25 A
Operating mode	Pulsed
Flat-top length	2 ms max
Maximum repetition frequency	2 Hz
Precision (uncertainty)	1000 ppm (1×10^{-3}) of nominal
Mechanical dimensions	One rack per six converters

Integration would be in the same rack space as for the existing steerer circuits. In principle the same DC cables can be reused, subject to an audit of their condition.

Circuits of the LT and LTB transfer lines

The following systems will be consolidated in the PSB–Linac4 transfer lines (LT and LTB lines) and are included for reference as these transfer lines are considered to be under the management of the Linac4 project. See Table 3.41

Table 3.41: Specification parameters for the consolidation of the LT.BHZ20, LT.BHZ30 and LTB.BHZ40 bending power converters.

Parameter	BHZ20, BHZ30	BHZ40
Peak current	561 A	174 A
Operating mode	Cycled	Cycled
Flat-top length	150 ms	150 ms
Maximum repetition frequency	1.1 Hz	1.1 Hz
Load inductance	95 mH	70 mH
Load resistance (without cables)	62 mΩ	43 mΩ
Precision (uncertainty)	100 ppm (1×10^{-4}) of nominal	
Mechanical dimensions	Three racks per converter	Two racks per converter

Bending magnets of the LT and LTB lines

The systems will be in operation from 2015 in building 355. It is proposed to move them to building 363 during LS2 to regroup all powering for the LT and LTB lines in the same building, which is also closer to the magnet.

Steerers of the LT and LTB lines

Affected circuits: LT.DHZ[40, 50], LT.DVT[40, 50], LTB.DHZ[10, 20, 30, 40], LTB, DVT[10, 20, 30, 40].

In total 12 power converters will be replaced to ensure all correctors in these transfer lines are using the same power and controls technology. The Mididiscap capacitor discharge power converter is used for all other steerers in this area and would be the most appropriate technical solution. See Table 3.42.

Table 3.42: Specification parameters for the consolidation of the LT line Steerer (DHZ and DVT [40, 50]) and LTB line Steerer (DHZ and DVT [10, 20, 30, 40]) power converters.

Parameter	Value
Peak current	25 A
Operating mode	Pulsed
Flat-top length	2 ms max
Maximum repetition frequency	2 Hz
Precision (uncertainty)	1000 ppm (1×10^{-3}) of nominal
Mechanical dimensions	One rack per six converters

Integration would be in the same rack space as for the existing steerer circuits.

QFN and QDN Quads of the LT and LTB lines

Affected circuits: LT.QDN[55, 75], LT.QFN[50, 60s], LTB.QFN10, LTB.QDN20

The existing power converters are reaching their end-of-life. In total, six power converters will be replaced with Maxidiscap capacitor discharge systems to ensure that all quads in these transfer lines are using the same power and controls technology. See Table 3.43.

Table 3.43: Specification parameters for the consolidation of the LT line Quadrupoles (QDN[55, 75], QFN[50, 60]) and LTB line Quadrupoles (QFN10, QDN20) power converters.

Parameter	Value
Peak current	200 A
Operating mode	Pulsed
Flat-top length	2 ms max
Maximum repetition frequency	2 Hz
Precision (uncertainty)	1000 ppm (1×10^{-3}) of nominal
Mechanical dimensions	One rack per three converters

It is noted that a recent optical study requested LT.QDN65 and LT.QFN.60 with different currents. These are actually cabled in series on the same power converter; thus if this request is maintained a new power converter and associated cabling will be required, bringing the total to seven new systems.

Integration would be in the same rack space as for the existing quad circuits, with perhaps an additional rack should the new circuit be integrated.

QFW and QDW Quads of the LT and LTB lines

Affected circuits: LT.QFW[70], LTB.QFW[30, 50], LTB.QDW[40, 60].

The magnets are of a solid yoke construction and therefore cannot be cycled; as such it is proposed to consolidate them with pulsed air-cooled magnets thus reducing power consumption and heat losses. The power converter, which is currently DC, must also be replaced.

In total, five power converters will be replaced with Maxidiscap capacitor discharge systems to ensure all quads in these transfer lines are using the same power and controls technology. See Table 3.44.

Table 3.44: Specification parameters for the consolidation of the LT line Quadrupoles (QFW70) and LTB line Quadrupoles (QFW[30, 50] and QDW[40, 60]) power converters.

Parameter	Value
Peak current	95 A
Operating mode	Pulsed
Flat-top length	2 ms max
Maximum repetition frequency	2 Hz
Precision (uncertainty)	1000 ppm (1×10^{-3}) of nominal
Mechanical dimensions	One rack per three converters

3.6.2 Main power supply

3.6.2.1 Introduction

The Proton Synchrotron (PS) Booster, is the smallest circular proton accelerator in the accelerator chain at the CERN Large Hadron Collider injection complex. The accelerator was constructed in 1972 and it is composed of four superimposed rings (synchrotrons) with a radius of 25 m.

The accelerator takes protons with an energy of 50 MeV from the linear accelerator Linac2 and accelerates them up to 1.4 GeV, ready to be injected into the Proton Synchrotron. The PS Booster is controlled with a pulse modulation with 1.2 s cycle length (repetition time of 1.2 s).

In the frame of the LIU project the particle energy in the Booster ring will be increased from the current 1.4 GeV to 2 GeV. This increase in energy is accompanied by an equal increase in the power requested by the main power converters. One of the main constraints of the project is to get the desired increase in particle energy with the lowest possible increase in rms current for the magnets.

This is the reason why the voltage across the magnet must be increased, enabling higher peak currents with faster acceleration.

As the increase in power and voltage could not be satisfied with the old power converters, it was decided to build a new, more powerful one.

3.6.2.2 PS Booster magnets

The PS Booster accelerator contains 264 magnets of 15 different types distributed along a central orbit length of 50π metres (~157 metres). The PS Booster magnets are divided into 16 sections as shown in Fig. 3.112.

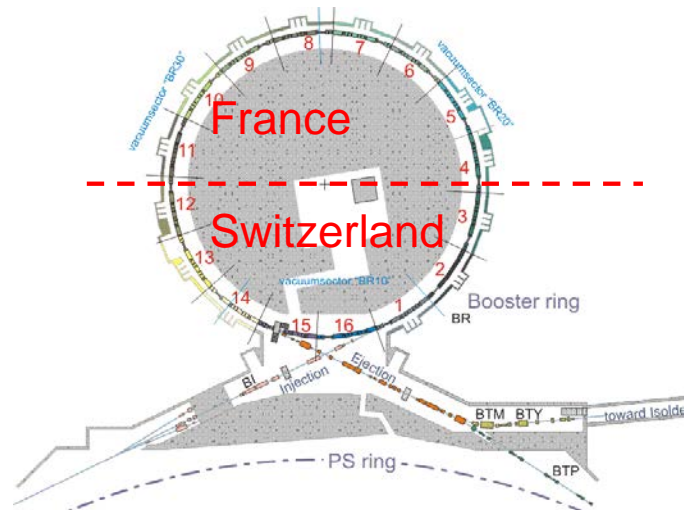


Fig. 3.112: PS Booster sections

The PS Booster is composed of total of 32 dipole magnets (192 mH) and total of 48 quadrupole magnets (8.8 mH). For every section there are two dipole magnets, two quadrupole focusing and one quadrupole defocusing magnets (see Table 3.45).

Table 3.45: PS Booster dipole and quadrupole magnet parameters

Magnet	Quantity	Single resistance (mΩ)	Single inductance (mH)	Total resistance (mΩ)	Total inductance (mH)
Dipoles normal configuration	30 + 1 ref	9.8	6	304	186
Dipoles special configuration	2	22.8	6	45.6	12
Quadrupole F	32	2.4	0.24	76.8	7.7
Quadrupole D	16	3.3	0.56	52.8	8.96

Pictures of the Booster dipole and quadrupole magnets are given in Fig. 3.113. Each of the dipole magnets consists of four parallel paths (rings) denoted 1 to 4. The four rings are presently connected in series as shown in Fig. 3.114.

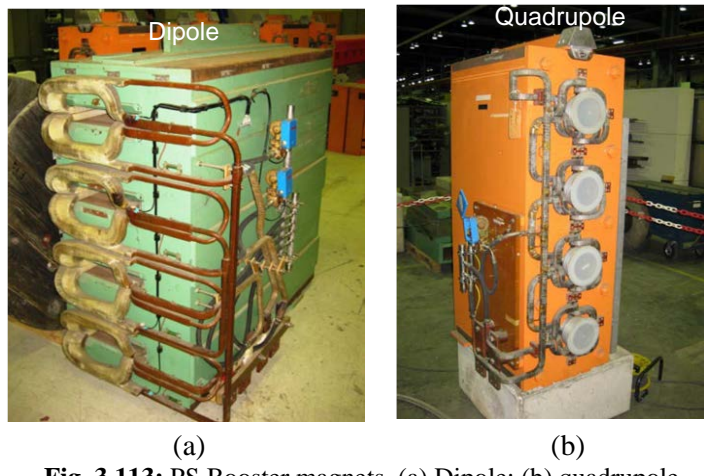


Fig. 3.113: PS Booster magnets. (a) Dipole; (b) quadrupole

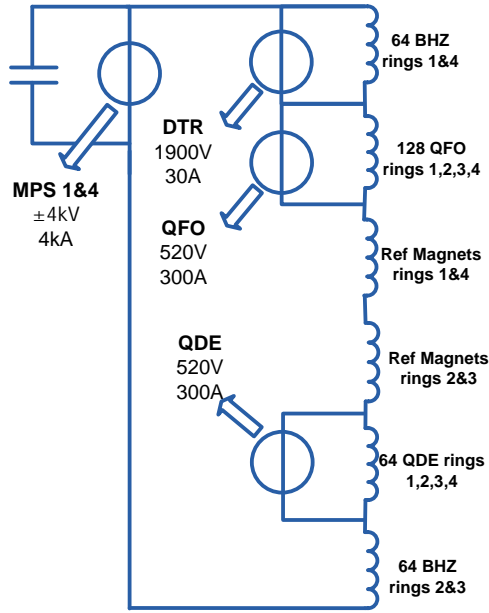


Fig. 3.114: Existing Booster magnet supply configuration

3.6.2.3 PS Booster magnets for the 2 GeV upgrade: a new connection

For the increase in beam energy to 2 GeV, a new configuration will be realized, where all dipoles and quadrupoles magnets are grouped following the schematic in Fig. 3.115. The outer rings of dipoles are connected in series together with the QFO magnets, while the inner dipole windings are connected with the QDE.

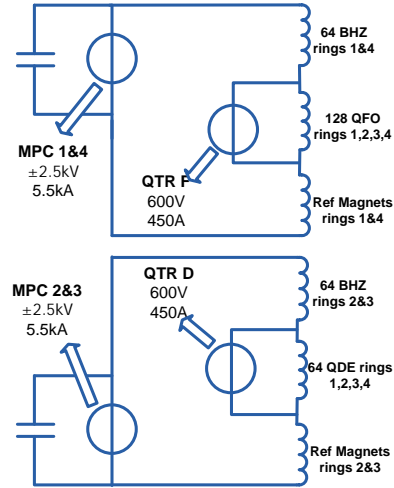


Fig. 3.115: Booster magnets and electrical connections

This way the field in the outer rings can be regulated without additional power converters.

Trims are only required to adjust the current in the quadrupoles.

Due to the new magnet connections the equivalent electrical parameters used for the dimensioning of each power converter are as reported in Fig. 3.116.

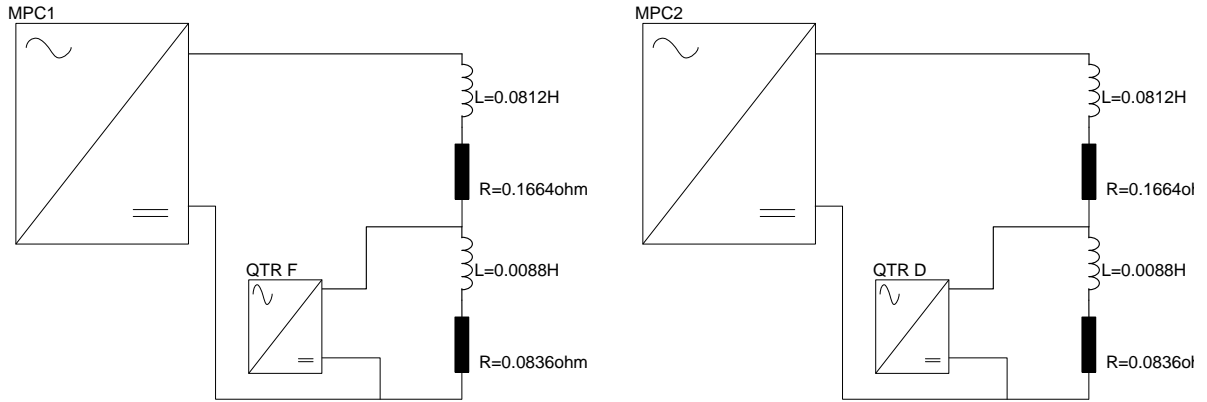


Fig. 3.116: Magnet electrical parameters used for converter dimensioning

The total impedance of the dipole and quadrupole magnets together is $L_{mag_{tot}} = 0.18 \text{ H}$, $R_{mag_{tot}} = 0.5 \Omega$.

Since the magnets will be reconnected on two separate strings, the parameters to be used for converter dimensioning are $L_{mag_{half}} = 0.09 \text{ H}$, $R_{mag_{half}} = 0.35 \Omega$.

For dimensioning of the trim converters, we use the quadrupole magnets impedance $L_{mag_{Qf/d}} = 0.0088 \text{ H}$, $R_{mag_{Qf/d}} = 0.0836 \Omega$.

As a result of the new magnet connections, it is possible to increase the maximum voltage generated by the MPS without surpassing the limiting voltage value of 4.6 kV [97] applied with respect to ground.

The peak output voltage for each magnet string is fixed to $V_{mag_{pk}} = \pm 2500 \text{ V}$

PROTON SYNCHROTRON BOOSTER

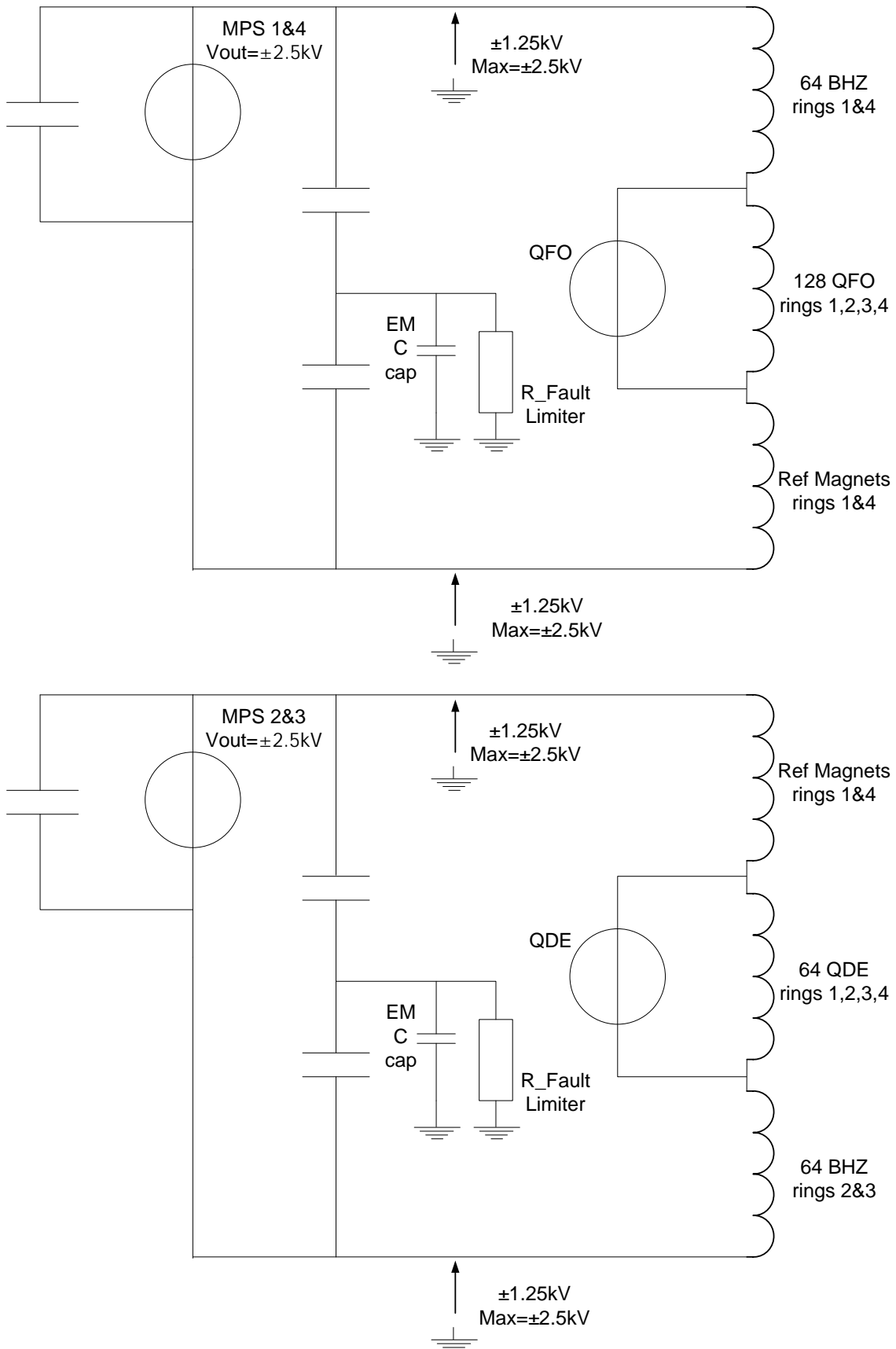


Fig. 3.117: MPS ground reference points

Given that the MPC converters will be grounded on the middle point of the output filter, the maximum low frequency value of the voltage to ground will be $V_{\text{earth max}} = \pm 1250 \text{ V}$

PSB cycle and main parameters

The PSB is characterized by a single magnetic cycle with a repetition rate of 1.2 s. The new target particle energy of 2 GeV will require a peak current of 5.2 kA on the magnets. The magnets limit the increase in rms due to cooling constraints; therefore the only solution is to increase the di/dt (i.e. the voltage) of the cycle. With a reference value of 5 kV_{pk} ($2 \times 2.5 \text{ kV}$) and taking into account the different limitations of the accelerator, the resulting cycle is reported in Fig. 3.118.

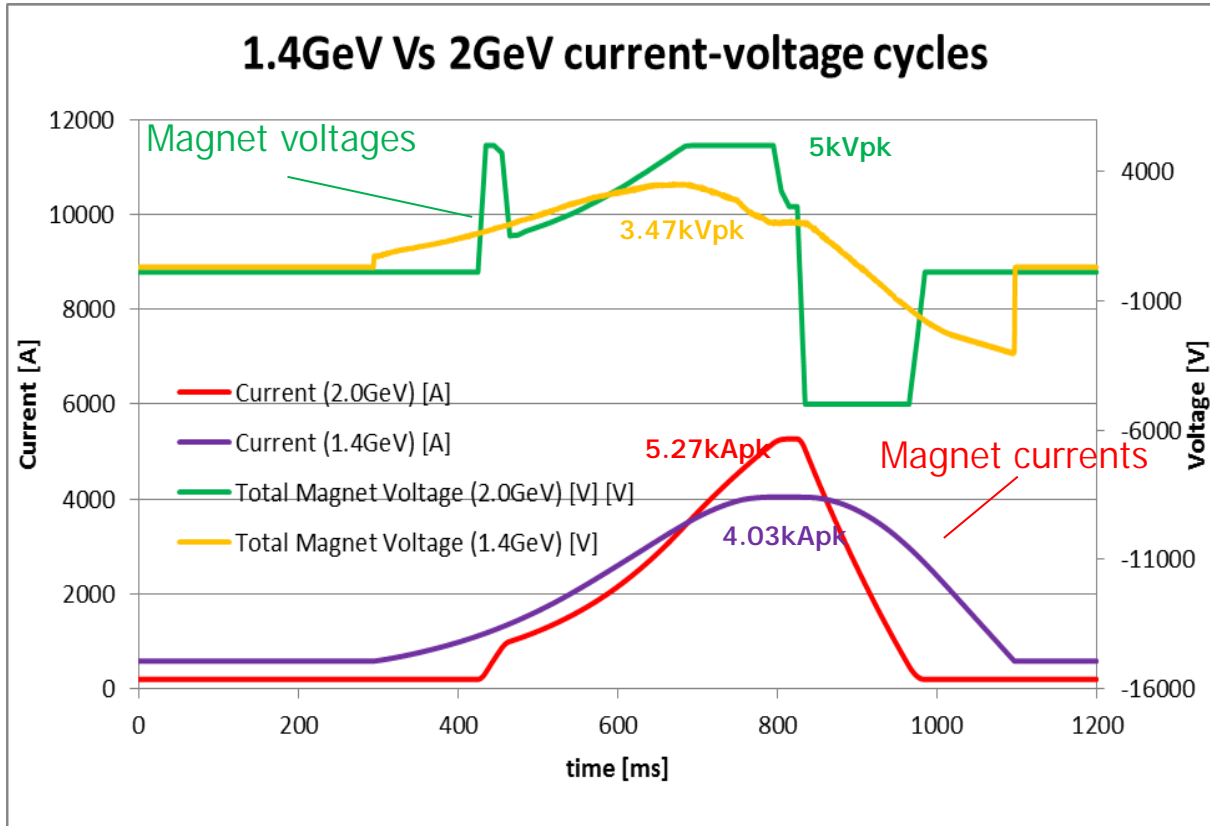


Fig. 3.118: 1.4 GeV vs. 2 GeV cycles: current and voltage

$$\Delta V_{\text{pk_Magnets}} = +40\%$$

$$\Delta I_{\text{pk_Magnets}} = +30\%$$

$$\Delta I_{\text{rms_Magnets}} = +10\%$$

Table 3.46 shows the main parameters of the 2 GeV and 1.4 GeV cycles together with the limiting values for the power converters.

Table 3.46: Main parameters of the new and present MPS

	New MPS (2 GeV)	Present MPS (1.4 GeV)
Cycle repetition	1.2 s	1.2 s
B field at injection	0.23 T	0.12 T
Kinetic energy at injection	160 MeV/c	50 MeV/c
Magnet current at injection	1080 A	580 A
B field at extraction flat top	1.13 T	0.86 T
Flat-top duration	20 ms	45 ms
Kinetic energy at extraction flat-top	2 GeV/c	1.4 GeV/c
Magnet current at extraction flat-top	5.3 kA	4 kA
Cycle rms current	2.49 kA	2.25 kA
Maximum cycle voltage at 2 GeV/1.4 GeV	± 5 kV (2×2.5 kV)	+3.47 kV – 3 kV
Number of cycles per year	10^7	10^7
Maximum power converters current	6 kA	4.5 kA
RMS power converter current	3 kA	2.3 kA
Maximum converter voltage	± 5.5 kV (2×2.75 kV)	+4.1 kV – 3.7 kV
Magnet stored energy	2.53 MJ	1.44 MJ
Peak power at the magnet terminals	26.5 MW	13.9 MW
Maximum apparent power on the 18 kV mains	3.5 MVA	15.2 MVA
Maximum active power on the 18 kV mains	3.5 MW	12.5 MW
Maximum reactive power on the 18 kV mains	0 MVar	14.7 MVar
Magnetic field ripple peak to peak	0.2 mT	0.2 mT
Maximum voltage ripple peak to peak	2.5 V _{rms} (on the single magnet string)	3.2 V _{rms}
Regulation	B field	

3.6.2.4 Present MPS configuration

The system was put into operation in 1982 and the transformers were renovated in 1996.

The MPS is composed of one main power converter (MPC) three quadrupole trims (QTR) and two dipole trims (DTR).

The main power converter

The present MPC (Fig. 3.119) is made up of four 12-pulse thyristor rectifiers directly coupled to the network and connected in series on the DC side plus one more as a spare.

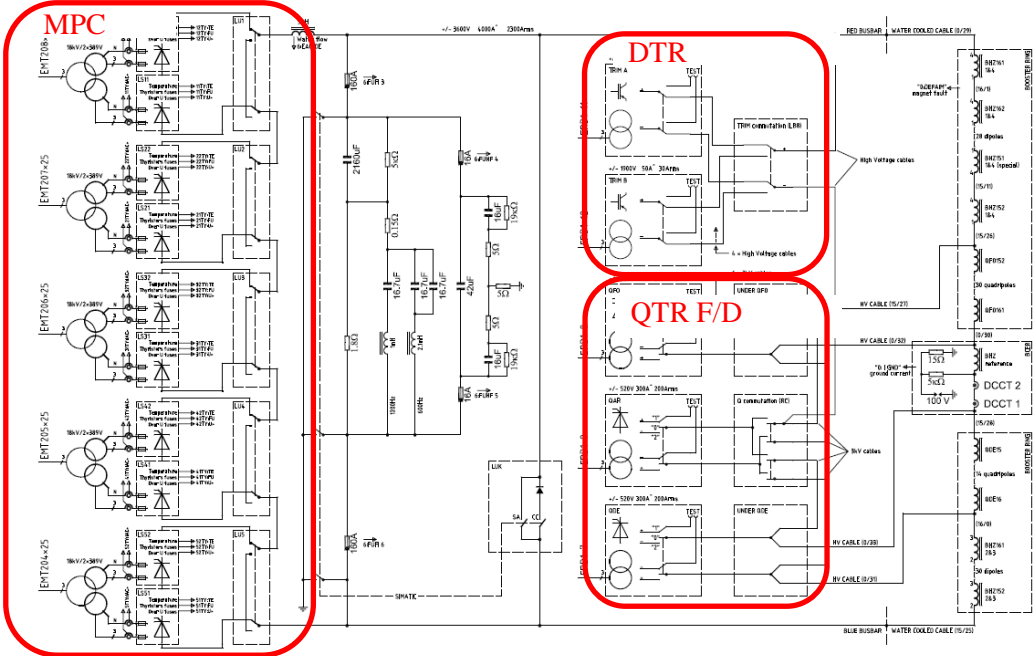


Fig. 3.119: Present Booster MPS: electrical scheme

Each of the thyristor groups is supplied by a three-windings transformer 18 kV/2 × 389 V.

Due to its thyristor structure, the present MPS takes all active power (instantaneously) from the AC network and as a consequence of the operation with low voltage and high current (i.e. during the flat-top) it requires a lot of reactive power.

Figure 3.120 shows that a peak of 12.5 MW and 14.7 MVar are required during a typical Booster cycle. Operation of the MPC requires a dedicated static Var compensator (SVC) located at the Meyrin site.

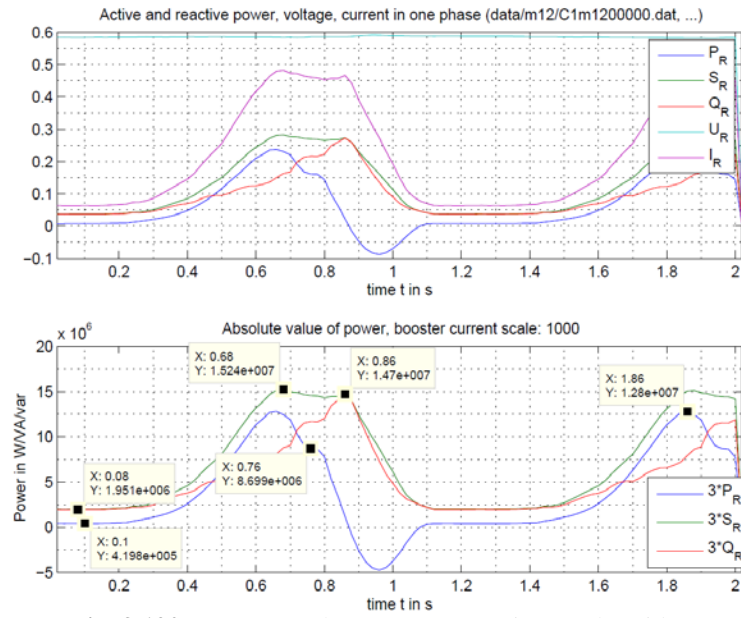


Fig. 3.120: Present total power consumption (18 kV side)

The trim converters

The present MPS is characterized by the presence of two QTR plus one as spare and one DTR plus one as spare.

The quadrupole trims converters

The present configuration is based on a thyristor rectifier bridge with an active filter on the DC side to improve ripple voltage performance (see Fig. 3.121 and Table 3.47).

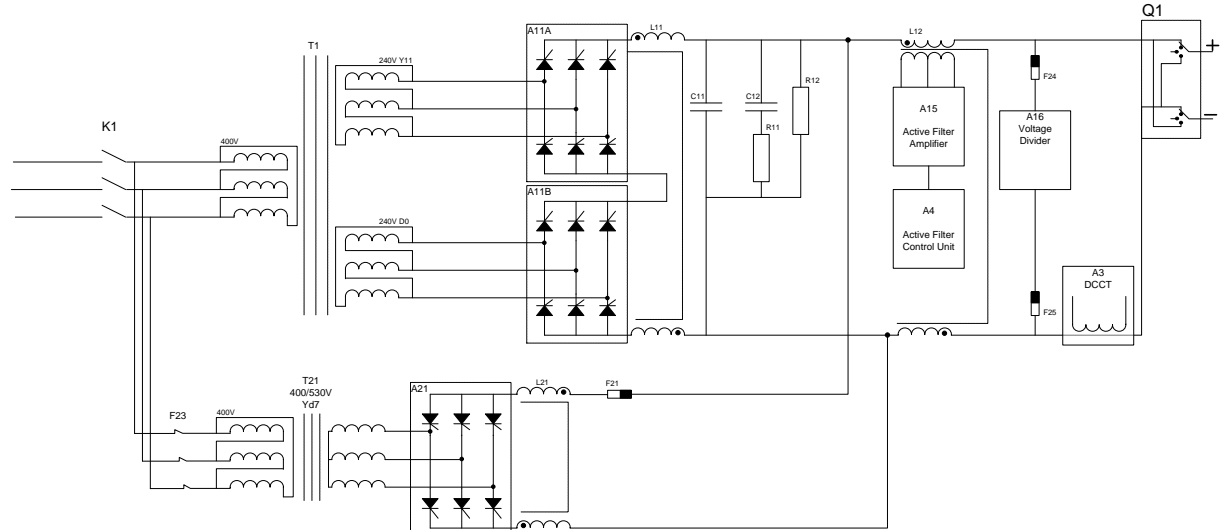


Fig. 3.121: Present QTR schematic

Table 3.47: Main parameters of the present QTR converter

Converter values		
I_{pkDC}	± 300 A	Peak current of the converter (DC side)
V_{pkDC}	± 350 V	Peak voltage of the converter (DC side)

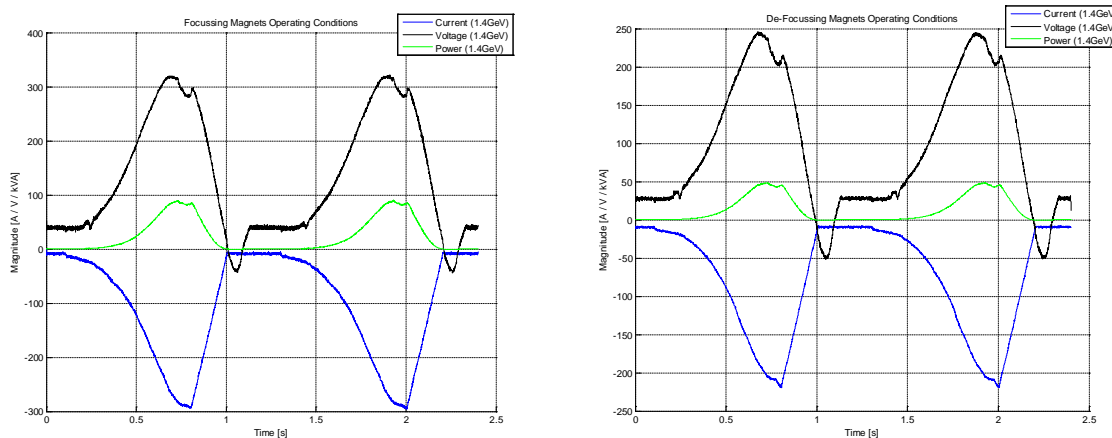


Fig. 3.122: (a) Focusing and (b) defocusing converter power operating characteristics

The dipole trims converters

The present DTR converter is realized with 4 H IGBT bridges connected in series as showed in Fig. 3.123. One of these units is connected to windings 1–4 of the dipole magnets and a second one is kept as a spare. See Table 3.48.

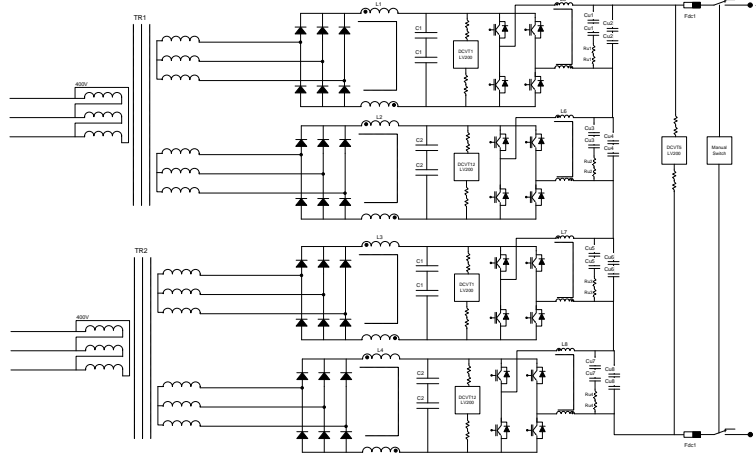


Fig. 3.123: Present DTR converter schematic

The goal of the dipole trims is to compensate for the difference between the inner and outer magnetic circuits by injecting a small current into the external windings (1 and 4).

Table 3.48: Main parameters of the present DTR converter

Converter values		
I_{pkDC}	30 A	Peak current of the converter (DC side)
V_{pkDC}	± 1900 V	Peak voltage of the converter (DC side)

Following the new magnet connection the DTR converter will not be required for the Booster 2GeV MPS.

3.6.2.5 Booster 2GeV MPS configuration

Given the re-configuration of magnet connections, the new MPS will be realized following the schematic shown in Fig. 3.124.

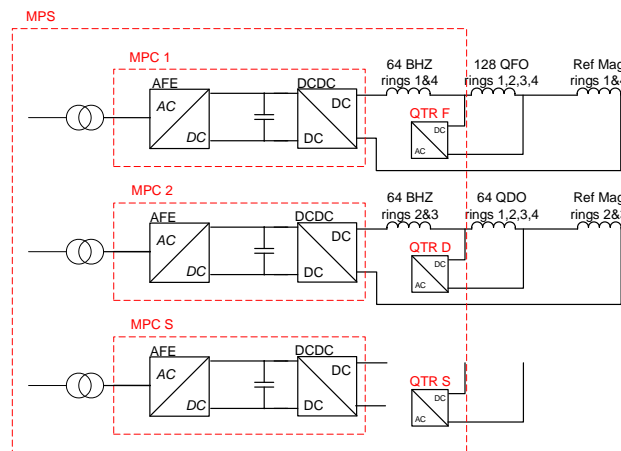


Fig. 3.124: New MPS configuration

The MPS comprises three identical sets of power converters. Two are used to supply the magnet strings and one is kept as a spare (Fig. 3.125). The MPC block is based on medium voltage drive technology, while the QTR is a low-voltage power converter.

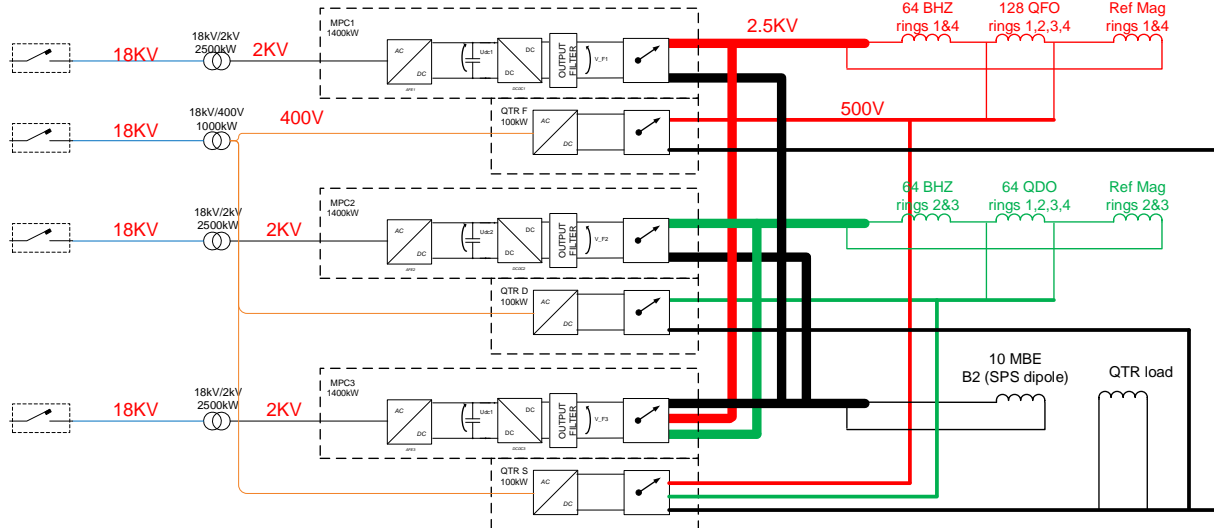


Fig. 3.125: New MPS schematic diagram

Each converter is equipped with an output switch that will allow it to be connected to the Booster magnets or to the test load for testing.

The spare converter will be able to connect to both Booster magnet strings and to the test load.

The main feature of the new MPS is the ability (of the MPC converter) to decouple the instantaneous load power from that taken from the network, via energy storage. The power taken from the AC network can therefore be limited to a maximum constant level much smaller than the peak, while the storage capacitor bank (the energy storage) takes the difference.

In addition, the MPC is equipped with an active front end (AC/DC active rectifier) that is able to control the input power factor to 1, thus eliminating the need for an SVC (Fig. 3.126).

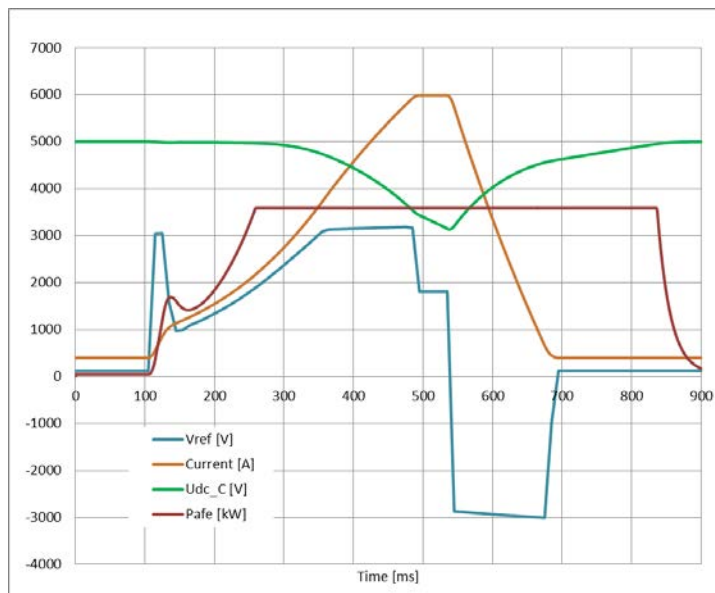


Fig. 3.126: AC power behaviour during a 900 ms Booster cycle

The Booster 2GeV main power converter

The new MPC will be based on IGBT/IGCT technology and 3Level configuration, and will use storage capacitors in order to decouple the load from the network. The front end with the AC network will be based on the same technology as the DCDC converter (Fig. 3.127). The DCDC converter will be realized with parallel branches for both the positive and negative legs with interleaving in order to increase the frequency of the ripple on the output voltage.

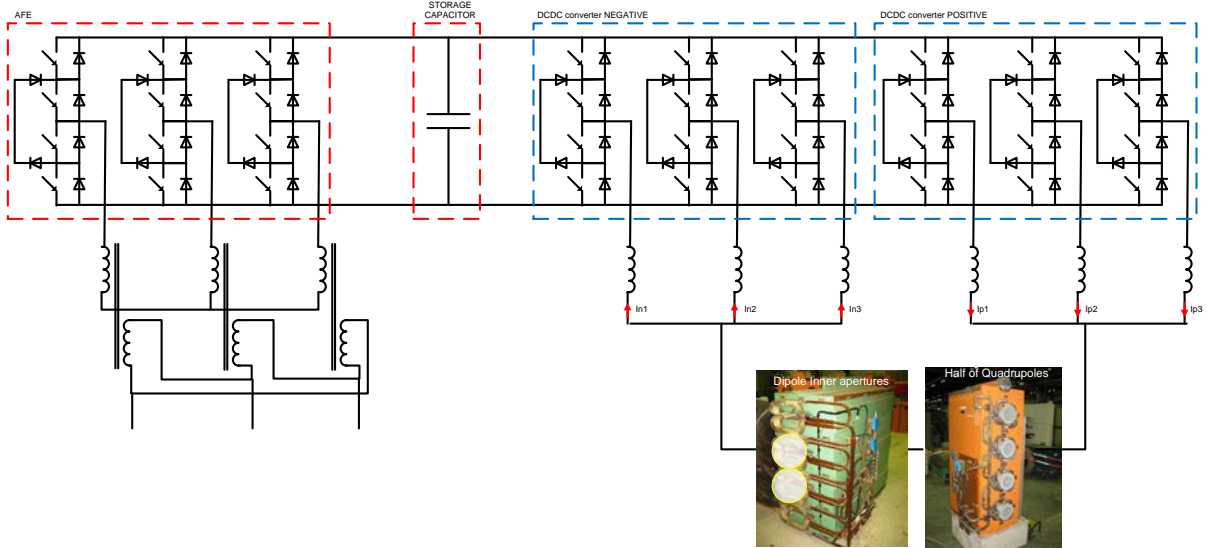


Fig. 3.127: IGBT based rectifier and DCDC converter

The front end with the AC network is an active one based on IGBT and it is only capable of absorbing active power from the network while generating sinusoidal currents.

Compensation of reactive power is therefore no longer needed.

The working principle is very similar to that of the POPS converter with the difference that in the Booster case there will not be floating converters and a much simpler structure will be required.

The Booster 2GeV quadrupole trim converter

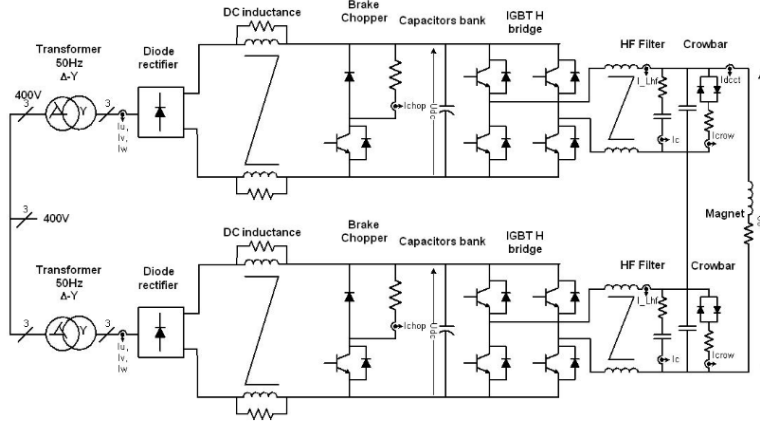
The quadrupole trim converters are inspired by the APOLO configuration (Fig. 3.128, Table 3.49).

For the main brick (APOLO), a 50 Hz transformer (galvanic isolation–voltage adaptation–phase shift), a diode rectifier and a DC-link filter are used for AC/DC conversion. An IGBT bridge (four quadrant operation) with an output filter is used for DC/DC conversion. The energy of the magnet is:

- recovered in a capacitor bank on the DC link during cycling mode of operation;
- dissipated in a brake chopper when energy storage is too low on the DC-link;
- dissipated in a bipolar crowbar in the event of a fault.

PROTON SYNCHROTRON BOOSTER

Two modules APOLO are assembled in series to increase the voltage capability (APOLO_2s):



APOLO_2s topology .vsd

Fig. 3.128: APOLO 2s (two series) topology

Table 3.49: APOLO power converter characteristics

Family name Configuration	APOLO – Auxiliary Power supply fOr the PS			
	Main brick	Parallel configuration	Serial configuration	Parallel configuration
HCR code	APOLO	APOLO_2p	APOLO_2s	APOLO_4p
V_out	HCRPADF	HCRPADG	HCRPADH	HCRPADI
I_out	450 V	450 V	900 V	450 V
	200 Arms/	400 Arms/	200 Arms/	800 Arms/
	450 Apeak	900 Apeak	450 Apeak	1800 Apeak
Power in	3×400 V / 50 Hz – 160 Arms	3×400 V / 50Hz – 320 Arms	3×400 V / 50 Hz – 320 Arms	3×400 V / 50 Hz – 640 Arms
Load conditions	1...100 mH 10 mΩ...0.48 Ω	1...100 mH 10 mΩ...0.24 Ω	1...100 mH 10 mΩ...0.96 Ω	1...100 mH 10 mΩ...0.96 Ω
Dimensions	Height: 2300 mm Width: 1800 mm Depth: 900 mm Weight: 1100 kg	Height: 2300 mm Width: 1800 mm Depth: 900 mm Weight: 1700 kg	Height: 2300 mm Width: 1800 mm Depth: 900 mm Weight: 1700 kg	Height: 2300 mm Width: 3200 mm Depth: 900 mm Weight: 3200 kg
Type	4 quadrants – switch mode power converter $F_{SW} = 6.5 \text{ kHz}$			
Application	Modulation: 2LF _{SW} (two level) or 3L2F _{SW} (three level with frequency doubling) This power converter is used in experimental areas, injector machines and test benches to power warm magnets, for DC or pulse applications			
Control type	RegFGC3 Crate Type 10 / Ethernet			
Precision performances	Current accuracy (one year): 100 ppm Current reproducibility (one day): 20ppm Current stability (1/2 hour): 20 ppm Current resolution: 16 bits			
Voltage ripple	xx mV _{rms} at $f = 20 \text{ Hz}-1 \text{ kHz}$ xx mV _{rms} at $f = 1 \text{ kHz}-150 \text{ kHz}$ xx mV _{rms} at $f = 150 \text{ kHz}-5 \text{ MHz}$			
General design	Altitude above sea-level: 300...600 m Operating ambient temperature: 0...+30°C Storage temperature: -25...+50°C			

Cooling	Relative humidity: 30...85% @30°C
	Pollution degree: II according to IEC 62103
	Overvoltage category: II according to IEC 62103
	Isolation level (to ground): 3 kVAC RMS (50Hz, 1 min)
	Water Forced (WF)
	<u>Losses</u>
	APOLO : 3100 W_Air / 2900 W_water_12 L/min
	APOLO_2p : 6200 W_Air / 5800 W_water_24 L/min
	APOLO_2s : 6200 W_Air / 5800 W_water_24 L/min
	APOLO_4p : 12400 W_Air / 11 600 W_water_58 L/min

In the case of the Booster 2GeV QTR, a higher insulation is required with respect to earth, therefore a special installation will be needed.

3.6.2.6 Booster 2GeV MPC: dimensioning criteria

The new target particle energy of 2 GeV will require a peak current of 5.2 kA on the magnets. As the magnets limit the increase in rms due to cooling constraints, the accelerating cycle is made faster. With a reference value of 2.5 kVpk and taking into account the limitation of the RF, the resulting cycle is reported in Fig. 3.129.

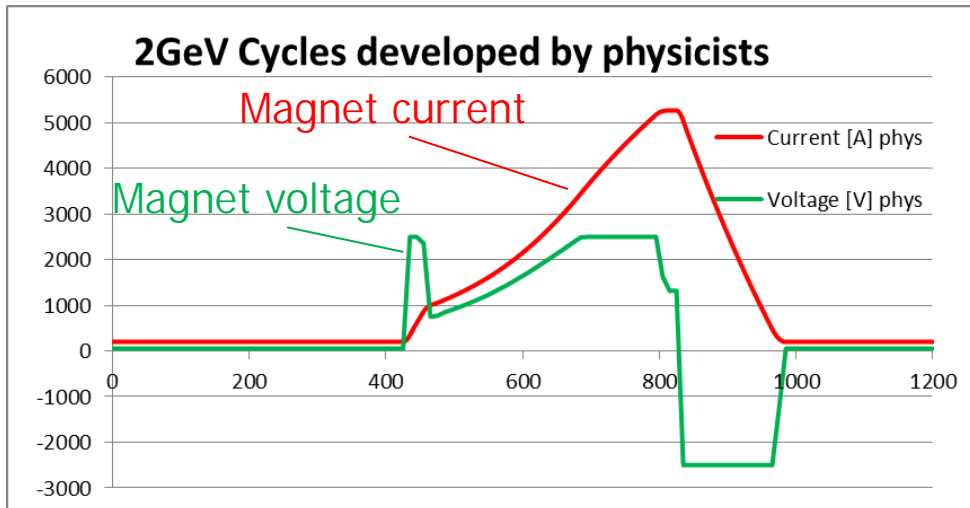
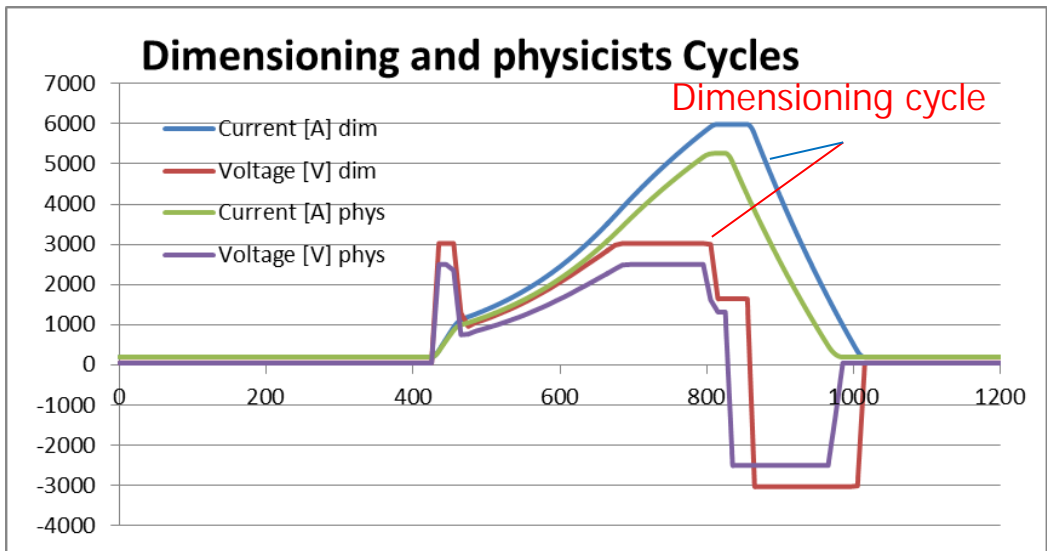


Fig. 3.129: Design of the new 2 GeV cycle

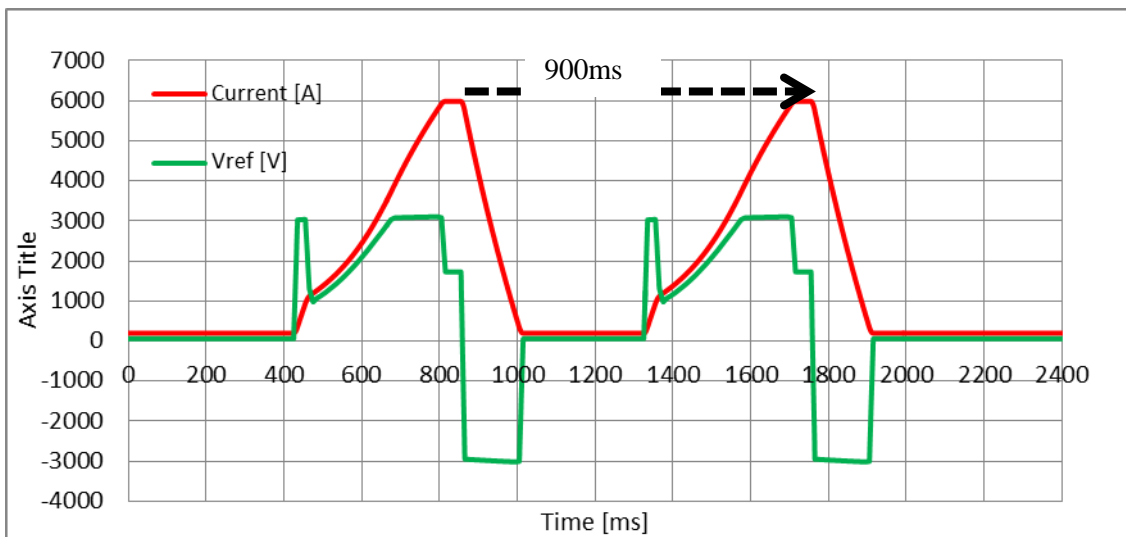
Dimensioning cycle

In order to keep an adequate margin, a larger cycle is considered for the dimensioning of the different power components (Fig. 3.130). MPC power components will be sized according to this cycle (see Table 3.50).

**Fig. 3.130:** New 2 GeV cycle for MPS dimensioning**Table 3.50:** Margins taken for MPS dimensioning

	Physics cycle	Dimensioning cycle
I_{pk}	5200 A	6000 A
I_{rms} (1.2 s)	2110 A	2572 A
V_{pk}	± 2500 V	± 3000 V

The worst condition for power converter dimensioning is when two of the cycles represented in Fig. 3.130 are executed one after the other with a short time between the two so as to simulate a false 900 ms cycle (Fig. 3.131) .

**Fig. 3.131:** New 2 GeV double cycle for dimensioning (false 900 ms)

Output voltage performance

Fig. 3.132 shows the specification for the output voltage ripple of the MPC.

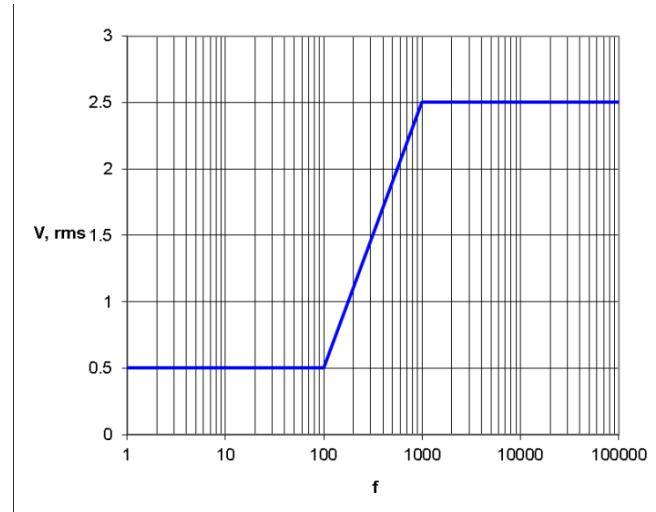


Fig. 3.132: Voltage ripple requirements for Booster 2GeV MPC

Voltage insulation to ground

Table 3.51 shows the values to be considered.

Main power transformers will be considered as singular cases.

Table 3.51: Voltage insulation level for MPS equipment

Insulation voltage level	
Power cables	$U_o = 6 \text{ kV } 50 \text{ Hz}$
Other equipment	$U_m = 7.2 \text{ kV } 50 \text{ Hz}$

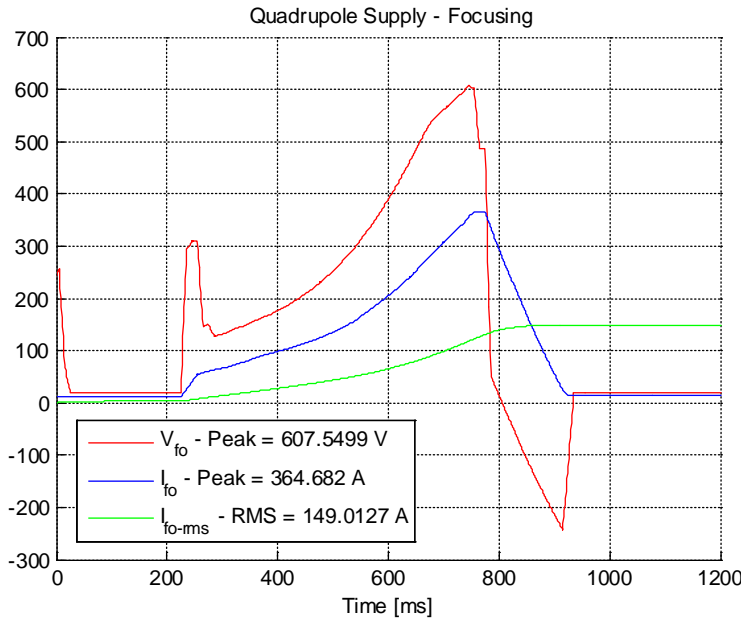
3.6.2.7 Booster 2GeV QTR: dimensioning criteria

The quadrupole trims converters provide some of the machine operation tuning degrees of freedom.

It is therefore very difficult to determine the correct dimensioning cycle as has been done for the MPC converters. Therefore a margin of error must be taken into account at this stage of the project.

Dimensioning cycle

We based our design on the following cycle (Fig. 3.133, Table 3.52) as the focusing magnets represent the worst conditions.

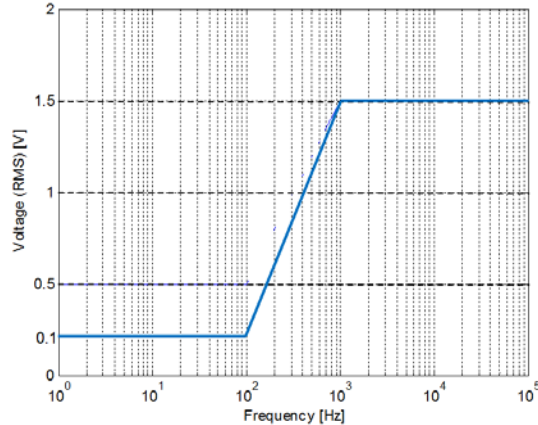
**Fig. 3.133:** Supply for quadrupole focusing magnets**Table 3.52:** Supply for quadrupole focusing magnets

	Operation values	Operation safety values 20% margin	Design values 30% margin
Current peak (A)	365	438	450 ^a
Current rms (A)	150	180	195
Voltage peak (V)	608	730	790

^a Limitation of the Apolo power converter (saturation of filter inductance)

Output voltage performance

Fig. 3.134 shows the specification for the output voltage ripple of the QTR.

**Fig. 3.134:** Output voltage ripple requirements for Booster 2GeV quadrupole power supplies

Following measurements on the present quadrupole power converters, we decreased the maximum allowed voltage ripple of the output voltage performance at low frequency (50 Hz) so as to decrease the annoying effect during the injection.

Voltage insulation to ground

The same considerations as for the MPC hold for the QTR (see Table 3.51).

3.6.2.8 Booster 2GeV cooling needs

The new MPS will be water-cooled. CERN group EN/CV is responsible for the design and installation of the cooling stations. A detailed specification is given in Ref. [98].

Cooling of the power converters

The power converters are directly cooled by a dedicated system designed and installed by EN/CV group. Requirements are reported in Table 3.53 and Fig. 3.134.

Table 3.53: Booster 2GeV power converter loss dissipation in water

	MPS		QPS	Spare circuit
	AFE + output filter	DCDC converter	quadrupole converter	
Number of units (N_u)	3	3	3	1
Losses in water per unit ($P_{\text{loss}U}$)	100 kW	77 kW	25 kW	30 kW
Water flow per unit (Q)	Q_1 : 36 m ³ /h	Q_2 : 36 m ³ /h	Q_3 : 5 m ³ /h	Q_{spare} : 5 m ³ /h
Inlet temperature (maximum) (T_{in})	30–35°C	30–35°C	30–35°C	30–35°C
Inlet water conductivity (μS/cm) at T_{in}	<1.5 μS/cm	<1.5 μS/cm	<1.5 μS/cm	<1.5 μS/cm
Estimated DP at Q	4.0 bar	4.0 bar	2.5 bar	2 bar
Total losses in water ($P_{\text{loss H}_2\text{O}}$)	500 kW			

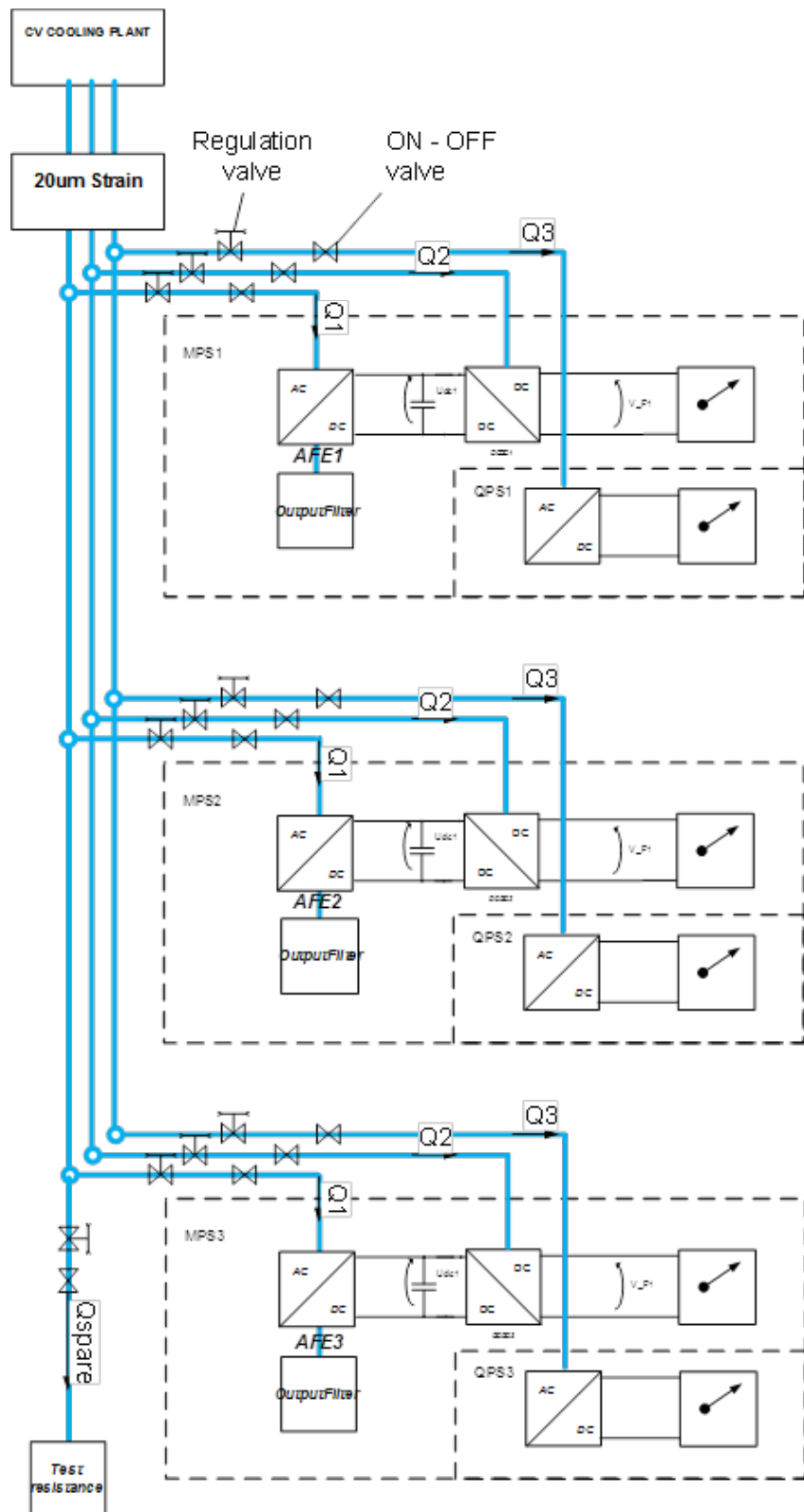


Fig. 3.135: MPS cooling schematic

Cooling of the load test magnets (in common with PS)

The POPS (main power supply of the CERN PS) test load is made up of 10 spare SPS magnets connected in series. Its impedance represents about 10% of the PS magnets that, in turn, corresponds to about the impedance of a single Booster magnet string:

$$L_{mag\text{ half}} = 0.09 \text{ H}, R_{mag\text{ half}} = 0.35 \Omega.$$

The same magnets will then be used for the commissioning of the Booster 2 GeV MPC.

These magnets are presently cooled by a PS cooling station common to other equipment that will undergo maintenance during LS2 and cannot therefore be used for commissioning of the power converters.

It has therefore been decided to make a modification to the present POPS dedicated cooling station, so that it can cool down the test load at the same time as the main POPS converter. This would allow the test load to be maintained independently of the PS ring, and to be available during LS2 for the commissioning of the Booster 2 GeV power converters.

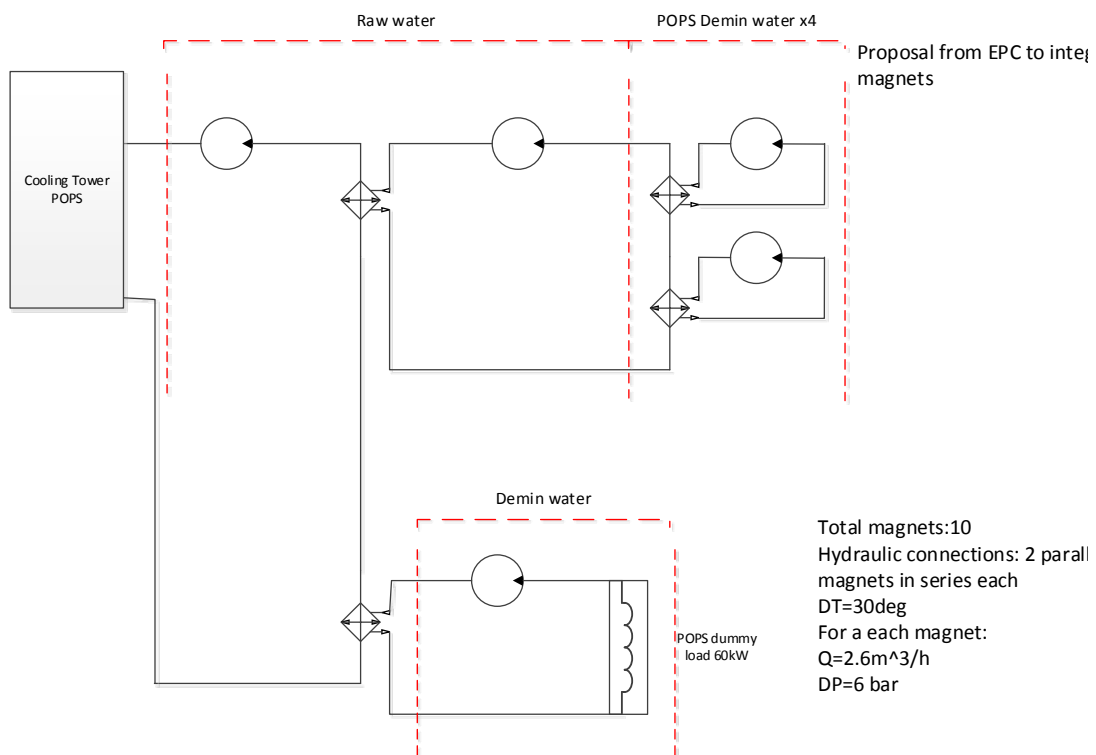


Fig. 3.136: Modification to include test load cooling

3.6.2.9 Booster 2GeV MPS cabling activities

The new MPS will be installed in a dedicated building to be realized before LS2 (building 245). During the first years after LS2, the present MPS power supply will work as back-up in case of failure of the new one.

It is therefore mandatory to install some switching cabinets to allow a smooth transition between the new and old configurations. These cabinets would need to be connected to the load and sources by means of power cables going from new building 245 to building 271.

In addition to the cables for the operation of the new and old MPS, cabling of the test magnets (in building 367) will be required for commissioning of the new Booster MPS.

For a detailed description of the cables to be installed, please see Ref. [99].

Power cabling for the MPS

Several cable paths are required to ensure the following functionalities:

Cables going outside building 245.

- i) The 18 kV power transformers cables: ensure 18 kV supply for the building 245 auxiliary transformer and the three MPC input transformers.
- ii) Booster magnet switch: this ensures switch-over between the old and new power converters in case of major problems (or for asynchronous commissioning). Magnets can be supplied either by the new or the old converter systems. A series of switching cabinets would need to be installed in building 271 for that purpose.
- iii) Building 245 auxiliary power supply to building 245 from building 271: auxiliary transformers are installed in building 245. The 18 kV cables will be installed from the ME25 substation to the building. In addition, safety network cables will be pulled from building 271 to building 245. Details on the dimensioning of these cables will be provided by EN/EL.

Cables connections inside building 245 (or close to it).

- i) Main AC power transformers: 6 kV cables need to be pulled from the three main power transformers to the power converters to provide main power.
- ii) Storage capacitors cables: 6 kV cables are used for connecting the storage capacitors in the respective rooms with the power converters in the converter hall.
- iii) Power converter internal cables: these are the cables to connect the AFE with the DCDC converters. They will be defined in a more advanced phase when the power converters are completely designed. As the converters are installed back-to-back, copper bus bars could be used.

Figure 3.137 shows the two cable paths for connection of building 245 with building 271. Figure 3.138 shows the cable switch connection logic to be realized in order to be able to switch between the new MPS configuration and the present one.

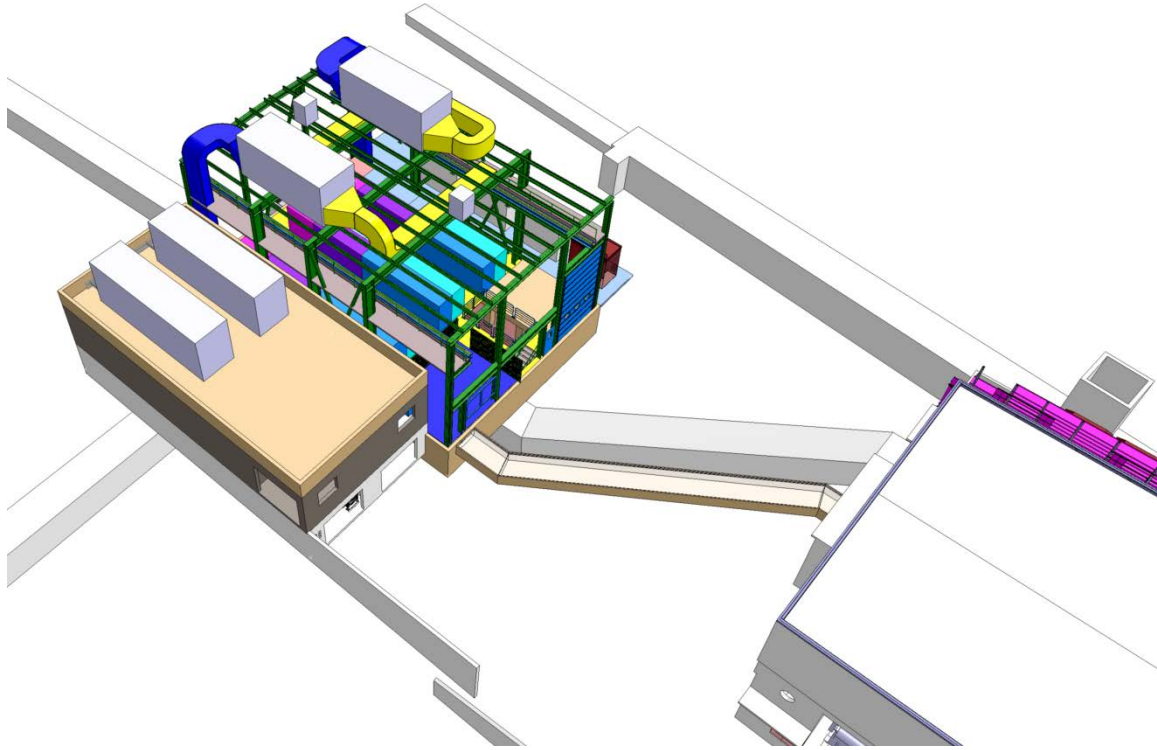


Fig. 3.137: Cable connections from building 245 to buildings 271/361 and ME25

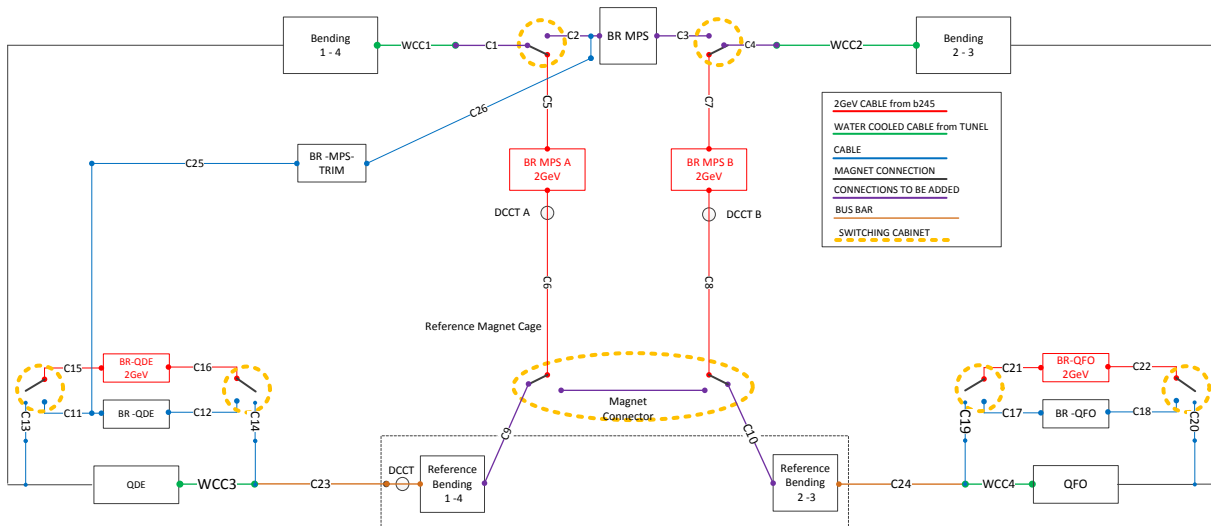


Fig. 3.138: Booster 2GeV magnet configuration

Power cabling of the test load magnets

The output of the MPC can be connected either to the Booster magnets or to a test load. Given its impedance, the POPS test load is the ideal dummy load for Booster MPC commissioning.

These magnets are located in building 367 and are presently used as a test load for POPS. A switching system will be installed that will allow the same dummy load to be used for either POPS or the Booster 2GeV. The new MPS will therefore be connected to building 367 for testing.

Fig. 3.139 shows the connection path required for cabling POPS test magnets to the new Booster MC.

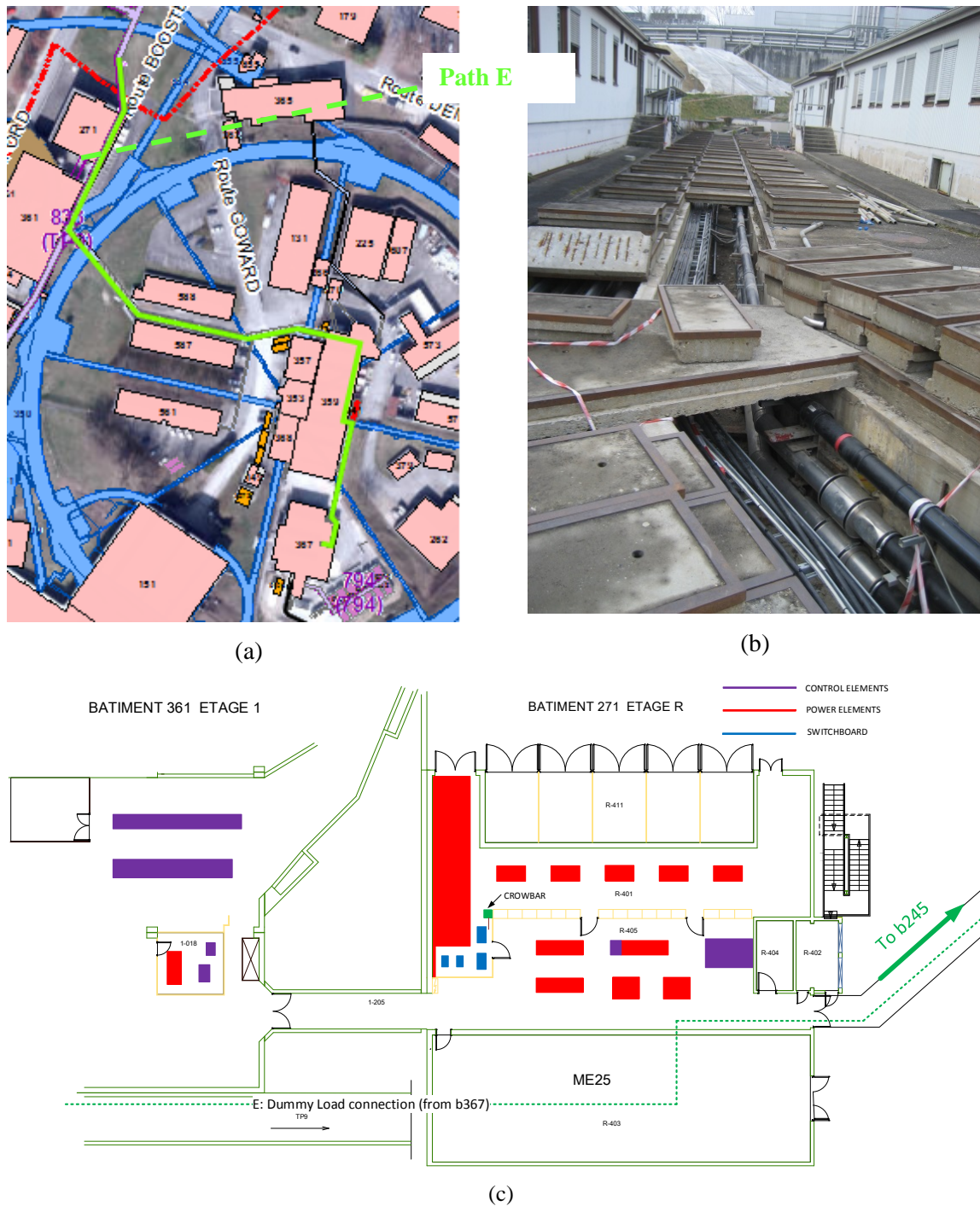


Fig. 3.139 a-c: Cable routing from building 245 to building 367

3.6.2.10 Project planning

The biggest challenge of project planning is to organize the activities to be performed before the start of LS2.

The construction of building 245 needs to be completed well in advance to allow EN-CV and EN-EL to install their equipment before the start of power converter commissioning. This date is fixed for March 2018.

Some of the activities need to be performed when the machines are off, i.e. during winter shutdowns:

- modification of the POPS cooling station to include test magnets: EN-CV;
- installation of 18 kV circuit breakers in ME25: EN-EL;
- cable connections from building 245 to building 367 for the test magnets: EN-EL;
- 18 kV cables connection from ME25 to building 245: EN-EL.

Figure 3.140 is a chart showing the general stages of planning, which are described below in greater detail.

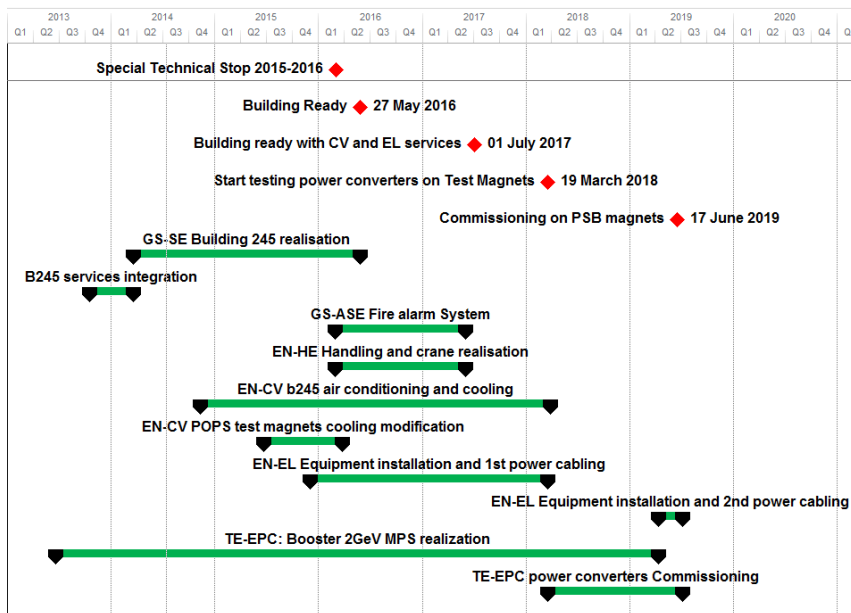


Fig. 3.140: Global Booster 2GeV new MPS project planning (macro-activities)

TE-EPC MPS realization project planning

Figure 3.141 shows the planning for MPS realization in greater detail.

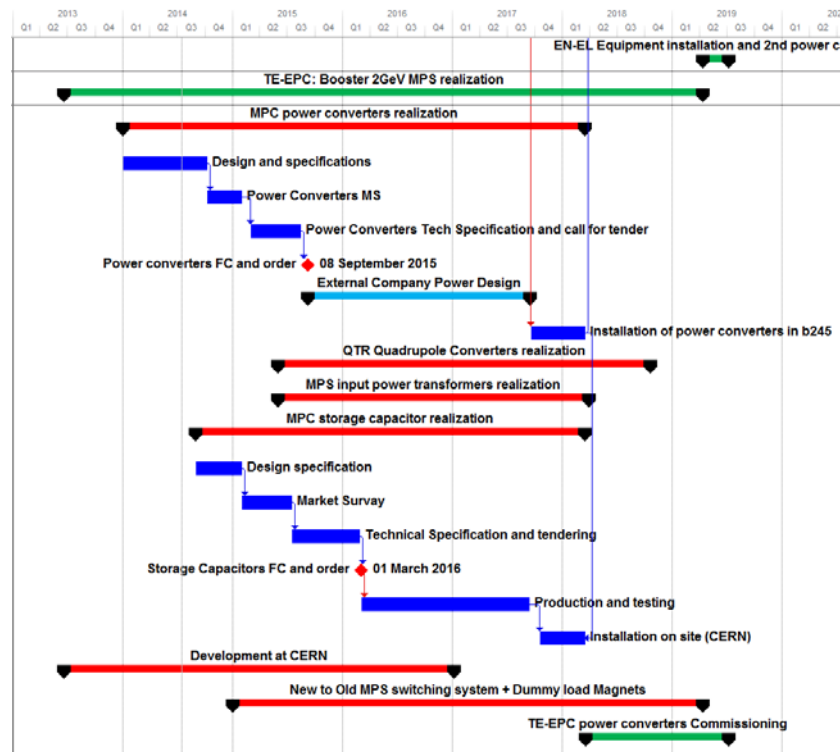


Fig. 3.141: TE-EPC MPS realization planning

Commissioning of the power converters

In order to commission the system efficiently, we need a test load with approximately the same size of the Booster magnets. The POPS test load is of the right size. The possibility of using this load would permit commissioning to continue independently from the Booster magnet activities. A tentative planning is shown in Fig. 3.142. It is therefore important to prepare the necessary cable connections and cooling modifications.

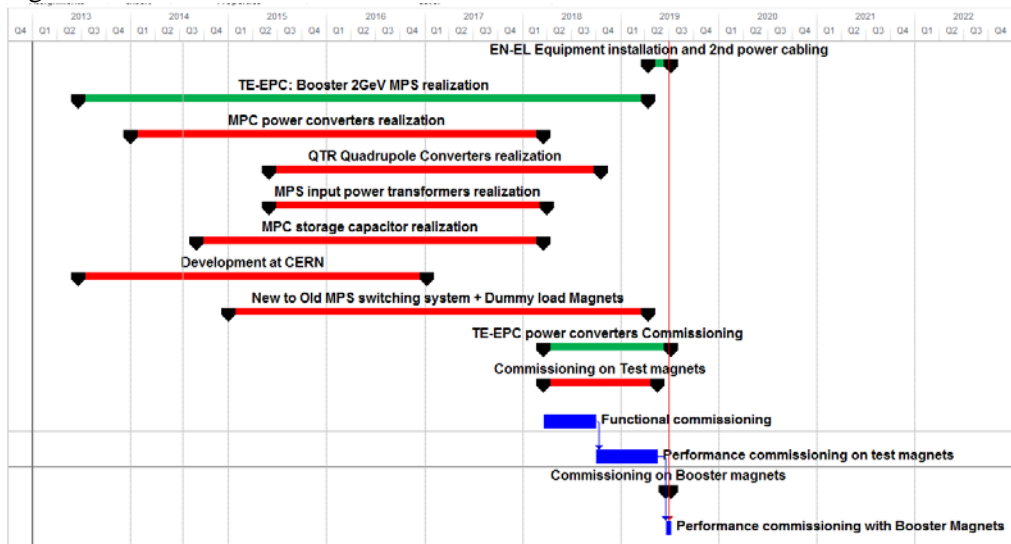


Fig. 3.142: TE-EPC MPS commissioning

The testing window at the beginning of LS2 is no longer necessary as we have decided to use the POPS testing magnets.

EN-EL electrical installations

The planning reflects the need to have all installations required for commissioning the MPS ready by March 2018 (see Fig. 3.143):

- installation of 18 kV circuit breakers in ME25: EN-EL;
- cable connections from building 245 to building 367 for the test magnets: EN-EL;
- 18 kV cables connection from ME25 to building 245: EN-EL.

The above activities will be carried out during a winter shutdown.

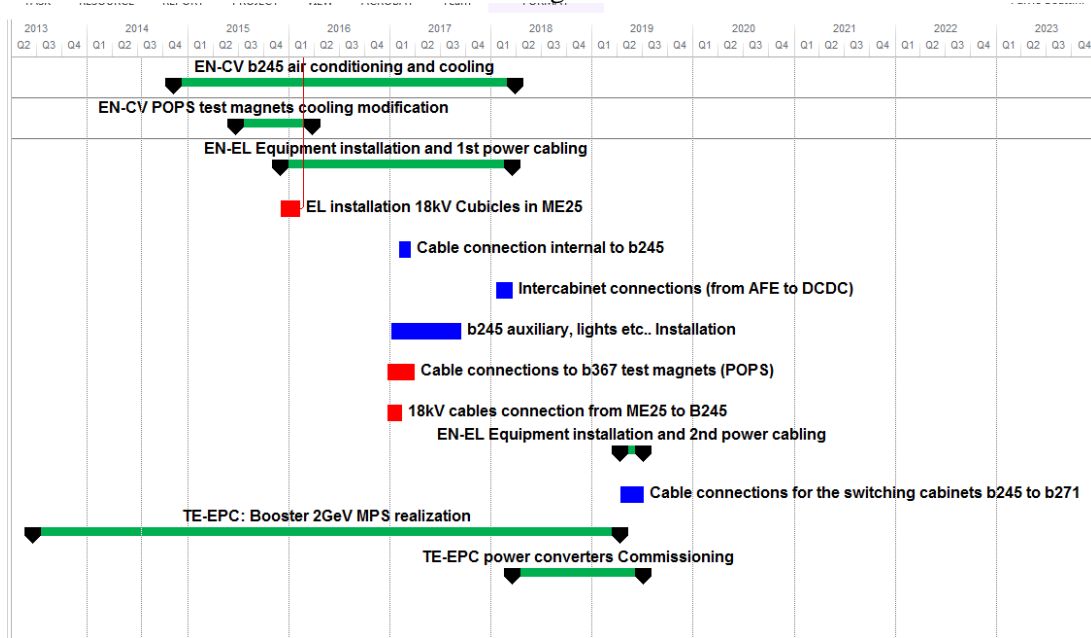


Fig. 3.143: EN-EL electrical installation

EN-CV cooling and air conditioning

The most critical activity for cooling and ventilation is the modification of the POPS cooling station to include test magnets. The realization will be carried out during a winter shutdown (Fig. 3.144).

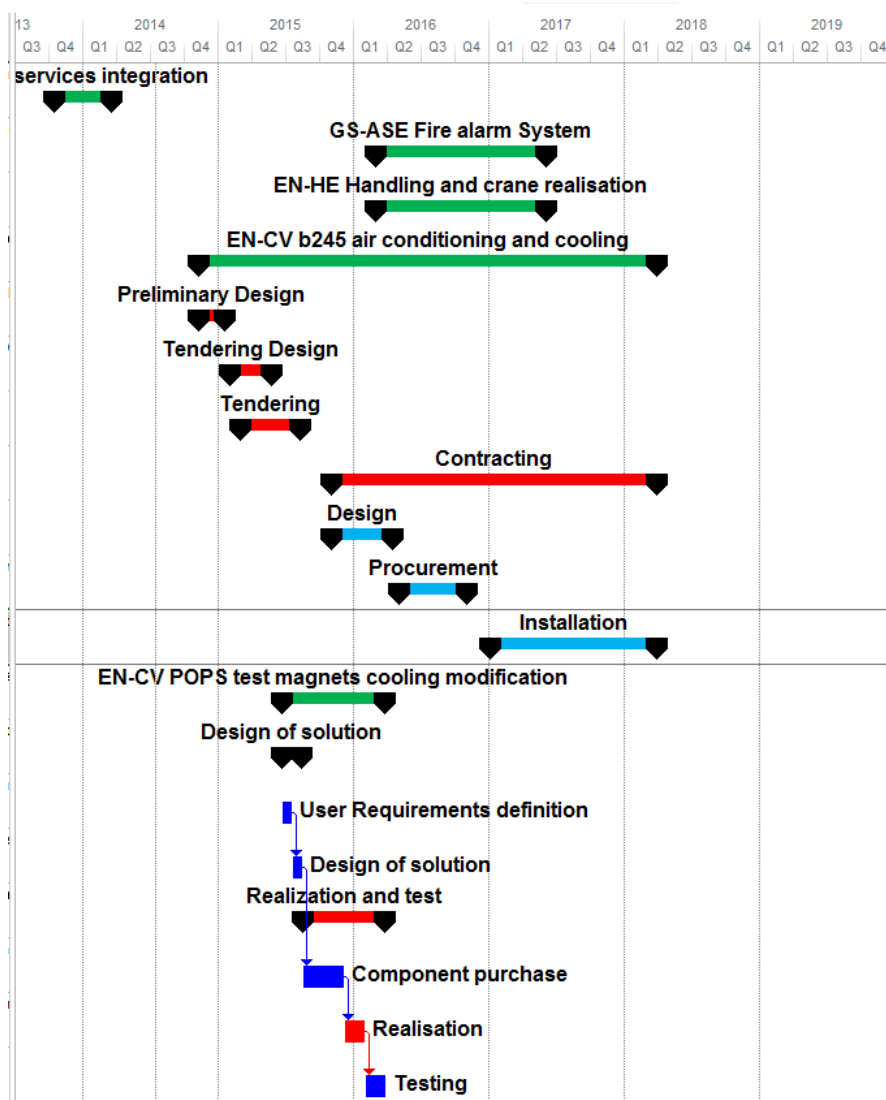


Fig. 3.144: EN-CV cooling installation

3.7 Beam instrumentation

3.7.1 Screen monitors

3.7.1.1 PSB injection BTVs (BI.BTV30)

These four BTV devices are presently mechanically attached to the BIr.SMV20 injection septa. During LS2, these septa will be replaced to prepare for H^- injection, with the new ones having a larger tank and different vacuum interface. The connection between the septum and the BI.BTV30 will therefore have to be modified. A new BTV design is not required, as only the flange on the BTV tank needs to be changed with a stand-alone bellows added between the two devices. Figure 3.145 shows the layout of the BI line around this BTV before and after the upgrade.

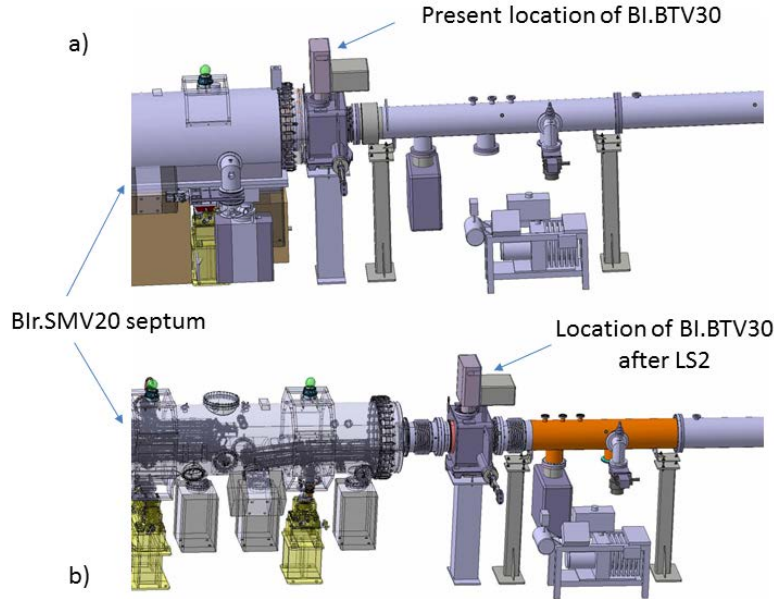


Fig. 3.145: (a) Present layout around BI.BTV30. (b) Layout around BI.BTV30 after the modification

3.7.1.2 PSB extraction BTVs

Currently, the BT.BTV10I and BT.BTV10S devices are installed in common tanks together with their respective extraction septa BT1.SMV10 and BT1.SMV4 (Fig. 3.146). An upgrade of the septa is foreseen before LS2 and it has been decided to separate the vacuum vessels of the septa and the BTVs. The design of this separate BTV tank was completed in 2012, with manufacture and installation taking place during LS1. The BTV instruments (screen movements plus detectors) will be moved from their present location to the new tank before LS2, following the planning of the septa upgrade.

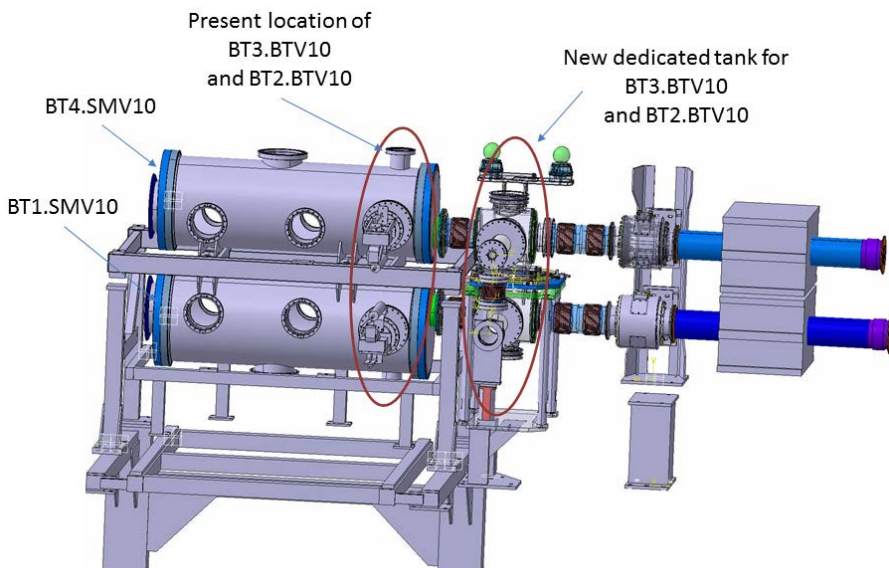


Fig. 3.146: Layout of the BT line around the septa BT1.SMV10 and BT4.SMV40 showing the current BTV locations and their future new vacuum tanks, which were installed during LS1.

The BT.BTV30 currently shares a tank with the BT2.SMV20 septum. This septum will also be upgraded before LS2 and again the BTV and the septum will have separate vacuum vessels in the new

design. The new BTV tank will be installed right after BT2.QN030 as shown in Fig. 3.147. The design of the tank is presently ongoing. The system will be installed during LS2.

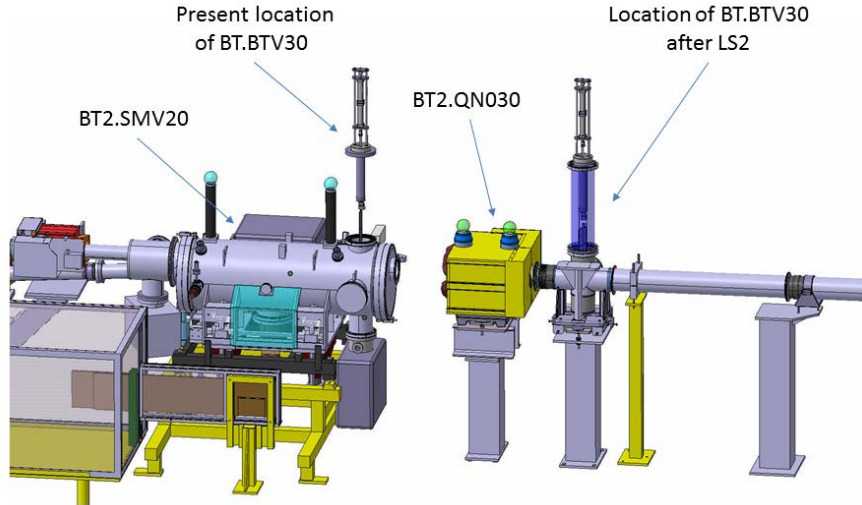


Fig. 3.147: Part of the layout of the BT line around BT2.SMV20 showing the present location of the BTV inside the septum and the upgrade with this BTV relocated after BT2.QN030.

3.7.2 Beam observation system (BTV) for the PSB H⁻ injection region

3.7.2.1 Description

With the connection of Linac4, the injection region of the PSB will radically change. The scheme used to inject the new H⁻ beam into the PSB is based on the charge-exchange principle using a stripping foil. An optical beam observation system (BTV), including a scintillating screen and radiation hard camera, is required for each of the four rings as the only means of verifying injection steering. It is requested that the same camera should allow monitoring of both the beam position and the integrity of the stripping foil.

The following main points have been specified for the observation stations:

- the position of the scintillating screen should be remotely controllable so that the screen is normally outside the beam path and only inserted when needed for beam measurements;
- the system should allow the observation of the beam and of the foil, but not necessarily at the same time;
- the system should allow easy and fast access for maintenance due to the high radiation levels expected;
- the system should allow quantitative beam measurements over a large range of beam intensities. This implies that a system of remotely controlled optical filters should be included to adapt the light intensity to the camera.

The major constraint for this project is the limited space available in the injection region for the observation station, implying a common vacuum chamber shared between the stripping foil and the BTV.

3.7.2.2 BTV screen specifications

The intensity on a 1 mm-thick Al₂O₃ BTV screen should not exceed 2.5×10^{12} particles due to the risk of damage due to heating. It is, however, possible that a maximum of 2.5×10^{13} H⁻ ions can be

injected. The screen should therefore survive a single shot of this intensity without damage. As an example, the energy density deposited by ionization for $2.5 \times 10^{13} \text{ H}^-$ ions is about 380 J/cm^3 , which gives an instantaneous temperature rise of 108°C . Assuming that the maximum allowable temperature rise of an Al_2O_3 screen is of the order of 500°C , and neglecting the beam blow-up and attenuation with multiple screen passages, the product of the intensity and the number of circulating turns must not in any case exceed 1×10^{14} as the screen would otherwise be destroyed.

The screen should cover an area $\pm 30 \text{ mm}$ vertically and $+25/-45 \text{ mm}$ horizontally around the nominal injected beam, which is located 80.9 mm away from the nominal PSB orbit. Figure 3.148 shows this geometry including the stripping foil. These screens will be constructed out of 1 mm -thick ceramic chromox material (Al_2O_3 doped with CrO_2) and engraved with calibration marks.

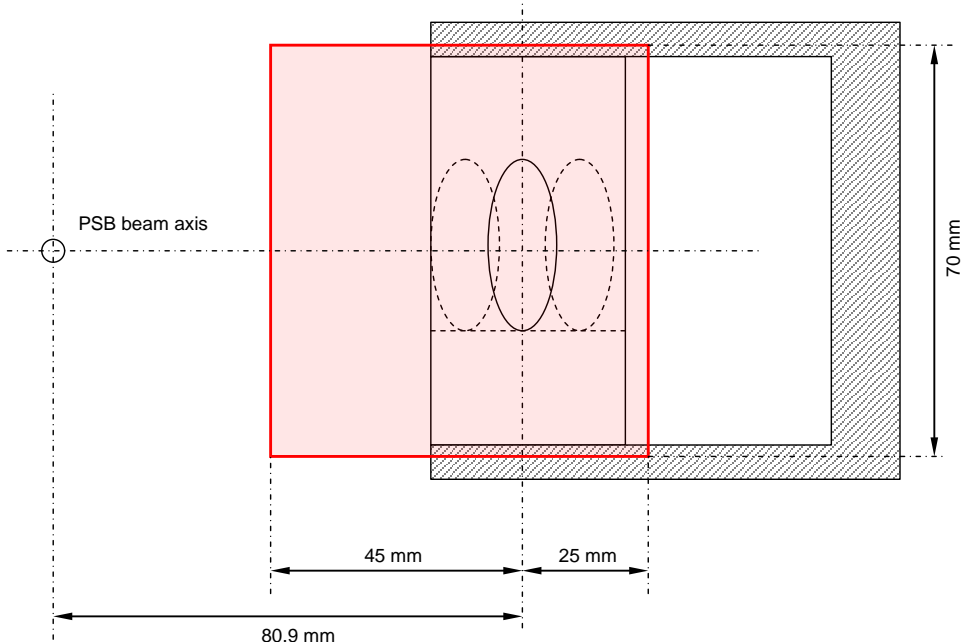


Fig. 3.148: Position of the chromox screen (red) and of the stripping foil holder (black) with respect to the injected and circulating PSB beam axes.

3.7.2.3 Optical line design

In order to observe the screen and the stripping foil with the same camera they need to be installed very close one to another, in order to be inside the depth of field of the focusing lens. Moving the camera or the lens in this compact and highly active area would be very difficult and would increase the requirements in terms of maintenance. The layout found to fulfil this requirement is shown in Fig. 3.149.

A mirror is positioned below the beam and reflects the images of the screen or of the stripping foil towards an observation viewport. The viewport itself is made of fused silica to avoid the browning that occurs for normal glass in radiation environments. The small, 5 mm difference in the distance of the camera from the screen and the foil makes the use of a single, fixed, optical system possible. A second mirror is required outside the viewport as there is not enough space to directly install the camera between the four rings. This limited space also means that the two mirrors have to be installed at an angle, which introduces some image distortion. The cameras will be located on the inside of the four PSB rings.

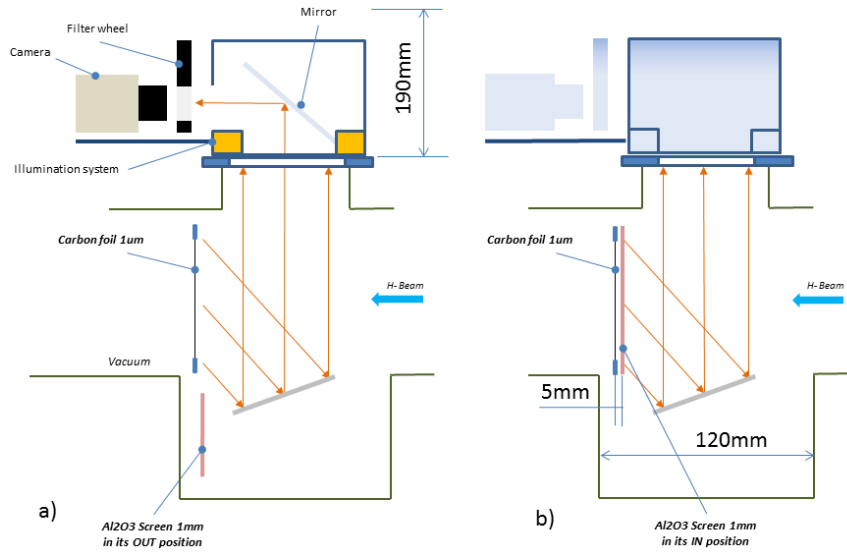


Fig. 3.149: Sketch of the optical line for beam and stripping foil observation. (a) Observation of the carbon stripping foil. (b) Observation of the scintillating screen (beam).

3.7.2.4 Mechanical design

The insertion and extraction of the screen is performed using a linear electrical actuator that controls the rotation of the screen around a pivot point. Due to the screen's vicinity to the 1 μm-thick carbon stripping foil all vibrations should be avoided; this is the reason why an electrical actuator was preferred to a pneumatic system.

A special camera support has been designed to cope with the limited space available. This support includes the second mirror, an illumination system, the camera support itself and a filter wheel. The mechanical design is shown in Fig. 3.150.

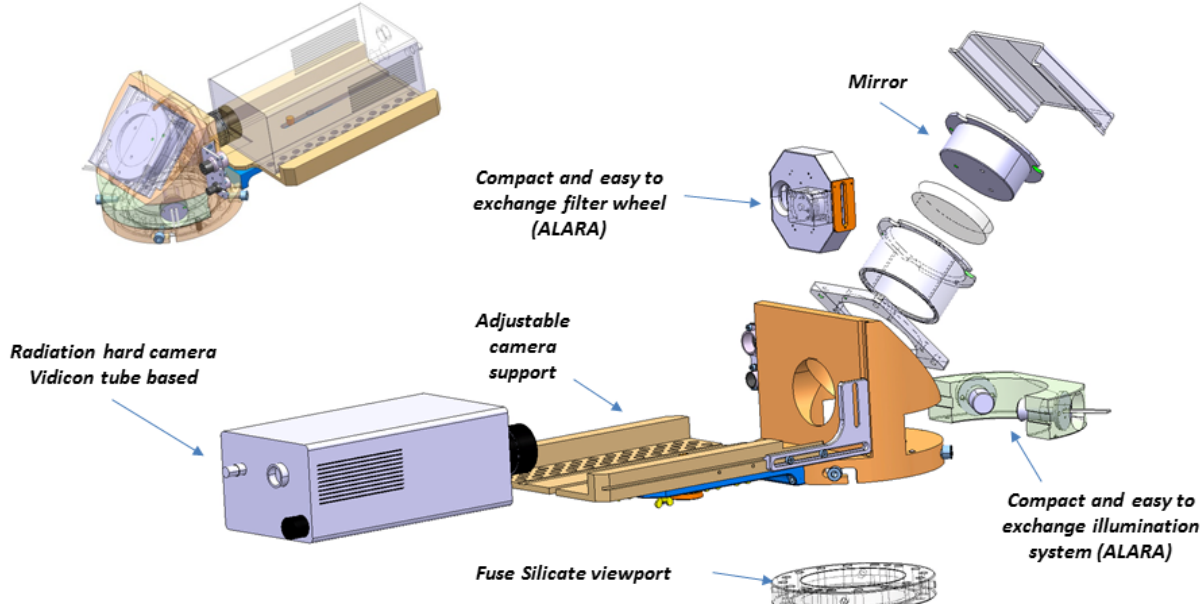


Fig. 3.150: 3D model of the camera support with all the required ancillaries (lights, filter wheel, etc.)

The complete mechanical system has been designed in such a way that any maintenance can be performed rapidly, with fast mounting and dismounting of the assembly.

The BTV screen and the stripping foil mechanism can interfere and damage each other. It is therefore important to ensure that the actuators can only be activated under safe conditions, with a hardware interlocking system preventing movement if this is not the case.

3.7.2.5 *Status and plans*

The design of this system is almost completed and a prototype of the screen actuator was built and tested in 2013, with over 300 in/out cycles performed under vacuum. The optical design has been validated by laboratory measurements.

The production of six actuators will be launched mid-2014, with two systems to be installed and tested in Linac4. One of these will be permanently installed for stripping foil studies, while the second will be temporarily installed for the half-sector test in 2015.

The production of camera supports has already been started and is expected to be complete by the end of 2014.

3.7.3 H^0/H^- intensity measurement at the injection dump

3.7.3.1 *Introduction and specifications*

Four internal H^0/H^- beam dumps, one per ring, will be installed downstream of the stripping foil unit to intercept the unstripped H^0/H^- particles as well as any H^- particles missing the foil. An intensity measurement of both the H^0 and H^- beam currents impacting the dump is required to allow an efficient setting-up of injection, to monitor the efficiency of the stripping foil and to protect the dump from a high-intensity beam impact by providing an interlock signal in case of stripping foil failure.

The H^0/H^- intensity will be measured using two, 1 mm-thick, titanium plates placed at a distance of a few centimetres from the front face of the dump. One plate will intercept the H^0 particles, while the other intercepts the residual H^- beam. As these beams traverse the titanium plates they are stripped of their remaining electrons, which are collected in the plates and can be read-out in a similar fashion to a Faraday cup. Both the dump and the monitor are placed inside the BSW4 chamber, the last of the four pulsed dipole magnets creating the injection bump.

The monitor specifications are described in detail in Ref. [100]. The system has to be robust and simple, for maintenance-free operation, withstanding a radiation dose of 0.1–1 MGy per year. It must also operate close to the pulsed magnetic field of the BSW4, which should not perturb the measurement by more than 0.1%. The monitor should also be able to survive the impact of a full Linac4 pulse ($2.5 \times 10^{13} H^-$ ions) in case of the failure of the stripping foil.

3.7.3.2 *Design*

Titanium is the material of choice for this monitor because it is a relatively low-Z material (leading to low activation) with a medium-level of conductivity ($2.3 \times 10^6 \Omega^{-1}$). This is considered the best compromise between the high conductivity needed for the read-out of the deposited charge and the low conductivity required by the presence of the pulsed magnetic field. The thickness of 1 mm is chosen to stop all the stripped electrons while avoiding current loops in the horizontal plane due to the presence of the vertical B field. The thermal load under normal operating conditions (2% of the full beam load) is of the order of 150 mW. In this configuration, the temperature increase for a full Linac4 pulse impact does not exceed 90 K.

A preliminary integration of the monitor in the BSW4 chamber is shown in Fig. 3.151. Each titanium plate is divided into two halves, with the cut placed at the centre of the expected H^- and H^0 beam envelopes. This additional feature, which is not explicitly required in the specifications [100], will add beam position information to the intensity. The monitor is inside the magnet, at a distance of

4 cm from the dump face [101], in a rather uniform vertical magnetic field of 0.18 T, which almost completely suppresses secondary electron emission from the monitor plates. Tracking simulations including the magnetic field map have shown that a 4 cm distance between the dump and the monitor is sufficient to prevent secondary particles from the dump hitting the monitor. The use of repelling electrodes is therefore avoided, greatly simplifying the integration in this area. As shown in Fig. 3.151, each monitor plate has two read-out cables, implemented for redundancy reasons and test purposes. The second cable can be used during testing to inject an external current pulse, as well as being available as a spare read-out cable. Kapton cables would have been the best solution, both for shielding purposes and for radiation hardness. Unfortunately they were ruled out for vacuum reasons, as their outgassing rate would have significantly increased the pumping time required after an intervention, which is a very critical point for this injection region. The baseline solution is therefore to use wires with ceramic tubes and beads as insulation.

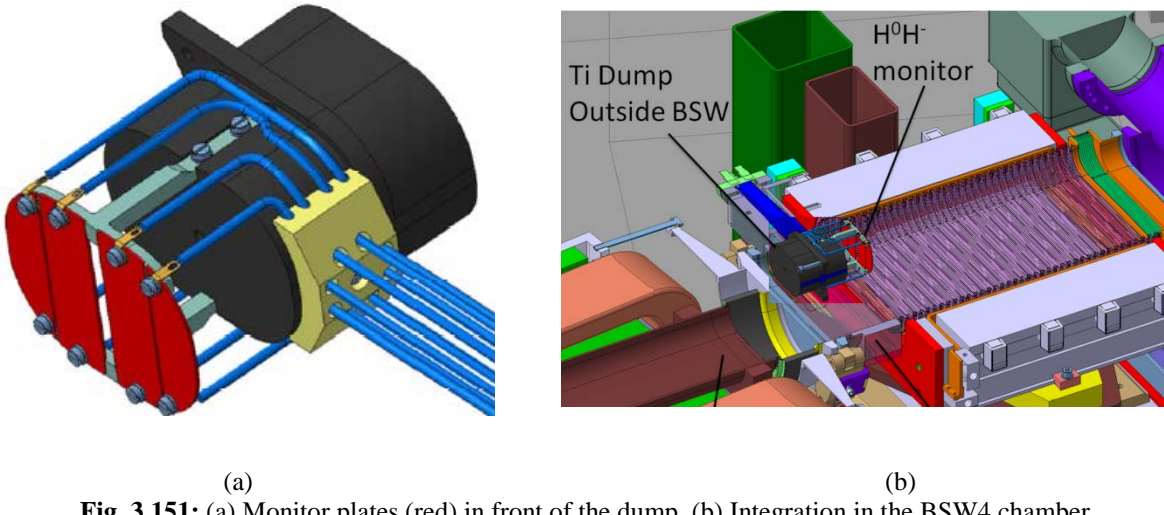


Fig. 3.151: (a) Monitor plates (red) in front of the dump. (b) Integration in the BSW4 chamber

3.7.3.3 Read-out electronics

During normal operation the current signal on the H⁰ plates is expected to be 2% of the Linac4 beam pulse current (nominally 40 mA), corresponding to a stripping foil efficiency of 98%. The level of unstripped H⁻ particles is normally expected to be very low (10^{-6} of the Linac4 beam pulse current), but it is possible that up to 2% of halo particles miss the foil and directly impact the dump [100]. Stripping foil degradation can be tolerated until the dump load reaches the safety limit of 10% of the full Linac4 pulse. This will be the threshold set for the interlock circuit.

The monitor is required to provide an integral measurement over the full injection time (which can vary from 50 ns up to 100 μ s), per H⁰ and H⁻ channel, per injection. After a first amplifying stage, the read-out electronics will be split into two parts. One circuit will be dedicated to the interlock, with a lower level of amplification, in order to prevent saturation in case of stripping foil breakdown. The other circuit will be used for current measurement under operational condition, using a higher level of amplification in order to get the best possible sensitivity for faint H⁻ currents.

3.7.4 Injection matching monitor

In order to verify the correct matching of the optical Twiss parameters of the Linac4 transfer line and the PS Booster, it is required to measure the transverse profiles of the injected beam on a turn-by-turn basis. An optical mismatch will induce an oscillation in the width of the measured profiles at twice the tune frequency. In order to measure and correct this mismatch it is necessary to determine the beam size to within a relative accuracy of a few percent. The acquisition of 20 successive turns is deemed adequate for the accurate quantification of the mismatch.

The injected beams will have transverse rms sizes of the order of 1 mm and currents up to 60 mA. To measure the profiles turn-by-turn it is necessary that the injected pulses are shorter than the PSB turn length (1.6 μ s). A pulse length of 0.5 μ s looks appropriate for this purpose. Profile measurement stations based on secondary emission grids, one per plane, have been identified as the best solution. By using grids of 24 carbon wires of 33 μ m diameter spaced by 0.4 mm it is possible to acquire the profiles with sufficient accuracy and sufficiently low perturbations from one turn to the next. Using the parameters mentioned above the maximum charge per turn on the central wire of the grid is estimated to be of the order of 15 pC.

Installing the front-end electronics near the detector heads would be the best solution in terms of noise and bandwidth. Unfortunately, the harsh radioactive environment of the PSB injection region rules out this option. A service room just above the injection region has been identified as the closest location where the electronics can be installed. Preliminary calculations indicate that by using suitable cables the noise level of the front-end electronics can be kept below 40 fC despite the 25 m cables. This would allow a signal-to-noise ratio of about 350.

More detailed studies are required to assess the effect of multiple scattering in the wires on the turn-by-turn profiles as well as on the thermal load. The addition of injection oscillations could be used to reduce this thermal load if necessary. The influence of electromagnetic noise from the pulsed elements of the injection region on the acquisition electronics also has to be studied and suitable compensation schemes identified.

On the mechanical side, a complete design study has to be undertaken before the fabrication of the monitors can start, with particular emphasis on their integration into the PSB ring.

3.7.5 Intensity watchdog

Intermediate bandwidth intensity monitors installed in each PSB ring (sector 8L1) will be upgraded during LS2 in order to measure injection efficiency and trigger an interlock in case of excessive losses with Linac4 beams. The upgrade consists of rewinding the existing toroids, pulling new signal cables and developing new front-end electronics.

The PSB injection watchdog will compare beam intensity between BIr.BCT20 (1 BCT per ring) and the intermediate bandwidth transformer in BRi.TMD.8L1 of the PS Booster on a ring-by-ring basis. The ring BCTs should measure the beam some 100 turns after the injection has taken place. A pure hardware-based watchdog is not deemed to provide sufficient flexibility for operation, so for this reason a hybrid architecture has been chosen, similar to that foreseen for the Linac4 accelerator. The software watchdog will calculate the total intensity given by the four BI transformers and that given by the four ring transformers for each user cycle, and compare the transfer efficiency with a predefined value on a per-user basis. If the loss value is above a pre-set threshold a software counter for that user cycle will be increased, with the beam injection inhibited when the counter reaches a user-defined limit.

The basic acquisition requirements are listed in Table 3.54, with more detailed information available here: <https://edms.cern.ch/document/1155020/1.0>.

Table 3.54: Expected performance of injection watchdog

Performance	Value
Intensity range	5×10^9 – 2.5×10^{13} charges
Resolution	1×10^9 charge
Accuracy	2%

3.7.6 PSB orbit and trajectory system

The PSB will be equipped with a Booster trajectory measurement system (BTMS) based on the successful upgrade of the PS orbit system, and is expected to comply with the specifications <https://edms.cern.ch/file/1233008/1.0/LIU-Position-Specs-V1.0.docx>. The horizontal and vertical difference signals, along with the sum signal from each BPM will be digitized by fast ADCs and the trajectories and averaged orbits of all particle bunches made available for the full acceleration cycle. All signal processing is done entirely in the digital domain using large FPGAs (Fig. 3.152).

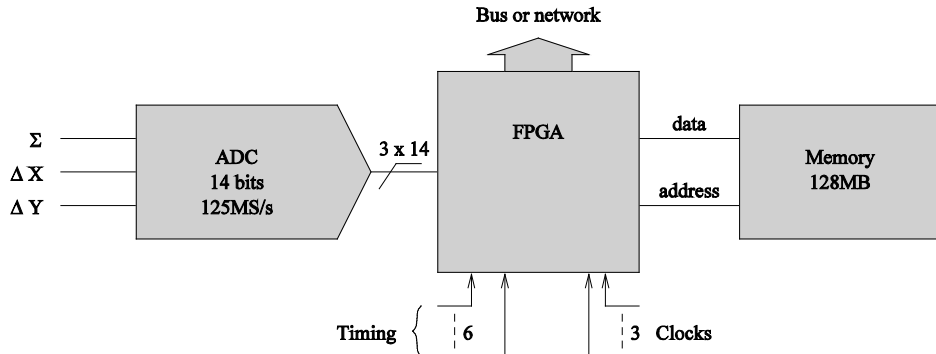


Fig. 3.152: Signal processing block diagram for one BPM

The TMS was originally developed for the PS in cooperation with the British Alpha Data Ltd-BEAM Ltd consortium. Except for the acquisition modules, all other hardware is standard off-the-shelf equipment. The acquisition system for the PSB is an upgraded version of the PS TMS, to deal with the PSB's multiple rings. This upgrade affects only the FPGA firmware and associated software, and will also be deployed on the PS TMS to avoid the parallel existence of several different versions.

The BTMS consists of four cPCI crates each containing six acquisition modules and one CPU board. These will be linked over a private Ethernet link to a system control computer that runs software to make the system appear as a single instrument (Fig. 3.153). A standard front-end computer (FEC), connected to both the private Ethernet link and to the accelerator control technical network (TN) interfaces the system to FESA and contains the hardware to generate timing signals, control the gain of BPM pre-amplifiers and generate test and calibration signals.

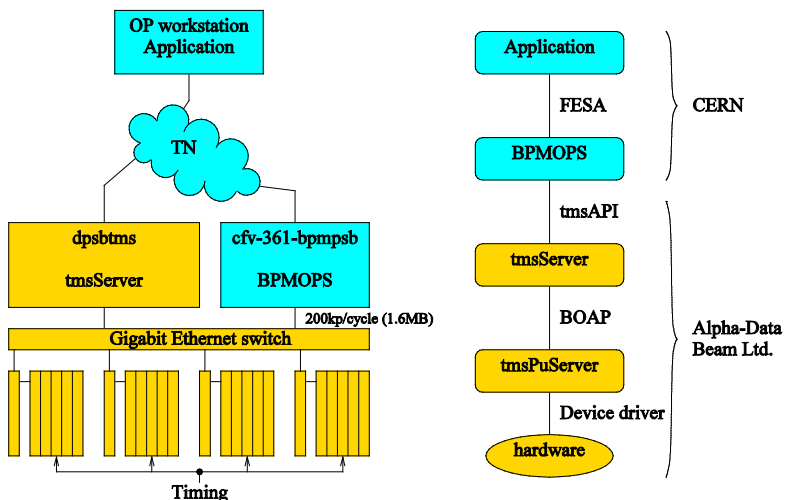


Fig. 3.153: BTMS block diagram

Figure 3.154 shows the layout of the system with four CPCI crates in buildings 37 and 361 and a centralized front-end server located in the BOR (building 361). All materials installed in the Booster ring tunnel will be entirely passive. Transformers provide the triple functionality of galvanic isolation, impedance transformation and separation of the electrode signals into Σ , X and Y components. Calibration and test signals will be injected close to the electrodes, improving the testability of the analogue signal processing chain over what is currently possible. Low-noise, variable gain amplifiers will be installed on the surface racks. The new head electronics is expected to provide the requested 200 μm resolution down to a beam intensity of $1 \times 10^{10} \text{ p}^+/\text{bunch}$.

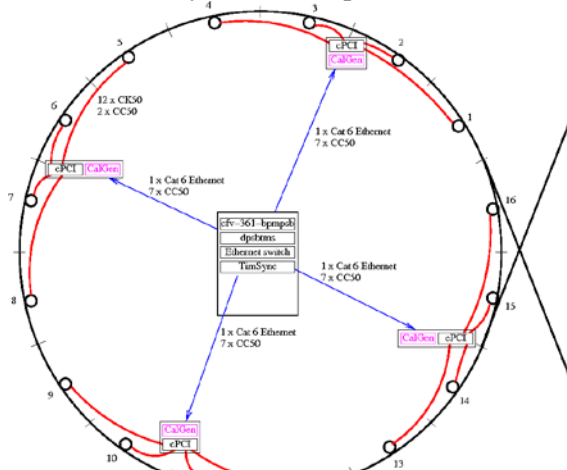


Fig. 3.154: BTMS layout in PSB buildings 37 and 361

Pending the installation of new cables the BTMS will operate alongside the existing orbit measurement, a multiplexed system allowing the measurement of a single PSB ring at a given time. Due to the incompatibility of the new BTMS front-end electronics with the old system, gain and calibration control specific to the BTMS will not be possible. The parallel BTMS system will therefore only provide good performance with fairly high-intensity beams, containing more than $1 \times 10^{11} \text{ p}^+/\text{bunch}$ (Fig. 3.155). It will, however, allow much of the system hardware, firmware and software to be debugged.

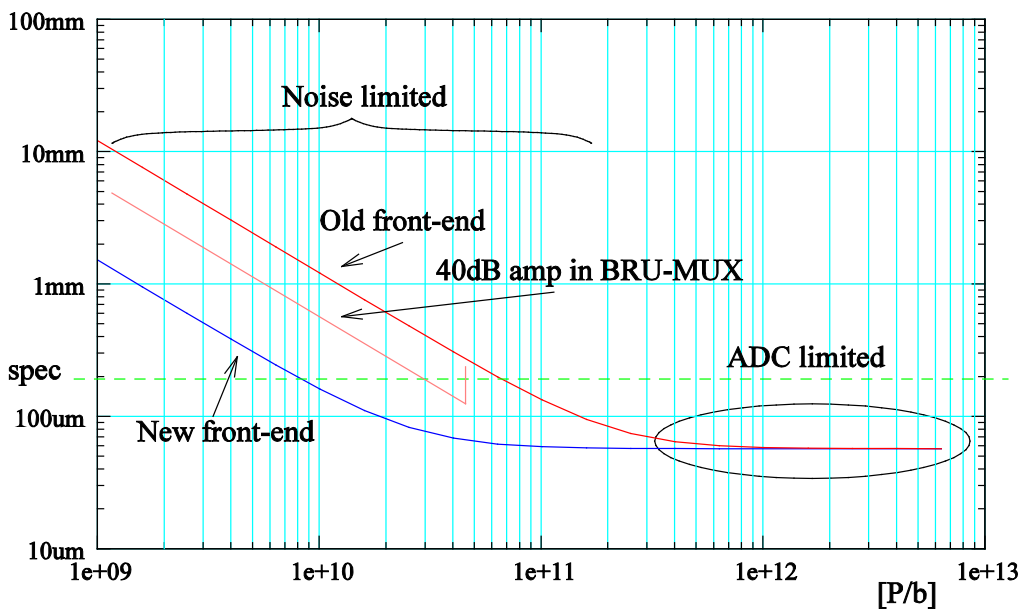


Fig. 3.155: Position resolution vs. beam intensity

The full, four-ring BTMS installation depends on the installation schedule of the new cables required and this is currently planned to take place during LS2.

3.8 Beam intercepting devices

3.8.1 PS Booster main dump

3.8.1.1 *Introduction*

The PS Booster main dump had been installed and in operation since the early 1970s. Even though it was initially designed to withstand beam energies reaching 800 MeV and intensities of 2×10^{12} particles per pulse, it had to cope with the various upgrades undergone by the PS Booster over the last four decades—up to the present 1.4 GeV.

In view of the upcoming energy upgrade after LS2, thermo-mechanical analyses were conducted and showed the need for a beam dump replacement. Consequently, a new dump has been designed, manufactured and installed during LS1, replacing the existing one in the same exact location—at the end of the PSB extraction line. This dump’s functional specification is mentioned in Ref. [102] and its technical specification in Ref. [103]. The constraints and requirements taken into account to design the new dump, the final design as well as the analyses done to support it are presented below. Additionally, a summary of the actual intervention carried out to dismantle the existing device and to install the new one is given in Section 3.8.1.6; special emphasis was laid on minimizing the human dose uptake throughout the entire operation.

3.8.1.2 *Loading and constraints*

This dump is located at the end of the BTM line, inside a cavity, which is right below the passage to ISOLDE—see Fig. 3.156.

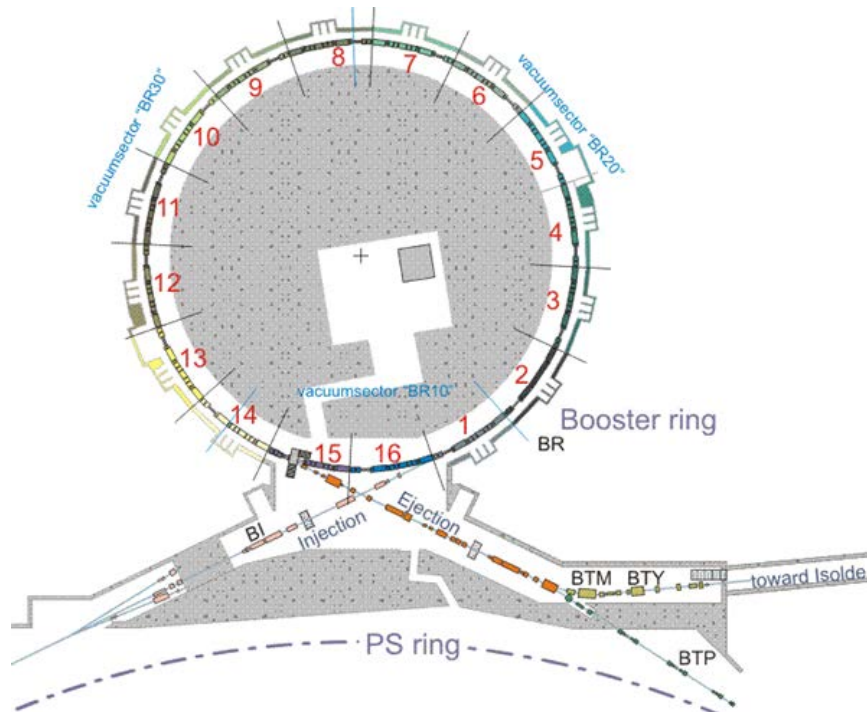


Fig. 3.156: Beam dump location

Similarly to the previous beam dump configuration (Fig. 3.157), a cylindrical dump core is surrounded by five shielding rings and the entire assembly is placed inside a 5 m-long cavity, 1 m in diameter. The cavity has existed since PS Booster construction in the early 1970s and has not been altered for the installation of the new beam dump. On the other hand, the beam dump assembly has been especially designed and manufactured in view of the PSB energy upgrade—a 3D model is shown in Fig. 3.158. The complete new design and its components are accurately illustrated in the technical drawings in Ref. [104].

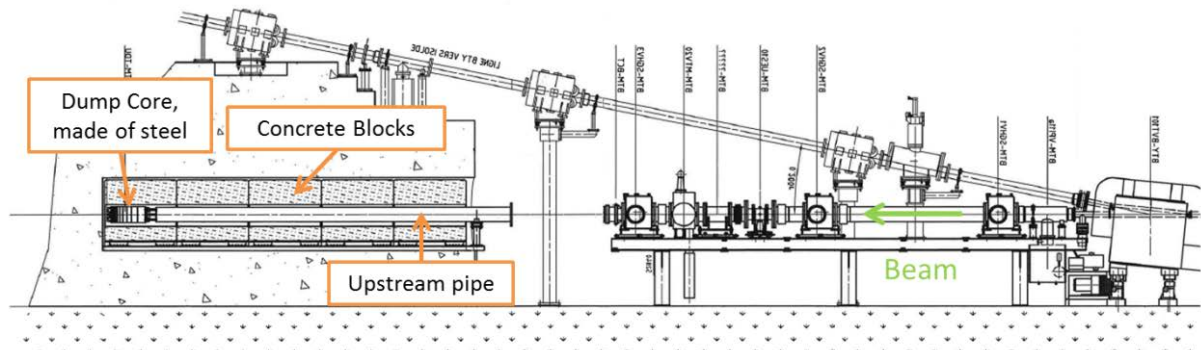


Fig. 3.157: Former PSB dump assembly (1972 to 2013)

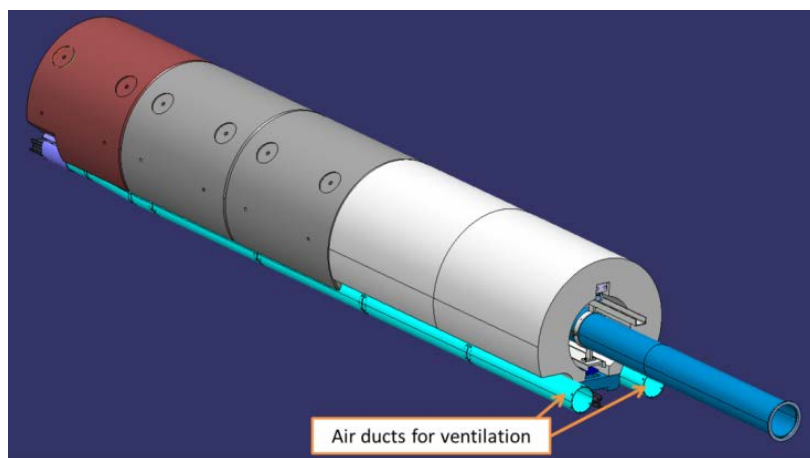
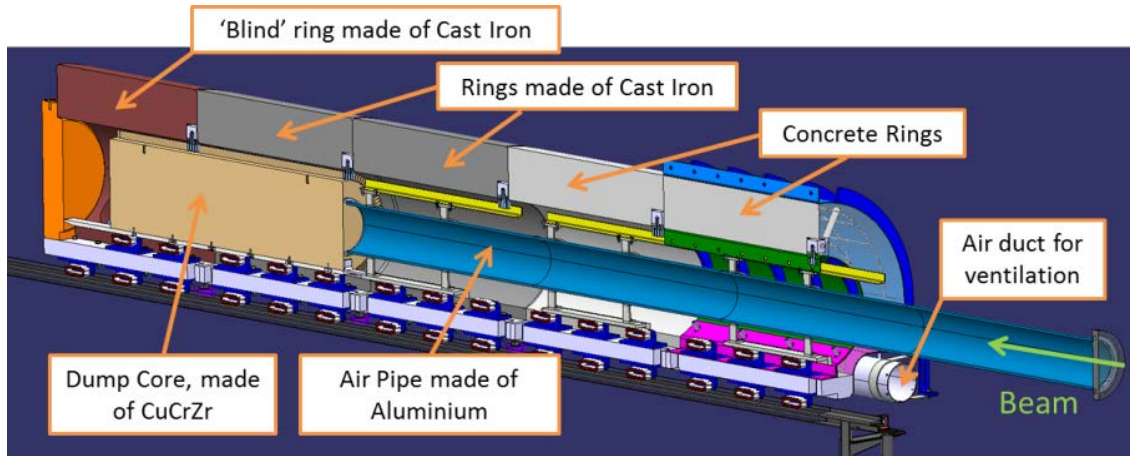


Fig. 3.158: Current PSB dump assembly (2013 to present)

The main beam loading parameters considered for the dump's design are summarized in Table 3.55. Some other design parameters and constraints, such as beam sizes at the dump core or the beam pulse structure are listed in the functional specification in Ref. [102].

During standard operation, it has been assumed that 10% of the extracted protons from the PS Booster will reach the dump. For commissioning periods, this value could temporarily increase up to 50% [102]. These constraints are already considered in the loading parameters presented in Table 3.55.

The beam dump has been designed for a lifetime of 25–30 years, excluding any further upgrade.

Table 3.55: PSB main dump design parameters for run 3 (after LS2)

Parameter	Value
Pulse current (A)	17.04
Pulse length (μs)	0.94
Average pulse period on the dump (s)	2.4
Maximum pulse intensity (proton/pulse)	1×10^{14}
Average power deposited in the dump (kW)	9.4

3.8.1.3 Vacuum and cooling

The beam dump, like the previous one, does not require vacuum conditions; beams will travel in air for about five metres—from the last beam-line element of the BTM line to the dump core. Nevertheless, in order to minimize the radiological impact, the activated air flowing along this path will be confined in a pipe, following radio protection experts' request.

The former beam dump, water-cooled by design, operated for the past two decades with no active cooling system, cooled only by natural convection with the air around it. The reason is that leakages in the water pipes were detected and could not be repaired, due to the difficulties in accessing the dump in such a constrained location.

Taking this past experience into account and, in order to opt for a much simpler and more reliable design, an active cooling system using air has been chosen for the new beam dump. Moreover, it complies with the recommendations from radio-protection experts, as air decay is much faster than that of water (tritium production)—see ‘Radiation Protection Constraints for the future PSB Beam Dump’ in Ref. [105].

As shown in Fig. 3.159, the cooling system is based on the intake of air from the PSB main ventilation channel, which is filtered, injected into two ducts that run inside the cavity under the shielding rings (see Fig. 3.158), and forced to flow around the dump core, cooling it from the back. The air is then expelled out of the cavity into the tunnel. The cooling parameters are summarized in Table 3.56.

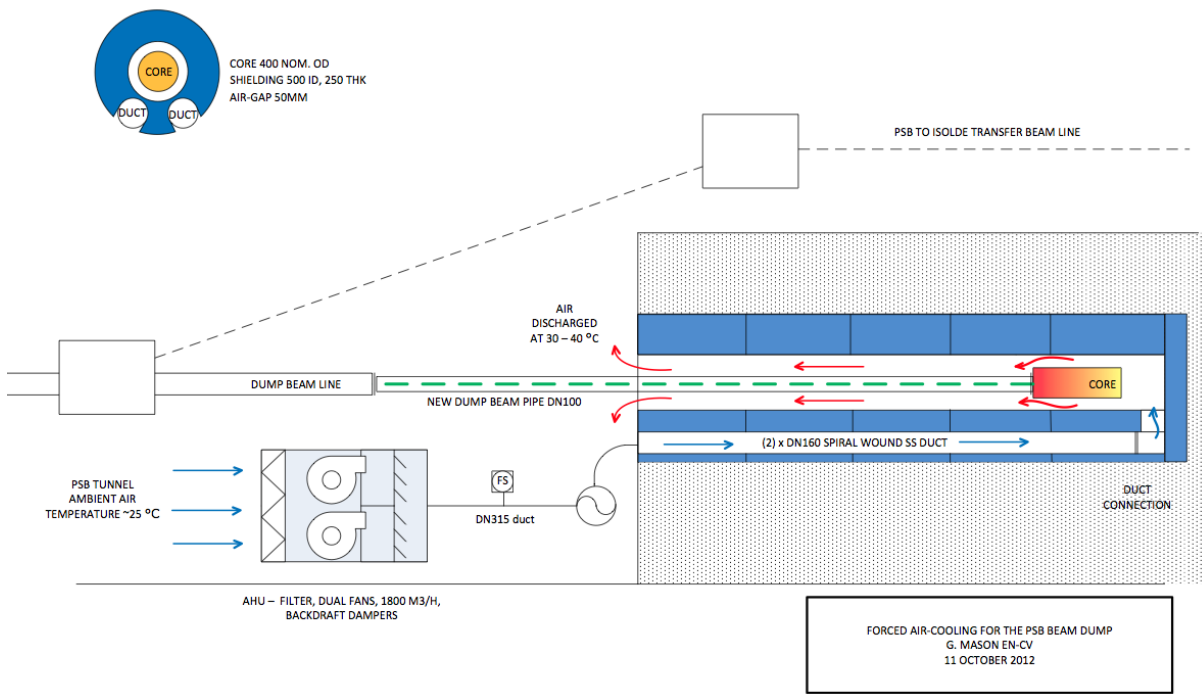


Fig. 3.159: Schematic of the cooling system for the PSB beam dump

Table 3.56: PSB main dump cooling parameters

Parameter	Value
Power to be extracted (kW)	10.7 ^a
Cooling system type	Forced air
Coolant working temperature (inlet) (°C)	20 (ambient temperature)
Nominal coolant flow (m ³ /h)	1800
Coolant temperature increase (estimate for the entire circuit) (°C)	17

^aThe power to be extracted is the sum of the power deposited in the dump core (9.4 kW) and in the shielding (1.3 kW)

The air handling unit (AHU) is composed of two independent fans, providing redundant operation in case of failure. All technical details are listed in Ref. [106].

3.8.1.4 Activation and maintenance

As described in Section 3.16, an assessment of the potential radiological hazards—arising mainly from the use of air as an active cooling system—was performed and it is available in Ref. [107]. The outcome of such assessment had the following consequences on the dump's design:

- a pipe (almost 5 m long) has been installed downstream of the last vacuum window, at the end of the BTM line, and runs up to the front face of the dump core (see Fig. 3.158). The aim is to minimize the radiological impact caused by the passage of the beam through air;
- the former shielding, in use since the early 1970s and composed of five concrete rings, was replaced by five new shielding rings. As advised by radio-protection experts, the three new innermost rings are made of cast iron, whereas the two outermost rings are made of concrete, in order to minimize the dose to workers by exposure during technical stops.

No maintenance is foreseen for the beam dump, due to its very difficult access and the high levels of radiation in its vicinity. Any maintenance work on the dump core would entail the partial

dismantling of the upstream BTM beam line, which would call for approval from an ALARA level III committee. An intervention to dismantle the beam-line elements would be very costly in terms of dose to personnel, in addition to the risk of repairing a highly active beam-intercepting device, such as the PSB dump.

On the other hand, the only element allowing repair is the AHU, being located outside the cavity, in an identified safe area beside the beam line, under the staircase towards the passage to ISOLDE—see Fig. 3.160.

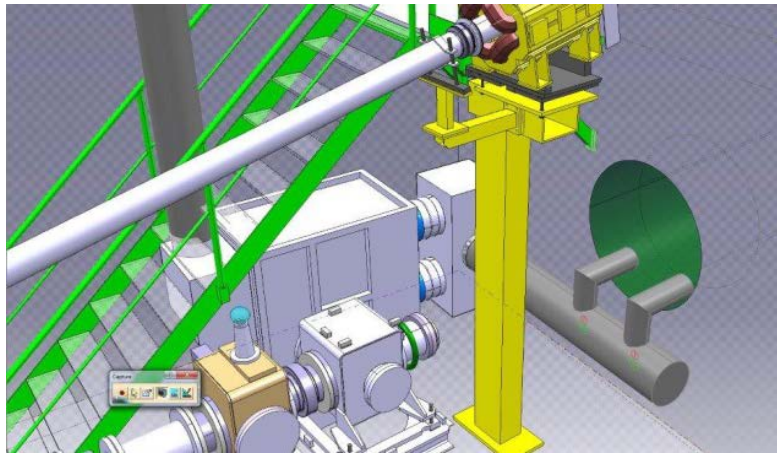


Fig. 3.160: AHU and air cooling ducts under staircase; beam dump cavity on the right; BTM and BTY beam-lines in the foreground.

3.8.1.5 Design and analyses

Design description

The beam dump core is a cylindrical block of copper alloy, measuring 1.5 m in length and 470 mm in diameter. In order to maximize heat exchange with the air flowing around it—and therefore optimize the cooling of the dump—thin fins have been machined longitudinally along its surface. The fins' final geometry is the result of an optimization study, involving computational fluid dynamics (CFD) simulations—this study can be found in Ref. [108].

Due to the manufacturer's size constraints, to guarantee the required material properties the dump core is split into three cylindrical pieces of equal diameters (see Fig. 3.161). These parts are held together by screws, exerting a force that has been calculated to ensure thermal contact. Details on these calculations are reported in Ref. [109].

As shown in Fig. 3.161, the front face of the dump core features two handles, to be used in the future for dismantling.

Five shielding rings surround the dump core, three of which are made of steel, whereas the other two are made of concrete. Their geometries are nearly the same, virtually covering the whole cavity (in width and length), but leaving a 30 mm gap between their inner diameter and the far end of the dump's fins, allowing for air flow.

Monte Carlo simulations [110] showed that irradiation of the cavity was beyond design parameters during the time that the previous dump was in use. Consequently, following advice on radiation protection, the far end of the cavity has been shielded and the new innermost shielding ring is therefore blind (see Fig. 3.158).

The upstream pipe, made of aluminium and nearly five metres long, has been manufactured in four equal sections coupled together. The reason for this is the possibility of disassembly without dismantling any of the elements of the optical line and avoiding cutting operations in a radioactive area—the distance between the last element of the optical line and the cavity is about 1.7 m.

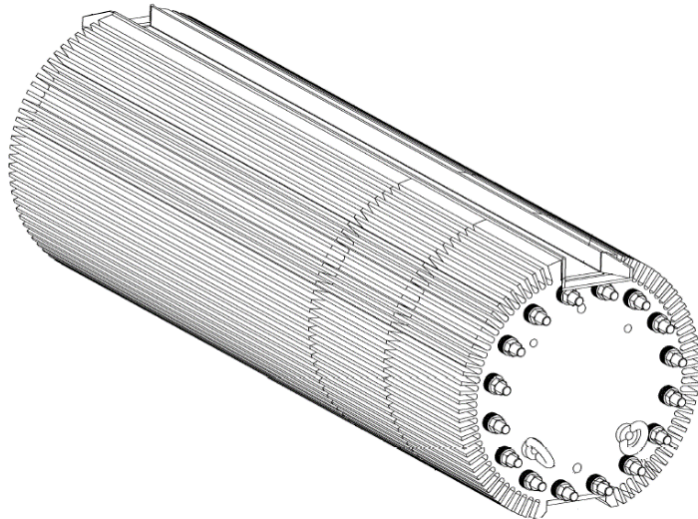


Fig. 3.161: PSB dump core (detailed view from technical drawing ‘PSB Main Dump Final Dump Core Assembly’, PSBTDE_0006).

Material choice

The dump core is made of a chromium zirconium copper C18150 alloy (CuCrZr), the main properties of which are listed in Table 3.57. This particular alloy has been selected for its high thermal conductivity (to dilute the incoming beam energy and evacuate the generated heat), its high density (to maximize efficiency and shielding), and its good mechanical properties at high temperatures (favouring long-term reliability) and for being corrosion resistant. The choice of material is also in line with radiation protection requirements.

Table 3.57: Dump core material properties (CuCrZr)

Property	Value
Density	8.94 g/cm ³
Young’s modulus	122 GPa
Yield strength	270 MPa
Tensile strength	450 MPa
Compressive strength	320 MPa
Maximum service temperature	300°C
Thermal conductivity	320 W/(m·°C)
Specific heat capacity	383 J/(kg·°C)
Thermal expansion coefficient	16.8 µstrain/°C

Thermo-mechanical behaviour under normal operating conditions

A complete thermo-mechanical analysis has been performed on the dump, in order to assess temperature and stresses during commissioning periods—i.e. the most restrictive conditions. FLUKA simulations [111] have served as the initial input to the analysis, providing a distribution of the energy deposited in the dump core and in its shielding after interaction with the beam (average power values are given in Table 3.57). In the second stage, CFD simulations have been used to model the forced-air

cooling, and were coupled with FEM thermo-mechanical analyses. As a result, temperature and stress maps of the dump and shielding have been produced—the outcome is presented in Figs. 3.162, 3.163 and 3.164.

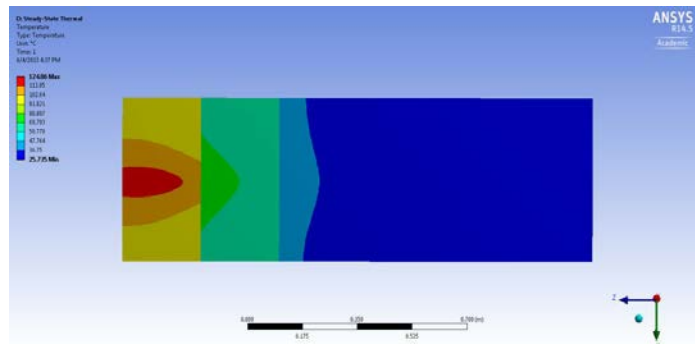


Fig. 3.162: Temperature profile ($^{\circ}\text{C}$) of dump core during normal operating conditions

A total power of 9.4 kW is deposited in the dump core, producing a temperature raise and leading to maximum temperatures of 134°C and maximum stresses of 94 MPa, both reached in the dump's front section.

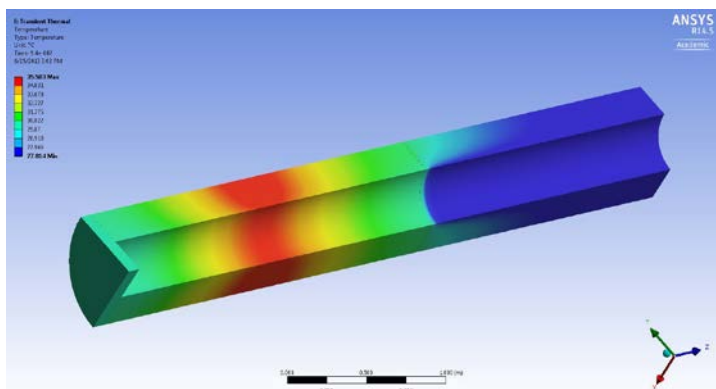


Fig. 3.163: Temperature profile ($^{\circ}\text{C}$) of shielding rings during normal operating conditions

Concerning the shielding rings, maximum temperatures of only 35°C and stresses of 1.8 MPa are reached, as a consequence of the 1.3 kW total deposited from the incoming beam (which are negligible when compared to the allowable values of the material).

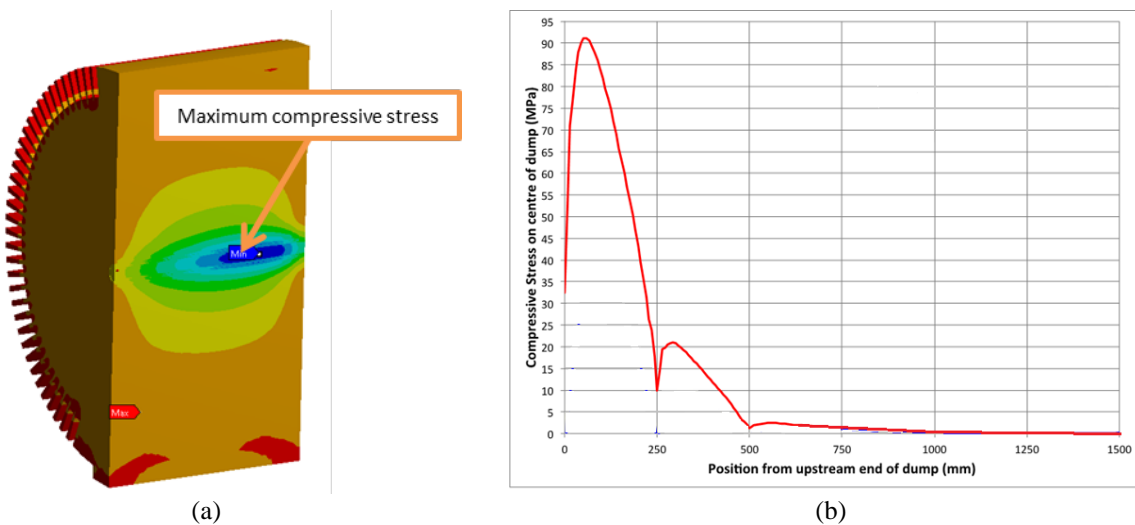


Fig. 3.164: (a) Distribution of stresses in the dump core's front section (250 mm in length); (b) compressive stresses along centre line of dump (MPa).

Two sets of analyses have been performed; the first (case 1) represents a desired scenario, assuming perfect contact at all times between the dump core's three sections; the second (case 2) represents the worst-case scenario, in which the spring washers holding the dump core together loosen, leading to a loss of thermal contact. The results of both analyses are compiled in Table 3.58.

Table 3.58: Maximum temperatures and stresses reached at dump core for both case studies

Value	Case 1 (normal operation)	Case 2 (failure of clamping system)	Limitations
Maximum operating temperature at dump core (°C)	134	153	Material's maximum service temperature = 300–350°C
Maximum (compressive) stress at dump core (MPa)	93	85	Material's compressive strength = 320 MPa

In both cases, the temperatures and stresses reached in the dump core are well below the material's limitations. For more information on the thermo-mechanical analyses carried out, see Ref. [112].

Thermo-mechanical behaviour of the dump core in accident scenarios

Two accident case scenarios—Involving failure of cooling system—have been analysed for the time span between LS1 and LS2. An average total power of about 2 kW has been assumed to reach the dump during this period, being consistent with the assumptions described in Section 3.8.2.2, Loading and constraints, i.e. 50% of the extracted beam from the PSB reaching the dump during commissioning periods.

Table 3.59 presents the results of both case studies, for which a significant reduction in the air flow has been considered, and compares them with nominal operation. In conclusion, even when the air flow becomes a ninth of the nominal flow, the temperatures reached in the dump core are lower than 200°C, which are well below the material's maximum service temperature (~300°C).

Table 3.59: Different case studies of cooling system failure

Case study	Cooling conditions	Dump maximum temperature (°C)	Air temperature (outlet) (°C)
Nominal conditions	Air flow: 1800 m ³ /h; Air temperature (inlet): 20°C	50	24
25% of nominal air flow	Air flow: 450 m ³ /h; Air temperature (inlet): 20°C	105	35
1/9 of nominal air flow	Air flow: 200 m ³ /h; Air temperature (inlet): 20°C	192	55

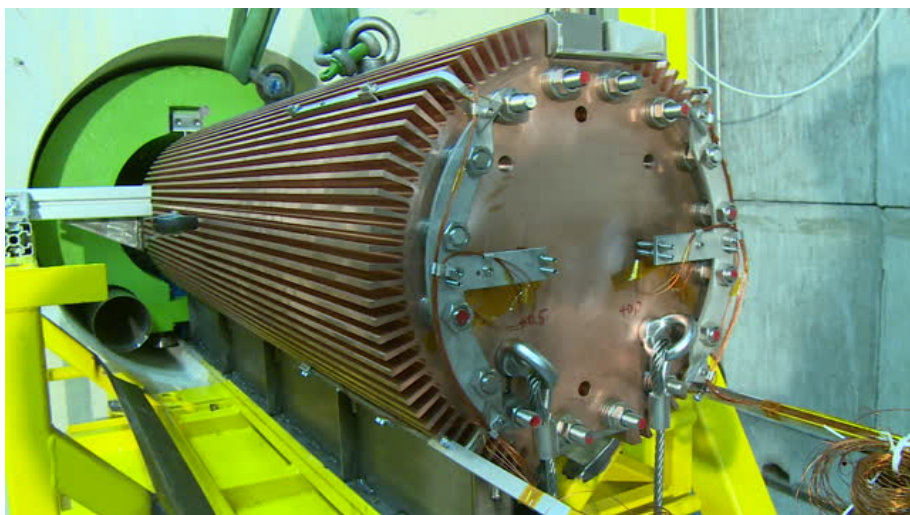
3.8.1.6 Installation

The installation of the new dump took place in October 2013 during LS1, as initially planned. The intervention involved the previous partial dismantling of the upstream BTM and BTY beam-lines, the extraction and disposal of the existing dump core and upstream pipe assembly and the five shielding rings. These elements were removed from the cavity, shielded in dedicated containers and safely transported to the ISR facilities, to be stored and eventually treated as radioactive waste. Following the disposal of the aged assembly, the cavity was inspected and decontaminated by radio-protection experts.

The actual installation started with the pre-assembly of the air ducts for ventilation, together with the new shielding rings. The assembly was later inserted into the cavity, making use of embedded rollers to glide it along a five-metre rail that runs lengthwise through the cavity. The rail is part of the former dump configuration, installed when the PS Booster started operation in the early 1970s. It has been preserved as a result of a structural analysis performed and an assessment on the admissible loads during insertion of the new components, see the report in Ref. [113].

Additionally, samples of concrete were extracted from the lower part of the front end of the cavity, in order to verify homogeneity in the material's composition and to ensure resistance. The results confirmed the structure's ability to withstand the new load—which is over 50% heavier than before.

Finally, the dump core was slid into the cavity, by means of sets of rollers that are embedded in the inner shielding ring (Fig. 3.165).

**Fig. 3.165:** Insertion of dump core inside cavity, October 2013

The actual intervention was carried out over a span of roughly four months, although it entailed a much longer preparation, ultimately including the approval from an ALARA level III committee. The series of meetings held during this preparatory procedure are compiled in Ref. [114].

3.8.2 Injection dumps

3.8.2.1 Introduction

Three new types of dumps are needed in the frame of the LIU Project for the injection of the 160 MeV beam from Linac4 to the PS Booster.

The first two are a pair of dumps that serve to intercept particles coming from the distribution of the Linac4 beam into the four rings of the PSB. During this splitting operation, two spur beams are generated, representing the head and the tail of the beam cross-section (Fig. 3.166), which have to be intercepted, also helping to protect the downstream distributor magnets. These dump blocks, hereafter called head and tail dumps, are integrated with the septum magnets as internal devices to the BI.SMV magnet tank, and share the vacuum with the circulating beam. The functional specification regarding these two dumps is in Ref. [115] while the technical specification is in Ref. [116]. There will be installed only one head dump and one tail dump and the drawings of the two are referenced in the CERN Drawing Directory CDD under the name ‘PSBTDI_00%’.

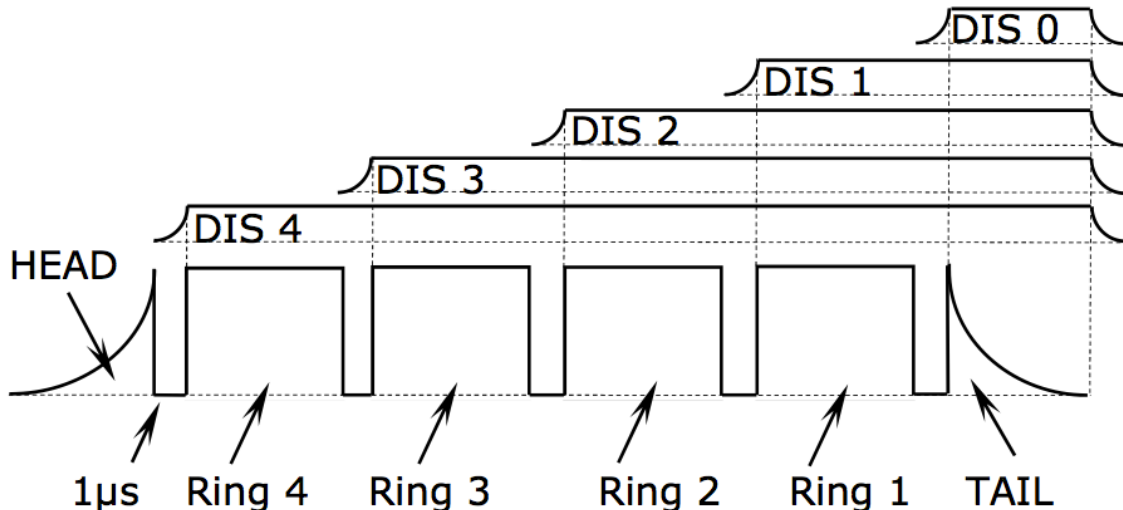


Fig. 3.166: Proposed Linac4 pulse structure (bottom) and BI.DIS timing (top) showing nominal operation with ~100 injected turns per ring [115].

The third dump is also an internal dump and is integrated with the BSW4 chicane magnet in the PSB injection region. This dump serves to intercept the unstripped H^0 and H^- particles that are generated from the stripping foil, due to its (very small) stripping inefficiency. Due to limitations in space, vacuum and activation considerations and due to electro-thermo-mechanical constraints, this dump is located outside and just after the BSW4 magnet but within its vacuum chamber, sharing the vacuum with the circulating beam. Due to radio-protection reasons, this dump is installed and uninstalled as a unique component together with the BSW4 magnet. The functional specification regarding this dump is also in Ref. [115] while the technical specification is in Ref. [117]. There will be four H^0/H^- dumps installed (one per PSB ring).

3.8.2.2 The head and tail dumps

Loading and constraints

These dumps are integrated into the BI.SMV septum tank assembly and are subject to the beam loading and constraints described in Ref. [115]. This beam loading is due to the splitting and separation of the Linac4 beam to match the four superposed PSB rings and is detailed in Table 3.60.

Table 3.60: Head and tail dump load cases

Parameter	Case 1: Accident	Case 2: Continuous	Case 3: Exceptional
Pulse current (mA)	40	0.5	20
Pulse length (μs)	400	50	20
Pulse repetition rate (Hz)	1.11	1.11	1.11
Maximum pulse intensity	1×10^{14}	1.56×10^{11}	2.5×10^{12}
Average beam power (W)	2841	4.4	71

The head dump is supported by the BI.SMV3 septum magnet, while the tail dump is positioned on BI.SMV1 (Fig. 3.167). The two dump cores are made of graphite R4550 and this choice has been driven by low activation requirements as well as constraints in maximum dimensions, low density, fast availability and price. Their longitudinal dimension is constrained by integration into the tank. The dimensions of the two dump cores are $108 \text{ mm} \times 40 \text{ mm} \times 200 \text{ mm}$ ($w \times h \times l$). The supports of these two dumps allow for a vertical positioning accuracy of about 0.5 mm.

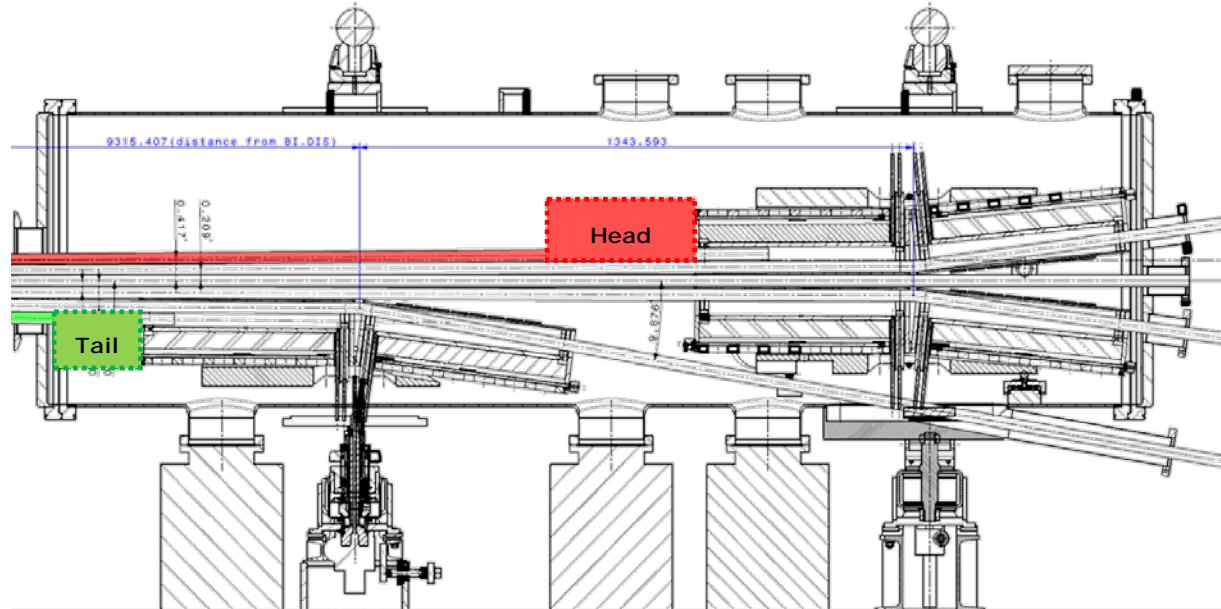


Fig. 3.167: Schematic layout of the BI.SMV magnets tank and of the position of the head and tail dumps

Vacuum and cooling

Both devices are internal dumps. To avoid high degassing in the continuous loading conditions (cases 2 and 3) an active cooling system is designed for the two dumps, to maintain the cores' maximum steady-state temperature always below 50°C. Also, an in situ bake-out system is integrated into the design and it allows a minimum of two baking cycles per year. The two dumps are cooled in series and the water-cooling circuit is designed according to the parameters reported in Table 3.61.

Activation and maintenance

No maintenance of the two magnets and of the two dumps is foreseen to take place in the tunnel; only when the BI.SMV tank is removed and brought to the surface.

Activation of the blocks is minimized by the choice of a light material for the core (graphite). Dedicated studies have been performed by DGS/RP, considering the dump cores as well as the surrounding environment and different scenarios for irradiation. These analyses and their results are detailed Section 3.16. The important results for the dump maintenance are reported in Ref. [118] and listed below:

- after 3 h (from the moment the beam is off), the magnet is the dominant source of radiation;
- the decrease of the dose rate slows down significantly after 3 h;
- expected dose rate at 1 m for case 3 is $<700 \mu\text{Sv/h}$ with 3 h cooling time after 1 week, and for case 2 is $<100 \mu\text{Sv/h}$ with 3 h cooling time after normal operation;
- tritium production in the water circuit remains at an acceptable level (4.6 kBq/year).

Table 3.61: Head and tail dump cooling parameters

Parameter	Value
Power to be extracted (W)	142 (2×71)
Cooling system type	External clamped piping Square external/round internal
Cooling pipe material	OFE copper UNS C10200
Minimum conducting internal cross-section (mm ²)	28
Coolant type	Water
Coolant working temperature (inlet) (°C)	25
Coolant working pressure (inlet) (bar)	7–10
Pressure drop in dump circuit (estimate) (bar)	0.2–0.35
Minimum coolant flow (l/min)	1.5
Nominal coolant flow (l/min)	2
Minimum–maximum coolant speed (m/s)	0.9–1.2
Coolant temperature increase (estimate) (°C)	5–10
Average water convection coefficient (estimate between 25°C and 30°C) (W/m ² K)	~6000

Design and analyses

Design description

The head dump comprises a graphite parallelepiped core that acts as an absorber of the beam. This is maintained, with the necessary gaps for thermal expansion in operation and during bake-out, within a 304 L stainless steel U-shaped support. On the top of this assembly, a copper counter-plate presses the copper cooling pipes against the graphite core, while a second copper plate clamps the bake-out heating system (Fig. 3.168).

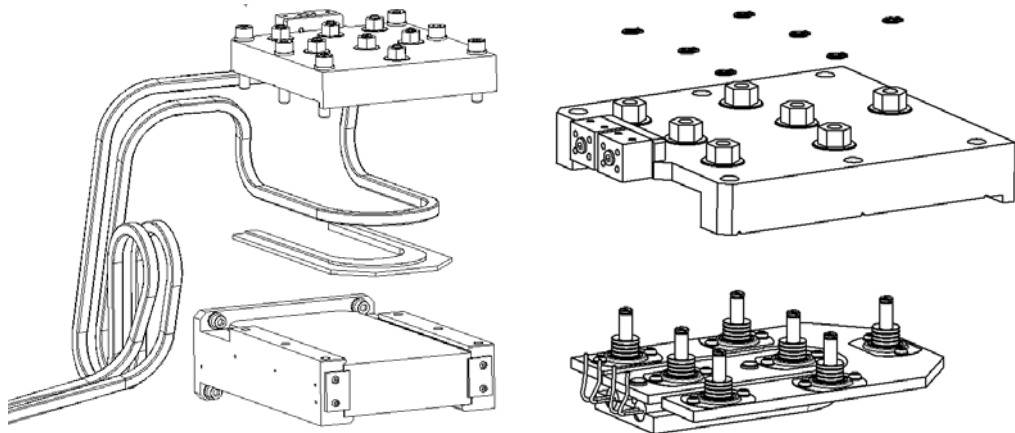


Fig. 3.168: Assembly of the head dump, details of clamping systems for the cooling channels and the bake-out system

The entrance and bottom surface of the dump are kept free for the beam impact. The whole head assembly is mounted on the front face of the BI.SMV3 septum magnet yoke, while the tail dump has exactly the same design but is mounted upside-down on the BI.SMV1 septum magnet (Figs. 3.169 and 3.170).

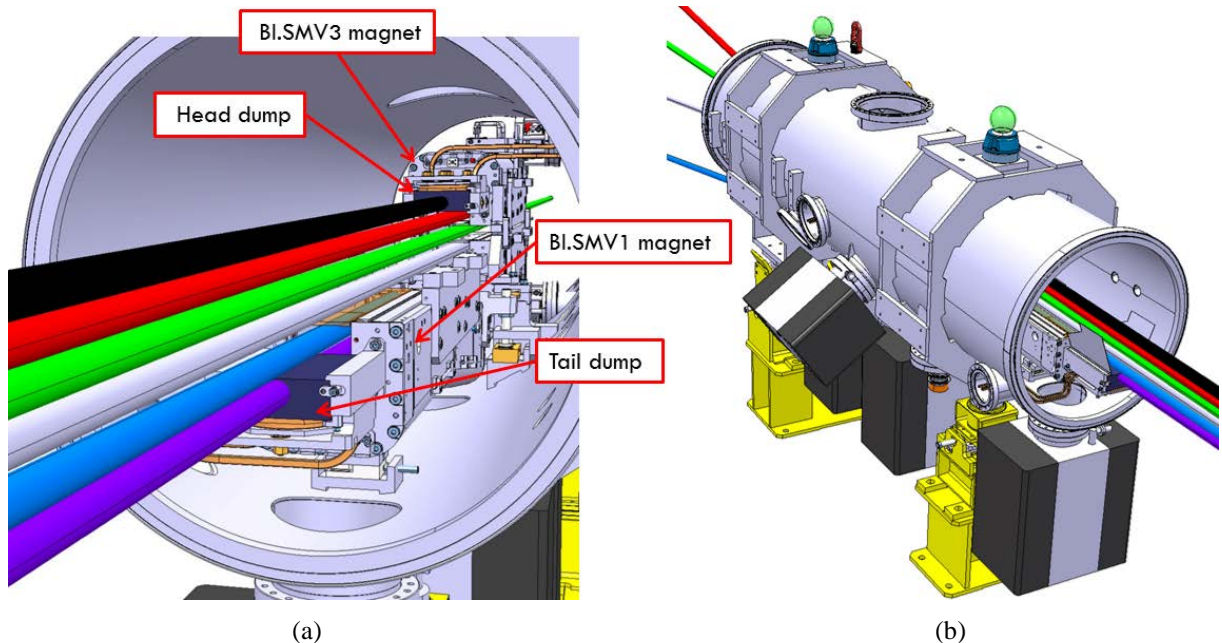


Fig. 3.169: Head and tail dumps within the BI.SMV magnet tank

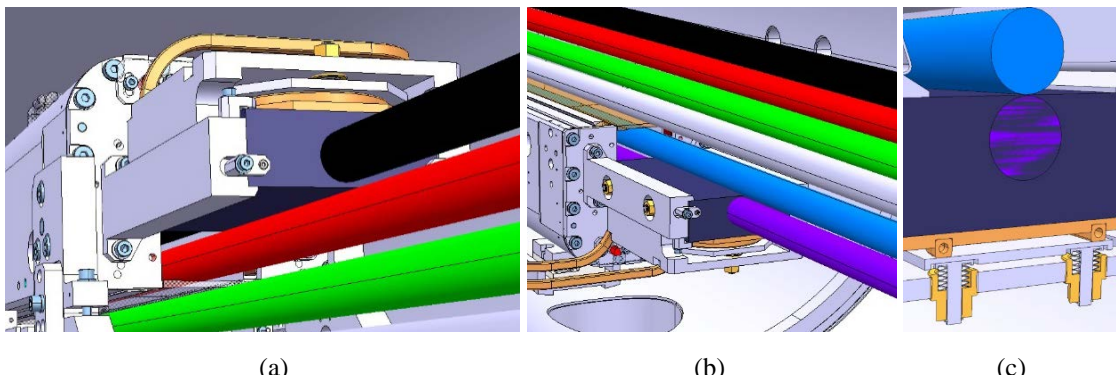


Fig. 3.170: (a) Detail of the head dump installed onto the BI.SMV3 septum magnet; (b) tail dump installed on BI.SMV1. (c) It can be noted that the circulating beam (in blue) ‘scrapes’ the upper surface of the tail dump.

In Figs. 3.171 and 3.172 the flanges used for dump maintenance and inspection, cooling pipes feed-through and electrical connexions can be seen.

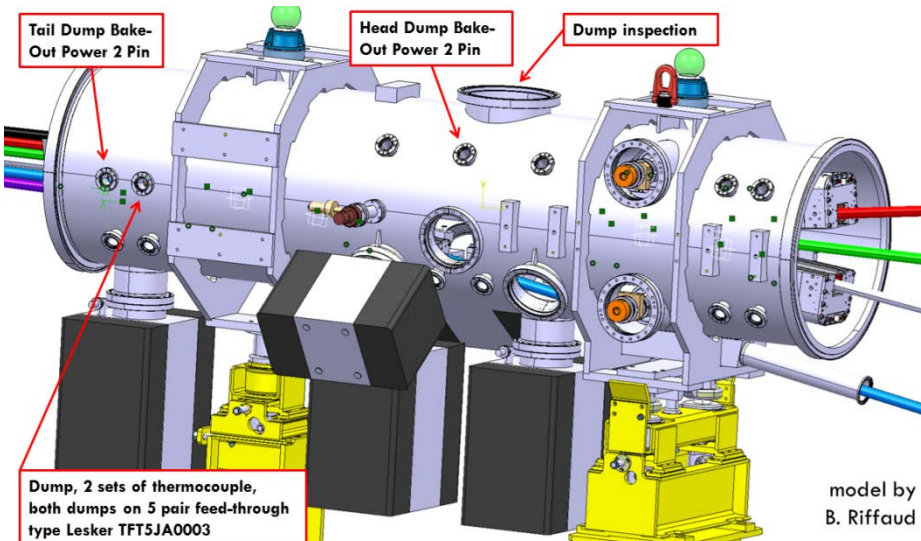


Fig. 3.171: Flanges on BI.SMV tank to be used for the dumps

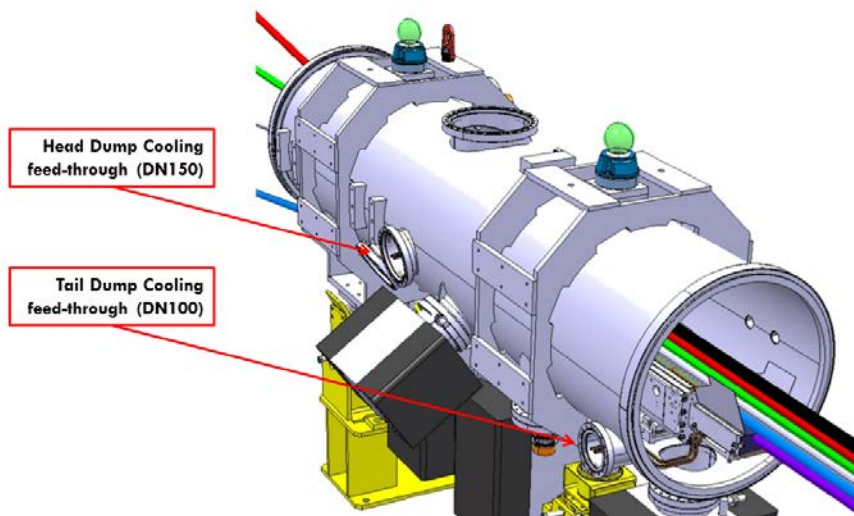


Fig. 3.172: Flanges on BI.SMV tank to be used for the dump cooling feedthrough

Thermo-mechanical behaviour of the dump core in an accident scenario

The model of the beam interaction in the dump was developed in FLUKA [111] and its output interpolated by ANSYS® for the thermo-mechanical analysis.

Fig. 3.173 shows the profile of maximum energy density deposited on the head dump core and the temperature rise at the end of one pulse, for the worst loading case. Results of the thermo-mechanical analysis are plotted in Fig. 3.174 and summarized in Table 3.62.

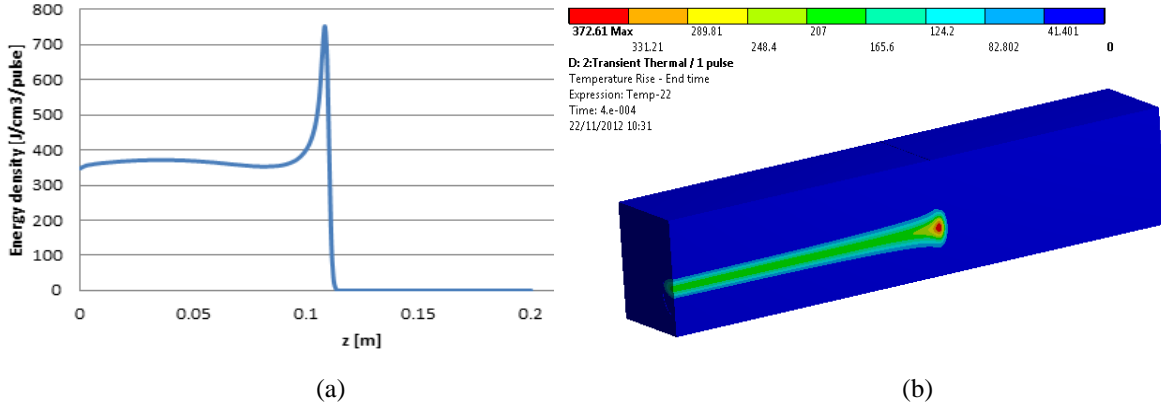


Fig. 3.173: (a) Profile of maximum deposited energy density in $\text{J}/\text{cm}^3/\text{pulse}$ during one pulse, loading case 1 (FLUKA), along the beam direction. (b) Temperature rise at the end of one pulse for loading case 1.

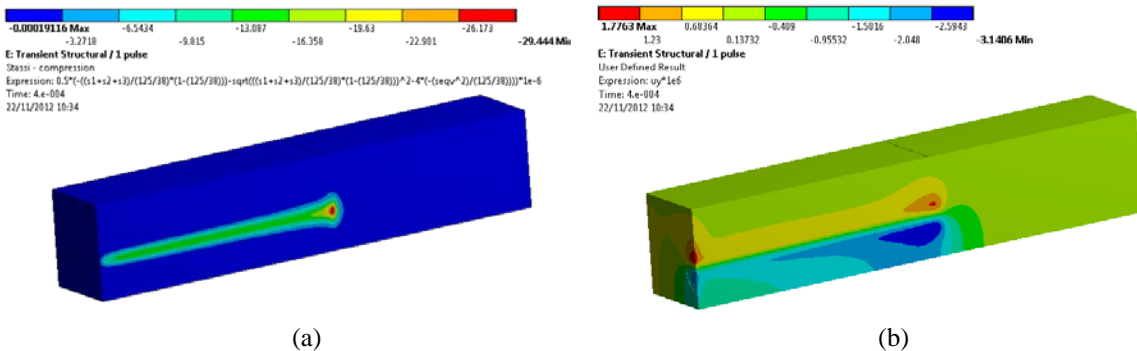


Fig. 3.174: (a) Stassi equivalent compressive quasi-static stress (MPa) in the head dump at the end of one pulse, loading case 1. (b) Approximation of the vertical deflection (μm) of the head dump core during one pulse, case 1.

Table 3.62: Head dump core maximum longitudinal elongation, maximum vertical deflection and maximum quasi-static equivalent Stassi compressive stresses.

Parameter	Case 1 ^a	Case 2 ^b	Case 3 ^b
Maximum surface temperature increase (K), no cooling	372.6	23	183
Maximum surface temperature increase (K), with cooling	372.6	1.1	18.2
Maximum longitudinal elongation (μm), no cooling	5.67	5.7	46.7
Maximum vertical deflection (μm), no cooling	-3.14	-4.831	-39.51
Maximum Stassi equivalent compressive stress (MPa), no cooling	-29.4	-8.85	-83

^aAt the end of one pulse only. ^bIn steady-state conditions.

Steady-state operation

A steady-state analysis has also been developed to evaluate the long-term behaviour of the core (temperatures and stresses after a few hours of irradiation when conditions are stable) as well as its

maximum longitudinal elongation and vertical deflection in nominally cooled operational conditions and also without water cooling (cooling failure scenario) for loading cases 2 and 3. Results are also summarized in Table 3.62. Results for the head dump with nominal active cooling are shown in Fig. 3.175. In all of these cases the steady-state temperature is found to be quite uniform over the whole of the dump core and no issues are highlighted. The same holds true for the tail dump.

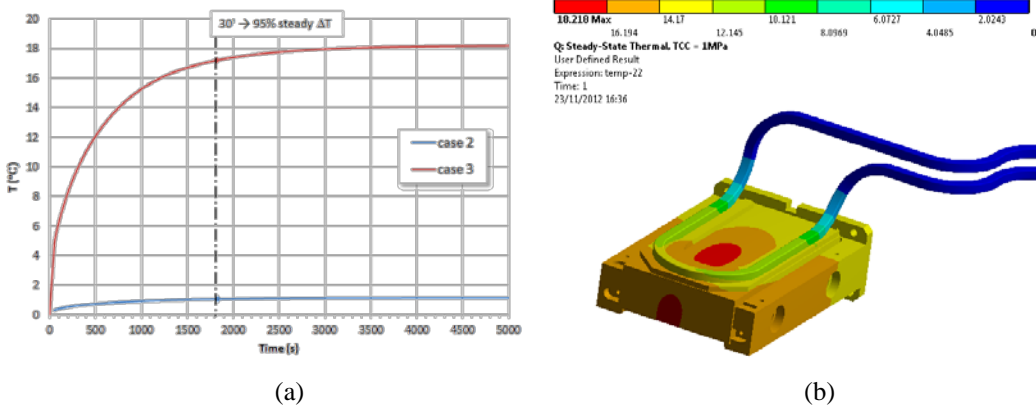


Fig. 3.175: (a) Transient increase of maximum temperature rise inside the dump core for the two continuous loading cases, with active cooling. (b) Steady temperature rise field in the head dump, case 3 with cooling.

3.8.2.3 The H^0/H^- dump

Loading and constraints

This dump is integrated into the BSW4 magnet assembly, in the new PSB injection region, and is subjected to the beam loading and constraints described in Ref. [117]. This beam loading is due to the unstripped particles coming from the upstream stripping foil unit, and is summarized in Table 3.63.

The dump sits outside and downstream to the BSW4 magnet, while remaining within its vacuum chamber. The dump indeed forms a unique assembly with the BSW4 magnet, and no dismantling or maintenance is foreseen taking place within the tunnel since the magnet itself serves to shield the ionizing radiation induced from the dump. Activities on this assembly are foreseen taking place only once the BSW4 magnet assembly is removed and brought to surface.

Table 3.63: H^0/H^- dump load cases

Parameter	Case 1: foil failure	Case 2: operational	Case 3: degraded
Pulse current (mA)	40	0.8	4
Pulse length (μs)	100	100	100
Pulse repetition rate (Hz)	1.11	1.11	1.11
Maximum pulse intensity	2.5×10^{13}	5×10^{11}	2.5×10^{12}
Average beam power (W)	710	14.2	71

The space allowed for the dump is longitudinally limited to 90 mm by the presence of the BR.BHZ11 dipole downstream. Hence a denser material has to be chosen with respect to the head and tail dumps. Also, the dump cross-section fully occupies the area defined by the envelope of the H^0 and H^- beams (80 mm \times 60 mm, $h \times v$) and does not result in an aperture restriction for the circulating H^+ beam.

Activation

The full activation study and radio-protection assessment are detailed in Refs. [119], [120] and [121] and reported in Section 3.16. The most important results for the H^0/H^- dump are:

- Future dose rates will be comparable to current ones in the PSB, with a collective dose of 2–5 mSv;
- The maximum individual dose is given by the replacement operation for the BSW4 magnet assembly; the dose is driven by the dump but results are within the requirements of a maximum of 2 mSv per person and per intervention;
- No intervention is foreseen to need an ALARA committee above Level 2.

The expected annual collective doses for different interventions are shown in Fig. 3.176. The calculation is based on various cooling times and for two materials (titanium alloy and silicon carbide).

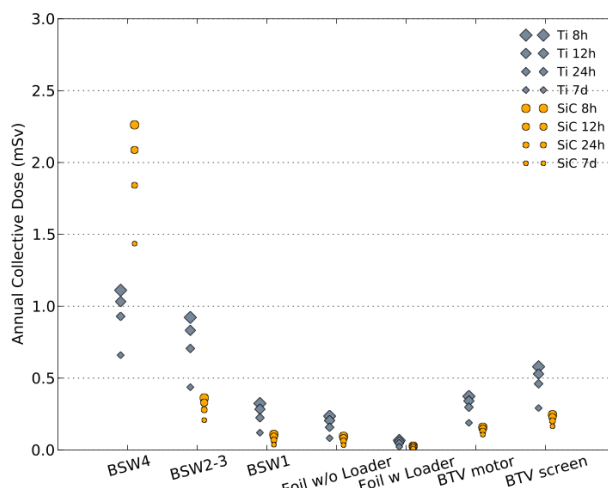


Fig. 3.176: Annual collective dose, in mSv, for several interventions within the new PSB injection region, for two different proposed dump materials (SiC ceramic and Ti alloy) and for several cooling times.

Vacuum and cooling

Due to space restrictions, it is not possible to integrate the dump with an in situ bake-out system, and the dump itself cannot be temporarily removed to do such a bake-out. This fact, together with other considerations, such as the degassing limit due to the presence of the stripping foil and the limited operational temperature of the BSW4 vacuum chamber and coils, forces the application of an active cooling system to maintain the dump at an acceptable steady temperature. The four injection dumps are cooled in series according to the parameters reported in Table 3.64.

Table 3.64: H^0/H^- dump cooling parameters

Parameter	Value
Power to be extracted, maximum average (W)	284 (4 × 71)
Cooling system type	External clamped square conduits
Cooling pipes material	Steel
Conduct internal cross-section (mm^2)	18
Coolant type	Water
Coolant working temperature (inlet) ($^\circ\text{C}$)	25
Coolant working pressure (inlet) (bar)	10
Minimum–maximum coolant flow (l/min)	1–2
Nominal coolant flow (l/min)	1.5

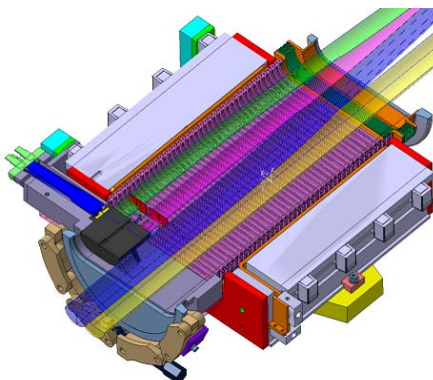
Parameter	Value
Minimum–maximum coolant speed (m/s)	0.76–1.51
Coolant temperature increase (estimate, whole circuit) ($^{\circ}\text{C}$)	5–2.5
Minimum–maximum pressure drop in dump circuit (estimate) (bar)	0.3–1.4
Average water convection coefficient (estimate between 25°C and 30°C) ($\text{W}/\text{m}^2 \text{ K}$)	4500
Required clamping pressure (bar)	10

Design and analyses

Each of the three load cases presented in Table 3.63 are very different to each other and none of them can be considered alone for the whole design of the dump. For example case 1 is considered for the quasi-static and dynamic studies of the structural integrity of the dump core, while cases 2 and 3 are considered for the estimate of the degradation of the material properties with time and for the analysis of activation.

Design description

The H^0/H^- dump comprises a 70 mm-long titanium core, which acts as an absorber of the beam and is shaped to cover the envelope of the two beams inside the BSW4 chamber. The dump is maintained in its position by a clamping support on a special stainless steel extension of the BSW4 vacuum chamber, between the chamber itself and the vacuum flange that connects the chicane magnet to the downstream BR.BHZ11 dipole. The dump is longitudinally positioned so that its entrance face is at a distance of 2 cm from the end of the BSW4 yoke end-plate and leaves a gap of a few millimetres to the vacuum chamber inner envelope (Fig. 3.177).



(a)

Fig. 3.177: (a) The inside of the BSW4 chicane magnet vacuum chamber and the internal H^0/H^- dump. The circulating H^+ beam is represented by the blue cylinder. The unstripped H^- particles will follow the green trajectory whilst the partially stripped neutral particles H^0 will impinge straight on the dump following the pink trajectory.

Outside this special extension, an additional, independent and detachable iron component acts as radiation shielding while a second incorporates the water conduits needed for the cooling of the dump (not represented in Fig. 3.177). There is no in situ bake-out system and no bake-out is foreseen for the dump before or after installation.

Finally, a current monitor is installed in front of the entrance face of the dump, allowing real-time measurement of the current due to the unstripped particles coming from the stripping foil unit (Fig. 3.178).

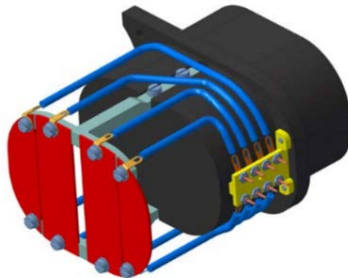


Fig. 3.178: The dump and current monitor. The plug-in system to allow easy assembly and connection of the dump with the monitor into its final position is also visible.

Material choice

After many iterations and tests of several candidate materials that would allow fitting the dump within the BSW4 magnetic field, titanium has finally been chosen. This choice also allows the possibility of positioning the dump outside the magnetic field. It also avoids a complicated bake-out system and many inconvenience and restrictions, such as a limitation of the lifetime, as would be the case with the use of ceramics or graphites.

The final material and specific alloy selection for the dump core has been driven by considerations such as space restriction, thermo-mechanical assessments, electrical compatibility with the environment, activation and vacuum constraints. Details of the selection are reported in Ref. [117]. The dump core, and possibly also its support, are made of an alpha-beta titanium alloy such as Ti₆Al₄V or, better, a beta-titanium alloy such as Timet® Ti-17 or Ti-10-2-3. All of the analyses and simulation results reported below have been done assuming the use of Ti₆Al₄V. The choice of one of the other beta alloys mentioned should only improve the results.

Thermo-mechanical behaviour of the dump core in an accident scenario

Fig. 3.179 shows the temperature field at the end of one pulse in the dump body, for the worst loading case (accident scenario). The resulting stress field at the end of the pulse for this load case is plotted in Fig. 3.180 while Fig. 3.181 shows the dynamic evolution in time of the maximum equivalent Von Mises stress inside the dump body, during the duration of the pulse. None of these analyses highlighted any problematic situation.

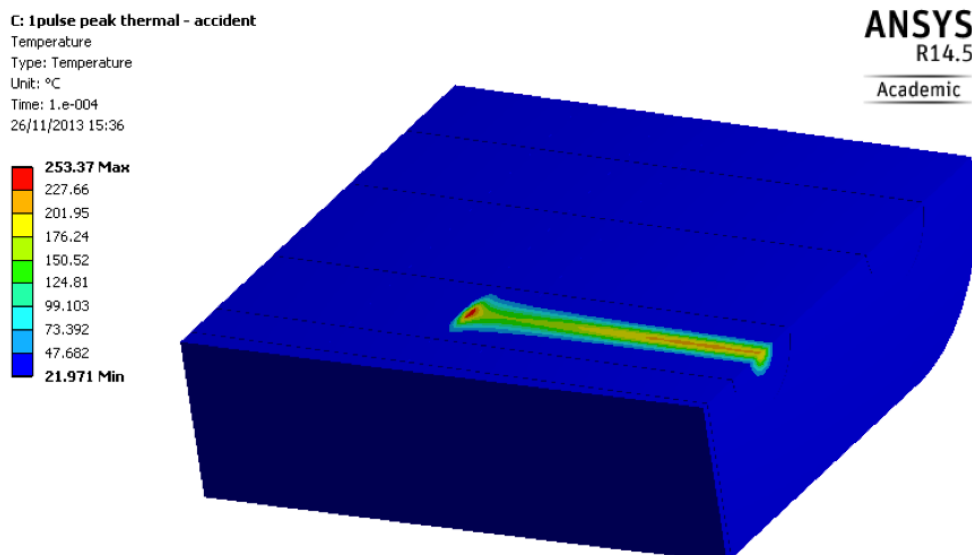


Fig. 3.179: Temperature (°C) of the titanium dump core at the end of one beam pulse for load case 1

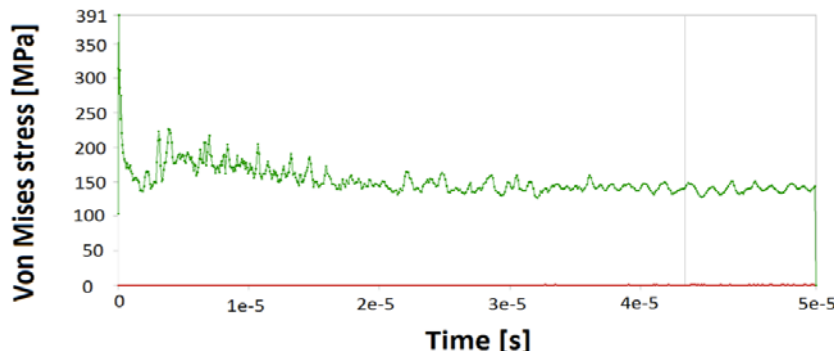


Fig. 3.180: Evolution of the maximum equivalent Von Mises stress in the dump core during a beam pulse of load case 1.

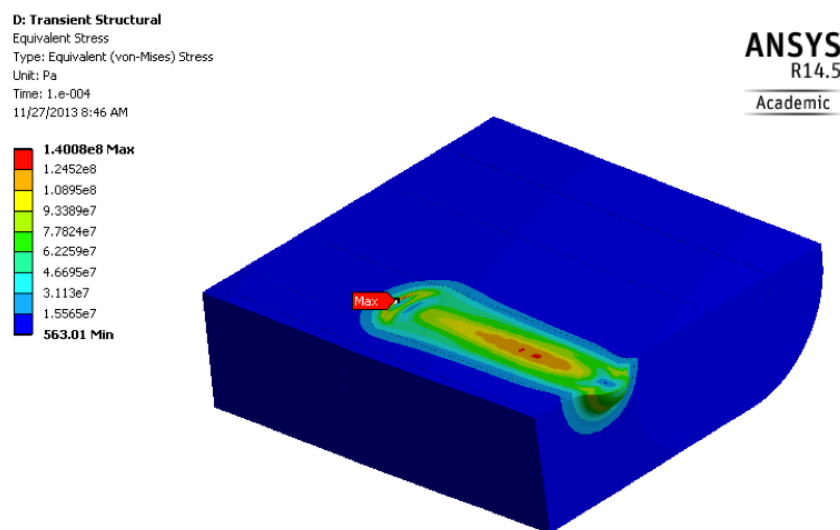


Fig. 3.181: Equivalent Von Mises stress field (Pa) in the titanium dump core at the end of one beam pulse for load case 1.

Steady-state operation

A steady-state analysis have been carried out to evaluate the long-term behaviour of the core (temperatures and stresses after a few hours of irradiation when conditions are stable) with nominal cooling conditions but also without water cooling (cooling failure scenario) for loading cases 2 and 3. The results are summarized in Table 3.65, where the maximum steady-state temperatures of all components are indicated for the various load cases. Results for the nominal load (case 2) with nominal active cooling are also shown in Figs. 3.182 and 3.183. In all these cases the steady-state temperature is found to be quite uniform for the components surrounding the dump, while the highest temperature gradient is concentrated within the dump core.

It has to be noted that due to the poor thermal conductivity of the components involved in the chain of heat evacuation from the dump to the cooling system, the cooling itself is not very effective and the assembly would meet the required temperature restrictions even without cooling. On the other hand, the steady-state temperatures found when the cooling is active are not the *maximum* temperatures reached in the assembly in operation: indeed, for the same reason as mentioned above, during the transient from the initial state to the final and steady state, the temperatures found are higher before the cooling starts to be effective (time delay due to the bad thermal conductivity of the parts involved) for a period of a few hours. This is clearly shown in Fig. 3.183.

Table 3.65: Summary of maximum steady-state temperatures of the assembly, for the various cases considered. Maximum transitory temperatures are indicated between brackets.

Component	Case 2 (°C)	Case 2, no cooling (°C)	Case 3 (°C)	Case 3, no cooling (°C)
Dump	45	51	122	151
Vacuum chamber	27	32	28	62
Vacuum flange	29 (34)	35	43 (56)	76

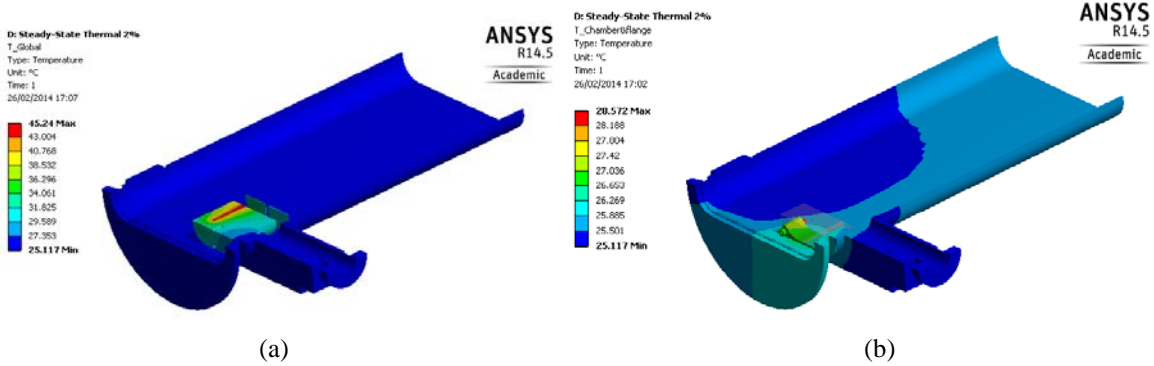


Fig. 3.182: Steady-state temperature distribution in the assembly dump, support and vacuum chamber for (a) load case 2 and (b) nominal cooling conditions.

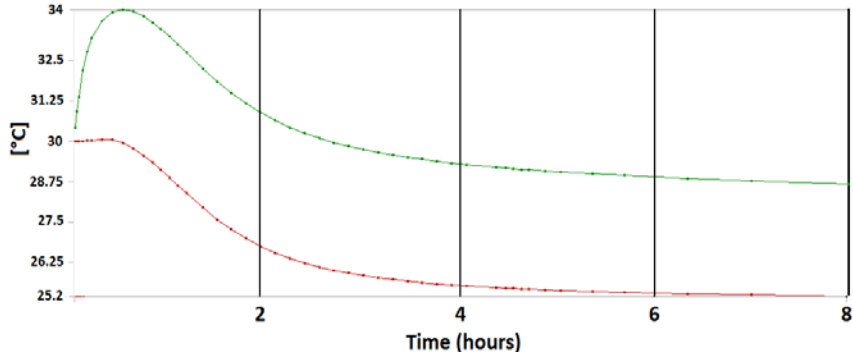


Fig. 3.183: Transient thermal behaviour (maximum in green and minimum in red) of vacuum chamber and flange for load case 2 and nominal cooling conditions.

3.9 Vacuum systems

3.9.1 Vacuum

A dynamic vacuum pressure in the range 10^{-8} – 10^{-9} mbar is required throughout the PSB machine, starting from the BI injection line to avoid beam loss due to residual gas.

The modified vacuum layout, i.e. the number, type, position and pumping speed of vacuum pumps and the position of sectorization valves, ensue from the requirement of guaranteeing ultimate pressure in the presence of a particular gas load. This gas load is estimated and not known in the new parts, as it follows from a certain number of unknown parameters, like cleanliness, material quality, etc. To ensure that the real gas load will be kept within the limits given by the layout, stringent specifications see Ref. [122] have been established and will be respected for the design, materials and treatments of components inside the vacuum volume of the PSB. Tests on individual items and global tests of vacuum vessels must then confirm compliance with the vacuum specification.

Vacuum controls ensure the safe operation of the ensemble and provide alarms for other systems, like the RF power and the septum magnets. A global consolidation of vacuum controls in the whole PS complex has been pursued for some years. The PSB itself has been completely overhauled with new vacuum controls, including the BI line as well as the extraction line to the PS, so modifications to the controls will only be required for new or displaced vacuum pumps and measuring devices.

3.9.2 Vacuum layout

The LIU-PSB vacuum system consists of the BI injection line inside the PSB tunnel, the PSB, the extraction line to the main dump and the injection line into the PS.

The LIU-PSB BI injection line is one vacuum sector with a total length of 25 m of beam tube; the last 10 m consists of four beam tubes in parallel giving a total of 55 m of beam tube. The PS Booster is separated into three vacuum sectors with a total length of 173 m per beam line. The PSB currently has a common vacuum system for the four beam lines. So to separate two vacuum sectors, four sector valves are required; the primary pumping, ion pumps, sublimation pumps and vacuum gauges are common for all four beam lines. The extraction line is separated into four vacuum sectors with a total length of 87 m. The reliability of the sector valves is very important, as the injection and extraction sectors have 12 sector valves per sector.

The existing PSB injection zone will be split into five new vacuum sectors by adding four new sector valves upstream of magnet BHZ162, and the four sector valves between sectors BR10 and BR20 will be moved upstream in front of magnet BHZ11 to allow for separate venting of the new H⁻ stripping foil mechanisms.

3.9.3 Vacuum equipment

The expected heavy gas load from the new horizontal septum magnets and the dumps inside the BI.SMH vacuum vessel will require a high pumping speed. To lower this gas load the magnets and dumps will be baked with an internal heating system before beam operation and the magnets and dumps will be water-cooled during operation.

There will be no modification to any vacuum chambers apertures except for the injection zone and in the BT.BHZ10 magnet. The new sizes of vacuum chambers are described in dedicated documents, see Refs. [123, 124]. Changes to any other vacuum chamber will be completed in the same materials and all vacuum tubes will have the same beam aperture as currently.

All vacuum sectors are equipped with separate pumping systems (turbo molecular pumps, ion pumps and titanium sublimation pumps), venting valves and vacuum gauges for each beam line.

The new injection sectors will be pumped by one common turbo-molecular pumping group down to 10⁻⁶ mbar using manual separation valves; and below this pressure separately pumped by sputter ion pumps.

All sealing systems in the PSB must be all-metal seals, and the vacuum clamps and flanges will be of the quick-connect type to minimize intervention time in activated zones.

The PSB is not a bakeable machine except for two septum magnets, which require a one-week bakeout after an intervention. Regular interventions are foreseen in the injector sector to change broken stripping foils. To minimize the start-up time after an intervention only non-porous materials and materials with a low outgassing rate similar to stainless steel will be used in the new installations in the PSB, see Ref. [122].

3.10 PSB extraction systems and PSB-PS transfer line

All systems from PSB extraction to PS injection, BT and BTP lines, and the PSB BTM measurement line need to transfer 1.4 GeV and 2.0 GeV beams after LS2. Hence, a 30% increase in the integrated magnetic fields for the 2 GeV beam, while keeping the available aperture for the bigger 1.4 GeV beam, is required in all lines after LS2. Equally, the power systems have to provide the range for the 1.4 GeV and 2 GeV beams. In case of hardware changes before LS2, 1.0 GeV beams also have to be transferred via the BT and BTM lines, and the BTY line for ISOLDE. The 1.0 GeV ISOLDE beams will be discarded after LS2.

3.10.1 Extraction and transfer line beam dynamics

A detailed description of the beam optics changes in the transfer lines is given in Ref. [125, 126].

The PSB extraction concept will remain unchanged when increasing the energy from 1.4 GeV to 2 GeV; the operational parameters of the extraction hardware will adapt to the increase in magnetic rigidity as described below. The same applies to the recombination kickers in the BT line. The recombination septa will have to be exchanged for longer magnets, implying a shift of the centre of deflection that can be rematched with the vertical correctors.

The switching dipole BT.BHZ10 will be replaced by a new magnet with a longer yoke, reusing the existing power supply. The dipole in the BTM.BHZ10 measurement line will be of a new design together with a new power supply.

Currently, only the BT line allows PPM of the hardware. Within the 2 GeV upgrade, the quadrupoles of the BTP line will be exchanged for a laminated design to provide full PPM capability for the PSB-to-PS transfer. This will allow optimizing of the optics for different beams, i.e. removing the horizontal dispersion mismatch for LHC beams that leads to emittance blow-up at PS injection and reducing the beam size for large emittance high-intensity beams to reduce losses during the injection process. Figure 3.184 shows the transfer line with horizontally matched dispersion at PS injection. In order to accomplish matching to the PS for three different optics scenarios, the present focusing structure is rearranged and an extra quadrupole added. The position of position monitors and correctors is adapted to the new quadrupole positions.

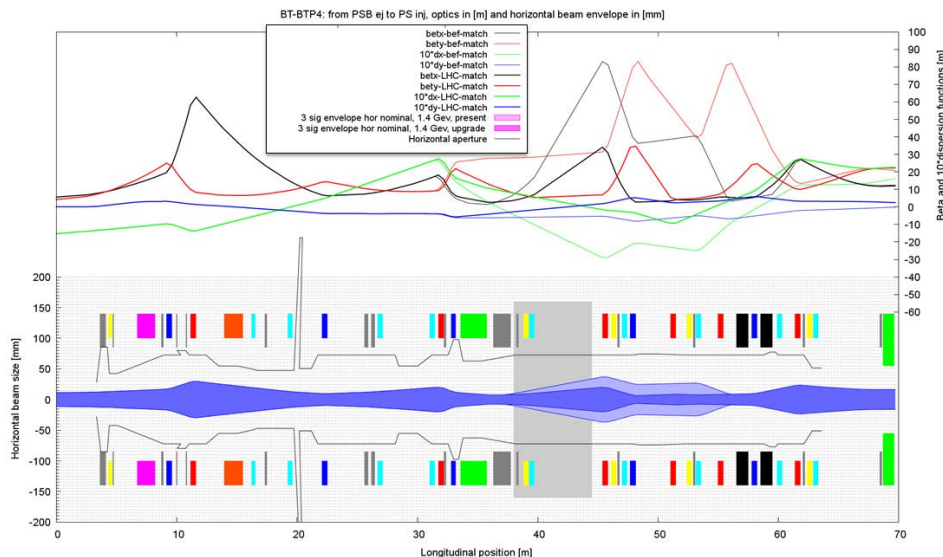


Fig. 3.184: Optics and horizontal beam envelopes for LHC beams from PSB extraction to PS injection

The maximum required quadrupole gradients can be reached for the last three quadrupoles in BTP without changing their length; the last two quadrupoles in BT and the first three in BTP have to

be increased in magnetic length from 466 mm to 570 mm. Also, the magnets with unchanged length will have new laminated yokes. The current inscribed pole diameter of 150 mm is sufficient for optics requirements.

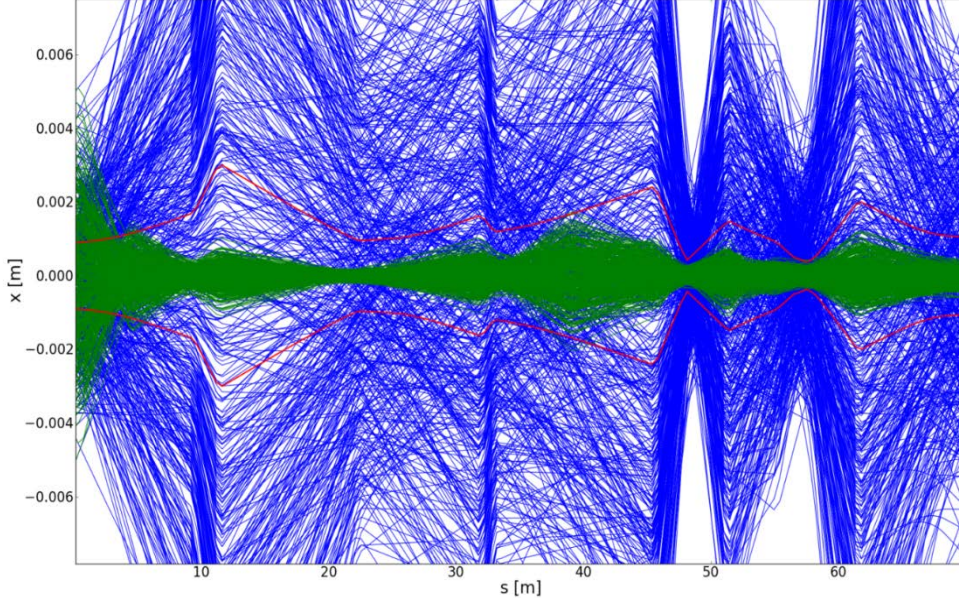


Fig. 3.185: Five hundred uncorrected (blue) and corrected (green) trajectories in the transfer line including misalignments and field errors. The maximum uncorrected trajectories peak at about 30 mm. The red line corresponds to the trajectory error taken into account in the calculation of the specified good field region in the magnets.

Trajectory correction studies have been performed with the error assignment shown in Table 3.66. The starting positions and angles were distributed according to the phase space distribution at PSB extraction. In the vertical plane there are many correction possibilities due to the recombination dipoles. In the horizontal plane, however, the trajectory correction performs sufficiently only when the extraction septum can be used as a corrector. It is envisaged that its implementation in the operational correction algorithm YASP will be tested in 2014. An additional pair of air-cooled steerers will be installed in the wall between PSB and PS zones as redundancy in case of failure of the one currently installed.

Table 3.66: Error assignment for trajectory correction studies

DS, DX ,DY 1 σ rms, cutoff 2 σ (mm)	DPHI, DTHETA, DPSI 1 σ rms, cutoff 2 σ (mrad)	Rel. error of integr. field along axis 1 σ rms, cutoff 2 σ
Quadrupole	0.2	1×10^{-3}
Dipole	0.3	4×10^{-3}
Corrector	0.3	4×10^{-5}
Monitor	0.3	

3.10.2 Extraction and transfer line systems

3.10.2.1 Booster extraction kicker BE.KFA14L1

The extraction kicker system consists of four delay line magnet modules pulsed in parallel for each Booster ring. The modules have 13 cells and are ferrite loaded with interleaved plate capacitors. They have a characteristic impedance of 25Ω and are terminated by a short circuit (Fig. 3.186).

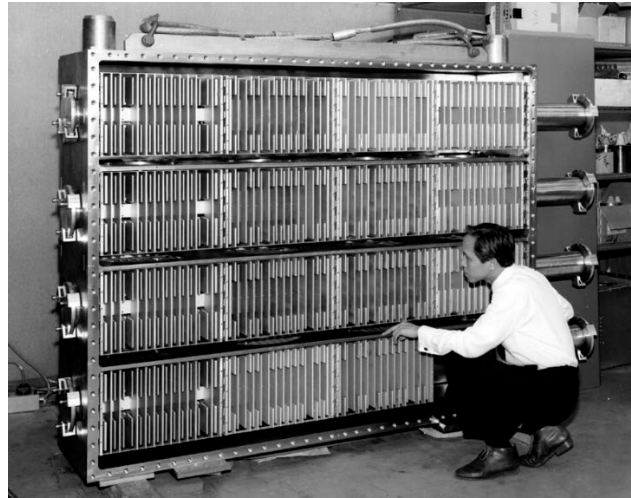


Fig. 3.186: BE.KFA14L1—16 kicker modules in a common vacuum tank

The pulse generator is mainly composed of a pulse forming line (PFL) discharged by a two-gap thyratron. A second thyratron acting as an inverse diode and a matched terminating resistor complete the generator to absorb negative reflections generated at the output of the magnets by the short circuit. The PFL is realized by four parallel-connected $25\ \Omega$ coaxial cables, which are filled with pressurized SF₆ insulating gas. At 1.4 GeV, the generators operate at 42.5 kV, with a maximum rating of 60 kV. The thyratron lifetime is more than ten years in the present working conditions.

In order to run at an energy of 2 GeV, the operating voltage will be increased to 55 kV, which only leaves a 10% margin relative to the maximum. The increased current will lead the magnet induction beyond the saturation of the ferrite yoke, which requires enlargement. In addition, it will increase the kick rise and fall time by about 5 ns. Table 3.67 summarizes the principal device parameters.

Table 3.67: BE.KFA14L1 extraction kicker magnet parameters for 1.4 GeV and 2 GeV

	Unit	1.4 GeV	2 GeV
Deflection angle	mrad		7.47
$\int B dl$	mT m	53	69
Effective length	mm		440
Gap height (<i>V</i>)	mm		70
Gap width (<i>H</i>)	mm		115
Operating voltage	kV	42.5	55
Kick rise time (1–99)%	ns	115	120
Kick rise time (2–98)%	ns	106	111
Pulse length (not adjustable)	ns		1500
Repetition rate	s	1.2	0.9

As an additional consequence, the magnets' reliability will significantly decrease and the production of a full operational spare becomes mandatory to avoid a long repair time in the event of failure. The thyratron lifetime will also decrease and will require extra maintenance.

3.10.2.2 Booster extraction septum BE.SMH

The present extraction septa BE.SMH (Fig. 3.187) use laminated steel magnet cores. The present magnetic field is around 0.35 T at the peak current of 7.2 kA. This design provides sufficient margin to increase the current to obtain the required field for operation with 2 GeV beams. A magnet block was successfully tested up to 11 kA, and the magnet behaviour is still sufficiently linear. However, the hydraulic circuit for the magnets will have to be modified so that the magnets can be cooled individually to cope with the additional heat dissipation due to the higher currents. The electrical series connections will need to be reinforced to withstand the higher mechanical loads as well as the increased rms current. The power convertor for this magnet is described in Section 3.6.

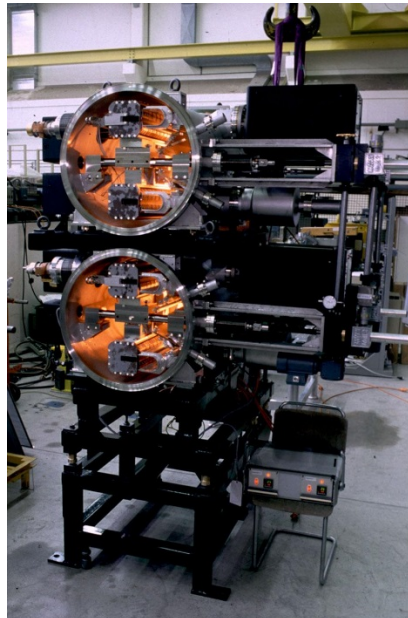


Fig. 3.187: BESMH with infra-red bake-out system activated

These modifications will be carried out on the operational spare magnet and, after this has been installed, the magnet removed from the ring will be upgraded. The exchange of the BESMH for its 2 GeV version can be planned for any shutdown that allows at least four weeks of access to the Booster extraction area, provided the radiation dose levels are acceptable. Table 3.68 summarizes the principal device parameters.

Table 3.68: BESMH extraction septa parameters for 1.4 GeV and 2 GeV

	Unit	1.4 GeV	2 GeV
Deflection angle	mrad	47	49
$\int B dl$	mT m	336	455
Physical length	mm		1000
Magnetic length	mm		949
Gap height (v)	mm		25
Gap width (h)	mm		78
Septum thickness (including magnetic screen)	mm		3.8
Yoke dimension ($h \times v$)	mm		130×120
Peak current (kA)	kA	7.0	9.6
Repetition rate (s)	s	1.2	0.9

3.10.2.3 Booster transfer septa SMV10

To maintain an acceptable lifetime and taking into account the high number of pulses annually, it is necessary to use longer magnets to achieve the required deflection at 2 GeV. Since the beam observation screen will be moved from the septum vacuum vessel to the adjacent vacuum chamber, the present vacuum vessels provide space for a 1300 mm magnet. Despite this increase in magnet length, it is expected that the lifetime of 2 GeV compatible septa magnets will nevertheless be reduced to four years. A new adjacent vacuum chamber will have to be designed and manufactured, to allow the installation of the beam observation system as well as the pumping group already installed in that area (see Section 3.7). Due to the increased yoke length, the vacuum is expected to degrade up to 25% with respect to present values, since the baseline design does not include changes to the vacuum pumping system on the septa vacuum vessels. Table 3.69 summarizes the principal septa magnet parameters. The power convertor for this magnet is described in Section 3.6.

Table 3.69: BT.SMV10 transfer line septum parameters

	Unit	1.4 GeV version	2 GeV version
Deflection angle	mrad	79.3	80
$\int B dl$	mT m	566	743
Physical length	mm	1060	1300
Magnetic length	mm	996	1224
Gap height (h)	mm	60.4	62
Gap width (v)	mm	102	116
Septum thickness	mm	5	5
Yoke dimension ($h \times v$)	mm	200×195	210×200
Peak current (kA)	kA	27.4	30.0
Repetition rate (s)	s	1.2	0.9

3.10.2.4 Booster transfer kickers KFA10 and KFA20 (recombination)

The KFA10 Recombination kicker system consists of two delay line magnet modules pulsed in parallel for each pair of Booster ring. The modules have 23 cells and are ferrite-loaded with

interleaved plate capacitors and speed-up saturating inductors. They have a characteristic impedance of 12.5Ω and are terminated by a short circuit.

The pulse generators are identical to those of the extraction kicker described in Section 3.10.2.1. At 1.4 GeV, they operate at 42.5 kV, for a maximum rating of 60 kV.

In order to run at an energy of 2 GeV, the operating voltage will be increased to 55 kV, which only leaves a margin of 10% relative to the maximum. The increased current will lead magnet induction beyond the saturation of the yoke, which is made from an old 4L1 grade ferrite with very low saturation, and is assembled with glue. The magnetic circuit will be entirely redone with a better grade of ferrite and without any gluing in order to improve vacuum performance.

The increased current will increase the kick rise and fall time by about 5 ns. The thyratron lifetime will also decrease and will require extra maintenance. Table 3.70 summarizes the principal device parameters.

As additional consequence, the magnets' reliability will significantly decrease and the production of a full operational spare becomes mandatory to avoid a long repair time in the event of failure.

Table 3.70: BT.KFA10 kicker magnet parameters for 1.4 GeV and 2 GeV

Parameter	1.4 GeV	2 GeV
Deflection angle (mrad) vertical	8.4	
$\int B dl$ (mT m)	60	78
Effective length (mm)	774	
Gap width (v) (mm)	53	
Gap height (h) (mm)	110	
Operating voltage (kV)	42.5	55
Kick rise time (1–99%) (ns)	105	110
Kick rise time (2–98%) (ns)	100	105
Pulse length (not adjustable) (ns)	1500	
Repetition rate (s)	1.2	0.9

3.10.2.5 Booster transfer septum BT.SMV20

This septum is used at slightly above its design current of 27.2 kA, which is equivalent to a deflection angle of 79 mrad (2010: 25.5 kA, 74 mrad). To maintain the estimated lifetime at present values, taking into account the high number of pulses annually, it is necessary to lengthen this magnet as well. The present vacuum vessel could provide space for the same 1300 mm magnet as used for the BT.SMV10, but the installed beam observation screen will be removed from the septum vacuum chamber. It is expected that the lifetime of the magnet will be around 4–5 years, depending on the number of pulses annually. A new adjacent vacuum chamber must be designed and manufactured, to allow the installation of the present beam observation system. Due to the increase yoke length, the vacuum is expected to degrade by up to 25% since the pumping speed on the septum vacuum vessel is not planned to be modified. Table 3.71 summarizes the principal septa magnet parameters. The power convertor for this magnet is described in Section 3.6.

Table 3.71: BT.SMV20 transfer line septum parameters

Parameter	2 GeV version
Deflection angle (mrad)	79
$\int B dl$ (mT.m)	734
Physical length (mm)	1300
Magnetic length (mm)	1224
Gap height (h) (mm)	62
Gap width (v) (mm)	116
Septum thickness (mm)	5
Yoke dimension ($h \times v$) (mm)	210×200
Peak current (kA)	39.6
Repetition rate (s)	0.9

3.11 Controls

The LIU for PSB involves work to be carried out by the BE-CO group as part of their daily work. But BE-CO does not foresee any upgrades/updates triggered specifically by/for LIU PSB. BE-CO will handle the requests by the equipment groups to follow their upgrades that, for example, could be installation of new FECs, providing additional timings or OASIS signals as required as part of their daily work. In fact, for that reason there is no funding allocated for these upgrades and we cannot provide detailed planning until the equipment groups know what they need and make their requests.

3.11.1 Upgrade of hardware platform for front-end computers

The operating system LynxOS has for a long time been marked as being obsolete. As a replacement, CERN is now using Scientific Linux in versions 5 and 6. As the latter is also available as a 64-bit version, CO started to move to 64 bit systems as well. The support missing for 64-bit CPUs of the existing old systems made it necessary to update the hardware.

An additional constraint on the selection of the new hardware system has been the availability of systems in 2U format for easy replacement of the existing systems. The new system had to support PCI slots for existing and new hardware cards and the availability of ATM for remote control and reboot.

With Kontron and KISS computers, CO is now using modern, stable and economically priced hardware and is prepared for the coming years. During LS1 and the ACCOR project, ~500 systems have already been replaced or added. About 50 systems are still scheduled to be renovated.

With this base, CO is prepared for upcoming demands from equipment groups for the LIU project.

3.11.2 Timing network

The timing distribution of the accelerator complex has seen some major upgrades carried out. All major upgrades have been completed; only minor issues are left for correction. No larger work is foreseen considering LIU.

On the hardware side, most of the old and obsolete TG8 timing cards in the FECs have been replaced by CTRV/CTRI. Not only have the front ends been renovated, but also the main servers providing central timing. The hardware has been upgraded to the new Kontron-based systems, and at the same time moved from LynxOS to Scientific Linux; timing devices have been moved from GM/FESA2 to FESA3.

In order to provide support for the new timing environment, the old TIMLIB (a library that provided connection to hardware timing receiver through a driver (the ctr or tg8 drivers)) has been replaced by LIBCTR and TGMLIB by TIMDT. (TGMLIB is a library providing access to telegrams with some history. Some access could be made through TIMLIB, but also through DTM for FECs without ctr or tg8.)

As the devices for central timing have been migrated to FESA3, the local timings (LTIM) have also been partially migrated to FESA3. LTIM is now available either in the old FESA2 style but also in FESA3 for 32-bit and 64-bit operating systems.

Another important point for PSB is that the AD timing network has been separated from the PSB timing network. This means that timing events for AD are no longer distributed on the PSB network.

3.11.3 Drivers

As a solid base for future driver development, CO has also moved from LynxOS to Linux, providing drivers for 32-bit operating systems and is also ready for 64-bit operating systems. Along with the migration to Linux, the recent tool for generation of drivers, driverGen II, has been replaced by a new tool, encore. This new tool is already heavily used by the equipment groups.

To provide a cleaner versioning scheme for drivers, the deployment scheme has been adapted to the CO standard of having a common versioning and deployment location of the driver libraries.

On the hardware side the FMC architecture has been developed. Based on Mezzanine cards it provides a new platform for the development of custom hardware.

To guarantee stable up-to-date FEC, a hardware configuration check tool has been developed and deployed. The tool is already used during runtime to determine if all of the drivers and firmware on the FEC comply with a valid version.

3.11.4 Control software framework

While there are still devices based on GM (the predecessor of FESA2) development had been started on renovating the FESA2 framework. These efforts led to the stable first release of the FESA3 framework. The latest release now available is 1.3.1. This version is available for the new 32-bit and 64-bit operating systems and is already used for operational devices.

FESA3 now uses a completely new tool chain. The central part is the open source development framework Eclipse. It is accompanied by SVN, which replaces the old and obsolete CVS used by FESA2 and by a new plugin that supports the necessary development steps.

The plugin is used to provide editors for all of the development stages and documents either in a XML source view or in a graphical XML editor mode. Additional buttons added to Eclipse by the plugin allow checking and generation of the FESA sources and makefiles. The sources can be compiled locally and deployed by the plugin and stored in the controls configuration database (CCDB) as well as in a version control system. The devices can be declared inside Eclipse and exported to the database. Adding new devices using this framework from a software point of view has become quite easy.

Given the new, more powerful, hardware, it is very likely that there will be no further action to be taken by CO when adding new hardware devices or software.

Development for FESA3 will continue and has already led to a second major version (FESA3.2), which is also already in production. The main change compared to FESA3.1 is the use of the newly developed transport protocol RDA3, provided by the middleware team.

3.11.5 Controls configuration database (CCDB)

The Controls Configuration Service (CCS) provides a collection of processes, tools and a common repository for all configuration data (a relational database) to provide configuration management facilities for the controls system for all CERN accelerators.

There have been numerous developments to enhance the service and to provide new functionalities driven by the requirements of the Renovation of the Controls of the Injector Chain Project. A new process was designed and implemented for the renovation (migration) of the software controls devices from one framework to another (e.g. GM devices migrations) and a dedicated user application provided to support this process. At the time of writing (July 2014) around 7000 devices have been renovated. In addition to the renovation of the devices stored in the controls configuration database (CCDB), improvements have been implemented in order to achieve smooth upgrades of the controls system through the propagation of configuration data from CCDB to other databases such as LSA/InCA DB, Layout, etc.

Other major developments in CCS related to the renovation of the injectors include the renovation of the hardware configuration domain (software and hardware configuration of FECs, drivers, etc.). Highlights in this area include the introduction of an operational support model for the FECs as well as improvements in the responsibility model, providing additional functionalities for drivers and hardware module configuration.

New functionalities currently under development are related to correlating configuration data with maintenance management data from the controls configuration and Infor (MTF) systems in order to help the controls installation team and the people in charge of equipment maintenance activities.

3.11.6 CMW, work on the middle tier

During LS1 the CMW team renovated the existing middle-tier-based RDA2 based on CORBA (which became an obsolete technology) and provided a replacement called RDA3. The most important new features are:

- a new generation of the CMW core communication infrastructure (client and server, Java and C++);
- integration of open-source transport library ZeroMQ (RDA2 used CORBA, which became an obsolete technology);
- improved scalability and performance for asynchronous calls and subscriptions (measured with timing team and internal tests).

RDA3 already triggered a lot of work related to integration with other middleware services and libraries, namely:

- new JAPC extension: jpc-ext-cmwrda3;
- integration with RBAC libraries;
- integration with the directory service;
- integration with the proxy infrastructure.

RDA3 is now operational with FGC gateways (PSB, LEIR, SPS), CGAFG (function generation), CGDIO flavours (digital input/output) (PSB, CPS, AD) as well as several other FESA3 classes of equipment groups (e.g. PowM1553 in AD and LEIR). The latest stable version of RDA3 is 1.0.1, which is also already used by FESA3 v. 2.0. There are currently no blocking points nor critical issues for operations related to RDA3.

Further work will comprise finishing the development and integration of the new proxy infrastructure needed for old RDA2 clients (which cannot migrate to RDA3), which have to connect to the new RDA3 servers. This also requires several extensions in the directory service.

3.11.7 InCA/LSA

After 10 years of experience with the existing and mature LSA APIs, it was time for a bigger refactoring to simplify and unify the APIs to make them simpler to use.

At the same time also the backend was renovated. The InCA servers have been improved so that now all communication (SET, GET and MONITOR) go through InCA. Before LS1 only SET always went through the server. For GET and MONITOR only a small subset of all devices/properties went via the InCA server. This reduces significantly the load on the FECs and network traffic, and therefore speeds up communication.

This improvement becomes very obvious and visible when opening working sets. While it took 5–15 s (or sometimes even much longer) this time has been reduced to 2–3 s.

In collaboration with CCS, the configuration of working sets and knobs has been moved from CCDB to LSA DB. Configuration data is now only kept in LSA DB. Before LS1 it was partially in CCDB and partially in LSA DB. Finally, tools have been implemented to configure content of working sets and knobs in a much more convenient way than as previously with the CCDB web tool.

3.12 PSB upgrade electrical infrastructure

3.12.1 Introduction

This document describes the modifications to the electrical network required by the PSB Energy Upgrade project. The feasibility study for the entire project, released in 2010, also included some preliminary requirements for the electrical infrastructure [127].

The present document focuses on the technical requirements; the planning and budget will be detailed in a following project note.

This document is based on data provided by users via meetings and emails. The users should provide a project note describing their requirements, such as the single line diagram of the low voltage distribution, to enable finalization of the technical design.

A new building, shown in Fig. 3.188, will host the power converters, together with the related auxiliary equipment. In addition, the new building will also host the new cooling and ventilation plant for the Booster magnets, which will replace the plant currently in service.

The modifications of the electrical infrastructure will also take into account the studies for the consolidation of the high voltage electrical network for 2025 [127]. The working principles of the autotransfer system for the Meyrin network and PSB complex are described in Ref. [128].

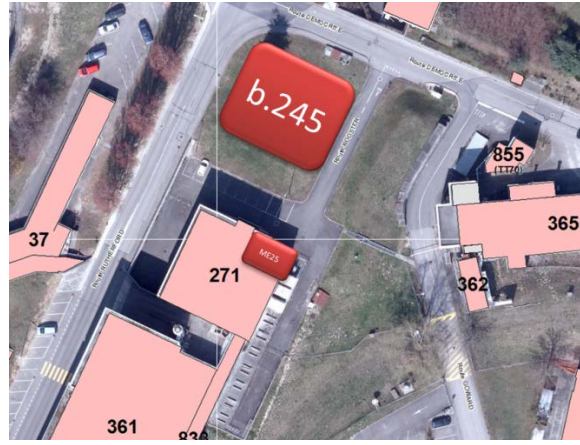


Fig. 3.188: Location of new building 245

3.12.2 Power requirements

The power requirements, communicated by the users, are summarized in Table 3.72. An additional margin, not included in the values below, will be taken into account.

As mentioned in the previous section, users should provide a technical note describing the loads and their characteristics.

It can be noticed that the cooling and ventilation loads are divided in two parts: the first, related to building 245 is considered to be general services; the second, related to the cooling of the Booster magnets, is considered as machine network.

Table 3.72: Power requirements

Type of network	User	Power [kW]	Comment	Reference
Machine	EN/CV	135	Water cooling and towers, buildings 237 and 245	M. Obrecht 19/03/2014
Machine	TE/EPC	392	Auxiliaries	F. Boattini 22/11/2013
Machine	TE/EPC	6750	N.3 transformer 2.7 MVA (two at 100%, one at 50%)	F. Boattini 22/11/2013
General services	EN/EL	70	Lights, sockets, OH crane, building 245	F. Boattini 19/03/2014
General services	EN/CV	153	HVAC, building 245	M. Obrecht 19/03/2014
UPS	TE/EPC	15	Auxiliaries that need UPS	F. Boattini 22/11/2013
Safety	EN/CV	8	Smoke extraction	M. Obrecht 19/03/2014
Safety	EN/EL	25	Emergency light, fire detection	F. Boattini 22/11/2013

3.12.3 PSB complex: HV electrical network

3.12.3.1 Status in 2013

The Booster complex is supplied from electrical substation ME25, located in building 271, as shown in Fig. 3.189.

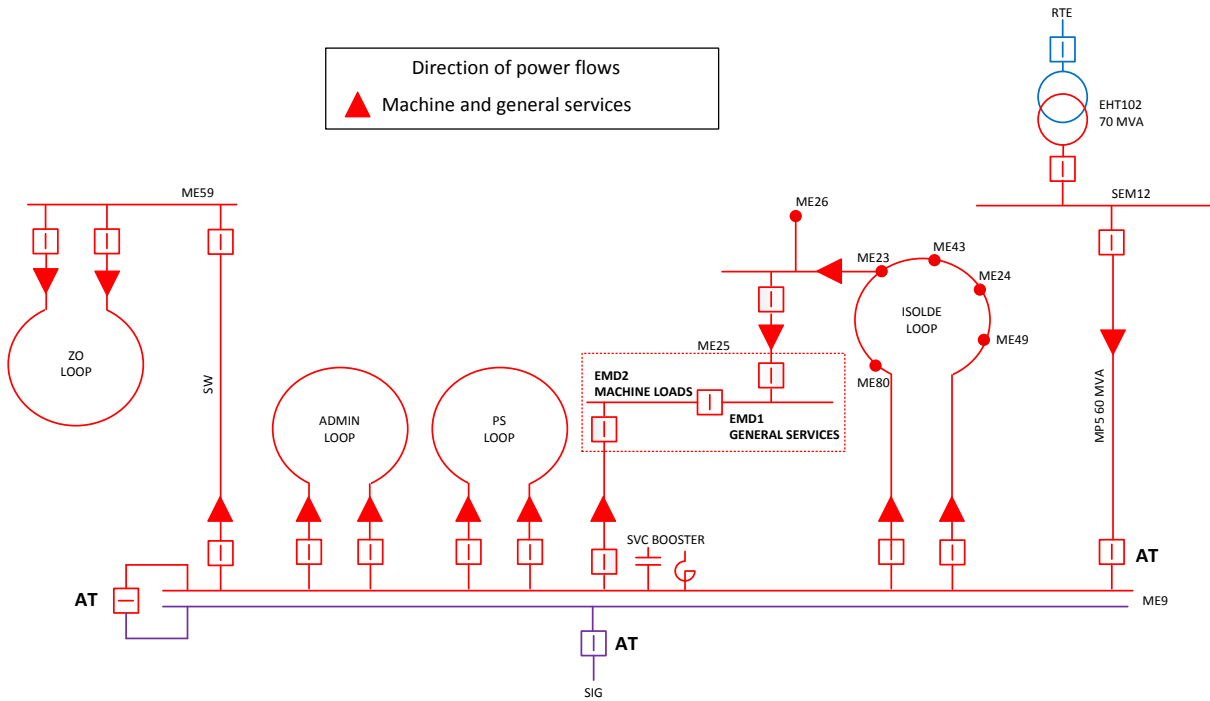


Fig. 3.189: Electrical network supplying ME25 (status in 2013)

Substation ME25 is, from a functional point of view, divided into two parts: EMD1 is dedicated to general services, and EMD2 is dedicated to the machine loads. The machine loads on EMD2 are compensated by the SVC Booster installed in ME9.

Detailed single line diagrams can be found in drawings in Refs. [129–131].

3.12.3.2 Transition LS1 to LS2

Figure 3.190 shows a schematic representation of the HV substation ME25. The dotted lines indicate the modifications to the existing switchgear related to the PSB upgrade project.

The HV switchgear is divided into three sections:

- EMD1, powered radially from ME23, supplies the general services;
- EMD2, powered from ME9, supplies the existing machine loads that are compensated for by the SVC Booster located in ME9;
- EMD3, powered from ME59, supplies the new machine loads.

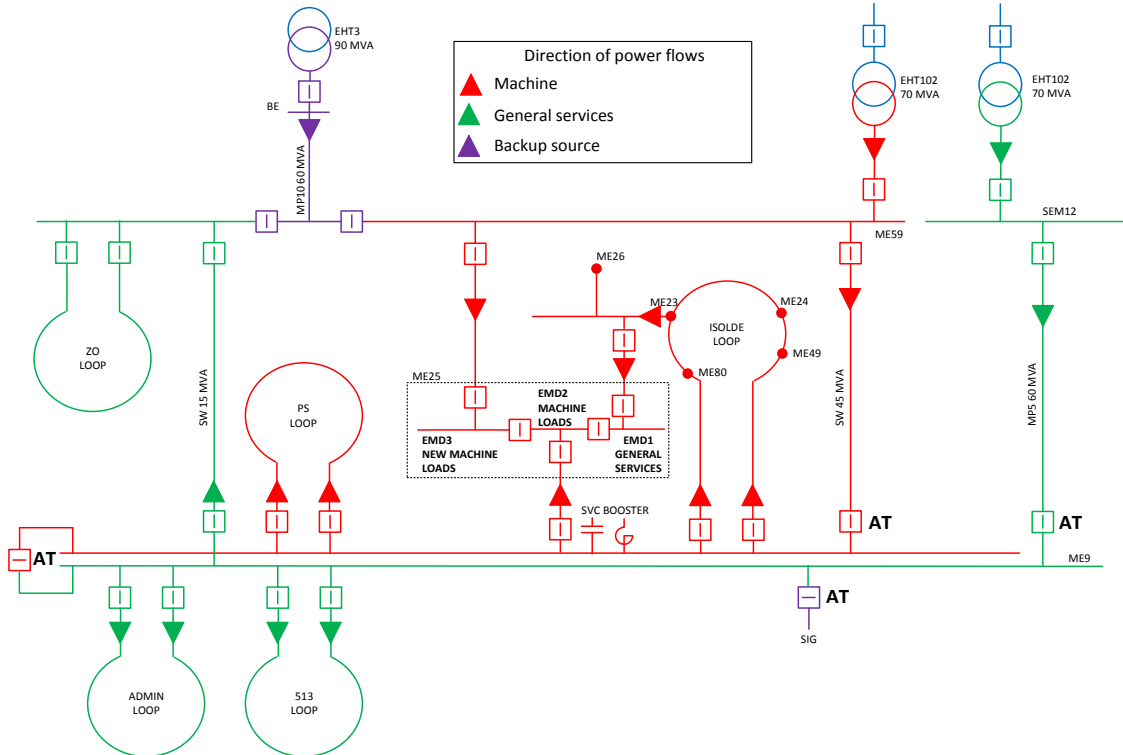


Fig. 3.190: Electrical network supplying ME25 (LS1 to LS2)

The network reconfiguration from LS1 to LS2 and its impact on the SVC Booster are described in Ref. [132]. The single line diagram (Fig. 3.191) [133] shows the electrical network in the period from LS1 to LS2.

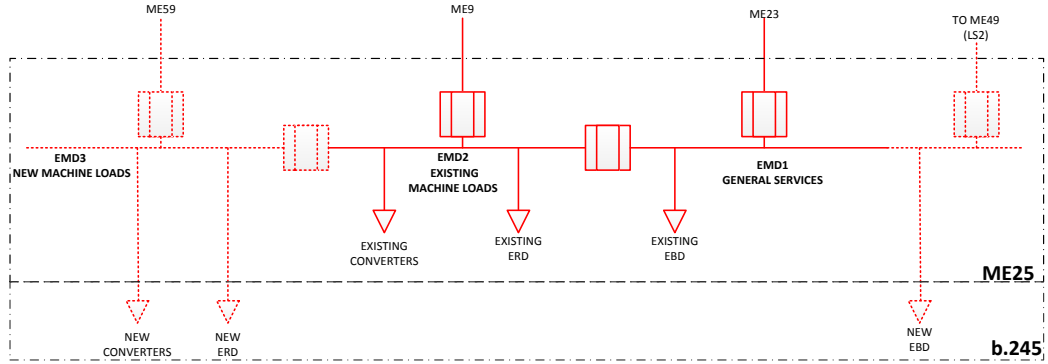


Fig. 3.191: ME25 modification to single line diagram

3.12.3.3 Configuration after LS2 ('2025 network')

As mentioned above, the project will take into account the existing studies related to the evolution of the HV electrical network [134].

These studies define, as one of the main strategies, the separation of general services and machine loads on the Meyrin site.

The objective is realized, in the case of the electrical distribution in the Booster complex, through the creation of a 'Booster loop' dedicated to the general services. In addition, electrical

substations ME24 and ME26, which contain only machine loads, would be removed from the loop Booster and supplied radially from ME25.

The separation of general services and machine network is represented schematically in Fig. 3.192, which focuses on the details of the Booster loop. The single line diagram of the ‘2025 electrical network’, which shows details for all the loops, can be found in Ref. [132].

The future modifications to the HV electrical network in the Booster complex, and in particular the separation of general services and machine loads, require a study to investigate the needs for SVC/filters on the Meyrin site, located in substations ME59 and ME9, for the period from LS2 onward.

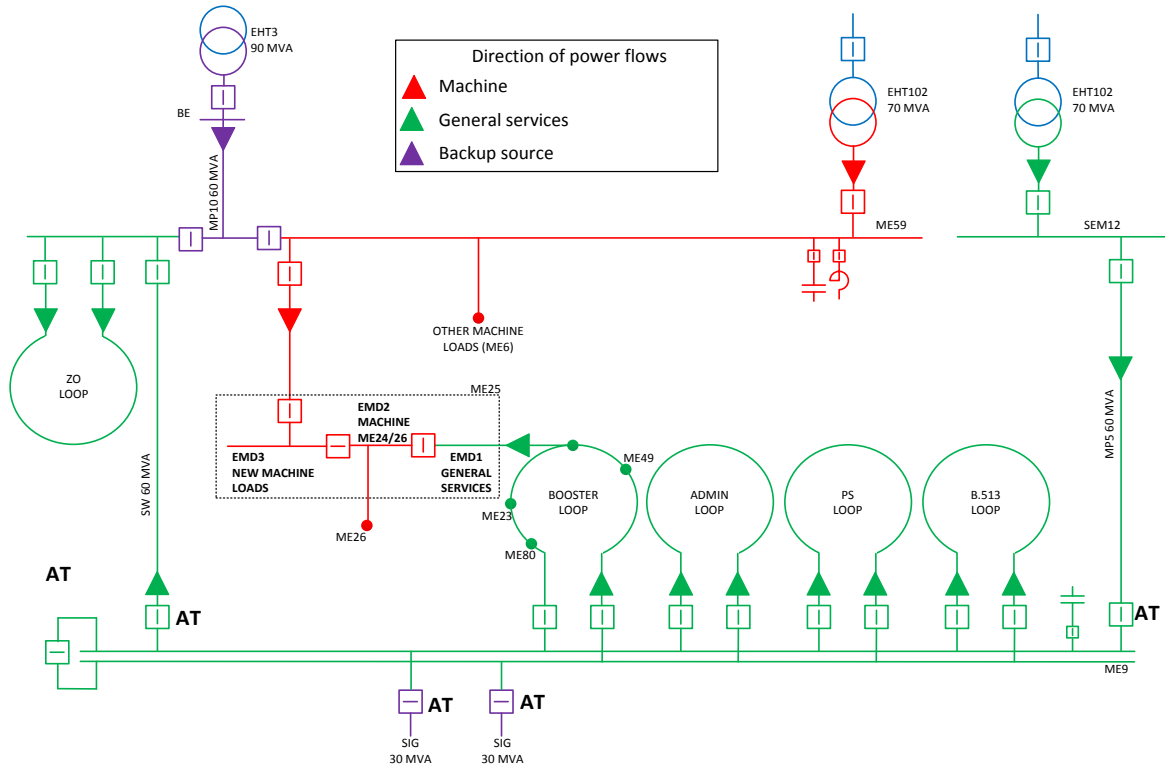


Fig. 3.192: Electrical network supplying ME25 (2025 configuration)

3.12.3.4 Technical description of the HV infrastructure

The proposed changes for ME25 are available as a single line diagram (see Ref. [135]). The main points can be seen in Fig. 3.193, with the numbers explained in the text below.

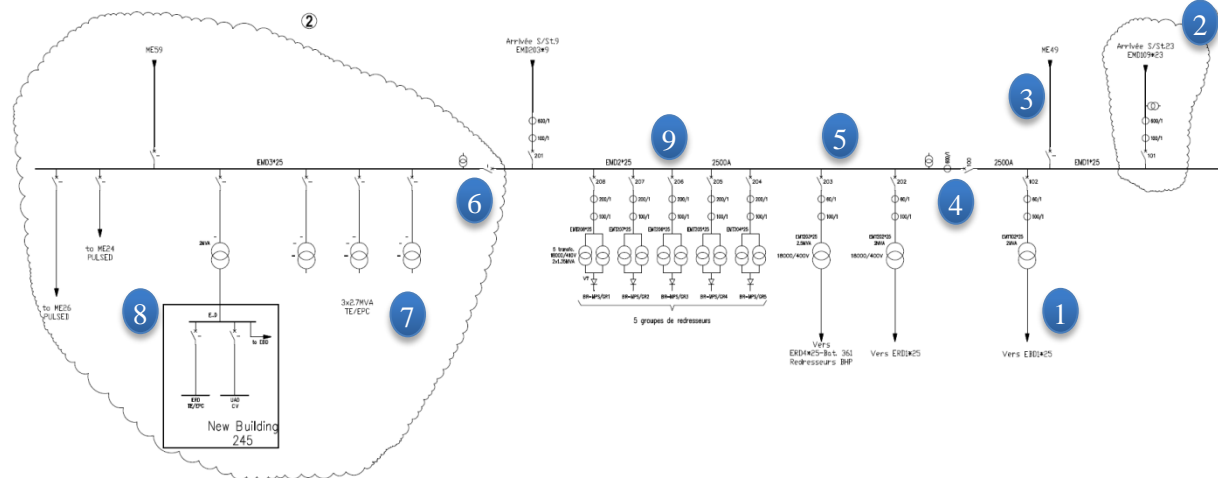


Fig. 3.193: Proposed single line diagram ME25

1. The general services of the building (lights, sockets, HVAC, etc.) are supplied from EMD1, via the LV switchboard EBD1*25 and an EBD switchboard located in building 245.
2. From LS1 to LS2: switchgear EMD1 is connected radially to the electrical substation ME23.
3. After LS2, the switchgear EMD1 will be connected to the Booster loop via electrical substations ME23 and ME49.
4. The coupling between EMD2 and EMD1 is open, to separate general service from machine loads.
5. Switchgear EMD2 supplies the existing machine loads.
6. The coupling between EMD2 and EMD3 is open, to separate the two machine busbars, dedicated respectively to existing and new loads.
7. The new power converters are supplied via three transformers connected to EMD3.
8. The machine services, represented by auxiliaries related to the power converters and the cooling and ventilation plan to the Booster magnets, are supplied via a transformer, which powers an EBD switchboard. This switchboard will supply smaller switchboards dedicated to the users: ERD for the auxiliaries of the power converters and UAD for CV loads.
9. After LS2, as shown in Fig. 3.192, the electrical substations ME24 and ME26, which contain only pulsed loads, will be supplied from EMD2. This step requires the disconnection of the existing power converters.

3.12.4 Technical description of the LV infrastructure

3.12.4.1 LV single line diagram

Figure 3.194 shows the draft of the LV single line diagram. This draft is based on the data provided by the users at this stage of the project. Further data will be provided by the users, to define elements such as the type of switchboards, the number of feeders in each switchboard and the type of switching devices (circuit breaker or switches). The full drawing can be viewed on CDD under the reference PS_EB_____7003 [136].

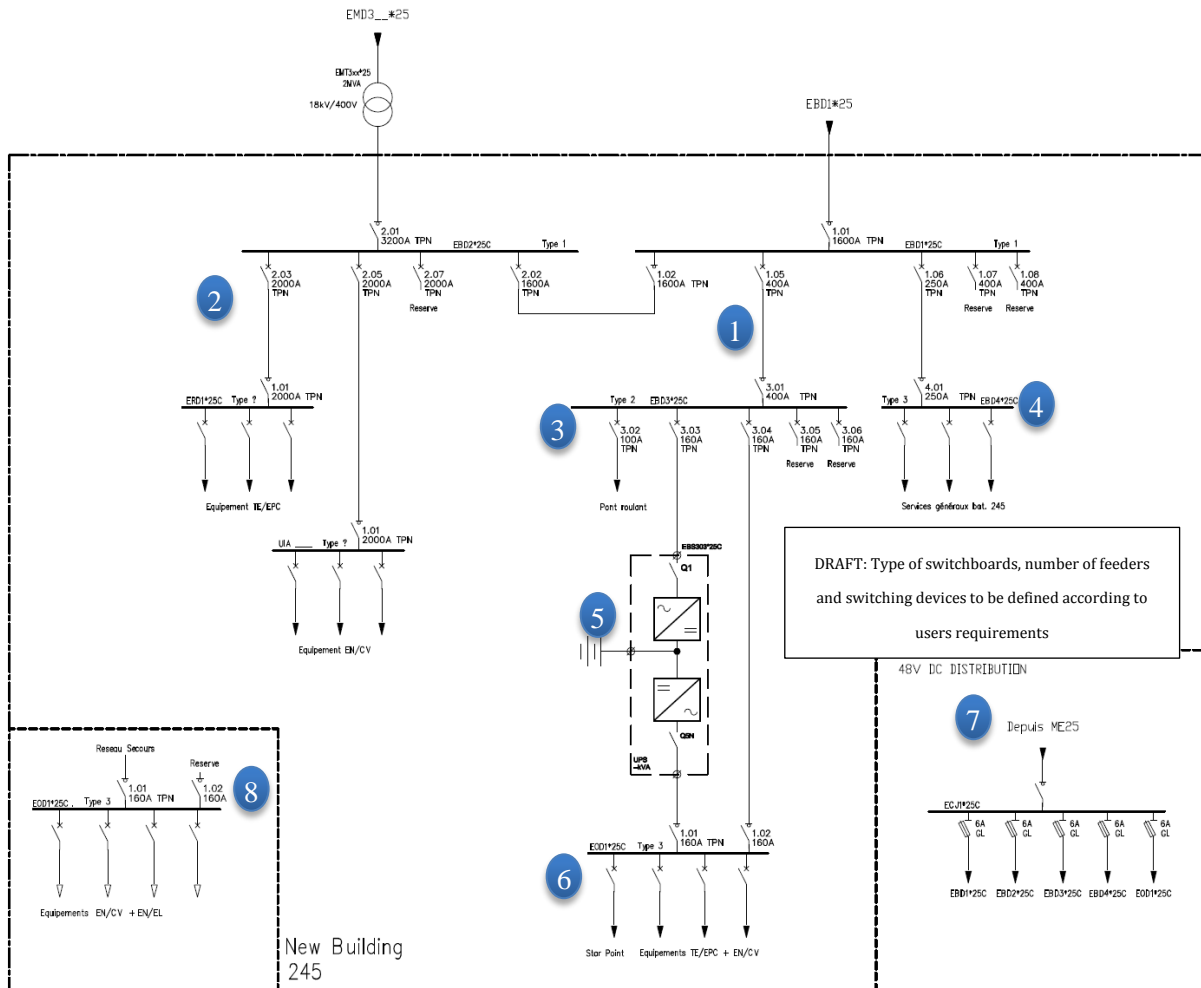


Fig. 3.194: Draft of the LV single line diagram

The main points are:

1. EBD1*25C type 2 LV switchboard supplying general services loads within the building, coupling to EBD2*25 for re-supply in the case of a failure of supply from EBD1*25;
2. EBD2*25C type 1 LV switchboard for supply of loads from the machine network that supplies TE/EPC and EN/CV process loads;
3. EBD3*25C type 2 LV switchboard supplying large calibre loads within the building (UPS, gantry crane);
4. EBD4*25C type 3 LV switchboard supplying all lighting and small power (socket outlets) general services within the building;
5. EBS303*25C redundant UPS providing continuity of supply to critical items of equipment with a battery autonomy of 10 minutes;
6. EOD1*25C type 3 LV switchboard supplying all critical loads from the UPS;
7. 48 V DC distribution originating from electrical substation ME25;
8. ESD1*25C type 3 LV switchboard supplying all life safety equipment.

3.12.4.2 Electrical distribution

One Hazemeyer type 1 electrical switchboard is to be located in the main electrical switchroom. The distribution board will be of an extendable modular type, containing electrical on-load isolators, air circuit breakers and moulded case circuit breakers (MCCB's). DIRIS type energy meters will be installed for major loads.

Power converter loads will be served by a dedicated ERD type switchboard supplied from the type 1 switchboard. Process cooling and ventilation loads will also be supplied by a dedicated UAD switchboard.

A Hazemeyer type 2 electrical switchboard will be installed to serve the main general services loads within the building (such as UPS, cooling and ventilation for the general areas of the building and the gantry crane). The type 2 electrical switchboard will be supplied from a new circuit breaker to be added to the EBD1*25 switchboard in the adjacent ME25 electrical substation. Power will be supplied through low voltage power cables installed in a cabling trench to the new building. A type 3 electrical switchboard to serve small calibre general services loads (lighting and power) will be connected downstream of the type 2 switchboard. A further type 3 electrical switchboard will be installed to supply loads from the UPS.

A third type 3 electrical switchboard will be installed to serve exclusively life safety loads (emergency lighting and smoke extraction). The switchboard will be supplied with a fire-rated cable from the nearest connection point to the diesel safety network, and all internal cabling will also be fire-resistant. This switchboard will be located outside, on an external wall of the building.

An additional 30% of outgoing circuit breakers will serve as spare capacity for future expansion to all switchboards.

The electrical switchboards will be unavailable for service during planned maintenance intervals, approximately once every 4–5 years (duration 1–2 days). The electrical switchboard will be continuously monitored by the EL SCADA system, reporting any electrical malfunctions to the TI desk in the CCC.

3.12.4.3 Electrical cable containment

Electrical cables will be distributed throughout the building on a dedicated electrical cable containment system. This will consist of a cable ladder for large cables (main feeds and sub-main distribution cables), cable tray, cable basket and telex for smaller auxiliary and final circuit cables. Cable containment will be installed throughout on a modular steel support system, which may contain common elements as coordinated with other services (such as cooling and ventilation).

Dedicated containment will be provided for all services not cut by the emergency stop (AUG) buttons for the building and supplies to and from the type 3 ESD switchboard. This containment will be identified with orange stripes.

3.12.4.4 Small power distribution

The type 3 switchboard will supply all lighting and small power loads within the building. The status of the distribution board will be monitored by the EL SCADA system, reporting any electrical malfunctions to the TI desk in the CCC.

Small power distribution within the technical areas of the building will be achieved by the installation of modular socket outlet boxes containing the following electrical outlets:

- four T-13 conventional plugs, protected by a single MCB plus RCD device;
- two 16 A 1 Ph CEE17 sockets protected by a single MCB plus RCD device;

- one 32 A 3 Ph CEE17 socket protected by a single MCB plus RCD device.

Offices and control rooms will be served with the installation of socket outlet strips, which may contain either five or ten socket outlets, protected by a single MCB plus RCD device. Sockets not protected by an RCD may only be installed for fixed equipment with the agreement of HSE. Equipment racks may also be supplied with socket outlet strips (e.g. IT racks), supplied from either the conventional network or a UPS source depending upon client requirements.

3.12.4.5 Lighting system

The building will be provided with a fluorescent lighting system for normal usage, designed to provide the following lighting levels:

- general circulation space and corridors: 100 lx, PIR controlled;
- technical halls and general equipment areas: 300 lx, switched;
- plant rooms: 300 lx, PIR controlled;
- offices and control room areas: 500 lx, switched;
- toilets (if applicable): 200 lx, PIR controlled.

A dedicated emergency lighting system will also be installed, based on Aprotec self-contained, self-test emergency light fittings. The emergency lighting system will activate in the event of a power failure or a scheduled test.

3.12.4.6 48 V DC power supplies

The building will be supplied with 48 V DC power from the adjacent ME25 electrical substation. The 48 V DC distribution will be used exclusively to serve EN/EL equipment such as switchboard auxiliaries and supply the action of local emergency stop buttons where required. A wall-mounted ECJ type enclosure will be installed in the electrical switchroom to provide 48 V DC distribution within the building.

3.12.4.7 UPS power supplies

A dual redundant UPS system will be installed to provide up to 10 minutes of autonomy for critical systems to allow for their safe shutdown in the event of a power failure. The UPS system will be installed in an accessible location to facilitate replacement and regular (3–5 year) battery changes. In the event of an equipment failure on one of the two UPS units, downstream loads will be serviced by the remaining unit. The UPS will be connected to a dedicated EOD type 3 distribution board, which will be monitored by the EL SCADA system in addition to the status of the UPS.

A risk assessment will be performed in accordance with IS5 regarding the action of the AUG on the UPS within the building. If the UPS is to be unaffected by the action of the emergency stop system then all downstream electrical equipment will be installed on dedicated containment and will be marked with fluorescent orange stripes to indicate that it will remain live during a general emergency power cut. In addition to the risk assessment, circuits downstream of the UPS may be provided with local emergency stop (AUL) buttons, located on or adjacent to the equipment supplied.

3.12.4.8 Emergency stop buttons

The 400 V supply to the building will be subject to the action of emergency stop buttons (AUG), which act on the 18 kV distribution network. In the event that an AUG affecting the building is pressed, the CERN fire brigade will be called immediately (Level 3 alarm) and all electrical power will be lost until it is restored by the EN/EL on-call service. A risk assessment will be conducted in

accordance with IS5 [137] to decide the scope of services affected by an AUG action within the building.

The building may also be fitted with local emergency stop (AUL) buttons, which disconnect all 230 V and 400 V electrical services to particular equipment, where decided by the equipment owner or supplied via UPS if not cut by the AUG. Any local emergency stop systems will be tested regularly under the responsibility of the building TSO.

3.12.4.9 Redundancy

The general electrical services within the building are provided on a non-redundant basis. The failure of any part of the distribution system will result in a loss of service for any downstream components until a repair is made.

The UPS systems are provided with $n + 1$ redundancy, such that the failure of either UPS unit within the building will have no effect on downstream services. However the associated distribution (cabling, switchboard) will be provided with a non-redundant configuration.

3.13 Cooling and ventilation

3.13.1 Introduction

This document describes the modifications to the cooling and ventilation infrastructure required by the LIU PSB Upgrade project, focusing on the technical requirements and the technical solutions foreseen.

The PS Booster complex will be affected by major modifications according to the need for consolidation of existing plants and those from the upgrade of the Booster.

Within the CV consolidation programme, it is proposed to refurbish completely the cooling and ventilations station for the PSB complex during LS2. The affected systems are the primary (raw water) and secondary (demineralized water) stations for water cooling, the chilled water production station and the ventilation station.

During the launch of the LIU PSB project the needs of all LS2 concerned stakeholders were reviewed and the preliminary results show that there are no major differences in the estimated heat loads with respect to the present situation; unless the advancement of the design work for the PSB equipment will modify this scenario, all of the CV stations will be refurbished keeping the same working parameters conditions as at present.

Therefore, the installed power for the water cooling will be 3.6 MW for a flow rate on the primary side of 465 m³/h and on the secondary side of 310 m³/h; the working pressure of the demineralized water will be between 12 and 13 bar at the exit of the station at a temperature of 25°C. The only modification on the cooling system with respect to the present condition is that the circuits for the surface premises will be separated from the circuit for the tunnel in order to avoid radio-protection issues in the future in mixing the water coming from the two zones. The new cooling station will be located in building 273 and in the adjacent building 141 provided that this building will be declassified from a radio-protection point of view.

Similarly, the flow rate for the air ventilation of the tunnel and the building are not foreseen to change from 32 000 m³/h for the air supply with a renewal of fresh air of 3000 m³/h and 35 500 m³/h extracted air.

The chilled water plant will be renewed keeping the same parameters since the needs of the PSB complex have not changed; however several consolidation actions are needed on the chilled water plants in this area (AD, PS, PSB) and a study will be launched to optimize the future configuration.

It worth pointing out that no refurbishment work is foreseen at present in the replacement of the distribution circuits (ducts and pipes) in the complex, since their condition is still considered to be acceptable; the increase of working pressure for the new magnets (requiring the replacement of all the piping) has not been confirmed by the group concerned.

Within the LIU PSB Upgrade project, the upgrade of the cooling and ventilation infrastructure will be limited to the cooling and ventilation systems dedicated to building 245 (shown in Fig. 3.188) housing the new main power supply converters with the related auxiliary equipment for the PSB as part of the PSB-LIU upgrade work.

3.13.2 New PSB-MPS building 245: water-cooling requirements

There are two main classes of equipment to be considered for water cooling:

- power converters:
 - main power converters (MPS);
 - quadrupole power converters (QPS);
- test resistance, to be connected in series with the dummy load.

Three identical MPS and three identical QPS will be installed, of which only two sets are necessary for operation and one is a spare. Due to the large number of elements to be cooled inside a single MPS, the cooling circuit is divided into two separated loops:

- one including an AFE converter, input reactor and filter/crowbar elements;
- one including a DCDC converter and decoupling inductors.

A total of 10 separated cooling loops are therefore required. Figure 3.195 shows the functional division into three identical lots, each having the same cooling requirements.

The cooling infrastructure dedicated to building 245 will be independent of that dedicated to the PS and PSB in order to allow functioning even when the PS and PSB systems are under maintenance.

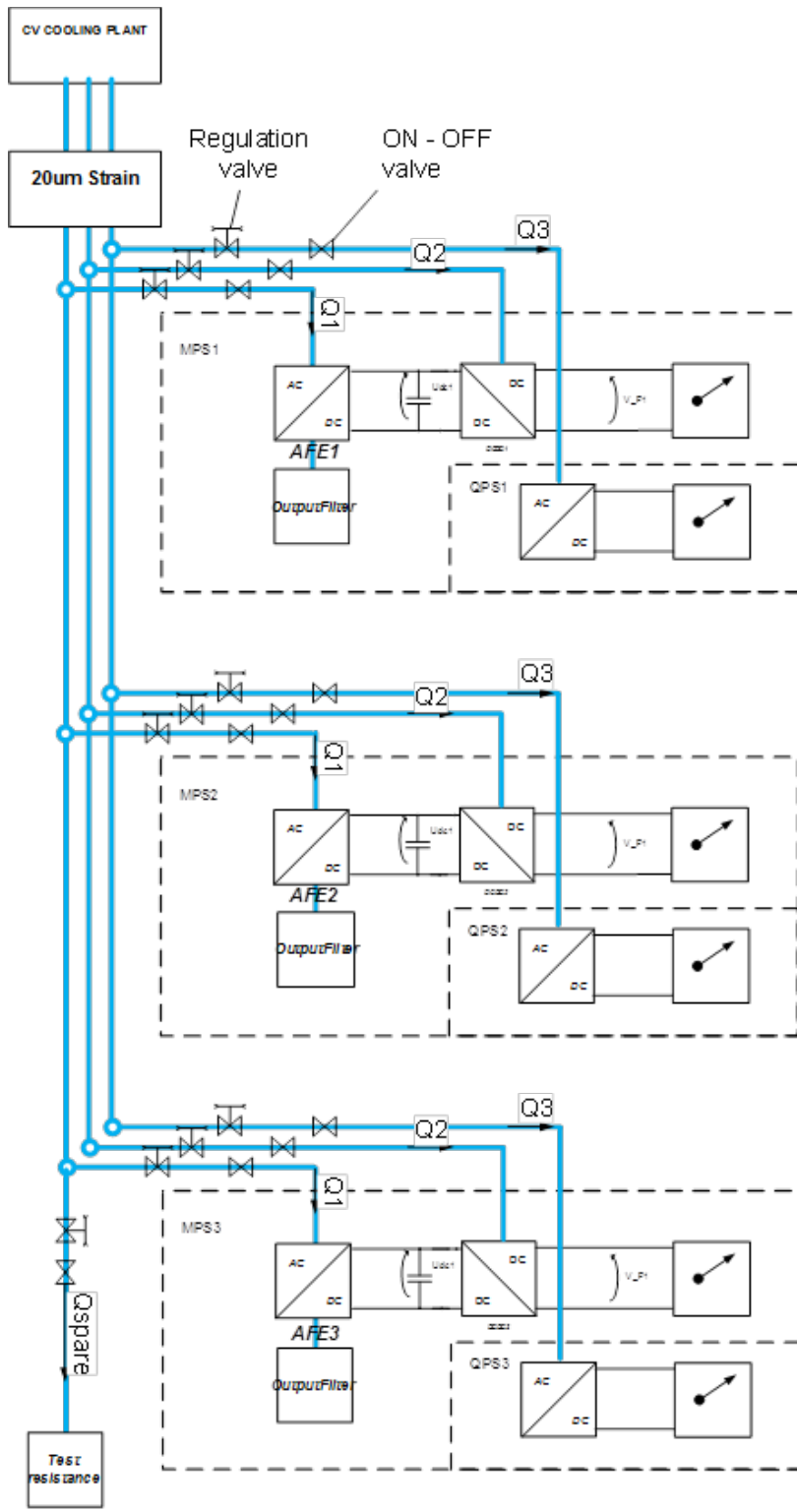


Fig. 3.195: Power converter water-cooling schematics

Total losses in water are estimated to be 470 kW. The spare converters only account for 30% of their inlet power, as they will only be tested at reduced power. Table 3.73 lists the heat loads per item of equipment.

Table 3.73: Booster 2GeV power converter loss dissipation in water

	MPS		QPS	Spare circuit
	AFE + output filter	DCDC converter	Quadrupole converter	
Number of units	3	3	3	1
Losses in water per unit	100 kW	77 kW	25 kW	30 kW
Water flow per unit	$Q_1: 36 \text{ m}^3/\text{h}$	$Q_2: 36 \text{ m}^3/\text{h}$	$Q_3: 5 \text{ m}^3/\text{h}$	$Q_{\text{spare}}: 5 \text{ m}^3/\text{h}$
Maximum inlet temperature (T_{in})	30°C–35°C	30°C–35°C	30°C–35°C	30°C–35°C
Inlet water conductivity ($\mu\text{S}/\text{cm}$) at T_{in}	<1.5 $\mu\text{S}/\text{cm}$	<1.5 $\mu\text{S}/\text{cm}$	<1.5 $\mu\text{S}/\text{cm}$	<1.5 $\mu\text{S}/\text{cm}$
Estimated differential pressure at Q	4.0 bar	4.0 bar	2.5 bar	2.0 bar
Total losses in water (Alu circuit)			500 kW	

The differential pressure is estimated on the basis of the present flow of the POPS converters without the strainer (20 μm filter) and heat exchanger.

Each of the 10 cooling loops for the power converters will be equipped with the following measurements available to the power converter control:

- flow rate;
- input temperature;
- output temperature;
- water conductivity.

3.13.2.1 Water-cooling principle

The cooling plant will be composed of a primary cooling circuit (cooling tower circuit), to be placed on the roof of the technical part of building 245, and a secondary circuit (distribution circuit), to be housed inside the CV technical room. The power converter supplies are cooled down with a closed loop demineralized water circuit.

The primary circuit will consist of a semi-closed loop cooling tower equipped with independent cells each fitted with its own fan. The independent cells will provide $n + 1$ redundancy.

The wet bulb design temperature will be 21°C. The circuit will be equipped with an automatic water treatment system (deconcentration, biocide, etc.) and filtration with automatic cleaning.

The water-cooling station will be implemented as indicated in Fig. 3.196.

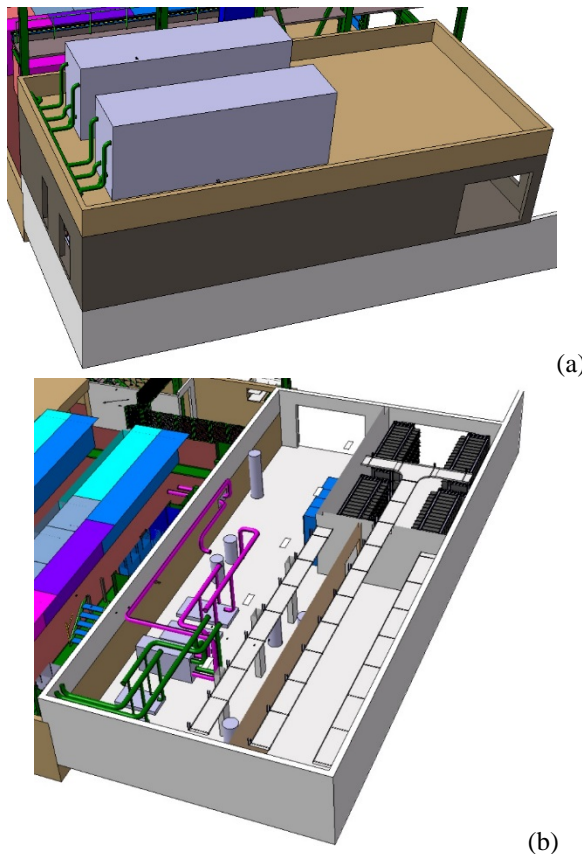


Fig. 3.196: Water-cooling plant (a) on the roof and (b) inside the building

3.13.3 New PSB-MPS building 245: ventilation requirements

Table 3.74 lists the areas requiring air conditioning.

Table 3.74: Booster 2GeV air conditioning requirements

	Temperature (°C)	Losses (kW)
Converter hall	26	160
Control room	Human range (18 in winter, 26 in summer)	4
Capacitor rooms	Human range (18 in winter, 26 in summer)	5 (per room)
False floor	26	15
EN/EL area	26	10

The operation of the air conditioning system is similar to that implemented for the POPS converters in building 367. The air is blown through the false floor at a temperature of 26°C and is pulled out by the fans located inside each power converter cabinet.

The design of the HVAC system will avoid the presence of air condensation in all seasons.

As for the cooling plant, the ventilation infrastructure dedicated to building 245 will be independent of that dedicated to the PS and PSB in order to allow functioning even when the PS and PSB systems are under maintenance (see Table 3.75).

Table 3.75: Electrical specifications for the cooling and ventilation infrastructure for building 245

Efficiency 55%	Equipment tag	Flow (m³/h)	Pipe diameter (mm)	Pressure (mCL)	Power absorbed (kW _a)	Power motor (kW _m)	Power consumed (kW _c)	Delta T (K)	Cooling capacity (kW _w)	Comment
3.245 – MPS Building										
<i>Water Cooling</i>										
Demin water pumps – Power Converter Circuit (Alum)	MPS-PED-1	252.4	DN 250	65	81.3	100		2	585	Duty/standby
Demin water pumps – Power Converter Circuit (Alum)	MPS-PED-2	252.4	DN 250	65	81.3	100		2	585	
3.245 PSB + MPS Cooling Towers – Combined Primary Water System										
Primary water pumps	PEP-1	86.3	DN 150	30	12.8	15		6	600	Duty/standby
Primary water pumps	PEP-2	86.3	DN 150	30	12.8	15		6	600	
Cooling tower	CT-1					20		600	Duty/standby	
Cooling tower	CT-2					20		600		

Table 3.75: Continued

Efficiency 60%							
Equipment	Equipment tag	Airflow (m ³ /h)	Pressure (Pa)	Power absorbed (kW _a)	Power motor (kW _m)	Power consumed (kW _c)	Delta T (K)
3.245 – MPS HVAC							
HVAC – Main hall	AHU-1	28 000	500	23.33	55	10	90
HVAC – Main hall	AHU-2	28 000	500	23.33	55	10	90
Heating – Main hall				20			
HVAC – Control room	FCU-1			8			
HVAC – Electrical room	FCU-2			4			
HVAC – Capacitor banks	UH-1, UH-2, UH-3			15			
Ventilation – Plant Rooms	Various			10			
Smoke Exhaust Fans (UPS)	UUUTI-1, UUUTI-2			8			
Total				445	290	kW	
						Allowance, FR cable	

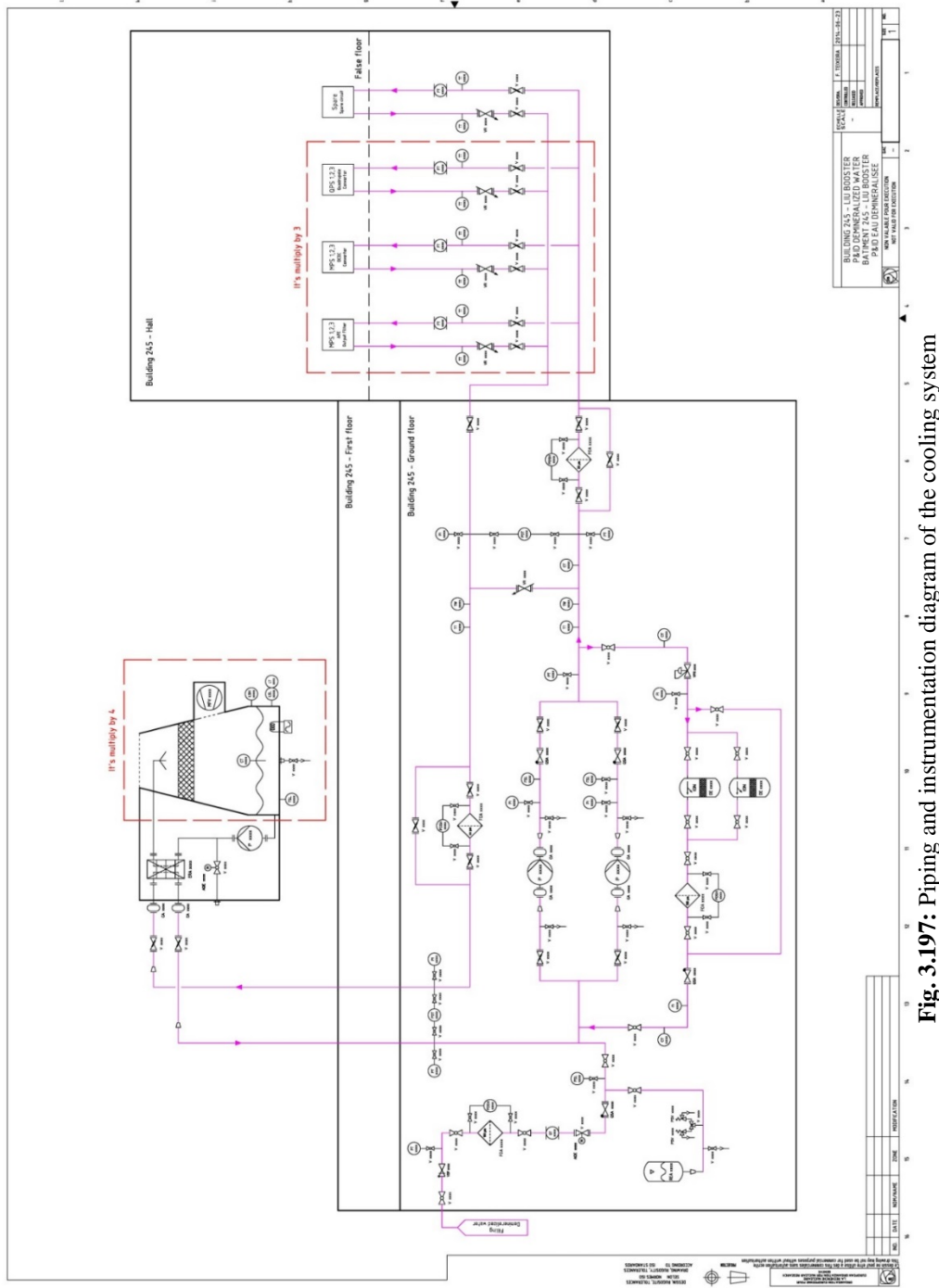


Fig. 3.197: Piping and instrumentation diagram of the cooling system

3.13.3.1 Ventilation principle

The two air-handling units will supply air into a plenum false floor. Air distribution to the openings on the power supply front doors will be ensured by means of floor grills (fitted with balancing dampers).

The power supplies are fitted with extraction fans at the top, inducing a flow of cool ambient air into the power supplies through openings on the lower part of their front doors.

The two air-handling units work on recycled air with a minimum of fresh air. They will work on the principle of indirect adiabatic cooling with high energy efficiency.

The ventilation system will be implemented as indicated in Figure 3.198.

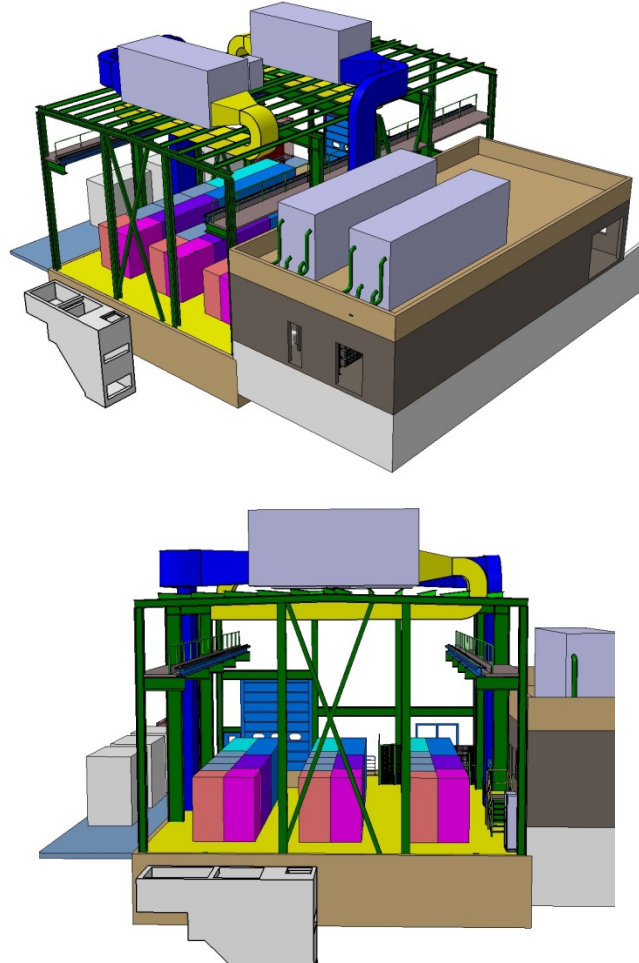


Fig. 3.198: Implementation of the ventilation system

For the heating and cooling of the control room and the capacitor rooms, an independent direct expansion system configured with a variable refrigerant volume will be installed.

In addition, there are two smoke extractors dedicated to the power converter hall, which are supplied through a secured electrical network.

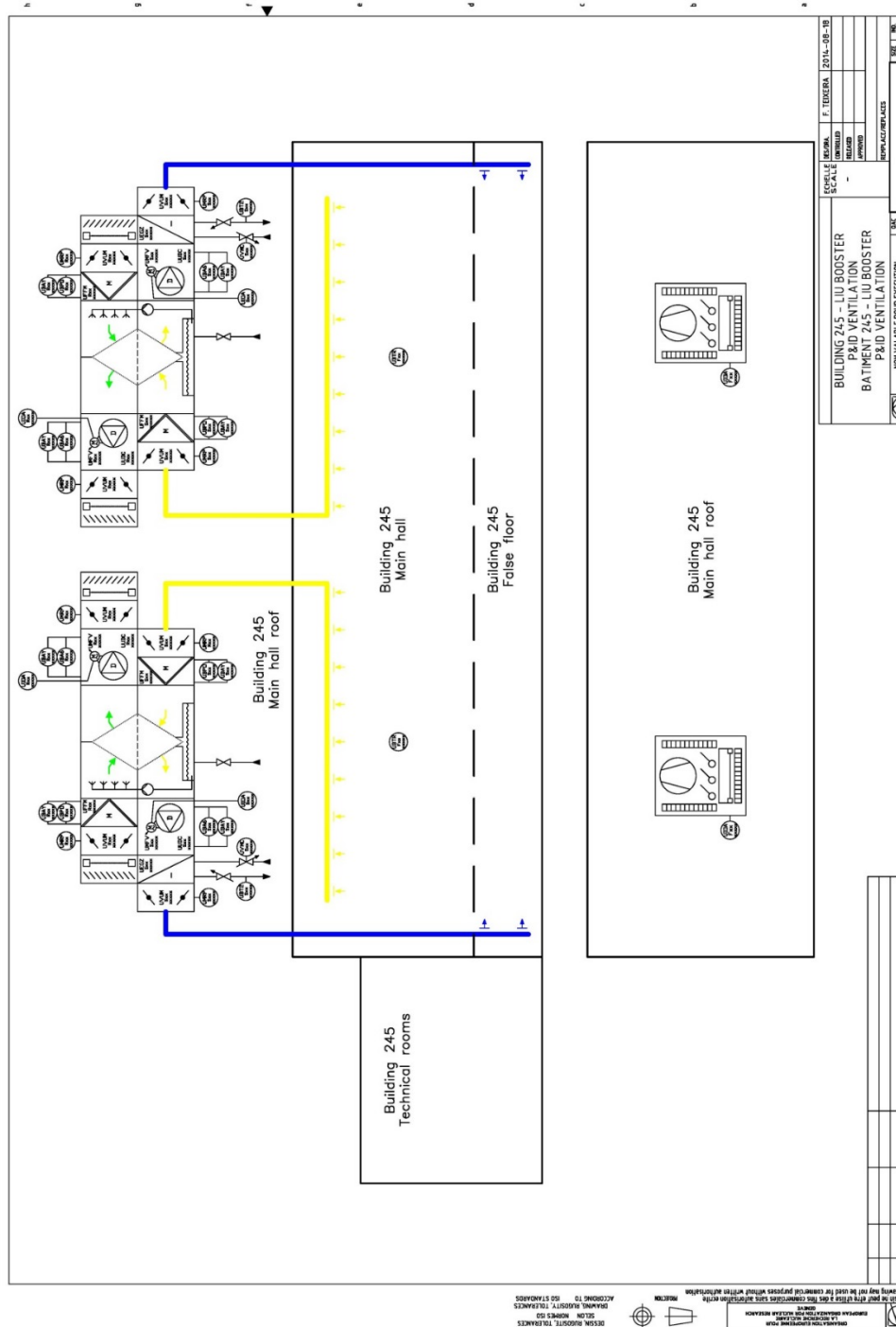


Fig. 3.199: Piping and instrumentation diagram of the ventilation system

3.14 Installation, transport and handling

3.14.1 Transport and handling equipment

3.14.1.1 Surface buildings

Building 245 will be equipped with an overhead crane. Depending on the final configuration of the equipment in this building some special tooling will be needed for installation.

The other building (building 361), which is used for handling operations for the components needed for the Booster upgrade, is already equipped with an overhead crane

3.14.1.2 Underground area

The tunnels are equipped with a series of cranes covering most areas. Some of the component installed for the PS were too heavy for the current cranes.

Figure 3.200 shows the equipment affected by the PSB upgrade.

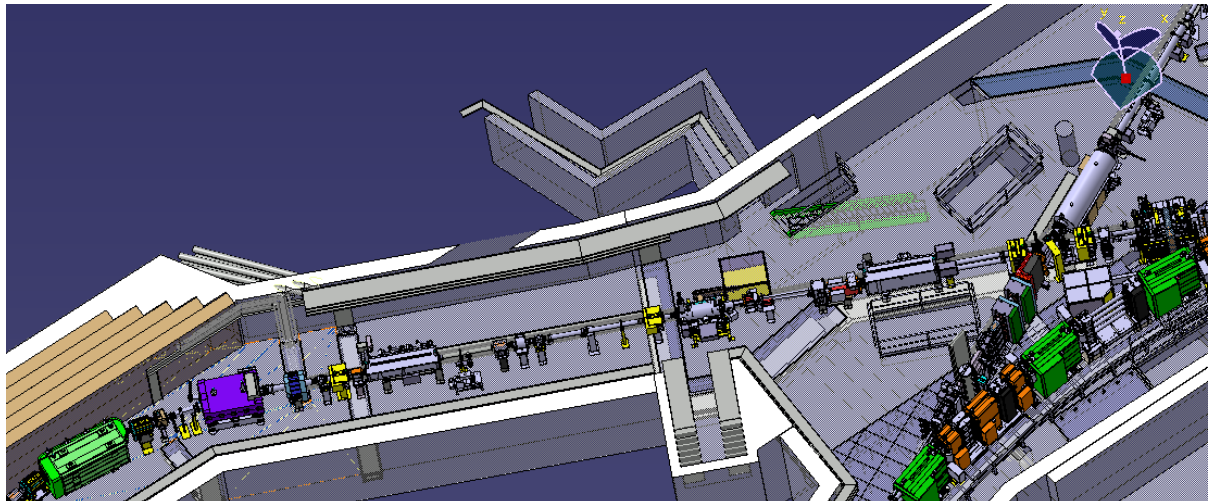


Fig. 3.200: BTM.BHZ10 and BT.BHZ10 (green and violet element)

Those elements would need to be removed through one of the PSB access shafts. A detailed study is needed for the two options in order to define the best method regarding the consequences for the planning and co-activities for the PSB upgrade.

Regarding the installation of the replacement magnets, the overall weight of a magnet is around 24 tonnes. A suitable option would be to transport the magnet in several pieces in the Booster and then assemble with the current overhead crane. Future maintenance and possible breakdown of these magnets would have to be considered as this would have an impact upon the operation of the PSB accelerator.

PSB triplet handling

Existing tooling exists for the handling of these pieces of equipment but it might not comply with the current handling standards. This might affect reconstruction of the equipment.

Two new transformers to be installed in the PSB

Two new transformers need to be installed in the junction area of the PSB. These transformers cannot not be installed at their planned position with the overhead crane; dedicated tooling for the installation of this equipment is needed.

Reference magnet

The reference magnet is currently installed in the middle of a false floor, a place where no suitable lifting equipment is available. For this reason, to remove the magnet two options might be considered: in situ disassembly, or the removal of the complete magnet; for the latter option reinforcement of the whole route out would be needed.

Other equipment

During the upgrade phase of the PSB other equipment will be upgraded. A detailed study will be carried out for installation in order to define the appropriate handling equipment.

3.14.2 Transport and handling services

All transport and handling needed for the upgrade, taking into account the upgrade of the accelerator itself and including the general service upgrade, will be provided during preparation and the upgrade phase. The details of the team involved in this upgrade will be prepared six months prior to the start of the work.

3.15 Civil engineering

3.15.1 Introduction

Building 245 is a new construction requested to host the new main power supply of the Booster accelerator ring, in the frame of the 2 GeV energy increase required by the LIU programme.

3.15.2 Proposed location

The proposed location for building 245 is the area between Booster road, Democrite road, Rutherford road and building 271, on the French part of CERN's Meyrin site.

The particular constraints of this area, to be taken into account in the design, are:

- the proximity of the French–Swiss border, and the requirement for any construction on the French side to maintain a minimum distance of 10 m from the border;
- the presence of technical gallery TP9 and tunnel TT6 under the new building;
- the existence of many electric and water networks in the area that need to be diverted.



Fig. 3.201: Proposed location for building 245

3.15.3 Proposed layout

The descriptions given below should be read in conjunction with the attached drawings ----.CE-1.0245.0001 and ----.CE-1.0245.0002A which show plans and sections of the proposed building (see Figs. 3.201 and 3.202).

The building will consist of:

- a hall, approximately 21 m long, 14.2 m wide and 12.4 m high, equipped with a 10-tonne overhead bridge crane and a false floor across the whole surface, for the power converters' installation;
 - a two-storey annex to the west of the hall, 19.2 m long, 9.2 m wide and 6 m high, for the storage capacitors bank and the electrical/HVAC services;
 - a concrete slab, 19.7 m long and 3.5 m wide, outside the building, at the eastern part of the hall, for electrical transformers.

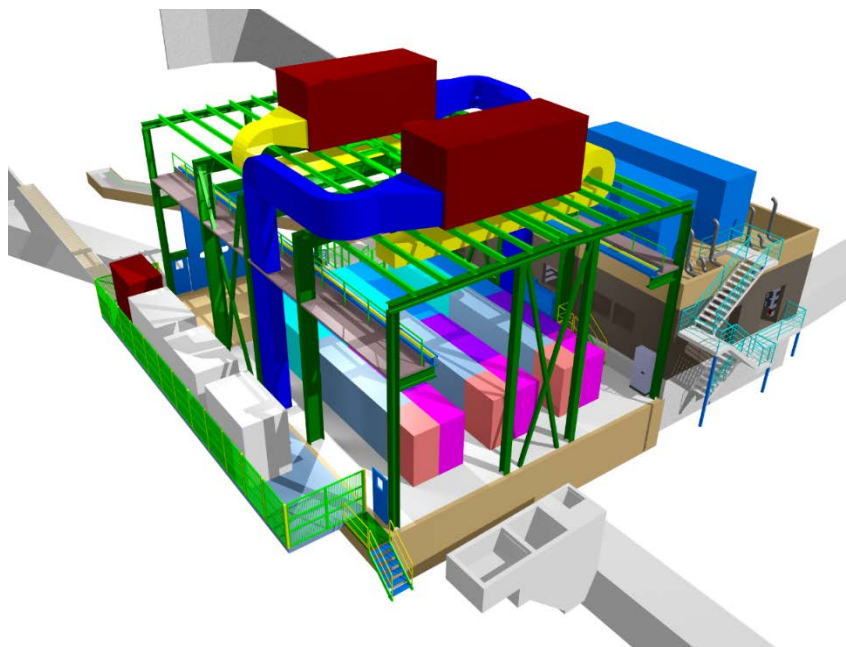


Fig. 3.202: 3D view of building 245 from the north

The building's entrances will be:

- on the south face, a sectional door for trucks, leading to the hall, and two double doors leading to the basement of the annex through a pit, for equipment and a stair for personnel;
- on the west face, a double door leading to the first floor of the annex from Rutherford road;
- on the north face, two doors leading to the first floor of the annex through a stair, allowing the access to the roof.

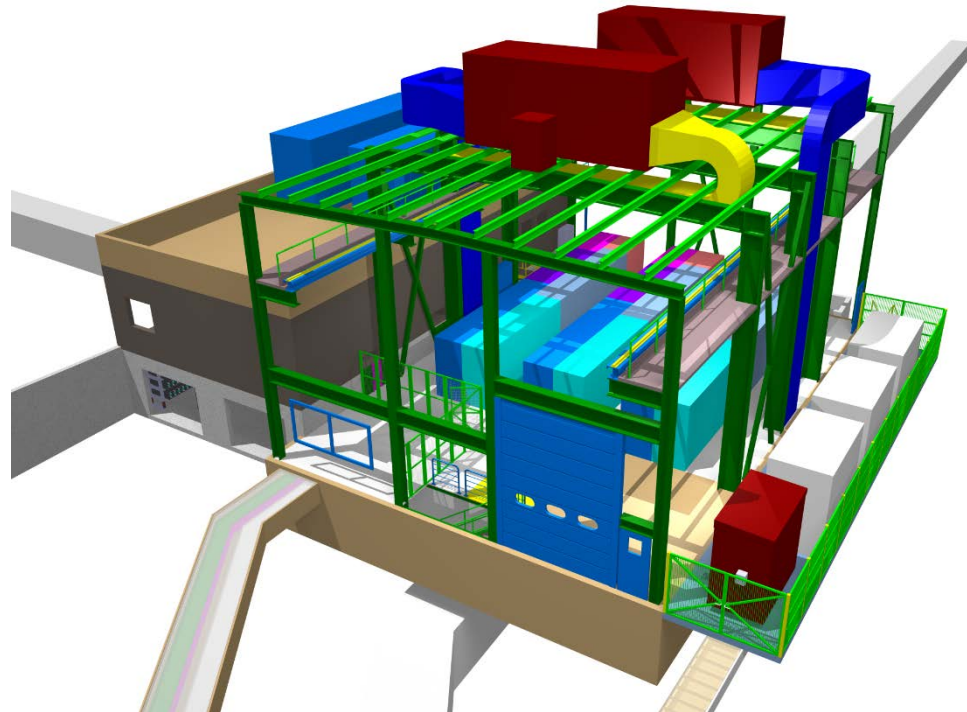


Fig. 3.203: 3D view of building 245 from the south

3.15.4 Civil engineering works

3.15.4.1 Preliminary works

The preliminary works for the construction of the building are:

- deviation of the existing networks in the area: sewage network, surface water, drinking water and industrial water;
- protection of existing electrical networks.

3.15.4.2 Foundation

According to the geotechnical study done in 2012, the ground under the proposed building is composed of a layer of heterogeneous backfill, over a layer of compact gravel backfill and a consolidated silty clay Würmian moraine, both overcoming the red sandstone of the Lower Chattian.

This ground does not contain a water table. However, depending on rainfall, water ingress can occur during excavations, mainly because of the presence of permeable layers and decompressed heterogeneous backfill. Any water inflow will need to be captured and removed from the site during the works, and a permanent drainage system around the peripheral walls will be necessary.

The loads from the building will be transferred into the compact materials (gravel or silty clay moraine) through additional depths of concrete, or directly into the molasse through deep foundations (piles).

The building will sit above the existing TP9 service tunnel, which will need to be reinforced to withstand the stress generated by the new building, or bridged to avoid this stress. The presence of tunnel TT6 deeper underground must also be taken into account in the design of the building's foundations.

Taking into account the presence of the above underground facilities and the networks in the area, the type of foundation proposed at this stage of the study consists of deep foundations (piles), avoiding these facilities and networks, supporting a concrete foundation structure composed of beams and slabs.

To ensure proper seating under the basement slab, the compressible soil will be replaced by a layer of compacted gravel.

Earthworks will be carried out using side slopes set to 1:1.

3.15.4.3 Building structure

The proposed type of structure for the two main work areas of building 245 is:

- for the converter hall: over ground level a steel frame structure with cladding, and for the basement a concrete structure with retaining walls;
- for the capacitors and services annex: a concrete structure;
- The facade and roof will be insulated with 180 mm of rockwool in accordance with current thermal standards.

3.15.4.4 Architectural building work and finishes

The amount of internal architectural building and finishing works is minimal, consistent with industrial type structures, and will include:

- unloading quay for lorries, in concrete, at the entrance to the converter hall;

- false floor in the converter hall;
- sanitaryware and waste water disposal;
- industrial doors, access doors and windows;
- stairs, walkways, balustrades and footbridges;
- rainwater gutters;
- painting of concrete floors and walls.

3.15.4.5 Car parks, roads, landscaping and external networks

Civil engineering works for the project will also include the car park, roads, surface water drainage and landscaping of the area around the new facility.

A trench measuring 1.5 m by 0.8 m between building 245 and the existing building 271 will enable electrical services and pipes to pass between the two structures.

Electrical transformers will be installed on a concrete slab outside the building on its eastern side. A second trench measuring 0.8 m by 0.25 m will allow the connection of the transformers to the 18 kV network.

The existing retaining wall between the Rutherford road and the parking for building 271 will be extended up to the new building.

As rainwater will be discharged into Swiss watercourses and the impermeable surface created by the project is larger than 500 m², a retention tank to collect the rainwater will be created in the area. The space under the slab in the capacitors room could be used for this.

3.16 Radiological protection

3.16.1 Injection dumps

The dumps for the future H⁻ injection system after the connection of Linac4 to the PS Booster are described in Section 3.8. There is one head and one tail dump as well as four internal injection dumps, denoted the H⁰/H⁻ dumps. The loading parameters for these dumps are specified in Ref. [138] and shown in Table 3.76.

Table 3.76: Loading assumptions for injection dumps of the Linac4 to PSB Injection, taken from Ref. [138].

	Annual load (H ⁻ /y)
Head dump	5.6×10^{18}
H ⁰ /H ⁻ dump (per dump)	5.78×10^{18}

Since there are four H⁰/H⁻ dumps, the number of protons absorbed by all of the H⁰/H⁻ dumps is approximately 4 times larger than that of the head dump. Together with the proposed material choices (see below), the radiological impact of the head dump will be much smaller than that of the H⁰/H⁻ dumps.

3.16.1.1 Head/tail dumps

Graphite has been proposed as the material for the head and tail dumps. From a radiation protection perspective, this is a very good choice.

After a waiting time of 3 h after the end of the beam period, the head dump is no longer the dominant contribution to the residual ambient dose rate. This is due to the fact that the most important radionuclide for such short waiting times is ^{11}C , which has a half-life of approximately 20 minutes. The waiting time prior to an intervention will have to be determined by dedicated work and dose planning, but respecting a waiting time of at least three hours before an intervention will always be a good optimization measure.

Even for an accidental distributor timing failure [138], the number of protons absorbed by the tail dump is very low. Its activation will thus be negligible.

3.16.1.2 H^0/H^- dumps

The baseline for the material choice for the internal H^0/H^- dumps is titanium. Graphite as a dump material has been ruled out due to its outgassing properties and including the radiological impact resulting from more complicated interventions. A radiological assessment of the current baseline and a comparison to silicon carbide (SiC) as dump material has been performed and been presented during a dedicated review meeting. It has been demonstrated, for the loading parameters [138] presented in Table 3.76, that:

- i) the estimated ambient dose equivalent rates are comparable to the current ambient dose rate levels in the PS Booster;
- ii) the estimated collective annual dose for the interventions in the PS Booster injection region is 2–5 mSv;
- iii) titanium and SiC are comparable with respect to the collective annual dose with a larger year-to-year variation for titanium;
- iv) the replacement of the BSW4 magnet, which houses the injection dump, has the highest maximum individual dose per intervention. However, this maximum individual dose per intervention is still compatible with the 2 mSv/person/intervention requirement;
- v) there is no intervention that will be above ALARA Level 2 [139].

Titanium has been adopted as the baseline material [140]. This decision was based partially on the conclusions of the radiological assessment as well as the swelling issues for SiC resulting in a larger uncertainty on the number of required interventions.

3.16.2 Main dump

The main beam dump of the PS Booster has been replaced in LS1. The description of the technical details of the new beam dump is given in Section 3.8. An assessment of the radiological hazards has been performed to ensure that the new beam dump complies with the CERN radiological safety requirements. The activation of air, its release to the environment and the resulting exposure of members of the public have been studied, in particular because the new beam dump is actively cooled by air. It has been demonstrated that:

- i) to minimize the radiological impact, the passage of the beam through air, i.e. part of the ventilation circuit of the PS Booster, has to be minimized;
- ii) the effective dose to members of the public from stray radiation and from releases to the environment is well below the dose objective of 1 $\mu\text{Sv}/\text{y}$;
- iii) the committed effective dose due to inhalation will be only a minor contribution to the total effective dose during access, even for very conservative intervention scenarios;
- iv) in the sense of the ALARA principle and under the assumption that the shielding will stay in place for the whole lifetime of the PSB beam dump, the current concrete ring shielding

surrounding the dump core will be replaced by low carbon steel to decrease the stray radiation intensity that penetrates the surface above the PSB beam dump. The ring shielding at the beginning of the dump cavern will be made of concrete or marble to reduce the exposure of workers during access.

3.16.3 Consolidation of water-cooling infrastructure

It is foreseen to consolidate the water-cooling infrastructure of the PS Booster during LS2. To implement the ALARA principle and best practices, it is required to separate the water-cooling circuits for elements inside the PS Booster machine, whose water content gets activated during operation, from the water-cooling circuits for surface infrastructure. In addition, uncontrolled leakage from water circuits containing activated water has to be avoided.

3.16.4 Collimation system

The current main aperture limitation installed in section 8L2 of the PS Booster will no longer be compatible with the planned increased injection and extraction energies. Therefore a new collimation system will be studied and installed. The design of the new collimation system will be optimized to limit the exposure of personnel during interventions as well as the amount of radioactive waste produced.

3.17 Machine interlocks

Machine interlocks are composed of two separate systems: the beam interlock system (BIS) and the magnet interlock system. The first system has been designed to protect the machine from accidental beam loss or from an equipment failure. The second system has been designed to protect the PSB magnets from overheating.

As a generic solution to the interlocking requirements existing throughout the CERN accelerators complex, the two interlock systems are identical to those already in operation for the LHC and many other machines (like Linac4) of the injector chain.

3.17.1 Beam interlock system

3.17.1.1 Overview

The beam interlock system (BIS) is the backbone of the beam-related protection. It takes inputs from subsystems, and inhibits beam operation if a subsystem indicates that there is a problem or that it is not ready for beam operation.

To ensure the overall protection of the PS Booster, it is foreseen that about sixteen different systems or subsystems are to be connected to the BIS (Fig. 3.204).

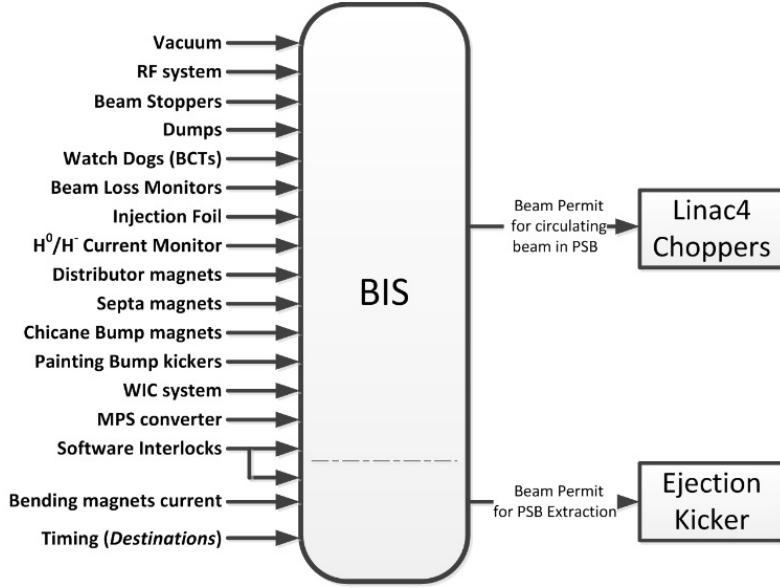


Fig. 3.204: The PSB beam interlock system links

The central element of the BIS is the beam interlock controller (BIC). Each BIC acts as a local concentrator, collecting up to 15 user permit signals (14 hardware and 1 software) from user systems and generating a local beam permit signal. This local beam permit is either an input for another BIC or an input for a selected system to carry on (or inhibit) the beam operation.

Generally, several BICs are needed to protect a machine; in Linac4 and PS Booster they are connected together through a two-layer structure, the ‘tree’ architecture (Fig. 3.205). It makes the connection of local beam permits from BICs attached to an interlock zone (in our case: PSB injection, PSB ring, PSB extraction) to the relevant actuator (Linac4 choppers or ejection kicker), through a special master controller. The latter is a special instance of the BIC as the equation implemented is not a simple ‘AND’ but it is an ‘OR of AND’. Therefore, additional conditions (like beam destination) could be taken into account for permitting safe beam transfers.

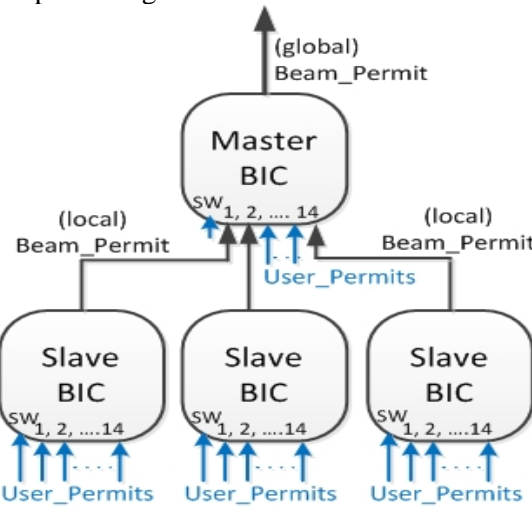


Fig. 3.205: The ‘tree architecture’ of the beam interlock system

PSB operation will be directly linked to Linac4 operation with the PSB being timing master for the combined control system. Thus, injection into the PSB or extraction from the PSB to certain destinations should be not possible in the event of equipment failure. It means that the Linac4 beam should be stopped as close to the source as possible to avoid activation.

Consequently, the BIS layout is adapted to PSB operation with Linac4 as injector. This will lead to a tree architecture, where three slave BICs (PSB inj-1, PSB inj-2 and PSB rings) are providing a local beam permit to the Linac4 Choppers master BIC. Their inputs involve the main elements in the PSB injection region and at extraction (see Fig. 3.206). The final injection permit into the PSB can only be given when both injection as well as extraction elements of the PSB are working correctly.

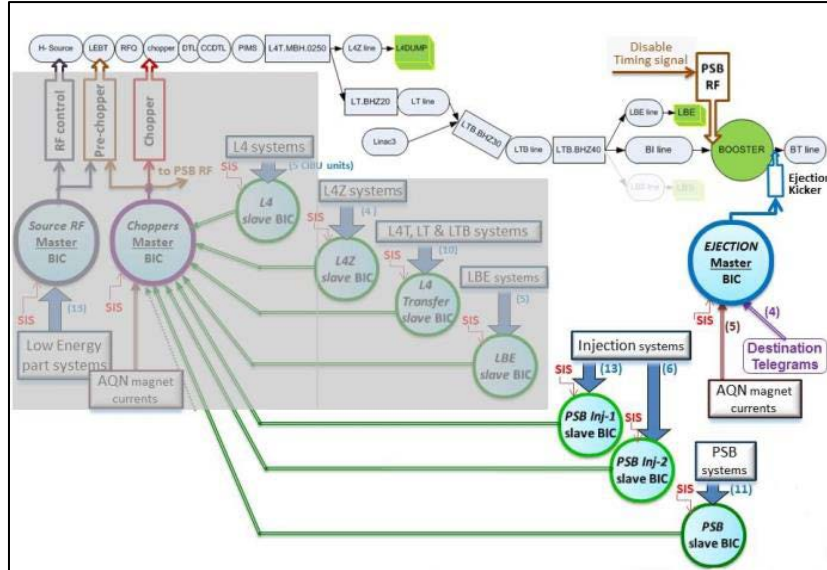


Fig. 3.206: The PSB beam interlock system layout (the grey area shows the Linac4 part of the BIS)

Together with four other slave BICs attached to the Linac4 part, the three slave BICs are connected to the Choppers master BIC (see Fig. 3.206). These together protect the different interlock zones in accordance with the four possible Linac4 beam destinations (Linac4 dump, LBE, PSB or PS). More details can be found in Ref. [141].

It should be noted that the above layout could be modified in the future. Thanks to the modular approach of the BIS, slave BICs could be added or moved in accordance with new requirements.

3.17.1.2 The BIS elements

The user interface unit

The user interface box is a small rack mounted module, installed in the user system rack (Fig. 3.207). Its role is to receive the redundant user permit signals supplied by the user system and transmit them to the beam interlock controller in a safe and reliable manner.



Fig. 3.207: Front and rear views of one user interface

This feature is realized via a simple, reliable and versatile interface. The input circuit of the user interface accommodates any type of hardware platform used by the user system.

In order to set its user permit ‘A’ signal to TRUE, the user system electronics needs to provide sufficient voltage (typically between 3 V and 25 V) across USER.PERMIT.A+ and USER.PERMIT.A- to turn the opto-coupler on (Fig. 3.208). The same should be applied to user permit ‘B’ signal.

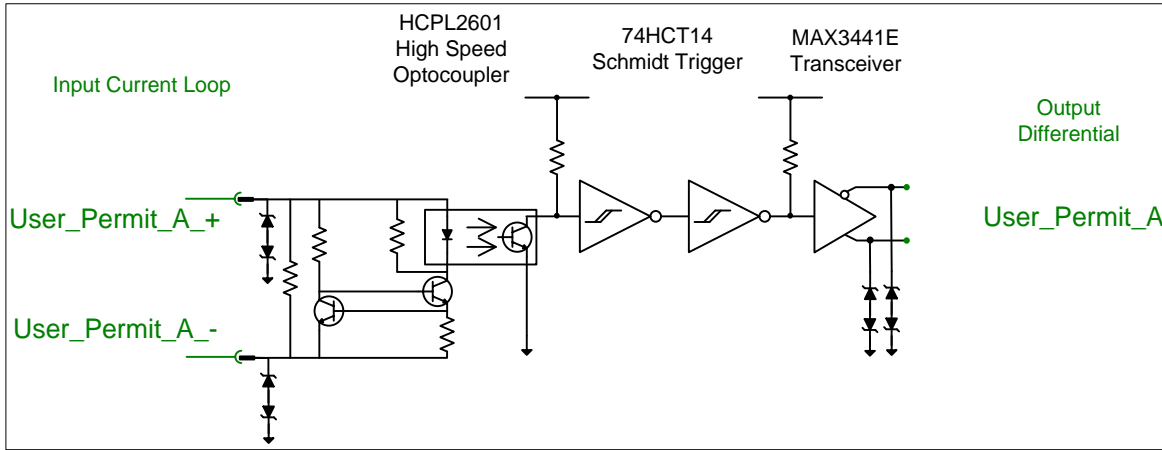


Fig. 3.208: Schematic of the user permit ‘A’ channel (‘B’ channel is identical)

The beam interlock controller

The beam interlock controller routes up to 14 redundant user permit signals provided by the user interface units to two redundant complex programmable logic devices (CPLD). The latter are used to AND together these inputs in order to determine the value of the (redundant) local beam permits.

On each BIC, one additional channel (i.e. the 15th input) is reserved for the calculated output of a software process (the software interlock system). The local beam permits will only be TRUE if all user permit signals, including the software channel, are all in the TRUE state.

The BIC boards and the cable connections from the user interfaces are embedded in a VME crate (Fig. 3.209). The beam interlock controller crate has been built to host up to two BICs and their user interfaces connections.

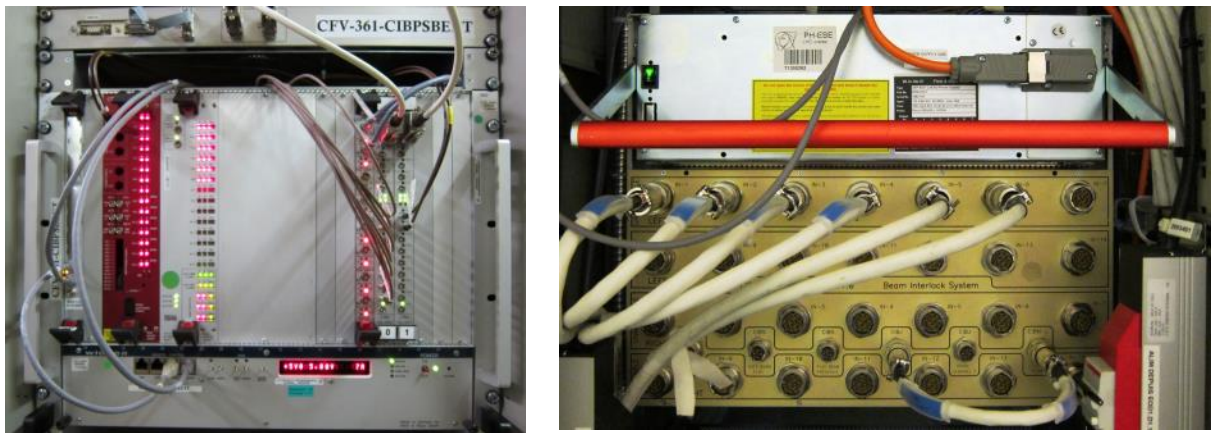


Fig. 3.209: Front and rear views of a beam interlock controller crate

The beam permit interface

The redundant beam permit signals are provided by the BIS to one or several system(s), known as actuators (or target systems). The latter should react to the two following conditions:

- allow the beam operation when the redundant beam permits are both TRUE;
- stop or inhibit the beam operation if one or both beam permit(s) is/are FALSE.

The redundant beam permit signals are transmitted over two copper cables using the RS-485 bus standard. A couple of interface card is provided to safely convert differential signals to/from TTL signals (Fig. 3.210). These two daughter cards (or the equivalent function) are embedded in the actuator's electronics.

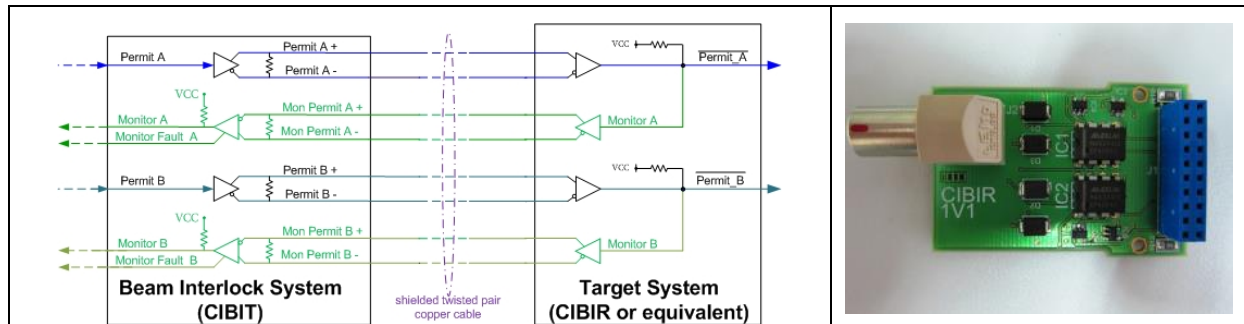


Fig. 3.210: Simplified schematics and top view of one beam permit interface card

3.17.1.3 Main features

- Redundancy: by design the BIS is fully redundant. This redundancy is maintained from the user permit connections right through to the actuator's connections.
- Safety: according to specifications set to meet the dependability requirements for LHC, the system must react with a probability of unsafe failure of less than 10^{-7} per hour (Safety Integrity Level 3 was used as a guideline).
- Fail-safe: any failure along the critical path signal transmission is designed to bring about a fail-safe state (i.e. beam permit = FALSE)
- Availability: the power supply redundancy is implemented in the controller's crates and also in the user interfaces units.
- Critical vs. non-critical: at the conception level, the critical functionality is always separated from the non-critical. Therefore, the monitoring elements are fully independent of the two redundant safety channels (Fig. 3.211).

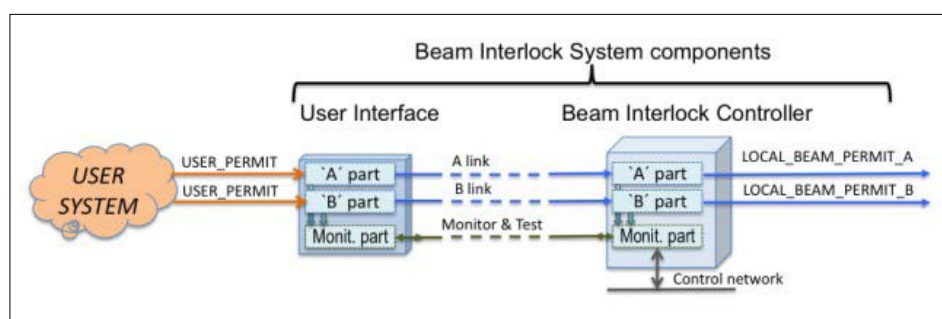


Fig. 3.211: Simplified view of the critical/non-critical paths

100% online test coverage: Using redundant channels in parallel with a monitoring channel, the system can be easily tested from end-to-end in a safe manner. This feature allows the BIS to be recovered ‘as good as new’.

3.17.1.4 Performance

- Reaction time: from user permit change detection to the corresponding local beam permit change, the response time is around 10 μs . The inner contribution of the two BIS elements (user interface electronics plus controller) is on the order of a few microseconds. To this value, one should add the propagation delay of the cable from the user interface to the BIC rack. This value is either negligible ($\sim 0.1 \mu\text{s}$) with a length of 20 m or significant ($\sim 5 \mu\text{s}$) with a length of 1000 m.
- Time stamping: the BIC includes a significant monitoring part; the latter is mainly handling a history buffer for logging anyesermit change through precise time stamping (UTC time) with 1 μs accuracy.

3.17.1.5 Operational tools

Pre-operational check

In order to ensure that the safety of the beam interlock system is not compromised during operation (e.g. after interventions, technical stops, etc.), a dedicated check compares the data read back from the installed hardware with the reference configuration stored in the configuration database. For instance, it compares the physically disabled channels with those defined in the configuration database. It also verifies that the user interfaces units are redundantly powered and their ID numbers match the connection to the correct user input. The BIS pre-operational checks can be launched remotely, either on a daily basis or before any fill (e.g. in the LHC it is part of the nominal cycle executed by the LHC sequencer).

On-line monitoring

Complementing the previous checks, the on-line verification verifies that several critical elements behave correctly. Each check compares data read back from the BIS to predefined settings. An alarm is generated if an error is detected. Different checks are performed, such as user permit consistency, beam permit consistency, user interface communication, timing reception quality, etc. The test also verifies that one of the redundant power supply units has not failed.

Supervision

Thanks to a dedicated FESA class, the status of the installed hardware can be visualized on the BIS graphical user interface (GUI). The latter provides the following features:

- an overall view of each BIC (states of all user permit and beam permit signals) and the connected user interfaces (Fig. 3.212);
- a plot of all changes per cycle/per channel with time markers.

In all cases, a filtering of masked, disabled or interlocking inputs is available.

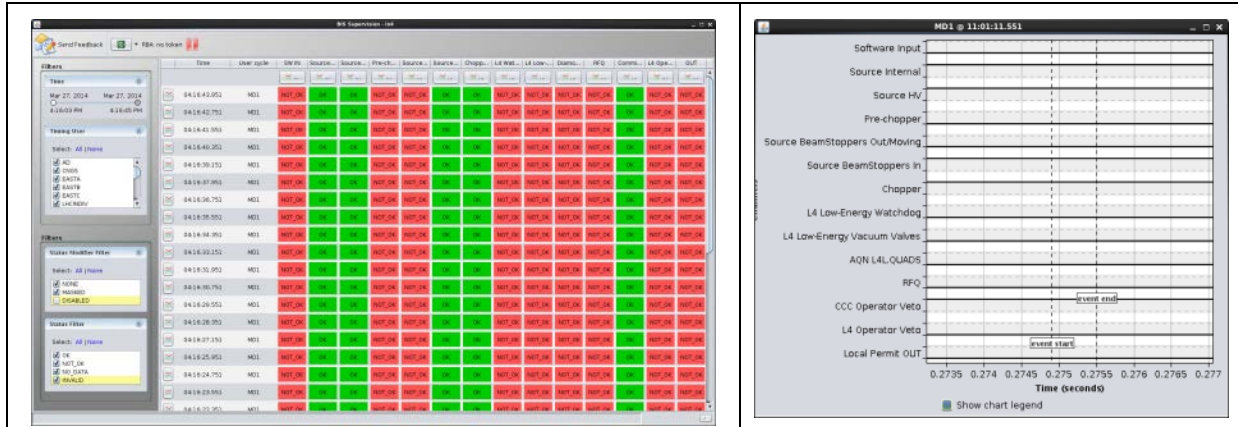


Fig. 3.212: Examples of BIS supervision views

3.17.2 Magnet interlock system

3.17.2.1 Principle

The warm magnet interlock system ensures protection against overheating of the normal conducting magnets. Risk of overheating is essentially due to the risk of a failure in the water cooling of such magnets. In the cooling circuit, one or several flow-meter(s) or pressure sensor(s) is/are installed to monitor the water flow. In addition, on each magnet several temperature probes (i.e. thermo-switches) are installed. The thermo-switch opens if the temperature exceeds a predefined value.

The opening of either one thermo-switch or one flow-meter switch is detected by the interlock controller, which then requests the abort of the power converter.

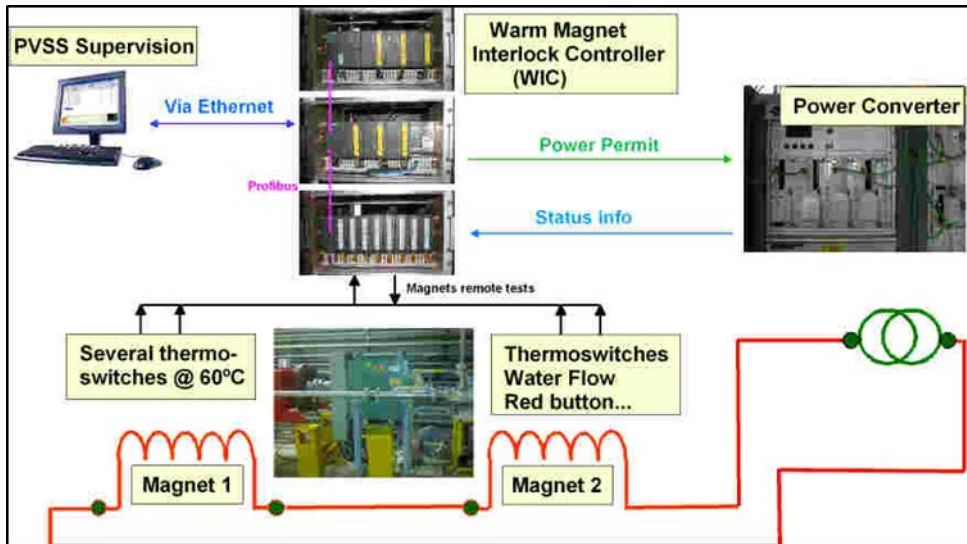


Fig. 3.213: Simplified layout of the WIC system (the magnet interlock boxes are not shown)

The warm magnet interlock controller

The central element of the magnet interlock system is known as the warm magnet interlock controller (WIC). The WIC is a PLC-based system. In order to optimize safety, the Siemens 'F' Series is used, offering a self-checking safety environment that ensures system integrity. The WIC performs self-testing of its own hardware and software to detect failures and corruption, and goes into a safe state in the event of an abnormality. The fail-safe state is to switch the power converters off.

It should be noted that no analogue values are transmitted or processed by the WIC. Only digital information is considered (either OK or NOT OK).

Generic solution

The WIC system has been designed for deployment in different areas by using a generic program and a homogenous hardware solution.

In order to adapt the interlock process to the existing layout, the hardware installation is described within a database (including magnet name, types, inputs and outputs addresses, power converters, interface types, etc.) The installation-specific installation is extracted in the form of a configuration file that is downloaded to the PLC along with the generic code base—the system will then configure itself in accordance with the installed hardware.

Magnet interlock box

As noted above, two different types of digital protection signals are used within the system:

- thermo-switches (several in series per magnet);
- pressure sensors/flow sensors.

In both cases, they are connected via a magnet interlock box, which is directly installed on the protected magnet (see Fig. 3.214).

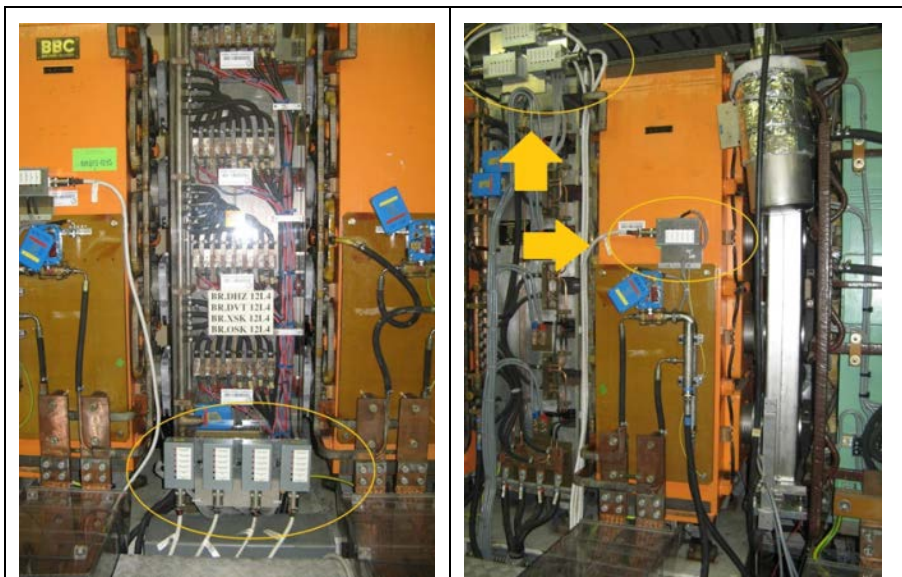


Fig. 3.214: Images of magnet interlock boxes installed on multipole magnets

3.17.2.2 The main components

The WIC system is composed of two essential parts:

- the PLC crate containing the CPU and the safety input modules (Fig. 3.215(a)). The latter collect the signals coming from various magnet sensors (thermo-switches and Elettas water-flow information) and the status input signals from the power converters;
- the chosen CPU (failsafe S7-315F-CPU from Siemens) offers a higher level of protection than a standard PLC, while still assuring a response time of less than 1 s;
- the PLC crate is powered by a redundant power-supply configuration;

- remote input/output crate(s) (see Fig. 3.215(b)). It contains the remote input/outputs used for collecting status signals from the magnets and delivering the signals for the remote tests and for delivering the power permit signals. A dedicated module is installed to give the redundant user permit signals to the beam interlock system.

Note: contrary to the input modules, the output modules used are not safety modules but are standard ones. For that reason two outputs of two different modules are connected in series to meet the dependability requirements.

The PLC crate is connected via a Profibus link to the remote input/output crates.

3.17.2.3 Remote testing

A remote test feature is implemented for facilitating as-good-as-new testing for the interlock system. This is performed using relays implanted into the magnet interlock boxes. These relays simulate the opening of the thermo-switches or the flow sensors. This feature is always guaranteeing system integrity; in particular, after interventions on the interlock cabling sensors or after a modification of the configuration file.

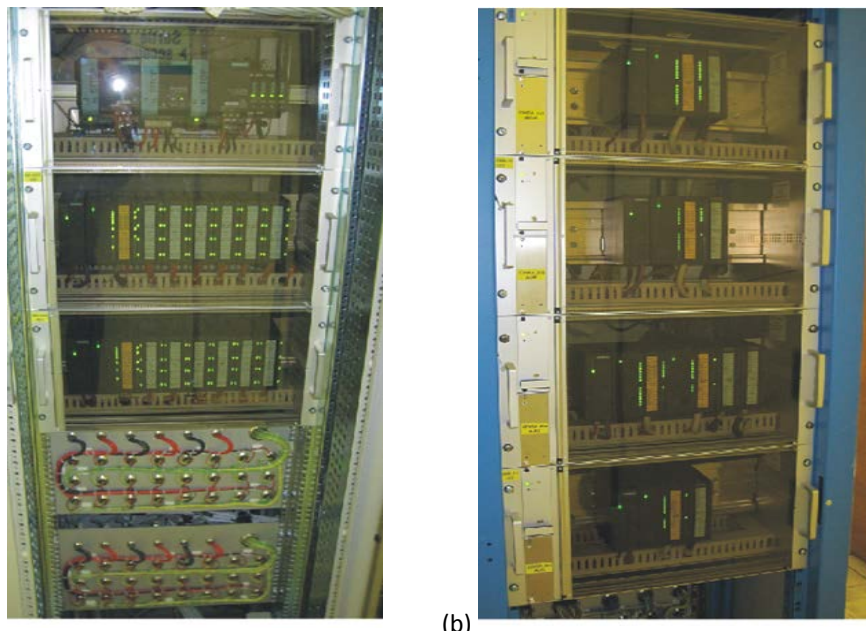


Fig. 3.215: (a) PLC crates containing CPU, redundant power supply and safety input modules; (b) remote input/output crates.

3.17.3 The layout

Four dedicated magnet interlock systems are installed around the Booster (itself divided into 16 periods):

- 1 WIC for the ‘main’ magnets: 1 PLC crate connected to 16 remote I/O units collecting signals from the magnets (BHZ, QFO and QDE) and one output crate controlling three power converters;
- 1 WIC called Aux1, connected to 16 inputs remote units collecting signals from the multipole magnets and two outputs crates controlling 22 power converters;
- 1 WIC called Aux2, connected to six input remote units collecting signals from the multipoles magnets and two outputs crates controlling 72 power converters;

- 1 WIC called Aux3, connected to five inputs remote units collecting signals from the magnets (horizontal and vertical dipoles, sextupoles and octupoles) and two output crates controlling 80 power converters.

A total of 177 circuits are protected by these four WIC systems:

- three circuits for the main magnets;
- 174 circuits for the multipole magnets.

More details on WIC deployment can be found in Ref. [142].

3.17.4 Supervision

A dedicated SCADA tool (based on WinCC) is provided for control and monitoring of the WIC system (Fig. 3.216). It allows the supervision of:

- the magnet statuses (Fig. 3.217(a));
- the power converter statuses (Fig. 3.217(b));
- the interlock process (history buffer);
- the communication statuses: Ethernet and Profibus;
- the signals to the BIS.

It also permits:

- the activation of the remote test (relays/magnet interlock box);
- the remote reset of eventual passivations of input modules.

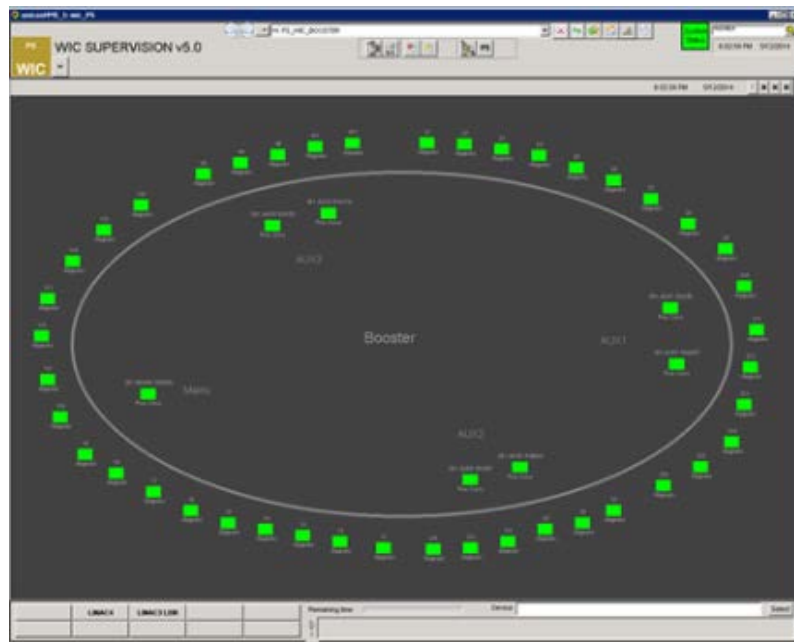


Fig. 3.216: Global view of PSB magnet interlocks system supervision

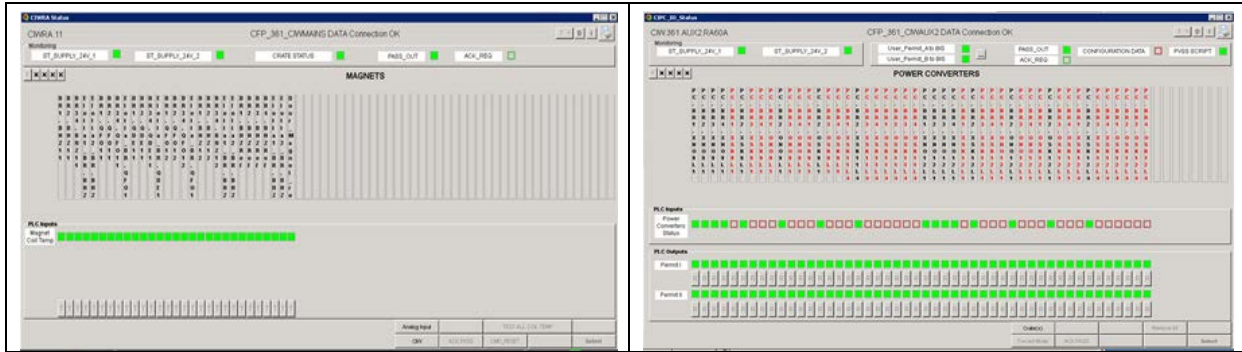


Fig. 3.217: (a) Status of magnet inputs; (b) outputs to power converters

3.18 Survey

For the LIU-PSB project, SU will provide all necessary support in terms of geometric measurements and alignments that will be requested by the different equipment groups. This is valid for all magnetic elements in the PSB ring itself, as well as for the injection and transfer lines.

Already in the design phase of equipment, SU is involved in the design effort for supports, feet/girders, moving tables and target positioning.

This is particularly important for the new injection region, where SU has to cope with the ALARA principle due to radiation issues in this region, combined with the fact that there are many different elements to align within tight accuracy requirements. Furthermore, the alignment methods have to be adapted to short distances and rather large vertical angles. This includes also the introduction of new and smaller target supports that allow measurement of all degrees of freedom without a supplementary tilt surface.

Concerning the PSB ring, two studies will be carried out:

- development of a transversal tilt measurement tool for the main dipole magnets, similar to the tool already used for the quadrupole magnets;
- study the possibility of replacing the existing dipole jacks, where an issue concerning radial and longitudinal movement could appear due to aging and non-availability of spare parts.

SU will also provide to the integration team the 3D scans requested before, during and after the completion of the project, to ensure a complete as-built documentation of the changes of lines and services.

Appendix 3.A

3.A.1 MPC dimensioning results

In this section we will report the results of the calculations performed to dimension the MPC part of the MPS. The QTR converters will be dimensioned in a later stage as they are much smaller in size.

As stated in Section 3.6.2.3 the MPC converter has been dimensioned on an artificial cycle where a design margin has been added.

Calculations are referred to the single magnet string (half of the total magnet impedance).

All calculations have been performed using a suite of Excel files, as shown in Table 3.A.1.

Table 3.A.1: Suite of Excel files used

Title	Description	Author	File Name
Booster2GeV_4MPSdimV5 _4500Vppack_1AFE_1DCD C_doubleCycle	General dimensioning of MPC converters	F. Boattini	Booster2GeV_4MPSdimV5_4500V ppack_1AFE_1DCD_doubleCycle. xslm
Booster2GeVMPSThermal_I EGTST2100GXH24A_V2In terpolLosses	Thermal analysis with IEGTs	F. Boattini	Booster2GeVMPSThermal_IEGTST 2100GXH24A_V2InterpolLosses.xls b
Booster2GeVMPSThermal_I GCT35L4510_DIODE_D13 31SHInterpolLosses	Thermal analysis with IGCTs	F. Boattini	Booster2GeVMPSThermal_IGCT35 L4510_DIODE_D1331SHInterpolL osses.xlsb
Booster2GeVMPSPressPack OutputVoltageV4_4500VpressPack	Output voltage analysis	F. Boattini	POPS_Type_TopoogyPressPack450 0V\Booster2GeVMPSPressPack OutputVoltageV4_4500VpressPack.xlsb

3.A.1.1 Booster 2 GeV MPC: electrical design

The electrical design is the calculation of all major component size. The double-cycle condition (Fig. 3.131) will be used as worst case dimensioning cycle.

Figure 3.A.1 shows the MPC converter layout, with all dimensioned power parts specified in Table 3.A.2.

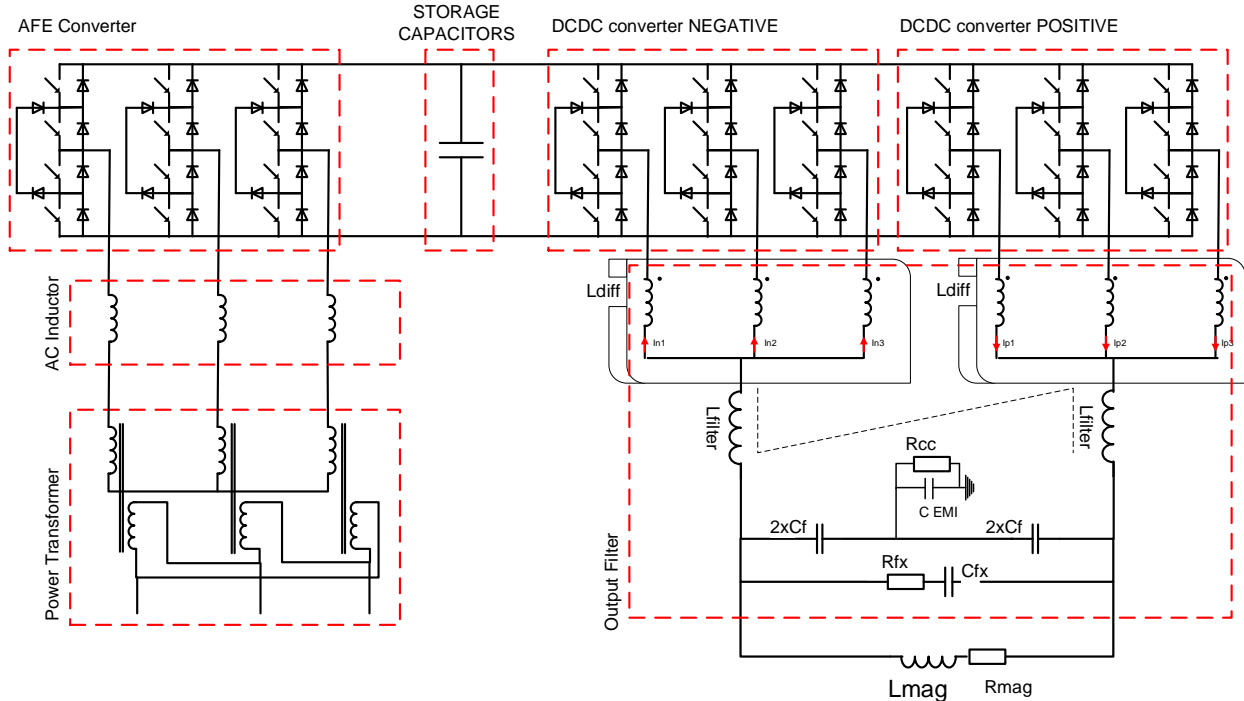
**Fig. 3.A.1:** MPC converter layout

Fig. 3.A.2 shows the simulations of the DCDC converter with the ‘false 900 ms’ double cycle. The power balance shows how the storage capacitor discharge provides the complement of power required by the magnets while the AFE only draws a constant much smaller value.

Fig. 3.A.3 shows the AFE input current at peak power from which the maximum load values for the converter can be drawn.

Fig. 3.A.4 reports the simulation of the storage capacitor current with the rms value.

3.A.1.2 Booster 2 GeV MPC: thermal design

The following data have been assumed for thermal calculation:

- IGBT switching frequency for DCDC converters: 333 Hz;
- IGBT switching frequency for AFE: 1000 Hz;
- the temperature is in a steady state as if the two cycles would repeat identically forever;
- the temperature reported is the differential temperature DT with respect to water temperature assumed to be <40°C.

Table 3.A.2: Power parts dimensioning

Quantity (total)			
Power transformer	3	Voltage	18 kV/1950 V
		Power	2.5 MW
		X_{cc}	8%
Input (AC) three-phase inductor	3	L	400 μ H (8%)
		$I_{nom/max}$	780 A _{rms} /1150 A _{rms}
		C	0.3 F
Storage capacitors	3	U_{dcmax}/U_{dcmin}	5000 V/3200 V
		NRG_stored/NRG_used	3.75 MJ/2.30 MJ
		Peak output current (the complete bank)	6 kA
ACDC converters	3	RMS output current (the complete bank)	1618 A
		Topology	Three phase, three-level NPC, IGBT-based active front end
		Active components	Presspack IGBT-IGCT 4500 V _{rms} 1700 A _{avg}
DCDC converters	3	I_{acnom}	780 A _{rms}
		I_{acmax}	1150 A _{rms}
		I_{pk} commutated	1730 A _{pk}
Output Filter	3	Topology	H bridge—three legs in parallel, three level NPC
		$I_{dcdc} (\times \text{leg})$	860 A _{rms}
		$I_{dcdcmax} (\times \text{leg})$	2000 A
		I_{dcdepk} commutated ($\times \text{leg}$)	2300 A _{pk}
Output Filter	3	Differential inductance for interleaving L_{diff}	Inductance value 2.8 mH
			I_{nom}/I_{max} 1000 A _{rms} /2600 A _{pk}
		Common mode inductance for filtering L_{filter}	L_{cm} 1 mH (coupled inductor L_{cm}) + 2 mH (separate CM inductor)
			I_{nom}/I_{max} 3000 A _{rms} /6500 A _{pk}
		C_f	Capacitance value 500 μ F
			V_{nom} 5 kV
		R_{fx}	Resistance value 2 Ω
			P_{rms} To be defined
C_{fx}			Capacitance value 3300 μ F
			V_{nom} 5 kV

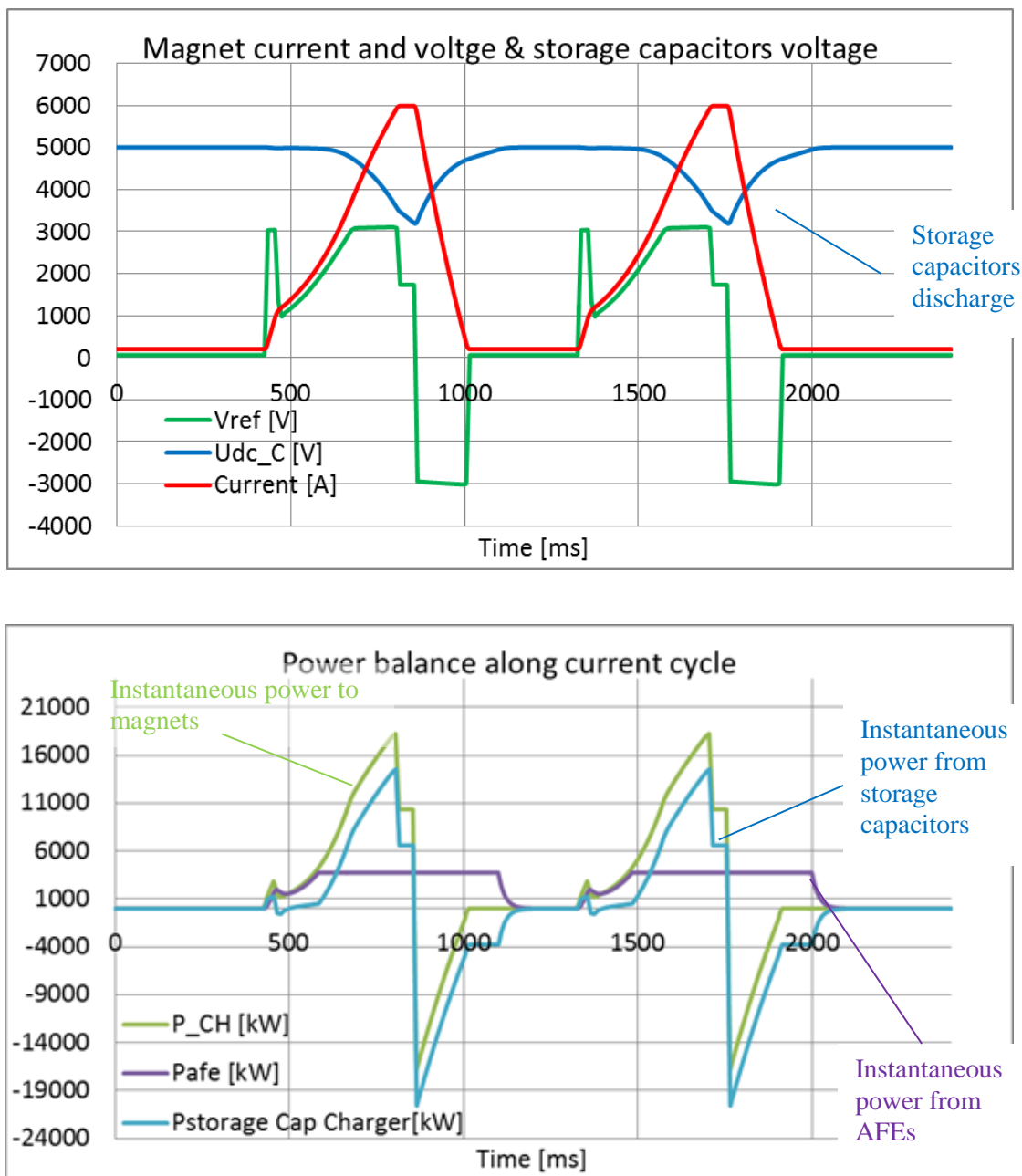


Fig. 3.A.2: MPC electric simulations: DCDC converter side. (a) Magnet current and voltage and storage capacitors' voltage; (b) power balance along current cycle.

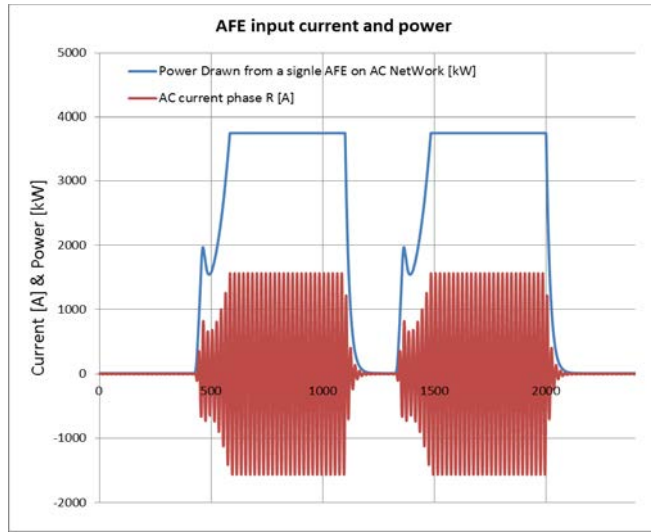


Fig. 3.A.3: MPC electric simulations: ACDC converter side

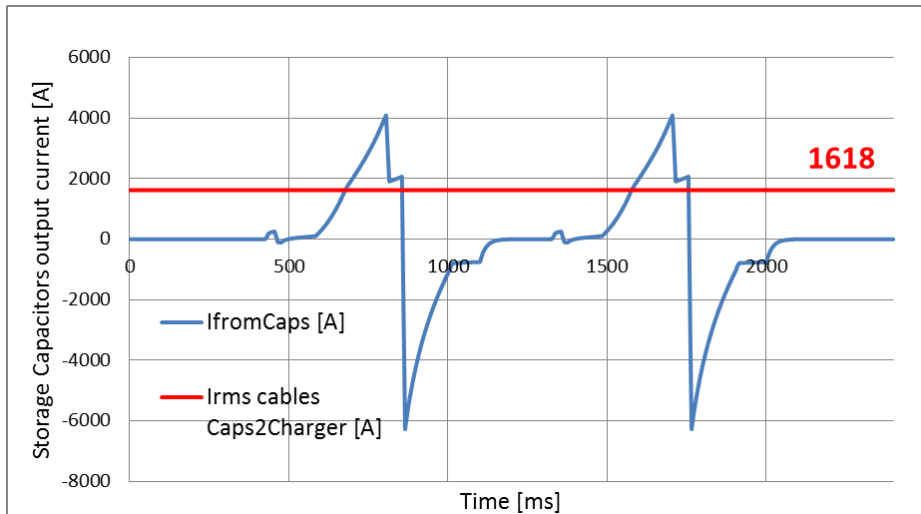


Fig. 3.A.4: Storage capacitor current

Figures 3.A.5–8 show thermal calculation of power converters components considering two different sets of IGBTs/IGCT from Toshiba and ABB.

In all cases the maximum DT is around 30°C and the maximum temperature is around 75°C.

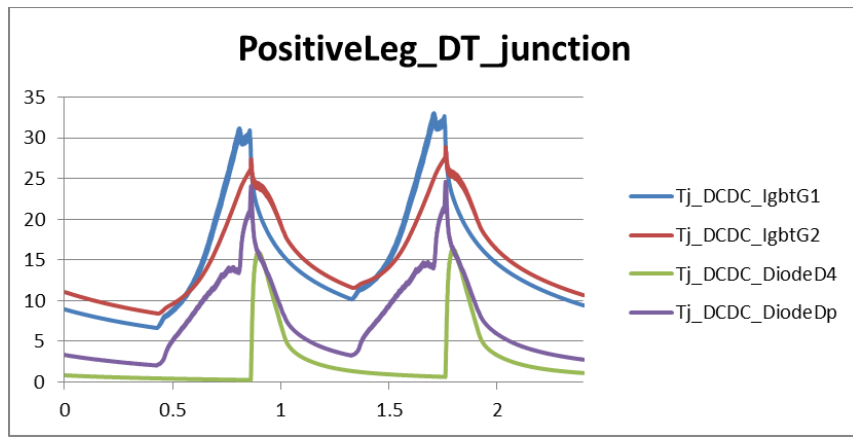


Fig. 3.A.5: DCDC thermal calculation with ABB IGCT 35L410 and Eupec diode D1331SH

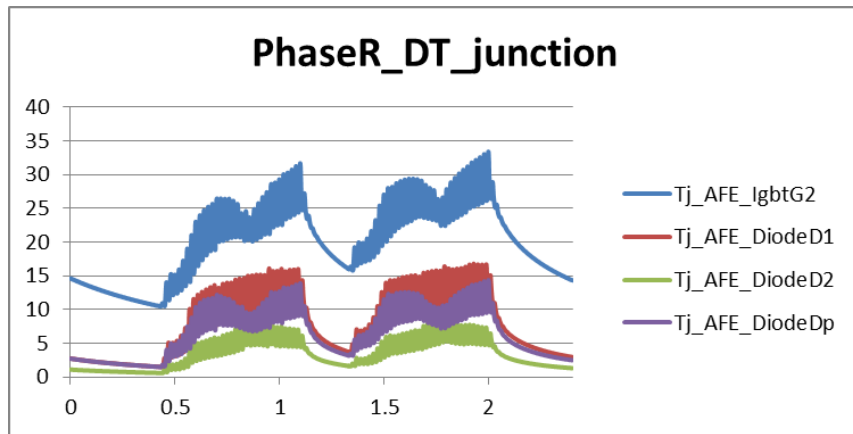


Fig. 3.A.6: AFE thermal calculation with ABB IGCT 35L410 and Eupec diode D1331SH

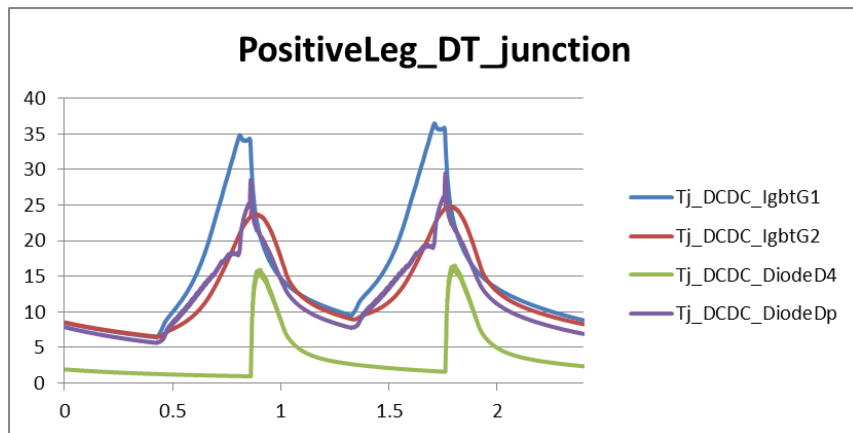


Fig. 3.A.7: DCDC thermal calculation with Toshiba IEGT ST2100GXH24A and diode

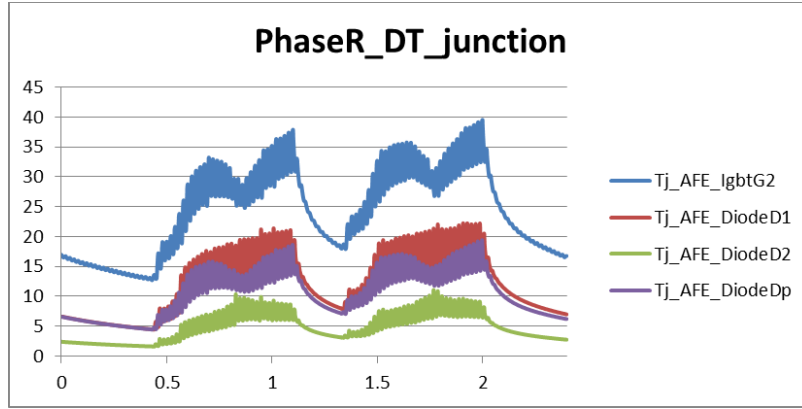


Fig. 3.A.8: AFE thermal calculation with Toshiba IEGT ST2100GXH24A and diode

3.A.1.3 Booster 2GeV MPC: output filter design

The output filter configuration is illustrated in Fig. 3.A.1. It has the classical LCRC configuration with the dumping guaranteed by the RC parallel branch.

The filter transfer function is:

$$\frac{\frac{s}{\alpha Kz} + 1}{\left(\frac{s}{\alpha} + 1\right) \cdot \left(\frac{s^2}{\omega_0^2} + \frac{2\delta}{\omega_0} \cdot s + 1\right)} = \frac{Rx \cdot Cx \cdot s + 1}{L_f \cdot Rx \cdot Cx \cdot C_f \cdot s^3 + L_f \cdot (C_f + Cx) \cdot s^2 + Rx \cdot Cx \cdot s + 1}. \quad (3.16)$$

Given the value reported in Table 3.A.2, the Bode plot and step responses are shown in Fig. 3.A.9.

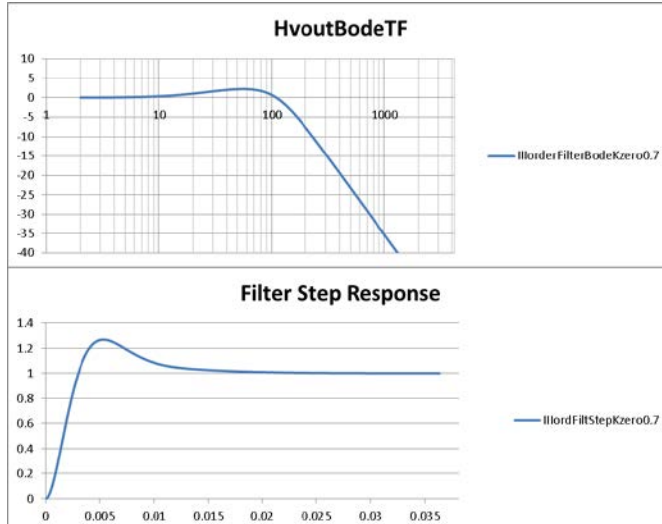


Fig. 3.A.9: Dynamic response of the output filter

The output voltage ripple depends upon the modulation index at which the DCDC converter is driven as is shown by Fig. 3.A.10.

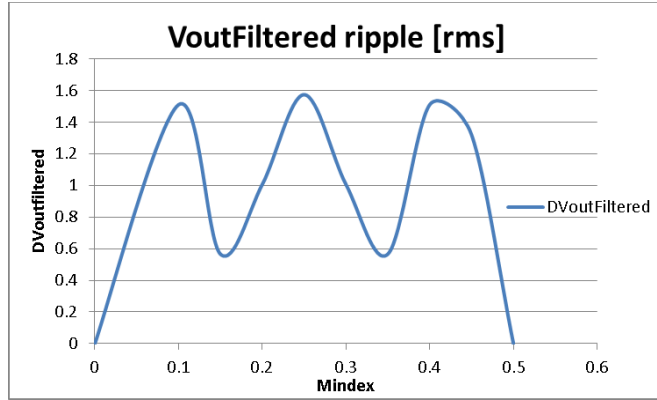


Fig. 3.A.10: Filtered output voltage as function of mod index

3.A.1.4 Booster 2GeV MPS: mechanical design and integration in building 245

A new building (building 245) will be realized to host the power converters and storage capacitors of the MPS.

Power converters and storage capacitors are installed inside the building, while power transformers will be placed outside but very close to it.

3.A.1.4.1 MPS power converters

The MPS will be realized by three identical cabinets rows each one made up of the following items (Fig. 3.A.11):

- MPC:
 - AFE: the AC/DC converter taking the power from the AC network;
 - DCDC: the DC/DC converter supplying the desired current profile to the magnets;
 - output filter and crowbar cabinet;
 - output selector switch;
- QTR:
 - power converter;
 - output selector switch.

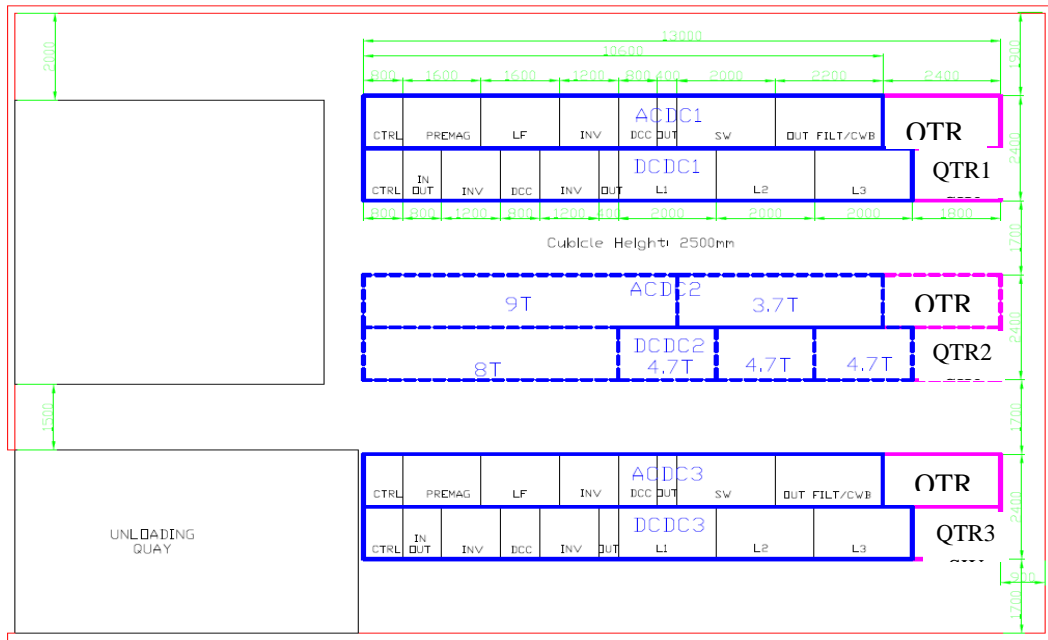


Fig. 3.A.11: Power converter layout

A.3.1.4.2 Storage capacitors

The storage capacitors will be arranged in racks and installed in appropriate rooms in building 245 (Fig. 3.A.12).

Each room is dedicated to a single power converter and hosts a total of 192 capacitors disposed on four separated racks (Fig. 3.A.13), for a total capacitance of 0.3 F..

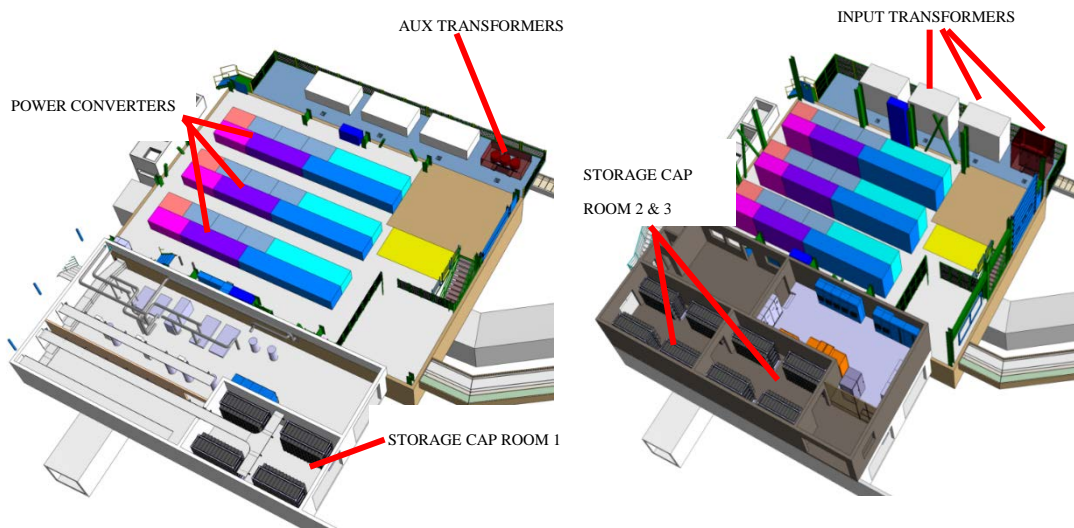


Fig. 3.A.12: Power converters and storage capacitors integrated into building 245

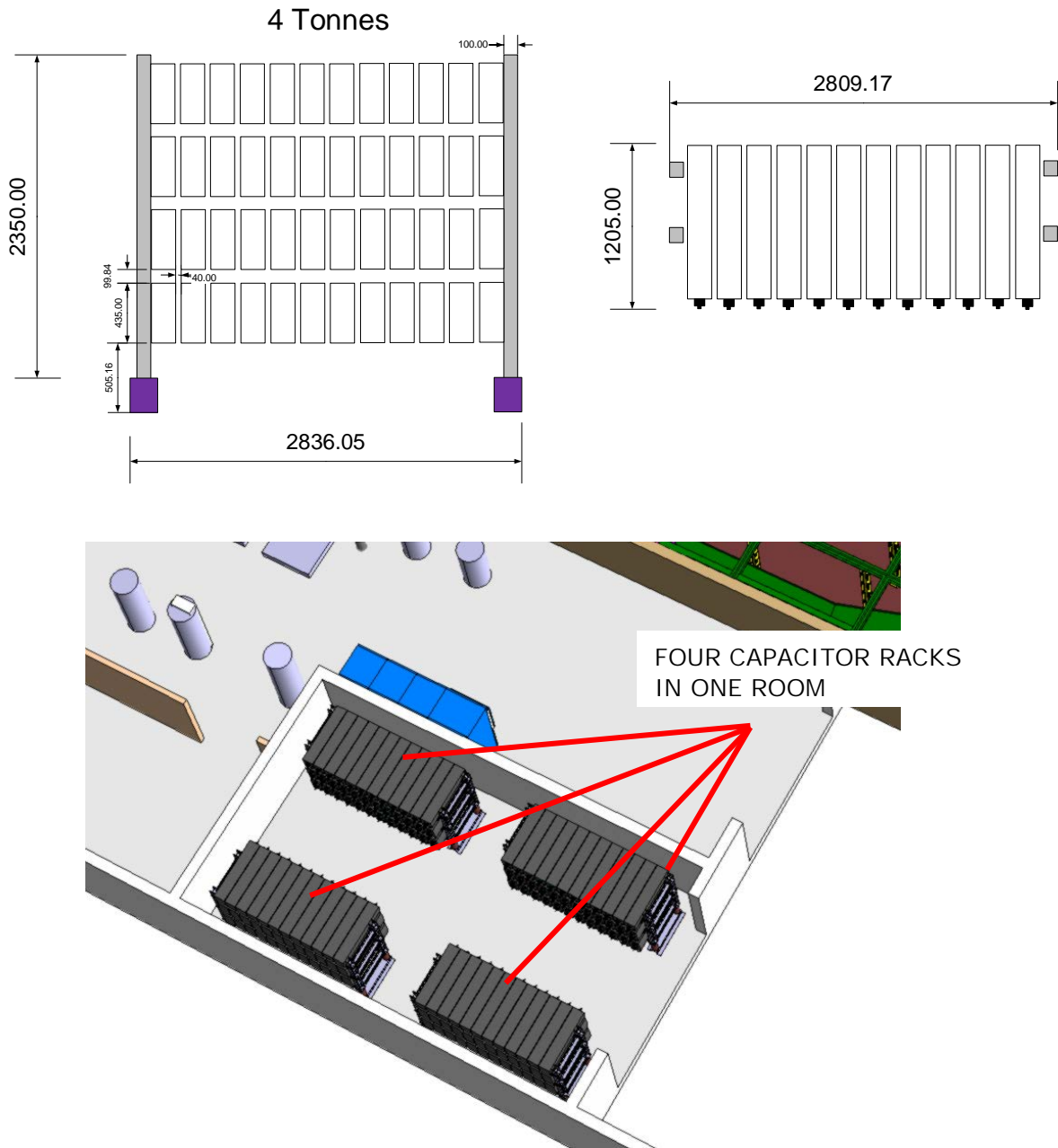


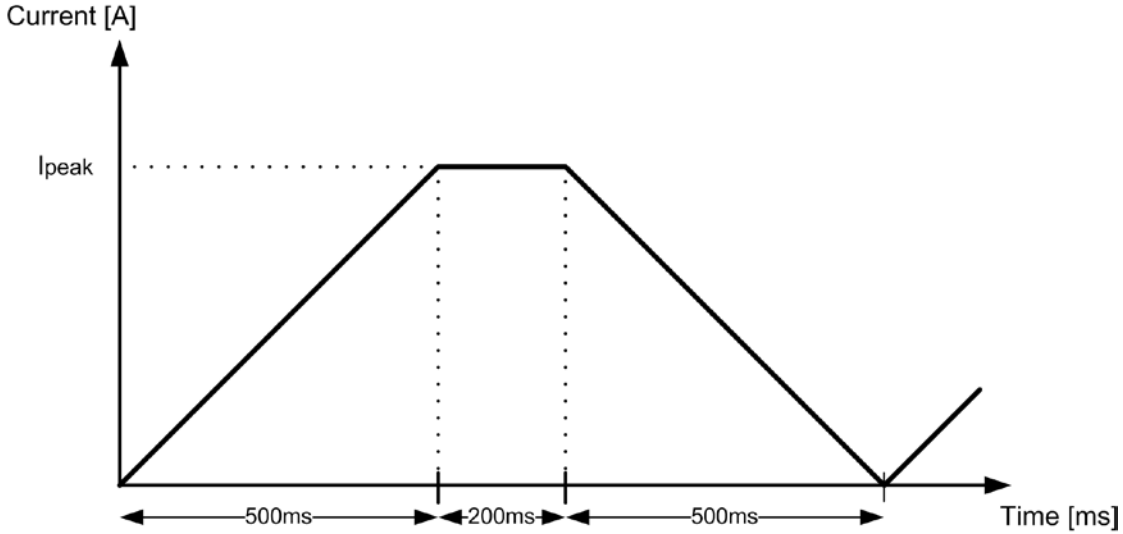
Fig. 3.A.13: Storage capacitor racks

3.A.2 Power supplies for extraction and transfer

3.A.2.1 RMS current reduction

The current into the magnets of the transfer lines is currently DC, with variations of the value according to the needs of the different users. For the upgrade of the transfer lines, a slow pulsed current will be used instead. This allows a higher current value during the transfer, while keeping a low rms value and therefore reducing the losses into the magnets. The resulting losses will be at the same level as previously.

The pulsed current cycle presented in Fig. 3.A14 uses the entire injection period (1.2 s) in order to minimize the dI/dt and therefore reduce the voltage requirement. For one quadrant converters, the decrease of the current will be done by the resistive voltage drop and the current may not reach zero before the new cycle.



$$\text{Magnet current: } I_{rms} = 0.583 I_{peak}$$

$$\text{Magnet losses: } P_{rms} = 1/3 P_{peak}$$

Fig. 3.A.14: Magnet current.

3.A.2.2 Converter upgrade

The new operation with pulsed current and increased peak current requires an upgrade of the control or of the rated power of some converters. Tables 3.A.3 and 3.A.4 summarize the changes to be done; in addition, replacement of all MiniDiscap with MidiDiscap.

Table 3.A.3: Converters with new control

Slot	Model
BE.SMH	ALG-2
BT.BHZ 10	BEN-250KW
BT.BVT 20	B1/IEP
BT.QNO 10	A2/IP
BT.QNO 20	A2/IP
BT.QNO 30	A1/IP
BT.SMV 20	ALG-1
BT1.SMV 10	ALG-1
BT2.DVT 10	A1/IP
BT3.DVT 10	A1/IP
BT3.DVT 40	A1/IP
BT4.SMV 10	ALG-1
BTM.QNO 05	S250A

Table 3.A.4: New converters (or relocation)

Slot	Existing model	
BT.QNO 40	A2/IP	New converter: S500
BT.QNO 50	A2/IP	New converter: S500
BT1.BVT 10	A2/IP	New converter: S500
BT2.DVT 20	A1/IP	Relocation of A2/IP
BT3.DVT 20	A1/IP	Relocation of A3/IP
BT4.BVT 10	A2/IP	New converter: S500
BTM.BHZ 10	B1/IEP	New converter: AuxPS
BTM.QNO 10	S250A	Relocation of A2/IP
BTM.QNO 20	S250A	Relocation of A2/IP
BTP.QNO 35	none	New converter: S500
BTP.QNO 55	none	Relocation of S250A
BTP.QNO 20	A1/IP	New converter: S500
BTP.QNO 30	A1/IP	New converter: S500
BTP.QNO 50	A1/IP	Relocation of S250A
BTP.QNO 60	A1/IP	Relocation of A2/IP

Tables

3.1.	Main parameters of the resistive wall calculation for the different vacuum chambers: thickness of the wall, electrical conductivity of the wall and background material.	41
3.2.	Vertical effective impedance of the elements included in the PSB impedance model for the mode $l = 0$. The last row shows the vertical effective impedance extrapolated from the measured coherent tune shift in Ref. [11]. In the horizontal plane the measured tune shift was almost negligible [11]	46
3.3.	Horizontal tune and instability occurrence time	48
3.4.	Parameters for the two types of simulated beams.....	53
3.5.	Main BIDIS magnet parameters	57
3.6.	Main BISMV (full) magnet parameters.....	62
3.7.	KSW magnet parameters	66
3.8.	Parameters of the KSW circuit	68
3.9.	Main BI.BSW magnet parameters	70
3.10.	List of Booster injection transfer line magnets	75
3.11.	Injection bending magnet parameters for 50 MeV and 160 MeV operations.....	77
3.12.	Injection dipole corrector magnets parameters for 50 MeV and 160 MeV operations.....	78
3.13.	Injection dipole corrector magnet BI.DHZ.DVT40 parameters for 160 MeV operations..	79
3.14.	Injection quadrupole magnets BI.QNO (10:60) parameters for 160 MeV operations.....	80
3.15.	Main bending magnet parameters for 1.4 GeV and 2.0 GeV operations	82

3.16.	Measured integrated field strength before and after the introduction of the laminated coil retain plate	83
3.17.	Focusing quadrupole magnet parameters for 1.4 GeV and 2.0 GeV operations.....	85
3.18.	Defocusing quadrupole magnet parameters for 1.4 GeV and 2.0 GeV operations.....	86
3.19.	List of Booster ejection transfer line magnets	87
3.20.	Recombination bending magnets, T-BV1 (new) parameters for 1.4 GeV and 2.0 GeV operations	90
3.21.	Recombination bending magnet, T-BV2 (new) parameters for 1.4 GeV and 2.0 GeV operations	90
3.22.	Recombination dipole corrector magnets, T-DVT parameters for 1.4 GeV and 2.0 GeV operations	92
3.23.	Correction dipole magnet parameters for 1.4 GeV and 2.0 GeV operations	94
3.24.	Correction dipole magnet parameters for 1.4 GeV and 2.0 GeV operations	95
3.25.	Horizontal switching magnet, PXMBHGAWWP parameters for 1.4 GeV and 2.0 GeV operations	98
3.26.	Horizontal bending magnet, BTM.BHZ10 parameters for 1.4 GeV and 2.0 GeV operations	99
3.27.	Quadrupole magnets, Triumf water parameters for 1.4 GeV and 2.0 GeV operations	100
3.28.	BT and BTP quadrupole magnet (new) parameters for 1.4 GeV and 2.0 GeV operations	101
3.29.	PSB B-train specifications	105
3.30.	C02 acceleration cycle relevant parameters.....	110
3.31.	C04 relevant parameters (single bunch, at extraction).....	111
3.32.	Main features of the DLLRF system	129
3.33.	Summary of changes in the PSB transverse feedback system	138
3.34.	Specification parameters for the vertical septum (BI.SMV) power converters	139
3.35.	Specification parameters for the vertical dipole (BI.BVT) power converters	141
3.36.	Specification parameters for the corrector magnet power converters.....	143
3.37.	Specification parameters for the injection chicane bump (BSW) power converters	144
3.38.	Specification parameters for the chicane correction (Qstrip trim) power converters	146
3.39.	Specification parameters for the consolidation of the BI line Quadrupole (QNO [10, 20, 30, 40, 50, 60]) power converters.....	148
3.40.	Specification parameters for the consolidation of the BI line Steerer (DHZ and DVT [10, 20, 30, 40]) power converters.	149

3.41.	Specification parameters for the consolidation of the LT.BHZ20, LT.BHZ30 and LTB.BHZ40 bending power converters.....	149
3.42.	Specification parameters for the consolidation of the LT line Steerer (DHZ and DVT [40, 50]) and LTB line Steerer (DHZ and DVT [10, 20, 30, 40]) power converters.....	150
3.43.	Specification parameters for the consolidation of the LT line Quadrupoles (QDN[55, 75], QFN[50, 60]) and LTB line Quadrupoles (QFN10, QDN20) power converters.....	150
3.44.	Specification parameters for the consolidation of the LT line Quadrupoles (QFW70) and LTB line Quadrupoles (QFW[30, 50] and QDW[40, 60]) power converters.....	151
3.45.	PS Booster dipole and quadrupole magnet parameters.....	152
3.46.	Main parameters of the new and present MPS	157
3.47.	Main parameters of the present QTR converter.....	159
3.48.	Main parameters of the present DTR converter.....	160
3.49.	APOLO power converter characteristics	163
3.50.	Margins taken for MPS dimensioning	165
3.51.	Voltage insulation level for MPS equipment.....	166
3.52.	Supply for quadrupole focusing magnets.....	167
3.53.	Booster 2GeV power converter loss dissipation in water	168
3.54.	Expected performance of injection watchdog.....	184
3.55.	PSB main dump design parameters for run 3 (after LS2).....	189
3.56.	PSB main dump cooling parameters.....	190
3.57.	Dump core material properties (CuCrZr).....	192
3.58.	Maximum temperatures and stresses reached at dump core for both case studies	194
3.59.	Different case studies of cooling system failure	195
3.60.	Head and tail dump load cases.....	197
3.61.	Head and tail dump cooling parameters.....	198
3.62.	Head dump core maximum longitudinal elongation, maximum vertical deflection and maximum quasi-static equivalent Stassi compressive stresses	201
3.63.	H^0/H^- dump load cases	202
3.64.	H^0/H^- dump cooling parameters	203
3.65.	Summary of maximum steady-state temperatures, in °C, of the assembly, for the various cases considered. Maximum transitory temperatures are indicated between brackets	207

3.66.	Error assignement for trajectory correction studies	210
3.67.	BE.KFA14L1 extraction kicker magnet parameters for 1.4 GeV and 2 GeV	211
3.68.	BESMH extraction septa parameters for 1.4 GeV and 2 GeV	213
3.69.	BT.SMV10 transfer line septum parameters.....	213
3.70.	BT.KFA10 kicker magnet parameters for 1.4 GeV and 2 GeV.....	214
3.71.	BT.SMV20 transfer line septum parameters.....	215
3.72.	Power requirements	219
3.73.	Booster 2GeV power converter loss dissipation in water	230
3.74.	Booster 2GeV air conditioning requirements	231
3.75.	Electrical specifications for the cooling and ventilation infrastructure for building 245	232
3.76.	Loading assumptions for injection dumps of the Linac4 to PSB Injection, taken from Ref. [146].....	242
3.A.1	Suite of Excel files used.....	255
3.A.2	Power parts dimensioning.....	257
3.A.3	Converters with new control.....	265
3.A.4	New converters (or relocation)	266

Figures

3.1.	Measured rms normalized average transverse emittance as a function of bunch intensity for 60 MeV, 100 MeV and 163 MeV [3]	37
3.2.	Intensity evolution for $Q_x = 4.28$, $Q_y = 4.53$ (programmed). In red, the measurement results with the error bar; in blue the simulations for an ideal lattice (no errors); in magenta the simulations with only field errors (Section 3.2.2); in black with the full set of field and alignment errors. For comparison, in brown, simulations with errors but no space charge [6].....	39
3.3.	Tomoscope profiles at (a) C450 and (b) C600 compared with simulated beam profiles (c) C450 and (d) C600 [6].....	39
3.4.	Vertical (full lines) and horizontal (dashed lines) generalized (driving+detuning) resistive wall impedance of the PSB at 160 MeV kinetic energy.....	42
3.5.	Vertical generalized impedance of the PSB at 160 MeV kinetic energy: comparison between the calculations assuming iron background in the magnets (full lines) and those assuming vacuum background (dashed lines).....	42
3.6.	Vertical driving (full lines) and detuning (dashed lines) impedance of the ferrite- loaded structure of the PSB extraction kicker at 160 MeV kinetic energy.....	43

3.7.	Horizontal driving impedance due to the coupling to the external circuits of the PSB extraction kicker at 160 MeV kinetic energy.....	44
3.8.	Total (a) horizontal and (b) vertical driving impedance of the PSB at 160 MeV and 1.4 GeV kinetic energy	45
3.9.	The PS Booster cycle: the full line shows the relativistic Lorentz factor (left vertical axis), the dashed line corresponds to the revolution frequency (right vertical axis). The blue lines indicate the cycle times at which unstable transverse oscillations and the related losses are observed.....	47
3.10.	The pick-up signals of the instability observed in the PSB with double-RF operation. (a) Standard operation, (b) flattened bunch profile, at the cycle time 493 ms, with $N_p = 500 \times 10^{10}$ ppb and a measured growth rate of 0.08×10^{-3}	48
3.11.	Summary for the growth rates of the horizontal instability in the PSB observed around the cycle time 386 ms. The vertical bars indicate the intensity thresholds of instability for RF operation with the corresponding colour.....	49
3.12.	Decay of KSW current as a function of time	51
3.13.	Ratio between final ε_f (after 100 μ s) and initial ε_i emittance for different non-ideal scenarios: (a) mismatched optics, (b) orbit offset, (c) reduced Linac4 current). A factor of two emittance blow-up is observed for the most conservative case (d)	52
3.14.	(a) Dipole and sextupolar component at BSW2. (b) Normalized strength required in the lattice quadrupoles, in absolute value, and in the special QDE3 and QDE14 equipped with trims for beta-beating compensation. The working point is $Q_x = 4.28$, $Q_y = 4.55$	53
3.15.	Vertical beta-beating at 1 ms after injection, before and after the correction with the trims on QDE3 and QDE14.	53
3.16.	Evolution during the fall of the chicane bump (~5000 turns) of (a) the HB beam rms normalized vertical emittance and (b) the HI beam intensity, for the case of (a) ceramic: only edge effects are taken into account and corrected; (b) inconel: edge and multipoles effects, only edge effects corrected; (c) inconel: edge and multipole effects, all corrected..	54
3.17.	(a) Current layout and (b) future layout study in CATIA (ST0428283) of the PSB BI injection line, giving main components and longitudinal positions (m).....	55
3.18.	Timing diagram of the PSB injection region for H^- injection [8].....	55
3.19.	Schematic of the PSB injection line with (a) the BI.DIS and (b) BI.SMV vertical separation schemes [35].....	56

3.20.	Possible Linac4 pulse structures and BI.DIS timing showing: (a) standard operation with 65–100 injected turns per ring, (b) operation with 0 injected turns for ring 3 and (c) pilot beam with 3–5 injected turns per ring	57
3.21.	Finite-element model of BI.DIS with the 1% field region plotted.....	58
3.22.	Assembly model of BIDIS (CATIA ST0221219)	59
3.23.	The BIDIS magnets being inserted in their vacuum vessel. In the background the spare vacuum vessel is waiting to be fitted out.....	59
3.24.	New BI.DIS system layout	60
3.25.	New BI.DIS control architecture	61
3.26.	Optimized angle and offset shown for the half magnets of SMV1 resulting from the simulations of the beam trajectory.....	62
3.27.	The BI.SMV complete vacuum tank assembly (CATIA ST0318018)	63
3.28.	Configuration of the PSB injection region, showing injected and circulating (first turn) beam envelopes of $\pm 4\sigma$ for $\pm 0.4\%$ $\Delta p/p$ variation.....	64
3.29.	Conceptual layout of the injection straight section, seen from the inside of the ring, showing the available space and position (mm) of the BSW magnets.....	65
3.30.	(a) Present and (b) future layout in PS Booster straight section 1	65
3.31.	(a) Present and (b) future layout in PS Booster 16L1	66
3.32.	KSW new ceramic chamber 3D and sectional views.....	66
3.33.	ORBIT simulations of the injected and circulating beams after five turns.....	67
3.34.	(a, b) CATIA 3D models and (c) schematic cross-section of the KSW magnet.....	67
3.35.	Finite-element model of the KSW magnet	68
3.36.	KSW magnet (a) before and (b) after impregnation	69
3.37.	Possible BI.KSW current waveforms. Not to scale	69
3.38.	Conceptual design of the generator, high current version.....	70
3.39.	(a) Temperature rise in carbon foil; (b) evolution of maximum temperature for high-intensity 1.3×10^{13} p^+ beam injected at 1.2 s intervals.	71
3.40.	Cross-section of stripping foil charger and handling system (CATIA ST411236).....	72
3.41.	Foil and support size and clearances required (a) for zero dispersion and (b) matched (-1.4 m) dispersion at injection point.....	73
3.42.	Example of the CERN normal conducting magnet identifier	74
3.43.	3D model of the new BI.BVT40 three aperture vertical injection magnet	76
3.44.	(a) Magnetic design showing Opera 3D model with a map of the magnetic flux density B on the yoke surface: both planes are excited, the value of B does not exceed 1.5 T; (b) field homogeneity of component B_x in GFR; vertical plane excited.....	78

3.45.	The BI.DVT.DHZ 40 magnet integrated on the support for the existing BI.DIS	79
3.46.	Opera 3D magnetic simulation of the pulsed quadrupole magnet (only one coil is displayed)	80
3.47.	Electrical schematic of the PS Booster main magnets as used at 1.4 GeV operations	81
3.48.	The PSB four aperture main dipole magnet.....	82
3.49.	(a) Poisson Superfish 2D simulation showing the effect of introducing the laminated side plate; (b) the prototype installation.....	83
3.50.	The four-aperture defocusing main quadrupole magnet	85
3.51.	Booster ejection layout (BE and BT line).....	91
3.52.	Booster to ISOLDE (BTY)	93
3.53.	The BT(1,2,3,4).DHZ10 corrector dipole magnets (PXMCXADWAP)	95
3.54.	Booster ejection layout (BTM and BTP line)	96
3.55.	(a) New BT.BHZ10 horizontal switching magnet 3D model; (b) magnetic flux distribution in the yoke; (c) field homogeneity in the GFR less than 10×10^{-3}	98
3.56.	Recombination quadrupole magnets in position BT2.QNO.10, BT3.QNO10.....	100
3.57.	The PSB B-train reference magnet in the Power House (building 361)	103
3.58.	The upgraded PS B-train prototype in the U101 reference magnet room.....	104
3.59.	Schematic layout of the 2 GeV PSB B-train.....	106
3.60.	Structure of the White Rabbit Ethernet data packets	107
3.61.	(a) 1.4×10^{13} and (b) 2.5×10^{13} C02 acceleration cycles	110
3.62.	Basic cell configuration. (a) Cell construction; (b) amplifier circuit.....	112
3.63.	MA core mounted on a copper cooling ring	112
3.64.	MA core temperature distribution ($^{\circ}\text{C}$).....	113
3.65.	(a) Single core impedance and R-L-C equivalent; (b) maximum voltage for 1 kW dissipation	113
3.66.	(a) Comparison of measured and simulated impedance; (b) equivalent circuit model	113
3.67.	Differential output amplifier: output circuit configuration	114
3.68.	Single-ended output amplifier: output circuit configuration.....	115
3.69.	Relative change of V_{GS} vs. received dose	116
3.70.	(a) Gap driving currents; (b) vector diagram	117
3.71.	Bunch reconstruction with DC and first four harmonic components (2.5×10^{13} protons, 200 ns, 1.81 MHz).	117
3.72.	(a) Computed accelerating cycle of 1.4×10^{13} protons; (b) gap voltage and beam and generator currents.....	118

3.73.	(a) Computed accelerating cycle of 2.5×10^{13} protons; (b) gap voltage and beam and generator currents.....	118
3.74.	MOSFET saturation currents. Green, VRF151; violet, SD2942; blue, MRF151; red, MRFE6VP6300	119
3.75.	System configuration	119
3.76.	System simulated response: (a) normal; (b) linearized (add 46 dB for absolute gain)	120
3.77.	Measured and simulated amplifier output impedance	120
3.78.	Simulated V_{Gap} (670 V, black) and drain currents (green and red) without beam.....	121
3.79.	Simulated V_{Gap} (670 V, black), I_{Beam} (1.4×10^{13} protons, stable phase $\sim 50^\circ$, blue), and drain currents (light blue and red).....	121
3.80.	PSB DLLRF block diagram for one ring after LS1. DDS: direct digital synthesiser; AD: analogue-to-digital FMC board; DAC: digital-to-analogue FMC board; DSP A, B, C: VXS-DSP-FMC-Carrier boards; RTM: rear transition module; Phase PU: longitudinal phase pick-up; TPU: transverse pick-up; CTRV, timing receiver module; Men A20: master VME board; BTrain: measured magnetic field.....	123
3.81.	VXS-DSP-FMC carrier board block diagram.....	124
3.82.	Picture of the main DLLRF modules	125
3.83.	Test system based upon the new DLLRF modules installed in February 2013 in the PSB RF cage for test purposes.....	125
3.84.	Rack layout in the BOR after LS1	127
3.85.	Block diagram of the RF interlock interface and its connections	128
3.86.	(a) The test PU; (b) new; and (c) present PU head amplifiers	132
3.87.	New PU head amplifier frequency response.....	132
3.88.	Digital signal processing board or BSP	133
3.89.	Beam synchronous digital signal processing block diagram	133
3.90.	800 W power stage board	134
3.91.	Water-cooling distribution diagram	134
3.92.	Water-cooling distribution	135
3.93.	First page of the PLC control menu	136
3.94.	PLC control hardware	136
3.95.	Oasis hardware installation	137
3.96.	New power supply for the power amplifiers.....	137
3.97.	New power attenuators	138
3.98.	MegaDiscap power converter topology	140
3.99.	Septum magnet current	140

3.100. Megadiscap power converter	141
3.101. Topology of the [± 600 A, ± 40 V] power converter	142
3.102. [± 600 A, ± 40 V] power converter.....	142
3.103. Topology of the Mididiscap power converter.....	143
3.104. Mididiscap power converter	143
3.105. Current ramp for the BSW magnets 2, 3 and 4.....	144
3.106. Overview of the BSW power converter system (1 ring).....	145
3.107. Topology of the BSW power converter using IGBTs.....	145
3.108. Cancun [± 50 A, ± 30 V] power converter	146
3.109. Current waveforms for the QCD circuits during injection	147
3.110. Trim function of the QCD circuit in sectors 3 and 14.....	147
3.111. Topology of the power converter for the QCD trim	147
3.112. PS Booster sections.....	152
3.113. PS Booster magnets. (a) Dipole; (b) quadrupole	152
3.114. Existing Booster magnet supply configuration.....	153
3.115. Booster magnets and electrical connections	153
3.116. Magnet electrical parameters used for converter dimensioning	154
3.117. MPS ground reference points.....	155
3.118. 1.4 GeV vs. 2 GeV cycles: current and voltage	156
3.119. Present Booster MPS: electrical scheme.....	158
3.120. Present total power consumption (18 kV side)	158
3.121. Present QTR schematic.....	159
3.122. (a) Focusing and (b) defocusing converter power operating characteristics.....	159
3.123. Present DTR converter schematic.....	160
3.124. New MPS configuration	160
3.125. New MPS schematic diagram.....	161
3.126. AC power behaviour during a 900 ms Booster cycle	161
3.127. IGBT based rectifier and DCDC converter.....	162
3.128. APOLO 2s (two series) topology	163
3.129. Design of the new 2 GeV cycle.....	164
3.130. New 2 GeV cycle for MPS dimensioning.....	165
3.131. New 2 GeV double cycle for dimensioning (false 900 ms)	165
3.132. Voltage ripple requirements for Booster 2GeV main MPC.....	166
3.133. Supply for quadrupole focusing magnets.....	167
3.134. Output voltage ripple requirements for Booster 2GeV quadrupole power supplies	167

3.135. MPS cooling schematic.....	169
3.136. Modification to include test load cooling	170
3.137. Cable connections from building 245 to buildings 271/361 and ME25	172
3.138. Booster 2GeV magnet configuration	172
3.139. Cable routing from building 245 to building 367	173
3.140. Global Booster 2GeV new MPS project planning (macro-activities).....	174
3.141. TE-EPC MPS realization planning	175
3.142. TE-EPC MPS commissioning.....	175
3.143. EN-EL electrical installation.....	176
3.144. EN-EL electrical	177
3.145. (a) Present layout around BI.BTV130. (b) Layout around BI.BTV30 after the modification	178
3.146. Layout of the BT line around the septa BT1.SMV10 and BT4.SMV40 showing the present BTV locations and their future new vacuum tanks which were installed during LS1.....	178
3.147. Part of the layout of the BT line around BT2.SMV20 showing the present location of the BTV inside the septum and the upgrade with this BTV relocated after BT2.QNO30.....	179
3.148. Position of the CHROMOX screen (red) and of the stripping foil holder (black) with respect to the injected and circulating PSB beam axes.....	180
3.149. Sketch of the optical line for beam and stripping foil observation. (a) Observation of the carbon stripping foil. (b) Observation of the scintillating screen (beam).	181
3.150. 3D model of the camera support with all the required ancillaries (lights, filter wheel, etc.)	181
3.151. (a) Monitor plates (red) in front of the dump. (b) Integration in the BSW4 chamber	183
3.152. Signal processing block diagram for one BPM	185
3.153. BTMS block diagram.....	185
3.154. BTMS layout in PSB buildings 37 and 361	186
3.155. Position resolution vs. beam intensity	186
3.156. Beam dump location	187
3.157. Former PSB dump assembly (1972 to 2013).....	188
3.158. Current PSB dump assembly (2013 to present)	188
3.159. Schematic of the cooling system for the PSB beam dump	190
3.160. AHU and air cooling ducts under staircase; beam dump cavity on the right; BTM and BTY beam-lines in the foreground.....	191

3.161. PSB dump core (detailed view from technical drawing ‘PSB Main Dump Final Dump Core Assembly’, PSBTDE_0006)	192
3.162. Temperature profile (°C) of dump core during normal operating conditions	193
3.163. Temperature profile (°C) of shielding rings during normal operating conditions	193
3.164. (a) Distribution of stresses in dump core’s front section (250 mm in length); (b) compressive stresses along centre line of dump (MPa).....	194
3.165. Insertion of dump core inside cavity, October 2013	195
3.166. Proposed Linac4 pulse structure (bottom) and BI.DIS timing (top) showing nominal operation with ~100 injected turns per ring [120]	196
3.167. Schematic layout of the BI.SMV magnets tank and of the position of the head and tail dumps.....	197
3.168. Assembly of the head dump, detail of clamping systems for the cooling channels and for the bake-out system.....	199
3.169. Head and tail dumps within the BI.SMV magnet tank	199
3.170. (a) Detail of the head dump installed onto the BI.SMV3 septum magnet; (b) tail dump installed on BI.SMV1. (c) It can be noted that the circulating beam (in blue) ‘scrapes’ the upper surface of the tail dump	200
3.171. Flanges on BI.SMV tank to be used for the dumps	200
3.172. Flanges on BI.SMV tank to be used for the dump cooling feedthrough.....	200
3.173. (a) Profile of maximum deposited energy density in J/cm ³ /pulse during one pulse, loading case 1 (FLUKA), along the beam direction. (b) Temperature rise at the end of one pulse for loading case 1	201
3.174. (a) Stassi equivalent compressive quasi-static stress (MPa) in the head dump at the end of one pulse, load case 1. (b) Approximation of the vertical deflection (μm) of the head dump core during one pulse, case 1.	201
3.175. (a) Transient increase of maximum temperature rise inside the dump core for the two continuous loading cases, with active cooling. (b) Steady temperature rise field in the head dump, case 3 with cooling.....	202
3.176. Annual collective dose, in mSv, for several interventions within the new PSB injection region, for two different proposed dump materials (SiC ceramic and Ti alloy) and for several cooling times.	203
3.177. (a) The inside of the BSW4 chicane magnet vacuum chamber and the internal H ⁰ /H ⁻ dump. The circulating H ⁺ beam is represented by the blue cylinder. The unstripped H ⁻ particles will follow the green trajectory whilst the partially stripped neutral	

particles H ⁰ will impinge straight on the dump following the pink trajectory.	
(b) Cross-section through the dump.	204
3.178. The dump and current monitor. The plug-in system to allow easy assembly and connection of the dump with the monitor into its final position is also visible.....	205
3.179. Temperature (°C) of the titanium dump core at the end of one beam pulse for load case 1	205
3.180. Evolution of the maximum equivalent Von Mises stress in the dump core during a beam pulse of load case 1.	206
3.181. Equivalent Von Mises stress field (Pa) in the titanium dump core at the end of one beam pulse for load case 1.....	206
3.182. Steady-state temperature distribution in the assembly dump, support and vacuum chamber for (a) load case 2 and (b) nominal cooling conditions.	207
3.183. Transient thermal behaviour (maximum in green and minimum in red) of vacuum chamber and flange for load case 2 and nominal cooling conditions	207
3.184. Optics and horizontal beam envelopes for LHC beams from PSB extraction to PS injection.....	209
3.185. Five hundred uncorrected (blue) and corrected (green) trajectories in the transfer line including misalignments and field errors. The maximum uncorrected trajectories peak at about 30 mm. The red line corresponds to the trajectory error taken into account in the calculation of the specified good field region in the magnets.....	210
3.186. BE.KFA14L1—16 kicker modules in a common vacuum tank	211
3.187. BESMH with infra-red bake-out system activated	212
3.188. Location of building 245.....	219
3.189. Electrical network supplying ME25 (status in 2013).....	220
3.190. Electrical network supplying ME25 (LS1 to LS2)	221
3.191. ME25 modification to single line diagram	221
3.192. Electrical network supplying ME25 (2025 configuration)	222
3.193. Proposed single line diagram ME25	223
3.194. Draft of the LV single line diagram	224
3.195. Power converter water-cooling schematics.....	229
3.196. Water-cooling plant (a) on the roof and (b) inside the building	231
3.197. Piping and instrumentation diagram of the cooling system.....	234
3.198. Implementation of the ventilation system.....	235
3.199. Piping and instrumentation diagram of the ventilation system.....	236
3.200. BTM.BHZ10 and BT.BHZ10 (green and violet element)	237

3.201. Proposed location for building 245	239
3.202. 3D view of building 245 from the north	240
3.203. 3D view of building 245 from the south.....	240
3.204. The PSB beam interlock system links.....	245
3.205. The ‘tree architecture’ of the beam interlock system.....	245
3.206. The PSB beam interlock system layout (the grey part shows the Linac4 part of the BIS).....	246
3.207. Front and rear views of one user interface.....	246
3.208. Schematic of the user permit ‘A’ channel (‘B’ channel is identical).....	247
3.209. Front and rear views of a beam interlock controller crate	247
3.210. Simplified schematics and top view of one beam permit interface card.....	248
3.211. Simplified view of the critical/non-critical paths.....	248
3.212. Examples of BIS supervision views.....	250
3.213. Simplified layout of the WIC system (the magnet interlock boxes are not shown).....	250
3.214. Images of magnet interlock boxes installed on multipole magnets	251
3.215. (a): Image of PLC crates containing CPU, redundant power supply and safety input modules. (b) remote input/output crates.	252
3.216. Global view of PSB magnet interlocks system supervision.....	253
3.217. (a) Status of magnet inputs; (b) outputs to power converters	254
3.A.1 MPC converter layout	255
3.A.2 MPC electric simulations: DCDC converter side. (a) Magnet current and voltage and storage capacitors’ voltage; (b) power balance along current cycle.	258
3.A.3 MPC electric simulations: ACDC converter side	259
3.A.4 Storage capacitor current	259
3.A.5 DCDC thermal calculation with ABB IGCT 35L410 and Eupec diode D1331SH	260
3.A.6 AFE thermal calculation with ABB IGCT 35L410 and Eupec diode D1331SH.....	260
3.A.7 DCDC thermal calculation with Toshiba IEGT ST2100GXH24A and diode.....	260
3.A.8 AFE thermal calculation with Toshiba IEGT ST2100GXH24A and diode	261
3.A.9 Dynamic response of the output filter.....	261
3.A.10 Filtered output voltage as function of mod index	262
3.A.11 Power converter layout	263
3.A.12 Power converters and storage capacitors integrated into building 245.....	263
3.A.13 Storage capacitor racks	264
3.A.14 Magnet current	265

References

- [1] LHC Performance Workshop, Chamonix, 2010,
<http://indico.cern.ch/conferenceOtherViews.py?view=standard&confId=67839>.
- [2] K. Hanke *et al.*, PS Booster energy upgrade feasibility study—First report,
<https://edms.cern.ch/document/1082646/3> (2010).
- [3] B. Mikulec, A. Findlay, V. Raginel, G. Rumolo and G. Sterbini, Tune spread studies at injection energies for the CERN PSB, proceedings HB2012, Beijing, 2012.
- [4] V. Forte *et al.*, SpaceCharge measurements in the PSB—MD report, CERN-ACC-NOTE-2014-0056 (2014).
- [5] E. Forest, A. Molodozhentsev, A. Shishlo and J. Holmes, Synopsis of the PTC and ORBIT integration, (KEK internal report (A), 2007-4, 2007).
- [6] V. Forte, E. Benedetto and M. McAtee, The CERN PS Booster space charge simulations with a realistic model for alignment and field errors, proceedings IPAC14, Dresden, 2014.
- [7] V. Forte *et al.*, PRST-AB, in preparation (2014).
- [8] P. Jackson, Masters thesis, University of Oxford, 2011.
- [9] G. Rumolo, LIU parameter tables. <https://edms.cern.ch/document/1296306/1>.
- [10] G.P. Di Giovanni, LIU-PSB upgrade. <https://twiki.cern.ch/twiki/bin/view/PSBUpgrade/>.
- [11] D. Quatraro, Ph.D. thesis, Bologna, University of Bologna, CERN-THESIS-2011-103, 2011.
- [12] O. Berrig, Private communication (2013).
- [13] K.Y. Ng, Space charge impedances of beams with non-uniform transverse distributions, FERMILAB-FN-0756, 2004.
- [14] C. Zannini, Ph.D. thesis, Lausanne, EPFL, CERN-THESIS-2013-076, 2013.
- [15] K.G. Nilanga *et al.*, *IEEE Trans. Magn.* **44** (2008) 438.
- [16] A. Asner, G. Brianti, M. Giesch and K.D. Lohmann, The PSB main bending magnets and quadrupole lenses, Third international conference on magnet technology, Hamburg, 19 -22 May 1970, proceedings DESY 1972 p. 798-811.
- [17] C. Zannini *et al.*, Effect of the TEM mode on the kicker impedance, proceedings IPAC 2012, New Orleans, (2012).
- [18] N. Wang, Ph.D. thesis, 2010.
- [19] N. Biancacci *et al.*, Impedance calculations for simple models of kickers in the non-ultrarelativistic regime, proceedings IPAC11, San Sebastian, Spain, 2011.
- [20] M. Barnes, private communication (2013).
- [21] <https://www.cst.com/>
- [22] S. Persichelli *et al.*, Finemet cavities impedance studies, CERN-ACC-NOTE-2013-0033 (2013).
- [23] C. Zannini, Status of PSB impedance calculations: Inconel undulated chambers, LIU PSB-Working group meeting, 30 May 2013.
<https://indico.cern.ch/getFile.py/access?contribId=5&resId=0&materialId=slides&confId=254489>.
- [24] F.J. Sacherer, Proc. IX Intern. Conf. High Energy Accel., Stanford, California, 1974.
- [25] C. Carter *et al.*, proceedings PAC'81, Washington DC, 1981.
- [26] V. Kornilov, S. Aumon, A. Findlay, B. Mikulec and G. Rumolo, MD on head-tail instability in the PS Booster, CERN-ACC-NOTE-2014-0025 (2013).
- [27] M. Aiba *et al.*, IPAC'10, Kyoto, Japan, TUPD013 (2010), p. 1949.
- [28] E. Benedetto *et al.*, proceedings IPAC'14, Dresden, Germany (2014).
- [29] C. Carli *et al.*, L4-PSB injection meetings, ABT website, Projects, Linac4-PSB (2011).

- [30] E. Benedetto, Minutes of the LIU-PSB Meeting, INDICO 274490 (2013).
- [31] C. Bracco *et al.*, Studies on Transverse Painting for H- Injection into the PSB, CERN-ATS-2011-277 (2011).
- [32] L. Petty, PSB injection line, EDMS/CDD PSBIHENS0032 vAG (2011).
- [33] J. Sanchez Alvarez, PBU-C-EP-0001, EDMS 1324759 (2013).
- [34] P. Bossard and F. Völker, Proc. MT-5, Frascati, 1975.
- [35] W. Weterings, PBU-MSMIA-EP-0001, EDMS 1178044 (2013).
- [36] B. Goddard and W. Weterings, L4-T-EP-0001, EDMS 963395 (2012).
- [37] M. Delonca and C. Maglioni, PBU-T-ES-0001, EDMS 1145567 (2013).
- [38] M. Angoletta *et al.*, Synchronisation between Linac4 and the PS Booster, CERN-ATS-Note-2010-052 (2010).
- [39] M. Paoluzzi, A Fast 650 V Chopper Driver, CERN-ATS-2011-026 (2011).
- [40] J. Borburgh *et al.*, proceedings EPAC'08, Genoa IT, WEPC141, (2008).
- [41] R.A. Barlow, PBU-MSMIA-ES-0001, EDMS 1339372 (2013).
- [42] M. Hourican *et al.*, *IEEE Trans. Appl. Supercond.* **22** (2012) 4000304.
- [43] M. Hourican *et al.*, PBU-MSMIB-EP-0001, EDMS 1170734 (2012).
- [44] W. Weterings, PBU-VCKC-CI-0001, EDMS 1214235 (2012).
- [45] J. Borburgh *et al.*, PBU-MKBSW-ES-0001, EDMS 1157402 (2014).
- [46] M. Martini and C.R. Prior, High-Intensity and High-Density Charge-Exchange Injection Studies into the CERN PS Booster at Intermediate Energies, proceedings EPAC'04, Lucerne, WEPLT028 (2004), p. 1891.
- [47] B. Goddard *et al.*, proceedings IPAC'10, Kyoto, THPEB030, 2010, p. 3951.
- [48] W. Weterings *et al.*, proceedings PAC'07, Albuquerque USA, TUPAN109, 2007, p. 1628.
- [49] P. van Trappen, PBU-TKSTR-EP-0001, EDMS 1367070 (2014).
- [50] P. van Trappen, Siemens ET200S CPU, private communication (2014).
- [51] J. Lopes and R. Lopez, NORMA—Conventions for identifiers of normal conducting magnets and components, <https://edms.cern.ch/document/1103449/2>.
- [52] A. Newborough, The modifications of the BI.BVT40 vertical dipole magnet in the Booster injection region with the LINAC 4, CERN TE/MSC/MNC, <https://edms.cern.ch/document/1188530/1>.
- [53] C. Carli, Beam dynamics for PSB injection (2012).
- [54] L. Vanherpe, Corrector Magnet for PSB Injection, CERN TE/MSC/MNC <https://edms.cern.ch/document/1277962/1.0>.
- [55] S. Pittet, L. Charnay and J.M. Cravero, Technical specification—Low power capacitor discharge converters. CERN (2010) <https://edms.cern.ch/document/1005478/3.1>.
- [56] W. Weterings, Modification to BI.DIS deflection angles and parameters of related equipment. CERN, <https://edms.cern.ch/document/1178044/1.0> (2010).
- [57] A. Aloev, Quadrupoles for the PS Booster injection line, CERN TE/MSC/MNC <https://edms.cern.ch/document/1297809/1>.
- [58] M. Benedikt and C. Carli, Operation of the CERN PS-Booster above 1 GeV, Saturation effects in the main bending magnets and required modifications, CERN Internal Note CERN/PS 9-059 (OP) (1998).
- [59] A. Newborough, M. Buzio and R. Chritin, Upgrade of the CERN Proton Synchrotron Booster bending magnets for the 2 GeV Energy Upgrade, *IEEE Trans. Appl. Supercond.* **23**.

- [60] A. Newborough, PSB Upgrade – Coil Force Measurements & Endurance Testing – April 2010.
<https://twiki.cern.ch/twiki/pub/PSBUpgrade/MinutesMeeting16September2010/MagnetTestsSM18.pdf>.
- [61] A. Blas, PSB magnetic cycle 900 ms, <https://indico.cern.ch/event/184980/>.
- [62] J. Cole and A. Newborough, PS Booster main magnet thermal switch interlock upgrade, <https://edms.cern.ch/document/1393802/1>.
- [63] J. Cole and A. Newborough, PS Booster quadrupole magnet hose connection upgrade, <https://edms.cern.ch/document/1393798/1>.
- [64] W. Bartmann and A. Newborough, BT line optics and BT.BHZ10, <https://indico.cern.ch/event/189318/>.
- [65] A. Aloev, Design Report for PS Booster transfer line switching magnet BT.BHZ10 (PXMBHGAWWP), <https://edms.cern.ch/document/1394217/1>.
- [66] J. Cole and S. Pittet, Upgrade study of magnet BTM.BHZ10, <https://edms.cern.ch/document/1282267/1>.
- [67] W. Bartmann, Optics of the ejection lines @2GeV and potential impact on hardware, <http://indico.cern.ch/event/274495/>.
- [68] J.L. Abelleira and W. Bartmann, New optics of the PSB measurement line (BTM), <https://indico.cern.ch/event/315820/>.
- [69] M. Buzio, R. Chritin, D. Cornuet, P. Galbraith and D. Giloteaux, Status and outlook of B-train systems for magnetic field control, ATC/ABOC days 2008, CERN (2008).
- [70] G. Bertotti, *Hysteresis in Magnetism* (Academic Press, San Diego, 1998).
- [71] P. Dreesen and I. Garcia Alfonso, A new B-train system for the PS accelerator, CERN PS/PO
- [72] M. Benedikt, F. Caspers and M. Lindroos, Application of magnetic markers for precise measurement of magnetic fields in ramped accelerators, CERN/PS 99-006 (OP) (1999).
- [73] M. Buzio, D. Giloteaux and D Oberson, PS Booster B-train upgrade, EDMS 1424058 (2014).
- [74] O. Andreassen, A. Beaumont, M. Buzio, F. Caspers, D. Cote, O. Dunkel, P. Galbraith, J. Garcia Perez, D. Giloteaux, G. Golluccio, C. Petrone and L. Walckiers, Upgraded B-train systems for magnetic field control in LHC injectors, TE Technical Meeting 08.03.2011, EDMS 1135199.
- [75] <http://www.ohwr.org/projects/show/spec>.
- [76] J. Serrano, P. Alvarez, M. Cattin, E.G. Cota, P.M.J.H. Lewis, T. Włostowski *et al.*, The White Rabbit Project, Proc. ICALEPCS TUC004, Kobe, Japan, 2009.
- [77] U. Dorda, M. Benedikt *et al.*, Status of the Medaustron ion beam therapy centre, proceedings IPAC 2012.
- [78] A. Beaumont, M. Buzio, R. De Oliveira, O. Dunkel, M. Stockner and T. Zickler, Printed circuit fluxmeter to measure the bending magnets of the MedAustron synchrotron, Proc. 17th International Magnetic Measurement Workshop, La Mola, Barcelona, 2011.
- [79] R. Garoby *et al.*, Upgrade plans for the LHC Injector Complex, proceedings IPAC2012, New Orleans, USA, 2012, p. 1010.
- [80] A. Findlay, private communication.
- [81] Nanocrystalline soft magnetic material FINEMET®, Hitachi Metals brochure HL-FMJ, <http://www.hitachi-metals.co.jp/e/products/elec/tel/pdf/hl-fm4-j.pdf>.
- [82] M.M. Paoluzzi *et al.*, Studies on a wideband, solid-state driven RF system for the CERN PS Booster, proceedings IPAC2012, New Orleans, Louisiana, 2012, p. 3749.
- [83] M.E. Angloletta, J. Bento, A. Blas, E. Bracke, A. Butterworth, F. Dubouchet, A. Findlay, F. Pedersen and J. Sanchez-Quesada, CERN's LEIR Digital LLRF: System overview and operational experience, proceedings IPAC'10, Kyoto, Japan, 2010, p. 1464.

- [84] M.E. Angoletta, A. Blas, M. Jaussi, P. Leinonen, T.E. Levins, J.C. Molendijk, J. Sanchez-Quesada and J. Simonin, A leading-edge hardware family for diagnostics applications and low-level RF in CERN's ELENA Ring, IBIC 2013, Oxford, 2013, TUPF28.
- [85] M.E. Angoletta, C. Carli, F. Caspers, S. Federmann, J. Molendijk, F. Pedersen and J. Sanchez-Quesada, An ultra-low-noise AC beam transformer and digital signal processing system for CERN's ELENA Ring, IBIC 2013, Oxford, 2013, TUPF27.
- [86] M.E. Angoletta, F. Caspers, S. Federmann, J. Molendijk, J. Sanchez-Quesada, P.J. Secouet, L. Søby, F. Pedersen and M. Timmins, Longitudinal beam diagnostics from a distributed electrostatic pick-up in CERN's ELENA ring, IBIC 2013, Oxford, 2013, WEPEF28.
- [87] T. Eriksson (editor) *et al.*, Upgrades and consolidation of the CERN AD for operation during the next decades, CERN-ACC-2013-0036 (2013).
- [88] M.E. Angoletta, Digital low-level RF, proceedings EPAC '06, Edinburgh, Scotland, 2008, p. 1847.
- [89] <http://www.vita.com>
- [90] M.E. Angoletta, A. Blas, A. Butterworth, A. Findlay, P. M. Leinonen, J.C. Molendijk, F. Pedersen, J. Sanchez-Quesada and M. Schokker, CERN's PS Booster LLRF renovation: plans and initial beam tests, proceedings IPAC'10, Kyoto, Japan, 2010, p. 1461.
- [91] M.E. Angoletta, A. Blas, A. Butterworth, A. Findlay, M. Jaussi, P. Leinonen, J. Molendijk and J. Sanchez-Quesada, PSB beam longitudinal blow-up by phase modulation with the digital LLRF prototype system, CERN-ACC-NOTE-2014-0007 (2014).
- [92] M.M. Paoluzzi, M.E. Angoletta, A. Findlay, M. Haase and M. Jaussi, Beam tests and plans for the CERN PS Booster wideband RF system prototype, IPAC'13, Shanghai, 2013, p. 2660.
- [93] M.E. Angoletta, A. Blas, A. Butterworth, C. Carli, M. Chalen, A. Findlay, H. Kozsar, B. Mikulec, J. Molendijk, M. Paoluzzi, F. Pedersen and J. Sanchez, Synchronisation between Linac4 and the PS Booster, CERN-ATS-Note-2010-052 (2010).
- [94] D. Perrelet, New 1-turn feedback for the PS 10 MHz cavities, CERN MSWG presentation, 27/8/2013, <https://indico.cern.ch/event/268549/contribution/4/material/slides/1.pdf>.
- [95] J. Belleman, A. Blas (ed.), J-L. Gonzalez, F. Caspers, W. Hofle, T. Kroyer, R. Louwerse, F. Pedersen, V. Rossi and J. Tuckmantel, PS transverse damping system for the LHC beams, AB/RF-Note-2005-027 (2005).
- [96] L. Arnaudon, M. Disdier, P. Maesen and M. Prax, Control of the LHC 400 MHz rf system (ACS), LHC Project Report 760 (2004).
- [97] BoosterBoosterA. Newborough, High_Voltage_test_procedure_PSB_V4, EDMS 1019755.V2.
- [98] F. Boattini, Booster2GeV_Cooling_specificationsV7, EDMS 1327071.v7.
- [99] F. Boattini, 1399168_V2_Booster_2GeV_cabling, EDMS 1399168_V2.
- [100] L4-T-EP-0003-rev 1.0, Measurement of beam current at the PSB H^0/H^- injection beam dump, EDMS n. 1069244.
- [101] PBU-T-ES-0007-rev 0.1, New baseline design for the H^0/H^- beam dump, EDMS 1347485.
- [102] W. Bartmann and B. Mikulec, PS Booster Dump Upgrade, PBU-T-ES-0002, EDMS 1229493.
- [103] A. Sarrió Martínez and A. Perillo-Marcone, The new Proton Synchrotron Booster Dump, EDMS 1392934.
- [104] E. Urrutia, B. Riffaud and A. Dallocchio PSB MAIN DUMP Technical drawings (CDD PSBTDE_ _ %).
- [105] R. Froeschl, Radiation Protection Constraints for the future PSB Beam Dump, EDMS 1345698, PSB Dump Design Review (2012).
- [106] G. Mason, LIU-PSB beam dump cooling system, EDMS 1250483.

- [107] R. Froeschl and P. Vojtyla, Radiological hazard assessment of the future PSB beam dump, CERN-DGS-2012-094-RP-TN, 2012 (EDMS 1243621).
- [108] BoosterG. Camplone and E. Da Riva: CFD thermal simulations for the air-cooling of the PSB dump upgrade, EDMS 1263715.
- [109] M. Garlaschè, PSB dump: Evaluation of cores joining, EDMS 1308583.
- [110] E. Nowak, V. Vlachoudis and M. Calviani, FLUKA PSB dump studies, ATS/Note/2012/098 TECH.
- [111] A. Fasso, A. Ferrari, J. Ranft and P.R. Sala, FLUKA: a multi-particle transport code, CERN-2005-10 INFN/TC 05/11, SLAC-R-773 (2005).
- [112] V. Venturi, New PSB dump study, EDMS 1309632.
- [113] M. Garlaschè, PSB dump insertion, EDMS 1302713.
- [114] A. Sarrio Martinez, PSB dump: ALARA procedure meeting (INDICO, LIU-PSB).
- [115] W. Weterings and B. Goddard: Loading assumptions for beam dumps of Linac4 PS Booster injection, L4-T-EP-0001 v.3.0, EDMS 963395.
- [116] C. Maglioni and M. Delonca, Design constraints and thermo-mechanical study of head & tail dumps, PBU-T-ES-0001 v.1.0, EDMS 1145567.
- [117] C. Maglioni, M. Delonca and A. Ouzia: The H⁰/H⁻ Dumps for the PSB Injection Region, PBU-T-ES-0006, EDMS 1293512.
- [118] R. Froeschl, RP status for the PSB injection head dump, EDMS 1251305.
- [119] R. Froeschl, Radiation protection assessment of the PSB H⁰/H⁻ injection dumps, LIU-PSB meeting on H⁰/H⁻ dump review, EDMS 1282829 (2013).
- [120] R. Froeschl, Radiation protection assessment of the titanium option for the future PSB H⁰/H⁻ injection dumps, EDMS 1341929.
- [121] R. Froeschl, Radiation protection studies for the future PSB injection region, in work, EDMS 1355930.
- [122] J. Hansen, Technical description of the LIU-PSB vacuum system. CERN EDMS 1247082.
- [123] W. Weterings, Design parameters for BI.BSW undulated vacuum chambers. CERN EDMS 1277821.
- [124] F. Carra, Preliminary FEM analyses on the new "Y" T-BH vacuum chamber, CERN EDMS 1301064.
- [125] W. Bartmann *et al.*, Upgrades for the CERN PSB-to-PS transfer at 2 GEV, IPAC'13, Shanghai, China.
- [126] W. Bartmann, PSB ejection lines, Review of the PSB ejection lines, <http://indico.cern.ch/event/274495/>.
- [127] EN/EL, Projet de consolidation et d'extension du réseau Haute Tension du CERN à l'horizon 2025, EDMS 1153990 (2012).
- [128] EN/EL, Consolidation of the electrical network in the Meyrin site: impact on the SVC Booster, EDMS 1309944 v.2 (2013).
- [129] EN/EL Drawing 18KV NORMAL SIMPLIFIED DIAGRAM – NOVEMBER 2013 CONFIGURATION, EDMS 808893 v.AH (2013).
- [130] EN/EL Drawing SCHEMA PRINCIPE DISTRIBUTION BT S/S—T.25—BAT.271, EDMS 221951 v.AF (2012).
- [131] EN/EL Drawing DISTRIBUTION MT SOUS-STATION 25, EDMS 221921 v.AC (1998).
- [132] S. Bertolasi and C. Bovet, Consolidation of the electrical network in the Meyrin site: Impact on the SVC Booster—Phase 2014 to LS2, EDMS 1309944 (2013).

- [133] EN/EL Drawing 18KV NORMAL SIMPLIFIED DIAGRAM—LS1 TO LS2 TRANSITION (2015), EDMS 1206604 v. AC (2013).
- [134] EN/EL Drawing 18KV NORMAL SIMPLIFIED DIAGRAM—2025 NETWORK, EDMS 1082784 v.AD (2012).
- [135] EN/EL Drawing PSEM_7002, EDMS 1335355 v.0 (2013).
- [136] EN/EL Drawing PS_EB_7003, EDMS 1336782 v.0 (2013).
- [137] Safety commission, IS 5 Emergency stops, EDMS 335742 v.2 (2001).
- [138] BoosterBoosterW. Weterings and B. Goddard, Loading assumptions for beam dumps of LINAC4 PS Booster injection, L4-T-EP-0001 Rev. 3.2, EDMS 963395 (2014).
- [139] ALARA Review Working Group, Final report, EDMS 1244380 (2013).
- [140] W. Weterings, New baseline design for the H^0/H^- beam dump, Presentation given at the LIU-PSB meeting 23/01/2014, INDICO Event 295767 (2014).
- [141] B. Mikulec *et al.*, Beam interlock specifications for Linac4, transfer lines and PS Booster, L4-CIB-ES-0001 v.1.0, EDMS 1016233.
- [142] P. Dahlen *et al.*, Magnet interlock system specifications for the PS Booster, EDMS 883871, in preparation.

Chapter 4

Proton Synchrotron

4.1 Introduction

The role of the Proton Synchrotron (PS) in the production of the beams for the Large Hadron Collider (LHC) is to preserve at maximum the transverse emittances defined by its injector, the PS Booster (PSB), and to manipulate the longitudinal phase space to define the bunch spacing required by the collider. For the production of the future HL-LHC (High Luminosity LHC) type beams, major upgrades are needed to eliminate the existing limitations, in particular related to space-charge and longitudinal instabilities.

4.1.1 Schemes for 25 ns beam production

The production of the 25 ns bunch spacing beam, which remains the baseline for the upgrade, is realized as follows (see Section 2.1). Linac2, or Linac4 in the future, fills each of the four PSB rings at 50 MeV (kinetic energy, 160 MeV for Linac4) on $h = 1$ (more precisely, each bunch is produced by filling a $h = 1 + 2$ bucket). Each PSB bunch, in total four, is transferred to the PS on $h = 7$ and, after 1.2 s, the PS receives two other PSB bunches. On the 1.4 GeV (kinetic energy, 2 GeV in the future) PS injection flat bottom, the six bunches are captured. Then, after a first acceleration to 2.5 GeV, they are triple split. The resulting 18 bunches are accelerated up to 26 GeV/c, where two consecutive double splittings produce the final bunch spacing of 25 ns creating a batch of 72 bunches. Prior to the transfer to the Super Proton Synchrotron (SPS), the bunches are rotated in the longitudinal plane to reduce the bunch length to about 4 ns. Up to four consecutive batches of 72 bunches are then injected in the SPS at 26 GeV/c, and accelerated to 450 GeV/c prior to extraction to the LHC. The longitudinal emittance is increased in the PS and SPS to reduce longitudinal instabilities, whereas transverse scraping is done in the SPS before reaching the extraction energy to eliminate tails.

Besides the classical production scheme, alternative ones were proposed to overcome the brightness limitation of the PSB. The most promising one, named BCMS (batch compression merging and splittings), comprises the injection of 2×4 bunches on the ninth harmonic in the PS, batch compression from $h = 9$ to $h = 14$ and bunch merging followed by a triple splitting all done at low energy instead of the triple splitting only. These involved RF gymnastics are performed at an intermediate kinetic energy ($E_k = 2.5$ GeV) to avoid transverse emittance blow-up due to space charge and to relax the requirements on the longitudinal emittance at injection.

The resulting 12 bunches are accelerated to the extraction flat top where two bunch splittings occur to obtain the final 25 ns bunch spacing (only one splitting is done for the 50 ns bunch spacing), as for the nominal scheme. The advantage with respect to the traditional scheme results from the smaller splitting factor of the PSB bunches (6 instead of 12). Before extraction to the SPS, 25 ns spaced bunches have the same transverse emittance but twice the intensity. Beams will be produced according to this scheme for the LHC Run 2.

4.1.2 Challenges of traditional schemes and proposed solutions

The double injection in the PS needed to maximize the number of bunches after the longitudinal splitting also requires very high intensity injected in the PSB. Every PSB bunch is split up to 12 times to get finally 72 bunches at 25 ns spacing at PS extraction, but fewer times for BCMS.

This requires Linac2 to inject a high-intensity beam with a limited brilliance, due to the multiturn injection process and large space charge (see Section 2.2). This issue will be solved with the connection

of Linac4, which will bring the injection energy from 50 MeV to 160 MeV, a clear advantage for space-charge limitations, but also will use H^- instead of protons, making the transverse painting more effective. It is expected that the brilliance of the PSB could be doubled thanks to the new linac. Once the first batch is injected from the PSB to the PS, there is a 1.2 s long waiting time on the PS flat bottom before the second injection can be delivered. During this period, the beam has a very large tune spread induced by the direct space charge, while the synchrotron period is of the order of 1 ms and there is a very large chromaticity in absolute value. The beam, due to the synchrotron motion, crosses many times the integer and the $4q_v = 1$ resonances, creating a transverse emittance increase and beam losses (see Section 4.2.1). The most robust solution to avoid this limitation is, for the fourth time in the PS history, to increase the injection energy, this time from 1.4 GeV to 2 GeV (see Section 2.3.1). The reduction of the direct space charge effect thanks to the energy increase leaves just enough space in the tune diagram to accommodate the tune shift expected for the future HL-LHC-type beams.

Once the triple-split beam is accelerated, right after transition crossing, coupled-bunch longitudinal instabilities are observed. The consequences are beam losses and a significant variation of longitudinal emittance and intensity along the extracted batch. This lack of reproducibility is a major source of losses, in particular capture losses, in the SPS. The preferred solution for this limitation is the use of a longitudinal damper, a function provided by a newly installed Finemet® cavity, as described in Section 4.5.1.

Electron cloud (EC) is regularly observed on the extraction flat top, even if there is no evident sign that the beam quality is affected. There is instead a clear horizontal instability appearing, together with EC, if the bunches are shorter than nominal or if the beam is kept artificially in the machine 50 ms longer than necessary (see Section 4.2.6). In case this becomes a limitation for the future beams, it was shown that the transverse damper (TD) can effectively delay the instability by about 10 ms.

4.1.3 Summary of upgrade interventions

The increase of the injection energy to 2 GeV is needed to reduce space-charge-induced transverse emittance blow-up experienced by the first batch injected on the flat bottom.

The new 2 GeV injection requires new injection elements and power converters (septum, kicker and injection bumpers described in Section 4.2.3). In addition to that, new magnets and power converters for orbit correctors and lattice quadrupoles used at low energy will also be produced to cope with the higher injection energy (see Section 4.3.3).

Head-tail (HT) instabilities (Section 4.2.4) on the injection flat bottom, which are currently cured by introducing linear coupling, will also be controlled thanks to the power upgrade of the TD together with the chromaticity control needed to avoid high-order modes.

A fast vertical instability, which was extensively studied on single-bunch beams, was observed also on a special high-intensity single-bunch LHC-type beam. Even if the future HL-LHC-type beams should be stable at transition, future studies with small longitudinal emittance beams will be done to confirm the extrapolation from past measurements (see Section 4.2.5).

As mentioned, the longitudinal coupled-bunch instability, if not cured, would limit the maximum intensity per bunch well below the 2.5×10^{11} ppb of the future HL-LHC-type beam. A new dedicated longitudinal damper, based on a Finemet® cavity and a new LL-RF (Low Lever Radio Frequency) system, was installed during Long Shutdown 1 (LS1) (see Section 4.5.1).

EC is observed during the 25 ns beam production but with no influence on beam quality, so this is not expected to be an issue in the future. In any case, studies carried out during the 2012–2013 run proved that the TD can effectively delay the appearance of the instability. In an alternative scheme, a faster final phase rotation may also be used. If EC would turn out, even after all the countermeasures deployed, to be a limitation, beam production schemes with reduced number of bunches, 48 for example, might be used instead. This, of course, would cause a minor reduction of the number of bunches in the

LHC, but would still make it possible to approach the HL-LHC requirements.

On top of the beam dynamics issues related to the production of the LHC-type beams, other limitations might appear during normal operation. A major one already appeared during the run with high-intensity beams used for neutrino production at the CERN SPS. The maximum beam current had to be reduced due to the too large radiation levels observed outside the PS tunnel in the injection and extraction regions, already present for nominal intensity. The original shielding built in 1958 is not any longer sufficient for the current intensities and losses. For this reason, following detailed Monte Carlo studies to assess the needed increase, also considering future high-intensity beams, civil engineering interventions took place in both regions during LS1 (see Section 4.8).

A similar limitation, related to the increase of the maximum circulating current and the reduced transverse emittances, will come from the internal beam dumps. The two internal dumps installed in the late 1970s will not be able to withstand the LHC-type beam at extraction energies and have to be replaced (see Section 4.10). All these interventions are also followed by the improvement of the beam instrumentation, as described in Section 4.9.

4.2 Beam dynamics

4.2.1 Space-charge and resonance compensation

4.2.1.1 *Introduction and motivation*

The production of the LHC beams in the CERN PS features a double-batch injection scheme, the two injections occurring at an interval of 1.2 s during the 1.4 GeV (kinetic energy) flat bottom [1]. This long waiting time on the injection plateau represents one of the main limitations for high-brightness beams: due to the large direct space charge tune shift, particles can cross deleterious betatronic resonances many times. Already in the past, to avoid too large losses or emittance blow-up during the production of the LHC-type beams, the injection energy of the PS was increased from 1 GeV to 1.4 GeV, based on studies presented in Ref. [2]. Today, for the very same reason, the injection energy has to increase from 1.4 GeV to 2 GeV, as proposed in Ref. [3], again to keep the direct space charge tune shift to reasonable values, of the order of -0.3 , for the production of the future HL-LHC-type beams.

A series of studies of the betatronic resonances [4] has also shown the most dangerous ones, which should be avoided in the choice of the future working points and that identify the maximum acceptable Laslett tune shift. As shown in Fig. 4.1, resonances can be identified by losses caused by their crossing. In addition to these resonances, a study revealed that the $4q_y = 1$ line is also excited, probably due to the coupling of space charge with a structure resonance [5]. This resonance cannot be seen in Fig. 4.1 because the beam used for the measurements had a very large emittance and low intensity: this particular line constitutes one of the main brightness limitations for the future LHC-type beams that the PS can produce.

The current operational working points are within the area $Q_x = [6.1, 6.24]$ and $Q_y = [6.1, 6.245]$, as illustrated in Fig. 4.1, to avoid resonances and damp HT instability using the transverse coupling introduced by the $Q_x - Q_y = 0$ resonance [6], in addition to linear coupling from skew quadrupoles.

The typical maximum detuning due to space charge of the nominal LHC-type beams produced for Run 1 is about -0.2 in the horizontal plane and -0.28 in the vertical one [1], which implies that the tune footprint is very close to and sometimes even overlaps the integer stop-band. Moreover, the high-luminosity LHC beam parameters [1] imply a detuning between -0.34 and -0.37 (for short bunches produced by the PSB, less for the options with longer bunches) even after the injection energy upgrade to 2 GeV, with an allocated budget for losses and transverse emittance growth for the PS of 5% each. Therefore, the understanding of the effect of the resonances depending on the beam tune spread and working point seems necessary.

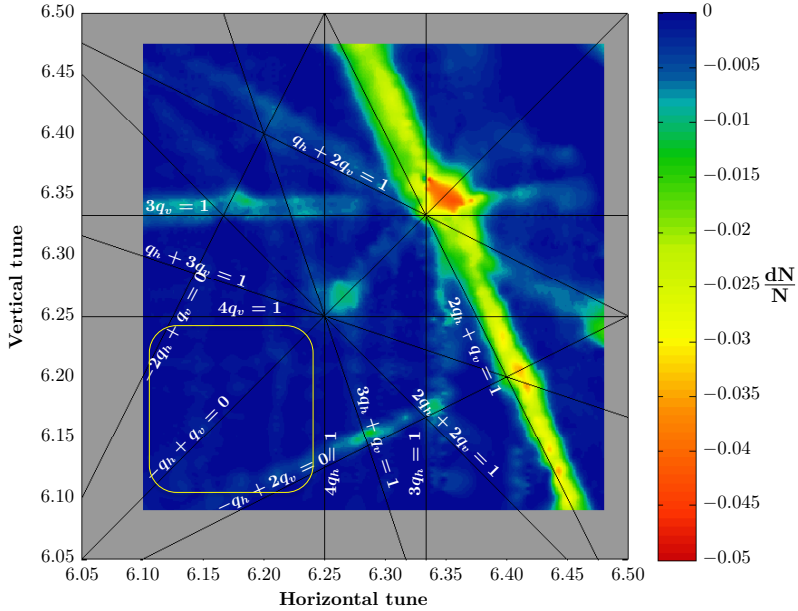


Fig. 4.1: Tune-loss map. The colour code indicates losses. The operational working area is identified by the rectangle.

4.2.1.2 Effect of the integer resonance

Measurement conditions

Emittance blow-up and its time evolution were measured for different tune spreads and working points in a previous study in the PS [2]. A similar study was repeated taking into account the current and future requirements in terms of losses, blow-up and beam parameters, to understand the limitations and necessary improvements.

The aim of this study is to measure the emittance blow-up and losses after 1.2 s at injection energy, representing the same conditions as for the first batch of the LHC beams. The working point $Q_x = 6.23$ and $Q_y = 6.255$ was chosen for the first measurements to have less than 5% losses. The transverse profiles were measured using a wire scanner, which averages the beam profile during about 1000 turns. Then, using the optics model ($\beta_{x,y}(s)$ and $D_x(s)$) of the machine, emittances could be computed from the beam profiles.

The bunch was compressed adiabatically during 20 ms after injection (see Fig. 4.2) using a ramp of the RF voltage to vary the space-charge forces. Then the beam is stored for 1.2 s at 1.4 GeV kinetic energy. Depending on the maximum voltage of the bunch compression, beams could have space-charge detuning.

The measurements were done with a single-bunch beam with 1.15×10^{12} protons, a 1σ normalized emittance of about $1.6 \mu\text{m}$ in horizontal and $1.25 \mu\text{m}$ in vertical planes, RMS momentum spread of 10^{-3} and a full bunch length of 180 ns before compression. The horizontal emittance did not show significant variations, since the maximum tune spread in the horizontal plane did not exceed -0.22 with a horizontal tune of $Q_x = 6.23$. Therefore, in the following sections, only the vertical emittance is shown. The space-charge forces are quantified using the maximum detuning due to space charge, which is estimated for the

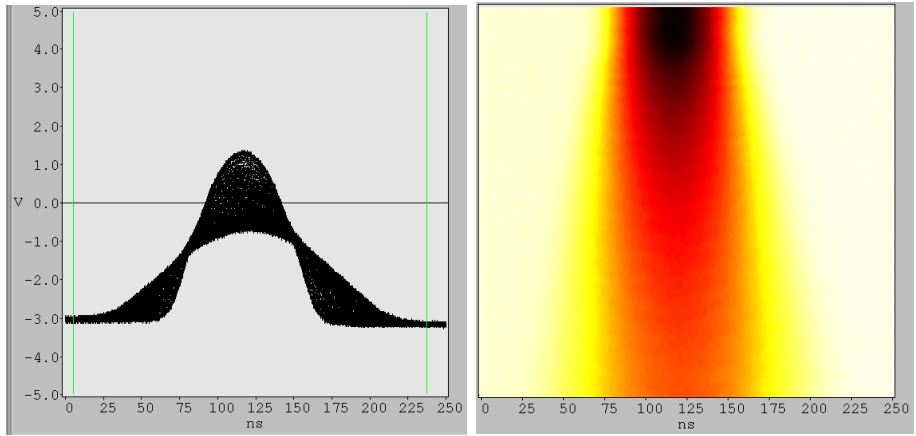


Fig. 4.2: Longitudinal beam profiles during an adiabatic bunch compression

different beams according to the following equations [7]:

$$\Delta Q_x = -\frac{\lambda_{\max} r_p}{2\pi\beta^2\gamma^3} \oint \frac{\beta_x(s)}{\sigma_x(s)[\sigma_x(s) + \sigma_y(s)]} ds, \quad (4.1)$$

$$\Delta Q_y = -\frac{\lambda_{\max} r_p}{2\pi\beta^2\gamma^3} \oint \frac{\beta_y(s)}{\sigma_y(s)[\sigma_x(s) + \sigma_y(s)]} ds, \quad (4.2)$$

where $\sigma_x(s) = \sqrt{\beta_x(s)\epsilon_x + D_x^2(s)(\Delta p/p)^2}$ is one standard deviation of the horizontal beam size and $\sigma_y(s) = \sqrt{\beta_y(s)\epsilon_y(s)}$ one standard deviation of the vertical beam size. Also, λ_{\max} is the maximum line density in units of number of protons/m, r_p the classical proton radius, β and γ the relativistic factors, $\beta_{x,y}(s)$ the horizontal/vertical beta functions at longitudinal position s , $\epsilon_{x,y}$ the horizontal/vertical physical emittances, $D_x(s)$ the horizontal dispersion function and $\Delta p/p$ the RMS momentum spread.

Results

Figure 4.3 presents the vertical emittance growth and losses for two working points and different tune spreads.

From the analysis of the data, the beam tune footprint seems to be limited between the $4(8)Q_y = 25(50)$ resonance and the integer resonance. Increasing the zero-current vertical tune decreases the effect of the integer resonance and therefore decreases the emittance blow-up. On the other hand, it increases the population of protons crossing the fourth-order resonance and therefore increases losses. The choice of the working point must be a compromise between emittance growth due to the integer resonance crossing and losses coming from the crossing of the fourth-order resonance.

For the same working point, losses are lower for higher tune spreads because a higher maximum detuning means fewer protons crossing the fourth-order resonance. These results support also the necessity of the 2 GeV injection energy upgrade: without that, the Laslett tune shift will be well beyond -0.3 for the future LHC-type beam with a consequent vertical emittance increase on the flat bottom well beyond the allocated budget.

The time evolution of the transverse emittance blow-up was also measured for different Laslett tune shifts. The results, presented in Fig. 4.4, show that there are two growth regimes. The first one is a fast growth of the emittance, which lasts less than 200 ms; the second one is much slower. The contribution of the two regimes to the final emittance increase depends on the tune spread.

This result could support the choice of single-batch production scheme for LHC beams, for which

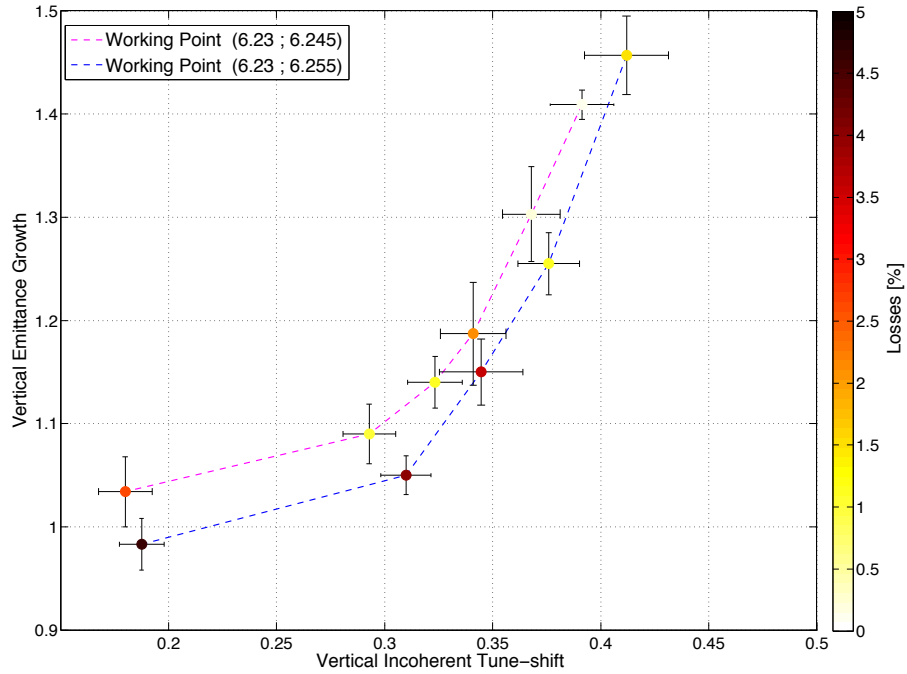


Fig. 4.3: Emittance growth and losses after 1.2 s at 1.4 GeV kinetic energy for two different working points.

a too large Laslett tune shift would be required ($> |-0.34|$), since bunches would then spend less than 200 ms at injection energy.

Further studies are planned to know the behaviour of the emittance growth during the first 200 ms. This study shows that the HL-LHC requirements in terms of emittance growth, losses and tune spread seem to very challenging to meet with the current conditions.

4.2.1.3 Resonance compensation

One of the ways to overcome space-charge limitations is to compensate resonances to reduce their harm on the beam. A compensation scheme was already used in the 1980s [8] using normal and skew sextupoles to compensate several third-order and the integer resonances. As seen in Fig. 4.1, the PS suffers mainly from two skew sextupolar resonances, $2Q_x + Q_y = 19$ and $3Q_y = 19$. The following study is to prove that we can compensate each of these naturally excited resonances.

Resonance modelling

Both of the mentioned resonances are excited for all conditions, even for the bare machine (only powering the main magnets and without any additional magnetic element). Therefore, we believe that the PS main magnets cause them. To estimate the magnetic errors induced by the main magnets, a 2D model of the magnets was simulated in OPERA®, including a misalignment error of the coil and the iron. A statistical study of 1000 models per magnet type and current level, using a Gaussian distribution of the errors, gives an estimation of the mean value of the magnetic components, as well as a standard deviation from this value. Implementing these values in PTC (polymorphic tracking code), one could estimate the driving term of each resonance and therefore its corresponding compensation.

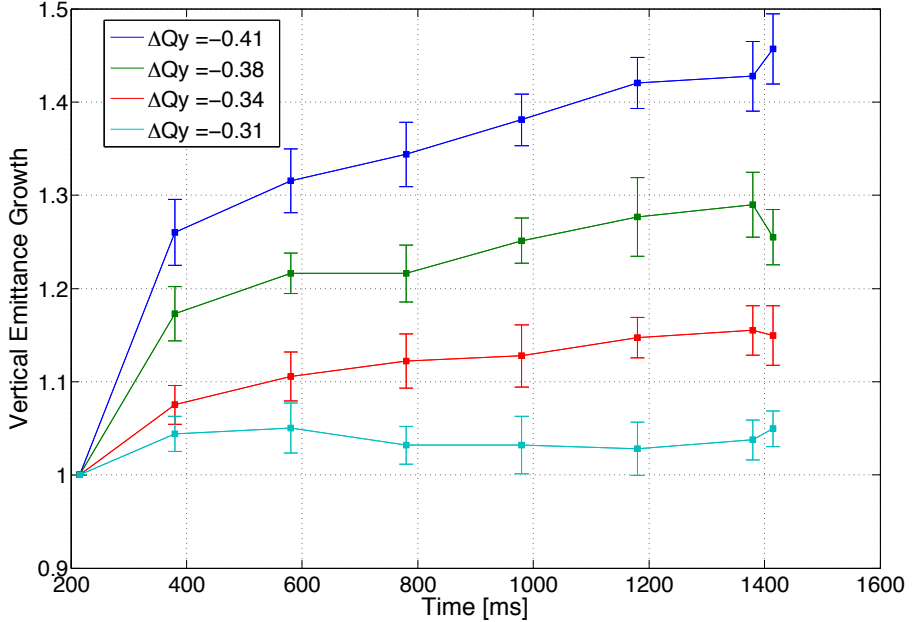


Fig. 4.4: Time evolution of the vertical emittance blow-up for four different space charge maximum detunings.

Compensation and results

During the 2012 winter shutdown, four skew sextupoles were installed in the straight sections 2, 52, 14 and 72. All were at the same position where they were in the 1980s except for the one in the section 72, which was in the section 64, but it is currently occupied. Including the four skew sextupoles in PTC, two compensation schemes were computed for each of the $2Q_x + Q_y = 19$ and $3Q_y = 19$ resonances. Then the correction currents were experimentally tried and gave the results of Fig. 4.5. Figure 4.5 shows the result of the compensation of the two resonances. As one could see, while compensating the $2Q_x + Q_y = 19$ resonance, the $3Q_y = 19$ resonance is enhanced. On the other hand, when compensating the $3Q_y = 19$ resonance, the $2Q_x + Q_y = 19$ resonance is reduced. A compensation scheme for both resonances was later computed, but, due to the limited available current from the power suppliers, it could not be tested. Further studies are planned after the restart of the PS in 2014, especially testing a compensation scheme of both the $3Q_y = 19$ and the integer ($3Q_y = 18$) resonances, in addition to compensating both the skew sextupolar resonances.

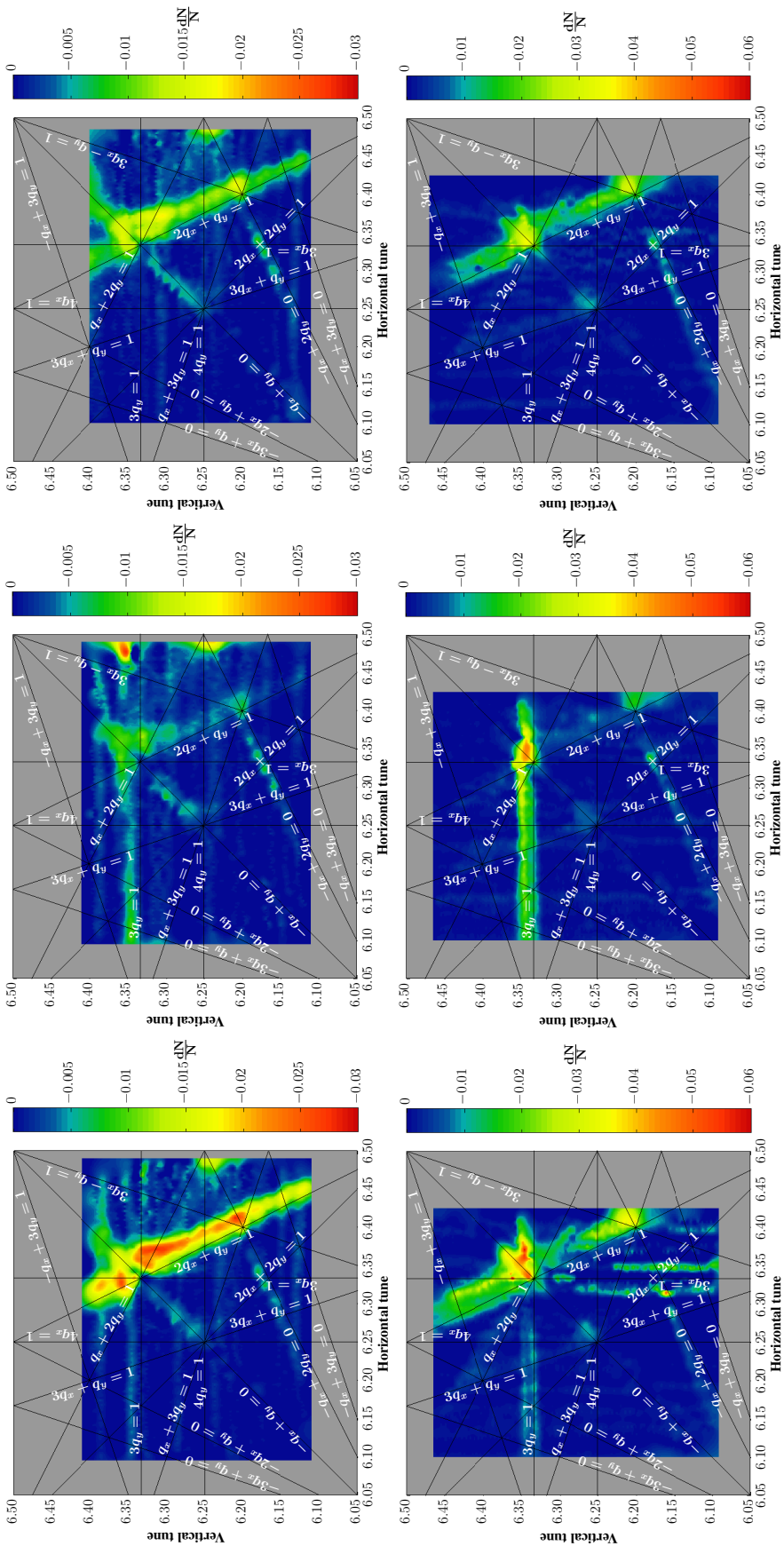


Fig. 4.5: Tune-loss maps for the two different compensation schemes: the first row is a horizontal scan of the tune space while the second row is a vertical one. The first column is the scan at 2 GeV, without any compensation. The second column is a scan while compensating the $2Q_x + Q_y = 19$ resonance and the third column is a scan while compensating the $3Q_y = 19$ resonance.

4.2.2 Control of the working point

4.2.2.1 Introduction

In the CERN PS the combined function main magnet units provide bending and focusing forces and small-intensity beams can be accelerated to nearly top energy, even without additional auxiliary magnets. However, in the PS a multitude of particle beams with different characteristics are produced in order to comply with the requirements of the physics users and, therefore, the sole use of the main magnets does not provide sufficient control over important machine parameters such as the working point. In particular, in view of the 2 GeV energy upgrade, the control of the working point and chromaticities at injection energy becomes even more important. The tunes should be chosen to avoid being too close to resonances that might be crossed due to the large direct space charge tune shift. The chromaticities should be corrected to help damping HT instabilities, as described in Section 4.2.4.

Whereas there are no dedicated sextupoles for the control of the working point, additional quadrupoles are distributed along the machine and allow us to move the working point to areas in the tune diagram which are more beneficial regarding betatronic resonances. These low-energy quadrupoles (LEQs) are alternately positioned to provide a pattern of focusing–defocusing magnets and are used to control the tunes from injection up to a kinetic energy of about 3.5 GeV.

The relationship between the currents flowing through these magnets and the measured tunes can be easily established by setting up the matrix equation

$$\begin{pmatrix} \Delta Q_x \\ \Delta Q_y \end{pmatrix} = \begin{pmatrix} 0.02045 & -0.01117 \\ -0.01089 & 0.02078 \end{pmatrix} \begin{pmatrix} \Delta I_F \\ \Delta I_D \end{pmatrix}, \quad (4.3)$$

which is in this representation only valid at the future injection energy $E_{\text{kin}} = 2$ GeV, as the matrix elements depend on the beam energy. Here Δ refers to an offset with respect to the bare machine value ($Q_x = 6.253$, $Q_y = 6.285$). Inversion of the matrix in Eq. (4.3) allows us to apply the desired offsets to the tunes, as the required currents can be calculated.

A disadvantage of the LEQs is that they do not offer means to correct chromaticity. Currently, this does not impose any operational restrictions at the PS, as the occurring head–tail instabilities on LHC beams can be cured by exploitation of linear coupling. However, this instability will become more important for higher intensity beams required by the HL-LHC, where linear coupling might no longer suffice to stabilize the beam. A chromaticity correction scheme at injection in combination with a TD system with appropriate bandwidth would therefore become inevitable (see also Section 4.4).

Today, linear chromaticity is corrected by a second group of magnets, the pole-face windings (PFWs) and the figure-of-eight loop (F8L), only above 3.5 GeV. For future use it is contemplated to extend their use and provide chromaticity correction already at injection energy.

The PFWs are special circuits mounted on top of the main magnet poles, divided, depending on their position within the main magnet unit, into a narrow and a wide circuit, while the F8L is a single winding crossing in the centre of the main magnet, having the form of a figure of eight. Altogether, the PFWs and the F8L constitute five independent circuits and, therefore, theoretically offer means to control both tunes as well as the linear chromaticities $\xi_i = \frac{\Delta Q_i / Q_i}{\Delta p / p}$ and one of the second-order chromaticities Q''_i . The correction currents and the parameters of interest are correlated by a matrix different from the one in Eq. (4.3), defined using the relation

$$\begin{pmatrix} \Delta Q_x \\ \Delta Q_y \\ \Delta \xi_x \\ \Delta \xi_y \\ \Delta Q''_{x,y} \end{pmatrix} = \mathbf{M}_{5 \times 5} \begin{pmatrix} \Delta I_{FN} \\ \Delta I_{FW} \\ \Delta I_{DN} \\ \Delta I_{DW} \\ \Delta I_{F8L} \end{pmatrix}. \quad (4.4)$$

4.2.2.2 Linearity of the machine at 2 GeV

In the absence of any auxiliary magnets or circuits, the working point of the PS is fully determined by the momentum of the beam, as the main magnets account for the dipole and quadrupole fields at the same time. With the available radial steering, the dependence of the tune on the momentum error can be measured, revealing the bare machine chromaticities $\xi_x = -0.83$ and $\xi_y = -1.12$ and a completely linear behaviour (see Fig. 4.6(a)). Using the LEQs does not alter this linearity and, therefore, the machine continues to behave linearly.

In order to correct linear chromaticity at energies above 3.5 GeV, the PFWs and the F8L are today used in three-current mode (3CM), meaning that the narrow and wide circuits of each half unit of the main magnet are powered with the same current. This approach only allows us to control three parameters, namely both tunes and either ξ_x or ξ_y . However, the implementation of a chromaticity correction scheme at injection aims for reducing the mode number of transverse HT instabilities and, therefore, control of linear chromaticities in both planes is desired. This requires us to operate the PFWs and the F8L in four-current mode (4CM), fixing, e.g., the current in the F8L to zero.

To examine the influence of these auxiliary circuits on the linearity of the machine, the working point was moved from the one of the bare machine to ($Q_x = 6.10$, $Q_y = 6.20$) by the PFWs in 4CM and the measured dependence of the tune on the momentum deviation is shown in Fig. 4.6(b). The appearing non-linearities and their correction were studied in detail [4] and the unbalancing of currents in the narrow and wide windings was understood to be the cause, most likely due to the asymmetric alignment of the PFWs.

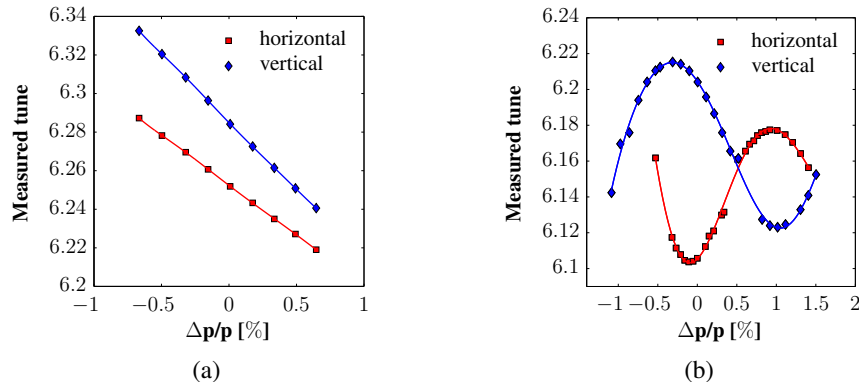


Fig. 4.6: Influence of auxiliary circuits on the linearity of the machine. (a) Bare machine. (b) Tune control with PFWs ($Q_h = 6.10$, $Q_v = 6.20$).

Using the matrix approach mentioned in Section 4.2.2.1, the correction of ξ_x and ξ_y with the PFWs and the F8L proved to be successful, while correction of the octupole components Q''_x and Q''_y was found to produce non-predictable results, making an operational implementation at low energy unlikely. The reason for this is not yet understood but under investigation.

4.2.2.3 Identification of resonances

Controlling the working point and eventually linear chromaticity requires us to use the PFWs in 4CM. Due to this fact, betatronic resonances that are not present for the bare machine could be excited and, depending on the chosen working point, degrade the beam quality. Therefore, beam loss based measurements, inspired by the technique used in Ref. [9], were conducted to identify destructive resonances [4].

To obtain a graphical illustration of the working point plane a single bunch of 1.2×10^{12} protons, with transverse normalized emittances (1σ) of $\varepsilon_x \approx 10$ mm mrad and $\varepsilon_y \approx 8$ mm mrad, was stored for 1.3 s at either 1.4 or 2 GeV, keeping the tune in one plane constant while changing it dynamically in

the other. Due to the large beam size, particles are quickly lost once the tunes enter into the stop-band of an excited resonance. This allows us to roughly estimate the relative strength and the width of all resonances by calculating the derivative of a beam current transformer signal. The measurement is then repeated for different constant tunes and interpolation of the data points on an equidistant grid leads to Fig. 4.7(a)–(d), where the colour scale represents beam loss.

For this beam the Laslett tune spread was calculated to be $\Delta Q_x = -0.05$ and $\Delta Q_y = -0.07$, sufficiently small to neglect multiple resonance crossings due to a large space charge neck tie, making the identification of single resonance lines possible.

Figure 4.7(a) and (b) show measurements at injection energy, where the tunes were controlled by the LEQs only. The strongest detected resonance is clearly the $2q_x + q_y = 1$ one, while the most interesting line concerning machine operation is the $3q_y = 1$ one (q being the fractional tune). The peculiarity of the measurement technique is that resonances are most efficiently detected when the scan is conducted perpendicular to the line. This causes the resonance $3q_y = 1$ to be visible in Fig. 4.7(b) but not in Fig. 4.7(a).

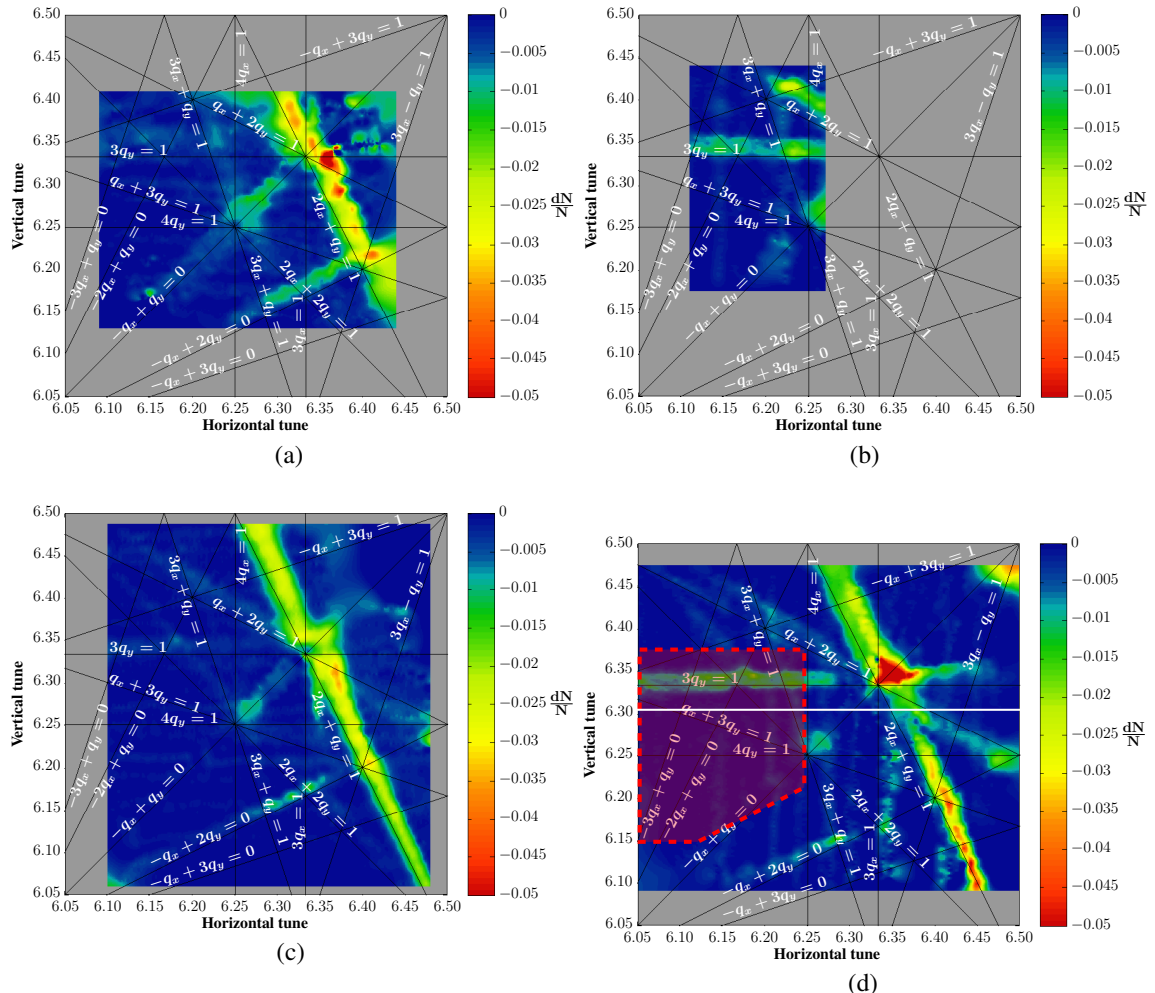


Fig. 4.7: Several graphical representations of the working point plane. (a) Horizontal scan at 1.4 GeV using the LEQs. (b) Detail of a vertical scan at 1.4 GeV using the LEQs. (c) Horizontal scan at 2 GeV using the PFWs in 4CM. (d) Vertical scan at 2 GeV using the PFWs in 4CM. The highlighted area appears to be free of severe resonances; the vertical fourth order is indicated by the white line.

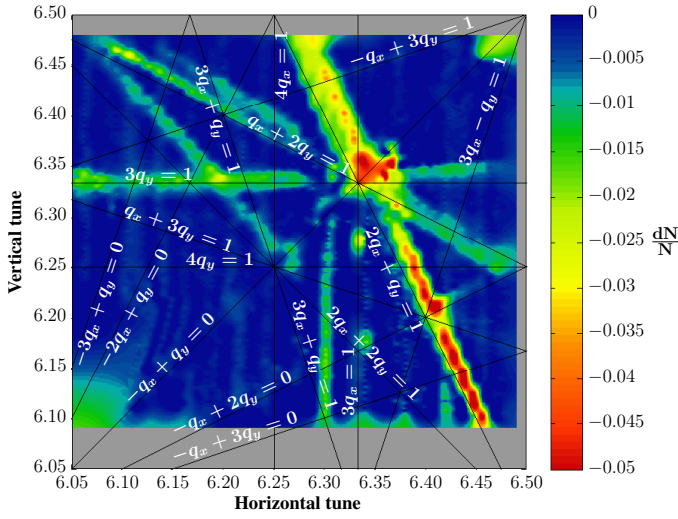


Fig. 4.8: Vertical scan at 2 GeV using the PFWs in 4CM and setting $\xi_x = -0.2$

Furthermore, measurements at 2 GeV using the PFWs in 4CM (with the current in the F8L being set to zero) are shown in Fig. 4.7(c) and (d). Most importantly, no additional resonances can be observed, the line $3q_y = 1$ remains equal in strength and width and the line $2q_x + q_y = 1$ even seems to be slightly reduced. Within the red highlighted area in Fig. 4.7(d), no resonances seem to be excited and these measurements therefore suggest this area to be the most beneficial within the working point plane, limited by the vertical integer- and third-order resonances.

Despite the non-linearities created by the PFWs (see Section 4.2.2.2), the same betatron resonances were found to be excited as in the bare machine, which led to the understanding that the observed resonances are mainly caused by magnetic errors within the main magnets. Based on this, a compensation scheme for resonances has recently been successfully tested and even allowed us to completely compensate the $3q_y = 1$ resonance (see Section 4.2.1).

In particular, Fig. 4.7(d) indicates the possibility of injecting beams with a maximum tune spread of $\Delta Q_y \approx -0.33$. However, the tune spread based on the demands of the HL-LHC is supposed to be $\Delta Q_y = -0.34$ in case of short bunches delivered by the PSB and about $\Delta Q_y = -0.3$ for longer bunches. A $\Delta Q_y = -0.34$ would not be reachable with a machine in this configuration unless the third-order resonance $3q_y = 1$ is compensated. Another issue concerns the resonance $4q_y = 1$, which is not visible in the presented measurements, but seems to be excited by the beam itself in the presence of high space charge (see Section 4.2.1).

If, additionally to controlling the working point with the PFWs, linear chromaticity is corrected, the characteristics of the excited resonances change and additional lines appear. Figure 4.8 shows a tune scan where ξ_x was set to -0.2 and the increased strength of the line $q_x + 2q_y = 1$ as well as the resonance $2q_x + 2q_y = 1$ are visible, which constitutes an additional restriction for the choice of the working point.

4.2.3 The PS 2 GeV injection

One of the most relevant limits of the high-brightness beams for the LHC is the space charge at the PS injection flat bottom (Section 4.2.1). A possible mitigation is to inject the beam into the PS at $E_k = 2$ GeV instead of the present $E_k = 1.4$ GeV. This energy increase is the baseline scenario for the LIU-PSB and LIU-PS projects (LIU: LHC Injector Upgrade) and it is expected to be commissioned after the Long Shutdown 2 (LS2).

The impact of hardware, optics and operation on the PSB and the PSB-to-PS transfer lines is

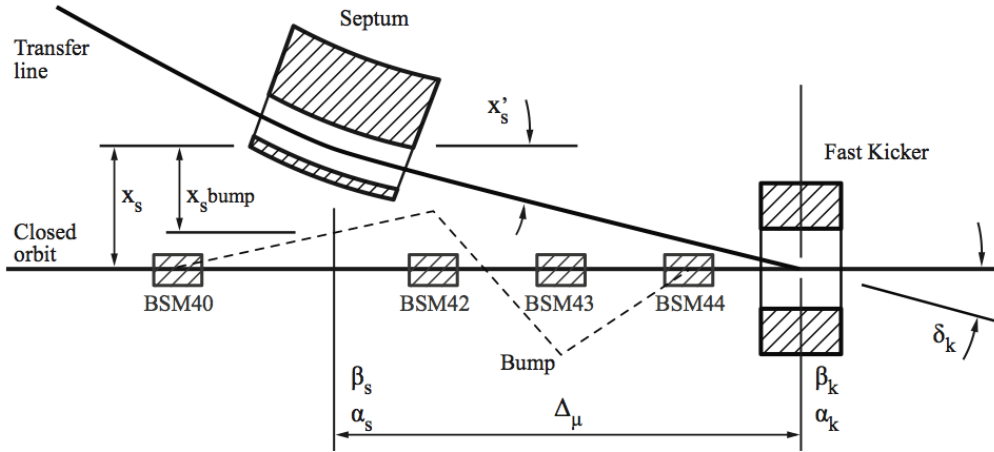


Fig. 4.9: Present injection region layout [15]

described in (3.10), whilst hereby we report the rationale that drives the specification and the proposed modifications of the PS injection hardware.

4.2.3.1 Requirements and specifications

The upgrade of the injection region of the PS has to provide a bunch-to-bucket transfer with high flexibility, allowing us to inject all beams (LHC beams or high-intensity beams) at 2 or at 1.4 GeV (using the present injection scheme) and providing enough aperture and margin for the injected and the circulating beams to minimize beam losses and consequent irradiation. Part of the irradiation issue has been addressed by reinforcing the tunnel radiation shielding during LS1 (see Section 4.8). To minimize the irradiation to the hardware and consequently ease its maintenance, particular attention has to be reserved for the high-intensity beams that, due to larger emittances and beam current, are responsible for most of the beam losses in the PS injection area.

The correctors and quadrupoles of the transfer line have to operate in pulse-to-pulse modulation (PPM) mode¹ to allow different settings in the same supercycle. In addition to optics matching, the transfer line has to provide, if requested, horizontal dispersion matching. The residual incoming vertical dispersion will stay unmatched: its impact on the emittance growth is marginal.

In the following we present in two separate sections the considerations related to the orbit and to the optics of the injection region.

4.2.3.2 The 2 GeV injection orbit

The work presented hereby is a summary of Refs. [10–15], where the different options are discussed in detail. An insight into the hardware and the operation sides of the new injection is given in Section 4.3. For the present injection scheme (Fig. 4.9), the septum is positioned at straight section 42 (SS42, $\theta_{\text{septum}} = 55$ mrad), the kicker in SS45 ($\theta_{\text{KFA45}} = 4.3$ mrad, terminated mode) and there are four injection bumpers (in SS40, 42, 43 and 44 providing respectively 3.5, -14.4, 12.0 and -6.1 mrad). The beam envelope at the injection region and at the septum location is shown in Fig. 4.10.

¹The BT - Beam Transfer - line is already fully PPM, whilst the BTP - Beam Transfer to PS - line needs to be upgraded.

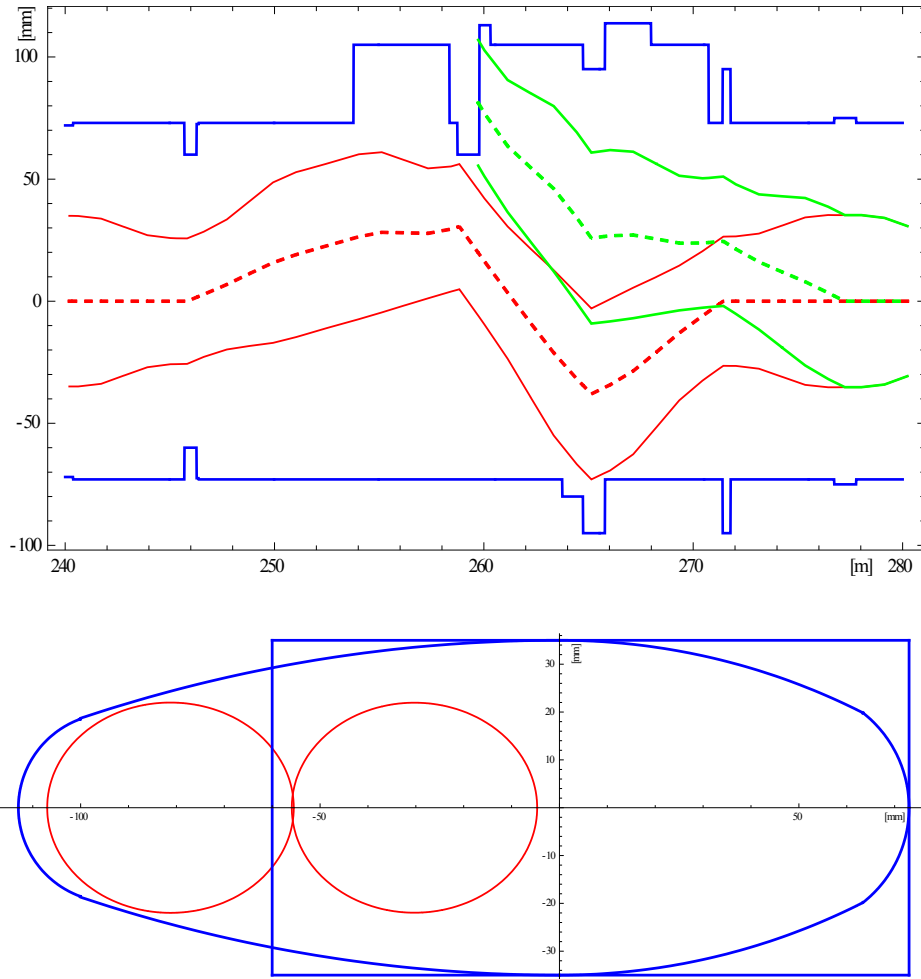


Fig. 4.10: The aperture at the injection region (top) and the beam envelopes at the septum (bottom) with the present injection at $E_k = 1.4$ GeV [13] (3σ envelopes for $\epsilon_n^x = 10$ and $\epsilon_n^y = 5$ mm mrad, $\sigma_{\Delta p/p} = 1.5 \times 10^{-3}$).

Passing from $E_k = 1.4$ GeV to 2 GeV, the beam momentum increases by 30%. This would imply a corresponding increase in the magnetic field of the injection hardware. Nevertheless, the septum and the kicker are operating already at their nominal limits and, therefore, to cope with the increased injection energy, three possible solutions were investigated.

- i) To move the septum from SS42 to SS41 in order to profit from a more favourable β_x [12]. This was finally excluded since the benefit is marginal with respect to the implication on the transfer line.
- ii) To redesign the septum in order to maintain the 55 mrad kick capability (it will be longer; the bumper 42 has to be integrated in it, and the BTP line survey has to be slightly modified) and to operate the kicker in short circuit. This can double the available kicker angle at the expense of a longer rise time (from $\tau_{2 \rightarrow 98\%} = 42$ to 78 ns [10]). The longer rise time is not fully compatible with $h > 7$ and could degrade the field uniformity, producing emittance dilution (LHC beams) and beam losses (high-intensity beams).
- iii) To redesign the septum in order to maintain the 55 mrad kick capability (it will be longer and the bumper 42 has to be integrated in it), to operate the KFA45 in terminated mode ($\theta_{KFA45} = 3.1$ mrad at $E_k = 2$ GeV) and to add a second kicker in section 53, with $\Delta\mu_{45 \rightarrow 53} \approx \pi$ ($\theta_{KFA53} =$

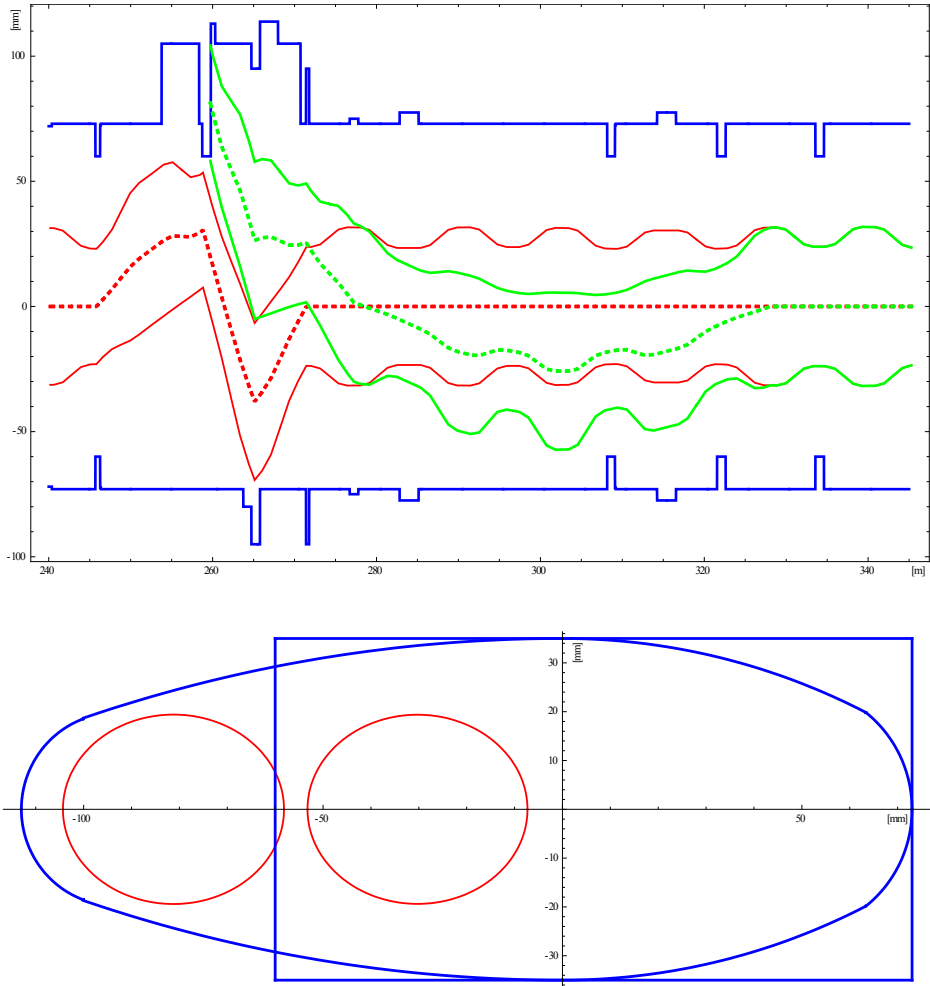


Fig. 4.11: The aperture at the injection region (top) and the beam envelopes at the septum (bottom) using KFA45 and KFA53 at $E_k = 2$ GeV [13] (3σ envelopes for $\epsilon_n^x = 10$ and $\epsilon_n^y = 5$ mm mad, $\sigma_{\Delta p/p} = 1.5 \times 10^{-3}$).

–1.2 mrad nominal and $\theta_{\text{KFA53}} = -1.5$ maximum at $E_k = 2$ GeV to obtain the full 4.3 mrad from the combined kicks).

The third solution is the only one compatible with the given requirements and it is the present baseline solution. Each bumper can cope with the increased beam momentum but for further flexibility in the injection region the present bumper 42 (that has to be replaced by one integrated into the longer septum) will be moved into section 41. In this configuration the angle and the position of the circulating beam orbit at the septum position can be fully controlled. The beam envelope at the injection region and at the septum location is shown in Fig. 4.11.

4.2.3.3 Proposal for the 2 GeV injection optics

Even with the proposed injection bump and septum/kicker settings, the high-intensity beam envelope (higher emittance) of the injected and circulating beams suffers from several aperture restrictions specifically in the horizontal plane (due to the bump and the dispersion). This issue can be addressed by a local optics perturbation trimmed during injection. This perturbation could reduce the overall horizontal beam size (from the interplay between β_x and D_x) at the expense of an increase of the vertical envelope.

In presence of an optics perturbation, all the bumps and the septum/kicker angles have to be slightly rematched and the position of the septum blade slightly optimized.

A complete study was performed in Ref. [13], where two possible hardware scenarios are envisaged, as follows:

- i) a global perturbation using the present quadrupoles in SS25 and SS5 (QKE16, $g = 0.86 \text{ T/m}$);
- ii) a local perturbation using new quadrupoles in SS33 and SS49 ($g = 1.24 \text{ T/m}$).

Beyond the intrinsic advantage of the local perturbation, having two additional quadrupoles in the machine (second scenario) allows more flexibility (it could be used together with the global perturbation) or as degrees of freedom to increase D_x for high-brightness beams in order to minimize space charge at injection.

The local optics perturbation is proposed as baseline scenario for the LIU-PS project. The beam envelope at the injection region and at the septum location is shown in Fig. 4.12.

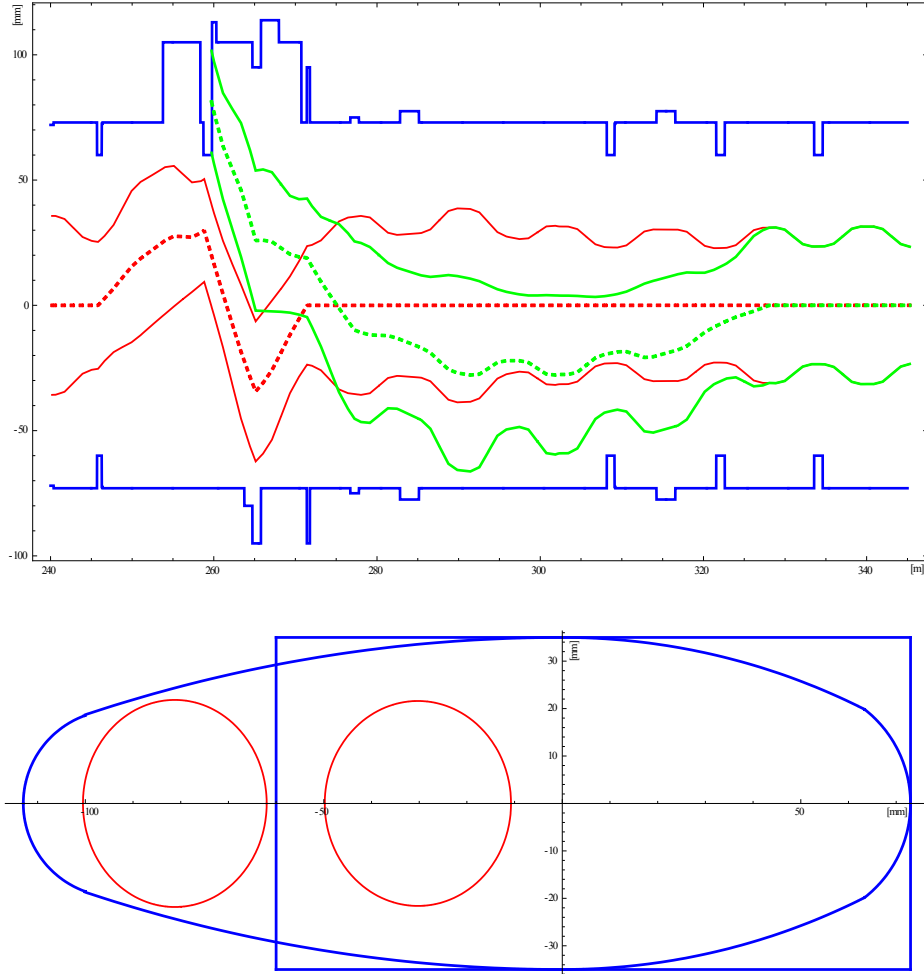


Fig. 4.12: The aperture at the injection region (top) and the beam envelopes at the septum (bottom) using KFA45 and KFA53 at $E_k = 2 \text{ GeV}$ with the addition of the doublet in SS33 and SS49 [13] (3σ envelopes for $\epsilon_n^x = 10$ and $\epsilon_n^y = \text{mm mad}$, $\sigma_{\Delta p/p} = 1.5 \times 10^{-3}$).

4.2.3.4 Conclusions

In order to mitigate the detrimental effect of the space charge at the PS injection plateau, an upgrade of the PSB extraction and the PS injection energy has been proposed as baseline LIU scenario.

The present PS injection septum and kicker cannot cope with this energy increase; therefore, it has been proposed to install a new and longer septum together with an integrated in-vacuum bumper and an additional kicker in SS53.

For high-intensity beams this solution is still critical concerning available aperture and beam losses. To address these issues, a local optics bump along the injection region has been presented and finally proposed. This solution would require the installation of two additional quadrupoles in SS33 and SS49.

4.2.4 The HT instability for the LIU-PS beams

4.2.4.1 Introduction

The HT instability is a coherent transverse single-bunch instability produced by the interaction between the beam and the machine transverse impedance (see Section 4.7.2): the wakes originated by the leading part of the bunch (head) will perturb the motion of the trailing particles (tail). This effect together with the interplay of the machine chromaticity and the intra-bunch synchrotron motion can give rise to a beam instability that shows up in growing bunch contortions produced by a phase shift between head and tail [16, 17].

Starting from the previous elements and in the linear approximation, the theory [17–19] describes the beam motion in a basis of natural modes. Each mode is related to a complex frequency shift, $\Delta\omega^2$; $\Im(\Delta\omega) > 0$ implies that the mode is unstable. If the injected beam or the noise of the machine excites an unstable mode, the instability will be triggered producing a deterioration of the beam quality (beam loss and emittance blow-up with consequent reduction of beam brightness). Usually the beam dynamics is dominated by the mode with the faster growth time.

By using simulation codes such as HEADTAIL [20], the effect of non-linear elements, dipolar and quadrupolar impedances, transverse coupling and transverse feedback (TFB) can be analysed in a more complete and realistic framework. For the PS case, the coupling between HT and EC (see Section 4.6) is not relevant, since the two phenomena take place at different moments in the cycle (the EC can occur at flat top while the HT instability is at flat bottom). Recent studies [21] show that the coupling between HT instability and space charge can be beneficial by slowing down the growth time of the HT instability.

4.2.4.2 Observation in the PS

In the PS, HT instabilities were systematically observed during the early commissioning and studies of the LHC beam [22] on the 1.2 s injection plateau needed for the double-batch injection. It was a horizontal instability with a growth time of the order of 100–200 ms for a bunch injected in an $h = 8, 4\sigma$ bunch length of 200 ns, $N_b = 200 \times 10^{10}$ ppb at $E_k = 1$ GeV injection. Depending on the chromaticity, the number of observed modes varied between $m = 3$ and $m = 8$. The beam loss was between 20 and 30%. The main reason responsible for the instability has been associated with the machine resistive wall impedance.

In general, there are three possible solutions to cure this instability:

- Landau damping using non-linear elements (octupoles);
- transverse coupling;
- TFB.

²Hereby we will adopt the physics notation $e^{-i\omega t}$ as alternative to the engineering notation $e^{j\omega t}$.

Starting from 1996, this instability was addressed by using transverse coupling [6, 23] because, at that time, the PS TFB could not cope with it. It was also to avoid strong non-linear elements in the optics.

Since then the HT instability was successfully suppressed in the PS by using the machine natural coupling, by introducing additional coupling using the skew quadrupoles, by setting the working points close to the main diagonal in the HT instability and by exploiting the asymmetry between the two planes (in terms of impedances and chromaticities).

The drawback of this approach is to restrict the machine operability to a confined space of parameters and in doing so reducing its overall flexibility. For example, with the new space-charge regime expected for the LIU (see Section 4.2.1) the choice of the working point has to be as flexible as possible in order to better accommodate the tune footprint. For these reasons, in the LIU perspective, the coupling solution becomes problematic.

During the 2012 run a new TFB was commissioned in the PS (see Section 4.4). This system appears now as the natural candidate to cure the HT instability: one of its goals is to address the HT instability issue at the injection energies ($E_k = 1.4$ GeV or 2 GeV, see Section 4.4) in the LIU parameter space, for a wide range of working points and without any residual coupling. In the following we will describe the principle, the potential and the preliminary results of this approach.

4.2.4.3 The HT instability cured by the TFB

In a linear system, the TFB can cure a specific HT instability if the faster growth time among the unstable modes, $\tau_i = \min_{m,n} \tau_{m,n} > 0$, is slower (larger) than the damping time provided by the TFB, τ_{FB} , that is,

$$\tau_i > |\tau_{FB}|. \quad (4.5)$$

After having introduced the terminology and some relevant considerations, in the following sections we will first present the damping time capability of the TFB and will afterwards compare it with the instability growth time.

The damping time of the feedback assuming uncoupled transverse motion and a pure resistive feedback is given by

$$\tau_{FB}(f) = -\frac{2\tau_r}{G(f)} < 0, \quad (4.6)$$

where τ_r is the beam revolution period and G is the TFB loop gain ($\Im(G(f)) = 0$ for a resistive feedback).

The TFB can be used to cure an instability, function referred to as feedback with the FB subscript, or as a damper with a D subscript to cancel an existing coherent movement, for example due to an injection error. In the damper context, the available power is the critical parameter as the goal is to cancel a high amplitude betatron oscillation before filamentation transforms it into an emittance blowup. The correction can be applied with a saturated signal (power amplifiers reaching their peak voltage value) or in linear mode (below saturation). The saturated approach allows for a faster linear decay whereas the linear approach, with its slower exponential decay, allows to treat, from the beginning, intra-bunch oscillations, caused for example by the observed injection kicker field ripple. Empirical measurements, taking into account the amplifiers' response to saturation, will determine the optimal choice for the loop gain in the damper mode.

In terms of power required by the final amplifier, P , in the first case we have $P \propto G_D x_{\max}^2$, whilst in the second case $P \propto G_{FB} x_{\min}^2$, where G_D represents the loop gain of the TFB as damper, G_{FB} is the loop gain of the TFB as feedback and x_{\max} and x_{\min} are respectively the maximum and minimum detectable beam positions in the linear regime. Since the maximum power, P_{\max} , that the power amplifier

can provide is fixed and independent of the gain and since the loop is optimized if $P \approx P_{\max}$ (keeping in mind that for stability $G_{\text{FB}} < 2$) in general, we have

$$0 < G_D \leq G_{\text{FB}} < 2. \quad (4.7)$$

The TFB has a power limitation that corresponds to a gain threshold $G_D = 0.04$ ($\tau_d(f) = 50 \tau_r$) below which the amplifiers remain in their linear range. Above it, they would peak at the bunch repetition rate, with $x_{\max} = 1.5 \text{ mm}$ at $E_k = 1.4 \text{ GeV}$. It follows that, for the HT instability suppression, we could theoretically operate with $G_{\text{FB}} = 1$ if $x_{\min} = \frac{G_D}{G_{\text{FB}}} x_{\max} = 60 \mu\text{m}$ is still a detectable signal, above the LSB level of the digital signal processing.

So, the TFB performance is limited by the final amplifier power if it operates as damper, whereas it is limited by the PU detection level, system noise and bandwidth when it operates as feedback. On the other hand, is worth noting that if the growth time of the unstable mode is faster than τ_r the feedback cannot cope with it (G should be greater than 2, and this would stabilize that specific mode but would drive unstable all the others). Fortunately, the HT instabilities that we are considering are ‘slow’ instabilities ($\tau_i \gg \tau_r$).

The TFB damping time

An extensive measurement campaign in the 2012–2013 run has been conducted to measure $G(f)$ of the TFB loop and to determine the devices limiting the overall performance. Combining all the elements in the loop chains (neglecting cable losses and parasitic mismatch), we obtain the loop gain: its value can be varied by using the PU amplifier setting. The results on τ assuming $t_r = 2.2 \mu\text{s}$ and $E_k = 1.4 \text{ GeV}$ are shown in Fig. 4.13: the τ_{FB} curve is computed assuming $G(f_0) = 1$ with $f_0 = 1 \text{ MHz}$, whereas the τ_D curve is computed with $G(f_0) = 0.04$.

It is worth noting that the feedback is not purely resistive for all frequencies (there is a dephasing within the loop); furthermore, the loop is unstable above 80 MHz (see 180 degrees phase rotation in Fig. 4.13) but with $\tau_{\text{FB}} > 1$. During the experiments this did not produce observable beam quality degradation, since the flat-bottom duration is on the same order as τ_{FB} . The phase rotation at $\approx 80 \text{ MHz}$ is produced by the sampling rate of the analogue-to-digital converter (ADC) clock ($200 \times f_{\text{rev}} \approx 86 \text{ MHz}$ at injection). Improvements of the system are under study to increase further its bandwidth reach (see Section 4.4).

The expected growth time and spectrum of the instability

In Ref. [24], a comparison of the PS case between Sacherer’s theory and direct simulation is presented. The results show that by varying the horizontal chromaticity between -1 and -0.1 with an uncoupled machine the theory and the simulation results are in good agreement. The faster HT instability predicted has $\tau_i = 32 \text{ ms}$ with $N_b = 1.6 \times 10^{12}$ and $E_k = 1.4 \text{ GeV}$. Doubling the bunch population, we expect to halve the rise-time constant ($\tau_i = 16 \text{ ms}$). Assuming parabolic bunches and a full length of the bunch of 180 ns from the bunch spectrum computation with $m = 10$, most of the power spectrum is confined below 50 MHz and has $\tau_i > |\tau_{\text{FB}}|$ (see Section 4.2.4.5 for details).

This leads us to the conclusion that the present system PS TFB can successfully stabilize the PS HT instability at $E_k = 1.4 \text{ GeV}$. At $E_k = 2 \text{ GeV}$ the maximum feedback gain before saturation will decrease but this in principle should not be a problem, since the HT instability growth time will decrease correspondingly, and the new power amplifiers will have a doubled saturation level. On the other hand, being closer to the transition will increase significantly the frequency range of the instability (see Section 4.2.4.5 for details). The improvement of the TFB power is justified by the damping of the injection errors at the higher energy and its increase in bandwidth is needed for curing the HT instability and the instability at flat top (i.e. same bunch population, higher energy).

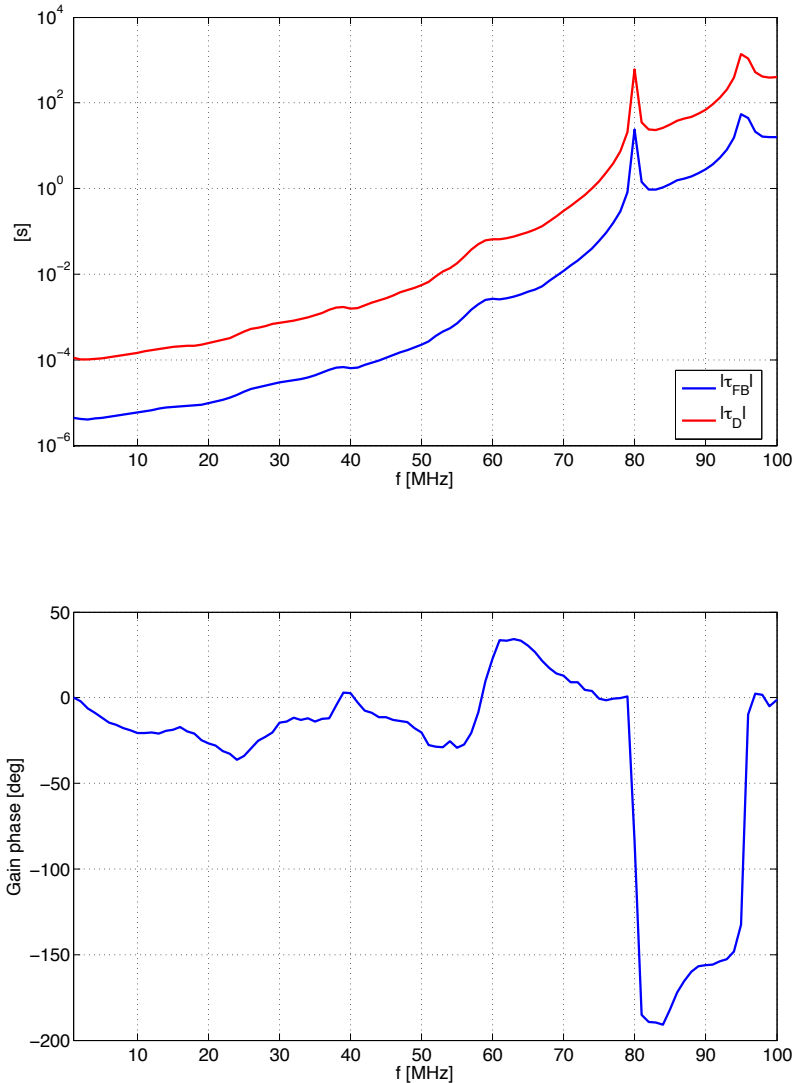


Fig. 4.13: The damping time of the feedback

4.2.4.4 Example of HT instabilities and TFB effectiveness

In the following we will present some results of beam-based measurements in the PS. In 2013 several study sessions were conducted in the PS to prove the effectiveness of the TFB. In the space of parameters explored (varying chromaticity and uncoupled machine), the TFB proved to be always capable of curing the instability. In Figs. 4.14 and 4.15 we show some examples of HT instability without and with the TFB.

In Section 4.2.4.5 we present in more detail the computation of the beam spectrum and the time constant of the instability using Sacherer's theory and formalism [17, 22].

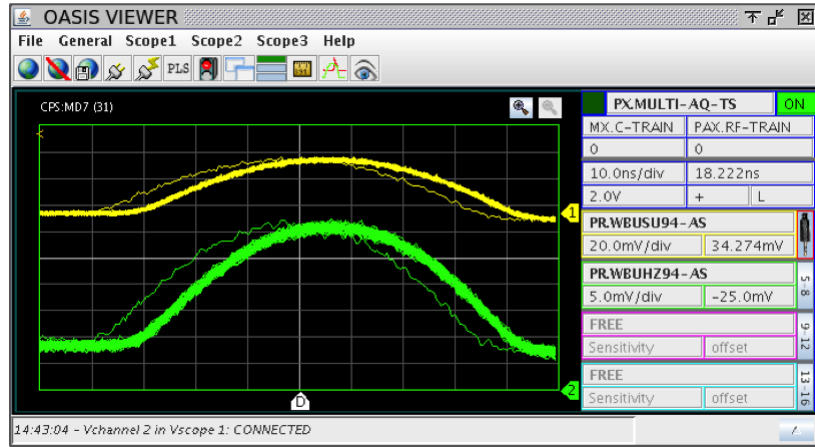
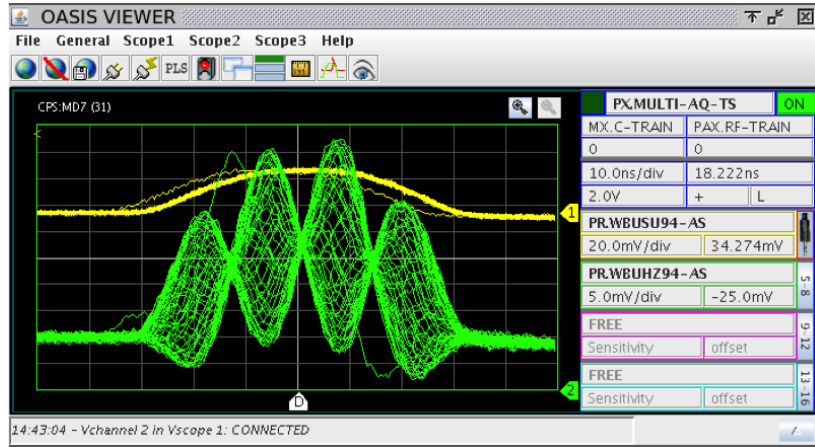


Fig. 4.14: With $\xi = -0.8$ and fully uncoupled machine. The signals in green and yellow represent respectively the horizontal position and sum signal along the bunch. The HT instability without TFB (above). The observation using the TFB (below): the instability has been successfully cured. It is worth noting that the frequency spectrum of the instability is extending up to ≈ 35 MHz.

4.2.4.5 Appendix

The machine impedance

The HT instability originates by the interaction of the PS wideband impedance. The main candidates for it are the resistive wall impedance ($Z_{RW\perp}$) and the broadband impedance ($Z_{BB\perp}$). From Ref. [22], we have

$$Z_{RW\perp} = (\text{sign } f - i) \frac{R}{b^3} \sqrt{\frac{\rho}{\pi \epsilon_0 |f|}} \quad (4.8)$$

and

$$Z_{BB\perp} = \frac{f_r}{f} \frac{R_T}{1 + i Q \left(\frac{f_r}{f} - \frac{f}{f_r} \right)} \quad (4.9)$$

with

- R = machine radius= 100 m,

- b = vacuum chamber radius = 3.5 cm,
- ρ = vacuum chamber resistivity = $9 \times 10^{-7} \Omega \text{ m}$,
- ϵ_0 = permittivity of free space = $8.85 \times 10^{-12} \text{ F/m}$,
- R_T = shunt impedance = 3 M Ω /m,
- f_r = vacuum chamber cut-off frequency = 1.4 GHz,
- Q = quality factor ≈ 1 .

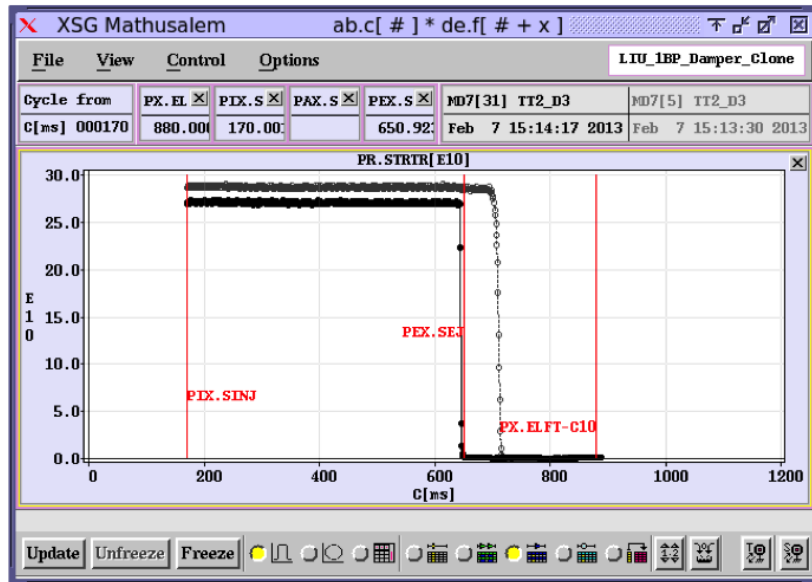
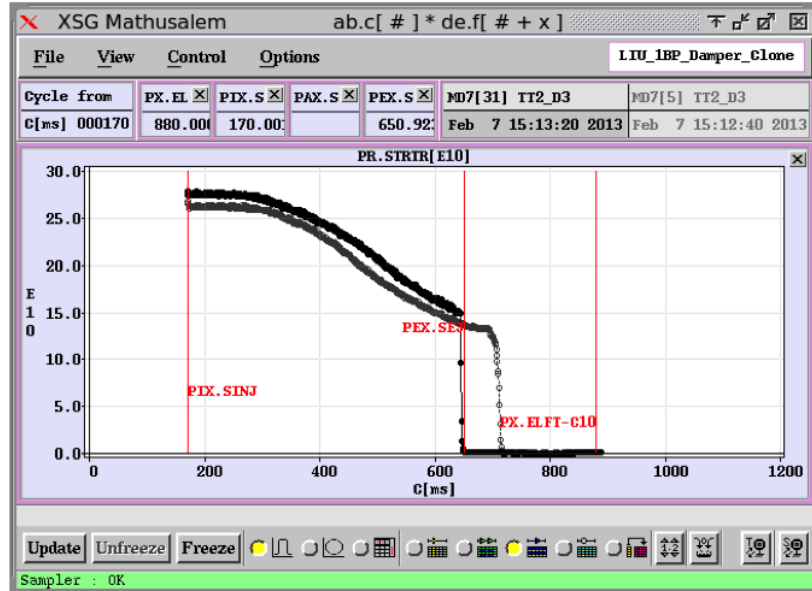


Fig. 4.15: With $\xi = -0.8$ and fully uncoupled machine. The signal represents the total charge in the ring during the cycle. The HT instability without TFB (above). The observation using the TFB (below): all measurable beam losses disappeared.

In Fig. 4.16 the two impedances (real part and imaginary part respectively with solid and dashed lines) are shown. In the frequency range between 0 and 100 MHz the resistive wall impedance is the dominant component.

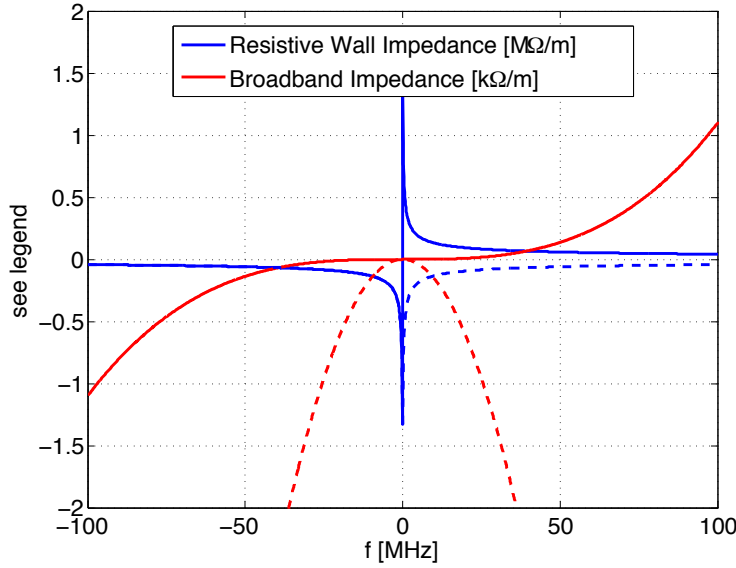


Fig. 4.16: Resistive wall and broadband impedances. The solid and dashed lines refer respectively to the real and imaginary parts. Note that the vertical scale is different and that the resistive wall impedance real part is 1000 times higher than the broadband impedance in the considered frequency range.

The beam spectrum of the instability

The HT instability oscillation spectrum for the different modes in the approximation of parabolic bunches can be expressed as

$$h_m(f) = (m+1)^2 \frac{1 + (-1)^m \cos(2\pi f \tau_b)}{((2f\tau_b)^2 - (m+1)^2)^2}, \quad (4.10)$$

where τ_b is the bunch full length duration.

In Fig. 4.17, the spectra of modes 1, 5 and 10 are represented assuming $\tau_b = 180$ ns. Up to mode $m = 15$ most of the spectrum is within 50 MHz for vanishing chromaticity.

The HT instability growth time

The instability growth time related to the m th mode can be expressed as

$$\tau_m = \frac{1}{\Im(\Delta\omega_m)} \quad (4.11)$$

with

$$\Delta\omega_m = -i \frac{1}{m+1} \frac{e c N_b}{4\pi Q_x \tau_b E/e} \frac{\sum_{p=-\infty}^{+\infty} Z_\perp(f_p^\perp) h_m(f_p^\perp - f_\xi)}{\sum_{p=-\infty}^{+\infty} h_m(f_p^\perp - f_\xi)} \quad (4.12)$$

and

$$f_p = (p + q_x) f_r + m f_s, \quad (4.13)$$

where

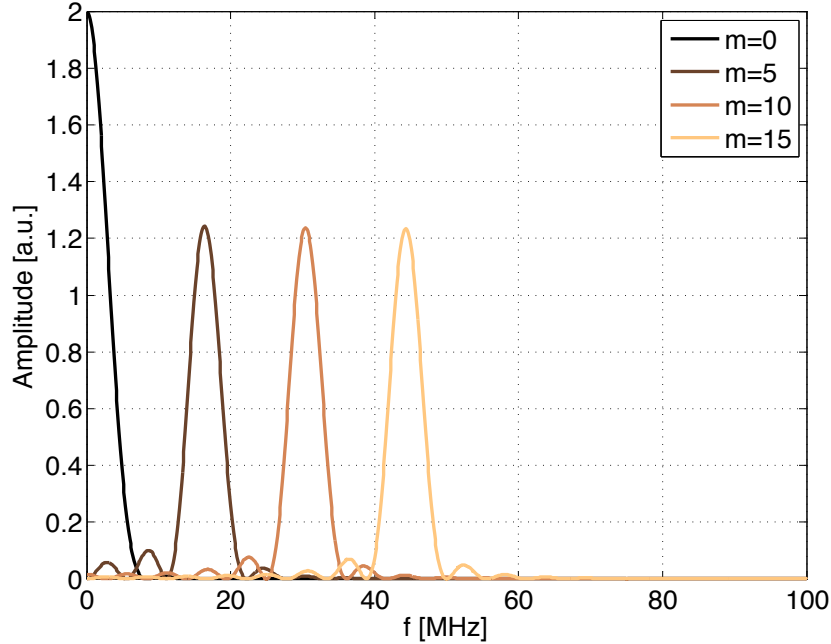


Fig. 4.17: Frequency spectrum of the different modes assuming a bunch length of 180 ns and parabolic bunch distribution for vanishing chromaticity.

- e = electron charge,
- c = speed of light,
- N_b = protons per bunch,
- Q_x = machine tune = 6.22,
- E = proton total energy,
- f_ξ = chromatic frequency = $\frac{\xi Q_x f_r}{\eta}$,
- $\xi = \frac{\Delta Q}{Q} / \frac{\Delta p}{p}$, machine linear chromaticity,
- f_r = beam revolution frequency,
- η = frequency slip factor = $\alpha_p - \gamma_r^{-2}$,
- α_p = momentum compaction factor = 0.027,
- γ_r = relativistic gamma,
- q_x = fractional tune,
- p = harmonic of fundamental frequency = $\dots, -1, 0, 1, \dots$,
- m = mode number = $0, 1, \dots$,
- f_s = synchrotron frequency = 540 Hz.

In Fig. 4.18, we plot τ_m for the modes $1, \dots, 15$ assuming a flat bottom $E_k = 1.4$ and 2 GeV and $N_b = 12 \times 2.3 \times 10^{11}$. For negative chromaticity, it is possible to conclude that $\tau > 16$ ms (Fig. 4.18). At higher energy we observe a slower time constant but a significant ‘chromatic compression’ of the different modes due to $|\eta(2 \text{ GeV})| < |\eta(1.4 \text{ GeV})|$ and its impact on f_ξ .

In Fig. 4.19, we plot the instability growth time versus the frequency when varying the chromaticity. For the frequency coordinate we considered the maximum of the spectrum of Fig. 4.17 (180 ns full bunch length) taking into account the chromatic shift. For the computation of the growth time constant

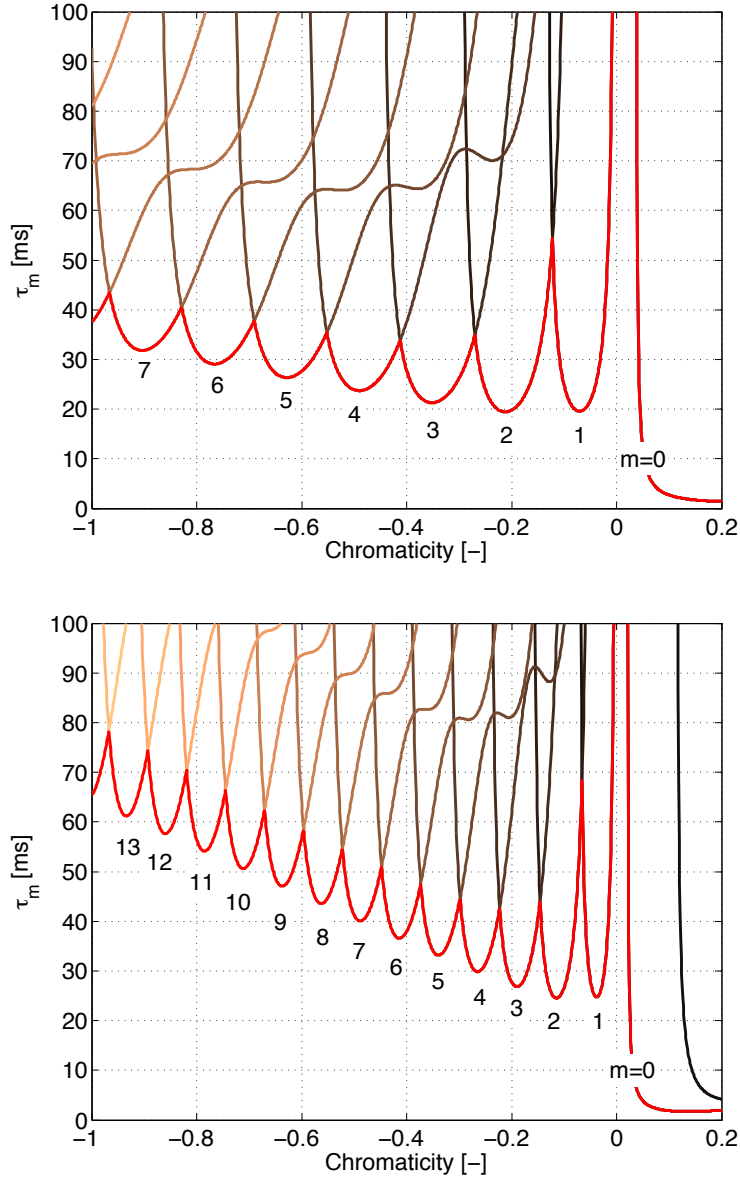


Fig. 4.18: Instability growth for the different modes at $E_k = 1.4$ GeV and 2 GeV (respectively above and below). We consider $N = 2.76 \times 10^{12}$ ppb, that is, 12.3×10^{11} ppb at top energy considering 12-fold splitting.

we assumed that $N = 2.76 \times 10^{12}$ ppb. We can conclude that for negative chromaticity we are within the capabilities of the present system at $E_k = 1.4$ GeV. On the other hand, at $E_k = 2$ GeV and for $\xi < -0.6$ the PS TFB cannot damp the instabilities. In Fig. 4.19, we show that by upgrading the power amplifier bandwidth (up to 100 MHz) and doubling the clock frequency of the DSPU we can recover the TFB performance even at higher injection energy.

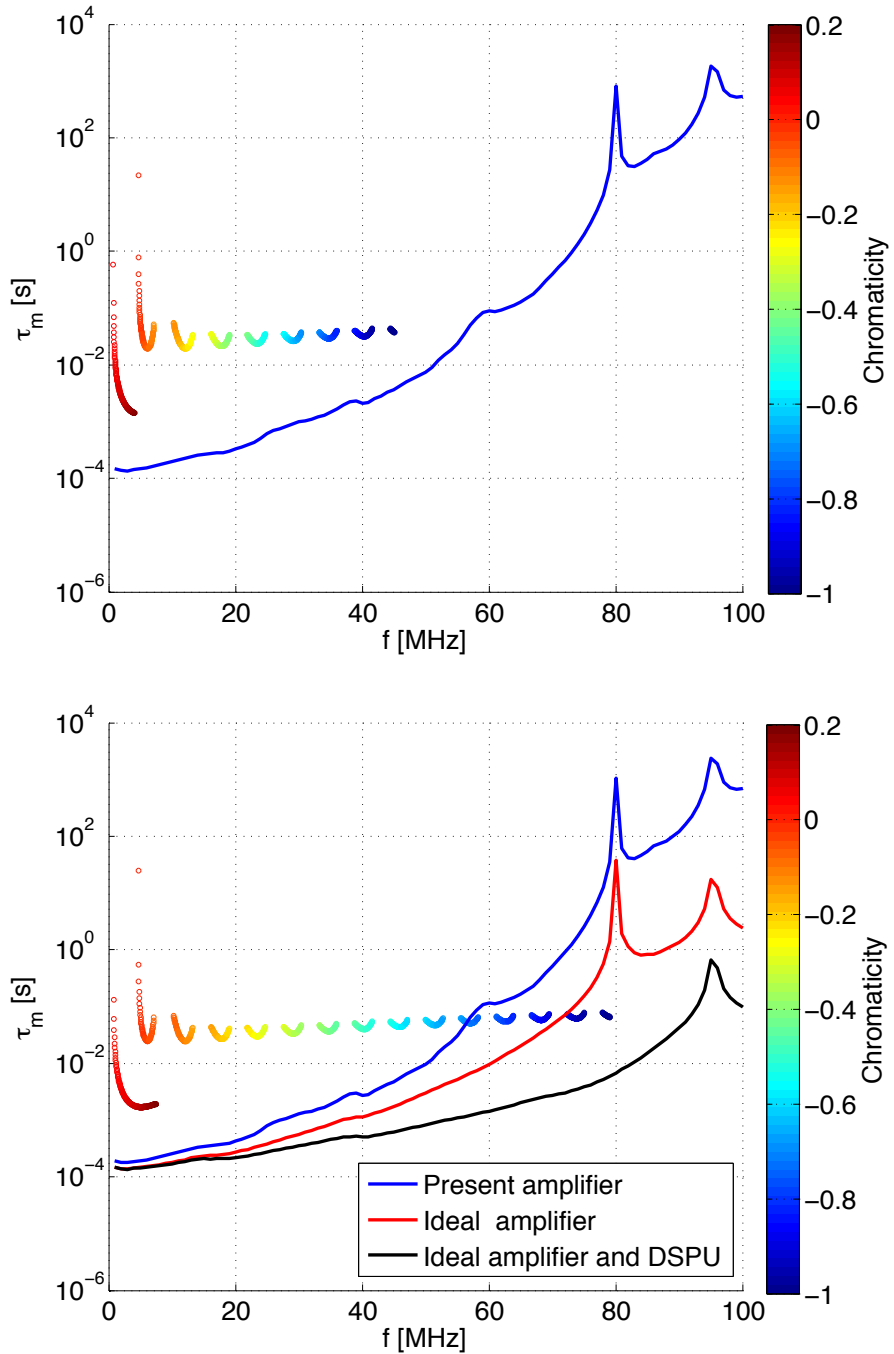


Fig. 4.19: By varying the chromaticity (colour coded in the plot), different modes with different frequency and growth time constant can be excited. For the frequency coordinate we considered the maximum of the spectrum of Fig. 4.17 (180 ns full bunch length) taking into account the frequency shift due to chromaticity. For the growth time constant we assumed $N = 2.76 \times 10^{12} \text{ ppb}$. The plots refer to $E_k = 1.4 \text{ GeV}$ and 2 GeV (respectively above and below).

4.2.5 Transition energy crossing for PS upgrade

4.2.5.1 Introduction

The PS upgrade project foresees accelerating through transition energy very bright LHC beams. The beam stability can be critical through transition due to the loss of Landau damping and special care is taken in the CERN PS to cross this region faster with a γ_t -jump. Métral *et al.* [25] observed in 2000 on a very intense single-bunch beam a fast vertical instability appearing around 6 GeV and which can induce large losses. More experimental works, described in Ref. [15], were performed a posteriori in 2010 to better understand the dynamics of this instability, here summarized in this report.

4.2.5.2 Transition energy

In a synchrotron, a relative energy error $\Delta p/p$ can be related to a relative change in the revolution frequency $\Delta f/f$ by the following relation:

$$\frac{\Delta f}{f} = \eta \frac{\Delta p}{p}, \quad (4.14)$$

where p is the momentum, f the revolution frequency and η the slip factor defined as

$$\eta = \frac{1}{\gamma_t^2} - \frac{1}{\gamma^2} \quad (4.15)$$

with γ the Lorentz energy factor and γ_t the value of γ at transition energy, given by the machine optics as

$$\frac{1}{C_0} \int \frac{D(s)}{\rho(s)} ds = \frac{1}{\gamma_t^2} \quad (4.16)$$

with C_0 the circumference, $D(s)$ the dispersion function and $\rho(s)$ the radius of curvature as a function of the longitudinal coordinate s along the ring. In many proton synchrotrons such as the CERN PS, the beam can be accelerated through the energy $\gamma = \gamma_t$, the so-called *transition energy*, where the slip factor becomes zero. The stable phase ϕ_s has to be shifted from $0 \leq \phi_s \leq \pi/2$ to $\pi/2 \leq \phi_s \leq \pi$ at $\eta = 0$ to preserve the stability of the synchrotron motion [26]. The other consequence of the transition crossing in a synchrotron is the frozen synchrotron motion. It can be easily seen by looking at the expression of the synchrotron angular frequency ω_s ,

$$\omega_s = \sqrt{-\frac{eh\eta V_{RF} \cos \phi_s}{2\pi\beta^2 E_{tot}}} \omega_0, \quad (4.17)$$

which goes to zero when $\eta = 0$: while approaching transition energy, the synchrotron motion performed by the particles is slowing down until it is totally frozen at $\eta = 0$. Once $\gamma > \gamma_t$, the motion slowly starts again. In fact, η measures the amount of phase slip for a single particle with respect to the synchronous particle over one revolution period for a given energy spread. An additional parameter can be used to measure at which moment the synchrotron motion can be considered frozen, the so-called *non-adiabatic time* T_c , defined as [27, 28]

$$T_c = \left(\frac{\beta^2 E_0 \gamma_t^4}{4\pi f_0^2 \dot{\gamma} h e V_{RF} |\cos \phi_s|} \right)^{1/3} \quad (4.18)$$

with e the charge of the particle, V_{RF} the total voltage, h the RF harmonic number, $\dot{\gamma}$ the change of γ with time, i.e. $d\gamma/dt$, and f_0 the revolution frequency. There is no clear distinction between adiabatic and non-adiabatic regions; the change from one to the other is very smooth. One can see that the non-adiabatic time increases with the transition energy.

Let consider the time t , with $t = 0$ being the transition energy. For $|t| < T_c$, the synchrotron motion is considered frozen and the longitudinal beam dynamics is *non-adiabatic*, meaning that the particle motion will not follow a change of the bucket shape. The time T_c is usually of the order of several milliseconds. In the case of the CERN PS, T_c is about 2 ms [15] near the transition energy.

4.2.5.3 γ_t -jump in the CERN PS

High-intensity beams are subject to many issues such as longitudinal emittance blow-up and stability problems. In the past, the intensity was limited at transition crossing due to a longitudinal microwave instability which induced severe losses and/or large dilution of the longitudinal phase space. However, another issue was the bunch length mismatch due to longitudinal space charge with respect to transition energy [29]. A possible solution is to catch up the bunch length after γ_t by changing dynamically the momentum compaction α_p or in other words η and increase as much as possible the speed of the transition crossing. This remedy used in the CERN PS since the 1960s, called *gamma transition jump* [30], is therefore an optics perturbation: it is performed with quadrupoles spread around the ring in doublets and triplets. The unperturbed optics is changed and hence the local dispersion function, allowing us to modify the momentum compaction factor η . The unperturbed γ_{tr} and the γ_{tr} -jump as nominally implemented in the CERN PS are compared in Fig. 4.20 and Fig. 4.21 shows the resulting momentum compaction factor η .

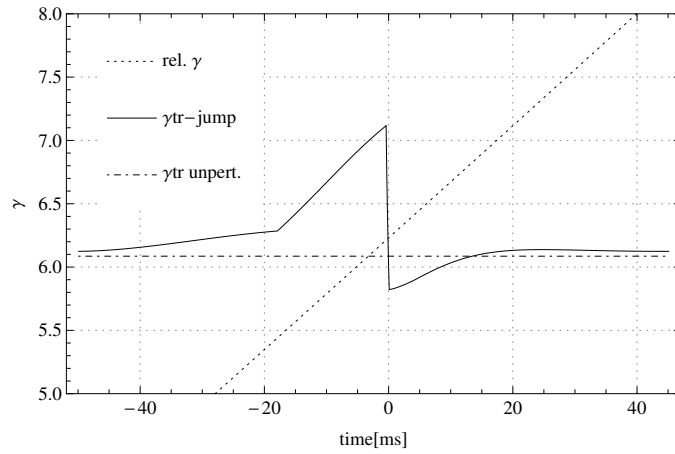


Fig. 4.20: Gamma transition jump in the CERN PS. The dotted curve represents the relativistic gamma as a function of time, the dot-dashed one is the unperturbed gamma transition and the plain curve shows γ_t with gamma transition jump.

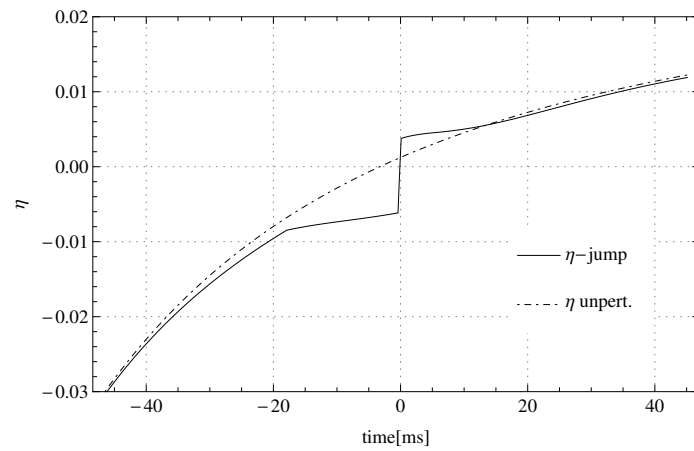


Fig. 4.21: Result of the momentum compaction η with the gamma transition jump in the CERN PS. The dot-dashed curve represents the unperturbed η as a function of time and the plain curve shows the one with gamma transition jump.

Instead of keeping γ_t constant with the energy, Fig. 4.20 shows that γ_{tr} is kept at a safe distance

from the curve of the Lorentz factor γ . Then a jump is performed of γ_{tr} by $\Delta\gamma_{\text{tr}} \simeq -1.24$ in $500 \mu\text{s}$; the transition crossing speed is $50\dot{\gamma}$ with $\dot{\gamma} = 49.9 \text{ s}^{-1}$. The transition energy is also made higher from 6.085 to about 6.2 with the γ_t -jump method. The doublets and triplets of the quadrupoles are powered by the currents as a function of time presented in Fig. 4.22. The jumps of the optics function η and γ_t are then triggered mainly by the doublets whereas the triplets are used to give the general shape of (η, γ_t) .

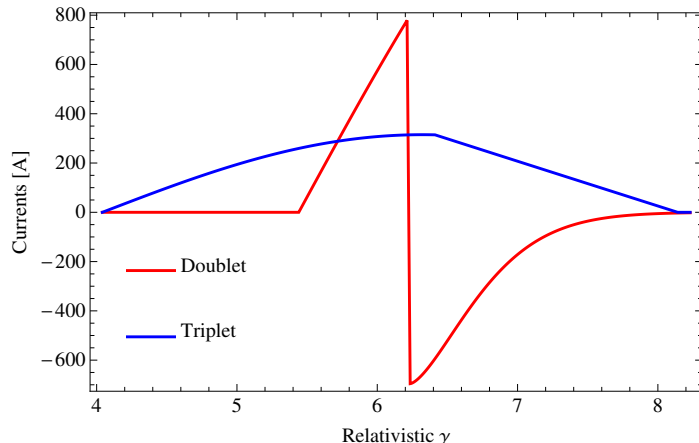


Fig. 4.22: Currents powering the gamma transition jump quadrupoles as a function of time. The γ_{tr} -jump is triggered while the currents of doublets are changing sign.

The gamma transition jump has been used in the CERN PS since the 1960s and has been a convenient method to cure many issues. However, the beam intensity has continuously increased over the years. The γ_{tr} -jump disadvantage is an increase of the transverse beam size due to a distortion of the beta function, very large at certain locations, resulting in severe aperture limitation [31].

In 2000, Métral *et al.* [25] measured near transition a fast vertical instability on the single-bunch-beam TOF, which they compared to the beam break-up instability observed in linacs. This instability was observed even with the use of the γ_{tr} -jump under certain conditions. Since then, more studies were performed of which the detailed results can be found in Ref. [15]. They will be briefly summarized in the next paragraph.

4.2.5.4 The fast vertical instability at transition in the PS

No γ_t -jump

While the beam crosses transition energy—here we suppose no γ_t -jump—with a given chromaticity and a longitudinal emittance and above a certain intensity threshold (Fig. 4.23(a)), a fast vertical instability develops within a few hundred turns. Using a wall-current monitor (WCM) as described in Ref. [32], one can measure on the vertical Δ -signal a high-frequency wave of about 700 MHz developing along the bunch starting close to the peak density, as illustrated in Fig. 4.23(b)—the beam is still stable—and Fig. 4.23(c)—the beam crosses transition and becomes unstable. The particles oscillating at high amplitude are lost in the vacuum very quickly and large losses can occur, as shown in Fig. 4.23(a).

The rise time of the instability is much faster than the synchrotron period (above 20 ms close to transition), meaning that this instability is not a classical HT kind. It has been observed [15], in agreement with the observations of Ref. [25], that this instability has a threshold in intensity for a given longitudinal emittance and chromaticity. Intensity threshold measurements were performed for two sets of vertical chromaticity—zero and slightly negative—and by varying the longitudinal emittance as presented in Fig. 4.24: the threshold can be increased linearly by longitudinal blow-up, which is a behaviour similar to the transverse mode coupling formalism for the computation of intensity threshold for a machine

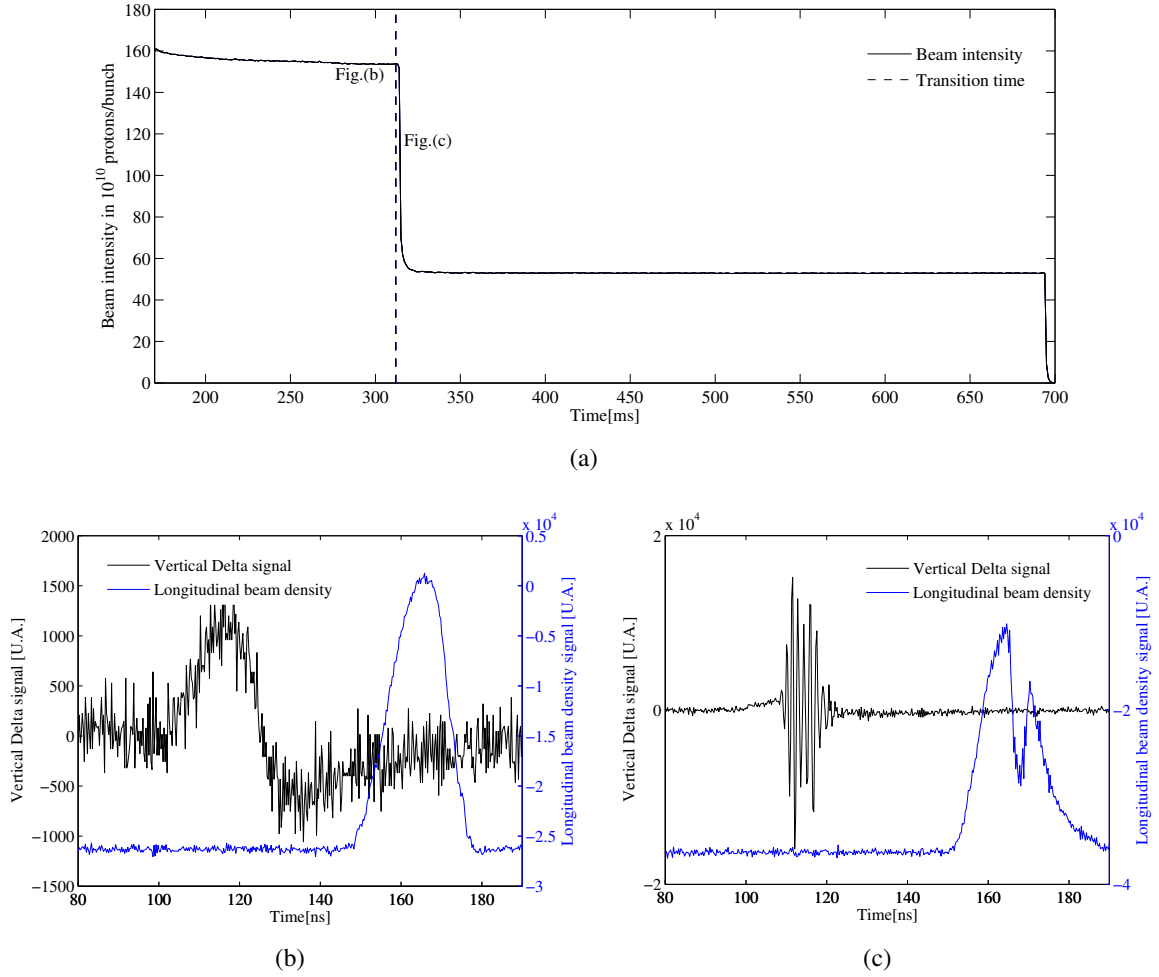


Fig. 4.23: Fast transverse instability observation close to transition energy with the WCM at a beam intensity presented in (a) and a longitudinal emittance of 2 eV s at 2σ : well before transition, the beam is stable (b) and, after transition, the vertical signal of the WCM shows that the beam is unstable (c). In (a) the dashed line shows the time of transition energy crossing.

with a broadband impedance and for a quasi-coasting beam [33] threshold in intensity. However, the formalism does not allow us to predict the measured intensity threshold [15].

Introducing chromaticity allows us as well to alleviate the instability, stabilizing the beam due to Landau damping, by introducing incoherent tune spread [28]

$$\Delta Q_\xi = |Q_0\xi + \eta(n - Q_0)|\Delta p/p \quad (4.19)$$

with Q_0 the bare tune, ξ the chromaticity and n the mode number of the sinusoidal wave. For no chromaticity, the Landau damping vanishes for $\eta = 0$. However, for non-zero chromaticity, here slightly negative, the time (or η) which triggers the instability will be different and therefore we can then define a threshold also in η , which varies linearly with the beam intensity. For the set of measurements $\xi_v < 0$ and, according to Eq. 4.19, the instability is triggered for $\eta > 0$; therefore, shortly after transition energy. Figure 4.25 illustrates this difference in η which triggers the instability, varied with respect to the beam intensity: if the chromaticity is slightly negative, the instability starts later in the cycle.

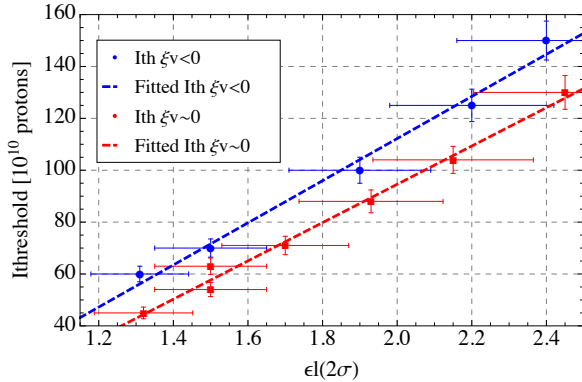


Fig. 4.24: Measured intensity threshold of the instability as a function of the longitudinal emittance for the two sets in chromaticity.

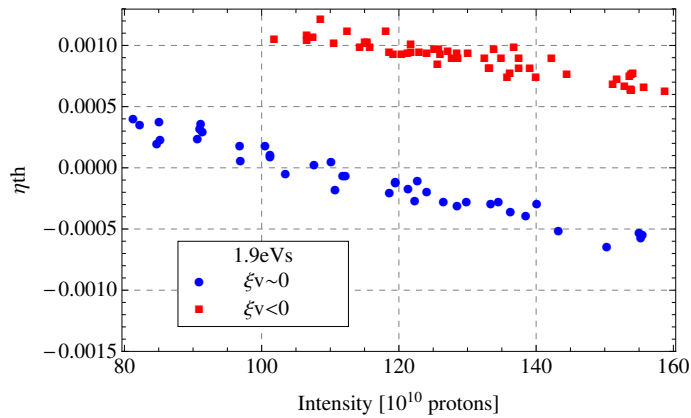


Fig. 4.25: η threshold as a function of the beam intensity for a longitudinal emittance of 1.9 eV s for a chromaticity close to zero and negative.

With γ_t -jump

As described in Ref. [25], the very intense single-bunch beam with 700×10^{10} protons can suffer from this fast vertical instability if a sufficient longitudinal blow-up is not applied before transition, even with the use of a gamma transition jump. However, the longitudinal blow-up increases the bucket filling; as a consequence, the TOF beam bucket is very full. Instead of using a longitudinal dilution to alleviate the instability, it would be more convenient to use for instance the chromaticity and the amplitude of the γ_t -jump.

As in the previous paragraph, measurements [15] of the intensity threshold were also done for a high-intensity single-bunch-beam TOF-like with the γ_t -jump for two sets of chromaticity through transition: slightly negative and with a quick change of vertical chromaticity from negative to slightly positive within a few milliseconds (Fig. 4.26). This is done by the PFWs mounted on the main magnets and the changing speed of their currents is limited as is the speed of the change of chromaticity.

The results of the intensity threshold with gamma transition jump are shown in Fig. 4.27: in comparison with the measurements without γ_t -jump, the intensity thresholds are increased by a factor of three, since the beam stays a shorter time in the non-adiabatic region. The slip factors which trigger the instability are 10 times larger.

However, the use of a quasi-chromaticity-jump in the vertical plane also increases considerably the

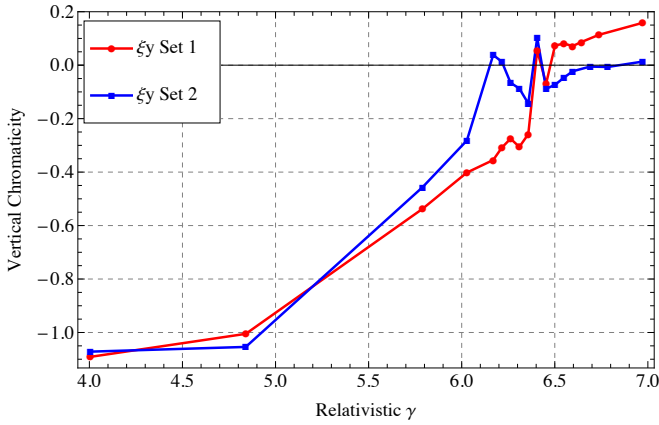


Fig. 4.26: Sets of vertical chromaticity for the instability measurements with gamma transition jump

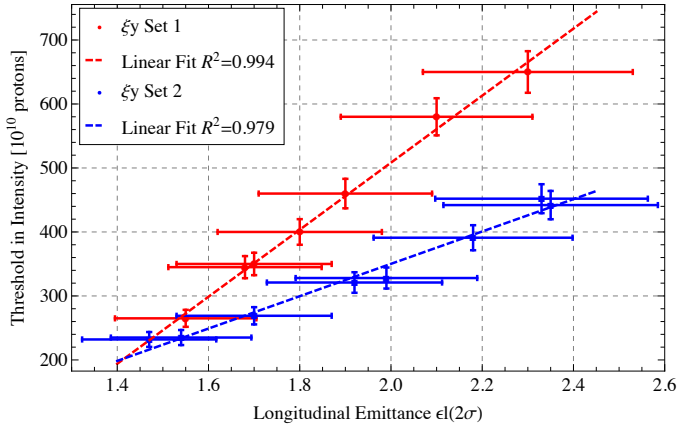


Fig. 4.27: Intensity threshold measurements with a gamma transition jump for two different working points.

threshold in intensity of the instability for the same reason of the loss of Landau damping as discussed in the previous paragraph. In fact, Ref. [34] proposed to correlate the variation of ξ_v with the variation of η , which seems to alleviate the instability; however, one has to note that the chromaticity-jump applied here is not as fast as the η variation due the limitation of the PFWs. For comparison, η changes within 500 μ s, whereas the chromaticity takes a few milliseconds.

Concerning the high-brightness LHC beams, it is very difficult to draw a definitive conclusion on the beam stability, based on a linear extrapolation of the data shown in Fig. 4.27 to small longitudinal emittances. Based on operational experience, it seems to be acceptable to assume that the beams will be stable, also thanks to a proper optimization of the gamma transition jump and the longitudinal beam parameters. A series of theoretical and experimental studies is planned to support this conclusion.

4.2.6 Electron Cloud studies in the CERN PS

4.2.6.1 Introduction

Indicators of the Electron Cloud were first observed in the CERN PS in 2001 during the last part of the cycle for the production of the so-called LHC-type beams, i.e. the beams of the type needed for the LHC filling. The production scheme of these beams in the PS is based on two or three steps of bunch splitting in order to obtain at the exit of the PS bunch trains with 50 ns or 25 ns spacing, respectively. In either case, the final stage of bunch splitting takes place at the flat top and is followed by adiabatic bunch

shortening and fast bunch rotation shortly before extraction [35]. Therefore, these beams only circulate in the PS for a few tens of milliseconds with a structure prone to EC formation (beam parameters are summarized in Table 4.1).

During this short time before extraction, EC was initially revealed in 2001 by the presence of a baseline drift in the signal from the PU as well as beam transverse instabilities purposely excited by keeping the adiabatically shortened 25 ns bunches in the PS for an additional 10 ms instead of rotating and ejecting them [36]. The transverse instabilities made a new appearance with 25 ns beams in 2006, after the long shutdown of the LHC injector chain of 2004–2006, and for a short time even seemed to affect even the operational LHC beams that were transferred to the SPS. A dedicated study of the problem showed that in reality the bunches were accidentally shortened to 10 ns or below (instead of the nominal 12 ns) during the phase of adiabatic shortening prior to the fast rotation. This observation suggested that the short bunches could initiate the EC build up earlier in the cycle and produce enough EC for a sufficiently long time as to render the beam visibly unstable. This was also confirmed by the fact that the instability could be avoided after the adiabatic bunch shortening was re-adjusted to lead to sufficiently long bunches (>11 ns) before the final bunch rotation [37, 38]. In March 2007, an experiment for dedicated EC measurements was set up at the PS to be able to directly measure the electron signal by using a shielded biased PU [39] and confirm its presence in the machine in the last phase of the LHC beams production. The experimental set-up was designed, built and mounted in the straight section (SS) 98 during the accelerator shutdown 2006–2007. Details of the set-up can be found in Ref. [39]. These studies confirmed that the EC develops during the last 40 to 50 ms before ejection, i.e. after the last double splitting and while the bunches get shortened by the RF gymnastics. Besides, they also showed that the EC can be locally suppressed by putting a sufficiently large voltage of either polarity onto a clearing electrode, even if the clearing efficiency depends on the magnetic field present in the region of the measurement in a non-trivial way.

Table 4.1: Relevant beam parameters in the PS during the flat-top RF gymnastics for the two bunch spacings of 50 and 25 ns.

	50 ns	25 ns
Beam energy [GeV/c]	26	
Bunch intensity [$\times 10^{11}$ ppb]	0.82–1.95	0.83–1.33
Bunch length [ns]	$15 \rightarrow 12 \rightarrow 4$	
Number of bunches	36	72
Transv. norm. emittances [μm]	1–2	2–3

In 2011, new systematic measurements of EC have been performed at the CERN PS with the goal of extracting the following information.

- Dependence of the EC build up evolution on some controllable beam parameters. The EC signals were recorded with both 25 and 50 ns beams and within a wide range of bunch intensities, covering present and possibly future operation. Besides, different bunch lengths could also be explored by removing the final steps of bunch rotation and adiabatic bunch shortening.
- A new collection of time-resolved experimental data of EC build up in some desired sets of beam conditions.

These sets of data can serve two purposes. First, comparing them with build up simulations will allow us to validate and improve the simulation model on which our tools are based. Second, by matching the simulations to the experimental data in all the different beam conditions, we can infer the surface properties of the PS vacuum chamber (maximum SEY – Secondary Emission Yield –, δ_{\max} , and reflectivity of the electrons at zero energy, R_0) and extrapolate then how much EC we can expect in the PS

with the higher intensity beams foreseen in the frame of the LHC-LIU project, and whether that can be detrimental to the beam.

In 2012–2013, the EC studies in the CERN PS were mainly devoted to describing the horizontal instability and damping it with the TFB system, as well as to exploring voltage settings to be used during the final manipulation of the 25 ns beams in order to shorten the time during which the EC builds up.

4.2.6.2 2011 activities

Measurements

In 2011, the Machine Development (MD) programme in the PS for EC studies took place in November and extended over several sessions to cover different sets of beam parameters. In particular, EC build up data were recorded for 25 ns and 50 ns beams. The bunch intensities were scanned in the ranges indicated in Table 4.1. The trigger for the data acquisition was set at extraction, when in normal conditions each bunch of the beam has been already fully rotated (4 ns bunch length). However, specifically for these measurements, the bunch length at this time for a fixed bunch intensity was also set to 6.5 ns or 15 ns by simply adjusting or fully removing, respectively, the final step of the fast bunch rotation. This allowed studying the dependence of the EC build up not only on the bunch intensity but also on the bunch length.

Several measurements of EC build up were taken with 50 and 25 ns beams and the results of the bunch intensity scan are displayed in Fig. 4.28. Each plot shows the EC signal over a time window slightly longer than one PS revolution time (2.1 μ s with 1.8 μ s length of the 36-bunch or 72-bunch train plus 300 ns gap). The bunch intensity was varied over a broad range.

The threshold for EC formation with 50 ns beams lies at about 10^{11} ppb and the measured signal increases monotonically with the bunch intensity. This is not entirely surprising, since the measurements were taken with zero magnetic field while the non-monotonic behaviour of the EC build up with the bunch intensity is more frequent in dipole regions. The shielded PU is installed inside a C-magnet, which was kept off during the MD sessions because the orbit perturbation it introduces would have required a specific correction. The scans with 25 ns beams covered a smaller intensity range, as labelled in Fig. 4.28, right-hand column. Here we can see that the threshold for EC formation is below 8×10^{10} ppb for 25 ns spaced beams and then again the EC signal increases with the bunch intensity.

The scans in bunch length for a fixed bunch intensity of 1.5×10^{11} ppb are plotted in Fig. 4.29 for both 50 ns (left) and 25 ns beams (right). From the left-hand plot it is clear that, while the difference between the build up with bunches of 4 and 6.5 ns is small, there is no sign of EC with 15 ns long bunches. This suggests that 50 ns beams might see the EC only in the very last phase of the beam production, i.e. during and after the fast bunch rotation. For 25 ns beams, while the difference between the EC build up with bunches of 4 and 6.5 ns is negligible, the EC is lower, yet still significant, with 15 ns long bunches.

Comparison with simulations

We have tried to fit the PS data with those from EC build up simulations [40]. First of all, the output of the code that should be compared with the measured signal is the electron flux to the wall. In a first approximation, we do not consider the holes in the vacuum chamber, which are expected to cause only a minor perturbation in a field-free region. In general, the simulated electron flux to the wall vanishes during the bunch passage, because initially all the electrons are drawn to the centre of the vacuum chamber by the passing bunch (e.g. during the first ~2 ns of a 4 ns long bunch) and they are gradually released only during the falling edge of the bunch, when they may reach the walls again. The fact that the measured signal does not exhibit this feature makes plausible a low-pass filtering of the signal (inherent to the measurement technique or due to electronics and/or cables) with a corner frequency in the range of some hundreds of MHz. Figure 4.30 shows measured and simulated signals, where the simulated signal, obtained with $\delta_{\max} = 1.6$ and $R_0 = 0.5$, was low pass filtered with a

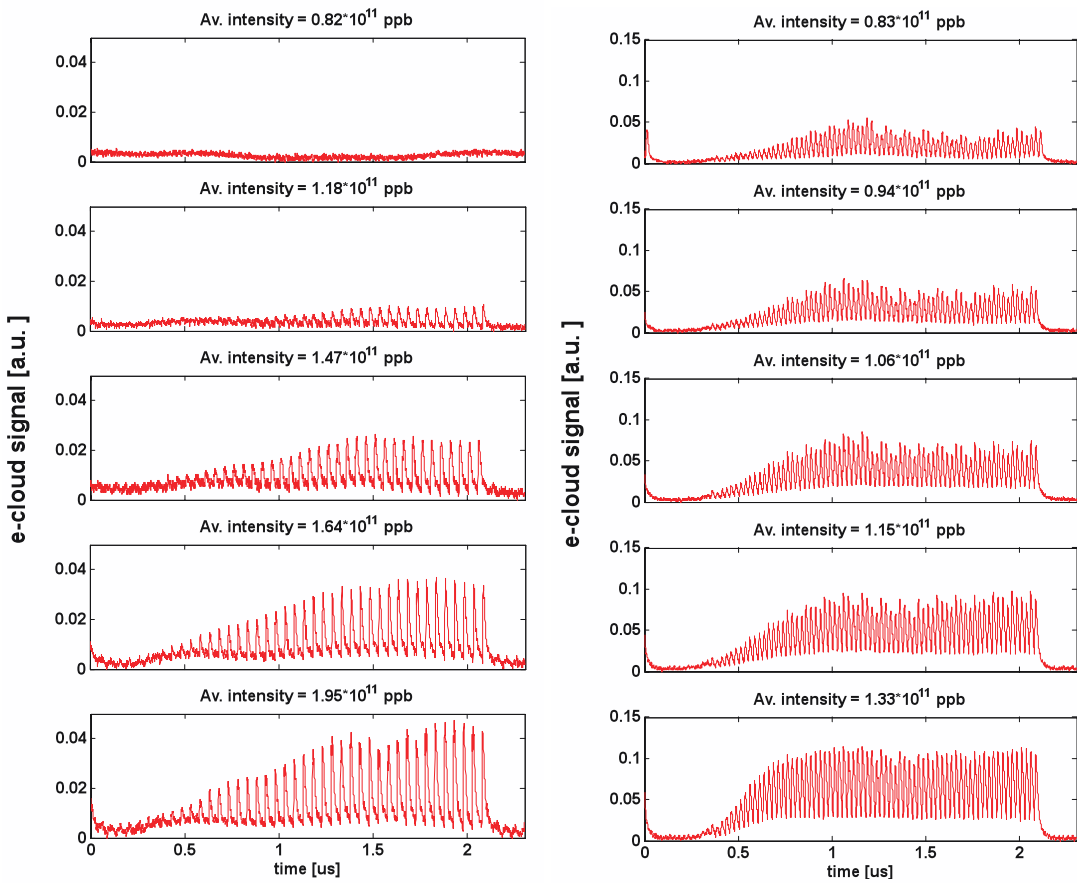


Fig. 4.28: E-cloud build up during passage of a 50 ns bunch train with 4 ns bunch length (left) and during passage of a 25 ns bunch train with 4 ns bunch length (right). The sometimes visible sawtooth behaviour follows a bunch-by-bunch intensity modulation present during the measurements.

corner frequency of 200 MHz. The impressive resemblance between the two suggests that our EC model correctly describes the phenomenon and the rationale applied for the data analysis is promising.

4.2.6.3 2012–13 activities

Within the LIU project, one of the outstanding questions to address is whether the EC instability, or incoherent EC effects, could degrade the beam quality on the time-scale of the nominal cycle for the high-intensity and high-brightness beams foreseen for the upgrade. In this framework, several studies were carried out in 2012–2013 in order to:

- further investigate the instability developing on the ‘stored’ 25 ns beam;
- check the possibility of using a modified 40 MHz RF voltage programme in order to limit as much as possible the exposure of the LHC beams to EC in the PS;
- use build up simulations to build a complete EC model of the PS vacuum chambers, identify new diagnostics tools (e.g. EC detector in a combined function magnet to be installed during LS1 [41], bunch-by-bunch stable phase shift measurement) and support their design. For this purpose, the possibility of simulating combined function magnets had to be implemented in the EC build up code PyECLLOUD [40] and was used for the characterization of the different chambers, as will be reported in the last following subsection.

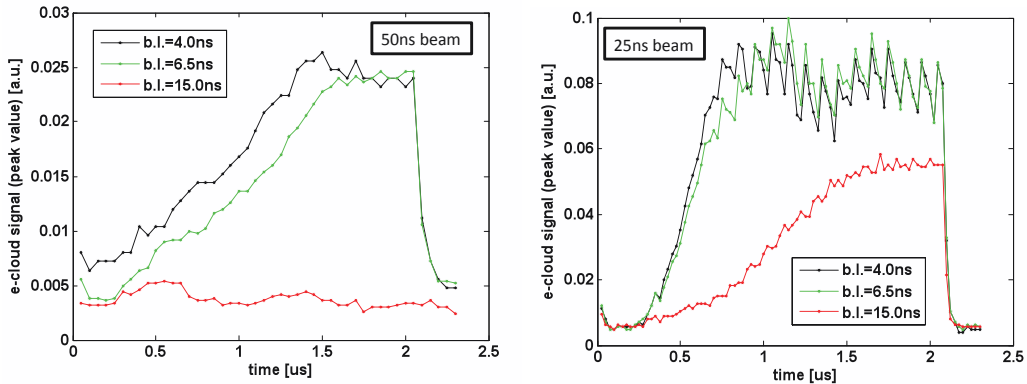


Fig. 4.29: Envelope of the build up during passage of a 50 ns (left) and a 25 ns (right) bunch train with 1.5×10^{11} ppb.

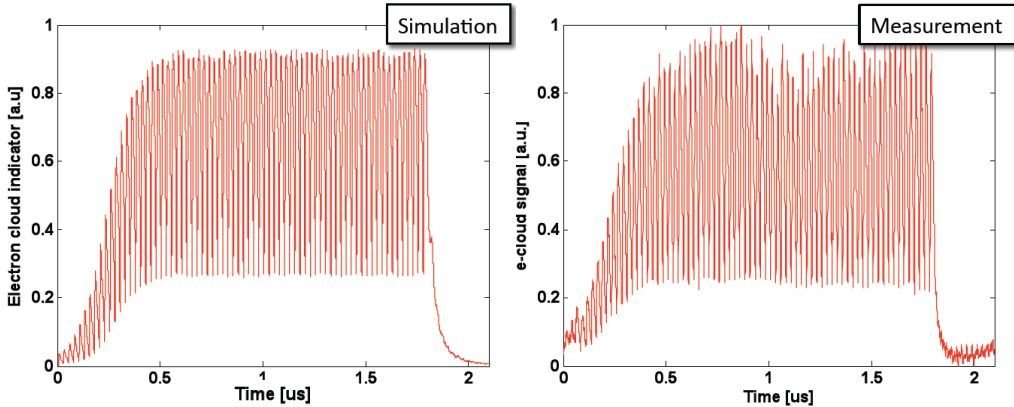


Fig. 4.30: E-cloud build up simulation (left) and measurement (right) for a 25 ns beam with 1.33×10^{11} ppb and 4 ns long.

Transverse instability

Several bunch-by-bunch position measurements were acquired on a modified cycle, in which the bunch rotation was removed and replaced by a 30 ms long flat top. In this cycle, the beam could be stored long enough after the adiabatic shortening ($h_{RF} = 84$, $V_{RF} = 100$ kV) to observe that the beam became transversely unstable (even for quite low intensities $\sim 6 \times 10^{10}$ ppb). The oscillation in the horizontal plane was much stronger than in the vertical plane. Actually, the spectral content of the vertical motion was concentrated around the horizontal tune, suggesting that the observed unstable motion observed also in the vertical plane is due to $x-y$ coupling. It could be noticed that the different bunches of the train have different behaviours, as shown in Fig. 4.31 (left). The rise time of the instability is almost the same for the bunches in the second half of the train and then it becomes longer for bunches towards the head. The first 10–15 bunches actually look stable during the 30 ms store. This kind of behaviour is consistent with the evolution of the electron density along the train in a typical EC build up. Moreover, the intra-train pattern revealed a clear coupled motion between bunches, whose mode number appeared to become larger when including bunches close to the train head, as shown in Fig. 4.31 (right). All these features look compatible with an EC-driven instability, although also other mechanisms (e.g. impedances) might need to be investigated.

In 2012 a new TFB was commissioned in the PS [42], which could also be tested on the instability described before with very encouraging results. Since the feedback cannot be operated in continuous-

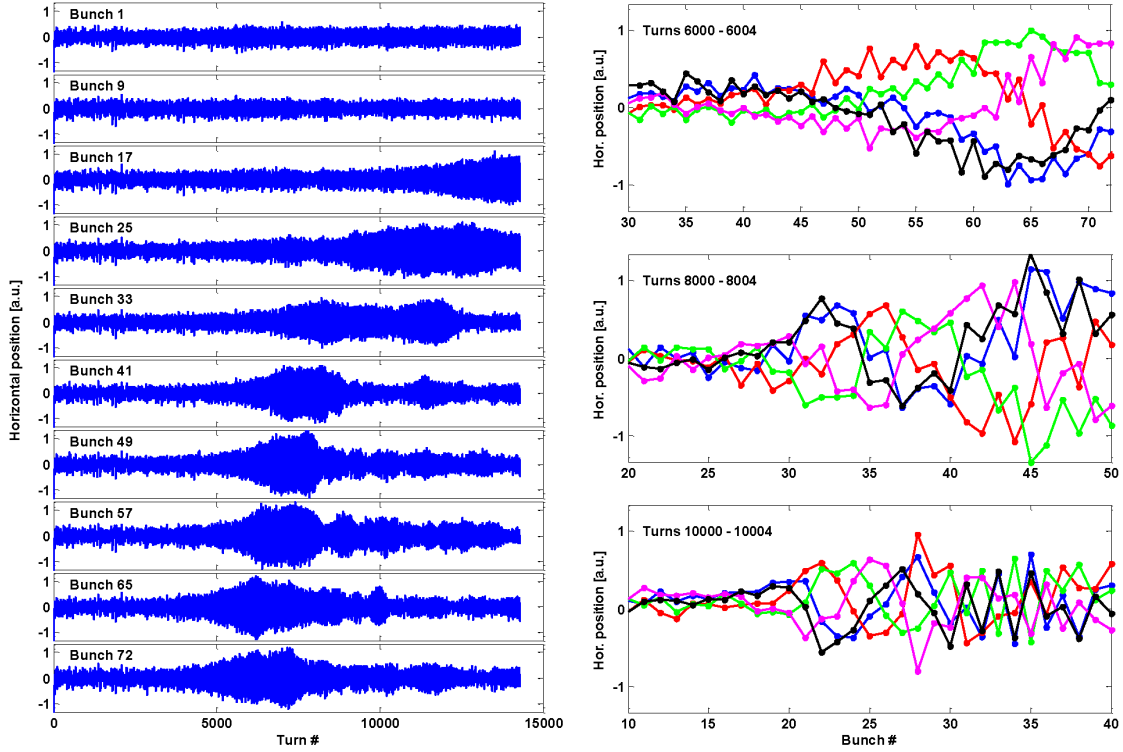


Fig. 4.31: (Left) evolution of the horizontal centroid position for selected bunches along the bunch train ($t = 0$ roughly corresponds to the beginning of the bunch shortening); (right) bunch-by-bunch position for five consecutive turns at different moments during the store (the horizontal scale is chosen in order to better visualize the unstable bunches).

wave (CW) mode, it could not suppress the instability altogether along the whole 30 ms store. On the other hand, the instability onset could be successfully delayed by about 10 ms, which could provide an important margin when compared to the time-scales of the bunch shortening in the nominal cycle.

Effect of the RF voltage programme

Simulations and measurements have shown that the EC build up in the PS is very sensitive to bunch length variations. Therefore, two modifications were introduced in the RF voltage programme in order to minimize the interaction of the beam with the EC: (1) the adiabatic bunch shortening was replaced with a bunch pre-rotation [43], which allows us to shorten the bunch length from 14 ns to 11 ns in a much shorter time, i.e. $\sim 600 \mu\text{s}$; (2) the 40 MHz RF voltage during the bunch splitting was reduced by 10%. Beam profile measurements confirmed that these modifications did not introduce any important degradation of the beam quality at the extraction from the PS.

For the tests the signal from a pressure gauge located in a straight section of the ring was used as a ‘time-integrated’ EC indicator. The effects of the modifications of the voltage programme on the pressure signal are shown in Fig. 4.32 for a bunch intensity of 1.25×10^{11} ppb (on the left) and 1.45×10^{11} ppb (on the right). It can be noticed that the strongest reduction of the pressure rise comes from the relatively small reduction of the voltage (and therefore slightly longer bunches) during the splitting, while the introduction of the double-bunch rotation has a non-negligible effect only for the lower intensity. Moreover, the combination of the two strategies gives an almost complete EC suppression for the lower

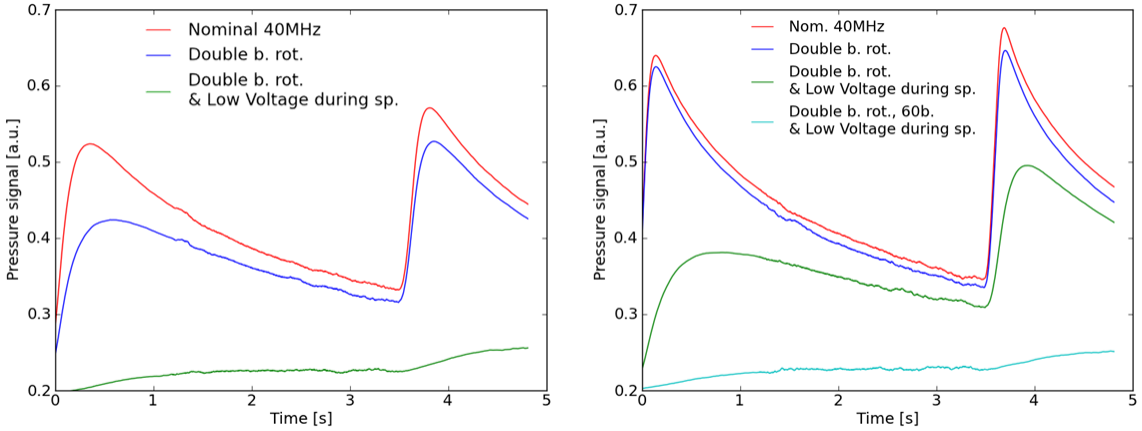


Fig. 4.32: Pressure measured with two consecutive LHC-type cycles (the beam is extracted at $t = 0$ and $t = 3.6$ s) for different RF manipulations. Comparison between two different bunch intensities: $\sim 1.25 \times 10^{11}$ ppb on the left and $\sim 1.45 \times 10^{11}$ ppb on the right.

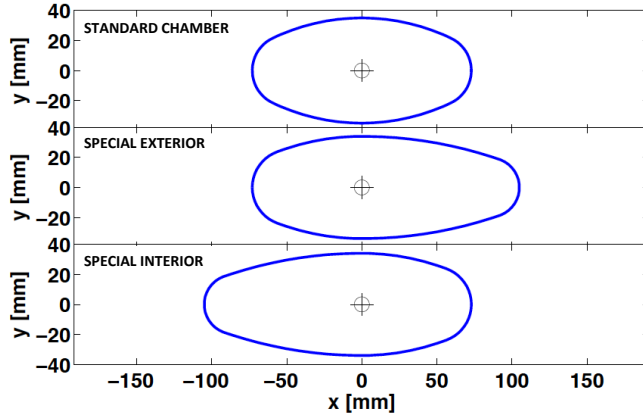


Fig. 4.33: Geometry of the three possible PS chambers analysed in the EC-parameter studies. From top to bottom: the standard chamber (width 146 mm, height 70 mm), the special exterior chamber (width 178 mm, height 68 mm) and the special interior chamber (width 178 mm, height 68 mm).

intensity, while a significant pressure rise is still observed for the higher one. In this last case, the EC could be almost completely suppressed only by reducing the number of bunches from 72 to 60, and hence increasing the empty gap in the ring from 300 ns to 600 ns. This is due to the fact that, especially when the bunches are longer (which implies a longer EC rise time), the ‘memory effect’ between subsequent turns plays an important role in the EC formation. Therefore, a smaller number of bunches, and hence an increased gap in the ring, can give an important mitigation for the EC. This means that alternative RF schemes based on batch compression, which are presently considered for the production of higher brightness LHC-type beams [44], should also be less critical in terms of EC effects thanks to the reduced number of bunches.

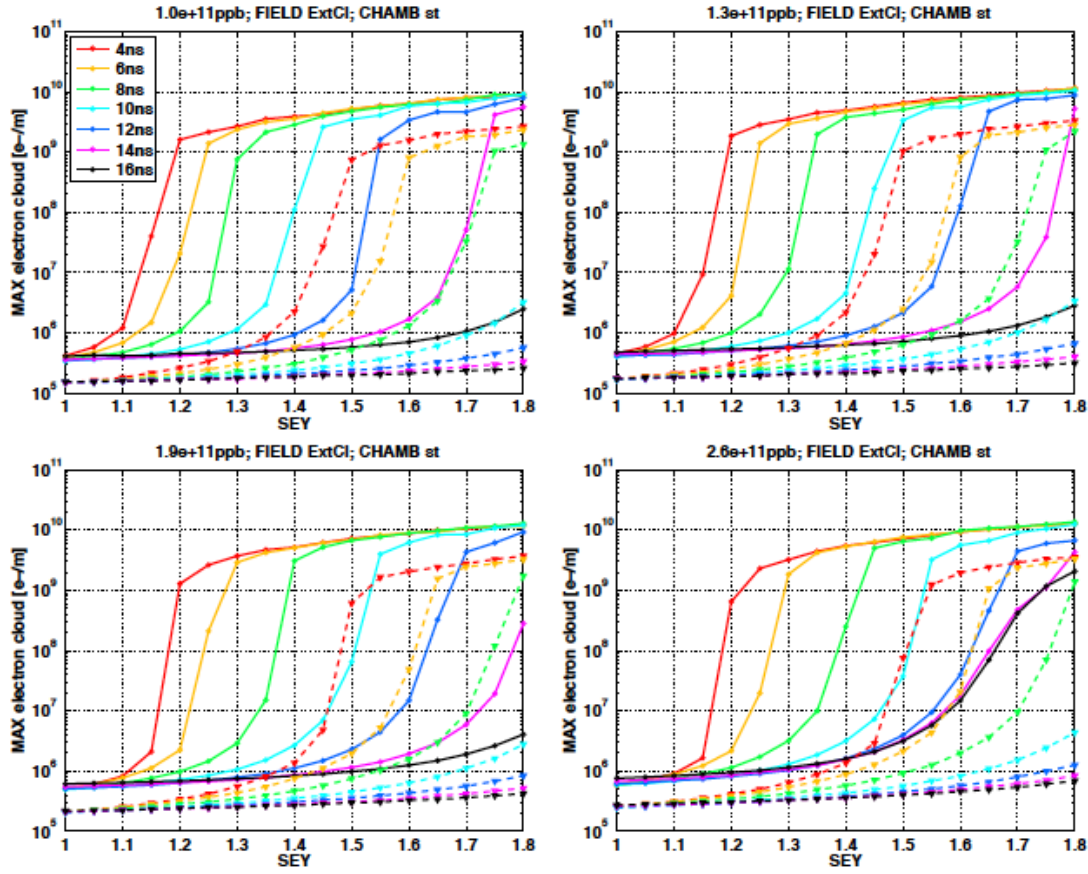


Fig. 4.34: EC line density as a function of the SEY for different bunch lengths (as labelled), for different values of bunch population ($1.0, 1.3, 1.9$ and 2.6×10^{11} ppb, from top left to bottom right, for two possible bunch spacings (25 ns solid lines and 50 ns dashed lines)).

Simulation scans

An intensive simulation campaign has been conducted in 2013 in order to characterize all the PS chambers (and different magnetic field configurations) in terms of EC formation. In this study, the relevant ranges of bunch length and population were covered, i.e. [4, 16] ns and [$10^{11}, 2.6 \times 10^{11}$], respectively. The bunch length range simply corresponds to the values really covered during the last part of the cycle of the LHC 25 ns beam production, namely after the last bunch splitting at 26 GeV/c up until extraction. The bunch population range has been chosen as to reasonably include values that can be reached nowadays and extend to the future LIU values. The main goal of these simulation scans was to determine SEY thresholds all around the PS machine in different operating conditions. To have this whole information would then allow:

- extrapolating the expected value of stable phase shift assuming a maximum SEY of about 1.6 (consistent with the EC data from the dedicated monitor with 25 ns beams, see previous section, and with 50 ns beams);
- defining the possible location for an in-magnet EC detector to allow for direct measurements after LS1.

Some examples of parameter studies are shown here in the following, while the full survey can be found in Ref. [45]. Three PS chambers were considered in the analysis; see Fig. 4.33.

For each chamber five possible magnetic field configurations have then been considered to cover all possible combinations, i.e. drift, open interior, open exterior, closed interior and closed exterior. An example of results from the vast parameter scan is shown in Fig. 4.34. EC build up thresholds were calculated for several values of bunch length (covering the whole part of the cycle in which the LHC beam structure has been already imprinted), several values of bunch population (covering present and future parameters) and 25 and 50 ns bunch spacing. For this special case, only the standard chamber has been considered and one configuration of magnetic field (external closed).

4.2.7 Longitudinal instabilities and transient beam loading

Coupled-bunch oscillations during acceleration above transition are the most stringent longitudinal limitation for the high-brightness beams in the CERN PS. While controlled emittance blow-up with a high-harmonic RF system may stabilize the beam, the maximum longitudinal emittance for LHC-type beams must remain compatible with a fixed emittance of about 0.35 eV s per bunch at extraction. To damp the instabilities without increasing the longitudinal emittance, a new coupled-bunch oscillation feedback with a dedicated kicker cavity was installed during LS1 and commissioned after the start-up in 2014 (see Section 4.5). An extensive study programme has been undertaken to improve the understanding of coupled-bunch instabilities in preparation of the installation of the new coupled-bunch feedback.

The thresholds of longitudinal single-bunch instabilities in the PS are expected to occur only beyond the intensity and density requirements of LHC-type beams, even after the upgrades. In the context of MD studies in the SPS in 2012, a single LHC-type bunch with a longitudinal emittance close to the nominal value of 0.35 eV s and an intensity of up to 4×10^{11} ppb has been produced in the PS without issues of longitudinal stability. Additionally, the high-intensity single-bunch beam for the nTOF (neutron Time Of Flight) experiment has a twice higher average longitudinal density, N_b/ε_1 , during acceleration and at transition crossing than the 25 ns LHC-type beam at an intensity of 2.4×10^{11} ppb (corresponding to about 10^{12} ppb during acceleration) [46]. The intensity per bunch is given by N_b and the longitudinal emittance by ε_1 .

In the ideal case all bunches in the batch of LHC type have the same intensity with identical longitudinal parameters. Transient beam loading during the bunch-splitting manipulations may introduce relative phase errors between RF systems along the batch, resulting in asymmetric splittings especially at the head of the batch. These relative phase errors due to transient beam loading can only be mitigated by reducing the effective impedance of the RF cavities participating in the bunch splittings.

4.2.7.1 Longitudinal coupled-bunch oscillations during acceleration

While the LHC-type beams in the PS are longitudinally stable below transition, coupled-bunch oscillations develop above a certain longitudinal density threshold during acceleration and on the flat top. To identify possible sources of impedance driving them, coupled-bunch oscillations have been observed along the cycle and their mode spectrum analysed. Assuming constant intensity per bunch at PS extraction, each bunch must have twice more intensity during acceleration for a final spacing of 25 ns than for the variant with 50 ns spacing (one splitting less on the flat top). For both variants, nominally 18 bunches are accelerated on harmonic $h = 21$. Since also the longitudinal emittance per bunch at extraction should be independent of the spacing, the emittance during acceleration with the 50 ns variant must not exceed half the bunch emittance for 25 ns final spacing. This implies that the longitudinal density, N_b/ε_1 , remains constant in both cases.

To measure coupled-bunch oscillations, the longitudinal emittance has been adjusted close to the stability limit applying controlled longitudinal blow-up. The profiles of all bunches are then recorded for a few periods of the synchrotron frequency every 70 ms. Gaussian fits are then applied to each bunch of each profile. This allows us to extract the dipole motion for all bunches, resulting in an oscillation amplitude, phase and frequency per bunch, the latter being close to the synchrotron frequency. The

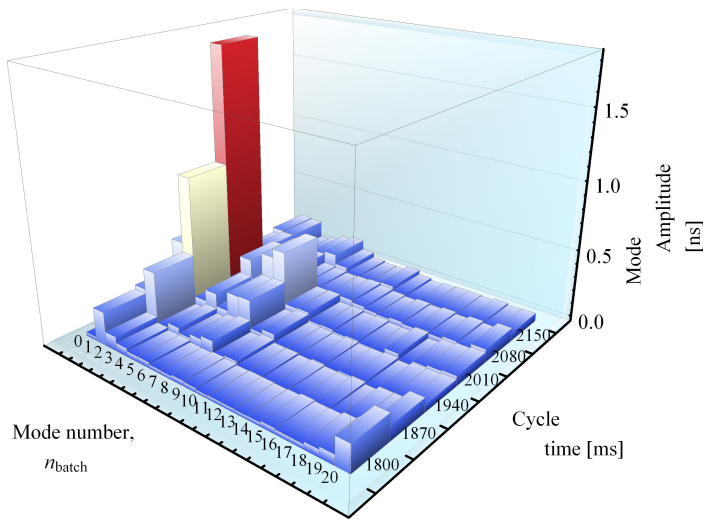


Fig. 4.35: Coupled-bunch mode spectrum during acceleration of 21 bunches in $h = 21$, averaged over 10 cycles for each measurement time ($N_b = 4.0 \times 10^{11}$ ppb, $\varepsilon_{1,RMS} = 0.14$ eV s).

amplitudes and phases per bunch can then be related to the mode amplitudes and phases by a discrete Fourier transform [47].

As a reference case for comparison with simulations, 21 bunches instead of the usual 18 bunches have been accelerated. Without empty buckets, spurious effects from the filling pattern are removed. Figure 4.35 shows the development of the mode spectrum along the cycle.

The mode number $n_{batch} = 2$, which, in the frequency domain, corresponds an upper synchrotron frequency sideband of the second and a lower sideband of the 19th revolution frequency harmonic, is excited most strongly. A self-stabilizing effect, most probably due to longitudinal emittance growth, can be observed towards the arrival on the flat top.

The mode pattern becomes more complicated for the usual batch of 18 bunches in $h = 21$, leaving three empty buckets for PS extraction and SPS injection kickers (Fig. 4.36).

Identical measurements performed in 2009 [48] already showed very similar mode patterns. Dipole modes with mode numbers around $n_{batch} = 1$ and $n_{batch} = 17$, corresponding to the 18th and 19th harmonics of the revolution frequency, are already present at 1730 ms (with respect to the arbitrary start of the cycle), shortly after transition crossing. The overall amplitude of the coupled-bunch oscillations increases, but the mode pattern remains very similar along the cycle. This excludes an impedance source at fixed frequency with a high quality factor being hit by a revolution frequency harmonic some time during the cycle.

With the 10 2.8 –10 MHz cavities as the most probable impedance source exciting the instabilities, simulations have been performed using the code LCBC (longitudinal coupled-bunch simulation code) [49]. The impedance model for the fundamental modes of the accelerating cavities has been extracted from transfer function measurements [47].

Figures 4.37 and 4.38 show the growth of the simulated coupled-bunch oscillation modes for 21 bunches and 18 bunches in $h = 21$, respectively.

The simulated mode patterns agree well with the measurements. In the case of 21 bunches, mode number $n_{batch} = 2$ is clearly predicted to be strongest. For 18 bunches in $h = 21$, the simulations show modes $n_{batch} = 1$ and 2 developing first, which again matches the experimental observations. Also, the simulated growth rates of the instabilities are compatible with the measurements. The oscillations develop slowly on a time-scale of a few hundred milliseconds.

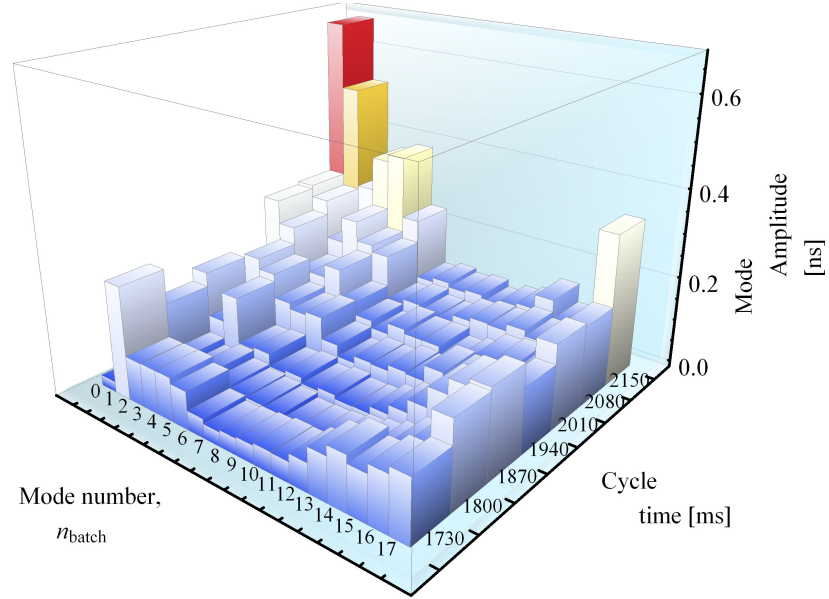


Fig. 4.36: Coupled-bunch mode spectrum during acceleration of 18 bunches in $h = 21$, averaged over 10 cycles for each measurement time ($N_b = 3.9 \times 10^{11}$ ppb, $\varepsilon_{l,\text{RMS}} = 0.13$ eV s).

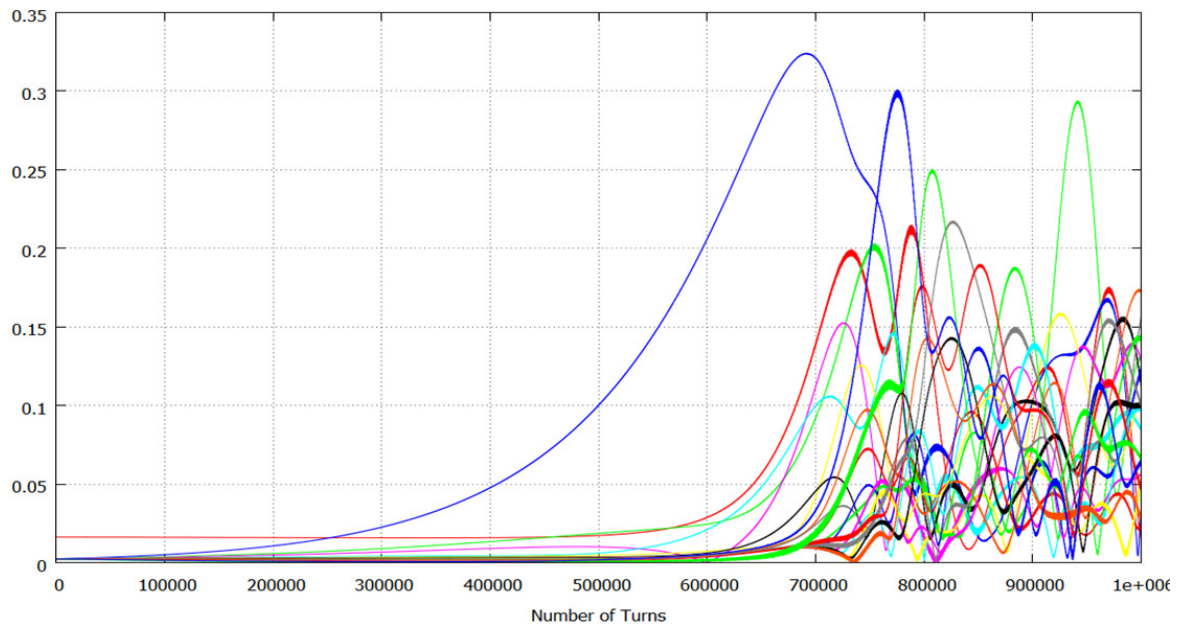


Fig. 4.37: Simulated growth of coupled-bunch modes under similar conditions as for the measurements with 21 bunches in $h = 21$ (compare Fig. 4.35).

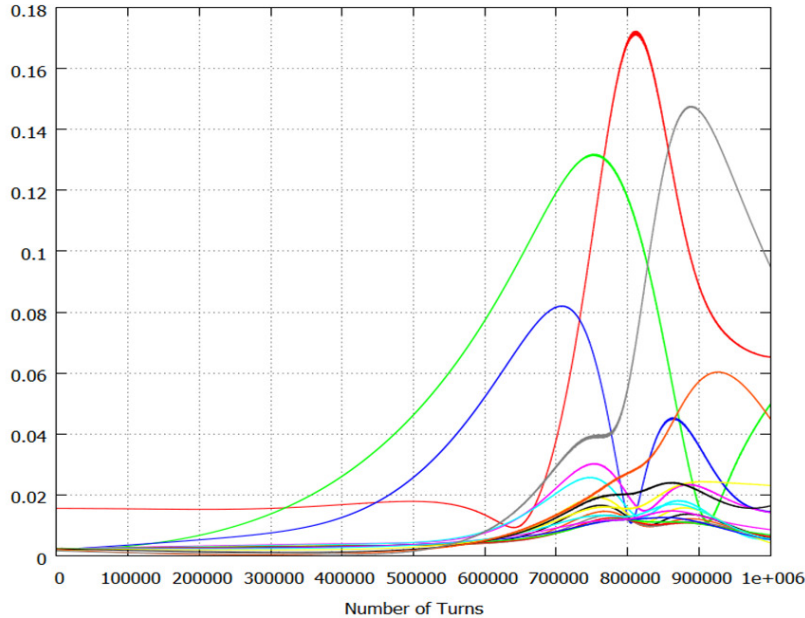


Fig. 4.38: Simulated growth of coupled-bunch modes under similar conditions as for the measurements with 18 bunches in $h = 21$ (compare Fig. 4.36).

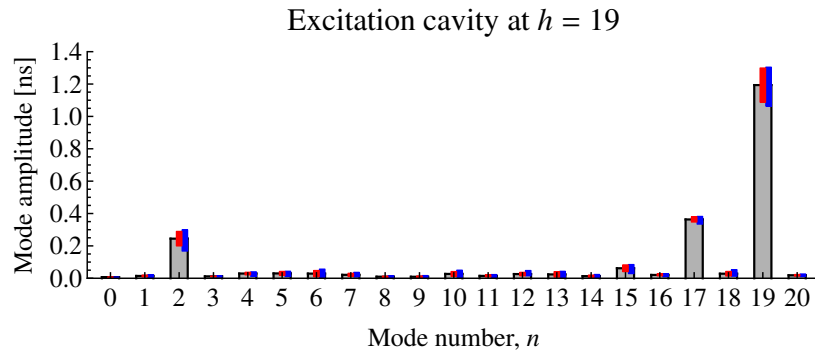


Fig. 4.39: Example mode spectrum of 21 bunches in $h = 21$, excited at the upper sideband of $19f_{\text{rev}}$ ($E \simeq 14$ GeV, average of five cycles, $\pm 1\sigma$ and min–max spread are indicated by the red and blue rectangles).

4.2.7.2 Excitation of coupled-bunch oscillations

Due to the nature of the instability, the cycle-to-cycle spread of the mode spectra measurements along the cycle is significant. To evaluate the behaviour of coupled-bunch oscillations more precisely, well-defined modes have therefore been excited by a feedback system in antiphase. For a filling pattern without gaps, a single mode can be excited strongly, accompanied only by the unwanted sideband at $n = 21 - n_{\text{exc}}$ and harmonics at $n = 2n_{\text{exc}}$ or $n = 2n_{\text{exc}} - 21$, as illustrated in Fig. 4.39.

A summary of measured mode spectra for excitation harmonics of $n_{\text{exc}} = 7, \dots, 20$ is illustrated in Fig. 4.40.

In all cases the excited mode appears most strongly ($n = n_{\text{exc}}$). Additionally, the unwanted sideband at $n = 21 - n_{\text{exc}}$ and harmonics at $n = 2n_{\text{exc}}$ or $n = 2n_{\text{exc}} - 21$ are detected.

The measured mode patterns become more complicated with the operational filling pattern for LHC-type beams in the PS, where only 18 bunches are accelerated, leaving a gap of three empty buckets for extraction purposes. With only 18 bunches the coupled-bunch mode number becomes n_{batch} and no

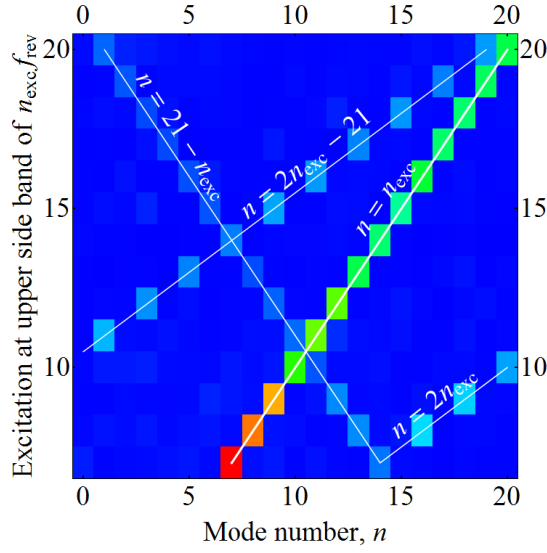


Fig. 4.40: Mode spectra measured after excitation of the upper sideband for 21 bunches at $h_{\text{RF}} = 21$ (full ring).

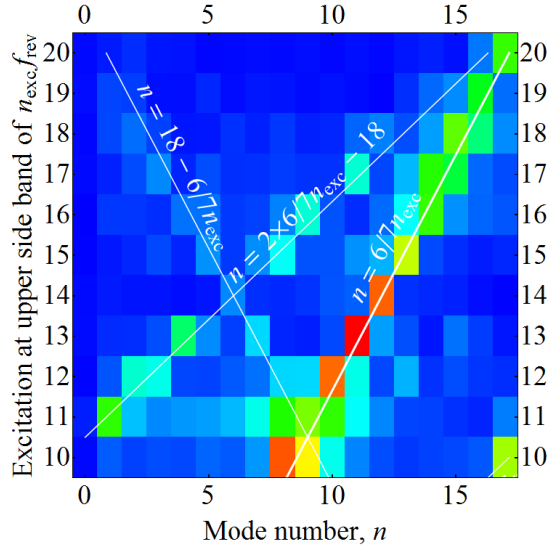


Fig. 4.41: Mode spectra measured after excitation of the upper sideband for 18 bunches at $h_{\text{RF}} = 21$ (6/7 filling).

longer corresponds directly to a harmonic of f_{rev} : each mode n_{batch} generates a spectrum of f_s sidebands due to the convolution with the filling pattern. However, for the relevant case of $18/21 = 6/7$ (86%) filling, the strongest mode(s) excited are well approximated by $n_{\text{batch}} = 6/7 \times n_{\text{exc}}$, as indicated in Fig. 4.41. Again, the excitation of the unwanted sideband and harmonic modes is observed.

From these mode scans it becomes clear that the coupled-bunch modes are only very weakly coupled to each other and that a feedback operating in the frequency domain can treat them successfully one by one.

4.2.7.3 Coupled-bunch oscillations on the flat top [48]

After arrival on the flat top, the batch is normally synchronized with the SPS on $h = 1$, before the splittings start. For a symmetric splitting of all bunches, coupled-bunch oscillations must not be present at this point. To allow for easier analysis of coupled-bunch instabilities on the flat top, the splittings

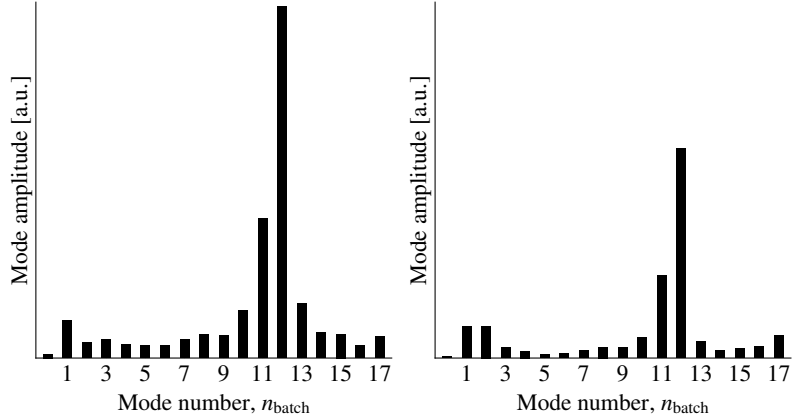


Fig. 4.42: Comparison of the coupled-bunch mode spectrum on the flat top for the LHC-type beams with 25 ns (left) and 50 ns (right) final bunch spacing. In both cases a batch of 18 bunches is kept at low voltage on $h = 21$ until extraction. The vertical scale of both plots is identical.

were disabled and the beam kept at low RF voltage at $h = 21$ for about 150 ms until extraction. Dipole oscillations develop especially at the tail of the batch. The same mode analysis procedure described above has been applied to the well-developed coupled-bunch oscillations close to extraction. The mode spectra, averaged over 10 cycles, are shown in Fig. 4.42.

The strongest modes present on the flat top are $n_{\text{batch}} = 11$ and 12, very different from the dominant modes observed during acceleration. This suggests that the driving impedance changes. Indeed, the configuration of the 10 2.8–10 MHz cavities is modified after the arrival on the flat top. During acceleration, all 10 MHz cavities are active, close to full voltage of 20 kV per cavity, and with their gaps open. To achieve the moderate RF voltages before the splitting on the flat top in a well-controlled fashion, nine of the 10 cavities are switched off in a sequence leaving only two active cavities. The unused cavities originally remain tuned close to the RF harmonic but are short circuited by one gap relay. It was found that the residual impedance of those short-circuited, inactive cavities represents an important part of the impedance driving the coupled-bunch instabilities on the flat top. First passive countermeasures to reduce the impedance of inactive cavities are already implemented since 2011: a second gap relay was installed on all 10 MHz cavities, and the detuning of unused cavities from $h = 21$ to $h = 6.5$ was implemented.

4.2.7.4 Transient beam loading

Transient beam loading causing phase slippage of one RF system with respect to another is deemed as a most important source of longitudinal beam quality degradation [48]. At the flat top the bunches are split either once (50 ns, $h = 21 \rightarrow 42$) or twice (25 ns, $h = 21 \rightarrow 42 \rightarrow 84$). The parameters of the cavities operated during these splittings are different in terms of shunt impedance, quality factor and direct feedback gain [50–52]; their transient beam loading behaviour also varies, causing their phase to slip with respect to each other during the passage of the batch. At intensities beyond nominal, transient beam loading compromises the longitudinal quality of the batch, since the symmetry of the bunch splittings becomes dependent on the position within the batch, resulting in unequal bunch intensities and emittances [46]. Figure 4.43 illustrates this effect for an LHC-type beam with 50 ns bunch spacing at an intensity of 1.9×10^{11} ppb.

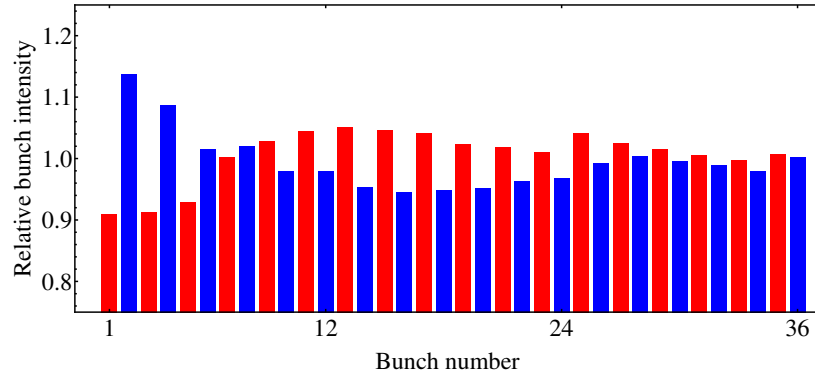


Fig. 4.43: Relative bunch intensity at extraction versus position within the batch (averaged over 10 cycles, LHC 50 ns, 1.9×10^{11} ppb) [48].

At extraction, a significant intensity variation from bunch to bunch and caused by the bunch splitting $h = 21 \rightarrow 42$ is clearly visible, especially at the head of the batch. This effect is caused by transient beam loading. The relative phase of the cavity return signals ($h = 21/42$) in the middle of the splitting is plotted for various batch lengths in Fig. 4.44.

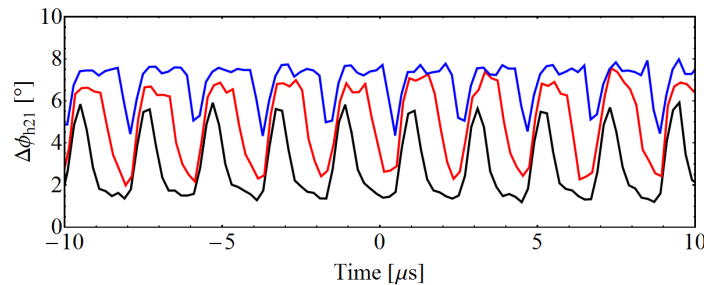


Fig. 4.44: Phase error between 10 MHz and 20 MHz versus time (50 ns bunch spacing, 1.9×10^{11} ppb, constant offsets removed). The vertical scale is in degrees with respect to the lower harmonic $h = 21$. The batch length is 12 (black), 24 (red) or 36 bunches (blue), corresponding to 2/7, 4/7 and 6/7 of the circumference. The periodicity is $1/f_{\text{rev}} = 2.1 \mu\text{s}$ [48].

The amplitude of the phase oscillations caused by transient beam loading is about 4° , similar to previous estimations based on the asymmetry of the bunch shape in the $h = 21 + h = 42$ double-harmonic RF system [53]. Due to insufficient time resolution of the measurement, the phase oscillations appear smaller in the 36-bunch case. Comparing forward and return phases of the cavities at $h = 21$ suggests that these cavities are more prone to transient beam loading than the 20 MHz cavity ($h = 42$).

However, while being an important issue for the larger bunch spacing of 50 ns and even more for obsolete 75 ns spacing, the 25 ns beam is much less prone to the inequality of bunch parameters due to transient beam loading. Its initial longitudinal emittance per bunch during the first splitting on the flat top ($h = 21 \rightarrow 42$) remains twice as large as the emittance of the bunches for a spacing of 50 ns. Hence, the bucket filling factor is twice larger and the bunches during splitting in first order $\sqrt{2}$ longer, which significantly relaxes the relative phase requirements during the splitting. The second splitting on the flat top ($h = 42 \rightarrow 84$) turns out to be less critical. Both cavities involved (especially the RF cavities at 40 MHz) have small bandwidth, exhibiting large direct feedback gain to reduce beam-induced voltage.

In addition, as described in Section 4.5.2, the high-frequency cavities will be upgraded with one-turn delay feedbacks (or the equivalent narrowband filter bank feedbacks), further reducing their phase deviations due to transient beam loading.

4.3 Injection and operation at 2 GeV

4.3.1 Magnetic injection devices

During the future 2 GeV operation, the beam will be injected in straight section 42 with a magnetic septum installed under vacuum to achieve the minimum separation between injected and circulating beams. To obtain the required integrated field strength for the 2 GeV beam, the septum magnet requires the full length of straight section 42 to be available. Since in this straight section a bumper for the injection bump is also located, a new bumper septum opposite the injection septum will be installed in the same vacuum vessel. Figure 4.45 shows a rendering of both the injection septum and the bumper septum installed in a common vacuum vessel.

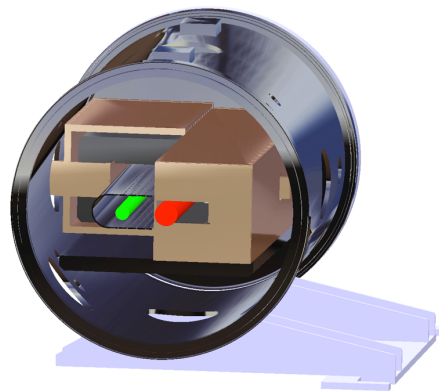


Fig. 4.45: Bumper septum (left) and injection septum (right) inside common vacuum tank

To maximize the acceptance, the bumper septum will be installed on the same movable support as the injection septum in the vacuum vessel. The position of the injection septum being remotely adjustable, the bumper septum will be displaced at the same time and as such the separation between injected beam and circulated beam is constant, independent of the position of the septa.

To achieve the required beam deflection and keep the magnet current to manageable levels, the injection septum uses the full length available in the vacuum vessel and no space remains for beam observation systems, i.e. inside straight section 42. Therefore, to observe the injected beam equipment will have to be installed at the end of the injection line, as close as possible to straight section 42, while to observe the beam after the septum the observation system may have to be integrated into the MU42 vacuum chamber. This is described in Section 4.9.

To provide more acceptance at injection, the dipole chamber is to be modified upstream of the septum (MU41), where the injected beam pipe (from the PSB) merges with the orbiting beam chamber halfway to the main dipole, similar to the way the MU chamber is installed after the extraction septum at straight section 16.

The power supplies for both the injection septum as well as the bumper septum are described in Section 4.3.4.

4.3.1.1 *Injection septum*

The new injection septum will be built to deliver 55 mrad at 2.0 GeV, with a physical length of 0.94 m and a gap field of 0.54 T. The injection septum is of the so-called ‘eddy-current’ type, i.e. the septum blade is not directly driven from the magnet power supply, but is part of a copper box around the magnet in which eddy currents are induced to keep the magnetic field inside the magnet gap.

In Ref. [54], the magnetic performance of this design was demonstrated. It was shown that the magnetic length of the septum is close to the physical length of the magnet and that a field homogeneity

of around $\pm 1\%$ can be achieved for the area close to the septum conductor (see Fig. 4.46).

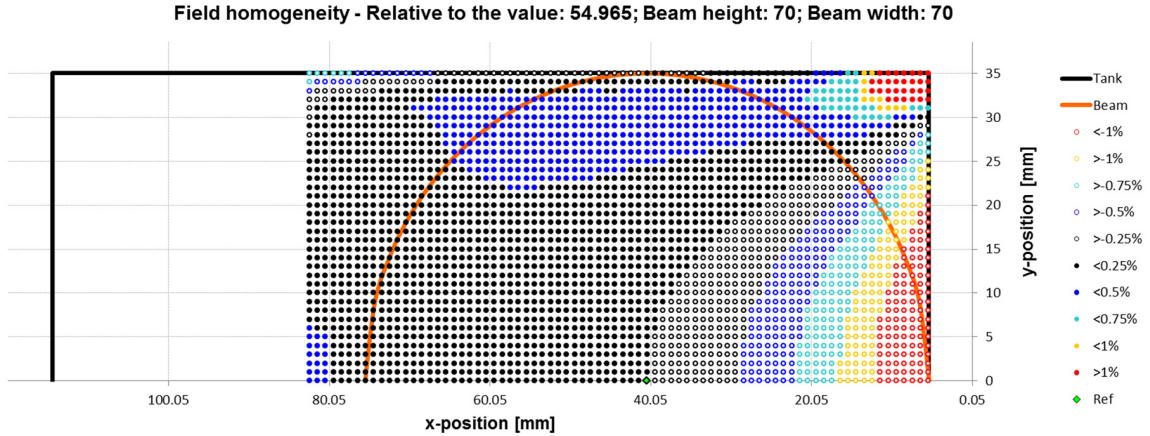


Fig. 4.46: SMH42 θ_x homogeneity map. Septum blade to the right

Following the aperture studies for the low-beta insertion [55], it was shown that the septum position should be adjustable between 49.6 and 62.2 mm. Taking into account the maximum horizontal beam size (for the 1.4 nTOF beam) and the sagitta of the beam in the magnet of 26 mm, the required horizontal magnet aperture (between conductors) is 113 mm. Beam transfer line studies have shown that the vertical aperture should be increased to the vertical acceptance of the PS, i.e. 70 mm.

To minimize the size of the septa under vacuum, and hence the gas load for the vacuum system as well as the space required for the vacuum vessel in the accelerator, it is essential to carefully choose the injection septum aperture as well as the remote positioning system stroke. In fact, the stroke of the remote displacement system directly determines the gap dimensions of the bumper septum to avoid it becoming an aperture restriction in the PS in one of the extremity positions. Table 4.2 summarizes the principal magnet parameters.

Table 4.2: Principal injection septum parameters

Physical length [mm]	940
Magnetic length [mm]	942
Septum thickness [mm]	5
Nominal septum position w.r.t. orbiting beam centre [mm]	56
Septum position range [mm]	49–63
Nominal angular septum position [mm]	10
Angular septum position range [mm]	0–10
Magnet gap height [mm]	70
Magnet gap width [mm]	113
Nominal deflection angle [mrad]	55
B_{gap} [T]	0.54
Integrated field strength [T m]	0.51
Peak current for nominal deflection [kA]	30.3
Pulse width, full sine [ms]	2
Magnet inductance [μH]	1.9
Magnet resistance [$\text{m}\Omega$]	0.1

To minimize the leak field next to the septum, the septum will be powered with a full sine wave. To further limit the leak field, and also to improve the vacuum for the orbiting beam, a beam impedance

screen made of mumetal should be foreseen, which will allow for dedicated vacuum pumping of the circulating beam area.

4.3.1.2 *Bumper septum*

To provide the required injection bump during injection, five bumpers are needed. Of the five bumpers used for the injection bump, four will be out-of-vacuum magnets around a thin-walled corrugated vacuum chamber (see Section 4.2.3). The fifth bumper (a septum) will be installed in the straight section adjacent to the injection septum. To minimize the continuous losses during injection of the circulating beam onto the septum blade, a faster fall time of the injection bumpers is advantageous. A pulse of 1 ms (instead of 1.6 ms presently) half sine is expected to be feasible. The tracking precision between different bumpers will be challenging for the bumper power supplies.

The bumper septum will be a single-turn magnet with an eddy-current septum conductor. The injection septum and bumper septum eddy-current shield will be shared by the two magnets. The magnet gap height is determined by the PS acceptance and the need for the installation of a beam screen inside the magnet aperture. It is foreseen to install thin (≤ 1 mm) plates parallel to the magnet poles to introduce a delay between the magnet current and the field seen by the orbiting beam, to obtain a delay as close as possible to the delay provoked by the vacuum chambers inside the four other outside-vacuum bumpers. In Ref. [54], it is shown that this compensation is feasible. The plates will be discontinuous with respect to the magnetic beam screen, to avoid an induced current loop when pulsing the bumper septum. The gap width is chosen such as to make sure that the magnet does not represent an aperture restriction for the orbiting beam when the injection septum is in the most outward position. The resulting magnet parameters are shown in Table 4.3.

Table 4.3: Principal bumper septum parameters

Physical length [mm]	300
Magnetic length [mm]	262
Septum thickness [mm]	~ 5
Magnet gap height [mm]	76
Magnet gap width [mm]	150
Nominal deflection angle [mrad]	13
B_{gap} [T]	0.461
Integrated field strength [T m]	0.121
Peak current for nominal deflection [kA]	27.9
Pulse width, half sine [ms]	1.0
Magnet inductance [μH]	0.7
Magnet resistance [$\text{m}\Omega$]	0.1

4.3.1.3 *Common vacuum vessel*

The common vacuum vessel to both septa will be equipped with dedicated pumping, and the system will be bakeable up to 200°C. High-power feedthroughs are installed on either side of the tank (one for each septum) and linked via a flexible stripline to the high-current bus bar. The system will be installed on self-centring feet and quick-disconnect flanges to minimize the time needed in case of an exchange.

4.3.2 *Injection kickers*

4.3.2.1 *Injection kicker KFA45*

The KFA45 kicker system has been installed in 1979 and has been upgraded several times since then to cope with new beam requirements. The latest modifications were made in 1994 to allow almost doubling

of the current in the magnets and in 2001 to improve kick rise and fall times [56]. An overview of one of the four modules composing the system is shown in Fig. 4.47.

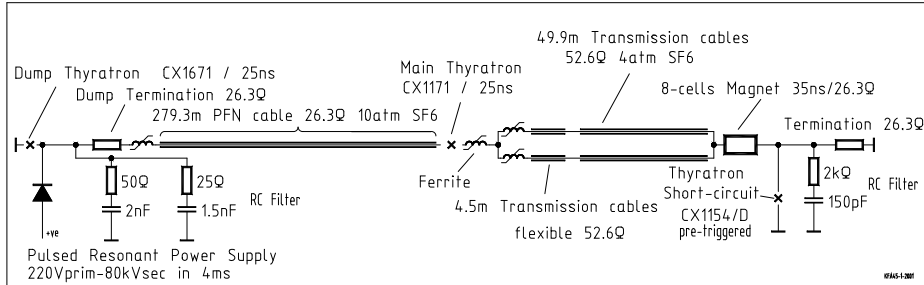


Fig. 4.47: KFA45 module layout

The magnet can be either terminated or short circuited at its end in a PPM operating mode. The use of the short-circuit mode allows for kick increase but deteriorates the rise time.

The main parameters of the system are given in Table 4.4.

Table 4.4: KFA45 system parameters

Parameter	Unit	Value (terminated)	Value (short circuited)
Deflection angle (nominal)	mrad	4.3	4.3
$\int B \cdot dl$ (max)	T m	0.0314	0.0601
Deflection angle (max) at 1.4 GeV	mrad	4.395	8.4
Deflection angle (max) at 2 GeV	mrad	3.38	6.5
System impedance	Ω	26.3	26.3
PFL voltage (max)	kV	80	80
Magnet aperture (w × h)	mm × mm	150 × 53	150 × 53
Kick rise time (1–99)%	ns	46	82
Kick fall time (99–1)%	ns	96	92
Kick length (max)	ns	2600	2600
Kick flat-top ripple	%	± 2	± 3
Post-kick ripple	%	± 1.25	± 1.5

The generators use very low loss SF₆-filled pulse-forming lines charged up to 80 kV. These cables are key elements in order to obtain fast rectangular kick pulses with low ripple and droop on flat top. As the lifetime of the present already aged cables is unknown, a market survey to find cables with equivalent characteristic must be launched. Market surveys made in the past were unfortunately not conclusive and this is a real concern for the future of PS kickers.

4.3.2.2 Second injection kicker KFA53

A second injection kicker vacuum tank will be installed in SS53 and used in conjunction with KFA45 for the high-intensity beams at 2 GeV. This kicker has to be as fast as KFA45. It will be made with delay line type magnets in order to have a matched system for an optimum pulse quality. As the straight section is partially occupied by a bumper, the estimated available physical length for new magnets is about 660 mm (\sim 730 mm flange to flange). A kick nominal value of -1.3 mrad is required. The magnet aperture dimensions are 140 mm wide and 53 mm high. In order to minimize the contribution of this new kicker to the PS impedance budget, coated ceramic shielding plates will tentatively be placed in the magnet aperture and connected to the beam pipe. This will entail an aperture height increase by at least 6 mm. The resistivity of the coating must be high enough in order not to alter the fast transition times of

the magnet. In order to minimize the effect of the plates on the kicker field, it is desirable to have two magnets pulsed in parallel with opposite current directions and plate surfaces connected as a F8L. This new feature introduced in the PS kickers will require considerable development time.

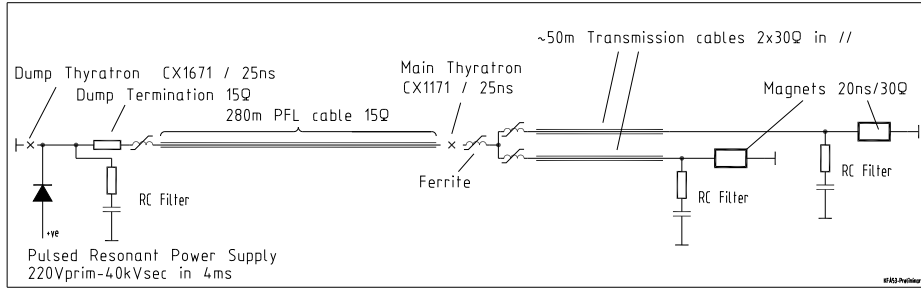


Fig. 4.48: KFA53 module layout

Table 4.5: KFA53 system parameters

Parameter	Unit	Value
Deflection angle (nominal)	mrad	1.3
$\int B \cdot dl$ (max)	T m	0.0187
Deflection angle (max) at 2 GeV	mrad	2
System impedance	Ω	15
PFL voltage (max)	kV	40
Magnet aperture (w × h)	mm × mm	140 × 59
Beam aperture (w × h)	mm × mm	140 × 53
Kick rise time (1–99)%	ns	46
Kick fall time (99–1)%	ns	92
Kick length (max)	ns	2600
Kick flat-top ripple	%	± 3
Post-kick ripple	%	± 1.5

Those preliminary considerations led us to design a system with two high-voltage generators, each supplying two very short magnets connected in parallel. The magnets will be short circuited at their ends inside the vacuum tank and their polarity will then not be reversible. The magnet impedance will be 30Ω .

At the time being, the available cables to build PFL (Pulse Forming Network) are of the RG220 type (50Ω and 60Ω). Their voltage is limited to 40 kV for safe operation (up to 50 kV occasionally) and their attenuation at 10 MHz is 5.7 dB/km compared to the 3 dB/km of the KFA45 PFL. The same problem arises for transmission cables from the high-voltage generator to the magnets. The attenuation of the actual KFA45 SF₆-filled transmission cables is 4 dB/km. The new generators have to be located near the magnets in order to limit the transmission cable length to less than 50 m.

As the nominal PFL voltage required for normal operation (with two generators) is 26 kV, with RG220 cables, it will not be possible to use only one generator in case of failure of the other, as the voltage required would be ~ 52 kV. So, the use of a 60 kV (minimum) SF₆-filled cable is highly desirable. It would improve system reliability and performance in one go. If SF₆-filled cable or equivalent is not available, a less performing and reliable but cheaper system with only two magnets will be considered.

The preliminary layout of one module is shown in Fig. 4.48.

The main tentative parameters of the system (assuming RG220-like cables) are given in Table 4.5.

4.3.3 Magnets

4.3.3.1 IPM magnets

The installation of one horizontal and one vertical ionization-profile monitor (IPM) requires the procurement of low field dipole magnets [57]. Both horizontal and vertical magnets will provide 0.2 T in a $50 \times 115 \text{ mm}^2$ cross-sectional window over a longitudinal path of 50 mm with a field homogeneity of 10^{-3} . The beam deviation once through the detector will have to be corrected in the opposite way in order to cancel the initial bending effect. One proposal is to apply the detector field and the correcting field in the same magnet. The alternative is to have the detector field and the correcting field magnets in different locations, thus being two independent pieces. The allocated space per horizontal and vertical detector is 700 mm and 1 m, respectively. The magnets shall be capable of being cycled in short time and therefore cannot generate high eddy current, thus requiring them to be made with laminated yokes.

4.3.3.2 Injection bumper magnets

The new injection scheme will employ five bumps, where four of them will be located in straight sections 40, 42, 43 and 44 and the fifth one will be integrated in the septum in SS 41 (see Section 4.2.1). A study [58] has shown that the present injection bumpers (see Fig. 4.49), originally designed to run at 0.8 GeV, can be operated at 2.0 GeV but under saturating conditions of 17%.

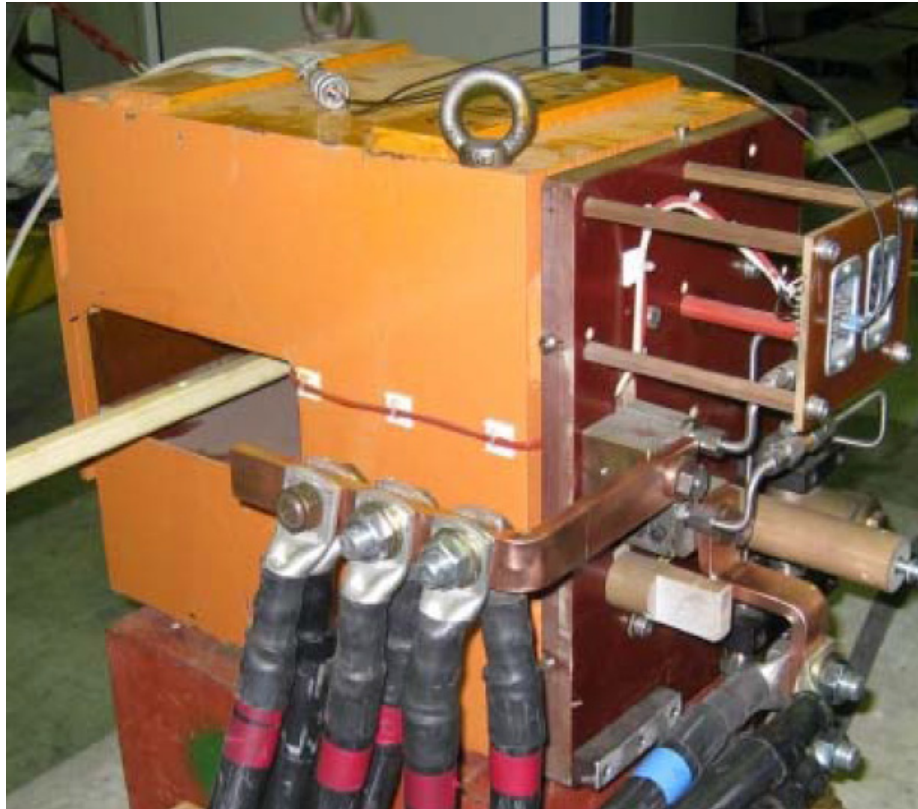


Fig. 4.49: Actual injection bumper magnet

However, we propose to design and manufacture new magnets, splittable into two upper and lower parts, in order to allow installation and possible interventions on these magnets without dismounting the vacuum chamber, as is needed for the present magnets.

The new magnet shall have the parameters described in Table 4.6.

Table 4.6: Injection bumper magnet parameters

Parameter	Value
Gap height	90 mm
Gap width	218 mm
Field at nominal current	0.77 T
Integrated field at nominal current	0.148 T m
Temperature rise of the conductor	10°C

4.3.3.3 Skew injection quadrupoles

Twenty-six small-aperture and 17 large-aperture skew quadrupoles are used at 1.4 GeV injection energy. These iron-free magnets are made of copper conductors impregnated in resin cast. A preliminary study made in winter 2011 [59] showed that both magnet types cannot provide the magnetic field amplitude required for 2 GeV injection under acceptable operating temperature: new magnets are therefore needed. Presently these magnets provide both a quadrupole and a vertical dipole correction. In the new magnets the required quadrupole strength can be achieved only if the dipole function is removed. This will require the installation of new separate vertical correctors, as described in Section 4.3.3.4.

4.3.3.4 Vertical correctors

Vertical corrector magnets are used today as an embedded version of the small-aperture skew quadrupoles (15 out of 26) and as iron-dominated magnets (four). As the new small-aperture skew quadrupoles will not include vertical correctors, 20 new vertical correctors to be installed in the straight sections are needed.

4.3.4 Power converters

4.3.4.1 Power converter for the SMH42 injection septum

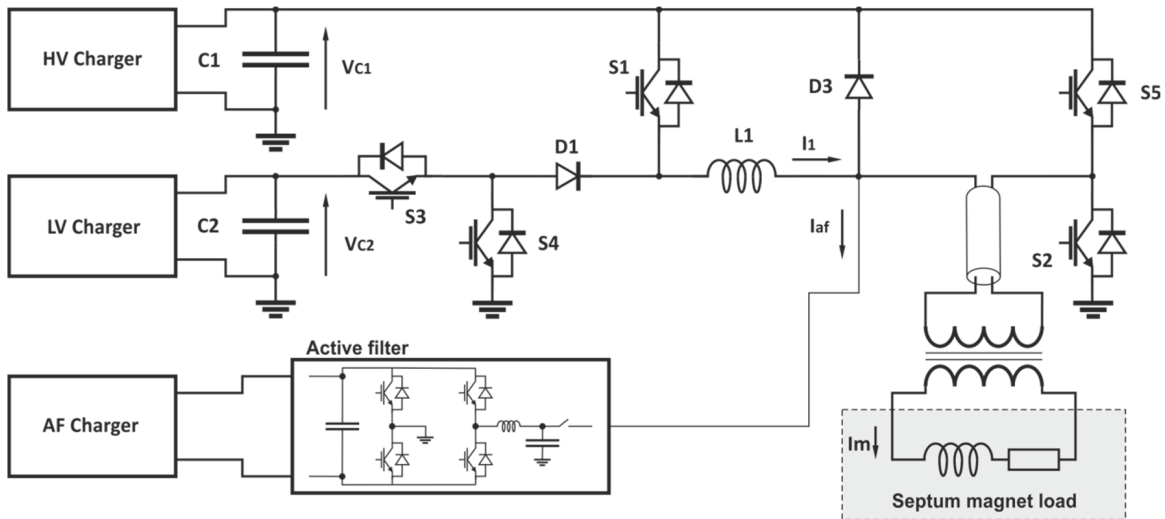
The injection septum magnet will use a different design to the existing magnet: instead of a direct-drive septum type it has been decided to install an eddy-current septum that presents some advantages like a more robust mechanical construction and the possibility of implementing a thinner septum blade. As regard to the converter requirements, this technological change has a strong impact, as the required current waveform is different than for a direct-drive septum. The existing power converter [60] delivers a positive current pulse with a third-harmonic shape and a high-precision flat top. For the eddy-current septum, a waveform with positive and negative parts is required in order to optimize the cancellation of the septum leakage field. The requirements for the power converter of the SMH42 septum magnet are summarized in Table 4.7.

With such a high operating current value, the best option is to install the converter in a surface building and a step-up (in current) transformer in the tunnel in order to reduce the converter voltage and the section of the linking power cables. This matching transformer has to be installed as close as possible to the septum magnet in order to reduce the inductance in the connecting bus bars.

Concerning the power converter, the ongoing studies indicate that the use of a MegaDiscaP [61] converter is a good option. Compared to the actual MegaDiscaP converters, which will be installed for the booster injection septum magnets, this particular application will require some modifications in order to deliver an output current waveform with positive and negative parts. Moreover, the MegaDiscaP converter output current capability, which is 2 kA at present, has to be raised to 2.6 kA and further studies and testing are still needed to validate this possibility. The corresponding converter topology is presented in Fig. 4.50.

Table 4.7: SMH42 parameters and operational requirements

Parameter		
Maximum operating current	31 kA	
Magnet inductance	1.9 μ H	
Magnet resistance	0.1 m Ω	
Maximum beam duration	3 μ s	
Output current precision	To be defined	
Operating current	1.4 GeV 23.3 kA	2 GeV 30.3 kA
Current waveform shape	Full sine or trapezoidal with positive and negative parts	

**Fig. 4.50:** Power converter topology for the SMH42 septum magnet

The MegaDiscaP converter ratings are given in Table 4.8.

Table 4.8: Ratings of the power converter for the SMH42 septum magnet

Parameter	
Maximum output voltage (primary of the matching transformer)	2.2 kV
Maximum output current (primary of the matching transformer)	2.6 kA
Matching transformer ratio	12
Output current precision	500 ppm
Input voltage (three phases with neutral)	400 V _{RMS}
Cooling	Forced air

In order to allow a high-precision flat top during the beam passage, a stabilization time of the output current is needed. The corresponding SMH42 current waveform is given in Fig. 4.51.

In order to minimize the leakage field in the fringe region of the septum magnet, a current pulse with a shorter duration would bring a significant advantage. Given the load parameters, this requirement leads to a higher operational voltage for the converter. As the semiconductors current capability decreases rapidly with the increase of their operational voltage, the implementation of shorter pulse duration is quite challenging and needs to be further studied with the MegaDiscaP topology.

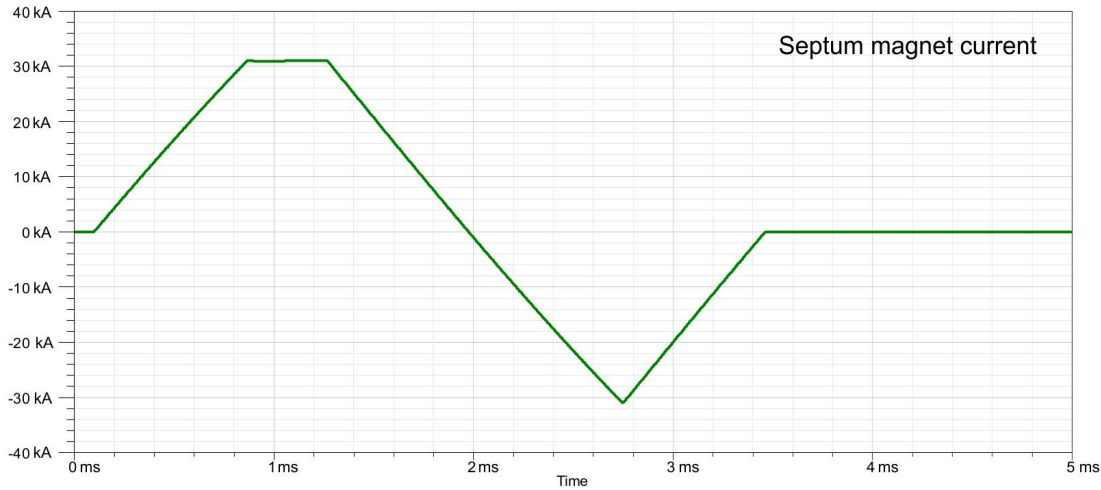


Fig. 4.51: SMH42 magnet current waveform with 2 GeV beam operation

4.3.4.2 Power converters for the injection bumpers

The future PS injection scheme will use five bumper magnets instead of four. One bumper magnet will be installed in the injection septum tank (under vacuum) and consequently it will present a completely different set of parameters compared to the others, thus presenting an additional difficulty to ensure a good tracking between the five magnet currents. The magnet parameters and operational requirements are presented in Table 4.9; it can be noted that the design of the four bumpers that are out-of-vacuum can still be modified to allow a better matching with the converters.

Table 4.9: Operational requirements and parameters of the injection bumpers

Parameter	BSM40, 41, 43, 44	BSM42
Maximum operating current	1.1 kA	28 kA
Magnet inductance	500 μ H	0.7 μ H
Magnet resistance	0.41 m Ω	0.1 m Ω
Output current precision	To be defined	To be defined
Current waveform shape	Half sine	Half sine
Operation mode	PPM	PPM
Maximum current pulse duration	1 ms	1 ms

Given the expected parameters of the bumper magnets and the required pulse duration, the use of capacitor discharge power supplies is a good option if the required tracking between the different magnet currents is of low precision. If the use of capacitor discharge power converters is possible, their corresponding ratings are given in Table 4.10.

Considering its high operational current, the BSM42 has to be supplied using a step-up (in current) transformer that will be installed in the tunnel gallery. In order to produce a half sine with 1 ms pulse duration, a capacitor discharge power converter is well adapted. The power converter parameters are given in Table 4.11.

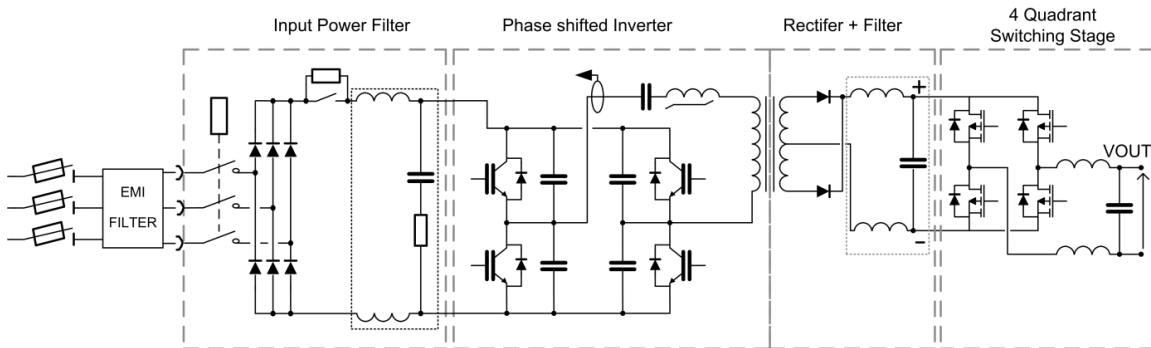
One of the critical points, which has not been totally addressed so far, is the relative precision (between the different bumper currents) that is required. Given the fact that the load parameters of the in- and out-of vacuum bumpers are completely different, and also that the installation of a matching transformer is required, the possibility of matching the different discharge circuits is more complicated but still feasible.

Table 4.10: Parameters of the power converters for BSM40, 41, 43 and 44

Parameter	
Maximum output voltage	1.8 kV
Maximum output current	1.2 kA
Capacitor bank value	190 μ F
Output current precision	1000 ppm
Input voltage (three phases with neutral)	400 V _{RMS}
Cooling	Natural air

Table 4.11: Parameters of the power converters for BSM42

Parameter	
Maximum output voltage (primary of the matching transformer)	2 kV
Maximum output current (primary of the matching transformer)	2.5 kA
Matching transformer ratio	12
Capacitor bank value	460 μ F
Output current precision	1000 ppm
Input voltage (three phases with neutral)	400 V _{RMS}
Cooling	Natural air

**Fig. 4.52:** Power: part-simplified architecture/topology

If the tracking between the different bumper currents has to be realized with high precision, the use of programmed converters has to be foreseen. This option would be challenging given the pulse duration of the output current and the operating voltage of the converters.

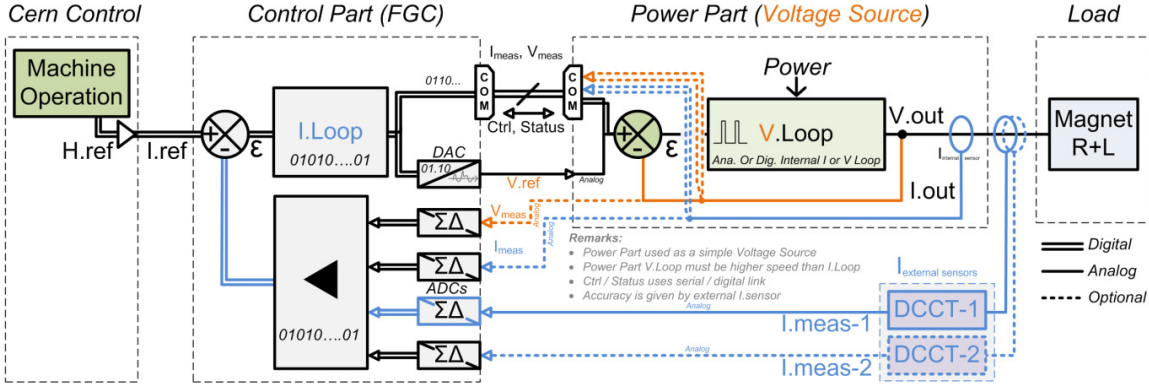
4.3.5 Low-energy power converters

4.3.5.1 Low-energy correctors

The 150 PS low energy correctors (CBE) are not yet critical for operation but help to improve the beam luminosity. The installed amplifiers worked well for more than 40 years. With the future LHC operation, the luminosity demand at the PS output increases and the CBE will become mandatory adds-on for LHC efficiency. See Table 4.12 for a summary of the different circuits.

It has first been decided to replace the existing amplifiers within the project of PS consolidation. The current ratings were then extended to cover the needs of the 2 GeV upgrade.

A digital CANCUN 20 A/75 V converter [62, 63] is currently under development and will be used for the upgrade. See Figs. 4.52 and 4.53 for the power converter topology and their regulation.

**Fig. 4.53:** Regulation control: simplified schematic**Table 4.12:** Circuit summary

	PR.DHZ	PR.DVT	PR.QDN	PR.QFN	PR.QSK
Quantity	50	20	20	20	40
Resistance [Ω]	2.5–3.5	0.9–4.4	2–3.2	2–3.2	2–4
Inductance [mH]	0.2–0.8	0.1–28	22–32	22–31	0.1–21
Time constant [ms]	0.07–0.3	0.02–31	7–13	7–12	0.03–8
I_{RMS} (max) [A]—magnet	10	6, 3.5	5.6	5.6	3.5
I_{RMS} (max) [A]—converter	20	20	20	20	20
I (max)	± 20	± 13	± 20	± 20	± 20
dI/dt (max) [A/s]	± 500	± 500	± 500	± 500	± 500
V (max) [V]	± 52.9	± 72	± 64	± 64	± 70.5
Induced voltage [V]	± 20	± 20	no	no	no
Precision [ppm]	1000	1000	1000	1000	1000
Ripple	0.5%	0.5%	0.5%	0.5%	0.5%
Switching frequency [kHz]	50	50	50	50	50

The corrector magnets do not have an embedded thermal protection and are currently protected by a thermal breaker at the power converter output. The breaker reaction time (1–2 s) is not representative of the thermal phenomena in the magnet and is today limiting operation, especially for the LHC long flat bottom.

The new digital current control will allow an RMS limitation over one supercycle, giving the opportunity to increase the peak current for some specific users.

4.4 The PS Transverse Damper

The PS Transverse Damper (TD) will be used to address three aspects of the PS beam dynamics to reach the LIU required performance.

- i) *The injection mis-steering due to a kick error.* This is expected to be an important source of the emittance growth which drove the specifications of the TD system: its damping constant has to be $< 110 \mu\text{s}$ — or less than 50 turns — for the 1.4 GeV injection energy while its bandwidth should cover the first betatron line at $Q = 6.1$ (40 kHz) up to 23 MHz corresponding to the ripple observed on the injection kicker bending field. Given the TD kicker design, this translates into the power specifications for the present driving amplifiers providing 3 kW per kicker plate. Considering a 2 GeV injection and maintaining the same time constant as the 1.4 GeV case, the required power

should be increased to 5 kW.

- ii) *The HT instability.* This effect is due to interplay between the machine transverse impedance, its chromaticity and the bunch longitudinal motion (see 4.2.4). It can have a detrimental effect on the beam characteristics up to preventing the beam transmission or degrading the beam emittance to an unacceptable level. The PS TD proved to be an valuable tool against this issue during the 2013 MD campaign.
- iii) *The transverse coupled instability at extraction.* In specific, not yet operational, conditions there have been observed coupled-bunch instabilities at the PS extraction flat top with the 25 ns bunch train. Investigations are ongoing to understand if similar instabilities will be present with the production LIU beams (see 4.2.6). Measurements demonstrate that the PS TD can delay by a significant amount of time the instability rise.

In addition to that, the TD can be used to excite the beam for tune and impedance measurements and also for the MD studies.

A description of the present system is provided in the following, highlighting its performance and limits. A more detailed description can be found in Refs. [64, 65]. The envisaged upgrade for 2015 will also be depicted.

A simplified block diagram of the present system from the PU to the kicker is shown in Fig. 4.54. In the plot only the horizontal plane is presented. The PU signal is amplified to match the input dynamic of the digital card (digital signal processing unit, DSPU). The output of the digital card is amplified, combined with the Q-meter signal and split on the input of the two power amplifiers that drive the two horizontal plates of the kicker. The matching between the output impedance of the power amplifier (50Ω) and the kicker impedance (100Ω) is performed with a transformer.

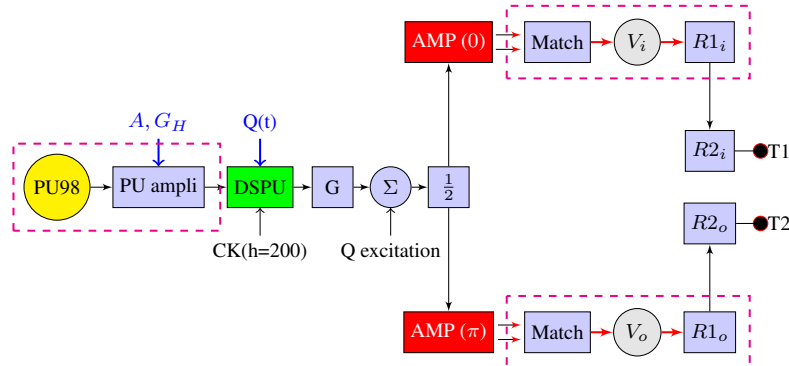


Fig. 4.54: The block diagram of the PS TFB. The magenta rectangles refer to the devices installed in the tunnel.

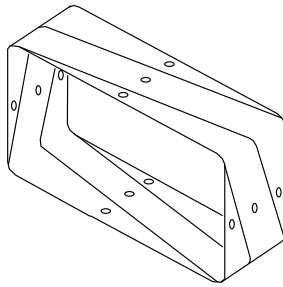
4.4.1 Description of the present system

The TD is composed of the subsystems described in the following sections.

4.4.1.1 The PU

The transverse PU [66, 67] (see Fig. 4.55 and Table 4.13) feeding the TD is positioned in section 98 (PU98, horizontal and vertical). Its low-noise pre-amplifier with a gain range of $-60 \rightarrow +40$ dB (-60 dB provided by attenuator in three steps of -20 dB and $+40$ dB provided by an amplifier in 255 steps of ≈ 0.155 dB) can be adjusted to the different beam flavour produced by the PS [66].

The pre-amplifier has a PPM attenuation common for all the three channels (horizontal, vertical and sum) and a PPM analogue gain per channel. The -10 dB bandwidth of the system is 60 MHz with

**Fig. 4.55:** The PU electrodes**Table 4.13:** The PU parameters

Aperture	$166 \times 80 \text{ mm}^2$
Length (in beam direction)	62 mm
Single-electrode capacitance	70 pF
Internal extra capacitance	30 pF
Transfer resistance (o.c.)	0.52Ω
S_x	174.3 mm
S_y	82.3 mm

less than 10 degrees of non-linear phase error on the entire amplification and attenuation range (Fig. 4.56).

At the moment, the transverse signals are not normalized and therefore the gain of the feedback loop varies along the bunch. A normalization circuit is under study; it would allow us to increase the -5 dB bandwidth up to 80 MHz by the virtue of the error over sum division. At the moment the error signal for the feedback is provided by the PU98 with the addition of a Hilbert filter (see Section 4.4.1.2) to set the betatron loop phase. This phase setting could also be obtained by using the available PU in section 02 (PU02), which is almost in betatron quadrature phase with respect to PU98.

4.4.1.2 The DSPU

There is one DSPU per plane clocked with harmonic 200 of the beam revolution frequency. This choice determines the bandwidth of the digital card at ≈ 30 MHz.

The signal from the PU pre-amplifier is a direct input for the DSPU: the PU pre-amplifier gain has to be set in order to match the ± 1 V ADC range of the DSPU.

The DPU is responsible for the following.

- i) Suppressing the revolution line harmonics, related to the closed orbit, using a notch filter.
- ii) Dephasing the error signal feeding the kicker by the correct betatron angle using the measured machine-tune information supplied by a function generator. A look-up table provides the Hilbert phase angle for PU98 and PU02 from the machine-tune value. It has been established from simulated values obtained from the machine and electronics model together with measurements achieved during the 2013 MDs. The results are in a very good agreement with the expectations [68].
- iii) Adjusting the delay between the PU and the kicker to keep the synchronism of the loop signal with the beam despite its varying revolution frequency.

Due to circuitry constraints, the maximum clock rate is limited to 100 MHz while the $h = 200$ clock

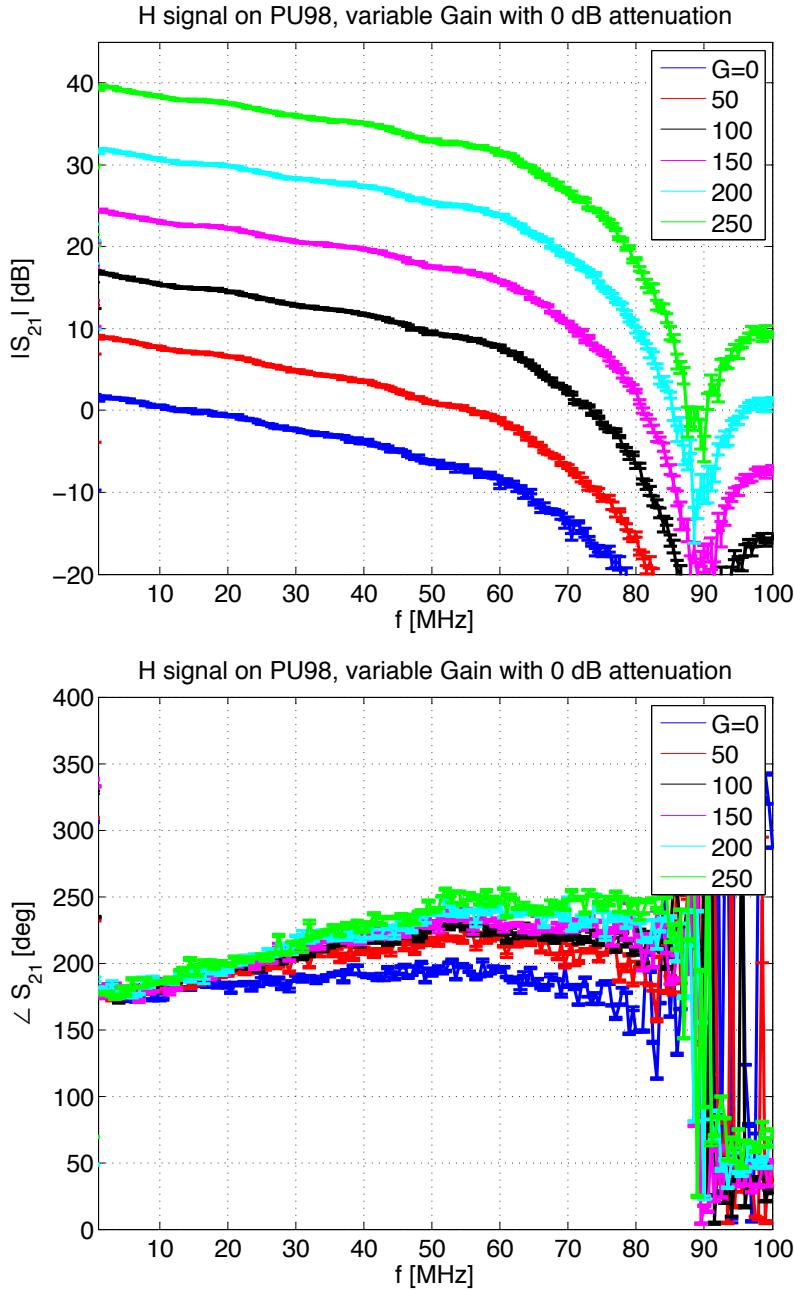


Fig. 4.56: The bandwidth of the PU pre-amplifier with variable amplification

ranges from 87.4 MHz up to 96 MHz with protons. In Fig. 4.57, top, the frequency response of the DSPU without signal processing is provided for a 80 MHz clock. Its -3 dB bandwidth is finally limited to about 30 MHz mainly due to the sample-and-hold effect ($\sin(x)/x$ amplitude shape). After the digital treatment the signal is converted by a digital-to-analogue converter (DAC) and sent to an additional programmable amplifier before being input to a combiner (used also for the tune measurement excitation) and a splitter feeding the pair of power amplifiers used for a given H or V plane. The programmable amplifier was used to adjust the output voltage of the DSPU (1 V_p) to the input saturation value of the final stage (550 mV_p). The frequency response of this post-amplifier is 80 MHz (-3 dB, Fig. 4.57, bottom). In the future a programmable amplifier should be used upstream of the DSPU to profit from its amplitude dynamic

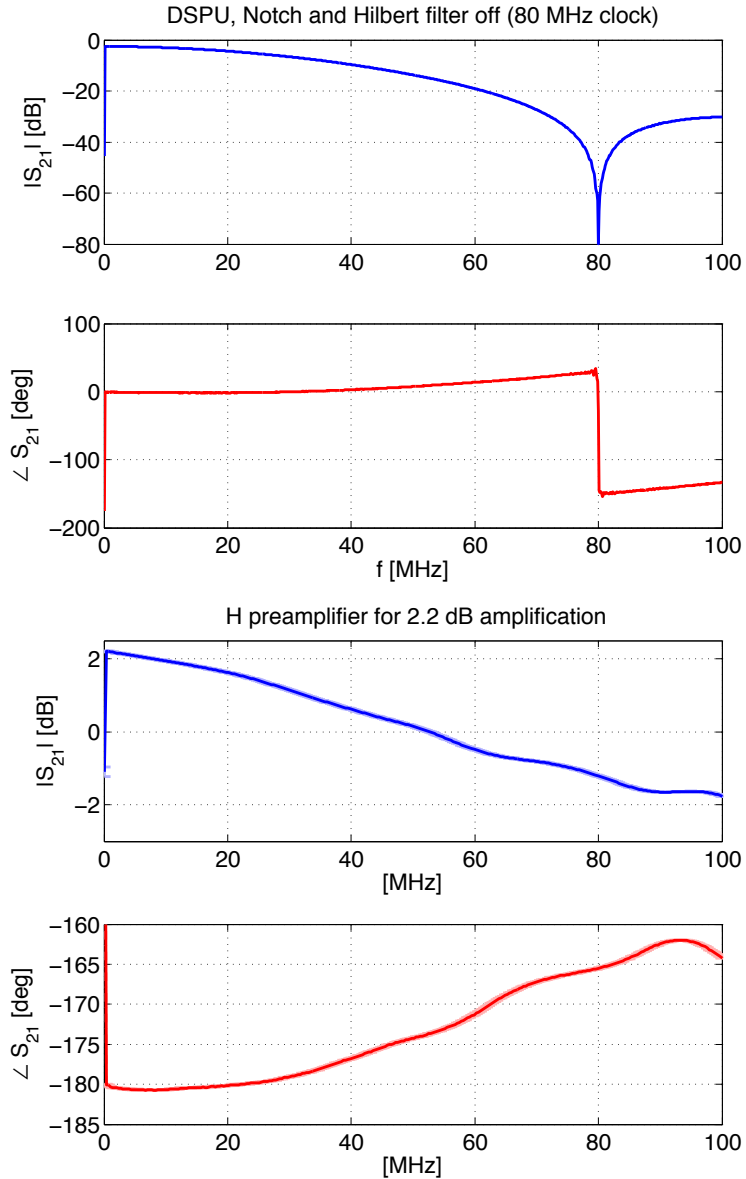


Fig. 4.57: The frequency response of the DSPU (amplitude with notch and Hilbert filters by-passed) for a clock of 80 MHz (top); the transfer function of the programmable amplifier used downstream of the DSPU (bottom).

range while the beam peak intensity changes or while orbit offsets are observed. There are also ongoing studies in collaboration with the SPS feedback team, for an option to suppress the closed orbit in an analogue way before the DSPU in order to further improve the signal-to-noise ratio of the system when facing beam radial offsets in the machine. At the moment, for an optimal setting, the closed orbit at the PU98 should be minimized all along the beam cycle.

4.4.2 The power amplifiers

There are two 3 kW power amplifiers per transverse plane. They work in push-pull mode, one per kicker plate. These devices are designed for a -3 dB bandwidth of 23 MHz representing the bandwidth bottleneck of the entire system. Figure 4.58 represents the frequency response of this device: it can be observed that a significant parasitic phase rotation starts only beyond 40 MHz. During the damping of

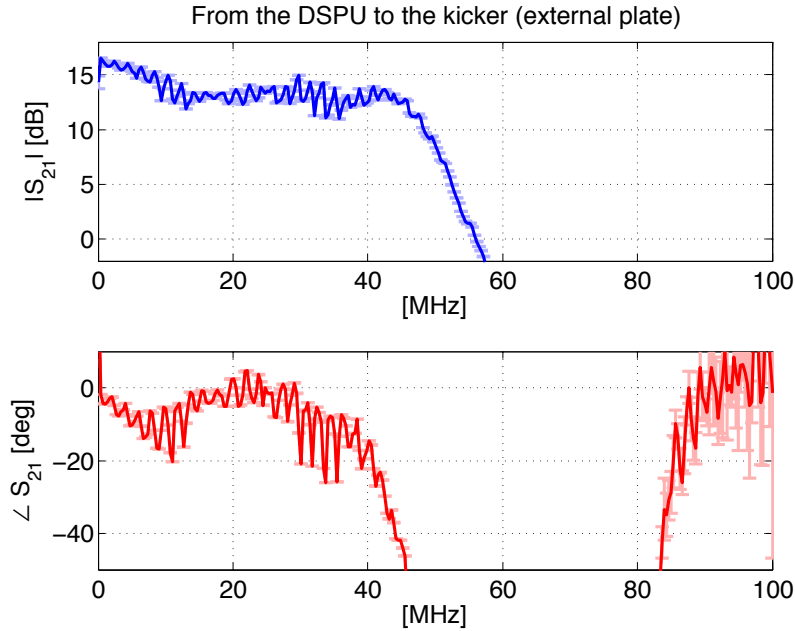


Fig. 4.58: Global frequency response of the DSPU including notch and Hilbert filters with pre-amplifier, power amplifier, matching network, kicker and final load. The response is dominated by the power amplifier itself. The observed ripple is due to the DSPU notch filter. The second trace corresponds to the non-linear phase.

the injection oscillations the final stage works at maximum power (at the limit of saturation, where the notion of bandwidth does not apply any more). Detailed measurements of the power amplifier in this regime were performed during LS1 in 2013–2014.

These amplifiers have been designed to provide a +57 dB voltage gain on each of the 2×1.5 kW RMS outputs to be combined (this means 550 mV_p at the input for 389 V_p on each $50\ \Omega$ output). This peak regime can be delivered only for a limited duration; the peak voltage gets reduced by 5.7 dB down to 0.8 kW CW with a time constant of ≈ 20 ms (see yellow trace in Fig. 4.59, top). In addition to this limit, the power amplifier output is not matched to $50\ \Omega$: this implies that the signal induced on the kicker by the beam will reach the amplifier and be reflected back to the kicker, potentially causing a cross talk between the different bunches (see Fig. 4.59, bottom). From preliminary investigations this cross talk appears to be negligible. The new power amplifiers will have a $50\ \Omega$ output impedance.

4.4.3 The damper kicker

A stripline kicker is installed in section 97 (SS97, see Fig. 4.60). It is a combined horizontal and vertical kicker (the optics in section 97 privileges the horizontal plane). The kicker has a characteristic impedance of $100\ \Omega$ in both planes. The power amplifier signal conveyed on a $50\ \Omega$ line is matched to it using a power transformer with a -3 dB bandwidth of 45 MHz.

4.4.4 Upgrade of the PS damper

To cope with the 2 GeV injection energy while preserving the same beam performances, the power amplifiers of the system have to be upgraded to 5 kW CW (3 kW CW down to 800 W CW presently). The delivery of the new power amplifiers is expected by the end of 2014 and their commissioning in 2015. With the new power amplifiers the problem of the matching of the output and the consequent reflection signals will be addressed. As explained, the power amplifiers are the bandwidth bottleneck of the system. For this reason, together with the increased power, the new devices will provide a -3 dB

PROTON SYNCHROTRON

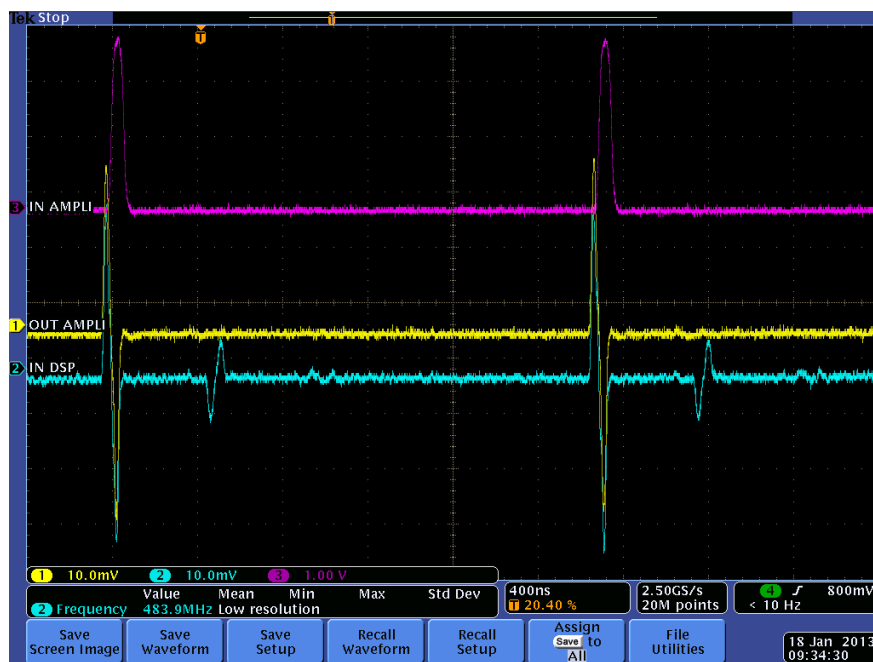
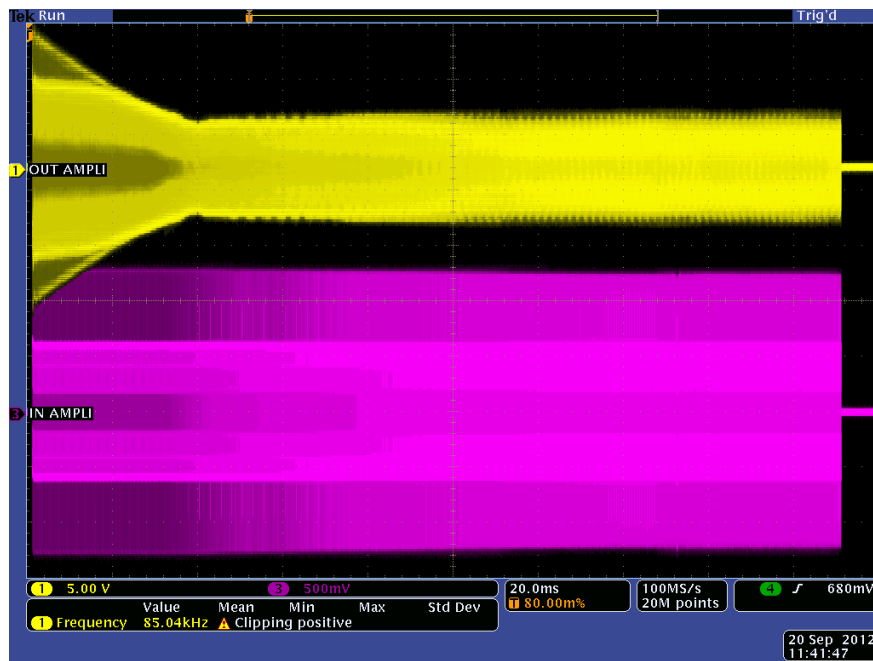


Fig. 4.59: The time progression of the peak detected voltage out of the power amplifier with its natural decay from 3 kW to 800 W transition (top, yellow trace); the beam-induced voltage observed on the kicker with its reflection as produced by the high-impedance power amplifier output (bottom).

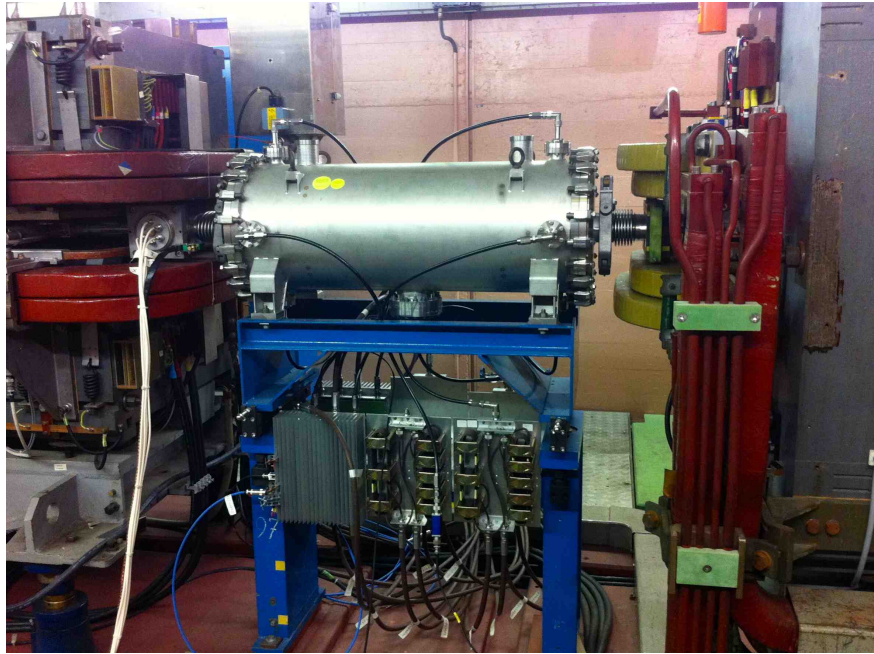


Fig. 4.60: The PS TFB kicker in PS SS97

Table 4.14: Comparison between the performance of the present amplifiers and the specification of the new amplifiers.

	Present amplifiers	New amplifiers
Peak power [kW]	3	5
CW power [kW]	0.8	5
-3 dB bandwidth [MHz]	23	100
Output impedance (to the load) [Ω]	50	50
Output impedance (from the load) [Ω]	$\neq 50$	50

bandwidth of 100 MHz. A comparison between the present and the new versions of the amplifiers is summarized in Table 4.14. With both the power and the bandwidth upgrade, the cure of the flat-top instability with the 25 ns bunch train should be improved. In order to cope with the power increase, the kicker impedance matching network will be fitted with upgraded ferrites.

Concerning the kicker, the hypothesis of its replacement by two dedicated 50Ω kickers (one vertical and one horizontal, for the purpose of avoiding the use of a matching network and optimizing the optics function in both planes), seems not viable, since it is too demanding for the power amplifiers.

By 2015 a new amplifier with a PPM gain control operated with a function generator should be put in place to optimize the loop working point along the cycle. After these upgrades, the bandwidth bottleneck will be the DSPU itself. One possible solution to overcome the latter is to use faster DACs in the DSPUs (hypothesis presently under investigation) or additional DSPUs controlling different frequency bands with a down- and up-frequency-conversion scheme.

4.5 RF

4.5.1 The longitudinal damper

4.5.1.1 Introduction

The longitudinal damper cavity for the new coupled-bunch feedback of the PS machine has to provide a correcting RF voltage to the circulating bunches to suppress the excitation of bunch oscillations. These oscillations are observed during acceleration and on the flat top with high-intensity LHC-type beams [48]. To improve longitudinal beam stability, a first dedicated coupled-bunch feedback has been installed in 2005 [69]. Two 10 MHz accelerating cavities driven by the signal from the feedback low-level electronics are used as longitudinal kickers. In addition to the up to 20 kV of voltage at the acceleration harmonic ($h = 21$, ~ 10 MHz), they produce a few kilovolts at once and twice the revolution frequency (~ 470 kHz and ~ 940 kHz) below their resonance frequency for the damping of coupled-bunch oscillations. Due to the limited bandwidth of the accelerating cavities, a damper covering all possible coupled-bunch modes is excluded. In the framework of the LHC-LIU project [70], it has therefore been decided to remove this limitation by installing a dedicated, wideband kicker based on the wideband frequency characteristics of Finemet magnetic alloy (MA) [71] and driven by solid-state amplifiers. However, installing a wideband cavity in the PS ring also introduces longitudinal impedance covering many revolution frequency harmonics. Special care must therefore be taken of the beam-loading effects in the new kicker cavity. The PS delivers beams with very different longitudinal parameters, amongst them also beams with much larger peak current than the beams required for the LHC, e.g. the high-intensity single bunch for TOF. Although the coupled-bunch feedback will not be active on such cycles, it must be ensured that the beam-induced voltage cannot damage the kicker cavity and its amplifier, even in case of a hardware fault.

4.5.1.2 Relevant parameters for the coupled-bunch feedback

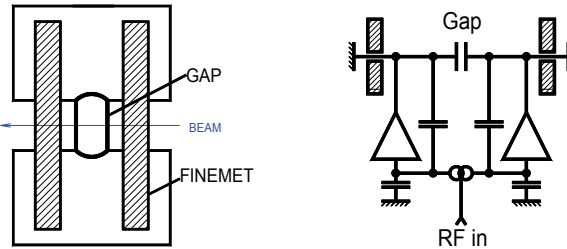
To detect longitudinal coupled-bunch oscillations in the frequency domain, the dedicated feedback picks up synchrotron frequency sidebands of the beam signal at harmonics of the revolution frequency. Demodulation and subsequent baseband filtering are applied to remove the strong component of the beam signal at exactly the revolution frequency harmonic. The filtered synchrotron sidebands alone are then amplified and remodulated with the correct phase to a multiple of the revolution frequency, f_{rev} [72]. The resulting signal, containing multiple carriers, is sent to the longitudinal kicker. As the new system will act on multiple harmonics of the revolution frequency simultaneously, depending on their relative amplitudes and phasing, the resulting voltage shape produced by the damper cavity cannot be foreseen deterministically.

According to the theory of coupled-bunch oscillations [73], each mode n , identified by its phase advance from a bunch of $n/2\pi$, appears as an upper synchrotron frequency sideband of the n th harmonic of the revolution frequency as well as the lower side of the $(h_{\text{RF}} - n)$ th harmonic; the RF harmonic, h_{RF} , being 21 during acceleration of the LHC-type beams with 25 ns and 50 ns bunch spacing in the PS. Due to the symmetry of sidebands, the kicker cavity should cover the frequency range either from ~ 0.4 to 5.5 MHz or from ~ 4.5 to 10 MHz. For easing the solid-state amplifier construction, the lower frequency range has been adopted for the kicker cavity. For the detection of the weak synchrotron frequency sideband close to the revolution frequency harmonics, the upper frequency is preferred. In particular, the harmonic content of the beam at once, twice and three times f_{rev} is very strong, which makes the sideband detection impractical.

Based on measurements with the existing coupled-bunch feedback, $V_{\text{mode}} = 1$ kV per mode is expected to be sufficient. Experience also showed that not all coupled-bunch modes are present simultaneously and with the same amplitude. The new feedback will therefore be designed to cope with five or six different modes and provide a maximum peak voltage of $V_{\text{max}} = 5$ kV to cope with the unforeseeable voltage shape. A power limitation will be specified at a later design stage. The parameters of the

Table 4.15: Feedback kicker basic requirements

Frequency range	0.4–5.5 MHz
RF voltage per sideband, V_{mode}	~ 1 kV
Maximum total RF voltage, V_{max}	~ 5 kV
Undamped shunt impedance at $n f_{\text{rev}}$	< 200 Ω

**Fig. 4.61:** Basic cell configuration

feedback kicker are summarized in the Table 4.15.

4.5.1.3 Power system description

As for the PSB prototype RF system [74], the PS longitudinal damper design is based on multiple RF cells each providing a fraction of the total RF voltage. Each cell consists of a ceramic gap with a Finemet FT-3L MA core on each side being push–pull driven by solid-state amplifiers (Fig. 4.61). For standardization, the ring dimensions are identical to those of the PSB, where the MA cross-section is 300 mm/200 mm/25 mm (outer diameter/inner diameter/thickness). Longitudinally, the cell is about 150 mm long. Both the amplifiers and MA cores are water cooled.

Thermal considerations

The maximum voltage achievable from one MA core is limited by the ability of removing the energy deposited in it. Among different cooling configurations, indirect cooling has been retained. For this, a water-cooled copper ring is placed on one of the core’s sides and isolated from the MA core by a thin kapton foil (Fig. 4.62). Detailed thermal simulations and measurements have been carried out. Figure 4.63 plots the simulation results for 750 W. Extrapolating from this data, the maximum temperature in the core is expected to be limited to below 100°C while dissipating 1 kW with inlet cooling water temperature of 30°C (3 l/min).

MA core impedance characterization

At low frequency the impedance of the cell is mainly dictated by the core characteristics; at high frequency the system capacitance becomes predominant. Figure 4.64, left-hand side, plots the measured impedance on one gap side with a single core inserted in the cell as well as its equivalent parallel R–L–C components. From the parallel resistance, the maximum voltage achievable on one core for a given power can be computed. Figure 4.64, right-hand side, plots these values for 1 kW.

The impedance behaviour can be easily fitted by a ladder R–L network. The system capacitance and the additional capacitance introduced by attaching the core to the cooling ring can complete the model that turns out being very convenient for Spice simulations. The measured and simulated curves as well as the equivalent lumped elements model are plotted in Fig. 4.65.

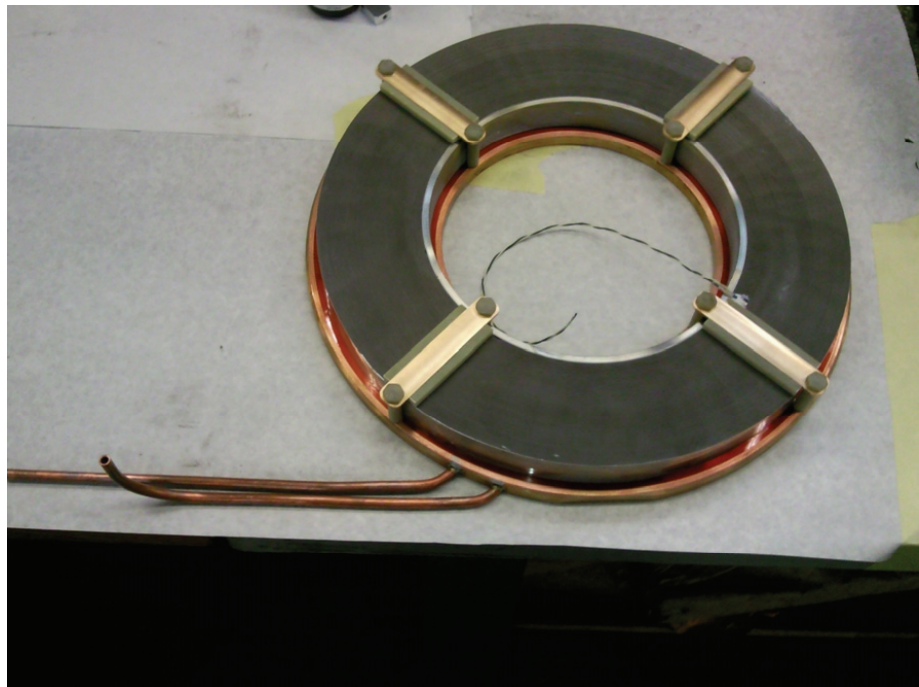


Fig. 4.62: MA core mounted on a copper cooling ring

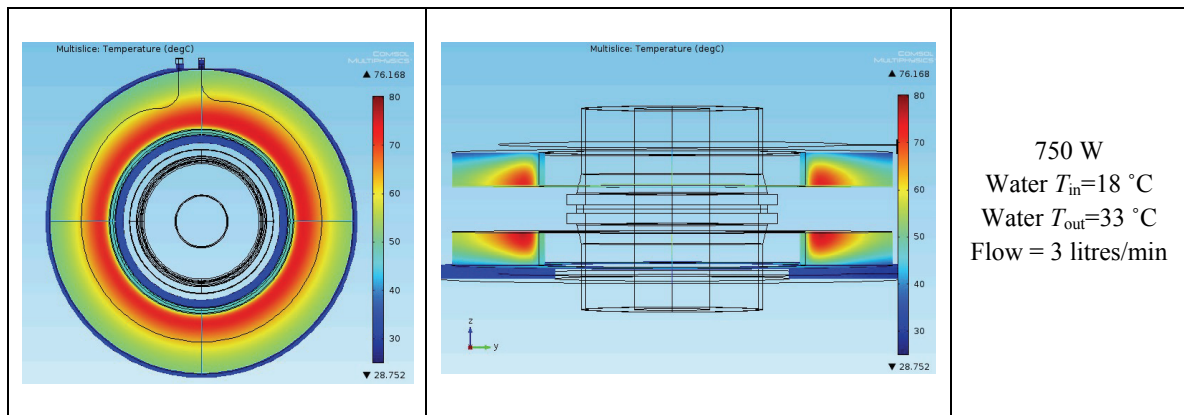


Fig. 4.63: MA core temperature distribution [$^{\circ}\text{C}$]

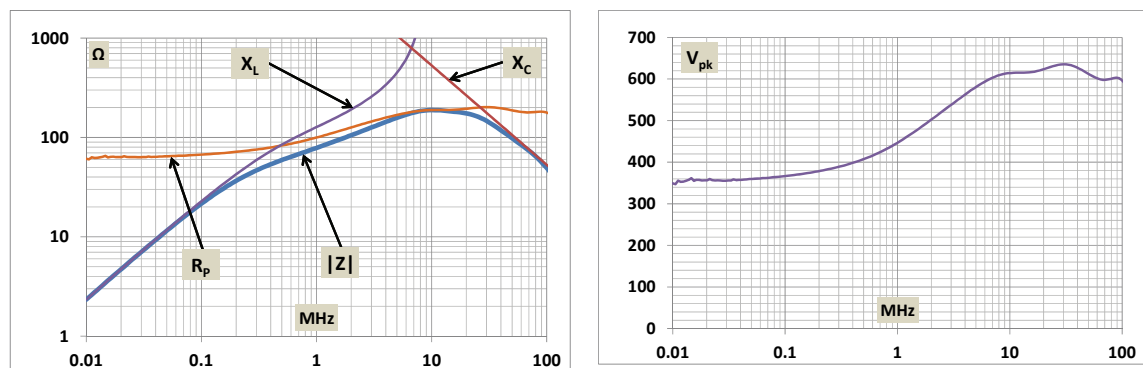


Fig. 4.64: Single-core impedance and R-L-C equivalent (left), maximum voltage for 1 kW dissipation (right).

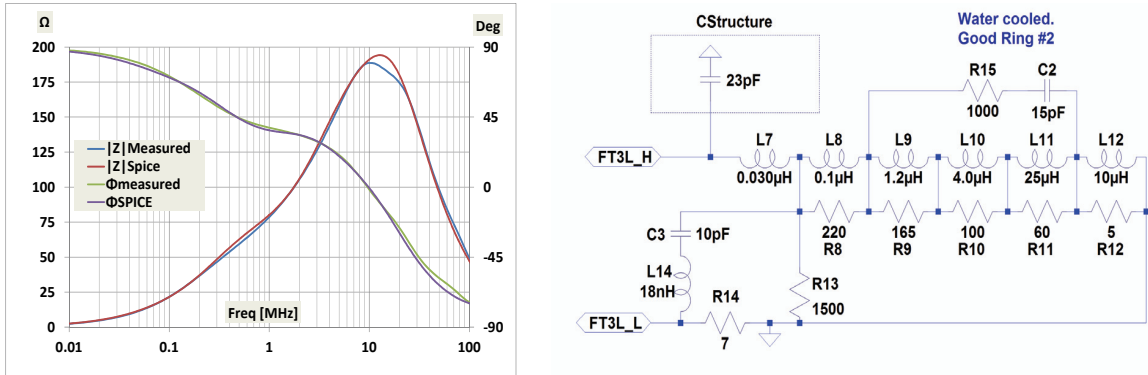


Fig. 4.65: Comparison of measured and simulated impedance (left); equivalent circuit model (right)

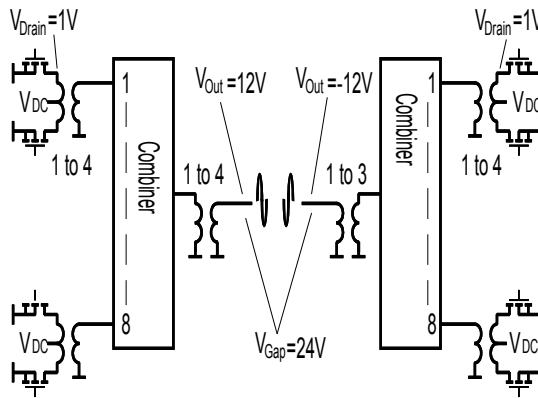


Fig. 4.66: Differential output amplifier—output circuit configuration

Amplifier output circuit configuration

The amplifier was originally designed for the PSB renovation programme where it had to fulfil strict vertical space limitations, as the four superimposed PSB vacuum chambers set the maximum available height. Longitudinally, the dimensions are set by the spacing required for the two MA cores, the cooling rings, the ceramic gap and the connection lines. All these limitations result in an available cabinet 295 mm deep, 323 mm high and 125 mm long. Sixteen 200 W amplification modules, the driver, the output combiners and transformers as well as the ancillary circuitry could be housed in this volume. In the first amplifier version (Fig. 4.66), the outputs of eight 200 W modules were combined and a 1-to-3 RF voltage transformer steps up the impedance to a nominal 50 Ω. The other eight 200 W modules were combined in the same way and driven in antiphase to obtain a differential output signal on two 50 Ω ports.

Each 200 W module contains an internal matching transformer with a 1-to-4 ratio, so that the overall voltage increase from a MOSFET's drain to the push-pull output is 24 times. To improve reliability, the maximum DC supply voltage has been reduced from the nominal 50 V to 40 V so that, considering the saturation voltage and other loss phenomena, the maximum gap voltage achievable in this configuration is ~ 750 V_{Peak}.

To increase the output voltage above 800 V_{Peak}, a single-ended version of the amplifier has been designed. It combines the sixteen 200 W modules in a single output and the output transformer has a 1-to-4 voltage transformation ratio (Fig. 4.67). Driving each gap side with one amplifier allows increasing the available power per cell to ~ 5 kW and the voltage to ~ 1 kV_{Peak}.

Using the single-ended amplifier version, to achieve the required 5 kV_{Peak} voltage with some

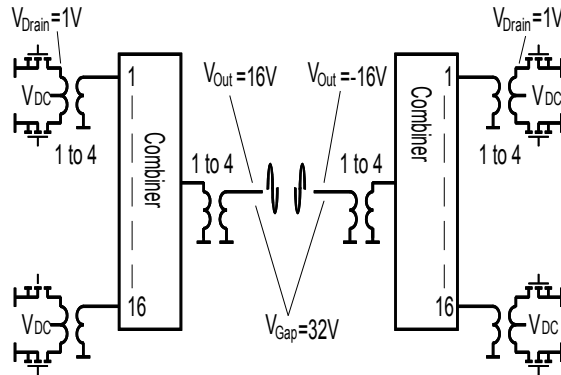


Fig. 4.67: Single-ended output amplifier—output circuit configuration

margin, a cavity composed of six cells will be used.

To evaluate the current available from the amplifier for compensating the wake fields induced by the beam current, it may be noticed that the current at the gap is transformed back to each drain as

$$I_{\text{Drain}} = I_{\text{Gap}} \times \frac{n}{N}, \quad (4.20)$$

where N is the number of combined 200 W modules and n is the voltage transformation ratio from the amplifier output to each MOSFET drain. So, for the two amplifier configurations, we have

$$\text{Differential output: } N = 8, n = 12, \quad \frac{I_{\text{Drain}}}{I_{\text{Gap}}} = 1.5, \quad (4.21)$$

$$\text{Single-ended output: } N = 16, n = 16, \quad \frac{I_{\text{Drain}}}{I_{\text{Gap}}} = 1. \quad (4.22)$$

MOSFET behaviour in radioactive environment and radiation shielding

Typically, MOSFETs submitted to radiation exhibit a threshold voltage (V_{TH}) shifting due to charges getting trapped in the gate isolating layer. For N-channel MOSFETs the shift is such that the device goes into conduction with lower V_{TH} values. This effect can be partly recoverable. Different MOSFET types were tested at the J-PARC Main Ring (MR) collimator to doses above 10 kGy. MRF151 is a standard device already in use in the PSB and employed in the test system. SD2942 and VRF151 are devices equivalent to MRF151 but the latter has enhanced V_{DS} characteristics. Differently from the previous models having V geometry, the MRFE6VP6300 is a modern L-type device with superior performance but lower maximum V_{GS} . Figure 4.68 plots the relative evolution of V_{GS} required for $I_{\text{D}} = 1 \text{ A}$ versus received dose until device failure. It can be noticed that all devices survived 2 kGy and react in a similar way but the L-MOS type seems less affected and stabilizes at some point.

Considering the active device sensitivity to radiation, PS straight section 02 (SS02) has been retained for its low radiation level. During 2012, with CNGS (CERN Neutrinos to Gran Sasso) high-intensity operation, the dose measured was about 1.6 kGy, which would limit the amplifier active devices lifetime to a single year. To increase the lifetime by a factor of 10, the amplifiers require some shielding that EN-STI-EET specialist [75] evaluated in 40 cm of steel. Figure 4.69 shows a 3D view of the foreseen installation. Installing such a shielding will necessarily impose us to move the amplifiers away from the cavity and thus introduce some electrical delay with effects on the overall system performance.

Despite the foreseen shielding, as shown in Fig. 4.68, the characteristic changes are already substantial for 150 Gy, which roughly corresponds to one year of operation. Some kind of compensation/correction measures must therefore be integrated in the amplifier bias circuitry.

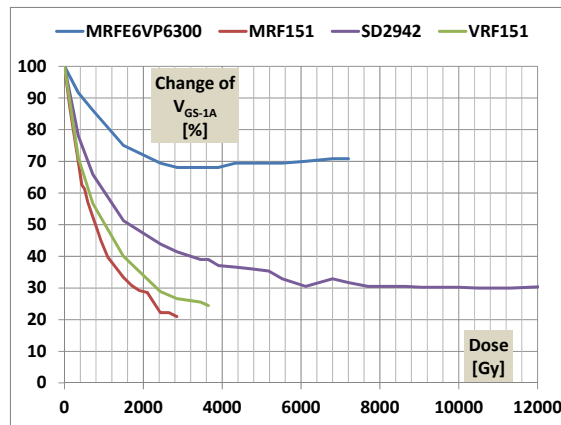


Fig. 4.68: Relative change of V_{GS} versus received dose

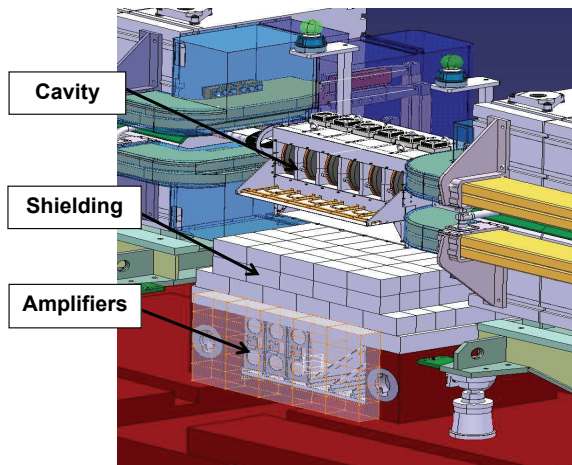


Fig. 4.69: 3D view of cavity, amplifiers and shielding in the PS SS02

Amplifier input circuit, bias adjustment and radiation compensation

The amplifier input circuit is composed of a driver amplifier acting as a high-impedance push-pull stage that drives all the 200 W modules gates in parallel. As the gate inputs almost behave as ideal capacitors, these resulting ports can be used as summing points for routing back the gap voltage signal through capacitors and implement a fast RF feedback loop. Due to this kind of coupling, the overall response is that of a low-pass network. An adequate high-pass section can linearize the response at low level.

To set the MOSFET's rest current as required for class-AB operation, the gate bias is simply fed through $10\text{ k}\Omega$ resistors to the gates. A power MOSFET of the same kind as used in the power stage implements a voltage generator proportional to its threshold voltage. This referenced generator is used to modulate the overall bias of the 200 W stages so as to automatically stabilize the working point versus any threshold voltage variations. Placing the sensing MOSFET on one of the power devices will provide thermal stabilization but, also, as it will have identical exposure to radiation, an automatic radiation compensation effect.

Gap impedance and connection line effect

The impedance experienced by the beam going through a gap is defined by the cell impedance, the amplifier output impedance and the connection transmission lines. Figure 4.70 shows the measured

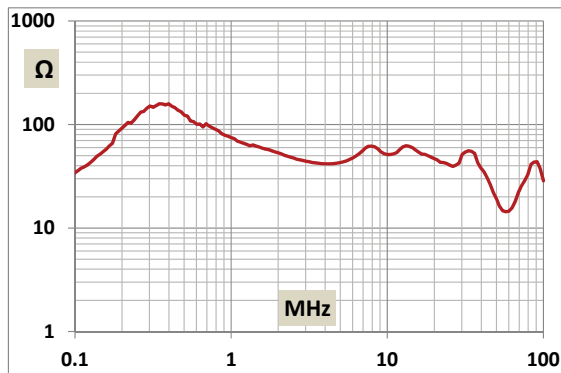


Fig. 4.70: Measured single-ended amplifier output impedance

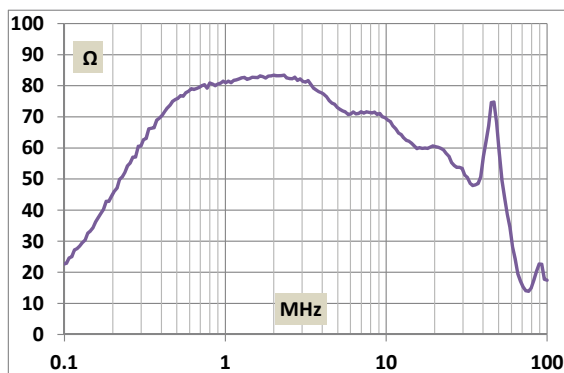


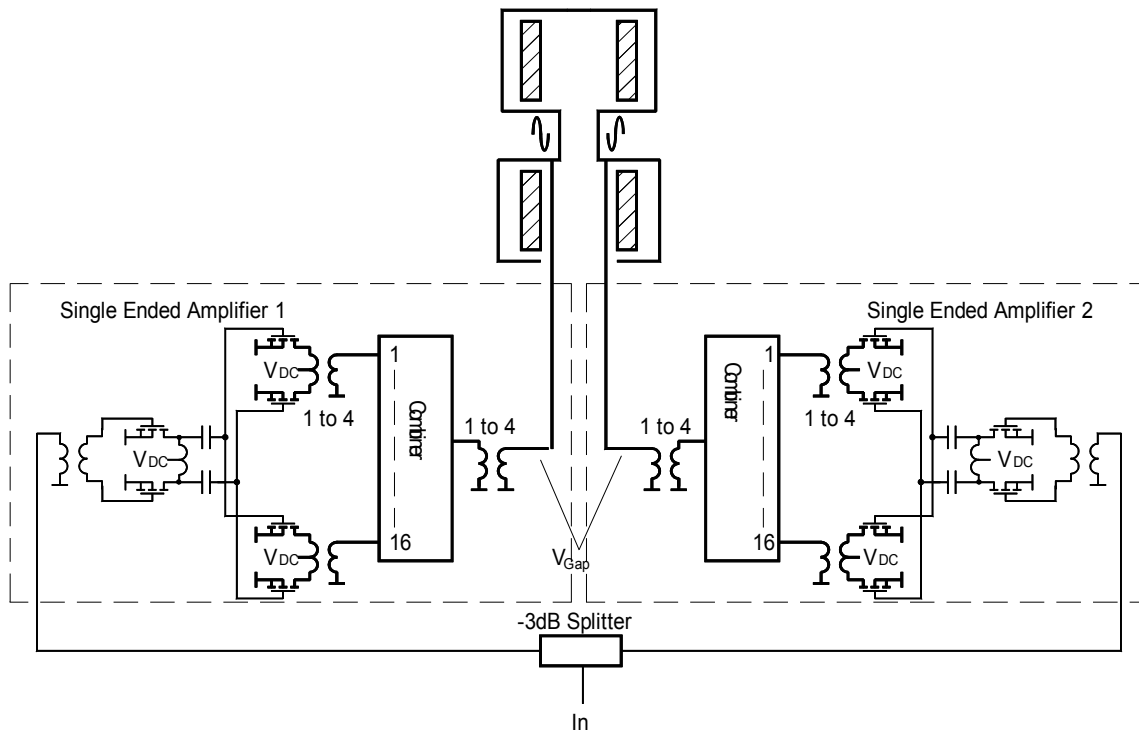
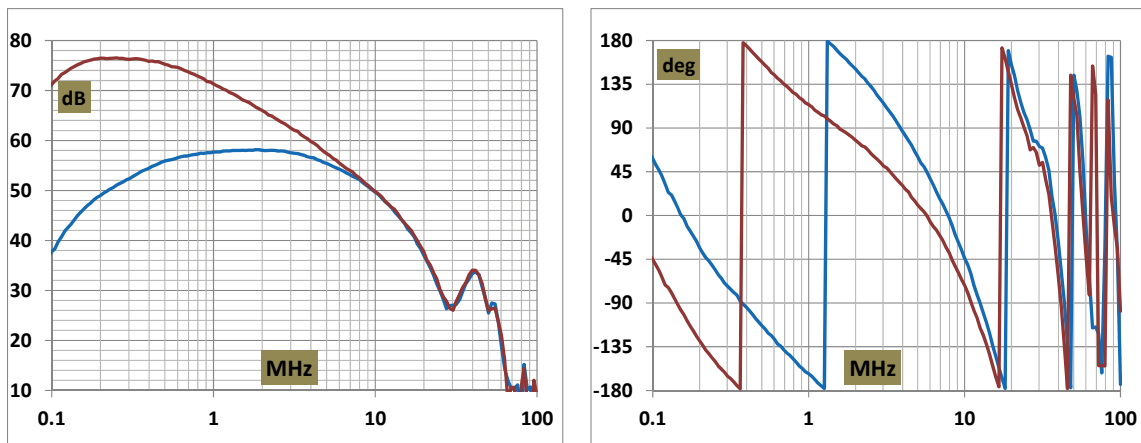
Fig. 4.71: Measured cell gap impedance with single-ended amplifiers and 4 ns cables

amplifier output impedance. It can be noticed that a rapid drop exists around 50 MHz. The distance between the cavity and the amplifier is ~ 1 m, which corresponds to 3–5 ns delay depending on the coaxial cable type. As shown in Fig. 4.64, left, around this frequency the cavity impedance is mostly capacitive and we can expect it to form a kind of parallel resonant circuit with the coaxial line having a length below $\lambda/4$ and thus inductive behaviour.

On the other hand, the falling amplifier output impedance can compensate the rising cavity cell impedance to form a fairly linear response. Figure 4.71 shows the gap impedance as seen by the beam when going through one gap connected to the amplifiers with 4 ns cables.

It must be noticed that any attempt at limiting the response just above 5 MHz by adding some lumped capacitance will have a dramatic influence on the amplifier current, as the required capacitance should be of the order of 1 nF and this would mean operating the amplifier on a mainly reactive load with very high reflected power. Moreover, the capacitance would enhance the impedance peaking visible around 45 MHz (Fig. 4.71) and bring it down in frequency. In the configuration described above, the six-cell system will then present a total impedance about 2.5 higher than the goal value listed in Table 4.15 (500 Ω instead of 200 Ω). As the present response already represents a reasonable compromise among the various limiting parameters, the task of further limiting the gap impedance will be taken by the low-level electronics in the form of a one-turn feedback loop or another technique.

Nevertheless, in the high-power electronics slight improvements may be possible by adding a moderate feedback to lower the impedance to ~ 60 Ω below 20 MHz. This requires additional studies in particular concerning the system stability.

**Fig. 4.72:** System configuration**Fig. 4.73:** System measured response: red: normal, blue: linearized

Amplifier response

The amplification system with two single-ended amplifiers is shown in Fig. 4.72. The overall response with the cavity connected through two 50Ω , 4 ns cables is shown in Fig. 4.73. Frequency-response linearization is achieved with a series 330 pF capacitor inserted between the driving generator and the amplifier input.

A complete Spice model has been made to evaluate some of the system parameters. The MOSFET device model VRF151 was made available by the manufacturer and the Finemet ring equivalent circuit is that derived from measurements and shown in Fig. 4.65. Table 4.16 lists the main parameters for a system developing 800 V_{Peak} at the gap and, in particular, shows the following.

Table 4.16: Simulated and measured amplifier parameters for the 800 V_{Peak} gap voltage

Freq. [MHz]	Simulated					Measured	
	I_{DPK} A	I_{DDC} A	P_{MOS} W	V_{GPK} V	$I_{\Sigma PK}$ A	I_{SUPP} A	I_{SUPP} A
0.5	9.2	3.4	77	1.9	0.06	115	100
1	5.0	2.8	39	1.3	0.10	96	72
2	3.1	1.6	23	0.8	0.16	57	53
5	2.5	1.4	27	0.9	0.36	50	74
10	4.7	2.5	55	1.5	0.71	84	100

- The peak and direct currents provided by each MOSFET device in the final stages (I_{DPK} and I_{DDC}) and the power (P_{MOS}) they dissipate.
- The gate driving voltage (V_{GPK}) and the relative current provided by the driver device ($I_{\Sigma PK}$).
- For comparison, the simulated direct current values are also compared with the measured ones under the same conditions.

Beam loading

While the coupled-bunch feedback is designed to stabilize LHC-type beams, the PS also accelerates beams with very different longitudinal structures for other users. As mentioned above, the beam-induced voltage in the kicker cavity is a critical issue due the large peak currents of these users compared to the peak currents with beams for the LHC. In particular, the high-intensity single bunch for the TOF experiment may attain a peak current of up to 100 A during the short-bunch rotation prior to extraction (Table 4.17). As the coupled-bunch feedback does not need to be active, the gaps can be short circuited by relays. Even with the parameters after the LIU [76], the maximum peak currents with an active coupled-bunch feedback are more than three times below this (absolute maximum parameters with inactive feedback in red, in green on cycles with the feedback active and blue with the gap open but not requiring damping).

The maximum foreseen beam peak current in the PS occurs with an LHC beam (25 ns bunch spacing) at transition crossing. Based on tomoscope measurements, the peak current of a beam with a total intensity of 1.28×10^{13} ppp (1.8×10^{11} ppb, delivered during scrubbing run in 2012) corresponds to an instantaneous peak current of 10.2 A. The shortest bunch length at transition is 18 ns (4σ , Gaussian). Following the LIUs (after LS2), the intensity per bunch from the PS will become up to 2.7×10^{11} ppb, which is a factor of 1.5 above the present maximum intensity for this beam. So, the maximum peak current on which the damper cavity will act becomes 15.5 A. The average direct beam current after the LIUs will be about 1.5 A and, in the simple short-bunch approximation, the RF current per spectral line will be of the order of 3 A.

This working condition corresponds to the beam being handled by the C10 RF system and requiring the damper action. In the last part of the accelerating cycle, the beam is handled by the higher frequency systems (20 MHz, 40 MHz and 80 MHz), the damper will not be used and the gap relays can be short circuited.

If, however, hot switching must be avoided, then higher beam peak currents can be reached with the 4 ns bunches at extraction. At the LIU goal intensity of 2.7×10^{11} ppb at 25 ns bunch spacing and 4.2×10^{11} ppb at 50 ns bunch spacing, the peak beam current is ~ 17.3 A and ~ 26.8 A, respectively.

The bunch rotation of LHC-type beams is short and the high peak currents are only reached for a few turns before ejection (< 1 ms).

These figures do not correspond to the absolute maximum instantaneous peak current circulating in the PS. Presently, during TOF cycles, the instantaneous peak current is ~ 20 A, but this value smoothly

Table 4.17: Beam characteristics

	2012	LIU parameters			
Beam type	LHC 25 ns	LHC 25 ns	LHC 50 ns	TOF	Fixed target
Damper	Active	Active	Active	Inactive	Possibly active
Beam intensity	1.28×10^{13} ppp	1.92×10^{13} ppp	1.48×10^{13} ppp	1.0×10^{13} ppp	Up to 4×10^{13} ppp
Direct current	1.0 A	1.5 A	1.16 A	0.8 A	3.2 A
Current per spectral component, short-bunch approximation	2 A	3 A	2.32 A	1.6 A	6.4 A
Peak current at transition	10.2 A	15.5 A	11.9 A	50 A	25 A
Bunch length	18 ns	18 ns	18 ns	40 ns	20 ns
Intensity per bunch at extraction		2.7×10^{11} ppb	4.2×10^{11} ppb	1.0×10^{13} ppp	Coasting beam
Peak current at extraction		17.3 A	26.8 A	100 A	
Bunch length		4 ns	4 ns	20 ns	
Duration of peak		~ 0.3 ms	~ 0.3 ms	~ 1 ms	

rises to ~ 50 A in ~ 50 ms at transition and then goes back to the initial value with a similar slope. Then, in the last ms just before ejection, the bunch is rotated in phase space so that it becomes very short and peak current rises from ~ 20 A to ~ 100 A.

The damper is not supposed to deal with this kind of beams and the gap should be short circuited in this condition.

4.5.1.4 Beam-induced voltage cancellation

The beam going through each gap will induce a voltage that, due to the wideband response, will be very similar to the beam pulse. Cancellation of the induced voltage can be done by injecting a current identical to that bunch current but with inverse phase. As seen in Section 4.3.3, for the single-ended amplifier configuration, each MOSFET has to provide the same amount of current as flowing at the gap.

As shown in Fig. 4.74, VRF151G, MRF151 and SD2942 drain current saturates at ~ 40 A while the more modern MRFE6VP6300 saturates at ~ 30 A.

The ratio between gap and drain currents, as discussed in Section 4.3.3, is unity for the single-ended amplifier version so that, in principle, the maximum foreseen 15.5 A having to be dealt with seem within the amplifier possibilities. Except for the MRFE6VP6300 device, the short peak at 27.6 A is also probably within the limits, as there only wake-field cancellation is required.

To evaluate the system ability to cancel out the wake fields, simulations with a simplified, feed forward (FF) compensation were done. The system simply consists in applying to the amplifier input, through a 100 pF capacitor, a voltage proportional to the beam current pulse delayed by 25 ns. As the signal does not contain any pre-distortion to take into account the system transfer function, the compensation is only ~ 6 dB, but this still provides interesting indications.

Figures 4.75 to 4.77 show the system response to a 10 MHz, 20 A beam current pulse. The left-hand column shows the simulated response without compensation and the right-hand one with compensation. As the total gap impedance is almost halved when paralleled by the amplifiers' output impedance, even without FF the power dissipated on each MOSFET is ~ 90 W, which is well within the device capabilities. Applying the FF results in a substantial reduction of the maximum gap voltage but the power dissipated on each MOSFET does not substantially change. What changes is the phase relation between drain voltage and current. The maximum drain peak current is still far away from maximum device satu-

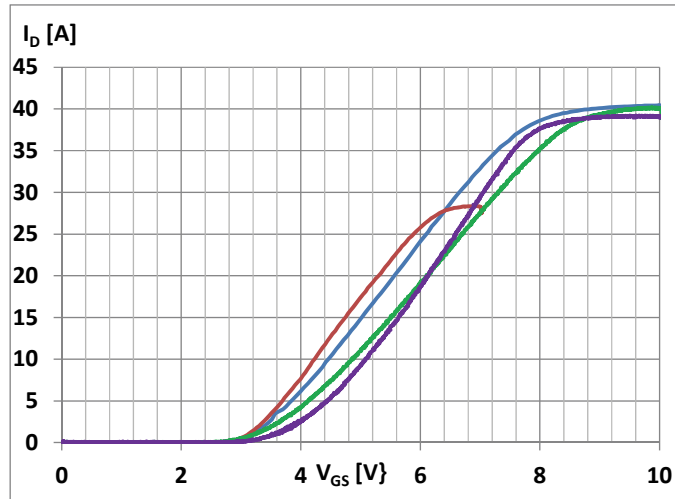


Fig. 4.74: Saturation MOSFET currents: green VRF151, violet SD2942, blue MRF151, red MRFE6VP6300.

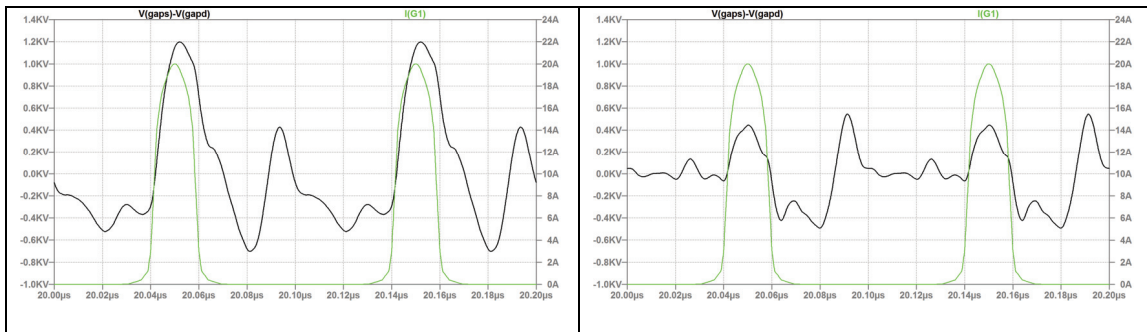


Fig. 4.75: Simulated gap voltage (black) and beam current (green) (left: no compensation, right: compensated).

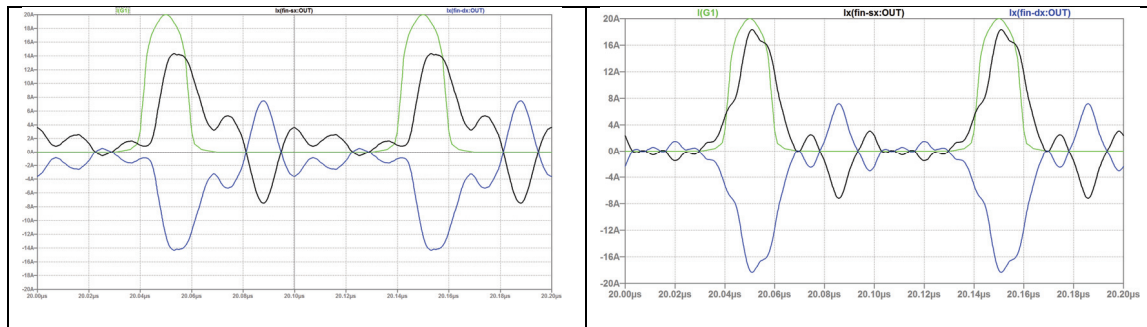


Fig. 4.76: Simulated amplifier output currents (black and blue) and beam current (green) (left: no compensation, right: compensated).

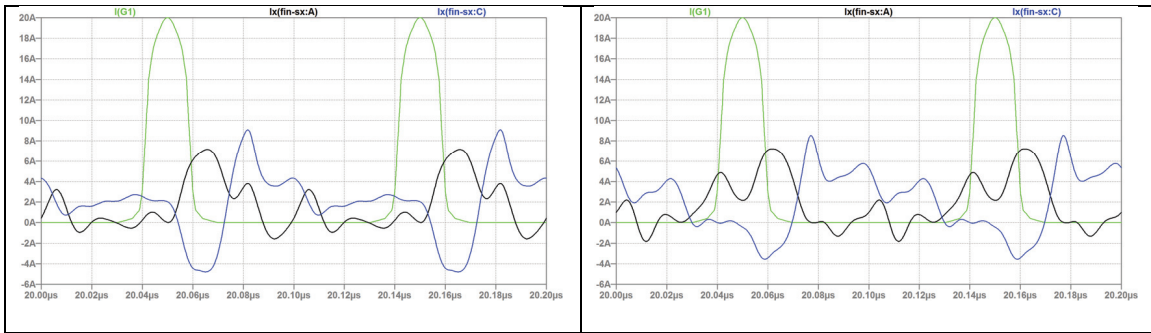


Fig. 4.77: Simulated drain currents (black and blue) and beam current (green) (left: no compensation, right: compensated).

ration, thus allowing, in principle, a far better wake-field cancellation. This of course requires drastically improving the FF system.

4.5.1.5 Overvoltage protection

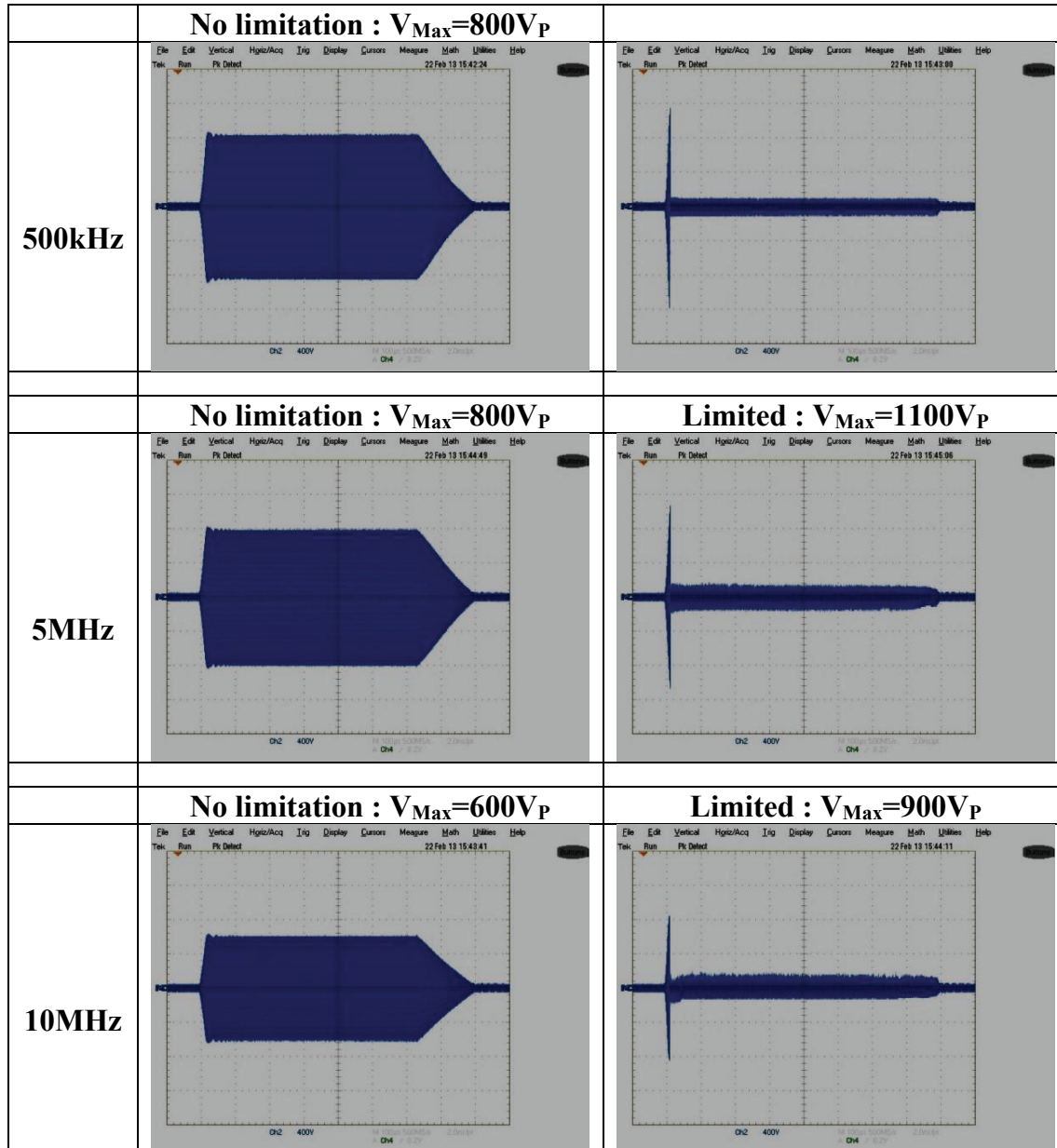
In case of misalignment or malfunctioning of the wake-field-compensation system, the voltage induced on the gap can reach very high values. Assuming the gap impedance to be 80Ω , a 30 A beam current will produce 2.4 kV across the gap. We have seen in Section 4.3.3 that the voltage transformation ratio from gap to drain is 32, so the drain voltage will reach ~ 75 V, to which the DC supply voltage has to be added. This makes a total drain voltage of ~ 120 V, which is already the breakdown value for MRF151 and SD2942 devices. For this reason the device selected for the amplifiers is VRF151, which has a maximum breakdown voltage of 160 V. But even this rugged device will not withstand the voltage induced by a 50 A or 100 A current of the TOF beam in case of gap circuit device failure. To protect the amplifiers from these extreme fault situations, gas spark gaps will be installed on each gap. EPCOS type EC 600 10 have a nominal voltage of 600 V. Figure 4.78 shows their behaviour when operated at RF voltages between 0.5 MHz and 10 MHz. The firing time is $20 \mu\text{s}$. Continuous operation of the spark gaps must be avoided. For this reason, dedicated electronics will monitor the gap relay status and gap voltage and detect spark gap current to eventually activate a spare gap relay to ensure the amplifiers' protection.

4.5.2 RF-HL

4.5.2.1 Introduction

The impedance presented by the accelerating cavities to the circulating beam during particle acceleration and beam manipulations is the source of two main classes of issues in the longitudinal plane: coupled-bunch instabilities and transient beam loading. The main strategy to fight against these sources of instability is represented by a new generation of one-turn feedback systems, developed within the LIU project, and by the implementation of a wideband longitudinal kicker cavity, driven by a digital LL-RF system, that aims at suppressing all the excited synchrotron frequency sidebands of the revolution frequency harmonics. These two main lines of attack are described in Sections 4.2.7 and 4.5 but of course the reason underneath the development of the instabilities remains the cavity impedance presented to the beam and here we describe different lines of action to reduce this impedance to the lowest possible value.

In Table 4.18 the PS beam characteristics for the LHC injection are summarized before and after the LS2 upgrade; as can be seen, the expected performance of the PS for the ultimate LHC beam foresees an increase by a factor 1.5 of the maximum beam intensity per bunch achieved so far.

**Fig. 4.78:** Behaviour of the spark gap voltage limiter at different frequencies**Table 4.18:** PS beam intensities per bunch with 25 ns bunch spacing

Bunch intensity	Achieved	After LS2
At injection	2.3×10^{12}	3.4×10^{12}
At extraction	1.8×10^{11}	2.7×10^{11}



Fig. 4.79: One of the 11 10 MHz RF cavities in the PS with its amplifier sitting in the cavity base

4.5.2.2 The 10 MHz system

The 10 MHz RF system consists of 10 cavities plus one hot spare that run in different tuning and voltage programme groups for all type of beams, including LHC beams. Each cavity consists of two accelerating gaps driven by a single RF power amplifier (see Fig. 4.79). When a group of cavities is not used, their accelerating gaps are short circuited with fast mechanical gap relays that reduce the equivalent impedance by 30 dB; nonetheless, the inductance associated with the relay connection can still resonate with the gap capacitance and excite some dangerous modes by the beam. It has been shown that a more effective way of avoiding excited modes under these circumstances is to park the cavity group at a non-integer harmonic of the revolution frequency.

However, when the cavities are in use, it is the task of the final amplifier to reduce the cavity impedance at the operating frequency as much as possible by applying a negative feedback on the cavity gap voltage.

The 10 MHz final and feedback amplifiers

The 10 MHz RF amplifier is a three-stage amplifier that adopts air-cooled tetrodes, YL1056, for the pre-driver and driver stages and a single RS1084 power tetrode for the final stage. The pre-driver and driver stages were added in the late 1980s with a feedback circuit that was at the time providing 20 dB of induced voltage attenuation at resonance [77]; the performance of the system was then progressively enhanced to the level of 26 dB, thus ensuring an adequate operation of the 10 MHz system with the strongest beams in 2001 [50]. That level appears to be a hard limit with the present components and topology of the amplifier.

The future upgrade of the amplifier performance is envisaging two distinct approaches: a limited-cost solution, where some key elements in the amplification chain are reviewed with the aim of achieving at least 28 dB of feedback gain (present is 24–26 dB) and a more extensive approach that could lead to substantial changes in the amplifier, up to the implementation of one amplifier per accelerating gap, or the replacement of the present system with a wideband system adopting the Finemet technology.

While the second approach has just started being considered and requires detailed studies with and without beam after LS1, the limited-cost solution has already entered the experimental phase. The existing final amplifier grid resonator is being replaced with a new design that results to be more efficient over the operating bandwidth, the RF tube working point is being reconsidered to increase the gain at each amplification stage, the RF feedback capacitive PU is also being reconsidered and the possibility of replacing the pre-driver stage with a solid-state amplifier is a possible option.

At the end of 2014 a prototype of an upgraded amplifier is going to be available for extensive testing with the test cavity in order to prepare its installation in the PS ring for the final validation. If successful, all amplifiers will be progressively upgraded with a feedback level higher than 28 dB already before LS2.

In the years 2015 and 2016 the more radical option will also be extensively studied to prepare for a prototype test in 2017 and for a decision on fabrication at the end of 2017. Again, the goal is to deliver a fully renovated system by 2020, in time for the start-up after LS2.

4.5.2.3 The 40 and 80 MHz systems

The 40 and 80 MHz RF systems [78, 79] are respectively made of two and three cavities that are used for bunch splitting (40 MHz only) and bunch rotation of the LHC beam. While one 40 MHz and two 80 MHz cavities are required during the proton cycle, leaving the remaining cavities as hot spares, one 80 MHz system is enough to produce the required bunch spacing for injection into the SPS during the ion cycle. However, when a proton and an ion cycle are present in the same supercycle, the three 80 MHz cavities are used and no hot spare remains available in the case of a failure of one system, since the cavity is tuned at two different frequencies with ions and with protons.

The cavities can provide a gap voltage of 300 kV and they are equipped with a mechanical, coaxial short circuit at the cavity gap to screen the circulating beam from the cavity when not in use. Since the mechanical short circuit cannot be operated in PPM mode, a direct wideband feedback system is implemented around the cavity and amplifier chain to reduce the cavity impedance seen by the beam.

The cavity detuning due to the beam loading represents an additional issue in the operation of the 40 MHz system, since the PS must also accelerate a so-called pilot, low-intensity beam and the nominal, high-intensity beam within the same supercycle. When the cavity is detuned due to the beam loading, an extra current is pulled from the anode high-voltage power supply to allow reaching the expected gap voltage, which may bring the power converter to its operational limit. In order to limit this effect, the cavity needs to be tuned at an intermediate frequency that is minimizing the consequences of the detuning effect at the two distinct beam currents.

The 40 and 80 MHz feedback system

The 40 and 80 MHz RF system is equipped with a high-gain fast RF feedback circuit around the cavity and amplifier chain, which delivers about 42 dB of feedback gain. Having considered the high quality factor of these cavities, the maximum group delay admissible for a stable loop operation with a 6 dB gain margin is about 250 ns. After having subtracted the delay related to the RF feedback chain, which includes solid-state amplifiers that must be kept away from high radiation fluxes, the available delay for the cables connecting to the final amplifier is limited to 120 ns.

The only possibility of pushing the RF feedback to higher gain would then be to reduce the group delay in the RF chain by reducing the group delay in the driving amplifiers and/or bringing them closer to the final amplifier that is directly connected to the cavity.

The study work aims at understanding if a different amplifier topology, with a reduced group delay in the feedback chain, would make an increase of the fast RF feedback gain possible. The technical difficulty of this enterprise can be understood by considering that a gain increase by 3 dB would require a reduction of the chain group delay by 40%.

The 80 MHz fast ferrite tuner

The 80 MHz RF system is used for bunch rotation just before the beam extraction to the SPS, to increase voltage gradient and hence improve the bunch shortening. Bunch shortening by bunch rotation is not required for the lead-ion beam, where adiabatic shorting is sufficient to reach a bunch length below 4



Fig. 4.80: One of the 80 MHz cavities with final RF amplifier; 40 MHz cavities look very similar

ns. At the same time the operation frequency changes between protons or other ion species: two cavities tuned at 80.110 MHz are used for protons, while one cavity tuned at 79.8765 MHz is operated for lead ions. Since three cavities are available in the PS ring, respectively in straight sections 8, 88 and 89, whenever a proton and an ion cycle co-exist in the same supercycle, all three cavities are used for the LHC beam production and there is no hot spare capability left.

In order to overcome this possible issue, especially with very long runs and reduced technical stops, it was proposed to explore the possibility of building a ferrite-based fast tuner, which would allow us to use the same cavity for both protons and ions by tuning it with ppm capability. This would allow recovering a full hot spare cavity, in case of need.

For realizing such a fast tuning system, the investigation started from the results obtained with the technique of perpendicularly biased ferrites, which has proven to be helpful to minimize losses in the ferrites; however, both polarization schemes are being tested on prototype equipment. The idea is to have an external inductance, strongly coupled to the cavity, which may be changed by means of a biasing current supplied by an external power supply. The change in the value of this inductance will produce a change in the cavity resonant frequency.



Fig. 4.81: Prototype equipment set-up during a measurement session

Extensive measurements on prototype equipment (see Fig. 4.81) are under way to assess the feasibility of the scheme, with the goal of building a working prototype before the end of 2014.

4.5.2.4 Conclusion

The different strategies aiming at a reduction of the equivalent impedance presented to the circulating beam by the RF cavities in the PS are still in the study phase. The testing of first prototypes in 2014 will allow evaluating a realistic margin for improvement and better estimating the cost of the upgrade. The results from the first measurements on the longitudinal kicker with the nominal beam will provide information on the effectiveness of this system in fighting multibunch instabilities and, eventually, steer decisions on the upgrade programme of the PS RF systems.

4.5.3 RF-low-level feedbacks and beam control

4.5.3.1 Low-level feedbacks and beam control

The upgrade of the longitudinal low-level feedbacks and the installation of a wideband damper are essential to preserve longitudinal beam stability in the PS with beam parameters foreseen after the LIU. Additionally, the upgrade of the beam control to a fully digital system is required to preserve the flexibility for present and future manipulations with the RF systems.

The longitudinal beam control systems generate the drive signals to all RF cavities based on the revolution frequency derived from the magnetic field, corrected by phase and radial position measurements of the beam. Table 4.19 summarizes the RF systems and their functions for the LHC-type beams.

While the main 2.8 –10 MHz and the 200 MHz RF systems are operated during acceleration and sweep with the increasing revolution frequency of the beam, all other RF systems are only used for RF manipulations at fixed energy and RF frequency.

Besides the low-level RF for the wideband longitudinal damper as described in Section 4.5.1, the upgrade within the LIU project comprises

- new one-turn delay feedbacks for the 11 main accelerating cavities including digital voltage control loops;
- one-turn delay feedbacks for the 40 MHz, 80 MHz and 20 MHz (of the order of priority);
- the upgrade of the longitudinal beam control to a fully digital implementation.

Table 4.19: RF systems for LHC-type beams in the PS

Frequency	Total RF			Ref.
	voltage	Number of cavities	Function	
2.8 –10 MHz	200 kV	10 (+1 spare)	Acceleration and RF manipulations	[80]
13.3 /20 MHz	20 kV	1 (+1 spare)	Flat-top splitting/rebucketing	[51]
40 MHz	300 kV	1 (+1 spare)	Flat-top splitting/bunch rotation	[81]
80 MHz	600 kV	2 (+1 spare)	Bunch rotation	[82]
200 MHz	100 kV	6	Controlled longitudinal blow-up	[83]
0.4 –5.5 MHz	5 kV	1	Coupled-bunch damping	Sec. 4.5.1

4.5.3.2 *Feedbacks with one-turn delay*

The cavities of all RF systems in the PS, with the exception of the 200 MHz cavities, are equipped with strong direct RF feedbacks around the amplifiers with gains between about 20 dB and 40 dB, depending on the system and its bandwidth. Additionally, the cavities at 10 MHz and 20 MHz have fast-switching gap relays to shield them almost completely from the beam when not in use. The impedance of the 200 MHz RF system is reduced by $\lambda/4 + n\lambda/2$ ($n = 1, 2, \dots$) stub lines with PIN diode switches to additionally load the cavities. As they are only active during the short longitudinal blow-ups, no further impedance reduction is required. Though installed as close to the cavities as possible, the achievable gain of the direct RF feedbacks remains limited by the bandwidth required, as well as by the group delays of amplifiers and cables. High feedback gain is only required close to the revolution frequency harmonics and a one-turn delay feedback had already been available around the 10 MHz RF cavities [84], reducing their impedance by an additional 12 dB. However, the previous one-turn delay feedback was incompatible with operation for LHC-type beams and not sufficiently flexible to allow, e.g., injection into $h = 7$ and $h = 9$. New feedback electronics has therefore been developed and installed on all 10 MHz cavities during LS1. The new system has been commissioned during the start-up 2014.

The gaps of the 40 MHz and 80 MHz cavities are equipped with a mechanical short circuit to shield them from the beam when not in use, but the mechanism cannot be actuated during each cycle. Hence, the residual impedance is visible to the beam during the whole cycle and a further reduction of the impedance by a one-turn delay feedback as planned within the LIU project will improve longitudinal stability. Though covered by LIU, adding a one-turn delay feedback to the 20 MHz cavities is of somewhat lower priority. These cavities are equipped with gap relays and are only active during less than 150 ms on the flat top.

10 MHz RF cavities

The 10 MHz RF cavities are equipped with a direct feedback around the high-power amplifier (see Section 4.5.2.2), the gain of which remains limited due to the large bandwidth. Further impedance reduction at the revolution frequency harmonics is achieved by a feedback system with a delay of one turn. Though already available for the antiproton production beam, new one-turn delay feedback electronics has been developed with LIU to cover also the LHC-type beams. In addition, the voltage-control loops have been renovated with both new systems available at the start-up after LS1.

One-turn delay feedback

A one-turn delay feedback system had originally been installed around the 10 MHz RF cavities [84] for the antiproton production beam to reduce transient beam loading effects during the batch compression RF manipulation. This hardware-based system was designed for a harmonic number range from 8 to 20, incompatible with the requirements for LHC-type beams.

The hardware development of a replacement for the one-turn delay feedbacks was therefore started

**Fig. 4.82:** PS feedback board

based on the electronics board for the same application in the LHC [85]. It features an increased resolution of 14 bits, full coverage of all harmonic numbers up to presently 32, as well as a fully digital and programmable implementation of the one-turn delay. Additionally, the new one-turn delay feedbacks only require a single swept clock at fixed harmonic number ($h_{\text{clk}} = 200$), improving operational stability and flexibility.

With respect to the initial development for the LHC, important modifications had to be made, requiring a complete redesign of the feedback electronics to allow:

- glitch-free adjustment of the delay chain covering the 10 % revolution frequency swing for protons;
- flexible handling of any harmonic number used for acceleration (presently $h = 7, \dots, 21$ for protons);
- restart of the feedback at an arbitrary harmonic number, making it suitable for all high-intensity beams, including all LHC-type proton beams.

Following the production of prototypes, the first series production was successfully completed in 2013 and a further series is expected during 2014. The new feedback board (Fig. 4.82) consists of in total four ADC and DAC channels with an Altera Stratix II field programmable gate array (FPGA).

To generate a signal delay of exactly one-turn delay, following the increase of the revolution frequency along the acceleration cycle, two independent fine delay line chains have been realized. Furthermore, the feedback board is equipped with serial data links to connect to the standard control function generators (3.2 MBit/s, CVORB) and fast serial receivers for, e.g., the real-time revolution frequency from the beam controls (40 MBit/s).

The one-turn delay feedback consists of three parts, which have all been integrated on the feedback board described above:

- a programmable notch filter cancels the effect of the feedback at the RF harmonic to avoid cross-talk with the voltage-control loop;
- a comb filter with its pass-bands at multiples of the revolution frequency harmonics;
- an automatic delay to stretch group delay of the signal processing in one complete revolution period.

During prototype tests, at least identical or better performance compared to the previous one-turn delay feedback has been achieved. With improved signal processing in place, significantly higher performance is expected. The new one-turn delay feedback is compatible with all beams in the PS, notably the multibunch beams for the LHC where the previous system could only reach marginal gain.

Notch filter. The programmable notch filter cancels any possible interaction between the voltage-control loop and the one-turn delay feedback, by removing any feedback gain around the RF harmonic. The

notch filter has been implemented as a second-order infinite impulse response (IIR) filter with the major advantage of being programmable to any fractional harmonic number ratio with respect to the clock harmonic h_{RF}/h_{clk} . Hence, the complete signal processing for one-turn delay feedback, voltage and future phase control loops only requires a single swept clock at a fixed harmonic number ($h_{clk} = 200$) and can be operated at any relevant RF harmonic. At the same time, the bandwidth of the notch filter can also be adjusted with the flexible IIR-based filter structure.

Comb filter. The comb filter provides feedback gain at all multiples of the revolution frequency. Since its transfer function does not depend on the harmonic number, a classical comb filter structure, feeding part of the output signal back via a first-in-first-out (FIFO) memory, has been chosen. The width of the comb filter pass-bands can be easily adjusted by bit shifting the signal in its internal feedback path.

One-turn delay. For the feedback to work in a wide range of harmonic numbers and revolution frequencies, the signal delay from the detection of the beam-induced voltage to the correction kick at the cavity gap must be adjusted to exactly one turn. In the new one-turn delay feedback, this delay has been separated into two stages. Based on the measured revolution period (respectively the frequency of the swept clock at $h_{clk} = 200$), the coarse delay is set in multiples of the clock period implemented in a FIFO-type memory. It is complemented by a delayed read clock of the FIFO memory, allowing the fine adjustment of the one-turn delay in steps of about 20 ps using digital delay lines. To avoid glitches when switching the delay, two fine delay lines in parallel have been set up such that a new fine delay value can be firstly programmed to the unused delay line and secondly switching to the delay line with the new value once eventual glitches have propagated through the delay chain. A glitch-free switching between both fine delay lines has also been developed. Once switched to the new delay line, the one used previously can be set to the subsequent value and this sequence continues periodically.

The new delay based on a FIFO memory combined with fine delay chains applied to the read clock can represent any programmable signal delay, with the advantage of being directly on the feedback module without the need for any physical cable delays.

Digital voltage- and phase-control loops

The feedback board for the new one-turn delay feedback has sufficient signal processing capacity to also handle the voltage and optionally the phase control of the 10 MHz cavities. Firstly, the RF voltage can be detected digitally in a narrow frequency band around the selected RF harmonic, reducing the influence of beam-induced voltage on all other harmonics. Secondly, a digital implementation allows a full control of the loop behaviour, e.g., minimizing its rise time for bunch-rotation RF manipulations. Finally, the new voltage-control loop directly accepts the standard function generator serial data stream (3.2 MBit/s) as voltage programme delivered by the recently renovated new voltage-control matrix.

The non-I/Q detector [86] allows the calculation of the gap voltage at any programmable harmonic number using a clock at fixed harmonic (again $h_{clk} = 200$). For the amplitude control, the resulting I/Q-pairs are converted to amplitude and phase applying the so-called CORDIC (coordinate rotation digital computer) algorithm. The detected gap voltage is then compared to the voltage programme. The loop error is fed to a PID-type regulator controlling the modulator for the drive RF signal to the amplifier chain of the cavity. In the digital domain this amplitude modulator simply multiplies the digitized RF from the beam controls by the output of the PID regulator.

Already in the after-LS1 era all 11 10 MHz cavities are equipped with the new voltage-control loops. Tests with a phase-control loop or an I/Q-based combined amplitude and phase control will follow. Additionally, it is also being studied to integrate the RF signal generation (so-called multiharmonic sources) directly into the feedback board, avoiding the redigitization of the RF signals from the beam control.

20 MHz RF cavities

The 20 MHz RF cavities are equipped with gap relays which allow hot switching during the acceleration cycle. The cavities are required to split LHC-type beams with final bunch spacings of multiples of 25 ns. They are operated at 20.03 MHz to split the bunches from 100 ns (bunch spacing during acceleration with $h = 21$) to 50 ns ($h = 42$) spacing. For bunch spacings of multiples of 75 ns, the cavities can be switched to 13.35 MHz to perform a splitting from 150 ns (bunch spacing during acceleration with $h = 14$) to 75 ns ($h = 28$) spacing. Hence, their impedance is only exposed to the beam during some 150 ms and their direct effect on the longitudinal beam stability and beam quality is expected to be minor. However, transient beam loading during the bunch splitting from 100 ns to 50 ns has an enhanced effect on the symmetry of the splitting along the batch.

The one-turn delay feedback hardware developed for the 10 MHz RF system clocked at $h_{\text{clk}} = 200$ directly covers the frequencies of 13.35 MHz ($h = 28$) and 20.03 MHz ($h = 42$) and no further adaptation will be required to add it to both 20 MHz cavities. The signal processing can be similar to the one of the 10 MHz one-turn delay feedback.

A special beam loading compensation feedback has been successfully tested for the Finemet cavity (see the section ‘Beam loading compensation’). Keeping in mind that the impedance curve of the 20 MHz cavities also remains fixed, the signal processing for this beam loading compensation feedback based on a bank of programmable narrowband filters may be the better choice to achieve maximum impedance reduction. This alternative will be studied in comparison to the one-turn delay feedback.

As the feedback for beam-loading reduction, the digital voltage-control loops can be identical to the new voltage control of the 10 MHz cavities.

40 MHz and 80 MHz RF cavities

The 40 MHz and 80 MHz RF cavities have slow mechanical short circuits. They provide excellent shielding of the cavities from the beam pipe when closed, but cannot be operated in PPM mode within the cycle. A cavity with open gap is hence affecting all beams during the complete cycles. Their resonance frequencies are fixed to the 84th (40.0529 MHz) and 168th (80.1058 MHz) revolution frequency harmonics for protons at flat-top energy. During acceleration the spectral components at $91f_{\text{rev}}, \dots, 84f_{\text{rev}}$ (40 MHz cavity) and $183f_{\text{rev}}, \dots, 168f_{\text{rev}}$ (80 MHz cavity tuned for proton operation) of the beam sweep through the cavity resonance. This does not perturb the beam during major parts of the cycle, as the bunches are relatively long; however, during transition crossing significant beam-induced voltages are observed in 40 MHz and 80 MHz RF cavities and longitudinal coupled-bunch instabilities are enhanced during acceleration on the flat top by the presence of these high-frequency cavities with open gaps [87].

The cavities are already equipped with a strong direct RF feedback [81, 82], which is also being revised in the framework of the LIU project, but, to reach even further reduction of their impedance, a comb-filter feedback with a one-turn delay will be added.

For the one-turn delay feedback of the 40 MHz cavities several implementation options based on the feedback module developed for the 10 MHz cavities are being investigated:

- analogue I/Q demodulation to an intermediate frequency, separate treatment of I and Q channels and analogue remodulation back to 40 MHz;
- direct sampling of the RF signal at 40 MHz and similar signal processing as for the lower frequency cavities, increased clock harmonic and replacement of the ADCs on the feedback board by faster ones;
- undersampling of the RF signals at 40 MHz and 80 MHz.

For the first choice, an I/Q demodulator and modulator prototype has been recently developed [88]. An existing beam-synchronous clock at $128f_{\text{rev}}$ internally generates phase-shifted local oscillators at $64f_{\text{rev}}$ (27.9 to 40 MHz). The intermediate frequency becomes $(84-64)f_{\text{rev}} = 20f_{\text{rev}}$ (8.7 to 9.5 MHz),

which is well within the frequency range to easily sample I and Q channels separately. The treatment of each channel (digital comb and notch filters combined with a one-turn delay) is equal to the signal processing of the feedback for the lower frequency cavities. The clock frequency for digitization could again be $128f_{\text{rev}}$. Remodulation back to 40 MHz provides the signal to be injected in the amplifier chain of the cavities.

The one-turn delay feedback systems for the 10 MHz cavities are presently clocked at $200f_{\text{rev}}$ (87.3 to 95.4 MHz), but it is envisaged to raise the clock harmonic to $256f_{\text{rev}}$ (111.8 to 122.1 MHz) to simplify the integration of the RF sources. The latter clock frequency harmonic would be sufficiently high to directly sample the signals of the feedback for the 40 MHz cavities. In this case analogue I/Q demodulation with associated amplitude and phase errors would not be required, resulting in a fully digital system, using only the existing feedback module for the one-turn delay feedback.

A decision on the implementation option will be taken, once conclusive tests with the 10 MHz one-turn feedback at the clock harmonic 256 have been performed. Again, a beam loading compensation feedback based on a bank of narrowband filters (see the section ‘Beam loading compensation’) could be an alternative to the one-turn delay feedback with the advantage of precisely controlling the notch phases while sweeping through the fixed cavity resonance.

Digital voltage-control loops can be easily added following the design choice for the beam loading reduction feedbacks.

Longitudinal beam control

The present longitudinal beam control for the LHC-type beams in the PS is composed of a mixture of analogue and digital electronics. The distribution of the uncorrected revolution frequency from the magnetic field measurement is already implemented fully digitally, as well as the drive RF signals to the cavities, which are generated from direct digital synthesizers (DDSs) [89]. The RF signals for the cavities of the main 2.8–10 MHz accelerating system are generated by a master–slave DDS system with so-called multiharmonic sources as slave synthesizers [90]. Following recent improvements [91], these synthesizers are programmable in harmonic number and phase along the cycle, resulting in full flexibility for advanced RF manipulations. The receivers for all beam phase and radial loops are still analogue superheterodyne receivers, requiring conversion of the input signals to a fixed intermediate frequency (10.7 MHz or 21.4 MHz) and subsequent phase detection.

Although the existing longitudinal beam control copes well with the present LHC-type beams, its flexibility and potential for future improvements remains limited. Additionally, reliable operation cannot be guaranteed on a time-scale of the next 10 to 20 years due to lack of spares and obsolete components. In addition, its operation and maintenance present a manpower-intensive task.

Fully digital technology has already been applied to the RF beam control of the Low Energy Ion Ring (LEIR) machine [92] and a second generation has been installed in the PSB during LS1 (see Section 3.5.5).

Several implementation options for a digital beam control in the PS are presently being considered:

- a digital beam control based on the hardware for the PSB (re-use of hardware only or both hardware and software, see Section 3.5.5) with additional developments for the high-frequency cavities;
- a beam control based on the one-turn delay feedback board or development of an enhanced version thereof, again with additional developments for the high-frequency cavities;
- the development of an improved one-turn delay feedback board, allowing higher clock frequencies and then covering all high-frequency cavities in the PS.

With the renovation of the voltage- and phase-control loops (see the section ‘Digital voltage- and phase-control loops’ for 10 MHz), each cavity will require a digital voltage programme. The generation

of the drive RF signal will be either moved directly into the hardware of the voltage and phase control or kept centrally with the beam control. The distributed solution with the RF source added to the feedback module of each cavity is presently envisaged for the PS 10 MHz RF system, requiring the synchronization of RF sources physically distributed over several racks and at least two buildings.

Beam control for the 10 MHz cavities

The 10 MHz RF system as the only system allowing acceleration requires sweeping drive signals in a frequency range of 2.8 MHz to 10 MHz at various harmonic numbers. To allow RF manipulations, all drive signals to these cavities must be derived from a common clock to guarantee that they remain synchronous with respect to the revolution frequency. The present multiharmonic source installation [90] operates with a tagged clock at the 128th harmonic of the revolution frequency, but the new one-turn delay feedback and the coupled-bunch feedbacks already use higher clock frequency harmonics of $h_{\text{clk}} = 200$ and $h_{\text{clk}} = 256$ (clocks without tagging). The beam detection for the beam phase and radial loops usually takes place at the same or a nearby harmonic as the RF, so the input frequency range for the receivers is again 2.8 MHz to 10 MHz. With the present beam-control system, phase and radial position measurements take an average of several turns, which unfavourably decreases the signal-to-noise ratio of low-intensity single bunches. Therefore, gating of the receivers with revolution frequency is being considered to increase the signal-to-noise ratio. In the digital beam control not only the drive signals will be synchronous with the revolution frequency, but also the numerical local oscillations for down conversion in the receivers, which simplifies the generation of bunch synchronous gates.

Beam control for the 20, 40 and 80 MHz cavities

The 20 MHz, 40 MHz and 80 MHz cavities are only required on the flat top of LHC-type beams and they are hence operated in narrow frequency ranges. For proton beams, only the 20 MHz and 40 MHz RF systems require a complete beam control with a beam phase loop locking them to the beam. Since the 80 MHz cavities are only needed during a fraction of the bunch rotation, their drive signal can be directly derived from the signal for the 40 MHz RF system. Assuming a clock harmonic of $h_{\text{clk}} = 256$ (122.1 MHz at the flat top) as already set up for the coupled-bunch feedback, the beam controls at both frequencies 20 MHz and 40 MHz are not expected to require any analogue down conversion. However, tests with the existing one-turn delay feedback board will be performed to confirm the assumption.

A different approach must be adopted for the beam phase loop locking the beam to one 80 MHz ($h_{\text{RF}} = 169$) RF cavity for adiabatic bunch shortening prior to extraction. This phase loop is only needed for ion beams on the flat top prior to the transfer to the SPS. Analogue I/Q down conversion to an intermediate frequency, an undersampling scheme or a higher sampling clock frequency ($h_{\text{clk}} = 512$) are being investigated. In addition, the ion phase loop at 80 MHz would profit significantly from a bunch synchronous gating of the beam signal. Only one, two or four out of 169 buckets are occupied, causing an important loss of signal-to-noise ratio with the present configuration of the phase loop.

Beam control for the 200 MHz cavities

With the upgrades of the LIU project, the function of the 200 MHz RF system in the PS remains unchanged. It only serves for the longitudinal emittance blow-up and to provide a 200 MHz structure during the five-turn extraction to the SPS. A complete beam control, including a beam phase loop, is therefore not needed for this system. The RF source generating a phase-modulated 200 MHz signal has been renovated recently [93]. However, seeing that the voltage-control and beam-frequency-control loops are still analogue, they should also be migrated to a fully digital implementation. At a RF frequency of 20 MHz, down conversion to an intermediate frequency, most probably in the 20 MHz range, is required.

Low-level RF system for the coupled-bunch feedback

As described in Section 4.5.1, a new Finemet cavity has been installed during LS1 to serve as a wideband kicker for the coupled-bunch feedback. Previously only two coupled-bunch modes could be damped simultaneously using two accelerating cavities as longitudinal kickers, while more modes were observed (see Section 4.2.7).

The low-level RF system for the Finemet cavity will detect coupled-bunch oscillations of all possible dipole modes ($n = 1, \dots, h_{RF}$, $h_{RF} = 21$) and generate a corresponding voltage at the synchrotron frequency sideband to damp them. As explained in Section 4.2.7, different frequency ranges for detection (from $11f_{rev}$ to $21f_{rev}$) and feedback kick (from f_{rev} to $10f_{rev}$) have been selected. This avoids the need to extract the synchrotron frequency sidebands close to the first few harmonics of the revolution frequency, while the Finemet kicker cavity can operate in an optimum frequency regime for this cavity type.

Additionally, the gain of the analogue direct wideband feedback around the amplifier of the Finemet cavity remains limited due to the large bandwidth requirements and its inherent delay. A dedicated low-level RF feedback has been foreseen, reducing the cavity impedance only close to the harmonics of the revolution frequency. The low-level RF part for the coupled-bunch feedback system installed during LS1 must therefore provide two major functionalities:

- i) reduce beam loading by impedance reduction of the Finemet-type wideband kicker cavity at the revolution frequency harmonics;
- ii) detect and damp synchrotron frequency sidebands associated to the presence of coupled-bunch oscillations.

The low-level RF system for the new coupled-bunch feedback will use the feedback board (Section 4.5.3.2) originally developed for the one-turn delay feedback, avoiding the need for dedicated hardware. The relevant frequency range of up to about 20 MHz can be covered by direct analogue-to-digital conversion.

Beam-loading compensation

The beam loading compensation feedback should provide an impedance reduction of the Finemet cavity by about 20 dB at ideally all revolution frequency harmonics up to 20 MHz. This reduction in addition to the gain of the direct RF feedback reduced the impedance of the one cell of the Finemet cavity to a few ohms, the same order of magnitude as, e.g., a WCM. Such a longitudinal impedance is not only considered insignificant to the longitudinal beam stability, but it also reduces the beam-induced voltage at the cavity gap and hence at the output of the transistor amplifier, which is directly coupled to the gap. It is important to point out that the longitudinal beam stability should not be compromised even in the case of the direct feedback alone [94]; however, the beam-induced voltage would exceed the safe limits at the output of the power amplifier (see Section 4.5.1).

Three different options have been investigated for reducing beam loading in the Finemet cavity: FF, one-turn delay feedback and a bank of narrowband filters. The first technique, FF, has been successfully tested with a PSB prototype Finemet cavity cell, where six harmonics of the revolution frequencies were damped with low-level RF electronics developed for the JPARC facility [95]. The achieved reduction of the beam-induced voltage (>26 dB) is well within the requirements but however difficult to evaluate without beam. A classical one-turn delay feedback [84] as foreseen for all other cavities within the LIU project (Section 4.5.3.2) has been considered as a second option. While being an excellent choice for cavities with changing impedance (as for the ferrite-loaded 10 MHz cavities) thanks to the relatively few parameters for its adjustment, it implies the same gain of the feedback electronics at the several revolution frequencies. Additionally, the delay setting to complete one revolution period is the same for all revolution frequencies within that bandwidth of the cavity. Seeing that the delay of the

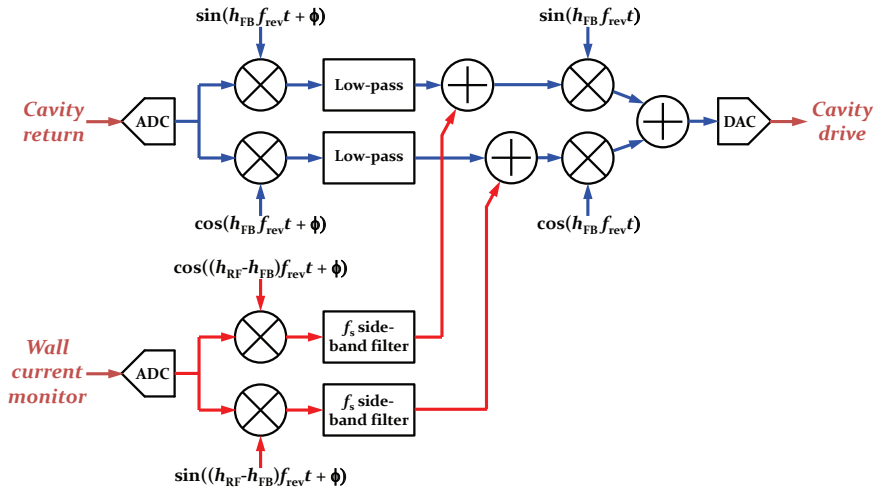


Fig. 4.83: Combination of beam loading compensation feedback (blue) and synchrotron frequency sideband processing for coupled-bunch damping (red).

Finemet cavity varies especially in the low-frequency regime, a sophisticated phase-compensation filter would be required to achieve high gain at large bandwidth.

It has therefore been suggested to compensate the beam-induced voltage by a bank of narrowband filter feedbacks [96], which damps each revolution frequency harmonic individually. With this configuration the gain, delay and phase are adjustable separately for each harmonic and its characteristics can be adapted to the impedance and delay behaviour of the Finemet cavity. Obviously, this flexibility comes at the expense of many parameters to be adjusted during setting up.

Following its digitization, the cavity return signal is firstly numerically down converted (in I and Q) to a zero intermediate frequency. A series of low-pass filters in the I and Q channels removes all components beyond the bandwidth (a few kHz) of the pass-band around the revolution frequency harmonic. The low-pass-filtered signal is then up converted back to its initial frequency. The harmonic number of this narrowband filter is selected by the numerical local oscillators for down and up conversion. The phase of the these numerically controlled oscillators comfortably adjusts the phase of the narrowband filter and even a virtual delay, τ , has been implemented by sweeping the phase according to $2\pi h f_{\text{rev}} \tau$. Multiple numerically controlled oscillators can be operated at different revolution frequency harmonics, synchronous with a common revolution frequency. This is needed for the coupled-bunch feedback part, where down and up conversion will be at different revolution frequency harmonics.

A prototype beam-loading compensation feedback has been tested around the Finemet cavity with low-intensity beam in 2014 and the expected reduction of the beam-induced voltage has been observed simultaneously at low (f_{rev}) and high frequencies (20 MHz). This compensation was observed from flat bottom to flat top, showing that the tracking of the virtual delay with the sweeping revolution frequency works correctly.

Coupled-bunch-instability damping

The detection of the synchrotron frequency sidebands indicating coupled-bunch oscillations will be implemented very similarly to the down conversion of the gap return signal. The beam signal from a WCM is again down converted in I and Q, filtered and up converted to then drive the Finemet cavity as longitudinal feedback kicker. Figure 4.83 shows a schematic view of a single branch of the coupled-bunch feedback, indicating the beam loading compensation filter (blue) and the contribution from the coupled-bunch feedback (red). In total 10 branches will be required, all implemented fully digitally on the same feedback board.

Following first tests with beam in 2014, the coupled-bunch feedback will be commissioned in 2015.

4.6 EC studies in the PS

4.6.1 Introduction

EC has been observed during normal operation of the PS, but without causing any degradation of the beam quality, since it appears only during the last stages of the cycle of the production of the LHC-type beams and the duration of the interaction with the beams is not long enough to trigger any instability; more details are given in Section 4.2.6. However, it is not yet clear whether the beams for the upgrade will be intrinsically stable. A series of machine and simulation studies has been carried out to identify the EC effects in the PS during the last few years [39, 97, 98]. This section starts with a short introduction of the existing EC measurement set-ups installed in the straight sections of the PS and then focuses on the new development of the EC measurement set-ups to be installed in the selected PS magnet during LS1. Considering the geometry and space limitation in the PS main magnet, two measurement developments have been discussed, carefully studied and presented.

4.6.2 The existing EC set-up in the PS

The first EC set-up in the PS was installed in straight section (SS) 98 in 2007. It consists of an elliptical vacuum chamber of bare stainless steel with dimensions $1050 \times 146 \times 70$ mm 3 . It is equipped with two button PUs on the top of the vacuum chamber; one Penning gauge installed close to the PUs and one special antechamber for a clearing electrode (stripline electrode) without aperture reduction (Fig. 4.84). The second set-up was installed in PS SS84 in 2008. Presently the vacuum chamber is coated with amorphous carbon. The details of the set-up, as well as the previous measurement results, can be found in Ref. [39].



Fig. 4.84: Picture of the existing EC experiment installed in PS straight section 98, containing two shielded button PUs, a shielded Penning gauge, a clearing electrode and a small dipole magnet [39].

4.6.3 New proposals for EC studies in the PS magnet

EC build up has successfully been measured and validated in the straight sections of the PS [39]; however, no direct diagnostics has been implemented inside any main magnet in the PS to gain a full understanding of the observed phenomena. According to the simulations, a dipole in a straight section does not represent the real situation in a combined function magnet due to the different geometries of the chambers and different magnetic fields. To be able to observe EC inside a combined function magnet of the PS is

therefore necessary in order to provide a prediction of the EC build up distribution in the PS magnets for higher intensity beams in the frame of the upgrade programme as well as validation of the EC simulation models and codes.

Most experiments either use retarding field analysers, button-type PUs (as the existing EC measurement set-up) and stripline electrodes to detect the electrons and beam-induced signals locally, or use microwave transmission or RF phase shift versus total beam intensity to determine the integrated EC density over a long section. Considering the geometries and space limitation of the PS magnet vacuum chamber, two measurement proposals have been considered and are discussed here.

4.6.3.1 Development 1: button-type PU in the PS magnet

By using the same principle as the existing EC monitor in the PS straight section, a similar shielded PU is planned to be installed. The ideal location to directly measure the EC density inside a magnet vacuum chamber is on the top/bottom of the vacuum chamber, perpendicular to the magnetic field. However, due to space limitation, the button-type PU together with the DN40 flange placed 30 degrees to the bottom part of the vacuum chamber will be installed in the horizontal direction where the only opening of the magnet coil is, as illustrated in Fig. 4.85. The PU, a ceramic block consisting of 96% Al_2O_3 coated with a thin layer of solvent-based Ag painting to create electrical conductance, is shielded from the main chamber with a 0.2 mm thick stainless steel sheet with a series of holes (1 mm diameter and 2 mm pitch) providing a geometrical transparency of 7%. The stainless steel shield is electrically grounded to the magnet vacuum chamber. The distance between the tip of the PU and the centre of the vacuum chamber is 12 mm. During the EC measurements, the displacement of the LHC beams can be arranged by the radial steering up to a maximum of 30 mm from the centre of the chamber towards the PU to maximize the electron-density signal. The first design version is provided in Fig. 4.85. Since the button-type PU is installed behind a shielding grid, it should not affect the beam-coupling impedance of the chamber. As seen in Fig. 4.85, the gap between the magnet coil is only 90 mm and this leads to a slight practical difficulty to insert and mount a DN40 flange into the magnet vacuum chamber. Therefore, a flexible stainless steel arm welded on the DN40 flange is introduced to make the insertion possible. The stainless steel arm can be bent and the distance between the flange and the grid to the vacuum chamber can still be well defined and fixed.

4.6.3.2 Development 2: EC measurement via electron–photon emission

Theory

Instead of directly measuring the electron current in the vacuum chamber, a new method to measure EC density via electron–photon emission is under development. This is based on cathodoluminescence, one of the phenomena that occurs when electrons are impinging on a surface, as demonstrated in Fig. 4.86a. The phenomenon of cathodoluminescence is illustrated in the energy diagram of Fig. 4.86b. A beam of electrons of energy E (hundreds of eV) is incident upon a solid face. After entering the system, the primary electrons subsequently generate secondary electrons. The amount of the secondaries generated by the primaries depends on the secondary electron yield of the surface and these electrons either escape from the surface to be detected as secondary electrons or fall back into the system and further decay, either radiatively or non-radiatively, to states at lower energy. If the decay is radiative the emitted photons can be detected. This process is known as inverse photoemission and has been intensively studied in the late 1970s. By using inverse photoemission spectroscopy (IPES), the studies of inverse photoemission of metals were carried out [99, 100]. The typical cathodoluminescence spectrum of clean Cu has been demonstrated by several authors [101, 102], as shown in Fig. 4.87. Both spectra are corrected for the system response and the position of the peaks does not change with energy.

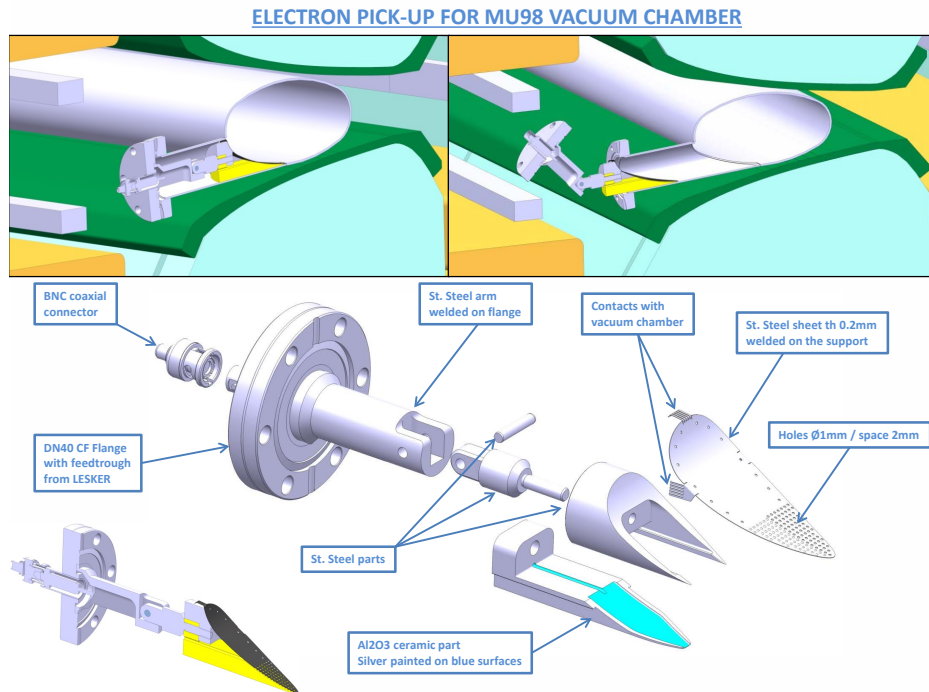


Fig. 4.85: Draft design of the MU98 vacuum chamber equipped with the shielded button-type PU (drawing by T. Capelli and C.F. Eymin).

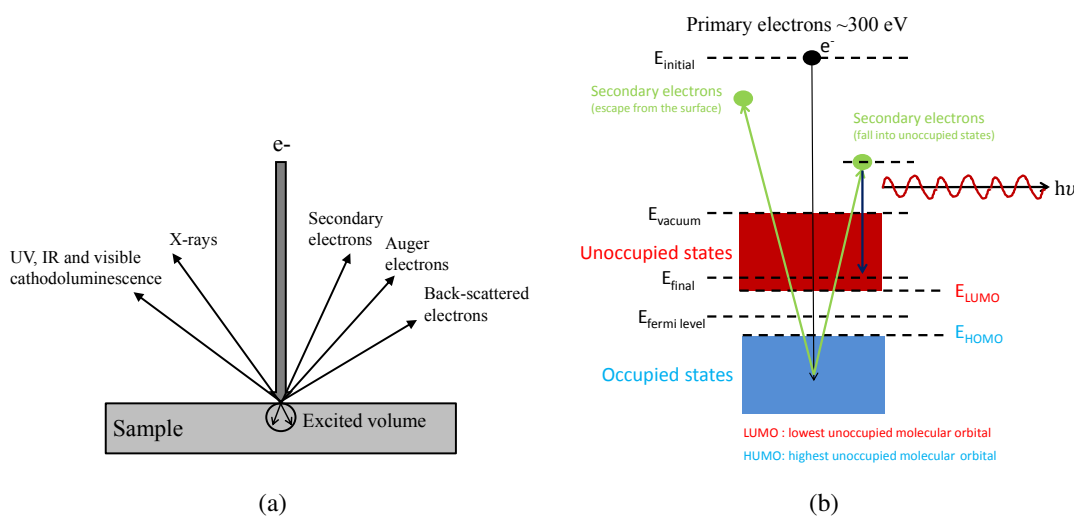


Fig. 4.86: (a) Phenomenology of electrons impinging on a surface. (b) Schematic of the principle of cathodoluminescence from a metal surface.

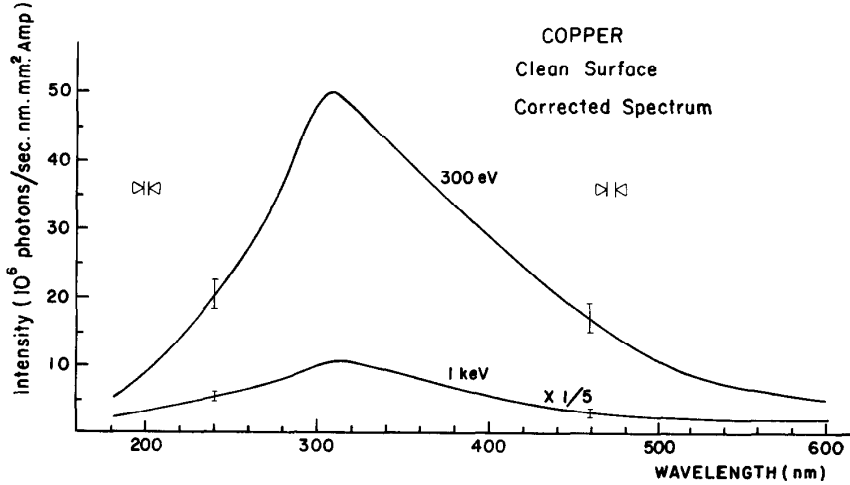


Fig. 4.87: Corrected cathodoluminescence spectra of clean Cu at electron energies 300 eV and 1 keV [101].

Experimental set-up in the laboratory

Unfortunately, no cathodoluminescence data has been found for stainless steel or other alloys that are normally used as the main material of vacuum chambers in the PS and other accelerators. In order to understand the electron–photon emission induced by electrons and estimate the radiation yield for the samples of our interest, we have built our own experimental set-up in the laboratory to perform cathodoluminescence measurements of various metal surfaces, similar to the one demonstrated in Ref. [101].

Figure 4.88 shows a schematic diagram of the experimental set-up in the laboratory for cathodoluminescence measurements in order to validate the photoemission yield on stainless steel surfaces and other alloys. The electron gun (Kimball Physics Inc. ELG-2) and the sample are placed inside the vacuum chamber at 10^{-9} mbar. The optical collimating lens, optical fibre, photospectrograph (Shamrock 303i) and CCD detector (iDus 420) provided by Andor are installed in air. To reduce the amount of background light coming from the electron gun, a low emission temperature barium oxide (BaO)-coated disc cathode to the electron gun is used. The BaO cathode is chosen for its low operating temperature of $T = 1150$ K aiming to minimize the thermal spread of electron velocities and avoid excess stray light in the near-ultraviolet region. The significant increase of photons in the measurement system after switching on the electron gun confirmed by the experimental data appears above 600 nm due to the black-body radiation from the BaO cathode and the investigated range of interest (200–600 nm) should not be influenced. The electron beam can be prevented from arriving on the sample surface either by using a grid with potential to block the beam inside the electron gun or by deflecting the beam onto the collector surrounding the electron gun, which is a copper tube biased with +45 V, as illustrated in Fig. 4.88. Both cases have been investigated to identify the ‘true’ background for the measurements. The latter was chosen to be presented as our standard background. The CCD detector is cooled using a thermoelectric (TE) cooler to -60°C in order to decrease the dark current and the dark count of the detection system is about 10 counts/s. The measurement system is unfortunately not completely screened and even minor variations of the light outside the vacuum chamber can therefore be detected by the CCD detector. To keep the experimental area as dark as possible is hence important to obtain good measurement results.

Experimental results in the laboratory

The detailed description of the experimental set-up as well as the complete measurement results of various metals and alloys is demonstrated elsewhere [103]. In this section, only the main results of the

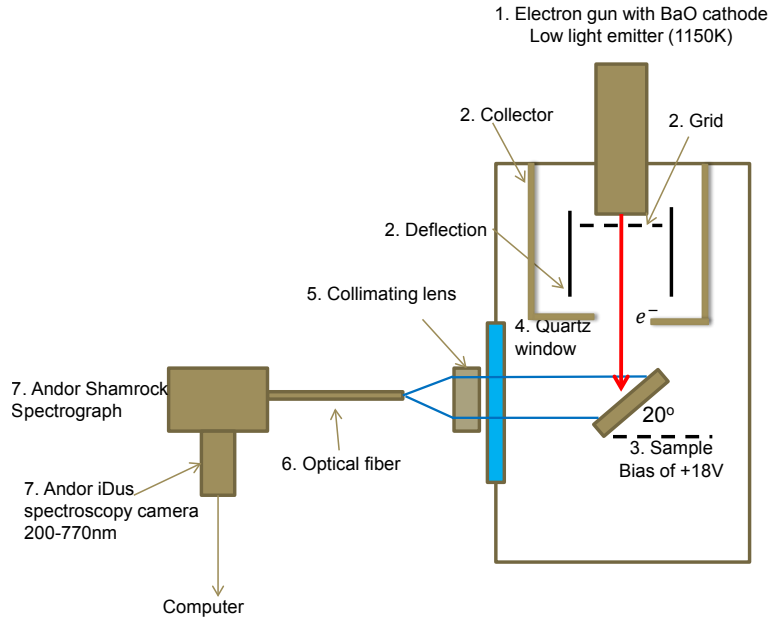


Fig. 4.88: Schematic diagram of the experimental set-up which implements the concept displayed in Fig. 4.86.

measurements obtained on oxidized stainless steel directly simulating the application for the EC measurements in the PS main magnet are presented.

The cathodoluminescence spectra of an oxidized stainless steel surface, uncorrected for the system response, are shown in Fig. 4.89. The bombarding electron energy is 300 eV and the current density on the stainless steel sample used for the investigations is $3 \mu\text{A}$ per 2 mm^2 and $9 \mu\text{A}$ per 2 mm^2 , respectively. The results were obtained by averaging 10 measurements of 60 s integration time with five accumulations. Accumulation must be performed due to the cosmic ray removal option in the CCD detector during the relatively long integration periods. Each scan is compared with the previous one, for the presence of unusual features, i.e. cosmic rays passing through the CCD and producing photoelectrons in a very small area due to low read noise of the CCD. The photon counts are clearly proportional to the electron current on the sample, as compared in Fig. 4.89(a) and 4.89(b).

In order to be confident that the experimental results can be explained on the basis of ideas concerning cathodoluminescence caused by recombination radiation, it is important to estimate our experimental radiation yield and compare it with the theoretical ones calculated by other authors [101, 104]. As explained in Ref. [104], the radiation yield of recombination radiation of light in a metal is expected to be in a range of 10^{-9} – 10^{-11} photons/electron, which is in reasonable agreement with the experimentally estimated yield on stainless steel of 5×10^{-11} photons/electron for $E = 300$ eV. The radiation yield on Cu at a bombardment energy of 300 eV is also estimated to be 10^{-11} photons/electron, as presented in Ref. [103]. These values combined with the EC-simulation data provided in Ref. [105] are later used to estimate the amount of photons that can be detected through a quartz window of DN63 size outside the PS main magnet vacuum chamber, as presented in Section 4.6.4.

4.6.4 Implementation in the PS

Magnet unit 98 (MU98), which consists of a standard stainless steel vacuum chamber, was chosen for the installation of EC monitors due to several reasons, such as the presence of low radiation dose in Sector 9 in the PS ring and the present close location to the existing electron monitor in SS98. Two flanges (one of DN35 for installation of a shielded PU and the other of DN63 for installation of an optical window)

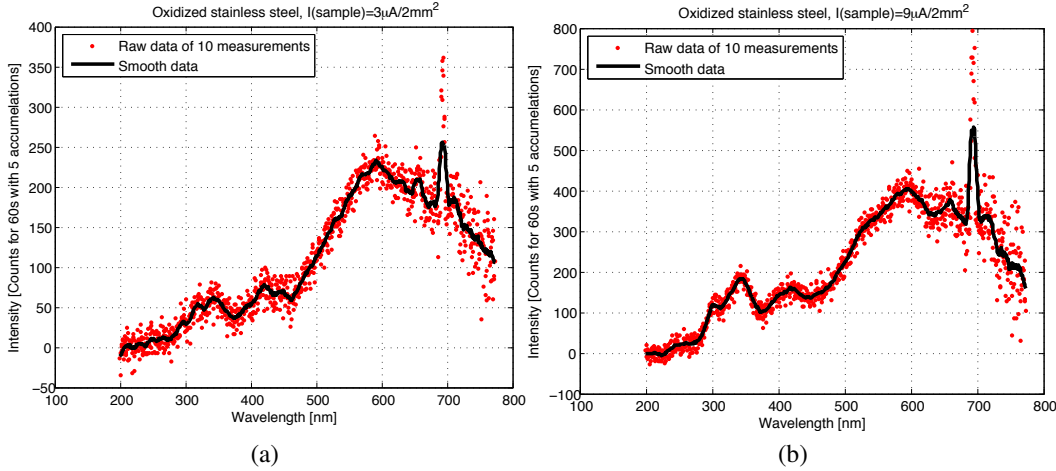


Fig. 4.89: Cathodoluminescence spectra of an oxidized stainless steel surface at electron energy of 300 eV. The spectra are uncorrected for the system response. (a) The measured current density on the sample is $3 \mu\text{A}$ per 2 mm^2 . (b) The measured current density on the sample is $9 \mu\text{A}$ per 2 mm^2 .

are added to the MU98 vacuum chamber, as shown in Fig. 4.90.

For the shielded PU, the similar electronics used for the existing PU in the SS98 will be applied for the measurement. Therefore, the solution is quite trivial.

However, for the photon detection in the PS, a detailed study to estimate the photon-detection yield as well as how to implement the electronics for the measurement in practice is needed. From the experimental radiation yield obtained in the laboratory combined with the results from the EC simulation provided in Ref. [105], the amount of the photons generated by the EC can easily be calculated and the estimated result is shown in Table 4.20.

Table 4.20: Estimation of the photons generated by EC with the LHC-type beams in the PS main magnet vacuum chamber.

EC bombardment area	$8.4 \times 10^2 \text{ mm}^2$
EC density	$1 \mu\text{A}/\text{mm}^2$
The number of electrons generated	$5.25 \times 10^{16} \text{ electrons/s}$
Experimental radiation yield of stainless steel	$5 \times 10^{-11} \text{ photons/electron}$
The number of photons emitted by the electrons	$2.625 \times 10^6 \text{ photons/s}$

Simulations by the Monte Carlo method have also been carried out to estimate the photon detection yield through the quartz window of DN63 size outside the PS main magnet vacuum chamber. By applying a high-reflectivity (about 85% for UV-VIS photons) coating in the flange, the photon detection yield on the quartz window can be improved by a factor of six according to the Monte Carlo simulation. The high-reflectivity coating is a Mylar foil with a reflective layer of Al/MgF₂ [106], which can easily be bent and inserted into the flange. This coating has proven high reflectivity in the UV range due to the non-oxidation of the aluminium layer prevented by MgF₂.

By assuming that the number of the photons emitted by the EC in the vacuum chamber is 2.625×10^6 photons, as demonstrated in Table 4.20, the number of the photons that can be detected through the quartz window outside the vacuum chamber can be estimated to be 2.1×10^5 photons/s. Since the EC development only occurs during the last 40–50 ms of the PS cycle, we estimate the photons that can be detected outside the vacuum chamber to be about 1×10^4 , which is a quite high value that can easily be measured with correct instrumentation.

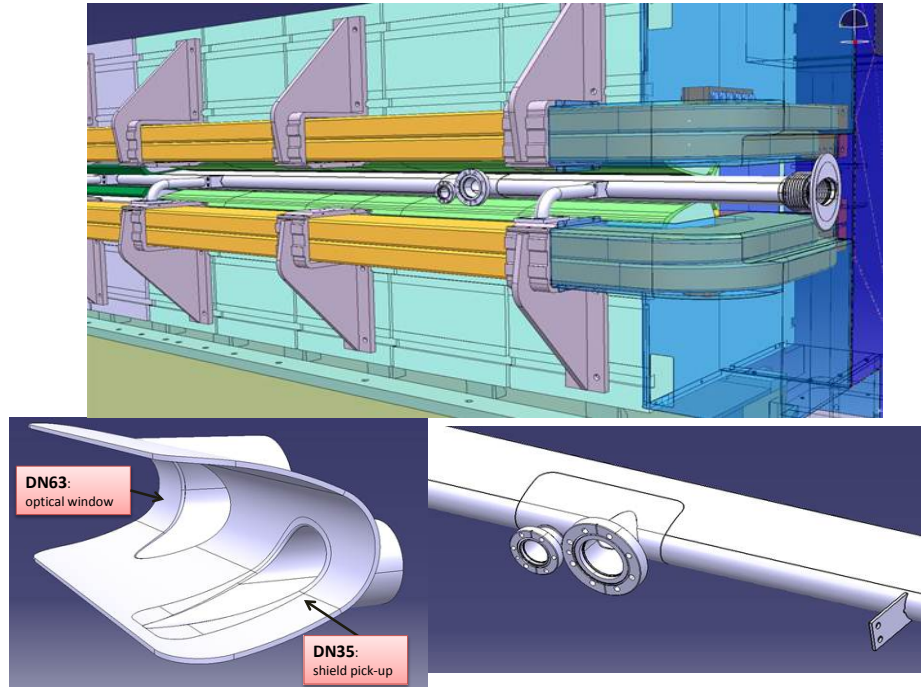


Fig. 4.90: Drawing of the MU98 equipped with two flanges for installation of the new EC monitors: DN35 for installation of the shielded PU and DN63 for installation of the optical window for detection of inverse photoemission (courtesy of T. Capelli).

The photon detector that will be used for the PS application will be a MCP-PMT of type PP0365G with an active area of 18 mm in diameter provided by Photonis. The photons emitted in the vacuum chamber will first go through the DN63 quartz window and then be collected through an UV lens that focuses the light into the MCP-PMT. This type of MCP-PMT has earlier been used at CERN. It has superior magnetic field immunity and is not expected to show any problem in the PS main magnet with a maximum value of 1.2 T. The final instrumentation for the MCP-PMT is still under development and will be reported soon.

4.7 Impedance models

4.7.1 Longitudinal impedance

The longitudinal coupling impedance is an important quantity to characterize the electromagnetic interaction of a particle beam with the surrounding elements, like kickers, radio-frequency (RF) cavities, diameter changes of the beam pipe, bellows and many other installations close to the beam. In particular, collective effects, triggered by these self-induced fields, may play an important role in beam stability and machine performance. Since a significantly higher beam intensity is planned for the PS in the framework of the LIU project, wake fields are expected to increase their influence on the beam dynamics, and their evaluation is important.

Due to the different effects on the beam dynamics, it is convenient to divide the study of the longitudinal coupling impedance into the broad- and narrowband ones. Concerning the broadband impedance, it influences the single-bunch dynamics and could lead to a bunch lengthening, an asymmetry in the bunch distribution and, if the effect is strong enough, even to microwave instability [107, 108], characterized by an increase of longitudinal emittance, thus deteriorating the beam characteristics. Also resonant modes, produced by narrowband impedances, are important to evaluate since they could produce the coupled-bunch instability, observed in the PS above transition energy [47], and which constitutes a ma-

ajor limitation in the beam intensity for this machine. The 10 MHz accelerating cavities are supposed to be, in this case, the main sources of the instability, and a detailed analysis of their impedance allows us to identify the main unstable coupled-bunch modes that should be damped by the longitudinal feedback.

4.7.1.1 Broadband impedance

In 2012 a measurement campaign [109], which has taken advantage of a better control of the longitudinal beam parameters, notably the capability of producing bunches with constant longitudinal emittance over a wide intensity range, has been carried out to determine the longitudinal broadband imaginary impedance of the PS.

The measurements, performed at a fixed momentum of $26 \text{ GeV}/c$ to minimize the effects of space charge and with a single-harmonic RF system at 40 MHz, used a single bunch with an intensity up to $N_p = 4.5 \times 10^{11}$ protons. The bunch was excited by white noise injected as an amplitude modulation of the voltage programme of the 40 MHz cavity, and a WCM (WCM95) was used to pick up the longitudinal beam signal. The spectrum of the incoherent quadrupole synchrotron frequency was then determined in amplitude and phase by the vectorial ratio of peak-detected beam signal and noise excitation and subsequent averaging over many individual acceleration cycles.

A typical averaged frequency spectrum is shown in Fig. 4.91.

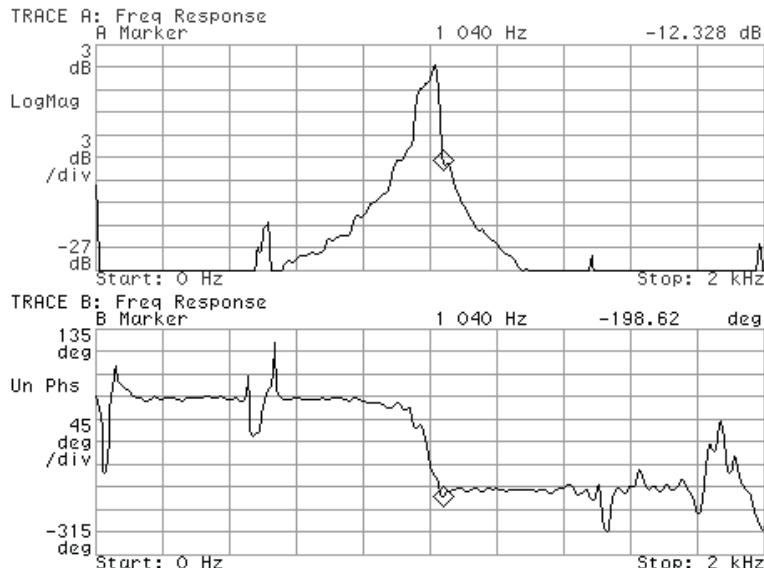


Fig. 4.91: Example screen-shot of amplitude and phase of the quadrupole beam transfer function for a bunch of about 9×10^{10} protons kept by 95 kV at 40 MHz. The diamonds indicate the zero-amplitude quadrupole synchrotron frequency.

The zero-amplitude quadrupole synchrotron frequency f_{2s} is given by the discontinuity of the phase curve following the 180° phase advance [110, 111], and it can be expressed as a function of the imaginary part of the broadband longitudinal impedance $\text{Im}[Z(p)]/p$. For a parabolic line density distribution, the relation is given by

$$\frac{f_{2s}}{f_{s0}} = 2 + \frac{12eN_p}{V_{RF}h \cos \phi_s \omega_0^2 \tau_b^3} \frac{\text{Im}[Z(p)]}{p} = 2 - \tilde{X} \frac{\text{Im}[Z(p)]}{p}, \quad (4.23)$$

where f_{s0} is the natural synchrotron frequency, V_{RF} the peak RF voltage, h the harmonic number, ϕ_s the synchronous phase ($\cos \phi_s < 0$ above transition), ω_0 the revolution frequency and τ_b the total bunch length.

Two series of single-bunch measurements at different RF peak voltages were made during two different MD sessions.

In Fig. 4.92, the measured quadrupole synchrotron frequency shift as a function of bunch intensity is shown, and from it an inductive broadband impedance of 18.4Ω has been obtained. This value is in agreement with previous measurements [112, 113].

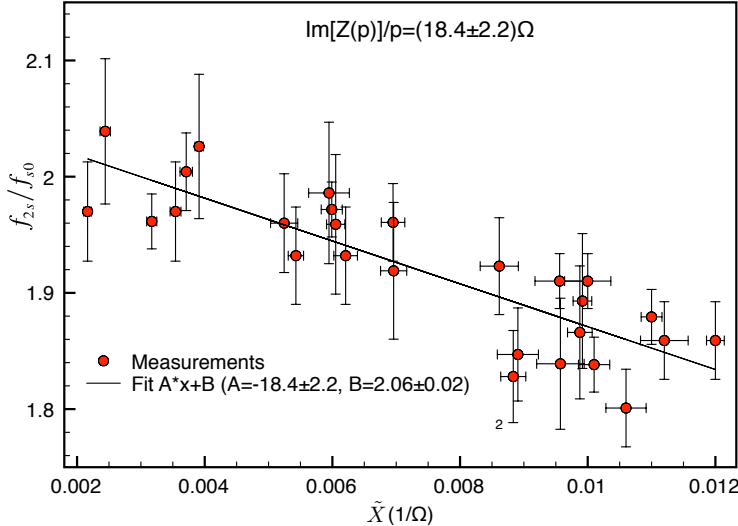


Fig. 4.92: Incoherent quadrupole synchrotron frequency shift obtained with the two sets of measurements.

The total longitudinal broadband impedance has also been evaluated by taking into account the individual contribution of what are considered the major sources of impedance: RF cavities, space charge, magnetic kickers, pumping ports, resistive walls, bellows and the many steps of the PS vacuum chamber. Concerning the RF cavities, the effects of the resonant modes due to the 10 MHz cavities (for a total of 10 cavities), one 20 MHz cavity, short circuited during the measurements, one 40 MHz, two 80 MHz and six 200 MHz cavities have been taken into account. All of them have been approximated by resonant oscillators, as their gaps are short compared to the bunch length and their first higher order modes are well above the fundamental resonance. Their contribution to the total machine broadband impedance is mainly resistive.

There are other sources of geometrical impedance, such as discontinuities of different kinds, shapes and sizes. We expect that they mainly contribute to the inductive part of the impedance, since the bunch spectrum is not able to excite diffracted fields propagating in the vacuum chamber. In Table 4.21 the contributions of the different elements to the machine impedance evaluated so far are summarized.

The study is still in progress and other contributions must be taken into account; however, the imaginary part of the total longitudinal broadband impedance estimated so far is close to the measured one. In order to compare the results, in Fig. 4.93 the analytical wake potential of a Gaussian distribution with $\sigma_G = 2.3$ ns and given by the sum of the several contributions is compared with the wake obtained by the measured inductive part of the impedance (\pm its uncertainty).

The total wake-potential budget can be approximated with a simple impedance model by observing that there is a small asymmetry in the wake, which is mainly due to the resistive contribution to the impedance of the RF cavities and the ferrite-loaded kickers. Of course, this contribution cannot be obtained with the measurements of the incoherent quadrupole synchrotron frequency shift, which gives only the imaginary part of the machine impedance. By using the Heifets–Bane model [114, 115], of which we maintain only the first two terms, the inductive and the resistive ones, with an inductance of $L = 5.86 \mu\text{H}$, which corresponds to $Z(p)/p = 17.5 \Omega$, and a resistance of $R = 316 \Omega$, which

Table 4.21: Impedance contribution of important machine elements evaluated at the bunch spectrum cut-off. For the RF cavities the fundamental mode parameters are reported, also by taking into account the fast RF feedback.

Machine element	$Z(p)/p$ at $\omega = 1/\sigma_G$
Space charge	$-1.9i\ \Omega$
Magnetic kickers	$(1.6+i\cdot 13.8)\ \Omega$
Pumping ports	$2.8i\ \Omega$
Resistive wall	$0.09(1+i)\ \Omega$
Steps	$0.96i\ \Omega$
Bellows	$0.85i\ \Omega$

f (MHz)	Q	R/Q (Ω)	Number of cavities	Comment
7.6	5	30	10	
20	4.6	43.5	1	Short circuited
40	70	33	1	
80	100	56	2	
200	130	28.5	6	

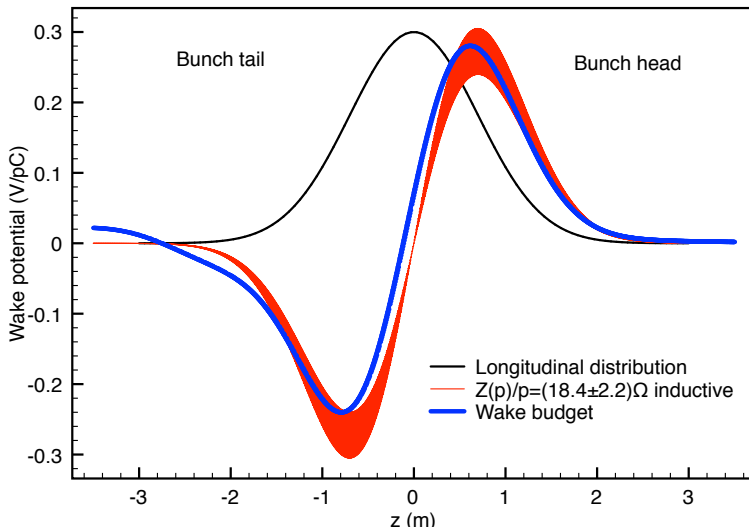


Fig. 4.93: Wake potential of a 2.3 ns Gaussian bunch given by the total impedance budget and by an inductive impedance model with $\text{Im}[Z(p)]/p = 18.4\ \Omega$.

corresponds to $Z(p)/p = 2.2\ \Omega$ if evaluated at the bunch spectrum cut-off, we obtain the wake potential represented by the black curve in Fig. 4.94. Also, a broadband resonator model can be used to fit the wake-potential budget with a resonant frequency of $f_r = 0.48$ GHz, $Q = 1$ and a shunt impedance of $R_s = 17.7$ k Ω , as shown by the red curve in the same figure. It is interesting to observe that this resonant frequency corresponds approximately to the frequency at which the real part of the kickers' longitudinal impedance has its maximum.

4.7.1.2 Narrowband impedance

Longitudinal coupled-bunch oscillations, which constitute an important limitation for the high-brightness beams accelerated in the CERN PS, are generated by narrowband impedances which produce long-range wake fields coupling the motion of multiple bunches over multiple turns. The principal source of this

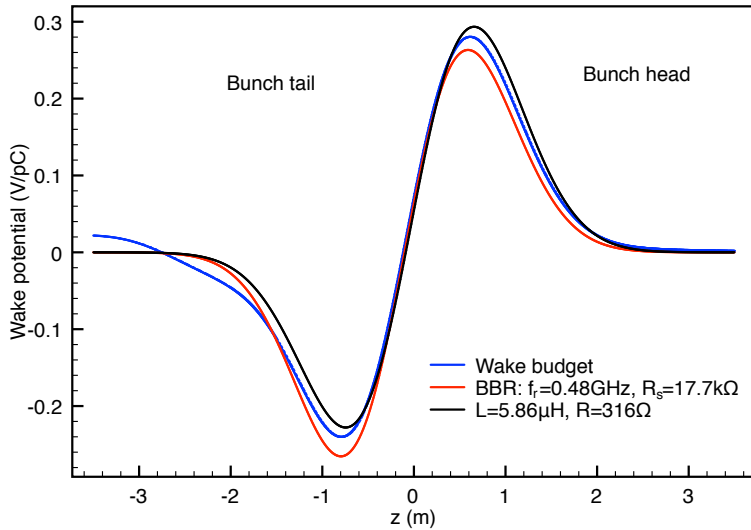


Fig. 4.94: Wake potentials of a 2.3 ns Gaussian bunch given by the Heifets–Bane model $Z(\omega) = (i5.86 \times 10^{-6}\omega + 316) \Omega$ and a broadband resonator with $f_r = 0.48$ GHz and $R_s = 17.7$ k Ω , compared to the total wake budget.

kind of impedance in the PS is supposed to be the fundamental mode of the 10 MHz cavities' system. Due to the feedback loop and the power amplifier, this impedance is not that of a pure resonator. A simplified model of the system, described in Ref. [47], is shown in Fig. 4.95.

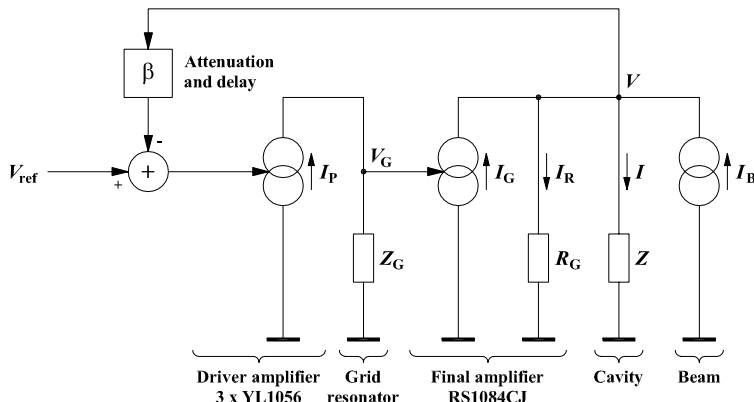


Fig. 4.95: Model of the 10 MHz RF cavity

According to the model, the impedance seen by the beam can be written as

$$Z_{\text{cav}} = \frac{1}{g_P g_G \beta Z_G + (R_G + Z)/(Z R_G)}, \quad (4.24)$$

where $Z_G(\omega)$ is the impedance of the grid resonator, g_P and g_G are the effective transconductances of driver and final amplifiers and β represents attenuation and delay of the feedback loop. The parameters of the impedance model have been evaluated by a fitting procedure to reproduce the measured open- and closed-loop transfer functions of 6 over the 10 cavities. The measurements were taken at harmonic seven ($f = 3.3$ MHz).

Coupled-bunch instability in the PS is observed above transition energy with harmonic 21, when the cavities work at 10 MHz. The impedance is supposed to remain the same as that of 3.3 MHz, just shifted in frequency, and its real part for the all 10 MHz cavities is shown in Fig. 4.96. In these conditions

the coupled-bunch unstable modes resulting from a time-domain simulation code [116] and produced by this impedance with uneven fill of 18 bunches over 21 buckets are the first ones, starting from mode $n = 1$ with the strongest growth rate. This analysis is in agreement with measurements carried out in 2010 [48].

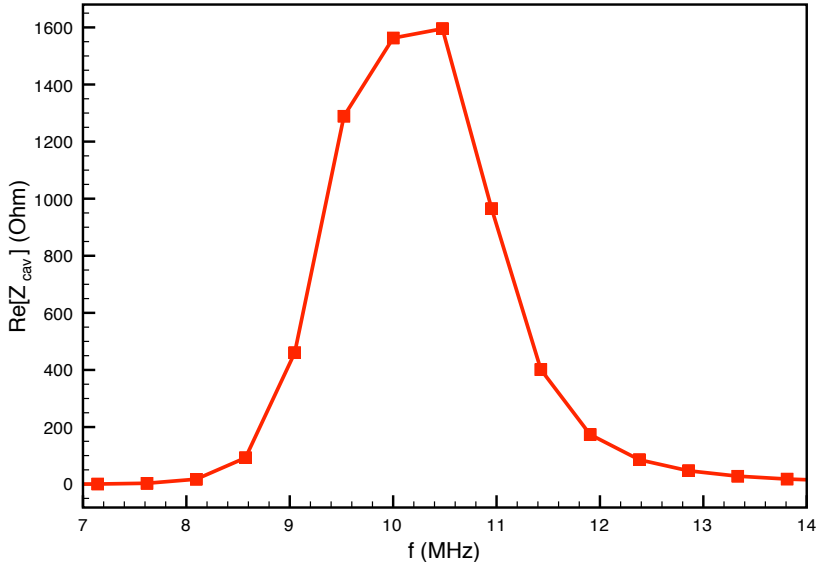


Fig. 4.96: Real part of the impedance of all the 10 MHz RF cavities

Other sources of impedance that could produce coupled-bunch instability are under investigation to determine their danger with respect to the 10 MHz cavity system, such as the 20 MHz, 40 MHz and 80 MHz cavities. A study has to be carried out also for the Finemet cavity [117] used as damper for the frequency-domain feedback system. Its longitudinal impedance, shown in Fig. 4.97, has a broad band so that stable and unstable frequencies generally tend to compensate each other, without exciting coupled-bunch oscillation modes. However, a more detailed analysis and the cavity impact on the beam dynamics must be evaluated.

4.7.2 PS transverse impedances: current and future

4.7.2.1 *Introduction*

As the beam intensity increases, the beam can no longer be considered as a collection of non-interacting single particles: in addition to the ‘single-particle phenomena’, ‘collective effects’ become significant. At low intensity a beam of charged particles moves around an accelerator under the Lorentz force produced by the ‘external’ electromagnetic fields (e.g. from the guiding and focusing magnets and RF cavities). However, the charged particles also interact with their environment, inducing charges and currents in the surrounding structures, which create electromagnetic fields called wake fields. In the ultrarelativistic limit, causality dictates that there can be no electromagnetic field in front of the beam, which explains the term ‘wake’. It is often useful to examine the frequency content of the wake field (a time-domain quantity) by performing a Fourier transform on it. This leads to the concept of coupling impedance (a frequency-domain quantity), which represents, for the plane under consideration (longitudinal, horizontal or vertical), the force, integrated over the length of an element, from a ‘source’ to a ‘test’ wave, a function of their frequency and normalized by their charges. In general, the impedance in a given plane is a non-linear function of the test and source transverse coordinates, but it is most of the time sufficient to consider only the first few linear terms. The linear coefficient of the impedance contribution that is proportional to the ‘source’ transverse offset is called here the dipolar impedance (as it does not depend on the ‘test’

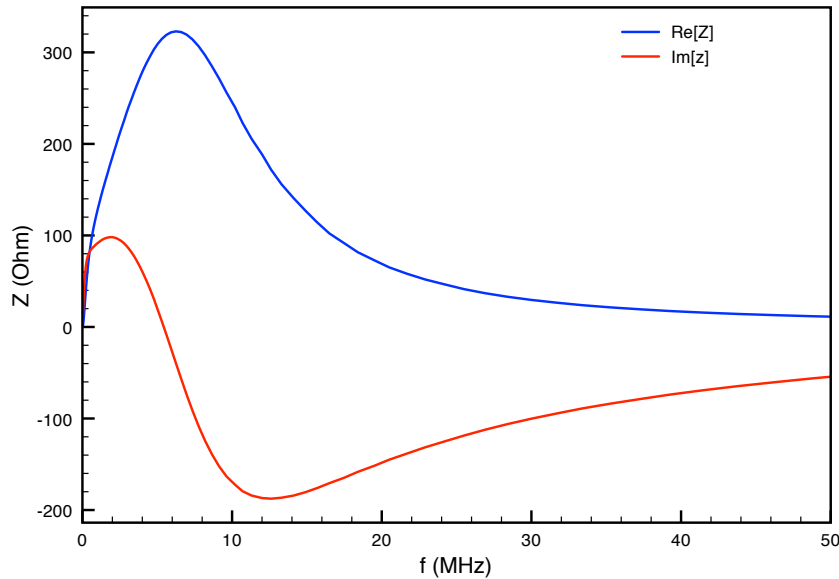


Fig. 4.97: Impedance of the Finemet cavity

particle feeling the wake field, similarly to the constant magnetic field created by a dipole), while the one that is proportional to the ‘test’ transverse offset is called the quadrupolar impedance (similarly to the magnetic field created by a quadrupole).

The wake fields (or impedances) can influence the motion of trailing particles, in the longitudinal and in one or both transverse directions, leading to energy loss and beam instabilities or producing undesirable secondary effects such as excessive heating of sensitive components at or near the chamber wall (called beam-induced RF heating). Therefore, in practice the elements of the vacuum chamber should be designed to minimize the self-generated (secondary) electromagnetic fields. For example, chambers with different cross-sections should be connected with tapered transitions; unnecessary cavities should be avoided; bellows should preferably be separated from the beam by shielding; plates should be grounded or terminated to avoid reflections; poorly conductive materials should be coated with a thin layer of very good conductor (such as copper) when possible, etc. In the case of beam instabilities, fortunately some stabilizing mechanisms exist, such as Landau damping, electronic feedback systems and linear coupling between the transverse planes if, for a transverse coherent instability, one plane is more critical than the other. Moreover, several beam or machine parameters can partly mitigate instabilities. All this translates into knobs which can be used in the control room to damp these instabilities: (i) transverse chromaticities, (ii) skew quadrupole current, (iii) Landau octupole current, (iv) gain(s) of the electronic feedback system(s) and (v) bunch length (and/or longitudinal profile). For the particular case of transition crossing (which is the case of the PS), it might be also needed to try and cross it as fast as possible, to prevent instabilities from developing.

Since the very first studies of LHC beams in the PS in 1993, a slow single-bunch horizontal HT instability of high order (with five to seven nodes in the standing-wave patterns) was observed [22]. After some detailed studies, this instability was then cured in 1999 by linear coupling between the transverse planes, introducing a small current in the skew quadrupoles [24,118,119]. This method has been used and proved to be reliable for more than 10 years (with neither Landau octupoles nor TFB) and it presented the advantage of using only linear optics. Furthermore, it was also well suited to the requirement by the LHC of a round beam, i.e. with similar transverse emittances, since emittance sharing or exchange was not an issue [120, 121]. However, on one hand, space-charge studies on the long (1.2 s) injection flat bottom revealed that in some cases the high (uncorrected, i.e. at around -1) chromaticities enhanced the slow

losses [122] and that it would be good to try and correct the chromaticities to increase the ‘space-charge limit’. On the other hand, new requests are coming for beams with unequal transverse emittances [123]. Past studies revealed that the TD would also be quite suitable to tackle this kind of instabilities [124], as beautifully confirmed in 2013 [125].

Besides, it has always been a challenge to minimize the perturbations to the beam at the moment of transition crossing, as many mechanisms can take place during this delicate process [126]. Indeed, transition energy is the moment when the synchrotron motion is frozen, and the beam is exceptionally sensitive to wake-field forces. In particular, a single-bunch fast vertical instability was already observed in 2000 [127] with the highest single-bunch intensity beam (for the neutron time-of-flight facility) when the longitudinal emittance was too small [128]. With the (global) broadband impedance model assumed at that time [129], the instability rise time was estimated using the beam-breakup formalism, giving a reasonable agreement with measurements [127]. Further simulation studies were then performed with the HEADTAIL tracking code [130], revealing that the same broadband impedance could reproduce the travelling wave measured in the second half of the bunch and that adding the direct space charge gives an even better (almost perfect) agreement with measurements [131]. A very detailed study of this single-bunch fast vertical instability has been carried out recently in Ref. [15], looking also at all the variety of mechanisms which take place at the PS transition crossing.

For the future operation at higher intensities and/or unprecedented beam brightness required by the LHC-LIU project [1], the specified TD should be sufficient to damp the injection instabilities and transition crossing should be possible without major issues. However, a careful follow up (and possibly minimization) of the transverse impedance is suggested to minimize the interplay with space charge, which is the main limitation at injection energy (to try and push further the ‘space-charge limit’) and to allow the possibility of accelerating high-intensity beams with lower longitudinal emittances through transition (which might be required in the future). It is therefore of paramount importance to estimate with some precision the current transverse coupling impedances of the PS, and to determine their main sources to be able on one hand to make reliable predictions for the future and on the other hand to try and reduce the impedance of these main contributors.

The current transverse impedance is discussed in Section 4.7.2.2, whereas the expected situation after the LIU-PS upgrade is analysed in Section 4.7.2.3.

4.7.2.2 Current transverse impedances

The current knowledge of the transverse impedances has been established by performing theoretical computations, electromagnetic simulations and beam-based measurements at the current (1.4 GeV kinetic) injection energy, the future (2 GeV kinetic) injection energy and the transition and top energies. These measurements consisted in measuring the transverse coherent tune shifts as a function of intensity (see Section ‘Measured transverse coherent tune shifts versus intensity’), studying the fast vertical instability at transition (see Section ‘Measured transition instability characteristics’) and trying to localize the main contributors (see Section ‘Localization measurements of the main contributors to the transverse impedances’). The analytical and simulation studies of particular equipment are discussed in the section ‘Theoretical/simulation studies of particular equipment’ and the estimated impedance budget is summarized in the section ‘Impedance budget evaluation’.

Measured transverse coherent tune shifts versus intensity

For a Gaussian bunch with RMS length σ_z and velocity $v = \beta c$, the tune shift ΔQ is related to the imaginary part of the total (dipolar + quadrupolar) transverse effective impedance Z_{\perp}^{eff} by [108]

$$\Delta Q = -\frac{\beta e I_0}{4\sqrt{\pi}\omega_0^2 Q_0 \gamma m_0} \frac{1}{\sigma_z} \Im \left[Z_{\perp}^{\text{eff}} \right], \quad (4.25)$$

where I_0 is the bunch current, Q_0 the zero-current betatron tune, γ the relativistic factor and m_0 the particle rest mass, and the effective impedance is defined as

$$Z_{\perp}^{\text{eff}} = \frac{\sum_{p=-\infty}^{\infty} Z_{\perp}(\omega') h(\omega' - \omega_{\xi})}{\sum_{p=-\infty}^{\infty} h(\omega' - \omega_{\xi})}, \quad (4.26)$$

where $\omega' = \omega_0(p + Q_0)$ with p an integer, $\omega_{\xi} = \omega_0 Q_0 \xi / \eta$ with ξ the chromaticity and η the slippage factor, and $h(\omega) = e^{-\omega^2 \sigma_z^2 / c^2}$ the power spectrum of the Gaussian zero azimuthal bunch mode.

For a parabolic bunch distribution, σ_z must be substituted with $\tau_b / 2\sqrt{\pi}$ [17], where τ_b is the total bunch length, and the power spectrum $h(\omega)$ has to be consequently modified.

If the bunch length remains approximately unchanged with intensity, Eq. (4.25) predicts a tune shift linear with bunch current, with a slope proportional to the transverse total effective impedance.

Several measurements of betatron tunes as a function of beam intensity have been taken, at 1.4 GeV kinetic energy [132], at 2 GeV kinetic energy [133] and extraction [132, 133]. In Fig. 4.98, examples of the measurement results for the horizontal and vertical planes are shown for the kinetic energy of 25 GeV.

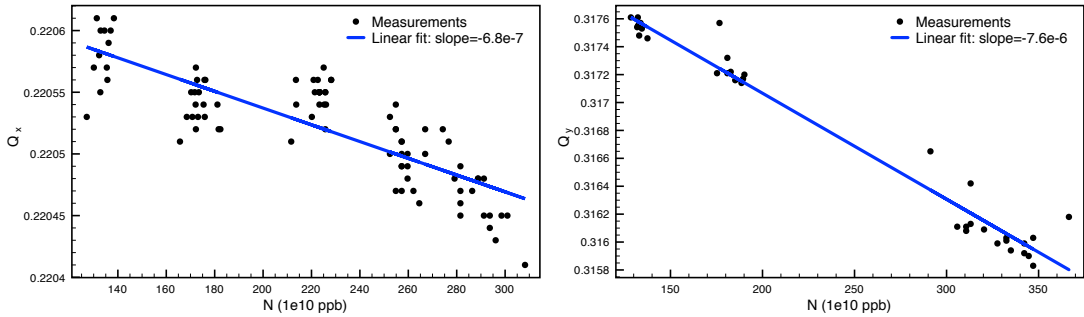


Fig. 4.98: Measurements of tune shift in the two planes (left and right) at a kinetic energy of 25 GeV

At injection (kinetic energy of 1.4 GeV), a horizontal total effective impedance of 3.5 MΩ/m and a vertical one of 12.5 MΩ/m were obtained in Ref. [132], where also a discussion and a comparison with older measurements can be found. The other measurements, made in the vertical plane during recent MD sessions in 2012–2013, give, at 2 GeV, $Z_{\perp,y}^{\text{eff}} = (9.6 \pm 1.0)$ MΩ/m [134].

The observed difference in the vertical plane between these two sets of measurements could be explained by the effect of the coherent indirect space charge, defined as the wake fields generated by a perfectly conducting infinitely smooth beam pipe: if we approximate the PS elliptical chamber with two parallel plates, its contribution to the imaginary part of the total effective impedance is 6 MΩ/m at 1.4 GeV and about 3.7 MΩ/m at 2 GeV, and if we consider a round chamber of 35 mm radius, we get 4.9 MΩ/m and 3 MΩ/m for the two energies. Resistive-wall and geometrical impedances are assumed not to depend on the energy, and we indeed observe that in both geometries the difference in the space-charge contribution ($6 \text{ M}\Omega/\text{m} - 3.7 \text{ M}\Omega/\text{m} = 2.3 \text{ M}\Omega/\text{m}$) is very close to the difference of the two sets of measurements ($12.5 \text{ M}\Omega/\text{m} - 9.6 \text{ M}\Omega/\text{m} = 2.9 \text{ M}\Omega/\text{m}$).

At 25 GeV, the contribution to the impedance of the coherent space charge becomes negligible. Indeed, at this energy, we are mainly dominated by resistive-wall and geometrical impedances. The measurements of Ref. [132] give $Z_{\perp,x}^{\text{eff}} < 1$ MΩ/m and $Z_{\perp,y}^{\text{eff}} = 6.1$ MΩ/m, while more recent measurements give $Z_{\perp,x}^{\text{eff}} = (0.39 \pm 0.03)$ MΩ/m and $Z_{\perp,y}^{\text{eff}} = (4.5 \pm 0.1)$ MΩ/m [133].

Measured transition instability characteristics

As mentioned in the Introduction, at high beam intensities, a fast vertical beam instability is observed in the vertical plane while crossing transition energy in the PS, producing an emittance blow-up and

beam losses [127]. The detailed study of this fast transverse instability, together with measurements, has been carried out in Ref. [15], and could give access to the real part of the dipolar transverse impedance. The characteristics of the instability were a travelling wave in the vertical position signals starting some hundreds of turns after the estimated transition crossing time with a strong spectral component between 600 MHz and 700 MHz. Heavy beam losses occur as a consequence of this instability in less than 1 ms, which is an order of magnitude smaller than the synchrotron period close to transition energy. The rise time of this instability as well as the intensity threshold were observed to increase with increasing beam longitudinal emittance (linearly for the intensity threshold). The momentum compaction threshold was also studied and did not seem to depend on longitudinal emittance, but depended on vertical chromaticity settings. Simulations with the HEADTAIL code were performed to find the shunt impedance of a broadband flat chamber impedance model with a quality factor $Q = 1$ and a resonant frequency $f_{\text{res}} = 1$ GHz that would match the measurement observables. In the frame of simple assumptions, it seemed that a vertical dipolar shunt impedance of $0.7 \text{ M}\Omega/\text{m}$ would be the best candidate to fit the rise time measurement dependence with longitudinal emittance as well as the travelling wave intrabunch motion at around 700 MHz, while a dipolar vertical impedance of $1.5 \text{ M}\Omega/\text{m}$ would better fit the vertical motion. It is interesting to note that these values inferred from instability measurements are quite close to the real part of the current impedance model shown in the following sections, in particular in Fig. 4.103, where it is observed that the real part of the PS impedance model is dominated by the impedance of the kickers (broad resonance of $1.4 \text{ M}\Omega/\text{m}$ at around 700 MHz). Also, as explained in Ref. [15], several mechanisms that damp instabilities were not accounted for in HEADTAIL simulations and could partly explain the disagreement. As a conclusion, the next step is to study the instability at transition with the new impedance model.

Localization measurements of the main contributors to the transverse impedances

In order to detect important sources of the transverse coupling impedance, a beam-based measurement was developed and applied to the PS in the vertical plane. It is called the impedance localization method [135, 136], and it is based on the variation of betatron phase beating with intensity: since the transverse tune, which is the total integrated betatron phase advance over the accelerator circumference, decreases linearly with intensity due to the imaginary total impedance of the full machine, a local impedance source produces a local phase-advance perturbation that is a phase beating along the machine. By varying the intensity of the beam, a phase-advance variation with intensity can be measured from a multiturn beam position monitor (BPM) system; the corresponding phase beating response matrix due to unknown local quadrupole errors, which represent the unknown impedance sources, can then be determined. The problem is therefore reduced to finding the sources of this response matrix. By means of the least-square method the location and amplitude of these impedances can as a result be reconstructed.

A first benchmark of the method was done to check its applicability to the PS [134]. The current of two quadrupoles, the QLS29 and QSE87, was varied from 2 A to 15 A in order to produce a tune shift of about 0.02 to mimic the effect of two impedance sources. Indeed, the phase-advance slope could be reconstructed and the quadrupole location correctly detected, as shown in Fig. 4.99.

The beam-based measurements, taken in the vertical plane with a kinetic energy of 2 GeV, show a similar behaviour with an additional average decreasing slope due to the distributed defocusing impedance sources. As reconstruction elements, only those reasonably believed to be important impedance sources have been chosen, like kickers, cavities, septa and dampers; 40 BPM monitors have been used for measuring the phase advance. As an example, for a measurement with 90 ns bunch length and intensity ranging from 10^{12} to 2×10^{12} ppb, in the upper part of Fig. 4.100 we show the detected impedance amplitudes and locations, together with the minimum accuracy threshold given by the noise level (horizontal red line), while the measured phase-advance slope and the least-square reconstruction are represented in the lower part of the figure.

The total impedance calculated by summing the contribution of each reconstruction element is

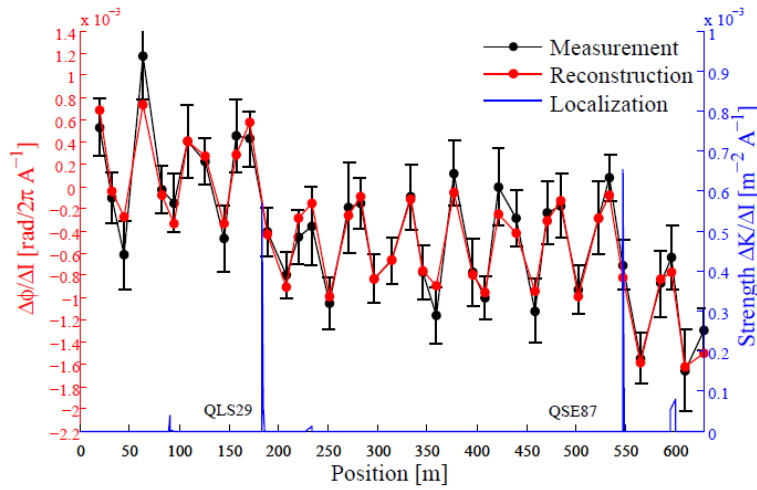


Fig. 4.99: Comparison between measured (black) and reconstructed (red) integrated phase advance slope versus longitudinal position around the PS, with intensity obtained by varying the current of two quadrupoles. The impedance locations are shown in blue and the two quadrupoles QLS29 and QSE87 are clearly identified.

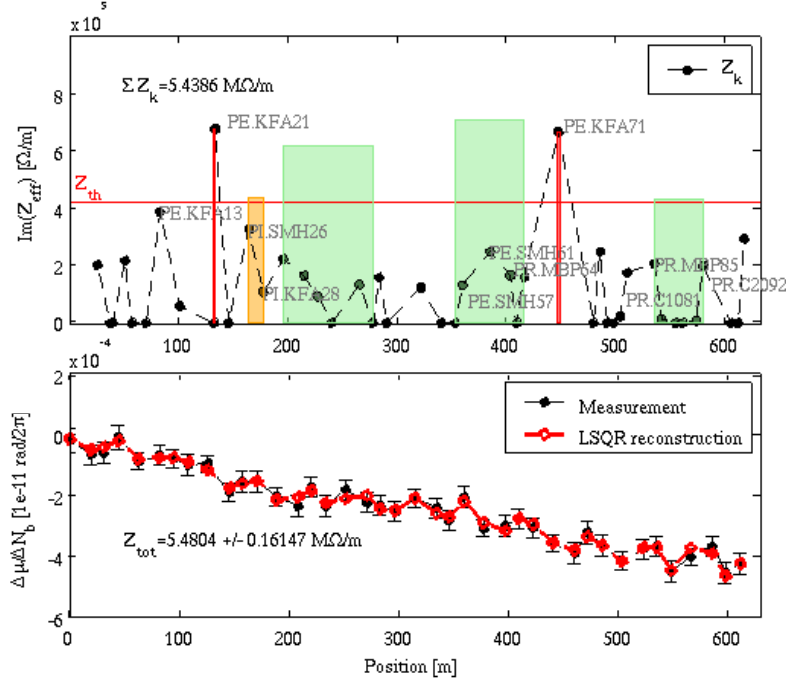


Fig. 4.100: Top: reconstructed impedances with spatial confidence bounds (Δs) and accuracy limit given by the noise level (horizontal red line); bottom: integrated phase advance slope and least-square reconstruction (LSQR).

about 9.5 $\text{M}\Omega/\text{m}$, in very good agreement with tune-shift measurements at the same energy (see the section ‘Measured transverse coherent tune shifts versus intensity’). Also, an estimate of the position uncertainty in the detection was obtained [134], as shown by the different colours in the upper part of the figure (narrow impedance locations in red, large ones in green). It is worth mentioning that the space charge and the resistive wall were subtracted from the measured slope. Kickers in sections 21 and 71 have been detected as principal sources of transverse impedance, being the only localized impedances appearing in all the measurements.

Theoretical/simulation studies of particular equipment

A work is in progress to evaluate the coupling impedance budget by taking into account the individual contributions of several machine elements.

Resistive-wall contribution

For the resistive wall, either a round chamber or parallel plates have been taken into account by using the code of Ref. [137].

By considering a machine made of stainless steel 316LN (about 70% of the total length) and of Inconel X750 alloy (about 20%), the transverse effective impedance is about the same for the two geometries: respectively 0.29 MΩ/m and 0.35 MΩ/m for the round chamber (35 mm radius) and parallel plates. For the parallel plates, the dipolar and quadrupolar impedance contributions are of the same sign for the vertical plane and the total vertical impedance is increased by a factor of 1.2 with respect to the round chamber case, but for the horizontal plane the parallel plates model gives zero total impedance due to the perfect compensation of dipolar and quadrupolar components of the impedance.

Indirect space charge contribution

In Table 4.22 we have summarized the results of the indirect space charge contribution. We expect that the parallel plates and the smaller round chamber can be used for the vertical plane, while an intermediate value between the two round pipes can be used for the horizontal plane.

Table 4.22: Indirect space charge contributions to the total transverse effective impedance at different kinetic energies for round chamber and parallel plates.

Kinetic energies	1.4 GeV	2 GeV	25 GeV
Flat chamber	6.0 MΩ/m	3.7 MΩ/m	44 kΩ/m
Round chamber ($r = 35$ mm)	4.9 MΩ/m	3.0 MΩ/m	36 kΩ/m
Round chamber ($r = 73$ mm)	1.1 MΩ/m	0.7 MΩ/m	8.2 kΩ/m

Kickers

Another important source of impedance is represented by the kickers, as resulting also from the localized impedance measurements (see the section ‘Localization measurements of the main contributors to the transverse impedances’). There are different kinds of kickers which give different contributions to the transverse effective impedance. Some of them (delay-line kickers) have a segmented ferrite inside, while others not. A comparison between CST Microwave Studio [138] simulations and measurements for the KFA13 [139] is shown in Fig. 4.101, revealing a very good agreement in particular for the vertical plane. Also, the other segmented kickers have been simulated in the same way, while, at the moment, for the lumped inductance kickers, which are not segmented, the impedance has been evaluated by using the field matching technique [140] also taking into account the quadrupolar impedance component [141]. The contribution of all the kickers is less than 0.03 MΩ/m in the horizontal plane and about 1.4 MΩ/m in the vertical one.

RF cavities

We have also taken into account the RF cavities, but a first estimate of the contribution of the 10 MHz cavities does not seem to indicate a strong impact in the transverse plane: indeed, as shown in Fig. 4.102, a value of less than 1 kΩ/m is obtained by considering the entire structure (in the figure only half a structure has been simulated).

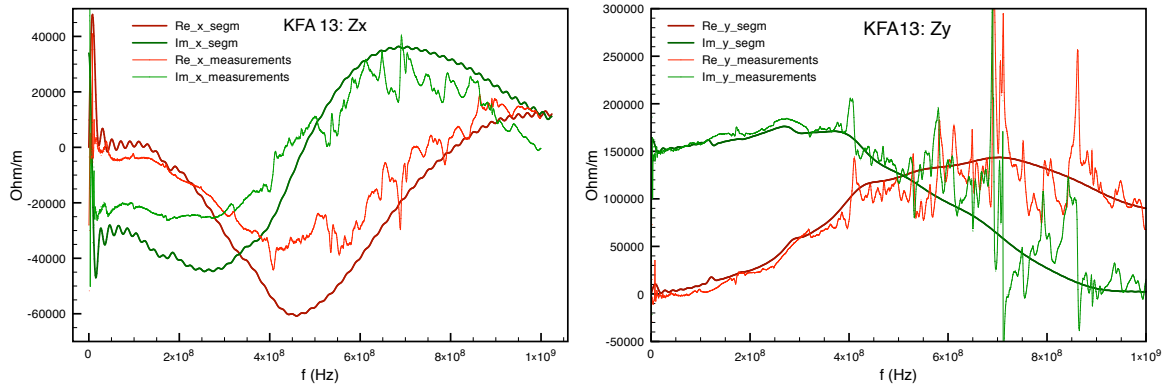


Fig. 4.101: Horizontal (left) and vertical (right) impedance of the kicker KFA13, comparison between simulations and measurements.

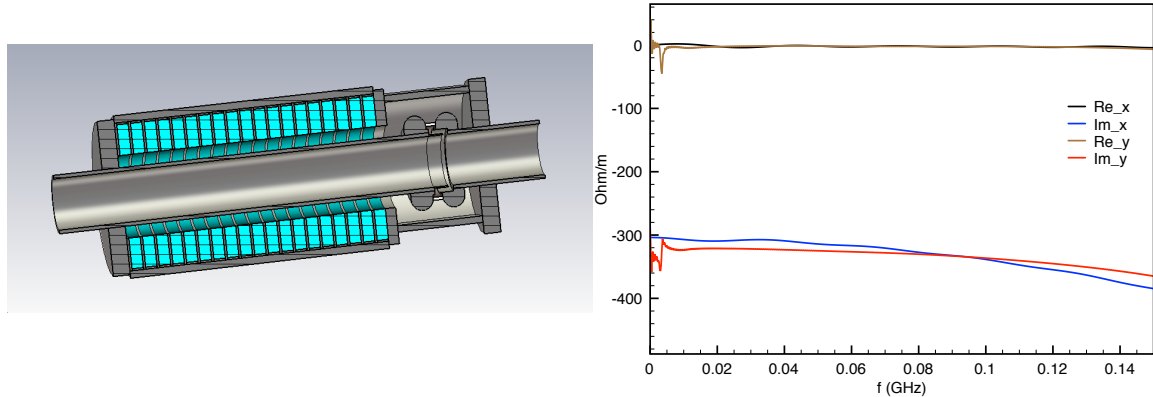


Fig. 4.102: Half 10 MHz cavity model simulated with CST and transverse impedance results

Other elements

Other elements, such as bellows, connections between the beam pipe and the vacuum pumps and other beam pipe step transitions have been evaluated because, notwithstanding their low impedance, due to their number, the total contribution cannot be ignored.

Previous simulations of the wire scanner tanks installed in 2011 showed transverse low frequency dipolar impedances of the order of $1 \text{ k}\Omega/\text{m}$ [142], but more refined simulations will be performed to confirm these low values.

Finally, a first estimate of the septa contribution (electrostatic and magnetic) does not seem to dramatically change the total budget, giving an effective impedance of some $\text{k}\Omega/\text{m}$.

A summary of the elements assessed so far is presented in Table 4.23. The updated list of elements and resulting model can be found on the CERN impedance web page [143].

In addition to these elements that were not evaluated or included in the model, several elements remain to be analysed, in particular instrumentation (e.g. PUs, BCT – Beam Current Transformer – and FBCT – Fast Beam Current Transformer).

Impedance budget evaluation

The total contribution to the effective impedance evaluated so far for the wake fields of individual elements, which is assumed independent of the beam energy, is about $1.9 \text{ M}\Omega/\text{m}$ in the vertical plane and

Table 4.23: List of PS elements that have been simulated and accounted for in the model and the corresponding imaginary part of the total effective impedance (horizontal and vertical). * The indirect space charge is given at 2 GeV; see Table 4.21.

Element	Number	Simulated?	Tool	In model?	Z_x [kΩ/m]	Z_y [kΩ/m]
Resistive wall	–	yes	Theory	yes	300	400
Indirect space charge *	–	yes	Theory	yes	1850	3000
Kicker KFA04	1	yes	CST	yes	3.5	97.7
Kicker KFA13	1	yes	CST	yes	25.4	120
Kicker KFA21	1	yes	CST	yes	23.2	123
Kicker KFA28	1	yes	Tsutsui	yes	25.4	130
Kicker KFA45	1	yes	CST	yes	33.5	154
Kicker KFA71	1	yes	CST	yes	70.8	368
Kicker KFA79	1	yes	CST	yes	29.0	121
Kicker BFA09	1	yes	Tsutsui	yes	57.2	155
Kicker BFA21	1	yes	Tsutsui	yes	48.2	150
Mag. septum SMH16	1	yes	CST	yes	5.1	-2.2
Mag. septum SMH26	1	no	As SMH16	no	–	–
Mag. septum SMH42	1	no	As SMH16	no	–	–
Mag. septum SMH57	1	no	As SMH16	no	–	–
Elec. septum SES23	1	no	As SES31	no	–	–
Elec. septum SES31	1	yes	CST	yes	–	–
RF cavities 10 MHz	11	yes	CST	yes	0.73	-0.47
RF cavities 20 MHz	2	no	–	no	–	–
RF cavities 40 MHz	2	yes	ABCI	yes	0.87	0.42
RF cavities 80 MHz	3	yes	ABCI	yes	0.84	0.60
RF cavities 200 MHz	6	yes	CST	yes	0.69	-1.12
Feedback kicker KFB97	1	no	–	no	–	–
WCM	2	yes	CST	yes	–	–
Beam dump	1	no	–	no	–	–
Vacuum-pump ports	100	yes	CST	yes	13.7	163
Steps	60	yes	CST	yes	23.3	143
Elliptical bellows	200	yes	CST	yes	0.31	177
Wire scanners FWS	5	yes	CST	no	–	–

0.02 MΩ/m in the horizontal plane. For the resistive wall and indirect space charge in the horizontal plane, we assumed the averaged contribution of an equal proportion of 35 mm and 73 mm radius beam chambers, while only the contribution of a 35 mm radius beam chamber is assumed for the vertical plane (see Table 4.24). The total horizontal effective impedance is very close to the measured one, at both 1.4 GeV and 25 GeV, while in the vertical plane a value of about 3 MΩ/m, independent of the energy, is still missing.

The transverse impedance obtained so far is shown in Fig. 4.103 for the real part and in Fig. 4.104 for the imaginary part as a function of frequency at 2 GeV.

As a result, some missing elements should only contribute to the total effective impedance in the vertical plane, and this suggests that other important cylindrical asymmetric impedance elements (either localized or distributed) have to be found in order to obtain a more accurate impedance model that could

Table 4.24: Comparison between estimated total effective impedance contributions (indirect space charge $Z^{\text{ind.s.c.}}$, resistive wall Z^{RW} , other simulated devices $Z^{\text{sim.devices}}$) and measured impedance from the current PS model.

E_k	Plane	$Z^{\text{ind.s.c.}}$	Z^{RW}	$Z^{\text{sim.devices}}$	Total model	Measured	Delta
1.4 GeV	x	3 MΩ/m	0.3 MΩ/m	0.02 MΩ/m	3.3 MΩ/m	3.5 MΩ/m	0.2 MΩ/m
2 GeV	x	1.85 MΩ/m	0.3 MΩ/m	0.02 MΩ/m	2.2 MΩ/m		
25 GeV	x	0.02 MΩ/m	0.3 MΩ/m	0.02 MΩ/m	0.34 MΩ/m	0.4 MΩ/m	0.06 MΩ/m
1.4 GeV	y	4.9 MΩ/m	0.4 MΩ/m	1.9 MΩ/m	7.2 MΩ/m	12.5 MΩ/m	5.3 MΩ/m
2 GeV	y	3 MΩ/m	0.4 MΩ/m	1.9 MΩ/m	5.3 MΩ/m	9.6 MΩ/m	4.3 MΩ/m
25 GeV	y	0.03 MΩ/m	0.4 MΩ/m	1.9 MΩ/m	2.33 MΩ/m	6.1 MΩ/m	3.8 MΩ/m

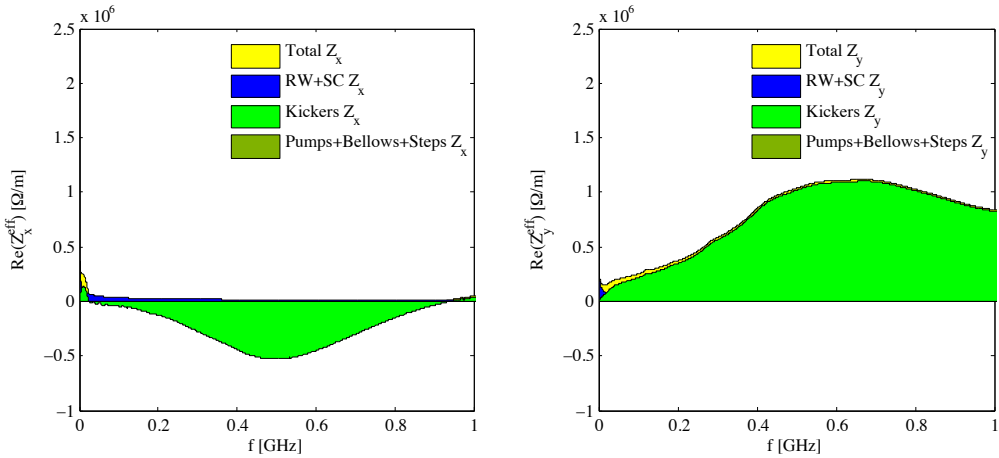


Fig. 4.103: Total real impedance budget obtained so far as a function of frequency

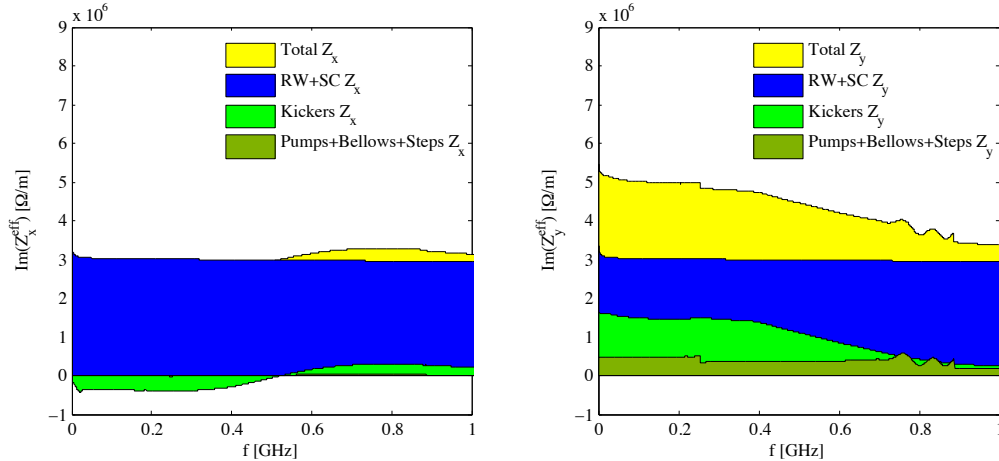


Fig. 4.104: Total imaginary impedance budget obtained so far as a function of frequency

explain the measured tune shift with intensity. Besides, multiparticle simulations with the HEADTAIL code are planned to check if the model reproduces the measured observables well, in particular the features of the vertical instability at transition.

4.7.2.3 *Expected situation after the LIU-PS upgrade*

Even though some choices for the LIU-PS baseline still remain to be made, several modifications have been envisaged to prepare the PS to accelerate beams needed to reach the HL-LHC performance. In particular, the new Finemet cavity has been simulated and the impact on the transverse impedance is expected to be small (of the order of 4 k Ω /m [144]). Other modifications include a new TFB, a new beam dump and new diagnostics (wire scanners, IPM and several PUs).

Other modifications will be required for other reasons, such as for instance the installation of a dummy septum in straight section 15 for the Multi Turn Extraction project [145]. Preliminary transverse impedance simulations did not reveal significant transverse modes, and a low-frequency dipolar impedance contribution of the order of 2 k Ω /m in both planes (for the orbiting position) and 70 k Ω /m for the extraction position has been found [146].

As a consequence, the changes known at the moment of writing do not seem to increase significantly the transverse impedance of the PS, and it is important to recall that transverse impedance has not been a limitation to produce LHC beams in past years. However, as mentioned in the Introduction, the higher brightness beams that could be required call for a tight control of the PS transverse impedance in order to keep more flexibility to increase intensity while decreasing longitudinal emittance.

New systematic impedance-localization and tune-shift measurements are planned for after-LS1 at the kinetic energies of 1.4, 2 and 25 GeV, in order to verify the machine status at the restart and complete the work done until now.

4.8 Radioprotection and civil engineering

4.8.1 Radiation protection requirements for the shielding improvements above the injection and extraction areas of the PS

4.8.1.1 *Introduction*

In 2010, the PS Radiation Working Group (PSRWG) was mandated to carry out an in-depth assessment of the radiation protection and radiation safety aspects of the PS considering current and future operation of the accelerator [147]. Several recommendations with proposed time lines [148] were established and, among others, the PSRWG recommended launching a civil engineering study for the implementation of additional shielding during LS1 in the injection region (Route Goward on top) and in the area of Septum 16 (ejection towards the TT2 beamline). For both areas, the current shielding must be improved, as it is not sufficient to cope with the beam losses and foreseen operational modes of the PS accelerator leading to unjustified exposure to stray radiation of the reference group (members of the public outside the CERN site boundary) as well as of personnel working in nearby buildings or using the Route Goward. In particular, based on the definition in the Safety code F (see Ref. [149]), a practice is considered optimized if it never gives rise to an annual dose above 10 Sv for members of the general public or 100 Sv for persons exposed because of their own professional activity. As some changes occurring in the frame of the LIU project, such as the injection of the PSB beam at 2.0 GeV (as compared to 1.4 GeV today) or the injection and ejection of beams with higher intensities, may further worsen the situation from a radiation protection standpoint, those two recommendations from the PSRWG have been followed up in the frame of the LIU-PS project.

The methodology used to determine the minimum shielding thickness to reduce the levels of stray radiation can be summarized as follows. Detailed geometries of the two areas concerned (see Ref. [150,151]) were implemented in FLUKA [152,153]. Measurement data from the area-monitoring system or dedicated radiation survey results were used to validate and adjust the beam-loss scenario considered in the simulation. Once the measured stray radiation levels were reproduced in the simulation with a good accuracy, future upgrade scenarios such as the injection at higher energy or beam intensities combined with CERN dose constraints were used to determine the required attenuation that the additional shielding must provide. More details of the approach and results for the two concerned areas are provided in the

following sections.

4.8.1.2 Shielding requirement for the injection area at the Route Goward

The Route Goward is the only road leading to the centre of the PS ring where several offices and technical infrastructure buildings for the PS are located. As a consequence, while most of the surface area on top of the PS is fenced off and not accessible during operation, the Route Goward must remain accessible at any time. In addition, the shielding thickness below the Route Goward is thinner (equal to 3.3 m) than in most areas around the ring (most areas are shielded with an earth thickness of 5 m or more). As a consequence, due to the increased stray radiation levels, the section of the Route Goward on top of the tunnel had to be classified as a Supervised Radiation Area.

The FLUKA analysis to assess the current radiological situation on top of the Route Goward is detailed in [150]. The beam-loss profile and intensity were reconstructed based on the measurements of the area-radiation monitor (named PAXS51) and a detailed stray radiation survey of the area. As an example, the dose rate levels calculated with FLUKA are shown on a horizontal layer at the altitude level of the Route Goward in Fig. 4.105. The results are normalized to an ambient dose equivalent rate level of $6 \mu\text{Sv/h}$ at the location of the PAXS51 monitor for comparison with the detailed survey results which were obtained with 2.25×10^{12} protons per second (pps) injected in the PS (higher beam intensity can be injected). Based on the measurements, it was estimated that the relationship between the dose equivalent rate and beam intensity is equal to $0.025 \mu\text{Sv/h}$ per 10^{10} protons injected at 1.4 GeV.

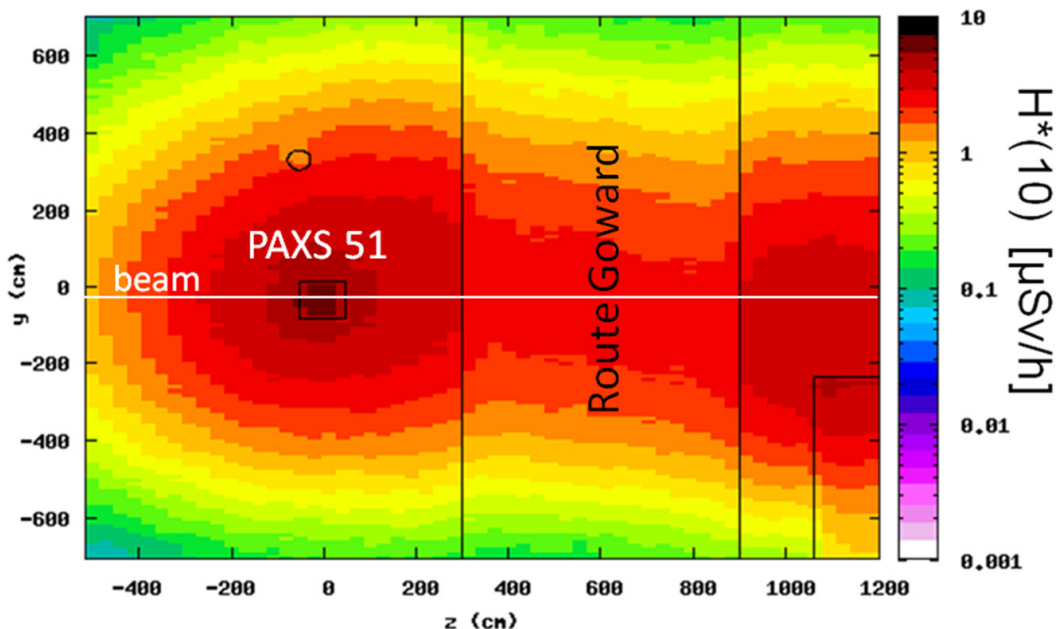


Fig. 4.105: Horizontal layer showing the dose equivalent rate above the Route Goward for 2.25×10^{12} pps injected in the PS.

Considering that, after the PSB upgrade, the injection energy will be raised from 1.4 GeV to 2.0 GeV and that the average injected intensity could increase to 1.1×10^{13} pps [154] (which is about 40% higher than what was initially considered in the PSRWG report), with the assumption that the beam-loss rate will remain constant, a maximum dose rate at the location of the PAXS51 monitor of $50 \mu\text{Sv/h}$ could be extrapolated. As the objective is to ensure that the Route Goward becomes a non-designated area, the additional shielding must ensure a reduction factor of the radiation levels equal to 50^3 . Increasing

³The limit for non-designated areas with a low occupancy factor is equal to $2.5 \mu\text{Sv/h}$ (see Ref. [155]).

the shielding above the injection area was technically challenging, as additional weight on the tunnel could lead to severe structural damage of the PS tunnel. For this reason the use of a concrete structure increasing the road level by 180 cm with lateral pillars to transfer the weight was found appropriate to reach the design objective. After several iterations, the final proposal resulting from the civil engineering study was validated with a detailed FLUKA calculation (see Ref. [150]).

4.8.1.3 Shielding requirement for the extraction area above Septum 16

The earth on top of the PS tunnel serves as the main shielding against stray radiation due to beam losses. Depending on the location along the beamline, the shielding thickness spans from 6 m to only 3 m in the ejection area, for example. From a radiation protection standpoint, the situation in the ejection area is a little different than in the injection area, as the area at the surface is part of the fenced exclusion zone on top of the PS ring and is therefore not accessible to personnel during beam operation. However, due to the weak shielding in this area and relatively high losses, the radiation exiting from the earth with an upward velocity has a sufficient intensity to be a source of exposure due to sky-shine effects (scattering with molecules in the atmosphere) for occupants of nearby buildings and for the reference group (general public outside the CERN site).

For the additional shielding specification (all details can be found in Ref. [151]), two design constraints were considered to account for exposure of personnel in nearby buildings and members of the reference group. For the exposure of personnel in nearby workplaces, a maximum dose equivalent rate of $30 \mu\text{Sv}/\text{h}$ at the surface above the ejection septum was recommended in the PSRWG report to ensure that the annual dose at the workplaces remains below $100 \mu\text{Sv}$ considering 2000 h of occupancy. For the reference group of the population, the annual external exposure due to beam losses in the ejection area must be limited to $5 \mu\text{Sv}$ considering 2550 h of typical high-intensity annual PS operation.

As for the injection area, the first step had been to validate the beam-loss assumptions and the FLUKA model with data from the fixed radiation monitoring system and from a detailed mapping of the dose rate levels in the area. For the comparison and design, the most penalizing of the Continuous Transfer (CT) and Multi-Turn Extraction (MTE) extraction schemes were considered (see [148] and references therein), as the beam-loss pattern is strongly correlated to the type of extraction. Indeed, while the overall beam losses distributed around the entire PS ring are higher for the CT extraction, in the Septum 16 area the losses are locally higher for MTE. For example, measurements performed at the surface above the PS extraction area during MTE extraction have shown dose rate values exceeding $200 \mu\text{Sv}/\text{h}$ for a beam intensity of $0.26 \times 10^{13} \text{ pps}$. If one considers the recommendation of $30 \mu\text{Sv}/\text{h}$ for the maximum dose rate at the surface, the possibility of operating with a factor of four higher intensity [154] and a reasonable safety margin, the required additional shielding must reduce the radiation levels by almost two orders of magnitude.

Three options with shielding thicknesses of 4.80 m, 5.6 m and 6.2 m as compared to 3.0 m in the actual configuration were considered. A comparison of the three cases with the actual configuration can be found in Table 4.25 considering a proton beam loss rate of 10^{11} pps in Septum 16.

From the table, it is concluded that the Option I (preliminary recommendation from the PSRWG study) is not sufficient and that only the last two options fulfil the two criteria. Furthermore, Option 3 would include an additional safety margin. The conclusions of the radio protection (RP) analysis were used as an input for the civil engineering studies and the solution retained is a combination of Options II and III with the thicker shielding in the most critical area. In addition to beam losses in Septum 16, the possibility of relocating a significant fraction of the beam losses in a dummy septum installed in SS15 was also considered and the proposal was also validated.

Table 4.25: Summary of the annual dose to workers at the closest workplaces (criteria 100 μSv for 2000 h of occupancy) and to the reference group (5 μSv for 2550 h of operation) due to the permanent loss of 10^{11} pps in the Septum 16 area. The three options are compared to the current shielding.

Shielding thickness above the PS SS16	Present 3.0 m	Option I 4.8 m	Option II 5.6 m	Option III 6.2 m
Surface dose equivalent rate	1200 $\mu\text{Sv}/\text{h}$	110 $\mu\text{Sv}/\text{h}$	25 $\mu\text{Sv}/\text{h}$	10 $\mu\text{Sv}/\text{h}$
Workplace exposure	2100 μSv	156 μSv	54 μSv	34 μSv
Reference group exposure	135 μSv	12 μSv	5 μSv	2.5 μSv

4.8.1.4 Conclusions

The shielding requirements were specified by the HSE unit for the injection and ejection areas before LS1 to allow the realization of the work while the PS is not operating. The additional shielding will allow the declassification of the Route Goward on top of the PS ring. For the extraction area, the shielding will be appropriate to comply with dose constraints for the reference group (general public) and workers in nearby buildings. For both shielding analyses, upgrades in intensity and energy (from the PSB) as well as new operational modes were taken into account using the most penalizing scenario. To conclude, it should be noted that while stray radiation levels will be reduced by additional shielding outside the tunnel, the beam losses should still be minimized as activation of the accelerator components and tunnel structure will still remain an important source of exposure for personnel intervening in the PS.

4.8.2 Civil engineering: Route Goward

4.8.2.1 Description of the project

The Route Goward is the only access road inside the ring of the PS. It is a two way traffic road, 5.80 m wide. The road passes over the buried PS tunnel in which ionizing radiation is emitted when the PS is in operation. The height of the fill material between the road and the top of the tunnel was 3.20 m.

To reduce the radioactivity, the Radioprotection Group requested to add 1.80 m of concrete above the tunnel and raise the level of the road (see Fig. 4.106).

As the resistance of the PS tunnel is insufficient to support such a height of concrete, a reinforced concrete bridge has needed to be created over the tunnel.

The bridge is supported by two walls of piles which also protect the side walls of the tunnel from the horizontal pressure due to backfill and the traffic loads (see Fig. 4.107).

These shielding improvement works, carried out in the first half of 2013, have involved:

- creation of a reinforced concrete bridge over the existing PS tunnel;
- raising the profile along the existing road;
- creation of retaining walls along the new profile of the road;
- backfill over the tunnel close to the road;
- reorganization of the parking lot served by the Route Goward;
- adaptation of existing facilities along the route (railings, lighting, guard rails, stairs, etc).

4.8.2.2 Design criteria

The basic design criteria used for civil engineering purposes are described in the EDMS document 1238434 v.1 ‘Convention d’utilisation 31132-CU-001’.

The main design parameters were:



Fig. 4.106: 1.8 m thick slab over PS tunnel

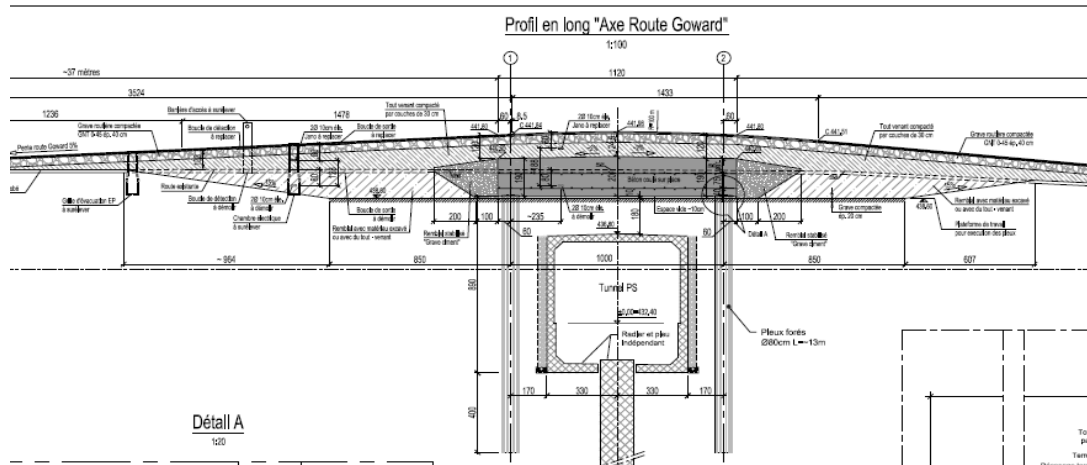


Fig. 4.107: Cross-section of Route Goward and PS (extract of drawing SYN1146000010-)

- to reduce the radiation level on the roadway, the reinforced concrete bridge had to have the following dimensions:
 - minimum height of concrete: 1.80 m;
 - minimum length: 11.20 m;
- next to the future bridge, the height of fill on the tunnel had to have the same level 441.20 as the rest of the PS tunnel;

- the future road had to be identical to the existing one: two lanes and 5.80 m wide;
- the slope of the road had to be less than or equal to 9.5%;
- the bridge had to be designed for the passage of vehicles representing a load of 12 tons per axle.

4.8.2.3 Special construction requirements

During the works, from March to July 2013, the PS tunnel was in shut-down period and maintenance activities were carried out in the tunnel.

Therefore, the access to the PS ring had to be maintained throughout all the construction phase and the traffic in the Route Goward could only be interrupted for short periods. For this reason a temporary road was constructed for light traffic at the beginning of the works (see Fig. 4.108).



Fig. 4.108: Temporary road

4.8.2.4 Geotechnical aspects

From the geological point of view, this sector of CERN has a large amount of fill surrounding the buried structures, sitting through a layer of silty Würmian moraine on the red sandstone which forms the bedrock of the Lake Geneva area and which is located underground at CERN. These geotechnical characteristics were taken into account in the design of the piles (see Fig. 4.109 for piling works).

4.8.2.5 Civil engineering works schedule

The main civil engineering works for the additional shielding on Route Goward were carried out from March to July 2013.



Fig. 4.109: Piling works

Some finishing works (second layer of black top, parking lot, etc) were carried out at the beginning of 2014, after the shielding works in Septum 16, in order to avoid damage related to the frequent and heavy traffic expected on the road during these works.

4.8.3 Civil engineering: Septum 16

4.8.3.1 Design parameters

The basic design criteria used for civil engineering purposes are detailed in the EDMS document 1252679. Figure 4.110 shows the final ground level required by RP in the Septum 16 area.

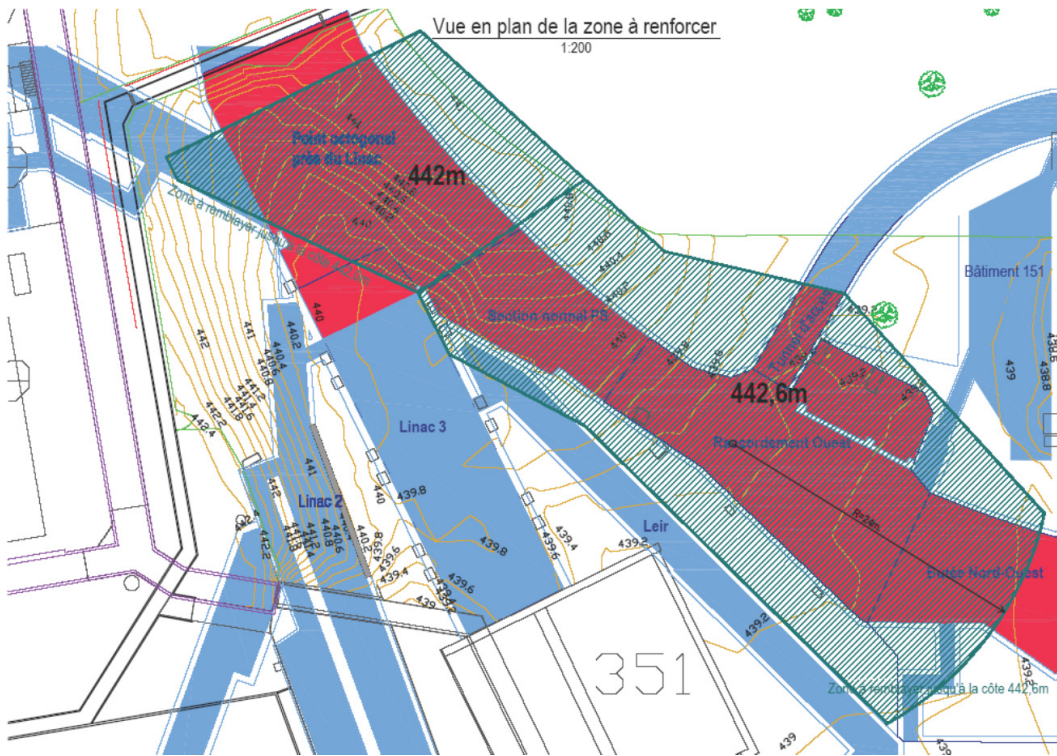


Fig. 4.110: Extent and finished level of backfill required in Septum 16

4.8.3.2 Description of the project

The description given below should be read in conjunction with EDMS document 1266026, which describes in detail the scope of the civil engineering design and work.

From the civil engineering point of view the Septum 16 area is quite a complex area, where, in addition to the PS tunnel, several underground structures converge. Constructed at different periods, these include the Linac3, Linac2 and LEIR beam-injection tunnels and the TT2 beam extraction tunnel (see Fig. 4.111).

Figure 4.110 details the extent and finished level of protective backfill in the septum area as required by the Radiation Protection service. To achieve this, it will be necessary to add a depth of earth of between 1.2 m and 3.4 m, depending on the area concerned.

Given that the existing structures are not strong enough to take the weight of the additional backfill, the proposed solution involves transferring the load onto a new load-bearing structure that will take the weight of the additional earth and redirect it into the bedrock underneath.

This new load-bearing structure will consist of a 1.10 m thick reinforced concrete slab sitting directly on the levelled surface of the existing tunnels. The additional depth of backfill will be placed directly on the unfinished slab.

To avoid placing a load on the existing structures in the weak areas, the slab will rest on drilled piles, or secant piles in areas subject to particularly heavy loads. In the places where the existing tunnels are made of large masses of concrete, the slab will rest on intermittent supports on the tunnel roof.

The shape of the slab with recesses and beams has been chosen to adapt to the static requirements and to the radioactive shielding needs.

Where LEIR and the PS converge, the geometric layout imposes a large span, which requires the slab to be supplemented by a large $2 \times 2 \text{ m}^2$ inverted beam.

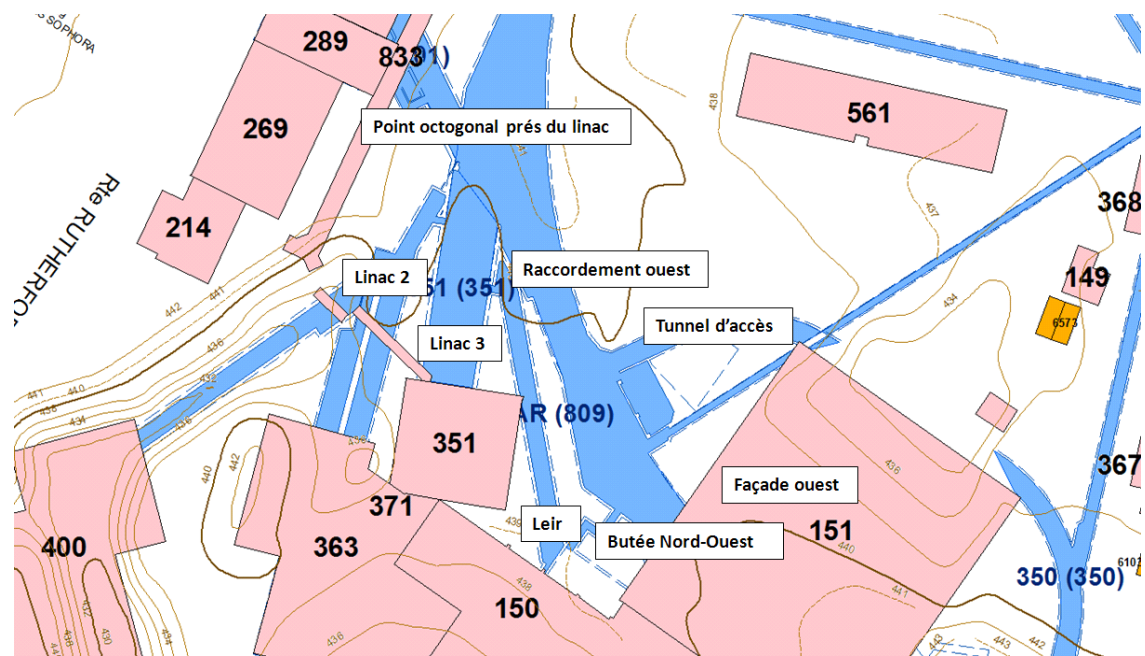


Fig. 4.111: Component structures of the Septum 16 area

Earth will not need to be removed but only temporarily stored on the work site. Ultimately, a small amount of earth will need to be brought in from outside in order to meet the radiation protection standards.

Figure 4.112 shows the various elements of the new load-bearing structure and Fig. 4.113 gives a bird's-eye view of the new slab.

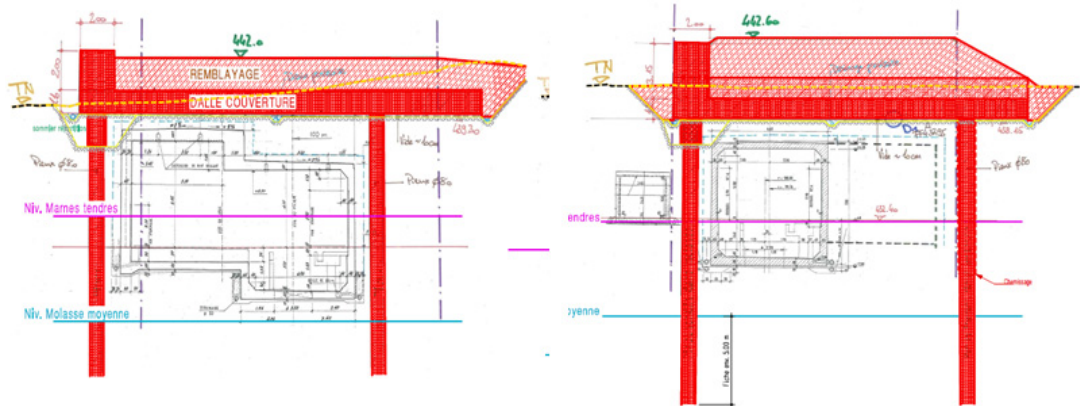


Fig. 4.112: Schematic plan of load-bearing system for additional backfill

To protect the existing structures, the transfer slab must guarantee that even after long-term deformation the load-bearing relief structure does not under any circumstances come to rest on the existing structures.

To this end, the slab will rest on a biodegradable honeycomb cardboard formwork that can be dissolved with water. This procedure guarantees that, once water has been injected to dissolve the cardboard, a void of 10 cm remains after concreting, which is more than enough to allow for the long-term deformation of the slab (see Fig. 4.114). As alternative, some parts of the slabs will rest on sand that will

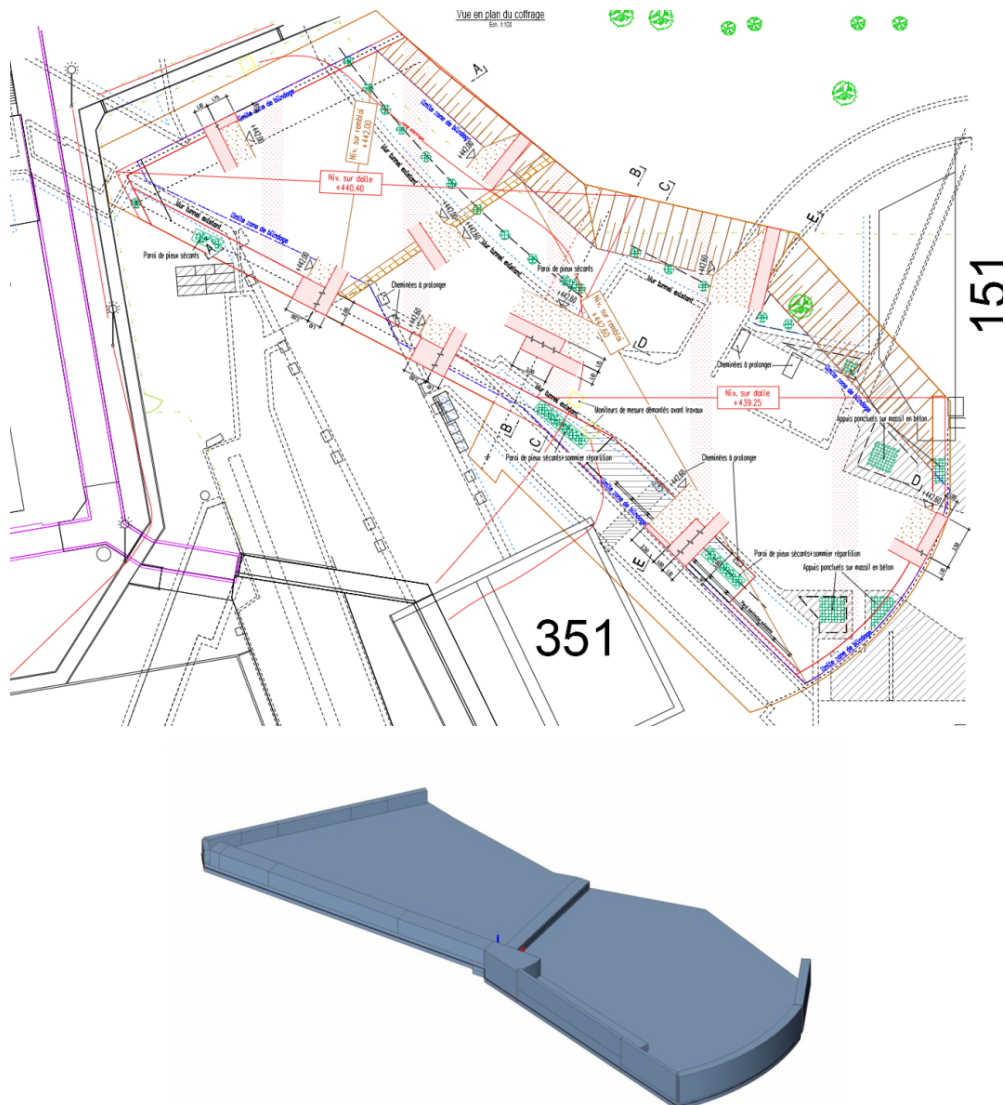


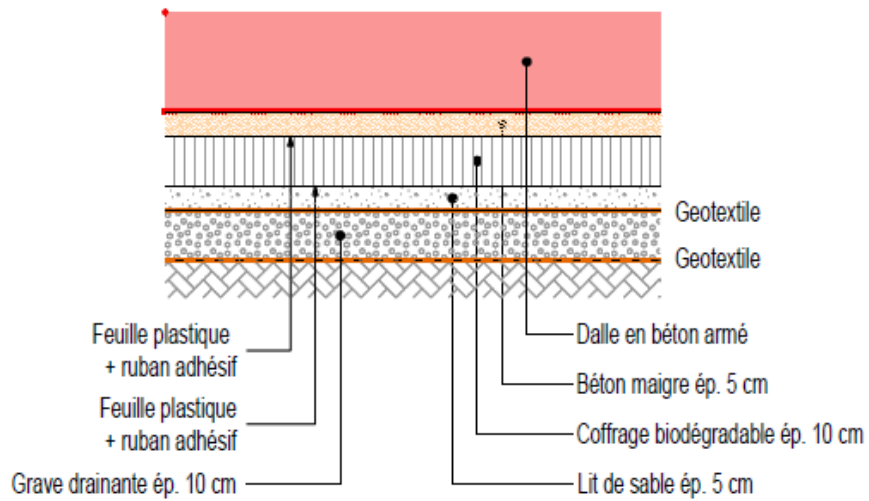
Fig. 4.113: Bird's-eye view of the new slab

be pumped away by pumping water. The sand together will the water is then recovered in drains built for this purpose.

These systems (the biodegradable formwork or sand) will guarantee that, under its own weight and in the long term, the load-bearing structure does not come into contact with the existing structure in the critical area.

The work to be carried out for this project includes the following:

- excavation of 1.20 m of earth across the entire area to be shielded;
- installing piles;
- placing the biodegradable formwork or sand;
- pouring the slab concrete;
- depositing the backfill.

**Fig. 4.114:** Biodegradable slab formwork**Fig. 4.115:** Site installations

4.8.3.3 Special construction requirements

During the work, which started in the second half of 2013 and finished in the first quarter of 2014, the PS tunnel was out of service. Nevertheless, the work site was classified as a ‘Radiation Area’ and personnel considered as occupationally exposed persons.

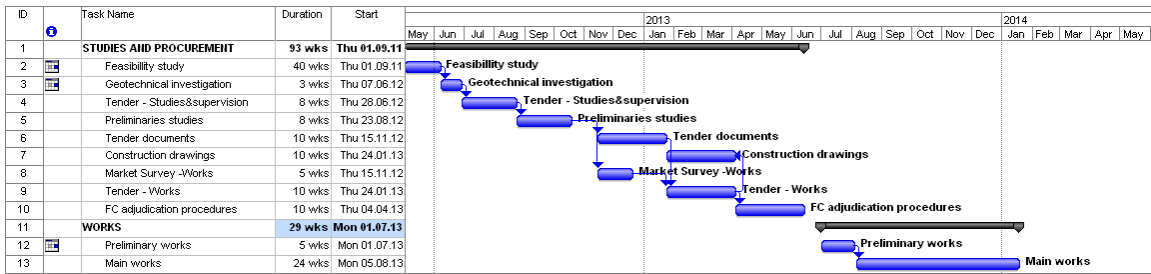


Fig. 4.116: Schedule of the civil engineering works



Fig. 4.117: New shielding on top of the extraction region

Additional constraints that have been taken into account are the following:

- The work must have no influence or impact on the existing structures.
- Conditions governing execution of the work and site access. There is only one possible access route, via Route Goward, at the PS. This means that the work will not be able to commence before the completion of the work on Route Goward. Figure 4.115 gives preliminary indications of site installations that would be necessary for the work.

4.8.3.4 Geotechnical aspects

From a geological point of view, this area of the CERN site has a large amount of fill surrounding the buried structures, which sit in a layer of silty Würmian moraine on the same red sandstone that forms the bedrock of the Lake Geneva area. These geotechnical characteristics have been taken into account in the design of the project.

4.8.3.5 Civil engineering work schedule

Figure 4.116 shows the schedule of the works and Fig. 4.117 a picture of the finished installation.

4.9 Beam instrumentation

4.9.1 Additional wideband PUs in the BTP line and PS ring

Transverse instabilities were studied in detail at PS injection, with bunch oscillations in both the horizontal and vertical planes clearly observed in the first couple of turns after PS injection for the CNGS and TOF beams. These might also be present for other high-intensity beams. To better understand the origin of the observed instabilities, which cause losses at PS injection, new large-bandwidth PUs have been requested in the BTP line. The full specifications for the new PUs can be found here: <https://edms.cern.ch/document/1259212/1.0>.

The vacuum chamber of the BTP line is slightly larger than that of the PS, so the proposed solution is to make a ~20% scaled-up version of the existing dual-plane wideband PUs already used in the PS

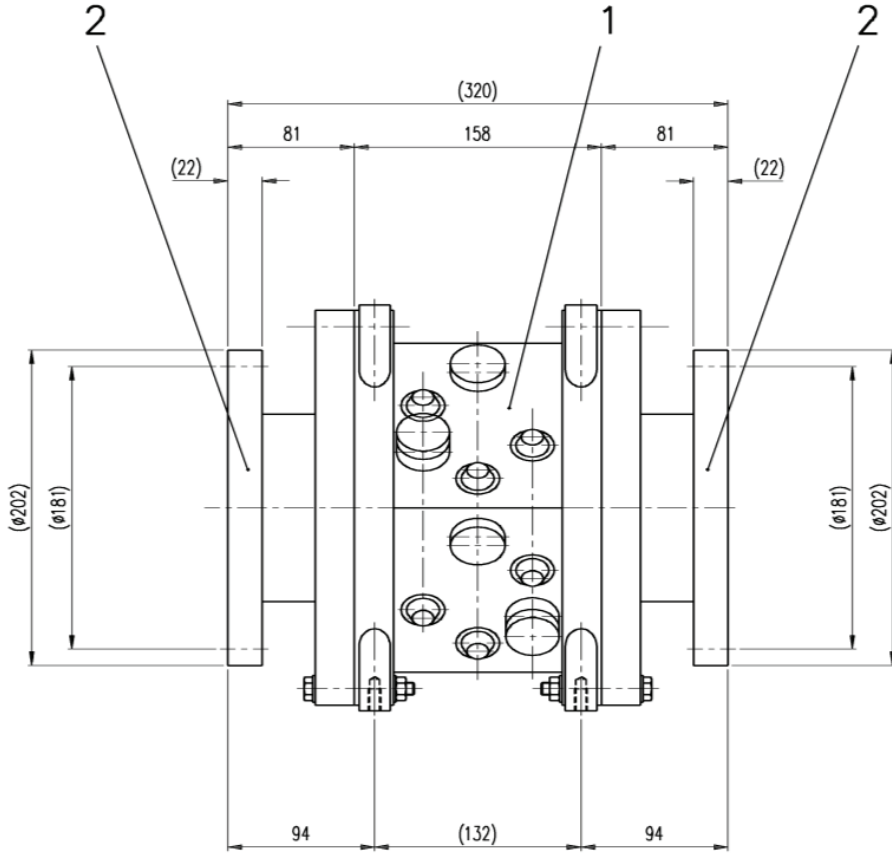


Fig. 4.118: Assembly drawing of the TT2 wideband PU

Table 4.26: Wideband PU characteristics

Aperture	$140 \times 140 \text{ mm}^2$
Length	140 mm
Electrode capacitance	$\sim 160 \text{ pF}$
Electrode transfer impedance	0.5Ω
Target bandwidth	200 kHz–250 MHz

and TT2 (Transfer Tunnel 2) lines (Fig. 4.118). The electrodes are cut to obtain a linear characteristic with respect to transverse displacement for both axes. Table 4.26 summarizes the properties of this PU. Installation is foreseen for 2017.

For the PS a second wideband PU, identical to one already installed in the ring, is requested. This is to enable the observation of bunch-by-bunch radial position during extraction of LHC-type beams (25 ns in particular) at two positions in the ring. Such a measurement is not possible with the standard orbit system. The acquisition system will also be identical to the one used for the existing PS wideband PU.

4.9.2 Modifications of the beam diagnostics around the PS injection septum

In view of the LHC injector upgrade, the PSB extraction and thus the PS injection energy will be upgraded from 1.4 GeV to 2 GeV. This change requires the upgrade of the PS injection septum in section

42. The new septum will take up the entire straight section 42 and leaves little or no space for the present beam-diagnostic instruments that are required to set up the injection and diagnose problems efficiently.

At present there are two beam-diagnostic systems integrated in, or attached to, the PS injection septum, a scintillating screen (BTV) upstream and a wire harp (SEM grid) downstream. These instruments make observation of the beam entering the PS through the septum possible.

The functionalities of these two instruments remain mandatory also with the new septum; therefore, a solution for their integration has to be found.

At present it is proposed to move them further upstream (BTV) and further downstream (SEM grid) of the present locations inside the envelope of the adjacent magnet units (41 and 42). The mechanical integration looks challenging and is further complicated by the fact that the instruments will be inside the magnetic field of the PS main magnets. The aim is to preserve the functionalities and accuracy of the present systems (see https://edms.cern.ch/file/1207510/1/PS_Inj_Diag_FuncSpec_8May2012_bis.pdf).

Two of the three BPMs in the BTP line will be moved such that one BPM is close to the septum while the second BPM should then be positioned $n \times \pi/2$ in phase advance upstream of the first BPM, where $n = 1, 3, 5$, etc.

4.9.3 Ghost and satellite detection

The ghost and satellite detection system to be installed in the PS will comply with the specifications given in <https://edms.cern.ch/file/1233006/1.0/LIU-Intensity-Specs-V1.0.docx>. The detector will be based on a new, high-bandwidth WCM (BCWM) and the analogue signals acquired with a new high-bandwidth, high-sampling-rate acquisition system.

A 3D model of the new BCWM foreseen for the PS SS03 is shown in Fig. 4.119. Two such devices will be installed in sector 3 of the PS ring: one will be used to cover standard operational requirements such as the tomoscope, 1000 turn intensity and OASIS measurement systems, while the other will be dedicated to satellite and ghost detection.

To detect satellite bunches it is necessary to implement a circuit that limits the voltage produced by the main bunches, while recovering faster than the time between two RF buckets, i.e. <25 ns. Commercial RF limiters typically need several microseconds to recover, and can therefore not be used. The limiter should also minimize any mismatch that could lead to reflections, which is another criterion by which commercial limiters fail, usually being totally reflective. A new limiting circuit is therefore under development to meet these specifications. It will consist of a partially matched bridge clipper followed by a more traditional crowbar-style limiter, implemented with Schottky diodes to ensure fast recovery (Fig. 4.120).

The main bunch signal will be attenuated by about 50 dB, while ghost bunches are attenuated by less than 30 dB, meaning that expected ‘visibility’ of the ghost bunches is improved by about 20 dB as shown in Fig. 4.121.

In the example shown in Fig. 4.121, a ghost bunch is simulated at a relative intensity of 1×10^{-3} at 25 ns after the main bunch. At the clipper output, the ghost bunch is at about 7×10^{-3} relative to the main bunch, a compression of the dynamic range required by nearly an order of magnitude. The residual reflection is clearly visible just before the 160 ns mark, and will require removal via digital post processing. The two new BCWMs are foreseen to be installed in 2014 and the electronics for the ghost detection by the start of 2015.

4.9.4 IPM

4.9.4.1 Description

Continuous beam size monitoring during the entire machine cycle is one of the priorities for PS operation. In addition, it is requested that the system is able to provide bunch-by-bunch profile recording. Such

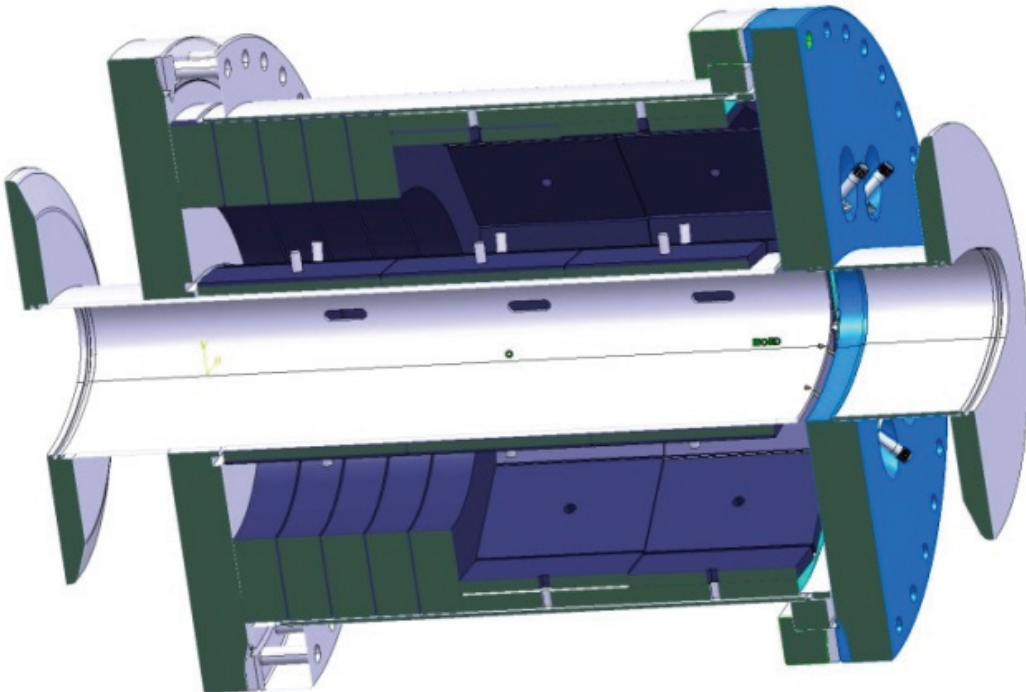


Fig. 4.119: The new PS WCM

measurements cannot be provided by the presently installed wire scanners, which can only perform two scans per cycle and may in future suffer wire sublimation due to the increased brightness of the beams after the upgrade. It is therefore planned to install an IPM for such measurements.

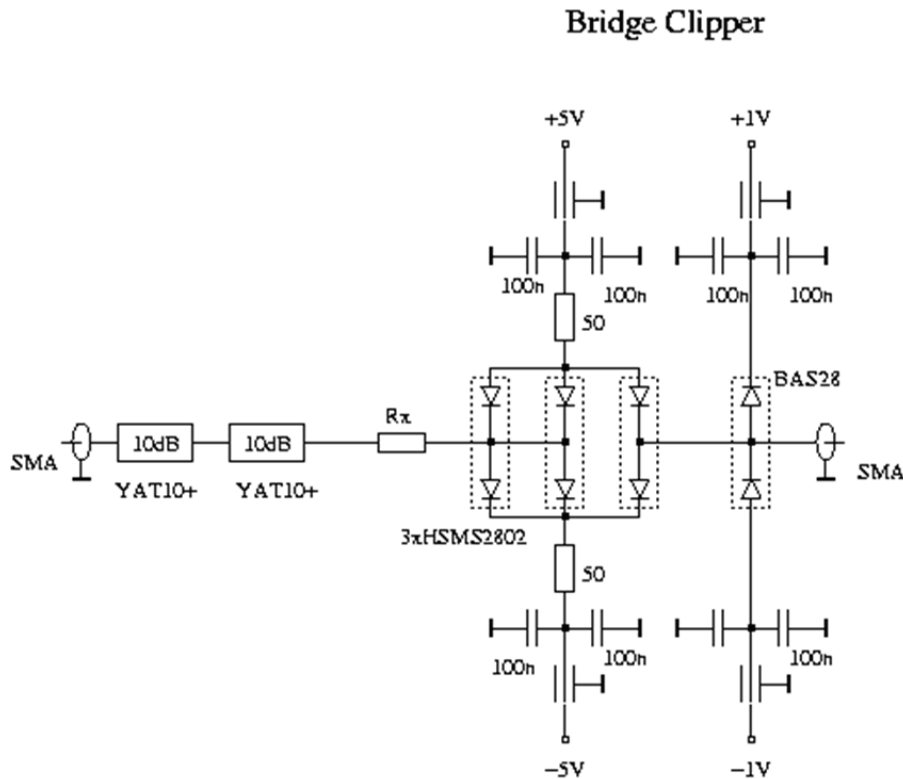
In order to measure bunches separated by 25 ns, the IPM must work in electron-collection mode. This requires the presence of a dipolar magnetic field to ensure that the electron trajectories spiral along the magnetic field lines, so keeping the registered profile undistorted by the space charge generated by the beam.

4.9.4.2 Acquisition system

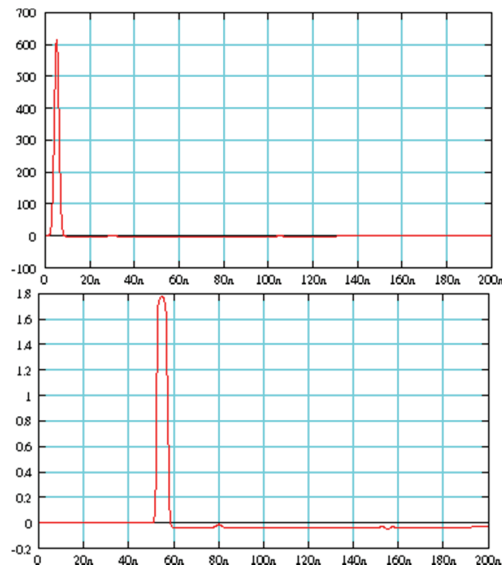
The PS specifications are unlikely to be met using traditional electron-detection systems. A detector based on a multichannel plate would quickly degrade in the high-radiation PS environment and a strip detector would be limited in both resolution and sensitivity. A study is therefore under way to see if the high-speed and high-duty-cycle requirements of the PS can be fulfilled by a new read-out system based on a hybrid silicon pixel detector. In this technology a pixellated sensor is bump bonded onto a pixellated read-out chip, allowing the signal from each pixel to be individually processed and digitized. The chosen chip—Timepix3—reads out a matrix of 256×256 pixels each of size $55 \times 55 \mu\text{m}^2$. It is currently (in 2014) the most versatile and one of the fastest hybrid pixel detector read-out chips available.

The limit at which the analogue front end can distinguish separate hits is about 2 MHz/pixel. Table 4.27 shows the maximum hit rate for the most demanding beams, which in the case of ion bunches reaches 1.6 MHz/pixel, still below this 2 MHz/pixel limit.

The chip can continually send data at a total hit rate of 80 MHz. In the case of 25 ns proton bunches this means that only two hits (electrons) per bunch and per turn can be transmitted. The full acquisition of a single-bunch profile will therefore require the addition of events from about 100 turns, i.e. $200 \mu\text{s}$.



J. Belleman—Match 2014

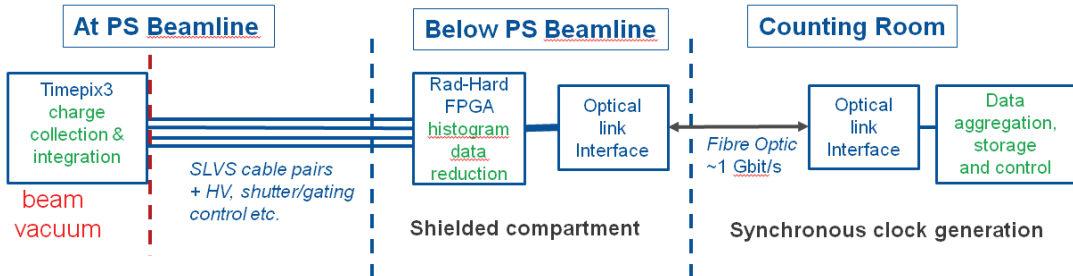
Fig. 4.120: Matched bridge clipping circuit**Fig. 4.121:** WCM raw output (upper) and clipper output signal (lower)

A schematic of the read-out system is shown in Fig. 4.122. The large amount of data (640 Mb/s) produced by a single Timepix3 chip is reduced by an FPGA-based front-end computer located in the

Table 4.27: Expected hit rates from the most demanding beams calculated for pressure of 10^{-9} mbar

Beam type	Beam energy [GeV]	Number of bunches	Bunch population [particles]	Number of electrons per bunch	Hit rate per pixel inside the bunch (maximum)	Hit rate per chip averaged over turn
P ⁺ , 25 ns	25	72	1.3×10^{11}	30	130 kHz	900 MHz
Pb 54 ⁺	1227	2	2.5×10^8	120	1.6 MHz	100 MHz

vicinity of the detector. An optical link is then used to send the reduced data to the acquisition electronics located outside the tunnel, where they are processed and sent to the control room and logging database. Beam-synchronous timing is also introduced at this stage to assign the correct bunch slots to the reconstructed data. In order to follow the bunch-splitting processes in the PS, beam-synchronous signal generation based on that developed for the PS trajectory measurement system is currently considered.

**Fig. 4.122:** Schematic of the proposed read-out system

The radiation level in the location of the Timepix3 chip is expected to reach about 10 kGy/year. This will lead to some radiation damage of the detector, resulting in a decrease of the depletion region and therefore signal amplitude. In order to limit the effect of this process, the detector will be cooled to about 0°C. A simple metallic plate connected to a cooling circuit and a chiller or a thermoelectric cooler is being investigated. The electronic chip itself should not suffer any damage at this level, although the ability to power cycle the system in case of single-event upsets is foreseen.

The FPGA-based front-end processor will be positioned as far as possible from the beam pipe and designed to be radiation tolerant, but will still need to be protected by additional shielding in order to reduce the accumulated dose to below 1 kGy/year.

4.9.4.3 Mechanical design

The new PS IPM must be designed to have:

- a beam aperture of 70 mm for the horizontal device and 146 mm for the vertical device;
- an accelerating potential of 20–30 kV combined with a magnetic field of 0.2 T;
- very good electric and magnetic field uniformity. Both fields must also be parallel;
- a shielded compartment within 2 m of the beamline to house the more radiation-sensitive components such as the front-end FPGA and chiller for the cooling system;
- a gas-injection system to have the possibility of imaging a single bunch within a single turn in the future.

The main mechanical elements of the IPM are the following:

- high-voltage electrodes isolated from the other elements;
- a detector assembly with room for up to four detectors on a cooling plate;
- a flange containing feedthroughs to which the detector structure is attached;
- a vacuum chamber;
- a dipole magnet to provide the required magnetic field.

The design should ensure the easy removal of the flange holding the detector structure to facilitate detector maintenance.

4.9.4.4 Status and plans

Experiments with 5 keV electrons and a thin-pixel detector attached to a Timepix1 chip have demonstrated the operational principle of such a device. The design of both the mechanical elements and the magnets is under way, while the final electronic development will start in autumn 2014. It is foreseen to install a single prototype system in the PS during an end of year technical stop before LS2, with the full installation of the final system done during LS2.

4.9.5 Matching monitor

In order to verify the correct matching of the optical Twiss parameters of the PSB-to-PS transfer line and the PS ring, it is required to measure the transverse profiles of the injected beam on a turn-by-turn basis. An optical mismatch will induce an oscillation in the width of the measured profiles at twice the tune frequency. In order to measure and correct this mismatch, it is necessary to determine the beam size to within a relative accuracy of a few per cent. The acquisition of 20 successive turns is deemed adequate for the accurate quantification of the mismatch.

This measurement currently uses three successive SEM grids. This method, however, does not allow the measurement of the mismatch directly, and relies on the knowledge of the PS optics functions with high accuracy, which is not necessarily the case.

It is therefore proposed to equip at least one of the three existing SEM grids in the PS ring with new electronics capable of acquiring the beam profiles on a turn-by-turn basis. This technique has already been tested in 2001 in a dedicated MD session [156]. On that occasion special front-end electronics was installed in the tunnel just for the measurements and then removed before it could be damaged by the high radiation level. A study is now necessary to identify possible radiation-hard front-end electronics or a scheme that employs deported electronics in the closest safe location.

The three existing SEM grid monitors are rather old and require a general overhaul of the mechanics, currently being undertaken under the auspices of the consolidation project. The requirements of the multturn acquisition will therefore be considered during the redesign of these monitors.

4.10 PS internal dump in the FLUKA Monte Carlo simulation

4.10.1 Introduction and motivation

The currently existing internal dumps are located in the straight sections 47 and 48 (SS47/48) of the PS. They are meant to absorb the accelerated proton beam in case of a dump request and to preserve the beam extraction towards East Area in case of not-extracted nTOF beams. The design of the dumps dates from 1975 and assumed an absorption of beams with an intensity up to 1×10^{13} ppp (protons per pulse) at a maximum beam energy of 24 GeV/c. Nowadays, both higher beam momentum and upgrade plans with increased beam intensity require a review of the internal dumps.

The aim of the presented study was thus to first review the status of the actual internal dump and to analyse the limitations of the actual design, as well as looking for a first general approach, possibly allowing for an increased beam intensity. Simulations with the FLUKA Monte Carlo code are based on

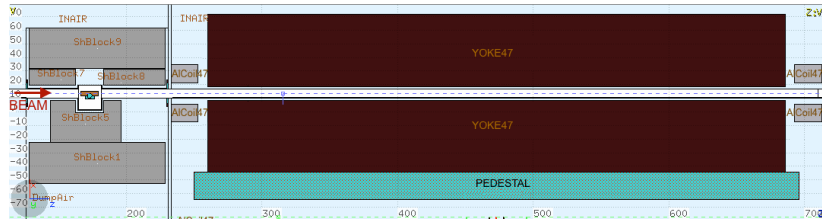


Fig. 4.123: FLUKA representation of the straight section 47 and downstream magnet MU47

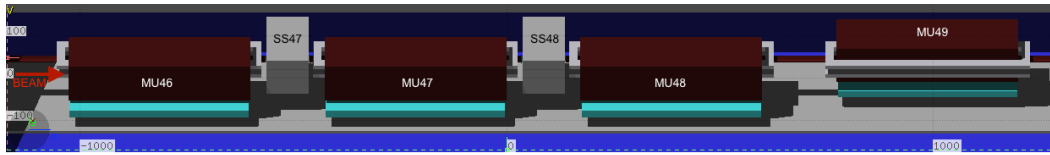


Fig. 4.124: FLUKA representation with extended geometry

the most critical parameters for both beam current and future beam profiles. Studies [160] were focused on the damage from the dose absorbed by the magnet coils, the energy distribution together with the induced temperature rise in the dump core and its nearby components. Moreover, the leakage of primary and secondary particles from the dump area was simulated to allow for a better analysis of the absorber efficiency as well as providing further information about the activation impact of the downstream beam elements. The final part of the preliminary study focused on the simulation of the residual dose in the straight section induced by both standard PS operation and dedicated beam dump cycles. The obtained FLUKA results were benchmarked with available ambient dose rate measurements for several cooling times, as well as passive dosimeter readings available for the area of concern. The conclusions from these first calculations led to the decision of performing a preliminary conceptual redesign study of the dump core, aiming for a possible solution capable of bearing the new maximum beam parameters in this context. The results of the preliminary calculations for the material choice and geometrical dump layout are presented in the last part of this report and [160].

4.10.2 Internal dump current state

4.10.2.1 Simulation conditions

Presented simulations considered in the first approach the close surrounding area of the straight section 47, since the design of the internal dump located in the straight section 48 is identical to the dump from the section 47. The FLUKA dump geometry includes the main dump elements, its surrounding shielding and the magnet—MU47 located downstream. The respective geometry elements are listed below:

- ‘the dump’ consists of a copper dump core, a stainless steel pipe (originally a cooling pipe, which is at the same time the assembling point to the moving system) and the stainless steel mounting structure located under the dump core (which assembles the pipe to the dump core). The dump structure is enclosed in a stainless steel vacuum tank;
- the ‘shielding’, the concrete blocks surrounding the dump;
- the ‘magnet’, a PS dipole magnet type S, which consists of the simplified yoke of rectangular shape (made of SS 316LN), an aluminium coil and pedestals (stainless steel). Updates of this previous FLUKA magnet design [158] included the distance between the yoke and the coils in order to better comply with the technical drawings [160, 161].

A longitudinal cut of the geometry used for first simulations is presented in Fig. 4.123.

In a further set of FLUKA studies, the geometry was extended to a cell of four magnets—from MU46 to MU49. Moreover, the curvature profile of the focusing and defocusing PFW elements were

applied, as well as a simplified shielding for the internal dump located in straight section 48. This design, as presented in Fig. 4.124, was used for the calculation of the distributed beam losses and the residual dose rate distribution in the area.

To determine the current design limitations, the most critical beam parameters were applied. Two beam profiles were used, both with a beam momentum of 26 GeV/c and a minimum Gaussian beam size with $\sigma_x = \sigma_y = 2$ mm, but with two different beam intensities [157]:

- ‘old beam’—refers to the currently used beam with a maximum beam intensity of 1×10^{13} ppp;
- ‘new beam’—most critical case for the future beam with the intensity of 5×10^{13} ppp.

4.10.2.2 Energy deposition

In order to study the induced temperature rise, either in the dump or in surrounding magnets and beam elements, calculations of the energy deposition were performed. An excessive amount of energy deposited in the dump can result in melting or a plastic deformation and damage of the dump core, due to the locally increased temperature. Moreover, the created particle showers (issuing from the hadronic and electromagnetic cascade) can affect the downstream magnet. It is important to note that the yoke lamination temperature of the PS dipole shall not exceed 60°C and the coil insulation temperature should be lower than 50°C [159]. The plot in the $z-y$ plane in Fig. 4.125 presents a graphical energy distribution over the straight section in which values were averaged for 20 cm around the vacuum tube.

To calculate the maximum temperature rise, first a simplified assumption was taken into account—an adiabatic process without a heat transfer to the surrounding elements. The adiabatic process is described by the equation

$$\Delta T = \frac{E}{V \times \rho \times C_p}, \quad (4.27)$$

where ρ is the material density, C_p the specific heat and E/V the deposited energy density. The parameters of the copper core used in this calculation are: $C_p = 0.385 \text{ J/g K}$ and $\rho = 8.96 \text{ g/cm}^3$. This results for a peak energy deposition of $E/V = 240 \text{ J/cm}^3/\text{pulse}$ in a temperature rise of $\Delta T = 69.5 \text{ K/pulse}$. In first approximation, the limiting material constraint was considered as the respective service temperature, T_s , which describes the maximum value at which a material can be used without changing its strength or other properties. For copper this is $T_s = 300^\circ\text{C}$. In case of a few pulses hitting the dump in a short period of time and a coinciding cooling failure, the temperature in the copper could exceed this value and possibly lead to partial damage in the dump core. Considering these results, it was agreed that particular care should be taken when operating the existing dump in quasi-continuous mode. In addition, ANSYS calculations will be carried out in order to study in more detail the temperature development in the core for various beam parameters.

In the magnet, the point in which the peak of the energy deposition is located is in the yoke at the depth of 2 cm in line along the beam axis, however with a maximum value which is lower than

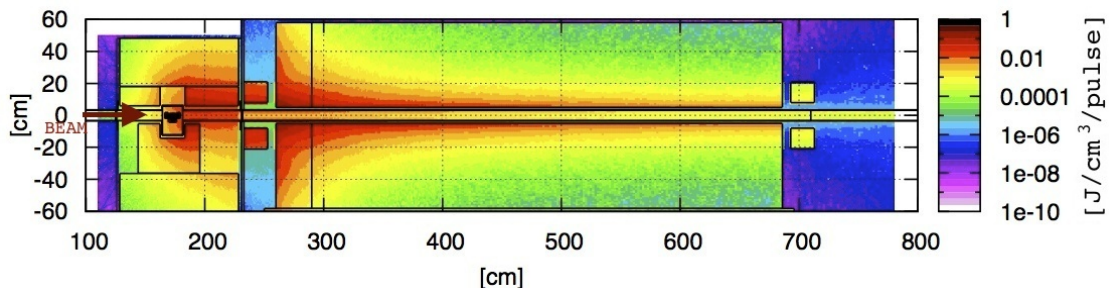


Fig. 4.125: Energy deposition in the dump area

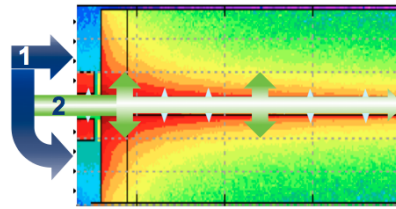


Fig. 4.126: Source of energy deposition in the magnet. (1) Frontal part interaction, (2) interaction along the vacuum tube.

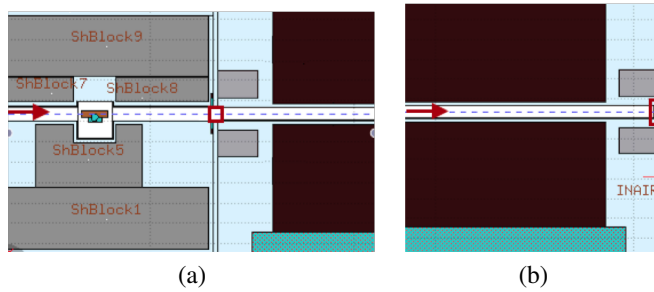


Fig. 4.127: Localization of the detector for particle leakage simulation. (a) Downstream area of the straight section. (b) Downstream area of the magnet.

1 J/cm³/pulse. Considering the material parameters for SS 316L, i.e. $C_p = 0.5 \text{ J/g K}$ and $\rho = 7.8 \text{ g/cm}^3$, results in a maximum temperature rise in the yoke which is lower than 1 K/pulse. Comparable energy deposition values can be found for the aluminium coil, which gives a similar negligible temperature rise.

Taking into consideration the total energy deposited in the yoke, 6.9 kJ/pulse, and in the coil, 1.5 kJ/pulse, it is important to estimate the fraction of the energy which could be absorbed by the dump shielding. If the contribution to the magnet heating from the beam dumping is comparable to the electrical heating, decreasing this value would be profitable due to the possibly limited efficiency of currently installed cooling. To determine the respective quantitative sources of energy deposition, two simulations were done (see Fig. 4.126). The first determined the energy deposition coming from the shower, which strikes the magnet from the frontal part, and the second the contribution from the particle scattering along the beam pipe and their respective showers. For the yoke, the frontal part is 47% of the total energy deposited in the yoke, for coils it is 65%. Unfortunately, it is not possible to further restrict the beam aperture (with an integrated absorber); thus, in order to significantly reduce the energy deposition in the magnet, a redesigning of the dump shielding on its own is not sufficient. Even with an ideal shielding (no energy deposition coming from the frontal part), the total energy will be reduced only by a factor of two. Therefore, a new dump core is required not only to stand the higher required beam intensities, but also to absorb more energy within the vacuum tube and to protect downstream installations.

4.10.2.3 Particle leakage

Quantifying the magnitude and energy distribution of the particles escaping the dump area, i.e. particle leakage, is important to better evaluate the possible damage and activation of elements located downstream of the internal dump. The particle spectrum was calculated in two positions in the vacuum tube cross-section: first in the downstream area of the straight section and second in the downstream area of following magnet (see Fig. 4.127) and the results are illustrated in Fig. 4.128.

It can be noticed that the spectrum of presented particles for the energies greater than 1 GeV is dominated by the charged hadrons—where pions and protons dominate. For the lower energies photons play the most significant role. It can also be noticed that the overall particle fluence decreases by one

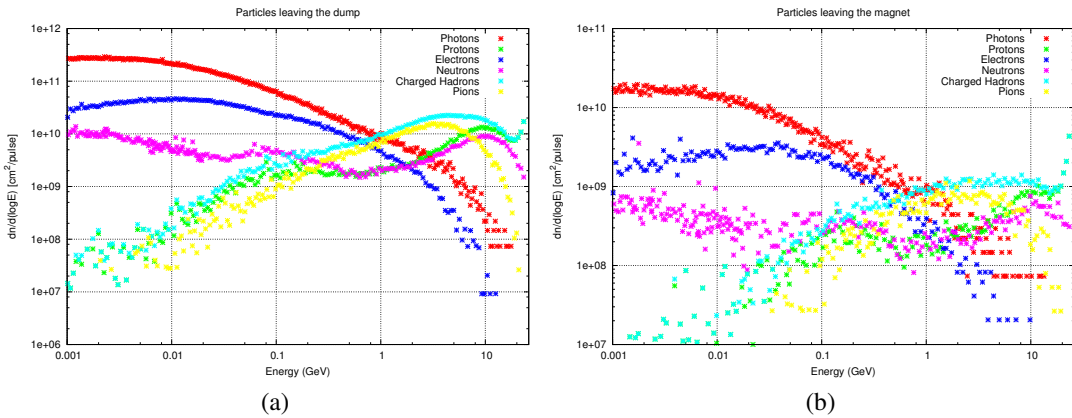


Fig. 4.128: Particle leakage. (a) Spectrum of neutrons, electrons and charged hadrons for the downstream area of SS. (b) Spectrum of neutrons, electrons and charged hadrons for the downstream area of magnet.

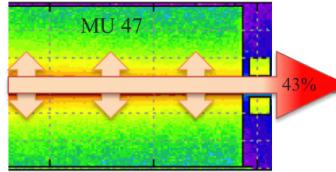


Fig. 4.129: Energy escaping the simulated geometry through the vacuum tube of MU47

order of magnitude after passing the magnet. That explains the energy deposited in the yoke, the beam pipe and surrounding elements.

In total, around 43% of the beam energy is escaping the simulated geometry (Fig. 4.129), mostly through the vacuum tube of the following magnet. As a result, approximately 20% of the primary beam energy is absorbed by the dump core and its surrounding shielding. Magnet 47 absorbs around 22% and the rest of the energy is mostly deposited on the vacuum tube and surrounding elements, such as tunnel, ground and magnet support.

4.10.2.4 Absorbed dose

Another calculation evaluated the possible long-term damage caused to the magnet coils and the dump by the absorbed dose. For the current beam conditions, the maximum absorbed dose in the coils varies around 50 Gy/pulse. For comparison, in the dump itself this value rises to 26 kGy/pulse; however, in this case, no insulating materials are concerned. For what concerns the actual limiting value of the coil materials used, it is expected that only minor degradation would be observed up to the order of MGy; thus, it can be assumed that beam dumps should not have a significant impact on coil damage.

Moreover, when comparing the calculated values for the dump operation with the actual measurements from high-level dosimeters (HLDs) distributed along the PS, it can be noticed that a standard dump operation (around 20 triggered dumps per year) yields a for the HLD at the localization of MU47 around 100 Gy/year, according to the simulation. On the other hand, measured values are of the order of 10 kGy. In more detail, the HLDs are passive dosimeters which measure the total ionizing dose integrated, usually, over a one- or two-year period. In the case of the PS, the dosimeters are located below the vacuum chamber, in the downstream edge of the magnets. The values from the last measurements (from February 2009 to March 2011) [162] from the magnets 46, 47 and 48 are: 27.47 kGy, 79.11 kGy and 31.24 kGy. This led to the conclusion that the measured dose values stem rather from the other sources

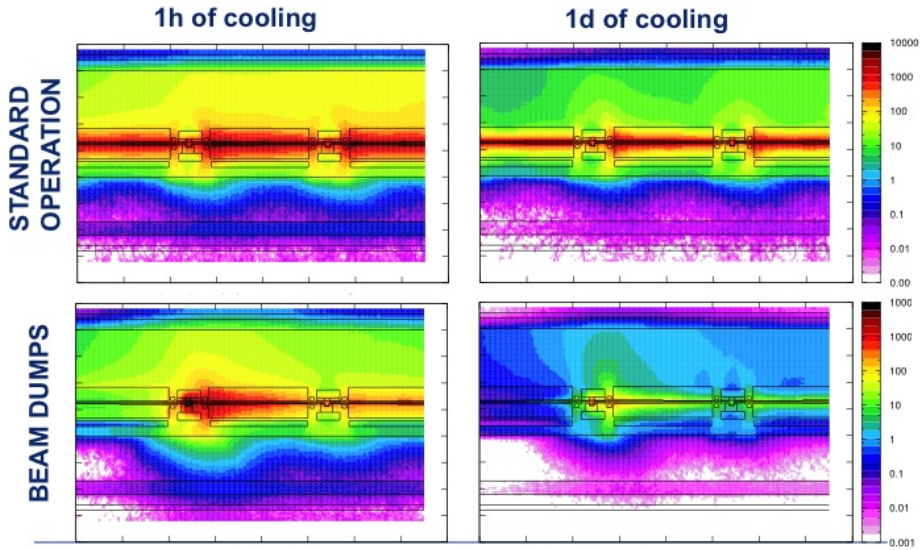


Fig. 4.130: Spatial distribution of the ambient dose equivalent $H^*(10)$ after 1 h and 1 day of cooling ($\mu\text{Sv}/\text{h}$).

of radiation—in the case of the PS most likely due to distributed beam loss.

4.10.2.5 Beam loss

To further investigate this assumption, the geometry in the calculation was extended, covering the area from SS46 up to MU49 (Fig. 4.124). Coherent with the longitudinal distribution of the values from the PS Radiation Survey [164], the losses were distributed along the beam pipe (vacuum chamber) simulating the inelastic interactions of the beam particles. In absolute terms, the total proton intensity for the period from February 2009 to March 2011 was assumed to be 18×10^{19} and the maximum beam loss in the PS of about 8%, in which 1.76% then derives from the section SS46–MU49 (based on the normalized survey measurement distribution [163]). Calculated values then result in: 65 kGy for MU46, 85 kGy for MU47 and 85 kGy for MU48, which are coherent within a ratio of 2.5 to the values measured by the HLDs. The relatively small incoherence is most likely a result of using only the most critical beam parameters for the calculations, while most of the beam losses occur for beams with lower energies [157]. Finally, the simulation nicely confirms that the major contribution to the dose absorbed by the elements located in this section actually derives from the beam loss.

Therefore, it is also important to calculate the energy deposited during the standard operation, in order to better quantify the respective heating and activation of the magnet. For the former, in the peak areas, located close to the vacuum tube, the deposited power density during a standard operation contribution does not exceed 0.6 mW/cm^3 . The resulting total power deposition for the magnet 47 and the magnet 48 in the yokes is then about 3.5 W. In the coils it is 0.61 W. This means that the averaged beam loss to the temperature rise is rather low and even higher losses over a shorter period of time should not become a limiting factor.

4.10.2.6 Residual dose

The final calculations of this first evaluation of the internal dump design referred to the ambient dose equivalent rate and its correlation to the values measured within the PS Radiation Survey [164]. In first approximation, for these simulations two basic operation scenarios were considered: one with the standard operation of 200 days and a beam intensity of 5×10^{12} pps per second plus 165 days of break (in this case the same beam-loss pattern like the one used in Section 4.10.2.5 was applied). A second scenario then assumed consecutive beam dumps over 60 s with a current of 5×10^{11} pps, then 20 days

of break and, after 10 cycles, a break of 185 days was assigned. Both annual cycles were repeated for 10 years; however, in the 10th year, the operation cycle stopped after 200 working days or last beam dump. See Fig. 4.131.

Detailed values from FLUKA calculations are presented in Fig. 4.132. They were compared to the PS Radiation Survey measurements [164]. An overall very good agreement was obtained (confirming the validity of the assumptions) and the observed differences can most likely be attributed to the differences in the assumed cooling times, the simplified constant assumption of the beam energy, the materials used for the geometry, the measurement uncertainties (distance from the vacuum tube) and finally also the scenario of the beam hitting only on the SS47 internal dump.

Figure 4.130 shows four plots for one hour and one day of cooling. While for shorter cooling times a not negligible contribution from the beam dump can be observed, such as from one day of cooling, this contribution significantly decreases. Therefore, for long cooling times the beam dumps do not play a significant role for the residual dose distribution in this area. Moreover, for this beam intensity, currently used shielding is sufficient. It attenuates the radiation produced by the beam dumps to acceptable levels outside the shielding, i.e. within 1 m distance from the dump and, after 1 month of cooling, the residual dose value from the dump operation scenario does not exceed $1 \mu\text{Sv}/\text{h}$. In the development of a new dump design, dedicated radioprotection studies shall be considered.

4.10.3 Upgraded beam parameters

4.10.3.1 Current design for the new beam parameters

For the beam intensity increased by a factor of five, a first approach was to simulate the current design. Based on the results of the previous sections, the most critical is clearly the impact of the deposited energy on the temperature rise in the dump core. Assuming no heat exchange and copper parameters used before, for the peak of the energy deposition, $1.2 \text{ kJ/cm}^3/\text{pulse}$, the temperature-rise peak would be around 340°C , whereas the already mentioned maximum service temperature for copper is only 300°C , confirming the need of a new dump core design.

4.10.3.2 Sandwich design

The redesign started with the investigation of proper material candidates. Based on generic calculations with the maximum beam parameters and a set of available dump materials, only those ones where the temperature rise from the deposited energy is lower than their service temperature were selected for a further preliminary study. Short-listed materials are:

- carbon composites—with $\rho = 1.7 \text{ Ug/cm}^3$, $C_p = 0.755 \text{ UJ/g }^\circ\text{C}$ and $T_s = 2000^\circ\text{C}$, while $\Delta T = 96$;
- titanium—with $\rho = 4.5 \text{ Ug/cm}^3$, $C_p = 0.54 \text{ UJ/g }^\circ\text{C}$ and $T_s = 540^\circ\text{C}$, while $\Delta T = 158$;

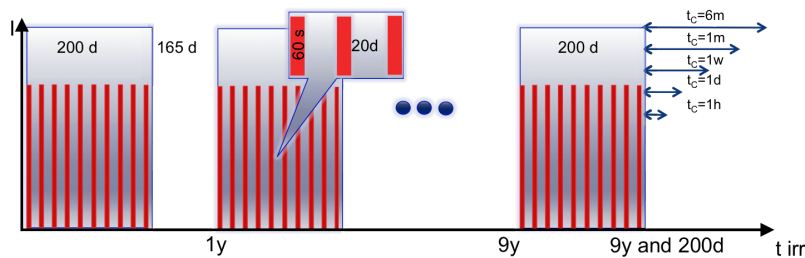


Fig. 4.131: Irradiation profile used for residual dose calculations. Red—beam-dumping scenario, blue—standard operation scenario.

cooling time	Upstream SS47				Downstream SS47				Upstream SS48				Downstream SS48			
	Inside		Outside		Inside		Outside		Inside		Outside		Inside		Outside	
1d 32h	106	271	97	156	272	207	260	84	100	53	141	101	173	109	276	79
1w 224h	68	58	59	48	161	45	165	50	64	37	89	72	109	66	182	46
1m 1470h	51	48	42	44	105	38	110	39	48	35	61	61	121	50	76	39
6m 187d	14	33	7	34	21	25	28	29	42	27	35	53	56	32	49	23

Fig. 4.132: Results for residual dose ($\mu\text{Sv}/\text{h}$) in FLUKA simulation (orange) and PS radiation survey measurements (blue).

- tungsten—with $\rho = 19.3 \text{ Ug/cm}^3$, $C_p = 0.134 \text{ UJ/g }^\circ\text{C}$ and $T_s = 2760^\circ\text{C}$, while $\Delta T = 2000$;
- molybdenum—with $\rho = 10.22 \text{ Ug/cm}^3$, $C_p = 0.25 \text{ UJ/g }^\circ\text{C}$ and $T_s = 550^\circ\text{C}$, while $\Delta T = 500$.

To absorb most of the energy within the relatively short dump core, and at the same time ensure a relatively low temperature rise in the material, it was decided to combine two or three materials in the form of a ‘sandwich’ (in a simplified way represented as an internal cylinder covered by larger and longer ones). For the inner material, one with a relatively low density was chosen, surrounded by medium and then highest density layers, the latter chosen for all cases as tungsten.

A first promising model contained a 15 cm long and 3 cm large cylinder made of carbon composites, which was surrounded by titanium with a total length of 25 cm and external radius of 4 cm and finally covered by a tungsten layer with a total length of 30 cm and an external radius of 5 cm. Simulations showed that, in this case, none of the materials would exceed the service temperature, but only a very limited amount of energy was absorbed and the maximum temperature rise in the tungsten layer (1300 K/pulse) together with the formation of shock waves could cause surface cracks or decrease the dump core lifetime. Other configurations were thus aiming for a higher intermediate density and length combination, where only a combination of two materials—titanium and tungsten—was tested. Unfortunately, in these cases, the tungsten temperature was raised to a maximum value of 1500 K/pulse (with sandwich of 15 cm titanium) or 1300 K/pulse (20 cm titanium). Therefore, a third material with density between titanium and tungsten was investigated to be placed in between; we opted for molybdenum as preliminary choice (knowing that possibly interesting composite materials would exist for a final design study): $\rho = 10.22 \text{ g/cm}^3$, $C_p = 0.25 \text{ J/g }^\circ\text{C}$ and $T_s = 550^\circ\text{C}$.

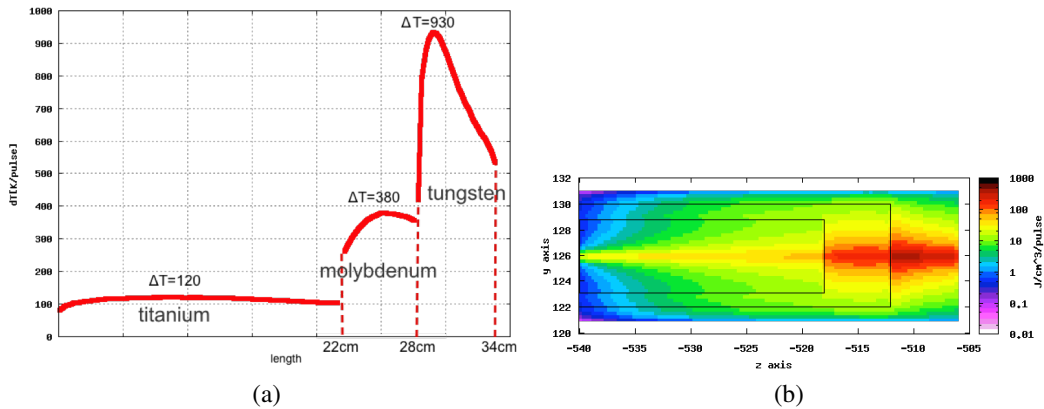


Fig. 4.133: (a) Temperature rise and (b) energy distribution in 34 cm titanium–molybdenum–tungsten sandwich dump core.

Although this molybdenum layer can significantly decrease the temperature rise in the tungsten, it almost reaches the service temperature ($T_s = 550^\circ\text{C}$)—with peak temperature rises around 450 K/pulse to 500 K/pulse (for the titanium length from 10 to 20 cm). To complete this first preliminary study, the

length of the titanium as a first cylinder was further extended by 2 cm. And, the length of the molybdenum was extended by another 2 cm to further reduce the peak temperature rise in tungsten. Results for this version are presented in Fig. 4.133, showing the maximum temperature rise along the sandwich and the energy distribution. It can be noticed that the temperature rise in the molybdenum decreased below 400 K/pulse and by using only 6 cm of molybdenum beyond titanium, the temperature rise in tungsten decreased to a value of 930 K/pulse.

This mentioned design could be a promising option for a first preliminary mechanical study of a new dump core. Further investigations of the thermomechanical behaviour, available materials to be used and a detailed mechanical design have to be iterated between the design and calculation teams, which shall soon lead to a design where all parameters can be further optimized.

In conclusion, this preliminary design study allowed us to very successfully benchmark the existing dump installation and analyse the main limitations associated to the dump itself and the elements, both for the operation of the existing dump, as well as for future dump designs. In further studies it is important to clarify two relevant constraints: (a) heating/cooling limitation of the downstream magnets—especially for such elements as PFW coils located close to the beam pipe; and (b) the maximum acceptable load for the movable parts of the dump.

Tables

4.1	Relevant beam parameters in the PS during the flat-top RF gymnastics for the two bunch spacings of 50 and 25 ns	317
4.2	Principal injection septum parameters	332
4.3	Principal bumper septum parameters	333
4.4	KFA45 system parameters	334
4.5	KFA53 system parameters	335
4.6	Injection bumper magnet parameters	337
4.7	SMH42 parameters and operational requirements	338
4.8	Ratings of the power converter for the SMH42 septum magnet	338
4.9	Operational requirements and parameters of the injection bumpers	339
4.10	Parameters of the power converters for BSM40, 41, 43 and 44	340
4.11	Parameters of the power converters for BSM42	340
4.12	Circuit summary	341
4.13	The PU parameters	343
4.14	Comparison between the performance of the present amplifiers and the specification of the new amplifiers.	348
4.15	Feedback kicker basic requirements	350
4.16	Simulated and measured amplifier parameters for the 800 V _{Peak} gap voltage	357
4.17	Beam characteristics	358
4.18	PS beam intensities per bunch with 25 ns bunch spacing	361
4.19	RF systems for LHC-type beams in the PS	366
4.20	Estimation of the photons generated by EC with the LHC-type beams in the PS main magnet vacuum chamber.	379
4.21	Impedance contribution of important machine elements evaluated at the bunch spectrum cut-off. For the RF cavities the fundamental mode parameters are reported, also by taking into account the fast RF feedback.	383
4.22	Indirect space charge contributions to the total transverse effective impedance at different kinetic energies for round chamber and parallel plates.	391
4.23	List of PS elements that have been simulated and accounted for in the model and the corresponding imaginary part of the total effective impedance (horizontal and vertical). * The indirect space charge is given at 2 GeV; see Table 4.21.	393
4.24	Comparison between estimated total effective impedance contributions (indirect space charge $Z^{\text{ind.s.c.}}$, resistive wall Z^{RW} , other simulated devices $Z^{\text{sim.devices}}$) and measured impedance from the current PS model.	394
4.25	Summary of the annual dose to workers at the closest workplaces (criteria 100 μSv for 2000 h of occupancy) and to the reference group (5 μSv for 2550 h of operation) due to the permanent loss of 10^{11} pps in the Septum 16 area. The three options are compared to the current shielding.	398
4.26	Wideband PU characteristics	407
4.27	Expected hit rates from the most demanding beams calculated for pressure of 10^{-9} mbar	411

Figures

4.1	Tune-loss map. The colour code indicates losses. The operational working area is identified by the rectangle.	288
4.2	Longitudinal beam profiles during an adiabatic bunch compression	289
4.3	Emittance growth and losses after 1.2 s at 1.4 GeV kinetic energy for two different working points.	290
4.4	Time evolution of the vertical emittance blow-up for four different space charge maximum detunings.	291
4.5	Tune-loss maps for the two different compensation schemes: the first row is a horizontal scan of the tune space while the second row is a vertical one. The first column is the scan at 2 GeV, without any compensation. The second column is a scan while compensating the $2Q_x + Q_y = 19$ resonance and the third column is a scan while compensating the $3Q_y = 19$ resonance.	292
4.6	Influence of auxiliary circuits on the linearity of the machine. (a) Bare machine. (b) Tune control with PFWs ($Q_h = 6.10$, $Q_v = 6.20$).	294
4.7	Several graphical representations of the working point plane. (a) Horizontal scan at 1.4 GeV using the LEQs. (b) Detail of a vertical scan at 1.4 GeV using the LEQs. (c) Horizontal scan at 2 GeV using the PFWs in 4CM. (d) Vertical scan at 2 GeV using the PFWs in 4CM. The highlighted area appears to be free of severe resonances; the vertical fourth order is indicated by the white line.	295
4.8	Vertical scan at 2 GeV using the PFWs in 4CM and setting $\xi_x = -0.2$	296
4.9	Present injection region layout [15]	297
4.10	The aperture at the injection region (top) and the beam envelopes at the septum (bottom) with the present injection at $E_k = 1.4$ GeV [13] (3 σ envelopes for $\epsilon_n^x = 10$ and $\epsilon_n^y = 5$ mm mad, $\sigma_{\Delta p/p} = 1.5 \times 10^{-3}$).	298
4.11	The aperture at the injection region (top) and the beam envelopes at the septum (bottom) using KFA45 and KFA53 at $E_k = 2$ GeV [13] (3 σ envelopes for $\epsilon_n^x = 10$ and $\epsilon_n^y = 5$ mm mad, $\sigma_{\Delta p/p} = 1.5 \times 10^{-3}$).	299
4.12	The aperture at the injection region (top) and the beam envelopes at the septum (bottom) using KFA45 and KFA53 at $E_k = 2$ GeV with the addition of the doublet in SS33 and SS49 [13] (3 σ envelopes for $\epsilon_n^x = 10$ and $\epsilon_n^y = 5$ mm mad, $\sigma_{\Delta p/p} = 1.5 \times 10^{-3}$).	300
4.13	The damping time of the feedback	304
4.14	With $\xi = -0.8$ and fully uncoupled machine. The signals in green and yellow represent respectively the horizontal position and sum signal along the bunch. The HT instability without TFB (above). The observation using the TFB (below): the instability has been successfully cured. It is worth noting that the frequency spectrum of the instability is extending up to ≈ 35 MHz.	305
4.15	With $\xi = -0.8$ and fully uncoupled machine. The signal represents the total charge in the ring during the cycle. The HT instability without TFB (above). The observation using the TFB (below): all measurable beam losses disappeared.	306
4.16	Resistive wall and broadband impedances. The solid and dashed lines refer respectively to the real and imaginary parts. Note that the vertical scale is different and that the resistive wall impedance real part is 1000 times higher than the broadband impedance in the considered frequency range.	307

4.17	Frequency spectrum of the different modes assuming a bunch length of 180 ns and parabolic bunch distribution for vanishing chromaticity.	308
4.18	Instability growth for the different modes at $E_k = 1.4$ GeV and 2 GeV (respectively above and below). We consider $N = 2.76 \times 10^{12}$ ppb, that is, 12.3×10^{11} ppb at top energy considering 12-fold splitting.	309
4.19	By varying the chromaticity (colour coded in the plot), different modes with different frequency and growth time constant can be excited. For the frequency coordinate we considered the maximum of the spectrum of Fig. 4.17 (180 ns full bunch length) taking into account the frequency shift due to chromaticity. For the growth time constant we assumed $N = 2.76 \times 10^{12}$ ppb. The plots refer to $E_k = 1.4$ GeV and 2 GeV (respectively above and below).	310
4.20	Gamma transition jump in the CERN PS. The dotted curve represents the relativistic gamma as a function of time, the dot-dashed one is the unperturbed gamma transition and the plain curve shows γ_t with gamma transition jump.	312
4.21	Result of the momentum compaction η with the gamma transition jump in the CERN PS. The dot-dashed curve represents the unperturbed η as a function of time and the plain curve shows the one with gamma transition jump.	312
4.22	Currents powering the gamma transition jump quadrupoles as a function of time. The γ_{tr} -jump is triggered while the currents of doublets are changing sign.	313
4.24	Measured intensity threshold of the instability as a function of the longitudinal emittance for the two sets in chromaticity.	315
4.25	η threshold as a function of the beam intensity for a longitudinal emittance of 1.9 eV s for a chromaticity close to zero and negative.	315
4.26	Sets of vertical chromaticity for the instability measurements with gamma transition jump	316
4.27	Intensity threshold measurements with a gamma transition jump for two different working points.	316
4.28	E-cloud build up during passage of a 50 ns bunch train with 4 ns bunch length (left) and during passage of a 25 ns bunch train with 4 ns bunch length (right). The sometimes visible sawtooth behaviour follows a bunch-by-bunch intensity modulation present during the measurements.	319
4.29	Envelope of the build up during passage of a 50 ns (left) and a 25 ns (right) bunch train with 1.5×10^{11} ppb.	320
4.30	E-cloud build up simulation (left) and measurement (right) for a 25 ns beam with 1.33×10^{11} ppb and 4 ns long.	320
4.31	(Left) evolution of the horizontal centroid position for selected bunches along the bunch train ($t = 0$ roughly corresponds to the beginning of the bunch shortening); (right) bunch-by-bunch position for five consecutive turns at different moments during the store (the horizontal scale is chosen in order to better visualize the unstable bunches).	321
4.32	Pressure measured with two consecutive LHC-type cycles (the beam is extracted at $t = 0$ and $t = 3.6$ s) for different RF manipulations. Comparison between two different bunch intensities: $\sim 1.25 \times 10^{11}$ ppb on the left and $\sim 1.45 \times 10^{11}$ ppb on the right.	322
4.33	Geometry of the three possible PS chambers analysed in the EC-parameter studies. From top to bottom: the standard chamber (width 146 mm, height 70 mm), the special exterior chamber (width 178 mm, height 68 mm) and the special interior chamber (width 178 mm, height 68 mm).	322

4.34	EC line density as a function of the SEY for different bunch lengths (as labelled), for different values of bunch population ($1.0, 1.3, 1.9$ and 2.6×10^{11} ppb, from top left to bottom right, for two possible bunch spacings (25 ns solid lines and 50 ns dashed lines)).	323
4.35	Coupled-bunch mode spectrum during acceleration of 21 bunches in $h = 21$, averaged over 10 cycles for each measurement time ($N_b = 4.0 \times 10^{11}$ ppb, $\varepsilon_{1,RMS} = 0.14$ eV s).	325
4.36	Coupled-bunch mode spectrum during acceleration of 18 bunches in $h = 21$, averaged over 10 cycles for each measurement time ($N_b = 3.9 \times 10^{11}$ ppb, $\varepsilon_{1,RMS} = 0.13$ eV s).	326
4.37	Simulated growth of coupled-bunch modes under similar conditions as for the measurements with 21 bunches in $h = 21$ (compare Fig. 4.35).	326
4.38	Simulated growth of coupled-bunch modes under similar conditions as for the measurements with 18 bunches in $h = 21$ (compare Fig. 4.36).	327
4.39	Example mode spectrum of 21 bunches in $h = 21$, excited at the upper sideband of $19f_{rev}$ ($E \simeq 14$ GeV, average of five cycles, $\pm 1\sigma$ and min–max spread are indicated by the red and blue rectangles).	327
4.40	Mode spectra measured after excitation of the upper sideband for 21 bunches at $h_{RF} = 21$ (full ring).	328
4.41	Mode spectra measured after excitation of the upper sideband for 18 bunches at $h_{RF} = 21$ (6/7 filling).	328
4.42	Comparison of the coupled-bunch mode spectrum on the flat top for the LHC-type beams with 25 ns (left) and 50 ns (right) final bunch spacing. In both cases a batch of 18 bunches is kept at low voltage on $h = 21$ until extraction. The vertical scale of both plots is identical.	329
4.43	Relative bunch intensity at extraction versus position within the batch (averaged over 10 cycles, LHC 50 ns, 1.9×10^{11} ppb) [48].	330
4.44	Phase error between 10 MHz and 20 MHz versus time (50 ns bunch spacing, 1.9×10^{11} ppb, constant offsets removed). The vertical scale is in degrees with respect to the lower harmonic $h = 21$. The batch length is 12 (black), 24 (red) or 36 bunches (blue), corresponding to 2/7, 4/7 and 6/7 of the circumference. The periodicity is $1/f_{rev} = 2.1 \mu\text{s}$ [48].	330
4.45	Bumper septum (left) and injection septum (right) inside common vacuum tank	331
4.46	SMH42 θ_x homogeneity map. Septum blade to the right	332
4.47	KFA45 module layout	334
4.48	KFA53 module layout	335
4.49	Actual injection bumper magnet	336
4.50	Power converter topology for the SMH42 septum magnet	338
4.51	SMH42 magnet current waveform with 2 GeV beam operation	339
4.52	Power: part-simplified architecture/topology	340
4.53	Regulation control: simplified schematic	341
4.54	The block diagram of the PS TFB. The magenta rectangles refer to the devices installed in the tunnel.	342
4.55	The PU electrodes	343
4.56	The bandwidth of the PU pre-amplifier with variable amplification	344
4.57	The frequency response of the DSPU (amplitude with notch and Hilbert filters bypassed) for a clock of 80 MHz (top); the transfer function of the programmable amplifier used downstream of the DSPU (bottom).	345

4.58	Global frequency response of the DSPU including notch and Hilbert filters with pre-amplifier, power amplifier, matching network, kicker and final load. The response is dominated by the power amplifier itself. The observed ripple is due to the DSPU notch filter. The second trace corresponds to the non-linear phase.	346
4.59	The time progression of the peak detected voltage out of the power amplifier with its natural decay from 3 kW to 800 W transition (top, yellow trace); the beam-induced voltage observed on the kicker with its reflection as produced by the high-impedance power amplifier output (bottom).	347
4.60	The PS TFB kicker in PS SS97	348
4.61	Basic cell configuration	350
4.62	MA core mounted on a copper cooling ring	351
4.63	MA core temperature distribution [°C]	351
4.64	Single-core impedance and R–L–C equivalent (left), maximum voltage for 1 kW dissipation (right).	351
4.65	Comparison of measured and simulated impedance (left); equivalent circuit model (right)	352
4.66	Differential output amplifier—output circuit configuration	352
4.67	Single-ended output amplifier—output circuit configuration	353
4.68	Relative change of V_{GS} versus received dose	354
4.69	3D view of cavity, amplifiers and shielding in the PS SS02	354
4.70	Measured single-ended amplifier output impedance	355
4.71	Measured cell gap impedance with single-ended amplifiers and 4 ns cables	355
4.72	System configuration	356
4.73	System measured response: red: normal, blue: linearized	356
4.74	Saturation MOSFET currents: green VRF151, violet SD2942, blue MRF151, red MRFE6VP6300.	359
4.75	Simulated gap voltage (black) and beam current (green) (left: no compensation, right: compensated).	359
4.76	Simulated amplifier output currents (black and blue) and beam current (green) (left: no compensation, right: compensated).	359
4.77	Simulated drain currents (black and blue) and beam current (green) (left: no compensation, right: compensated).	360
4.78	Behaviour of the spark gap voltage limiter at different frequencies	361
4.79	One of the 11 10 MHz RF cavities in the PS with its amplifier sitting in the cavity base	362
4.80	One of the 80 MHz cavities with final RF amplifier; 40 MHz cavities look very similar	364
4.81	Prototype equipment set-up during a measurement session	365
4.82	PS feedback board	367
4.83	Combination of beam loading compensation feedback (blue) and synchrotron frequency sideband processing for coupled-bunch damping (red).	373
4.84	Picture of the existing EC experiment installed in PS straight section 98, containing two shielded button PUs, a shielded Penning gauge, a clearing electrode and a small dipole magnet [39].	374
4.85	Draft design of the MU98 vacuum chamber equipped with the shielded button-type PU (drawing by T. Capelli and C.F. Eymin).	376

4.86	(a) Phenomenology of electrons impinging on a surface. (b) Schematic of the principle of cathodoluminescence from a metal surface.	376
4.87	Corrected cathodoluminescence spectra of clean Cu at electron energies 300 eV and 1 keV [101].	377
4.88	Schematic diagram of the experimental set-up which implements the concept displayed in Fig. 4.86.	378
4.89	Cathodoluminescence spectra of an oxidized stainless steel surface at electron energy of 300 eV. The spectra are uncorrected for the system response. (a) The measured current density on the sample is $3 \mu\text{A}$ per 2 mm^2 . (b) The measured current density on the sample is $9 \mu\text{A}$ per 2 mm^2	379
4.90	Drawing of the MU98 equipped with two flanges for installation of the new EC monitors: DN35 for installation of the shielded PU and DN63 for installation of the optical window for detection of inverse photoemission (courtesy of T. Capelli).	380
4.91	Example screen-shot of amplitude and phase of the quadrupole beam transfer function for a bunch of about 9×10^{10} protons kept by 95 kV at 40 MHz. The diamonds indicate the zero-amplitude quadrupole synchrotron frequency.	381
4.92	Incoherent quadrupole synchrotron frequency shift obtained with the two sets of measurements.	382
4.93	Wake potential of a 2.3 ns Gaussian bunch given by the total impedance budget and by an inductive impedance model with $\text{Im}[Z(p)]/p = 18.4 \Omega$	383
4.94	Wake potentials of a 2.3 ns Gaussian bunch given by the Heifets–Bane model $Z(\omega) = (i5.86 \times 10^{-6}\omega + 316) \Omega$ and a broadband resonator with $f_r = 0.48 \text{ GHz}$ and $R_s = 17.7 \text{ k}\Omega$, compared to the total wake budget.	384
4.95	Model of the 10 MHz RF cavity	384
4.96	Real part of the impedance of all the 10 MHz RF cavities	385
4.97	Impedance of the Finemet cavity	386
4.98	Measurements of tune shift in the two planes (left and right) at a kinetic energy of 25 GeV	388
4.99	Comparison between measured (black) and reconstructed (red) integrated phase advance slope versus longitudinal position around the PS, with intensity obtained by varying the current of two quadrupoles. The impedance locations are shown in blue and the two quadrupoles QLS29 and QSE87 are clearly identified.	390
4.100	Top: reconstructed impedances with spatial confidence bounds (Δs) and accuracy limit given by the noise level (horizontal red line); bottom: integrated phase advance slope and least-square reconstruction (LSQR).	390
4.101	Horizontal (left) and vertical (right) impedance of the kicker KFA13, comparison between simulations and measurements.	392
4.102	Half 10 MHz cavity model simulated with CST and transverse impedance results	392
4.103	Total real impedance budget obtained so far as a function of frequency	394
4.104	Total imaginary impedance budget obtained so far as a function of frequency	394
4.105	Horizontal layer showing the dose equivalent rate above the Route Goward for 2.25×10^2 pps injected in the PS.	396
4.106	1.8 m thick slab over PS tunnel	399
4.107	Cross-section of Route Goward and PS (extract of drawing SYN1146000010-)	399
4.108	Temporary road	400

4.109	Piling works	401
4.110	Extent and finished level of backfill required in Septum 16	402
4.111	Component structures of the Septum 16 area	403
4.112	Schematic plan of load-bearing system for additional backfill	403
4.113	Bird's-eye view of the new slab	404
4.114	Biodegradable slab formwork	405
4.115	Site installations	406
4.116	Schedule of the civil engineering works	406
4.117	New shielding on top of the extraction region	406
4.118	Assembly drawing of the TT2 wideband PU	407
4.119	The new PS WCM	409
4.120	Matched bridge clipping circuit	410
4.121	WCM raw output (upper) and clipper output signal (lower)	410
4.122	Schematic of the proposed read-out system	411
4.123	FLUKA representation of the straight section 47 and downstream magnet MU47	413
4.124	FLUKA representation with extended geometry	414
4.125	Energy deposition in the dump area	414
4.126	Source of energy deposition in the magnet. (1) Frontal part interaction, (2) interaction along the vacuum tube.	415
4.127	Localization of the detector for particle leakage simulation. (a) Downstream area of the straight section. (b) Downstream area of the magnet.	415
4.128	Particle leakage. (a) Spectrum of neutrons, electrons and charged hadrons for the downstream area of SS. (b) Spectrum of neutrons, electrons and charged hadrons for the downstream area of magnet.	416
4.129	Energy escaping the simulated geometry through the vacuum tube of MU47	416
4.130	Spatial distribution of the ambient dose equivalent H*(10) after 1 h and 1 day of cooling ($\mu\text{Sv}/\text{h}$).	418
4.131	Irradiation profile used for residual dose calculations. Red—beam-dumping scenario, blue—standard operation scenario.	418
4.132	Results for residual dose ($\mu\text{Sv}/\text{h}$) in FLUKA simulation (orange) and PS radiation survey measurements (blue).	419
4.133	(a) Temperature rise and (b) energy distribution in 34 cm titanium–molybdenum–tungsten sandwich dump core.	420

References

- [1] S. Gilardoni *et al.*, The high intensity/high brightness upgrade program at CERN: status and challenges, Proc. HB2012, Beijing, China, 2012.
- [2] R. Cappi *et al.*, Measurement and reduction of transverse emittance blow-up induced by space charge effects, Proc. PAC 93, Washington, DC, USA, 1993.
- [3] M. Giovannozzi *et al.*, Possible improvements to the existing pre-injector complex in the framework of continued consolidation, Proc. Chamonix 2010 Workshop LHC Performance.
- [4] A. Huschauer, Working point and resonance studies at the CERN proton synchrotron, CERN-THESIS-2012-212 (2012).
- [5] R. Wasef *et al.*, Space charge effects and limitations in the CERN proton synchrotron, Proc. IPAC2013, Shanghai, China, 2013.
- [6] R. Cappi *et al.*, Control of coherent instabilities by linear coupling, CERN/PS2001-010 (AE) (2001).
- [7] K. Schindl *et al.*, Space charge, CERN/PS 99-012 (DI) (1999).
- [8] Y. Baconnier, Tune shifts and stop bands at injection in the CERN proton synchrotron, CERN/PS 87-89(PSR) (1987).
- [9] G. Franchetti, B. Franczak and P. Schütt, A benchmarking experiment in SIS for dynamic aperture induced beam loss, GSI-Acc-Note-2004-05-001 (2004).
- [10] J. Borburgh, S. Aumont, W. Bartmann, S. Gilardoni, B. Goddard, L. Sermeus and R. Steerenberg, Feasibility study of a CERN PS injection at 2 GeV, Proc. IPAC2011, San Sebastián, Spain, pp. 3–5.
- [11] W. Bartmann, B. Balhan, J. Borburgh, J. Cole, S. Gilardoni, B. Goddard, O. Hans, M. Hourican, L. Sermeus, R. Steerenberg and C. Yu, Upgrades for the CERN PSB-to-PS transfer at 2 GeV, Proc. IPAC2013, Shanghai, China, pp. 404–406.
- [12] S. Aumont, B. Balhan, W. Bartmann, J. Borburgh, S. Gilardoni, B. Goddard, M. Hourican, L. Sermeus and R. Steerenberg, Feasibility of 2 GeV injection into the CERN PS, Proc. IPAC2011, San Sebastián, Spain, pp. 343–347.
- [13] C. Yu, S. Gilardoni, S. Aumont, W. Bartmann, J. Borburgh and G. Arduini, Beam envelope optimization for PS injection at 2 GeV, 2012, to be published.
- [14] R. Steerenberg, PS Protons Injection Diagnostics, EDMS 1207510.
- [15] S. Aumont, Ph.D. thesis, 2012, <http://infoscience.epfl.ch/record/180214>, CERN-THESIS-2012-261 (2012)
- [16] C. Pellegrini, *Nuovo Cimento LXIV* (1969), pp. 447–473
- [17] F.J. Sacherer, Transverse bunched beam instabilities: theory, 9th Int. Conf. High-energy Accelerators, 1974, pp. 347–351.
- [18] F.J. Sacherer, Theoretical aspects of the behaviour of beams in accelerators and storage rings, First Course Int. School Particle Accelerators, ‘Ettore Majorana’ Centre for Scientific Culture, Erice, Italy, 1976.
- [19] J.-L. Laclare, CAS: Advanced Accelerator Physics, 1985.
- [20] G. Rumolo and F. Zimmermann, Practical user guide for HEADTAIL, SL-Note-2002-036-AP (2002).
- [21] A. Burov, *Phys. Rev. ST Accel. Beams* **12**(4) (2009) 044202.
- [22] R. Cappi, Observation of high-order head-tail instabilities at the CERN-PS, CERN-PS-95-02-PA (1995).
- [23] E. Métral, Ph.D. thesis, CERN-THESIS-1999-074 (1999).
- [24] E. Métral, G. Rumolo, R. Steerenberg and B. Salvant, Simulation study of the horizontal head-tail

- instability observed at injection of the CERN proton synchrotron, Proc. PAC2007, Albuquerque, NM, US, pp. 4210–4212.
- [25] E. Métral *et al.*, Beam break-up instability in the CERN PS near transition, CERN-PS-2000-017-AE (2000).
 - [26] S.Y. Lee, *Accelerator Physics*, 2nd ed. (World Scientific, 1999).
 - [27] E. Métral and G. Rumolo, Collective effects, USPAS Course, 2009.
 - [28] K.Y. Ng, *Physics of Intensity Dependent Beam Instabilities*, 1st ed. (World Scientific, 2006).
 - [29] A. Sorensen, *Part. Accel.* **6** (1975) 141.
 - [30] W. Hardt, Gamma transition jump scheme in the CPS, CERN-MPS-DL 74-3, 1974.
 - [31] S. Aumont *et al.*, Study of beam losses at transition crossing at the CERN PS, CERN-AB-2008-015 (2008).
 - [32] G.C. Schneider, A 1.5 GHz wide-band beam-position and intensity monitor for the electron–positron accumulator, CERN-PS-87-44-BT (1987).
 - [33] E. Métral, Stability criteria for high intensity single bunch beams in synchrotrons, Proc. EPAC2002, Paris, France, pp. 1532.
 - [34] E. Métral, Crossing transition with TMCI, RLC CERN Internal Meet., 2006.
 - [35] R. Garoby, Status of the nominal proton beam for LHC in the PS, CERN/PS 99-13 (RF) (1999).
 - [36] R. Cappi *et al.*, *Phys. Rev. ST Accel. Beams* **5** (2002) 094401.
 - [37] R. Steerenberg and M. Morville, Accelerator Performance Committee Meet., 15 December 2006.
 - [38] R. Steerenberg *et al.*, Nominal LHC beam instability observations in the CERN proton synchrotron, Proc. 22nd Particle Accelerator Conf., Albuquerque, NM, USA, 25–29 June 2007.
 - [39] E. Mahner, T. Kroyer and F. Caspers, *Phys. Rev. ST Accel. Beams* **11** (2008) 094401
 - [40] G. Iadarola and G. Rumolo, PyECLOUD and build up simulations at CERN, Proc. ECLOUD’12 Workshop, Isola d’Elba, Italy, 5–9 June 2012.
 - [41] S. Gilardoni *et al.*, The PS upgrade programme: recent advances, WEPEA042, Proc. 4th Int. Particle Accelerator Conf., Shanghai, China, 12–17 May 2008.
 - [42] A. Blas *et al.*, Beam tests and plans for the CERN PS transverse damper system, WEPME011, Proc. 4th Int. Particle Accelerator Conf., Shanghai, China, 12–17 May 2008.
 - [43] H. Damerau *et al.*, Electron cloud mitigation by fast bunch compression in the CERN PS, Proc. 11th European Particle Accelerator Conf., Genoa, Italy, 23–27 June 2008.
 - [44] H. Damerau *et al.*, RF manipulations for higher brightness LHC-type beams, WEPEA044, Proc. 4th Int. Particle Accelerator Conf., Shanghai, China, 12–17 May 2008.
 - [45] S. Rioja-Fuentelsaz, G. Iadarola and G. Rumolo, Electron cloud simulation studies for the CERN-PS in 2012 and 2013, CERN ATS Note, in course of publication.
 - [46] H. Damerau, RF issues with (beyond) ultimate LHC beams in the PS in the Lin4 era, unpublished presentation at the LIU Day, Thoiry, France, 2010.
 - [47] H. Damerau, S. Hancock, C. Rossi, E. Shaposhnikova, J. Tuckmantel and J.-L. Vallet, Longitudinal coupled-bunch instabilities in the CERN PS, PAC07, Albuquerque, NM, USA, 25–29 June 2007.
 - [48] H. Damerau, S. Hancock and M. Schokker, Longitudinal performance with high-density beams for the LHC in the CERN PS, ICFA-HB2010, Mohrschach, Switzerland, 2010, p. 193.
 - [49] M. Bassetti, A. Ghigo, M. Migliorati, L. Palumbo and M. Serio, A time domain simulation code of the longitudinal multibunch instabilities, Internal Note G-19, Frascati, Italy, 1993.
 - [50] D. Grier, The PS 10 MHz cavity and power amplifier, PS/RF/Note 2002-073, CERN, Geneva, Switzerland (2002).
 - [51] M. Morville, R. Garoby, D. Grier, M. Haase, A. Krusche, P. Maesen, M. Paoluzzi and C. Rossi,

- The PS 13.3–20 MHz RF systems for LHC, PAC03, Portland, OR, USA, 2003, p. 1725.
- [52] M. Benedikt (ed.), The PS complex as proton pre-injector for the LHC – design and implementation report, CERN 2000-03, CERN, Geneva, Switzerland, p. 47.
- [53] C.M. Bhat, F. Caspers, H. Damerau, S. Hancock, E. Mahner and F. Zimmermann, Stabilizing effect of a double-harmonic RF system in the CERN PS, PAC09, Vancouver, BC, Canada, 2009, p. 4670.
- [54] V. Pricop and B. Balhan, SMH 42 and Bumper 42 eddy current septum feasibility study, CERN, EDMS 1265116.
- [55] C. Yu, Low beta insertion aperture assessment, to be published.
- [56] K.D. Metzmacher and L. Sermeus, The PS injection kicker KFA45 performance for LHC, CERN PS/PO/Note 2002-015 (2002).
- [57] M. Sapinski, O. Keller and B. Dehning, Proposal for the PS beam gas ionization monitor, BI Tech Board, CERN, 2014.05.15.
- [58] D. Bodart, Use of the PS bumper injection septum magnets after the PS Booster upgrade at 2.0 GeV, EDMS 1171781.
- [59] D. Bodart, Evaluation of the magnets for the upgrade at 2.0 GeV injection energy, EDMS 1398184.
- [60] J.M. Cravero and J.P. Royer, The new pulsed power converter for the septum magnet in the PS straight section 42, CERN PS/PO/Note 97-03 (1997).
- [61] J.M. Cravero, C. De Almeida Martins, R. Garcia Retegui, N. Wassinger, M. Benedetti, A new multiple-stage converter topology for high power and high precision fast pulsed current sources, 13th European Conference on Power Electronics and Applications, 2009.
- [62] S. Pittet, Operational specification of the PS low energy correctors (CBE), EDMS 773856.
- [63] <http://te-epc-lpc.web.cern.ch/te-epc-lpc/convertisers/cancun/general.stm>.
- [64] J. Belleman, A. Blas, J.-L. Gonzalez, F. Caspers, W. Hofle, T. Kroyer, R. Louwerse, F. Pedersen, V. Rossi and J. Tuckmantel, PS transverse damping system for the LHC beams, AB-Note-2005-027 (2005).
- [65] A. Blas, J. Belleman, E. Benedetto, F. Caspers, D. Glenat, R. Louwerse, M. Martini, E. Métral, V. Rossi and J. Sladen, The New CERN PS Transverse Damper, CERN-ATS-2009-074 (2009)
- [66] J. Belleman, PS transverse feedback pick-up, <http://jeroen.home.cern.ch/jeroen/tfpu/overview.shtml>.
- [67] J.M. Belleman, A proposal for new head electronics for the PS orbit measurement system, AB-Note-2003-057-BDI (2003).
- [68] G. Sterbini, A. Blas and S. Gilardoni, MD studies on the relation between the Hilbert angle and the tune in the PS damper, Technical Report, in preparation.
- [69] J.-L. Vallet, Faisceaux PS pour LHC : Amortissement des instabilités longitudinales de modes couplés, Accelerator Performance Committee, 2005.
- [70] R. Garoby *et al.*, Status and plans for the upgrade of the LHC injectors, CERN-ATS-2013-059 (2013).
- [71] Nanocrystalline soft magnetic material FINEMET®, Hitachi Metals brochure HL-FM9, www.hitachi-metals.co.jp/e/products/elec/tel/pdf/hl-fm9-e.pdf.
- [72] B. Kriegbaum and F. Pedersen, Electronics for the longitudinal active damping system for the CERN PS booster, PAC77, Chicago, IL, USA, 1977, p. 1695.
- [73] F. Pedersen and F. Sacherer, Theory and performance of the longitudinal active damping system for the CERN PS booster, PAC77, Chicago, IL, USA, 1977, p. 1396.
- [74] M.M. Paoluzzi *et al.*, Studies on a wideband, solid-state driven RF system for the CERN PS booster, IPAC2012, New Orleans, LA, USA, 2012, p. 3749.
- [75] M. Brugger, private communications.

- [76] R. Garoby *et al.*, Upgrade plans for the LHC injector complex, IPAC2012, New Orleans, LA, USA, 2012, p. 1010.
- [77] R. Garoby *et al.*, RF system for high beam intensity acceleration in the CERN PS, PAC1989, Chicago, IL, USA, 1989.
- [78] R. Garoby, The PS 40 MHz bunching cavity, CERN-PS-97-039-RF, CERN, Geneva, Switzerland (1998).
- [79] D. Grier *et al.*, The PS 80 MHz cavities, CERN-PS-98-021-RF, CERN, Geneva, Switzerland (1998).
- [80] H.-Ch. Grassmann, R. Jankovsky and W. Pirk, *Siemens Rev.* **44** (1977) 166.
- [81] R. Garoby, M. Morville, E. Jensen, A. Mitra and R.L. Poirier, The PS 40 MHz bunching cavity, PAC97, Vancouver, BC, Canada, 1997, p. 2093.
- [82] D. Grier, E. Jensen, R. Losito and A.K. Mitra, The PS 80 MHz cavities, EPAC98, Stockholm, Sweden, 1998, p. 1773.
- [83] D. Boussard, The PS 200 MHz RF system, present situation and future prospects, CERN-SPS/ARF/78-6, CERN, Geneva, Switzerland (1978).
- [84] F. Blas and R. Garoby, Design and operational results of a ‘one-turn-delay feedback’ for beam loading compensation of the CERN PS ferrite cavities, PAC91, San Francisco, CA, USA, 1991, p. 1398.
- [85] V. Rossi, General purpose digital signal processing VME-module for 1-turn delay feedback systems of the CERN accelerator chain, PAC09, Vancouver, BC, Canada, 2009, p. 2186.
- [86] T. Schilcher, RF applications in digital signal processing, CERN-2008-003, CERN, Geneva, Switzerland (2008), p. 249.
- [87] H. Damerau and S. Hancock, Update on longitudinal performance of LHC beams in the PS, unpublished presentation, Machine Studies Working Group Meet., CERN, Geneva, Switzerland (2011).
- [88] T. Truszcynski, A quadrature frequency converter in a feedback loop of high frequency cavities in the proton synchrotron at CERN, CERN-THESES-2013-025, CERN, Geneva, Switzerland (2013).
- [89] F. Blas, J. Boucheron, B.J. Evans, R. Garoby, G.C. Schneider, J.P. Terrier and J.L. Vallet, Digital beam controls for synchrotrons and storage rings in the CERN PS complex, EPAC94, London, England, 1994, p. 1568.
- [90] R. Garoby, Multi-harmonic RF source for the anti-proton production beam of the AD, CERN PS/RF/Note 97-10, CERN, Geneva, Switzerland (1997).
- [91] H. Damerau, S. Hancock and M. Schokker, Recent improvements of the RF beam control for the LHC-type beams in the CERN PS, IPAC10, Kyoto, Japan, 2010, p. 2716.
- [92] M.E. Angoletta and A. Findlay, First experience with the new LEIR digital beam control system, CERN AB-Note-2006-003-RF, CERN, Geneva, Switzerland (2006).
- [93] H. Damerau and G. Konstantinou, 200 MHz RF source for the CERN PS, LLRF 2011 Workshop, DESY, Hamburg, Germany, 2011.
- [94] S. Persichelli, M. Migliorati, M. Paoluzzi and B. Salvant, Impedance studies for the Finemet® loaded longitudinal damper, IPAC14, Dresden, Germany, 2014, p. 1708.
- [95] F. Tamura, C. Ohmori, M. Yoshii, K. Hasegawa and M. Paoluzzi, Beam test of the CERN PSB wide-band RF system prototype in the JPARC MR, IPAC14, Dresden, Germany, 2014, p. 3385.
- [96] D. Boussard, H.P. Kindermann and V. Rossi, RF feedback applied to a multicell superconducting cavity, EPAC88, Rome, Italy, 1988, p. 985.
- [97] G. Rumolo and G. Iadarola, Electron cloud in the CERN accelerators (PS, SPS, LHC), Joint INFN-CERN-EuCARD-AccNet Workshop Electron-cloud Effects, 2012.
- [98] G. Iadarola, H. Damerau, S. Gilardoni, G. Rumolo, G. Sterbini, C. Yin Vallgren, M. Pivi and

- S. Rioja-Fuentelsaz, Electron cloud studies for the upgrade of the CERN PS, 4th Int. Particle Accelerator Conf., 2013.
- [99] V. Dose, *Appl. Phys.* **14** (1977) 117.
 - [100] N.V. Smith, *Rep. Prog. Phys.* **51** (1998) 1227.
 - [101] B.G. Papanicolaou *et al.*, *J. Phys. Chem. Solids* **37** (1976) 403.
 - [102] N.V. Smith, *Prog. Surf. Sci.* **21** (1986) 295.
 - [103] C. Yin Vallgren *et al.*, note in preparation.
 - [104] P.G. Borzyak, I.I. Geguzin, V.N. Datsyuk, I.A. Konovalov, Yu.A. Kulyupin and K.N. Pilipchak, *Zh. Eksp. Teor. Fiz.* **80** (1981) 1514.
 - [105] G. Rumolo, G. Iadarola and S. Rioja-Fuentelsaz, Electron cloud simulation studies for the PS main chambers, Technical Notes (Future).
 - [106] T. Schneider and C. David, NA62 Mylar reflection coating with Al/MgF₂, <http://ph-news.web.cern.ch/content/na62-mylar-reflection-coating-almgf2> (2013).
 - [107] H. Wiedemann, *Particle Accelerator Physics* (Springer, 2007).
 - [108] A.W. Chao, *Physics of Collective Beam Instabilities in High Energy Accelerators* (John Wiley, 1993).
 - [109] M. Migliorati, S. Persichelli, H. Damerau, S. Gilardoni, S. Hancock and L. Palumbo, *Phys. Rev. ST Accel. Beams* **16** (2013) 031001.
 - [110] D. Boussard and J. Gareyte, CERN SPS Improvement Report No. 181, CERN, Geneva, Switzerland (1980).
 - [111] E.N. Shaposhnikova, CERN SL/94-19 (RF), CERN, Geneva, Switzerland (1994).
 - [112] S. Hancock, private communication.
 - [113] R. Cappi *et al.*, Measurements of the PS low-frequency inductive broad-band impedance, PPC Meet., PPC, December 2001, <http://psdoc.web.cern.ch/PSdoc/ppc/ppc011214/emetral.pdf>.
 - [114] L. Palumbo, V.G. Vaccaro and M. Zobov, CERN 95-06, CERN, Geneva, Switzerland (1995), pp. 331–390.
 - [115] S. Heifets, SLAC/AP-93, SLAC, Menlo Park, CA, USA, 1992.
 - [116] S. Bartalucci *et al.*, *Part. Accel.* **48** (1995) 213.
 - [117] S. Persichelli *et al.*, Impedance studies for the PS Finemet loaded longitudinal damper, CERN-ACC-2014-0113 (2014).
 - [118] R. Cappi, R. Garoby and E. Métral, Collective effects in the CERN-PS beam for LHC, Proc. Workshop Instabilities of High Intensity Hadron Beams in Rings, BNL, Upton, NY, USA, 28 June–1 July 1999.
 - [119] E. Métral, *Part. Accel.* **62**(3–4) (1999) 259.
 - [120] E. Métral, Simple theory of emittance sharing and exchange due to linear betatron coupling, CERN/PS 2001-066 (AE) (2001).
 - [121] A. Franchi, E. Métral and R. Tomàs, *Phys. Rev. ST Accel. Beams* **10** (2007) 064003.
 - [122] G. Franchetti and I. Hofmann, Resonance trapping due to space charge and synchrotron motion, Theory, Simulations and Experiments, Proc. HB2006 Workshop, Tsukuba, Japan, 2006.
 - [123] A. Burov and A. Valishev, Circular modes and flat beams for LHC, CERN Accelerator Physics Forum, 1 October 2012.
 - [124] M. Benedikt *et al.* (eds.), LHC design report, Vol. III: The injector chain, CERN-2004-003 (2004).
 - [125] G. Sterbini, Progress in the PS (Xverse damper, resonance compensation, impedance ...), CERN LIU 2013 Review, 12 April 2013.
 - [126] E. Métral and D. Mohl, Transition crossing, ‘Fifty years of the CERN Proton Synchrotron: Volume 1’, CERN-2011-004 (2011), 172 pp.

- [127] R. Cappi, E. Métral and G. Métral, Beam breakup instability in the CERN PS near transition, Proc. 7th EPAC, Vienna, Austria, 26–30 June 2000, p. 1152.
- [128] S. Hancock and E. Métral, Ghost bunches and blow-up losses with high-intensity beams, CERN PS/RF Note 2002-198 (2002).
- [129] R. Cappi *et al.*, Recent studies on transverse beam behaviour at the CERN PS, CERN/PS 89-39 (PA) (1989).
- [130] G. Rumolo and F. Zimmermann, *Phys. Rev. ST Accel. Beams* **5** (2002) 121002.
- [131] G. Rumolo and E. Métral, Simulations of single bunch collective effects using HEADTAIL, Proc. ICAP 2006, Chamonix, France.
- [132] S. Aumon, H. Bartosik, P. Freyermuth, O. Hans and S. Gilardoni, CERN ATS-Note-2011-NNN (2011).
- [133] N. Biancacci and S. Persichelli, private communication.
- [134] N. Biancacci *et al.*, Proc. IPAC 2013, Shanghai, China, p. 3106.
- [135] D. Brandt, P. Castro, K. Cornelis, A. Hofmann, G. Morpurgo, G.L. Sabbi, J. Wenninger and B. Zotter, Proc. PAC 95, Dallas, TX, USA, p. 570.
- [136] G. Arduini, C. Carli and F. Zimmermann, Proc. EPAC 04, Lucerne, Switzerland, 2004, p. 1339.
- [137] N. Mounet and E. Métral, Proc. HB2010, Morschach, Switzerland, 2010, p. 353.
- [138] CST AG, Darmstadt, Germany, <http://www.cst.com>.
- [139] E. Métral, F. Caspers, M. Giovannozzi, A. Grudiev, T. Kroyer and L. Sermeus, CERN-AB-2006-051 (2006).
- [140] H. Tsutsui, Proc. EPAC 2000, Vienna, Austria, 2000, p. 1444.
- [141] C. Zannini *et al.*, CERN-BE-Note-2010-006, CERN, Geneva, Switzerland (2009).
- [142] B. Salvant *et al.*, Electromagnetic simulations for the new PS wire scanner, CERN BE/ABP-ICE Meet., 28 July 2010.
- [143] CERN impedance website: <http://impedance.web.cern.ch/impedance/>, under the dedicated PS machine web page.
- [144] S. Persichelli *et al.*, Finemet cavity impedance studies, CERN-ACC-NOTE-2013-0033 (2013).
- [145] M. Giovannozzi *et al.*, Proposal of a dummy septum to mitigate ring irradiation for the CERN PS multi-turn extraction, Proc. IPAC12, 2012.
- [146] S. Persichelli *et al.*, Dummy septum impedance studies, MTE Meet. 74, 2 May 2013, http://ab-project-mte.web.cern.ch/AB-Project-MTE/Minutes/2013/0502/Impedance_02_05_2013.pdf.
- [147] P. Collier and R. Trant, Memorandum, Mandate of the PS Radiation Working Group, EDMS 1142920, 2010.
- [148] PS Radiation Working Group Report, CERN-ATS-2011-007, EDMS 1142005, 2011.
- [149] Safety code F: Radiation protection, EDMS 335729, 2006.
- [150] S. Damjanovic, M. Widorski and S. Gilardoni, Shielding studies for the Route Goward/PS crossing, RP Technical Note CERN-DGS-2011-065-RP-TN, EDMS 1161799, 2012.
- [151] S. Damjanovic, S. Roesler and M. Widorski, Shielding studies for the ground level above straight section 16 of the PS, RP Technical Note CERN-DGS-2011-066-RP-TN, EDMS 1161800, 2012.
- [152] A. Ferrari, P.R. Sala, A. Fassò and J. Ranft, FLUKA: a multi-particle transport code, CERN-2005-10 (2005), INFN/TC 05/11, SLAC-R-773. 2005-10 (2005), INFN/TC 05/11, SLAC-R-773.
- [153] G. Battistoni, S. Muraro, P.R. Sala, F. Cerutti, A. Ferrari, S. Roesler, A. Fassò and J. Ranft, The FLUKA code: description and benchmarking, Proc. Hadronic Shower Simulation Workshop 2006, Fermilab, 6–8 September 2006 [M. Albrow and R. Raja (eds.), *AIP Conf. Proc.* **896** (2007) 31].
- [154] M. Lamont, private communications.

- [155] D. Forkel-Wirth and T. Otto, General safety instruction: Area Classification, RGE Section 9/S3-GSI1, EDMS 810149, 2006.
- [156] M. Benedikt *et al.*, Injection matching studies using turn by turn beam profile measurements in the CERN PS, DIPAC 2001, Grenoble, France.
- [157] S. Gilardoni, private communication.
- [158] S. Damjanovic, private communication.
- [159] D. Bodart, private communication.
- [160] W.S. Kozlowska and M. Brugger, Report from FLUKA Monte Carlo simulations for PS internal dump, CERN (2014), <https://edms.cern.ch/document/1403161/1>.
- [161] The CERN proton synchrotron magnet, MPS/Int. DL 63-13, 31 May 1963.
- [162] I. Brunner *et al.*, High-level dosimetry results for the CERN high energy accelerators, Annual Report for 2009 and 2010, CERN-DGS-2012-027-RP-TN (2012).
- [163] J.P. Saraiva and M. Brugger, Radiation levels at CERN's injectors and their impact on electronic equipment, CERN (2013).
- [164] G. Dumont, Radiation survey results 2013 comparison 32 h & 2 months 2011–2012 vs 2013 PS complex, MSGW, 9 April 2013.

Chapter 5

Super Proton Synchrotron

5.1 Overview

The demanding beam performance requirements of the High Luminosity LHC (HL-LHC) project and the available beam characteristics from the pre-injectors translate into a set of requirements for the SPS as HL-LHC injector. The baseline upgrade path has been defined to remove or mitigate the identified limitations in intensity, stability, emittance preservation and availability. In this section, the performance requirements for the SPS and the known limitations are reviewed in the light of operational experience up to and including LHC run 1, and the objectives of the SPS upgrade are summarized. The present and expected machine performance reach is compared, and the few remaining decisions that still need to be made concerning upgrade options are detailed. The technical details of the specific SPS upgrades in progress are then described, accompanied by relevant machine studies and simulation results.

5.1.1 Summary of performance requirements and limitations for SPS

The HL-LHC requires 25 ns bunch spacing, with 2.3×10^{11} p⁺ per bunch and up to four batches of 72 bunches per SPS extraction. The assumed accelerated intensity in the SPS is 2.5×10^{11} p⁺, to allow for scraping and losses, with a transverse emittance of 2.3 μm and 288 bunches per transfer.

For the SPS, the main limitations come from the beam-loading at very high beam intensity, which reduces the RF voltage available; longitudinal instabilities linked to the longitudinal impedance; the electron cloud effect, which at 25 ns can make operation impossible through high vacuum or instabilities; and the high stored beam energy, which requires significant upgrades of all beam intercepting protection devices in the ring and transfer lines. The instrumentation requires major changes to be able to reliably characterize the very bright beams, and changes to other systems like the magnet interlocking and vacuum sectorization are designed to improve availability, another key requirement for HL-LHC [1].

5.1.2 SPS upgrade baseline

The present status of the LIU-SPS upgrade baseline is based on the large amount of progress made in the past decade or so on many fronts [2]. Intensive tests of scrubbing were used to benchmark simulations and test new methods [3], with the various effects and dependencies now well understood. With a well-scrubbed machine the electron cloud was not a limitation for the 50 ns operational LHC beams, but effects were seen with high bunch intensity for 25 ns spacing, with some transverse emittance blow-up on the trailing bunches in the batches. The amorphous carbon coating [4], which should significantly reduce the Secondary Electron Yield (SEY), was fully validated as a mitigation measure, and a sputtering technique was demonstrated that does not require the removal of the vacuum chamber from the magnet.

The low-gamma transition optics (Q20) was deployed operationally [5], after intensive testing and development, necessitating re-commissioning of the RF beam control, re-matching of the extraction systems and transfer lines to LHC and a re-set-up of the transfer line protection collimators. With these optics the transverse bunch stability significantly increased although longitudinal stability remains a limitation. The work on identification of relevant impedance sources continues [6]. In addition, the transverse brightness increased from an average of 0.92×10^{11} p⁺/μm to 1.05×10^{11} p⁺/μm. It is interesting to note that the achieved brightness is already very close to the HL-LHC target of 1.09×10^{11} p⁺/μm—the challenge is to conserve this performance with double the bunch intensity.

A series of LIU-SPS technical reviews [7] has examined remaining open questions and limited the upgrade possibilities to a much more focused baseline. The existing scraper system will be retained, with the magnetic bump solution documented as a Technical Design [8]. The existing extraction system will also be kept, with some improvements to cooling and a reduction in the total number of kickers. The internal beam dump absorber block will be upgraded to withstand full LIU beam parameters, and an external block in an existing transfer line investigated for high-energy beams is being investigated. The pumping of the ZS electrostatic septa will be improved and remote voltage modulation implemented. Local correction of the extraction orbit will be implemented using the extraction bumpers, but no general closed orbit correction system for high energy is required.

During LS1, the 800 MHz RF system is being extensively renovated and its voltage will be doubled. The existing transverse damper system is also being upgraded with new low-level controls and dedicated pick-ups. The preparation for the upgrade of the 200 MHz RF [9] is ongoing with the prototyping of the power amplifiers under way, the design of the new power couplers in progress and the layout change to the RF cavities and associated SPS straight section defined.

Following the successful test of the wideband (intra-bunch) transverse damper demonstrator in closed-loop mode with a single bunch [10], the design of a multi-bunch prototype is now under way.

Concerning beam instrumentation, performance upgrades of almost every system have been defined and specified. Work is progressing with the pulling of fibres and cables for the upgrade of the large distributed orbit and loss systems. Prototyping of specific systems is in progress, for example a new high-resolution wire scanner.

5.2 Longitudinal beam dynamics

5.2.1 Introduction

Since a few years the SPS has been able to deliver at top energy up to four LHC batches with an intensity of 1.6×10^{11} p/bunch for 50 ns bunch spacing and 1.2×10^{11} p/bunch for 25 ns beam, all with nominal bunch length (below 1.6 ns) and longitudinal emittance (below 0.6 eVs). During the SPS operation in 2012 single bunches with intensity up to 3.0×10^{11} were also successfully accelerated in the SPS to 450 GeV and used in the machine development (MD) studies both in the SPS and LHC. However all these beams suffer from various limitations, which in the longitudinal plane include particle losses, beam instabilities and beam loading. Much higher intensities are required by the LIU project for HL-LHC scenarios. Existing and future limitations are discussed below together with their possible cures.

5.2.1.1 Beam losses

In the past beam loss was one of the most serious intensity limitations for the LHC beams in the SPS [11]. These losses may have different origins (aperture and RF voltage restrictions, electron cloud, transverse and longitudinal instabilities, working point, space charge effect, beam loading). The total losses for operational 50 ns LHC beams in the SPS normally did not exceed 8% and they were mainly low energy losses (at injection, capture and on the 10.6 s long flat bottom). However losses increase with total intensity and during MD studies at the end of 2012 were significantly higher for 25 ns beam with injected bunch intensity of 1.5×10^{11} , so that only 1.3×10^{11} p/b could reach the SPS flat top.

PS-SPS transfer

The longitudinal bunch parameters at SPS injection are determined by the PS beam production scheme. In particular, to fit into the 200 MHz RF bucket of the SPS, the LHC bunches before extraction in the PS are rotated in the longitudinal phase space by a quarter of the synchrotron period

acquiring a specific S-shape with increased particle population in the bunch tails and therefore a higher probability of particle losses during capture in the SPS, see Fig. 5.1(a). Detailed studies and simulations [12] show that, because of this S-shape, reducing bunch length at injection does not necessarily lead to capture loss reduction and, for a given RF voltage programme in the PS, losses mainly depend on longitudinal emittance and less on bunch length. However, increasing the voltage amplitude (using spare cavities or power source) of the 40 MHz RF system (from 300 kV to 600 kV, preferred option), see Fig. 5.1(b), or of the 80 MHz RF (from 600 kV to 900 kV) during bunch rotation may reduce existing losses or significantly increase the margin for injection of future higher intensity bunches with larger longitudinal emittances, see Fig. 5.2. Indeed, an increase of injected emittance with intensity was observed during operation and MD studies, and sometimes it was done on the SPS request to improve beam stability and quality in the SPS. In measurements a loss reduction from 5.2% to 2.3% was achieved for 50 ns LHC beam with bunch intensity of 1.6×10^{11} , in good agreement with predictions based on simulations [13].

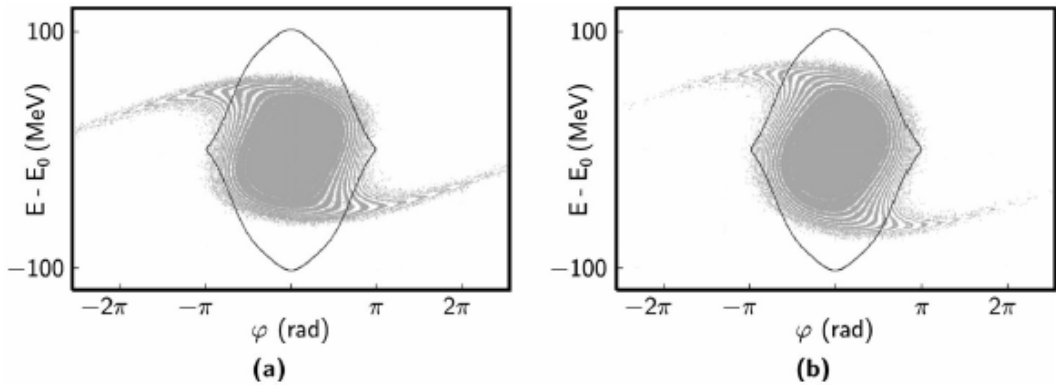


Fig. 5.1: Bunch shapes in longitudinal phase space at SPS injection [13]: (a) PS operational conditions ($V_{40\text{MHz}} = 300$ kV and $V_{80\text{MHz}} = 600$ kV); (b) rotation with $V_{40\text{MHz}} = 600$ kV, $V_{80\text{MHz}} = 600$ kV and optimal timings; simulations done with code ESME. The SPS bucket shown for the typical SPS RF capture voltages (in the Q26 optics): $V_{200\text{MHz}} = 2$ MV and $V_{800\text{MHz}} = 0.34$ MV in phase.

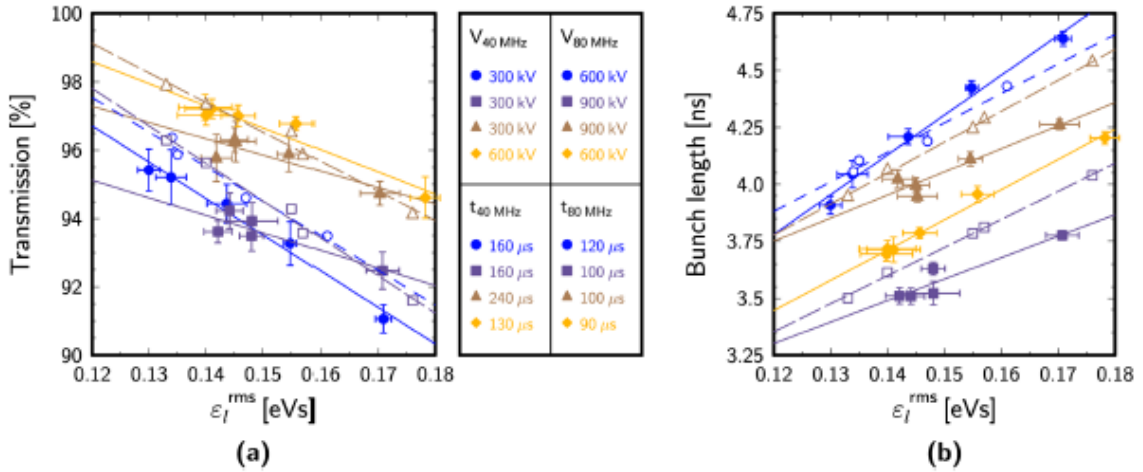


Fig. 5.2: Dependence of beam transmission on (a) emittance and (b) bunch length [13]. Full and empty symbols (solid and dashed lines) mark experimental and simulation results, respectively. The circles correspond to operational settings, the squares to earlier optimization attempts based on bunch length. The triangles and diamonds show the results obtained using additional $V_{80\text{MHz}}$ or $V_{40\text{MHz}}$ voltage, respectively (no simulations for the latter case), for the rotation with optimized timings. The bunch length is obtained from a 4σ Gaussian fit in all cases.

5.2.1.2 Beam instabilities and their cures

At the present the longitudinal beam instabilities in the SPS are the main intensity limitation for future high-intensity beams. The threshold of these instabilities is decreasing with beam energy reaching a minimum on the flat top [13]. The instability of the operational beams is cured by increased Landau damping, which is achieved by the use of the 800 MHz RF system as a Landau cavity in bunch shortening mode throughout the cycle and by controlled emittance blow-up performed with band-limited noise during the second part of acceleration.

In the middle of 2012 the SPS nominal optics (Q26) has been changed to the optics with lower transition energy ($\gamma_t = 18$ instead of $\gamma_t = 22.7$), for which the expected increase in the longitudinal coupled bunch instability threshold is proportional to a change in the slip factor $\eta = \gamma^2 - \gamma_t^{-2}$ (see the section below).

The beam quality monitors (BQM) [14] control longitudinal beam parameters both in the SPS (bunch length, pattern and beam stability) and in the LHC, preventing extraction to the LHC of bunches that are too long. Maximum allowed longitudinal bunch length at the SPS flat top is defined by losses during the capture by the LHC 400 MHz RF system with a bucket length of 2.5 ns. Due to the limited RF voltage at the 200 MHz in the SPS (7.5 MV for nominal LHC intensity) this leads also to a limitation of the maximum longitudinal emittance that can be transferred to the LHC. At the end of the 2012 run the average bunch length at SPS extraction was 1.6 ns (in the Q20 optics) with maximum allowed BQM bunch length setting at 1.9 ns.

Low transition energy (Q20)

Existing in the past intensity limitation in the transverse plane (TMCI) was significantly relaxed due to implementation of the new (Q20) optics with lower transition gamma [15, 16], however the beneficial effect in the longitudinal plane is less obvious due to the limited 200 MHz RF voltage available in the SPS. Indeed, for lower transition energy the expected increase in longitudinal coupled-bunch instability threshold is proportional to the slip factor $|\eta|$. However for the same longitudinal parameters the required voltage also scales as $|\eta|$. The maximum voltage (7.5 MV) is already used for beam transfer to the LHC, but the controlled emittance blow-up can also be reduced for the same intensity. For stability in the Q20 optics one needs a smaller emittance $\varepsilon \sim \eta^{-1/2}$, which gives the same bunch length τ in the two optics, since the threshold for the loss of Landau damping scales as $N_{th} \sim \varepsilon^2 \eta \tau$ [13]. This scaling was practically confirmed by measurements performed in 2011 and 2012 [15, 16]. Significant improvement in beam stability was obtained on the flat bottom. However, on the flat top the high harmonic RF system was still insufficient for stability of 50 ns beam with ultimate bunch intensity, and one needs in addition the controlled emittance blow-up that nevertheless is smaller than in nominal optics. Indeed, in the Q26 optics the controlled emittance blow-up was performed twice during the cycle. The first blow-up was with mismatched voltage at injection (2 MV) where due to filamentation the initial nominal emittance of 0.35 eVs was increased to 0.42 eVs. This emittance blow-up is practically absent in the Q20 optics. In the middle of 2012 the Q20 optics became operational for the LHC beams, and from this moment, for the same intensity, bunches delivered to the LHC had smaller longitudinal emittance (around 0.5 eVs for 50 ns spaced beams). This smaller emittance could potentially create problems due to the IBS on the LHC flat bottom and special batch-by-batch longitudinal emittance blow-up was developed and tested in the LHC [17].

Single bunch intensity effects

The SPS intensity limitations are due to both single-bunch and multi-bunch effects. The most important single bunch effect in the longitudinal plane is loss of Landau damping, caused by the reactive impedance of the ring ($I_m Z/n$), leading eventually to an instability with a growth rate defined mainly by the resistive impedances. In the SPS the threshold for the loss of Landau damping is reducing with beam energy so that high-intensity bunches become unstable earlier during the

acceleration ramp [13]. Single bunch instability driven by high-frequency impedance is also often called microwave instability. The microwave instability was one of the main intensity limitations for the SPS as an injector for the LHC and it was eliminated up to ultimate intensities during the SPS impedance reduction campaign in 1999 to 2001 [11]. The result of this instability is uncontrolled longitudinal emittance blow-up. Strong dependence of bunch length on intensity recently was observed in the SPS for single bunches with intensities similar to that required by the HL-LHC project, see Fig. 5.3. This bunch lengthening cannot be explained by potential well distortion (PWD) due to defocusing voltage induced in the SPS reactive impedance and implies that most probably the threshold of microwave instability is hit during the cycle. The possible source of this instability has been identified as resonant impedance at 1.4 GHz observed in measurements with long bunches [18].

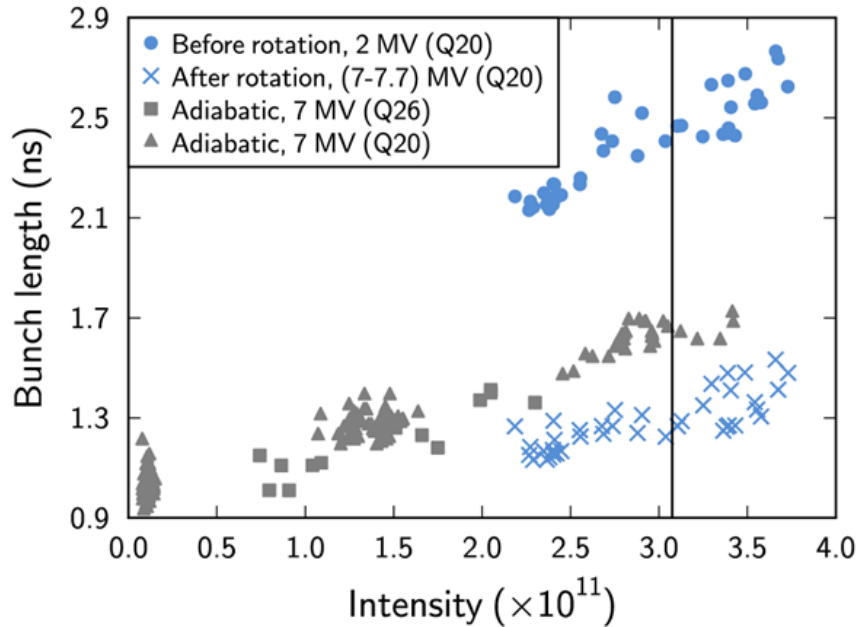


Fig. 5.3: Bunch length on the SPS flat top measured as a function of bunch intensity in the two different SPS optics (Q20 and Q26).

Nevertheless the effect of PWD also exists and should be taken into account when considering the RF voltage required for higher bunch intensities (see below). Indeed, for a bunch with an intensity of 2.5×10^{11} and length of 1.7 ns the induced voltage is in the range 1.2–1.9 MV (depending on bunch profile).

Measurements on the flat bottom (with phase loop on) show that the single bunch instability threshold strongly depends on the capture voltage. Bunches are much more stable in the matched capture voltage (1 MV for Q26 optics), which was impossible to use in operation with the LHC beam with the Q26 optics due to beam loading leading to beam losses, but became possible with the Q20 optics.

Multi-bunch effects

The longitudinal coupled-bunch instability of the LHC beam in the SPS is characterized by a very low intensity threshold. In the Q26 optics a single 50 ns batch with 2×10^{10} p/bunch becomes unstable during acceleration above ~ 200 GeV/c with feedback and feedforward systems (around 200 MHz) in operation; at injection the coupled-bunch instability was observed at $\sim 1.1 \times 10^{11}$ /bunch.

As expected from the calculated threshold for the coupled-bunch instability [13], the threshold clearly depends on energy and longitudinal emittance: more dense bunches become unstable earlier in

the cycle. Therefore, larger emittance (and higher voltage) is required to stabilize bunches with higher intensity (Fig. 5.4).

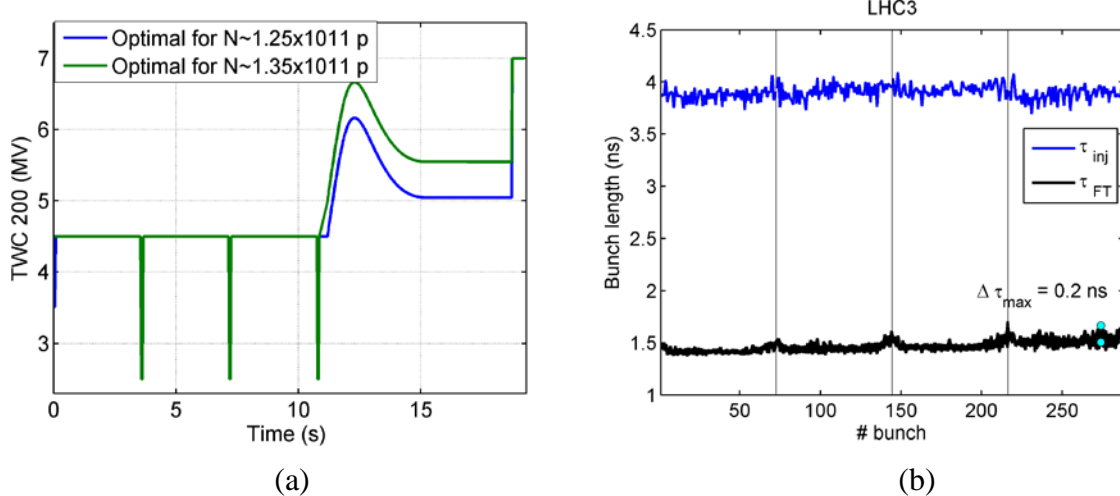


Fig. 5.4: (a) Voltage programmes used in the SPS for the 25 ns beam in the Q20 optics for two different beam intensities (optimized for reduction of particle losses). (b) Bunch-by-bunch length on the flat bottom (blue curve) and flat top (black curve) for 25 ns beam with an intensity of $1.25 \times 10^{11} \text{ p/b}$.

Multi-bunch effects are caused by narrow-band impedances that are able to couple motion of the subsequent bunches in the batch. This coupling is stronger for batches with shorter bunch spacing, as it is a case for beams with 25 ns bunch spacing in comparison with 50 ns spacing. A comparison of the LHC beams with different bunch spacing T_b shows that the energy threshold scales roughly as $1/E_{\text{th}} \sim N_b/T_b$. Indeed, in measurements the 50 ns beam with a bunch intensity of $N_b = 1.6 \times 10^{11}$ was unstable around 160 GeV/c and the 25 ns beam with $N_b = 1.2 \times 10^{11}$ at 110 GeV/c. In the Q26 optics high-intensity 25 ns and 50 ns beams were also at the limit of stability on the 26 GeV/c flat bottom, but they are stable in the Q20 optics.

However, the final emittance also increases with bunch intensity, so that in the Q20 optics the 25 ns beam with $1.35 \times 10^{11} \text{ p/b}$ has an emittance of 0.47 eVs and the 50 ns beam with $1.6 \times 10^{11} \text{ p/b}$, an emittance of 0.46 eVs. In the Q26 optics, before the change, the average emittance of similar 50 ns beam was 0.5 eVs [19].

Expected future performance

Unless serious measures are taken, future beam performance will be limited by existing longitudinal instabilities and lack of RF voltage. Planned actions include continuing studies of beam instabilities (both single bunch and multi-bunch), identification of guilty impedance sources and, if possible, their reduction as well as upgrade of the 200 MHz and 800 MHz RF systems. With the foreseen upgrade of the 200 MHz RF system the effect of beam loading will be reduced as well as the impedance of the whole system, and more voltage will be available for higher intensities. However, more voltage will also be required due to controlled (or uncontrolled) longitudinal emittance blow-up (to avoid loss of Landau damping and beam instabilities) and the effect of potential well distortion discussed above. In Fig. 5.5 both required and available voltages are shown versus beam intensity (RF current) for different configurations of the RF system and its operation mode (continuous or pulsing).

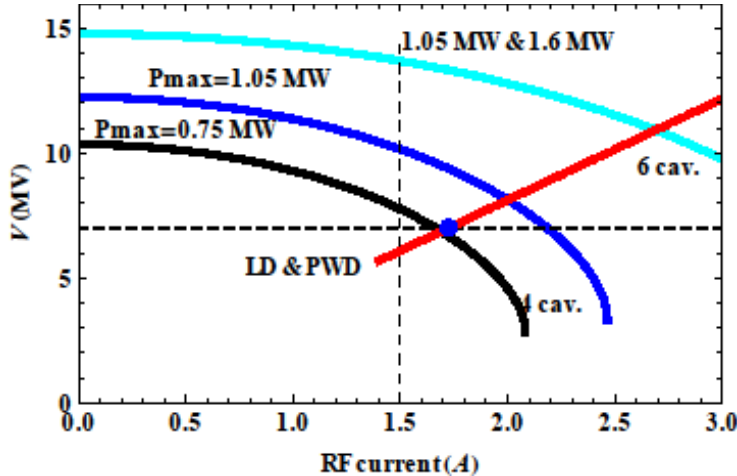


Fig. 5.5: The total 200 MHz voltage as a function of the RF current (the 200 MHz harmonic for 25 ns bunch spacing) available now from four cavities with power of 0.75 MW at cavity input in continuous mode (black solid curve) and with power of 1.05 MW at cavity input in the pulsing mode, possible after LLRF upgrade (blue curve) together with the situation after the full RF upgrade which includes four 3-section cavities with 1.05 MW and two 4-section cavities with 1.6 MW in pulsing mode (magenta curve). The vertical dashed line indicates the RF current of 1.47 A corresponding to the 25 ns beam with nominal intensity of 1.15×10^{11} p/b. The blue symbol shows the reference point used for red line indicating the voltage needed for higher intensity due to the effects of potential well distortion (PWD) and loss of Landau damping (LD).

Voltage required to avoid the loss of Landau damping can be estimated from the required emittance ε as $V \sim \varepsilon^2$. Assuming that threshold bunch intensity $N_{\text{th}} \sim \varepsilon^{5/2}/V^{1/4}$, the required RF voltage is proportional to bunch intensity $V \sim N$. Similar scaling of voltage with intensity can be obtained from the (simplified) microwave instability threshold. Taking also into account the reduction of the effective voltage due to the PWD (see above) a larger RF voltage is needed for higher beam intensities. For scaling for high intensity, the reference point can be taken from results of measurements during MD at the end of 2012 (Q20 optics), where marginally stable 25 ns beam with an intensity of 1.35×10^{11} p/bunch and average bunch length of 1.7 ns was obtained at the SPS flat top (shown with a blue circle in Fig. 5.5). In the present RF configuration, with a 750 kW power limit, bunch length will already be 10% longer for bunch intensities around 1.45×10^{11} , see Table 5.1. In pulsing mode with 1.05 MW per cavity (possible only after the LLRF upgrade), a bunch intensity of 1.5×10^{11} can be reached without performance degradation and 1.7×10^{11} with 10% longer bunches. One can see that, unless undesired emittance blow-up is reduced, the HL-LHC request can be satisfied only with longer extracted bunches and probably with increased capture losses. Even if the limitation on flat top can be removed (200 MHz RF system in the LHC), voltage required during acceleration will still be at the limit even for increased acceleration time.

Table 5.1: SPS intensity limitations for 25 ns beam in present situation and in different scenarios of the 200 MHz RF system upgrade.

Scenario			Maximum bunch intensity	
Number of cavities with N sections	Power per cavity	Operation mode	No performance degradation	10% longer bunches
2 × 5 sections + 2 × 4 sections	750 kW	Continuous	1.35×10^{11}	1.45×10^{11}
2 × 5 sections + 2 × 4 sections	1.05 MW	Pulsing	1.5×10^{11}	1.7×10^{11}
4 × 3 sections	1.05 MW	Pulsing	2.1×10^{11}	2.5×10^{11}
2 × 4 sections	1.6 MW	Pulsing	2.1×10^{11}	2.5×10^{11}

Apart from the potential increase in the average bunch length for high intensities, there is a limitation due to large bunch-to-bunch length variation created during controlled emittance blow-up. The bandwidth of the applied noise should follow the synchrotron frequency spread inside the bunch in a double RF system. However, beam loading in the 200 MHz and 800 MHz RF systems leads to bunch-by-bunch variation of the phase shift between the two RF systems and corresponding modification of the synchrotron frequency distribution [20]. This in turn creates difficulties with controlled emittance blow-up and beam quality degradation (non-uniform bunches). A similar problem is observed for beams with large bunch-by-bunch length or intensity variation of injected beams due to the effect of the PWD.

5.3 Transverse beam dynamics

5.3.1 Low gamma transition optics

The transverse mode coupling instability (TMCI) at injection [21] and the electron cloud (EC) driven single bunch instability [22] were identified as potential intensity limitations soon after the first studies with LHC-type beams in the SPS. For a given longitudinal emittance ε and a matched RF bucket, the intensity thresholds for the TMC [23] and the single bunch EC [24] instabilities as well as the longitudinal instabilities encountered in the SPS scale with the slippage factor $\eta = 1/\gamma_t^2 - 1/\gamma^2$. The SPS optics used for LHC beams until 2012 has a gamma transition of $\gamma_t = 22.8$. This optics is called Q26 due to the integer part of the betatron tunes ($Q_x = 26.13$, $Q_y = 26.18$). A plot of the optics functions is shown in Fig. 5.6(a). Since LHC beams are always injected above transition, reducing the transition energy of the lattice results in a higher slip factor throughout the acceleration cycle and consequently better beam stability [25]. In the frame of the LIU project, a new optics with lower transition energy has been developed [26]. Compared to the Q26 optics, the working point in this so-called Q20 optics is lowered by 6 integer units in both planes ($Q_x = 20.13$, $Q_y = 20.18$) and the transition energy is reduced to $\gamma_t = 18$. A plot of the corresponding optics functions is shown in Fig. 5.6(b). Note that the average beta functions are increased by about 30%, however the maxima remain at the same level. Although the Q20 optics has a significantly higher dispersion function in the arcs, the SPS vacuum chambers provide sufficient aperture for the LHC-type beams due to their small transverse emittance.

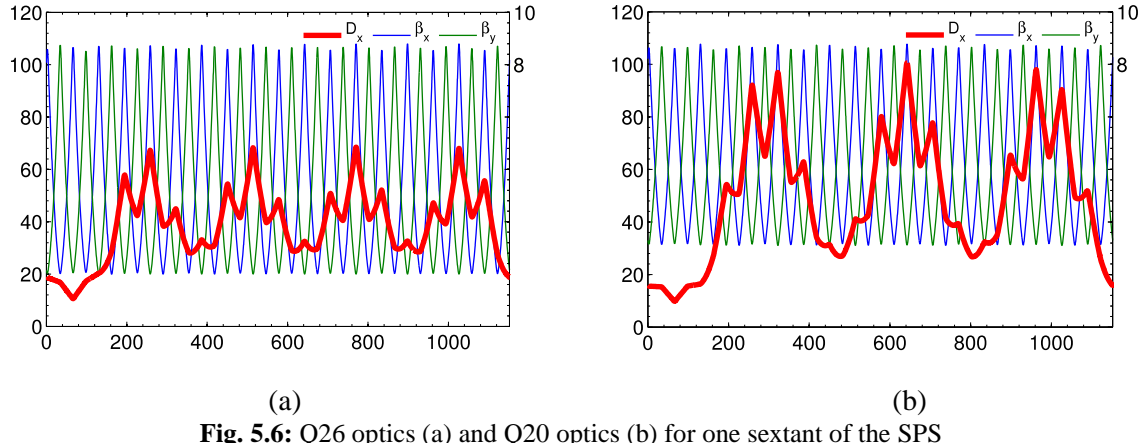


Fig. 5.6: Q26 optics (a) and Q20 optics (b) for one sextant of the SPS

Figure 5.7 shows the phase slip factor η normalized to its value in the Q26 optics ($\eta_{\gamma t} = 22.8$) as function of the gamma transition for injection and for top energy. The largest relative increase of the slip factor is obtained at injection energy, where η is about three times higher in the Q20 optics compared to the Q26 optics. Significant improvement of beam stability is therefore achieved, especially in the low energy part of the acceleration cycle, as demonstrated in a series of machine development sessions and in simulations studies. These results will be discussed in more detail below. The implementation of the Q20 optics did not require any hardware modification and thus after preparation and set-up of the LHC transfer lines for the new SPS optics [27], it was also possible to test its performance and reliability in routine operation for LHC filling for a period of a few months since September 2012 until the beginning of LS1 with excellent results [28]. Due to the improved beam stability and the successful test in routine operation Q20 will be the default machine configuration for LHC beams in the SPS in the future.

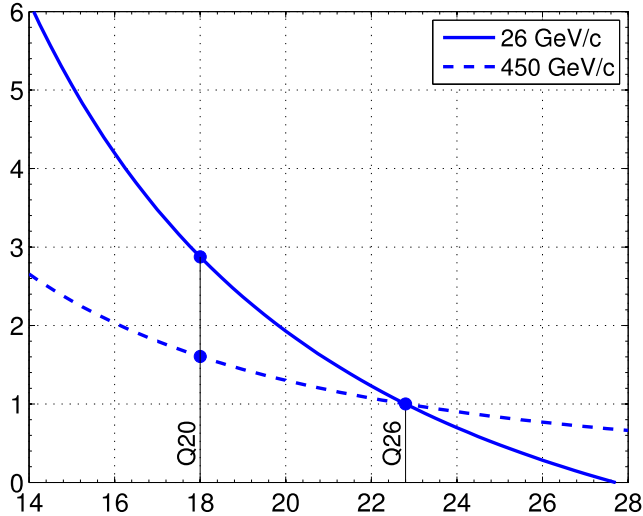


Fig. 5.7: Phase slip factor η relative to the value of the Q26 optics as a function of the gamma transition for injection and extraction energy. The values of $\gamma_t = 22.8$ and $\gamma_t = 18$ indicated in the graph correspond to the Q26 and Q20 optics, respectively.

5.3.2 Transverse mode coupling instability at injection

The vertical single bunch TMCI at injection is one of the main intensity limitations in the Q26 optics. For bunches injected with the nominal longitudinal emittance $\varepsilon = 0.35$ eVs, the corresponding

instability threshold is around $N_{\text{th}} \approx 1.6 \times 10^{11}$ p/b (with vertical chromaticity adjusted close to zero) [29]. The instability results in emittance blow-up and fast losses as shown in Fig. 5.8(a). Slightly higher intensities can be reached when increasing chromaticity, however at the expense of enhanced incoherent emittance growth and losses on the flat bottom. Analytical models based on a broadband impedance predict that the instability threshold with zero chromaticity scales like $N_{\text{th}} \propto |\eta|\varepsilon/\beta_y$ [23], where β_y denotes the vertical beta function at the location of the impedance source. Thus, the instability threshold can be raised by injecting bunches with larger longitudinal emittance. However, the beam transmission between PS and SPS is degrading for larger longitudinal emittances unless additional cavities in the PS are used for optimizing the bunch rotation at extraction [30]. On the other hand, a significant increase of the instability threshold is expected in the Q20 optics even with the nominal longitudinal emittance, since the product of the slip factor and the vertical beta function at important impedance sources ($\eta\beta_y$) is about 2.5 times higher compared to Q26. This has been verified in measurements with high-intensity single bunch beams as shown in Fig. 5.8(b). Due to the higher slip factor in the Q20 optics, the RF voltage of the 200 MHz RF system was increased to $V_{200} = 4$ MV compared to $V_{200} = 1.4$ MV used in Q26 in order to maintain the same bucket area. In both optics, the 800 MHz cavity was operated in bunch shortening mode at 10% of the voltage of V_{200} . In these conditions, the instability threshold in the Q20 optics for chromaticity close to zero and the nominal longitudinal emittance of $\varepsilon = 0.35$ eVs at injection was found at around $N_{\text{th}} \approx 4.5 \times 10^{11}$ p/b. Furthermore, the TMCI intensity threshold of the Q20 and the Q26 optics was characterized as a function of the longitudinal emittance at PS extraction and the bunch intensity at PS extraction [31], as shown in Fig. 5.9. In the case of the Q26 optics, a linear dependence of the intensity threshold as a function of the longitudinal emittance is observed, as expected from analytical models. In the Q20 optics the TMCI intensity threshold is about 2.5 times higher. In addition to the strong TMCI at high intensity, an area of ‘weak instability’ is observed in the Q20 optics for longitudinal emittances below $\varepsilon \approx 0.32$ eVs and intensities in the range 1.1×10^{11} p/b $< N < 2.3 \times 10^{11}$ p/b. It should be emphasized that this slow instability is not of concern for LHC beams, as they are injected with higher longitudinal emittance. The experimental observations in the two SPS optics have been reproduced in excellent agreement in numerical simulations [31] using the wake functions obtained from the SPS impedance model, which includes the wall impedance, the kicker magnets, the BPMs, the RF cavities and flanges. Figure 5.10 shows the vertical growth rate as a function of longitudinal emittance and intensity for the two optics as obtained with the macro particle code HEADTAIL. In these simulations both the 200 MHz and the 800 MHz RF systems as well as the measured non-linear chromaticity were taken into account. The threshold intensities are similar to those observed in the measurements. In particular, the area of slow instability experimentally found in the Q20 optics is reproduced in the simulations.

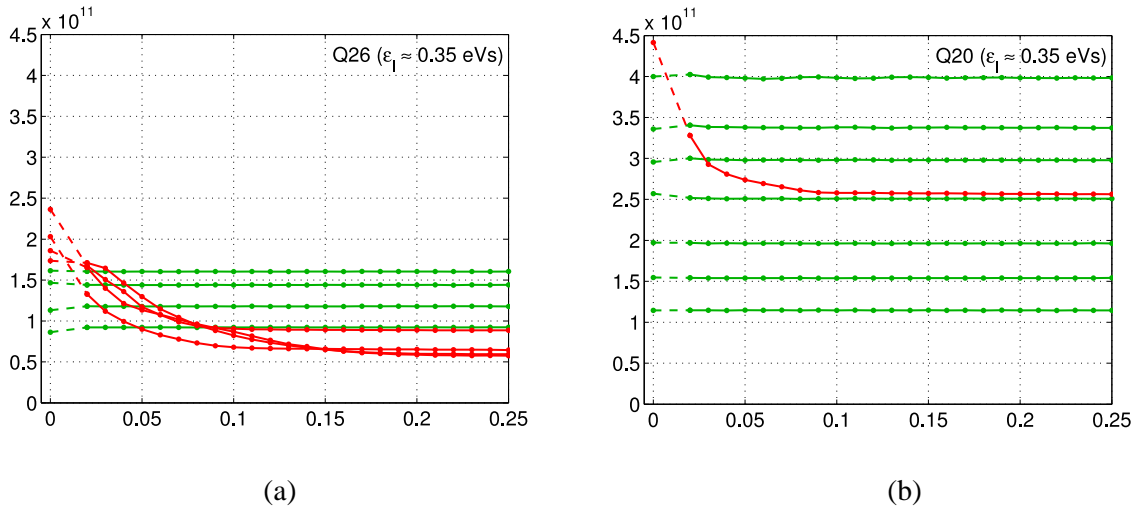


Fig. 5.8: Intensity as function of time after injection in (a) the Q26 optics and (b) the Q20 optics. Red traces indicate unstable beam conditions and green traces correspond to stable conditions.

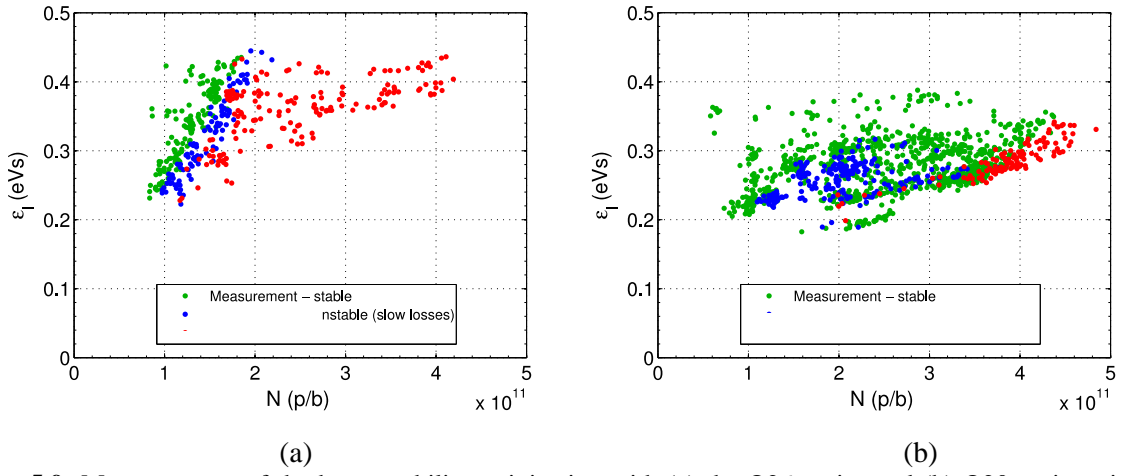


Fig. 5.9: Measurements of the beam stability at injection with (a) the Q26 optics and (b) Q20 optics with low vertical chromaticity. Green points correspond to stable cases. Unstable cases are marked by red dots if losses occurred within the first 1000 turns after injection ('fast losses') and blue dots if losses occurred later in the cycle.

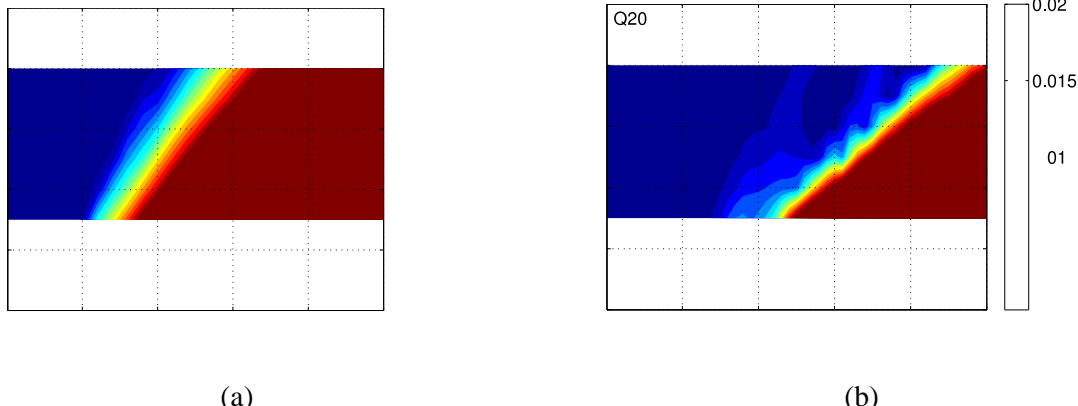


Fig. 5.10: Vertical growth rate as a function of the intensity per bunch and the longitudinal emittance as obtained from a series of HEADTAIL simulations for (a) the Q26 optics and (b) the Q20 optics. The colour scale is clipped, i.e. areas in red correspond to growth rates of 0.02/turns or higher.

It is concluded that with the Q20 optics the TMCI is not of concern for the beam parameters envisaged by the HL-LHC, even for the scenarios with 50 ns beams, which require significantly higher intensities per bunch compared to the 25 ns beams.

5.3.3 Simulation study of the electron cloud-driven single bunch instability

The electron cloud effect can be a serious performance limitation for the 25 ns LHC beams in the SPS and mitigation strategies have therefore been developed. The threshold of the single bunch electron cloud-driven instability in the SPS has been studied in numerical simulations using HEADTAIL [24]. Figure 5.11 shows the threshold electron density as a function of the synchrotron tune Q_s and of the beta functions at the location of the interaction with the electron cloud.

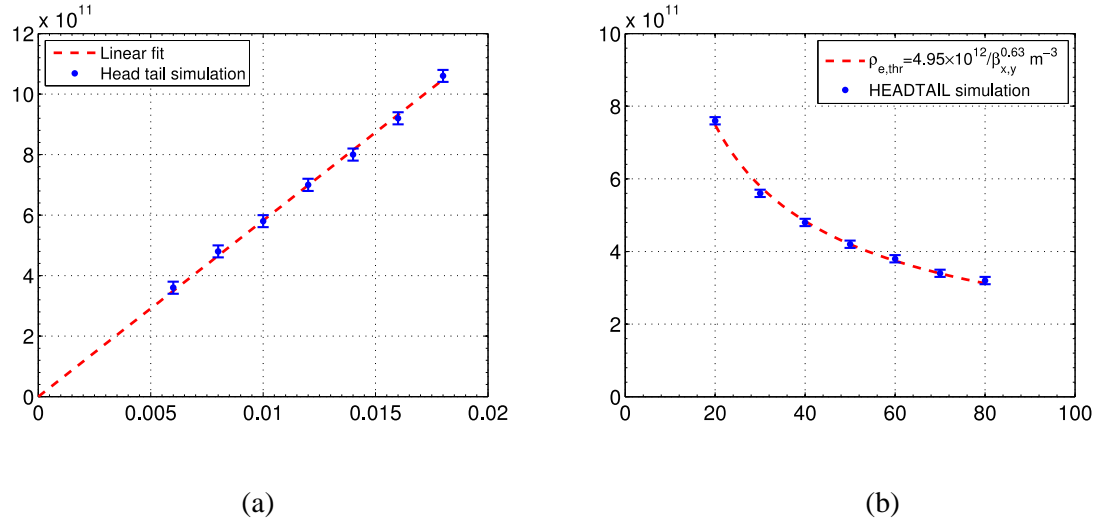


Fig. 5.11: Instability threshold density as a function of the synchrotron tune for constant longitudinal bunch parameters (a) and as function of the beta functions at the location of the electron cloud interaction (b).

The faster synchrotron motion in the Q20 optics for RF parameters matched to the nominal longitudinal bunch parameters at the flat bottom results therefore in about two times higher threshold electron densities for the single bunch instability compared to the Q26 optics in simulations for drift spaces and MBB dipole magnets, as shown in Fig. 5.12 for different intensities per bunch, despite the slightly increased beta functions.

As shown in experimental studies in 2012 [32], the measures for suppressing the electron cloud formation and/or the implementation of the high bandwidth feedback system are essential for avoiding beam quality degradation due to emittance blow-up along the train for high beam intensities, even with the higher threshold for the electron cloud instability in the Q20 optics.

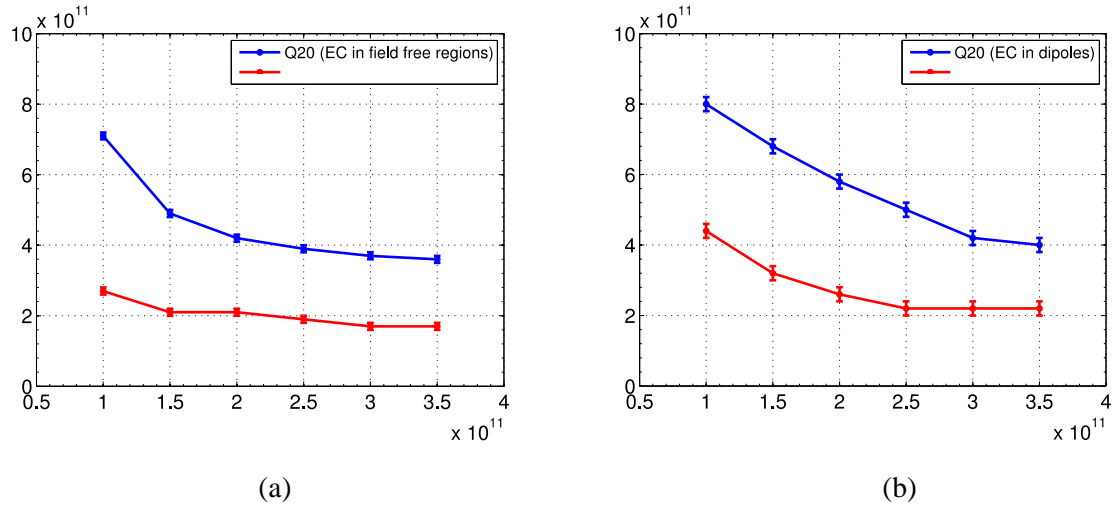


Fig. 5.12: HEADTAIL simulations yielding the instability threshold density as a function of intensity per bunch comparing the Q26 with the Q20 optics for field-free regions (a) and for the electron cloud located in MBB dipole magnets (b), assuming the corresponding average beta functions in the respective locations.

5.3.4 Space charge

The incoherent space charge tune shift calculated for the requested parameters of the 25 ns HL-LHC beam at SPS injection, i.e. at an intensity of 2.6×10^{11} p/b and normalized transverse emittances of $1.89 \mu\text{m}$, is about $\Delta Q_x, \Delta Q_y \approx 0.10, 0.17$ in the Q20 optics (and about 15% higher in the Q26 optics due to the smaller dispersion function). To maintain equal beam parameters along the bunch train, beam loss and emittance blow-up on the long flat bottom (10.8 s for accumulating four injections from the PS) have to be kept as small as possible in a regime with a relatively strong space charge.

A working point scan was performed with the Q20 optics during machine studies in 2012 in order to study emittance growth and losses for a high-brightness beam at flat bottom [33]. The measurements were performed with a 50 ns beam with an intensity of about 1.95×10^{11} p/b and transverse emittances of about $\epsilon_n \approx 1.1 \mu\text{m}$, as obtained with the batch compression and bunch merging (BCMS) scheme [34] in the PS. For each working point, the transverse emittances were measured with the wire scanners in turn acquisition mode (average profile along the bunch train) at the end of the 10.8 s flat bottom of the LHC cycle. Single batches were used for this experiment in order to study the blow-up along the entire injection plateau. Figure 5.13 shows the tested working points on the tune diagram together with the corresponding emittance measurements at the end of the flat bottom for a single batch of 24 bunches with transverse damper on. First, the horizontal tune was varied from $Q_x = 20.07$ to $Q_x = 20.23$ while the vertical tune was kept at approximately $Q_y \approx 20.19$. For each setting, a single batch of 24 bunches of the 50 ns BCMS beam was injected in five consecutive cycles and the transverse beam profiles were measured with the wire scanners in turn acquisition mode (average profile along bunch train) at the end of the 10.8 s long injection plateau. For each plane and each working point, the emittance is determined from a single Gaussian fit of the corresponding overlapped measured profiles and the error bars are determined by the fit uncertainty. A significant horizontal emittance blow-up was observed for horizontal tunes below $Q_x = 20.13$, while practically constant emittances were found for higher horizontal tunes. In a similar scan in the vertical plane, significant emittance blow-up is observed for vertical tunes close to the integer resonance, while the sum of the two transverse emittances is preserved for vertical tunes above $Q_y = 20.19$. This is consistent with the calculated incoherent space charge tune spread of $\Delta Q_x = 0.11$ and $\Delta Q_y = 0.20$ for a bunch length of $\tau \approx 3$ ns and an rms momentum spread of $\delta p/p_0 \approx 1.5 \times 10^{-3}$. For all the working points studied, the losses on the injection plateau were typically of the order of 1% and the total transmission up to flat top was about 93% (without scraping). The preservation of the beam brightness along the flat bottom for working points sufficiently far above the integer resonances was also demonstrated with

bunch-by-bunch emittance measurements for the same beam but with three injections from the PS. Figure 5.14 shows an example of the emittances along the train for the working point $Q_x, Q_y = 20.17, 20.23$. The measurement shows that the emittance of the first batch, which is stored for more than 10 s, is equivalent to the two batches injected later. The bunch-to-bunch variation within the batches originates from the pre-injectors. This beam was already successfully delivered to the LHC with the Q20 optics for LHC machine studies at the end of 2012.

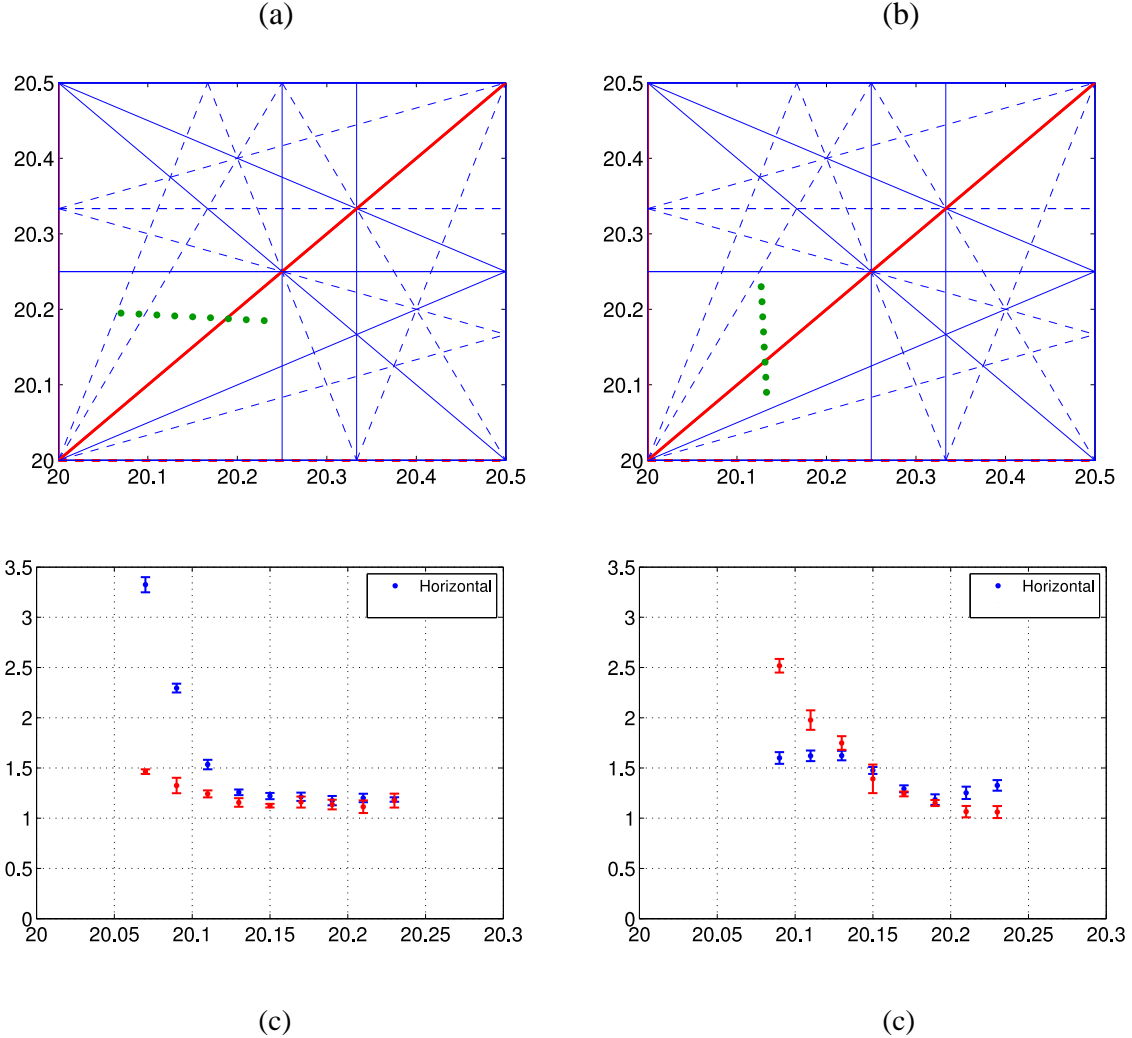


Fig. 5.13: Average transverse emittance of 24 bunches measured at the end of the SPS flat bottom for different horizontal tunes (a, c) and for different vertical tunes (b, d) as indicated by the green dots in the tune diagrams.

Based on the above results and considering the budgets for emittance blow-up and losses defined in Table 2.4, which permit slightly more blow-up in the SPS than observed in the measurements, the presently maximum acceptable space charge tune shift in the SPS for an optimized working point is $\Delta Q_y = -0.21$. The corresponding achievable beam brightness for this tune shift is shown in Fig. 5.15 in terms of transverse emittance as function of intensity both at SPS extraction including the tolerated losses and emittance blow-up. As these studies were performed with the highest beam brightness available from the PS in 2012, the maximum tolerable space charge tune shift on the SPS injection plateau might be even higher.

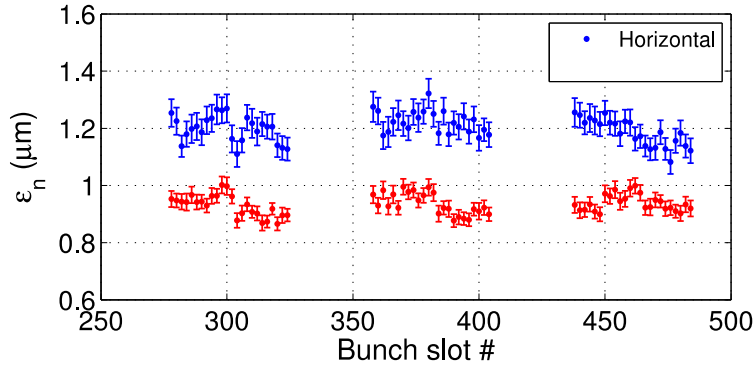


Fig. 5.14: Bunch-by-bunch emittance measurement at the end of the flat bottom for three batches of the 50 ns BCMS beam at the working point $Q_x, Q_y = 20.17, 20.23$.

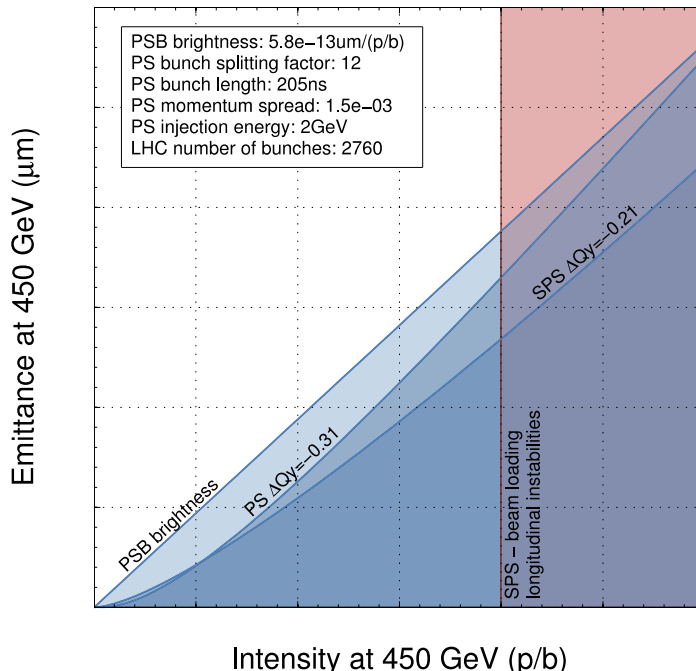


Fig. 5.15: Transverse emittance as a function of intensity for a space charge tune shift of $\Delta Q_y = 0.21$, as achieved during machine studies with the 50 ns BCMS beam in 2012.

5.4 RF power systems (200 MHz, 800 MHz)

5.4.1 200 MHz RF system

The 200 MHz RF system in the SPS is the main RF system used for acceleration of all beams. It has a travelling wave (TW) structure and consists of four cavities, two of them with five sections and two with four sections.

For stability of future high-intensity LHC beams in the SPS larger (than current) longitudinal emittance and therefore bucket and voltage amplitude will be necessary, but less voltage will be available due to the effect of beam loading in the existing system with maximum peak RF power per cavity of 1 MW. This issue will become critical for beam acceleration and especially for beam transfer into the 400 MHz RF system of the LHC. Currently the maximum total voltage available at nominal

LHC intensity is 7.5 MV. The power per cavity is limited by power amplifiers, fundamental power couplers and feeder lines to 700 kW in continuous operation (full ring, CNGS type beam) and up to 900 kW in pulsed operation (LHC beam). With an adequate upgrade of the present equipment a higher value of 1.05 MW is possible in pulsed mode for an LHC beam filling less than half of the ring. The power per cavity during the LHC cycle in two different optics is shown in Fig. 5.16(a) for 200 MHz cavities of different length (consisting of four and five sections). It corresponds to the voltage programmes with constant filling factor in momentum shown in Fig. 5.16(b). One can see that more voltage is necessary in the Q20 optics than in the Q26 for acceleration of bunches with the same longitudinal emittance. It is also clear that for intensities above the nominal, RF power required during the cycle in both optics exceeds the present limit of 0.7 MW. Note that for higher intensity, the required increase in longitudinal emittance should also be taken into account.

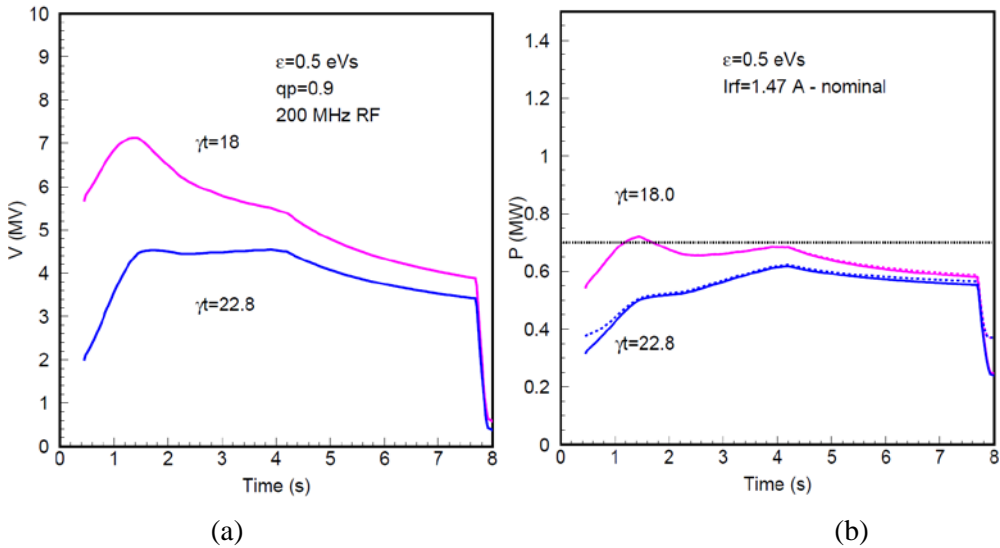


Fig. 5.16: (a) Voltage programmes corresponding to the constant filling factor in momentum for emittance of 0.5 eVs in the two different SPS optics. (b) Corresponding RF power per 200 MHz TW cavity having four (solid line) and five (dashed line) sections during the LHC acceleration cycle for nominal 25 ns beam intensity.

Therefore more voltage is required for transfer of beams with higher intensity to the LHC. On the other hand, the existing two five-section cavities can provide much less voltage already at nominal current with power of 0.7–0.75 MW Fig. 5.17 (a) and become practically useless for ultimate intensity even with RF power of 1 MW/cavity, Fig. 5.17 (b).

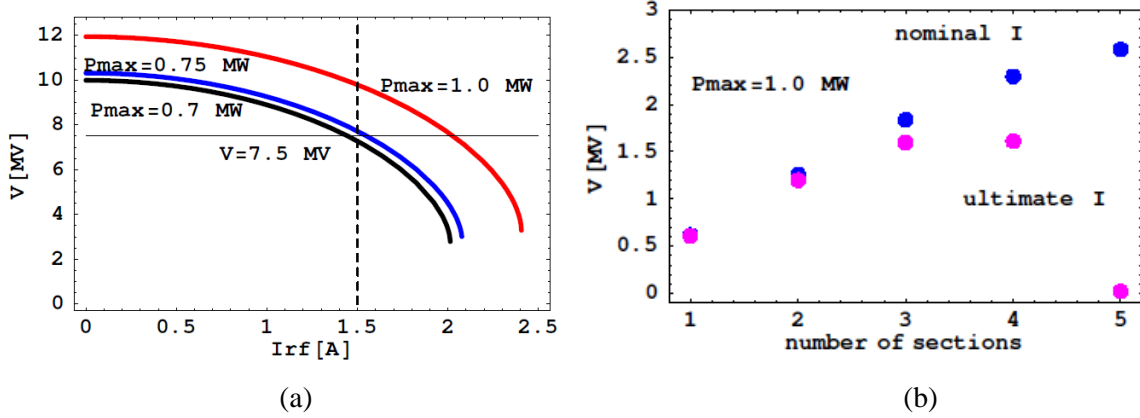


Fig. 5.17: (a) Total voltage available on the SPS flat top as a function of RF current in the present configuration (four cavities) for different RF power. The vertical line corresponds to the 25 ns beam with nominal intensity. (b) RF voltage per 200 MHz TW cavity with different number of sections for nominal and ultimate beam current.

The proposed solution [9] is to shorten the two long cavities and using the sections thus freed, together with two spare to install two extra cavities with corresponding power plants of 1.7 MW each. After this upgrade, the performance of the SPS RF system with high-intensity beams will be significantly improved and at the same time the overall peak impedance of the system will be reduced by 20%.

5.4.2 800 MHz RF system

Two TW cavities are installed in the SPS, but only one is currently connected to the power supply; this is used in everyday operation and during MDs for beam stabilization against longitudinal single- and multi-bunch instabilities. The total voltage seen by the beam is

$$V(\varphi) = V_{200} \sin\varphi + V_{800} \sin(4\varphi + \varphi_2). \quad (5.1)$$

The 800 MHz voltage is applied for all LHC beams from injection to extraction in bunch shortening mode (in phase) and with $V_{800} = V_{200}/10$. This ratio is defined by additional considerations concerning beam stability in a double RF system (monotonic dependence of the synchrotron frequency on synchrotron oscillation amplitude inside the bunch) [35]. The 800 MHz phase φ_2 is locked to the 200 MHz voltage, but the relative phase should be programmed during the cycle according to the variation of the stable phase 4 φ s. For bunch shortening above transition the phase should be $\varphi_2 = -4 \varphi_s + \pi$. Absolute phase is calibrated at the start of each run from beam measurements (bunch tilt at injection and beam stability during the cycle).

The second cavity, with its high impedance, has so far been idle. The foreseen upgrade includes putting it into operation together with a power upgrade for the operational cavity and serious improvements in the LLRF control (new one-turn feedback and later a feedforward system). Similar to the 200 MHz TW RF system, the effect of beam loading will also reduce the available voltage for higher beam intensities, however the 200 MHz voltage and therefore the 800 MHz voltage will be required due to larger longitudinal emittances.

After power upgrade the maximum 200 MHz voltage at lower intensities should be 15 MV and 10 MV at a maximum HL-LHC bunch intensity of 2.5×10^{11} p/b (25 ns spacing). The available (per cavity) 800 MHz voltage is shown in Fig. 5.17 as a function of current component at 800 MHz I_{rf} for the present 100 kW RF power at cavity input (Fig. 17(a)) and 150 kW after the power upgrade (Fig. 17(b)). Note also that only one cavity is currently connected to RF power, and two cavities will be operational after the upgrade providing that the voltage is sufficient, also taking into account that it is used at the level of (1/10–1/5) of the main 200 MHz voltage amplitude.

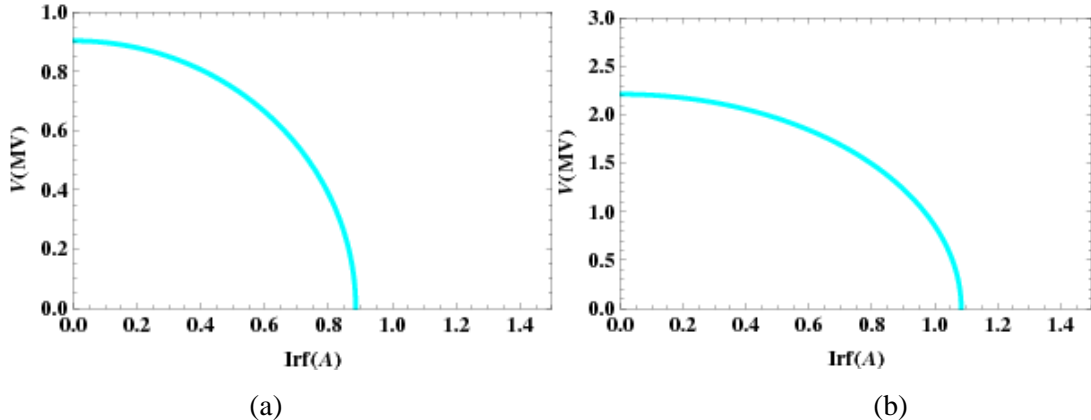


Fig. 5.18: The available 800 MHz voltage per cavity as a function of I_{rf} (beam current component at 800 MHz) with 100 kW RF power at cavity input (a) and after upgrade with 150 kW RF power (b). Nominal 25 ns beam corresponds to $I_{rf} = 0.45$ A and 25 ns with a bunch intensity of 2.5×10^{11} p/b to $I_{rf} = 1.0$ A (assumed form-factor of 0.33).

5.4.2.1 Existing system

The SPS-RF started up in 1976 with two accelerating cavities. Since 1980, for the new role of the SPS as a proton-antiproton collider, there are four power plants operating at 200 MHz (Fig. 5.19).

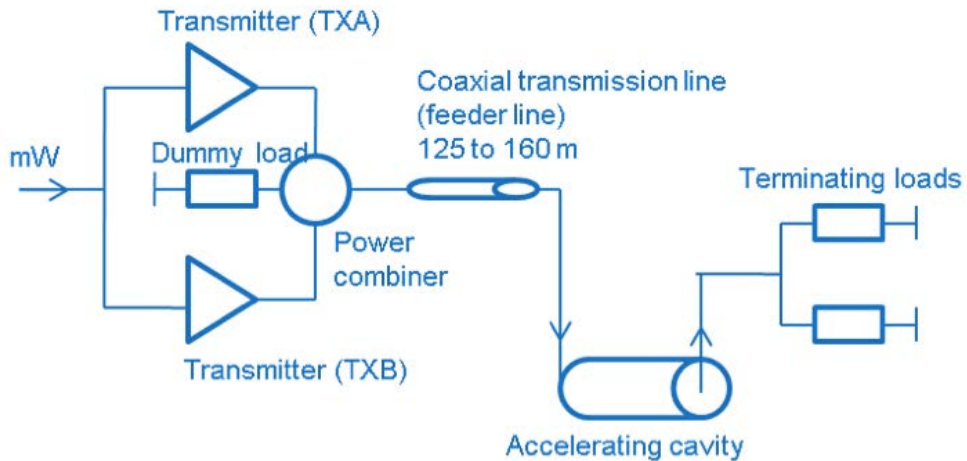


Fig. 5.19: Configuration of one of the four 200 MHz power plants

5.4.2.2 Motivation for the upgrade (Elena)

With the present four-cavity configuration we will have difficulties at high-intensity LHC beam in the SPS. Increasing number of shorter cavities with two extra power plants should significantly improve the RF performance for higher LHC intensities.

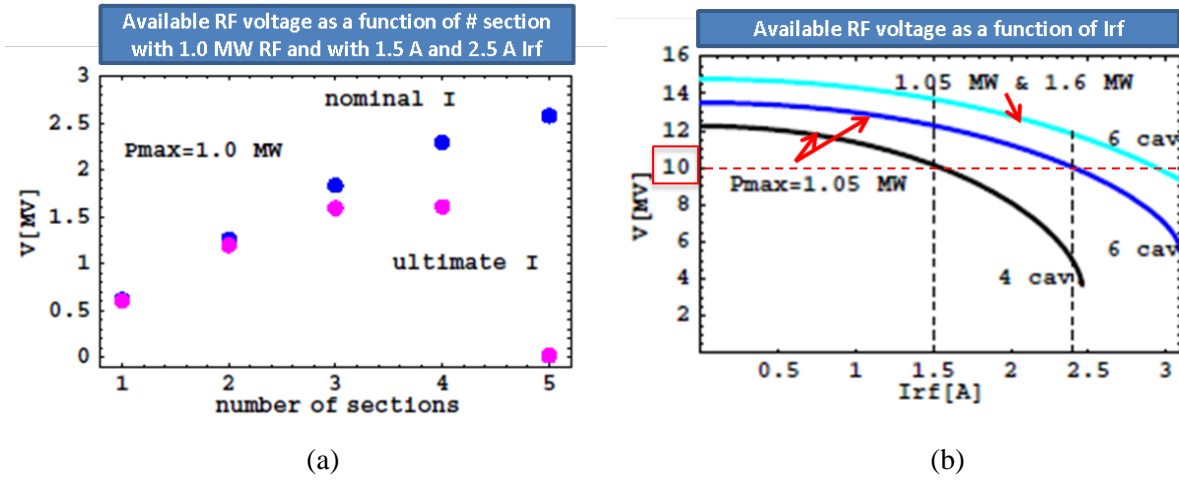


Fig. 5.20: Voltage limitation due to power available from amplifiers (a) as a function of the number of sections per cavity, for nominal and ultimate current, and (b) as a function of I_{rf} for 4, 5 and 6 sections.

The best new compromise is six cavities:

- 4 × 3-section cavities with 1.05 MW;
- 2 × 4-section cavities with 1.6 MW.

To provide 1.6 MW peak to the cavity input in pulse mode ($10 \mu\text{s}/43 \text{ kHz}$ and $3 \mu\text{s}/172 \text{ kHz}$) the new amplifiers will be able to deliver 1.9 MW at the tube output. The maximum average power over 30 s sliding is 600 kW due to thermal limitations of the coaxial lines.

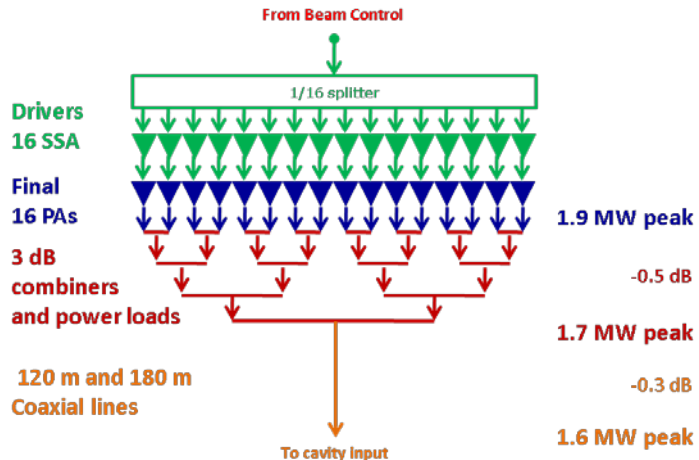


Fig. 5.21: Power at the cavity input and amplifier output

5.4.2.3 LIU-SPS RF 200 MHz upgrade project

The project is made of four main activities:

- existing amplifiers upgrade;
- new RF amplifiers;
- new RF building;
- LSS3 tunnel integration.

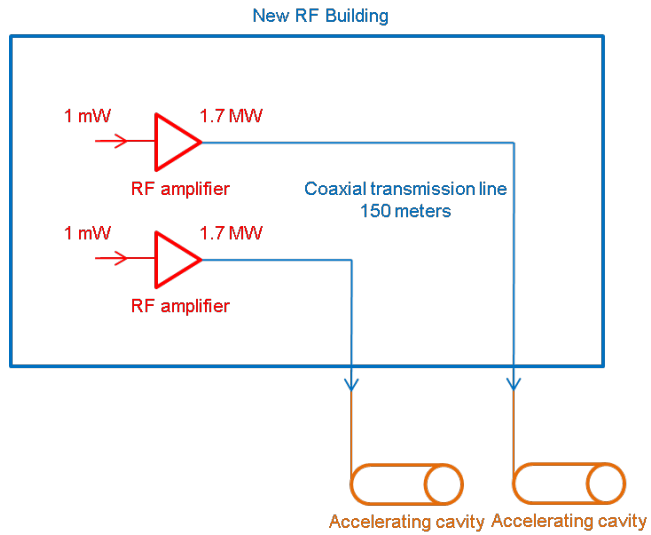


Fig. 5.22: LIU-SPS 200 MHz RF upgrade project main activities: building BAF3, amplifiers and LSS3 tunnel integration.

The new RF amplifier subproject is itself made of four contracts:

- drivers (SSA);
- finals (technology not yet decided);
- combiners (3 dB above 100 kW);
- transmission lines (coaxial, 345 mm outer).

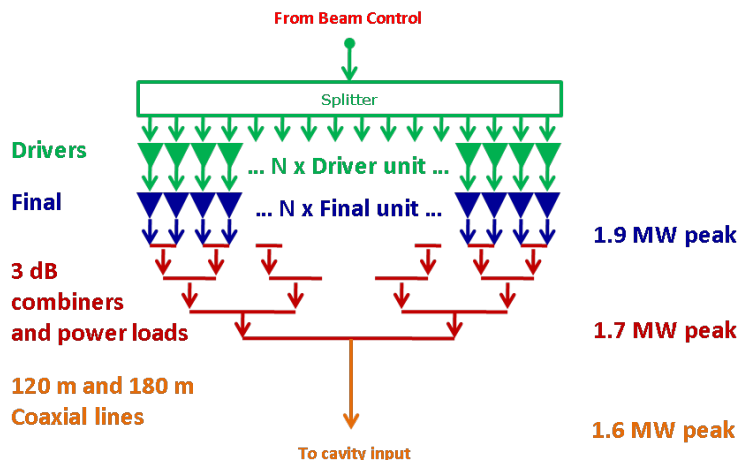


Fig. 5.23: LIU-SPS 200 MHz RF upgrade project amplifiers contracts: drivers, finals, combiners and power loads and coaxial lines.

A major improvement to existing systems will be to have individual driver per final. Combiners and lines will be the same as for existing systems.

5.4.2.4 Upgrade of the present systems

Amplifiers for the present systems, Siemens and Philips plants, have been in operation since 1976 and 1981, for 38 and 33 years of operation, respectively (Fig. 5.24). These systems have been upgraded several times to achieve higher performances. The last major upgrade was the modification of the high voltage power supplies to allow a pulsed mode operation. This was done beginning of the century to allow an operation with 12 μ s pulses at 43 kHz repetition rate.

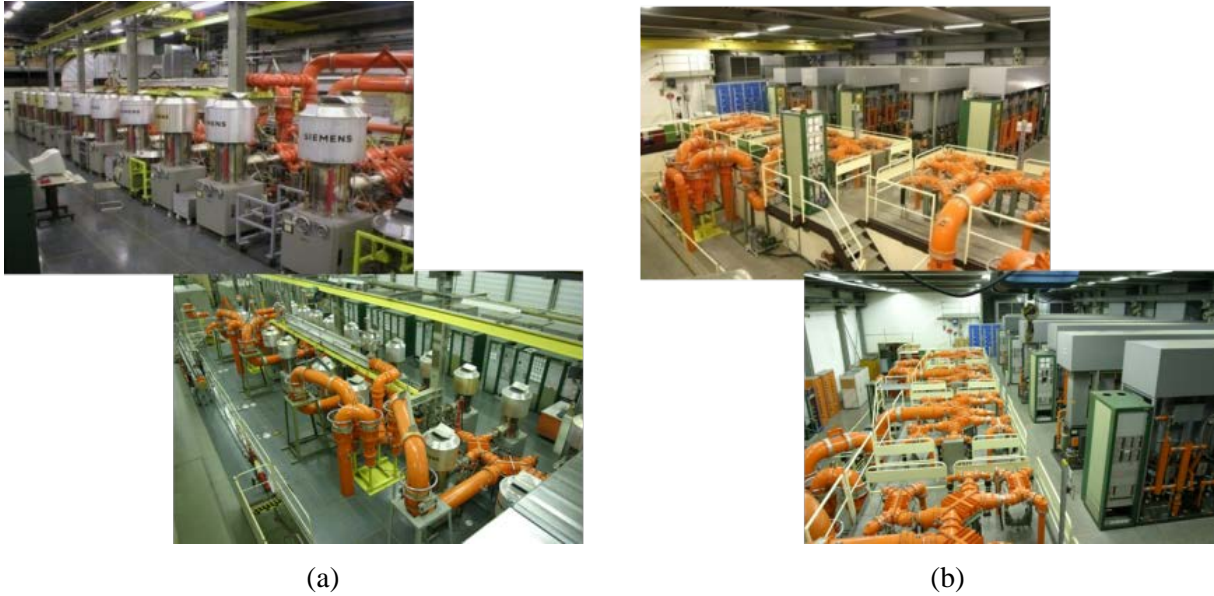


Fig. 5.24: (a) The Siemens power plant has been in operation since 1976; (b) the Philips power plant has been in operation since 1981.

With the new scheme of operation, several modifications will have to be implemented. It will again consist mainly of modifications to the high voltage power supplies, to allow operation in continuous wave (CW) mode as well as in pulsed mode with $12\text{ }\mu\text{s}$ pulses at 43 kHz repetition rate and $3\text{ }\mu\text{s}$ pulses at 172 kHz repetition rate. The target in pulse mode is 1.1 MW at the amplifier output, i.e. 1.05 MW at the cavity input, and the target in continuous wave mode is 600 kW at the amplifier output.

In addition to the high voltage power supplies modification and re-cabling, an important air-cooling plant upgrade has to be done to allow higher power. One must also keep in mind that these new operation ratings will be much more demanding and one must be ready to pay for new tubes.

Several options have been looked at to completely upgrade the systems with new technologies. We have considered using the present system with a higher consumption of tetrode as the base line and compared it to a diacrod option, a high power tetrode option, an Inductive Output Tube high power tetrode (IOT) option and to a solid state amplifier option. It turned out that the costs for upgrading and operation of other systems over a period of 20 years, including infrastructure modifications, operation and maintenance costs, would be:

- 1.6 time higher with diacrod;
- 2 times higher with high power tetrodes;
- 2.8 times higher with IOT;
- 3 times higher with solid state, even if operation and maintenance costs are reduced.

This is mainly explained by acquisition costs and infrastructure modification costs. Indeed, we already have the infrastructure for the present systems, and even if we have to modify the filtering of the high voltage power supplies, no infrastructure modifications are required. So, even if we have to be ready to buy a huge amount of tubes for the new operating scheme, this largely remains the ‘less expensive’ option. In addition, these systems have been proven to be very reliable over the last decades, which is not yet the case with new technologies.

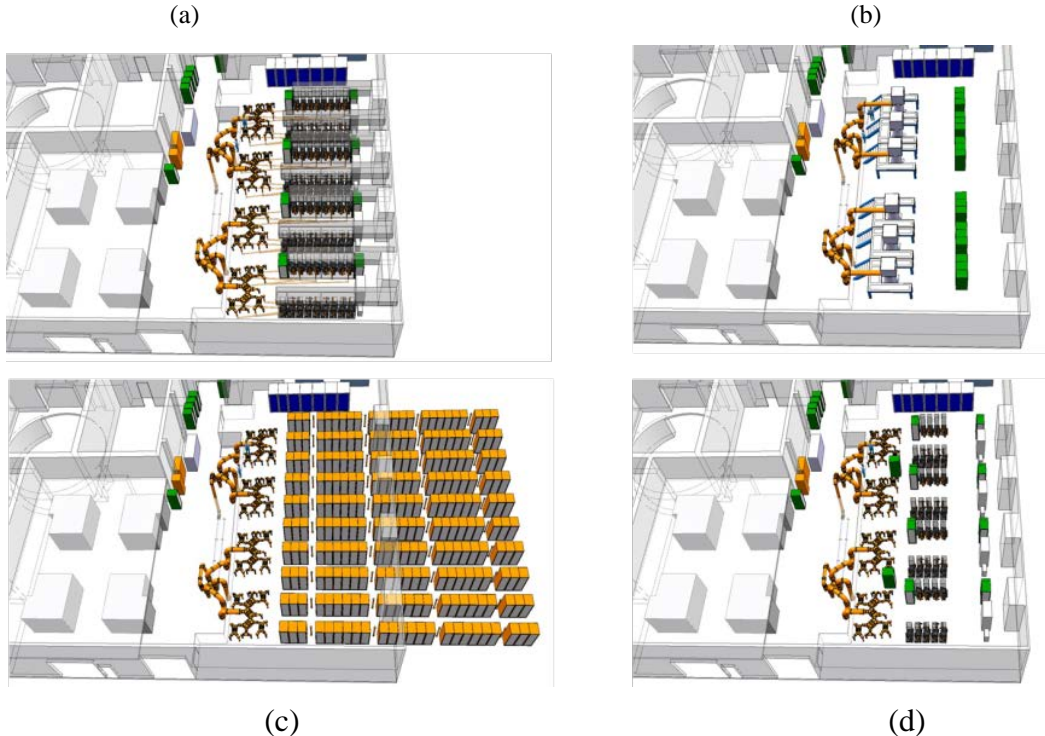


Fig. 5.25: Renovation of the Philips plant, comparison of technologies footprint: (a) present tetrode system, (b) diacrode, (c) SSPA and (d) IOT.

In March 2013, at the end of the last run period, we tested the present system up to its limit, with the implementation of quick modifications (a few additional capacitors in high voltage power supplies and in amplifiers). We were able to reach slightly above the requested power levels in various operation modes. We learned all weaknesses of the system regarding these new ratings, and solutions are being implemented. It is not only upgrading the high voltage power supplies and thermal cooling systems, but it is also implementing new high voltage swing filtering in the amplifiers themselves. This was not expected and will be deployed over the coming years.

As one can see in Figure 5.26, system 3 was lower in peak ratings. This is explained by the unavailability of one out of the sixteen tubes in operation. In previous operational mode, it was always possible to operate the system with one to two tubes out of order, and still be able to deliver the requested power. These tests have shown that with new machine requirements, all amplifiers will have to be operational. Any single fault will lead to degraded ratings. There will be no more margins.

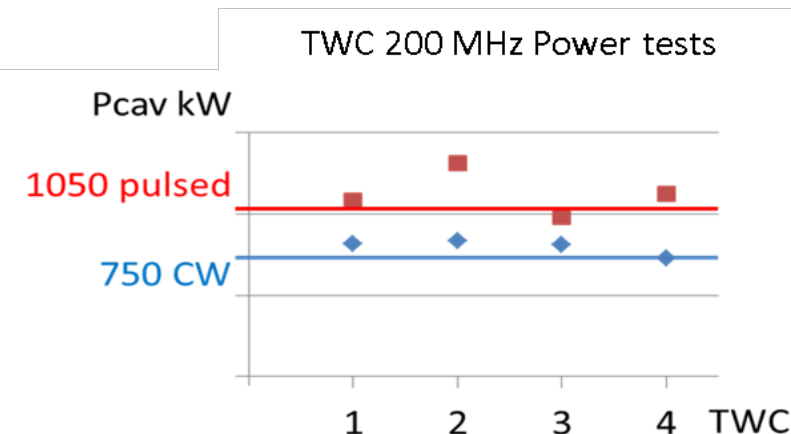


Fig. 5.26: Tests results of maximum ratings achieved in March 2013

5.4.2.5 New building

Several places have been checked in the SPS to host new cavities. It was necessary to find places where a surface building would also be available with the required infrastructure such as electrical networking and a water-cooling plant. Three SPS points have been good candidates: LSS3, LSS4 and LSS5. None of the SPS places have proposed an available building to host the amplifiers. So it was inevitable that a new building would be built. Point 3 is already an RF point, and electrical networking as well as water networking have required a minimal upgrade compared to other points. The upgrade of these networks remains nevertheless quite important, in this case minimal not being a synonym for small. In addition, the availability of gallery GT10, close to the shaft, has helped making the decision for the new RF plant location.

For the new amplifiers, whatever the technical solution selected; SSA, tetrodes, IOT or diacrode, the same building will be provided. Indeed, when looking at a possible place, the best possible location was found to be between BA3 and BB3 (Figs. 5.27 and 5.28).

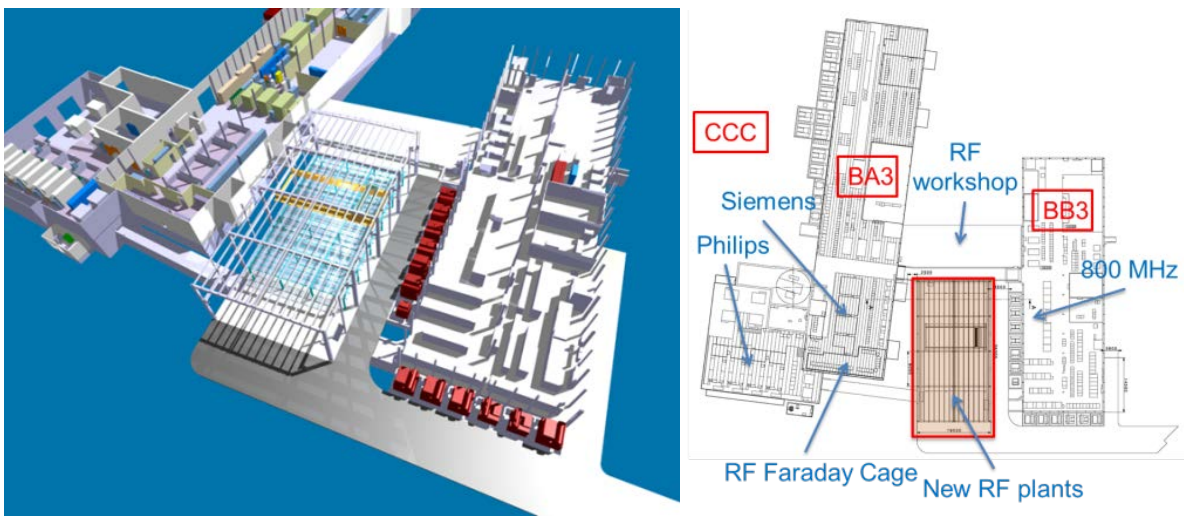


Fig. 5.27: 3d Implantation of the new BAF3 (a), Prévessin site, between BA3 and BB3 (b)

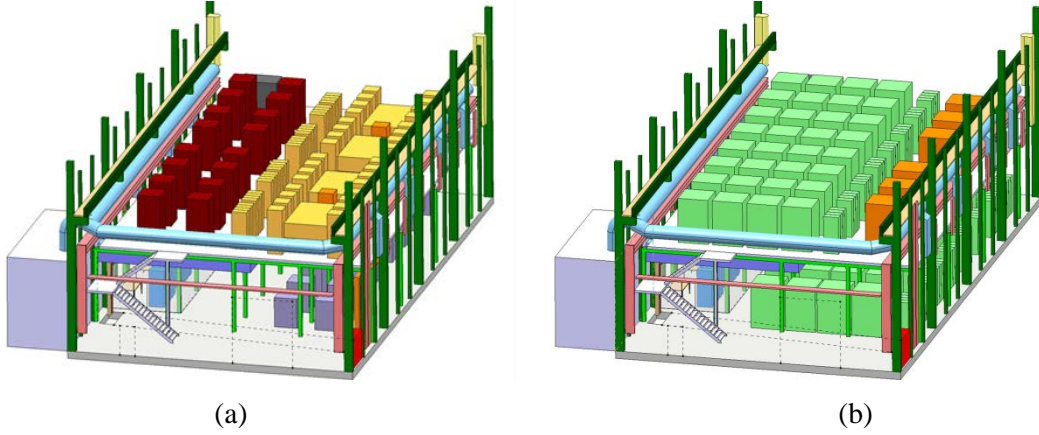


Fig. 5.28: Two possible configurations of the building with (a) tetrodes or (b) SSPA option

A key point is the availability of the GT10 gallery, connecting BB3 to BAE3, which is almost empty, allowing us to have access within a small length to the BA3 shaft going down to the SPS tunnel. The length between the amplifiers and the cavities has to be as short as possible to minimize losses in line.

One has to remember here that losses of -1 dB is a loss of 25% of the power. With all the ceramics and connectors we will have with the power lines, we optimistically estimated the losses of the 150 m of transmission line to -0.3 dB, i.e. almost 7.5% of the power. One can easily understand why we have tried to shorten the 350 mm coaxial line lengths.

The new building BAF3 will then be exactly above the GT10 Gallery (Fig. 5.29).



Fig. 5.29: The GT10 gallery, a few cable trays to be removed to allow the 350 mm coaxial transmission line to go to the LSS3 shaft.

The maximum footprint of the building will be a ground floor of $19.5 \text{ m} \times 36 \text{ m}$, almost 700 m^2 . This is taking into account existing buildings and their peripheral equipment such as high voltage transformers for BB3 and ventilation units for BA3. In order to maximize the available space, a metallic mezzanine has also been foreseen for the building. It will provide almost all the available surface of the building, except for a truck discharging area. In total the RF-available footprint will be almost 1000 m^2 .

We decided to build it as an industrial building. There will be no windows and no light openings in the ceiling of the building. The main idea is to minimize any water infiltration as we experienced it with older buildings at CERN. The building will be very similar to BA3 and BB3, with a metallic frame structure and metallic panels for the walls (Fig. 5.30).

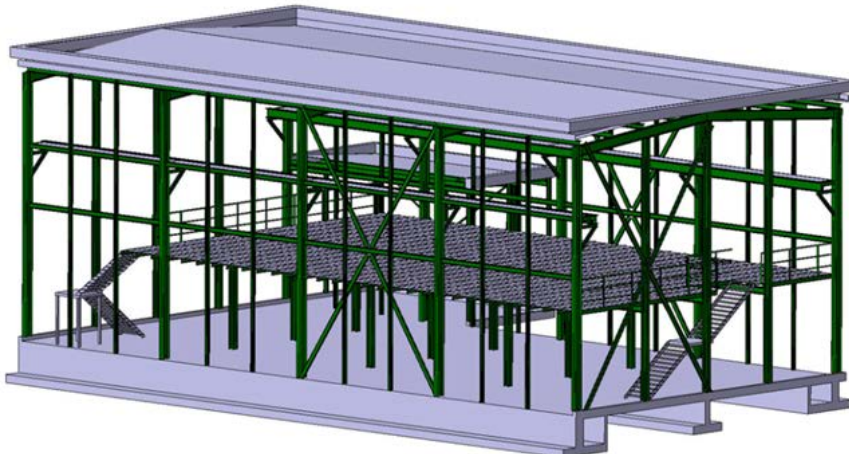


Fig. 5.30: Metallic frame structure of the building. Mezzanine inside will be defined once the technology of the finals has been selected.

A standard 10-tonne crane has been specified in order to move any heavy item in the building. The final height has been defined in such a way that, up to 3 m height, items can be installed under the mezzanine and 3 m-high items can be installed on the mezzanine. Changing the lights has been a deep problem with many of the old SPS buildings. Taking this experience into account, the crane will also be used for lighting maintenance within the building. All of these considerations lead to a total height of 12 m.

5.4.2.6 Amplifiers

Regarding a new request of 1.6 MW peak per cavity, we looked at the weak items.

The first one is the cavity itself, which we have never tested up to these voltage levels. However, based on previous experience with copper cavities, we believe that they will sustain the increase of voltage.

The second limiting item is the fundamental power coupler. In any case, for integration reasons, this device has to be re-designed. The present ones have been tested up to 800 kW 12 μ s/43 kHz in pulsed operation and up to 500 kW in continuous wave operation. As there are two couplers per cavity port, i.e. four fundamental power coupler per cavity in total, this allow us to feed the cavity with power up to 1.0 MW in continuous wave mode and up to 1.6 MW peak in pulsed operation. We are therefore confident that a new fundamental power coupler can be designed for these values at a minimum.

The next limiting items are the coaxial lines. With 350 mm outer diameter lines, we are already at the largest size we can use with respect to the frequency. These lines are built with an aluminium outer conductor and a copper inner conductor. The maximum single length available is 6 m. Large triangular ceramics are used to maintain the inner copper line centred on the outer aluminium line. These ceramics are also used in all angles we need for going from the amplifiers to the cavities. Keeping the system simple without adding complex cooling of the inner line, and taking into account all these items; aluminium, copper and ceramics, the absolute maximum power ratings for the coaxial lines are 1.75 MW peak power with respect to 870 kW average power. However, with these values, the inner copper line will be heated to 120°C. To ensure availability of the systems and stable operation, we have to reduce these numbers down to 1.7 MW peak power with respect to 600 kW average power over 30 s sliding. This is the power that can be fed to the first piece of line on the amplifier side. With the (optimistic) -0.2 dB losses along the line, it is possible to obtain absolute maximum ratings of 1.6 MW peak power on the cavity input side (Fig. 5.31).

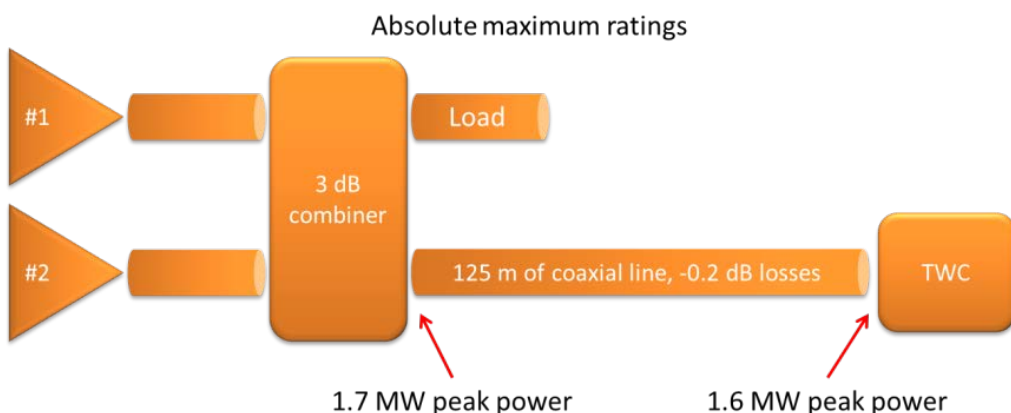


Fig. 5.31: Absolute maximum ratings of 1.6 MW at the cavity input

Looking at the amplifier parameters, and taking into account all the limiting parameters described above, the absolute maximum ratings for the amplifiers have been defined as follow:

- peak power: 1.7 MW maximum with 10 μ s/43 kHz or 3 μ s/172 kHz;
- average power: 600 kW (sliding over last 30 s);
- must be reliable 24/24 hours, 300/365 days with a 2 month winter technical stop and a 1 day stop every 8 weeks;
- minimum 20 years of operation with 3 years of operation plus 1 year off cycle;
- qualified solution must be demonstrated to be reliable under scientific operation, not just broadcast operation.

Specific bandwidth, gain saturation and phase distortion have also been required in order to guarantee a correct low level feedback operation (Fig. 5.32).

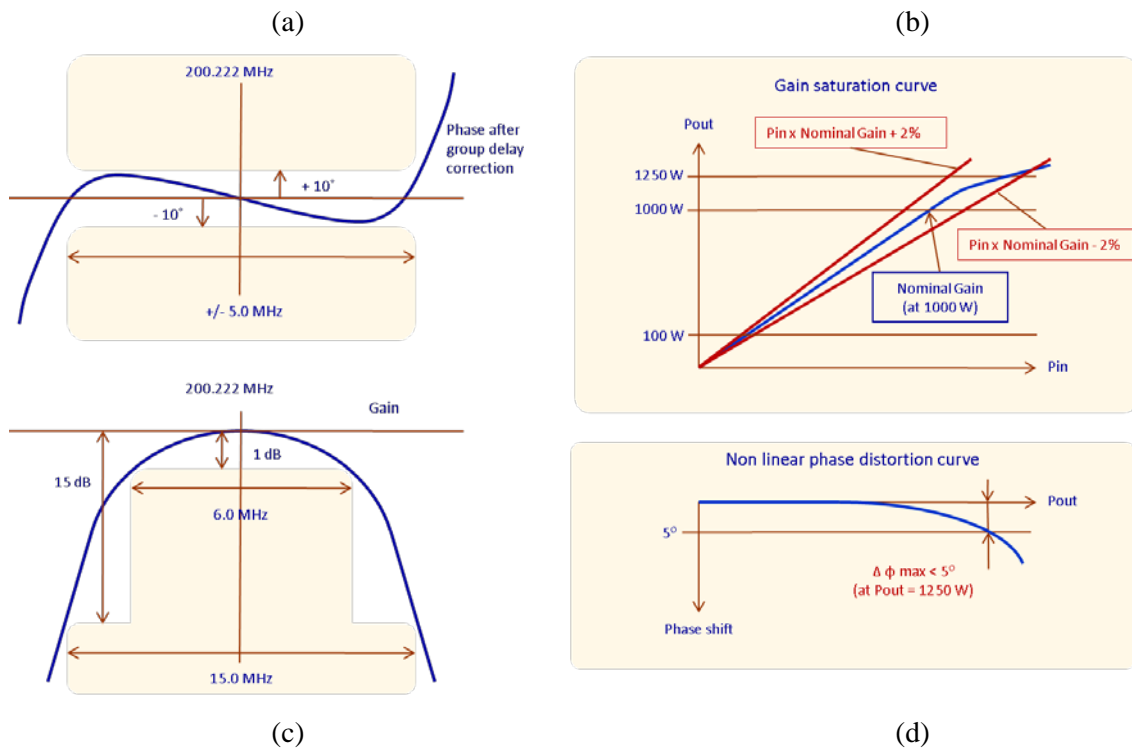


Fig. 5.32: Specific bandwidth (a), gain saturation (b), gain (c) and phase distortion (d) requirements

In order to qualify drivers and finals, several tests have been requested from the single unit level up to the whole system level:

- test 1 and 2 are in continuous wave, simulating coast operation;
- test 3 and 4 are with long pulse operation of 5 s pulse length and 0.1 Hz repetition rate, simulating CNGS type operation;
- test 5 and 6 are with 12 μ s pulse length and 43 kHz repetition rate, simulating LHC proton operation;
- test 7 and 8 are with 12 μ s pulse length and 43 kHz repetition rate, simulating LHC ion operation.

To be as close as possible to SPS operations, a supercycle composed of all these test has been defined. All systems will be qualified applying these tests for 1 min each over a supercycle of 8 min over 48 h (Fig. 5.33).

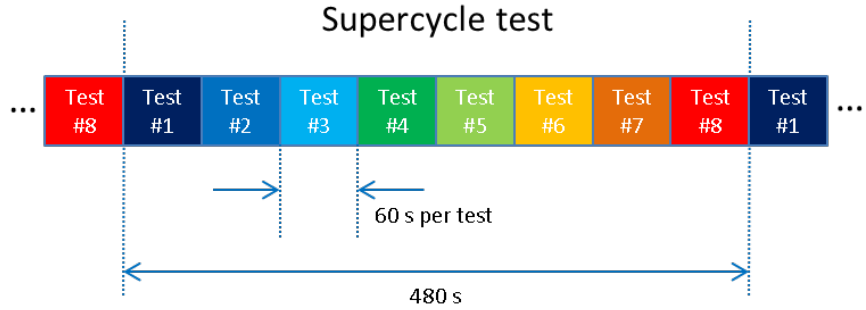


Fig. 5.33: Test to be applied to all subsystems for qualification

An additional RF test will be applied to all RF items. This is the short circuit test. It consists of applying the eight tests described above to amplifiers on a short circuit instead of a load. We will then repeat the eight cycles with the devices matched and suddenly unmatched with a special triggered short circuit (Fig. 5.34). It will be repeated for several unmatched phases. This test will be one of the most demanding and will prove the reliability of any single RF item.

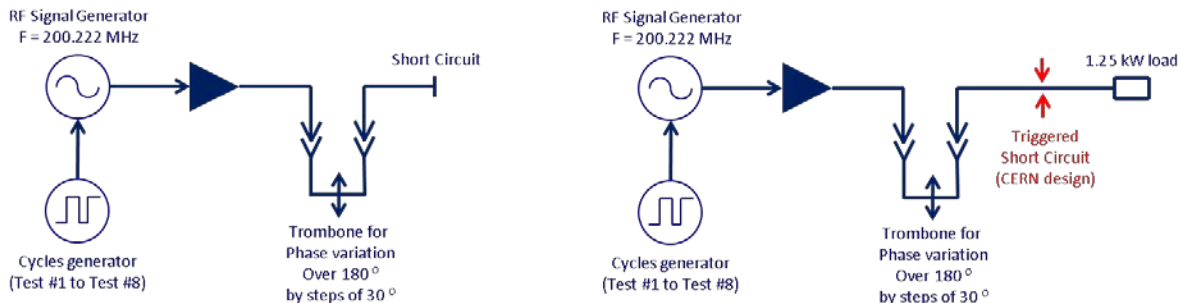


Fig. 5.34: Short circuit test: unmatched condition and matched and triggered unmatched condition

Again, to be as close as possible to SPS operation, a short circuit supercycle composed of all the eight tests has been defined. It will be repeated with the short and triggered short test for 5 s each. This 40 s supercycle will be repeated for half an hour.

Once all of these qualification tests have been done, there will be a final long duration test that will be performed onto a pre-series set for qualification. It will consist of applying the supercycle for 1000 h to several pre-series units in parallel (Fig. 5.35). If a single item fails, the whole system will be disqualified.

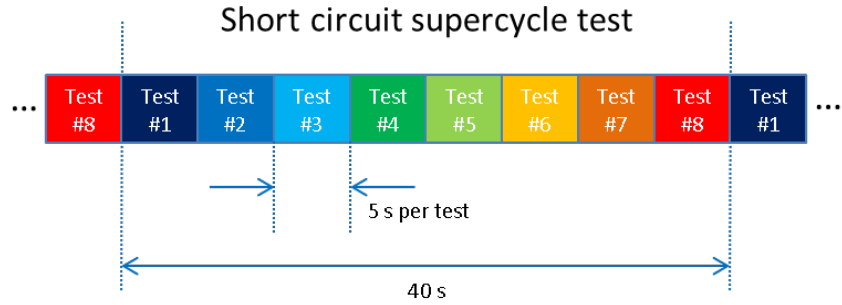


Fig. 5.35: Short circuit test with unmatched and triggered unmatched conditions, over all phases, to be applied to all RF subsystems for qualification.

5.4.2.7 *Finals*

Several options have been looked at for the final amplifier stage. Many suppliers have been contacted to check availability of the technologies. The options that have been considered are:

- 2×1.7 MW peak klystron;

the klystron option has quickly been removed from the list as none of the known suppliers wanted to go further in this direction. Indeed, at this frequency and power ratings, no klystron currently exists. A special design would have to be launched requiring a special, very long vacuum furnace.

- $2 \times 2 \times 970$ kW peak diacrodies;

the option with two diacrodies is one of the most promising. Los Alamos has already designed an amplifier operating at exactly the correct frequency. It has been tested up to 3 MW in ms pulsed mode, with average power of hundreds of kW. Tests have been made jointly with CERN in the frame of TIARA [9, 36]. An option with two diacrodies combined and a third as an active spare would be easily implemented (Fig. 5.36). This would offer a very available system.

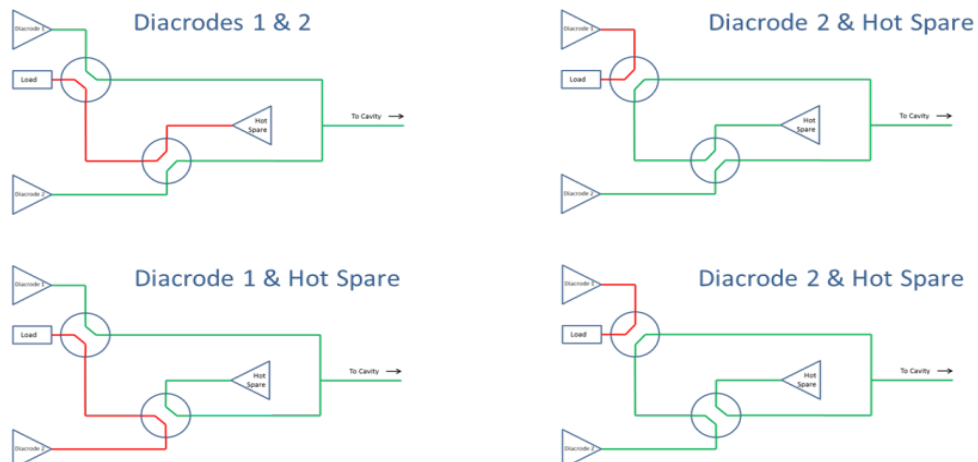


Fig. 5.36: Proposal with two diacrodies and a third additional one as a hot spare

- $2 \times 8 \times 225$ kW IOTs;

an IOT system has been proposed, but there are no IOTs that operate at this frequency. In addition, this option would have imposed a higher high voltage operating value. This option has then been down-selected.

- $2 \times 8 \times 225$ kW tetrodes, equivalent to Siemens or $2 \times 16 \times 106$ kW tetrodes, equivalent to Philips;

as we have a very long and good experience with tetrodes at CERN, tetrode options have been considered. As we want to be able to operate the system even if one of the tube fails, the eight-tube option would have required too much power. Indeed none of the existing tetrodes would have allowed the system to be operative with seven out of eight tubes and still provide full power to the cavities. Not having the possibility of switching off-line any tube has been considered to be too risky for this project. With a 16 tetrode system, it has been found out that even with 14 out of 16 operating tubes, the requested power would still be available. To date, this remains one of the considered options, along with the diacrod solution.

- $2 \times 2048 \times 830$ W SSA, equivalent to ‘SOLEIL’;

regarding the SSPA amplifiers, demonstrated to be reliable by SOLEIL, a pre-study has shown that the available space in the new building would have been too small (Figs. 5.37 and 5.38). In addition, with our BA3 and BB3 facilities, the 18 kVAC network is available at a low cost and is already sized for the new amplifiers. Downsizing the voltage from 18 kVAC to 400 VAC, as requested by SSPA solution, would result in consequent additional costs. The cost of the amplifier itself would have already been much more expensive than a tube option, as recently experienced with our driver contract. All of these parameters together have driven us to not consider SSPA as an option for the final stage.

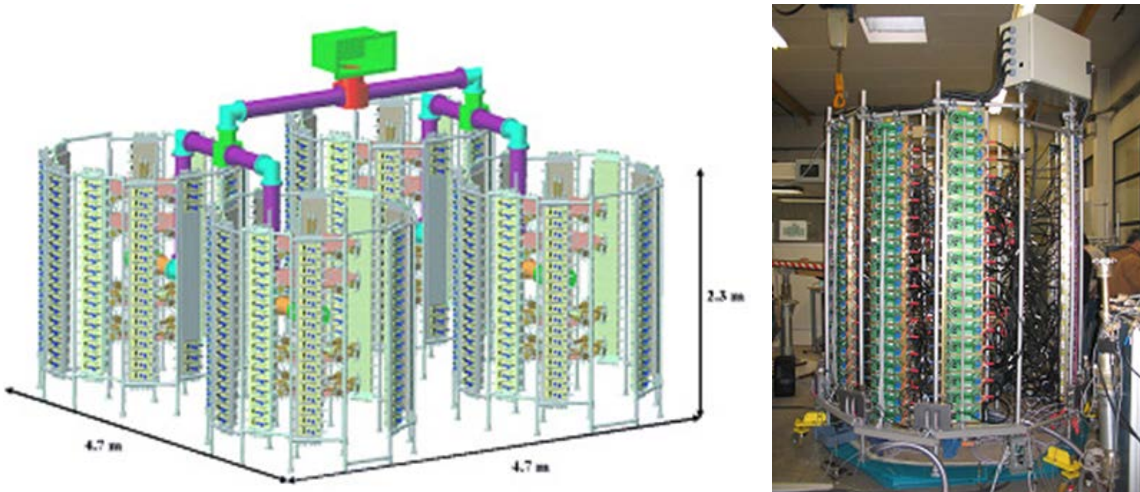


Fig. 5.37: SOLEIL amplifiers reliably in operation since 2007

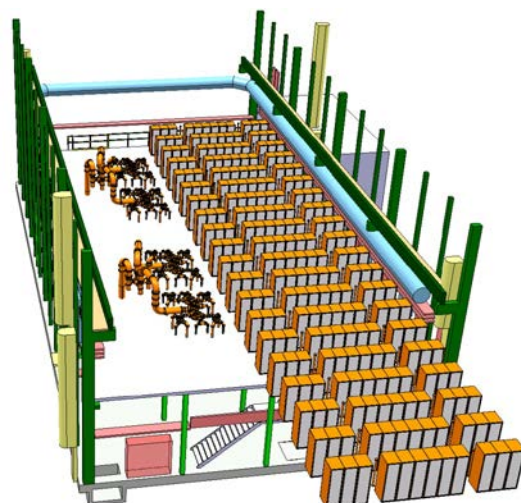


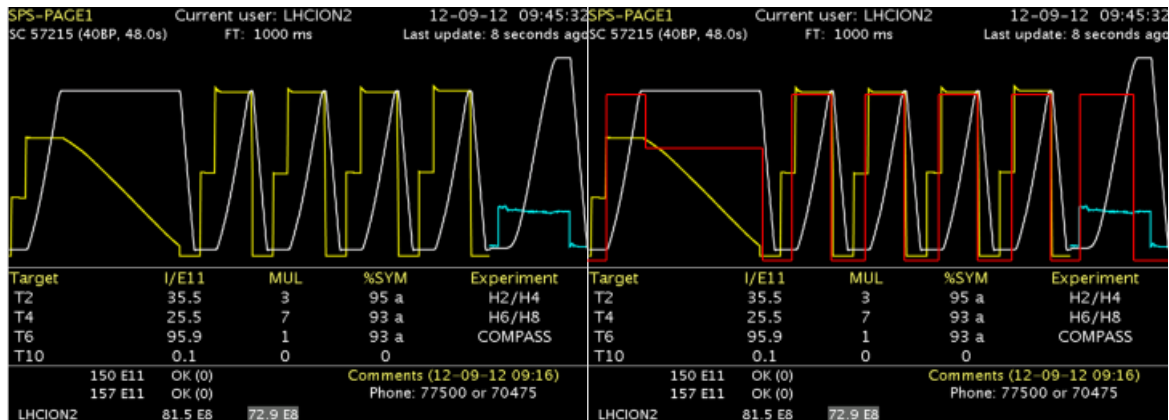
Fig. 5.38: Preliminary SSPA integration study showing that even with a rack solution the new RF building would have been too small.

5.4.2.8 Drivers

Regarding the frequency range, and the power ratings, a solid state amplifier solution has been found to be the most appropriate for building the driver stage. It has several advantages, such as:

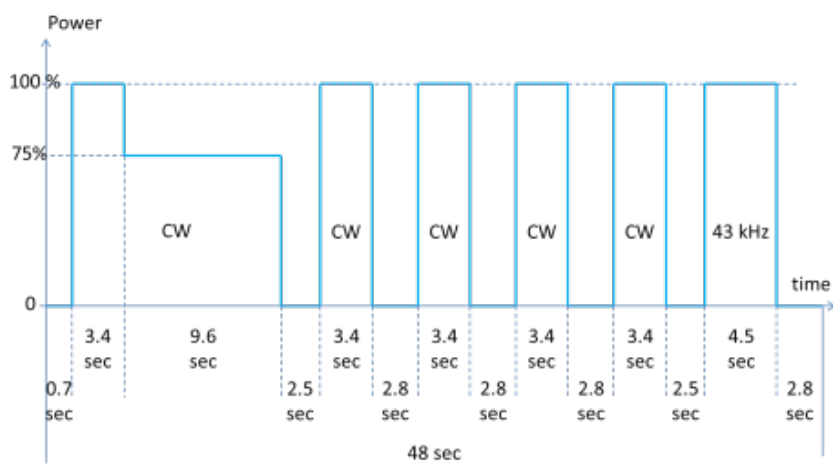
- largely available on the market;
- it is easy to build a redundant system;
- there is no need for a high voltage power supply;
- as a combination of several small units, it is easy to have one driver unit per final unit, instead of a chain of drivers split at its last stage into several sub-outputs to several driver final units, as is the case with the present SPS system
- if limited to several tens of kW, it is easy to combine using $\lambda/4$ wavelength transmission lines.

Regarding all of the kinds of RF cycle that we will have to provide during operation, when regarding the transistors available on the market, we have decided to ask for a brick of power rated at 1.25 kW peak with respect to 700 W average power, Fig. 5.39.



(a)

(b)



(c)

Fig. 5.39: Example of a SPS supercycle; with proton and CNGS operated in continuous wave mode (a) and LHC injection (b) operated in pulsed mode at 43 kHz 50% (c). Average power is almost 55% of maximum power. For a driver amplifier operated at 1.25 kW peak, this leads to 688 W average power.

With two amplifiers of 1.9 MW peak and each amplifier with 16 tetrodes (Fig. 5.40), for an operation with even 14 out of 16 tetrodes, each tetrode will provide up to 175 kW peak.

Taking into account ageing, the maximum gain of the tetrode will be 13 dB, the driver is then:

- 175 kW, 13 dB + 1 dB losses due to the driver combiner and cables = 11 kW.

The driver will then be a combination of nine units of $1.25 \text{ kW} = 11.25 \text{ kW}$ and the total number of drivers will then be $2 \times 16 \times 9 = 288$ units. With 12 additional spares and 12 pre-series for qualification test, this leads to a grand total of 312 units.

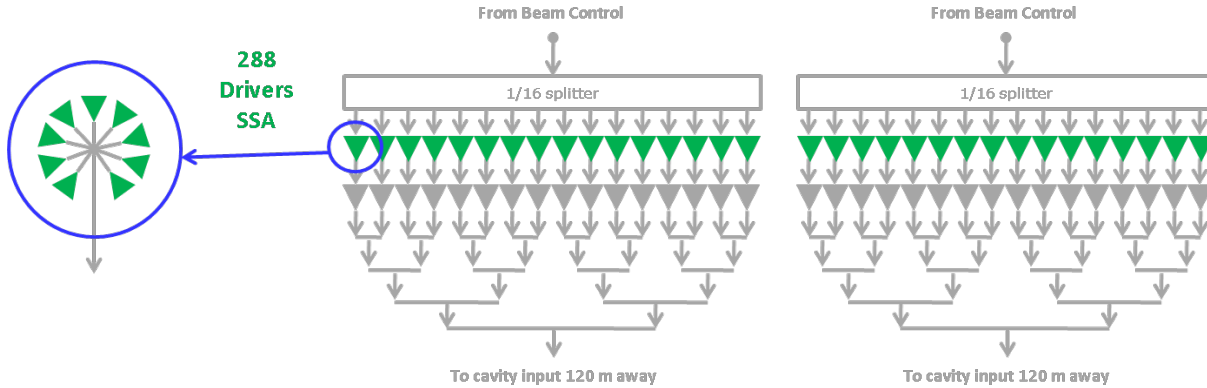


Fig. 5.40: Driver configuration with a 2×16 tetrodes option

With two amplifiers of 1.9 MW peak and each amplifier with $2 + 1$ diacrododes, each diacrodode providing 950 kW peak + 0.3 dB losses due to the final combiner = 1020 kW peak.

Taking into account ageing, the gain of the diacrodode is 12.5 dB, the driver is then: 1015 kW, 13 dB + 0.6 dB losses due to the driver combiner and cables = 66 kW.

The driver will then be a combination of 54 units of $1.25 \text{ kW} = 67.5 \text{ kW}$ and the total number of drivers will then be $2 \times 2 \times 54 = 216$ units (Fig. 5.41). With 32 additional spares and 12 pre-series for qualification tests, this leads to a grand total 260 units.

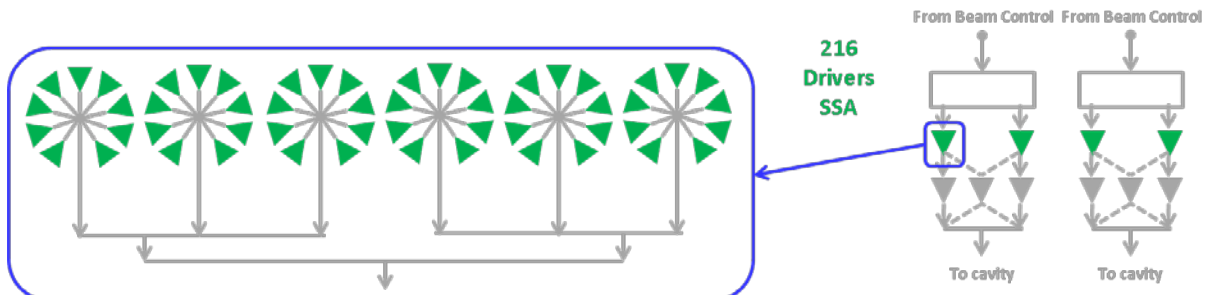


Fig. 5.41: Driver configuration with a 2×2 diacrododes option

As the decision of the technology for the final is not yet decided, the contract for the drivers has been made to allow placing an order of up to 320 driver units.

5.4.2.9 Combiner and coaxial lines

From the surface building to the cavity, we will re-use the same 50Ω coaxial transmission lines that have been in operation in the SPS since 1976. These are 345 mm aluminium outer diameter transmission lines with 150 mm copper inner diameter transmission lines. The inner diameter is maintained coaxially with large triangular pieces of Al_2O_3 ceramic that have specially been designed for these transmission lines (Fig. 5.42). The maximum length of such a transmission line is a straight piece of length 6 m (Fig 5.43). From the surface building to the cavity, it is 150 m to the first cavity and 180 m to the second cavity (Fig. 5.44). We will also have to take into account thermal dilation of the lines in order to allow movement of the external pipe and not overstress the ceramics. In the centre

of each ceramic, there is a specially designed connector system that allows the inner copper pipe to slide along the connector. The RF finger of this special contact must not greatly stress the ceramic to not to break it, while ensuring perfect RF continuity, noting the huge power that is transmitted along the lines.



Fig. 5.42: Specially designed ceramic maintaining the inner line coaxial to the outer line. The special RF finger inner connector is also visible, as well as the specific suspending system.



Fig. 5.43: Preparation and assembly of a piece of 6 m length of a 345 mm coaxial line. A special lifting craft is mandatory when installing these heavy transmission lines, which are suspended from the ceiling.

Even if these lines could be air cooled, thanks to the design of the ceramic, the complexity of such a cooling system is very constraining. It has been decided to stick with a ratings value for operation without any additional cooling system. The maximum operating value will have to remain below 600 kW average power over 30 s. With this average rating, the inner copper line will remain under 120°C. The 1.9 MW peak power delivered by the final is within the peak value maximum ratings for such a coaxial line.



Fig. 5.44: A very important tip is not forgetting, when designing the path of such large transmission lines, the 180° U-shapes, which are the only way to disconnect a part of the main path. With about 150 m of lines, we will have to integrate a few of these to be able to exchange a faulty item if necessary.

Whichever technology is selected for the final amplifiers, we will have to combine the output power of the sub-units to provide the total output power to feed the cavities. With the requested power ratings, 3 dB combiners adding two power inputs as with the present systems have since 1976 been proven to be reliable (Fig. 5.45). We will do a reverse-engineering of the combiners that are in use with the present Siemens and Philips power plants, in order to provide fully compatible equipment:

- if the final solution is a combination of 16 tetrodes, we will first have three stages of the same 500 kW CW 3 dB combiners. We will then have one stage of 1.0 MW CW input combiner;
- if the final solution is a combination of two diacrodes, we will only have the last 1.0 MW CW input combiner.

For CW power the performance has already been demonstrated. However, even if calculations have shown compliance up to full peak power, the 3 dB combiners still have to be tested up to full peak power.

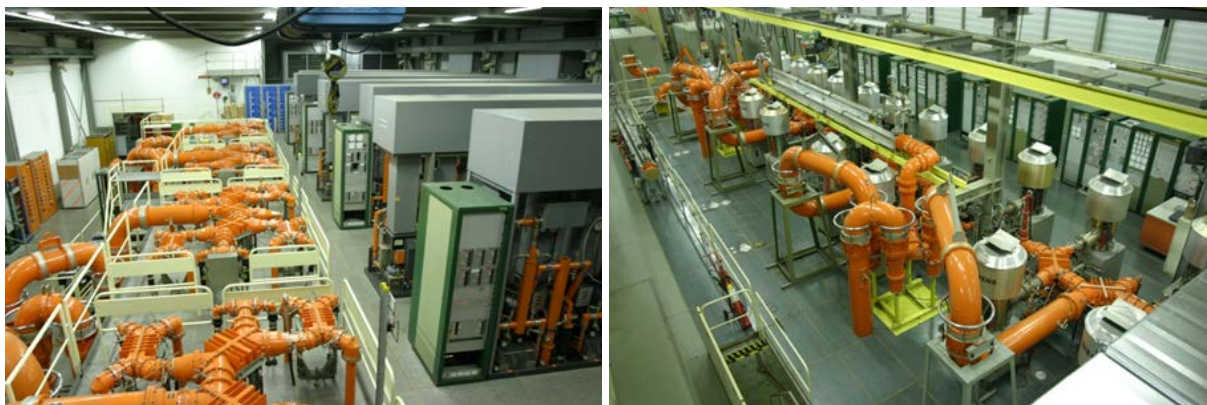


Fig. 5.45: (a) The 500 kW 3 dB combiners; (b) the 1 MW 3 dB combiners. These have been in operation with the present systems since 1976 without a single default.

Power loads that are to be connected to the fourth port of the combiners will also be re-designed at CERN. Regarding a power level of up to 200 kW peak, a new design will be developed and made compatible with the present systems. Regarding power up to 500 kW, we will re-use the recent design (2001) made for the present combining systems and for the cavities themselves (Fig. 5.46). It has

proven to be reliable for the last ten years of operation. The window isolating the air side to the water side has been designed like a coupler power window, with an Al_2O_3 coaxial ceramic, tested up to 800 kW peak power. When power above 500 kW peak will be needed, we will connect several loads in parallel through a $\lambda/4$ wavelength network to match the impedance.



Fig. 5.46: The recently (2001) re-designed RF power loads rated at 500 kW CW and 800 kW peak power

One has to keep in mind that any additional losses due to combining system, ceramics in the transmission lines or transmission lines themselves will induce additional overheating. The induced overheating will generate a mismatch of the lines by modifying the geometry (Fig. 5.47), again inducing additional losses. The -0.1 dB losses estimated per 3 dB combiner and the -0.3 dB losses estimated as overall losses from the lines are all optimistic values. However, regarding the size of the line and the construction of the adaptors to perform matching measurements, it is difficult to make a better estimate. Regarding these parameters, 1.9 MW peak power at the output of the tubes to provide 1.6 MW at the cavity input must be understood to be a best estimate value at the cavity input. It could be that additional losses in the combining system or additional losses in the transmission lines have a great reducing effect. Indeed, one must remember here that -0.1 dB corresponds to a loss of 2.5% of power.



Fig. 5.47: In the past, two ways of welding the outer lines have been tested. (a) The initial linear weld showed less stability than the helicoidally welded line shown in the picture. (b) The 350 mm to N adaptor.

Calibration of such adaptors is not easy. When looking for a level of losses at 0.1 dB, any detail will have a deep impact.

LSS3 re-arrangement

Travelling wave cavities are built from a section of cavity (Fig. 5.48). Since 1980, we have two cavities made of four sections and two cavities made of five sections, for a total of 18 sections in LSS3. In addition, we have three spare sections, which have, however, never been equipped with all peripherals such as drift tubes, fundamental power couplers, HOM filter and field antennas.



Fig. 5.48: (a) A section of cavity in the lab equipped with its drift tubes; (b) a four-section cavity in the SPS-LSS3, fully dressed with its fundamental power couplers, power loads and other peripherals.

With the proposed upgrade project, we will increase the total number of sections in operation, having 20 sections distributed over six cavities instead of 18 sections distributed over four cavities. We will then have four cavities made of four sections and two cavities made of five sections. The four-four section cavities will be fed by the present system, which is able to deliver 1.05 MW peak to the cavities, while the two-five sections cavities will be fed by the new amplifiers, delivering 1.6 MW peak to the cavities (Fig. 5.49).

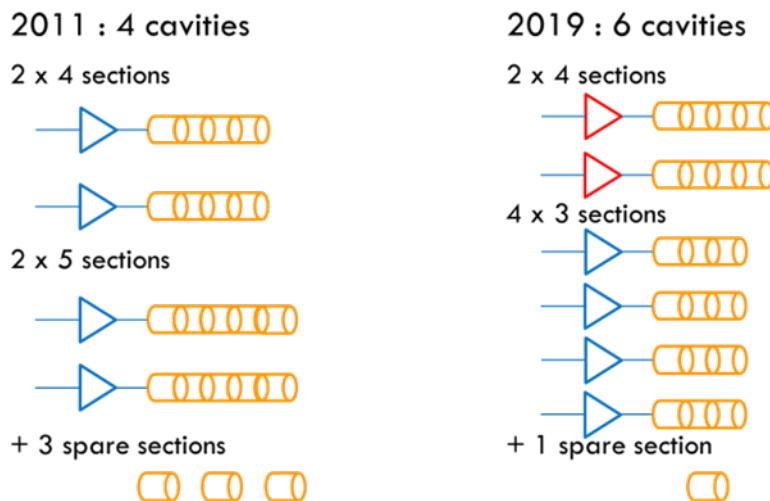


Fig. 5.49: Proposed upgrade scheme: from (a) four cavities to (b) six cavities in the SPS LSS3

The decision regarding the total number of cavities had been made taking into account the available space in LSS3, the available total number of sections of cavities, the cross-section space available enabling installation of coaxial transmission lines, and the need for specific elements to remain at their present locations for machine optics reasons (Figs. 5.50 and 5.51). Taking all of these parameters into account has driven us to the proposed compromise. Within the four straight sectors, there will be all six cavities with, in addition, the two 800 MHz travelling wave cavities. This remains compatible with the few devices that cannot be moved. Some other kickers that are currently inside these four sectors will be moved to the ex-standing wave cavities areas at both sides of the straight sectors. All parameters have been checked and the new locations have been agreed by all owners. Seven pick-ups will move from inside the area to other locations, inside and outside the area. In the meantime, free space has also been made for the high bandwidth kicker and pick-up project. During winter 2012–2013, we already cleaned old cables from sector 314 and sector 321. This enabled us to move pick-ups in sector 314 and free the space to integrate a new kicker in sector 321.

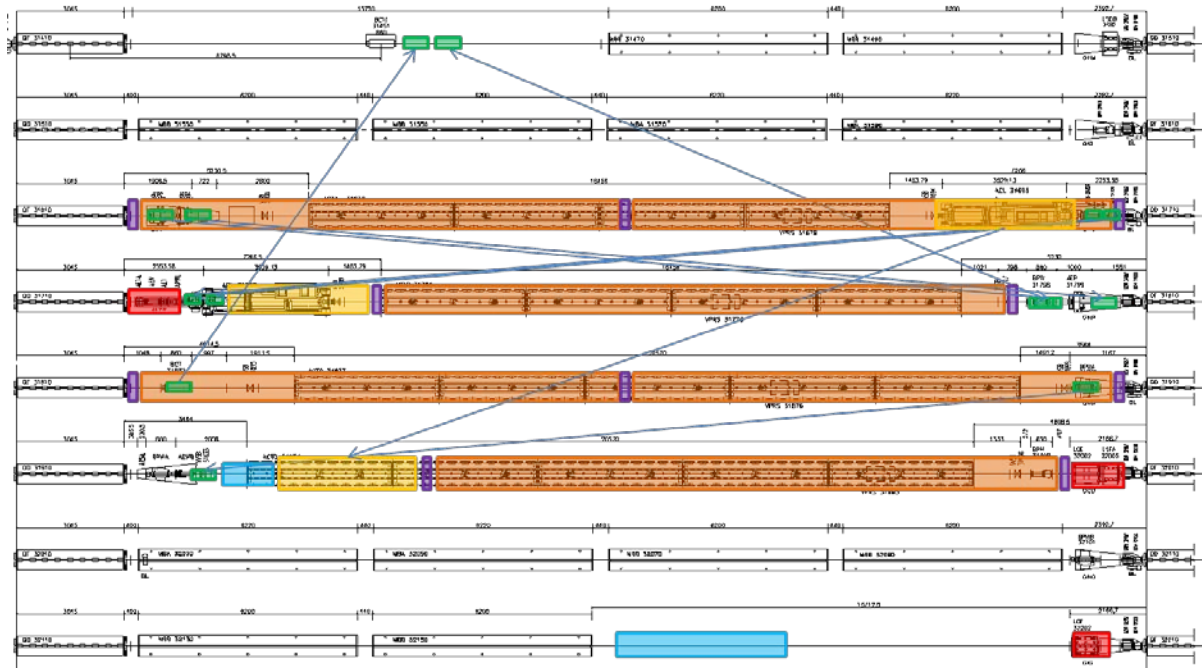


Fig. 5.50: The main limiting available space was the configuration of LSS3 itself. Some devices have to remain at their present locations due to machine optics constraints.

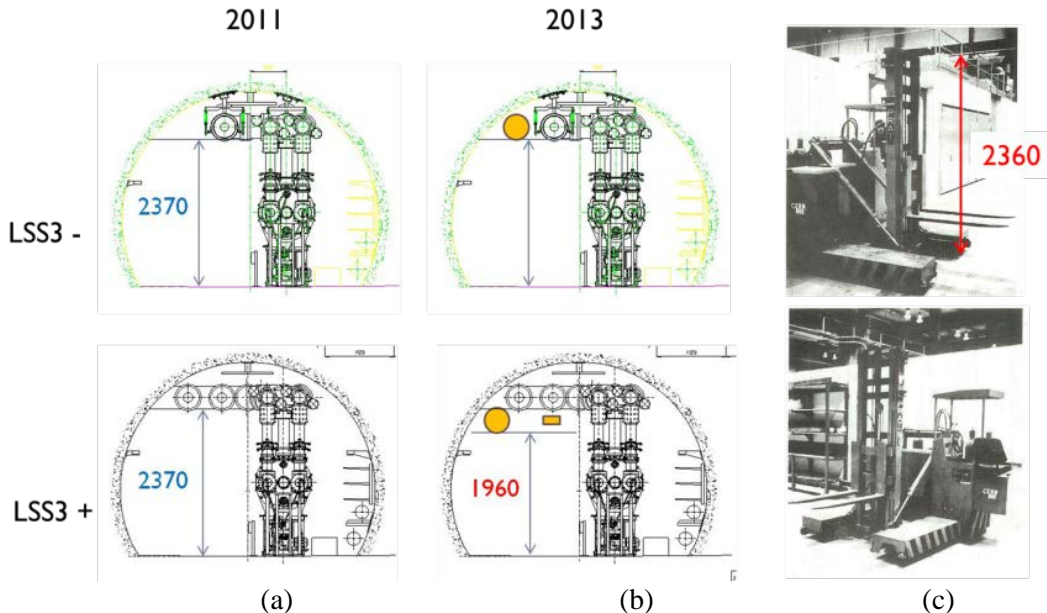


Fig. 5.51: Cross-section space available for LSS3- (a) and LSS3+ (b), abd vertical clearance (c) has been one additional limiting parameter to define the number of cavities that we can install in LSS3.

During 2001 to 2004, we had a SPS realignment campaign during which we disassembled all four cavities. Thanks to this we have all needed specific tooling (Fig. 5.52). We also know that it will be a huge amount of work involving a lot of people, and that perfect coordination between all of the actors will be mandatory for success.



Fig. 5.52: Specific tooling, a dedicated truck, to move each single section of cavity

5.4.2.10 New RF fundamental power couplers

With the present couplers, integration is not possible as each cavity will be too long by about 30 cm. A new coupler has to be designed. In any case, we had to design a new fundamental power coupler as the maximum ratings have increased incredibly. Indeed, these travelling wave cavities have been designed to be fed by two fundamental power couplers at the input and two fundamental power couplers at the output to dissipate the unused power into $50\ \Omega$ loads. The initial power rating was of about 375 kW CW per fundamental power coupler in the 1980s. In the late 1990s, after almost 20 years of operation,

some couplers started to fail with metallized ceramics. We have already made the first upgrade, changing the ceramic axis. The current design allows an increase of the transmitted power up to 500 kW CW per fundamental power coupler. Tests have even been made up to 800 kW peak power for a short duration (Fig. 5.53). The new design will have to allow the same average power level with, in addition, the capability of more than 800 kW peak power over a long duration basis.

As we will have to considerably increase the power rating of the fundamental power couplers, a known weak device within the current fundamental power coupler is the connection between the fundamental power coupler and the cavity. Indeed, the fundamental power coupler is connected to the cavity through a spring contact inside the cavity vacuum side. This does not allow very efficient cooling of the connection, limiting the average power. In addition, due to the coupling element shape itself, the total length of the spring contact is reduced; this also limits the maximum current that can flow through the contact itself, limiting the peak power. The new coupler device will have to take both parameters into consideration, average and peak power, to ensure the required ratings (Fig. 5.54).



Fig. 5.53: Current fundamental power coupler under test in early 2000. Power levels up to 500 kW and 800 kW peak power have been tested for a short duration.

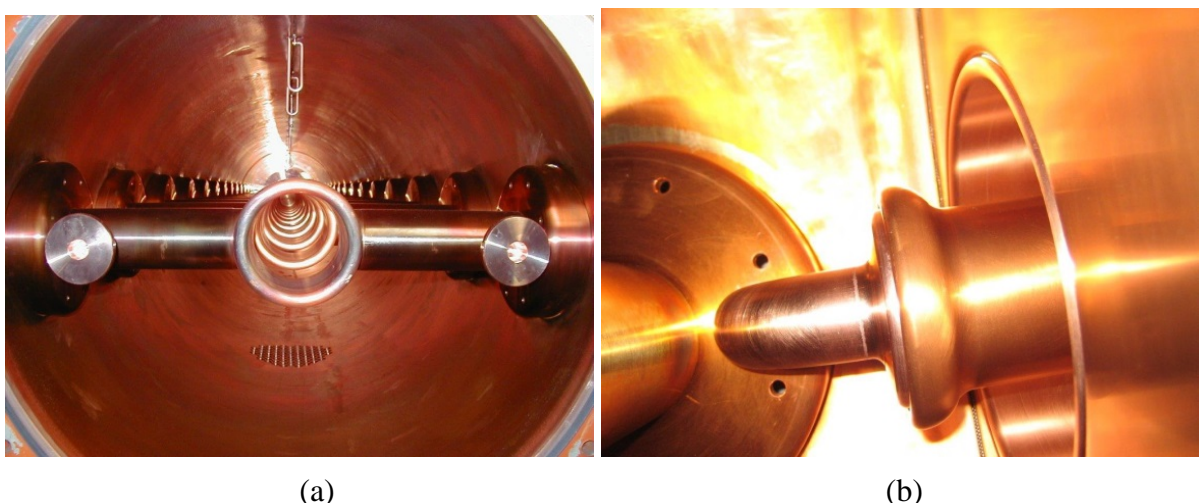


Fig. 5.54: Coupling element on the first drift tube connecting the coupler to the cavity (a). The size of this coupling element (b) has been designed for 375 kW CW and peak power. It was not modified for the upgrade in 2000, and has operated at up to 500 kW peak power. It will have to be improved for 800 kW peak power.

5.4.2.11 Schedule

The project has been split in three main activities:

- new RF power amplifiers and Low Level RF;
- LSS3 tunnel integration;
- new RF building.

All RF devices should be ready by the beginning of 2017 in order to start long duration tests and qualification. LSS3 tunnel integration will take place during the first part of Long Shutdown 2 (LS2), when all present cavities will be disassembled to a section level (Fig. 5.55). All pick-ups will be moved to their new locations, and cavities will be reassembled following the new proposed scheme. The total duration of that phase will be a minimum of 9 months. We will then have a second period of 9 months shared between high-power tests and RF conditioning of the cavities, and low level RF commissioning (Fig. 5.56). All new systems will be operational by beginning 2019, at the end of Long Shutdown 2

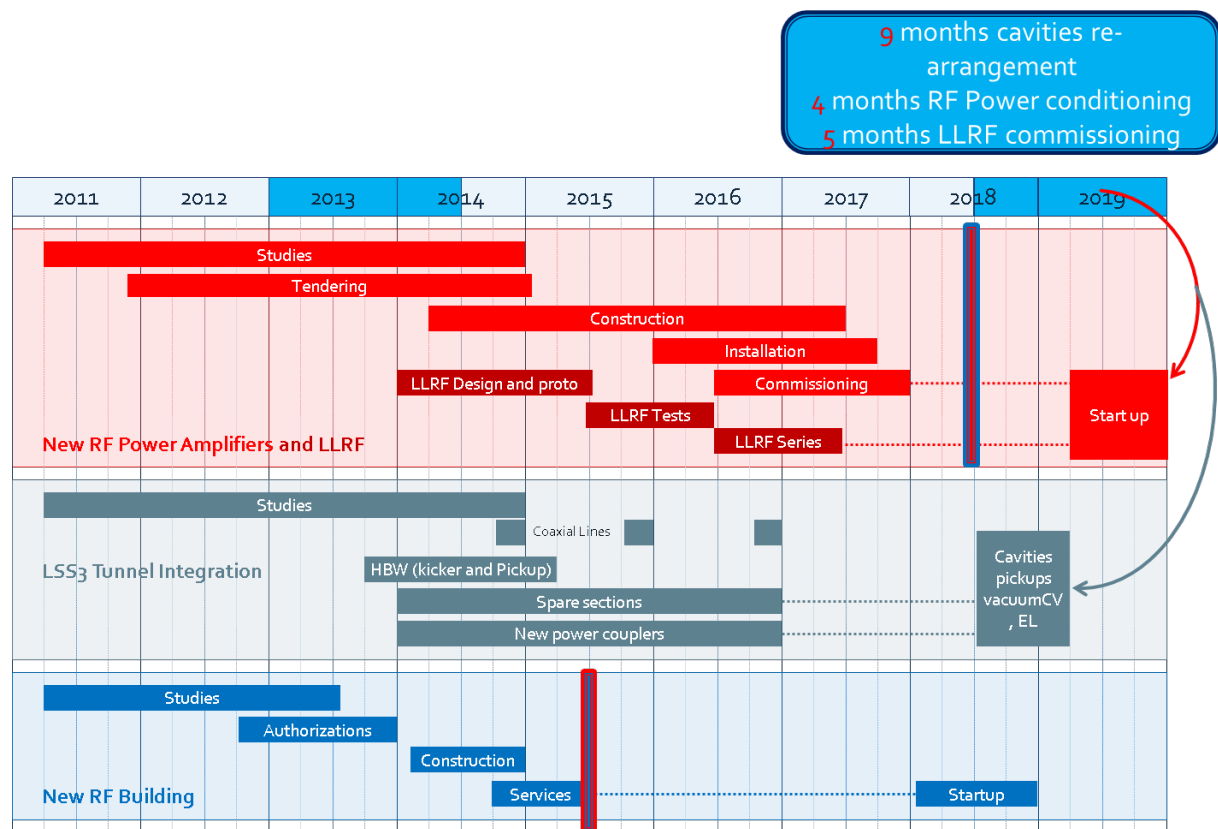


Fig. 5.55: Global schedule of the project. The new RF building will be ready by mid-2015. The drivers contract was placed in March 2014. The finals contract has been launched.

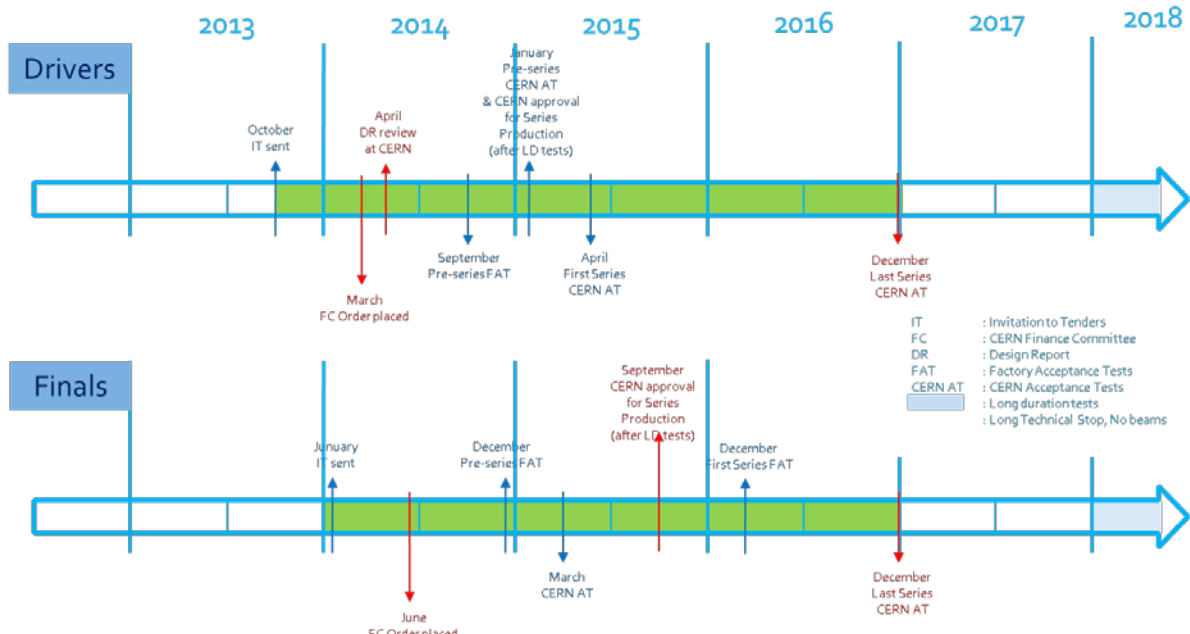


Fig. 5.56: Drivers and finals detailed schedule. The goal is to have all amplifiers delivered by the beginning of 2017 to launch long duration tests far in advance of the operation run to debug the systems.

5.5 LLRF upgrade and control

5.5.1 The 800 MHz system

5.5.1.1 Background and motivation

The 800 MHz system is essential in the SPS: above 2×10^{10} protons per bunch the LHC-type proton beams are unstable without it. In 1998, to deal with the beam loading of the high-intensity proton beams for LHC in the 800 MHz travelling wave cavities and in the absence of an RF feedback, the cavity voltage was sampled at the revolution frequency during the passage of the beam. This method had to be abandoned because the 800 MHz beam current is too dependent on bunch distribution and hence the beam loading varies strongly along the bunch train. In 2001 it was realized that improved voltage control was required for the 800 MHz travelling wave cavities to obtain optimal stabilization of the beam in bunch shortening mode. Another justification for improved regulation are the requirements of the controlled longitudinal emittance blow-up of the proton beam delivered to the LHC. This is realized by injecting phase noise into the 200 MHz cavities. The spectrum of the noise must track the synchrotron frequency that depends on the 200 MHz and 800 MHz voltage seen by the beam. For good performances, similar synchrotron frequency distributions are thus required for all of the bunches. Due to the present 800 MHz beam loading this is not the case and therefore the controlled longitudinal emittance blow-up is not optimal, resulting in bunch parameters varying along the batch (mainly variation of bunch length), and capture losses at LHC transfer caused by the longer bunches.

5.5.1.2 Proposed upgrade

Perturbations to the cavity voltage come from various sources: TX noise and drifts, beam-induced voltage. With the 800 MHz travelling wave cavities, beam loading is the main cause. The classic method for reduction of transient beam loading is the use of strong RF feedback. The accelerating field is measured, compared to the set value, and a correction is sent to the amplifier. In the case of a long loop delay (long distance between the generator and cavity), an alternative was designed in 1985,

the one-turn delay feedback (OTFB) that reduces the impedance only in narrow frequency bands around the revolution frequency sidebands of the RF frequency [37]. This will indeed reduce the transient beam loading (as the beam current is periodic at the revolution frequency), and will improve the coupled-bunch instability threshold (for the cavity impedance at the fundamental), as long as the frequency bands include the synchrotron sidebands. This method was successfully applied to the SPS 200 MHz cavities [38, 39], to the SPS 352.2 MHz superconducting cavities during the LEP era and to numerous other machines. Feedforward is also of common use for the reduction of beam loading; the RF component of the beam current is measured with a pick-up. After proper filtering and amplification, it creates a generator drive that reduces the beam-induced voltage. Feedforward is sensitive to drift of the amplifier response. OTFB and feedforward are included in the new cavity controller. These systems will cover the frequency range of both LHC and fixed target beams. Also planned is the possibility to modulate the cavity phase and amplitude over one turn. For the short ions bunches, a longitudinal damper (dipole and quadrupole) can be implemented, with a bandwidth limited by the bandwidth of the closed-loop response of the LLRF-TX-Cavity system (a few MHz). Controlled longitudinal emittance blow-up could be achieved by injecting phase noise into the 800 MHz cavities. ON-OFF amplitude modulation can also be used to save RF power, with a beam occupying only a fraction of the SPS ring. The new system includes a local loop around the Transmission Line (TX) to make the outer feedback insensitive to the TX gain and phase changes, and to locally reduce the noise produced by the high Level (TX). This regulation is called klystron polar loop in the LHC and Linac4 designs [40]. Finally, it contains built-in observation memories for diagnostics and post mortem. All settings will be programmable per cycle, with functions when they need to be changed during the acceleration ramp.

Figure 5.57 shows the diagram for the cavity controller. The core of the system is the cavity loops module. It receives, as input, the vector sum of the 200 MHz accelerating voltage in order to achieve precise alignment between fundamental and fourth harmonic RF. The 800 MHz component of the beam current is received from a pick-up, and used as input to the feedforward system. It is important to estimate the accelerating RF voltage seen by the beam, in each passage through the 800 MHz cavity (37 cell-long travelling wave structure). Antennas have been installed on (almost) all cells, and an RF network has been designed to generate the vector sum of these signals, with insertion of time-of-flight delay for each antenna, and individual fine adjustment of attenuation and phase. This vector sum RF signal is the input to the OTFB. The hardware (custom-designed VME card) is very similar to the Linac4 system, while the firmware (FPGA) is different. Broadband beam loading compensation in a travelling cavity calls for sophisticated algorithms [38]. The full cavity controller will occupy one VME crate (per cavity). For details on the hardware see Ref. [43]. A prototype system will be tested at SPS restart at the end of 2014. It will then be made operational during the 2015 run.

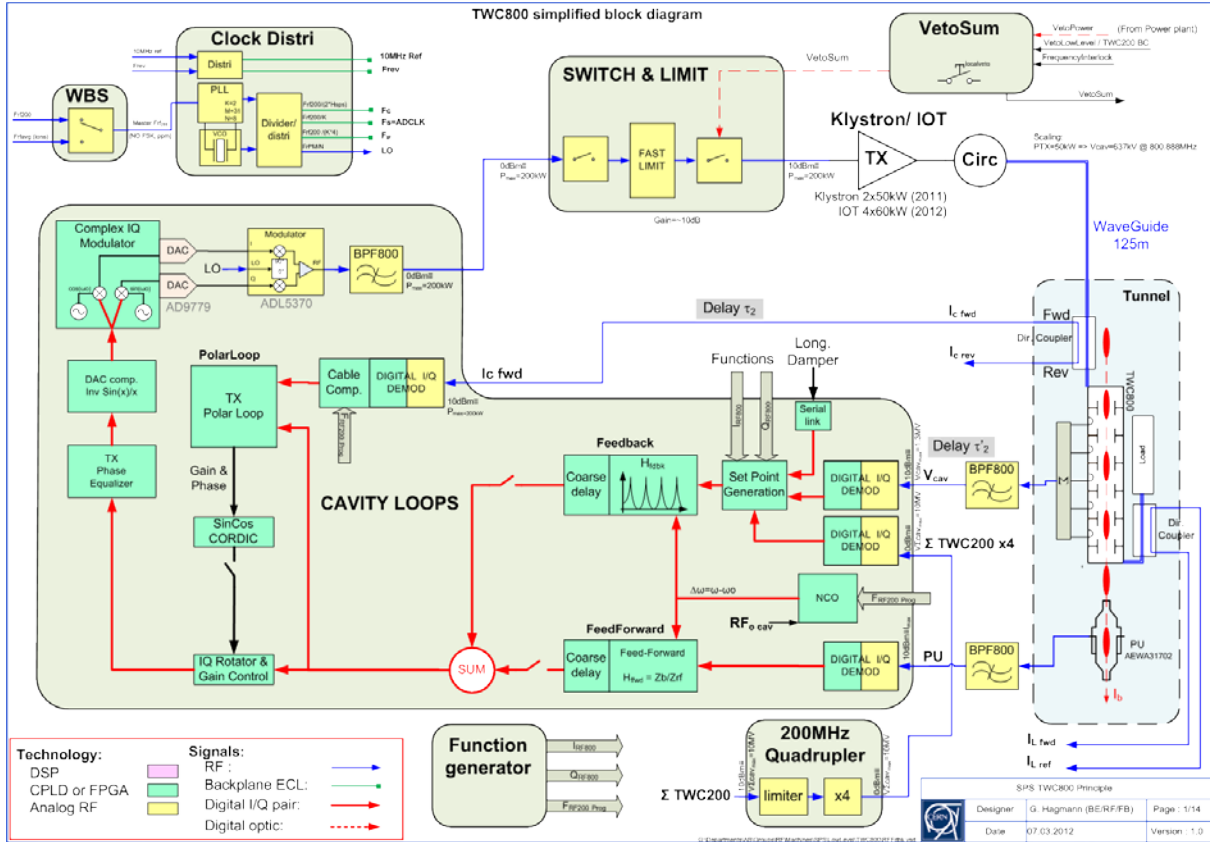


Fig. 5.57: The 800 MHz cavity controller

5.5.2 The 200 MHz system

5.5.2.1 Background and motivation

The original cavity controller designed in 1976 [41] included amplitude and phase loops regulating the field measured with an antenna in the centre cell of the 200 MHz travelling wave structure (43 or 54 cells long). The regulation time constant is a few milliseconds. In the early 1980s, with the increase of beam intensity, transient beam loading compensation was required. Using antennas in all cells, a vector sum RF signal was generated (with adjustment of time-of-flight, gain and phase), and the first OTFB system was installed in 1985, with one processing chain per pair of cavities. In the late 1990s the system was upgraded for the LHC beam: one processing chain per cavity, higher bandwidth OTFB, addition of a feedforward system [37, 38] and implementation of a longitudinal damper (dipole mode) acting on two cavities used as narrow-band kickers. All of these upgrades were added while keeping the original amplitude and phase regulation loops operational. That implies separate RF demodulation for each system, and summing of their outputs at the 200 MHz RF frequency. This is far from optimal as it requires fine phase alignment of the various systems. Setting-up is time-consuming and must be re-done after an intervention on the power system (replacement of a tube, for example). It is also very sensitive to drifts. In addition the design has been concentrating on LHC beams using the Q26 optic, with a synchrotron frequency remaining below 400 Hz. The performance in term of impedance reduction (coupled bunch instabilities) is therefore reduced with the Q20 optics (synchrotron frequency as high as 1 kHz). The longitudinal damper gain is also much reduced. Finally, all settings are adjusted manually. There is no possibility for cycle-dependent settings in one supercycle and no function. ON-OFF amplitude modulation over the turn is not possible. The present system occupies four crates per cavity.

5.5.2.2 Proposed upgrade

When the design of the LHC 400 MHz cavity controller was started, the limitations of the SPS 200 MHz system were well known and better solutions were found for the LHC. The SPS will now benefit from the LHC experience. The key is a unique demodulation and modulation for all regulation loops. With this principle, it is very easy, for example, to keep the longitudinal damper kick in quadrature with the cavity voltage (dipole mode). The new 200 MHz cavity controller will have all of the features listed above for the 800 MHz system (except for the alignment with the 200 MHz system as it is considered to master). OTFB and feedforward will cover the frequency range of both LHC and fixed target beams. All systems will be designed to cope with larger values of synchrotron frequency. Figure 5.58 shows a possible frequency response for the OTFB. The gain remains large over a ± 3 kHz band, well in excess of the requirements for Q20 protons. This type of filter will be implemented in the 800 MHz system first.

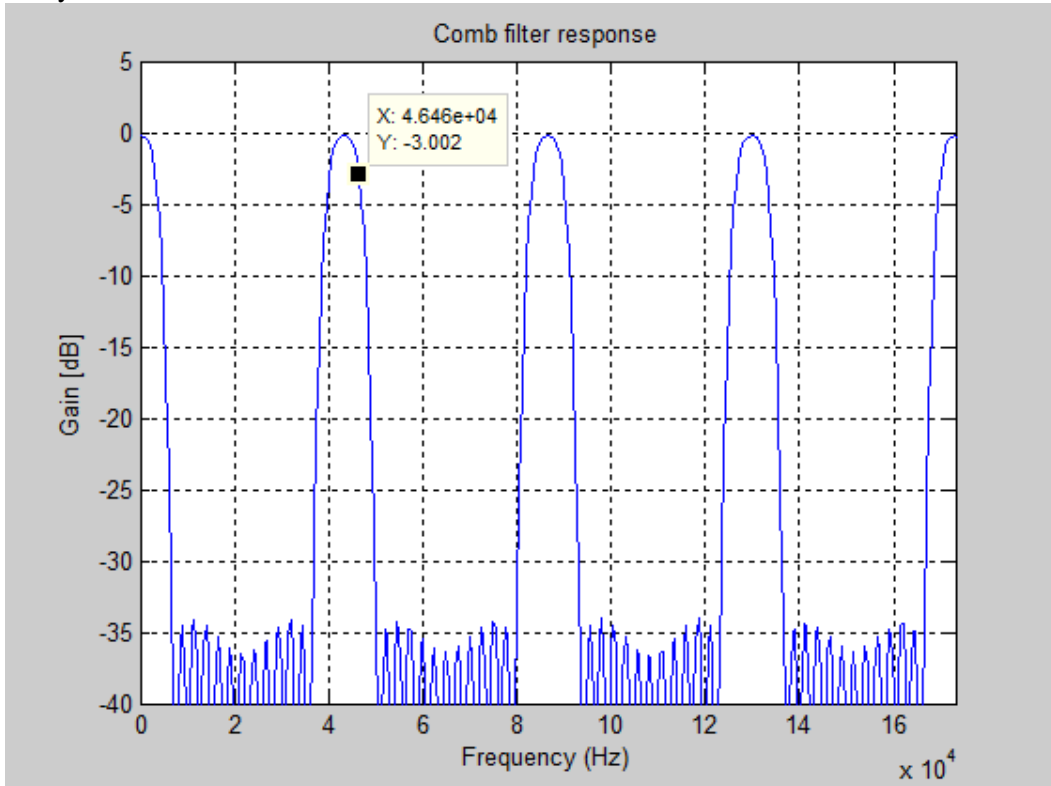


Fig. 5.58: OTFB response with ± 3 kHz band around each revolution frequency sideband

The voltage set-point need not be constant. Modulation along the turn will be possible: ON-OFF amplitude modulation to save RF power with a beam filling only a portion of the ring, pulsing the RF in a portion of the ring for adiabatic capture of individual batches, fast voltage steps for bunch rotation, individual FM modulation of the RF cavities at slightly different frequencies to implement slip stacking, etc.

With travelling wave cavities, the beam current can induce voltage at frequencies where the TX cannot give compensation [42, 43]. These discrete frequencies are a function of the number of cells. Having cavities of different lengths, we could design a global feedback that acts on the drive of the 54-cell cavities to compensate the beam loading in the 43-cell cavities and vice versa. This was proposed 14 years ago but not implemented [37]. It could be implemented if these discrete frequencies are identified as a problem.

The 200 MHz cavity controller upgrade will be launched after the 800 MHz is fully operational. It will use similar hardware. We plan on one VME crate per cavity.

5.5.3 Beam control

5.5.3.1 Background

The SPS LLRF consists of cavity controllers responsible for the regulation of the cavity field (presented above), and a beam control system, using beam-based measurements (radial position, beam phase), generating a master RF signal used as reference by the fundamental and harmonics systems. As the beam parameters (bunch intensity, number of bunches) can be very different for the various cycles, the beam control contains hardware that is dedicated to one type of beam (ions for example). Analog switches driven by the machine timing commute between these signals during the SPS supercycle. The trend is to replace this switching of analog signals with cycle-dependent programming (driven by the timing) of a unique hardware wherever possible. A complete renovation of the SPS beam control is not planned before LHC LS2. Below is given a list of planned limited-size upgrades and a wish-list for mid-term improvements.

5.5.3.2 Proposed upgrade

Protons and ions

The frequency programme, generating a 200 MHz RF from measurement of the bending magnetic field in a reference magnet, is made cycle-dependent. The new module will be used at SPS restart in 2014.

To keep good lifetime during slip stacking, two beam-based phase loops are needed. New hardware is required.

The frequency response of the radial, synchro and phase loop should be made programmable through each cycle's ramp, according to the varying synchrotron frequency.

For cycles ending in slow extraction, the beam should be locked on a reference frequency on flat top, to keep its parameters constant during the extraction process.

Ions

The LHC ion beam suffers much from the SPS RF noise during the 39.6 s-long SPS filling plateau, resulting in a triangular shape in bunch parameters when injected into the LHC [39]. The first bunches injected into the SPS end up in the LHC with a lower intensity than those injected just before the start of the SPS ramp. A major source of RF noise was found to be the generation of the 500 MHz clock used by the SPS master direct digital synthesizer (DDS). A low-noise module is ready for SPS restart in 2014.

Another improvement would be to avoid AM/FM modulation during the SPS filling plateau by filling with a fixed harmonic RF. Transition from this fixed harmonic system to fixed frequency acceleration before the start of the ramp, must be studied.

5.6 Transverse feedback systems

5.6.1 Upgrade of bunch-by-bunch SPS transverse feedback

5.6.1.1 Motivation and issues of the current system

The SPS transverse damper [44] is installed in point 2 of the SPS. It is used to damp injection oscillations in the horizontal and vertical planes and as a feedback system to provide stability for coupled bunch oscillations predominantly driven by the resistive wall impedance. Without feedback the beam is unstable above a total intensity of 5×10^{12} protons, developing rigid dipole coupled bunch

oscillations, both for LHC-type beams with bunch spacing equal to a multiple of 25 ns and for fixed target beams with 5 ns bunch spacing.

The last upgrade of the SPS damper system dates back to the late 1990s and was aimed at increasing the bandwidth from 6 MHz to 20 MHz, the maximum frequency required to damp all possible rigid dipole coupled bunch modes with the LHC-type beams at 25 ns bunch spacing. On this occasion the power system with tetrode amplifiers in the tunnel as well as the low-level systems were upgraded [40].

Requirements for the future use of this system have evolved since the 1990s, which make it necessary, together with obsolescence issues in the area of controls, to upgrade the system in the framework of the LIU project. The principal issues with the current system are:

- obsolescence of control of the equipment (G64 hardware and software) and the MIL-1553 field bus;
- incompatibility of the present pick-up signal processing with the requirements of the scrubbing beam with 5 ns bunchlets;
- sharing of pick-ups between the beam orbit measurement system (MOPOS) and the transverse feedback with a future incompatibility between the planned MOPOS upgrade and the use of the same pick-ups for the transverse feedback system;
- despite achieving 20 MHz bandwidth the current digital hardware does not permit bunch synchronous sampling of the LHC-type beams with 25 ns bunch spacing; consequently efficient feedback on a single bunch such as that required for combined tests with crab cavities and transverse feedback is not possible; single bunch damping is also needed for the proton beam used for pPb collisions in LHC for efficient injection oscillation damping at the shorter than nominal batch spacing of 200 ns, which was originally not foreseen;
- remote diagnostics and setting-up such as with the new digital system for the LHC transverse feedback system (ADT) is not possible, decreasing operational efficiency;
- the range of intensities per bunch is higher for the LHC-type beams than originally planned, spanning from a few 10^9 per bunch to over 3×10^{11} ; hardware for automatic gain switching between cycles is required to be able to adapt pick-up signal levels;
- the original scheme required a phase advance of 90° between the sets of two pick-ups used, which is not the case for the new Q20 optics; the optimal adjustment of the feedback phase for the Q20 optics requires processing of the signals and phase adjustment individually per pick-up as is done in the LHC ADT system;
- upgrading the signal processing to LHC standards would permit the testing of new features in the area of abort gap cleaning and transverse blow-up efficiently in the SPS before deployment in the LHC;
- the current system cannot be used for ions due to the FSK modulation (frequency modulation) scheme used for the 200 MHz RF system; the upgraded damper systems will permit feedback on the bunched ion beam used for the LHC permitting shorter than nominal batch spacing for ions, thus increasing the luminosity potential in LHC for ion physics.

5.6.1.2 Upgrade of system with new dedicated pick-ups

The upgraded system will use a new set of pick-ups dedicated and exclusively used for the transverse damper. These new pick-ups are standard SPS BPH and BPV pick-ups as well as a set of two coupler pick-ups of type BPCR. All pick-ups are provided by the BE-BI group. They will be installed with the associated new cabling during LS1 in regions around point 2 of the SPS as close as possible to the existing dampers to ease signal and clock delay equalization. Low-loss 7/8" smooth cables are used to

provide a high signal quality with cable installation and quality control representing a significant fraction of the effort for the upgrade. The locations of the pick-ups are outlined in the corresponding ECRs [44, 45]. There are six new pick-ups in total:

- two BPH pick-ups: BPH 202.03 and BPH 204.06, horizontal electrostatic pick-ups;
- two BPV pick-ups: BPV 205.05 and BPV 207.05, vertical electrostatic pick-ups;
- two BPCR pick-ups: BPCR 214.59 and BPCR 221.72, equipped with electrodes for both planes, dedicated to LHC-type beams.

The electrostatic pick-ups will be used as currently with high-input impedance pre-amplifiers installed in pits in the tunnel close to the respective pick-ups. The existing head amplifiers provide a bandwidth of 100 MHz for sum and difference signals and will be used for the standard fixed target beam with 5 ns bunch spacing. This type of beam is not entirely bunched at injection and thus calls for beam oscillations detected in the baseband. The pick-up head amplifier system is perturbed by the electron cloud effect [46] and therefore cannot be used for the LHC-type beams. Should the electron cloud effect become an issue with the fixed target beams one would have to consider producing a coated version of an electrostatic pick-up or apply a sufficiently high solenoid field in the pick-up to suppress locally the electron cloud effect in the pick-up [46]. The fixed target head amplifiers may require consolidation outside the LIU project at a later stage.

For all LHC-type beams, including variants for scrubbing and ion beams, with bunch spacings of multiples of 25 ns as well as single bunch beams, the beams are entirely bunched at injection permitting the use of a system similar to that in the LHC, which uses 50Ω coupler type pick-ups with electronics installed on the surface down-converting the pick-up signals and sampling synchronously each bunch [47]. The LO frequency for down-conversion will be 200 MHz as compared to 400 MHz in the LHC. The couplers of type BPCR are optimized for this frequency with the maximum of their transfer function at 200 MHz. The scrubbing beam with splitting of bunches at injection requires a separate set of electronics with direct digitization or analogue demodulation at 40 MHz. Likewise, a separate set of electronics will be used for the ion beam with its special requirement for clocking.

Figure 5.59 shows the geographical location of pick-ups and kickers around point 2 of the SPS with respect to the SPS RF in BA3. Pick-up cabling from the tunnel to the surface is at least 250 m and significantly longer for the more distant pick-ups BPH.202 and BPH.204. The geometrical layout together with the changing frequency during acceleration, the fixed delays in fibres and cables as well as the frequency shift keying used for the ion beam imposes compensation of delays and phases at various points in the damper installation.

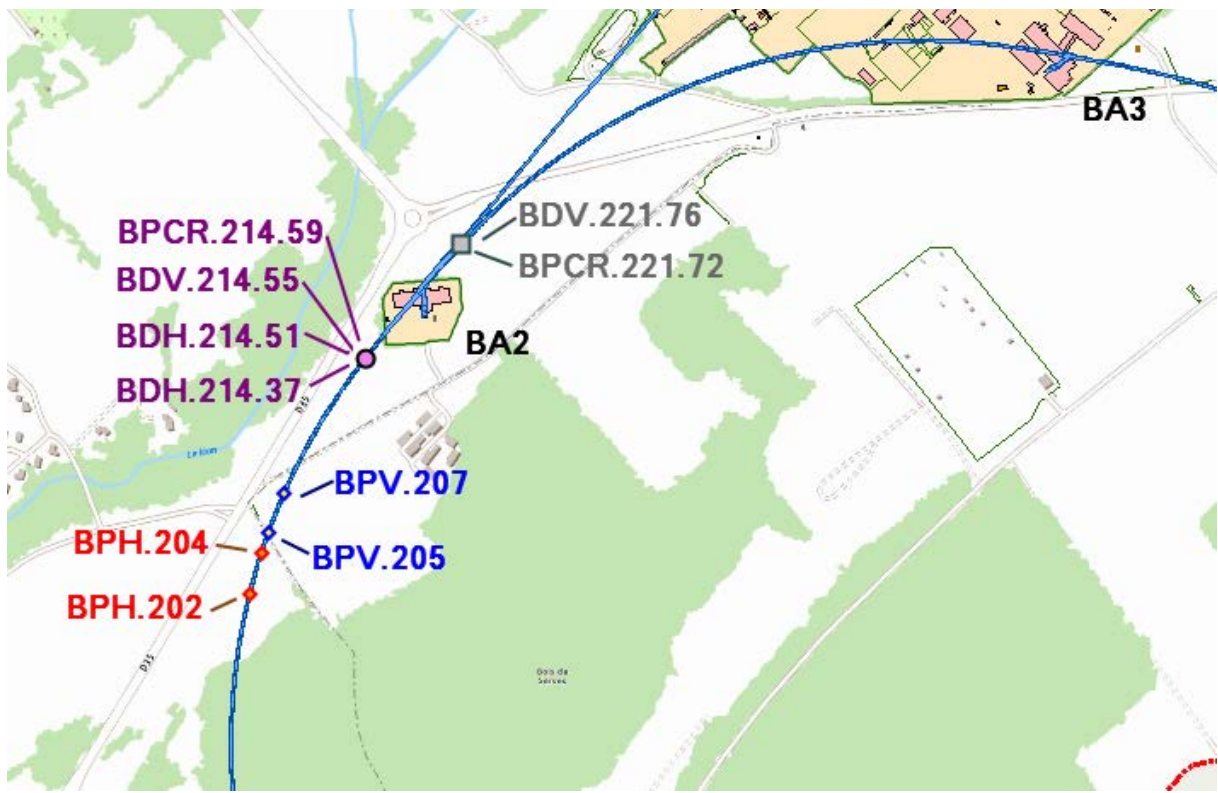


Fig. 5.59: Geographical location of damper kickers and pick-ups in BA2 with respect to the SPS RF system in BA3. The beam travels clockwise from BA2 to BA3 (~1.152 km).

5.6.1.3 Fibre optic links and local clock generation in BA2

For the LIU upgrade new fibre links are being installed between the BA3 Faraday cage and BA2, replacing the existing links. With the introduction of the new pick-ups and the requirement within the LIU project to provide damping for the bunched ion beam, the signal transmission and clock generation scheme for BA2 is being upgraded.

Figure 5.60 summarizes the planned fibre links between BA3 and BA2 and the local clock generation scheme in BA2.

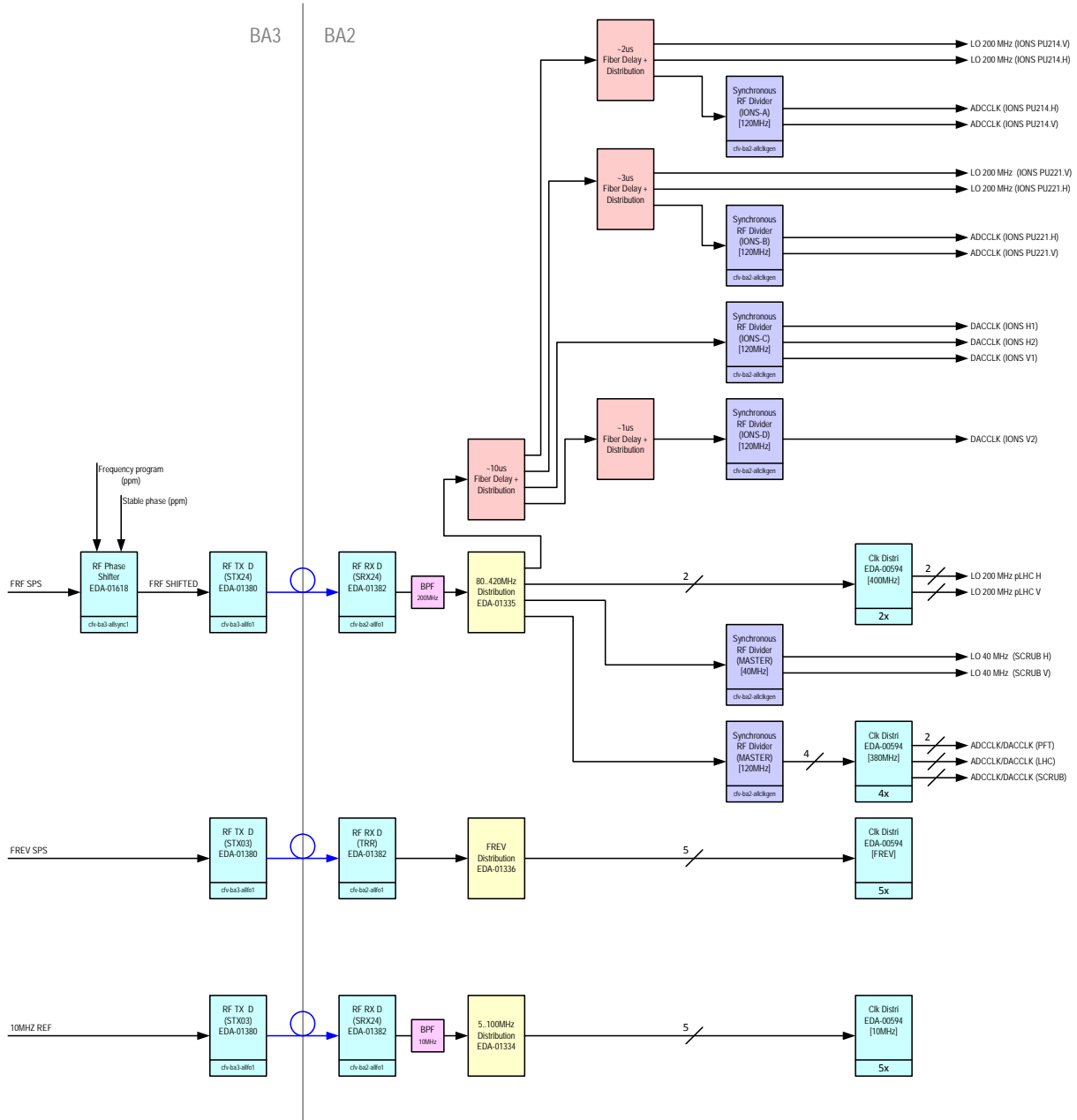


Fig. 5.60: Summary of the planned fibre links between BA3 and BA2 and the local clock generation scheme in BA2.

Three new fibre links (see Fig. 5.60) will be established for the start-up in 2014 (additional fibres reserved as spares):

- 200 MHz RF from the SPS beam control systems;
- revolution frequency from the SPS beam control systems;
- 10 MHz reference (originates from the LHC RF 10 MHz GPS disciplined oscillator in SR4) as a reference for instrumentation and measurements.

Local 40 MHz, 120 MHz and revolution frequency signals will be generated in BA2 by synchronously dividing the 200 MHz RF. The dividers will be reset prior to beam injection using the revolution frequency to synchronize.

Figure 5.61 shows the evolution of the scrubbing beam injected into the SPS, immediately after injection (Fig. 5.61(a)). This beam is produced by injecting with a 180° phase error leading to bunchlets spaced at 5 ns developing during the first tens of turns after injection. Also shown in Fig. 5.61(b) are the corresponding amplitudes of the components at multiples of 40 MHz from a turn-by-turn spectrum of this beam. As damping times of 20 turns are to be achieved it can be seen that only 40 MHz and 80 MHz are suitable RF beam components for a down-conversion scheme. However, the 40 MHz beam signal could be spoiled by the electron cloud effect due to the repetitive nature of the electrons hitting the pick-up. Tests are required with actual beam, and flexibility will be built into the system to change the down-conversion frequency from 40 MHz to 80 MHz, with 80 MHz expected to be less polluted by the electron cloud effect.

The 120 MHz clock, proposed for the sampling of the pick-up signals and the digital processing, is most easily taken as the third harmonic of the 40 MHz, clock similar to the present damper system. For the proton beams the sampling frequency generation (120 MHz) is straightforward, with a fine adjustment of the clocks possible on the digital board. The proton LHC beams require a 200 MHz RF for the down-conversion of the standard beams, and a 40 MHz RF is foreseen as baseline for the down-conversion of the scrubbing beam.

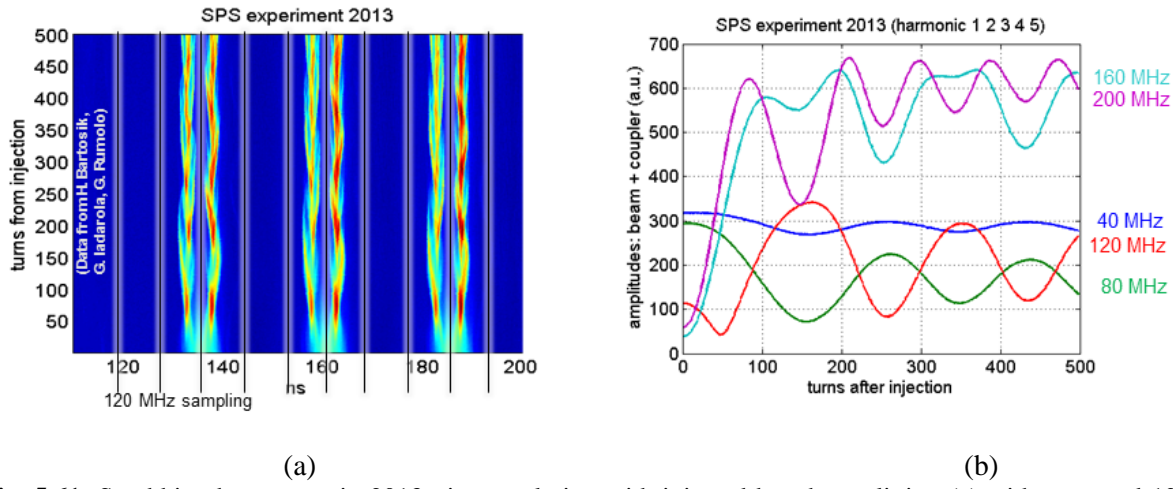


Fig. 5.61: Scrubbing beam tests in 2013: time evolution with injected bunches splitting (a) with proposed 120 MHz sampling clock and (b) components at multiples of bunch frequency of 40 MHz.

The acceleration scheme for ions with an FSK modulation of the RF within the turn requires a separate scheme for clocking and down-conversion. The damper system with pick-ups for LHC-type beams, which will be also used for ions, is distributed over two azimuthal positions (see Fig. 5.59) in half-period 214 and half-period 221. Due to the electronic delay in cables and hardware for each of the two azimuthal locations two separate RF frequencies must be generated: one for detection (down-conversion and ADC clock) and one for driving the kickers (DAC clock). The FSK modulation must be shifted in time to align with the passage of the beam. This is achieved by the four branches of fibre delays in Fig. 5.60 shown in red. The largest delay is required to compensate for the azimuthal position with respect to BA3.

To illustrate the complexity of the ion scheme note that this requires four different 120 MHz clocks and two different 200 MHz RF signals, whereas for the standard proton LHC beam a single 120 MHz clock and a single 200 MHz RF is sufficient.

5.6.1.4 Signal processing after the LS1 upgrade

Signal processing is carried out within a single VME module that comprises electronic boards for analogue amplification and down-conversion and a single board with ADCs, DACs and an FPGA for

digital signal processing. Separate instances of this board are required for each beam type and for each plane (horizontal and vertical). The beam types that need to be distinguished are:

- standard LHC-type proton beams;
- scrubbing beam (5 ns bunchlets);
- bunched ion beam;
- fixed target beam.

Solutions have not been studied for ion beams that are not bunched at multiples of 25 ns, such as the fixed target ion beam after de-bunching and re-capture, and the upgraded ion beam during the process of slip-stacking. Separate electronics would be required for these cases.

LHC standard proton and ion beams and the scrubbing beam use down-conversion schemes with LOs at 200 MHz (standard beams) and 40 MHz (scrubbing beam). Figure 5.62 shows an overview of standard LHC beam signal processing. For each plane eight signals will be digitized: The in-phase (I) and quadrature (Q) component of the down-converted sum and difference signals of the set of two BPCR pick-ups. Two independent output channels with DACs provide the analog signals for the set of two dampers in the respective plane. Similar to the existing damper system, a summing point is provided per damper (signal combiner chassis) that adds signals from the four independent processing channels for the different beam types and provides analog inputs for beam excitation purposes (not shown in Fig. 5.62).

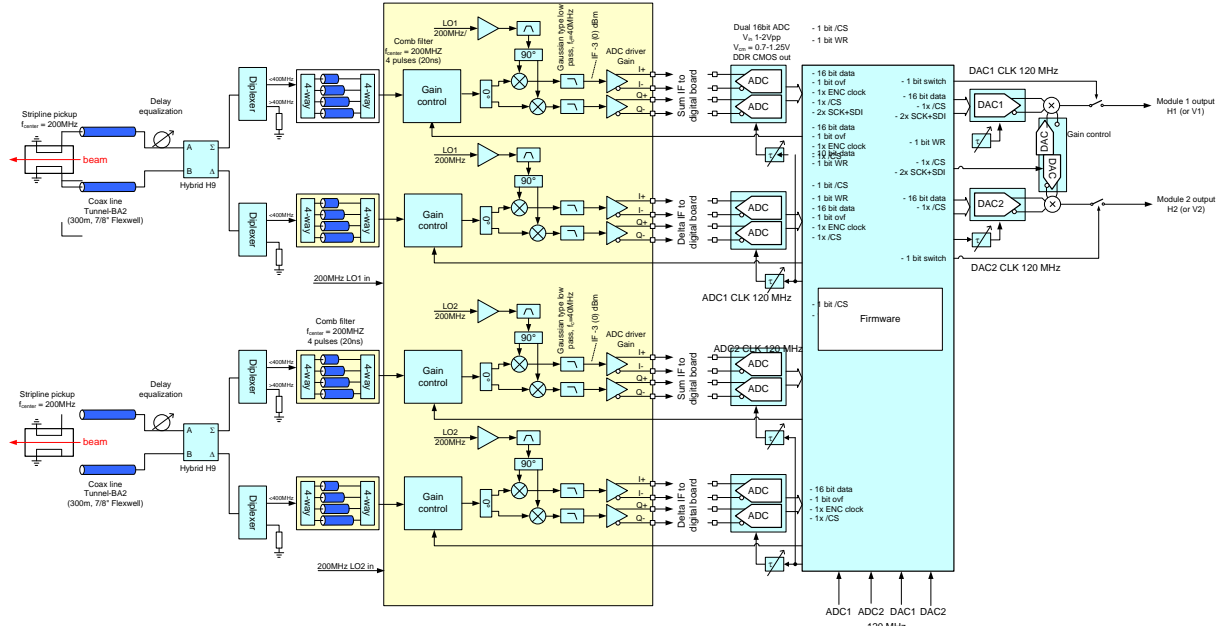


Fig. 5.62: Overview of the damper signal processing for LHC-type beams. A total of eight instances of this VME module are needed (one per beam type and plane).

For the fixed target beam the down-conversion is not needed and only half of the signals need to be digitized. Note that the scheme in Fig. 5.62 foresees the supply of four 120 MHz clocks and two LOs, which will be all different in the case of ions, as explained above. The firmware will combine the complexity of the LHC transverse damper BeamPos module [47] and the LHC DSPU module [48] in one single FPGA.

The signal combing chassis, not depicted in Fig. 5.62, will also provide an input per damper for injecting a signal generated by BE-BI for the measurement of the transverse tune. Additional

inputs are provided for hardware checks and to connect an external network analyser for transfer function measurements, the latter in particular being used for setting-up purposes.

5.6.1.5 Expected performance

For the power system with tetrode amplifiers in the tunnel and kickers that only use the electric field, a modest consolidation effort is under way in the framework of the LIU project to streamline maintenance and ensure reliable operation over the next decade. The performance will be maintained with the maximum kick strength for the Q20 optics essentially unchanged at the 5% level with respect to the Q26 optics. The kick strength scales with $\beta^{1/2}$. Q20 and Q26 optics are compared in Table 5.2.

Table 5.2: Optics parameters and machine position of damper systems for LHC beams

Damper	β (m) Q26	β (m) Q20
H1: BDH 214.37	77	79
H2: BDH 214.51	67	71
V1: BDV 214.55	39	43
V2: BDV 221.76	45	49

Figure 5.63 shows field computations [49] of the existing horizontal and vertical kickers [50], which will not be modified. The computations confirm the previously assumed kick strength [51] that permits damping times to be maintained at 0.5 ms (20 turns) as can currently be reached with both optics. The new digital signal processing will permit improvement of the performance for higher frequencies towards 20 MHz by carefully correcting the phase response of the power amplifiers. A truly bunch-by-bunch damper with flat frequency response can be implemented if needed, as tested in the LHC [52].

Table 5.3 summarizes the performance in terms of kick strength at low frequency. A drop in kick strength by 3 dB is expected in between 4.5 MHz to 6 MHz with an estimated 20% kick strength remaining available at 20 MHz.

Table 5.3: Kick strength (total of two systems per plane) of dampers up to 100 kHz assuming for the horizontal plane 2.9 kV (TH 561 tube) and the vertical plane 2.6 kV (RS 2048 CJ tube).

Plane	Length/gap (mm/mm)	Δp eVs/m	kV transverse	μrad at 26 GeV/c
H	$2 \times 2396/142$	3.3×10^{-4}	98	3.8
V	$2 \times 1536/38$	7.2×10^{-4}	215	8.3

5.6.1.6 Summary of new system

In summary the upgraded system will be capable of providing damping times of 0.5 ms for all LHC-type beams, standard proton and ion beams and the scrubbing beam. The modern digital system will permit tailoring of the bandwidth of the system.

All features developed for the LHC such as observation of bunch-by-bunch oscillations, transverse blow-up by injection of noise, beam gap cleaning and excitation for the purpose of tune measurement, can also be made available in the SPS. They require, however, a considerable effort in the development of software interfaces dedicated to SPS operation.

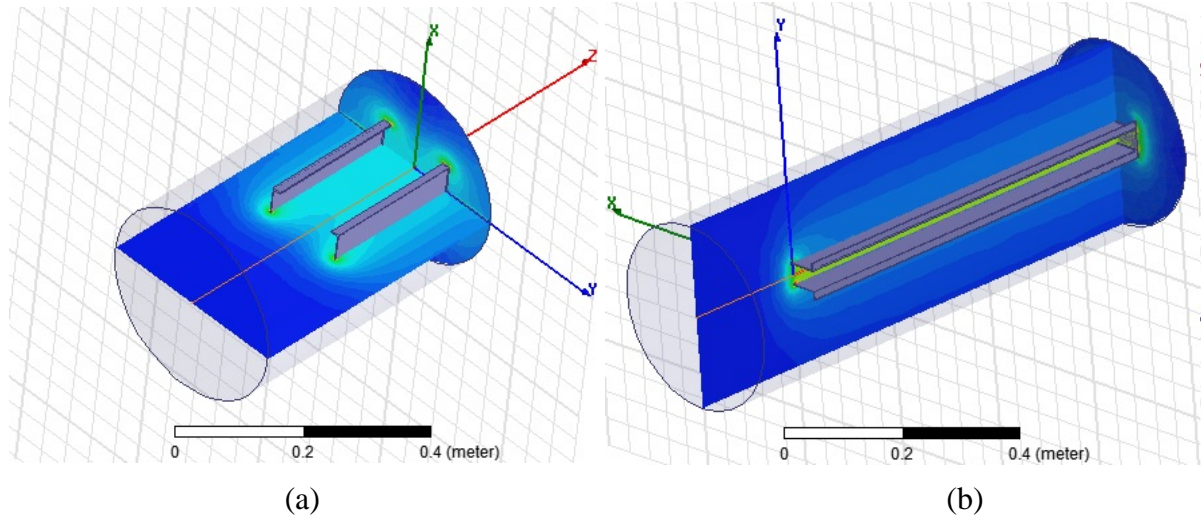


Fig. 5.63: Field distribution computed by HFSS for the horizontal (a) and vertical (b) kickers for verification of the kick strength [54].

5.6.2 New high-bandwidth transverse feedback system

5.6.2.1 Motivation and background

The electron cloud effect causes in the SPS a vertical transverse single bunch instability with intra-bunch motion [53]. To cure this type of instability a dedicated transverse feedback is planned. Motivation, feasibility, scope and planning were reviewed in 2013 [54]. This new feedback system is complementary to the previously described coupled bunch instability feedback system that only acts on the centre of gravity of oscillation due to the limited bandwidth of the kicker system. Figure 5.64 shows the principal elements of the feedback system.

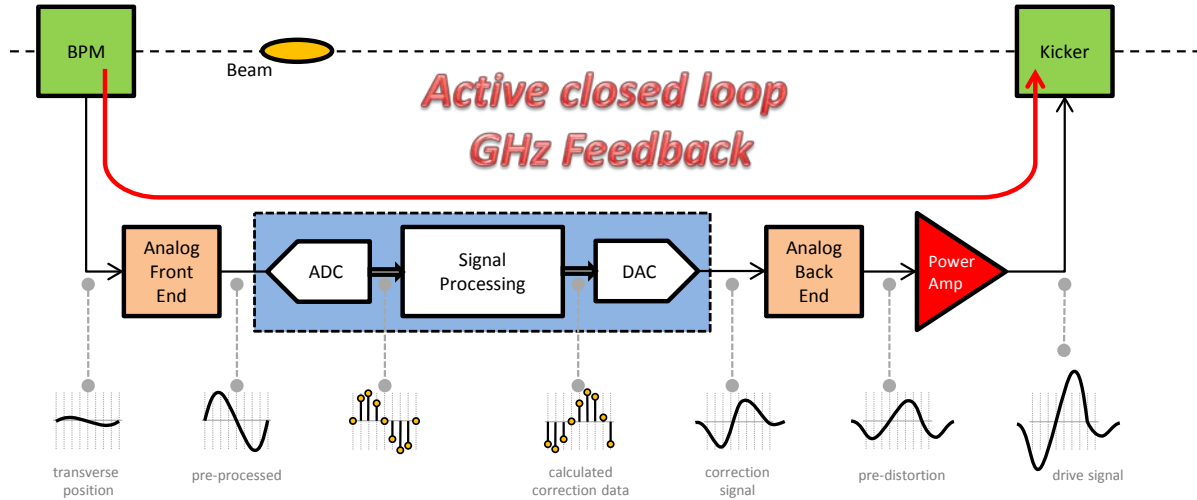


Fig. 5.64: High-bandwidth transverse feedback system with digital sampling of intra-bunch motion

Research and development for this system started in 2008 with head-tail simulations [55, 56] implementing a feedback system for bunch parameters for an increased injection momentum of 55 GeV/c in the SPS with beam provided by a new injector synchrotron for the SPS, the PS2. These initial simulations demonstrated that such a system: i) is feasible in the sense that it can suppress the coherent intra-bunch motion; and ii) needs a bandwidth of around 1 GHz. It was also shown that at

very high gain less bandwidth is needed (a minimum of 300 MHz); however, a rigid dipole feedback similar to the existing feedback with a bandwidth of 20 MHz was shown to be insufficient. The electron cloud effect couples intra-bunch modes such that acting on one frequency (or mode) also has an effect on other frequencies (modes). The need for 1 GHz bandwidth is also supported by observations at injection into the SPS [61] of electron instability, as shown in Fig. 5.65.

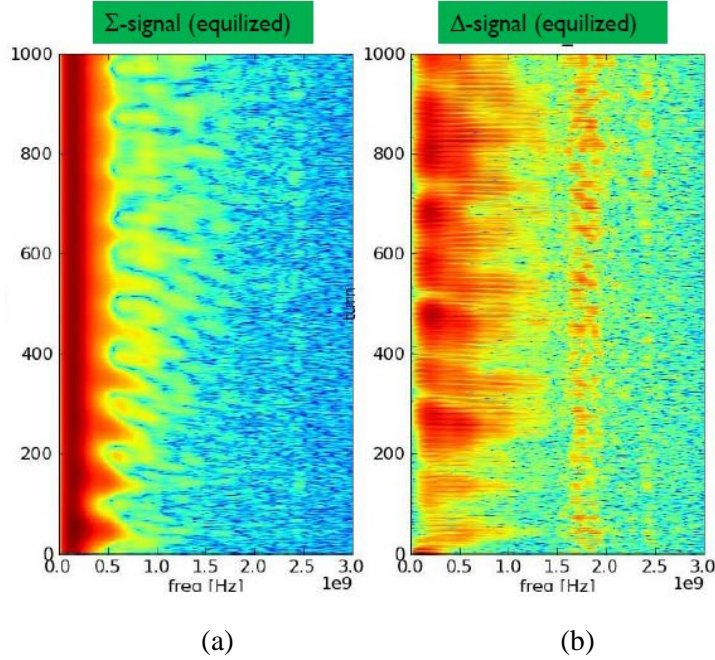


Fig. 5.65: Spectrum of sum (a) and difference (b) signal of a bunch subject to the electron cloud instability [57]. Spectral contents at 1.6 GHz and 2.5 GHz are artefacts due to higher order modes in the pick-up.

Design estimates for the feedback were proposed in 2009 [58]. Subsequent studies [59–62] have focused on implementing in a more detailed way numerical simulations of the feedback system together with the electron cloud effect for an SPS injection energy of 26 GeV/c that, in the LIU upgrade programme, will remain the future injection energy. In all of these studies active feedback has been shown to cure the coherent oscillation for the case of the Q26 optics. The case for the Q20 optics and the challenges of making the signal processing work at high synchrotron tune are discussed in Ref. [63].

Ultimately, the aim is to reduce the observed transverse emittance increase caused by the electron cloud effect. Studies to quantify the improvement have been undertaken, and it could be shown in simulation that emittance increase is reduced [60, 62]. The scenario envisaged is to run with feedback on, permitting the chromaticity that is currently used to cure the instabilities to be reduced, which is expected to have an additional positive effect on incoherent particle loss and emittance increase.

Although the motivation to implement the high bandwidth transverse feedback system in the SPS comes from the need to cure the electron cloud instability and support efficient scrubbing of the SPS, the approach to curing intra-bunch motion by feedback is generic and can also be used for the case of impedance-driven intra-bunch motion, such as that caused by the transverse mode coupling instability (TMCI) [54, 63]. This type of instability is observed in the SPS, and feedback algorithms to cure it have been tested in simulation of the SPS with success. There are further applications of the feedback in other accelerators such as the PS and the LHC, in which different intra-bunch oscillations are observed or suspected to cause beam blow-up and particle losses. In the context of crab cavities, an intra-bunch feedback could help to reduce the effect of residual head-tail oscillations by amplitude noise in the crab cavities and oscillations induced by the combined effect of RF noise and a non-

closure of the crabbing motion. A combined test of the feedback together with crab cavities in the SPS can therefore lead to a case for the deployment of a head-tail motion damper in the LHC.

5.6.2.2 Key specifications for hardware

The two key parameters to specify the hardware for are the *bandwidth* of the system and the *maximum kick strength* required. Bandwidth simulations at 26 GeV/c with 4σ bunch lengths of the order of 3 ns have consistently shown that a bandwidth of much less than 1 GHz is sufficient, i.e. 300 MHz to 500 MHz [55, 56, 59–61]. During the ramp the bunch length shrinks, reaching approximately 1.5 ns at extraction to the LHC, a factor of 2 less than at injection. A similar mode of higher order for the long and short bunch—order meaning the number of nodes of oscillation across the bunch for the time projection of the bunch signal—should result in a maximum required frequency for the feedback that is twice as high for a bunch of half the length. In the absence of simulations it is therefore reasonable to set the maximum frequency to around 1 GHz.

The lower frequency of the feedback will range between 20 MHz and 40 MHz with details to be specified at a later stage of the project. A lower cut-off frequency of close to 20 MHz would permit having an overlap with the existing coupled bunch feedback, permitting damping with the high bandwidth damper coupled bunch modes from 20 MHz to 100 MHz for a 5 ns-spaced beam. For this damping the SPS currently relies on octupoles and chromaticity. A cut-off frequency of lower than 40 MHz is also required to shape the signal in the time domain to independently treat successive bunches at 25 ns.

The required maximum kick strength is determined by the resolution of the system, and the maximum transient error signal, from which one would like to enable the feedback to recover, without saturation. Simulations have been carried out to approach the kick strength requirements from the resolution point of view [61]; however, as the simulations are driven by numerical noise from modelling with macro-particles they are prone to uncertainties. The alternative approach is to fix a maximum oscillation level, for example at injection, from which one would like to recover. These maximum oscillation levels occurring at injection must be determined in MDs after LS1 when the bunch-by-bunch damper will have been upgraded and the situation for the future can be correctly assessed.

The existing pick-up BPW319.01 used as a kicker for the vertical plane in the prototype experiments, with four 100 W amplifiers driving the four electrodes, develops a maximum kick strength of 1.2 kV transverse, at low frequency [64]. This can move the beam by 46 nrad at 26 GeV/c, which would correspond to 3.6 μm at $\beta = 100$ m, taking 60 m as the beta function for the kicker. A target has been set to provide a 10-times larger kick strength, which would permit recovery without saturation from larger oscillation amplitude. At injection of the beam the existing coupled bunch feedback will first reduce the rigid dipolar injection errors from the level of ~ 1 mm to less than 50 μm before the high bandwidth feedback can be switched on. The large kick strength with the existing feedback permits carrying out this task in less than a quarter of a synchrotron period, the timescale at which the intra-bunch motion grows.

5.6.2.3 Feedback algorithms and reduced model

Feedback algorithms using FIR and IIR filters have been developed and checked in simulation. Reduced models are being fitted to intra-bunch motion from both experimental observation and numerical multi-particle simulation [65–68]. The objective of the reduced models is to describe the intra-bunch motion by a set of coupled oscillators. The reduced model can then be used to design feedback algorithms best suited for efficient and fast damping, which as a consequence will also determine the technical design and resources need for signal processing on the FPGA.

5.6.2.4 *Digital hardware and beam tests*

Digital prototype hardware has been developed that features digitization of up to 4 GS/s of the intra-bunch motion and tested with beam [69–73]. In practice, in machine experiments 3.2 GS/s has been used for facilitating the synchronization with the SPS of the parallel processing inside the dedicated FPGA that runs 1/16 of the sampling frequency, which coincides with 3.2 GS/s for the SPS 200 MHz RF frequency. The final digital hardware will be modified to provide a high-enough sampling rate for the short bunches at the SPS flat top of 450 GeV/c. This may call for sampling frequencies higher than the present 4 GS/s maximum when, for shorter bunches, frequencies in excess of 1 GHz are to be damped. Final specifications for the digital system will be drawn up after successful feedback tests with new kickers and the 1 GHz analog bandwidth foreseen after LS1 [54].

5.6.2.5 *Pick-ups and kickers—path from research and development demonstrator system to final system*

The prototype system used before LS1 uses exponential couplers as pick-ups and kickers [58, 74]. In order to achieve a 1 GHz bandwidth it is mandatory to compensate the phase response. Analogue phase compensating circuits have been developed for feedback prototyping [75] and have been used in beam experiments; for the final system, digital techniques as used in the LHC damper are foreseen [53]. Machine layout, as well as different pick-up and kicker designs, were reviewed in 2013 [57]. With respect to the pick-up design it has been emphasized that good closed orbit rejection is mandatory, and passive schemes to achieve this have been proposed [76].

Different concepts for the system and kicker designs [68] have been compared with respect to their transverse shunt impedance, which defines for a given RF power the available kick strength and machine impedance. The results are summarized in the kicker design reports. Three different kicker concepts were compared:

- separate kickers for different frequency bands with low Q cavities for the higher frequencies and a strip-line kicker for low frequencies;
- an array of short strip-lines;
- a slotted waveguide kicker, including a broadband version that features a strip-line within a slotted waveguide [77], already known from stochastic cooling systems as a ‘Faltin’ type kicker [78].

Table 5.4 summarizes the retained options for the next stage of prototyping, with more details available in the kicker design report [77]. Strip-lines have an advantage for the lower frequency end, while the slot-line develops more kick strength towards 1 GHz, where the strip-line shunt impedance rolls-off. Due to the complementary advantages (different frequency ranges) the review in 2013 [57] recommended that prototypes of both types of kicker be developed, with the strip-line kickers being the priority.

Table 5.4: Comparison of transverse voltage kicks for different kicker options assuming different power amplifiers for strip-lines (100 mm length) and slot-line kicker (1 m length); two amplifiers are needed with a rating as in the table to power the two sides of the kicker individually [64].

Kicker type	Number	Power (W)	V_{\perp} (250 MHz) (kV)	V_{\perp} (500 MHz) (kV)	V_{\perp} (1 GHz) (kV)
Strip-lines	4	500	7.3	6.3	3.2
Strip-lines	44	100	35.9	31.2	15.5
Slot-line	1	500	3.3	3.6	4.6
Slot-line	1	2000	6.6	7.2	9.3
Slot-line	6	300	15.3	16.7	21.5

In order not to limit the power handling capabilities the prototype feedthroughs are specified to handle RF power in the kW range. With four Faltin-type kickers and 2 kW power feeding each side of the kicker, one could reach 26.4 kV transverse volts (at 250 MHz), which would permit damping of a $\sim 20 \mu\text{m}$ oscillation, a realistic size for an oscillation that can still be detected, at 450 GeV/c with 10 turns damping time. Such a high kick strength may not be required for steady operation to guarantee stability if there are no transients to damp. Clearly a 10-bit digitization gives a small margin for orbit variations while an 8-bit digitization, as in the current prototype system, would be just sufficient to discriminate at 10 μm oscillations within a range of acceptance of $\pm 1 \text{ mm}$. A good rejection of the closed orbit before digitization, as proposed in Ref. [76], is therefore highly desirable.

In a staged deployment it is planned to initially install two strip-lines and one Faltin-type kicker, to test these structures with beam between LS1 and LS2. The final decision will then be taken on the numbers and types of kickers to be installed during LS2. The experience gained with damping transients at injection will serve to refine the requirements for 450 GeV/c for the final system to be deployed in LS2.

5.6.2.6 Implementation and commissioning planning

The implementation will be staged with three distinct phases. After the successful completion of stage 1 in 2013 (results from the first stage have been documented and reviewed in Ref. [60]), which comprised closed loop experiments on a single bunch using existing kickers and pick-ups with prototype electronics at 3.2 GS/s sampling rate and limited power and bandwidth, the second stage will aim at testing new kickers with beam as well as closed loop experiments on bunch trains, subject to the electron cloud effect.

The second stage is scheduled to take place between LS1 and LS2 with new digital hardware running at 8 GS/s also being considered. The parameters for the final system can only be fixed towards the end of stage two, for deployment of a full system in the vertical plane in the SPS during LS2. Commissioning of the full system would then take place during the first year of running after LS2.

5.7 Electron cloud

5.7.1 Observed and simulated performance, limitations

For many years the electron cloud in the SPS has been an object of intensive simulation study. One of the main goals was to determine the values of SEY thresholds for its formation in the different types of SPS beam chambers, in an attempt to deduce which ones would be expected to be critical for both present and future LHC beams. In the SPS there are six main different types of vacuum chamber: two types are used in the main dipoles (MBA and MBB), two in the quadrupoles (QD and QF) and two in the drift spaces (A or B type). The different sizes mainly reflect the change of the beta functions in the nominal optics. The electron cloud build-up has been studied in both dipole chambers and drift space chambers. The quadrupoles have not yet been simulated, because they only cover less than 10% of the

ring circumference. Nevertheless, they are likely to be affected by significant electron cloud down to very low bunch populations, as we know from the LHC. After LS1, a quadrupole with a strip monitor covering half of its inner pipe wall will again be connected to the electronics for electron cloud detection in order to establish this issue experimentally and to obtain information on the speed of scrubbing. A and B type drift chambers are both circular and have a radius of 88 or 65 mm, respectively. Figure 5.66(a,b) shows the SEY threshold as a function of bunch intensity at both 26 GeV/c and 450 GeV/c in these chambers. The following features can be observed:

- the SEY thresholds are mostly decreasing with bunch current, but tend to change slope for 50 ns beams with bunch populations above 2×10^{11} ppb;
- there exist regions in which 50 ns can create a worse electron cloud than 25 ns;
- the SEY thresholds become very low (close to 1.05) for 25 ns beams in drift B and with bunch currents above 2×10^{11} ppb.

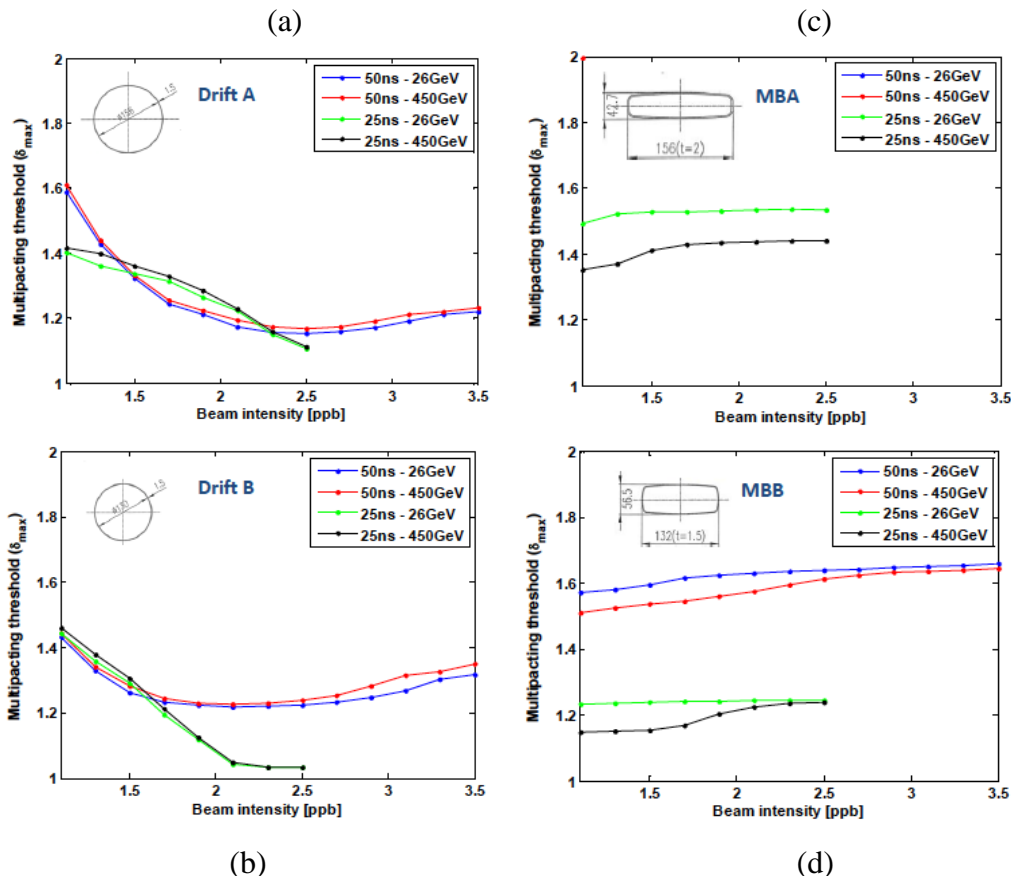


Fig. 5.66: Threshold SEY for electron cloud formation in different types of SPS chambers, as a function of the bunch intensity. (a) Drift A; (b) drift B; (c) dipole MBA; (d) dipole MBB.

The vacuum chambers in dipoles also come in two different sorts with almost rectangular shape: the MBB type, characterized by a height of about 56.5 mm and 132 mm width; and the MBA type, flatter than the MBBS and thus more suited to regions with lower vertical betatron functions, characterized by a height of 43 mm and 156 mm width. In Fig. 5.66(c,d), the SEY threshold is displayed as a function of the bunch population for both 25 and 50ns beams at injection and top energy. Also in this case the dependencies are not trivial and exhibit the following features:

- the SEY thresholds do mostly increase with bunch current. When they do not, the behaviour tends to be flat, indicating then little dependence of the SEY threshold on the bunch intensity in these intensity ranges;

- the SEY thresholds of the 50ns beam lie above 2.0 in the MBA chambers;
- the SEY thresholds can become in general very low (around 1.2) for 25ns beams in MBB chambers.

Considering all the results of the above study, it is evident that the most dangerous chambers in the SPS, in terms of favouring electron cloud build-up for the present and future LHC beam intensities, are the drift B and the MBB types, which exhibit the lowest SEY thresholds at almost all intensity ranges. In particular, it is especially worrisome that both these chambers exhibit SEY thresholds below 1.3, which seems to be the saturation value for scrubbing of Stainless Steel (StSt) in some of the laboratory measurements [79]. In some cases the SEY in laboratory conditioning decreases to 1.1, accompanied by a increase in carbon concentration. The behaviour has still to be clarified. Besides, StSt samples exposed to the SPS beam and then extracted from the machine have generally shown SEY values around 1.5 (see below). Presently, it still remains unclear whether we still have an electron cloud in some of the SPS regions, because the observed pressure rise is several orders of magnitude lower than that observed in previous years and the nominal 25 ns beam is not really any longer affected by significant electron cloud effects [80]. While the future strategy against the electron cloud will only be defined after LS1, it is clear, meanwhile, from simulations and LHC experience that the critical regions that might need coating (if overall machine scrubbing is insufficient or too long) would be drift B, MBB and the quadrupoles (amounting to about 50% of the whole machine). This would allow the conditions for the electron cloud to be completely harmless to the beam to be easily met, which has been roughly identified as electron cloud suppression over at least two-thirds of the whole SPS ring.

Experimentally, the electron cloud (EC) effect has been observed to be a clear performance limitation for the SPS since LHC-type beams were first injected into the machine, since the year 2000. At that time a severe pressure rise was observed all around the machine, together with transverse beam instabilities (which could be suppressed by increasing chromaticity), important losses and emittance blow-up on the trailing bunches of the train. These observations triggered several machine studies in order to understand the performance limitations coming from EC effects; and periodic (yearly) scrubbing runs with 25 ns beams were introduced in order to cope with EC (a detailed description of the 2012 scrubbing run is presented in Ref. [3]). As a consequence the SPS could deliver beams with 50 ns bunch spacing and intensities up to 1.6×10^{11} ppb within transverse emittances smaller than 2 μm without any limitation coming from the EC. The situation is different at 25 ns bunch spacing.

In 2012, using a new operation mode of the SPS wire scanners, the evolution of the transverse emittances could be measured bunch-by-bunch, showing no blow-up when storing the full bunch train with nominal intensity (1.15×10^{11} ppb, 4×72 bunches) for more than 10 s at injection energy. Moreover, the best beam lifetime was obtained with small positive vertical chromaticity settings, while in the past large chromaticity was needed for curing fast EC-driven instabilities. This confirms that scrubbing accumulated over the years was enough to suppress any beam degradation due to EC effects for the nominal bunch intensity on the cycle timescale, and this beam could indeed be regularly delivered to the LHC for the scrubbing run towards the end of 2012. Further experiments performed on the LHC filling cycle with the SPS low γ_t optics (Q20) showed that it was possible to inject the full train of the 25 ns beam with up to about 1.35×10^{11} ppb without transverse emittance blow-up and preserve the beam quality up to extraction energy, as shown in Fig. 5.67 (a). For higher intensities (about 1.45×10^{11} ppb injected) a transverse instability was observed after the injection of the third and fourth batches, leading to emittance blow-up (see Fig. 5.67(b)) and particle losses on the trailing bunches of the injected trains. Larger bunch intensities (1.6×10^{11} ppb) were injected into the SPS during the scrubbing run, revealing average emittance values of 5 μm in the horizontal and 4.5 μm in the vertical plane even with only two injected batches at flat bottom. The observed pattern on the bunch-by-bunch emittance observed for this case was typical of EC effects, but other sources (e.g. impedances) were also considered to be potential limitations at that stage.

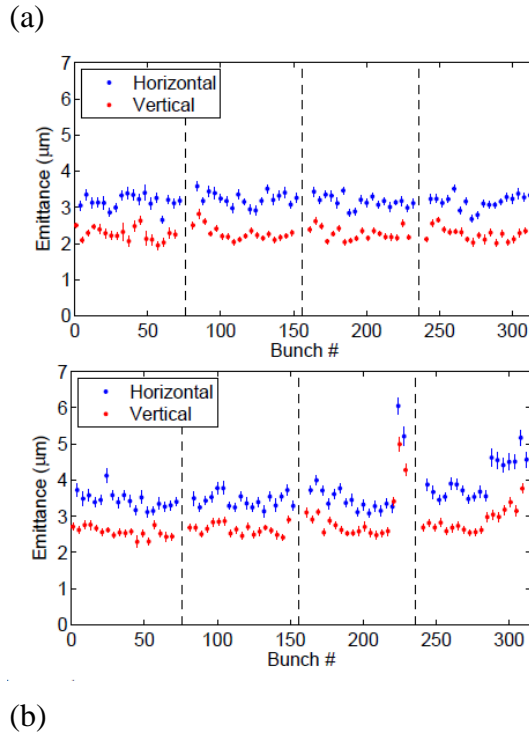


Fig. 5.67: Bunch-by-bunch emittances measured at SPS extraction energy for 4×72 bunches of the 25 ns LHC beam with (a) 1.34×10^{11} ppb injected; (b) 1.44×10^{11} ppb injected.

Apart from the beam performance, some diagnostics tools were set up to measure quantities related to EC in order to characterize the status of the machine [3] and the dependence of the EC on the various beam parameters. The dynamic pressure rise on the pressure gauges of the ring is considered to be related to the electron-stimulated desorption provoked by the EC. In the measurements on gauges in the arcs close to the MBB magnets a pressure rise is observed when injecting the 25 ns beam at nominal intensity, but this rise is orders of magnitude lower than that found in early 2000. This is obviously due to the accumulated scrubbing in most of the arcs. As expected, the pressure rise increases with beam intensity. The pressure rise time-pattern related to the EC could be distinguished from that induced by slow losses by modifying the 200 MHz RF cycle.

A further diagnostics set-up that is used for a direct measurement of the lateral distribution of the EC current are the strip detectors, often called EC monitors (ECM). They measure EC current to the wall in stainless steel vacuum chambers of MBA and MBB cross-section inserted in dipoles with $B = 0.12$ T, which corresponds to the field at injection energy. For the beam intensity in the range of interest the current is localized on two symmetric stripes, which are located about 10 mm on the left and on the right with respect to the beam position. Figure 5.68 shows how the distance between the stripes increases for higher bunch intensity. This can be explained as a combined effect of the energy given to the electrons by the bunch charge—or electric field—and the energy dependence of the secondary electron curve. This displacement could be relevant for the accumulated scrubbing effect on the beam pipe if beam parameters are changed. The amount of current depends on the number of bunches, as a consequence of the time necessary to build up the EC. It is interesting to note that at least 24 bunches (25 ns nominal intensity) are necessary to induce a measurable current in an MBA profile, whereas the MBB profile displays a current at 12 bunches: this confirms the higher sensitivity to EC of the MBB profile.

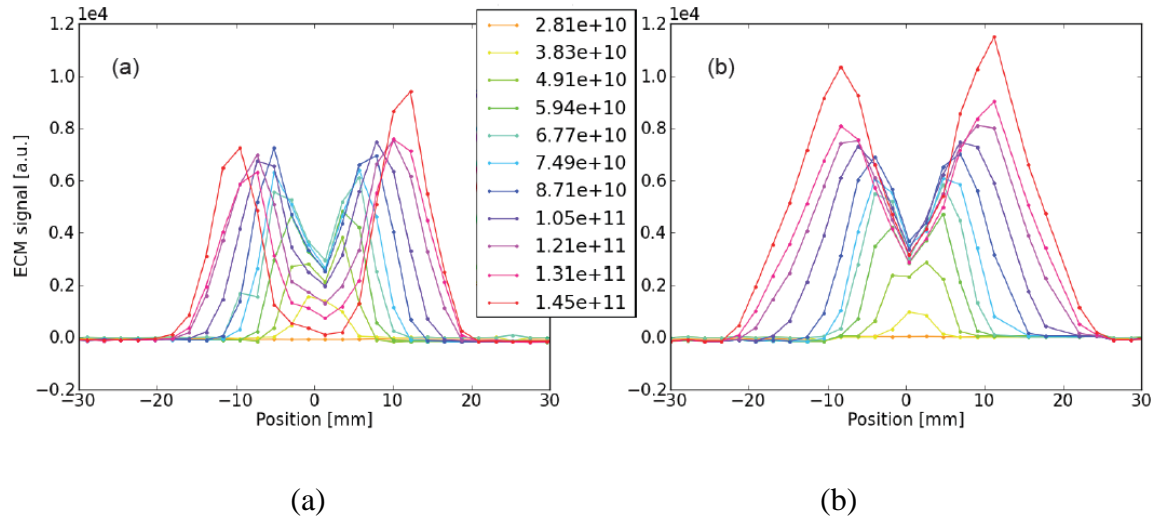


Fig. 5.68: Horizontal distribution of the electron flux in two strip detectors with (a) MBA; (b) MBB shaped chambers for 72 25ns spaced bunches with different bunch intensities.

A further measurement of the EC was made through microwave transmission. In principle the method could enable a measurement of the integrated EC density over the length of propagation of the microwave, through the dependence of the transmission on the charge density. The set-up in the SPS showed a difference between a carbon-coated dipole chamber, where no influence of EC was found, and a stainless steel dipole chamber, where the influence of the beam on the transmission was observed [81]. In a more recent set-up a difference in the signals given by a nominal and ultimate intensity LHC beam was observed, as a further confirmation of the intensity dependence of the EC.

Two mitigation techniques will be discussed below as potential solutions to suppress or reduce the EC for the beams required within the LIU scheme. In addition to those techniques the ‘transparent’ clearing electrodes were tested in ECM. Since they will no longer be discussed, we summarize briefly here the main findings. The set-up was based on the plasma spray alumina and tungsten coating developed at KEK [3]. The electrodes were effective in suppressing the EC in the central region of the beam pipe even with moderate voltages, but showed pronounced EC on the sides where the insulator was apparent. In a subsequent measurement in the laboratory, it was found that the SEY of the central tungsten region was around 1.3 and therefore below the one of StSt. Such a device was not investigated more deeply due to the effect of the apparent insulating stripes and the difficulty of applying such a solution to the SPS vacuum chambers: for instance, to limit deformation of the stainless steel plates during application of the layers a preliminary vacuum firing at 950°C was mandatory.

5.7.2 Mitigation by scrubbing

The first solution proposed for mitigation of the EC is beam scrubbing. Beam scrubbing is known to occur in particle accelerators and is known to be related to a decrease of the SEY on the walls of the vacuum beam pipe. The mechanism of this decrease is still debated, but the key ingredients seem to involve a beam-induced cleaning of the surface and the increase and/or graphitization of the carbon concentration on the surface. All effects can be induced in laboratory experiments with an electron source of the proper energy; but, for example, the origin of the carbon, as surface diffusion, bulk impurity or residual gas, has not yet been clarified.

Beam scrubbing effects have been observed on the liners installed in the strip detectors of the SPS. These measurements can help to understand the beam-induced conditioning process in the machine, but the differences between the ECM and the real bending magnets of the SPS might be relevant. In fact, the interplay between the horizontal confinement of the electrons in the dipolar

magnetic field and the presence of the holes in the grid of the ECM for electron detection might affect (probably slow down) the conditioning process, as the holes can locally suppress the electron cloud. The conditioning in the ECM has been observed to be faster in the central channels: there the current decreases faster as a function of beam time compared to the total current of the ECM. This was confirmed by moving the beam sideways on a conditioned chamber and observing the increase of the EC current and the localization of the scrubbing. A comparison of the EC current in MBB and MBA profiles after scrubbing with 25 ns beams clearly demonstrates the lower SEY threshold for the EC in MBB: indeed, the scrubbing could eliminate the current in the MBA profile for 50 ns beams, whereas EC was still well measurable in MBB.

In order to measure the value of the SEY as reduced by the beam scrubbing in SPS, a mobile sample set-up was installed in the machine [82, 3]. The set-up enabled measurement of the SEY of a plate on the bottom of a dipole with magnetic field at the injection value without exposing the sample to air. The magnetic field was switched on only during the MD runs in the machine. Various measurement runs showed that the conditioning was occurring around the central region of the beam pipe, in agreement with the findings in the ECM. Figure 5.69 shows that the maximum SEY in the part that was mostly scrubbed was close to 1.5, compared to more than 2 on the sides. A higher carbon concentration was also found in the central scrubbed region. It is known that in the machine the quadrupoles and dipoles, which have been in operation for a long time, exhibit visible dark stripes along the surface of the vacuum chamber, typically at the azimuthal locations where the EC is at its strongest. An RF shield from a quadrupole presenting such traces was recently cut, and the maximum SEY measured on the dark stripes was as low as 1.38. This measurement was obviously done after air exposure of the concerned surface.

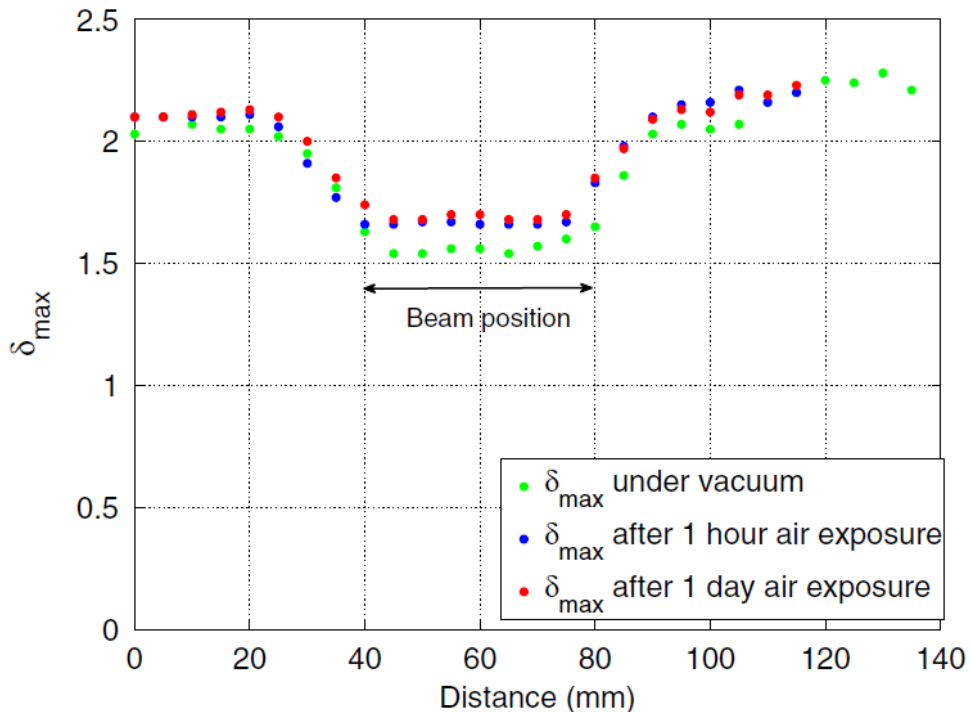


Fig. 5.69: Profile of SEY on the mobile removable sample of stainless steel (2009)

These values give an estimate of the SEY level that can be reached by conditioning with the present beams, but they are also consistent with SEY measurements done *in situ* in the past [83] on copper surfaces without an applied magnetic field. As a comparison the conditioning in the lab showed that in various cases it is possible to go below an SEY of 1.3 by using a sufficiently high dose and

electron energy, but the lowest achievable SEY was found to change from 1.1 to 1.3 in a non-reproducible way.

As a general rule, it seems clear that when conditioning the machine for suppression of the EC, the type of beam used for conditioning cannot be the same as the type of beam that will be used in the machine, since after some scrubbing the EC current decreases and becomes less effective for conditioning. The ideal scheme would imply using a scrubbing beam that has a lower SEY threshold for inducing an EC than the operating beam.

The idea of facilitating the scrubbing process by enhancing the EC while keeping the beam stable with high chromaticity was proposed in order to speed up the scrubbing process for the SPS [3]. Exploratory simulation studies in this direction were performed in 2011, when different options compatible with the beam types attainable in the SPS were investigated. In particular, the options of enhancing the EC via deliberately increasing the fraction of uncaptured beam or with tighter bunch spacings such as 5 ns, hybrid (10 + 15) ns or (20 + 5) ns, which can be accommodated in the 200 MHz main SPS RF system, were the object of detailed EC simulation campaigns to compare their potential. The outcome of these studies indicated that one of the most promising techniques for EC enhancement consists of creating beams with the aforementioned hybrid bunch spacings with about nominal charge per bunch, i.e. 1.1×10^{11} ppb. The higher frequency of the beam electric field with a shorter time for the EC decay between subsequent bunch passages is the underlying reason for the EC enhancement with the hybrid bunch spacings. However, the techniques initially envisaged to produce these beams, i.e. slip stacking in the SPS or RF manipulations in the pre-injector Proton Synchrotron (PS), turned out to be inapplicable due to technical limitations of the RF systems in the two accelerators. At this point, a novel production scheme was proposed to create a beam with the required (20 + 5) ns spacing. Long bunches (10 ns full bunch length) in 25 ns-spaced trains could be injected from the PS on the unstable phase of the 200 MHz SPS RF system. Ramping up the RF voltage shortly after injection from 1 MV to 3 MV to capture the long bunches in two neighbouring buckets would then result in the generation of 5 ns-spaced ‘doublets’ out of each incoming PS bunch. This scheme was successfully tested in the SPS first with a single bunch, and then with a train of 72 bunches with 25 ns bunch spacing [84]. Figure 5.70 shows the doublet creation in the SPS, with the bunch splitting effectively taking place in the first 50 turns and the readjustment of the bunches to their buckets in the following few synchrotron periods. Another test took place in 2013, in which a second PS train was injected into the SPS while one train of doublets was already circulating. The goal of this test was to prove that the decrease-increase of the RF voltage required for the injection of the second train would not cause excessive capture losses for the circulating beam.

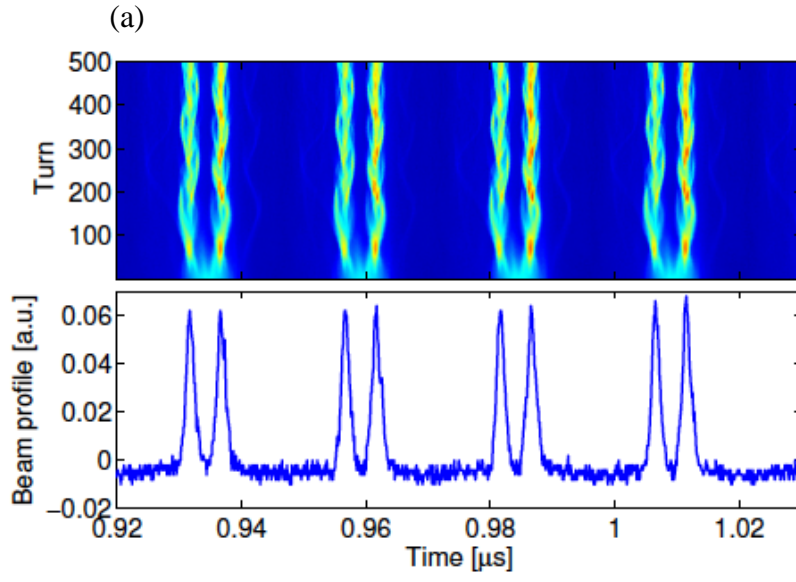


Fig. 5.70: Longitudinal beam profile (zoom on four of the 72 bunches): (a) evolution during the first 500 turns after injection; (b) snapshot at turn 500.

Electron cloud simulations run with PyECLLOUD in preparation of this doublet experiment showed that doublets can provide larger scrubbing doses and have significantly lower EC build-up thresholds than nominal 25 ns beams, as long as their intensity is above 1.5×10^{11} p/doublet. This is illustrated in Fig. 5.71 for both the MBA type chamber and the MBB type chamber. The enhancement effect should be mostly visible in the region of SEY below 1.55 for the MBA and below 1.25 for the MBB (i.e. the threshold for EC build-up for nominal 25 ns beams). As the 25 ns beam was produced in 2012 without significant beam quality degradation and with no important pressure rise in the SPS arcs (see above) it is believed that the SPS was then operating in these SEY regions.

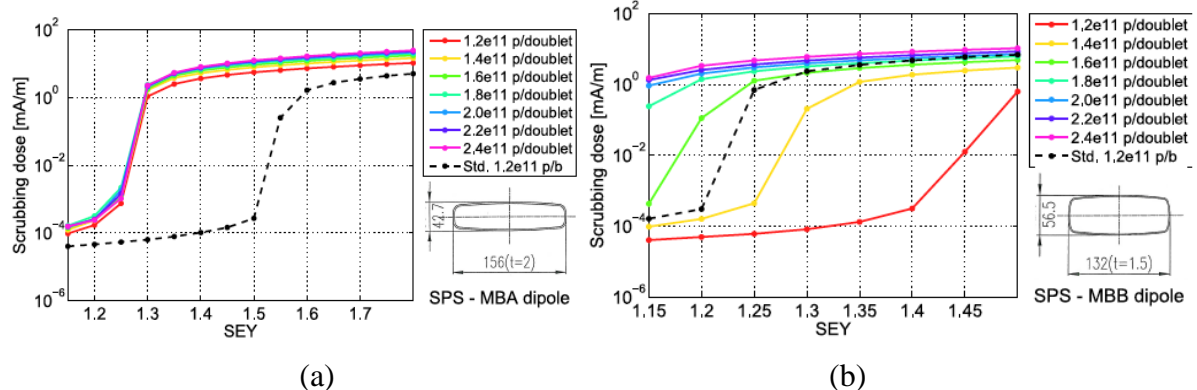


Fig. 5.71. Electron scrubbing flux in the SPS MBA (a) and MBB (b) chamber as a function of the maximum SEY for different values of the intensity per doublet (solid lines, colours labelled) in comparison with the nominal 25 ns beam (dashed line)

For a direct comparison between the two beam types, a standard 25 ns beam with 1.7×10^{11} p/b and a doublet beam with the same intensity per doublet were injected on consecutive SPS cycles, each with a length of 4 s. The effect of the enhanced EC in the SPS with doublet beams was immediately observed, with a dynamic pressure rise in the arcs that was about four times the value measured with the standard beam. Furthermore, the signals from the EC detectors (both MBB and MBA chamber types) also provided a direct measurement of the stronger EC production, as displayed in Fig. 5.72(a, c). However, albeit increasing the electron flux on the chamber walls, the doublet beam covers a

different region compared to the two stripes created by the standard beam. This observation was already anticipated by build-up simulations with a high degree of accuracy, as shown in Fig. 5.72(b, d). The consequence is that radial steering in the dipoles is needed to scrub the required part of the SPS chambers with the doublet beam. The proof-of-principle of the production and efficiency of the doublet beam in the SPS, as well as the validation of our simulation tools for predictions, was an essential milestone for considering this beam as a future option for scrubbing the SPS after LS1.

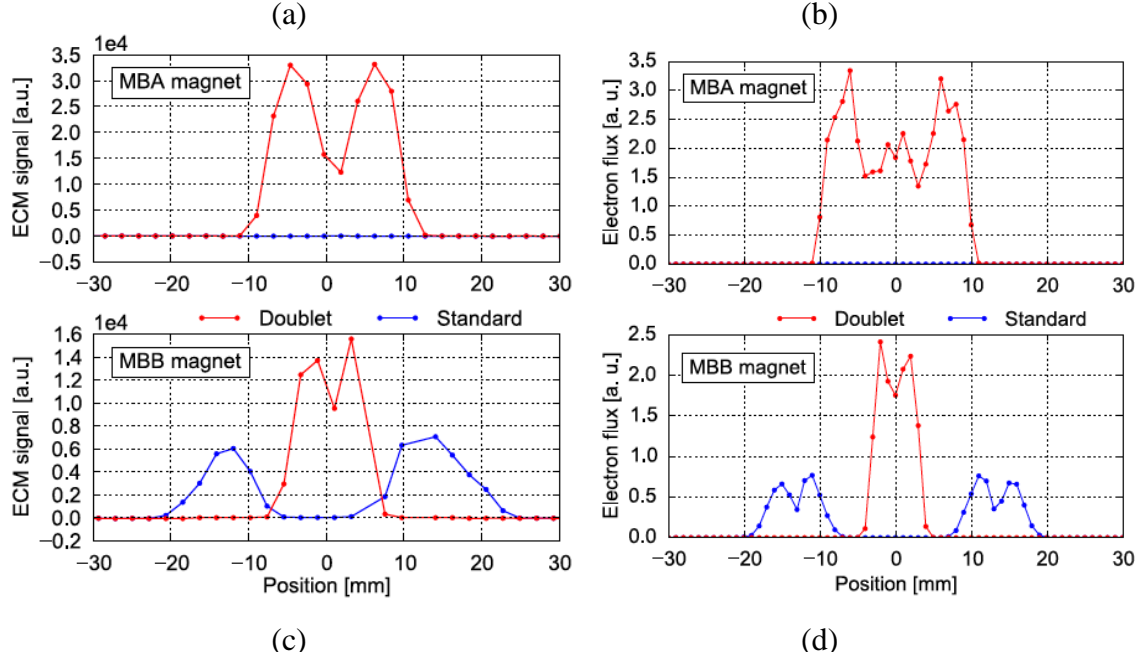


Fig. 5.72: Electron signal from the SPS electron cloud monitors in (a, b) an MBA chamber; (c, d) an MBB chamber as a function of the horizontal position. The blue traces are the measured (a, c) or simulated (b, d) signals with the standard 25 ns beam; and the red traces are those from the doublet beam.

5.7.3 Mitigation by amorphous carbon coating

The SEY of the beam pipe is a surface effect and can therefore be reduced by a thin-film coating having the suitable properties. Amorphous carbon coatings for long beam pipes, which are captive in the bending magnets of the SPS, were developed at CERN and applied to ECM monitors and a few test dipoles and quadrupoles of the machine. Once the coating technique was established all the liners with carbon coatings installed in the ECM showed complete suppression of the EC [82] current even after months of venting for 25 ns beams. The ‘oldest’ carbon-coated ECM liner, which was inserted in 2008, is still in the SPS and did not show any loss of effectiveness in terms of electron cloud suppression during the 25 ns runs. The measurements of RF transmission through carbon-coated bending magnets showed that the signature of the EC was below the noise level and in any case significantly lower than for the usual stainless steel vacuum chambers. Only the pressure measurements did not show a sharp difference between coated and uncoated sections (a few dipoles) of the SPS. For this reason a carbon-coated drift section [3] was equipped with solenoids, so that the contribution of the EC to the pressure could be measured by switching on and off the axial magnetic field. The pressure gauge at the centre of the coated drift section showed a minor change (due to finite conductance) compared to the gauges at the edge of the section, where the magnetic field was suppressing the EC occurring in the stainless steel part of the beam pipe. This has again demonstrated the effectiveness of the carbon for the EC suppression. Last but not least, a multipacting experiment was set up in the lab by stretching a W wire along an ECM in a small dipole. The multipacting was easily induced with the available power level in a stainless steel vacuum chamber, but the threshold of

necessary power was by far too high to induce any current in the case of a carbon-coated chamber [85].

5.7.4 Planning

In case scrubbing is not sufficient for suppressing the electron cloud effect with the high beam intensity and small transverse emittance required for the HL-LHC, or in case the reconditioning process is very slow after large parts of the machine are vented (like during a long shutdown), the inner surface of the SPS vacuum chambers has to be coated with a low SEY material. As described above, the solution developed at CERN is to produce a thin film of amorphous carbon using DC hollow cathode sputtering directly inside the vacuum chamber. The suppression of the electron cloud in coated prototype vacuum chambers has been fully validated with beam in the SPS.

The coating of the entire machine circumference of the SPS with amorphous carbon is a major work, which requires careful preparation and planning of resources (as all magnets need to be transported to a workshop). The decision whether the SPS needs to be coated, or if scrubbing as electron cloud mitigation is sufficient, has therefore to be taken not later than mid-2015. After the long shutdown, a scrubbing run of about two weeks will be performed during the startup at the end of 2014 with the goal of recovering operational performance, as it is expected that the good conditioning state of the SPS will be degraded due to the long period without beam operation and the related interventions on the machine. Another scrubbing run will be performed in the first half of 2015 in order to scrub the machine for high-intensity 25 ns beams. The final decision about the coating will be based on the experience during this period and on the outcome of experimental studies with the high-intensity 25 ns beams.

Since amorphous carbon coating is the main alternative to scrubbing, a coated section of four half cells of the machine, including the dipoles, quadrupoles and RF shields, will be installed during LS1 in 2014 and suitable pressure gauges will be placed to monitor the effect of the coating for static and dynamic vacuum. In parallel, the results from the carbon-coated ECM vented during LS1 will be followed at the restart of the machine. If these tests show a positive result in terms of pump-down time and dynamic vacuum and the decision is taken to coat the entire ring, the planning is to first equip a single arc (sextant) of the SPS during LS2. This will enable a larger scale testing without a too severe modification of the SPS, which would be simultaneous with the start of operation of Linac4. Coating an entire sextant involves complex logistics, since it has been established that the magnets must be displaced, coated, put back in place and realigned. This could mean that they are lifted up to the surface into a dedicated workshop or that they are coated in the ECX5 cavern. The cleaning of the vacuum chambers before coating is a safety issue. From the radio-protection point of view, in the event of wet cleaning it has been established that the main contamination can be easily removed by wiping with a cloth with solvents before a common detergent cleansing. This was successfully applied to a magnet that had received a grazing beam impact. However, wet cleaning would involve additional safety and logistics issues if the coating is to be done in the tunnel of the machine (leaks of liquids, etc.). In principle, plasma cleaning should be possible and will be tested in the near future.

Such a schedule involves the design and construction of a prototype of the coating plant in the years 2016–2017, which will be required to accomplish the task within the available shut-down time. It will also be a module of the larger plant needed to coat all the remaining arcs of the machine in an acceptable time, always assuming that the results from the coated single arc are positive.

In case of unforeseen issues with the coated section an oxygen plasma treatment can be envisaged in order to remove the coating. This has already been successfully applied on shorter chambers in the lab after coating.

5.8 Beam scraping

5.8.1 Introduction

The LHC beams in the injectors have large non-Gaussian transverse tails that are lost on the transfer line collimators during injection into the LHC. If the tail population is not reduced, the beam losses can be high enough to trigger a protection beam dump and delay the operation of the LHC. During LHC run 1, beam scraping in the SPS became an essential part of operation with LHC beams in the injectors. The scrapers were also used for beam diagnostics and for intensity reduction. The scraping is done in the SPS towards the end of the ramp at 409 GeV. For high-intensity LHC physics beams, around 3% of the intensity is usually removed to obtain sufficiently clean injections. In each transverse plane, a 1 cm-long graphite blade is swept through the beam tails to intercept and scatter high-amplitude particles and remove them from the beam. Because of orbit drifts, the scraper position needs to be adjusted on a daily basis, but this is now a standard procedure for the SPS operators. The scrapers are located in LSS1, with a spare set just upstream of the operational ones. Another set of scrapers is installed in LSS5, which is not currently used. The SPS scraper system is simple, but proved to be efficient and robust during operation. Although concerns were raised about the lifetime of the mechanical system, it worked reliably throughout the run.

At the end of run 1, a special machine development test was carried out to assess the endurance of the present scraper blades. During the test, the full SPS beam was scraped with the spare blades, which were then removed and inspected. The inspection showed that the blades had undergone structural changes. This can reduce scraper performance, but no substantial breakage is expected and no substantial reduction in performance was observed during the tests [8, 86].

For the LIU project, the present scraping system was evaluated with respect to the increased beam intensity and improved emittance. In addition, a new scraper system, relying on a fixed mask and a magnetic bump, was studied and the feasibility was demonstrated in dedicated machine development studies. The technical design report [8] was fully prepared and contains details that will be summarized here.

5.8.2 Beam scraping on fixed mask

The proposed system relies on a magnetic bump moving the beam onto a fixed mask as illustrated in Fig. 5.73. This method allows for a larger block to absorb the beam tails. The magnetic bump is created by four bumpers in each plane, two before and two after the scraper block, allowing orthogonal steering of position and angle of the beam at the scraper.

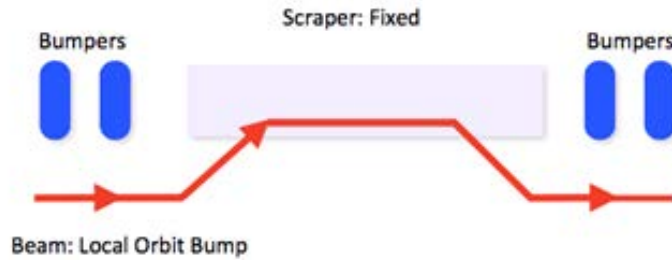


Fig. 5.73: The new concept of beam scraping relies on a magnetic bump and a fixed block. By using four bumpers per plane one can obtain orthogonal steering of angle and position of the beam.

After considering all SPS long, straight sections, LSS6 was chosen. The layout is given in Fig. 5.74. In the horizontal plane the four existing extraction bumpers were found to be suitable. In the vertical plane two existing and two new bumpers are used. Due to integration issues at one of the new bumper locations, a new bumper design with a smaller size was also proposed.

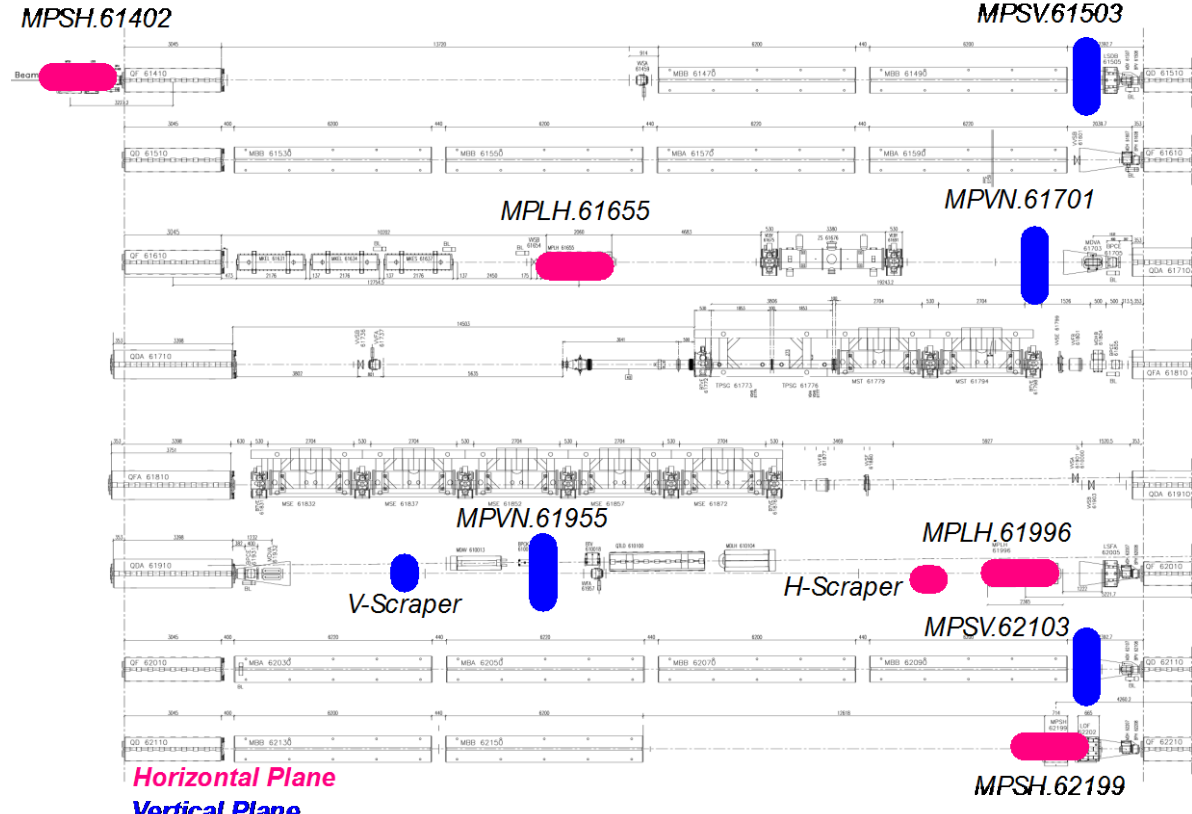


Fig. 5.74: The proposed layout for the scraper in LSS6 consists of four bumpers in each plane. In the horizontal plane the extraction bumpers are used. In the vertical plane two existing bumpers can be used, but the scheme also requires installation of two new bumpers.

5.8.3 Feasibility studies

During 2012, machine development studies were carried out to prove the feasibility of this scraping concept. For these studies the extraction bumpers in LSS6 were used to create a bump onto TPSG.61773 (protection shield for the extraction septa) for scraping a low-intensity beam of one bunch. The studies were performed only in the horizontal plane due to the availability of bumpers and the fixed mask.

The main goal of the machine studies was to demonstrate that the new scraper method successfully removes transverse tails. After adjusting the bump height and angle, the beam profile was measured using the wire scanners and the results clearly show that the tails were successfully removed, see Fig. 5.75.

During the tests a single-cycle scraper scan was also successfully tested proving that the system is flexible enough to be used to measure the beam profile within one cycle. This is not possible with the current scraper system. This exercise also demonstrated that the system has a higher flexibility and could easily be used to scrape multiple times within one cycle.

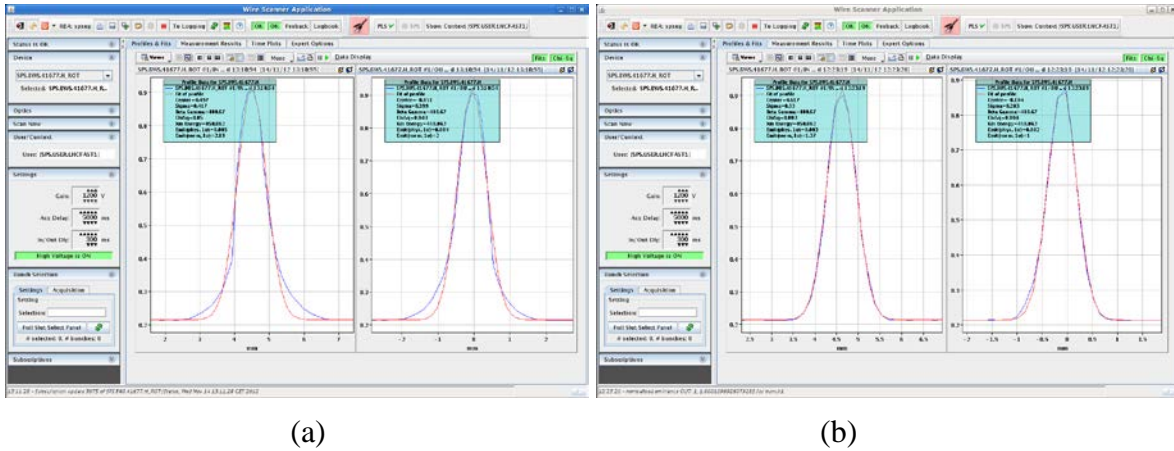


Fig. 5.75: Beam profile (a) before and (b) after scraping, measured by the SPS wire scanners. The profiles show that the tails have been successfully removed by scraping on the TPSG using a magnetic bump.

The magnetic bump scraping also proved to be faster and sharper with respect to the current scraper, see Fig. 5.76. The time per scraping is limited by the 150 ms stable field region of the bumpers. An angular scan of the bump angle versus scraping efficiency showed the importance of the correct set-up of the bump angle.

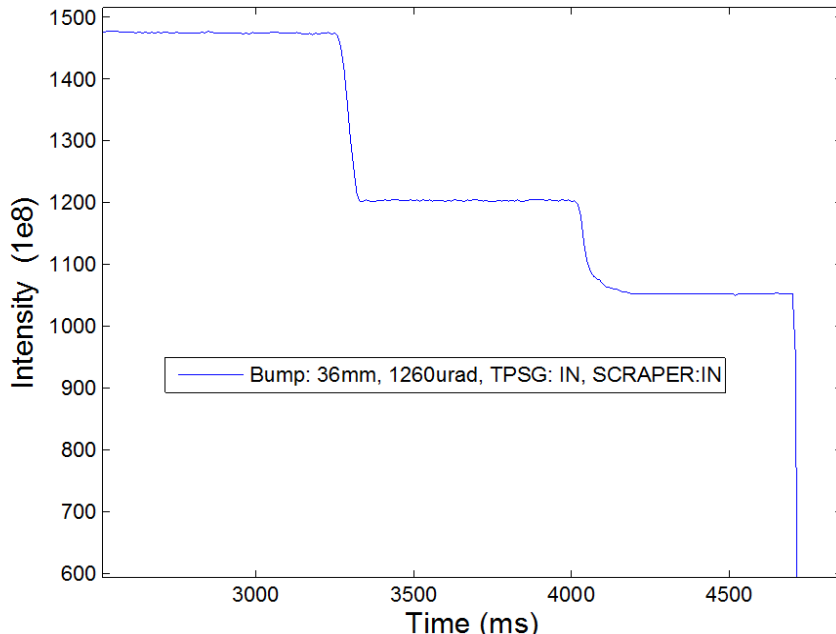


Fig. 5.76: Beam intensity measurement during a cycle where the beam was scraped both using the magnetic bump onto the TPSG (first intensity drop) and using the operational scraper (second intensity drop).

5.8.4 Operational flexibility and limitations

Because the bumpers operate very fast, it is possible to scrape multiple times within a cycle to scan, for example, a beam profile, as was shown during the machine development tests. However, in the case of a magnetic bump, failures of the bumper power converters could cause severe damage to equipment. Sufficient interlocking would have to be worked out. For the extraction bumpers a similar interlock system is already in place, but would need to be extended to allow multiple scrapes within a cycle if necessary. The interlocking requirements could limit the operational flexibility.

5.8.5 Material studies

Simulations coupling FLUKA to SixTrack were performed to assess the energy deposition in the current operational scraper and in the proposed, upgraded one. The peak energy deposition in the long block is significantly lower than that in the present scraper, since the interactions of the beam particles with the absorber are diluted over a larger length, with a much lower survival probability and thus reduced number of passages through the block. On the other hand, totals are dramatically different, due to the different volumes of material available for absorbing particle showers. Many recommendations for input in the material choice are also presented in the design report.

The aforementioned results were obtained with no synchrotron motion activated in SixTrack (i.e. 4D tracking), and emulating the rising of the bump actually moving the block towards the beam: these approximations were not expected to have a relevant effect on typical energy deposition values. Figure 5.77 shows the effects on the peak energy deposition (adiabatic estimation) once these approximations are removed [87]: the absorber block is oriented at the natural angle of the magnetic bump, and the relative angle between the absorber and the beam decreases while the bump is raised, by $\sim 15 \mu\text{rad}$ for each σ spanned by the bump. The addition of the synchrotron motion (thus performing the tracking in 6D) lowers the values, since the impact parameter is further diluted.

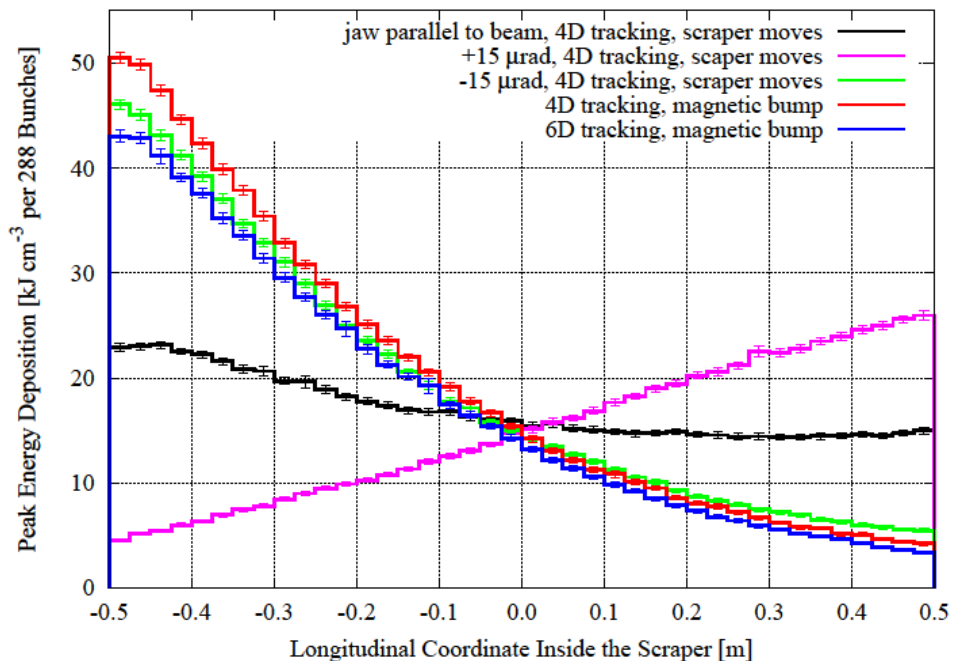


Fig. 5.77: Longitudinal profile of the peak energy deposition for different simulation settings

5.8.6 Radiation protection considerations

The current system is located in the BA1 area close to the SPS beam dump system, and the additional radiation caused by scraping is considered negligible in comparison to the radiation from the beam dump block. However, an intervention in this area exposes personnel to significant doses and maintenance is expected to be necessary.

For the fixed scraper, less maintenance is foreseen, which is an advantage in terms of radiation. Some increase of radiation is to be expected in BA6, however, if the system is installed there.

5.8.7 Endurance test of the present scraper blades

As mentioned earlier a material endurance test was carried out at the end of LHC run 1 with the present scraper system in the SPS. While sweeping the scraper blades through the beam, the energy deposition is concentrated around the edge actually facing the beam. For the test the entire beam was scraped, thus the blade was moved to the centre of beam distribution.

Figure 5.78 shows a map of the energy deposition expected in adiabatic assumptions for the test of the horizontal blade, as estimated with the FLUKA-SixTrack coupling. The values are so high that local material removal can reasonably be expected. Indeed, during the test, relevant vacuum spikes were registered at the kickers just upstream of the scrapers (see Fig. 5.79). Moreover, inspection [86] revealed that the morphological structure of the graphite in the region of the chamfer was actually modified (flake-like shapes, see Fig. 5.80), and a substantial increase in the porosity (~30%) was estimated.

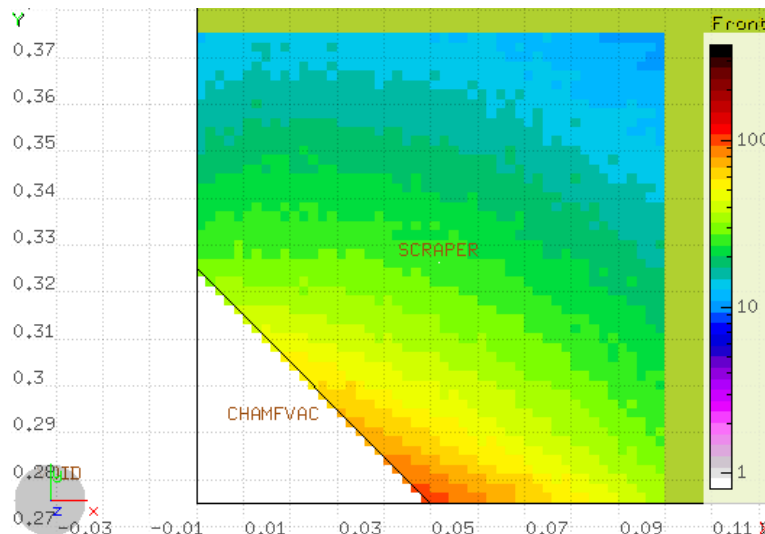


Fig. 5.78: Map of energy deposition expected in adiabatic assumptions for the test of the horizontal blade; the map (transverse cut) is zoomed on the region of the chamfer facing the beam, at the longitudinal centre of the blade. The blade is swept through the beam from top to bottom.

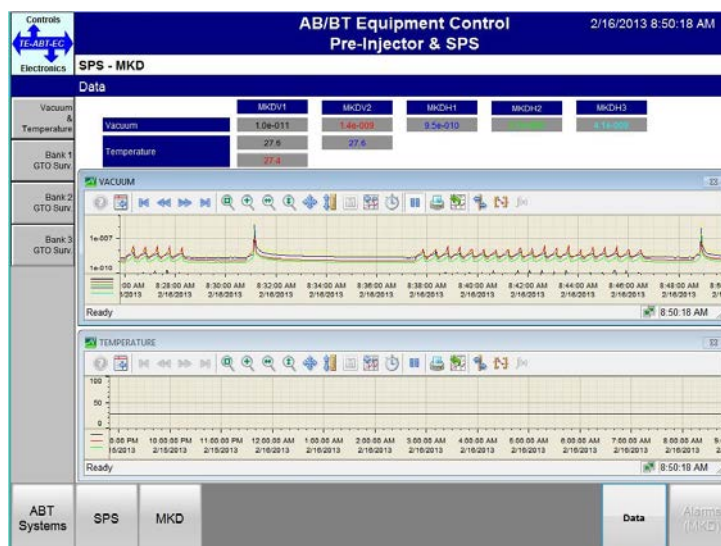


Fig. 5.79: Time profile of the vacuum in the region of the kickers just upstream of the scrapers under test. Two relevant spikes are clearly visible: one at ~08:31 AM, when the vertical blade was tested, and the other one at ~08:49 AM, when the horizontal blade was tested.

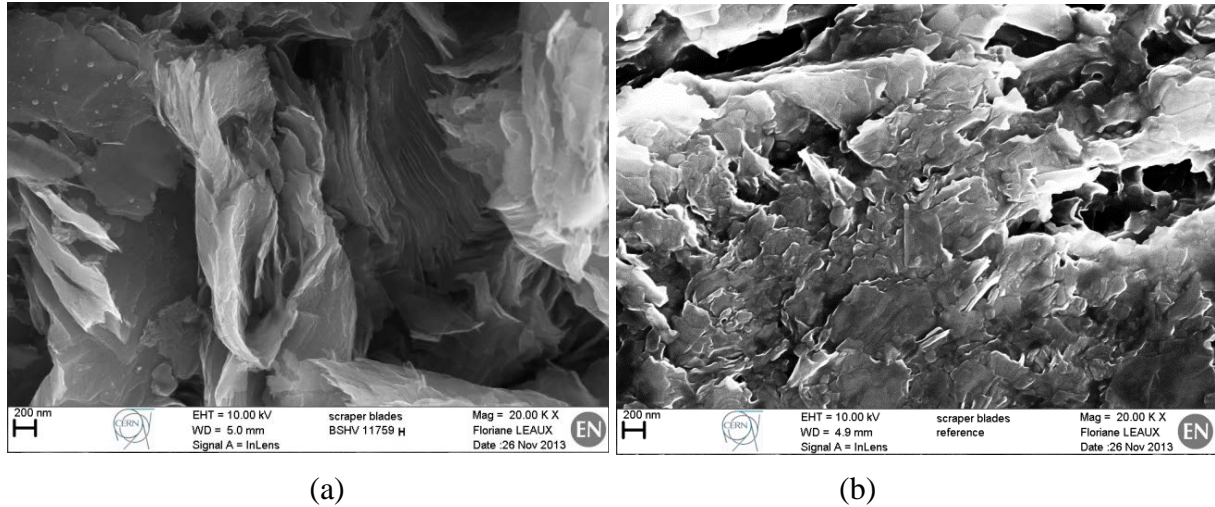


Fig. 5.80: SEM images of the horizontal scraper blade after the test. (a) In the region of the chamfer affected by the beam; (b) in a region far from the chamfer (shown as reference).

The local increase in the porosity is reflected in a decrease of the local density of the material, possibly affecting the performance of the blade, in particular the time required for scraping. Nevertheless, thanks to the blade movement and the damage being extremely localized, the beam particles will start to see other material of a regular density (see Fig. 5.81), without affecting too much the operation of the blade, unless the whole face has been consumed. As proof, regular scraping was verified before and after testing each blade, and no visible detriment in the performance was registered (see Fig. 5.82).

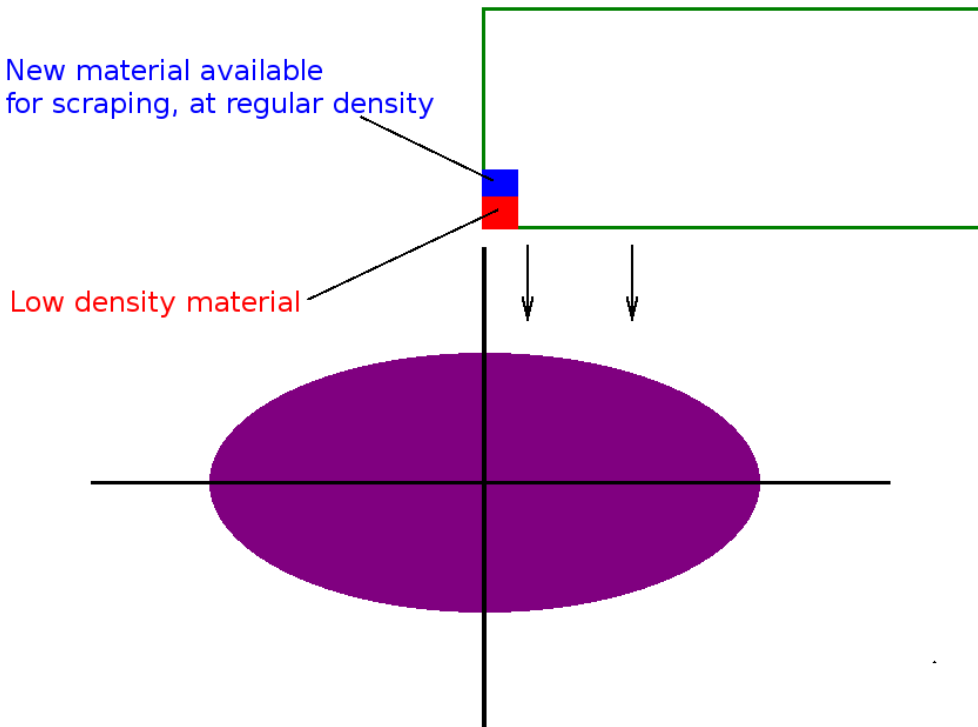


Fig. 5.81: Schematics of the consumption of the scraper blade

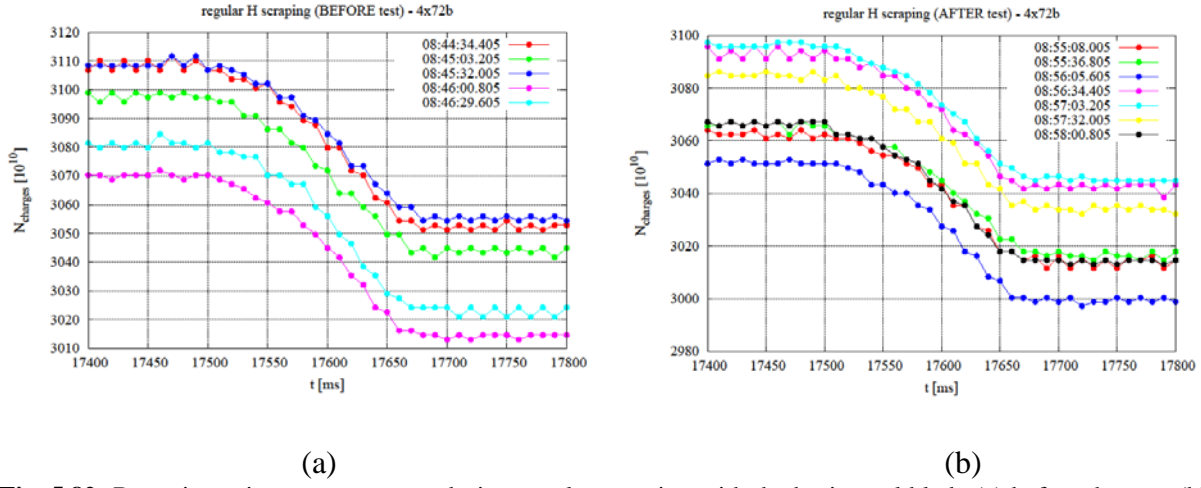


Fig. 5.82: Beam intensity measurements during regular scraping with the horizontal blade (a) before the test, (b) after the test.

5.8.8 Summary

In January 2013 a review of the scraper system was organized [88]. Several aspects of the current system and a possible upgraded system with a fixed mask were discussed. Some more advanced techniques were also presented, but these are not yet developed enough to be considered. After the review it was decided that the current system has no serious issues and should be kept. However, the new design is prepared for rapid implementation in case the current system reveals problems in the future.

5.9 Dump system

The SPS internal beam dump is installed in Long Straight Section 1. It is formed by two main absorber blocks (TIDH and TIDVG), two vertical kickers (MKDV), three horizontal sweepers (MKDH), three misaligned quadrupoles (QDA117, QFA118 and QDA119) and two SEM grids (TFDH/V). Other two absorbers, TIDP and TBSJ, are used for off-momentum collimation and injection beam stopper, respectively.

The TIDH is the absorber block used for dumping the low-energy beams (14 GeV to 28.9 GeV), while the high-energy beams (102.2 GeV to 450 GeV) are dumped onto the TIDVG; between these ranges a clean dump cannot be made. The TIDVG is a 4.3 m absorber block, made of 2.5 m of graphite, 1 m of aluminium, 0.5 m of copper and 0.3 m of tungsten.

The three misaligned quadrupoles form a closed orbit bump that helps the MKDV to vertically deflect the beam towards the absorbers. The orbit bump is closed, with a maximum amplitude of 7 mm (both planes) for the Q26 optics (fixed target beams). It is not closed and also less effective (about 35%) for the Q20 optics (LHC and ion beams). Even in these conditions, the beam is still dumped 10 mm below the TIDVG top edge, which is the safe margin for the absorber block [89, 90]. Hence, for future operation, modification of the dog-leg is not foreseen [91].

Depending on the beam energy, the MKDVs deflect the beam either onto the TIDH or the TIDVG. The MKDV tracking function is shown in Fig. 5.83(a). The combined waveforms of the MKDV and the MKDH (Fig. 5.83(b)) are such that the whole beam is spread onto a relatively large part of the absorber block front face. In fact, the MKDV waveform is designed to provide oscillation of $\pm 15\%$ around the nominal kick strength, to give increased dilution of the dumped beam. The current kicker parameters are summarized in Table 5.5. [92, 93]

A simulated example of beam loading on the TIDVG front face due to the LHC-BCMS ($1.15 \times 10^{11} p^+$ /bunch, $\varepsilon_{x,y} = 1.39 \pi$ mm mmrad, 240 bunches) is shown in Fig. 5.84.

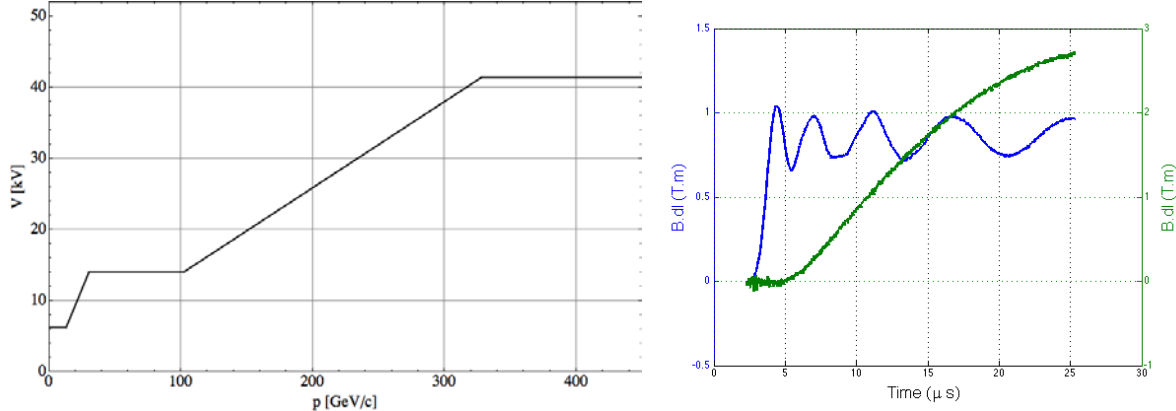


Fig. 5.83: (a) MKDV energy tracking function. (b) MKDV (MKDVA + MKDVB) waveform in blue and MKDH (2 × MKDHA + MKDHB) waveform in green.

Table 5.5: Dump kicker parameters [108]

Parameters	Unit	MKDVA/B	MKDHA/B
H_{ap} (full)	mm	75/83	97.1/106.1
V_{ap} (full)	mm	56/56	56/60
Length	m	2.56	1.256
Rise time	μs	1.1	23
Maximum voltage (2012)	kV	41.4	9.9
Kick strength	T.m	0.49/0.41	0.92/0.77

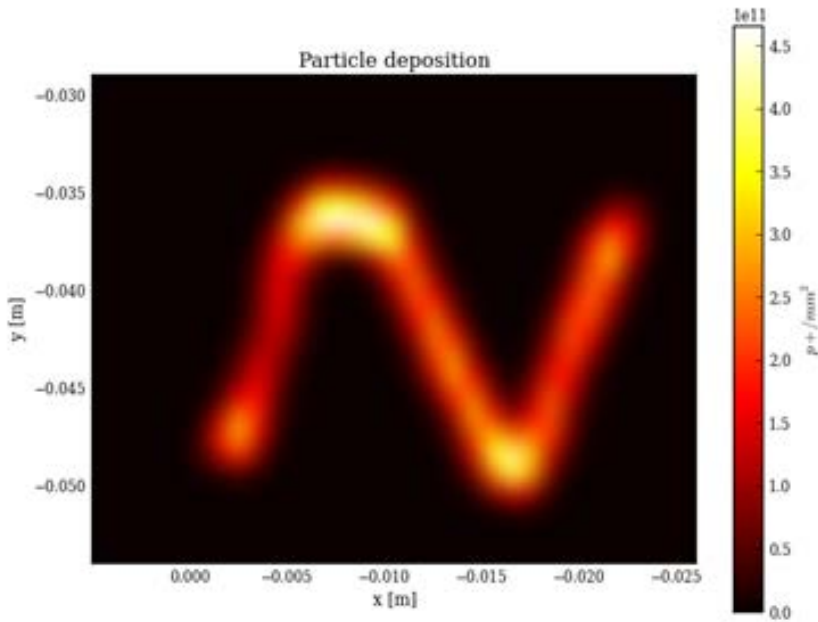


Fig. 5.84: Simulation of particle deposition on the front face of the TIDVG for LHC-BCMS beam. The maximum simulated proton density considering an ideal machine is $4.6 \times 10^{11} \text{ p}^+/\text{mm}^2$ [94].

5.9.1 Limitations and proposed upgrades of the present system

The initial SPS beam dumping system was built for energies lower than the current ones. During its lifetime the system has been upgraded several times to make it suitable for the increasing demands. Although the system performance has been greatly improved, there are still several major issues affecting it:

- outgassing of the TIDVG, which causes vacuum pressure rise in the downstream MKP injection kicker;
- MKDV reliability issues due to the topology;
- MKDV switches limitation, which translates into a forbidden dump energy range;
- activation of the area around the TIDVG.

Furthermore, the required performance of the TIDVG will change due to the high-brightness (LIU and HL-LHC) beams.

5.9.1.1 Outgassing

The most likely sources of outgassing in the TIDVG are graphite and tungsten driven by temperature rise and material contamination; hence, the most critical case is when the graphite exceeds the bake-out temperature. This happens when the beam is repeatedly dumped, when the graphite is exposed for a long time to atmospheric air, or when a new absorber block is installed [91].

The main effect is seen in the downstream injection kicker, where the vacuum pressure rises up to 1×10^{-6} mbar, preventing further beam injection due to the risk of high voltage breakdown.

Possible solutions to this problem may be: increase the longitudinal distance or the pumping speed (possibly using NEG materials) between the TIDVG and MKP; separate the graphite block from the circulating beam aperture (a solution explored in Ref. [91]); modify the material composition of the TIDVG.

5.9.1.2 MKDV powering

The current MKDV power system is based on three pulse forming networks (PFNs). Each is connected to a composite switch, i.e. thyratron and ignitron, as shown in Fig. 5.85 (lefthand side). This configuration leads to two main problems: the effective redundancy in case of magnet breakdown is reduced by the presence of a third common PFN, and the gas switches do not permit coverage of the whole SPS energy dynamic range [93], leading to a ‘forbidden zone’ of the dump system.

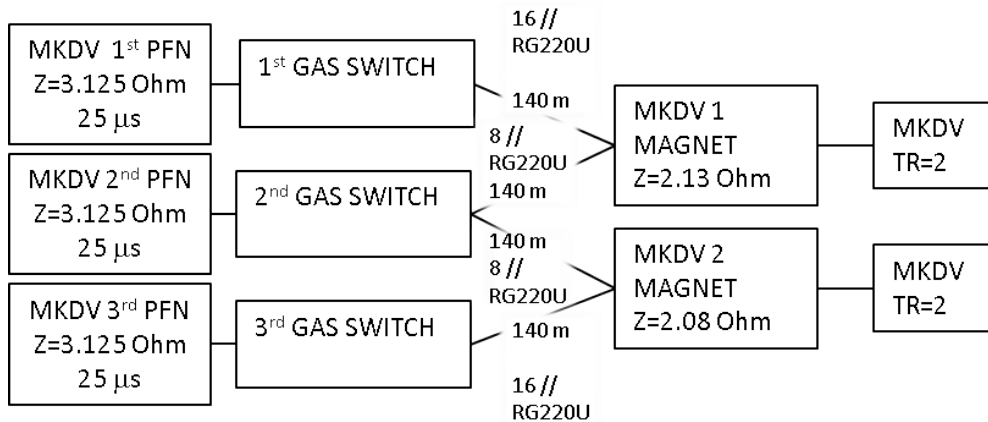


Fig. 5.85: Schematic view of the MKDV current connection [93]

The forbidden energy range can be observed in the lefthand side of Fig. 5.83. Between 14 GeV and 28.9 GeV the beam is dumped on the TIDH; between 102.2 GeV and 450 GeV the beam is dumped on the TIDVG; between 28.9 GeV and 102.2 GeV the MKDV voltage is kept constant resulting in a progressive deflection of the beam between the TIDH and the TIDVG and hence an increase in losses around the SPS.

The nominal operational voltage of the MKDV is 52 kV. Between 2006 and 2010 there have been several modifications of the MKDV [93]; moreover, in 2011 the maximum voltage was clamped at 44 kV due to magnet sparking, and in 2012, due to switch weaknesses, it was clamped at 41.4 kV [91].

An upgrade of the power system is already foreseen. In order to provide the required redundancy for the kicker system, each magnet will be equipped with its own PFN and switch. Also, the switches will be different from the current ones. These will be semiconductor switches, like those already installed in the MKDHs, made of a stack of modified gate turn off (GTO) devices. This will entail a slightly longer rise time, i.e. about 1.3 μs, but also a broader dynamic range, which will significantly reduce the ‘forbidden zone’. The powering system upgrade will also produce a different current waveform (Fig. 5.86), although the overshoot of ±15% will be preserved [89].

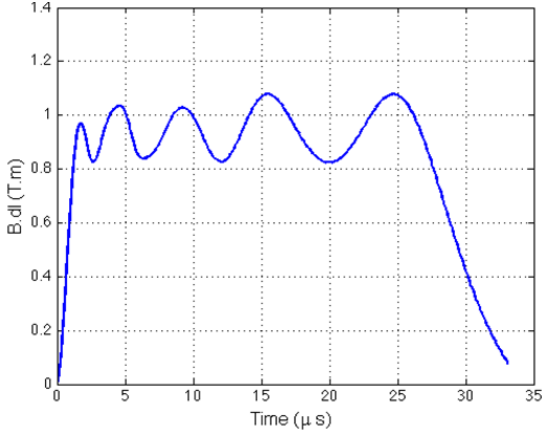


Fig. 5.86: MKDV integrated field waveform at 47 kV using GTO switches [89]

5.9.1.3 Activation

The number of protons per year dumped on the TIDVG since 2006 is shown in Fig. 5.87. This, together with the fact that it is the vertical machine bottleneck, makes the high-energy absorber the most radioactive element of the whole SPS. This imposes very strict rules about access to the TIDVG area. Depending on the preceding operation, it may be necessary to wait weeks before having the possibility of accessing this area safely. The best scenario to reduce activation in LSS1 is an external dump.

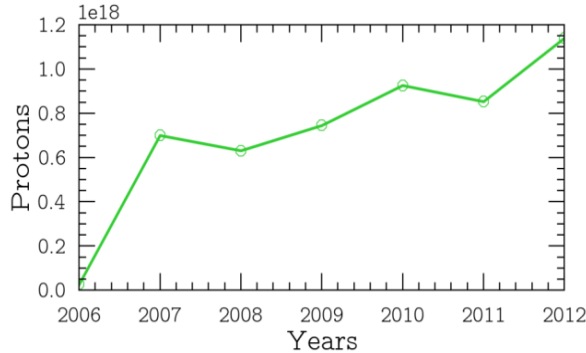


Fig. 5.87: Total number of protons dumped on the TIDVG per year from 2006 to 2012

5.9.1.4 Beam loading on the TIDVG

To quantify the beam loading on the TIDVG due to the foreseen high-brightness beams, particle tracking studies have been performed with MAD-X [106], also taking into account the upcoming MKDV upgrade (LS2).

The most critical failure scenarios are all related to the MKDV and MKDH power equipment. Six different possible cases have been analysed:

1. self-triggering of an MKDV power switch;
2. failure to fire of one MKDV power switch;
3. flashover in the MKDV;
4. flashover in the MKDH;
5. complete failure of the MKDH;
6. complete failure of the MKDV (This does not produce any beam load on the TIDVG).

Failure cases 1 and 3 are considered to be the design cases for the new TIDVG block. Case 2 is not been explicitly considered. The very low operating voltage of the MKDH means that cases 4 and 5 are very unlikely (neither has been seen before), therefore they are considered as ‘beyond design’. The results of these studies are summarized in Table 5.6, which refers to the beam types listed in Ref. [106].

Table 5.6: Maximum beam loading on the TIDVG front face for different failure scenarios

	LHC (Achieved—BCMS)	LIU (BCMS)	Requested HL-LHC	Probability of failure
Nominal [p^+/mm^2]	4.6×10^{11}	1.13×10^{12}	1.09×10^{12}	-
Maximum p^+ density [p^+/mm^2] Failure 1	4.2×10^{11}	8.32×10^{11}	8.1×10^{11}	1/year (after MKDV upgrade)
Maximum p^+ density [p^+/mm^2] Failure 3	4.7×10^{11}	9.7×10^{11}	9.6×10^{11}	Few times per year
Maximum p^+ density [p^+/mm^2] Failure 4	6.6×10^{11}	1.48×10^{12}	1.4×10^{12}	Never seen before
Maximum p^+ density [p^+/mm^2] Failure 5	2.43×10^{12}	3.6×10^{12}	3.42×10^{12}	Never seen before

5.9.2 External dump design

A first design study for an SPS external dump was done in Ref. [91]. The initial conclusion is that such a system will suffer heavy operational limitations (not enough apertures to extract Fixed Target (FT) beams below 100 GeV) due to aperture limitations in the SPS extraction channels.

As noted above, the high-brightness beams represent a challenge for the SPS dump system, and hence the need to investigate external solutions for them. Due to their high energy and small emittance, the already existing extraction channels (LSS4 and LSS6) represent ideal locations to extract the beam from the SPS. The external dump will then be used only for scheduled LHC-type beam dump, hence the internal one will be kept for emergency and FT beam dumps.

Two different positions and designs have been explored. The first one is to use the extraction system in LSS4 and then branch off from TI8 towards a new dedicated tunnel. The second possibility is to extract from LSS6 and slightly modify TT61 in order to host the dilution system and the absorber block.

5.9.2.1 Extraction from LSS4

The transfer line linked to the extraction system in LSS4 is TT40. It is the common part of TT41, which points towards the CNGS area, and TI8, which is the transfer line dedicated to the injection of beam 2 into LHC. TT41 branches off from TT40 with a switch; instead TI8 is the continuation of TT40.

The switch magnets (MBS) are usually used to physically separate two beam lines. They are a series of C-shaped bending magnets and they have been considered in the following study. A good location to install a system to branch off towards the beam dump is at the beginning of TI8, where

there are five bend-free FODO cells. Half a cell will be occupied with six MBS to provide the required deflection for the separation.

One of the main reasons to have an external beam dump is the activation of the absorber block. Therefore, a minimal wall thickness of 3 m between the dump cave and the adjacent tunnel is required to shield it properly. To satisfy this requirement, two additional MBA (horizontal normal conducting bend) will be installed in the dump line. The deflection ensured by these magnets translates into a separation of 10 m from TI8 (Fig. 5.88) after 130 m; which is where the absorber block is foreseen to be.

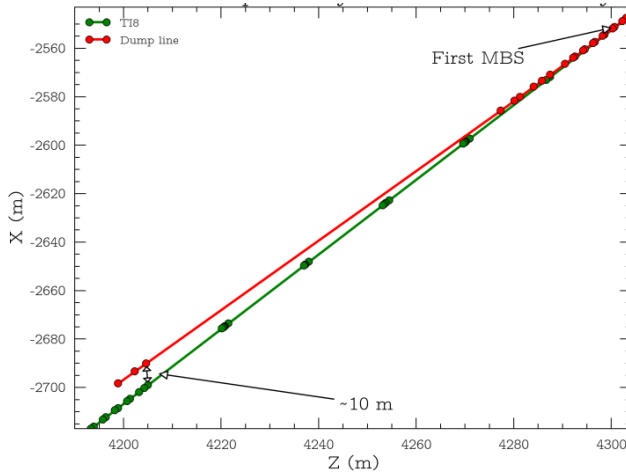


Fig. 5.88: Geometry of the TI8 line and the proposed external dump line in MAD-X coordinate system

One quadrupole, QNL, is used between the MBS and MBA to keep enough beam focusing to pass through the downstream apertures of the bending magnets. The lattice functions of the whole line are shown in Fig. 5.89(a).

There will be no more quadrupoles to control the beam focusing; hence the dilution required at the absorber block is obtained by letting the beta-functions drift in the free space before the dump (Fig. 5.89(b)). This strategy of diluting the beam is very sensitive to orbit errors; therefore a detailed error analysis has to be done to prove the reliability of this solution. Another option to obtain the required beam density at the dump block is to use ‘sweepers’, as in the internal beam dump.

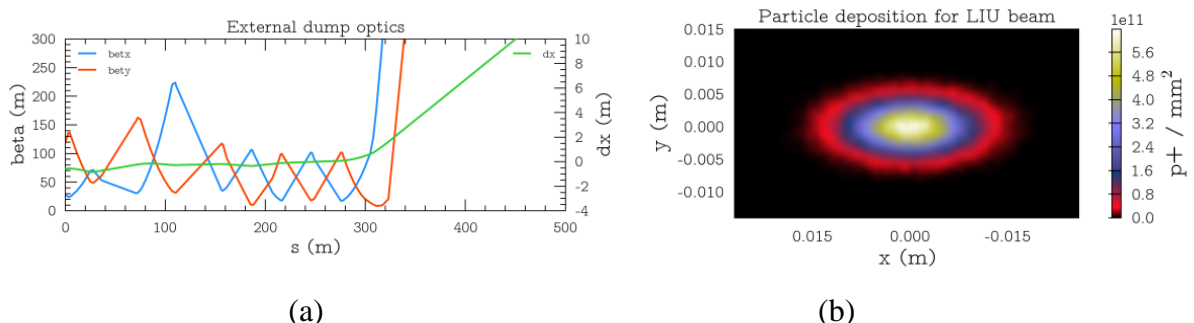


Fig. 5.89: (a) Optics from the SPS LSS4 extraction point to the external absorber block. (b) Particle distribution on the dump block for an LIU-BCMS beam.

5.9.2.2 Extraction from LSS6

The SPS beams that are extracted from LSS6 pass through the transfer line TT60. Once in this transfer line, the beams have two options: a set of eight C-shaped MBS magnets deflect the beam either to TI2 for LHC injection (left, power off) or to HiRadMat (right, power on). The distance between the two

beamlines is further increased by using independent bending magnets. One possible location for the beam dump is the central tunnel in Fig. 5.90, called TT61, as it is not currently used.

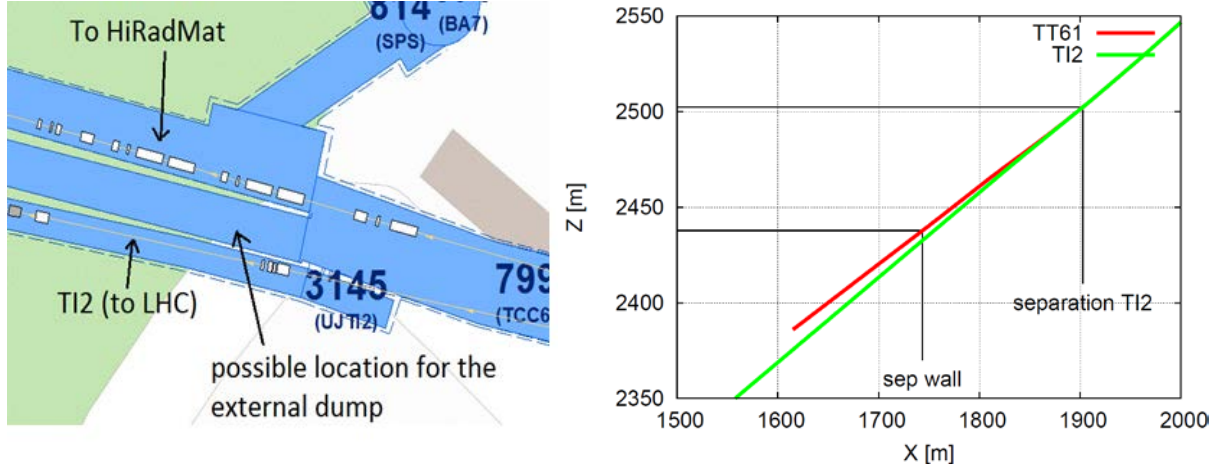


Fig. 5.90: (a) TT60 tunnel branch off into TT61, TT66 and TI2. (b) Geometry of the TT61 and TI2 transfer lines

Once the beam is totally separated from TI2, we currently apply a horizontal deflection to bend the beam to the right towards HiRadMat. After TT66.QTLD.660200, this deflection is done by two MBBs with positive magnetic field. These magnets would therefore be substituted by a set of four C-shaped magnets (MBS), which would make the switch between both lines (TT61 and TT66). They would be powered at zero current for the beam dump option. Downstream, another set of four MBS magnets would be needed. They would have a powering option opposite to the previous one: off for HiRadMat and on for beam dump (negative sign of the magnetic field). After the two sets of switches, two pairs of bending magnets need to be installed, each of them with opposite sign, in order to reach the tunnel with the proper angle and at the required position.

The option of dumping the beam following the same inclination as for the tunnel is discarded. A large amount of muons above 1 GeV would be produced, and this would require shielding the tunnel with more than 100 m of iron. Active shielding, i.e., by means of a dipole magnet that could bring the muons out of the tunnel does not appear to be a feasible option, due to the large energy spectrum of the muons and the fact that antimuons are also produced. For these reasons, the dump should be horizontal, with zero slope (Fig. 5.91). This is the safest option from the radio-protection point of view, as the muon shower generated by the protons on the target, which would produce intolerable levels of radiation, does not reach the surface. This would require the excavation of the tunnel by about 3.5 m (Fig. 5.92(a)). The location of the dump has been defined so that it is at least 3 m from the adjacent area (Fig. 5.92(b)), meaning the radiation does not influence the sensitive equipment in HiRadMat.

An alternative option to reduce/limit the civil engineering work required is to find the optimum dump block inclination. This angle has to be defined to obtain the required muon shielding from the earth profile.

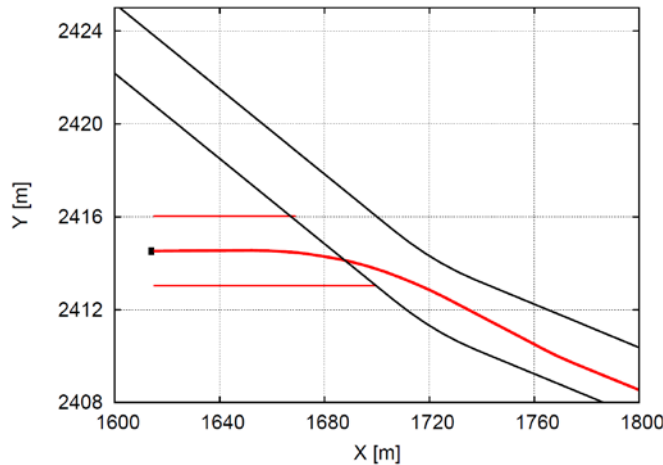


Fig. 5.91: Vertical cross-section of the actual TT61 tunnel (in black) and proposed beam trajectory (in red)

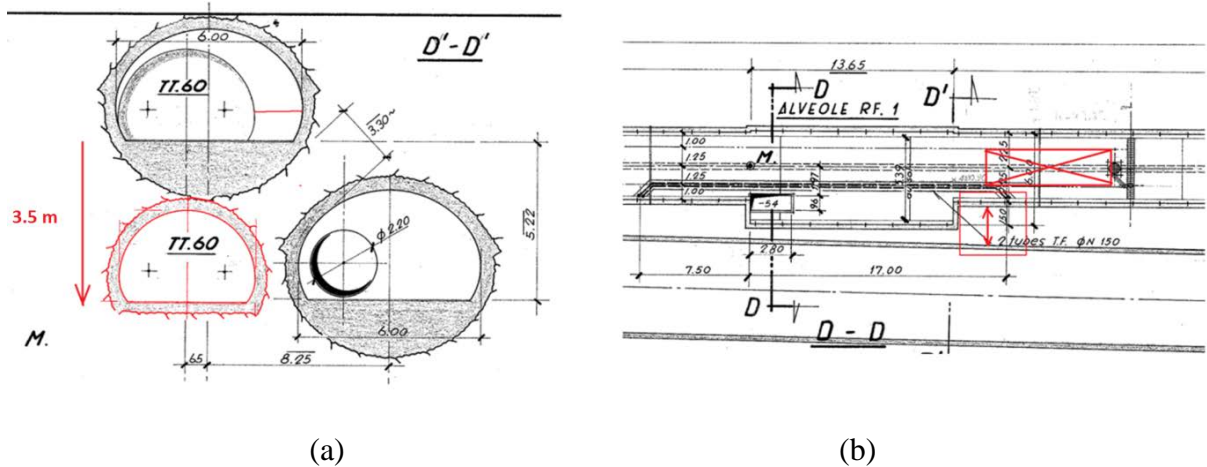


Fig. 5.92: (a) Vertical section and (b) horizontal section drawings of the two tunnels, indicating a possible location for the beam dump.

5.9.3 Conclusions

The SPS internal beam dump has been presented, and known issues of the current system, together with already proposed upgrades, have been summarized. The design of an external beam dump system has started, considering two different locations for it.

Concerning the internal dump system, the foreseen upgrades of the kicker powering system will contribute to solving or alleviating the current issues. Studies are also on-going to reduce dump block outgassing. Further studies are still required to quantify the effect of the possible failure scenarios on the absorbing blocks and the whole machine equipment. A conceptual design report on the LIU-SPS TIDVG will be released soon.

The design of an external dump for LIU and HL-LHC beams has started. Two possibilities are currently being investigated. Both will require civil engineering work to host the absorber block, taking into account all the constraints, such as air activation and the secondary showers produced. More detailed studies will be done to quantify the feasibility and reliability of these external systems while optimizing the available resources.

5.10 SPS to LHC transfer line collimators

5.10.1 Motivation

The maximum energy stored in the beam transferred and injected from the SPS to the LHC for LIU is 4.8 MJ, enough to damage accelerator equipment if lost in an uncontrolled way. Monitoring systems are in place to stop SPS extraction in case of, for example, wrong currents in magnet power supplies. Transfer line collimators (TCDIs) are located at the end of the lines to catch fast failures that can occur while the beam is already extracted. The transfer line collimators were originally designed to withstand 288 bunches of ultimate LHC intensity with 25 ns spacing and to attenuate the beam to a safe level for downstream equipment and the LHC. The normalized brightness N_0/ε_0 in the beam for LIU BCMS is a factor of 3 higher than that for which the TCDIs were designed. For the LIU era, the current TCDIs would not be able to guarantee protection and would not be robust enough to survive beam impact. Therefore the LHC transfer lines will need a new collimation system for LIU beam operation

5.10.2 Requirements

5.10.2.1 Attenuation

The LHC transfer line collimation system consists of three collimators per plane with 60° phase advance between two collimators to guarantee full phase space coverage. In this way it is a generic protection system, protecting against any failure upstream of the collimation section. The original design is described in detail in Ref. [95].

From the TT40 damage test [90], a protection device at 450 GeV needs to attenuate the TT40 test normalized beam brightness to $2.3 \times 10^{12} \text{ p}^+$ in 3.5 μm emittance to not damage copper (Cu) (for perpendicular impact and for a typical range of beta functions, conservative). For ultimate intensity this corresponds to a reduction of the brightness by a factor of 20.

$$\frac{2.3 \times 10^{12}}{3.5 \times 10^{-6}} > \frac{N_{\text{after TCDI}}}{\varepsilon_{\text{after TCDI}}} = \frac{N_0}{\varepsilon_0} \cdot \frac{1}{A} = \frac{288 \cdot 1.7 \times 10^{11}}{3.5 \times 10^{-6}} \cdot \frac{1}{20}. \quad (5.2)$$

For the LHC nominal to ultimate beams, this condition is fulfilled with 1.2 m-long graphite transfer line collimators. The design of the LHC ring collimators with exactly that length was therefore adequate. The differences from the ring collimator system are cooling and jaw tapering. Cooling is not needed in the transfer lines nor tapering of the jaws for RF fingers. The transfer line collimation system was completed with stainless steel masks in front of the downstream magnets to protect them from particle showers started in the collimator.

The proposed beam parameters required from the injectors for the LHC high luminosity operation are summarized in Table 5.7. For the most stringent scenario, with BCMS beams, the required *attenuation factor from the TCDIs* is 64. This implies making the TCDIs longer while keeping the material density low for the reason of robustness. For graphite R4550 (1.83 g/cc) or BN5000 (1.9 g/cc) it would require an active jaw length of 1.9 m, conservatively neglecting the blow-up due to multiple Coulomb scattering.

Table 5.7: LIU beam parameters assumed for TCDI studies, 288 bunches per SPS transfer

	Bunch population ($\times 10^{11}$)	ε (μm)
LIU nominal	2.3	2.1
LIU BCMS	2.0	1.3

5.10.2.2 Robustness

The impact of a full LIU 25 ns batch on a TCDI collimator will create high stresses in the material. Particularly problematic are tensile stresses in graphite and carbon materials in the case of shallow impact parameters in the order of 1σ . The temperature and hence maximum stress is reached in the first 20 cm of the jaw, see Fig. 5.93. The larger the beam size at the collimator, the lower the stress in the material. It has therefore been decided to discard a number of the current TCDI locations with too small beta functions. The new TCDI locations should provide a spot size of at least 0.16 mm^2 for a BCMS beam:

$$\sigma_x \cdot \sigma_y > 0.16 \text{ mm}^2 \quad (5.3)$$

This corresponds to a maximum temperature increase of 1500°C in graphite materials for LIU BCMS beam impact.

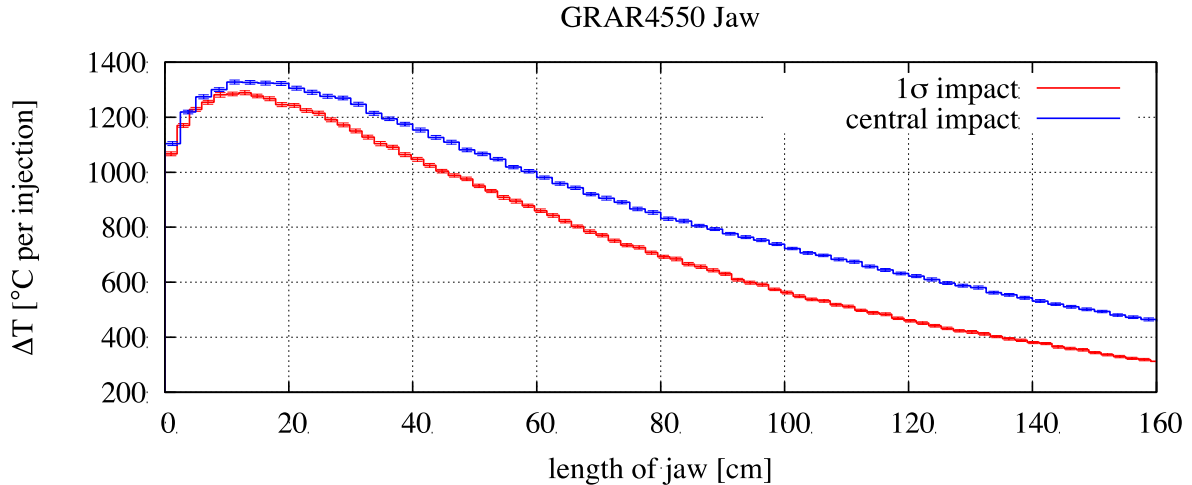


Fig. 5.93: Maximum increase in temperature along the collimator jaw for different impact parameters in graphite R4550 with BCMS beam at the TCDI in TI 2 with the smallest spot size, but fulfilling the spot size criterion. $\beta_x = 39.74 \text{ m}$, $\beta_y = 105.17 \text{ m}$.

However, even with this increased spot size with respect to the original TCDI locations, the stresses are above robustness limits for materials like graphite or boron-nitride; see Table 5.8 for graphite. The relevant robustness criterion for graphite is the Mohr-Coulomb criterion. For the material to survive a certain stress load, the safety factor F_s has to be larger than 1. The definition of this safety factor is:

$$F_s = \left[\frac{\sigma_1}{\sigma_{\text{Tensile limit}}} + \frac{\sigma_3}{\sigma_{\text{compressive limit}}} \right]^{-1} \quad (5.4)$$

where σ_1 is the maximum principal stress at a given point in the material and σ_3 the minimum principal stress. For LIU BCMS beam impact in a graphite TCDI, $F_s = 0.9$ at the most critical point in the material.

A number of other materials such as silicon carbide or even lower density carbon fibre-reinforced carbon have been investigated with Fluka and ANSYS. None of these are suitable. A summary of advantages and disadvantages of the most promising materials is given in Table 5.9.

Table 5.8: Stress maxima from ANSYS calculations in a TCDI jaw of graphite R4550 for a 1σ impact parameter of LIU BCMS beam, full batch. Values exceed the limit for tensile stresses. No dynamic effects (e.g. shock waves) have been included.

Traction		Compression		Maximum T
Maximum value (MPa)	Limit (MPa)	Maximum value (MPa)	Limit (MPa)	(°C)
32	29	80	118	1400

Table 5.9: Compilation of materials tested in simulation. Material density, advantages and disadvantages are listed.

Material	Density (g/cc)	Advantage	Disadvantage
BN5000	1.9	Low-density material Excellent material properties at low temperatures	Poor material properties at high temperature (Expected temperature $\sim 1300^\circ\text{C}$ for LIU beam impact)
Graphite R4550	1.8	Low-density material. Known material available in bulk block pieces for collimator jaws	LIU foreseen load above tensile stress limit
CFC	1.7	It might be able to withstand the beam in case orientation of fibres follows the maximum and minimum principal stress direction through the material	Available properties to be confirmed Manufacturing issues: difficulty in guaranteeing a surface flatness below 40 μm , in making bulk block pieces with the fibres in preferred directions, etc. ANSYS is not able to simulate what happens at the interface matrix–fibre. HiRadMat tests are needed Principal stress directions are strongly dependent on material properties, very often really hard to obtain from the suppliers. Material characterization tests are needed

As a consequence of these investigations, the LIU TCDIs are currently being planned as sacrificial absorbers to be replaced in the case of full beam impact. The design of the support and vacuum systems has to be done such that quick removal and installation of a spare is possible (quick plug-in like LHC ring collimators [96]). The new locations of the TCDIs in the transfer line should allow easy access.

Studies are ongoing to try to avoid this potential complication for LIU operation with TCDIs. For instance, the feasibility of increasing the beam size at the TCDIs even further should be considered.

5.10.3 LIU TCDIs for TI 2 and TI 8—possible layout

For reliability and sufficient flexibility, collimators longer than ~ 1.5 m are produced in several modules. An obvious solution for the transfer line collimators would therefore be to reuse the existing TCDI design from LHC runs 1 and 2 and install at each LIU TCDI location two original 1.2 m-long

TCDIs. A schematic of the new LIU TCDI assembly is shown in Fig. 5.94. The total required length in the transfer line is 3.5 m per collimator location.

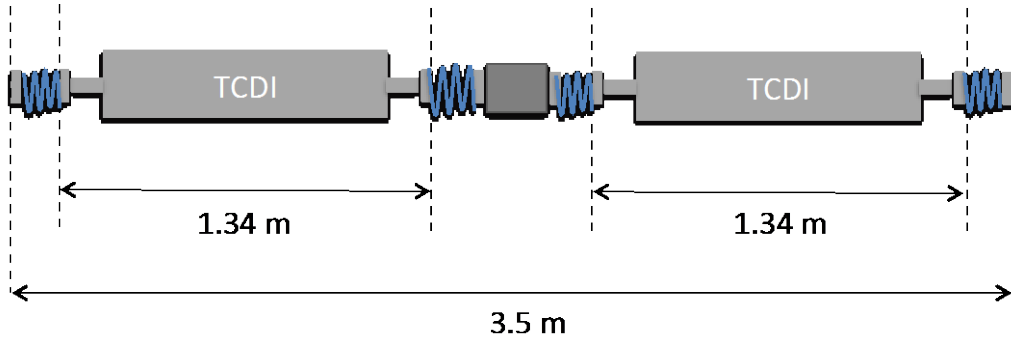


Fig. 5.94: Layout of $2 \times$ TCDI assembly for LIU. The total length required is 3.5 m. A double bellows is used between the TCDIs to have the possibility to exchange just one in the event of damage. A vacuum pumping port can be installed at the beam pipe between the bellows.

In TI 2 enough space and flexibility with optics are available at the current locations to reserve 3.5 m for the LIU TCDIs. The proposed locations also include the required 5 m distance to the downstream element. Table 5.10 gives the preliminary locations of the end of each collimator ensemble. No integration studies have been carried out to check possible interference with vacuum equipment and the requirement of new masks in front of quadrupoles.

Table 5.10: Preliminary locations of 3.5 m-long TCDI collimator assemblies in TI 2. The spot size at the collimators and the phase advance between two neighbouring TCDI couples are also given. An emittance of $2.1 \mu\text{m}$ is used for the spot size.

TI 2	s (exit) (m)	β_x (m)	β_y (m)	$\sigma_x \sigma_y$ (mm 2)	$\Delta\mu$ ($^\circ$)
TCDIH.NEW1	2970.130	94.642	77.24	0.374	0.0
TCDIH.NEW2	3016.370	45.9	94.59	0.289	60.2
TCDIH.NEW3	3096.170	50.227	219.54	0.46	54.1
TCDIV.NEW1	2952.67	237.79	22.59	0.32	0.0
TCDIV.NEW2	3026.57	72.94	64.56	0.30	57.4
TCDIV.NEW3	3109.17	50.50	223.54	0.47	61.6

Space and optics are more constrained in TI 8. In this first version the spot size criterion, 5 m distance to the next element and 3.5 m-long spaces for transfer line collimators in TI 8 could only be achieved by adding 10 quadrupole power supplies to increase the number of individually powered quadrupoles, see Table 5.11, and shifting one quadrupole plus corrector, BPM and mask, see Table 5.12. The new LIU TCDI locations are given in Table 5.13. One additional vertical collimator (not in Table 5.13) would be needed in front of the MSI to protect the vertical aperture bottleneck at that location. As for TI 2, interference with vacuum elements has not been checked. A detailed integration study will have to come.

Table 5.11: List of individually powered quadrupoles in TI 8 needed to host the LIU transfer line collimators as presently proposed:

Quadrupole
QIF.86200
QID.86300
QIF.86400
QID.86500
QIF.86600
QID.86700
QIF.86800
QID.86900
QIF.87000
QID.87100

Table 5.12: Elements in TI 8 that need to be shifted to make space for the 3.5 m-long transfer line collimator ensemble. Details need to be finalized.

Element	Moved by (m)
TCDIM.87658	−4.252
MQID.87700	−4.252
BPMI.87704	4.363
MCIAV.87704	4.443

Table 5.13: Preliminary locations of 3.5 m long TCDI collimator assemblies in TI 8. The spot size at the collimators and the phase advance between two TCDI couples are also given. The numbers refer to the exit of the collimators. An emittance of 2.1 μm is used for the spot size. One additional vertical TCDI in front of the MSI at an already existing TCDI location would be needed to protect the vertical aperture bottleneck at that location. It is not part of this list.

TI 8	s (exit) (m)	β_x (m)	β_y (m)	$\sigma_x \sigma_y$ (mm2)	$\Delta\mu$ ($^\circ$)
TCDIH.NEW1	2390.48	43.83	96.17	0.28	0.0
TCDIH.NEW2	2432.65	47.66	89.18	0.285	64.2
TCDIH.NEW3	2457.35	20.9	195.39	0.28	62.2
TCDIV.NEW1	2440.63	28.66	135.33	0.27	0.0
TCDIV.NEW2	2504.06	181.36	23.38	0.29	58.5
TCDIV.NEW3	2550.25	89.81	100.56	0.42	56.2

5.10.4 Summary and outlook

A new transfer line collimation system between the SPS and the LHC will be required for the LIU era. The brightness of the LIU beams will be a factor of 3 above that for which the collimators have been designed, and they will not attenuate the impacting intensity enough to protect equipment downstream. Another issue will be the robustness of the jaw material against beam impact.

Sufficient beam attenuation can be guaranteed by using two TCDIs, one after the other, per collimator location. Integrating the new TCDIs is currently being worked on in TI 2 and TI 8. To date, however, no material has been found that will survive LIU beams at the new locations of the transfer line collimators. The new TCDIs are therefore sacrificial absorbers and need to be replaced in the event of beam impact.

Further studies are ongoing to fully exploit the optics flexibility in the transfer lines and increase the spot sizes at the collimator locations as much as possible. This could possibly remove the

robustness limitation. A robustness test of a collimator jaw prototype in HiRadMat with LIU beam brightness is strongly recommended.

5.11 Beam instrumentation

5.11.1 Orbit and trajectory monitoring system upgrade

5.11.1.1 Introduction

The SPS orbit and trajectory measurement system consists of 216 beam position monitors (BPM) distributed along the SPS accelerator ring as summarized in Table 5.14. Most of them are single-plane electrostatic shoe-box pick-ups, based on linear-cut electrodes. The large aperture resonant BPMs (BPA and BPD), used in the injection and fixed target extraction regions have been replaced with strip-line BPMs during LS1. Apart from these modifications it is not foreseen to change the other pick-ups as part of the SPS orbit system upgrade.

Table 5.14: The currently installed BPM types used for position measurement in the SPS

Monitor types	Physical beam aperture (mm)	Quantity	Section	Comment
BPH	$44 \times 154 (v \times h)$	103	Rectangular	Electrostatic shoe-box
BPV	83×83	94	Square	Electrostatic shoe-box
BPA	269	4	Circular	Resonant cavity (LSS2)
BPD	269	2	Circular	Resonant cavity (LSS1)
BPCN	76	7	Circular	Strip-line BPM
BPCE	206	6	Circular	Strip-line BPM (LSS 4 and 6)
Total		216		

The current acquisition system is based on a homodyne receiver working at 200 MHz with four, individually switchable gain stages capable of covering a total dynamic range of 90 dB. Parts of this system date from the start of the SPS, with the last upgrade concerning the digital acquisition itself taking place over 10 years ago. In addition to the obsolescence of the electronics used and the limited spare parts available, the system is plagued by several issues, notably:

- the reliance on accurate phasing between long cables, many of which have to be periodically replaced due to radiation damage;
- position offsets depending on the bunch-filling pattern;
- a multiplicity of calibration tables to cope with the various gain settings possible.

It is nevertheless capable of providing turn-by-turn position measurements for the complete SPS acceleration cycle and orbit measurements with better than $50 \mu\text{m}$ rms resolution for high-intensity proton beams.

5.11.1.2 New system—introduction

The new SPS system being developed aims at replacing the existing electronics while maintaining or improving its performance taking into account the requirements from LIU.

The SPS currently accelerates proton and lead-ion beams. Proton bunch spacing extends from 5 ns up to 23 μs with a bunch charge dynamic range from $\sim 1 \times 10^9$ to 50×10^{10} . Pb^{82+} bunch spacing varies from 75 ns to 125 ns with a bunch charge from $\sim 5 \times 10^8$ to 2×10^{10} . The typical machine parameters for protons and lead ions have been reviewed to comply with the foreseen LHC injector

upgrade programme [97]. Table 5.15 summarizes the parameters for the different cycles currently available in the SPS.

Table 5.15: SPS beam types expected for the LHC operation period. The nominal number of batches (N_{bat}) varies between one and four for protons, but exceptionally this number can be larger for SPS MDs (up to eight for electron cloud studies). For ions the number of batches is in the range 1–13.

Type	Bunch spacing (ns)	Bunch number	Bunch charge (10^{10})	Bunch length (4σ , ns)
FT/CNGS	5	400–4000	0.1–2	1–4
LHC25NS	24.96	$N_{\text{bat}} \times 72$	1–50	1–4
LHC50NS	49.92	$N_{\text{bat}} \times 36$	1–50	1–4
LHC75NS	74.88	$N_{\text{bat}} \times 24$	1–50	1–4
LHC single bunch	524.4–2022.6	1–16	0.2–50	1–4
LHC ion/Pb ⁸²⁺	100	$N_{\text{bat}} \times 4$	0.05–2	1–4

Bunch charge spans a dynamic range of 74 dB, assuming that special ion operation will not go below 5×10^8 charges per bunch. With the additional 6 dB required to account for the effect of position variations in BPM signals, the full dynamic range required for position processing electronics is ~ 80 dB.

5.11.1.3 New system—specifications

The following acquisition modes have been requested

- Closed orbit: the system will provide a closed orbit measurement every millisecond (single gated PS batch, averaged over 40 turns) for each SPS cycle (up to 100 s).
- Injection: the system will automatically publish the 50 first turns of each cycle (one measurement per batch, for every PS batch).
- Trajectory: the system will provide up to 10 000 turns of trajectory data for a selected PS batch for all channels per cycle.
- Extraction interlock: at least three BPMs around each fast extraction point (presently LSS4 and LSS6) will be used to interlock the beam position before extraction with connection to the SPS extraction interlock systems.
- Ring interlock: To protect the SPS ring against very fast beam position excursions two BPMs in each plane, separated in phase by $\sim 90^\circ$ will be capable of directly dumping the beam by providing an input to the SPS ring beam interlock loop.

It is specified that the new system will have a closed-orbit position resolution for LHC-type beams of 0.4 mm to 0.1 mm for bunch intensities of 2×10^9 to 2×10^{11} charges respectively over $\pm 20\%$ of the BPM aperture. Turn-by-turn resolution for the same intensity range will be between 1 mm to 0.4 mm, while the absolute accuracy will be better than 0.5 mm rms excluding mechanical alignment tolerances.

The interlock modes will, as far as possible, be independent of fast timing signals and not require cycle specific gain settings.

The beam-synchronous timing, currently distributed in the SPS surface buildings, will allow using both RF-related signals and pre-programmed events. To keep the acquisition synchronous to selected batches, the system will use the turn clock (43.4 KHz SPS revolution frequency), bunch clock (40 MHz for LHC beams) and injection pre-pulses.

5.11.1.4 New system—electronic acquisition chain

In order to cope with the high dynamic range required, while still being able to measure individual PS batches, the analog front-end electronics will be based on logarithmic amplifiers.

5.11.1.5 Position measurement principle

Beam position x can be derived from the logarithmic difference of BPM signals on opposite electrodes A and B as follows:

$$x = \frac{A-B}{A+B} \Leftrightarrow \frac{A}{B} = \frac{1+x}{1-x}. \quad (5.5)$$

Consider the series expansion of the natural logarithm:

$$\ln \frac{1+x}{1-x} = 2 \left(x + \frac{x^3}{3} + \frac{x^5}{5} + \dots \right). \quad (5.6)$$

Converting to decibels and using the first term leads to:

$$\log \frac{A}{B} \cong 2 \frac{x}{\ln 10}. \quad (5.7)$$

Then, for small beam displacements, the log ratio gives a good approximation of x :

$$x = \frac{\ln 10}{2} (\log A - \log B). \quad (5.8)$$

5.11.1.6 Front-end electronics

The architecture of the front-end electronics [98] is depicted in Fig. 5.95.

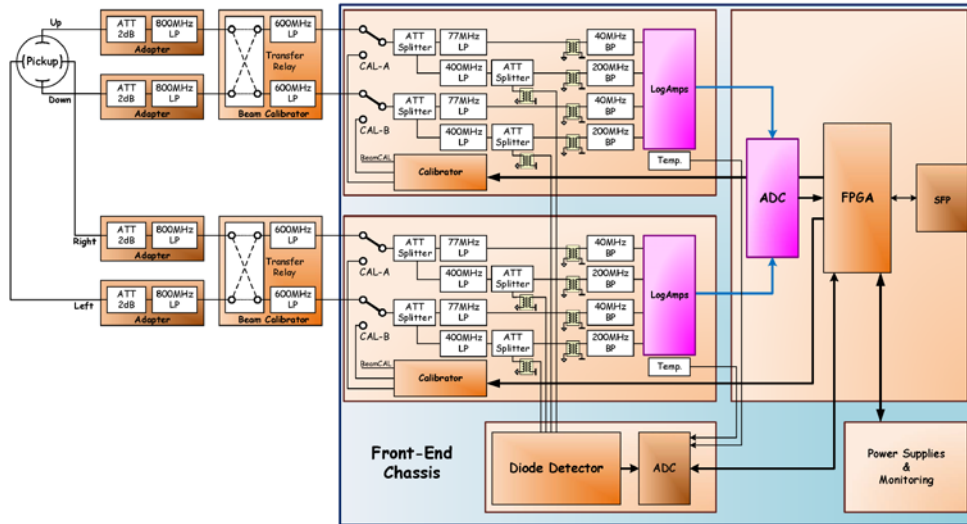


Fig. 5.95: Front-end electronics diagram for the new SPS orbit and trajectory system

In order to reduce both power dissipation and bunch length dependence during beam acceleration, the low-pass filtering scheme has been distributed over three elements: the pick-up adapter that performs electrode impedance matching, the beam-based calibrator circuit and the input filters in the front-end chassis. The signals from each electrode are split into three parallel detection chains (40M Hz low and high sensitivity and 200 MHz) with different input filters and gain stages to

cover the high dynamic range and the different beam patterns possible in the SPS. Signals from opposite electrodes are processed by the same dual logarithmic amplifier.

Optional diode detectors [99] are foreseen, in parallel to the logarithmic processing chain, to achieve even more accurate orbit measurements. The resulting position and intensity information is digitized using an octal 14-bit 10 MSa/s ADC. Finally, the data are serialized and transmitted through optical fibres [100] over long distances (up to 1 km) to the VME digital acquisition hardware [101], which is located in six auxiliary surface buildings.

The front-end integrates both internal and beam-based calibration capabilities using RF switches, remotely controlled via the optical link.

The front-end board is designed to be located in the tunnel, where a dose rate of 100 Gy/y is expected in the worst condition. For this reason, analog components, such as logarithmic amplifiers, ADC-drivers and voltage regulators, as well as several families of small form-factor (SFP) bidirectional optical transceivers have been tested for radiation hardness [102].

Additional radiation hardness tests will be performed in the SPS and at the PS-CHARM facility in order to validate the final version of the digital front-end electronics.

5.11.1.7 Acquisition system architecture

The front-end electronics will be located in dedicated crates underneath the beam-pipe in the SPS tunnel. Each station will transmit its data via a radiation-hard optical link to the associated surface building (BA). The use of such radiation-hard optical links has been a success in the LHC, considerably reducing installation costs by eliminating the need for long, high-quality coaxial cables. A complete fibre-optic infrastructure is therefore being installed in the SPS by the EN-EL-CF team, which is dimensioned to fulfill the requirements of a future BLM upgrade. This installation will be completed during LS2.

The surface buildings will contain the VME-based digital processing electronics and CPU ultimately providing the position data to applications in the control room. These electronics will be based on a new VME FMC carrier (VFC) board developed by the BE-BI group and is foreseen to be the common acquisition platform for the majority of future BE-BI developments. This is equipped with a large FPGA, substantial memory and four SFP inputs for the orbit system along with one SFP for Ethernet and one SFP for beam synchronous timing.

Deployment of a test system is foreseen in 2014, followed in 2015 by one full BA equipped with non-radiation-resistant front-ends working in parallel to the existing system. Full deployment of the radiation-qualified electronics in all BAs will take place in LS2.

5.11.2 Fast beam current transformer system upgrade

The fast beam current transformer (BCT) system in the SPS is specified to measure individual bunch intensities for LHC beams at a level of 1%. The current system suffers from several shortcomings that make this impossible. First of all, despite the relatively high overall bandwidth of the system, imperfections in the toroid design combined with the long cables used mean that a proportion of the signal from each bunch inevitably leaks into the next 25 ns slot. In addition, recent observations in the LHC have unveiled a dependency on the beam intensity measurement both with beam position and bunch length.

This system is essential for understanding the origin of instabilities leading to beam losses and for optimizing other accelerator systems such as the RF and correctly gating injection kickers. It is therefore foreseen that both the detector and acquisition systems will be upgraded to provide a true bunch-by-bunch measurement capable of fulfilling the specifications.

The choice of detector will be between a commercial (ICT) toroid being developed in collaboration with Bergoz Instrumentation, St-Genis-Pouilly, France and an in-house development based on a wall current transformer (BCWT), with a design similar to the inductive pick-ups used in CTF3. These are currently being installed for testing in the LHC, where their performance will be verified with beam at the beginning of 2015. If the beam tests prove to be conclusive, the best solution will be adapted for installation in the SPS ring during LS2.

The principle of the integrating current transformer (ICT) being developed by Bergoz Instrumentation is sketched in Fig. 5.96. It consists of two magnetic cores (4) enclosed in a common copper shell (1) installed over a ceramic insert (6) on a conducting beam pipe (8). A dielectric slit (2) incorporated into the copper shell allows the capacitance of the shell to be influenced by external capacitors (3). In this configuration the copper shell is seen by the magnetic cores as a single-turn primary winding that induces current in the secondary winding (5) of the ICT.

The capacitive copper shell significantly limits the spectrum of the current seen by the magnetic cores, resulting in an output pulse much longer than the beam pulses. When the beam passes through the ICT, it induces an equal but opposite charge on the capacitive shell. This charge is temporarily stored in the shell capacitance. As the shell, loaded by the magnetic cores, discharges an electric current flows. This current is seen by the encased toroids as a single-turn primary winding.

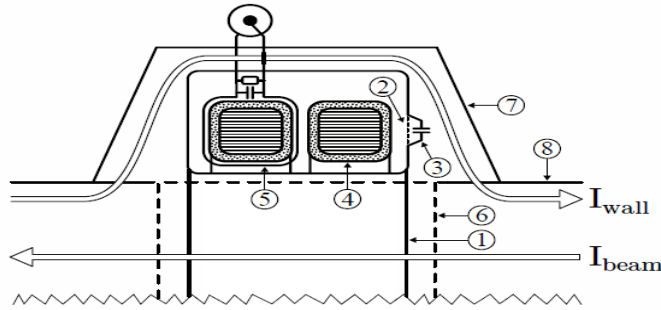
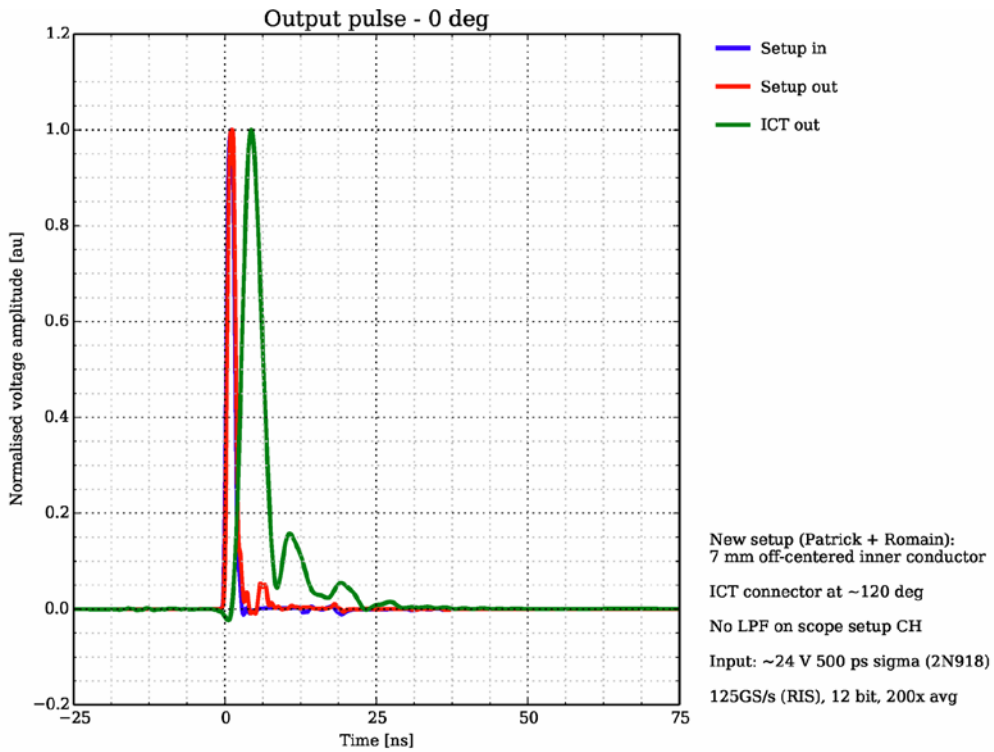


Fig. 5.96: Cross-section through an integrating current transformer

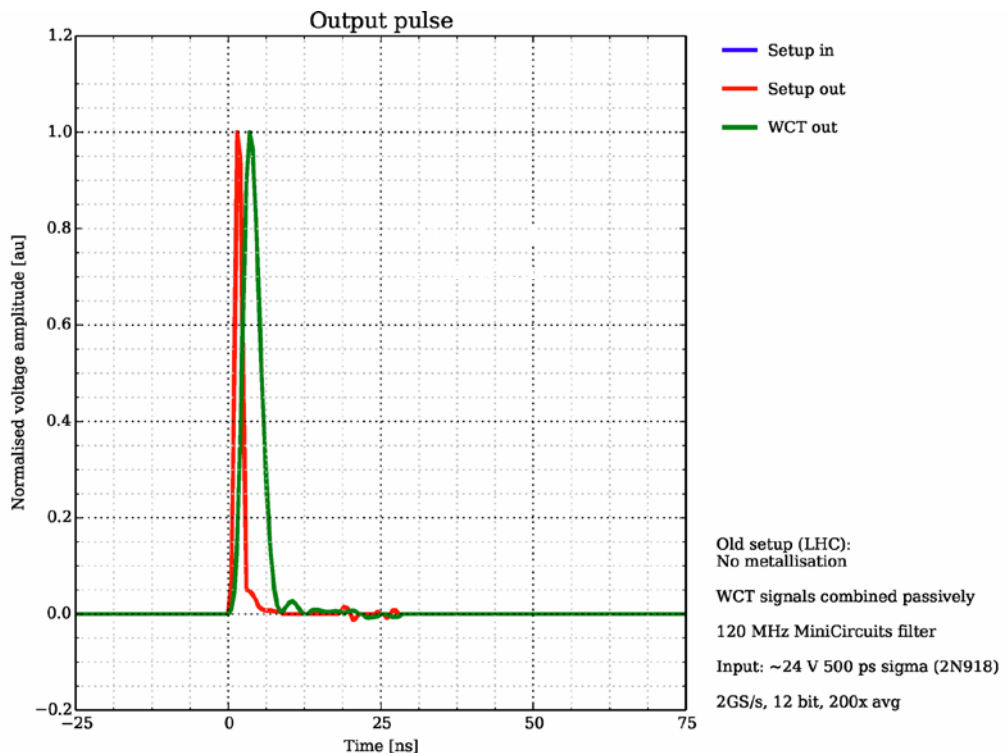
The pulse response of the Bergoz ICT measured in a coaxial set-up is shown in Fig. 5.97 (green curve). Some ringing at the end of the pulse leaking into the next 25 ns bunch slot can be observed. The charge carry-over to the following bunch slot is estimated to be 2.4%, which could be corrected for by de-convoluting the response in the time domain.

In the CERN-developed WCT the beam image current passes through the primary windings of RF transformers. The secondary windings are combined to one output, providing the beam current signal. The WCT is built in two halves and can be clamped onto an existing vacuum chamber, without any need to open the beam vacuum. A first prototype has been built and tested in the laboratory. The result is the excellent impulse response shown in Fig. 5.98, with 99.8% of the charge being collected within the first 25 ns bunch slot.

The acquisition electronics for this monitor will also be upgraded, making use of the fast sampling, high-resolution ADCs now commercially available. Studies have shown that less than 1% measurement error can be achieved by sampling the output from either the ICT or WCT at 500 MHz with 11 effective ADC bits. The proposal is therefore to buy a commercially available, fast-sampling FPGA Mezzanine card (FMC) capable of being mounted on the new BE-BI acquisition platform (VME FPGA card (VFC)) being developed for future upgrades, including the LIU-funded SPS orbit system.

**Fig. 5.97:** Pulse response of the Bergoz ICT

A first prototype has been built giving the excellent impulse response shown in Fig. 5.98, resulting in 99.8% of the charge being collected within the first 25 ns bunch slot.

**Fig. 5.98:** Pulse response of the CERN WCT

5.11.3 Head-tail monitor system upgrade

The current system was designed to measure chromaticity but has subsequently mainly been used for the observation of beam instabilities. A schematic layout of the SPS head-tail monitor set-up is shown in Fig. 5.99. A 60 cm-long strip-line coupler followed by a 180° hybrid provides the sum and difference signals for each measurement plane. This length of coupler allows the wanted signal and reflection from the downstream end of the strip-line to be fully decoupled for bunches of up to 4 ns in total length. These signals are fed into a fast-sampling (>2 GS/s), high analogue bandwidth (>2 GHz) digital oscilloscope that is connected to a VME front-end acquisition crate via an Ethernet link.

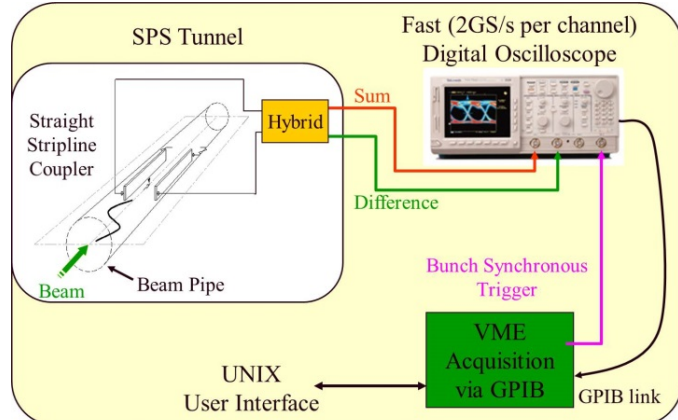


Fig. 5.99: Original head-tail monitoring system in the SPS

The oscilloscope is triggered by bunch synchronous timing signals. Combining this with the fast-frame capabilities of the oscilloscope allows one bunch (25–50 ns worth of data) to be captured over many SPS turns (up to 2000). In this way it is possible to track the evolution of the signal from a single, specific bunch. Even though the bunch synchronous timing has an rms jitter of only 100 ps, the sum signal still has to be acquired to enable the difference signal to be accurately re-aligned for each turn. In this way, the timing jitter is reduced to well below the sampling frequency.

The main aim of upgrading the existing head-tail monitor is to allow even more detailed observation of transverse intra-bunch instabilities. Compared to the existing system, a higher sampling rate and much larger memory buffer is required. The current oscilloscope will therefore be replaced by modern fast digitizers. A recent market survey identified a new product that provides an analogue bandwidth in excess of 8 GHz with a sampling speed of 20 GS/s. The board has an internal memory of 16 GB, enabling the storage of up to 1 s worth of data at the full sampling speed. It is also equipped with a powerful FPGA to filter and pre-process the data. A first unit was purchased in 2013 and will be tested in the PS for ghost and satellite detection during 2014. If this proves successful, a full deployment in the SPS is then foreseen for the 2015 run.

5.11.4 Upgrade of the SPS synchrotron light monitor

Visible synchrotron radiation (SR) in the SPS was measured for the first time in late 1979, when an experiment aiming at observing dipole edge radiation emitted by relativistic protons was successfully carried out. It consisted of a light intensity measurement using a photomultiplier, and image acquisition using a Vidicon camera with a silicon target. Signals on the photomultiplier were detected from a proton beam as weak as 10^{11} particles, while images were captured for energies greater than 350 GeV and a proton intensity higher than 6×10^{12} . Following this experiment, visible synchrotron radiation was used during ppbar operation to monitor the beam size evolution while in store. Since then the system has only been used periodically for testing and has been, for several years, no longer operational.

In order to continually monitor the brightness of the SPS beams to the LHC a monitor capable of measuring the beam size at extraction is required. Until now the SPS has relied on the use of wire scanners, but this has two drawbacks. Firstly the instrument lifetime is compromised if used systematically on each SPS pulse, and secondly wire damage is possible when used with high-brightness beams. A profile monitor based on synchrotron light could solve both of these issues. It is therefore planned to refurbish the SR monitor of the SPS as part of the LIU project.

The synchrotron light extraction system of the SPS is located in LSS5. The visible SR light is generated from the falling edge of the MBB52130 dipole and rising edge of the MBB52150 dipole. It is extracted after 19 m using an in-vacuum rectangular mirror (BRSC). The system refurbishment focuses mainly on re-designing and re-implementing the optical system used to guide and focus the SR light, and the deployment of a new camera. The calibration target (BSRF) installed between the two dipoles will also be upgraded to allow for a better alignment accuracy of the optical system and to measure its magnification.

5.11.5 Spectral components of the source

Figure 5.100 shows the calculated extracted power spectrum (integrated over the area of the extraction mirror) of the visible edge radiation emitted from the two bending magnets. The calculations show that the SR is concentrated above 500 nm, thus the lenses to be used should be optimized for near-infrared operation. Figure 5.100 also shows a comparison with the light emitted by the same bunch passing through the LHC undulator at 450 GeV. Experience with this LHC undulator radiation, using the same type of camera proposed for the SPS, has shown that for these light intensities it is possible to measure a single pilot bunch (5×10^9 protons) in a single turn.

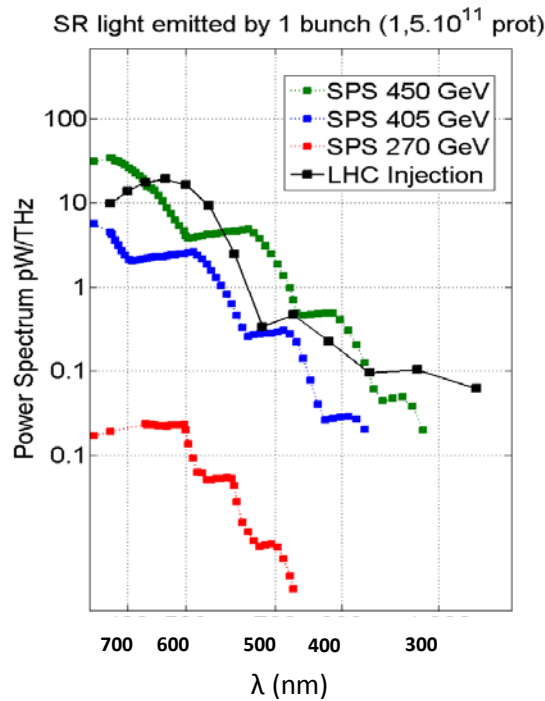


Fig. 5.100: Power spectrum of the visible SR integrated over the area of the extraction mirror

5.11.6 Source size

Table 5.16 summarizes the optics parameters at the location of the SPS BSRT. For normalized beam emittances in the range 1–3 mm mrad, the corresponding beam size at the BSRT location are 534–644 μm in the horizontal plane and 394–682 μm in the vertical plane. The horizontal dispersion value is not negligible and increases the horizontal beam size by 109% for $\varepsilon_n = 1$ μm and by 46% for

$\varepsilon_n = 3 \mu\text{m}$ at 450 GeV. This implies that precise horizontal beam size measurements (5% error or less) are only possible if the momentum spread and the dispersion are known with good accuracy (combined error <10%).

Table 5.16: Optics parameters at the SPS BSRT location

	Horizontal	Vertical
Beta function (m)	31.147	74.55
Dispersion (m)	1.563 4	0

The new layout of the SR optics will consist of a two-stage imaging system using high-quality apochromatic lenses with a focal length of $f = 800$ mm and $f = 18$ mm, coupled to a gated, intensified, analogue camera. The present acquisition chain (analogue camera \Rightarrow frame grabber \Rightarrow software) is limited to about 16 frames/s but will be upgraded to 50 frames/s in the near future. Even with this increased frame rate, assuming that single-bunch-single-turn images can only be detected for energies above 400 GeV, this still means that only one PS batch of 72 bunches could be individually measured per cycle. In order to measure more batches the gate would need to be extended to cover groups of up to four bunches, which would nevertheless still provide a good indication of the general quality of the LHC beam in the SPS.

5.11.7 Plans and schedule

The modifications described above will be implemented during LS1 with the refurbished BSRT system tested at the restart of the SPS in 2014. After a first phase investigating the real working conditions (light intensity, background radiation, etc.) a detailed design for the control system will be prepared, including automatic dynamic settings to cope with light intensity variations during the cycle.

The hardware of the acquisition chain is foreseen to be upgraded in 2015 by introducing a faster frame grabber allowing the acquisition of images at 50 frames/s. A second upgrade phase is also foreseen in which the analogue camera is replaced by an intensified digital camera (ZYLA). This camera will initially be tested in the laboratory to assess its characteristics and develop the required control software. A test in a radiation environment (probably in the LHC where the radiation is lower than in the SPS) will also be needed to assess its suitability for the SPS.

5.11.8 Upgrade of the SPS ionization profile monitor

As part of the LIU project the upgrade of the SPS ionization profile monitor (IPM) will be completed, to make it identical to the one constructed for the LHC. An IPM collects electrons produced from the interaction of the beam with residual gas by accelerating them with an electric field and guiding them using a dipolar magnetic field. These electrons are then multiplied by an in-vacuum multi-channel plate detector and converted to light using a phosphor scintillator screen. The beam image is then registered using a specially-designed optical system and a radiation-hard camera. It is hoped that the upgraded system will be fully operational in 2014, providing average beam size measurements throughout the SPS cycle.

The camera currently used can be gated down to 10 ns, but the decay time of the phosphor (P46) is 300 ns, meaning that the system is unable to perform bunch-by-bunch measurements at 25 ns. If, at a later stage, a bunch-by-bunch measurement capability is to be introduced, then a faster phosphor or a readout concept similar to that foreseen for the new PS IPM would need to be implemented.

5.12 Vacuum system

5.12.1 Halving the length of long vacuum sectors

The longest vacuum sectors of the SPS are located in the arcs. Their length varies between from 400 m to 450 m, depending on the sector. The division of these vacuum sectors by installing new sector valves is advantageous because of the following.

- In the case of venting to air, the beam pipe length exposed to air is reduced and the vacuum cleaning and beam scrubbing are better preserved. This is of particular interest as far as electron cloud phenomena are concerned.
- Using the same number of turbomolecular mobile groups, the pumping time before starting the ion pumps is reduced and consequently the time of intervention.
- The longest vacuum sectors in the SPS ring are those ending in 10 (i.e. 110, 210, etc.) and 60 (i.e. 160, 260, etc.) with six (12 half cells) and seven (14 half cells) periods, respectively. They will be denoted as x10 and x60. Figures 5.101 and 5.102 show the layout of a long arc with arrows indicating the position of sector valves and the equivalent network.

An extensive calculation by means of the electrical network–vacuum analogy has been carried out to evaluate the effect of the modification on the pumpdown curves. Each component of the vacuum line has been represented by an electrical network that can be easily studied by means of dedicated software, for example LTSpice and PSpice. The vacuum conductance of each component of the vacuum line has been calculated by Molflow, a Monte Carlo-based software program written by R. Kersevan.

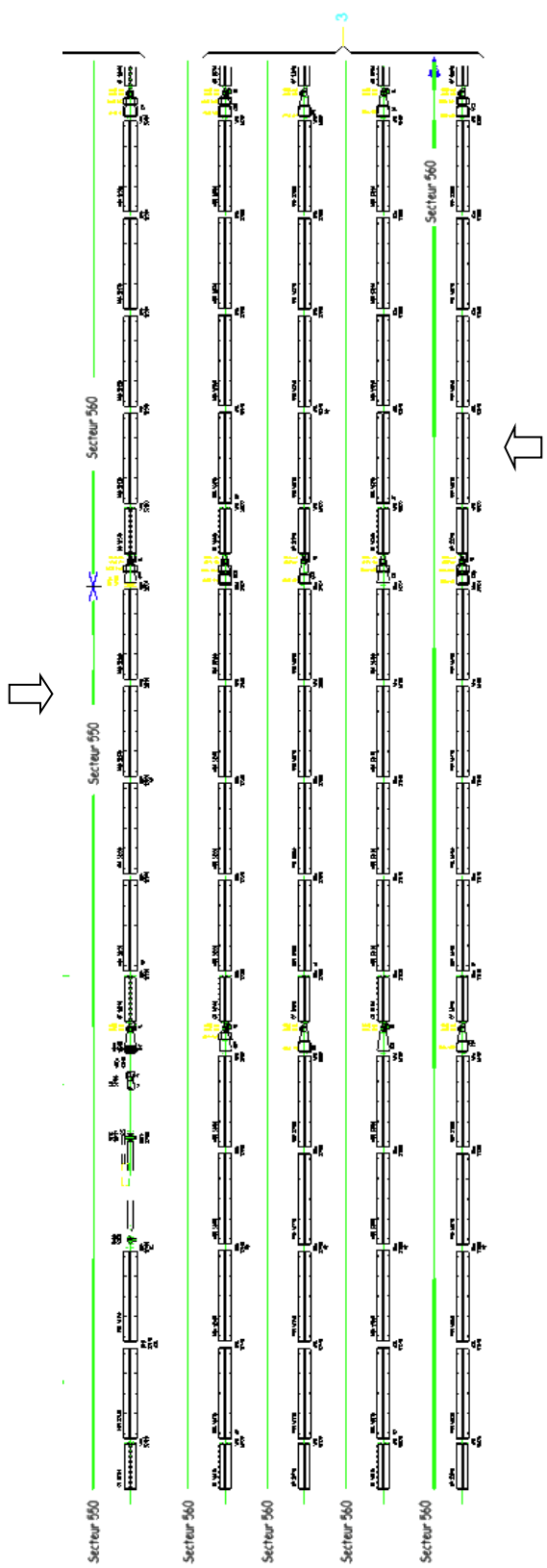


Fig. 5.101: Secteur 560 lay-out

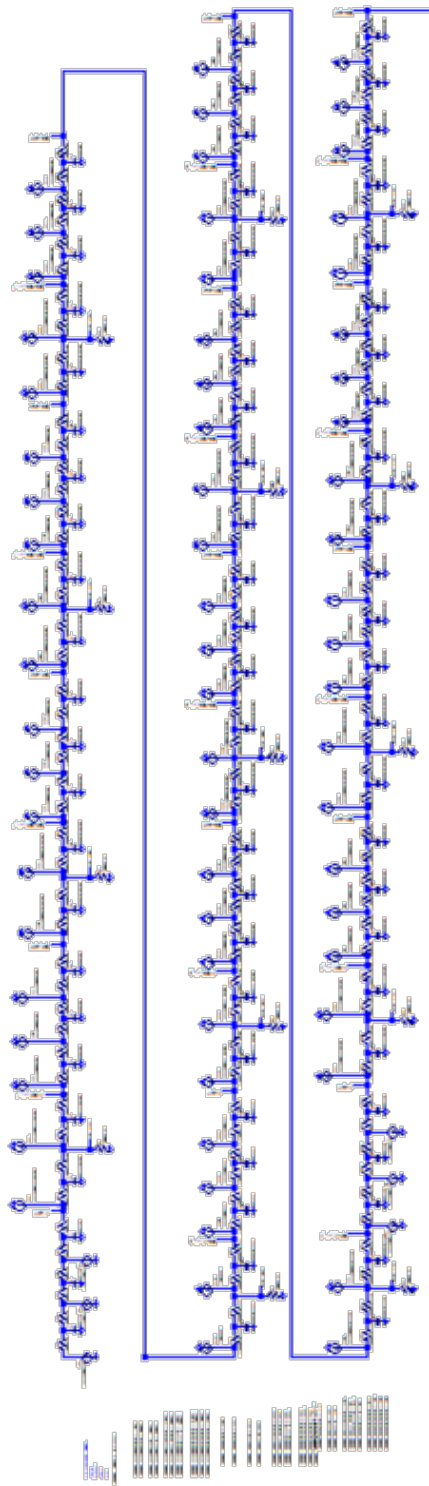


Fig. 5.102: Equivalent electrical network for sector 560

In Fig. 5.103 an example of calculated pumpdown is shown for an x10 sector. Firstly, air is pumped down to 10^{-2} mbar using one Roots pump ($30 \text{ m}^3/\text{h}$). Then, assuming an outgassing rate for water vapour of $2 \times 10^{-9} /t[\text{h}] \text{ mbar l/s cm}^2$ and using four 70 l/s TMP groups, the system is pumped down to 10^{-5} mbar. Finally, the ion pumps are switched on. The time required to switch on the ion pumps is reduced by a factor of 2 when the vacuum sector is halved.

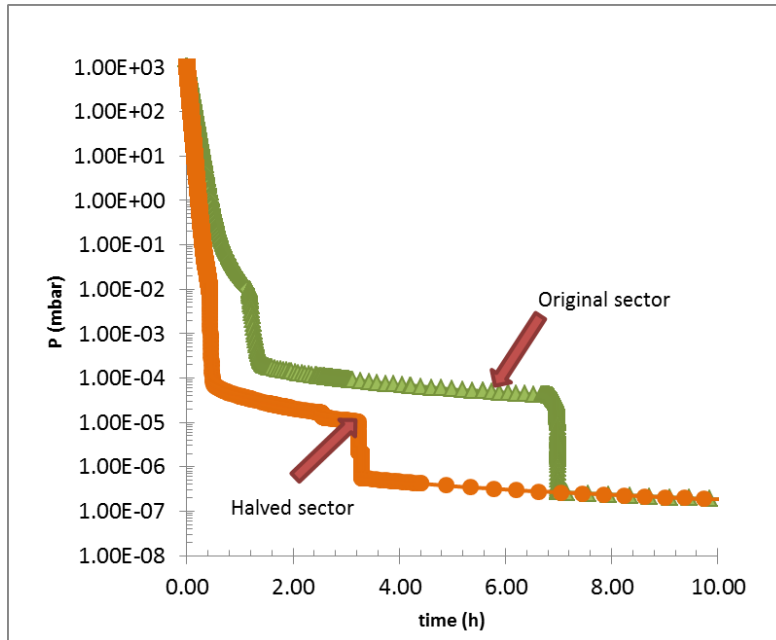


Fig. 5.103: Comparison between calculated pumpdown curves for original (green) and halved (orange) x10 vacuum sector

As a consequence of the modification of the vacuum sectors, new instrumentation will be necessary for interlock purposes.

5.12.2 x10 vacuum sectors

Sectors x10 are 384 m long. It is proposed that a new VVSA valve (DN 100 all-metal sector valve) is installed in the position x0701 to divide the original sector into two identical new sectors. The new sector length is 192 m. Hereinafter we call the first halved sector x11 and the second x12.

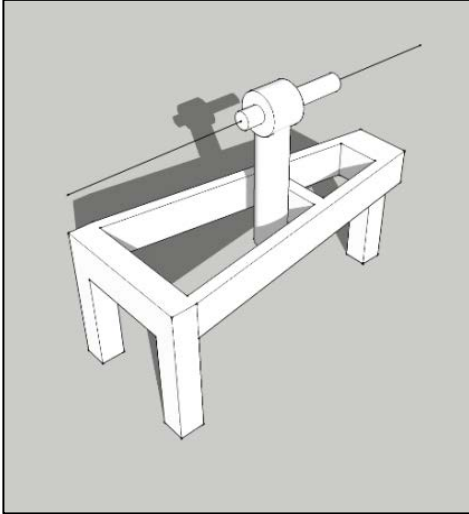
In sector x10 the vacuum gauges (Penning and Pirani) are located in position x0660 that will remain in halved sector x11. The proposed position for new gauges in sector x12 is x0720. In Table 5.17 the positions of the proposed new sector valves are shown. Two new roughing valves (VVR) have to be installed in each new sector. This layout assumes that the venting to air will be carried out through VVRs.

Table 5.17: Proposed vacuum layout for the halved x10 vacuum sectors

Sector		Valve					
Sector x11	VVSA x0101	VVR x0140	VVR x0280	VVR x0480	VG x0660	VVR x0680	VVSA x0701
Sector x12	VVSA x0701	VG x0720	VVR x0740	VVR x0880	VVR x1080	VVR x1280	VVSA x1301

VVSA, sector valve; VVR, roughing valve; VG, vacuum gauges.

The positions for the new valves are located between a MBB dipole and a QD quadrupole. These short straight sections consist of a LOD magnet and a circular chamber DN86 (QD type). In Fig. 5.104 it is shown that there is enough space for the installation of a new VVSA valve. A new support and chamber has to be designed and produced for each sextant. These supports should take into account that the new VVSA will be a different model from the old VVSA, with a slight change in the body height. This has to be taken into account during the design of the support to be compatible with both valves.

**Fig. 5.104:** Scale drawing showing the space required for x0701 valves

VPI (ion pumps) can be controlled by the same power supplies at both sides of the new valve. New cabling will be needed to allow independent control of each sector.

Position 20701 in sextant 2 will be occupied by a new position monitor [44]. The valve and the gauges in this sextant should be displaced to the next free position (20901 and 20940). The sectors in 211 and 212 will have a length of 224 m and 160 m, respectively.

5.12.3 x60 vacuum sectors

In sectors x60 the total length is 448 m. It is proposed that a new VVSA is placed at x3101, dividing the original sector in two new sectors: one 256 m long and the other 192 m long. Hereinafter we call the first halved sector x61 and the second x62, respectively.

In sector x60 the vacuum gauges (Penning and Pirani) are located in position x2940 and $(x + 1)0060$, which will remain in halved sector x61 and x62, respectively. The proposed position for new gauges in sector x12 is x3160. In Table 5.18 the proposed sectorization is shown. Two new VVR

have to be installed in each new sector. This layout assumes that the venting will be carried out through VVRs.

Table 5.18: Proposed sectorization for x60 vacuum sector

Sector		Valve					
Sector x61	VVSA	VVR	VVR	VVR	VG	VVR	VVSA
	x2301	x2340	x2560	x2840	x2960	x3080	x3101
Sector x62	VVSA	VG	VVR	VVR	VVR	VG	VVSA
	x3101	x3160	x3140	x3280	x3480	(x + 1)0060	(x + 1)0080
							(x + 1)0101

VVSA, sector valve; VVR, roughing valve; VG, vacuum gauges.

A new support and chamber have to be produced for each sextant. Only the chamber has to be designed. These supports should take into account that the new VVSA will be a different model from the old VVSA, with a slight change in the body height. This has to be taken into account during the design of the support to be compatible with both valves.

VPI (ion pumps) can be controlled by the same power supplies at both sides of the new valve. New cabling will be needed to allow independent control of each sector.

5.12.4 Improving protection for kicker MKDH 11757

Located in BA1, the MKDH 11757 kicker is vented to atmospheric pressure every time that an intervention on the scraper is needed (Fig. 5.105). Figure 5.106 shows the position of the existing valve (VVSB 11772) and the position of the same valve once it will be displaced right before the scraper (not shown in this non-updated drawing). BSHV 11759 has to be displaced the length of the valve.

This activity is foreseen to be completed during LS1.

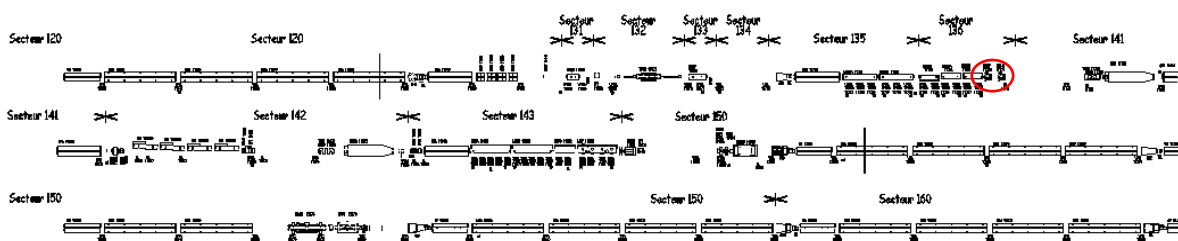


Fig. 5.105: MKDH 11757 in LSS1

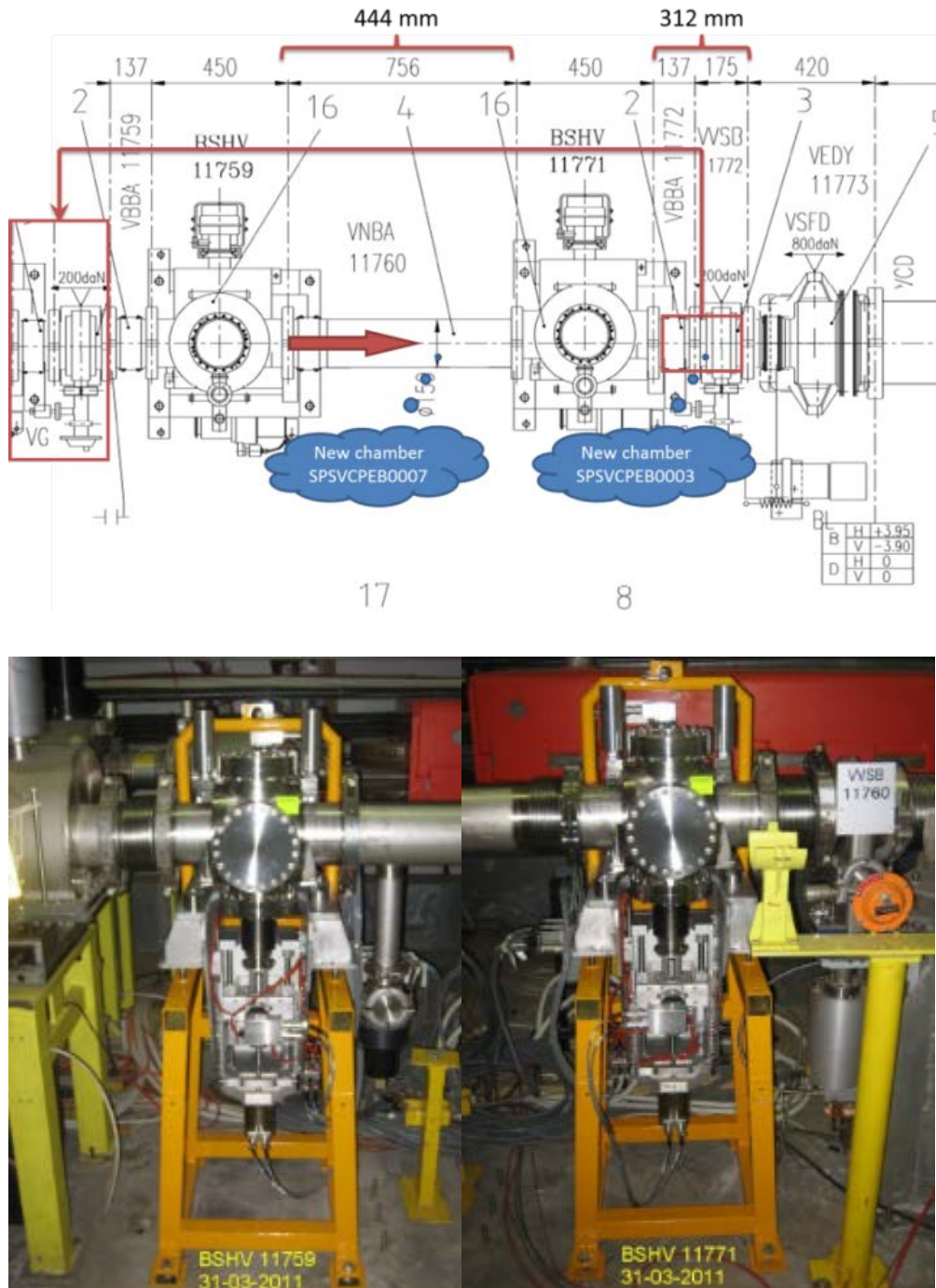


Fig. 5.106: Equipment that has to be displaced to relocate VVSB 11772

5.12.5 Protection of TIDVG dump

The TIDVG dump is located in LSS1. The vacuum sector of the dump (142) is delimited by three sector valves. In the downstream position the VVSB 11903 is relatively close to the dump and no improvement is necessary. In the upstream direction, because the vacuum chamber bifurcates, the sector valves are tens of meters away from the dump (see Figs. 5.107 and 5.108). Therefore, if an intervention on the injection septum magnets or in the last part of TT10 is needed, the dump is vented to atmospheric pressure, leading to a potential loss of conditioning.

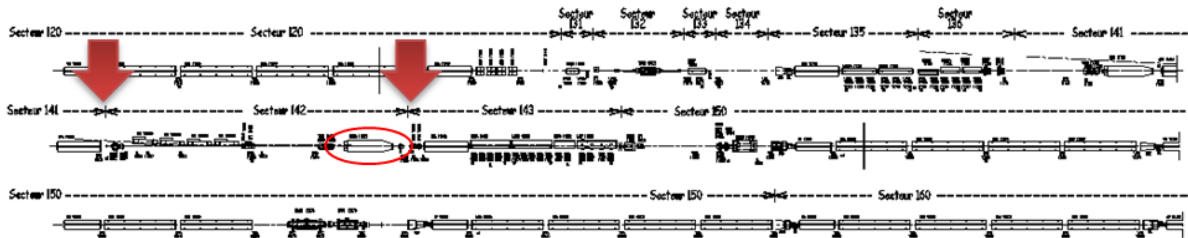


Figure 5.107: Position of the sector valves in the vacuum sector where the TIDVG is installed

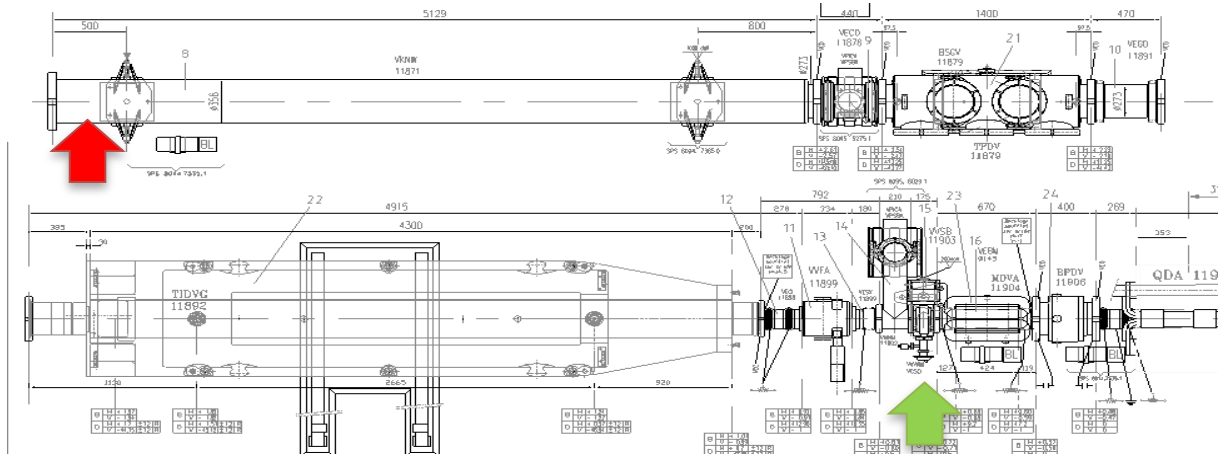


Fig. 5.108: positions of the existing VVSB valve (green arrow) and the new proposed VVSF valve (red arrow). Chamber VKNW ($l = 5129$ mm, $\varnothing = 356$ mm) has to be replaced by two new chambers that have yet to be designed.

Dump conditioning is better preserved if a sector valve is installed directly in the large vacuum chamber connected to the TIDVG. Because the vacuum chamber diameter is 386 mm, the proposed sector valve is a VVSF, which has a nominal diameter of 400 mm (see Fig. 5.109).

VVSF valves are already installed in LSS2 and LSS6. Despite the clear benefits from the dump sectorization, it should be mentioned that these kinds of valves are not standard products; they are expensive and bulky and they require particular maintenance. In addition, it is important to underline that the dump area is highly radioactive; thus, *the benefits of the new sectorization should be evaluated also in the context of the ALARA principle*.



Fig. 5.109: Picture of a VVSF valve

5.12.6 Re-sectorization of RF cavities

During LS2, new RF cavities will be installed in LSS3 as part of the SPS upgrade. The installation of two new VVSB sector valves is required to sectorize the new vacuum chambers. Figure 5.110 shows the lay-out of the new sectors.

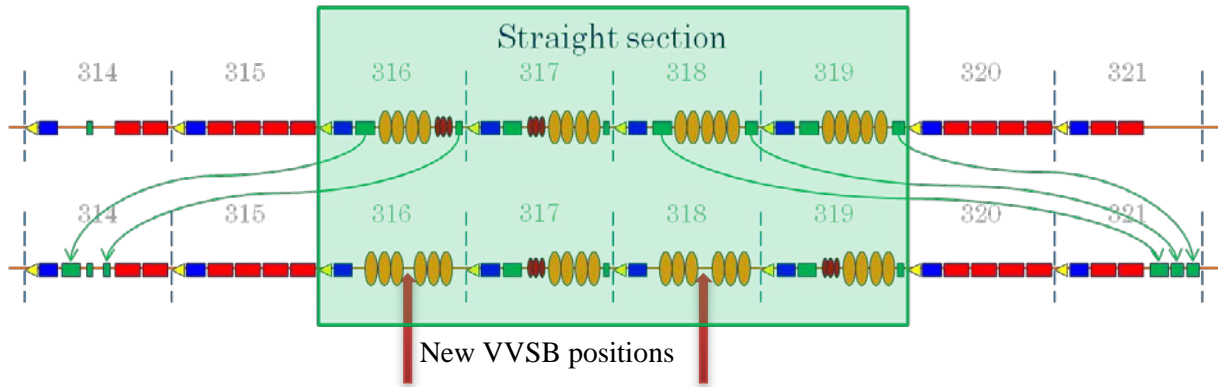


Fig. 5.110. New RF cavities layout for the SPS upgrade

In parallel with the re-sectorization the full vacuum system of the six cavities will be consolidated (new ion pumps).

The reconnection of the cavities during LS2 will require training and the development of a procedure to ensure the tightness of connection between tanks.

5.12.7 Fast valves

The fast valves in SPS are safety equipment that protect elements (kickers and septa) where a risk of water inrush exists. This equipment is actuated by a gauge that detects an abnormal increase of pressure. Most of the fast valves are located in areas where the dose rate is high. The position of the fast valves is summarized in Table 5.19.

Table 5.19: List of fast valves in SPS

VVFA 11901	VVFA 61460
VVFA 21701	VVFA 61737
VVFB 21801	VVFB 61801
VVFB 21877	VVFB 61877
VVFA 41698	VVFA 61957
VVFA 610213 (TT60)	

There are two different type of valves, VVFA and VVFB, installed in the SPS. VVFA are VAT valves with an aperture of 150 mm, and electrically operated. VVFB are valves of 250 mm aperture and pneumatically operated. These valves are not leak-tight and their function is to slow the increase of pressure until the sector valve is closed. These valves were developed 40 years ago and only old spares are available. New alternatives will be developed to ensure the effective protection of new equipment. New valves have to fulfil the following: radiation tolerance, low conductance when closed and short time of response (tenths of milliseconds).

The fast valve (VVFA) in position 11901 (after the TIDVG) was installed to protect the kickers MKP. It is operated in a very hot environment and this will increase with higher beam intensity. Several interventions were required to open the valve after failure. In case of water inrush from the

MSIs the dump is not protected, even if the MKPs are protected. During LS1 this valve will be suppressed to minimize the risk of an intervention in this environment [45].

5.12.8 Costs

Material costs are listed in Table 5.20. The breakdown considers valves, mechanical parts and control equipment including instrumentation and cabling.

Table 5.20: Material costs for vacuum sectorization

Element	Activity	Cost (KCHF/unit or m)	Quantity	Total cost (KCHF)	VSC FTE M- Week	VSC FSU control and vacuum (kCHF)
VVSA	Halving long sectors	22.5	12	270		
VVSA + VG (Pirani and Penning) cabling and control	Halving long sectors	-	12	413.3		
VG (Pirani and Penning)	Halving long sectors	3	12	36		
Valve Support	Halving long sectors	2	12	24		
New vacuum chambers	Halving long sectors	2.5	12	30		
VVR	24	4.5	24	108		
Valve support	Displacement of VVSB 11772	2	1	2		
New vacuum chamber	Displacement of VVSB 11772	2.5	1	2.5		
VVSF	TIDVG sectorization	Reused	1	0		
VVSF cabling and control	TIDVG sectorization	-	1	7.8		
New vacuum chambers	TIDVG sectorization	2.5	4	10		
VVSF support	TIDVG sectorization	2	1	2		
Total				905.6		
Halving long sectors					14	70
TIDVG					2	3
VVSB11772					1.5	3
Total					21	86

5.12.9 Conclusions

The proposed modifications to SPS sectorization will considerably shorten the intervention time after air venting of the longest vacuum sectors. Kicker magnets will be better protected and the conditioning of the TIDVG dump better preserved. The activities should be fitted into the schedule of the IVM section in LS1 and LS2.

5.13 Impedance budget

In the framework of the SPS upgrade project an accurate impedance model is needed in order to determine its effect on the beam stability and assess the impact of the new devices to be installed in the machine, with both the present and future beam parameters [103].

The SPS impedance model is obtained by summing the contributions of the different devices along the machine (β -weighted for the transverse impedance). Analytical models, 3-D simulations and bench measurements are used to estimate these contributions. The SPS impedance model is dynamical because it needs to be updated to include newly identified impedance sources as well as modifications of installed elements or new elements.

5.13.1 Transverse impedance model

The present version of the SPS transverse impedance model, which we present here, includes the following contributions.

- Kicker magnets. They are likely to be the most important impedance source in the SPS. In a very simple approximation a SPS ferrite loaded kicker can be modelled as two parallel plates of ferrite. For this simple geometrical model all the impedance terms (longitudinal, driving and detuning horizontal and vertical impedances) have been calculated analytically. CST 3D simulations were found to be in very good agreement with the analytical results. The excellent agreement between analytical model and numerical simulations can be read as an important benchmark for the simulation code in the correct solution of electromagnetic problems involving dispersive materials such as ferrite. In the framework of an improvement of the kicker impedance model we performed a step-by-step simulation study starting from the simplest model and introducing one by one the new features that make the model gradually closer to reality. This approach allows for a good understanding of the different contributions brought to the kicker impedance by the different aspects. First, the ferrite is assumed to be C-shaped and the whole finite length device is inserted into the vacuum tank and equipped with an inner conductor [104]. In order to further approach a more realistic model other aspects have to be included: the cell longitudinal structure, also called segmentation, which determines a significant increase of the beam coupling impedance for the SPS injection kickers (due to the short cell length) and the serigraphy for the SPS extraction kickers. All the details about the SPS kicker impedance model can be found in Ref. [105].
- Wall (resistive wall and indirect space charge), based on analytical calculation taking into account the different SPS vacuum chambers [105].
- Beam position monitors, based on CST 3D simulations [106].
- RF cavities, based on CST 3D simulations [107].
- Broadband impedance from step transitions, based on the information for the SPS flanges collected during the task force for the identification of the longitudinal impedance source responsible for the impedance peak at 1.4 GHz observed during beam measurements [108]. The broadband impedance of the SPS transitions has been calculated as:

$$Z_{\text{transitions}} = \sum_{i=1}^N Z_i n_i \quad (5.9)$$

where N is the number of different transition types, Z_i is the broadband impedance of the transition i and n_i is the number of occurrence of transition type i . The broadband impedance contribution of each type of transition has been obtained by means of CST 3D EM simulations.

Figure 5.111 shows the full SPS impedance model including all the impedance sources analysed, weighted by the respective length and beta functions for the horizontal and vertical impedances. As we will see, the impedance model of Fig. 5.111 can explain the measured coherent tune shifts. Moreover, HEADTAIL simulations based on this impedance model show a good agreement also with instability measurements.

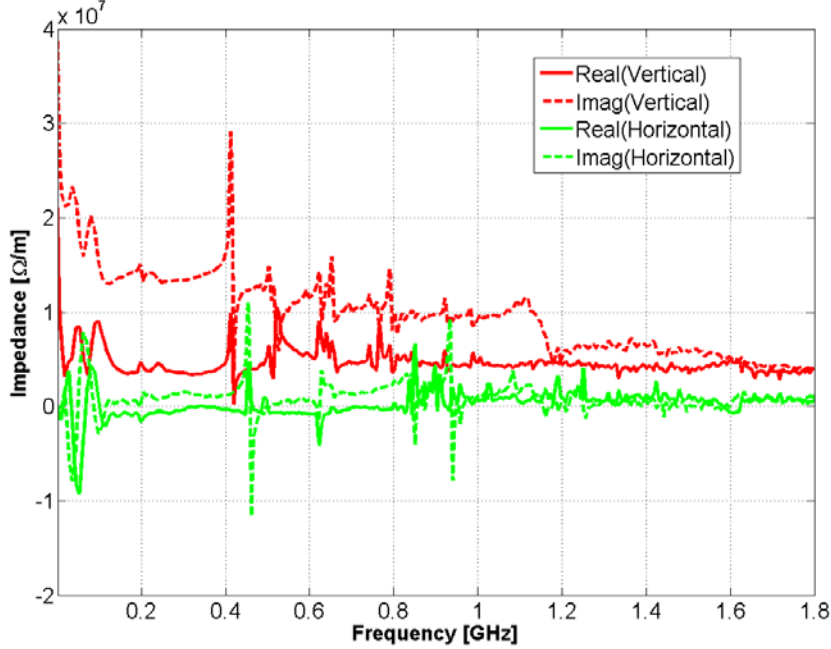
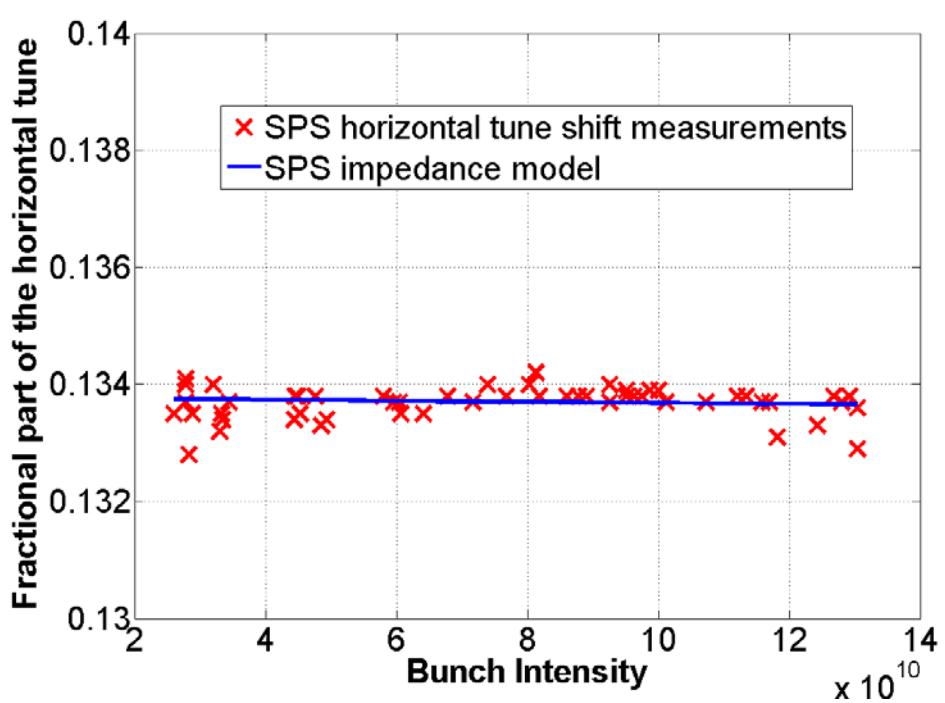
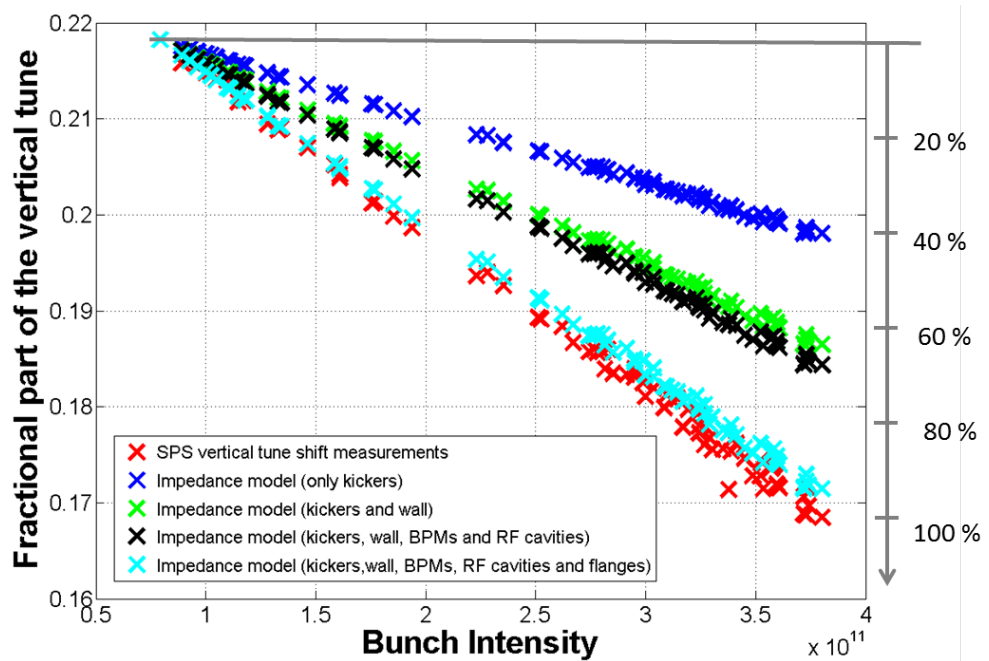


Fig. 5.111: Total vertical (red) and horizontal (green) generalized impedance of the SPS

Comparison with tune shift measurements

Tune shift measurements give integrated information about the effective impedance of a machine, which depends on both its full impedance and the length/shape of the bunch used for the measurements. The effective impedance is calculated for the mode $l = 0$ assuming a Gaussian bunch and is directly related to the tune shift (e.g. Ref. [109] (Eq. 6.207)). The measurements are performed on a single circulating bunch of particles. The tune is measured as a function of the bunch intensity. The bunch length is also measured and recorded for each intensity. For the Q20 optics the vertical tune shift measured during 2012 led to an estimated SPS vertical effective impedance of $18.3 \pm 0.7 \text{ M}\Omega/\text{m}$. The uncertainty of impedance propagation has been calculated in Ref. [109] (Eq. 6.207) for the uncertainty of the tune shift measurements. A direct comparison between measurements and the impedance model is shown in Fig. 5.112, where we compare the vertical tune measurements with the tune obtained from Ref. [109] (Eq. 6.207), using as an input the effective impedance of the partial SPS impedance model and the measured bunch intensity and bunch length for each point. Figure 5.112 shows that kicker magnets are the main broadband impedance source of the SPS (about 40% of the measured coherent tune shift). It is also important to underline that step transitions represent more than 20% of the SPS impedance and that thanks to its contribution the SPS transverse impedance model now explain more than 90% of the measured coherent tune shift. The SPS impedance model also predicts a very small horizontal tune shift (almost flat) in agreement with the tune measurements (see Fig. 5.113).



5.13.2 SPS longitudinal impedance model

5.13.2.1 Travelling wave cavities

The SPS has a double RF system. This comprises two sets of two 200 MHz travelling wave cavities (TWC), [41], and two 800 MHz TWC. The current impedance model for the fundamental pass-band of the cavities is:

$$Z(f) = R \left\{ \left(\frac{\sin(\tau/2)}{\tau/2} \right)^2 - 2j \frac{\tau - \sin(\tau)}{\tau^2} \right\} \quad (5.10)$$

with $\tau = l/v_g(f)/(\omega - \omega_0)$ where l is the total length of the cavity and $v_g(f)$ the frequency-dependent group velocity. Table 5.21 shows the parameters used in the model.

Table 5.21: Parameter list used in the TWC impedance model

	Centre frequency (MHz)	τ at centre frequency (μ s)	R ($M\Omega$)
200 MHz TWC short	200.222	3.56	1.752
200 MHz TWC long	200.222	4.47	2.760
800 MHz TWC	800.888	2.07	1.938

In addition, the impedance model includes a higher order mode (HOM) at 629 MHz. This HOM is modelled as a resonator of $R = 388 \text{ k}\Omega$ and $R/Q = 1560$.

Kicker magnets

Kicker magnets have been studied in detail [105]. Figure 5.114 shows the total kicker magnet longitudinal impedance. The blue and red traces are the real and imaginary parts of the longitudinal impedance. The black lines show the eight-resonator model fit that is used in beam dynamics simulations. Detailed information on the impedance fit can be found in Refs. [110, 111].

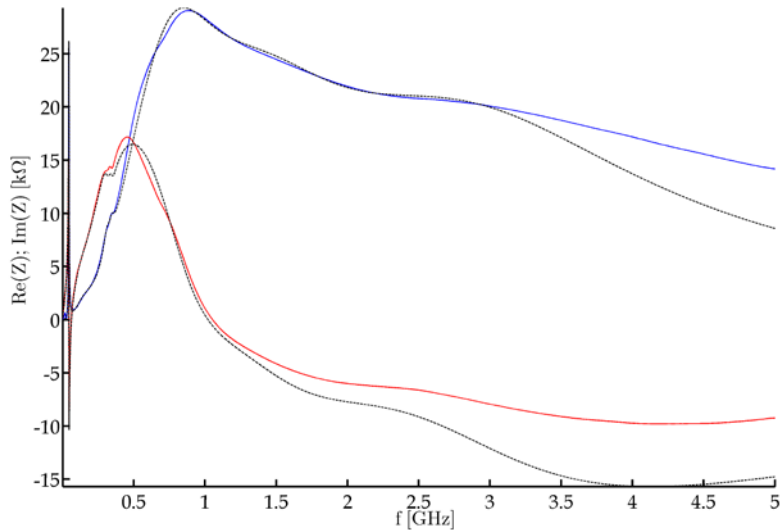


Fig. 5.114: Total SPS kicker magnet longitudinal impedance. The blue and red lines show the real and imaginary parts of the impedance, respectively. The black line shows the real and imaginary part of an eight-resonator model fit used for beam dynamics studies.

MKE kickers—effect of serigraphy

A fast extraction kicker system to meet the LHC and CNGS specifications was installed in the SPS and successfully used in extraction tests in 2003. Since the beam-induced heating of these devices was observed to be critical, each kicker was equipped with a cooling system. The beam-induced heating is directly related to the beam power loss through the real part of the longitudinal impedance. Impedance reduction techniques were investigated in order to solve the issue of the beam-induced heating. The final solution of using silver fingers printed by serigraphy directly on the ferrite was implemented in 2007 [112]. Before the long shutdown of all CERN accelerators (LS1) only one SPS extraction kicker out of eight had not yet been serigraphed. Therefore, it is very important to estimate the beam coupling impedance of the serigraphed SPS extraction kickers.

Figure 5.115 shows the simulated longitudinal impedance for the MKE with and without serigraphy. As expected, serigraphy results in a strong reduction of the real part of the longitudinal impedance over a broad frequency range [112]. The broadband peak shifts from ≈ 600 MHz to ≈ 3.3 GHz. At the same time the serigraphy introduces a clear resonance at 44 MHz. This resonance was studied in detail and recognized to be a quarter wavelength resonance on the silver fingers [105]. The impedance model of the SPS extraction kicker shown in Fig. 5.115 is consistent with the beam-induced heating observed in the machine [105].

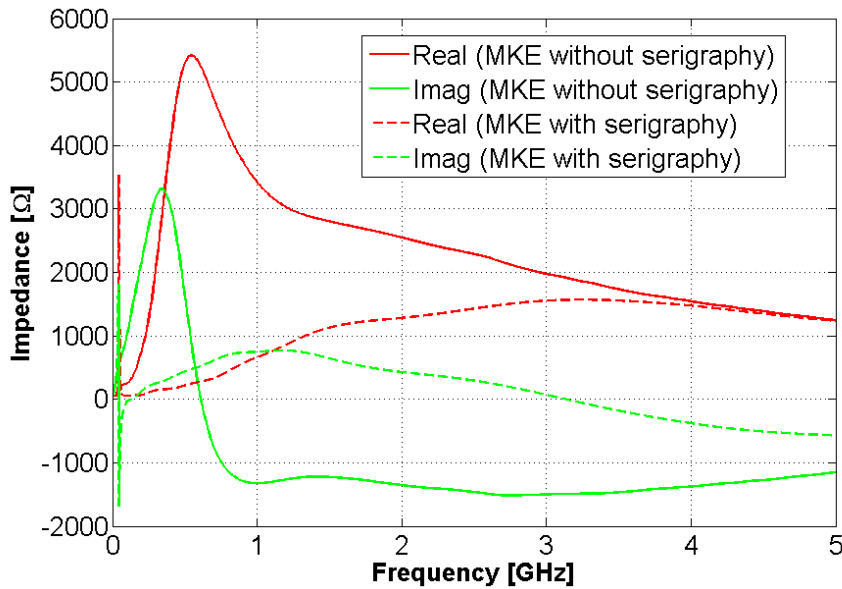


Fig. 5.115: CST 3D simulations of the longitudinal impedance for the SPS extraction kicker (MKE-L) with and without serigraphy.

Vacuum flanges

The latest addition to the longitudinal impedance model are the vacuum flanges. A layout survey of the SPS machine has been carried out to determine the total number and type of dangerous flanges and to estimate their impedance contribution. Detailed information on the SPS flange design can be found in Ref. [113]. Figure 5.116 shows a flange in the SPS and the model used in simulations to assess its impedance.

The longitudinal coupling impedance of the SPS was already studied by G. Dôme in 1973–1974, see Refs. [114, 115]. As a result, cylindrical resistors were placed all around the ring to damp the resonances created, not only by the flanges, but also by other elements such as pumping ports. The locations of where these dumping resistors are located can be found in the original layouts. There are two types of damping resistors, 25 mm and 54 mm long.

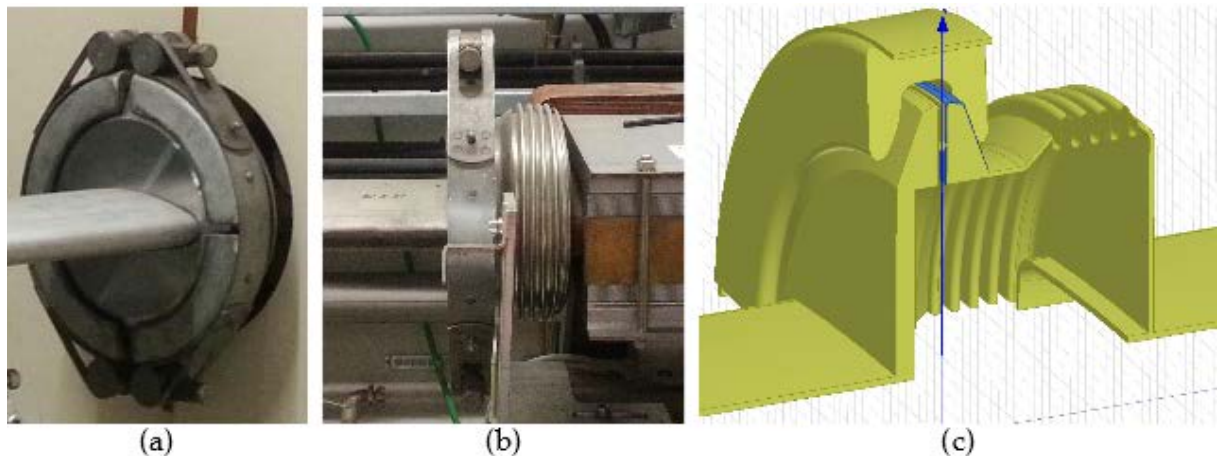


Fig. 5.116: An SPS flange. (a) Front view of a flange in the SPS. (b) Lateral view of a flange with a short bellows. (c) Model used to calculate the impedance of an enamelled flange with a short bellows.

Simulations

The aforementioned layout survey found nine types of flanges frequently used in the SPS. All of the different cases have been carefully simulated. The commercial software HFSS was used to run the simulations. Analogous to the method used to calculate beam loading in the CLIC main Linac [116], an ‘on-axis’ plane wave was used as a source to calculate the beam-induced field inside the SPS flanges.

A realistic model based on official layouts of the SPS flanges, see Fig. 5.116(c), has been built in order to obtain accurate impedance values. The flanges are, as a first step, classified in terms of their surrounding magnets. In addition, two other characteristics have to be accounted for: whether or not the flange is enamelled and/or has a bellows. For instance, Fig. 5.116(c) shows one-quarter of an enamelled flange with a short bellows between two MBA magnets. Beam pipes and bellows in the SPS are made of 304L/316L stainless steel. A conductivity of 1.35×10^6 S/m has been used to model the stainless steel in the simulations. Additionally, a 0.2 mm thick enamel layer ($\epsilon_r = 3$ and $\tan\delta = 0.01$) has been used for the appropriate cases.

Table 5.22 shows the most relevant resonances found in the flanges. The first, second and last entries of the table show resonances in the special cases where vertical and horizontal beam position monitors (BPV and BPH, respectively) are involved. The ‘Amount’ column shows the total number of each particular type of flange in the SPS. The ‘Impedance’ and ‘ R/Q ’ columns show the total values, i.e. impedance of a single flange times the amount of flanges in the SPS. Finally, the ‘Damping resistor’ column states whether or not each type of flange should have a damping resistor inside and its type. It must be highlighted that, at present, the damping resistors have not been included in the simulations. There is an ongoing effort to accurately account for them and assess their influence.

The enamelled flanges are open and inhomogeneous resonators. Radiation losses are dominant for all enamelled flanges in Table 5.22. Therefore, low Q values (<400) are obtained in these cases. Because of the lack of radiation in the non-enamelled flanges, higher Q values have been found. The entries of Table 5.22 can be divided in three groups. Resonances are around 1.25 GHz, 1.4 GHz and 1.6 GHz.

The 1.4 GHz resonances in Table 5.22 are the biggest flange contribution to the SPS impedance. The first two enamelled types have a low Q (around 275), a combined impedance around $1.9 \text{ M}\Omega$ and a high R/Q value of $7 \text{ k}\Omega$. The last, high Q , resonance is the highest single flange contribution to SPS impedance, $3.7 \text{ M}\Omega$, and adds an additional $1 \text{ k}\Omega$ to the R/Q of the previous enamelled types.

Additionally, the first two resonances around 1.25 GHz have similar Q and a total longitudinal impedance and R/Q values around $1.6 \text{ M}\Omega$ and $4.5 \text{ k}\Omega$, respectively. Considering now the 1.6 GHz resonances, we find very different Q values. The total impedance and R/Q contribution is $0.7 \text{ M}\Omega$ and $1.6 \text{ k}\Omega$, respectively.

Table 5.22: Most relevant flange resonances sorted by ascending resonant frequency

Flange type	Enam el	Bello ws	Amou nt	Frequen cy (GHz)	Impedanc e ^a (kΩ)	Q^a	R/Q^a (Ω)	Dampi ng resistor ^b
BPV-QD	Yes	Yes	90	1.21	630	315	2010	No
BPH-QF	Yes	Yes	39	1.28	1030	400	2495	Long
QF-MBA	Yes	Yes	83	1.41	1600	268	5985	Short
MBA- MBA	Yes	Yes	14	1.41	300	285	1040	Short
QF-QF	No	Yes	26	1.41	3765	1820	2060	Short
QF-QF	No	No	20	1.61	590	980	600	No
BPH-QF	Yes	Yes	39	1.62	120	120	1015	Long

^aThe damping resistors have not been included in the simulations. ^bThis column states whether or not the flange should have a damping resistor and its type

5.13.2.2 Measurements

Both enamelled and non-enamelled flanges have been measured in different configurations and with different methods to assess the accuracy of simulations. Bead-pull measurements have been found to be the best way to characterize the resonances of vacuum flanges.

A non-enamelled MBA-QF and a MBA-MBA enamelled flange both with short bellows have been measured using the bead-pull method with and without a damping resistor. Figure 5.117 shows the set-up used for the measurements. The phase of the transmission coefficient between two very weakly coupled ad hoc probes was measured as an on-axis longitudinal needle passed through the vacuum flange. From the obtained profile, the R/Q of the resonance can easily be calculated.

**Fig. 5.117:** The bead-pull measurement set-up

Table 5.23 shows the comparison between simulations and bead-pull measurements. Very good agreement is observed for the R/Q values without damping resistor. The resonant frequencies were accurately predicted by simulations and do not shift significantly due to the presence of the damping resistors. In addition, this set of measurements shows that the unloaded Q of the resonances and, therefore the impedance, is reduced around 5.5 and 3.5 times for the non-enamelled and enamelled cases, respectively. Finally, it must be highlighted that the R/Q of the resonances is not reduced significantly due to the presence of damping resistors.

Table 5.23: Comparison between simulations and bead-pull measurements

	Damping resistor		Resonant frequency (GHz)	Q	R/Q (Ω)
MBA–QF Non- enamelled	Simulated	No	1.415	1800	82
	Measured	No	1.401	1100	$85 \pm 2.5\%$
	Measured	Short	1.395	200	$81 \pm 2.5\%$
MBA–MBA Enamelled	Simulated	No	1.410	285	75
	Measured	No	1.415	270	$79 \pm 5\%$
	Measured	Short	1.415	75	$65 \pm 5\%$

Beam position monitors

The SPS longitudinal impedance model also includes the BPMs. So far, two types of BPMs have been analysed, those for the horizontal plane (BPH) and for the vertical plane (BPV). There are 106 BPHs and 93 BPVs in the SPS ring. Table 5.24 summarizes the most relevant BPM resonances. More details on the BPMs' impedance analysis and results can be found in Refs. [117, 111].

Table 5.24: Most relevant BPM resonances. The values in the table already take into account the total number of BPMs in the machine.

	Frequency (GHz)	R ($k\Omega$)	Q	R/Q (Ω)
BPH	1.0	350	770	450
BPH	1.6	600	690	870
BPH	1.8	300	900	330

Low frequency $Im(Z)/n$

Table 5.25 shows the known contributions for the low frequency imaginary part of Z/n . The contributions of the SPS cavities have been calculated dividing the cavity's R/Q by n_r . The f_{max} column states the frequency at which $Im(Z)$ changes its sign. For the vacuum flanges and BPMs, the values have been calculated via wake field simulations. In this case, the f_{max} column states approximately up to what frequency $Im(Z)/n$ is constant.

Table 5.25: Known contributions to the low frequency constant $\text{Im}(Z)/n$

	Number	$\text{Im}(Z)/n$ (Ω)	f_{\max} (MHz)
200 MHz TWC—long	2	2.72	200
200 MHz TWC—short	2	2.18	200
200 MHz TWC—HOM	4	0.11	630
800 MHz TWC	2	0.35	800
Vacuum flanges	589	0.97	400
BPMs—H	106	0.11	400
BPMs—V	96	0.05	400

The complete SPS longitudinal impedance model

Figure 5.118 shows the total SPS longitudinal impedance (in black) after the contribution from all the aforementioned elements are summed. The same plot also shows the partial contribution from the flanges, BPMs and kicker magnets. The SPS longitudinal impedance is dominated by the 200 MHz TWCs at $4.2 \text{ M}\Omega$. The second biggest contributors are the 800 MHz cavities and the vacuum flanges whose peak amplitude is around $1.8 \text{ M}\Omega$.

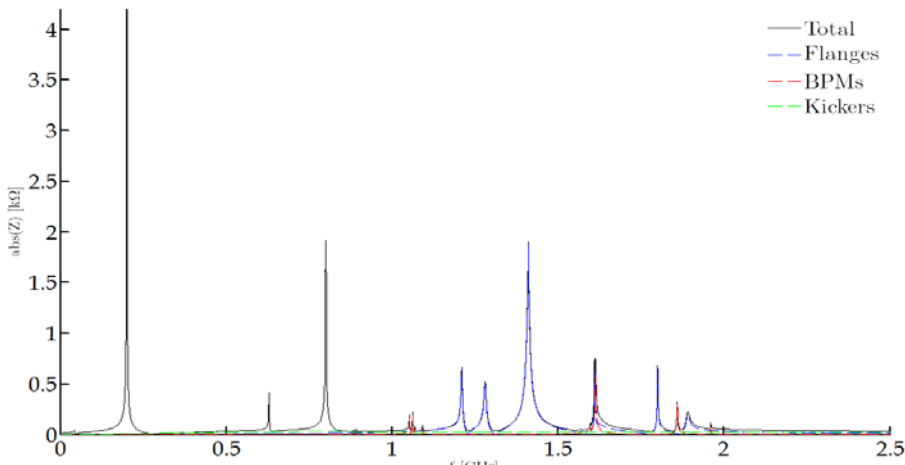


Fig. 5.118: Total SPS longitudinal impedance in lineal vertical scale. The blue, red and green lines represent the contribution of the flanges, BPMs and kicker magnets, respectively.

A more detailed view of the current impedance model can be obtained by plotting the same information on a logarithmic scale. Figure 5.119 shows, as an analogy to Fig. 5.118, the total, flange, BPM and kicker longitudinal impedance contributions. It is now clear that the kicker magnets contribute as a $\approx 25 \text{ k}\Omega$ offset at high frequencies. The 44 MHz serigraphy peak is also visible in this plot. Aside from the 200 MHz and 800 MHz TWC peaks, the 630 MHz HOM peak is also clearly visible now. Above 1 GHz, the spectrum is dominated by the resonances coming from the vacuum flanges and BPMs.

Finally, Table 5.26 shows the main contributors to the longitudinal SPS impedance. A resonator model approximation has been used to build the table for the TWCs and kickers so that the entries are

easily comparable. Table 5.26 shows three main contributors to the SPS impedance, i.e. the 200 MHz and 800 MHz cavities and the 1.4 GHz flange resonance. On the other hand, main contributions for R/Q come from the kicker magnets and, again, the 200 MHz cavities.

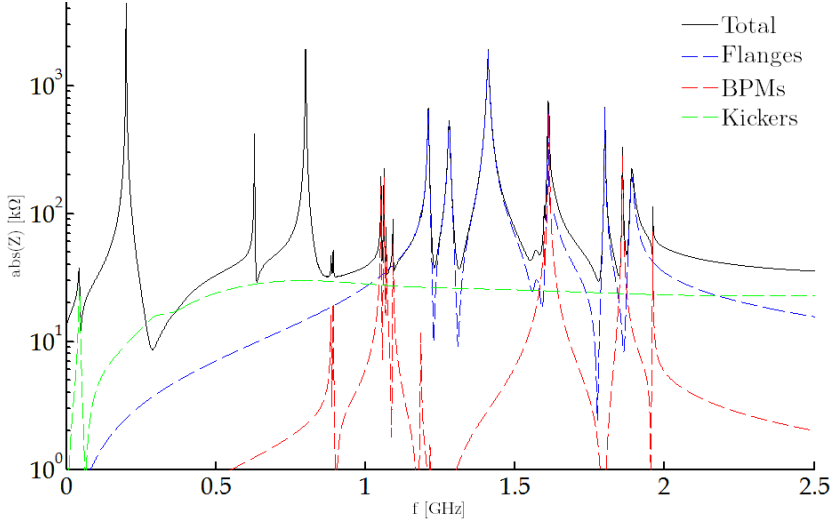


Fig. 5.119: Total SPS longitudinal impedance on a logarithmic vertical scale. The blue, red and green lines represent the contribution of the flanges, BPMs and kicker magnets, respectively.

Table 5.26: Main impedance contributors to longitudinal SPS impedance

	Frequency (MHz)	R ($k\Omega$)	Q	R/Q (Ω)
Serigraphy	44	26	11	2 400
200 MHz TWC— long	200	2 760	150	18 400
200 MHz TWC— short	200	1 750	120	14 600
200 MHz TWC— HOM	630	390	250	1 560
800 MHz TWC	800	1 940	300	6 460
Kickers	810	20.5	1	20 500
Vacuum flanges	1 200	630 + 500	250	4 500
Vacuum flanges	1 400	1 875	200	9 300
Kickers	1 500	12	1	12 000
Vacuum flanges	1 600	630	395	1 600
BPM—H	1 600	600	685	870
Kickers	3 000	14.5	1	14 500

5.13.3 Kicker impedance heating and mitigation

Beam observables, like beam-induced heating measurements, have been used to validate the longitudinal impedance model of the MKE with and without serigraphy [105].

The power lost by a beam passing with revolution frequency $f_0 = \omega_0/2\pi$ through a device having longitudinal impedance $Z_{||}(\omega)$ can be expressed as:

$$\Delta W = (f_0 e N_{\text{beam}})^2 \sum_{p=-\infty}^{p=\infty} \left(|\bar{\Lambda}(p\omega_0)|^2 \operatorname{Re}[Z_{||}(p\omega_0)] \right) \quad (5.11)$$

where e is the charge of the particle, N_{beam} is the number of particles in the beam and $\bar{\Lambda}(p\omega)$ the beam spectrum. Applying Eq. (5.11) with the impedance model shown in Fig. 5.118, we can calculate the power lost in an SPS extraction kicker by a typical LHC beam in the SPS. The calculation can be carried out for several values of bunch length, covering the range swept over a typical 25 ns or 50 ns beam production cycle. In order to compare it with direct heating observations, we need to consider the dynamics of the beam with the time. In addition, two more aspects need to be taken into account: the beam intensity is changing while the beam is being injected, and the bunch length changes along the energy ramp. The calculations of the beam-induced heating on the SPS extraction kicker with and without serigraphy showed a good agreement with the measurements [105].

The beam-induced heating of the SPS extraction kicker with serigraphy strongly depends on the frequency (about 44 MHz for the present design) of the resonance due to the serigraphy itself. This resonance is directly related to the finger pattern (in particular to the finger lengths). Fig. 5.120 shows the dependence of the beam-induced heating on the frequency of the peak due to the serigraphy assuming that shunt impedance and the quality factor of the resonance are unchanged. This picture gives guidelines to optimize in terms of beam-induced heating the present SPS extraction kickers. This optimization would help to run the SPS at the LIU beam intensities. In fact the beam-induced heating on the MKE with serigraphy for LIU beams is expected to be comparable to the heating observed in 2012 on the MKE without serigraphy, which was limiting operation during scrubbing runs.

However, after the serigraphy of the last extraction kicker according to the impedance model and heating measurements, the SPS injection kickers (MKPs) are likely to become the limiting elements in terms of heating. They are expected to show a beam-induced heating significantly higher than the heating observed in 2012 on the MKE without serigraphy with LIU beams. Figure 5.121, based on the kicker impedance model, shows the expected power loss in W/m on the MKE with serigraphy and MKP11955 for both 25 ns and 50 ns beam at the LIU intensities. The power loss for the MKE without serigraphy at the 2012 intensities is also displayed as a reference.

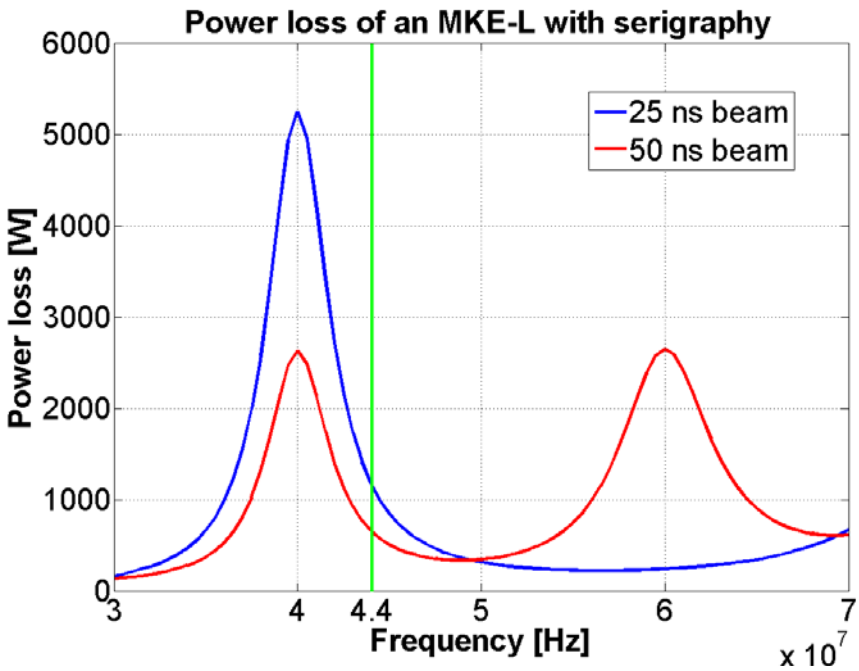


Fig. 5.120: Power loss as a function of the frequency of the peak due to the serigraphy assuming that shunt impedance and the quality factor of the resonance are unchanged.

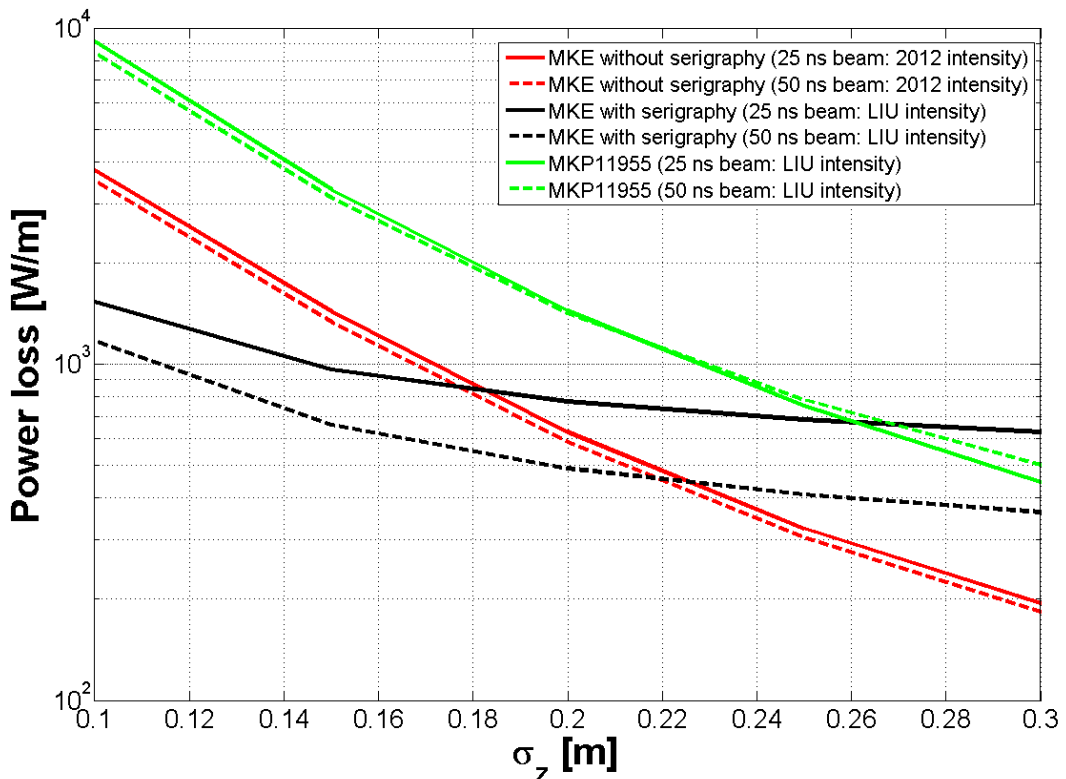


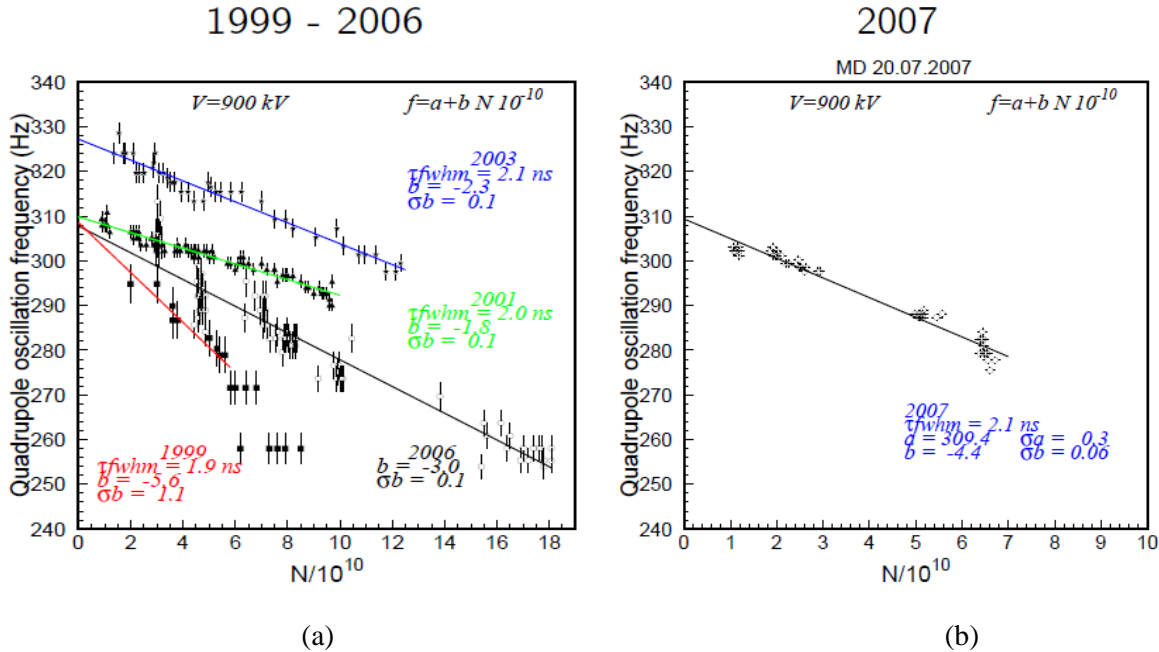
Fig. 5.121: Comparison between the power loss of the MKE without serigraphy for 2012 beam intensities and the MKE with serigraphy and MKP11955 for LIU beam intensities.

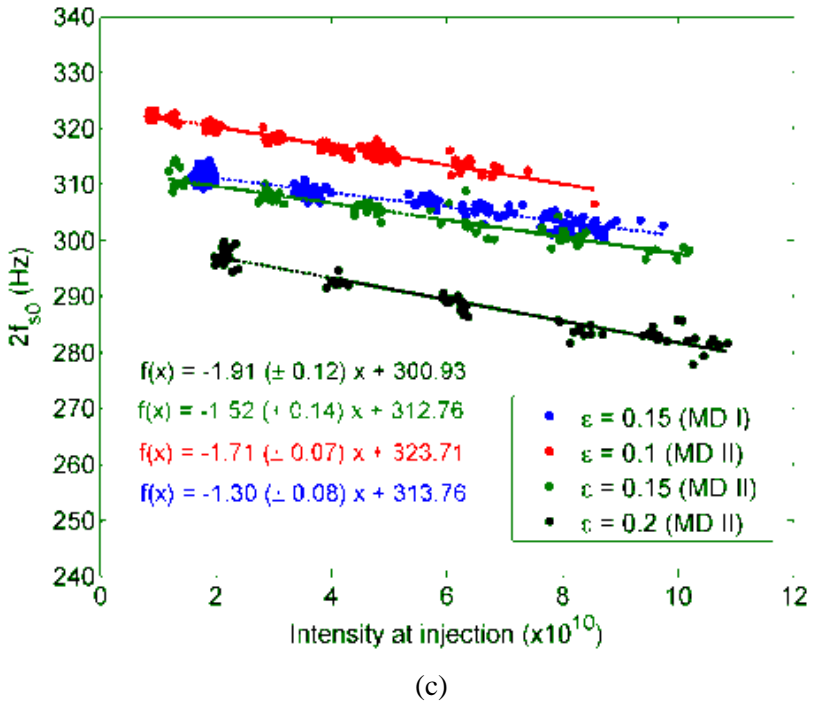
5.13.4 Beam measurements

5.13.4.1 Broadband impedance

Beam measurements in the SPS are performed to verify an existing impedance model of the machine, to follow up the impedance changes and to identify unknown impedance sources. Single-bunch measurements are used to see the effects associated with broadband impedances, and multi-bunch beams are used to study narrow-band impedances. The reactive part of the low frequency impedance can be estimated from measurements of synchrotron frequency shift with intensity, and the resistive part from synchronous phase shift with intensity as well as from instability growth rates and machine element heating (see below).

Measurements of the quadrupole synchrotron frequency shift with intensity using a single bunch injected into the SPS at 26 GeV/s were performed from 1999 to monitor the evolution of the low-frequency inductive impedance [118], see Fig. 5.122. The method of measurements (injection into mismatched voltage of 900 kV) requires bunches with a variable intensity, but constant bunch length and emittance. The beam is prepared in the SPS injector chain and its production scheme has evolved with time, which makes a comparison not always easy. The 2001 data shows that after the impedance reduction programme the low-frequency inductive impedance had been reduced by a factor of 2.5 [119]. In the following years a significant increase in impedance was observed due to the installation of eight MKE kickers for extraction to the LHC. After 2006 the serigraphy [120] was applied almost each year on some MKE magnets, with full shielding expected in 2014, and results can be seen in Fig. 5.122 (c) and Fig. 5.123.

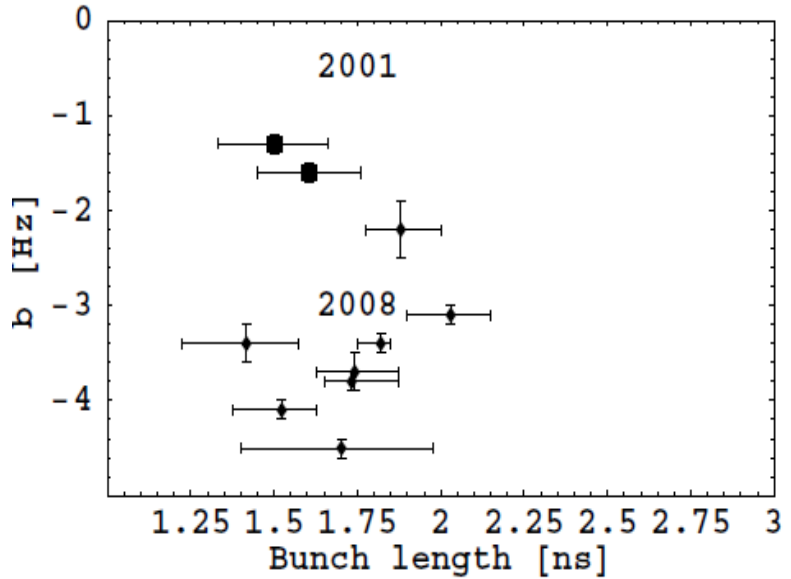




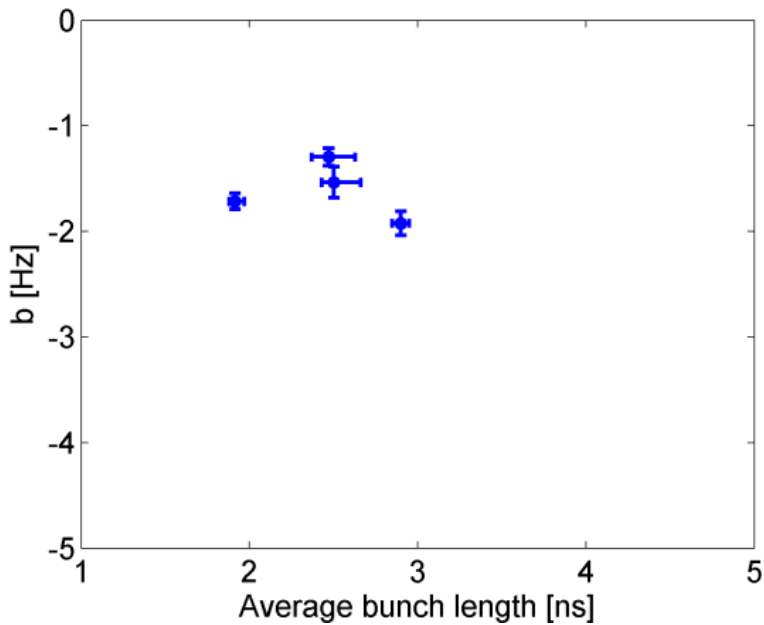
(c)

Fig. 5.122: Measurements of the quadrupole synchrotron frequency shift at 26 GeV/c in the SPS during the period from 1999 to 2006 (a), in 2007 (b) and 2013 (c).

Slope b in hertz from the fit $f2s = a + b N/10^{10}$, measured in 2001 and 2008, are shown in Fig. 5.123(a) and can be compared with the measurements done in 2013, Fig. 5.123(b). Due to the strong dependence of slope b on bunch length the results are presented vs. bunch length (which is the average bunch length during approximately the first 10 quadrupole oscillations after injection in the SPS). Comparison of the results of macro-particle simulations [121] (using the present SPS impedance model and bunch distribution similar to the experimental one) with measurements indicates that some inductive impedance is still missing in the SPS impedance budget, especially for shorter bunches (thus at higher frequencies). Missing impedance is even larger if one takes into account the space charge effect, which gives a negative (capacitive) contribution around 1.5Ω .



(a)



(b)

Fig. 5.123: Slopes $|head|$ of the quadrupole synchrotron frequency shift with intensity measured at 26 GeV/c with different injected longitudinal emittances in (a) 2001 and 2008 and (b) in 2013. The results are plotted versus measured average bunch length (4 σ Gaussian fit) during quadrupole oscillations. One can clearly see reduction in the slope in 2013 due to serigraphy of the MKE kickers.

In the past, after the identification of the impedance driving the microwave instability on the flat bottom, a significant reduction of the SPS impedance has been achieved thanks to shielding of ~ 800 inter-magnet pumping ports. This impedance was found by observing the spectrum of long (~ 25 ns) single bunches injected into the SPS with RF off and bunch intensity ($\sim 2 \times 10^{10}$) above the instability threshold [122]. In 2001, when the impedance reduction programme was completed, practically no peaks could be seen for bunch intensities below 8×10^{10} . However for higher intensities bunch modulation appeared at frequencies around 1.4 GHz. These measurements were repeated in 2007 and more recently, in 2011 to 2013 [6], see Fig. 5.124. After intensive search the peak at 1.4 GHz has been

identified as an impedance of vacuum flanges (see below) with high R/Q ($\sim 9 \text{ k}\Omega$) and relatively low Q (~ 200), similar to the impedance of the pumping ports. These accidental cavities were also always damped by ceramic resistors (at least the majority of them) to reduce the risk of coupled-bunch instabilities. The results of beam simulations [123] done for different measured particle distributions using the SPS impedance model, which includes the contribution from flanges (with 90% of damping resistors in place), are shown in Fig. 5.124. One can see that the peak amplitude at 1.4 GHz (as compared to the 200 MHz peak with known impedance) varies a lot, but practically for all cases it is lower than the average peak amplitude obtained in the measurements with the same bunch intensity. The agreement is achieved if impedance used in simulations is approximately 20% larger.

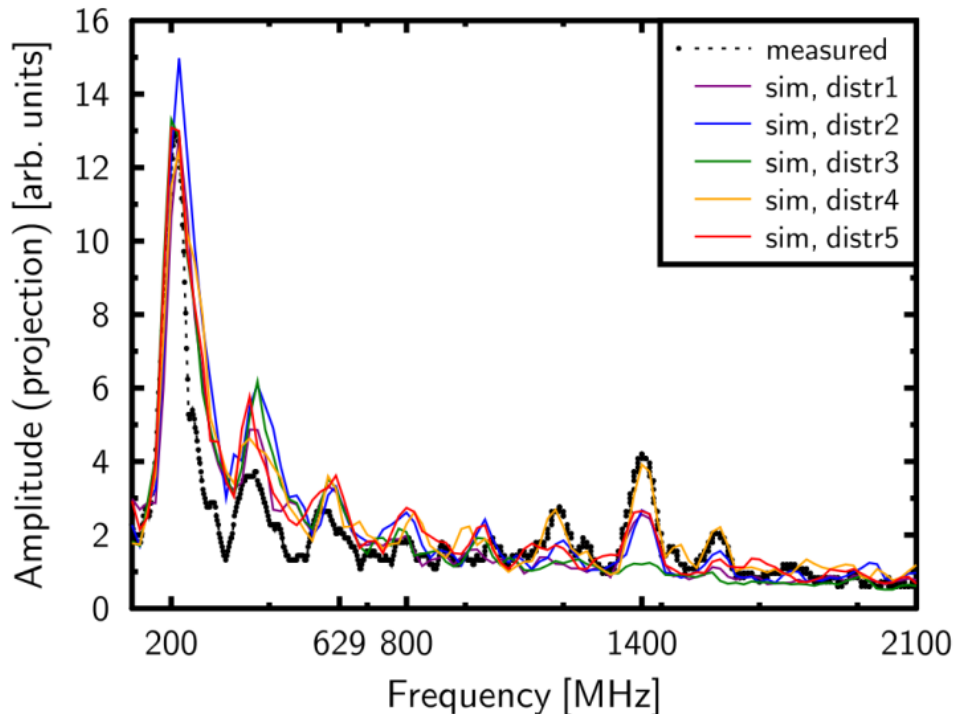


Fig. 3.124: Projection of bunch spectrum evolution of long bunches ($\sim 25 \text{ ns}$) with intensity of 1×10^{11} after injection into SPS with RF off in measurements (black dashed line) and simulations with different (reconstructed from PS tomography) distributions in the present SPS impedance model [123].

5.13.4.2 Narrow-band impedance

The impedance source of longitudinal multi-bunch instability is not known, but one can make a few conclusions about its parameters based on existing beam observations. The instability threshold observed during ramp of one batch is similar to two, three or four batches. The instability starts at the same time (energy) for all batches. The fact that there is coupled motion for the 50 ns spacing and no coupling between batches with a 225 ns gap point to a resonant impedance at frequency $f_r = \omega r/(2\pi)$ with relatively low quality factor Q , in the range:

$$50 \text{ ns} < 2Q/\omega_r < 225 \text{ ns}. \quad (5.12)$$

This short-range wake is compatible with different impedance sources, starting from the main impedance of the 200 MHz RF system, which has a quality factor of ~ 200 . The list of other possible candidates is presented in Table 5.26. One can see that the idle 800 MHz RF cavity with its very high impedance and $Q = 300$ would also satisfy this condition, which for $f_r = 0.8 \text{ GHz}$ becomes $120 < Q < 560$. This is why the foreseen upgrade of the 800 MHz RF system is a very important step for impedance reduction. The results of this improvement can already be seen with beam at the end of

2014. The impedance of vacuum flanges with their approximate quality factor of 200 can also satisfy condition (1).

5.14 Electrostatic septa

In the past, in particular just after the LHC commissioning, high spark rates and vacuum activity was observed in the ZS electrostatic septa in LSS2, when high-intensity 25 ns beam was accelerated in the SPS for the LHC. Both the high spark rate phenomenon as well as the vacuum level in the ZS are interlocked, and each one of these interlocks removes the high voltage from the ZS, and the injection veto for the SPS is raised. To prevent the LHC from being affected, the north extraction (for which the ZS are used) was stopped when LHC beam was required. Although this may be acceptable during dedicated LHC filling, it is nevertheless a limiting factor for the north extraction, since the switching off and back on again of the ZS is not possible on a cycle-to-cycle basis. The ramp-down of the ZS main voltage takes several tens of seconds. Consequentially, this approach would prevent parasitic MDs with high-intensity LHC cycles in the SPS. To improve this ramp up/down time, tests were made to reduce only the main voltage of the ZS during LHC beam operation of the SPS [124]. A 20% reduction in main voltage allowed LHC high-intensity beam in the SPS, while keeping the spark rate sufficiently low to avoid an interlock. However, vacuum activity, in particular in ZS 4 and ZS 5, was observed, leading to triggering of the ZS vacuum interlock.

Over time, the use of the LHC high-intensity beam induced less and less vacuum activity. This contributed to conditioning of the ion trap surfaces by the LHC beam. The origin points towards electron cloud activity in the region, but the ion traps inside the ZS anode provide a vertical electrical field in the circulating beam area. Studies [125] have shown that a voltage between 500 V and 5 kV is effective at suppressing the electron cloud. Since the ion traps are powered with -3 kV and -6 kV , it was assumed this could not occur inside the ZS anode. A dedicated MD [126] confirmed the lower threshold of 500 V, but also showed that it was beneficial for the vacuum activity to bias the cathode to at least several tens of kV. The exact value of the bias voltage depends on the beam intensity. These experimental results point either to an electron cloud being produced between the ZS, i.e. in the pumping modules (MP) between each ZS tank, since the aperture transition and hence the impedance continuity, between the alternating MP and ZS equipment sequence, is abrupt. Alternatively it can also be shown that the length of the ion trap electrodes (3 m) is in the same order of magnitude as half of the 25 ns beam wavelength. The LHC beam may well induce a significant voltage on the ion trap electrodes, particularly since these are supplied with their bias voltage via a high impedance network external from the ZS tanks. This may provoke a temporary loss of bias voltage seen by the beam and cancel the electron cloud's suppressing effect from the ion traps.

The upgrade of the ZS can therefore be split into two principal topics. The first topic is vacuum improvements, which aim at avoiding the creation of an electron cloud in the pumping modules, and moving the vacuum pumping directly to where it is needed, i.e. onto the ZS themselves instead in adjacent equipment (MP). To preserve the effect of conditioning by beam scrubbing, sectorization of each ZS will be studied in case venting of only 1 ZS is needed. The second topic will address the beam impedance of the ZS extraction system. This topic will aim at keeping the transition of the geometry between ZS tanks as smooth as possible, to reduce beam impedance, and also looks into reducing the beam impedance of the ZS tanks themselves as much as possible. In this context the preservation of the bias voltage of the ion traps, while high-intensity beam is present in the SPS, is also studied.

5.14.1 Vacuum improvements

The principal modifications planned to improve the vacuum in the ZS concern the installation of the vacuum pumps directly onto the ZS vacuum vessels [127]. New vacuum vessels will be equipped with additional extrusions on the underside to allow the installation of vacuum pumps (see Fig. 5.125).

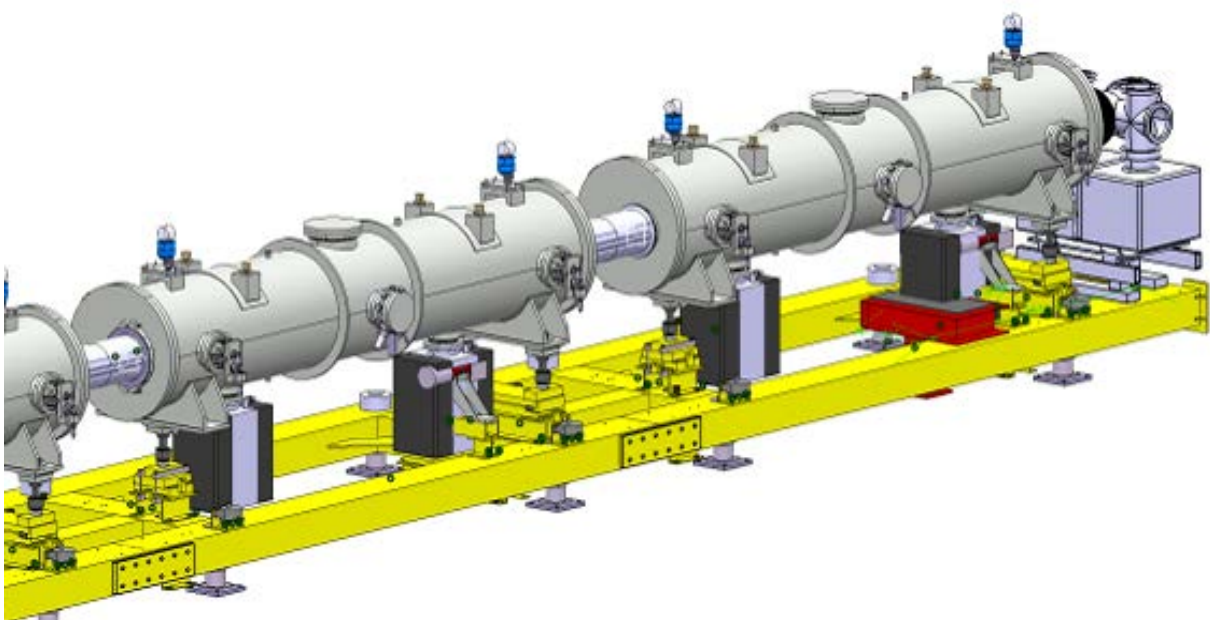


Fig. 5.125: Modified ZS tanks with ion pump installed below (black) with the aim of replacing the MP (grey box behind).

This allows the actual MP between the ZS tanks to be redesigned to have a more coherent aperture with respect to the beam acceptance of the ZS, and at the same time continue to be the support for the beam instrumentation in the ZS region. It will be studied if sufficient space can be allocated for sector valves on each side of each ZS, to allow the installation of a preconditioned ZS, without the need to vent the entire ZS section as is currently done. This would also preserve the conditioning effect of the ion trap surfaces seen by the beam from the scrubbing effect that the use of high-intensity beam seems to provide.

5.14.2 Impedance reduction

Beam impedance measurements [128] were conducted on an MP and a ZS. Until now, it has not been possible to measure a MP attached to a ZS, due to space constraints. The results of wire measurements in the ZS are shown in Fig. 5.126. Measurements were made with the ion trap and anode connections open, grounded (shorted) or connected to the ion trap connection box. There is a clear effect due to these terminations below 200MHz. The circuits used during operation suppress many resonances seen when the terminations are open or shorted.

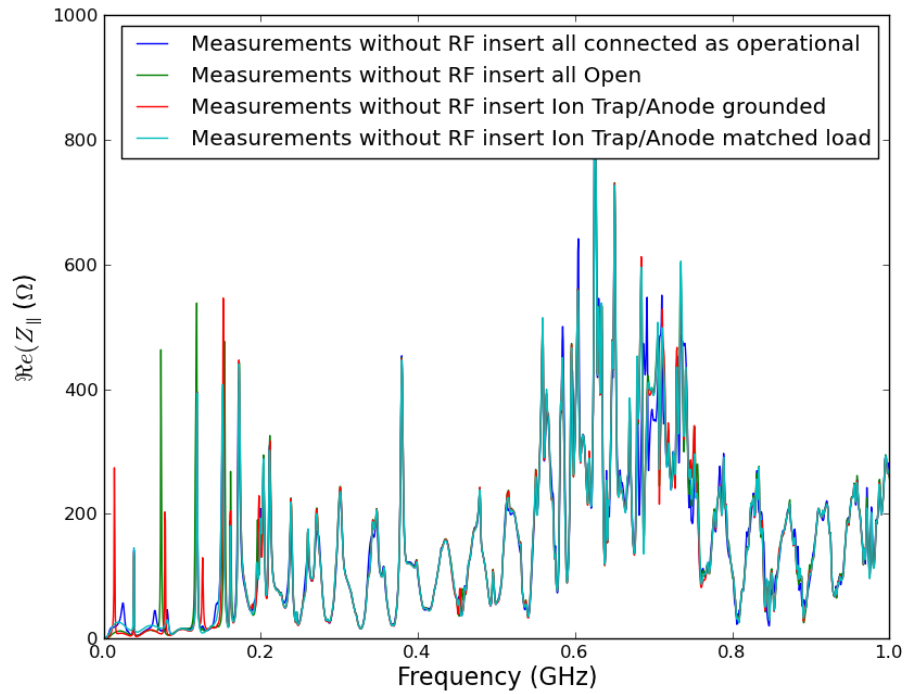


Fig. 5.126: Impedance of ZS as a function of frequency, with the ion trap and anode connection open, grounded (short) or connected to the ion trap connection box.

In an effort to reduce the impedance seen by the beam, an insert was developed between the vacuum vessel flange and the anode. This insert effectively makes a direct contact between the flange and the anode support. Although this short-circuits the anode measurement resistor (external to the ZS tank, in the ion trap connection box, see Fig. 5.127), it can be seen (Fig. 5.128) that the impedance spectrum up to 500 MHz are effectively suppressed. An increase of resonances around 620 MHz to 660 MHz with the presence of the insert can be noticed, while a new series of resonances (broadband?) between 1.2GHz and 1.35 GHz is measured.

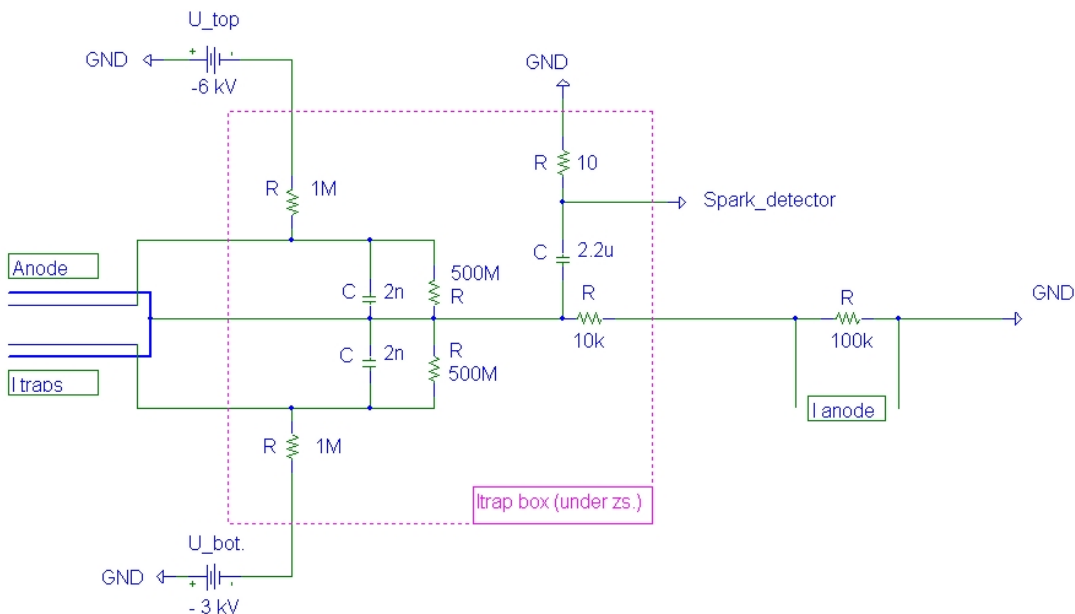


Fig. 5.127: Simplified HV circuit of ion traps (U_{top} , $U_{\text{bot.}}$) circuits and anode current (I_{anode}) measurement resistor.

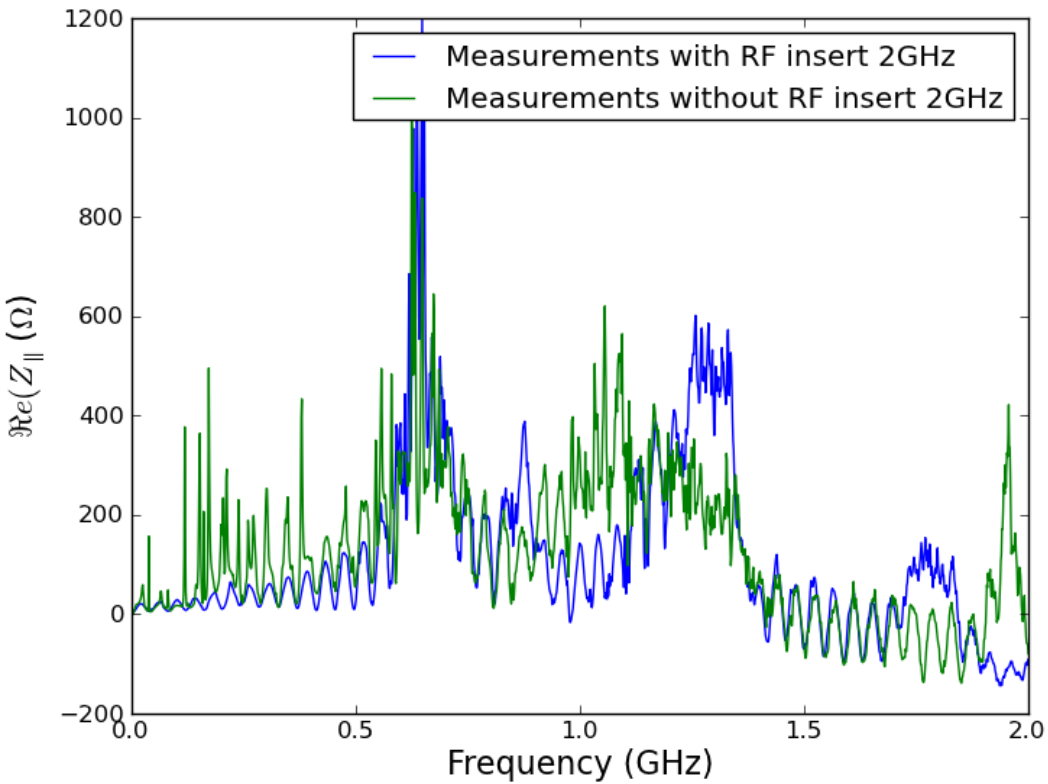


Fig. 5.128: The real component of the longitudinal impedance of the ZS with and without the impedance insert (grille) up to 2 GHz.

The LIU project aims to reduce the beam impedance as seen by the beam from the ZS itself. As demonstrated by the first tests with the RF insert, the impedance can be improved and the aim is to develop a shielding that improves impedance at lower frequencies, but also avoids introducing resistance at frequencies above 1 Ghz.

In parallel, the ion trap connection box will be improved; this connects the ion trap power supplies to the ion trap electrodes (see Fig. 5.127). It will be investigated how the impedance can be reduced between the power supplies and electrodes, with the aim of maintaining the vertical field even with high-intensity beam in the SPS, but without increasing the risk of increasing the spark rate of the ZS or allow too much energy to be dissipated during sparking and causing damage to the ZS wires. Since short-circuiting of the anode with the RF insert prevents the spark counter system from being connected to the anode, separate connections to the upper and lower ion trap electrodes are needed to link to ion trap spark counter systems.

To allow variation of the main and ion trap voltage as a function of the SPS cycle, the interlock levels, spark counting and maximum current setting need to be modified from cycle to cycle. This must prevent erroneous interlocks for current drawn when the voltage is being modified. The maximum current required to ramp up the main voltage relatively fast is significantly higher than the current allowed when at flat top, to avoid damage to the high voltage components when sparking occurs. All modifications will be deployed first at the ZS test facility (ZSTF) in LSS6. Although the operating conditions are not exactly identical to LSS2, it is considered to be a safe approach to validate new developments before deploying them to the actual extraction channel equipment.

5.15 Extraction protection elements upgrade

5.15.1 Purpose

Several types of septa protection elements are in use in the SPS extraction channels. For the two extraction channels towards the LHC in LSS4 and LSS6 two different diluters are in use, the TPSG4 and TPSG6, respectively. The TSG4 is designed to protect the thick under vacuum magnetic septa (MSE), while the TPSG6 is designed to protect the thin under vacuum magnetic septa (MST). Their purpose is to protect the magnetic septa (MS) downstream from damage by energy deposition from the beam, up to a full beam impact onto the extraction equipment. Two criteria are considered to be of importance to the survival of the MS coils:

- to protect MS copper coil from being deformed, a temperature rise of the copper will be limited to a maximum ($\Delta T_{\text{cu}} < 80 \text{ K}$);
- to avoid a vacuum leak from the coil cooling circuit to vacuum, a pressure rise in the water will be limited to a maximum:
 - $\Delta P < 50 \text{ bar}$ (TPSG4 to protect thick septum MSE);
 - $\Delta P < 25 \text{ bar}$ (TPSG6 to protect thin septum MST).

For the present design the nuclear calculations were done at CERN for ‘ultimate’ intensity LHC-type beam (see Table 5.26) and the subsequent thermal and dynamic mechanical calculations were performed at CRNS4 [129, 130]. The results of these calculations were presented in Ref. [131]. The first conclusion was that the requirement to limit the temperature rise of the copper in the magnet coil is not the dominating requirement. However, the limit imposed on the water pressure rise in the water in the cooling channels in the magnet coil clearly drives the design of the diluters. It was shown to limit the water pressure rise in the MSE to 50 bar; the copper temperature rise is limited to 15 K. Similarly, to limit the water pressure rise in the MST to 25 bar, the associated copper temperature rise in the magnet coil is below 8 K.

As can be seen in Fig. 5.129, the calculations predict that the instantaneous temperature rise of the diluting blocks upon full impact of the ultimate intensity LHC-type beam is significant, but remain acceptable for the materials used. More critical is the maximum mechanical stress to which each block is subject, as a result of the thermal expansion and the resulting shockwave inside each block. The Stassi criterion is suitable for isotropic brittle materials having different tensile and compressive strength. The equivalent Stassi stress is calculated on the basis of the Von Mises equivalent stress, the ratio between the compressive and tensile strength and the hydrostatic pressure. In Fig. 5.130 the corresponding Stassi ratio is indicated for each block of the TPSG4. The results are acceptable for the graphite blocks, being well below the failure limit for the Carbon Composite (CC) blocks, but the stress ratio is high for the titanium and Inconel blocks. It is currently considered that this is acceptable, since these alloys have a ductile behaviour.

Temperature rise and Stassi values are shown for the TPSG6 in Figs. 5.131 and 5.132. Even for the metallic blocks, the stress levels remain below the plastic deformation limits.

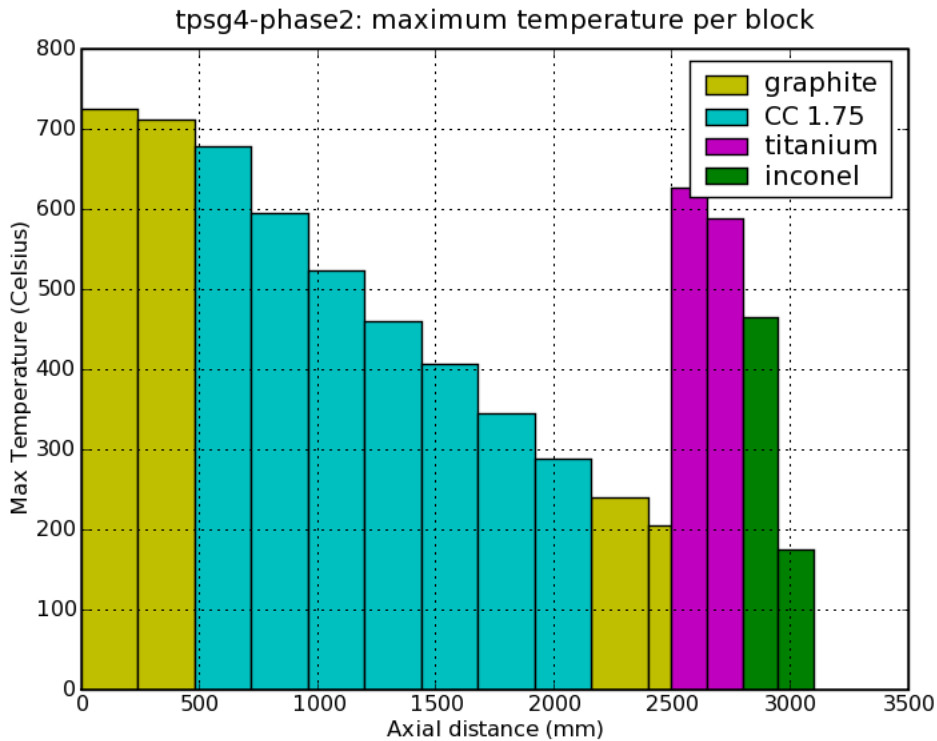


Fig. 5.129: Temperature in the diluting blocks of TPSG4, as a function of their longitudinal position upon full impact of the ultimate intensity LHC-type beam of the SPS.

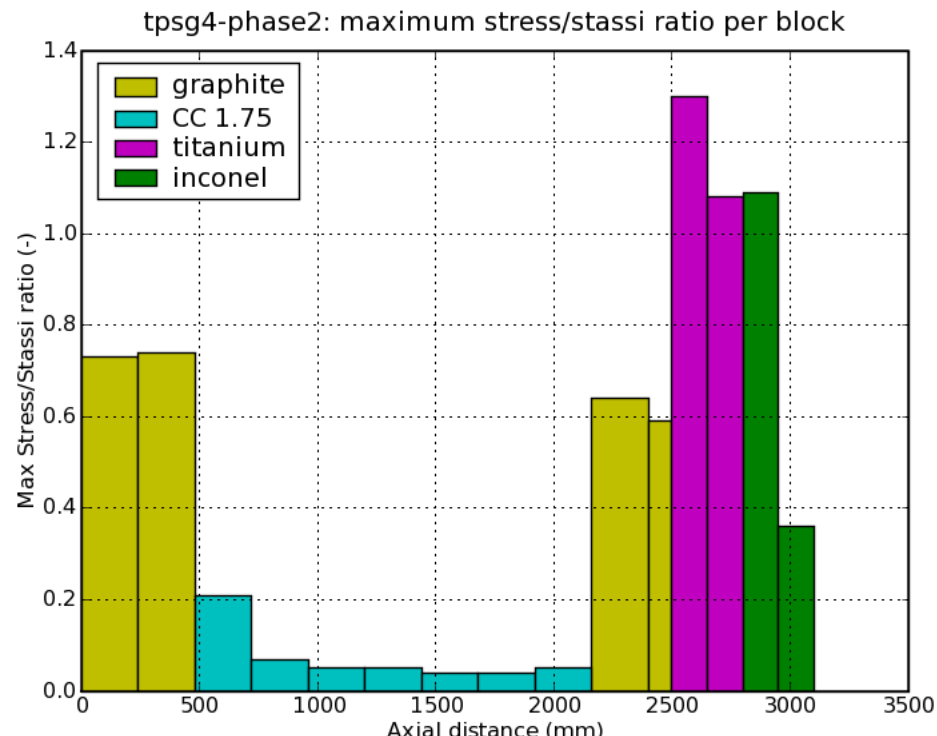


Fig. 5.130: Maximum Stassi ratio in each block of the TPSG4, as a function of their longitudinal position upon full impact of the ultimate intensity LHC-type beam of the SPS.

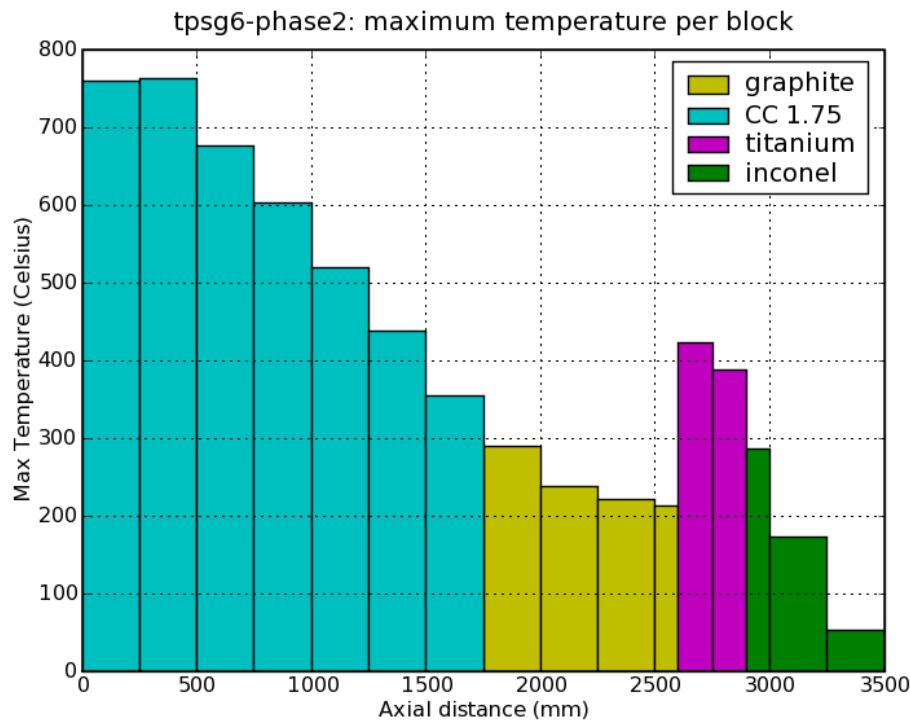


Fig. 5.131: Temperature in the diluting blocks of TPSG6, as a function of their longitudinal position upon full impact of the ultimate intensity LHC-type beam of the SPS.

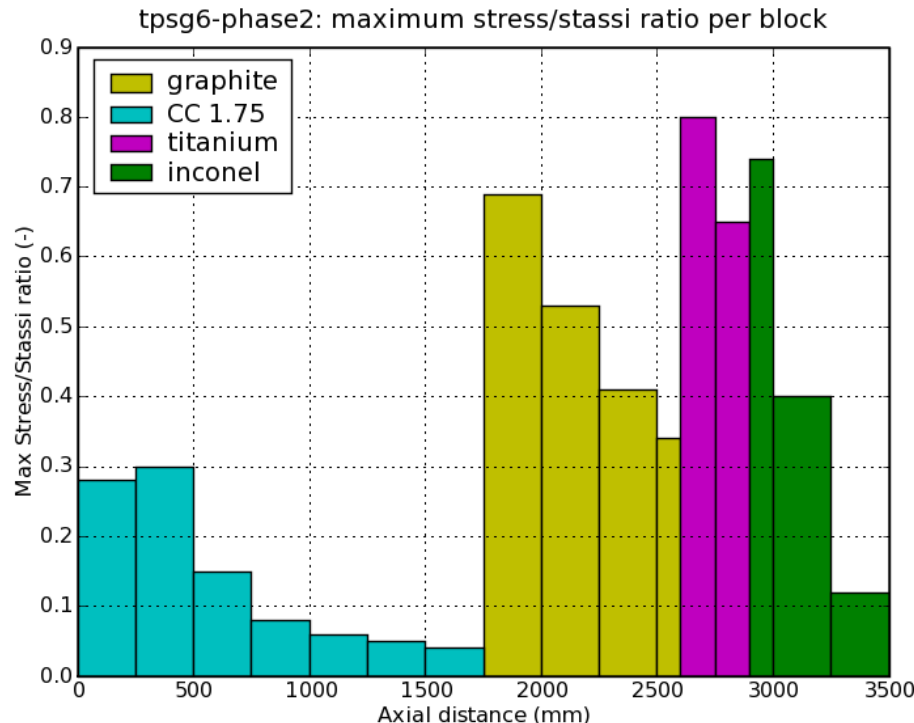


Fig. 132: Maximum Stassi ratio in each block of the TPSG6, as a function of their longitudinal position upon full impact of the ultimate intensity LHC-type beam of the SPS.

5.15.2 Validation of existing design and failure assumptions

As described above, TPSG4 and TPSG6 [132] are designed to be compatible with the ultimate LHC beam parameters (see Table 5.27). Nevertheless, the assumption that exceeding the Stassi limit for ductile materials is acceptable (titanium and Inconel blocks) as well as the assumptions for the non-isotropic behaviour of the CC material, need to be validated before further upgrades can be studied. Therefore a first test was made at the CERN HiRadMat facility in 2012, where a TPSG4 was installed in front of an MSE. The MSE was not electrically powered, but during impact of the SPS nominal LHC beam (see Table 5.27) directly onto the TPSG4, the cooling circuit was pressurized to nominal operating pressure. Both TPSG4 and MSE were kept under vacuum and the beam entered the set-up via a purpose-built beam window made of beryllium. At each impact of the beam onto the TPSG4, the vacuum rose but the ion pumps did not trip. Although the detailed inspection of the TPSG4 and MSE is still to be finished at the time of writing, it is assumed from the swift vacuum recovery that the MSE cooling circuit is not damaged.

It is expected that an LHC beam with higher than nominal (ideally ultimate) intensity should become available in SPS by the end of 2014. Although the longitudinal emittance will not be within specification for this higher intensity beam, a new test of the TPSG4/MSE is of interest and will be pursued.

Table 5.27: Principal beam parameters assumed for the design of the septa extraction protection elements (diluters) TPSG4 and TPSG6.

	Nominal	Ultimate	LIU-SPS
Momentum (GeV/c)	450	450	450
Time structure	25	25	25
Bunch intensity (number of protons)	$\text{ns} \times 72 \times 4$ 1.1×10^{11}	$\text{ns} \times 72 \times 4$ 1.7×10^{11}	$\text{ns} \times 72 \times 4$ 2.5×10^{11}
Total intensity (number of protons)	3.2×10^{13}	4.9×10^{13}	7.2×10^{13}
Beam size H (mm)	0.97	0.97	0.75
Beam size V (mm)	0.40	0.40	0.30

5.15.3 Upgrade

If the tests at HiRadMat confirm that the assumptions taken for its design are valid, studies will be needed to predict their behaviour at LIU-SPS intensity. Even if these studies confirm that the present design sufficiently protects the MS at LIU-SPS intensities, more spare diluters need to be built: it is known that the mechanical properties of CC degrade with an integrated radiation dose [133], so they will have to be regularly changed. On the other hand, if the diluters protect the MS sufficiently but are themselves damaged they might be used as sacrificial diluters, provided that the damage is limited.

If the study shows that the present diluters do not protect the MS sufficiently or the diluters are significantly damaged during impact, the absorption length will have to be increased. This would imply the installation of an additional girder upstream of the quadrupole in front of the existing TPSG4, the position of which needs to be adjusted and controlled separately with relation to the extraction channel remote displacement system. However, for the TPSG6 it might be possible to free some additional space directly in front of the TPSG6. If this is sufficient, a similar solution as anticipated for the TPSG4 would have to be envisaged. A study how to free the required space and the layout of the diluters' absorbing structure is still to be studied.

5.16 Orbit stability and correction

The trajectories in the SPS-to-LHC transfer lines drift and must be corrected frequently. Each correction campaign costs significant time and reduces the availability for LHC physics. The variations are seen mainly in the horizontal plane. An analysis of the origin of the trajectory variations revealed several sources. The ripple in the 20 kA power supply for the SPS extraction septum (MSE) is one of the main sources of variation for both transfer lines. After the improvement of the ripple between LHC runs 2011/2012, the shot-by-shot stability was greatly improved, but now trajectory drifts prevail. The other source is suspected to come from the SPS orbit itself [134, 135]. Towards the end of LHC run 1, SPS orbit data during LHC physics beam cycles was collected and analysed to localize the source of the orbit drifts.

5.16.1 Orbit at extraction through BPM fit

In the extraction region, a large orbit bump of more than 35 mm is applied to move the circulating beam as close as possible to the extraction septum and reduce the required strength of the extraction kicker. The data from the larger aperture BPMs in the extraction region have large errors and cannot be used directly to define the beam position and angle at the extraction point. A fit based on many BPMs was used to obtain a better estimate. Each orbit is fitted using the function

$$X(s) = [A \times (\mu(s)) + B \times \cos(\mu(s))] \times \sqrt{\beta(s)} + \frac{dp}{p} \times D(s), \quad (5.13)$$

which represents a betatron oscillation plus a dispersion trajectory due to momentum offset. The fit parameters A , B and dp/p are calculated by a least squares fit routine in Python.

Because the orbit in the SPS is not stored automatically, only data from October to December 2012 were saved and available for analysis. The orbits have been stored at $t = 18\,500$ ms, which is 110 ms after the start of the flat top. Further, this data has been filtered using injection quality check (IQC) data to only include orbits where the beam was successfully extracted to the LHC. To observe orbit changes, the difference orbit with respect to a reference early in the period was used. In the plots the reference time is marked by a vertical grey line.

The calculated fit parameters A , B and dp/p are given in Fig. 5.133. Except for a few orbits, dp/p is small. Transfer with large momentum offset is normally stopped by the SPS beam quality monitor (BQM) before extraction and is most likely an artefact of longer than normal rephasing early at the flat top. The phase advance of the drift has also been calculated: $\mu_0 = \tan^{-1}(B/A)$.

For orbits close to the reference the fraction B/A can be very large and thus fluctuate strongly. Nevertheless, the phase changes over time, indicating that there is more than one source.

The resulting position and angle at BPCE.61805 (for TI2) are given in Fig. 5.134 and for BPCE.41801 (TI8) in Fig. 5.135. In the horizontal plane the orbit drifts away from the reference by over a millimetre within a week. In the vertical plane the orbit is stable.

Another indication for SPS orbit drifts came from the frequent necessity to re-adjust the SPS scraper position. The LHC physics beams are scraped before each extraction. Fig. 5.136 shows the evolution of the beam position at the scraper and the horizontal scraper setting. The scraper position mostly follow the orbit drift, but some changes could also be related to changes in scraped intensity.

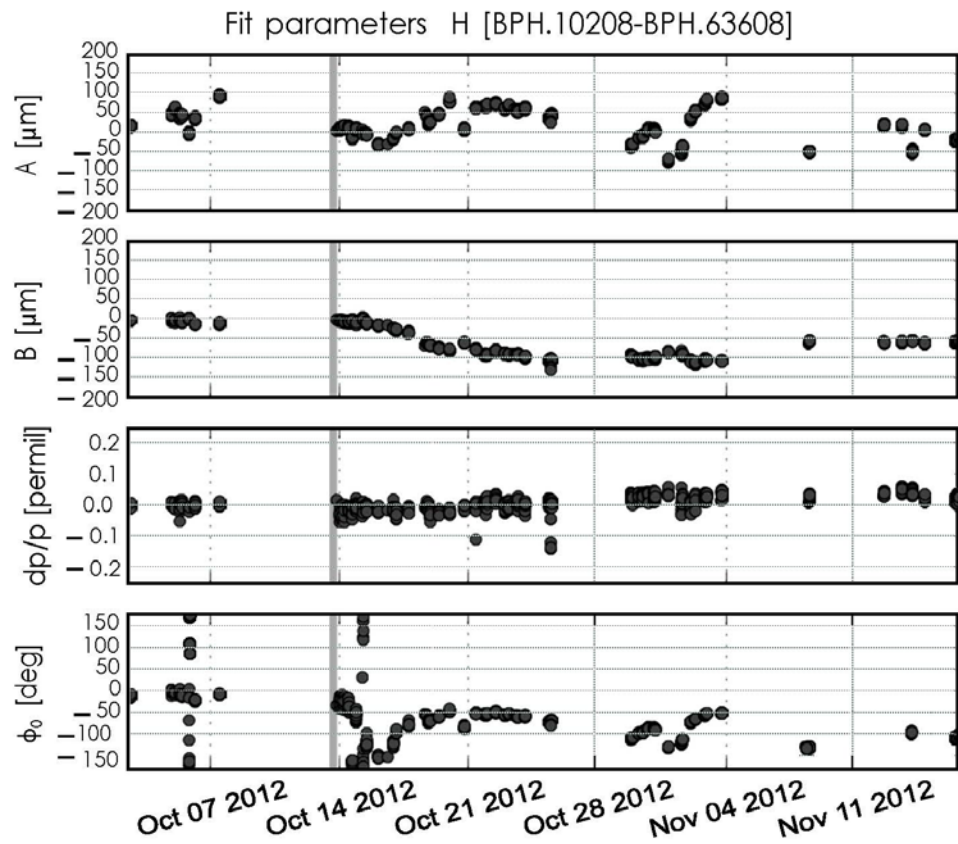


Fig. 5.133: The evolution of the fit parameters A , B and dp/p are shown for the orbit data in the horizontal plane. The bottom plot shows the phase advance $\mu_0 = \tan^{-1}(B/A)$ calculated from the fit parameters.

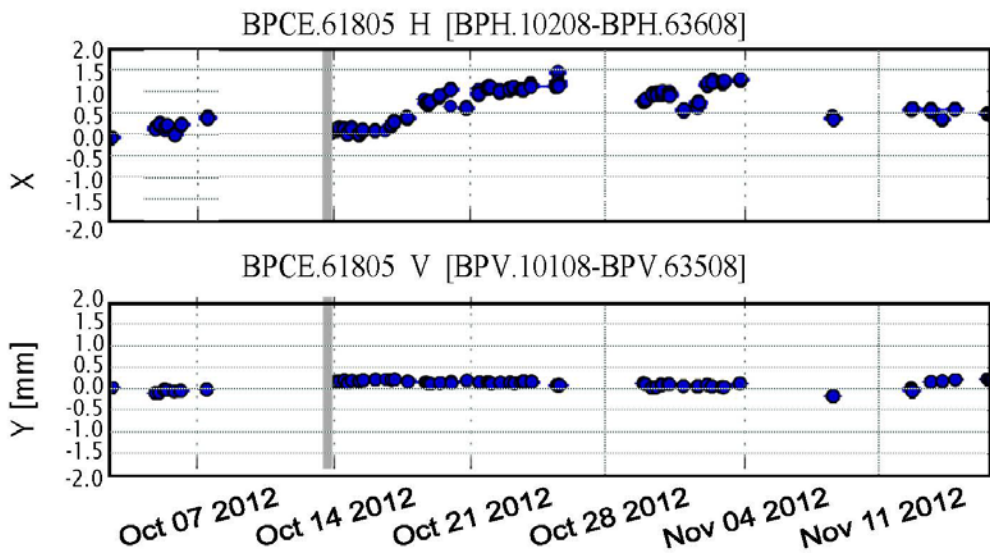


Fig. 5.134: The SPS orbit at extraction to TI2 is calculated at BPCE.61805. In the horizontal plane variations of 1.4 mm are observed. Within the period of one week the effect is already strong. In the vertical plane the variations are 0.4 mm throughout the whole period.

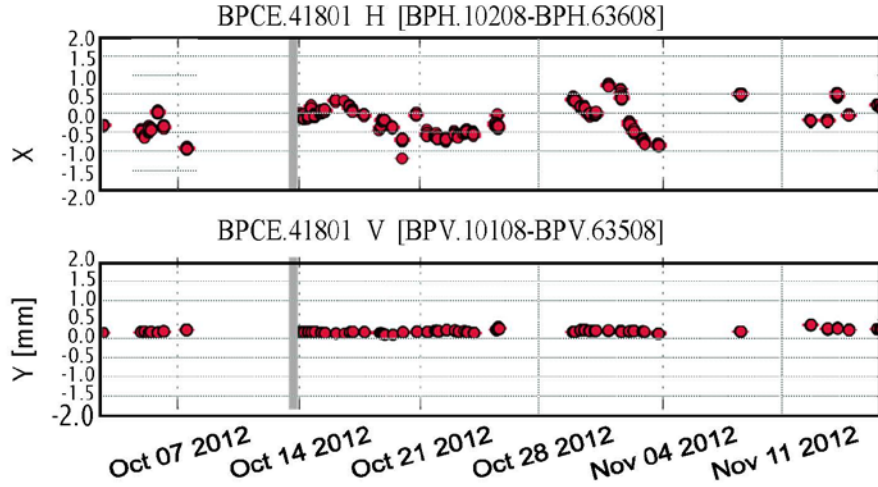


Fig. 5.135: The SPS orbit at extraction to TI8 is calculated at BPCE.41801. In the horizontal plane the drift is 1.8 mm, while in the vertical plane it is only 0.3 mm.

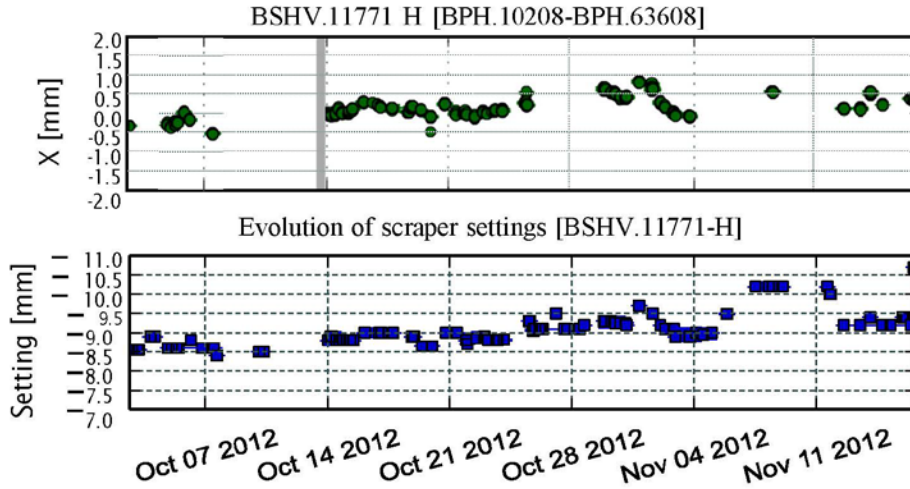


Fig. 5.136: Calculated position at the scraper BSHV.11771 in the horizontal plane versus the scraper settings in the same period.

5.16.2 Source investigations

The orbits have also been analysed by model independent analysis (MIA) [136]. Through singular value decomposition MIA separates the temporal and spatial eigenmodes of the orbit data. The spatial eigenmodes with significant eigenvalues can be used to identify the sources of variation. The eigenvalues found in the analysis of the orbit data are given in Fig. 5.137. In the horizontal plane there are two large eigenvalues that correspond to betatron oscillations. The actual sources are linear combinations of the two eigenvectors. As there are two betatron modes there are a minimum of two sources. Also, the largest eigenvalue in the vertical plane corresponds to a betatron oscillation, but as the orbit variations in the vertical plane are small we do not consider them further.

To further probe the sources, the analysis period is divided into smaller periods. The data have not been stored continuously, so that there are gaps as can be seen from Figs. 5.133–5.154. Natural selections for periods are therefore 13 October to 24 October and 29 October to 4 November. Because there are many injections per point in time, these periods still provide sufficient data for analysis.

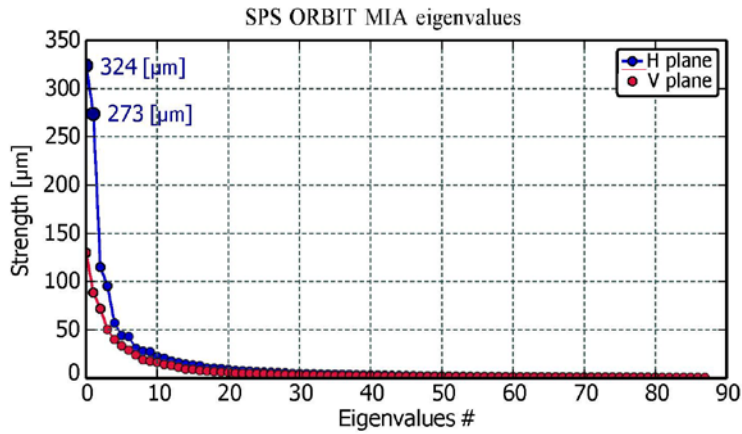


Fig. 5.137: Analysis of the orbit shows that there are two strong eigenmodes in the horizontal plane. Both correspond to betatron oscillations.

5.16.2.1 Period 1: 13 October to 24 October

Over these 10 days, the orbit drift in the horizontal plane is clearly present with drifts of over 1 mm at both extraction BPMs. By running MIA on these 323 orbits, only one eigenmode stands out, see Fig. 5.138. The eigenvalue is 359 μm , which is of the same order as the eigenvalues for the whole period. The corresponding spatial eigenmode is fitted to MAD-X simulations of errors on the bumpers and septa in LSS4 and LSS6. See Table 5.28 for a list of extraction elements and the total strength of each element or series of septa as it was operated during this period. The best match is found to be MST.6 or MSE.6, see Fig. 5.139. These two elements are very close in phase (6.3°) and it is therefore difficult to distinguish between them.

The circulating beam only sees stray fields from the septa. The MSE stray field depends on the distance from the septum [137]. Because of the extraction bump this distance does in fact vary strongly over the length of the septum magnet. Therefore a model of the bump and septum was made to estimate the effect of the stray field due to a 1 mm change of the orbit, see Fig. 5.140. The outcome of the study is, however, that the stray field of the MSE and MST in LSS6 give additional orbit deviations of only 14 μm and 7 μm peak-to-peak respectively, which is too small to explain the drifts. A measurement with beam is planned to investigate if the actual stray fields are stronger than previously measured. For the septa, unused compensation coils are available, but the effect of the stray field needs to be better understood.

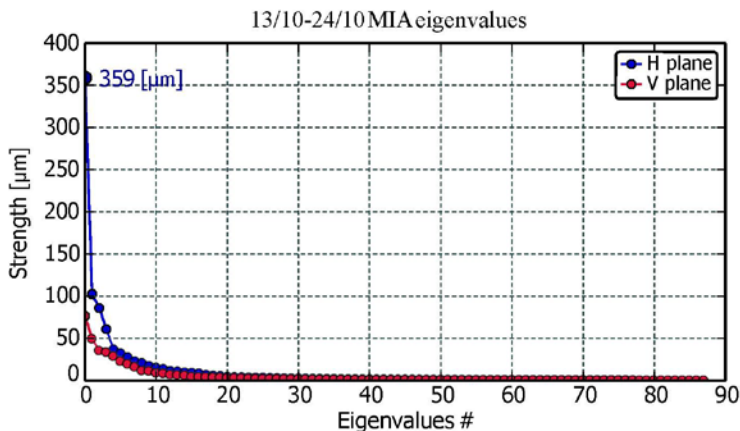


Fig. 5.138: Taking a shorter time period (13 October to 24 October) only one eigenmode is significant

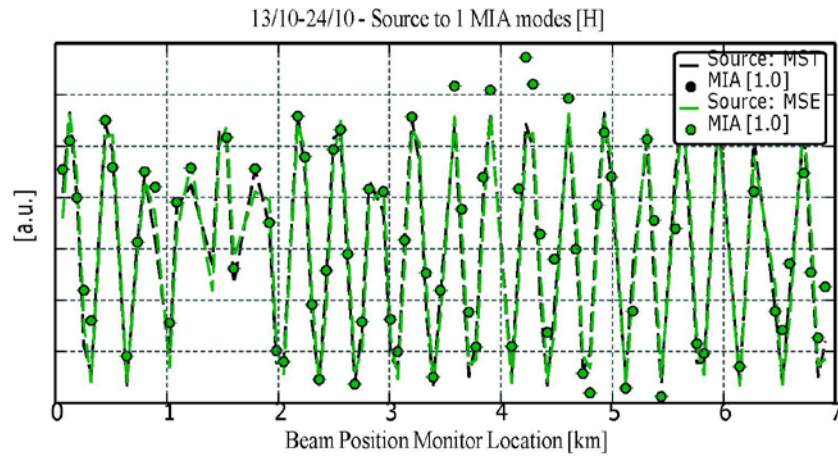


Fig. 5.139: For the period 13 October to 24 October the best match to the source is found to be the MST or MSE in LSS6

Table 5.28: SPS Extraction elements (TI2 and TI8)

Element	Phase advance (μ)	Strength (mrad)
MPSH.41402	11.367 392 89	0.236 9
MPLH.41658	11.591 082 32	0.276 1
MPLH.41994	11.920 895 68	0.317 7
MPSH.42198	12.111 166 57	0.117 1
MSE.418	11.758 746 73–11.803 729 48	12.122 5
MPLH.61655	18.294 938 03	0.459 5
MPLH.61996	18.634 250 68	0.122 4
MPSH.62199	18.820 405 73	0.345 7
MPSH.61402	18.078 609 98	0.031 7
MST.617	18.439 856 22–18.445 897 01	1.063 8
MSE.618	18.463 479 14–18.493 374 34	8.780 0

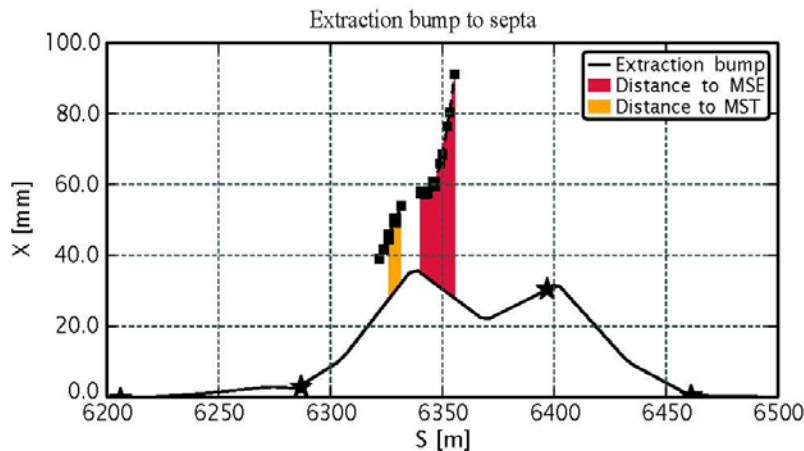


Fig. 5.140: The effect of the stray fields of the MST and MSE in LSS6 are simulated using the distance of the bump to the septa.

5.16.2.2 Period 2: 29 October to 4 November

The second period is shorter, but still shows significant orbit drift. For this period the drift is stronger at BPCE.41801. This data set contains 179 orbits saved over 5 days. For this period there is also only one significant eigenvalue of 345 μm , see Fig. 5.141. By matching the eigenmode to the MAD-X simulations, the best match is MPSH.62199 (or MPLH.61655, 189° upstream), see Fig. 5.142. The eigenmodes for the two periods do not match the same sources. For the bumpers, logged current variations were used to simulate the effect on the orbit, but this effect is also much too small to explain the observed orbit deviations.

Another puzzle is the possible correlation of the orbit drift at the extraction point with the local temperature, see Fig. 5.143. To date the origin of this correlation, if true, has not been found.

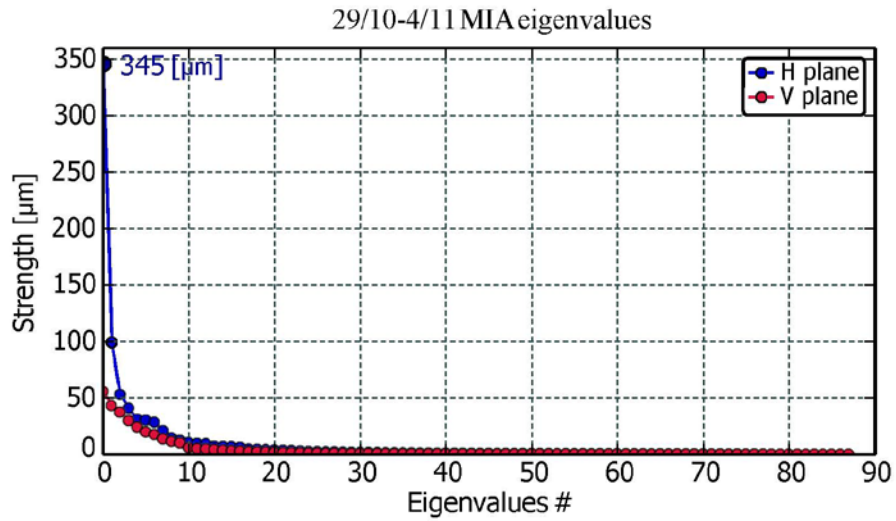


Fig. 5.141: For the second isolated period there is also only one significant eigenmode

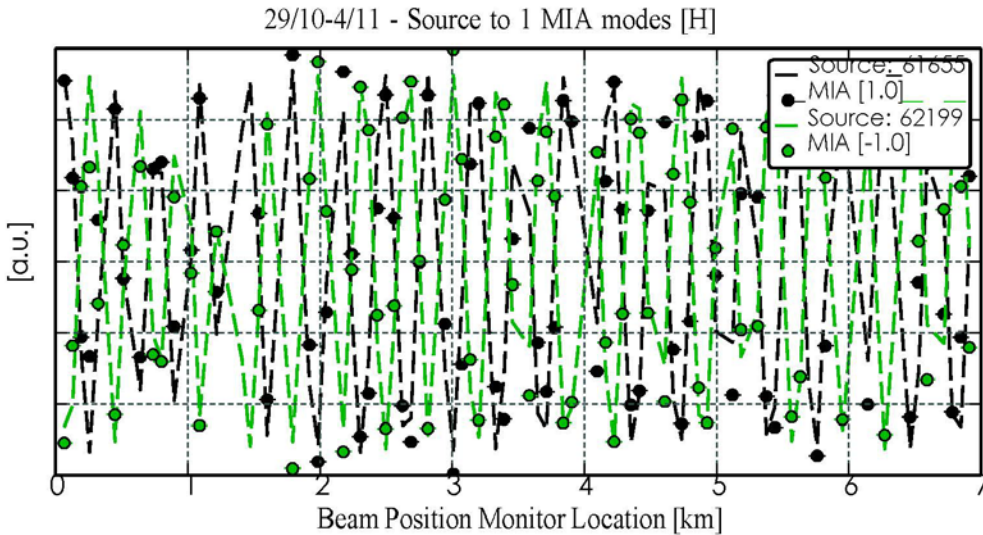


Fig. 5.142: For the period 29 October to 4 November the best match is MPSH.62199 or MPLH.61655

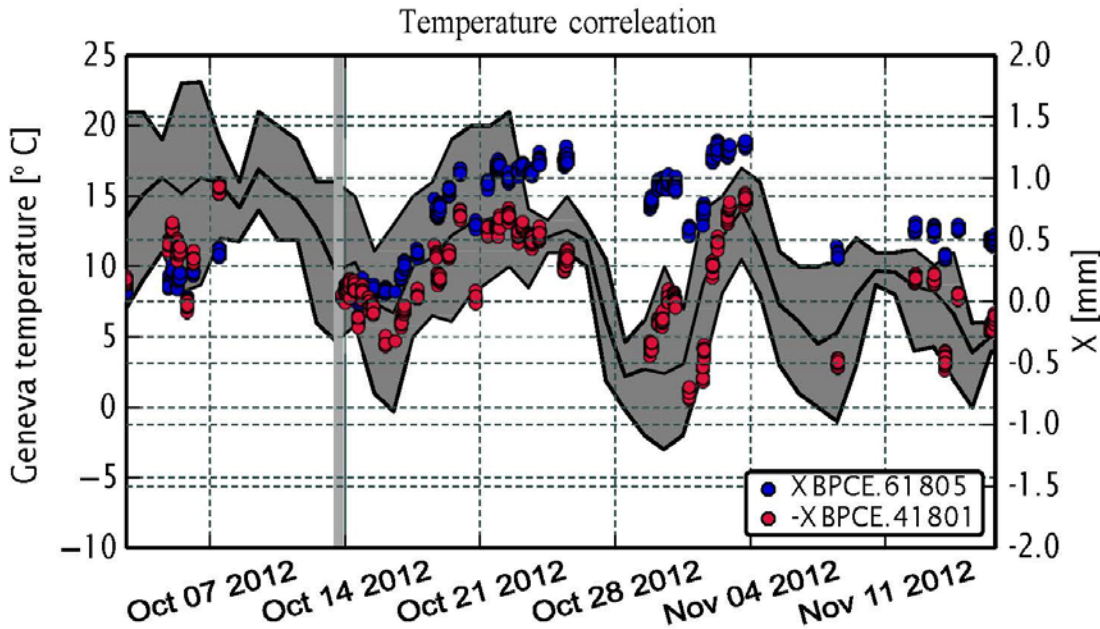


Fig. 5.143: The drifts at extraction match fairly well to the outside temperature

5.16.3 Orbit correction strategies

As the source of the orbit drift is not fully understood and might not be possible to correct, we have looked into the effectiveness of either a global orbit correction or a local correction at the extraction points by using the interlocked bumpers and without resorting to the BPCE's erroneous orbit data.

A total of 1001 measured orbits have been used for creating the MAD-X models reproducing the same orbit changes at the BPMs with relation to an arbitrary chosen golden orbit, namely the first one recorded. The resulting orbits have been globally corrected either using all SS4 and SS6 bumpers through a SVD algorithm or using the MAD-X MICADO algorithm with up to two correctors. In the SVD algorithm the two largest singular values have been retained.

For the local correction three different methods for analysing the orbit differences and interpolate position and angle at the extraction septum have been considered:

- ‘fake correction’ using all correctors¹ through a SVD; the closed orbit and its derivative due to the correctors alone is then computed (the number of correctors is actually the largest reasonable number of elements);
- Fourier analysis;
- amplitude-phase-momentum fit.

By any of these three methods we get an analytical expression of the orbit allowing to evaluate the change of the beam position and angle at the septum. The four bumpers are used to create a local bump correcting position and slope while keeping the orbit unchanged outside (four constraints).

Figures 5.144 to 5.146 illustrate the three methods of orbit analysis on one particular orbit difference.

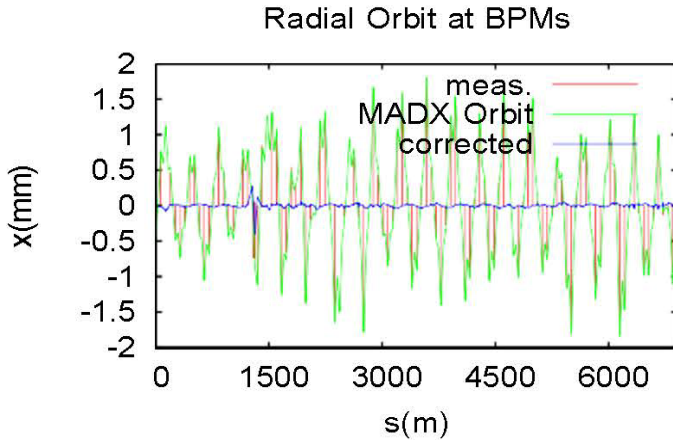


Fig. 5.144: Example of ‘fake correction’: in red the actually measured orbit at the BPMs, in green the closed orbit obtained with the MAD-X model, in blue the closed orbit after the correction via SVD.

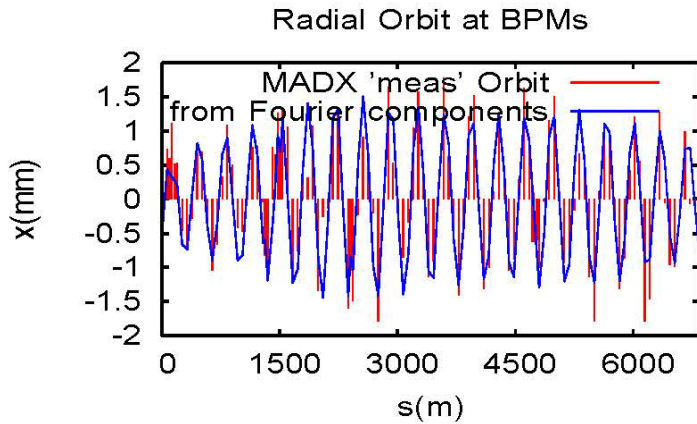


Fig. 5.145: Example of Fourier analysis of the BPM data: in red the MAD-X orbit at the BPMs, in blue the closed orbit obtained by summing the Fourier components 19, 20 and 21.

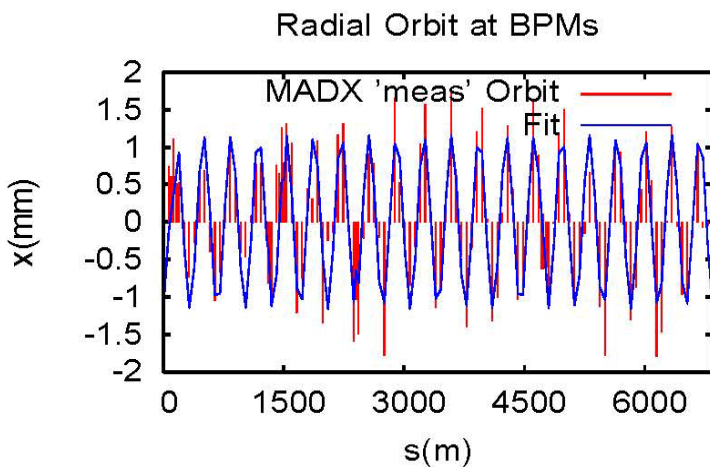


Fig. 5.146: Example of amplitude-phase-momentum fit: in red the MAD-X orbit at the BPMs, in blue the trajectory obtained by fitting all BPM data with a free oscillation and a momentum offset.

The corresponding ‘actual’ position and angle errors at the MSE.61852 (MAD-X model) and their values inferred through the three different methods are quoted in Table 5.29.

Table 5.29: $(\Delta x, \Delta x')$ at MSE.61852

	x (mm)	x' (mrad)
MAD-X	0.935	-0.020
Fake correction	1.002	-0.021
Fourier	0.682	-0.016
Fit	0.825	-0.013

Results for the 1000 difference orbits, without calibrations errors and using all available BPMs, with the exception of the BPCEs, are summarized in Tables 5.29 and 5.30 for SS6 and SS4, respectively. For the Fourier analysis, orbits have been computed by summing the harmonic components 20 ± 2 and 20 ± 7 , 20 being the integral part of the SPS horizontal tune.

The effect of random calibration errors and missing BPMs have been studied for the most promising methods, namely fake correction and Fourier analysis. Results are summarized in Table 5.31 for SS6 with 50% missing monitors and 25% calibration errors (one seed).

The kicks required for correcting the 1000 difference orbits at SS6, without BPMs errors, are shown in Figs. 5.146 and 5.147 for the fake correction method and Fourier analysis, respectively.

The corrections are relatively small and it is crucial to prove that such small kicks may be precisely set. Measurements of the bumpers' power supply stability are ongoing.

Table 5.30: SS6

	$A^2 x$ (μm)
Uncorrected	0.0081 ± 0.0062
Fake correction	$0.952 \times 10^{-4} \pm 0.9092 \times 10^{-4}$ Fourier
Fourier analysis (20 ± 2)	0.0020 ± 0.0027
Fourier analysis (20 ± 7)	0.0025 ± 0.0018
Fit (all BPMs)	0.0053 ± 0.0081
Eight bumpers (SVD)	0.0032 ± 0.0053
Two bumpers (Micado)	0.0037 ± 0.0053

Table 5.31: SS4

	$A^2 x$ (μm)
Uncorrected	0.0058 ± 0.0055
Fake correction	$0.429 \times 10^{-4} \pm 0.631 \times 10^{-4}$
Fourier analysis (20 ± 2)	0.0028 ± 0.0022
Fourier analysis (20 ± 7)	0.0014 ± 0.0014
Fit (all BPMs)	0.0077 ± 0.0079
Eight bumpers (SVD)	0.0020 ± 0.0019
Two bumpers (Micado)	0.0018 ± 0.0026

Table 5.32: SS6

A^2x (μm)	
Uncorrected	0.0081 ± 0.0062
Fake correction	$0.667 \times 10^{-3} \pm 0.701 \times 10^{-3}$
Fourier analysis (20 ± 2)	0.0028 ± 0.0028

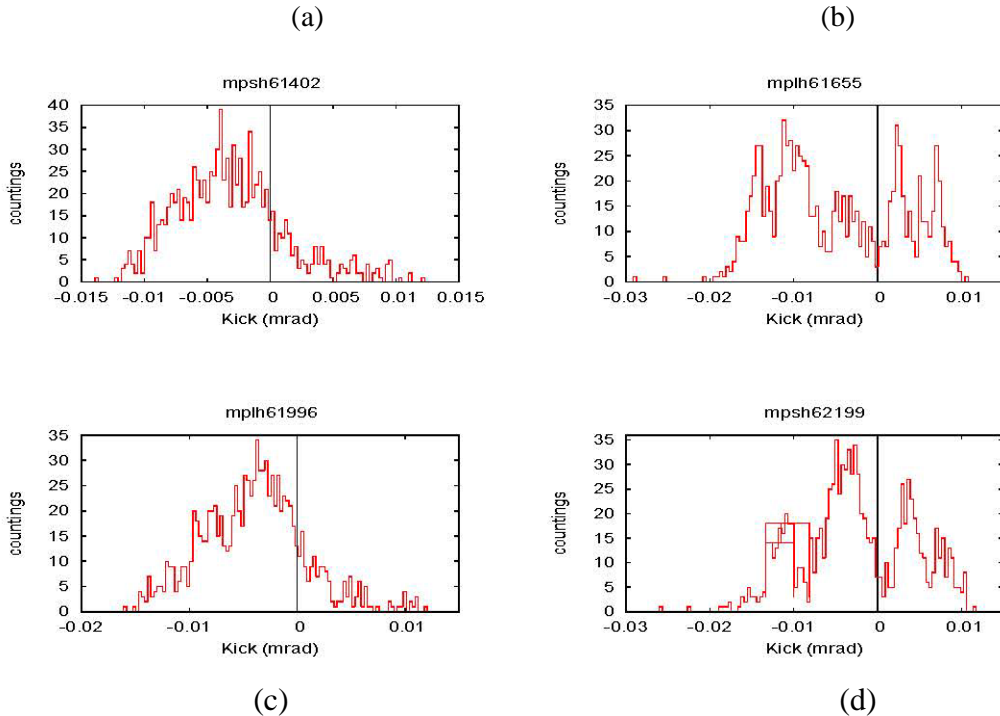


Fig. 5.147: ‘Fake’ correction kicks. (a) MPSH.61402 ($\theta_0 = 0$). (b) MPLH.61655 ($\theta_0 = 0.512$ mrad). (c) MPLH.61996 ($\theta_0 = 0.094$ mrad). (d) MPSH.62199 ($\theta_0 = 0.398$ mrad).

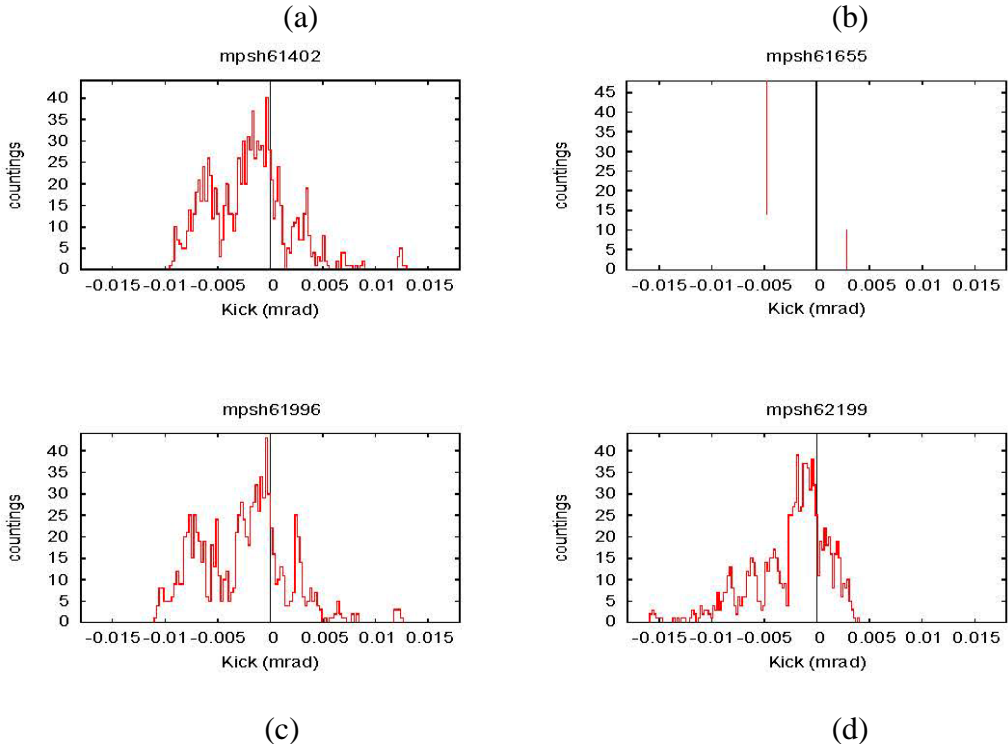


Fig. 5.148: Fourier analysis kicks. (a) MPSH.61402 ($\theta_0 = 0$). (b) MPLH.61655 ($\theta_0 = 0.512$ mrad). (c) MPLH.61996 ($\theta_0 = 0.094$ mrad). (d) MPSH.62199 ($\theta_0 = 0.398$ mrad).

The trajectory amplitude due to errors in position Δx_0 and slope $\Delta x'_0$ at the extraction septum is given by:

$$A^2 x \equiv \beta x \Delta x'^2 + \gamma z \Delta x'^2 + 2\alpha x x_0 x'_0. \quad (5.14)$$

The collimators limit the transfer line aperture to 4.5σ around an empirically found golden trajectory. Considering a 3σ beam envelope and adding in quadrature betatron and trajectory contributions to the actual beam size, the excursions at the extraction septum should be such that

$$(\sqrt{\beta_x A_x})^2 + (3\sqrt{\beta_x \epsilon_x})^2 < (4.5\sqrt{\beta_x \epsilon_x})^2, \quad (5.15)$$

i.e.

$$\hat{A}^2 x < 11.25 \epsilon_x = 0.082 \text{ m}, \quad (5.16)$$

where $\epsilon_x = \epsilon N_x / (\beta \gamma) rel = 7.3 \text{ nm}$ ($\epsilon N_x = 3.5 \mu\text{m}$).

It is worth noting that the uncorrected amplitudes (see Tables 5.30 and 5.31) already satisfy the criteria. The presence of large tails and/or large momentum deviations, however, can make the limit on $\hat{A}^2 x$ tighter. During the run 2012–2013, drifts of the extracted beam trajectories and losses in the LHC have been observed that may be related to the observed SPS orbit drifts. Therefore it has been decided to implement the fake correction and the Fourier analysis methods and gain experience with these two methods when SPS operation resumes.

Tables

5.1.	SPS intensity limitations for 25 ns beam in present situation and in different scenarios of the 200 MHz RF system upgrade.....	442
5.2.	Optics parameters and machine position of damper systems for LHC beams	485
5.3.	Kick strength (total of two systems per plane) of dampers up to 100 kHz assuming for the horizontal plane 2.9 kV (TH 561 tube) and the vertical plane 2.6 kV (RS 2048 CJ tube).	485
5.4.	Comparison of transverse voltage kicks for different kicker options assuming different power amplifiers for strip-lines (100 mm length) and slot-line kicker (1 m length); two amplifiers are needed with a rating as in the table to power the two sides of the kicker individually [68].....	490
5.5.	Dump kicker parameters [108].....	507
5.6.	Maximum beam loading on the TIDVG front face for different failure scenarios.....	511
5.7.	LIU beam parameters assumed for TCDI studies, 288 bunches per SPS transfer.....	515
5.8.	Stress maxima from ANSYS calculations in a TCDI jaw of graphite R4550 for a 1σ impact parameter of LIU BCMS beam, full batch. Values exceed the limit for tensile stresses. No dynamic effects (e.g. shock waves) have been included.	517
5.9.	Compilation of materials tested in simulation. Material density, advantages and disadvantages are listed.....	517
5.10.	Preliminary locations of 3.5 m long TCDI collimator ensembles in TI 2. The spot size at the collimators and the phase advance between two neighboring TCDI couples are also given. An emittance of $2.1 \mu\text{m}$ is used for the spot size.....	518
5.11.	List of individually powered quadrupoles in TI 8 needed to host the LIU transfer line collimators as presently proposed	519
5.12.	Elements in TI 8 that need to be shifted to make space for the 3.5 m long transfer line collimator ensemble. Details need to be finalized.....	519
5.13.	Preliminary locations of 3.5 m long TCDI collimator ensembles in TI 8. The spot size at the collimators and the phase advance between two TCDI couples are also given. The numbers refer to the exit of the collimators. An emittance of $2.1 \mu\text{m}$ is used for the spot size. One additional vertical TCDI in front of the MSI at an already existing TCDI location would be needed to protect the vertical aperture bottleneck at that location. It is not part of this list.....	519
5.14.	The currently installed BPM types used for position measurement in the SPS	520
5.15.	SPS beam types expected for the LHC operation period. The nominal number of batches (N_{bat}) varies between one and four for protons, but exceptionally this number	

can be larger for SPS MDs (up to eight for electron cloud studies). For ions the number of batches is in the range 1–13.	521
5.16. Optics parameters at the SPS-BSRT location.....	528
5.17. Proposed vacuum layout for the halved x10 vacuum sectors.....	533
5.18. Proposed sectorization for x60 vacuum sector.	534
5.19. List of fast valves in SPS.....	537
5.20. Material costs for vacuum sectorization	538
5.21. Parameter list used in the TWC impedance model.....	542
5.22. Most relevant flange resonances sorted by ascending resonant frequency	546
5.23. Comparison between simulations and bead-pull measurements	547
5.24. Most relevant BPM resonances. The values in the table already take into account the total number of BPMs in the machine	547
5.25. Known contributions to the low frequency constant $\text{Im}(Z)/n$	548
5.26. Main impedance contributors to longitudinal SPS impedance.....	549
5.27. Principal beam parameters assumed for the design of the septa extraction protection elements (diluters) TPSG4 and TPSG6.....	553
5.28. SPS extraction elements (TI2 and TI8)	568
5.29. $(\Delta x, \Delta x')$ at MSE.61852.....	572
5.30. SS6.....	572
5.31. SS4.....	572
5.32. SS6.....	573

Figures

5.1. Bunch shapes in longitudinal phase space at SPS injection [14]: (a) PS operational conditions ($V_{40\text{MHz}} = 300$ kV and $V_{80\text{MHz}} = 600$ kV); (b) rotation with $V_{40\text{MHz}} = 600$ kV, $V_{80\text{MHz}} = 600$ kV and optimal timings; simulations done with code ESME. The SPS bucket shown for the typical SPS RF capture voltages (in the Q26 optics): $V_{200\text{MHz}} = 2$ MV and $V_{800\text{MHz}} = 0.34$ MV in phase.....	437
5.2. Dependence of beam transmission on emittance (a) and bunch length (b) [14]. Full and empty symbols (solid and dashed lines) mark experimental and simulation results, respectively. The circles correspond to operational settings, the squares to earlier optimization attempts based on bunch length. The triangles and diamonds show the results obtained using additional $V_{80\text{MHz}}$ or $V_{40\text{MHz}}$ voltage, respectively (no simulations for the latter case), for the rotation with optimized timings. The bunch length is obtained from a 4σ Gaussian fit in all cases.	437

5.3.	Bunch length on the SPS flat top measured as a function of bunch intensity in the two different SPS optics (Q20 and Q26).....	439
5.4.	(a) Voltage programmes used in the SPS for the 25 ns beam in the Q20 optics for two different beam intensities (optimized for reduction of particle losses). (b) Bunch-by bunch length on the flat bottom (blue curve) and flat top (black curve) for 25 ns beam with intensity of 1.25×10^{11} p/b.....	440
5.5.	The total 200 MHz voltage as a function of the RF current (the 200 MHz harmonic for 25 ns bunch spacing) available now from four cavities with power of 0.75 MW at cavity input in continuous mode (black solid curve) and with power of 1.05 MW at cavity input in the pulsing mode, possible after LLRF upgrade (blue curve) together with the situation after the full RF upgrade which includes four 3-section cavities with 1.05 MW and two 4-section cavities with 1.6 MW in pulsing mode (magenta curve). The vertical dashed line indicates the RF current of 1.47 A corresponding to the 25 ns beam with nominal intensity of 1.15×10^{11} p/b. The blue symbol shows the reference point used for red line indicating the voltage needed for higher intensity due to the effects of potential well distortion (PWD) and loss of Landau damping (LD).	441
5.6.	Q26 optics (a) and Q20 optics (b) for one sextant of the SPS.....	443
5.7.	Phase slip factor η relative to the value of the Q26 optics as a function of the gamma transition for injection and extraction energy. The values of $\gamma_i = 22.8$ and $\gamma_t = 18$ indicated in the graph correspond to the Q26 and Q20 optics, respectively	443
5.8.	Intensity as function of time after injection in the Q26 optics (a) and in the Q20 optics (b). Red traces indicated unstable beam conditions and green traces correspond to stable conditions	445
5.9.	Measurements of the beam stability at injection with (a) the Q26 optics and (b) Q20 optics with low vertical chromaticity. Green points correspond to stable cases. Unstable cases are marked by red dots if losses occurred within the first 1000 turns after injection ('fast losses') and blue dots if losses occurred later in the cycle.....	445
5.10.	Vertical growth rate as a function of the intensity per bunch and the longitudinal emittance as obtained from a series of HEADTAIL simulations for (a) the Q26 optics and (b) the Q20 optics. The colour scale is clipped, i.e. areas in red correspond to growth rates of 0.02/turns or higher.	445
5.11.	Instability threshold density as a function of the synchrotron tune for constant longitudinal bunch parameters (a) and as function of the beta functions at the location of the electron cloud interaction (b).....	446

5.12. HEADTAIL simulations yielding the instability threshold density as a function of intensity per bunch comparing the Q26 with the Q20 optics for field free regions (a) and for the electron cloud located in MBB dipole magnets (b), assuming the corresponding average beta functions in the respective locations	447
5.13. Average transverse emittance of 24 bunches measured at the end of the SPS flat bottom for different horizontal tunes (a, c) and for different vertical tunes (b, d) as indicated by the green dots in the tune diagrams.	448
5.14. Bunch-by-bunch emittance measurement at the end of the flat bottom for three batches of the 50 ns BCMS beam at the working point $Q_x, Q_y = 20.17, 20.23$	449
5.15. Transverse emittance as a function of intensity for a space charge tune shift of $\Delta Q_y = 0.21$, as achieved during machine studies with the 50 ns BCMS beam in 2012... .	449
5.16. (a) Voltage programmes corresponding to the constant filling factor in momentum for emittance of 0.5 eVs in the two different SPS optics. (b) Corresponding RF power per 200 MHz TW cavity having four (solid line) and five (dashed line) sections during the LHC acceleration cycle for nominal 25 ns beam intensity.	450
5.17. (a) Total voltage available on the SPS flat top as a function of RF current in the present configuration (four cavities) for different RF power. The vertical line corresponds to the 25 ns beam with nominal intensity. (b) RF voltage per 200 MHz TW cavity with different number of sections for nominal and ultimate beam current....	451
5.18. The available 800 MHz voltage per cavity as a function of I_{rf} (beam current component at 800 MHz) with 100 kW RF power at cavity input (a) and after upgrade with 150 kW RF power (b). Nominal 25 ns beam corresponds to $I_{rf} = 0.45$ A and 25 ns with a bunch intensity of 2.5×10^{11} p/b to $I_{rf} = 1.0$ A (assumed form-factor of 0.33). . .	452
5.19. Configuration of one of the four 200 MHz power plants	452
5.20. Voltage limitation due to power available from amplifiers.....	453
5.21. Power at the cavity input and respectively at the amplifier output.....	453
5.22. LIU-SPS 200 MHz RF upgrade project main activities: building BAF3, Amplifiers, LSS3 tunnel integration.....	454
5.23. LIU-SPS 200 MHz RF upgrade project amplifiers contracts: drivers, finals, combiners and power loads and coaxial lines	454
5.24. (a) The Siemens power plant has been in operation since 1976; (b) the Philips power plant has been in operation since 1981.....	455
5.25. Renovation of the Philips plant, comparison of technologies footprint: present tetrode system, diacrod, SSPA, IOT (or high power tetrode).	456

5.26. Tests results of maximum ratings achieved in March 2013	456
5.27. Implantation of the new BAF3, Prévessin site, between BA3 and BB3	457
5.28. Two possible configurations of the building with tetrodes or SSPA option	457
5.29. The GT10 gallery, a few cable trays to be removed to allow the 350 mm coaxial transmission line to go to LSS3 shaft.....	458
5.30. Metallic frame structure of the building. Mezzanine inside will be defined once the technology of the finals will be selected.....	458
5.31. Absolute maximum ratings of 1.6 MW at the cavity input	459
5.32. Specific bandwidth, gain saturation and phase distortion requirements.....	460
5.33. Test to be applied to all subsystems for qualification.....	461
5.34. Short circuit test: unmatched condition and matched and triggered unmatched condition	461
5.35. Short circuit test with unmatched and triggered unmatched conditions, over all phases, to be applied to all RF subsystems for qualification.....	462
5.36. Proposal with two diacrodes and a third additional one as hot spare	462
5.37. SOLEIL amplifiers reliably in operation since 2007.....	463
5.38. Preliminary SSPA integration study showing that even with a rack solution the new RF building would have been too small.....	463
5.39. Example of a SPS supercycle; with proton and CNGS operated in continuous wave mode and LHC injection operated in pulsed mode at 43 kHz 50%. Average power is almost 55% of maximum power. For a driver amplifier operated at 1.25 kW peak, this leads into 688 W average power.....	464
5.40. Driver configuration with a 2×16 tetrodes option	465
5.41. Driver configuration with a 2×2 diacrodes option.....	465
5.42. Specially designed ceramic maintaining the inner line coaxial to the outer line. The special RF finger inner connector is also visible, as well as the specific suspending system.....	466
5.43. Preparation and assembly of a piece of 6 m length of a 345 mm coaxial line. A special lifting craft is mandatory when installing these heavy transmission lines, which are suspended from the ceiling.....	466
5.44. A very important tip is not forgetting, when designing the path of such large transmission lines, the 180° U-shapes, which are the only way to disconnect a part of the main path. With about 150 m of lines, we will have to integrate a few of these to be able to exchange a faulty item if necessary.	467

5.45. (a) The 500 kW 3 dB combiners; (b) the 1 MW 3 dB combiners. These have been in operation with the present systems since 1976 without a single default	467
5.46. The recently (2001) re-designed RF power loads rated 500 kW CW and 800 kW peak power.....	468
5.47. In the past, two ways of welding the outer lines have been tested. (a) The initial linear weld showed less stability than the helicoidally welded line shown in the picture. (b) The 350 mm to N adaptor. Calibration of such adaptors is not easy. When looking for a level of losses at 0.1 dB, any detail will have a deep impact.	468
5.48. (a) A section of cavity in the lab equipped with its drift tubes; (b) a four-section cavity in the SPS-LSS3, fully dressed with its fundamental power couplers, power loads and other peripherals.	469
5.49. Proposed upgrade scheme: from (a) four cavities to (b) six cavities in the SPS LSS3 ...	469
5.50. The main limiting available space was the configuration of LSS3 itself. Some devices have to remain at their present locations due to machine optic constraints.....	470
5.51. Cross-section space available has been one additional limiting parameter to define the number of cavities that we can install in LSS3.....	471
5.52. Specific tooling, a dedicated truck, to move each single section of cavity	471
5.53. Current fundamental power coupler under test in early 2000. Power level up to 500 kW and 800 kW peak power have been tested for a short duration.....	472
5.54. Coupling element on the first drift tube connecting the coupler to the cavity. The size of this coupling element has been designed for 375 kW CW and peak power. It was not modified for the upgrade in 2000, and has operated at up to 500 kW peak power. It will have to be improved for 800 kW peak power	472
5.55. Global schedule of the project. The new RF building will be ready by mid-2015. The drivers contract was placed in March 2014. The finals contract has been launched.	473
5.56. Drivers and finals detailed schedule. The goal is to have all amplifiers delivered by the beginning of 2017 to launch long duration tests far in advance of the operation run to debug the systems.	474
5.57. The 800 MHz cavity controller	476
5.58. OTFB response with ± 3 kHz band around each revolution frequency sideband	477
5.59. Geographical location of damper kickers and pick-ups in BA2 with respect to the SPS RF system in BA3. The beam travels clockwise from BA2 to BA3 (~1.152 km).....	481
5.60. Summary of the planned fibre links between BA3 and BA2 and the local clock generation scheme in BA2	482

5.61. Scrubbing beam tests in 2013: time evolution with injected bunches splitting (a) with proposed 120 MHz sampling clock and (b) components at multiples of bunch frequency of 40 MHz.....	483
5.62. Overview of the damper signal processing for LHC-type beams. A total of eight instances of this VME module are needed (one per beam type and plane).....	484
5.63. Field distribution computed by HFSS for the horizontal and vertical kickers for verification of the kick strength [54].	486
5.64. High-bandwidth transverse feedback system with digital sampling of intra-bunch motion.....	486
5.65. Spectrum of sum and difference signal of a bunch subject to the electron cloud instability [61]. Spectral contents at 1.6 GHz and 2.5 GHz are artefacts due to higher order modes in the pick-up.....	487
5.66. Threshold SEY for electron cloud formation in different types of SPS chambers, as a function of the bunch intensity. (a) Drift A; (b) drift B; (c) dipole MBA; (d) dipole MBB.....	491
5.67. Bunch-by-bunch emittances measured at SPS extraction energy for 4×72 bunches of the 25 ns LHC beam with (a) 1.34×10^{11} ppb injected; (b) 1.44×10^{11} ppb injected.....	493
5.68. Horizontal distribution of the electron flux in two strip detectors with (a) MBA; (b) MBB shaped chambers for 72 25ns spaced bunches with different bunch intensities.....	494
5.69. Profile of SEY on the mobile removable sample of stainless steel (2009).....	495
5.70. Longitudinal beam profile (zoom on four of the 72 bunches): (a) evolution during the first 500 turns after injection; (b) snapshot at turn 500.....	497
5.71. Electron scrubbing flux in the SPS MBB chamber as a function of the maximum SEY for different values of the intensity per doublet (solid lines, colours labelled) in comparison with the nominal 25 ns beam (dashed line).....	497
5.72. Electron signal from the SPS electron cloud monitors in (a, b) an MBA chamber; (c, d) an MBB chamber as a function of the horizontal position. The blue traces are the measured (a, c) or simulated (b, d) signals with the standard 25 ns beam; and the red traces are those from the doublet beam.	498
5.73. The new concept of beam scraping relies on a magnetic bump and a fixed block. By using four bumpers per plane one can obtain orthogonal steering of angle and position of the beam.....	500
5.74. The proposed layout for the scraper in LSS6 consists of four bumpers in each plane. In the horizontal plane the extraction bumpers are used. In the vertical plane	

two existing bumpers can be used, but the scheme also requires installation of two new bumpers	501
5.75. Beam profile (a) before and (b) after scraping, measured by the SPS wire scanners. The profiles show that the tails have been successfully removed by scraping on the TPSG using a magnetic bump.	502
5.76. Beam intensity measurement during a cycle where the beam was scraped both using the magnetic bump onto the TPSG (first intensity drop) and using the operational scraper (second intensity drop).....	502
5.77. Longitudinal profile of the peak energy deposition for different simulation settings	503
5.78. Map of energy deposition expected in adiabatic assumptions for the test of the horizontal blade; the map (transverse cut) is zoomed on the region of the chamfer facing the beam, at the longitudinal centre of the blade. The blade is swept through the beam from top to bottom	504
5.79. Time profile of the vacuum in the region of the kickers just upstream of the scrapers under test. Two relevant spikes are clearly visible, one at ~08:31 AM, when the vertical blade was tested, and the other one at ~08:49AM, when the horizontal blade was tested.....	504
5.80. SEM images of the horizontal scraper blade after the test. (a) In the region of the chamfer affected by the beam; (b) in a region far from the chamfer (shown as reference).....	505
5.81. Schematics of the consumption of the scraper blade.....	505
5.82. Beam intensity measurements during regular scraping with the horizontal blade (a) before the test, (b) after the test.	506
5.83. (a) MKDV energy tracking function. (b) MKDV (MKDVA + MKDVB) waveform in blue and MKDH ($2 \times$ MKDHA + MKDHB) waveform in green.	507
5.84. Simulation of particle deposition on the front face of the TIDVG for LHC-BCMS beam. The maximum simulated proton density considering an ideal machine is $4.6 \times 10^{11} \text{ p}^+/\text{mm}^2$ [106].....	508
5.85. Schematic view of the MKDV current connection [109].....	509
5.86. MKDV's integrated field waveform at 47 kV using GTO switches [106].....	510
5.87. Total number of protons dumped on the TIDVG per year from 2006 to 2012	510
5.88. Geometry of the TI8 line and the proposed external dump line in MAD-X coordinate system	512
5.89. (a) Optics from the SPS LSS4 extraction point to the external absorber block. (b) Particle distribution on the dump block for an LIU-BCMS beam.	512

5.90. (a) TT60 tunnel branch off into TI2, TT61 and TT66. (b) Geometry of the TT61 and TI2 transfer lines.....	513
5.91. Vertical cross-section of the actual TT61 tunnel (in black) and proposed beam trajectory (in red).....	514
5.92. (a) Vertical section and (b) horizontal section drawings of the two tunnels, indicating a possible location for the beam dump	514
5.93. Maximum increase in temperature along the collimator jaw for different impact parameters in graphite R4550 with BCMS beam at the TCDI in TI 2 with the smallest spot size, but fulfilling the spot size criterion. $\beta_x = 39.74\text{m}$, $\beta_y = 105.17\text{m}$	516
5.94. Layout of $2 \times$ TCDI assembly for LIU. The total length required is 3.5 m. A double bellows is used between the TCDIs to have the possibility to exchange just one in the event of damage. A vacuum pumping port can be installed at the beam pipe between the bellows.	518
5.95. Front-End electronics diagram for the new SPS orbit and trajectory system.....	522
5.96. Cross-section through an integrating current transformer	524
5.97. Pulse response of the Bergoz ICT	525
5.98. Pulse response of the CERN WCT.....	525
5.99. Original head-tail monitoring system in the SPS	526
5.100.Power spectrum of the visible SR integrated over the area of the extraction mirror.....	527
5.101.Sector 560 lay-out.....	530
5.102.Equivalent electrical network for sector 560	531
5.103.Comparison between calculated pumpdown curves for original (green) and halved (orange) $\times 10$ vacuum sector	532
5.104.Scale drawing showing the space required for x0701 valves	533
5.105.MKDH 11757 in LSS1.....	534
5.106.Equipment that has to be displaced to relocate VVSB 11772	535
5.107.Position of the sector valves in the vacuum sector where the TIDVG is installed.....	536
5.108.Positions of the existing VVSB valve (green arrow) and the new proposed VVSF valve (red arrow). Chamber VKNW ($l = 5129\text{ mm}$, $\emptyset = 356\text{ mm}$) has to be replaced by two new chambers that have yet to be designed	536
5.109.Picture of a VVSF valve.....	536
5.110.New RF cavities layout for the SPS upgrade	537
5.111.Total vertical (red) and horizontal (green) generalized impedance of the SPS	540
5.112.Vertical tune versus bunch intensity. Measurements performed in September 2012.....	541

5.113. Horizontal tune versus bunch intensity. Measurements performed in March 2013	541
5.114. Total SPS kicker magnet longitudinal impedance. The blue and red lines show the real and imaginary parts of the impedance, respectively. The black line shows the real and imaginary part of an eight-resonator model fit used for beam dynamics studies.....	543
5.115. CST 3D simulations of the longitudinal impedance for the SPS extraction kicker (MKE-L) with and without serigraphy	544
5.116. An SPS flange. (a) Front view of a flange in the SPS. (b) Lateral view of a flange with a short bellows. (c) Model used to calculate the impedance of an enamelled flange with a short bellows.....	544
5.117. The bead-pull measurement set-up.....	546
5.118. Total SPS longitudinal impedance in lineal vertical scale. The blue, red and green lines represent the contribution of the flanges, BPMs and kicker magnets, respectively.....	548
5.119. Total SPS longitudinal impedance in logarithmic vertical scale. The blue, red and green lines represent the contribution of the flanges, BPMs and kicker magnets, respectively.....	549
5.120. Power loss as a function of the frequency of the peak due to the serigraphy assuming that shunt impedance and the quality factor of the resonance are unchanged.....	551
5.121. Comparison between the power loss of the MKE without serigraphy for 2012 beam intensities and the MKE with serigraphy and MKP11955 for LIU beam intensities	551
5.122. Measurements of the quadrupole synchrotron frequency shift at 26 GeV/c in the SPS during the period from 1999 to 2006 (a), in 2007 (b) and 2013 (c).	553
5.123. Slopes $ b $ of the quadrupole synchrotron frequency shift with intensity measured at 26 GeV/c with different injected longitudinal emittances in (a) 2001 and 2008 and (b) in 2013. The results are plotted versus measured average bunch length (4σ Gaussian fit) during quadrupole oscillations. One can clearly see reduction in the slope in 2013 due to serigraphy of the MKE kickers.	554
5.124. Projection of bunch spectrum evolution of long bunches (~ 25 ns) with intensity of 1×10^{11} after injection into SPS with RF off in measurements (black dashed line) and simulations with different (reconstructed from PS tomography) distributions in the present SPS impedance model [142]	555

5.125. Modified ZS tanks with ion pump installed below (black) with the aim of replacing the MP (grey box behind).....	557
5.126. Impedance of ZS as a function of frequency, with the ion trap and anode connection open, grounded (short) or connected to the ion trap connection box	558
5.127. Simplified HV circuit of ion traps (U_top, U_bot.) circuits and anode current (I_anode) measurement resistor.....	558
5.128. The real component of the longitudinal impedance of the ZS with and without the impedance insert (grille) up to 2 GHz	559
5.129. Temperature in the diluting blocks of TPSG4, as a function of their longitudinal position upon full impact of the ultimate intensity LHC-type beam of the SPS	561
5.130. Maximum Stassi ratio in each block of the TPSG4, as a function of their longitudinal position upon full impact of the ultimate intensity LHC-type beam of the SPS	561
5.131. Temperature in the diluting blocks of TPSG6, as a function of their longitudinal position upon full impact of the ultimate intensity LHC-type beam of the SPS	562
5.132. Maximum Stassi ratio in each block of the TPSG6, as a function of their longitudinal position upon full impact of the ultimate intensity LHC-type beam of the SPS	562
5.133. The evolution of the fit parameters A , B and dp/p are shown for the orbit data in the horizontal plane. The bottom plot shows the phase advance $\mu_0 = \tan^{-1}(B/A)$ calculated from the fit parameters.	565
5.134. The SPS orbit at extraction to TI2 is calculated at BPCE.61805. In the horizontal plane variations 1.4 mm are observed. Within the period of one week the effect is already strong. In the vertical plane the variations are 0.4 mm throughout the whole period.....	565
5.135. The SPS orbit at extraction to TI8 is calculated at BPCE.41801. In the horizontal plane the drift is 1.8 mm, while in the vertical plane it is only 0.3 mm	566
5.136. Calculated position at the scraper BSHV.11771 in the horizontal plane versus the scraper settings in the same period	566
5.137. Analysis of the orbit show that there are two strong eigenmodes in the horizontal plane. Both correspond to betatron oscillations	567
5.138. Taking a shorter time period (13 October to 24 October) only one eigenmode is significant.....	567
5.139. For the period 13 October to 24 October the best match to the source is found to be the MST or MSE in LSS6.....	568
5.140. The effect of the stray fields of the MST and MSE in LSS6 are simulated using the distance of the bump to the septa.....	568

5.141. For the second isolated period there is also only one significant eigenmode.....	569
5.142. For the period 29 October to 4 November the best match is MPSH.62199 or MPLH.61655	569
5.143. The drifts at extraction match fairly well to the outside temperature.....	570
5.144. Example of ‘fake correction’: in red the actually measured orbit at the BPMs, in green the closed orbit obtained with the MAD-X model, in blue the closed orbit after the correction via SVD.....	571
5.145. Example of Fourier analysis of the BPM data: in red the MAD-X orbit at the BPMs, in blue the closed orbit obtained by summing the Fourier components 19, 20 and 21 ...	571
5.146. Example of amplitude-phase-momentum fit: in red the MAD-X orbit at the BPMs, in blue the trajectory obtained by fitting all BPM data with a free oscillation and a momentum offset	571
5.147. ‘Fake’ correction kicks. (a) MPSH.61402 ($\theta_0 = 0$). (b) MPLH.61655 ($\theta_0 = 0.512$ mrad). (c) MPLH.61996 ($\theta_0 = 0.094$ mrad). (d) MPSH.62199 ($\theta_0 = 0.398$ mrad).....	573
5.148. Fourier analysis kicks. (a) MPSH.61402 ($\theta_0 = 0$). (b) MPLH.61655 ($\theta_0 = 0.512$ mrad). (c) MPLH.61996 ($\theta_0 = 0.094$ mrad). (d) MPSH.62199 ($\theta_0 = 0.398$ mrad).	574

References

- [1] M. Lamont, How to reach the required availability in the HL-LHC era, Proc. RLIUP Workshop, Archamps, p. 139 (2014).
- [2] B. Goddard *et al.*, Progress with the upgrade of the SPS for the HL-LHC era, Proc. IPAC4, Shanghai, China, p. 2624 (2013).
- [3] G. Iadarola *et al.*, Electron cloud and scrubbing studies for the SPS in 2012, CERN-ATS-Note-2013-019 MD (2013).
- [4] C. Yin Vallgren *et al.*, Performance of carbon coatings for mitigation of electron cloud in the SPS, Proc. IPAC2, San Sebastian, Spain, p. 1590 (2011).
- [5] H. Bartosik *et al.*, Operational performance of the LHC proton beams with the SPS low transition energy optics, Proc. IPAC4, Shanghai, China, p. 3945 (2013).
- [6] T. Argyropoulos *et al.*, Identification of the SPS Impedance at 1.4 GHz, Proc. IPAC4, Shanghai, China, p.1793 (2013).
- [7] LIU-SPS workshops, special meetings and reviews, <https://indico.cern.ch/category/3494/>.
- [8] O. Mete *et al.*, Feasibility studies in view of a new LIU-SPS scraping system, CERN-ACC-NOTE-2013-0016 (2013).
- [9] E. Shaposhnikova, E. Ciapala and E. Montesinos, Upgrade of the 200 MHZ RF system in the CERN SPS, CERN-ATS-2011-042 (2011).
- [10] J.D. Fox *et al.*, First results and analysis of the performance of a 4 GS/s intra-bunch vertical feedback system at the SPS, Proc. IPAC4, Shanghai, China, p. 3070 (2013).
- [11] P.Collier *et al.*, The LHC injector chain, LHC Design Report, vol. III, Chapter 16.2 (2004).
- [12] H. Timko *et al.*, PS to SPS beam transfer, PRST AB 16, 051004 (2013).

- [13] E. Shaposhnikova, Longitudinal stability of the LHC beam in the SPS, CERN SL-Note-2001-031 HRF (2001).
- [14] G. Papotti *et al.*, The SPS beam quality monitor, from design to operation, Proc. IPAC11, San Sebastian, Spain, p. 1849 (2011).
- [15] H. Bartosik *et al.*, Experimental studies with low transition energy optics in the SPS, CERN-ATS-2011-086 (2011).
- [16] H. Bartosik *et al.*, Increasing instability thresholds in the SPS by lowering transition energy, Proc. IPAC12, New Orleans, USA, p. 3096 (2012).
- [17] T. Mastoridis *et al.*, Batch by batch longitudinal emittance blow up MD, CERN ATS-Note-2012-050 MD (2012).
- [18] T. Argyropoulos *et al.*, Identification of the SPS impedance at 1.4 GHz, Proc. IPAC13, Shanghai, China, p. 1793 (2013).
- [19] T. Bohl, Bunch parameters of the 50 ns LHC type beam for the Q26 and Q20 optics, CERN Internal Note-2013-16 v00.02 (2013).
- [20] T. Argyropoulos *et al.*, Controlled longitudinal emittance blow-up in a double RF system at CERN SPS, Proc. ICFA workshop HB2010, Morschach, Switzerland, p. 86 (2010).
- [21] G. Arduini *et al.*, Observation of a fast single bunch transverse instability on protons in the SPS, AB-Note-2003-093-MD (2003).
- [22] G. Arduini *et al.*, The Electron Cloud Instability of the LHC Beam in the CERN SPS, LHC-Project-Report-637 (2003).
- [23] E. Mètral, Overview of single-beam coherent instabilities in circular accelerators, Proc. 1st CARE-HHH-APD Workshop on Beam Dynamics in Future Hadron Colliders and Rapidly Cycling High-Intensity Synchrotrons, Geneva, p. 89 (2004).
- [24] H. Bartosik *et al.*, Impact of low transition energy optics to the electron cloud instability of LHC beams in the SPS, CERN-ATS-2011-087 (2011).
- [25] E. Shaposhnikova, Longitudinal stability of the LHC beam in the SPS, SL-Note-2001-031-HRF (2001).
- [26] H. Bartosik *et al.*, Optics considerations for lowering transition energy in the SPS, CERN-ATS-2011-088 (2011).
- [27] G. Vanbavincckhove *et al.*, Beam Transfer to LHC with the Low gamma-Transition SPS Optics, CERN-ACC-2013-0106 (2013).
- [28] Y. Papaphilippou *et al.*, Operational Performance of the LHC Proton Beams with the SPS Low Transition Energy Optics, CERN-ACC-2013-0124 (2013).
- [29] B. Salvant *et al.*, Probing intensity limits of LHC-Type bunches in CERN SPS with nominal optics, CERN-ATS-2011-176 (2011).
- [30] H. Timko *et al.*, Experimental and simulation studies of the PS-to-SPS beam transfer efficiency, CERN-ATS-Note-2012-059 PERF (2012).
- [31] H. Bartosik, Beam dynamics and optics studies for the LHC injectors upgrade, CERN-THEESIS-2013-257 (2013).
- [32] G. Iadarola *et al.*, Recent Electron Cloud Studies in the SPS, CERN-ACC-2013-0115 (2013).
- [33] H. Bartosik *et al.*, Experimental Studies for Future LHC Beams in the SPS, CERN-ACC-2013-0151 (2013).
- [34] H. Damerau *et al.*, RF Manipulations for Higher Brightness LHC-Type Beams, CERN-ACC-2013-0210 (2013).
- [35] E. Shaposhnikova, T. Bohl and T. Linnecar, Beam transfer functions and beam stabilisation in a double RF system, Proc. PAC05, Knoxville, TN, USA, p. 2300 (2005).

- [36] C. Tanguy, Report of the survey realized at the TIARA workshop on RF power generation, TIARA-NOTE-WP3-2013-003 (2013).
- [37] P. Baudrenghien *et al.*, Reducing the impedance of the travelling wave cavities feed-forward and one turn delay feed-back, Proc. 10th Workshop on LEP-SPS Performance, Chamonix, France, p. 102 (2000).
- [38] P. Baudrenghien *et al.*, Control of strong beam loading. Results with beam, Proc. 11th Workshop of the LHC, Chamonix, France, p. 67 (2001).
- [39] D. Manglunki *et al.*, The first LHC p-Pb run: performance of the heavy ion production complex, Proc. IPAC4, Shanghai, China, p.2648 (2013).
- [40] W. Hoefle, LHC Design Report, vol III, CERN-2004-003, p. 97 (2004).
- [41] G. Dome, The SPS acceleration system, travelling wave drift-tube structure for the CERN SPS, Proc. Proton Linear Accel. Conf., Chalk River, Ontario, p.138 (1976).
- [42] P. Baudrenghien *et al.*, The LHC low level RF, Proc. EPAC06, Edinburgh, UK, p.1471 (2006).
- [43] G. Hagmann and P. Baudrenghien, LLRF and commissioning, LIU-SPS Coordination meeting, 12 December 2013, <https://indico.cern.ch/event/277739/>.
- [44] W. Hofle and C. Boccard, EDMS 1251693, <https://edms.cern.ch/document/1251693/1> (2013).
- [45] W. Hofle and C. Boccard, EDMS 1251695 <https://edms.cern.ch/document/1251695/2> (2013).
- [46] W. Hofle, Progress with the SPS damper, 11th Chamonix Workshop, Chamonix, 2001, CERN-SL-2001-003 DI, (2001).
- [47] P. Baudrenghien and D. Valuch, Beam phase and transverse position measurement module for the LHC, LLRF07 Workshop, October 2007, Knoxville TN, USA, <https://edms.cern.ch/document/929563/1> (2007).
- [48] P. Baudrenghien, W. Hofle, G. Kotzian and V. Rossi, Digital signal processing for the multi-bunch LHC transverse feedback system, Proc. EPAC'08, Genoa, Italy, p. 3269 (2008).
- [49] G. Kotzian, CERN, unpublished (2014).
- [50] W. Hofle and R. Louwerse, The deflectors of the SPS transverse damper – measurements and calculations, SL-Note-97-45-RF (1997).
- [51] W. Hofle, Towards a transverse feedback system and damper for the SPS in the LHC era, *Particle Accelerators 1997*, vol. 58 (OPA, Amsterdam), p. 269 (1997).
- [52] W. Hofle, G. Kotzian and D. Valuch, Performance of the LHC transverse damper with bunch trains, Proc. IPAC'13, Shanghai, China, p. 3022 (2013).
- [53] G. Arduini, T. Bohl, K. Cornelis, W. Hofle, E. Metral and F. Zimmermann, Beam observations with electronic cloud in the CERN PS and SPS Complex, Ecloud'04, Napa, USA, 2004, CERN-2005-001 (2005).
- [54] LIU Review of the high bandwidth damper system, 30 July 2013, <https://indico.cern.ch/event/260522/> (2013).
- [55] J.R. Thompson, J.M. Byrd, W. Hofle and G. Rumolo, Headtail feedback module: implementation and results, CERN-AB-2008-070 (2008).
- [56] J.R. Thompson, J.M. Byrd, W. Hofle and G. Rumolo, Initial results of simulation of a damping system for electron cloud-driven instabilities in the CERN SPS, PAC'09, Vancouver, Canada, p. 4713 (2009).
- [57] R. de Maria *et al.*, Performance of exponential couplers in the SPS with LHC type beam for transverse broadband instability analysis, Proc. DIPAC'09, Basel, Switzerland, p. 83 (2009).
- [58] J.D. Fox *et al.*, Feedback techniques and SPS e-cloud instabilities – design estimates, Proc. PAC'09, Vancouver, Canada, p. 4135 (2009).
- [59] J.-L. Vay *et al.*, Simulation of a feedback system for the attenuation of e-cloud driven instability, Proc. PAC'09, Vancouver, Canada, p. 4716 (2009).

- [60] J.-L. Vay *et al.*, Simulation of e-cloud driven instability and its attenuation using a feedback system in the CERN SPS, Proc. IPAC'10, Kyoto, Japan, p. 2438 (2010).
- [61] R. Secondo *et al.*, Simulation results of a feedback control system to damp electron cloud single-bunch transverse instabilities in the CERN SPS, Proc. PAC'11, New York, NY, p. 1773 (2011).
- [62] M.T.F. Pivi *et al.*, Multi-particle simulation codes implementation to include models of a novel single-bunch feedback system and intra-beam scattering, Proc. IPAC'12, New Orleans, LO, p. 3147 (2012).
- [63] K. Li *et al.*, Modelling and studies for a wideband feedback system for mitigation of transverse single bunch instabilities, Proc. IPAC'13, Shanghai, China, p. 3019 (2013).
- [64] J.M. Cesaratto *et al.*, A wideband slotted kicker design for SPS transverse intra-bunch feedback, Proc. IPAC'13, Shanghai, China, p. 3073 (2013).
- [65] C.H. Rivetta *et al.*, Mathematical models of feedback systems for control of intra-bunch instabilities driven by e-clouds and TMCI, Proc. PAC'11, New York, NY, p. 1621 (2011).
- [66] O. Turgut *et al.*, Identification of bunch dynamics in the presence of e-cloud and TMCI for the CERN SPS ring, Proc. IPAC'11, San Sebastian, Spain, p. 811 (2011).
- [67] O. Turgut *et al.*, Identification of intra-bunch dynamics using CERN SPS machine measurements, Proc. NA-PAC'13, Pasadena, CA, p. 1861 (2013).
- [68] J.D. Fox *et al.*, Excitation of intra-bunch vertical motion in the SPS – implications for feedback control, SLAC-PUB-15046 (2012).
- [69] J. Dusatko *et al.*, A 4 GS/s instability feedback system processing system for intra-bunch instabilities, Proc. IPAC'13, Shanghai, China, p. 3067 (2013).
- [70] J.M. Cesaratto *et al.*, First results and analysis of the performance of a 4 GS/s intra-bunch vertical feedback system at the SPS, Proc. IPAC'13, Shanghai, China, p. 3070 (2013).
- [71] J. Dusatko *et al.*, The hardware implementation of the CERN SPS ultrafast feedback processor demonstrator, Proc. IBIC'13, Oxford, UK, p. 124 (2013).
- [72] J.D. Fox *et al.*, A 4 GS/s feedback processing system for control of intra-bunch instabilities, Proc. IBIC'13, Oxford, UK, p. 323 (2013).
- [73] C.H. Rivetta *et al.*, Control of intra-bunch dynamics at CERN SPS ring using 3.2 GS/s digital feedback channel, Proc. NA-PAC'13, Pasadena, CA, p. 1430 (2013).
- [74] T. Linnecar, The high frequency longitudinal and transverse pick-ups used in the SPS, CERN-SPS-ARF/78/17 (1978).
- [75] K. Pollock *et al.*, Signal equalizer for SPS ecloud/TMCI instability feedback control system, Proc. IBIC'12, Tsukuba, Japan, p. 424 (2012).
- [76] G. Kotzian, W. Hofle, R.J. Steinhagen, D. Valuch and U. Wehrle, Evaluation of strip-line pick-up system for the SPS wideband transverse feedback system, Proc. IBIC'13, Oxford, UK, p. 690 (2013).
- [77] J.M. Cesaratto *et al.*, SPS wideband transverse feedback kicker: design report, SLAC-R-1037, Stanford, CA (2013).
- [78] L. Faltin, Slot-type pick-up and kicker for stochastic beam cooling, Nucl. Instrum. Methods 148, 449.83 (1978).
- [79] C.Yin Vallgren, Ph.D. thesis, CERN-THEESIS-2011-063 (2011).
- [80] G. Iadarola *et al.*, Electron Cloud and Scrubbing Studies for the LHC, Proc. IPAC'13, Shanghai, China, p.1331 (2013).
- [81] S. Federmann *et al.*, Electron Cloud Measurements of Coated and Uncoated Vacuum Chambers in the CERN SPS by Means of the Microwave Transmission Method, Proc. IPAC10, Kyoto, Japan, p. 1497 (2010).

- [82] C. Yin Vallgren *et al.* Amorphous carbon coatings for the mitigation of electron cloud in the CERN Super Proton Synchrotron, Phys. Rev. ST Accel Beams **14** 071001 (2011).
- [83] J.M. Jimenez *et al.* Electron cloud with LHC-type beams in the SPS : A review of three years of measurementsLHC Project Report 632, (2003).
- [84] G. Iadarola *et al.*, Recent Electron Cloud Studies in the SPS, Proc. IPAC13, Shanghai, China, p.2525 (2013).
- [85] P. Costa Pinto *et al*, Radio-Frequency Multipacting as Quality Control of Coatings for E-Cloud Suppression, Proc. IPAC13, Shanghai, China, p. 3403 (2013).
- [86] F. Leaux, Microscopic inspections of irradiated graphite scraper blades, <https://edms.cern.ch/document/1339153/1> (2013).
- [87] A. Mereghetti *et al.*, SixTrack-Fluka active coupling for the upgrade of the SPS scrapers, IPAC13, Shanghai, p. 2657 (2013).
- [88] LIU-SPS Beam Scraping System Review, <http://indico.cern.ch/event/221617/> (2013).
- [89] F. Velotti, Design Requirements of the LIU-SPS TIDVG, <https://edms.cern.ch/document/1323812/1.0> (2014).
- [90] V. Kain *et al.*, Material damage test with 450 GeV LHC-type Beam, 2005, Proc. PAC'05, Knoxville, TN, USA, p.1607 (2005).
- [91] F. Velotti *et al.*, Performance improvements of the SPS internal beam dump for the HL-LHC beam. Proc. IPAC'13, Shanghai, China, p.3231 (2013).
- [92] G. Arduini, E. Carlier, L. Ducimetiere and G. Robin, Extension of the SPS beam dumping interlock and surveillance system, CERN SL-Note-97-68-BT (1997).
- [93] V. Senaj *et al.*, Upgrade of the Super Proton Synchrotron vertical beam dump system, CERN-ATS-2010-134 (2010).
- [94] Karel Cornelis, personal communication.
- [95] H. Burkhardt, B. Goddard, V. Kain and W. Weterings, Function and concept of TCDI transfer line collimators, LHC-TCDI-ES-0001, EDMS 433291 (2004).
- [96] R. Assmann *et al.*, Beam cleaning and collimation system, LHC Design Report, vol. I, CERN (2004).
- [97] K. Cornelis *et al.*, Machine parameters of relevance for beam instrumentation after LHC injectors upgrade, <https://edms.cern.ch/document/1215595> ver. 1.0, (2012).
- [98] J. Gonzalez *et al.*, Development of a high dynamic range beam position measurement system using logarithmic amplifiers for the SPS at CERN, Proc. IBIC Conf., Oxford, UK, p. 89 (2013).
- [99] M. Gasior, J. Olexa and R.J. Steinhagen, BPM electronics based on compensated diode detectors—results from development systems, CERN-ATS-2012-247 (2012).
- [100] C. Deplano *et al.*, LogAmp electronics and optical transmission for the new SPS beam position measurement system, *J. Inst.* **8** C12008 (2014).
- [101] A. Boccardi, On-going electronic development in the CERN Beam Instrumentation Group: challenges and solutions for the measurement of particle accelerator beam parameters, *J. Inst.* **8** C03006 (2013).
- [102] C. Deplano *et al.*, Radiation resistance testing of commercial components for the new SPS beam position measurement system, Proc. IBIC Conf., Oxford, UK, p. 686 (2013).
- [103] G. Rumolo, LIU parameter tables, <https://edms.cern.ch/document/1296306/1> (2014).
- [104] C. Zannini *et al.*, Effect of the TEM mode on the kicker impedance. CERN-ATS-2012-082, (2012).
- [105] C. Zannini, PhD thesis, Lausanne, EPFL, CERN-THESIS-2013-076 (2013).
- [106] B. Salvant *et al.*, Coupling impedance of the CERN SPS beam position monitors. CERN-ATS-2009-046 (2009).

- [107] B. Salvant *et al.*, Update of the SPS impedance model, CERN-ATS-2010-077 (2010).
- [108] J.E. Varela, Short update on the SPS vacuum flanges, CERN SPS Upgrade Working Group, <http://paf-spsu.web.cern.ch/> (2013).
- [109] A.W. Chao, Physics of Collective Beam Instabilities in High Energy Accelerators, Wiley, New York, Wiley (1993).
- [110] H. Timko, Latest results of simulations of the SPS impedance, CERN SPS Upgrade Working Group, <http://paf-spsu.web.cern.ch/> (2013).
- [111] J.E. Varela, Update on the SPS longitudinal impedance, CERN SPS Upgrade Working Group, <http://paf-spsu.web.cern.ch/> (2014).
- [112] T. Kroyer *et al.*, Longitudinal and transverse wire measurements for the evaluation of impedance reduction measures on the MKE extraction kickers, CERN-AB-Note-2007-028 (2007).
- [113] M. Mathieu, Les raccords à vide démontables du SPS, Internal Note, SPS/SME/76-3, (1976).
- [114] G. Dôme, Longitudinal coupling impedance of cavities for a relativistic beam, Internal Note, LABII/RF/Note/73-2 (1973).
- [115] G. Dôme, Longitudinal coupling impedance of resonant elements along the SPS ring, Internal Note (1974).
- [116] O. Kononenko, A. Cappelletti and A. Grudiev, Compensation of transient beam-loading in the CLIC main linac, Proc. Linear Accelerator Conf., LINAC2010, Tsukuba, Japan, p.1093 (2010).
- [117] B. Salvant, Update on the SPS impedance: ZS PMs and BPMs, CERN SPS Upgrade Working Group, <http://paf-spsu.web.cern.ch/> (2013).
- [118] E. Shaposhnikova *et al.*, Reference measurements of the longitudinal impedance in the CERN SPS, Proc. PAC09, Vancouver, Canada, p.1098 (2009).
- [119] T. Bohl, T. Linnecar and E. Shaposhnikova, Impedance reduction in the CERN SPS as seen from the longitudinal beam measurements, Proc. EPAC02, Paris, France, p.1446 (2002).
- [120] E. Gaxiola *et al.*, The fast extraction kicker system in SPS LSS6, Proc. EPAC06, Edinburgh, UK, p.3125 (2006).
- [121] A. Lasheen *et al.*, talk at CERN LIU-SPS BD WG meeting 14 March 2014.
- [122] T. Bohl, T. Linnecar and E. Shaposhnikova, *Phys. Rev. Lett.* **78 N16** 2109 (1997).
- [123] H. Timko *et al.*, talk at CERN LIU-SPS BD WG meeting, 24 October 2013.
- [124] J. Borburgh and B. Balhan, Impact of multi-cycling on the ZS electrostatic septa, Multi Cycling Study Group meeting, 8 April 2005.
- [125] G. Rumolo, E-cloud build up simulations for ZS, SPS Upgrade Study team meeting, 22 April 2010.
- [126] J. Borburgh *et al.*, Observations and measurements on the ZS during the SPS MD, SPS Upgrade Study team meeting, 20 May 2010.
- [127] J. Borburgh, Possible ZS improvements, LIU-SPS ZS electrostatic Septum Upgrade Review, 20 February 2013.
- [128] H. Day *et al.*, ZS impedance measurements, SPS Upgrade Study team meeting, 30 January 2014.
- [129] L. Massidda and F. Mura, Dynamic structural analysis of the TPSG4 & TPSG6 beam diluters, CERN-AB-2006-015 (2005).
- [130] L. Massidda and F. Mura, Analysis of the water dynamics for the MSE-coil and the MST-coil, CERN-AB-2006-016-ATB (2005).
- [131] L. Massidda, Workshop on Materials for Collimators and Beam Absorbers, CERN, 5 September 2007.

- [132] J. Borburgh *et al.*, Modifications to the SPS LSS6 septa for LHC and the SPS septa diluters, Proc. EPAC2006, Edinburgh, UK, p.2565 (2006).
- [133] N. Simos, personal communication, HiRadMat Scientific Board Meeting, 23 April 2012.
- [134] L. Drosdal *et al.*, Analysis of LHC transfer line trajectory drifts, Proc. IPAC'13, Shanghai, p.2864 (2013).
- [135] L. Drosdal *et al.*, Sources and solutions for LHC transfer line stability issues, Proc. IPAC'12, New Orleans, p.3025 (2012).
- [136] J. Irwin *et al.*, Model-Independent Beam Dynamics Analysis, Phys. Rev. Lett. **82**, 1684 (1999).
- [137] R. Chritin and P. Leclère, Mesures magnétiques d'un aimant dipôle de type MSE, SL-Note 99-053 MS (1999).

Chapter 6

Common Beam Instrumentation

6.1 Beam loss measurement

The existing beam loss monitoring (BLM) systems in the Proton Synchrotron Booster (PSB) and Proton Synchrotron (PS) use outdated electronics based on old aluminium cathode emission monitors (ACEM). This type of detector has a limited dynamic range, requires frequent calibration and was not designed with reliability in mind. Most importantly, these are commercial products that are no longer manufactured and only a very limited amount of spares are available. The LIU project goal of providing high intensity, low emittance beams from the LHC injectors requires a full upgrade of their Beam Loss Monitors (BLM) systems in order to correctly identify loss locations and implement machine protection. The LIU baseline is to upgrade the PSB and PS with systems similar to what is currently being developed for Linac4, with their transfer lines equipped with the same system as part of the Beam Instrumentation group consolidation requests. The Super Proton Synchrotron (SPS) is to be consolidated at a later stage with a different type of electronics that is more suited to its large ring architecture.

The main design goals for the new injector BLM system are to cover a high dynamic loss range and to provide high reliability and availability, all based on a generic, modular and highly configurable architecture [1]. With this in mind the acquisition electronics will be compatible with several detector types. In the majority of cases the detectors will be ionization chambers similar to those used in the LHC. Nevertheless, several other types, e.g. secondary emission monitors, diamond detectors and Cherenkov detectors, may be used to cover particular needs at specific locations. Double-shielded coaxial cables will be used to transport the signal between the detector and the front-end electronics, to minimize the amount of electro-magnetic noise introduced. The digitization will be based on a new design concept that allows the measurement of currents from 10 pA to 200 mA, equivalent to a dynamic range in the order of 10¹⁰. The processing part of the system will keep track of several integrated loss windows, ranging from 2 µs to 1.2 s, for each detector. As well as providing this data on-line to the control room and storing it in databases for subsequent analysis, the calculated loss values for each channel will also be continuously checked against predefined threshold values both at the hardware and software levels. When these thresholds are exceeded, the BLM system, through its direct connection to the beam interlock system (BIS), will have the ability to block future beam injections. The processing is provided by a field programmable gate array (FPGA), providing the flexibility to implement the specific requirements of each accelerator, while still maximizing reliability. A block diagram of the architecture of the system can be seen in Fig. 6.1.

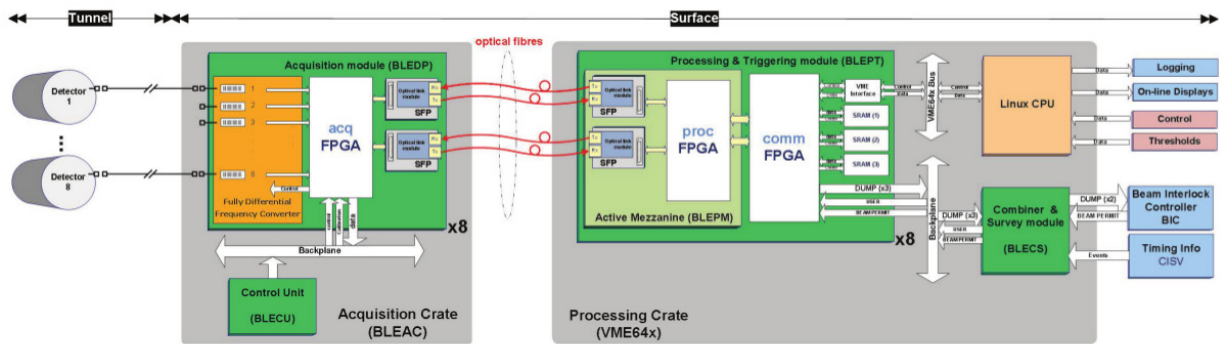


Fig. 6.1: Overview of the BLM system under development for the CERN injector complex. Beam Loss Electronics (BLE), Dual Polarity module (BLEDP), Acquisition Crate (BLEAC), Control Unit (BLECU),

Combiner and Survey module (BLECS), Processing and Triggering module (BLEPT), Processing Mezzanine (BLEPM), Beam Interlock Controller (BIC), Safe Machine Parameters Receiver (CISV), Small form-factor pluggable transceiver (SFP)

6.1.1 Acquisition electronics

The analogue acquisition electronics will be controlled by an FPGA, and will have the ability to automatically switch between two acquisition methods depending on the current seen at the input. For an input current in the range between 10 pA and 30 mA a fully differential current to frequency converter (FDFC) will be used, assisted by an analogue to digital converter (ADC) for fine interval sampling (see Fig. 6.2). Currents above 20.3 μ A will be measured via direct sampling by a second ADC.

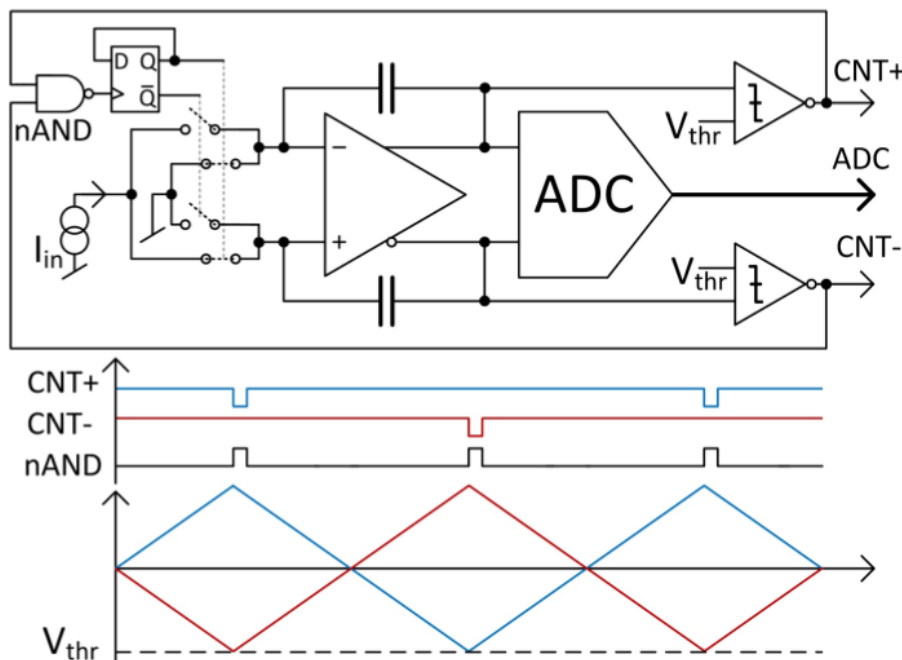


Fig. 6.2: Fully differential current to frequency converter

The principle of operation of the FDFC is as follows. The input current is directed to the positive or negative branch of the differential integrator by analogue switches. This charges the capacitor of the connected branch while at the same time discharging the capacitor of the opposite branch. Both branches are connected to analogue comparators that create a negative pulse as soon as the voltage reaches the threshold V_{thr} . The pulses from both comparators are combined by a NAND gate, which toggles a flip-flop, forcing a change of connection for the input current to the two branches [2]. By counting the number of times the input is switched the amount of input charge received within a given time can be calculated. The collected number of switches is read at regular intervals and the ADC is then used to provide the fractional part of the charge still remaining on the capacitor. Laboratory tests have shown that this system is capable of measurement over 10 orders of magnitude [3].

The acquisition crate will be able to host up to eight BLEDP modules, with each module digitizing the current from eight input channels in parallel. An FPGA device located on each BLEDP module is responsible for controlling the analogue circuitry, collecting the input data and transmitting them to the processing electronics through a point-to-point multi-gigabit optical link.

6.1.2 Processing electronics

The processing modules are hosted in Versa Module Eurocard bus (VME) crates together with the front-end computer and timing receiver modules. These processing modules are the standard Beam Instrumentation carrier board, the digital acquisition board (DAB)64x, fitted with an active mezzanine containing an FPGA device. The mezzanine also provides two small form-factor pluggable (SFP) transceiver connectors that can be used to provide a bi-directional multi-gigabit optical link or gigabit Ethernet.

The data received from the acquisition modules will be processed using FPGAs to provide an update of the losses measured for each of the channels every 2 μs . These values will then be used to create a summary for each channel for permanent logging and for operational displays. For assistance with more detailed analysis of loss mechanisms, the system will store shorter integrals in memory to allow the evolution of the losses over the cycle to be displayed.

The processing modules will also continuously update the losses observed in several integration windows for each channel. These will be checked against interlock threshold values for each window and provide an over-threshold signal when the threshold is exceeded. The over-threshold signals from all eight processing modules residing in one crate will propagate through backplane daisy-chain lines to the combiner module, which has a direct connection to the beam interlock system.

6.1.3 Installation and planning

A total of 32 BLM detectors have been installed and connected in the L2 straight section of each PSB period during LS1, and will be commissioned during 2015. A further 18 channels are foreseen for the new PSB injection region and will be ready for installation at Linac4 connection. The remaining part of the system, which includes 32 channels in the L3 straight section of each period and 28 channels in the ejection region, will be installed during LS2. A new type of detector, the flat ionization chamber (FIC), is currently being produced in collaboration with Institute of High Energy Physics (IHEP, Protvino, Russia) to address the space constraints of the L3 position. All other ionization chamber detectors are expected to be of LHC design.

For the PS ring it is proposed to replace the existing system with 100 new channels based on LHC ionization monitors using the electronics described above.

It is also planned to consolidate the transfer line BLM systems between the PSB and PS as well as those from the PS to the SPS with the same detectors and acquisition chain. A request for the necessary funding for this has been made to the consolidation project.

The SPS beam loss system is not expected to be upgraded before LS3 due to manpower constraints, and will therefore not form part of the LIU project.

6.2 Beam loss observation system

The request for observation systems to allow bunch-by-bunch, turn-by-turn loss evaluation will be fulfilled using diamond detectors. These detectors have a large dynamic range, a response time of a few nanoseconds and have demonstrated the possibility of measuring bunch-by-bunch losses on a turn-by-turn basis in the LHC. It is foreseen to install eight such detectors in the PSB injection region, up to 16 at various locations in the PS ring and two diamond detectors in the SPS extraction regions. The PSB and PS systems will provide analogue signals to Open Analogue Signal Information System (OASIS) to allow fast loss observations to be correlated with other machine events. Initial acquisition of the SPS monitors will be based on fast sampling oscilloscopes, with the aim of moving to an in-house solution by LS2.

6.3 New wire scanner system

To cope with increasing requirements in terms of accuracy and system reliability, and to deal with the much brighter beams foreseen after LIU completion, a new beam wire scanner is under design for the CERN accelerator complex. The ease of operation of these devices should also be improved to avoid the need to manually shift the dynamic range for different beam parameters. To overcome the limitations of the existing wire scanner systems [4] the design is based on a new concept. It eliminates the need for moving bellows by placing all of the moveable parts of the rotational scanner in the beam vacuum, and replaces the current shower acquisition detector, consisting of a scintillator attached to a photomultiplier, with a diamond-based sensor connected to high dynamic range acquisition electronics. The main system requirements are a wire speed of 20 m s^{-1} , a beam-width determination accuracy of $2 \mu\text{m}$ and a common design base for all fast wire scanners at CERN.

6.3.1 System design

The selected solution uses a permanent magnet rotor placed in the vacuum chamber and coupled to the stator through a wall of low magnetic permeability material. With this design, the use of bellows is no longer required, removing the related constraints of maximum acceleration and cycle lifetime. The rotor is fitted to a shaft supported by roller bearings coated with a vacuum-compatible solid lubricant. In addition to the rotor, the shaft holds all of the other moving parts located in the vacuum: the absolute angular position sensor for the motor's feedback control loop, the forks holding the thin wire and the disk for the optical incremental encoder used for accurate angular position determination (see Fig. 6.3).

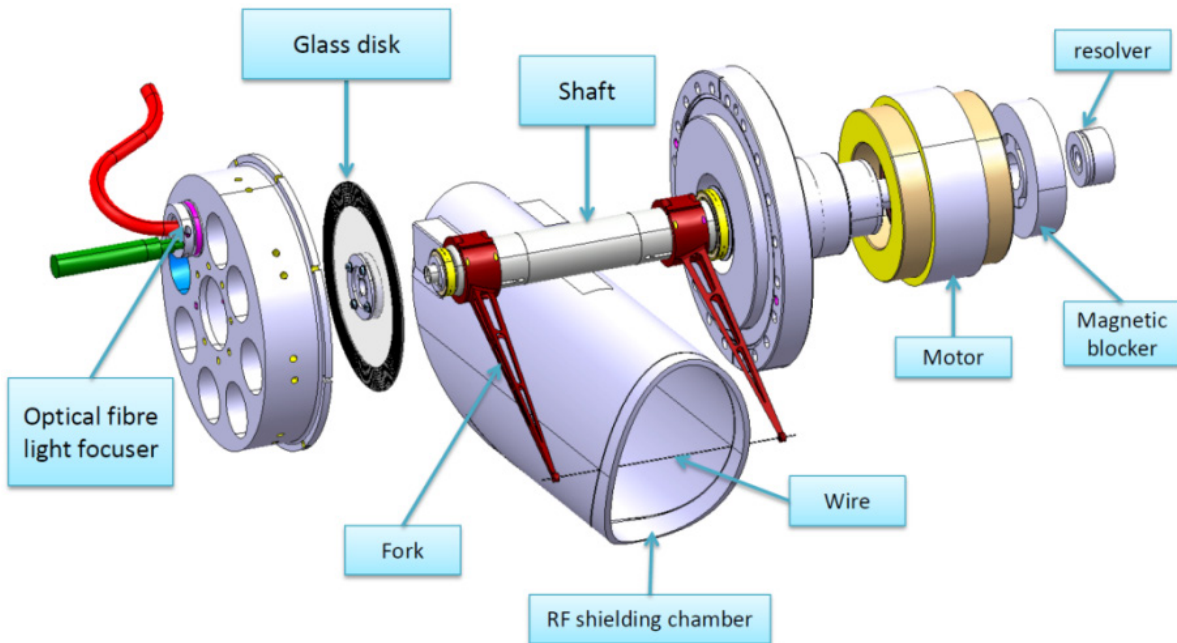


Fig. 6.3: Elements of the wire scanner located in the beam vacuum

6.3.2 Incremental optical angular sensor

The high-precision determination of angular position [5] is achieved using a principle similar to that used by a compact disk reader. A glass disk with a micrometre pattern of photo-lithographed chrome is placed inside the vacuum chamber and fixed to the scanner shaft. An optical single-mode fibre with associated feedthrough routes a laser beam onto a lens, which focuses the light onto the disc surface. The laser is coupled back into the same fibre using the reflective property of the chrome, meaning that only one fibre is required per measurement head. To increase the reliability of the system a second

measurement head samples the disk at a location 180° from the first. As the disk spins with the shaft the micrometre pattern on the chrome is detected, allowing an accurate measurement of the angular position. The laser emitters, splitters and receivers will be located in the surface building and only the optical fibre will make the link to the scanner system in the accelerator tunnel.

Reproducibility was determined by comparing the two angular position measurement systems after correction for the eccentricity of the optical disk pattern. Figure 6.4 shows the error (difference between the two sensors) as a function of the angular position and its distribution. For a typical wire scanner fork length of 10 cm this translates into a position reproducibility error of $1.07 \mu\text{m}$. The absolute accuracy is given by the photo-lithographic process and is of the same order as the reproducibility uncertainty.

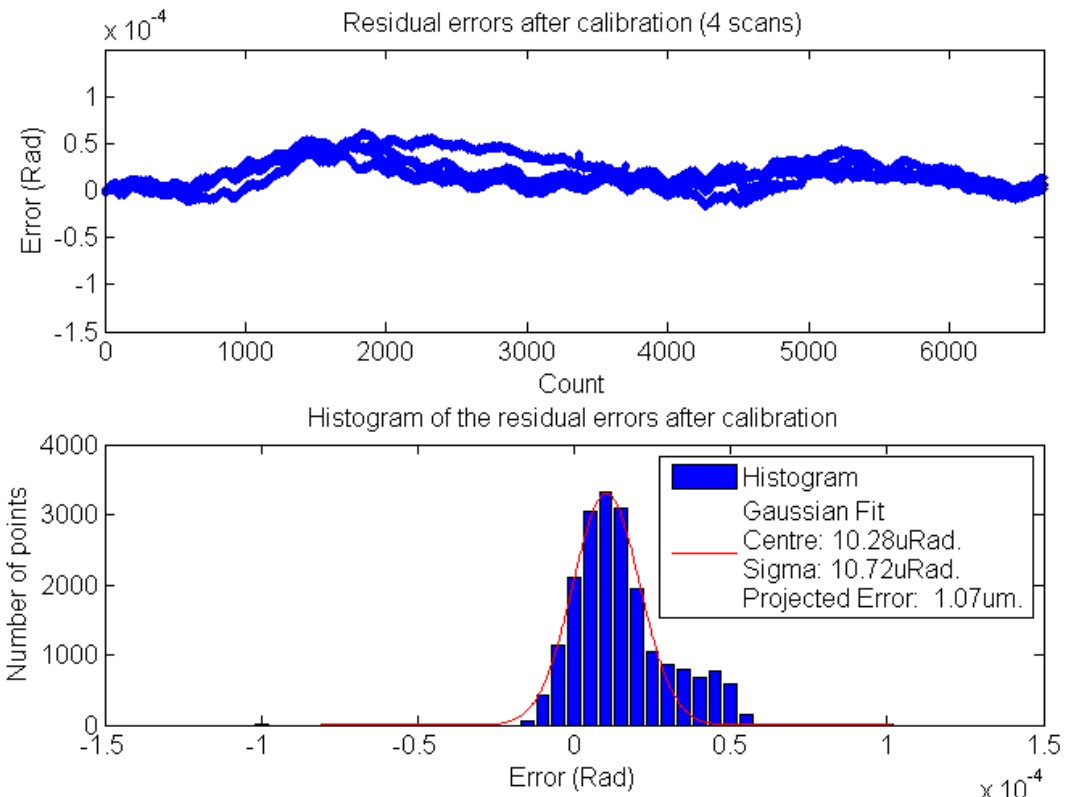


Fig. 6.4: Reproducibility measurements of the optical disk based incremental angular position sensor. Top: difference between two sensors versus the disk pattern count for one full rotation. Bottom: distribution of the reproducibility error.

6.3.3 Control and acquisition electronics

The main guideline for the topology concept of the system is defined by the design rules for high-reliability systems.

- Minimization of complexity. Achieved by limiting the electrical connections and number of sub-systems, while avoiding channel multiplexing, to have a continuous connection between the drive and scanner.
- Separation of critical and non-critical functions. Accomplished by integrating the safety functions directly inside the hardware of every instrument, with the higher-level software only taking care of setting-up, triggering, analysing and recording measurements.
- Integration of early failure detection. These features are integrated inside the system's intelligent drive, constantly monitoring the condition of the hardware.

Figure 6.5 shows the global architecture of the new beam wire scanner, illustrating how the electronics is separated into two distinct parts comprising the intelligent three-phase Pulse-Width Modulated (PWM) drive, and the acquisition and supervision modules.

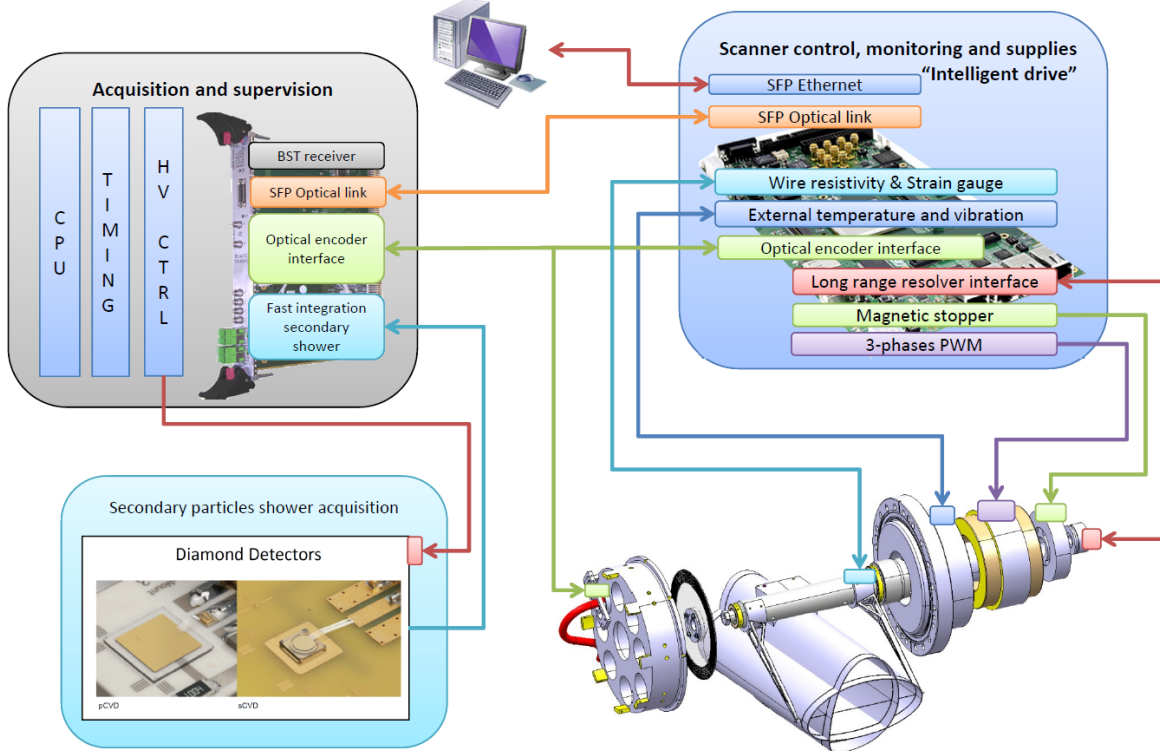


Fig. 6.5: Topology of the new beam wire-scanner system

The intelligent drive electronics contains all of the functions critical for maintaining instrument integrity. It will be constructed as a fully customized box that directly connects the different parts of the scanner such as the resolver and optical encoder, the motor and the wire, as well as the early failure detection and safety systems [6]. The intelligent drive avoids active electronics in the tunnel areas in order to ease design, increase reliability and simplify preventive and corrective maintenance. Copper cables, some up to 250 m in length, will therefore be required, with the effect of any electromagnetic interference being studied.

The acquisition and supervision electronics are responsible for receiving information from various external systems, triggering measurements, taking data and making this data available to external clients for visualization and long-term storage.

The existing secondary shower detection system, based on a scintillator connected to a photomultiplier, covers the large dynamic range required by a combination of optical filter and photomultiplier gain settings. However, for a given setting the available range is very small, often making it difficult to operate. It is therefore proposed to replace this system with a detection system based on diamond detectors. In order to make use of the inherent high dynamic range of the diamond detector a new, radiation-hard front-end electronics system capable of bunch-by-bunch measurements at 40 MHz needs to be developed. It is currently foreseen that this will be based on one of two Application-Specific Integrated Circuit ASICs being tested for the LHC experimental upgrade: the QIE10 chip (a 17-bit dynamic range charge integrator and encoder developed by the Compact Muon Solenoid (CMS) collaboration or the so-called 'ICECAL' chip, a low-noise analogue gated integrator with 12-bit dynamic range developed by the LHCbeauty (LHCb) collaboration. This electronics system would be located in the tunnel near the detector. It would transmit its data to the acquisition

and supervision electronics on the surface via a radiation-hard optical link, using a high-speed serializer and deserializer chip (GBT - GigaBit Transceiver) and the Versatile link Transmitter/Receiver (VTRx), both under development for the upgrade of LHC experiments. In this way it is hoped that a much larger dynamic range will be covered for a given front-end setting, making the system easier to operate while also eliminating the need for long signal cables.

6.3.4 Planning

The new wire scanner project has three main subtasks, namely the design and production of the mechanical system, the control electronics and the acquisition electronics.

The mechanical design for a prototype system is nearly complete, with the tank to house the mechanism installed in the SPS during LS1. A laboratory mechanism is already available and will be used to qualify the design using laboratory electronics before the end of 2014. A second mechanism will be built for installation in the SPS during the 2014 end-of-year technical stop.

The main system control algorithms will be tested on the prototype mechanism by the end of 2014. It is then aimed to have a prototype intelligent drive ready for installation and beam testing in the SPS during 2015.

The acquisition electronics for the diamond detector will be prototyped in the SPS in 2014, and it is foreseen that a final design will be started in 2015.

It should be possible to achieve a fully common design for the SPS and PS systems, while modifications will be required in order to fit such a system into the tight space constraints given by the PS Booster. The initial integration study for the PS Booster will start in 2014.

The current baseline, provided sufficient resources are made available, is to install all of the new scanners into the injectors during LS2. This comprises one horizontal and vertical scanner per ring in the PS Booster, two horizontal and vertical scanners in the PS, and two horizontal and vertical scanners in the SPS. The main outstanding issue is the effect of the wire and mechanism on the beam in terms of impedance and, vice versa, the effect of RF heating upon the wire due to the beam. Several possibilities for impedance reduction are currently under study.

6.4 DC beam current transformers

The ring Direct-Current (DC) beam current transformer (BCT) systems (PSB, Low Energy Ion Ring (LEIR) and PS) will be upgraded with new electronics derived from the LHC DC Current Transformer (DCCT) system. The analogue part will be installed in the technical stop during week 51, 2014 to replace the original electronics, which was installed in 1993. The front-end electronics has been standardized across the three accelerators, while digital acquisition has been upgraded from the obsolete 12-bit MPV908 to the 16-bit VD80, with the associated new front-end software, in time for the 2014 start-up with beam. Modification of the β normalization (2 GeV plus new B train) is under study. Once this upgrade is complete the new system is expected to fully comply with the specifications defined in [7].

Figures

6.1. Overview of the BLM system under development for the CERN injector complex.....	593
6.2. Fully differential current to frequency converter.....	594
6.3. Elements of the wire scanner located in the beam vacuum	596

6.4. Reproducibility measurements of the optical disk based incremental angular position sensor. (a) Difference between two sensors versus the disk pattern count for one full rotation.	
(b) Distribution of the reproducibility error.....	597
6.5. Topology of the new beam wire scanner system.....	598

References

- [1] C. Zamantzas, M. Alsdorf, B. Dehning, S. Jackson, M. Kwiatkowski and W. Vigano, System architecture for measuring and monitoring beam losses in the injector complex at CERN, Proc. IBIC2012. Tsukuba, Japan, (2012), TUPA09, <http://jacow.org/>.
- [2] W. Vigano, B. Dehning, E. Effinger, G. Venturini and C. Zamantzas, Comparison of three different concepts of high dynamic range and dependability optimised current measurement digitisers for beam loss systems, Proc. IBIC2012, Tsukuba, Japan, (2012), MOPA09, <http://jacow.org/>.
- [3] W. Vigano, B. Dehning, E. Effinger, G. Venturini, M. Kwiatkowski and C. Zamantzas, 10 orders of magnitude current measurement digitizer for the CERN beam loss system, CERN-ACC-2014-0001, 2014.
- [4] G. Baud, B. Dehning, J. Emery, J-J. Gras, A. Guerrero and E. Piselli, Performance assessment of wire-scanners at CERN, IBIC2014, Oxford, UK, (2014), TUPF03, <http://jacow.org/>.
- [5] J. Sirvent Blasco, Masters thesis, UMH, Elche, Alicante, Spain, 2012
<https://cds.cern.ch/record/1491608/files/CERN-THESIS-2012-159.pdf>
- [6] J. Emery, Beam scanner control, monitoring and supplies part, engineering specification, CERN EDMS No1318827.
- [7] J.-J Gras *et al.*, Functional specifications for beam intensity measurements as part of the LHC injectors upgrade project (2012) <https://edms.cern.ch/file/1233006/1.0/LIU-Intensity-Specs-V1.0.docx>.

Chapter 7

Commissioning and Optimization

7.1 General considerations

The objective of the LHC Injectors Upgrade (LIU) project is to deliver beams with adequate characteristics for reaching the goal of the High Luminosity LHC (HL-LHC) project (see Chapters 1 and 2). The actions foreseen in the context of the LIU consist of installing new equipment, renovating/upgrading existing equipment and implementing new schemes of beam production. Most tasks will take place during the next long LHC shutdown period, Long Shutdown 2 (LS2). They can be divided into two main categories:

- operation-critical;
- non-critical.

The operation-critical modifications concern systems that have to perform according to specification in order to be able to produce operational beams as at present, requiring a full commissioning before beam delivery for physics can start. The non-critical modifications can be fully commissioned at a later stage when the ‘basic’ machine is operational, e.g. during parallel or, if necessary, dedicated machine development sessions. It is essential that the equipment affected by the non-critical modifications does not degrade beam performance of the ‘basic’ machine. Prior to commissioning a complete list will be drawn up attributing each modification to one of the two categories.

The commissioning of each piece of equipment and every process will take place in a well-organized and staged manner according to detailed planning with clear hand-over milestones. The following successive phases can be distinguished, which generally require the full availability of general services such as electricity, cooling water and ventilation:

- training of the operations team;
- hardware commissioning;
- dry runs;
- commissioning with beam;
- validation up to former operational beam characteristics;
- study and optimization up to the LIU goals in terms of beam characteristics (see Chapter 1 and 2).

These phases are described in the following sections.

7.1.1 Training

Although members of the operations team are frequently involved in the tasks of the equipment groups, formal training on the new or upgraded systems and processes is required to ensure efficient and safe exploitation. This training will be given by specialists during dedicated training sessions towards the end of the long shutdown period, during which the upgrade will take place. Detailed planning of these training sessions has to be set up in due time.

7.1.2 Hardware commissioning

For the hardware commissioning phase it is assumed that all equipment is fully installed and connected, in the tunnel and in the equipment rooms. It is also assumed that general services, such as electricity, cooling water and ventilation, are fully operational. Hardware commissioning, which will take place in the last part of the long shutdown, has the aim of checking that equipment is functional and properly interconnected. The absence of beam during this period will allow relatively easy access to the tunnel if interventions are required. These tests, where applicable, will cover:

- electrical connections (quality, heating, etc.);
- equipment cooling (hydraulic pressure, flow, etc.);
- equipment heating when powered at specified rms power (thermography);
- verification of polarity (connections, magnetic field, etc.);
- signal transmission;
- failure scenarios (actions following interlocks, etc.).

These tests will be done locally and will not rely on the full availability of controls and timing system, as in this phase of commissioning they might not yet be fully operational.

The responsibility for hardware commissioning lies with the equipment specialists. The coordination of hardware tests, however, will be ensured by the machine technical coordinator. Each piece of equipment for which hardware commissioning has been completed and validated by the equipment specialists will be declared as being available for dry runs.

7.1.3 Dry runs

For this phase, the entire infrastructure including controls and timing system has to be operational, and all equipment and application software has to be available. The aim of the dry run is to test and validate entire equipment chains and processes without having beam in the machine; nonetheless this involves all controls and diagnostics.

Responsibility for dry runs lies with the operations team, which will need close collaboration with the equipment specialists and members of the controls group. Each piece of equipment or process that has passed the dry run, perhaps after several iterations, will be declared available for commissioning with beam.

7.1.4 Commissioning with beam

Once the dry-run phase has been completed the theoretical settings will be loaded for each piece of equipment and/or process, after which a beam with reduced intensity and beam size (e.g. a pencil beam) will be used to commission the machine. Correct functioning of the diagnostics systems will play a vital role in the optimization of settings, hence in obtaining the required beam performance.

As mentioned above, the operation-critical systems and processes will need to be commissioned with beam from the start (i.e. upgraded injection). The non-critical systems and processes, however, can be commissioned at a later stage, possibly during parallel or dedicated machine development sessions (e.g. longitudinal damper).

The responsibility for commissioning with beam lies with the operations team in close collaboration with machine supervisors, beam physicists and equipment specialists.

7.1.5 Validation

The operational commissioning process ends with the validation phase, where the goal is to reach and possibly exceed the beam characteristics available before the shutdown. Each piece of equipment and process for which the required performance has been reached will be officially declared operational.

7.1.6 Optimization

The LIU goals in terms of beam characteristics are, by definition, in unknown territory. Reaching them will require fine optimization and extensive beam physics studies in all of the accelerators. Progress in performance has to propagate along the cascade of accelerators, from the lowest up to the highest energies. In other terms, the Super Proton Synchrotron (SPS) will only be confronted with the most challenging beams once Linac4, Proton Synchrotron Booster (PSB) and Proton Synchrotron (PS) have reached their own LIU goals.

If the desired performance cannot be obtained it should be clarified whether this is related to a technical or a beam physics limitation requiring more profound studies. Time may be needed during shutdowns and/or technical stops to modify installed equipment.

7.2 PSB

7.2.1 Scope

The main modifications taking place in the PSB during LS2 are listed in Table 7.1. They are meant for:

- charge exchange injection of the Linac4 beam at 160 MeV kinetic, with the possibility of painting in the horizontal and longitudinal phase planes;
- bringing the transfer energy to the PS up to 2 GeV kinetic energy;
- increasing the accelerated beam intensity by a factor of up to 2.

Table 7.1: Main modifications to the PSB during LS2, with estimated hardware commissioning durations

Upgrade activity	Hardware commissioning and dry runs (months)
Replacement of all equipment in the injection region	3 (maximum)
Replacement of the power supply for the main magnets	11.5 (independent)
Upgrade or replacement of ejection/recombination/transfer equipment	5
Upgrade/replacement of RF systems	5
Upgrade of old instrumentation and installation of new-beam instrumentation	3 (maximum)

7.2.2 Preparation phase before LS2

According to current planning, Linac4 will have reached the nominal beam energy of 160 MeV by the end of 2015, and it will be subject to a reliability run during most of 2016.

The opportunity of having the 160 MeV H⁻ beam available will allow testing of as much of the PSB injection equipment as possible. For that purpose, half of a PSB injection section will be installed at the end of 2015 in the Linac4-to-PSB transfer line, and tested with beam during the first half of 2016 (half-sector test). That will allow gaining of valuable experience with the new hardware,

controls, application software and, in general, with the new injection principle. This phase will help correct potential design flaws and accelerate the setting-up of the PSB at the end of LS2.

7.2.3 Hardware commissioning and dry runs following LS2

During hardware commissioning the equipment experts have to check in detail the newly installed equipment, as well as all existing equipment under their responsibility. In particular, the cable removal and cable installation campaign, as well as the numerous installation activities inside the tunnel and in the equipment galleries, justify this precaution. The hardware commissioning period follows the installation phase and is individually timed for each piece of equipment. Testing should proceed as soon as all the boundary conditions are fulfilled, i.e. when the equipment is cabled and ready to be powered and controlled, vacuum and cooling, etc. are available if needed, and the different testing steps are permitted by machine/access conditions. One major lesson from the Spallation Neutron Source (SNS) ring commissioning was that the equipment set the pace for the overall duration of the commissioning phase

Dry runs will be organized as soon as equipment becomes available. An essential prerequisite is for the control infrastructure to be in an operational state with all applications ready and tested from the CERN Control Center (CCC).

7.2.4 Beam commissioning up to validation

After the successful completion of dry runs on all systems (Radio Frequency (RF), beam instrumentation, power supplies, etc.), beam commissioning will begin, provided that the following additional conditions are met:

- the Linac4 beam is fully characterized in the transverse emittance measurements beam line (called LBE line) and the requested commissioning beam is ready;
- correct operation of Linac4 pre-chopper and chopper as main actors for the beam interlock system, to avoid beam being sent to head- and tail dumps of the distributor, as well as losses during distributor kicker switching between rings, and finally to provide an adequate beam structure for injection into the PSB;
- the Linac4 beam synchronized with all PSB injection systems (distributor, vertical septum, beam instrumentation, magnets, chicane and painting bump, PSB RF, etc.);
- magnets' polarity checked (quadrupoles and corrector magnets in the BI line);
- beam interlock system validated;
- new magnetic cycle prepared;
- extensive support from equipment and controls specialists, especially during the first phase of beam commissioning;
- availability of optics models for the injection region and the PSB rings with extensive support from beam physicists present in the control centre (optics checks, injection process, re-matching of the injection line, issues with orbit closure, etc.).

A very-low-intensity beam from Linac4 of $0.5 \mu\text{s}$ length should be used first, with the software interlock system (SIS) in place to guarantee the intensity limit. This beam will be injected successively into the four rings, and it will serve to check/calibrate beam interlock and test injection systems with their beam instrumentation. This phase is expected to take 1 to 2 weeks.

Once beam has been centred on H^0/H^- dumps and with all ring equipment available (especially RF and beam instrumentation) the setting-up will continue with preliminary adjustment of trajectories/orbit and transverse tunes in the PSB. When the beam will circulate for $\sim 10\text{--}20$ turns with

an orbit around $\sim\pm 5$ mm, the RF will be switched on and RF adjustment will begin. Tune measurement will then be possible, allowing refinement of the working point and adjustment of injection bumper magnets (BSW) and injection kicker magnets (KSW) bump closure to minimize injection oscillations. It is estimated that 4 weeks will be necessary to complete this work programme.

The next step will be to adjust beta-beating compensation, measure transverse emittances and check apertures in all rings. Commissioning of the matching monitor will begin. The duration of this phase is estimated to be 1 week.

Acceleration up to 2 GeV will then be set up, involving completely new main power supply (MPS) and high-power RF equipment. All RF loops have to be functional as well as synchronization of ejection timings to the external dump. Resonance compensation will be necessary, starting with pre-loaded functions for the multipole correctors. The energy of the different rings will be equalized using the length-integrated trim field (Bdl) power supplies. After adjustment of extraction and recombination systems, aperture scans will be performed at the septa location. This phase will take 3 weeks.

Preparation of the LHCprobe beam will be the logical next step, both because it is of a low intensity ($5 \cdot 10^9$ p) and because it is probably the first beam required by the downstream machines. Properly working beam instrumentation and fine control of RF and magnetic elements will be essential for tailoring intensity and emittances in all phase planes. A total of 3 days should be sufficient for achieving the LHCprobe nominal parameters and adjusting the PSB to PS (BTP) beam line to make it available to the PS.

The setting-up of the multiple operational beams will then take place (STFPRO, LHC production beams, ISOLDE, AD, etc.) [1] by progressively increasing the injected beam intensity and optimizing painting at injection and, in general, the adjustments in all phase planes. If given the highest priority, the LHC production beam could be available after two more weeks. Afterwards, it will take three more months to adjust the multiple operational beams in parallel with the delivery of beams to the PS and to make the PSB work reliably according to its specifications. Requirements on beam instrumentation are especially stringent from the very beginning of that phase.

7.2.5 Summary of beam commissioning planning

The different beam commissioning and validation phases and their respective durations are summarized in Table 7.2. No contingency is included for dealing with unplanned difficulties (e.g. foil breakage, etc.).

Table 7.2: Successive beam commissioning and validation phases and their estimated durations

Milestone	Phase	Duration [weeks]
	First injections	2
	First turn and closed orbit	4
	Optics and aperture	1
	Accelerate and extract	3
	Produce the LHCprobe beam	0.5
Availability of LHCprobe beam		10.5
	Setting-up of LHC production beam	2
Availability of LHC production beam with pre-LS2 beam characteristics		12.5
	Setting-up of other operational beams in parallel with delivery of beam to the PS	13
Validation of all operational beams at pre-LS2 performance level		25.5

Approximately 10.5 weeks of beam commissioning are needed before delivering the first beam (LHCprobe) to the PS. If absolutely necessary, a low-intensity/higher emittance beam could be delivered earlier to the PS (after ~6 weeks), by preparing ring 3 alone. The completion of beam commissioning of the other rings in parallel with the regular delivery of beam to the PS would, however, require four more weeks. In any case, the total time required with beam until the pre-LS2 beam characteristics are available for all operational beams adds up to ~6 months.

7.2.6 Optimization

Many machine development (MD) sessions will be needed for checking how far the beam characteristics can be improved, understanding potential new limitations and finding means to circumvent them. Additional methods like longitudinal painting will be tested and optimized in view of reaching the LIU goals in terms of beam characteristics from the PSB.

This phase will take place in parallel with the physics run. Its successful completion will only be possible if adequate MD time is made available and if all equipment in Linac4, transfer lines and PSB are reliably working according to their specifications. Beam instrumentation, in particular, should be fully operational from the beginning. The duration will depend on the amount of allocated beam time and on the availability of adequate specialists.

7.3 PS

7.3.1 Scope

Although some of the PS upgrades are implemented during LS1, the main and most critical ones will be done during LS2. This is summarized in Table 7.3.

The main performance improving changes after LS2 will be:

- the increase of the injection energy into the PS up to 2 GeV kinetic;
- the reduced beam loading effects on RF cavities and the increased RF voltages at 40 MHz and 80 MHz.

Table 7.3: Overview of the equipment and processes concerned by the upgrade

Item	Commissioning	Criticality
Beam production scheme (BCMS)	After LS1	Non-critical
Resonance compensation	After LS1	Non-critical
Transverse damper	After LS1	Non-critical
Longitudinal damper	After LS1	Non critical
Working point control	After LS1	Non critical
Injection energy	After LS2	Operation-critical
Low-energy correctors	After LS2	Operation-critical
Internal dump	After LS2	Operation-critical

The other upgrades (low-energy correctors, internal dump, etc.) will improve safety, ease of operation and reliability.

7.3.2 Preparation before LS2

The batch compression, merging and splittings (BCMS) scheme, which was only demonstrated during test periods at the end of run 1, will have to be set up for reliable operation at high luminosity with 25 ns bunch spacing in the LHC during run 2.

The equipment installed during LS1 will be tested during machine development sessions and progressively put into operation during run 2.

Combined with an improved modelling and control of the working point using the pole face windings, the compensation of resonances permitted by the new sextupoles will help handle beams with large space charge-induced tune shift. That should improve performance of operational high-intensity beams (e.g. Antiproton Decelerator (AD), neutrino Time-of-Flight (nToF)) as well as accelerate setting-up after LS2 with the higher brightness beams from the PSB.

Once equipped with the required amplifiers and low-level RF, testing of a new longitudinal damping system will start at the beginning of 2015. Before the beginning of LS2 it should be operational, suppressing longitudinal coupled bunch instabilities, improving the quality of beam gymnastics and reproducibility of beam characteristics, especially for the LHC.

7.3.3 Hardware commissioning and dry runs following LS2

The injection energy increase from 1.4 GeV to 2 GeV kinetic will be obtained with upgraded or new equipment that requires dedicated and extensive commissioning before the first beam.

The renovated power converters of the low-energy correctors should be exercised and demonstrate adequate and with identical rise times.

The upgraded RF systems should be conditioned up to their new and higher nominal voltages.

The upgraded and newly installed diagnostics for injection will also require commissioning.

7.3.4 Beam commissioning up to validation

After the successful completion of dry runs on all systems, beam commissioning will begin. The estimated duration of the successive phases is given in Table 7.4.

Table 7.4: Successive beam commissioning and validation phases and their estimated durations

Milestone	Phase	Duration (weeks)
	First injections, closed orbit at low energy	1.5
	Optics and aperture	1
	Setting up of RF, Accelerate and extract ^a	3
	Produce the LHCprobe beam	0.5
Availability of LHCprobe beam		6
	Additional time for setting-up of LHC production beam	2
Availability of LHC production beam with pre-LS2 beam characteristics		8
	Setting-up of other operational beams in parallel with delivery of LHC-type beam to the SPS	4
Validation of all operational beams at pre-LS2 performance level		12

^a The mentioned re-commissioning times assume restarting with the existing RF low-level beam control and a possible fast switching between the current and new beam controls. If this is not the case an additional 4 to 5 weeks will have to be added to the re-commissioning.

7.3.5 Optimization

Machine development sessions, parallel and dedicated, will be required following the initial commissioning of the LHC beams (as mentioned in Table 7.4) in order to explore the parameter space, not only for the LHC beams, but also for the other non-LHC physics beams, such as for SPS fixed target, nTOF, East Area and AD. These MD sessions rely on good performance of the different beam diagnostics systems and the availability of sufficient trained staff to run the MD sessions, with support from the OP group.

7.4 SPS

The following tasks, which must be completed during LS2, will have a major impact on the LS2 schedule:

- 200 MHz RF upgrade;
- aC-coating of six sectors;
- implementation of an external beam dump and replacement of the internal one.

Many other systems are also being upgraded and the re-commissioning with beam will be extremely challenging in view of the need to deliver beam immediately to the LHC for luminosity production. The end of the injector upgrade work in LS2 will therefore require a very well-organized and complete set of commissioning tests to prepare for nominal operation with beam, the scope of which will include individual system tests and powering, control system integration tests, dry runs from the CCC, machine cold check out and beam commissioning.

The main boundary conditions are the length and timing of LS2, set at 18 months from Q3 2018 onwards, the scope of the work to be done (summarized below), and the planning for the beams to be delivered to the LHC. Clearly, manpower and experts' availability for the commissioning phases is also a key factor but this will not be discussed here, under the assumption that the CERN groups involved take the necessary steps to ensure that adequate qualified support is available.

In the following sections the scope of the LS2 work in the SPS is recalled, and the main commissioning steps outlined, together with the presently estimated durations and known dependencies. The expected performance evolution after LS2 is also described, in terms of reasonable assumptions on the available beam characteristics, together with a proposed overall strategy for the commissioning of the full LIU beams.

7.4.1 Scope

For the LIU project, the main SPS upgrades implemented during LS2 are listed in Table 7.5, together with the estimated time for hardware commissioning/dry runs. Note that these preliminary estimates do not take into account any co-activities.

Table 7.5: Main SPS upgrade items in LS2, with estimated commissioning time

Upgrade activity	Hardware commissioning and dry runs (months)
200 MHz RF system (high power and low-level)	6.5
Amorphous Carbon (aC) coating of six sectors	12 (tbc)
Improve ZS pumping and impedance	1
Reduce the impedance of kickers	2
Upgrade the extraction protection system	1
Install new external high-energy beam dump	3
Exchange internal beam dump (TIDVG) core	2
Add a new wide-band transverse damper	3
Renew/improve beam instrumentation	3
Improve vacuum sectorization of the arcs	1
Upgrade the injection damper for ions	3
New injection system with 100 ns rise-time kicker for ions	4

The tunnel work on the 200 MHz RF systems during LS2 involves 6 months of cavity rearrangement in LSS3: 18 existing cavity sections with their services have to be displaced and re-installed, two new cavity sections will be added, as well as six new couplers.

Electron cloud is one of the major limiting factors for 25 ns beam operation. One promising suppression technique consists of coating vacuum chambers with a thin film of amorphous carbon. Over the years a technology was developed for treating the chambers in the magnets without the need for dismantling. Nevertheless, this has to be done in a special workshop on the surface. After LS1, four SPS half-cells will be coated and their performance will be evaluated with beam. The aim for LS2 will be to coat 90% of the SPS: more than 700 dipoles, the main quadrupoles, long straight sections, pumping port shields and perhaps the short straight sections as well. A first plan for magnet flow between tunnel and surface workshop has been presented. The maximum estimated flow consists of six magnets in and six magnets out per day, yielding 12 months in total, including commissioning for this activity.

A new external beam dump will have to be installed. Although the definitive solution will only be defined at the end of 2014, it will in any case necessitate underground civil engineering, and completing this task during LS2 will be challenging.

Among the many other activities, a major one is the modification of the injection system to reduce the injection kicker rise-time to 100 ns for ions.

7.4.2 Preparation before LS2

Several systems will have already been installed or upgraded and commissioned before LS2, including the transverse damper and the 800 MHz RF system with new high-power and low-level RF systems.

The 200 MHz upgrade activity has already started, and the new building will be handed over at the end of 2015. The amplifiers will be installed inside and tested on dummy loads before the beginning of LS2.

7.4.3 Hardware commissioning and dry runs following LS2

The time required for hardware commissioning and dry runs of the newly installed equipment is given in Table 7.5.

A total of 6.5 months will be necessary for commissioning the 200 MHz RF systems immediately after installation. From the logistics point of view, transport through LSS3 will be prohibited for a total of 12.5 months.

Commissioning of the new injection system for ions will be the next most time-consuming (4 months) activity.

7.4.4 Beam commissioning up to validation

According to this analysis, 16.5 months will be necessary for the SPS to be ready to receive beam from the PS. Beam commissioning will be very challenging due to the modified RF hardware combined with a new RF beam control, therefore a minimum of 1.5 months have to be reserved. Depending on the electron cloud situation in the SPS and the required vacuum conditioning (the machine will have been at atmosphere over many months), it is expected that at least another 1.5 months have to be added to be ready to send the current nominal LHC production beam to the LHC (1.15×10^{11} p+/bunch at 25 ns, around 2.5 μm transverse emittance). This is summarized in Table 7.6.

Table 7.6: Successive beam commissioning and validation phases and their estimated durations

Milestone	Phase	Duration (months)
	Injection and acceleration of low-intensity beam	1.5
Availability of LHCprobe beam		1.5
	Setting-up of LHC production beam (including vacuum conditioning)	1.5
Availability of LHC production beam with pre-LS2 beam characteristics		3
	Setting up of RF, Accelerate and setting-up of other operational beams in parallel with delivery of beam to the LHC ^a	2
Validation of all operational beams at pre-LS2 performance level		5

^aThe availability of the new external and internal beam dumps will be essential for proceeding as quickly as possible with the setting-up of these other beams.

7.4.5 Optimization

The commissioning of the final HL-LHC beams with double the brightness is expected to take around two years of parallel machine development and dedicated tests. Many new systems and functionalities must be commissioned across the complex, including a completely new type of injection in the PSB (160 MeV H⁺) with brand-new hardware, and it is expected that much of run 3 will be needed to learn how to operate and optimize the adjustment of the newly installed equipment and to routinely produce the new beams.

The necessary studies and machine development can tentatively be scheduled as follows:

- a. One day per week until the end of 2020: establish high-intensity 25 ns (2.5×10^{11} p+/bunch) beam with few bunches, working on the following subjects:
 - damper;
 - longitudinal transfer;
 - longitudinal stability;
 - transverse stability;
 - beam losses;
 - instrumentation;
 - beam characterization.
- b. One day per week during 2021: establish high-intensity 25 ns (2.5×10^{11} p+/bunch) beam with 72–288 bunches, working on the following subjects:
 - longitudinal transfer;
 - electron cloud;
 - longitudinal stability;
 - transverse stability;
 - beam losses;
 - instrumentation;
 - beam characterization;
 - conditioning of beam dumps.

Clearly, many details remain to be worked out, including the time-sharing between machines and the exact order of the different steps, as well as the split with physics beams. However, it is clear that significant dedicated commissioning time will need to be planned across the injector complex throughout 2020 and 2021 at least, with the likelihood of continuing in 2022 and even of having more dedicated blocks during 2023 when the LHC is scheduled to be off for LS3. It should be noted that, in addition to the proton beam, ion beams and associated equipment also need commissioning, including the slip-stacking in the SPS and the new faster rise-time ion injection system.

If this commissioning strategy is adopted, and assuming 12 h per week can be dedicated to LIU beam commissioning through 2020 and 2021, then a total of about 18 days per year integrated commissioning time would be available. This is not particularly long, given the number of upgrades made in all of the machines and the ambitious beam performance target, and it may be that more dedicated time will need to be made available. A few, longer, 3–4 day periods may be useful and should be planned in, probably to coincide with LHC technical stops—the need for any extra dedicated time can be judged during 2020, and should possibly already be planned as a review or

checkpoint midway through 2020, when progress can be examined and the strategy adjusted if required. Clearly, to ensure that these important beam time requests are met will need a general and high-level agreement on beam time sharing between LIU beam commissioning, other SPS MD and the SPS physics programme.

7.5 Integrated planning

The analysis given above of the estimated time required for recovering pre-LS2 performance from the different accelerators of the injector complex is summarized in Table 7.7. The main conclusion is that, to fit within the allocated slot of 18 months of beam stop in the LHC, beam commissioning in the PSB, PS and SPS have to begin after no more than 12.5, 15 and 16.5 months, respectively. A first estimate prepared for the Review of LHC and Injectors Upgrade Plans [2] in October 2013 showed that this will not be easy, especially in the PSB, where an extensive amount of cabling work is on the critical path. A detailed schedule remains to be prepared, making optimum use of the access time during the machine stops before LS2, and taking properly into account all of the activities (e.g. SPS external dump and 100 ns rise-time kickers).

Table 7.7: Preliminary estimates of shutdown time required for the LHC injectors during LS2 [2]

	Month																					
	1		//	13		14		15		16		17		18		19		20				
	1	2	//	1	2	1	2	1	2	1	2	1	2	1	2	1	2	1	2			
	LS2 start End of beams in LHC			Start of Beam commissioning in injectors												Start of Beam commissioning in LHC						
PSB	PSB LS2 works (Linac4 connection + 2 GeV upgrade)			Beam commissioning LHCprobe				LHC PRO D														
PS	PS LS2 works (2 GeV injection + RF upgrades etc.)						Beam commissioning LHCprobe		LHC PRO D													
SPS	SPS LS2 works (200 MHz high-power RF upgrade + aC coating + external beam dump + 100 ns rise-time injection kickers for ions)									Beam commissioning LHCprobe		LHCprod (with scrubbing)										
LHC	LHC LS2 works													Beam commissioning								

Tables

7.1.	Main modifications to the PSB during LS2, with estimated hardware commissioning durations	603
7.2.	Successive beam commissioning and validation phases and their estimated durations	606
7.3.	Overview of the equipment and processes concerned by the upgrade	607
7.4.	Successive beam commissioning and validation phases and their estimated durations	608
7.5.	Main SPS upgrade items in LS2, with estimated commissioning time	609
7.6.	Successive beam commissioning and validation phases and their estimated durations	610
7.7.	Preliminary estimates of shutdown time required for the LHC injectors during LS2 [2] .	612

References

- [1] B. Mikulec, PSB beam parameter summary table 2011, EDMS 1167797, 2011.
- [2] B. Mikulec *et al.*, Work effort in the LHC injector complex for the upgrade scenarios, Proc. RLIUP, Archamps, 2013,
<https://indico.cern.ch/event/260492/session/2/contribution/13/material/paper/1.pdf>



LHC Injectors Upgrade



CERN-ACC-2014-0337 - 15 / 12 / 2014